AusIMM

CSIRO

PERTH, AUSTRALIA AND ONLINE
8-10 NOVEMBER 2021

IRON ORE CONFERENCE 2021

Conference Proceedings

PRIMETALS TECHNOLOGIES

IRON ORE CONFERENCE 2021

Sustainability in a Changing World

8–10 NOVEMBER 2021
PERTH, AUSTRALIA

The Australasian Institute of Mining and Metallurgy
Publication Series No 6/2021

Published by:
The Australasian Institute of Mining and Metallurgy
Ground Floor, 204 Lygon Street, Carlton Victoria 3053, Australia

All papers published in this volume were peer reviewed before publication.

ISBN 978-1-922395-01-6

ORGANISING COMMITTEE

Ralph Holmes HonFAusIMM(CP)
Conference Organising Committee Chair

Erick Ramanaidou
Conference Organising Committee Co-chair

Keith Vining
Conference Organising Committee Co-chair

John Clout FAusIMM

Jim Cribbes FAusIMM

Peter Fisher MAusIMM

Tom Honeyands FAusIMM

Brian McDonald MAusIMM

Kylie Nettleton

Alan Ooi MAusIMM

Nishka Piechocka

Clayton Simpson MAusIMM

Camilla Stark

John Tsalapatis

John Visser FAusIMM

AUSIMM

The AusIMM Event Management Team

REVIEWERS

We would like to thank the following people for their contribution towards enhancing the quality of the papers included in this volume:

Heath Arvidson MAusIMM
Cameron Boyle MAusIMM
Stewart Brand MAusIMM
Joffre Buswell MAusIMM
Simon Campbell-Hardwick MAusIMM
John Clout FAusIMM
Jim Cribbes FAusIMM
Tim Donohue
Eugene Donskoi
Hamid Doostmohammadi MAusIMM
Peter Fisher MAusIMM
Cathy Galli MAusIMM
Diana Greenup MAusIMM
Ralph Holmes HonFAusIMM(CP)
Tom Honeyands FAusIMM
Alan Irving FAusIMM(CP)
Lou Jelenich
Liming Lu
Georgia Manning MAusIMM
Elardus Mare MAusIMM
Brian McDonald MAusIMM
Angus McFarlane
Kylie Nettleton
Alan Ooi MAusIMM
Mike Peterson
Nishka Piechocka
Brian Povey FAusIMM(CP)
Mark Pownceby
Erick Ramanaidou
Walid Salama
Clayton Simpson MAusIMM
Philippa Sjoquist MAusIMM
Camilla Stark
Barry Tan MAusIMM(CP)
John Tsalapatis
Adel Vatandoost MAusIMM
Michael Verrall
Keith Vining
John Visser FAusIMM
Denis Yan MAusIMM

FOREWORD

The 2021 Iron Ore Conference is the ninth in the very successful international Iron Ore Conference series jointly hosted by the Australasian Institute of Mining and Metallurgy (AusIMM) and Australia's Commonwealth Scientific and Industrial Research Organisation (CSIRO). These conferences are held every two years and cover the latest technological developments in the world's iron ore industry, including ore genesis, geology, exploration, characterisation, mining, processing and market outlook. They also provide unparalleled opportunities for everyone involved in the iron ore industry, including geologists, geophysicists, geochemists, geostatisticians, mining engineers, mineralogists, metallurgists, managers, operators, consultants, research providers, engineering companies, equipment manufacturers, and analytical and metallurgical service providers, to network and share their experience and expertise. The theme of the Iron Ore Conference 2021 is 'Sustainability in a Changing World' as we address the many challenges the world is currently facing, including global warming and the ongoing COVID pandemic.

These conference proceedings include a number of keynote papers as well as 60 technical papers. The technical papers were sought from a wide range of areas from ore genesis through to processing and beneficiation, as well as automation, big data, machine learning, sustainability, technical marketing and health, safety and environment. After reviewing the abstracts submitted and selecting those relevant to the iron ore industry and conference theme, the full papers subsequently submitted were peer reviewed prior to acceptance and publication by the AusIMM. I trust you will find these proceedings a valuable permanent record of the papers that were presented at the Iron Ore Conference 2021.

In conclusion, I would like to thank the conference organising committee, the AusIMM Events Department, authors, paper reviewers, and all the sponsors and exhibitors, particularly Primetals Technologies for sponsoring these conference proceedings as well as BHP as the Major Sponsor of the conference. Thanks also go to Malvern Panalytical, Epiroc and Metso Outotec Australia Limited as Gold Sponsors. I welcome you to the Iron Ore Conference 2021 both at the well-appointed Perth Convention and Exhibition Centre and online, and trust that you will find it an enjoyable and rewarding event.

Yours faithfully,

Dr Ralph Holmes, BSc, PhD, HonFAusIMM(CP), FAIP

Conference Chair, Iron Ore Conference 2021

CSIRO Mineral Resources

SPONSORS

Platinum Sponsors

BHP

Gold Sponsors

Epiroc

Malvern Panalytical
a spectris company

Metso:Outotec

OZ MINERALS

Networking Event Sponsor

FMG Fortescue
The New Force in Iron Ore

Coffee Cart and Breaks Sponsor

ALS

Name Badge and Lanyards Sponsor

RioTinto

SPONSORS

Technical Session Sponsors

LONGi®
The Experts in Magnetic Technology

Conference Proceedings Sponsor

PRIMETALS
TECHNOLOGIES

Conference App Sponsor

AMC
consultants
mine smarter

Destination Partner

BUSINESS
EVENTS
PERTH


GREEN STEEL FOR A ZERO-CARBON WORLD

CONTENTS

Agglomerate bonding phase advances

Alternative fuel sources for ironmaking

Exploration and geology

Geophysics

Machine learning, big data and automation

Mining

New equipment and processes

Online and downhole assay measurement

Ore characterisation and geometallurgy

Processing and beneficiation

Project development and optimisation

Sustainability and climate change

Tailings

Technical marketing

Agglomerate bonding phase advances

Development of a cold bonding technology to high-grade iron ore concentrate

J Caron[1], M Athayde[2], F Lavoie[3] and R Joyce[4]

1. Analyst – Projects and Innovations, Quebec Iron Ore, Montreal Quebec H3B 4N4. Email: JCaron@mineraiferquebec.com
2. Senior Corporate Metallurgist, Quebec Iron Ore, Montreal Quebec H3B 4N4. Email: MAthayde@mineraiferquebec.com
3. Technical Marketing Manager, Quebec Iron Ore, Montreal Quebec H3B 4N4. Email: FLavoie@mineraiferquebec.com
4. Head of Technology, Binding Solutions, Materials Processing Institute, Middlesbrough TS6 6US. Email: Rjoyce@bindingsolutions.uk

ABSTRACT

Decarbonisation has become a major challenge for the global steelmaking industry, turning towards new technologies aimed at carbon footprint reduction, which on its own accounts for approximately 9 per cent global emissions. The iron and steel industry represents a 'hard to abate' sector, where much of efforts are currently being deployed into initiatives aiming to decarbonise the ironmaking through the use of green hydrogen, carbon capture utilisation and storage and state-of-the-art operation of current technologies, while little efforts being deployed to find carbon-efficient solution to iron ore burden preparation, where high-grade iron concentrate will increase in importance to ironmaking regardless of the chosen reduction route. Quebec Iron Ore (QIO), a subsidiary of Champion Iron Limited (Champion), produces high-grade hematite concentrate with one of the lowest carbon global footprints. Still, QIO is partnering with its clients to the development of burden solutions to minimise CO_2 emission, in the seek for a decarbonised steel.

In a strong technological partnership, Binding Solutions Limited (BSL) has developed a novel, cold-binding technology to provide a cleaner, more cost-effective alternative to induration. The technology allows miners and steel producers to reduce Capex significantly and reduce energy consumption and CO_2 emissions by 90 per cent. QIO and BSL have partnered to adapt the disruptive cold binding technology developed by BSL to QIO's concentrate to produce a high-quality low emissions iron ore agglomerate.

This paper describes the efforts taken to further develop BSL's cold binding technology and its application to QIO's high-grade iron ore concentrate to produce a hematite cold bonded briquette (hCBB) showing comparable performances with high quality seaborne fired pellets.

INTRODUCTION

The Bloom Lake iron mine property is located approximately 13 km north of Fermont, Quebec, and 10 km north of the Mont Wright iron ore mining complex, property of ArcelorMittal Mines Canada. The Bloom Lake mine facilities include a 32 km railway that connects to the 395 km Quebec North Shore and Labrador (QNS&L) railway to efficiently transport the high-quality hematite concentrate to a loading port located in Sept-Iles, Quebec.

The Bloom Lake mining complex was initially commissioned in December 2009 with a nameplate capacity of 7.5 million tons per annum of high-grade hematite concentrate. Five years later, the declining iron ore concentrate prices combined with the high operating costs resulted in the termination of the operations at the Bloom Lake site. The site was idled in December 2014 and put under care and maintenance during the Companies Creditor Arrangement process. The site was acquired by Quebec Iron Ore (QIO), a subsidiary of Champion Iron Limited (Champion), in April 2016 and restarted in February 2018 after major work was completed on-site to improve profitability. The Bloom Lake mining complex is now going through an expansion phase (Phase 2) that will come online in the second half of 2022 and will double the site production to 15 million tons per annum of high-grade iron ore concentrate.

In its actual operation, QIO is selling a high-grade iron ore concentrate on the Asian, mostly Japan, China and Korea, European and Middle East markets. The lower contaminant level is ideal to upgrade sintering blends compared with eastern ores, especially with its low alumina content, improving considerably the sinter strength and coke consumption. Notably, the ultra low level of alkalis improves the blast furnace operation and lower phosphorus has been noticed as being a great contribution to improving hot metal quality, together with lower sulfur input.

The current hematite concentrate features a high Fe content (>66 per cent) and low levels of contaminants: Al_2O_3 <0.27 per cent, Na_2O <0.01 per cent, K_2O <0.01 per cent, P <0.015 per cent and S <0.015 per cent.

In today's state-of-the-art, only two technologies are predominantly used to agglomerate iron ore concentrate: sintering and pelletising. About 80 per cent of QIO production is processed through sintering process at client's facilities, while 20 per cent is being pelletised to serve as burden to DRI modules. The greenhouse gases (GHG) client's emissions due to QIO concentrate agglomeration amount to 0.904 Mt CO_{2e} annually, for a production of 7.5 Mt/a. Table 1 focuses on the GHG emissions generated by the fuel combustion required for these two thermal agglomeration processes.

TABLE 1

GHG emissions related to principal agglomeration processes.

	Unit	Sinter Plant	Pelletising Plant
Typical Fuel Used		Bunker C	Bunker C
Heating Value of Fuel Used	MJ/L	42.50	42.50
Fuel Co_{2e} Emission	kg/L	3177	3177
% Iron in Concentrate	%	66.2	66.2
Coke Proportion	%	4.70	1.43
Typical Bentonite Proportion	%	1.50	1.05
Typical Limestone Proportion	%	13.20	0.04
Typical Dolomite Proportion	%	1.50	0.00
% Iron in Mix	%	54.93	64.64
% Iron after Induration	%	59.91	65.43
Total Agglomeration Energy	MJ/t	1400	800
Admixed Coke Energy (25.03 MJ/kg)	MJ/t	1176	358
Fuel Consumption	L/t	5.26	10.40
GHG Emission (Fuel + Coke)	CO_{2e} kg/t	133.60	68.61
GHG Emission (Fuel + Coke)	**CO_{2e} Kg/% Fe**	**2.23**	**1.05**

In pelletising plant, the energy consumption is around 800 MJ/t of pellet. For sinter plant, the melt of fluxes and phase changes observed in the iron-bearing minerals requiring up to 1400 MJ/t of pellet (Iljana, 2017). The values presented in Table 1 do not include the GHG emissions generated by the fluxing agents and coke production.

The aim of the cold pelletising project is to develop a hCBB (hematite based Cold Bonded Briquette) that can replace the traditional routes of sintering and pelletising, while significantly reducing the greenhouse gas generation. The goal is to achieve a product that competes with broadly available direct feed products for the blast furnace market, in term of chemical, physical, and pyro-metallurgical parameters.

Cold bonding challenges

In pelletising, high temperature process with sintering of smaller particles together and creation of larger cohesive solids, without extensively melt of iron ore. The atoms diffuse across the iron oxide particle boundaries, binding them together and creating one solid piece (Eisele and Kawatra, 2003). For sinters, the bonding mechanism is rather the melting and re-solidification of iron oxides and slag phases, as the process reaches a temperature beyond the eutectic point of the solution of iron oxides and gangue (ratios of CaO, MgO, SiO_2 and Al_2O_3).

On the other hand, cold bonding processes, to avoid fusing particles and phase changing at high temperature, will exploit the bonding properties of a binder to agglomerate the iron ore particles. Cold bonded processes encompass binding mechanisms at lower temperatures. Activated by a catalyst, a binder may recrystallise and form chemical liaisons between the iron ore particles, holding them together. Examples of cold bonding processes include carbonate bonding, cement bonding, hydrothermal bonding, rust bonding, organic binders, and polymer bonding (Dutta *et al, 1992)*. Several studies have failed in the endeavour to find a proper binder, cold binding application for primary iron ore agglomeration has been overlooked because of the incapacity to develop an agglomerate having the physical properties suitable for seaborne transport and related handling. The pellet strengths obtained with different cold bonding methods vary between 13.4 to 266.8 daN (Halt, Roache and Komar Kawatra, 2015). Cold bonding has seen renewed interest in recent years for a simple reason: these methods will consume less energy than thermal induration and will regenerate less GHG. Different materials have been selected, carbonate, cement or hydrothermal bonding, the binder consists in the hydration of calcium carbonate. The thermal conversion of the type of binder is rapidly initiated at 750°C (Karunadasa *et al*, 2019). The binder will decompose into carbon dioxide and calcium oxide, leaving the pellet without any cohesion strength once the reaction is completed. Some challenges are specifically inherent to the cold bonded processes. For example, briquettes are generally cured for expressive longer periods of time than the processes time of fired pellets. The curing area and stockpile design must be thought adequately. Also, the binder proportion representing a higher fraction of the briquette weight in cold bonded processes, the level of contamination with refractory element like aluminium and magnesium is likely to be higher. The higher binder fraction results also in a lower iron content. The right balance of reducing and refractory elements in overall pellet must be addresses to obtain a chemical signature suitable for blast furnace use. Finally, the binders used in cold bonding processes are not involving sintering iron ore or slag. This represents another challenge: the binders must resist the high temperature condition occurring in the blast furnace and maintain the pellet's integrity.

In a competitive iron and steel market, plants are operated in the most efficient way possible. With the older cold bonding methods, the main drawbacks were low cohesive strength, lower iron content and lower furnace operational stability than typical fired pellets, and an increased slag rate and coke rate in the furnace due to the added gangue.

Binder formulation development

Binding Solutions Limited (BSL) were established in 2011 by experienced metallurgical, mineral and chemistry experts. Having previously worked in the production of chemical plants in the Middle East, the founders were introduced to a major steel producer in the region who had issues with a gross excess of waste and by-products. This led to a project with the aim of introducing a 'zero waste' strategy at the works, to encompass the reuse or repurposing of by-products and also consider the overall energy use.

Within the project there was a vast amount of iron oxide fines of which the steel company had started to agglomerate using a cementitious binder. This had led to serious operational problems and has to be ceased. Binding Solutions transferred knowledge developed from an unrelated project, where a binder was developed for use in high-grade electronics products. A similar product was developed for the binding of iron ore, which was successfully trialled. The technology was transferred to an integrated Blast furnace/BOF Operation in the UK. The company has been in a significant further R&D phase and continual expansion to the present day. In the present project on primary iron ore, the significant challenge was to achieve the appropriate balance of physical and metallurgical properties, in particular the thermal stability and reducibility parameters.

Previous cold bonding technologies have generally focused on either organic or inorganic binder systems. For this project, a hybrid inorganic-organic binder was formulated. By using a hybrid system, BSL can use the strengths of each system to overcome the weaknesses of the other. The inorganic portion of the binder provides a strong polymerised bond with the iron oxides and brings thermal stability. It was designed to sustain a temperature of around 1100°C, avoiding lower temperature degradation observed in blast furnace with traditional binders. Unlike cementitious binders, no thermal conversion is occurring around 750°C. This characteristic leaves much more leeway to maintain cohesion up to the hCBB's sintering point. The organic portion of the binder provides bonding with both the iron oxides and the inorganic binder, to give the required physical properties. Additionally, the organic content aids the manufacturing process and aids stability, when in the unhardened phase.

Using this hybrid system allows the hCBB to achieve the required properties, at a low level of binder addition when compared to alternative systems. The gangue content is kept within parameters as the binder content is not excessive. A good hCBB must be sufficiently strong to allow a successful seaborne transport and to be used within a blast furnace. For this, the hCBB product must maintain its integrity, in terms of fines generation, volume and shape, under the handling and transportation required for shipping to foreign markets. It must also show equivalent reducing properties than typical acidic fired pellet. As well, it should contain a high % of total iron, therefore a low % of binder, to reduce the slag formation and insure a high yield of hot metal.

The aim of the project was to develop a hCBB suitable for blast furnace uses with a significant burden ratio. The physical and metallurgical properties for a blast furnace application must be at least as good as fired acidic pellets.

MATERIALS AND METHODS

A 2000 kg hematite concentrate was first grinded and sized to obtain different grain size distribution to be tested. Various PSD tested for briquette production, ranging from P80 ≤ 45 µm to P80 ≤ 140 µm, in the BSL laboratory located in Middlesbrough, United Kingdom. The grinded hematite produced was manually feed into a mixer. It was weighed and placed in the mixer before the homogenisation process starts. The binders are weighed out from bulk storage and poured in the mixer while in function. The hydration process takes place during the mixing with the addition of water up to different moisture content. The mixer speed and mixing period were set based on material type.

Two methods were used at the laboratory to form briquettes: extruding and roller-pressing (pillow shape). The extruder uses a system of barrels and cylinders to propel the iron ore matrix through a die to create the desired shape of pellets. On the other hand, briquettes are produced with a roller press. The hematite concentrate is fed between two counter-rotating rollers, which are furnished with synchronised moulds that defining the briquette shape. On passing through the roller gap, the material is compacted and formed into briquettes.

Handling and transport resistance

This feature can vary according to multiples aspect of the briquettes, the chemical composition of the binder, the moisture content in the homogenisation phase, the hematite grain size distribution, the pellet overall shape and size and the curing conditions (temperature, pressure, % moisture etc). The degradation by abrasion was assessed with the ISO3271:2015 test: Abrasion Index (% <0.5 mm) and Tumble Strength (% >6.3 mm). Aiming a more extensive degradation evaluation, the axial and shear constraint resistance were tested with a custom-made drop test, developed at COREM, Quebec (Martinovic, Ouellet and Paquet, 1998). This test assesses the briquette breakage (chips or -6.3 + 0.5 mm) and degradation by abrasion (dust or -0.5 mm). The 10 m drops to which the hCBB is submitted makes it possible to simulate the stress conditions caused by transportation and handling.

Reducibility

Several variables can influence the reducibility of the hCBB such as their size, the iron ore grain size distribution, and their chemistry. The influence of these variables on the briquette reducibility were evaluated by carrying out two ISO standard test protocols: the ISO 7215*:2015 – Relative

Reducibility measuring the final degree of reduction after 180 minutes, and the ISO 4695*:2015 – Reducibility R40, measuring the rate of reduction until 60 per cent of reduction is reached.

RESULTS AND DISCUSSION

Many features of hCBB can impact its overall quality. Some of these consist in the chemical signature, the physical resistance, the binder proportion, the moisture content, their shape and size or the iron ore grain size distribution. Other variables are related to the operational parameters of the agglomeration equipment chosen, which include the operating conditions (temperature and pressure) and the curing conditions (temperature, pressure, % moisture, duration). This section presents an overview of the hCBB properties under study and the way they were evaluated.

Hcbb size

To evaluate the basic quality properties, pillow shaped briquettes of 40 mm × 30 mm were produced with a roller press, using a PSD of P80 ≤ 140 µm. The samples were recovered after the reduction tests and were mounted in polished coatings for examination under an optical microscope (reflected light). Figure 1 shows the microscopic mineralogy of a briquette, after a Static-LTD ISO 4696–2*:2015 reduction test. The reduction process mainly presents itself as a steady progression from the briquette periphery, typical of a topochemical phenomenon where the impact of particle assembly predominates on their intrinsic reduction properties. This emphasises the importance of a size offering the smallest surface/volume ratio.

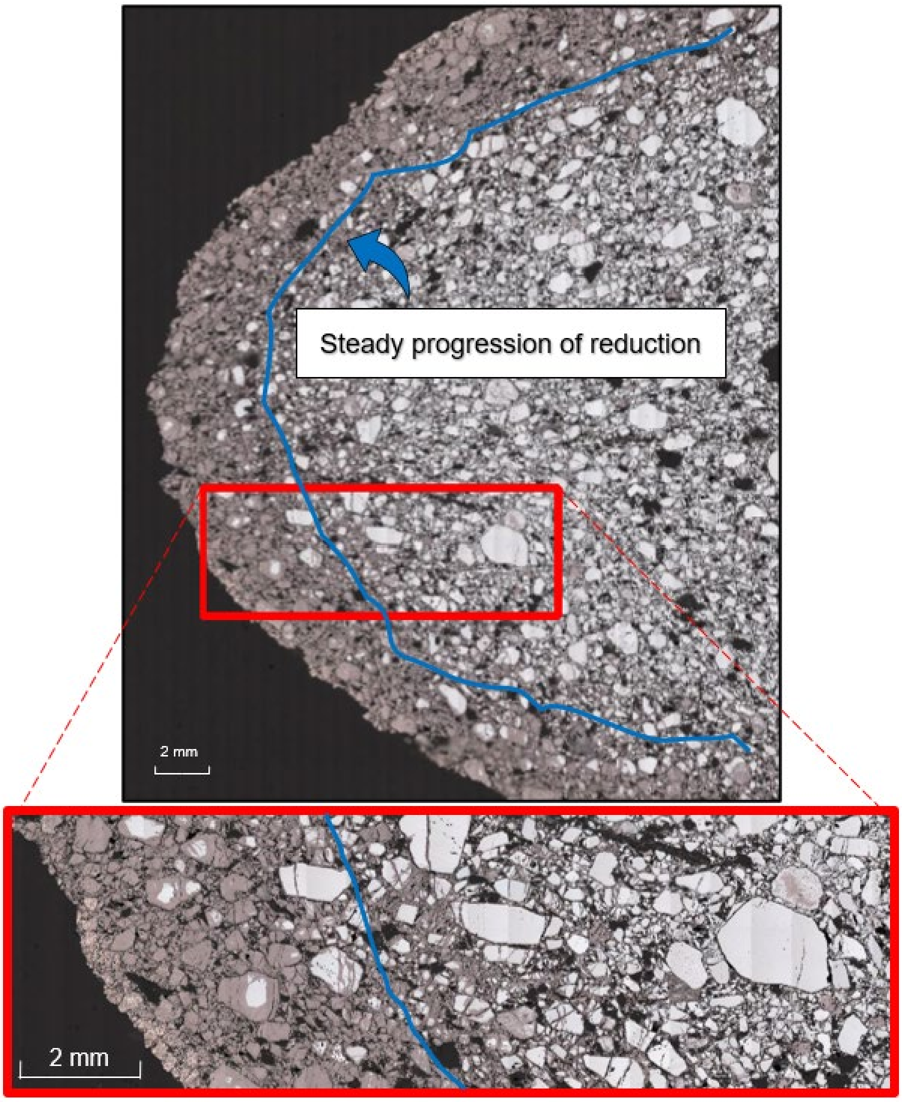

FIG 1 – Microscopic view of 40 mm × 30 mm briquette (roller pressed), after Static-LTD ISO 4696–2*:2015.

The aim was consequently to reduce the surface/volume ratio of the briquettes, which is possible by reducing their overall size and elongation. At this point, the extrusion was proven to be the preferred agglomeration process, allowing efficient production of small dimension briquettes with a length equal to the diameter. In addition, a major loss of productivity was observed with roller presses when the size of the briquettes decreased. When the individual mass of smaller briquettes is not sufficient for them to come off freely from the roller press, great slowdowns in production were expected. Thus, extruded briquettes of 20 mm diameter were produced, using the same PSD of P80 ≤ 140 µm.

To compare the effect of size on reduction, ISO 4695*:2015 – Reducibility R40 tests were performed on whole hCBB (20 mm) and crushed hCBB (~10 mm pieces), of same length. Figure 2 reports the R40 values obtained.

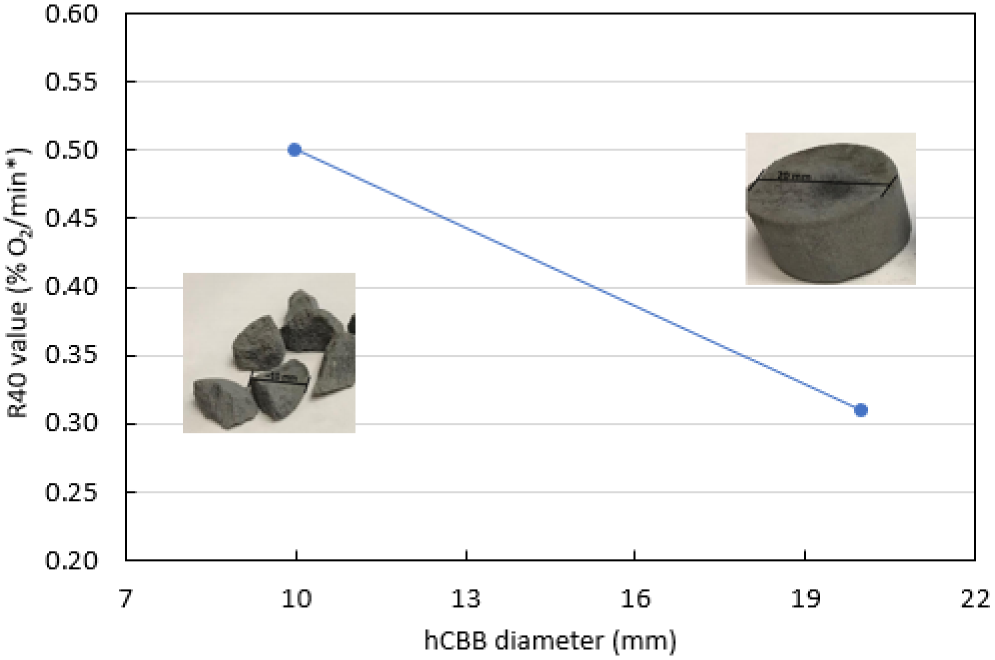

FIG 2 – Reducibility R40 – ISO 4695*:2015 results on different hCBB sizes. *The R40 value were calculated with the total mass loss recorded during the R40 test, as prescribed in the standard.

The 20 mm diameter hCBB shows a rate of reduction of 1.6 × 10^{-2} per cent O_2/min/mm of diameter. This rate increases to 5.0 × 10^{-2} per cent O_2/min/mm of diameter when compared to the ~10 mm pieces. This result is in concordance with the topochemical reduction progression observed in Figure 1.

The smaller the hCBB is, the higher the reduction degree will likely to be. It is also possible to notice in Figure 1 that the top size particles are not reduced at the periphery of the briquette. This observation suggests that a uniformed and fine iron ore grain size distribution will lead to higher overall rate of reduction and ultimate reduction degree.

Grain size distribution

The effect of the grain size distribution on reduction was assessed on 12 mm diameter and 12 mm length hCBB obtained from extrusion. Two different PSD were compared: P80 ≤ 55 µm and P80 ≤ 90 µm. ISO 4695*:2015 – Reducibility R40 and ISO 7215*:2015 – Relative Reducibility tests were performed on both PSD hCBB. Figure 3 shows the R40 and relative reduction values obtained.

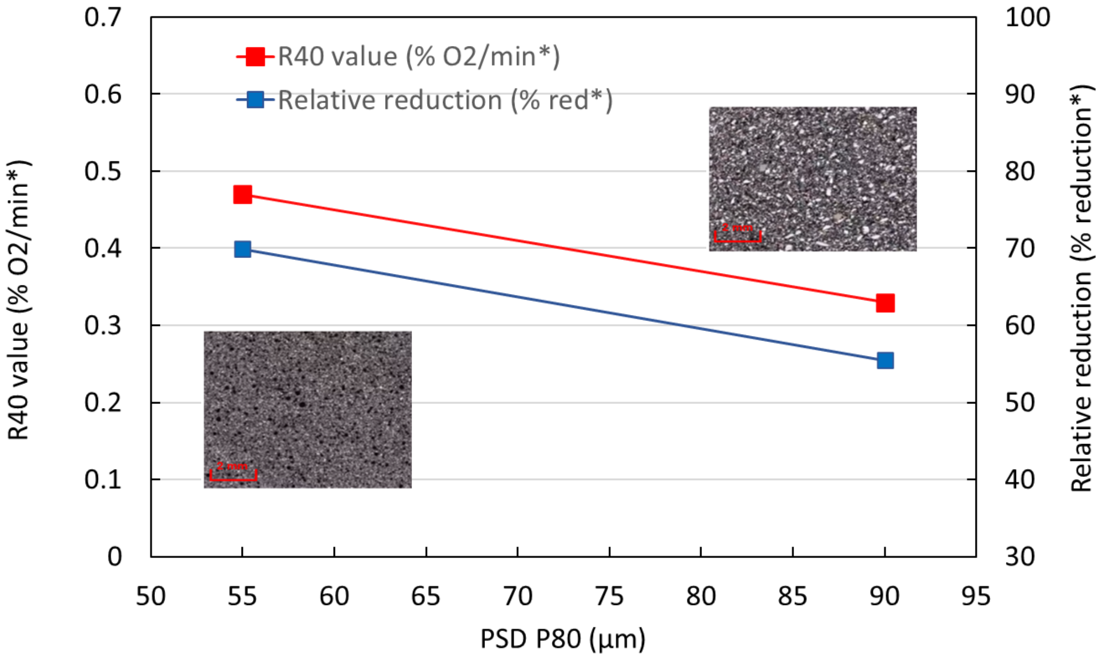

FIG 3 – R40 (ISO 4695*:2015) and Relative Reducibility (ISO 7215:2015) results with different PSD. *The R40 and relative reduction values were calculated with the total mass loss recorded during the tests, as prescribed in the standard.

The graph in Figure 3 shows a significant increase of reduction rate and final degree of reduction when passing from a P80 ≤ 90 µm PSD to a P80 ≤ 55 µm PSD. This result is also in concordance with the observations of un-reduced top size particles in Figure 1 with coarser grain size distribution. More uniform and finer PSD are likely to lead to faster reducing hCCB.

The proper PSD design is key to adequate briquette physical resistance required. A spread distribution of grain size leads to a higher degree of compaction during extrusion, therefore a stronger physical resistance of the briquette. A trade-off study (Figure 4) between the briquettes resistance and its reducibility properties is likely the pathway to an overall optimised product.

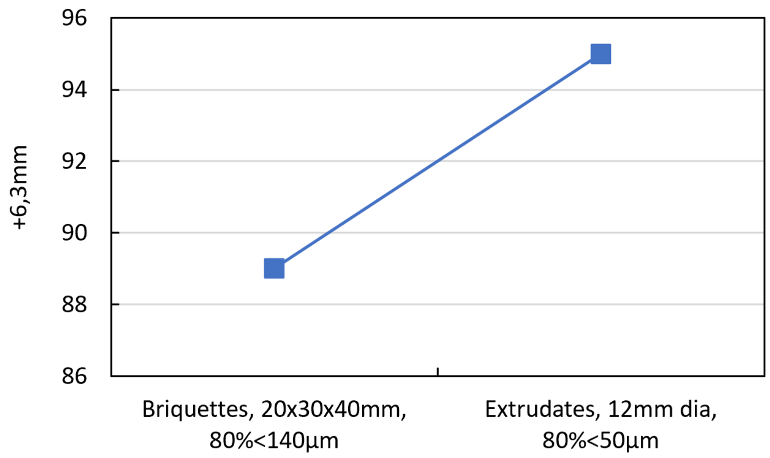

FIG 4 – Resistance of transportation measure through Thumble Index – on different hCBB.

The analysis of the cold bonded briquettes reducibility results to lead to questioning the accuracy of reducibility ISO tests for col agglomerated briquettes. Indeed, hCBB, not being fired, display a different chemical signature that might not met the prerequisite of ISO tests to the characterisation of cold bonded agglomerates.

Using chemical signature to calculate reducibility for hCBB

Different than the industrial reactor ISO tests are performed under isothermal conditions, where the objective is repeatability. The pre-heating and cooling are performed under nitrogen saturated atmosphere in order to prevent the first stages of iron ore reduction from happening since the test environment should be free of carbon monoxide. Once the temperature plateau is reached, all mass loss is considered to be oxygen mass loss due to reduction of iron ore. To verify this prerequisite of ISO tests, a TGA test was performed on standard fired pellets and cold bonded briquettes. The TGA setting were to represent the increase of temperature during the pre-heating phase of ISO 7215:2015 Relative Reducibility test, ie from room temperature to 900°C, under saturated N_2 atmosphere.

Figure 5 shows the results of a TGA test carried out between the two products. As the mass loss for the standard fired pellets is less than 0.5 per cent, the recorded mass loss for the cold bonded briquette is about 4.5 per cent.

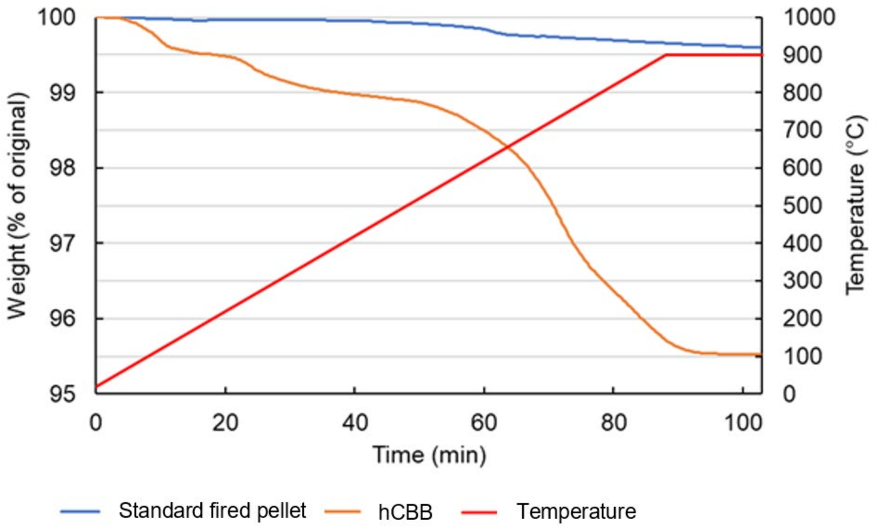

FIG 5 – TGA mass loss for control (fired) and cold bonded samples.

This test suggests that a certain amount of mass loss is possible during the pre-heating phases with hCBB. Therefore, the hypothesis of an inert atmosphere during the pre-heating phase of R40 and Relative Reducibility ISO tests is not valid for hCBB and the percentage of reduction cannot be calculated from the mass loss after the pre-heating phases.

Alternatively, the percentage of reduction can be calculated based on chemical analysis of total Fe, metallic Fe and Fe^{3+} ($K_2Cr_2O_7$ titration):

$$\%\,reduction = \frac{1.5 - \left(\frac{O}{Fe}\right)}{1.5\,\times\,100}\; where\; O/Fe \; \frac{\left(\frac{16(Fe_{tot} - Fe_{met} - Fe^{3+})}{55.85}\right) + \left(\frac{Fe^{3+} \times 3 \times 16}{2 \times 55.85}\right)}{16} \Bigg/ \frac{Fe_{tot}}{55.85} \qquad (1)$$

This approach based on the chemical signature of the iron allows to capture the key difference between hCBB and fired pellets and is thought to be a better way to assess the reducibility properties of cold bonded agglomerates.

To quantify the discrepancy between the reduction calculation methods, ISO 4695*:2015 – Reducibility R40 and ISO 7215*:2015 – Relative Reducibility tests were performed on extruded hCBB of 12 mm diameter with PSD of P80 ≤ 45 µm. The results of the tests, calculated with the two methods are presented in Figure 6.

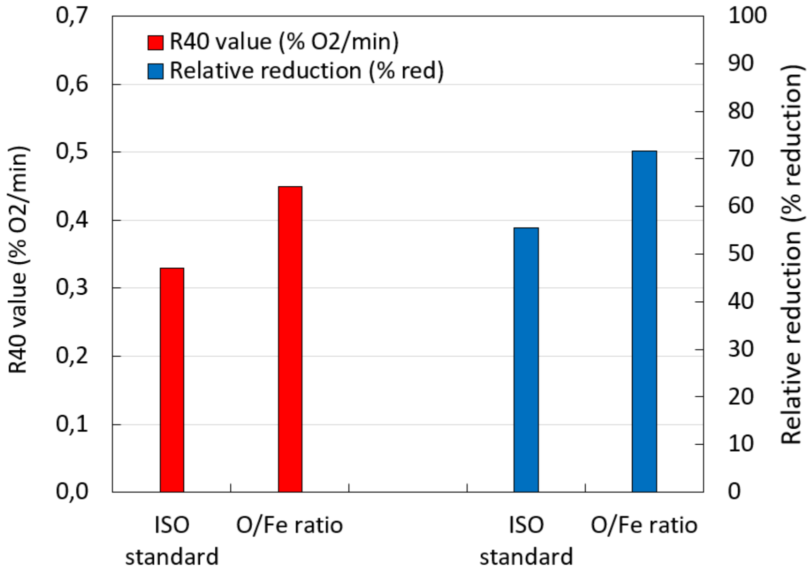

FIG 6 – hCBB reducibility tests results based on ISO standard and O/Fe ratio.

The reducibility results highlight the discrepancy between the ISO standard R40 and relative reducibility values, compared to the value obtained based on chemical analysis of O/Fe ratio with Equation 1. The reduction rate increases from 0.30 per cent O_2/min to 0.45 per cent O_2/min when using the chemical analysis of reduction instead of the mass loss solely. The final degree of reduction also increases from 0.55.5 per cent to 71.6 per cent, which is in good agreement with most of blast furnace operations and may indicate a good operation and stability

The hCBB integrity was not compromised in any of the metallurgical tests and Figure 7 shows the resulted hCBB post-tests. It is to be noted that virtually no physical degradation is noticeable. Also, it is an important results as high blast furnace permeability at the elaboration zone, where the effectiveness will lead to lower coke rate and high furnace productivity.

FIG 7 – 12 mm diameter hCBB after R40 (ISO 4695*:2015) and Relative Reducibility (ISO 7215:2015) tests.

A much further development was conducting on extruded smaller agglomerates and finer particles, to improve the results observed so far. The hCBB of 12 mm diameter with PSD of P80 ≤ 55 µm a smaller format where the aspect ratio (diameter/length) is equal to 1, with a uniformed and fine iron ore grain size distribution.

The complete assessment of quality for production and iron burden utilisation can be seen at Table 2, The PSD of P80 ≤ 55 µm combined with a 12 mm size hCCB succeeded in reconciling a high physical resistance with high reducibility properties. In order to evaluate further the degradation, the

10 m drop test was applied, in parallel to the traditional tumble test, results of 86.9 per cent $_{-6.3\ \text{mm}}$ and 2.0 per cent $_{-0.5\ \text{mm}}$ in the same average interval of seaborne trade pellets values of 92.4 per cent $_{-6.3\ \text{mm}}$ and 1.5 per cent $_{-0.5\ \text{mm}}$ (Martinovic, Ouellet and Paquet, 1998). From the metallurgical performance, a greater reducibility rate of 0.67 per cent O_2/min was observed compared with typical commercial acid pellets value for BF of 0.4 to 0.6 per cent O_2/min (Fruehan, 1999). It shows a greater potential to reduce even further coke rate by improving the effectiveness of blast furnace preparation zone.

TABLE 2

Proof of concept on 12 mm extrudated hCBB.

Property	Indicator	Standard	Unit	Value
Handling and transport resistance	10 m Drop test	COREM	-6.3 mm (%)	86.9
			-0.5 mm (%)	2.0
	Tumble strength	ISO3271:2015	+6.3 mm (%)	95.7
			-0.5 mm (%)	4.2
Reducibility	Reducibility R40	ISO 4695*:2015	(% O_2/min)	0.47[1]/0.67[2]
	Relative Reducibility	ISO 7215*:2015	%	69.9[1]/76.1[2]

[1] The R40 and relative reduction values were calculated with the total mass loss recorded during the tests, as prescribed in the standard.

[2] Reduction based on chemical analysis of O/Fe ratio with Equation 1.

The 10 m drop test results of 86.9 per cent -6.3 mm and 2.0 per cent -0.5 mm are slightly below the range of seaborne trade pellets values of 92.4 per cent -6.3 mm and 1.5 per cent -0.5 mm (Martinovic, Ouellet and Paquet, 1998) and will be optimised through subsequent phases of testing. The reducibility rate of 0.67 per cent O_2/min is higher than the typical commercial acid pellets value for BF of 0.4 to 0.6 per cent O_2/min (Fruehan, 1999).

The reducibility results presented highlight the importance to properly evaluate the ISO standard R40 and relative reducibility in the iron burned development, as far the cold bonded product is concerned. An important performance of the hCBB was observed when properly compared to the value obtained based on chemical analysis of O/Fe ratio with Equation 1. The ISO standard underestimated the rate of reduction by 42.55 per cent and underestimated the final degree of reduction by 8.14 per cent. Further evaluation of the cohesive zone and industrial performance will have to reconsider the use of ISO tests for the characterisation and evaluation of the benefits of product cold bonded.

GHG CONSIDERATIONS

When comparing the usual agglomeration techniques, such as pelletising and sintering, with the cold bonding technique described in this paper, the GHG reduction is impressive.

In addition to excluding emissions from fluxing agents and coke, the technique eliminates the need for fuel combustion. The production of the binder generates around 63.2 kg of CO_{2e} per t. All things considered, the cold-bonded briquette generate 1.58 kg of CO_{2e} per t of hCBB, compared to 133.60 and 68.61 for sinters and fired pellets, respectively.

The actual production of QIO concentrate is agglomerated into sinters (80 per cent) and fired pellets (20 per cent). The GHG emissions related to QIO concentrate agglomeration amount to 904 482 t CO_{2e} annually, for a production of 7.5 Mt/a. This number could be lowered to 18 850 t CO_{2e} annually, with the cold bonded technology describe in this paper. This would represent a reduction of 98.7 per cent GHG emissions.

CONCLUSION

The aim of the project was to develop a suitable and alternative product to blast furnace with physical and metallurgical properties for a blast furnace application at least as good as fired acidic pellets.

The results shows that hCBB is sufficiently strong to allow a successful seaborne transport and it must demonstrate equivalent, whether not superior, reducing properties to typical acidic fired pellet.

Furthermore, hCBB presented satisfactory high heat resilience. The binder retained its strength under the stringent and high temperature conditions prevailing in blast furnaces. Degradation of the hCBB was minimum, compared with traditional products. The results showed the reduction process in the bast furnace shall accept this new iron burden product. The adoption of the new developed product will have to be evaluated with adaptation of traditional ISO method is needed to be adjusted, to do not underestimate it real performance in the blast furnace.

QIO has been successful in design a new concept that allow a decarbonised hot metal production from a blast furnace with a stable contribution the iron burden, like a traditional ferrous product. Further studies will assess in much more details the performance of hCBB in the cohesive zone. The outcomes of this work will be the subject of a subsequent publication which will present the results from further stages of experimentation.

ACKNOWLEDGEMENTS

The authors are grateful for the assistance of the BSL staff for providing their valuable observations and technical knowledges and to the Champion Iron management team who have been supportive in the development of decarbonising solutions to support the iron and steelmaking industry.

REFERENCES

Dutta, D K, Bordoloi, D, Gupta, S, Borthakur, P C, Srinivasan, T M and Patil, J B, 1992. Investigation on cold bonded pelletization of iron ore fines using Indian slag-cement, *International Journal of Mineral Processing*, 34:149–159.

Eisele, T C and Kawatra, S K, 2003. A review of binders in iron ore pelletization, *Minerals Processing and Extractive Metallurgy Review*, 24(1):1–90.

Fruehan, R J, 1999. AISE Steel Foundation. *The Making, Shaping, and Treating of Steel*, Pittsburgh, PA: AISE Steel Foundation.

Halt, J A, Roache, S C and Komar Kawatra, S, 2015. Cold Bonding of Iron Ore Concentrate Pellets, *Mineral Processing and Extractive Metallurgy Review*, 36(3):192–197, DOI: 10.1080/08827508.2013.873863

Iljana, M, 2017. Iron Ore Pellet Properties Under Simulated Blast Furnace Conditions, Investigation on Reducibility, Swelling and Softening, PhD thesis, University of Oulu, Faculty of Technology, Oulu, Finland.

Karunadasa, K S P, Manoratne, C H, Pitawala, H M T G A and Rajapakse, R M G, 2019. Thermal decomposition of calcium carbonate (calcite polymorph) as examined by in-situ high-temperature X-ray powder diffraction, *Journal of Physics and Chemistry of Solids*, 134(2019):21–28, https://doi.org/10.1016/j.jpcs.2019.05.023

Martinovic, T I, Ouellet, G, and Paquet, G, 1998. Influence of Thermal Treatment and Handling Conditions on Fired Pellet Physical Properties, *1998 Ironmaking Proceedings*.

Ancient to modern ironmaking – examining the effect on the behaviour of phosphorus and other impurities in iron ore by doping with calcium oxalate ($CaC_2O_4.H_2O$)

S Hapugoda[1], V Nunna[2], H Han[3], M I Pownceby[4] and L Lu[5]

1. Senior Experimental Scientist, CSIRO, Pullenvale, Brisbane, Queensland 4069, Australia. Email: sarath.hapugoda@csiro.au
2. Senior Research Scientist, CSIRO, Pullenvale, Brisbane, Queensland 4069, Australia. Email: venkata.nunna@csiro.au
3. Research Officer, CSIRO, Pullenvale, Brisbane, Queensland 4069, Australia. Email: hongliang.han@csiro.au
4. Senior Principal Research Scientist, CSIRO, Clayton, Victoria 3168, Australia. Email: mark.pownceby@csiro.au
5. Principal Research Scientist, CSIRO, Pullenvale, Brisbane, Queensland 4069, Australia. Email: liming.lu@csiro.au

ABSTRACT

Charcoal produced from *Syzygium Zeylanicum* (local name: Yakada Maran = iron killer) trees were widely used in ancient Sri Lankan iron smelting practices. In this study, relict charcoal from *Syzygium Zeylanicum* tree trunks, branches and leaves were analysed for the first time. Unusually high concentrations of calcium oxalate ($CaC_2O_4.H_2O$ – CaOX) crystals were identified preserved in plant cell structures by optical mineralogy and SEM analysis. Thermogravimetric Analysis (TGA) of CaOX showed that it displayed three decomposition stages, releasing H_2O at 177°C, CO at 493°C and CO_2 at 750°C. Following the identification of CaOX in Sri Lankan charcoal, a series of reduction tests on a low-grade, high-P iron ore fine sample (high SiO_2: 5 wt. per cent; Al_2O_3 4 wt. per cent; P: 0.135 wt. per cent) doped with CaOX were carried out at various temperatures. Samples were analysed by XRF, SEM and EPMA to determine the degree of reduction and the effect of reduction on the deportment of impurities, in particular P. Reduction tests at 800°C and 900°C with 5 wt. per cent CaOX showed that the reducibility increased to over 65 per cent. At temperatures above 900°C, P was located mainly within a fine, interstitial glass matrix suggesting that the CaOX flux enhanced removal of P from iron-rich pre-cursor phases to form glass. Preliminary magnetic separation tests to remove the P-rich interstitial glass were unsuccessful due to the fine grain size. Further complete reduction tests at temperatures above 1200°C with addition of coke to convert the iron oxides into Fe_m were conducted with samples doped with 10 wt. per cent CaOX, 10 wt. per cent $CaCO_3$ and equivalent undoped samples. Results confirmed the preferential P-incorporation into a glassy matrix in the CaOX samples although some rare P incorporation into the metallic phase was noted. Experimental results, including comparisons with the $CaCO_3$ fluxed and undoped samples, are discussed in view of the potential for CaOX flux for removing P (and potentially other impurities) from P-rich iron ores.

INTRODUCTION

Evidence for the earliest production of high carbon steel in South Asia is found in the Samanalawewa area of Sri Lanka where thousands of archaeological sites have been found (Seneviratne, 1985; Karunatilaka, 1991; Juleff, 1996, 1998). Wootz steel was produced in India and Sri Lanka in furnaces powered by monsoon winds and artefacts have been dated to 300 B.C. using radiocarbon dating techniques. In one of the most recent archaeological discoveries in Lanka, ironmaking furnaces along with samples of steel, dating to 200 BC, were discovered from a village in Hingurakgoda in north-west Sri Lanka. The discovery of these artefacts supported previous discoveries made in Anuradapura, Sigiriya, Ala Kola Weva, Kuratiyaya, and Nikavatana (all locations in North Western Province, Sri Lanka) in support of ancient Syrian records that 'Sivhala' (Lanka), once was home to the world's best steelmaking technology. Recent studies have suggested that the ancient Lankan furnaces may have provided the source material for the legendary Damascus swords following export of steel to the middle east. Coomaraswamy (1908) believed that iron slag heaps discovered in nearly every district of Ceylon (Sri Lanka) showed the vastness of the iron smelting industry in ancient times and may have extended to earlier times. For example, studies by Karunaratne and

Adikari (1994) have shown that the earliest known age for iron smelting, based on C14 dating of iron slag found in a proto-historic context in an archaeological site from Aligala in Sigiriya, to be ca. 998–848 BC.

Syzygium Zeylanicum is a species of plant in the family Myrtaceae endemic to Sri Lanka (Ashton *et al*, 1997) and it has been reported that the *Syzygium Zeylanicum* tree species had been preferentially exploited for charcoal from the 3rd century BC onwards (Coomaraswamy, 1908; De Silva, 2011; Solangaarachchi, 1999; 2011). The local (Sinhalese) name for *Syzygium Zeylanicum* is 'Yakada Maran' which is translated as 'Iron Killer' plant. Although the use of charcoal from *Syzygium Zeylanicum* is described by many, the actual reason for its use has not been investigated. Anoop and Bindu (2014) conducted a pharmacognostic and physico-chemical study on leaves of *Syzygium Zeylanicum* and reported the presence of calcium oxalate crystals in cell structures while Franceschi and Nakata (2005) described calcium oxalate formation in plants and that the Ca oxalate crystals formed specific shapes and sizes.

In the current study, we provide a detailed examination of charcoal produced from *Syzygium Zeylanicum* tree stem, branches, and leaves, and characterise slag iron from ancient ironmaking sites in Sri Lanka. Given that high quality steel was produced from Sri Lanka, it was hypothesised that the presence of calcium oxalate may be a key factor in iron production. From our observations we then conduct our own experimental studies into the use of calcium oxalate as a dopant during iron ore reduction. The effect of adding calcium oxalate on the distribution of phosphorus, a key iron ore impurity element, is discussed.

CHARACTERISATION OF CHARCOAL MADE FROM *SYZYGIUM ZEYLANICUM*

Charcoal from *Syzygium Zeylanicum* tree stem (Figure 1a), branches and leaves (Figure 1b) were prepared by burning dried pieces of each material above 100°C in a large steel barrel, covered with a lid. The charcoal produced from burning the tree stem and branches was typically observed to be solid pieces as shown in Figure 1d.

The charcoal (both from tree stems and branches) was set in epoxy resin, polished, and observed under the optical microscope, SEM and EPMA (Electron Probe Micro Analyser). High magnification optical micrographs (Figures 2a and 2b) and SEM backscattered electron (BSE) images (Figures 2c and 2d) showed that calcium oxalate (CaOX) crystals developed excessively within cell structures parallel to the tree stems or branches and was present in almost every particle examination. The EPMA spot analysis results on individual calcium oxalate crystals showed a CaO content of between 45–57 wt. per cent (average 47 wt. per cent, with a std. dev. of 3.5 wt. per cent from 20 spot analysis). Several SEM EDS spectra (as Figure 1h) were obtained on Ca oxalate crystals – these confirmed that the crystals contained Calcium (Ca), Carbon (C) and Oxygen (O) only and were consistent with the material being CaC_2O_4 (Figure 1i).

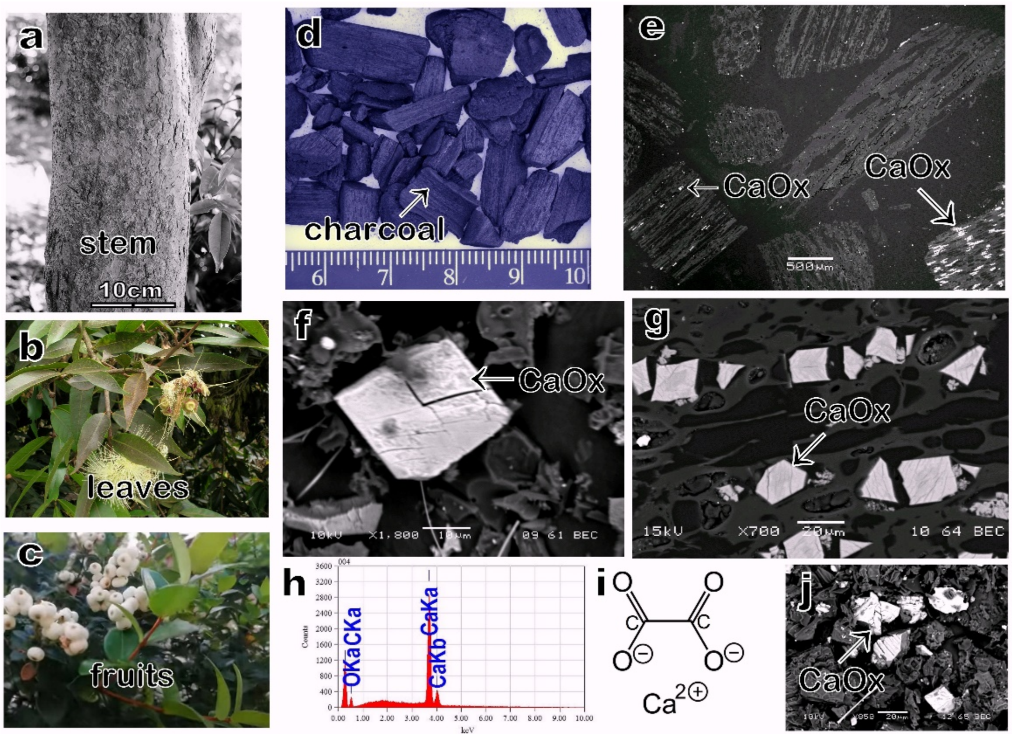

FIG 1 – Images of *Syzygium Zeylanicum* (local name: yakada maran = iron killer). a) stem of the tree, b) leaves and branches, c) fruits, d) charcoal made from tree stem, e) SEM backscattered electron image of polished charcoal, f) magnified SEM backscattered electron image of a typical calcium oxalate crystal, g) SEM backscattered electron image of charcoal showing Ca oxalate crystals and some pull-out spaces during polishing, h) EDS X-ray spectrum taken on a Ca oxalate crystal showing characteristic Ca, C and O X-ray peaks, i) calcium oxalate atomic structure, and j) SEM backscattered electron image showing separated Ca oxalate crystals in crushed charcoal.

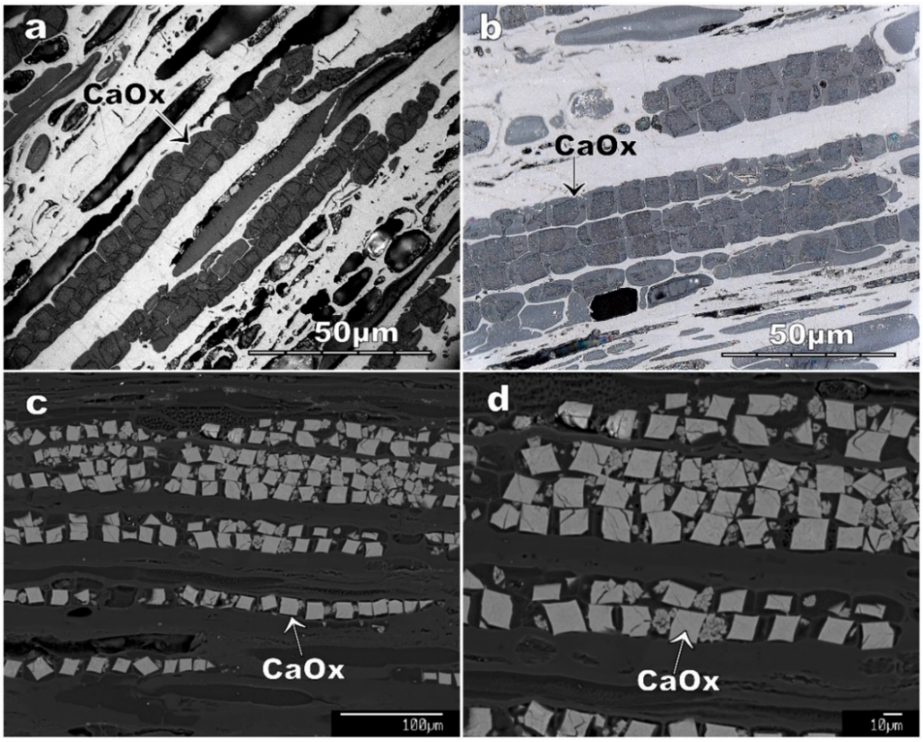

FIG 2 – Optical micrographs (a and b) and SEM backscattered electron images (c and d) showing excessive calcium oxalate (CaOx) crystal development in *Syzygium Zeylanicum* (Yakada Maran) plant cell structures.

CHARACTERISATION OF SLAG IRON SAMPLES

Slag iron can be found in almost every district in Sri Lanka usually near famous archaeological sites, ancient temples, or ancient ruins. Several large iron slag samples were collected from three locations closer to archaeological sites at Madawala Ulpatha (Central Province GPS X-186673.44, Y-264757.83, Lat. 7.61741, Lon. 80.67118, Panwila (Central Province, GPS X-194538.227 Y-246328.045, Lat. 7.36486, Lon. 80.70917), Belihul Oya (Sabaragamuwa Province, Lat. 6.70494, Lon. 80.78740). Samples were broken into several pieces and representative pieces from each sample are shown in Figure 3. These types of slag iron samples are common, well-preserved, and still fresh and very hard. In some cases, pores were filled with clay/soil with quartz (SiO_2) particles. Sample SL-10 (Figure 3a) was massive/hard with smaller pores, less soil attached and displaying a brownish yellow stain due to the presence of secondary goethite-Fe $(OH)_3$. The sample SL-012 (Figure 3b) displayed a rope-like structure, with larger pores within and with some soil attached to the sample surface. The sample SLSH-4S (Figure 3c) was dense and with few larger circular pores and had some goethite staining on the surface. The sample SLSH-02 (Figure 3d) displayed a large amount of minor pores filled with soil near the surface, however, the sample was internally very dense and fresh inside with no soil infiltration. Sample SLSH-01 (Figure 3e) had both hard dense (fresh) and medium-hard porous parts. Many of the pores were filled with clay/soil. The sample SLSH-03 (Figure 3f) displayed a coral-like structure with several tubular structures that were connected at one end. It also had some soil attached to the surface but was fresh and hard inside.

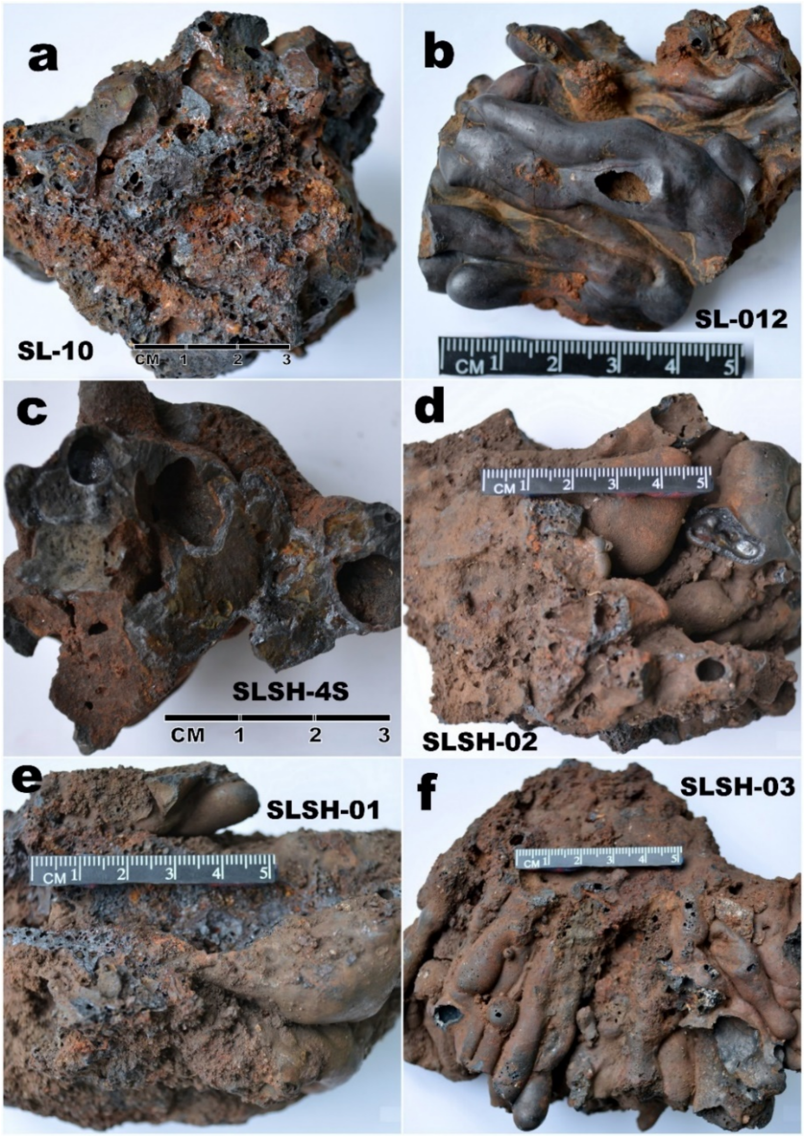

FIG 3 – Slag Iron samples from proximity to possible ancient smelting sites in Sri Lanka.

Table 1 contains chemical analysis data for two representative slag iron samples. Care was taken to remove as much soil and quartz particles attached to the samples before analysis. The chemical analysis data indicates that the samples had total Fe contents of between 45–51 wt. per cent, SiO_2 between 18.7–21.6 wt. per cent, Al_2O_3 between 7.3–8.5 wt. per cent and CaO ranged from 0.75–2.45 wt. per cent. As expected, the SiO_2 content was high in the slag and CaO was low indicating most likely low-basicity iron smelting conditions. The calcium (CaO) contents are low, and silica (SiO_2) contents are high in supergene goethite iron ores most likely used in iron smelting (Ranasinghe, 1986). Calcium for the smelting processes may have added from widely available dolomitic crystalline limestone (marble – limestone) deposits in the island. The phosphorus content in the slag was significant and close to 0.4 per cent wt. per cent (P_2O_5 = 1.8 wt. per cent) and MgO (0.74–0.92 wt. per cent) and TiO_2 (0.47–0.52 wt. per cent) were also low. Potassium, K_2O (0.64–0.78 wt. per cent) in the slag had most likely come from minor amounts of clay/soil attached to the samples. Manganese (Mn) is also significantly high in samples.

TABLE 1

Chemistry of Sri Lankan slag iron samples.

Ele./Oxide (wt.%)	Fe	Fe(Calc)	SiO_2	Al_2O_3	TiO_2	Mn	CaO	P	S	MgO	K_2O	Zn	Pb	Cu
SL-012	51.05	51.08	18.71	7.36	0.47	1.49	0.76	0.396	0.037	0.74	0.783	0.019	0.003	0.004
SLSH-02	45.51	45.51	21.64	8.49	0.52	3.08	2.45	0.335	0.043	0.92	0.645	0.026	0.005	0.014
SLSH-02 Rpt	45.55	45.49	21.66	8.51	0.52	3.08	2.45	0.334	0.044	0.91	0.643	0.025	0.005	0.014
Ele./Oxide (wt.%)	Cu	Ba XRF	V	Cr	Cl	As	Ni	Co	Sn	Sr	Zr	Na	LOI 371	LOI 900
SL-012	0.004	0.163	0.01	0.02	0.026	-0	0.003	0.003	-0	0.01	0.019	0.04	-0.82	-5.34
SLSH-02	0.014	0.133	0.013	0.02	0.005	-0	0.006	0.016	0.001	0.024	0.022	0.07	-0.58	-5.35
SLSH-02 Rpt	0.014	0.132	0.013	0.02	0.004	-0	0.006	0.016	-0	0.022	0.021	0.06	-0.58	-5.34

Several slag iron samples were qualitatively analysed by XRD (X-Ray Diffraction analysis for the mineralogy. A typical XRD pattern for one of the specimens-SLSH-01 is shown in Figure 4 The major and minor minerals identified in the sample were: fayalite (Fe_2SiO_4), hercynite ($FeAl_2O_4$), wüstite (FeO), quartz (SiO_2), magnetite (Fe_3O_4), maghemite (Fe_2O_3), hematite (Fe_2O_3) and cohenite (Fe_3C).

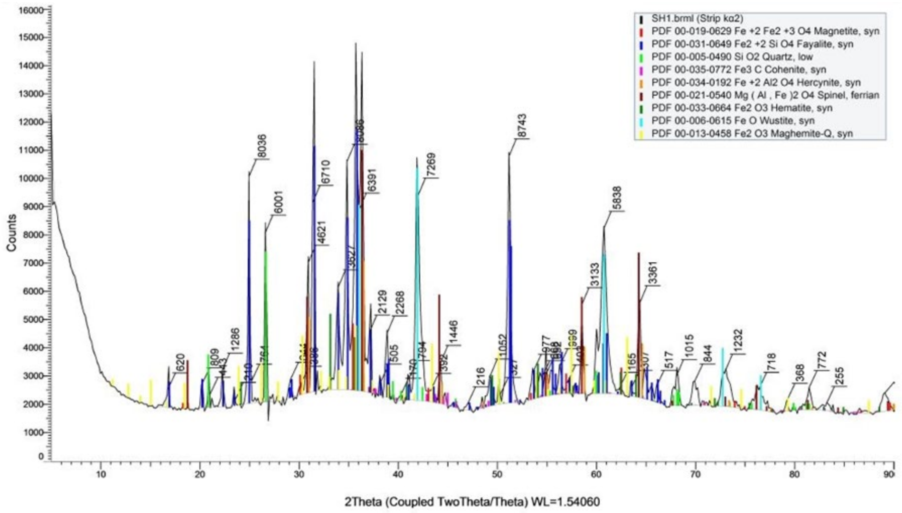

FIG 4 – XRD pattern for the slag iron sample SLSH-01.

Several representative slag iron samples were mounted in 25 mm round polished blocks. Despite the slag samples being sourced from various locations, the textures and mineralogy of the slag samples were alike with typical textures characterised by a network of wüstite formed within a matrix of fayalite, spinel, and glass. The major and minor mineral phases identified in all the studied slag iron samples were: wüstite (FeO), olivine-fayalite ($FeSiO_4$), spinel (hercynite-$FeAl_2O_4$), metallic iron (Fe) and a glass phase. Under the optical microscope wüstite, hercynite, fayalite, metallic iron, glass, hematite, goethite, minor quartz (embedded) and some flux particles were recognised. Within two iron slag samples (Figure 5b) relict charcoal particles (most cell structures are replaced with goethite) were identified. In optical images shown in Figure 5a, predominantly wüstite in a fayalite/spinel (hercynite)/minor glass matrix can be seen. Most of the large spinel crystals displayed zoning and some spinel particles contained wüstite inclusions. The edges of some of the large spinel particles were recognised as being converted into wüstite. In the SEM backscattered electron image shown in Figure 5c, metallic Fe particles and wüstite can be seen in a fayalite/spinel (hercynite/glass) matrix while in Figure 5d, few metallic Fe particles and a network of wüstite can be recognised in a spinel (hercynite) glass matrix. In a colour enhanced SEM backscattered electron image (Figure 5f), wüstite (orange), metallic Fe (red), fayalite (green), spinel-hercynite (blue and light blue) and glass (dark blue) can be recognised. Spinel (hercynite) crystals (in Figure 5f) clearly display zoning within individual crystals.

The polished samples were coated with a thin (10 nm) carbon film using a QT150T (Quorum Technologies) carbon coater before examination by EPMA. A JXA 8200 Electron Probe Microanalyzer fitted with five Wavelength Dispersive (WD) detectors were used for the compositional analyses. The analyses were conducted at an accelerating voltage of 15 kV and a probe current of 15 nA. The standards used for quantitative analysis were from Charles M. Taylor Co. (Stanford, California) and included: hematite (Fe_2O_3) for Fe, kyanite (Al_2SiO_5) for Al, pure MgO standard for Mg, rutile (TiO_2) for Ti and wollastonite ($CaSiO_3$) for Ca and Si. The METAL-ZAF correction (atomic number: Z, adsorption: A, fluorescence: F) procedure supplied with the electron probe was applied to all analysis to correct for matrix effects. The average accuracy of the EPMA measurements was estimated to be 1 wt. per cent. Both Fe^{2+} and Fe^{3+} are present in the samples, however, only the metal cation concentrations can be measured by EPMA. For the presentation purposes only therefore, all iron cation weight percentages measured by EPMA were converted to oxide percentages such as 'Fe_2O_3' from the measured Fe wt. per cent.

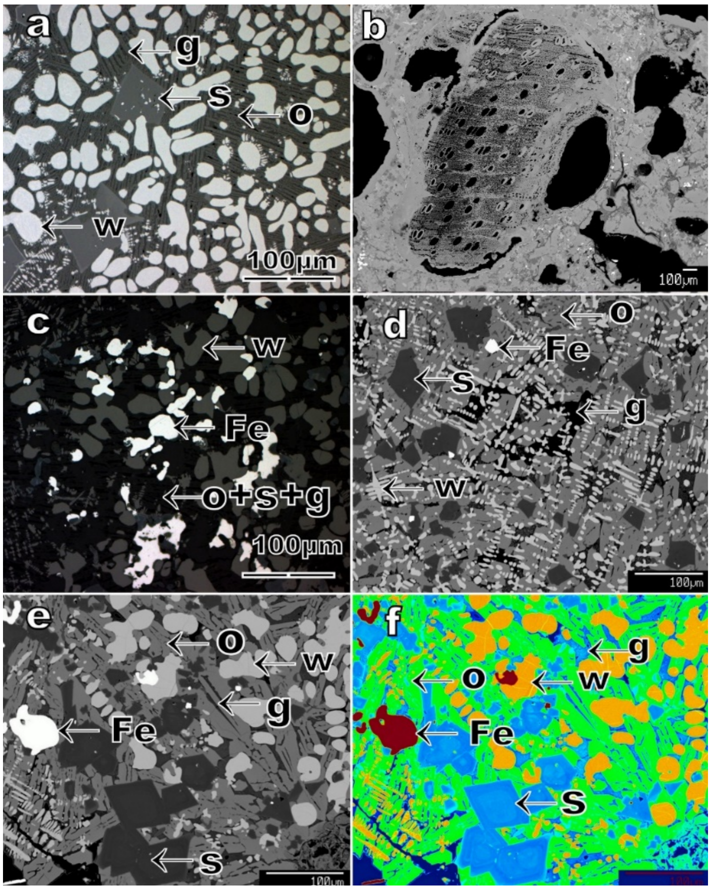

FIG 5 – Representative optical micrographs and SEM backscattered electron images of the iron slag samples: a) optical micrographs displaying the typical slag iron mineralogy and textures, b) SEM backscattered electron image displaying a preserved charcoal particle in the slag, c), d). and e) SEM backscattered electron images displaying typical slag iron mineralogy and textures, and f) colour enhanced SEM image the image shown in (e) (orange = wüstite, green = olivine (fayalite),

dark blue = slag (glass), light blue = spinel (hercynite), red = metallic iron). Key to abbreviations used: W = wüstite, O = olivine (fayalite), g = slag (glass), s = spinel (hercynite), Fe = metallic iron.

Table 2 displays the average (STDEV is in brackets) EPMA analysis data from individual mineral phases in several slag iron samples studied. The main aim was to locate the phosphorus containing phases/phase within the slag samples. In slag sample SLSH-01 the main mineral/metal/amorphous phases identified were metal-Fe, glass phase, silicate minerals within glass, pyrolusite, goethite, fayalite (olivine), spinel, and wüstite. Fayalite and goethite contained significant amounts of Mn (>5 wt. per cent) and minor amounts of Mn in glass (average 1.4 wt. per cent). The most significant observation was that phosphorus was mainly concentrated within the glass phase with an average content of 1.7 wt. per cent P). In sample SL-10, metal-Fe, fayalite, glass phase, spinel and two wüstite phases (Fe 74 wt. per cent and Fe 78 wt. per cent) were the main phases analysed. Phosphorus contents were significantly low in all phases however, compared to an average of 0.9 wt. per cent P recognised in the glass phase. In sample SLSH-4S, metal-Fe, fayalite, glass, spinel and wüstite were the main phases analysed. In the slag sample SLSH-09 metal-Fe was not present, and the main mineral phases identified were fayalite, spinel, wüstite, glass phases and secondary minerals such as goethite (filling cell structures in relict charcoal) and hydro-hematite along cell structures. In slag sample SLSH-02, the main mineral/metal and amorphous phases analysed were metal-Fe, fayalite, wüstite, spinel, magnetite, glass phase, minor hydro-hematite, minor pyrolusite and some quartz particles (most likely mixed with slag at a later stage). The phosphorus content in most of the mineral phases analysed was very low. In comparison, the glass phase had an average phosphorus content of 1.2 wt. per cent P. In slag sample SL-012, the main mineral/metal/amorphous phases identified were metal-Fe, fayalite, glass phase, spinel, wüstite, silicate minerals within glass, magnetite, and secondary minerals such as goethite and hydro-hematite (both were related to later infillings of cell structures in relict charcoal preserved in the slag). Phosphorus was mainly concentrated within the glass phase which had an average phosphorus content of 1.2 wt. per cent P. In slag sample SLSH-03, metal-Fe was absent, and the main mineral/amorphous phases analysed were fayalite, glass, spinel, wüstite, hematite and minor particles of quartz. Like the other slag samples, the phosphorus was mainly concentrated within glass with an average of 1.29 wt. per cent P.

The EPMA data strongly suggest that in the Sri Lankan iron slag samples, phosphorus has been preferentially partitioned into the slag phase instead of reporting to the metal. This observation suggests that possibly, the presence of the Ca oxalate derived from the charcoal has a positive effect during ironmaking in that it leads to lower P levels in the hot metal. This observation was therefore explored further through preliminary reduction experiments whereby the P-rich iron ore was fluxed with Ca oxalate. The experimental procedure and results are detailed in the following section.

TABLE 2

Quantitative EPMA analysis data for the mineral phases in the iron slag samples.

Sample No.	Phase	O	Si	Ca	Fe	Mn	Al	P	Ti	Mg	Total	No. of analysis
SLSH-01	Metal-Fe	0.27(0.18)	0.01(0.03)	0(0)	100.63(0.26)	0.25(0.29)	0.02(0.08)	0.01(0.02)	0.01(0.01)	0(0.01)	101.21(0.55)	16
SLSH-01	Slag (glass)	39.24(1.31)	16.21(1.66)	8.19(1.55)	19.23(1.25)	1.41(0.63)	9.07(0.79)	**1.7(0.34)**	0.49(0.33)	0.02(0.01)	95.56(1.7)	8
SLSH-01	Silicate	47.27(0.66)	30.98(0.42)	0.57(0.17)	4.73(0.3)	0.37(0)	9.73(0.17)	0(0)	0.01(0.01)	0.08(0.02)	93.76(0.77)	2
SLSH-01	Pyrolusite	36.34(0.92)	0.29(0.26)	0.22(0.23)	0.83(0.87)	62.35(1.07)	0.97(0.42)	0.03(0.04)	0(0)	0.32(0.38)	101.35(1.62)	3
SLSH-01	Goethite	29.93(0.41)	0.29(0.18)	0.19(0.28)	61.11(1.74)	6.84(1.93)	0.25(0.19)	0.08(0.13)	0.03(0.04)	0.26(0.33)	98.98(2.39)	5
SLSH-01	Olivine (Fayalite)	33.41(0.34)	14.2(0.23)	0.53(0.22)	46.13(1.34)	5.35(1.08)	0.25(0.35)	0.19(0.09)	0.05(0.05)	1.18(0.43)	101.3(0.7)	17
SLSH-01	Spinel	37.62(0.55)	0.13(0.04)	0(0)	32.81(0.44)	2.27(0.41)	27.76(0.22)	0.01(0.01)	0.34(0.08)	1.17(0.07)	102.11(0.63)	13
SLSH-01	Wüstite	24.47(0.37)	0.18(0.15)	0.2(0.41)	73.58(0.69)	1.25(0.69)	0.38(0.14)	0.14(0.26)	0.42(0.22)	0.06(0.01)	100.68(0.66)	10
SL-10	Metal-Fe	0.02(0.04)	0.03(0.06)	0(0)	100.54(0.4)	0.23(0.06)	0.06(0.11)	0.02(0.02)	0.02(0.03)	0.01(0.01)	100.91(0.5)	6
SL-10	Olivine (Fayalite)	33.46(1.6)	13.56(1.02)	1.54(0.67)	44.87(1.76)	6.16(1.02)	0.35(0.36)	0.4(0.1)	0.06(0.05)	1.74(0.56)	101.87(3.61)	22
SL-10	Slag (glass)	36.34(0.3)	15.66(0.24)	11.04(0.24)	20.26(0.83)	1.69(0.12)	8.65(0.54)	**0.9(0.2)**	0.31(0.07)	0.07(0.02)	94.03(0.65)	20
SL-10	Spinel	38.63(1.96)	0.09(0.04)	0.01(0.02)	30.04(1.1)	2.15(0.38)	29.57(0.96)	0.02(0.01)	0.18(0.09)	2.5(0.69)	103.17(2.46)	28
SL-10	Wüstite-1	23.67(1.34)	0.11(0.09)	0.04(0.1)	74.24(1.57)	2.25(0.57)	0.49(0.19)	0.03(0.06)	0.45(0.24)	0.1(0.02)	101.36(2.61)	26
SL-10	Wüstite-2	17.67(0.37)	0.08(0.01)	0(0)	78.88(1.04)	2.19(0.09)	0.23(0)	0.01(0.01)	0.19(0.01)	0.05(0.01)	99.29(0.53)	3
SLSH-4S	Metal-Fe	0.74(0.92)	0.03(0.06)	0(0)	100.22(0.58)	0.22(0.38)	0.33(0.41)	N/A	0.05(0.04)	0.02(0.02)	101.39(0.58)	7
SLSH-4S	Olivine (Fayalite)	35.79(0.35)	14.11(0.14)	1.1(0.66)	46.23(1.06)	1.48(0.47)	0.34(0.38)	N/A	0.08(0.04)	1.07(0.23)	100.21(0.65)	23
SLSH-4S	Slag (glass)	41.03(2.23)	18.07(1.86)	6.66(1.28)	14.06(2.85)	0.79(0.5)	10.42(1.56)	N/A	0.3(0.28)	0.04(0.02)	91.37(3.77)	14
SLSH-4S	Spinel	39.49(0.35)	0.1(0.04)	0.01(0.01)	28.99(0.82)	0.89(0.52)	27.84(0.24)	N/A	0.39(0.05)	1.42(0.09)	98.27(0.67)	10
SLSH-4S	Wüstite	24.67(0.26)	0.12(0.13)	0(0.01)	73.93(0.73)	0.41(0.41)	0.12(0.06)	N/A	0.2(0.04)	0.06(0.04)	99.51(0.76)	10
SLSH-09	Metal-Fe	0.3(0.14)	0.08(0.23)	0.01(0.02)	101.15(0.59)	0.11(0.17)	0.03(0.09)	N/A	0.02(0.03)	0.02(0.02)	101.72(0.55)	10
SLSH-09	Goethite (wood cell filling)	34.14(5.74)	2.39(1.24)	0.25(0.59)	58.29(3.98)	0.42(0.86)	0.42(0.96)	N/A	0.06(0.09)	0.05(0.11)	96.01(1.52)	6
SLSH-09	Hematite (hydro-hematite)	25.59(4.11)	1.57(0.27)	0.26(0.37)	68.48(1.9)	1.05(1.47)	0.75(1.02)	N/A	0.18(0.23)	0.1(0.15)	97.99(0.76)	4
SLSH-09	Olivine (Fayalite)	30.9(0.61)	14.25(0.19)	0.38(0.12)	47.36(1.35)	3.91(0.09)	0.14(0.05)	N/A	0.04(0.04)	1.83(0.98)	98.82(0.9)	17
SLSH-09	Slag (glass1)	33.1(2.22)	17.16(1.35)	6.05(3.38)	21.65(3.15)	0.92(0.4)	7.42(1.07)	N/A	0.24(0.12)	0.02(0.01)	86.55(4.79)	8
SLSH-09	Slag (glass2)	33.13(0.63)	16.98(0.22)	7.85(0.08)	14.24(0.38)	1.26(0.05)	10.66(0.18)	N/A	0.08(0.04)	0.13(0.01)	84.33(0.69)	6
SLSH-09	Spinel	35.96(1.27)	0.16(0.23)	0.05(0.16)	32.21(1.05)	1.41(0.14)	28.12(0.9)	N/A	0.31(0.15)	1.91(0.36)	100.13(1.4)	20
SLSH-09	Wüstite	22.82(1.88)	0.26(0.32)	0.04(0.07)	73.64(1.03)	1.47(0.69)	0.41(0.19)	N/A	0.36(0.25)	0.16(0.14)	99.16(0.87)	23
SLSH-02	Metal-Fe	0.3(0.02)	0.01(0.01)	0.01(0.01)	103.25(1.55)	0.05(0.03)	0(0)	0(0.01)	0.01(0.01)	0.01(0.01)	103.63(0)	6
SLSH-02	Olivine (Fayalite)	33.09(0.94)	13.78(1.64)	0.75(0.94)	47.15(2.24)	5.06(1.31)	0.19(0.21)	0.21(0.11)	0.04(0.03)	1.23(0.78)	101.47(1.31)	32
SLSH-02	Spinel	37.24(0.72)	0.13(0.05)	0(0.01)	32.62(1.69)	2.09(0.5)	27.66(0.66)	0.01(0.01)	0.35(0.16)	1.56(0.65)	101.66(1.57)	20
SLSH-02	Wüstite	23.89(0.95)	0.13(0.1)	0(0.01)	74.15(0.84)	1.71(0.58)	0.49(0.25)	0.01(0.02)	0.36(0.16)	0.1(0.08)	100.84(0.87)	24
SLSH-02	magnetite	29.83(2.08)	0.34(0.5)	0.01(0.02)	70.4(1.23)	0.46(0.51)	0.08(0.1)	0.03(0.02)	0.08(0.2)	0.02(0.04)	101.25(0.75)	7
SLSH-02	Slag (glass)	38.53(3.25)	16.64(1.47)	6.95(2.38)	20.48(2.5)	1.91(0.77)	8.4(1.58)	**1.23(0.74)**	0.47(0.5)	0.37(1.43)	94.8(5.28)	20
SLSH-02	Pyrolusite	37.82(0.88)	0.12(0.06)	0.13(0.15)	0.57(0.55)	57.77(3.13)	1.82(0.93)	0.03(0.03)	0(0)	0.08(0.09)	98.34(1.81)	8
SLSH-02	Hematite (hydro-hematite)	31.66(1.55)	0.38(0.19)	0.18(0.26)	63.89(1.09)	2.77(3.6)	0.17(0.14)	0.21(0.2)	0.03(0.03)	0.18(0.29)	99.47(1.54)	4
SLSH-02	Quartz	54.59(0.06)	47.24(0.01)	0(0)	0.37(0.21)	0.33(0.47)	0.01(0.01)	0.02(0.02)	0.01(0.01)	0(0)	102.57(0.61)	4
SL-012	Metal-Fe	0.02(0.03)	0.01(0.01)	0(0)	100.73(0.66)	0.04(0.03)	0(0.01)	0.01(0.01)	0.01(0.02)	0(0.01)	100.83(0.66)	37
SL-012	hematite)	31.25(0.87)	0.78(0.85)	0(0)	64.71(2.51)	0.05(0.02)	0.01(0.01)	0.01(0.01)	0.03(0.02)	0(0)	96.84(2.49)	4
SL-012	Goethite (cell)	40.38(0.78)	2.65(0.07)	0.35(0.07)	43.06(0.35)	0.24(0.01)	8.67(0.71)	0.18(0.02)	0.04(0)	0.58(0.01)	96.14(0.39)	2
SL-012	magnetite	29.43(0.66)	0.29(0.06)	0(0)	70.35(0.38)	0.07(0.03)	0(0)	0(0.01)	0.01(0.01)	0(0)	100.15(0.93)	5
SL-012	Olivine (Fayalite)	34.14(0.61)	14.36(0.12)	0.62(0.31)	45.37(1.13)	5.03(0.42)	0.2(0.07)	0.11(0.05)	0.04(0.03)	2.09(0.55)	101.95(0.78)	30
SL-012	Slag (glass)	35.27(1.31)	16.65(0.91)	7.81(0.76)	19.51(2.98)	1.52(0.35)	8.16(0.7)	**1.22(0.18)**	0.17(0.07)	0.09(0.07)	90.39(1.69)	58
SL-012	Spinel	39.81(0.76)	0.1(0.1)	0(0.01)	30.31(1.84)	1.67(0.08)	29.15(1.04)	0.01(0.01)	0.18(0.21)	2.7(0.67)	103.92(0.72)	31
SL-012	Wüstite	24.97(1.54)	0.09(0.06)	0(0)	73.49(0.96)	1.83(0.59)	0.45(0.15)	0.01(0.01)	0.22(0.13)	0.29(0.18)	101.34(0.98)	31
SL-012	Silicate (glass)	43.29(1.75)	31.01(0.61)	1.43(0.23)	1.25(1.28)	0.09(0.09)	10.75(1.54)	0(0.01)	0.02(0.02)	0.03(0.03)	87.86(4.47)	6
SL-012	Silicate (glass)	37.45(1.03)	19.31(0.05)	2.48(0.06)	30.58(0.37)	0.94(0.02)	6.13(0.1)	0.18(0.01)	0.21(0)	0.58(0.03)	97.86(1.25)	6
SLSH-03	Olivine (Fayalite)	32.92(0.69)	14.11(0.15)	0.72(0.47)	48.28(1.36)	2.77(0.48)	0.21(0.07)	0.12(0.03)	0.03(0.02)	1.65(0.34)	100.82(1.09)	11
SLSH-03	Slag (glass)	36.54(0.74)	16.96(1.13)	10.3(0.75)	17.28(1.94)	0.72(0.32)	8.59(0.61)	**1.29(0.22)**	0.07(0.04)	0.07(0.09)	91.82(1.31)	45
SLSH-03	Spinel	36.19(0.04)	0.34(0.09)	0(0)	40.25(0.22)	0.76(0)	23.59(0.55)	0.02(0)	0.56(0)	0.14(0)	101.84(0.72)	5
SLSH-03	Wüstite	24.2(0.56)	0.12(0.08)	0(0.01)	74.43(0.37)	0.98(0.35)	0.5(0.07)	0.01(0.01)	0.19(0.14)	0.2(0.14)	100.63(0.91)	11
SLSH-03	Hematite	29.76(0.2)	0(0)	0.08(0.03)	70.71(0.52)	0.18(0.03)	0.26(0.07)	0(0)	0.04(0.04)	0(0)	101.03(0.61)	5
SLSH-03	Quartz	53.96(1.33)	46.37(0.4)	0(0)	0.16(0.02)	0.02(0.02)	0(0)	0.01(0.01)	0.02(0.03)	0(0)	100.54(1.8)	5

TABLE 2 continued.

Sample No.	Phase	O	Si	Ca	Fe	Mn	Al	P	Ti	Mg	Total	No. of analysis
SLSH-01	Metal-Fe	0.27(0.18)	0.01(0.03)	0(0)	100.63(0.26)	0.25(0.29)	0.02(0.08)	0.01(0.02)	0.01(0.01)	0(0.01)	101.21(0.55)	16
SLSH-01	Slag (glass)	39.24(1.31)	16.21(1.66)	8.19(1.55)	19.23(1.25)	1.41(0.63)	9.07(0.79)	**1.7(0.34)**	0.49(0.33)	0.02(0.01)	95.56(1.7)	8
SLSH-01	Silicate	47.27(0.66)	30.98(0.42)	0.57(0.17)	4.73(0.3)	0.37(0)	9.73(0.17)	0(0)	0.01(0.01)	0.08(0.02)	93.76(0.77)	2
SLSH-01	Pyrolusite	36.34(0.92)	0.29(0.26)	0.22(0.23)	0.83(0.87)	62.35(1.07)	0.97(0.42)	0.03(0.04)	0(0)	0.32(0.38)	101.35(1.62)	3
SLSH-01	Goethite	29.93(0.41)	0.29(0.18)	0.19(0.28)	61.11(1.74)	6.84(1.93)	0.25(0.19)	0.08(0.13)	0.03(0.04)	0.26(0.33)	98.98(2.39)	5
SLSH-01	Olivine (Fayalite)	33.41(0.34)	14.2(0.23)	0.53(0.22)	46.13(1.34)	5.35(1.08)	0.25(0.35)	0.19(0.09)	0.05(0.05)	1.18(0.43)	101.3(0.7)	17
SLSH-01	Spinel	37.62(0.55)	0.13(0.04)	0(0)	32.81(0.44)	2.27(0.41)	27.76(0.22)	0.01(0.01)	0.34(0.08)	1.17(0.07)	102.11(0.63)	13
SLSH-01	Wüstite	24.47(0.37)	0.18(0.15)	0.2(0.41)	73.58(0.69)	1.25(0.69)	0.38(0.14)	0.14(0.26)	0.42(0.22)	0.06(0.01)	100.68(0.66)	10
SL-10	Metal-Fe	0.02(0.04)	0.03(0.06)	0(0)	100.54(0.4)	0.23(0.06)	0.06(0.11)	0.02(0.02)	0.02(0.03)	0.01(0.01)	100.91(0.5)	6
SL-10	Olivine (Fayalite)	33.46(1.6)	13.56(1.02)	1.54(0.67)	44.87(1.76)	6.16(1.02)	0.35(0.36)	0.4(0.1)	0.06(0.05)	1.74(0.56)	101.87(3.61)	22
SL-10	Slag (glass)	36.34(0.3)	15.66(0.24)	11.04(0.24)	20.26(0.83)	1.69(0.12)	8.65(0.54)	**0.9(0.2)**	0.31(0.07)	0.07(0.02)	94.03(0.65)	20
SL-10	Spinel	38.63(1.96)	0.09(0.04)	0.01(0.02)	30.04(1.1)	2.15(0.38)	29.57(0.96)	0.02(0.01)	0.18(0.09)	2.5(0.69)	103.17(2.46)	28
SL-10	Wüstite-1	23.67(1.34)	0.11(0.09)	0.04(0.1)	74.24(1.57)	2.25(0.57)	0.49(0.19)	0.03(0.06)	0.45(0.24)	0.1(0.02)	101.36(2.61)	26
SL-10	Wüstite-2	17.67(0.37)	0.08(0.01)	0(0)	78.88(1.04)	2.19(0.09)	0.23(0)	0.01(0.01)	0.19(0.01)	0.05(0.01)	99.29(0.53)	3
SLSH-4S	Metal-Fe	0.74(0.92)	0.03(0.06)	0(0)	100.22(0.58)	0.01(0.02)	0.33(0.41)	N/A	0.05(0.04)	0.02(0.02)	101.39(0.58)	7
SLSH-4S	Olivine (Fayalite)	35.79(0.35)	14.11(0.14)	1.1(0.66)	35.74(0.56)	0.07(0.02)	0.34(0.38)	N/A	0.08(0.04)	1.07(0.23)	88.3(0.68)	23
SLSH-4S	Slag (glass)	39.96(3.27)	17.57(1.86)	5.59(1.3)	12.79(3.02)	0.02(0.02)	10.42(1.56)	N/A	0.3(0.28)	0.02(0.02)	86.68(5.07)	14
SLSH-4S	Spinel	39.49(0.35)	0.1(0.04)	0.01(0.01)	28.99(0.82)	0.04(0.03)	27.84(0.24)	N/A	0.39(0.05)	1.42(0.09)	98.27(0.67)	10
SLSH-4S	Wüstite	24.67(0.26)	0.12(0.13)	0(0.01)	73.93(0.73)	0.02(0.02)	0.12(0.06)	N/A	0.2(0.04)	0.06(0.04)	99.12(0.7)	10
SLSH-09	Metal-Fe	0.3(0.14)	0.08(0.23)	0.01(0.02)	101.15(0.59)	0.11(0.17)	0.03(0.09)	N/A	0.02(0.03)	0.02(0.02)	101.72(0.55)	10
SLSH-09	Goethite (wood cell filling)	34.14(5.74)	2.39(1.24)	0.25(0.59)	58.29(3.98)	0.42(0.86)	0.42(0.96)	N/A	0.06(0.09)	0.05(0.11)	96.01(1.52)	6
SLSH-09	Hematite (hydro-hematite)	25.59(4.11)	1.57(0.27)	0.26(0.37)	68.48(1.9)	1.05(1.47)	0.75(1.02)	N/A	0.18(0.23)	0.1(0.15)	97.99(0.76)	4
SLSH-09	Olivine (Fayalite)	30.9(0.61)	14.25(0.19)	0.38(0.12)	47.36(1.35)	3.91(0.09)	0.14(0.05)	N/A	0.04(0.04)	1.83(0.98)	98.82(0.9)	17
SLSH-09	Slag (glass)	33.1(2.22)	17.16(1.35)	6.05(3.38)	21.65(3.15)	0.92(0.4)	7.42(1.07)	N/A	0.24(0.12)	0.02(0.01)	86.55(4.79)	8
SLSH-09	Slag (glass)	33.13(0.63)	16.98(0.22)	7.85(0.08)	14.24(0.38)	1.26(0.05)	10.66(0.18)	N/A	0.08(0.04)	0.13(0.01)	84.33(0.69)	6
SLSH-09	Spinel	35.96(1.27)	0.16(0.23)	0.05(0.16)	32.21(1.05)	1.41(0.14)	28.12(0.9)	N/A	0.31(0.15)	1.91(0.36)	100.13(1.4)	20
SLSH-09	Wüstite	22.82(1.88)	0.26(0.32)	0.04(0.07)	73.64(1.03)	1.47(0.69)	0.41(0.19)	N/A	0.36(0.25)	0.16(0.14)	99.16(0.87)	23
SLSH-02	Metal-Fe	0.3(0.02)	0.01(0.01)	0.01(0.01)	103.25(1.55)	0.05(0.03)	0(0)	0(0.01)	0.01(0.01)	0.01(0.01)	103.63(0)	6
SLSH-02	Olivine (Fayalite)	33.09(0.94)	13.78(1.64)	0.75(0.94)	47.15(2.24)	5.06(1.31)	0.19(0.21)	0.21(0.11)	0.04(0.03)	1.23(0.78)	101.47(1.31)	32
SLSH-02	Spinel	37.24(0.72)	0.13(0.05)	0(0.01)	32.62(1.69)	2.09(0.5)	27.66(0.66)	0.01(0.01)	0.35(0.16)	1.56(0.65)	101.66(1.57)	20
SLSH-02	Wüstite	23.89(0.95)	0.13(0.1)	0(0.01)	74.15(0.84)	1.71(0.58)	0.49(0.25)	0.01(0.02)	0.36(0.16)	0.1(0.08)	100.84(0.87)	24
SLSH-02	magnetite	29.83(2.08)	0.34(0.5)	0.01(0.02)	70.4(1.23)	0.46(0.51)	0.08(0.1)	0.03(0.02)	0.08(0.2)	0.02(0.04)	101.25(0.75)	7
SLSH-02	Slag (glass)	38.53(3.25)	16.64(1.47)	6.95(2.38)	20.48(2.5)	1.91(0.77)	8.4(1.58)	**1.23(0.74)**	0.47(0.5)	0.37(1.43)	94.8(5.28)	20
SLSH-02	Pyrolusite	37.82(0.88)	0.12(0.06)	0.13(0.15)	0.57(0.55)	57.77(3.13)	1.82(0.93)	0.03(0.03)	0(0)	0.08(0.09)	98.34(1.81)	8
SLSH-02	Hematite (hydro-hematite)	31.66(1.55)	0.38(0.19)	0.18(0.26)	63.89(1.09)	2.77(3.6)	0.17(0.14)	0.21(0.2)	0.03(0.03)	0.18(0.29)	99.47(1.54)	4
SLSH-02	Quartz	54.59(0.06)	47.24(0.01)	0(0)	0.37(0.21)	0.33(0.47)	0.01(0.01)	0.02(0.02)	0.01(0.01)	0(0)	102.57(0.61)	4
SL-012	Metal-Fe	0.02(0.03)	0.01(0.01)	0(0)	100.73(0.66)	0.04(0.03)	0(0.01)	0.01(0.01)	0.01(0.02)	0(0.01)	100.83(0.66)	37
SL-012	hematite)	31.25(0.87)	0.78(0.85)	0(0)	64.71(2.51)	0.05(0.02)	0.01(0.01)	0.01(0.01)	0.03(0.02)	0(0)	96.84(2.49)	4
SL-012	Goethite (cell)	40.38(0.78)	2.65(0.07)	0.35(0.07)	43.06(0.35)	0.24(0.01)	8.67(0.71)	0.18(0.02)	0.04(0)	0.58(0.01)	96.14(0.39)	2
SL-012	magnetite	29.43(0.66)	0.29(0.06)	0(0)	70.35(0.38)	0.07(0.03)	0(0)	0(0.01)	0.01(0.01)	0(0)	100.15(0.93)	5
SL-012	Olivine (Fayalite)	34.14(0.61)	14.36(0.12)	0.62(0.31)	45.37(1.13)	5.03(0.42)	0.2(0.07)	0.11(0.05)	0.04(0.03)	2.09(0.55)	101.95(0.78)	30
SL-012	Slag (glass)	35.27(1.31)	16.65(0.91)	7.81(0.76)	19.51(2.98)	1.52(0.35)	8.16(0.7)	**1.22(0.18)**	0.17(0.07)	0.09(0.07)	90.39(1.69)	58
SL-012	Spinel	39.81(0.76)	0.1(0.1)	0(0.01)	30.31(1.84)	1.67(0.08)	29.15(1.04)	0.01(0.01)	0.18(0.21)	2.7(0.67)	103.92(0.72)	31
SL-012	Wüstite	24.97(1.54)	0.09(0.06)	0(0)	73.49(0.96)	1.83(0.59)	0.45(0.15)	0.01(0.01)	0.22(0.13)	0.29(0.18)	101.34(0.98)	31
SL-012	Silicate (glass)	43.29(1.75)	31.01(0.61)	1.43(0.23)	1.25(1.28)	0.09(0.09)	10.75(1.54)	0(0.01)	0.02(0.02)	0.03(0.03)	87.86(4.47)	6
SL-012	Silicate (glass)	37.45(1.03)	19.31(0.05)	2.48(0.06)	30.58(0.37)	0.94(0.02)	6.13(0.1)	0.18(0.01)	0.21(0)	0.58(0.03)	97.86(1.25)	6
SLSH-03	Olivine (Fayalite)	32.92(0.69)	14.11(0.15)	0.72(0.47)	48.28(1.36)	2.77(0.48)	0.21(0.07)	0.12(0.03)	0.03(0.02)	1.65(0.34)	100.82(1.09)	11
SLSH-03	Slag (glass)	36.54(0.74)	16.96(1.13)	10.3(0.75)	17.28(1.94)	0.72(0.32)	8.59(0.61)	**1.29(0.22)**	0.07(0.04)	0.07(0.09)	91.82(1.31)	45
SLSH-03	Spinel	36.19(0.04)	0.34(0.09)	0(0)	40.25(0.22)	0.76(0)	23.59(0.55)	0.02(0)	0.56(0)	0.14(0)	101.84(0.72)	5
SLSH-03	Wüstite	24.2(0.56)	0.12(0.08)	0(0.01)	74.43(0.37)	0.98(0.35)	0.5(0.07)	0.01(0.01)	0.19(0.14)	0.2(0.14)	100.63(0.91)	11
SLSH-03	Hematite	29.76(0.2)	0(0)	0.08(0.03)	70.71(0.52)	0.18(0.03)	0.26(0.07)	0(0)	0.04(0.04)	0(0)	101.03(0.61)	5
SLSH-03	Quartz	53.96(1.33)	46.37(0.4)	0(0)	0.16(0.02)	0.02(0.02)	0(0)	0.01(0.01)	0.02(0.03)	0(0)	100.54(1.8)	5

IRON ORE REDUCIBILITY TESTS WITH Ca OXALATE

Analysis of Thermoanalytical curves of whewellite ($Ca(C_2O_4).\ H_2O$), or naturally occurring hydrated form of Ca oxalate, by Földvári (2011) has shown that whewellite has three stages of decomposition: first endothermic dehydration of crystalline water at 220–230°C via $Ca(C_2O_4).H_2O \rightarrow CaC_2O_4 + H_2O$; second, a combination of endothermic and exothermic reactions of elimination and burning of CO at around 500°C according to the reactions $CaC_2O_4 \rightarrow CaCO_3 + CO$ and $2CO + O_2 \rightarrow 2CO_2$ and; third, an exothermic reaction occurring at about 900°C involving the reaction $CaCO_3 \rightarrow CaO + CO_2$.

Preliminary reduction tests with high-phosphorus (P=0.135 wt. per cent) ore sample (Dukino, England and Kneeshaw, 2000), which was grinded to -1 mm size, doped with 10 per cent (wt.) calcium oxalate monohydrate: $Ca(C_2O_4)$. H_2O were conducted using a microwave heating facility and a CO/CO_2 gas ratio of 40/60. Details regarding the microwave heating apparatus were previously presented in Nunna, Hapugoda and Pownceby (2017) and Nunna *et al* (2021).

Table 3 summarises the reduction test conditions, the chemistry of the raw iron ore sample used and the reduced products after experiments conducted at the two temperatures, 800°C and 900°C. To examine the effect of the Ca oxalate on the partitioning of P in the reduced iron ore, we deliberately selected These two temperatures were selected as the complete decomposition of calcium oxalate is completed above 800°C according to the Thermoanalytical results described above. Results of heating experiments conducted in air and then in air with the addition of calcium oxalate indicated there was no FeO formed. However, when using the CO/CO_2 reduction atmosphere results, with or without calcium oxalate, showed a significant increase in the amount of FeO generated (up to 60 per cent increase) with the greatest amount occurring after doping with calcium oxalate.

TABLE 3

Results of quantitative phase analysis on the iron ore feed and the products after microwave heating under various conditions.

Sample	Test Tem. (C°)	Add./Air/ Red. Gas	FeO (wt.%)	Fe (wt.%)	SiO_2 (wt.%)	Al_2O_3 (wt.%)	TiO_2 (wt.%0	Mn (wt.%)	CaO (wt.%)	P (wt.%)	S (wt.%)	MgO (wt.%)	K_2O (wt.%)	Zn (wt.%)	Na_2O (wt.%)	LOI1200
HP-01	Raw Ore		-0.1	57.84	4.11	4.11	0.1	0.46	0.11	0.134	0	0.18	0.03	0.004	0.02	6.57
HP-17	800	Air	-0.1	61.75	5.61	4.45	0.11	0.51	0.11	0.143	-0	0.2	0.03	0.004	0.016	0.13
HP-18	800	CaOX/Air	-0.1	60.58	5.59	4.5	0.11	0.45	2.02	0.139	0.001	0.18	0.033	0.005	0.028	0.06
HP-19	800	CO/CO_2 40/60	5.33	61.87	5.93	4.6	0.12	0.44	0.1	0.145	-0	0.2	0.032	0.004	0.014	-0.51
HP-20	800	CaOX/CO/CO_2 40/60	8.84	61.37	5.5	4.34	0.11	0.44	1.92	0.141	0.001	0.18	0.032	0.004	0.02	-0.9
HP-21	900	Air	-0.1	61.75	5.71	4.49	0.11	0.36	0.1	0.14	0.002	0.18	0.028	0.005	0.013	0.13
HP-22	900	CaOX/Air	-0.1	60.75	5.46	4.31	0.11	0.48	1.78	0.14	0.012	0.2	0.029	0.004	0.022	0.11
HP-23	900	CO/CO_2 40/60	5.12	62.17	5.7	4.52	0.11	0.44	0.1	0.145	-0	0.18	0.029	0.004	0.017	-0.56
HP-24	900	CaOX/CO/CO_2 40/60	8.75	61.46	5.48	4.27	0.11	0.42	1.94	0.137	0.006	0.16	0.029	0.004	0.022	-0.88
HP-24 Rpt	900	CaOX/CO/CO_2 40/60	8.65	61.38	5.49	4.3	0.11	0.42	1.93	0.137	0.004	0.16	0.029	0.004	0.025	-0.82

The results of the phase identification and QPA using X-ray diffraction of the reduced products are given in Table 4. The QPA results are relative weight percentages and do not include any unidentified or amorphous material which may exist in the samples. Like the FeO content increase observed in the chemical analysis data, the XRD determination of magnetite contents in reduced products confirm the increased effect of doping with calcium oxalate as magnetite content increased by up to 50–65 per cent when using the calcium oxalate with compared to the use of CO/CO_2 without calcium oxalate addition. The results also indicated that small amounts of feldspar and SFCA (possibly the mineral khesinite) both formed only under the calcium oxalate doping conditions in air and in reducing gas atmospheres.

TABLE 4

Results of quantitative phase analysis (relative wt.% of crystalline phases) in reduced samples.

Sample	Test Tem. (C°)	Add./Air/ Red. Gas	Crystalline phase concentration (relative wt%)						
			Magnetite	Hematite	Quartz	Cristobalite	Mullite	Feldspar	Khesinite (SFCA?)
HP-17	800	Air		94.1	0.7	3	2.2		
HP-18	800	CaOX/Air		93.6	0.9	1.1	1.6	2.8	
HP-19	800	CO/CO_2	19.6	74.1	0.6	3.3	2.4		
HP-20	800	$CaOX/CO/CO_2$	29.9	62.9	0.7	1.7	1.7	2.4	0.7
HP-21	900	Air		94.9	0.4	3	1.7		
HP-22	900	CaOX/Air		93.3	0.3	1.4	2.1	1.9	1.1
HP-23	900	CO/CO_2	17.2	78	0.2	2.9	1.7		
HP-24	900	$CaOX/CO/CO_2$	32.1	60.1	0.3	1.7	2.1	1.6	2

Figure 6 shows representative SEM backscattered electron images (Figure 6a, Figure 6b and Figure 6c) and a comparison of phosphorus in slag (glass) and SFCA (Figure 6d) of the reduced P-rich iron ore sample (0.134 wt. per cent P) at 800°C doped with calcium oxalate (10 wt. per cent). It was observed that there were number of calcium phosphate crystals formed (Figure 6a, Figure 6b and Figure 6c) within the glass matrix in the calcium oxalate doped sample. To confirm the identity of (up to 17 wt. per cent) high-phosphate (up to 17 wt. per cent P) crystals, they were analysed by both SEM EDS and EPMA analysis and results indicated that they were in fact apatite crystals. Magnetite, hematite and SFCA were almost free from any phosphorus and, other than the individual apatite crystals, phosphorus was mainly located within the glass matrix which had significantly high phosphorus contents of up to 5 wt. per cent P (Figure 6d). There were comparatively very low or zero phosphorus contents noted within SFCA particles (see Figure 9a). The details of EPMA and SEM results of the slag phases are discussed later in the paper.

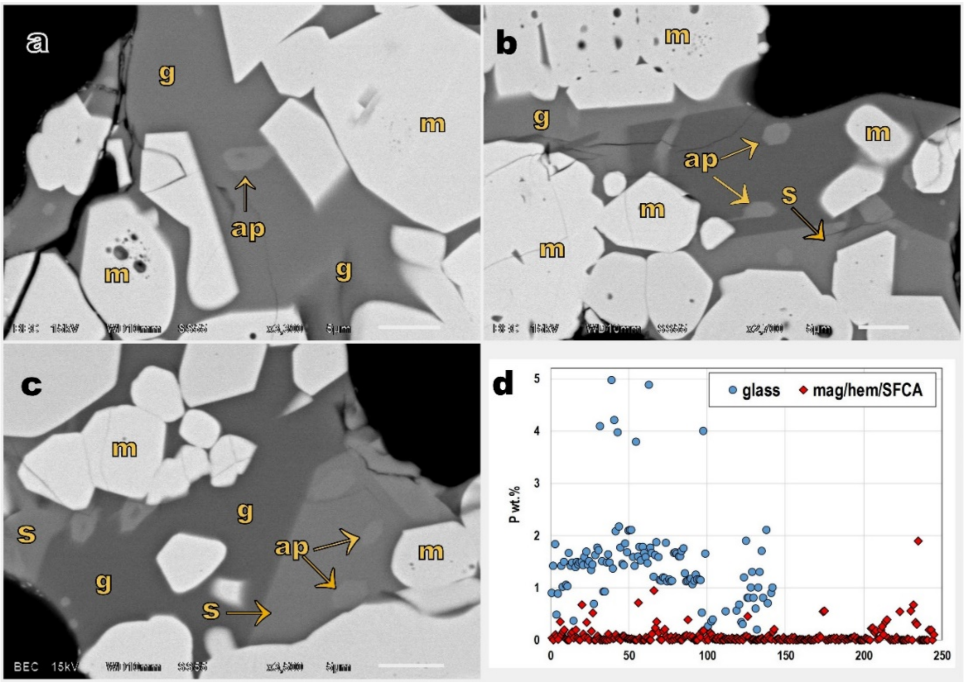

FIG 6 – SEM backscattered electron images of reduced sample at 800°C with CaOX, (a, b and c) and (d), plot of phosphorus contents in glass and slag of the P-rich iron ore sample doped with calcium oxalate (5 wt.%) and reduced at 800°C with CO/CO_2 40/60. Key to abbreviations used: g = glass, ap = apatite – $Ca_5PO_4.OH$, m = magnetite, h = hematite, s = SFCA.

SINTER ANALOGUES WITH CaOX AND $CaCO_3$

Sinter analogues were prepared to compare the effect of $CaCO_3$ when replaced with calcium oxalate with the same weight amount of each. Table 5 display the chemical composition of each sinter analogues and the calculated basicity is 2.5 and 1.7 respectively with $CaCO_3$ and calcium oxalate. In the complete reduction tests to test the behaviour of phosphorus the same conditions were used (same weights of $CaCO_3$ and calcium oxalate). Total time of sintering was 4 minutes, and all samples were quenched in water to cool them rapidly.

TABLE 5

Test conditions of sinter analogues with calcium oxalate and calcium carbonate.

Fe_2O_3 (g)	**SiO_2 (g)**	**$CaCO_3$ (g)**	**MgO (g)**	**$Al(OH)_3$ (g)**	**Total**	**Basicity**	**Temperature °C**
3.925	0.25	1.1161	0.1	0.1265	5.5176	2.5	1220, 1240, 1280, 1360, 1400
Fe_2O_3 (g)	**SiO_2 (g)**	**$Ca(C_2O_4).H_2O$ (g)**	**MgO (g)**	**$Al(OH)_3$ (g)**	**Total**	**Basicity**	**Temperature °C**
3.925	0.25	1.1161	0.1	0.1265	5.5176	1.7	1220, 1240, 1280, 1360, 1400

Figure 7 compare the sinter analogues prepared by using $CaCO_3$ (left column images of Figure 7) and calcium oxalate (right column images of Figure 7) at several temperatures. At lower temperatures of 1220°C and 1240°C both sinter from $CaCO_3$ and calcium oxalate displayed similar textures and slightly similar mineralogy. Amount of magnetite was always higher in calcium oxalate samples compare with the $CaCO_3$ samples. Samples sintered over 1280°C started to display very clear differences with each other. At 1280°C magnetite, skeletal hematite and glass contents were comparatively higher and SFCA was less in calcium oxalate sinter sample. At the temperatures of 1360°C and 1400°C the samples were totally different. SFCA was completely disappeared in calcium oxalate samples and at 1360°C and 1400°C magnetite/glass was the only mineral/amorphous phases observed in calcium oxalate sinter samples. As seen in Figure 7g and Figure 7i SFCA was still present in $CaCO_3$ sinter samples. The calculated sinter basicity of two sinter mixtures were 2.5 for the $CaCO_3$ tests and 1.7 for the calcium oxalate tests. In another test with same conditions in sinter samples prepared, some SFCA was still present at the basicity of 1.67 with $CaCO_3$ at the temperature condition of 1400°C.

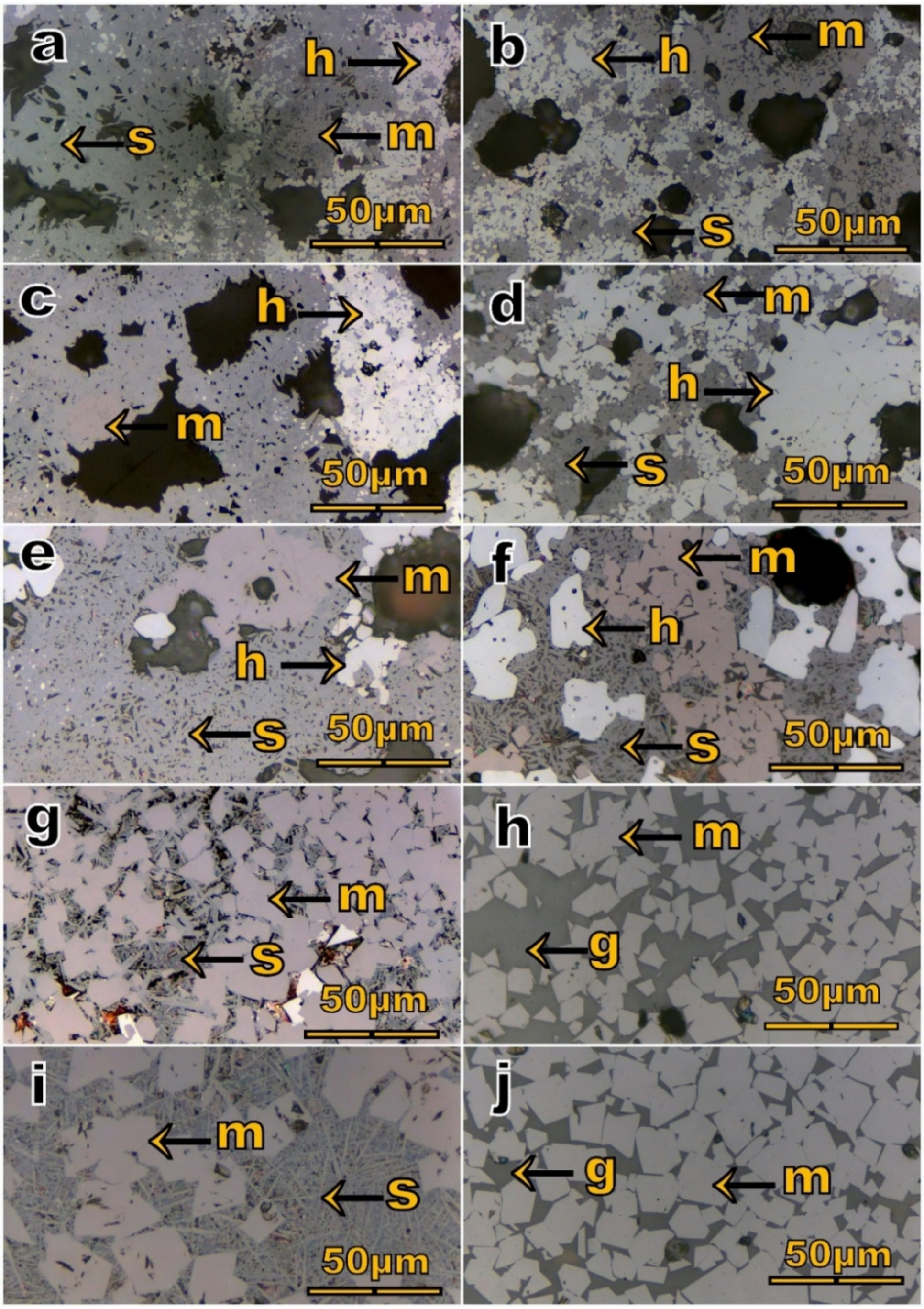

FIG 7 – Comparison of the sinter analogues prepared by using $CaCO_3$ (left column) and calcium oxalate (right column) at several temperatures. a) $CaCO_3$/1220°C, b) calcium oxalate/1220°C, c) $CaCO_3$/1240°C, d) calcium oxalate/1240°C, e) $CaCO_3$/1280°C, f) calcium oxalate/1280°C, g) $CaCO_3$/1360°C, h) calcium oxalate/1360°C, i) $CaCO_3$/1400°C, j) calcium oxalate/1400°C. Key to mineral phases: m=magnetite, S=SFCA, g=glass, h=hematite.

REDUCTION TESTS WITH $CaC_2O_4.H_2O$ AND $CaCO_3$

To further test the effect of calcium oxalate on partitioning of phosphorus during ironmaking, complete reduction tests to produce metallic iron and slag were conducted. Han *et al* (2014) explained a similar approach by completely reducing high-P iron ores doped with $CaCO_3$ and separating high-P containing glass from metallic iron by magnetic separation. There is a possibility of applying the similar technique to remove the metal-Fe from high-P glass from this process (doped with calcium oxalate) or use the calcium oxalate treated high-P ores in ironmaking process directly. It was also noted that the reduced samples doped with calcium oxalate were strong and difficult to crush compare to others. There is also a scope that calcium oxalate can be used in pellet making to increase the pellet strength. Su *et al* (2017), investigated the effect of high Na_2O addition for dephosphorisation efficiency of low-basicity converter slag and decrease the consumption of solid CaO. A reference sample of Brockman high-P ore with phosphorus content of 0.135 wt. per cent was selected. Compressed pellets were prepared by mixing 10 grams of -1 mm sized high-P ore, 3 g of coke, thoroughly mixed with either calcium oxalate or $CaCO_3$ (to examine if the effect was simply due to the presence of calcium) and a reference ore sample with coke without adding fluxes (Table 6). Samples were placed in graphite crucibles and were completely reduced separately in a horizontal furnace. At first the samples were slowly pre-heated to 900°C and kept for 15 minutes, and then the temperature was gradually increased to 1250°C for 30 minutes to allow the ore to be completely reduced to metal-Fe and slag. Samples were then removed from the furnace and let air-cooled.

TABLE 6

Complete reduction tests with a high-P ore doped with $CaCO_3$, calcium oxalate and a reference sample without any of the fluxes.

High-P Ore (g)	Coke (g)	$CaCO_3$ (g)	Calcium Oxalate (g)	Temperature (pre-heated) 900°C	Temperature final 1250°C
10	3	1	0	15 minutes	30 minutes
10	3	0	1	15 minutes	30 minutes
10	3	0	0	15 minutes	30 minutes

After cooling the completely reduced samples were mounted in epoxy resin and polished for optical microscopy, SEM and EPMA analysis. Figure 8 compares optical micrographs of the high-P ore samples reduced with calcium oxalate, $CaCO_3$ and reference sample without any of the fluxes. Visual observations indicated that the highest metallic iron (Fe) was from the sample mixed with calcium oxalate and metallic Fe particles appears to be somewhat similar size (Figure 8a), followed by the $CaCO_3$ fluxed sample with range of metal Fe sizes (Figure 8c). The lowest amount of metallic Fe was observed to be present in the un-fluxed sample (Figure 8e).

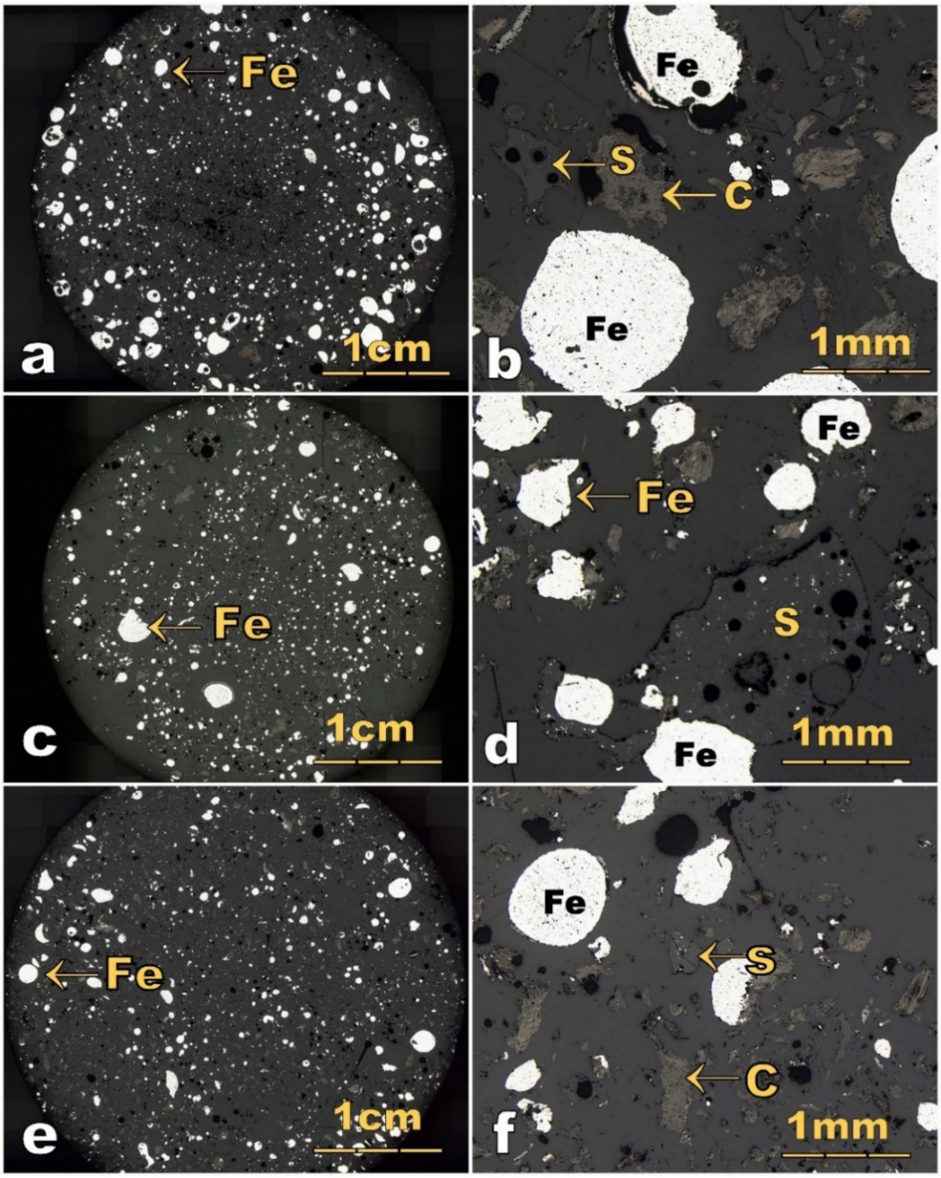

FIG 8 – Optical micrographs of the completely reduced P-rich ore samples. Images a) and b) are ore samples reduced with calcium oxalate, images c) and d) are ore samples reduced with $CaCO_3$, and images e) and f) are ore samples reduced without any fluxes. Key to abbreviations used: Fe = metal-Fe, s = slag (glass), c = unreacted coke particles.

Metallic iron (Fe) particles and slag phases (glass and silicates) in all three samples were analysed by EPMA and the measured phosphorus (P) contents in the metal-Fe and slag phases in the three respective samples are plotted in Figure 9a (calcium oxalate doped sample), Figure 9b ($CaCO_3$ doped sample) and Figure 9c (reference sample without any of the fluxes).

It was observed that phosphorus contents in the metal-Fe produced in the calcium oxalate doped sample were very low whereas most of the slag (glass) analyses showed very high contents of phosphorus. In comparison, the metal-Fe analysis results from the $CaCO_3$ doped and the reference sample indicate higher levels of phosphorus incorporated in the metal-Fe. Results also indicate that phosphorus in the slag (glass) phase from the calcium oxalate doped sample was somewhat evenly distributed while the glass in the $CaCO_3$ doped and the un-fluxed reference sample showed scattered values of phosphorus contents, some higher values, and some very low values. Figure 9a displays the phosphorus contents in glass and SFCA from calcium oxalate doped samples heated at 800°C. It was clearly observed that the phosphorus was mainly within the glass phase and that the phosphorus contents in SFCA phase was very low.

It was also noted that in all three samples (calcium oxalate doped, $CaCO_3$ doped and the reference sample) a few very high phosphorus analyses within some of the larger metallic iron particles were reported by SEM EDS analysis. Additional EPMA spot analysis indicated these tiny regions contained phosphorus contents that ranged from 1–12 wt. per cent P. Further analyses confirmed that these were very small, localised areas within large metallic Fe particles and not spread throughout metal Fe particles. It was anticipated that these phosphorus were released to metallic Fe from relict rare earth particles or rare apatite found within the high phosphorus ore because none of the phosphorus EPMA analysis of hematite/goethite particles of high-P ore reported such high level of phosphorus (MacRae *et al,* 2011) and the highest phosphorus levels in few goethite partials within high-P ore was reported from EPMA analysis was 1 wt. per cent. Within some glass particles of the Ca-oxalate doped sample large concentrates of calcium-aluminium feldspar was identified (Figure 8d). It appears that most of the metallic Fe particles are in contact with feldspar and EPMA analysis of feldspar indicated that feldspar did not contain any phosphorus in them.

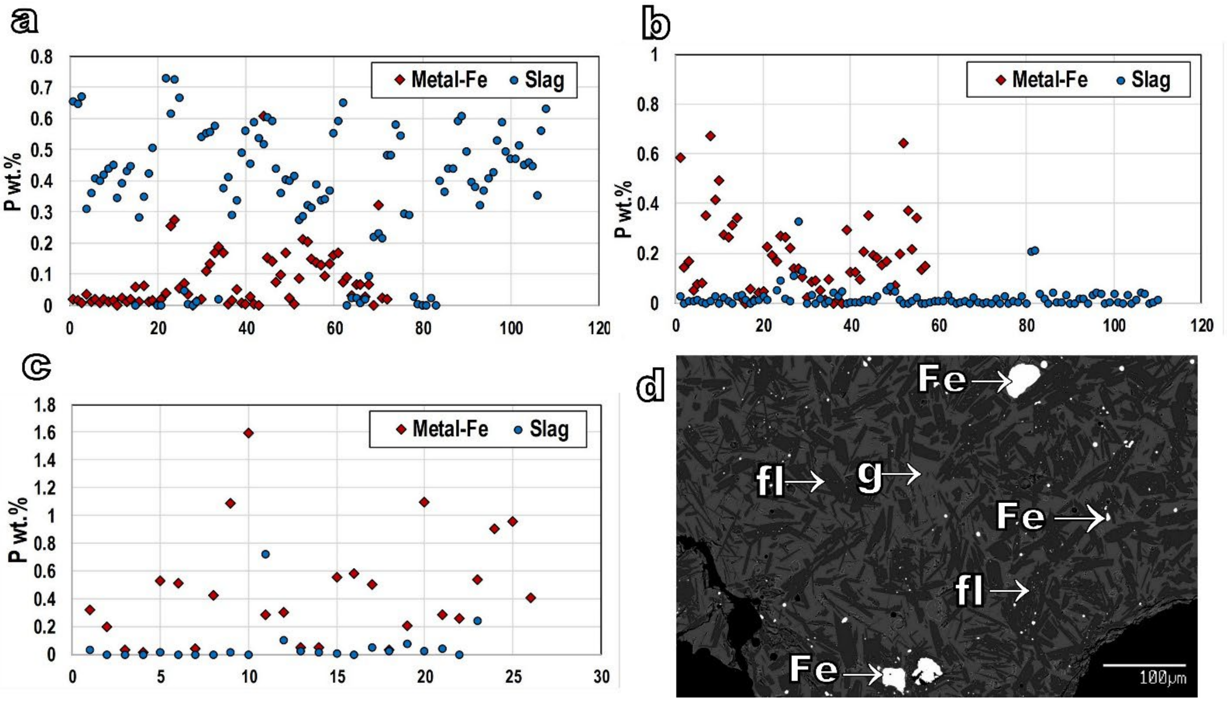

FIG 9 – Comparison of phosphorus (P wt.%) contents (a, b and c) in reduced samples and (d), metal-Fe (Fe), glass (g) and feldspar (fl) formed in CaOX doped/reduced sample.
(a) Phosphorus in metal-Fe and glass in CaOX doped and completely reduced sample.
(b) Phosphorus in metal-Fe and glass in $CaCO_3$ doped and completely reduced sample.
(c) Phosphorus in metal-Fe and glass in completely reduced reference sample without flux.

HIGH PHOSPHORUS BROCKMAN ORE REDUCTION TEST WITH CaOX

Australian high phosphorus Brockman ore with Fe content of 57.8 wt. per cent, P content of 0.135 wt. per cent, SiO_2 5.14 wt. per cent, Al_2O_3 4.11 wt. per cent, CaO 0.11 wt. per cent and MgO 0.19 wt. per cent. was doped with 3 wt. per cent $CaC_2O_4.H_2O$ (calcium oxalate monohydrate- molecular weight 146.11) and mixed with 10 wt. per cent coke to make a mixture with basicity of 2.26 (CaO 8.95 wt. per cent and SiO_2 3.95 wt. per cent in the mixture before adding the coke). The mixture was pulverised for two minutes and the 10g pellets were prepared. The pellets were placed in a graphite crucible and slowly heated in air to 900°C in a horizontal tube furnace and kept for 15 minutes. Then the temperature was increased to 1280°C and kept for 30 minutes. The reduced sample was quenched in water and a polished section was prepared for optical and SEM analysis. The reduced sample was predominantly consisting of metallic-Fe, feldspar, slag (glass), wüstite and minor magnetite (Figure 10b). SEM EDS analysis was performed on large number of separate slag (glass) and metallic-Fe particles and the phosphorus contents (wt. per cent) in slag and metallic-Fe is displayed in Figure 10a. SEM, EDS analysis of over 130 individual glass particles (average P=1.57 wt. per cent) and 140 individual metallic-Fe particles (average P=0.03 wt. per cent) has shown excellent phosphorus partition between them. Majority of glass particles analysed contained phosphorus over 1 wt. per cent and majority of metallic-Fe had no phosphorus in them. Table 7 display the average compositions for metallic-Fe, slag (glass), feldspar, magnetite and wüstite from SEM EDS analysis. The Fe content in slag (glass) was significantly low and majority of silica was located within glass and feldspar while alumina was manly confined to feldspar.

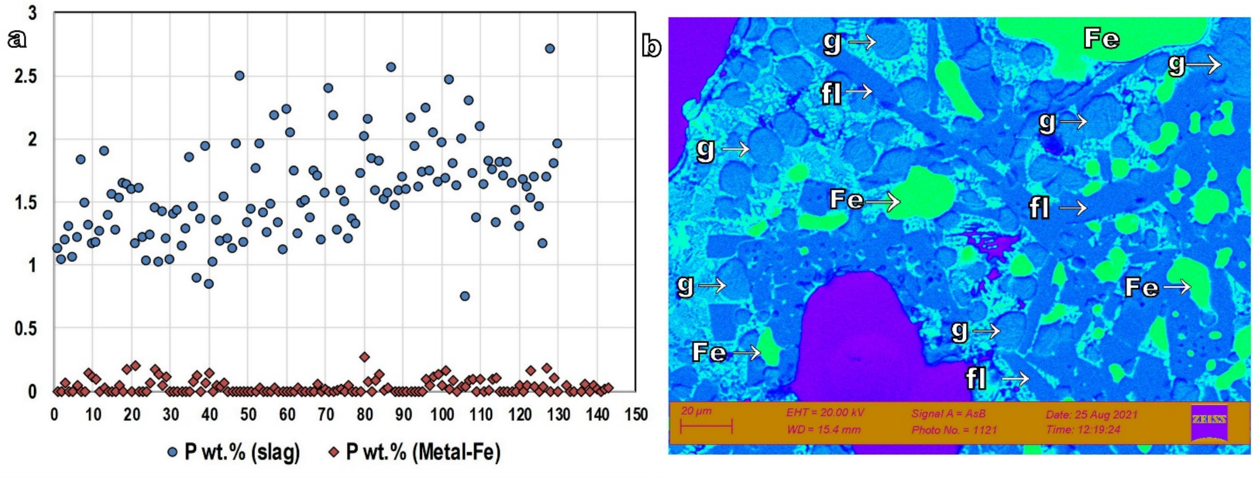

FIG 10 – Comparison of phosphorus (P wt.%) contents (a) in slag and metal-Fe in reduced sample and (b), metal-Fe (Fe), slag phase glass (g) and feldspar (fl) formed in CaOX doped/reduced sample.

TABLE 7

SEM EDS analysis of Fe-metal, slag (glass), feldspar, wüstite and magnetite in CaOX doped and sample reduced at 1280°C.

phase	Oxygen (O)	Magnesium (Mg)	Aluminium (Al)	Silicon (Si)	Phosphorus (P)	Calcium (Ca)	Titanium (Ti)	Iron (Fe)	Total	No. of analysis
Fe-metal	0±0	0.06±0.08	0.32±0.09	0.18±0.06	0.03±0.05	0.91±0.31	0.04±0.07	97.21±0.42	99.31±0.04	142
slag	38.32±2.67	0.21±0.11	0.22±0.19	10.87±1.04	1.57±0.37	45.25±2.53	0.09±0.12	3.24±1.55	99.92±0.31	129
Feldspar	39.19±2.15	0.15±0.23	17.55±2.08	8.22±0.82	0.03±0.04	32.53±1.66	0.06±0.09	2.21±0.9	99.98±0.09	33
Magnetite	25.53±2.18	0.28±0.3	0.68±0.35	0.14±0.21	0.03±0.04	3±1.63	0.05±0.1	69.99±3.51	99.91±0.1	17
Wustite	22.95±0.59	0.09±0.1	0.32±0.28	0.05±0.06	0.02±0.04	0.65±0.39	0.03±0.05	75.69±1.38	100±0	16

CONCLUSIONS

Charcoal from *Syzygium Zeylanicum* plant has been used as a reductant in ancient iron smelting processes in Sri Lanka. The iron produced after using charcoal or wood from such plant material is of exceptional quality with low impurities, in particular phosphorus. Ethnographic evidence indicates that the pre-industrial smelters of Sri Lanka found it convenient to utilize charcoal as a fuel basis. Deep mining was not the most convenient method of extracting raw material under such conditions. There was no compelling reason on the part certain technological implications involved in the process of production, magnetite ores (Fernando, 1986; Jayewardene, Balasooriya and Weerakoon, 2014) may not have been extensively worked during the Proto-Historic period, though the same cannot be inferred for the subsequent periods.

The present study analyses of slag samples from various locations showed that the phosphorus contents in metallic Fe, wüstite, fayalite and spinel in slag was extremely low and phosphorus was mainly restricted into the slag (glass) phase. Further test work on charcoal produced from the *Syzygium Zeylanicum* plant indicated high levels of calcium oxalate phase. Therefore, it was suspected that there is a significant effect on iron ore reducibility and phosphorus separation from high-P ores by using charcoal or wood which contained high percentage of calcium oxalate within.

The reduction tests were conducted using calcium oxalate and the results have shown that the calcium oxalate significantly enhanced the reducibility of a high-P iron ore by up to 50–65 per cent compared with no flux conditions. It has also shown that it could be a good alternative to the $CaCO_3$ for reducing high alumina ores as the raw ore used in this study had high alumina level of close to 4 wt. per cent of Al_2O_3. At low temperatures (800°C and 900°C) under reducing conditions it was observed that the slag (glass) produced in calcium oxalate doped samples contained significantly high amounts of phosphorus and other Fe phases such as hematite, magnetite and SFCA were devoid of phosphorus. In reduced samples (calcium oxalate doped and reduced at 800°C and 900°C), high-phosphorus glass was formed as small interstitial space filling grains between magnetite/hematite/SFCA particles and apatite/high phosphate crystals were also formed within glass. The attempt to separate glass from other was unsuccessful with grinding down the reduced sample to -100 microns and followed by the magnetic separation due to the fine size. Dissolving high phosphorus containing glass with acids and separate the liquid from reduced ore (high with phosphorus) to reduce the phosphorus may be a possible technique to investigate. Complete reduction tests of high-P ore doped with calcium oxalate confirmed that the phosphorus was mainly restricted in slag (glass) phases when the high-P ore was doped with calcium oxalate and completely reduced. Phosphorus separation/partition behaviour between calcium oxalate and calcium carbonate fluxed samples seems quite different. Therefore, there is a good indication that calcium oxalate can be used to reduce high-P, high alumina ores at low temperatures and to retain phosphorus from mixing with metallic iron. Further investigations need to be conducted to check the effectivity of calcium oxalate in retaining phosphorus in slag by fine tuning the experimental conditions such as reduction temperature/gas atmosphere and basicity levels (balancing CaO/SiO_2) in the mixture.

ACKNOWLEDGEMENT

The authors wish to thank CSIRO Mineral Resources for permission to publish the paper and for the financial support of this work. The external reviewers are thanked for their valuable comments and improvements to the paper. Dr Nathan Webster, CSIRO is acknowledged for providing XRD analysis. The authors acknowledge the facilities, and the scientific and technical assistance of the Centre for Microscopy and Microanalysis (CMM) at University of Queensland.

REFERENCES

Anoop, M V and Bindu, A R, 2014. Pharmacognostic and Physico-Chemical Studies on Leaves of Syzygium zeylanicum (L.) DC, *International Journal of Pharmacognosy and Phytochemical Research 2014–15*, 6(4):685–689.

Ashton, M S, Gunathilake, S, Zoysa, N De, Dissanayake, M D, Gunathilake, N and Wijesundera, S, 1997. A Field Guide to the Common Trees and Shrubs of Sri Lanka, Syzygium zeylanicum, yakada maran (S)/maranda (T), (DP 11:431), N, 10, tree, WHT Publications (Pvt.) Limited, p 293, plant 33.

Coomaraswamy, A K, 1908,1956 (2003), Mediaeval Sinhalese Art: Being a Monograph on Mediaeval Sinhalese Arts and Crafts, Mainly as Surviving in the Eighteenth Century, with an Account of the Structure of Society and the Status of the Craftsmen, Pantheon Books, 1956 – Art – 344 pages.

Dukino, R D, England, B M and Kneeshaw, M, 2000. Phosphorus distribution in BIF-derived iron ores of Hamersley Province, Western Australia, *Trans Instn Min Metall (Sect B: Appl Earth Sci),* 109, September–December 2000.

Fernando, L J D,1986. Science education series No 17 Mineral resources of Sri Lanka. Natural Resources Energy and Science Authority. Part II, Ch. VI.

Földvári, M, 2011. Handbook of thermogravimetric system of minerals and its use in geological practice, Occasional Papers of the Geological Institute of Hungary, vol 213, p 134.

Franceschi, V R and Nakata, P A, 2005. Calcium Oxalate in Plants: Formation and Function, *Annul. Rev. Plant Biol*. 56:41–71.

Han, H, Duan, D, Wang, X and Chen, S, 2014. Innovative Method for separating Phosphorus and Iron from high-Phosphorus Oolitic Hematite by Iron Nugget Process, *Metallurgical and Materials Transactions B*, The Minerals & Material Society and ASM International, vol 45B, 1634, October 2014.

Jayewardene, D T, Bbalasooriya, N W B and Weerakoon, W A P, 2014. Geochemical Characteristics of Hydrated Iron-Ore Deposit in Dela, Sri Lanka, *Journal of Geological Society of Sri Lanka,* 16(2014):43–52.

Juleff, G, 1996. An ancient wind-powered Iron smelting Technology in Sri Lanka, *Nature*, 379(4):60–63.

Juleff, G, 1998. Early Iron and Steel in Sri Lanka: A study of the Samanalawewa Area (Materialien Zur Allgemeinen Und Vergleichenden Archeaologie,), December 31, Philipp von Zabern, 422 p.

Karunaratne, P and Adikari, G, 1994. Further studies in the settlement archaeology of the Sigiriya-Dambulla region, (Eds. S Bandaranayake and M Morgren), pp 55–60, Postgraduate Institute of Archaeology, University of Kelaniya, Colombo, Sri Lanka.

Karunatilaka, P V B, 1991. Metals and metal use in ancient Sri Lanka, University of Peradeniya, Lanka Journal of Humanities, vol. XVII & XVIII, 1991–1992, pp 104–118, URI: http://hdl.handle.net/123456789/2224.

MacRae, C M, Wilson, N C, Pownceby, M I and Miller, P R, 2011. The Occurrence of Phosphorus and Other Impurities in Australian Iron Ores, *AusIMM Iron Ore Conference*.

Nunna, V, Hapugoda, S and Pownceby, M I, 2017. Study of microwave-assisted magnetising roasting and mineral transformation of low-grade goethite ores. In: *Proceedings Iron Ore 2017*. Australasian Institute of Mining and Metallurgy, Melbourne, pp. 575–582.

Nunna, V, Hapugoda, S, Pownceby and Sparrow, G J, 2021. Beneficiation of low-grade, goethite-rich iron ore using microwave-assisted magnetizing roasting, *Minerals Engineering,* 166(2021):106826.

Ranasinghe, S P, 1986. Iron Ore Deposits of Sri Lanka, Geological Society of Sri Lanka, Department of Geology, Univ. of Peradeniya, Sri Lanka, L J D Fernando Felicitation volume, pp. 33–44.

Seneviratne, S, 1985. Iron Technology in Sri Lanka: a preliminary study of resource use and production techniques during the early iron age, *The Sri Lanka Journal of the Humanities,* 9:129–178. Peradeniya: University of Peradeniya.

De Silva, M A T, 2011. Evolution of Technological Innovations in Ancient Sri Lanka, ISBN 978–955–665–140–9, Vijitha Yapa publications, 444 p.

Solangaarachchi, R, 1999. History of Metallurgy and Ancient Iron Smelting, *Vudurava*, 19(1):30–40.

Solangaarachchi, R, 2011. Ancient Iron Smelting Technology and the settlement pattern in the Kiri Oya basin in the dry zone of Sri Lanka, PhD thesis, University of Florida, 2011.

Su, C, Lv, N, Yang, J, Wu, L, Wang, H and Dong, Y, 2017. Effect of high Na_2O addition on distribution of phosphorus in low basicity converter slag, *J. Iron Steel Res. Int*, https://doi.org/10.1007/s42243–018–0096–1(0123456789().,-volV)(0123456789().,-volV).

Characterisation of SFCA phases in iron ore sinter by combined optical microscopy and electron probe microanalysis (EPMA)

S Hapugoda[1], L Lu[2], E Donskoi[3], M I Pownceby[4] and H Han[5]

1. Scientist, CSIRO, Pullenvale, Brisbane Qld 4069. Email: Sarath.Hapugoda@csiro.au
2. Principal Research Scientist, CSIRO, Pullenvale, Brisbane Qld 4069. Email: Liming.Lu@csiro.au
3. Project Leader, CSIRO, Pullenvale, Brisbane Qld 4069. Email: Eugene.Donskoi@csiro.au
4. Senior Principal Research Scientist, CSIRO, Clayton Vic 3169. Email: Mark.Pownceby@csiro.au
5. Research Officer, CSIRO, Pullenvale, Brisbane Qld 4069. Email: Hongliang.Han@csiro.au

ABSTRACT

Iron ore sinter mineralogy and its associated macro-/micro – structure has a strong impact on sinter quality. At a macroscopic scale, sinter ideally consists of a strong, porous matrix which bonds relict ore nuclei together. Microscopically, the sinter matrix (solidified from the melt part of the initial sinter mix) generally consists of complex calcium ferrites known as SFCA, secondary magnetite and hematite grains (precipitated from the primary sinter melt), glass and silicates. Depending on the conditions under which the sinter structure is formed, two major forms of SFCA with different morphologies are generally recognised, ie fine micro-platy SFCA (usually termed SFCA-I) and coarse columnar/prismatic SFCA. Detailed optical microscope observations of several pot grate and compact sinter samples revealed the presence of a variety of fine, coarse and dense forms of both types of SFCA. The controlled cooling tests revealed that cooling rate has an impact on the form and size of SFCA crystals. In this work, EPMA analysis of SFCA compositions from a variety of pot grate and compact sinter samples are presented. Results show that the SFCA types exhibit a broad range of complex compositions within the system $Fe_2O_3/CaO/SiO_2/Al_2O_3/MgO/TiO_2/MnO_2$. Although SFCA-I and SFCA are known to be crystallographically distinct and with different, well-defined ranges in composition, there was considerable overlap in compositions of the experimental sinter samples. The development of SFCA textures depend on several parameters including the local chemistry and conditions including the maximum temperature attained and the cooling rate, within the sinter bed, thereby suggesting that SFCA identification based on morphology alone may be erroneous.

INTRODUCTION

Sinter can constitute over 65 per cent of the total ferrous burden in modern blast furnace ironmaking operations (Lu *et al,* 2009) and, hence, plays an important role in determining the productivity and energy efficiency of the blast furnace. Sinter mineralogy and its associated macro – and micro-structure has a direct relationship to sinter quality and strength. At a macroscopic scale, sinter ideally consists of a strong, porous matrix which bonds relict ore nuclei together (Figure 1). Microscopically, the solidified sinter matrix (produced from the melt part of the initial sinter mix) generally consists of complex calcium ferrites known as SFCA, glass and silicates (eg larnite – Ca_2SiO_4), as well as secondary magnetite and hematite grains (precipitated from the primary sinter melt). Depending on the conditions under which the sinter structure is formed, two major forms of SFCA with different morphologies, chemistry and crystal structure (Shigaki, Sawada and Gennai, 1986; Scarlett *et al,* 2004b; Webster, Pownceby and Madsen, 2013; Webster *et al,* 2012, 2014) are generally recognised. These are fine micro-platy SFCA (SFCA-I) and coarse-columnar or coarse short-prismatic SFCA. Fine micro-platy SFCA has in the past been considered a desirable sinter bonding phase, due to its interlocked structure and micro-porous nature, which makes the sinter stronger and more reducible. The sinter matrix acts as a glue which bonds the sinter structure together and as a result it plays a key role in achieving sinter quality. The bonding phases (sinter matrix) make up most of the phases within sinter and thus strongly influence the overall sinter properties. These phases are formed during the sintering process at temperatures above about 1000–1100°C and contain a large variety of minerals, mainly complex calcium ferrites (ie SFCA phases) in association with iron oxides and a limited amount of silicates. Sinter bonding phases such as SFCA have been studied extensively because of their important role in determining key sinter quality parameters such as reducibility

(Kitamura, 1985; Bristow and Waters, 1991) and reduction degradation (Shigaki, Sawada and Gennai, 1986; Loo, Wan and Howes, 1988). More recently, Pownceby *et al* (2015) have shown that the sinter matrix, which includes the solid SFCA phases and pores, directly influences other sinter quality parameters such as strength before and after reduction. These are important parameters as Reduction properties (RDI/RI) and other metallurgical properties (ie TI-Tumble Strength) have a significant influence on the coke rate and the blast furnace productivity. Thus, the types of phases present in sinter, their composition, amount/volume fraction, morphologies have a very strong influence on sinter properties. Similarly, the presence and type of pores in sinter can, either increase or decrease RI as well as RDI depending on whether they are open or closed. The phases that are present around the pores will also affect these parameters.

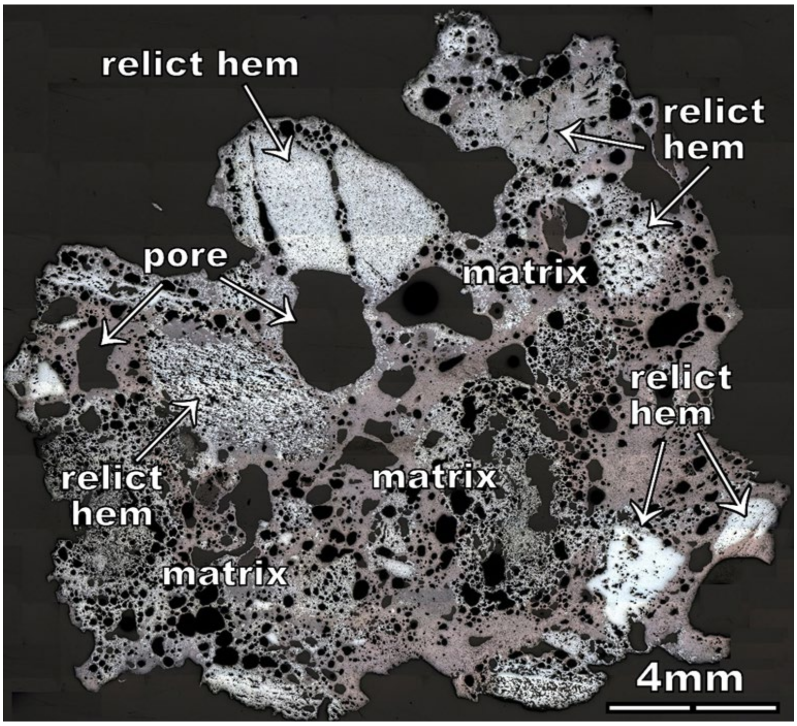

FIG 1 – Optical micrograph of a sinter lump particle displaying sinter nuclei (hematite) bonded by a matrix consisting of SFCA-magnetite-hematite±glass/larnite.

Quantification of iron ore sinter mineralogy (Hapugoda *et al,* 2016, 2019) is traditionally carried out by point counting of various sinter phases under the optical microscope using an identification scheme based on reflectivity, colour and morphology. More recently the classification of iron ore sinter minerals has been through X-ray diffraction (XRD) a technique that classifies minerals based on their crystal structure. *In situ* powder XRD investigations have also been conducted (Scarlett *et al,* 2004a, Webster, Pownceby and Madsen, 2013) into the formation of SFCA and the observation of intermediate phases with respect to time and temperature. Electron beam-based techniques have also been employed in sinter classification. For example, automated techniques such as the QEMSCAN technique has been successfully used by Tonzetic and Dippenaar (2011). This technique was especially useful for its ability to distinguish magnesio-ferrites from calcium-bearing magnetite and calcium ferrite phases from SFCA. Scanning Electron Microscopy and Electron Microprobe Analysis has also been used to analyse and characterise iron ore sinter (Pimenta and Seshadri, 2002; Patrick and Pownceby, 2001; Hancart, Leroy and Bragard, 1967; Ahsan, Mukherjee and Whiteman, 1983; Hsieh and Whiteman, 1989; Yang and Loo, 1997; Stenlake, Pepper and Ostwald, 1981; Ostwald, 1981; Dawson, Ostwald and Hayes, 1985). While the e-beam techniques have proved useful characterising many of the phases found in iron ore sinter, especially the incorporation of trace impurities and deciphering the complex chemistry of the various SFCA phases, they have difficulty in deciphering between Fe^{2+}/Fe^{3+} minerals (eg magnetite and hematite).

In this paper we utilise optical microscopy and an optical image analysis (OIA) system and sinter phase classification scheme developed by CSIRO (REF) to characterise sinter and to compare the sinter mineralogy produced from different sinter blends. In the sinter phase classification scheme, three main types of SFCA phases are included. These are: SFCA-I (fine microplaty type SFCA), SFCA (coarse platy/columnar or prismatic/tabular SFCA) and dense SFCA. The identification is primarily based on the size, shape and texture of the SFCA. Examples of these phases are shown in Figure 2, where the dense verities of SFCA are presented in Figure 3. Recent analysis of major elements in these phases by Electron Probe Microanalysis (EPMA) techniques have also shown that they have wide variation in chemistry (REF). Therefore, for the better identification of these SFCA phases under the optical microscope and to correlate the major element chemistry, a variety of pot-grate and compact sinter samples were analysed by EPMA. Initially we provide a review of SFCA morphological types followed by an examination of SFCA types determined from an optical analysis of sinter samples obtained from pot-grate tests conducted on various sinter blends. To better understand the relationship between SFCA texture/morphology and composition we then conducted quantitative EPMA studies on the identified SFCA textural types.

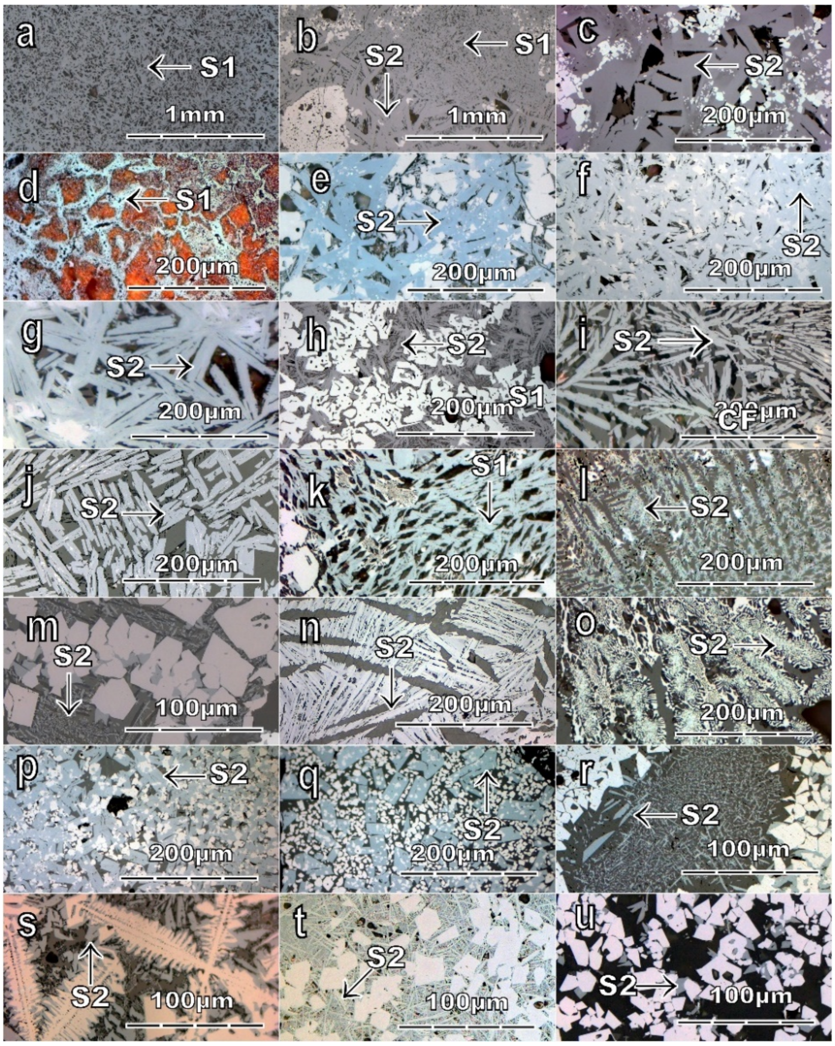

FIG 2 – Optical micrographs showing various SFCA morphologies and textures in iron ore sinter (S1=SFCA-I, S2=SFCA).

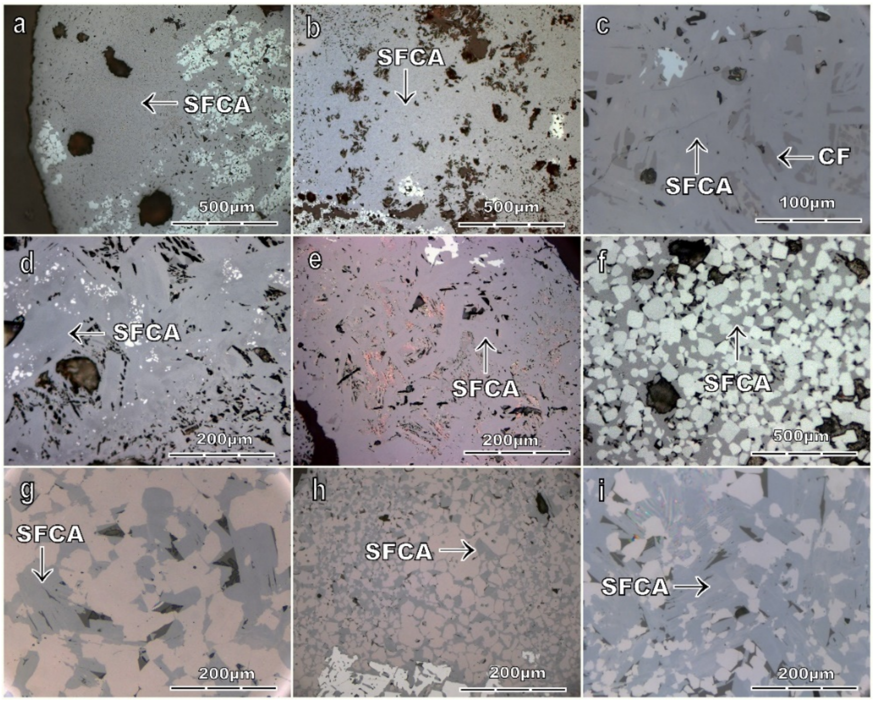

FIG 3 – Optical micrographs of common dense type SFCA morphologies.

SFCA morphological/textural types based on optical microscopy

Tonzetic and Dippenaar (2011) provided several descriptive names for the 'SFCA' group of minerals. Terms most encountered in literature for the fine SFCA-I (smaller than 10 microns) type include (but are not limited to); acicular SFCA, acicular calcium ferrite, SFCA-I, fine platy SFCA, fibrous SFCA, finely fibrous SFCA, irregularly shaped SFCA, low T morphology SFCA and needle-like dendritic/eutectic SFCA. The most common names used for SFCA (larger than 10-micron size) are worm SFCA, dense SFCA, columnar SFCA/intermediate columnar SFCA, tabular SFCA, prismatic SFCA, lath-shaped/flaky SFCA, crystalline SFCA. Other names for both varieties include silico-ferrites, monocalcium ferrite, complex calcium ferrite and dense/blocky SFCA (when the SFCA displays dense texture with less porosity and no define crystal margins are visible). Even though the XRD is crucial in distinguishing between SFCA and SFCA-I, at present the most used approach by researchers is based on the observed texture by microscopic examination (under optical microscope or SEM). Examination of Figure 2a and 2c however illustrates that depending on the orientation of the crystals, the platy SFCA-I often exhibits a fine microplaty, needle-like or fibrous texture. In addition to these two SFCA types, recent work by Hapugoda *et al* (2016) and Honeyands *et al* (2017), indicated that they are further able to identify another morphology which is dense SFCA. The dense varieties of SFCA are shown in Figure 3. Gan *et al* (2015), differentiates between four SFCA morphologies, with two having similar compositions to SFCA (acicular and columnar) and the other two similar to SFCA-I (platy and granular). Frequently, a relation between morphology and chemical composition is presented in the literature, but as shown previously, analyses tend to differ substantially and are often incomplete. For example, fine microplaty SFCA (SFCA-I) are thought to have high Fe, Ca and low Al contents, as opposed to coarse columnar or plates (SFCA) which have low Fe, low Ca and high Al (Ahsan, Mukherjee and Whiteman, 1983). As summarised in Nicol *et al* (2018), different opinions concerning a relation between the attained sintering temperature and the subsequent morphology exist as well (eg Sasaki and Hida, 1982). Previous studies (Mežibrický and Fröhlichová, 2016), to determine the differences between acicular (SFCA-I) and columnar (SFCA) structural types, indicated that the different 'SFCA' phases can form similar microstructures at certain conditions. The similarities in composition of the two phases gives them a similar colour and contrasts in both optical and electron microscopes giving rise to significant difficulties in differentiation between both different phases and microstructures. This indicates that more advanced techniques than that currently used may be required to differentiate between the phases. Honeyands *et al* (2017) compared the terminology and classification of SFCA phases and microstructures between labs, with four types of SFCA in the final classification system. These were, platy SFCA-I, prismatic SFCA, blocky SFCA and dendritic SFCA, with blocky and dendritic considered as subtypes of prismatic. Three techniques were used to attempt to differentiate phases: XRD, reflected light microscopy (incorporating optical image analysis) and EPMA.

Varieties of SFCA types based on size, crystal morphology and texture can be observed in iron ore sinter (Figure 2). In Figure 2a, a fine variety of SFCA is shown and the SFCA crystals display a network exhibiting a microplaty texture. Close examination reveals there are two sizes (very fine microplates, less than 5-micron size forming a relative dense texture and fine microplaty plates, larger than 5-micron size). The two fine and very-fine SFCA areas are hard to separate as the two textures developed together as patches in the same area. In most of the previous studies this type of SFCA (Figure 2a) would be categorised as SFCA-I. In Figure 2b, three SFCA textures near a primary hematite particle can be recognised with textures similar to that in Figure 2a and another texture characterised by relatively larger microplates or flakes larger than 10-micron size. The difference between these three SFCA types is the relative differences in size and porosity and it was noted that all three types displayed a similar reflectance under the optical microscope (reflected light). In optical point counting the two fine texture varieties shown in Figure 2b are considered as SFCA-I and the coarse variety is considered to be the SFCA. In Figure 2c, large columnar or long prismatic shaped SFCA was observed and close examination showed that there is significant variation in reflectivity (grey/dark grey) indicating compositional variation within the SFCA particles. Primary hematite or partially reacted hematite forming subhedral hematite can be observed within larger SFCA flakes. Due to the higher particle size, the SFCA in Figure 2c is categorised as SFCA. In Figure 2d, irregular/dense SFCA is formed near a high-alumina particle (most likely ochreous goethite) and this type of SFCA would be categorised as SFCA-I in optical point counting. Figure 2e, Figure 2f and Figure 2g display the most common SFCA texture in iron ore sinters. Large laths or flakes of SFCA are formed with varying amounts of magnetite, glass and larnite. Frequently magnetite is formed within SFCA crystals and has irregular crystal shapes and displays diffused/mixed boundaries with SFCA. It is difficult to confirm whether magnetite with irregular crystal shapes is secondary or whether these are reduced partially reacted hematite particles. Various sizes of this type of SFCA can be recognised and the morphology is described as coarse micro-platy, flaky or columnar. In Figure 2h microplaty SFCA is associated with secondary skeletal hematite. This SFCA is morphologically very similar to the SFCA in Figure 2a and Figure 2b, however the crystal size is comparatively large and therefore categorised as SFCA. In Figure 2i, thin and long, platy SFCA displays a dendritic pattern with contained pores within the SFCA crystals. Because of the larger size, these would be categorised as SFCA. The SFCA in Figure 2j shows columnar crystal shapes with crystals having become more rectangular in appearance. Close examination revealed the presence of resorbed fine magnetite within the SFCA. In Figure 2k, the SFCA is dense and has no shape and is frequently associated with larnite. This type of SFCA is difficult to categorise into SFCA-I or SFCA but is often counted as SFCA-I. In Figure 2l, the SFCA has been formed as an irregular network within a glass-rich matrix. Being often associated with glass, this type of SFCA is classified as SFCA. In Figure 2 m, irregular crystals of SFCA with varying sizes are associated with magnetite and glass and classified as SFCA. In Figure 2n, large plates of SFCA with different reflectivity can be recognised and these are typically associated with larnite. Long platy SFCA can either be SFCA or calcium ferrite (CF). In Figure 2o, SFCA has been formed with magnetite within a glass-rich matrix and displays a worm-shaped texture. Due to the association with magnetite and glass these are categorised as SFCA. In Figure 2p and Figure 2q, SFCA is associated with magnetite and glass and display a tabular short prismatic crystal habit. Compared with the SFCA in Figure 2p, the SFCA in Figure 2q has developed into perfect, short prismatic crystals. Being associated with magnetite and glass this type of SFCA is classified as SFCA. In Figure 2r, a network of fine acicular SFCA has been formed within glass. Even with the smaller size, this type is classified as SFCA because of the association within glass. In Figure 2s, SFCA can be seen formed around skeletal secondary magnetite. Although the grain size can be very small this type of SFCA is classified as SFCA as it is associated with magnetite and glass. In Figure 2t, thin fine, acicular SFCA is formed within a glass-rich matrix. This texture was frequently observed in high temperature sinter (from tests above 1360°C) and categorised as SFCA. In Figure 2u, a few smaller irregular shaped SFCA particles are observed with a majority of glass and either magnetite or wüstite. Due to being associated with magnetite/wüstite and glass, this SFCA would be classified as SFCA.

Based on the above observations, it can be summarised that SFCA can be formed in various sizes (ultrafine, fine, medium and coarse) and several crystal morphologies and textures. The general practice to classify them into either SFCA-I or SFCA, depending on the size, crystal morphology, texture and association (primary or secondary hematite, magnetite, glass, wüstite) therefore has potential to result in incorrect identification.

Dense-SFCA morphological/textural types

In pot grate or compact iron ore sinters, a variety of SFCA with a typically dense appearance can be observed (Honeyands *et al,* 2017; Hapugoda *et al,* 2016). Several dense SFCA morphologies were identified optically and the most common varieties are shown in Figure 3. In Figure 3a and 3b dense SFCA was closely associated with fine microplaty SFCA and it seems that dense appearance is developed by the intergrowth of fine SFCA (less than 10 microns in size). We propose therefore, that this variety of dense SFCA can be incorporated into the fine microplaty SFCA category. In Figure 3c, 3d and 3f, the dense SFCA appears to have been formed by the intergrowth of coarse platy SFCA (higher than 10 microns in size) as the crystal outlines of some of the coarse platy SFCA particles can still be recognised. This variety of dense SFCA was categorised as SFCA (not SFCA-I). The optical classification is purely based on crystal size and however, uncertainty remains as to whether this coarse SFCA is actually SFCA-I. In Figure 3f and 3h, dense SFCA is associated with secondary subhedral hematite and secondary magnetite respectively – again, uncertainty further remains as to whether these are SFCA-I or SFCA crystals. However, in optical identification these types are most likely classified as SFCA rather than SFCA-I due to the size of the SFCA crystals. In Figure 3g and 3i, it can be observed that the dense SFCA has been formed by the intergrowth of coarse columnar or short prismatic tabular SFCA and therefore usually categorised as SFCA (not SFCA-I) under the optical characterisation.

In summary the dense SFCA types have similar reflectance and therefore, the dense SFCA was categorised as either SFCA-I or SFCA by identifying the nature (size and crystal outlines of intergrown SFCA type) of the associated SFCA variety. As for the SFCA classification discussed above, we emphasise however, the classification based on the crystal size and texture of SFCA is still questionable as discussed in the following sections.

EXPERIMENTAL

Over many years, CSIRO has conducted pilot scale pot-grate sinter tests to evaluate various sinter blends and to examine their metallurgical properties. Sample data from over 220 individual pot-grate sinter tests with varying basicity levels (Table 1) were selected for the optical mineralogy and the various forms of SFCA phases (ie Figures 2 and 3) were identified. The SFCA phases were later analysed by EPMA. The EPMA results were obtained on sinter from several blends with different basicity levels to compare the chemical composition of the sinter phases including; fine-microplaty SFCA-I (SFCA types similar to those marked as S1 in Figure 2a, 2b and 2d), coarse-columnar SFCA (SFCA types similar to those marked as S2 in Figure 2c, 2e, 2f, 2g, 2i and 2f), short-prismatic SFCA (SFCA types similar to those marked as S2 in Figure 2p, 2q and 2u) and variety of dense SFCA phases. Samples were mounted in 32 mm round polished blocks. The polished samples were coated with a thin (10 nm) carbon film using a QT150T (Quorum Technologies) carbon coater before examination by EPMA. A JXA 8200 Electron Probe Microanalyser fitted with five Wavelength Dispersive (WD) detectors were used for the compositional analyses. The analyses were conducted at an accelerating voltage of 15 kV and a probe current of 15 nA. The standards used for quantitative analysis were from Charles M. Taylor Co. (Stanford, California) and included: hematite standard-Fe_2O_3 for Fe, kyanite standard-Al_2SiO_5 for Al, pure MgO standard for Mg, rutile standard-TiO_2 for Ti and wollastonite standrad-$CaSiO_3$ for Ca and Si. The METAL-ZAF correction (atomic number: Z, adsorption: A, fluorescence: F) procedure supplied with the electron probe was applied. The average accuracy of the EPMA measurements was estimated to be 1 wt. per cent. Both Fe^{2+} and Fe^{3+} are present in the samples, however, only the metal cation concentrations can be measured by EPMA. For the presentation purpose only, all iron cation weight measured by EPMA was therefore converted to oxide percentages such as 'Fe_2O_3' from the measured Fe wt. % to represent the iron oxide percentages.

To understand the SFCA-I/SFCA formation under different basicity levels, temperature and cooling rates, in this study sinter powder analogues (compressed pellets) with basicity values 1.67, 2.5 and 3.5 were prepared with synthetic powders (Fe_2O_3, CaO, Al_2O_3, MgO and SiO_2) and pressed pellets were oven dried for 6 hours at 100°C prior to the sintering. The samples were heated at the desired temperature in air inside a horizontal furnace for 4 minutes by gradually (four steps at one minute each) inserting the sample inside a Ni crucible. The pellets were heated at seven different temperatures of 1200°C 1220°C, 1240°C, 1280°C, 1320°C, 1360°C and 1400°C. One set of samples were air cooled and another set of samples at the same basicity level/temperature conditions were water quenched to cool down rapidly. Duplicate samples with same conditions were prepared for optical microscopy and XRD analysis.

RESULTS AND DISCUSSION

Optical point counting results

Detailed studies of iron ore sinter by Pownceby and Clout (2003) have shown that the characterisation of sinter cannot be achieved only through analysis of overall sinter chemistry, since each phase present in sinter can potentially have a wide variation in chemical composition due to its origin and/or due to solid solution within individual phases. In addition, each phase may appear in different morphologies with different characteristics. Therefore, in addition to chemical analysis, there is a need to characterise sinter in terms of the mineralogy and spatial arrangement of the various phases. Over the years, CSIRO has developed a sinter phase characterisation procedure and a classification scheme (Hapugoda *et al,* 2016) for iron ore sinter, which considers major sinter bonding phases such as SFCA and other secondary sinter phases such as secondary magnetite, secondary hematite, glass and larnite as well as un-reacted ore and flux particles. Association of sinter phases, sinter pore (open and closed) structure and macroscopic and microscopic porosity were also considered in the development of the classification scheme. The bonding phases (sinter matrix) make up most of the phases within sinter and thus strongly influence the overall sinter properties. These phases are formed during the sintering process at temperatures above about 1000–1100°C and contain a large variety of minerals, mainly complex calcium ferrites in association with iron oxides and a limited amount of silicates. The complete scheme includes major components such as primary and secondary hematite, fine micro-platy SFCA (SFCA-I) and columnar-prismatic SFCA (Figure 2), dense SFCA (Figure 3), secondary magnetite, glass, larnite (di-calcium silicate) phases and the remaining fluxes. Representative sinter samples from over 220 pot grate sinter tests were manually point counted. Point counting was carried out on 40 mm diameter polished sections of sinter split from 2 kg representative samples of the optimum sinter product, which was collected after plug processing and roll crushed to -1 mm (also used for sinter chemical analysis). The finest sinter particles (below 0.1 mm) were removed by screening. For each sinter sample, a minimum of 1000 points were counted across a grid covering the whole surface of the polished block. From the results percentage of SFCA-I, SFCA and total of other phases were calculated. Close examination (as discussed in the dense-SFCA morphological types section above) of dense SFCA types indicated that the dense appearance was primarily due to the intergrowth of SFCA crystals and therefore by carefully selecting and adding the dense SFCA particle counts separately to either SFCA-I or SFCA, (depending on the size) total counts were performed. The final percentages of SFCA-I, SFCA and total of other phases is presented in the triangular plot shown in Figure 4. For the 220 pot-grate sinter samples, the majority (over 95 per cent of samples) had sinter blend basicity values close to 2.0 and were made from various ore-blend compositions. Most of the sinter samples examined in this study were optimised blends and therefore showed favourable sinter metallurgical properties based on RDI, RI and TI test results.

According to the point counting results (Figure 4), the SFCA-I contents varied from 1.7–42.0 per cent with an average SFCA-I content of 6.93 per cent (STDEV=4.29). The SFCA contents varied from 4.7–44.5 per cent with an average SFCA content of 23.68 per cent (STDEV=6.73). Out of the 220 sinter samples, in 75 samples the SFCA-I content was below 5 per cent (while the SFCA content was below 5 per cent only in 5 samples), in 176 samples the SFCA-I content was below 10 per cent, while, comparatively, in 38 samples the SFCA content was between 10–20 per cent. In 168 samples, the SFCA content was above 20 per cent and in 35 samples the SFCA content was above 30 per cent. The majority of high-quality sinter (as determined by sinter productivity analysis) had SFCA-I between 5–10 per cent and SFCA between 10–35 per cent). Although the preferred SFCA type for the good quality sinter has previously been indicated to contain predominantly fine microplaty SFCA-I type, from the above observations, it can be observed that in the high-quality pot-grate sinter samples studied, the SFCA phase (coarse plates larger than 10 microns) and coarse columnar-prismatic together, over 10-micron size) was well dominant over fine microplaty (less than 10-micron size) SFCA-I phase.

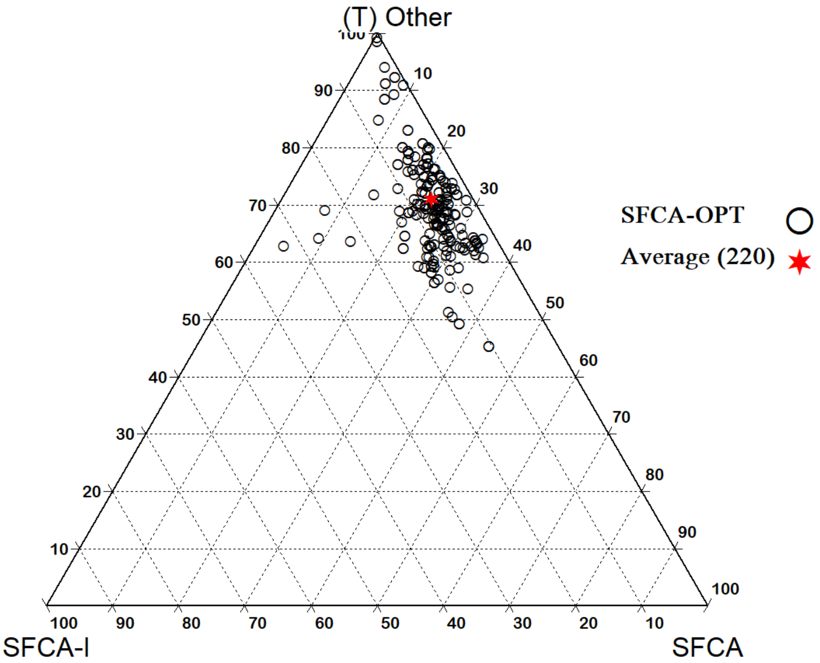

FIG 4 – Optical point counting data (volume per cent) for SFCA-I, SFCA and total of other phases including magnetite, hematite, glass and larnite (labelled as Other – (T)), in over 200 pot-grate sinter samples.

EFFECT OF BASICITY, TEMPERATURE and COOLING RATE ON SFCA MORPHOLOGY

Effect of basicity/temperature

As indicated above, sinter bonding phases such as SFCA have been studied extensively because of their important role in determining key sinter quality parameters such as reducibility (Kitamura, 1985; Bristow and Waters, 1991) and reduction degradation (Shigaki, Sawada and Gennai, 1986; Loo, Wan and Howes, 1988). Pownceby *et al* (2015) have shown that the sinter matrix, which includes solid SFCA phases and pores, directly influences sinter quality parameters such as strength before and after reduction. Zhang *et al* (2012) found that it is beneficial to the formation of complex calcium ferrite to enhance the basicity of low silica sinters. The acicular SFCA-I (the fine microplaty SFCA-I) was increased with the enhancing basicity and reached the peak at basicity 2.8, then the columnar or platy SFCA formed and the bonding strength decreased. Webster *et al* (2014) studied the effects of processing parameters such as basicity on their formation and decomposition may assist in improving efficiency of industrial iron ore sintering operations. According to Webster *et al* (2014) increasing basicity significantly increased the thermal range of SFCA-I, from 1363 K to 1533 K (1090°C to 1260°C) for a mixture with basicity, B = 2.48, to ~1339 K to 1535 K (1066°C to 1262°C) for a mixture with B = 3.96 and to ~1323 K to 1593 K (1050°C to 1320°C) at B = 4.94. Increasing basicity also increased the amount of SFCA-I formed, from 18 wt. per cent for the mixture with B = 2.48 to 25 wt. per cent for the B = 4.94 mixture. Higher basicity of the starting sinter mixture will, therefore, increase the amount of SFCA-I, considered to be more desirable of the two phases. Basicity did not appear to significantly influence the formation mechanism of SFCA-I. It did, however, affect the formation mechanism of SFCA, with the decomposition of SFCA-I coinciding with the formation of a significant amount of additional SFCA in the B = 2.48 and 3.96 mixtures but only a minor amount in the highest basicity mixture. Basicity related studies by Umadevi, Rameshwar and Mahapatra (2014) has also shown that at higher basicity, normally, the formation of more quantity of SFCA phase takes place.

In Figure 5, compact sinter samples from three different basicity levels (1.67, 2.5 and 3.5) and three different temperature conditions (1240°C, 1280°C and 1400°C) are compared. All samples were quenched in water. At 1240°C the sinter samples from all three basicity values at 1.67, 2.5 and 3.5 had variable amounts of dense SFCA, very fine microplaty SFCA (below 5-micron size) and medium sized SFCA (around 10-micron size).

The SFCA textures were compared by the size and shape only and uncertainty remains whether these are SFCA-I or SFCA. Comparison of all three samples at 1240°C (Figure 5a, 5b and 5c) showed that the sample at a basicity of 1.67 had relatively coarse plates of SFCA while at B=2.5, fine and coarse SFCA were evenly mixed and in the sample at B=3.5, coarse SFCA was dominant over fine SFCA. At 1280°C and B=1.67 the sinter was characterised by an assemblage composed of microplaty SFCA/glass/magnetite with minor hematite. The SFCA phase was medium in size (below 10-micron size) and relatively homogeneous in terms of grainsize. At 2.5/1280°C the SFCA morphology consisted of fine flakes (microplates?) were mixed with medium sized flakes. Compared with the sample at 1.67/1280°C this sample had overall less magnetite. At 3.5/1280°C the sinter sample displayed flat plates of SFCA and the sizes of SFCA was relatively even throughout the sample and the sinter contained less magnetite. At 1.67/1400°C the sinter consisted mainly of magnetite and glass. There were very few acicular SFCA particles observed (Figure 5g). In comparison, at 2.5/1400°C the sinter assemblage consisted of magnetite with SFCA/glass matrix. The SFCA was characteristically thin, evenly sized (around 10 micron) and evenly distributed in glass matrix. The texture at 3.5/1400°C was similar to the sinter texture developed at 2.5/1400°C however, the SFCA content was much higher and acicular SFCA crystals were very much thicker/larger than in the 2.5/1400°C sinter sample. By comparing the magnetite/glass/SFCA contents in Figure 5g, 5h and 5i at the same temperature of 1400°C with increasing basicity from 1.67 to 2.5 and then to 3.5, the glass content decreased, magnetite content slightly decreased and SFCA content significantly increased.

From the above observations it can be concluded that basicity and temperature conditions have significant impact on SFCA formation and morphology. Lower basicity levels and higher temperatures favoured magnetite/glass formation and higher basicity levels favoured higher SFCA (perhaps both types, however this is optical identification of SFCA and therefore the type of SFCA is uncertain) formation.

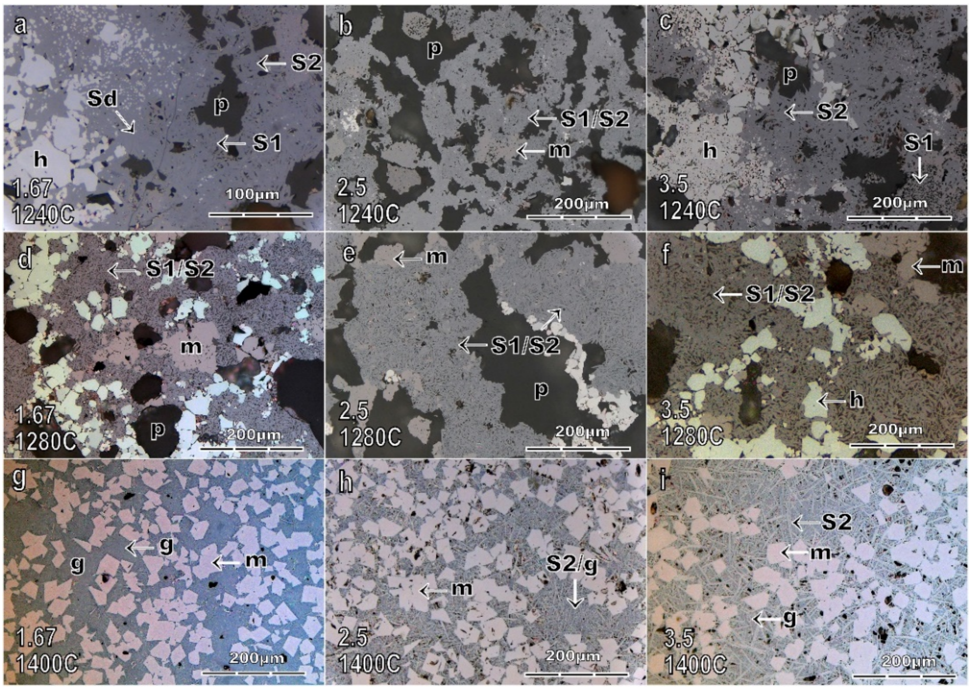

FIG 5 – Optical micrographs of compact sinter analogues at different basicity levels and temperature conditions. a) basicity 1.67/temperature 1240°C, b) basicity 2.5/temperature 1240°C, c) basicity 3.5/temperature 1240°C, d) basicity 1.67/temperature 1280°C, e) basicity

2.5/temperature 1280°C, f) basicity 3.5/temperature 1280°C, g) basicity 1.67/temperature 1400°C, h) basicity 2.5/temperature 1400°C, i) basicity 3.5/temperature 1400°C.

Effect on SFCA morphology with cooling rate

To compare the effect of cooling rate on sinter mineralogy, SFCA formation, morphology and texture, a series of tests were conducted at various basicity levels, temperature conditions and cooling rates. At the same basicity and temperature conditions, samples were quickly quenched in cold water and a duplicate sample allowed to cool in air permitting slow crystallisation. Representative optical images are displayed in Figure 6 to show the effects of cooling rate at the different basicity values and temperatures. Quenched and air-cooled samples at a basicity of 1.67 and at temperature level of 1280°C, are compared in Figure 6a and 6b. In both samples, the SFCA that developed displayed similar morphologies being fine-microplaty and dense in parts. However, the magnetite content was comparatively higher and the hematite content concomitantly lower in the rapidly quenched sample and the pores were significantly larger in the air-cooled sample. In comparison, a significant change in mineralogy was observed in the quenched and air-cooled samples at a basicity level of 1.67 and a temperature of 1400°C. The quenched sample contained mainly magnetite and glass/minor silicates and very few SFCA particles (Figure 6c). Compared with the quenched sample, the air-cooled sample contained less magnetite and glass and the main mineralogy was magnetite, prismatic SFCA, glass and larnite (Figure 6d). Completely different mineralogy and textures were also observed in the quenched and air-cooled samples at the basicity level of 2.5 and temperature 1360°C. The quenched sample (Figure 6e) contained a higher amount magnetite, glass and thin acicular SFCA and the air-cooled sample (Figure 6f) contained less magnetite and glass and large crystals of SFCA developed. Similar variations were observed in quenched and air-cooled samples at a basicity 2.5 and a temperature of 1400°C. Like the quenched sample at 1360°C (Figure 6e), the SFCA was acicular (Figure 6g), however, clear size differences were observed in the quenched sample at 1400°C (compare the images Figure 6e and 6g). The slower, air-cooled samples (Figure 6f and 6h) displayed similar mineralogy and textures, however it was observed that compared to the sample run at basicity 2.5, in the 1360°C sample, the magnetite content was higher than in the sample run at 1400°C. Clear differences were also observed in the quenched and air-cooled samples at the basicity level of 3.5 and temperature 1400°C. In both samples, SFCA was thin and acicular in the rapidly quenched sample (Figure 6i) and thick and platy in air-cooled sample (Figure 6j). It was also observed that the magnetite content was lower and the glass content was higher in the quenched sample compared to the air-cooled sample.

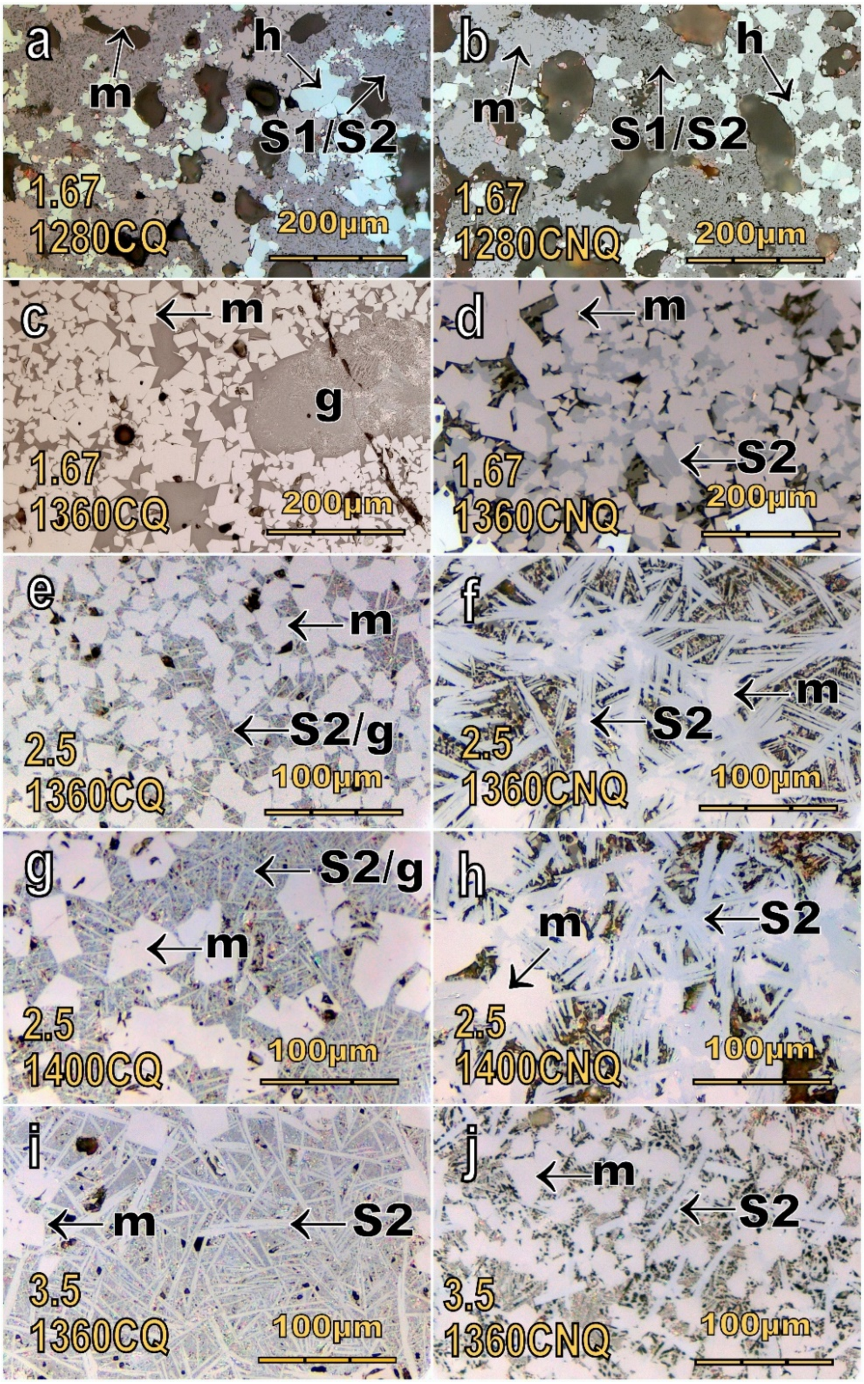

FIG 6 – Optical micrographs of compact sinter analogues at different basicity and cooling rates (Q=rapid cooled quenched in water, NQ=no quenching-slow air cooled). M=magnetite, S1=SFCA-I, S2=SFCA, g=glass, h=hematite. a) basicity 1.67/temperature 1280°C rapid cooled, b) basicity 1.67/temperature 1280°C slow cooled, c) basicity 1.67/temperature 1360°C rapid cooled, d) basicity 1.67/temperature 1360°C slow cooled, e) basicity 2.5/temperature 1360°C rapid cooled, f) basicity 2.5/temperature 1360°C slow cooled, g) basicity 2.5/temperature 1400°C rapid cooled, h) basicity 2.5/temperature 1400°C slow cooled, i) basicity 3.5/temperature 1360°C rapid cooled, j) basicity 3.5/temperature 1360°C slow cooled.

X-RAY DIFFRACTION (XRD) ANALYSIS

The relative SFCA-I and SFCA contents as well as the total content of all other phases derived from quantitative XRD data are shown in Figure 7 for selected sinter blends. Also, in Figure 7, point counting results (volume per cent) for several pot-grate sinter is included for comparison. Blend1 (basicity 2.0) and Blend1 (basicity 2.8) were prepared from the same ore; however, the basicity values were different (adding different ratios of CaO and SiO_2). When the basicity was increased from 2.0 to 2.8, the SFCA-I and SFCA contents and the total SFCA content increased significantly. In comparison, point counting data for the same samples showed similar total SFCA contents, however, point counting SFCA-I results were not compatible (point counting percentages of SFCA-I were much lower) than determined value of XRD data. This indicates that the SFCA-I/SFCA discrimination under optical microscopy had some errors and the distinction between the fine/coarse classification of SFCA-I/SFCA may not correct. Blend2R1 (basicity 1.9) and Blend2R2 (basicity 1.9) in the plots were also prepared using the same ore mixture but with different basicity levels but the two runs were conducted with different fuel (coke) levels. The XRD data showed that even with same ore blend and the same basicity, the SFCA formation and contents were variable due to the different fuel levels. The XRD data for the Blend3 (basicity 2.15) and Blend4 (basicity 1.5) again showed that the higher basicity favoured higher SFCA contents however at the lower basicity level of 1.5 the total SFCA content was lower. Samples Blend-A to Blend-G in the plot were seven pot-grate sinter samples from same ore blend and the basicity values gradually increased from Blend-A (basicity 1.2) to Blend-G (basicity 2.8). The point counting data showed that both SFCA-I and SFCA contents and the total SFCA content was increased with the increasing basicity levels. At very low basicity levels (basicity levels of 1.2 and 1.5), the total SFCA contents were comparatively lower than the total in tests conducted at higher basicity levels. For example, the total SFCA content at a basicity of 1.2 was around 9 per cent (volume) compared to 54 per cent (volume) at the basicity level of 2.8. However, there were some discrepancies as some pot-grate sinter samples showed conflicting results to the assumption that to the basicity level increase then accordingly, corresponding SFCA-I content too will be increased. The point counting data showed the same ore blend sinter with basicity value of 2.0 had SFCA-I 22 per cent (volume) and SFCA 25 per cent (volume). The same ore blend with basicity 3.5 had SFCA-I 16 per cent (volume), SFCA 46 per cent (volume). These results showed that the SFCA-I per cent was comparatively lower in higher basicity sinter. In another test the total SFCA contents in lower and higher basicity levels were significantly close, specially the SFCA-I contents (basicity level of 2.09 SFCA-I 7 per cent/SFCA 26 per cent (total SFCA 33 per cent), at the basicity level 2.8 SFCA-I 8 per cent, SFCA-29 per cent (total SFCA 37 per cent).

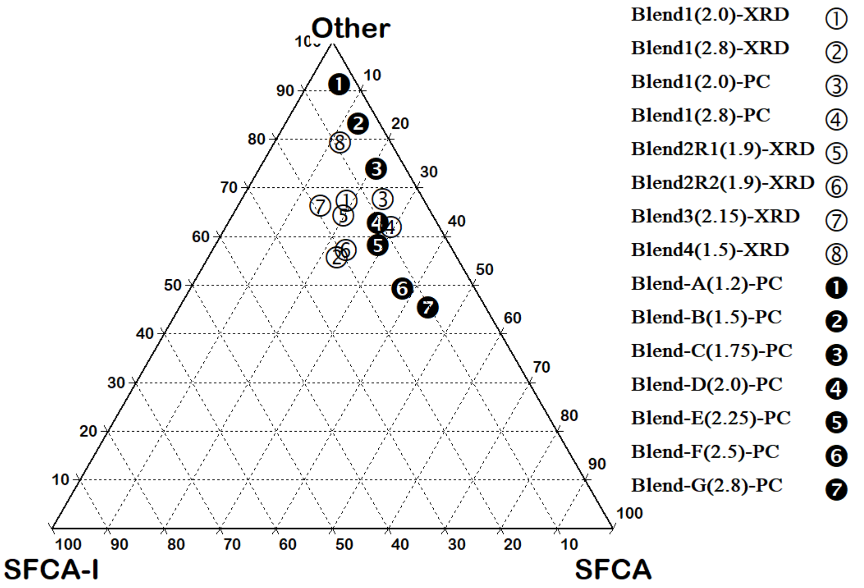

FIG 7 – Comparison of XRD and point count data (volume per cent) for SFCA-I, SFCA and total of other phases (including magnetite, hematite, glass and larnite) in pot-grate sinter from various blends under different basicity conditions.

Table 1 provides results from a comparison of XRD data for SFCA-I, SFCA and other calcium ferrites in compact sinter under various temperature-basicity conditions. The XRD data demonstrated that the higher basicity favours the formation of SFCA, however at higher basicity level (B=3.5) and temperature conditions above 1320°C SFCA was not stable and γ-CFF ($Ca_2Fe_{15.588}O_{25}$) was the stable phase. At temperature conditions above 1220°C SFCA-I was not formed in any of the samples while at higher temperature of 1400°C, SFCA was formed only at moderate basicity levels (B=2.5) and at the basicity level of 3.5 only γ-CFF ($Ca_2Fe_{15.588}O_{25}$) was stable. At the lower basicity level of

B=1.67 SFCA was unstable above 1320°C. From these observations it can be concluded that the basicity levels and temperature conditions greatly influence the formation of SFCA types such as SFCA-I, SFCA or γ-CFF ($Ca_2Fe_{15.588}O_{25}$) and the stability of these phases in sinter. At the basicity level of 2.5 and the temperature of 1200°C significant amount of SFCA-I has been formed; however, SFCA-I was not formed at the temperature conditions above 1220°C. However, in Figure 5b image display the sinter formed at the basicity level of 2.5 and temperature of 1240°C. The SFCA particles are fine and display a microplaty texture and therefore difficult to distinguish whether they are SFCA-I or SFCA. As XRD results indicate there was no SFCA-I in the sample it can be argued that SFCA too can display the fine-platy textures that are like SFCA-I. Figure 5c display the sinter from the test at basicity level of 3.5 and the temperature condition of 1240°C. XRD results indicated that there was no SFCA-I. Part of the Figure 5c image SFCA texture is similar to the SFCA-I. Therefore, the SFCA-I optically identified as S1 in image should be SFCA not SFCA-I. At the basicity level of 1.67 no SFCA-I was reported the temperature conditions above 1200°C. However, in Figure 5d SFCA display textures like that of SFCA-I. Same observations can be seen on Figure 5e, XRD analysis indicated that there was no SFCA-I, however SFCA in image display fine-platy SFCA which are realistically SFCA (according to XRD analysis). Based on XRD analysis, at the basicity level of 2.5 and temperature condition of 1360°C there was no SFCA-I formed. The SFCA in Figure 6e (quenched sample) display acicular texture and are fine in size while SFCA in Figure 6f are platy and coarse in size. Based on this comparison it can be considered that SFCA too can formed as fine or coarse crystals depending on the cooling rate. At the basicity level of 3.5 and the temperature condition of 1360°C γ-CFF ($Ca_2Fe_{15.588}O_{25}$) was formed. Figure 6i and 6j display the textures of γ-CFF ($Ca_2Fe_{15.588}O_{25}$) phase that are like SFCA. From the above observations it can be concluded that different phases of SFCA-I, SFCA and γ-CFF ($Ca_2Fe_{15.588}O_{25}$) can develop similar textures and the optical classification based on the size and texture may not be accurate.

TABLE 1

Comparison of XRD data for SFCA-I, SFCA and other calcium ferrites in compact sinters run under various temperature conditions and basicity levels.

Basicity	T C°	SFCA	SFCA-I	2CaO.Fe_2O_3 (C_2F)	CaO.Fe_2O_3 (CF)	γ-CFF ($Ca_2Fe_{15.588}O_{25}$)
2.5	1200	29	21.5	nd.	nd.	nd.
2.5	1220	34.2	nd.	6.8	nd.	nd.
2.5	1240	59.7	nd.	nd.	nd.	nd.
2.5	1280	53.9	nd.	nd.	nd.	nd.
2.5	1320	25.7	nd.	nd.	nd.	nd.
2.5	1360	35.6	nd.	nd.	nd.	nd.
2.5	1400	19.7	nd.	nd.	nd.	nd.
3.5	1200	22.3	nd.	8.2	15.7	nd.
3.5	1240	49.4	nd.	1.6	nd.	nd.
3.5	1280	31.1	34.5	nd.	nd.	nd.
3.5	1320	nd.	nd.	nd.	nd.	40.8
3.5	1360	nd.	nd.	nd.	nd.	35.2
3.5	1400	nd.	nd.	nd.	nd.	23.4
1.67	1200	23.6	10.6	1.2	nd.	nd.
1.67	1240	48.2	nd.	3.7	nd.	nd.
1.67	1280	32.6	nd.	nd.	nd.	nd.
1.67	1320	nd.	nd.	nd.	nd.	nd.
1.67	1360	nd.	nd.	nd.	nd.	nd.
1.67	1400	nd.	nd.	nd.	nd.	nd.

ELECTRON PROBE MICROANALYSIS (EPMA) AND SEM IMAGING RESULTS

EPMA analysis was performed on sinter samples from two blends with different basicity levels to compare the chemical composition of sinter phases including fine-microplaty SFCA (SF), coarse-columnar SFCA (SC), short-prismatic SFCA (SP) and other phases.

Based on analysis by Hancart, Leroy and Bragard (1967) and Ahsan, Mukherjee and Whiteman (1983), SFCA in industrial plant sinters typically contain 60.01–75.78 wt. per cent Fe_2O_3 (also contains FeO), 12.59–15.39 wt. per cent CaO, 2.3–10.05 wt. per cent SiO_2, 3.8–9.5 wt. per cent

Al_2O_3 and 0.66–1.66 wt. per cent MgO. Mumme, Clout and Gable (1998) reported that SFCA-I phase found in industrial plant sinters contained comparatively higher 81.3–83.0 wt. per cent Fe_2O_3 than in SFCA, 12.6 wt. per cent CaO, 1.07 wt per cent SiO_2 and 1.9 mass per cent Al_2O_3. Webster *et al* (2012) found that SFCA in industrial sinter was comprised of 60–76 wt. per cent Fe_2O_3, 3–10 wt. per cent SiO_2, 13–16 wt. per cent CaO, 0.7–1.5 per cent MgO, 4–10 wt. per cent Al_2O_3, while SFCA-1 contained 84.4 wt. per cent Fe_2O_3, 12.8 wt. per cent CaO, 0.9 wt. per cent SiO_2, 2.2 wt. per cent Al_2O_3, which is equivalent to a chemical composition of $(Fe_2O_3)_{5.3}(SiO_2)_{0.16}(CaO)_{2.3}(Al_2O_3)_{0.22}$. Honeyands *et al* (2017) reported average SFCA-I composition in a sinter particle contained Fe (54.6 per cent), Ca (9.1 per cent), Si (1.3 per cent) and Al (1.3 per cent) plus a small amount (0.5 per cent) of Mg. Their sinter sample appears to be had more variation in the SFCA-I than in the sample reported by Mumme, Clout and Gable (1998) however, they noted that there is a lack of previously reported quantitative data for SFCA-I and its compositional range remains unknown. Honeyands *et al* (2017) also reported a second variant of the SFCA morphological type characteristically contained a high proportion of Mg (1.5 per cent) and Fe (56.9 per cent) and low Ca (6.5 per cent), Al (1.1 per cent) and Si (0.9 per cent). The exact nature of this phase was unknown however it was noted that its composition is very similar to an unknown phase first noted in pot grate and laboratory sinter by Webster *et al* (2012).

SEM backscattered imaging

SEM backscattered images provide useful information related to the different phases and the chemical variation within the same phase. SEM colour map technique based on electron back scattering can be used to create elemental maps to understand minor element variations within a small area. Figure 8 shows SEM backscattered electron images of fine microplaty SFCA (labelled as S1 in Figure 8a and 8b), coarse platy SFCA (labelled as S2 in Figure 8b, 8c, 8d, 8e and 8f), dense SFCA (labelled as S2 in Figure 8c) and prismatic SFCA (labelled as S2 in Figure 8g, 8h and 8i). In Figure 8b the images show that fine microplaty SFCA and coarse platy SFCA formed next to each other in close vicinity. In comparison, Figure 8c shows that fine microplaty SFCA and dense SFCA formed next to each other.

In Figure 8a, 8b and 8c SFCA appears to be homogeneous by the appearance (reflectivity) however, EPMA analysis confirmed that there were significant differences in chemistry within a small area. In Figure 8g significant variation in grey colour (dark grey and light grey variations in the same SFCA crystals) reflect low and high Fe zones within the same SFCA crystals. In Figure 8d, 8e (colour induced) and 8f clear chemical zonation of SFCA can be recognised. Prismatic SFCA in Figure 8g, 8h and 8i (colour induced) to display some fine chemical zonation. While the caution was taken to analyse the SFCA particles away from magnetite, some SFCA and magnetite (such as in Figure 8f) display a diffusive boundary and due to the presence of subsurface magnetite EPMA analysis can be inaccurate. In Figure 8e magnetite (green) SFCA (blue) and glass/larnite (purple) zones are shown. SFCA light blue crystals display colour differences (zones) of blue – light blue indicating the chemical zonation within SFCA. In Figure 8d and 8f SFCA display light grey-dark grey zones indicating the chemical differences. In Figure 8h (SFCA-light grey) and 8i (SFCA-blue) display some homogeneity.

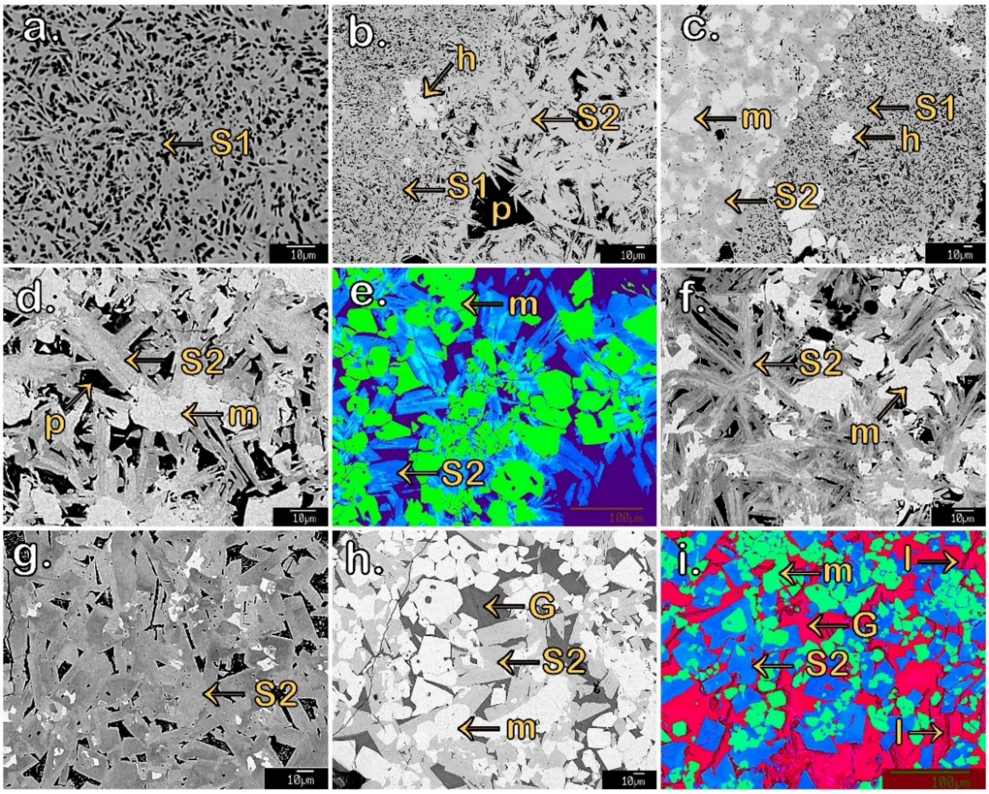

FIG 8 – SEM backscattered electron images displaying various SFCA morphologies. S1=SFCA-I, S2=SFCA, m=magnetite, h=hematite, l=larnite, G=glass, p=pore. Images a, b, c, d, f, g and h are SEM backscattered images which can show the chemical differences of the mineral phases; and images e and i are the colour induced backscattered images to enhance the chemical differences of the phases in the images.

EPMA data (element concentrations as wt. per cent)

Figure 9 shows a comparison of the measured Fe_2O_3, CaO, MgO, SiO_2 and Al_2O_3 data from the EPMA conducted on over 360 different SFCA particles (irrespective of their particle size, morphology, or texture and neglecting whether they are SFCA-I or SFCA) in a single pot-grate sinter sample. The SFCA particles were mainly separate SFCA particles which either can be SFCA-I or SFCA. The sinter blend chemistry was: Total Fe (56.05 wt. per cent), CaO (10 wt. per cent), MgO (1.5 wt. per cent), SiO_2 (5 wt. per cent) and Al_2O_3 (2.43 wt. per cent) and the resulting sinter had the chemistry of: Total Fe (56.05 wt. per cent), FeO (6.63 wt. per cent), CaO (10.12 wt. per cent), MgO (1.5 wt. per cent), SiO_2 (4.84 wt. per cent) and Al_2O_3 2.49 wt. per cent).The plot in Figure 9 displays a comparison of other elements such as CaO, MgO, SiO_2 and Al_2O_3 against decreasing Fe_2O_3 content (wt. per cent). The EPMA data indicated the existence of range of SFCA compositions varying with Fe_2O_3:42–89 wt. per cent, with an average of 77.1 (STDEV=6.0) wt. per cent, CaO: 0–38.0 wt. per cent with an average of 13.2 (STDEV=5.3) wt. per cent, MgO: 0–17.0 wt. per cent with an average of 2.0 (STDEV=3.6) wt. per cent, SiO_2:0–17 wt. per cent with an average of 3.7 (STDEV=2.7) wt. per cent and Al_2O_3:1.1–8.9 wt. per cent with an average of 3.7 (STDEV=1.4) wt. per cent. All SFCA analysis displayed minor concentrations of TiO_2 and MnO_2. Some of the SFCA compositions with higher CaO concentrates might be calcium ferrite (CF) rather than SFCA. Two clusters of compositions, one with higher Fe_2O_3 contents and an MgO content of around 9.0 per cent and one MgO cluster with around 17.0 per cent with lower concentrations of all other elements, are considered as two magnesium ferrite varieties. Except for the two high Mg clusters it was hard to recognise other clusters in related to CaO, Al_2O_3 or SiO_2.In general, with decreasing Fe_2O_3 content the weight percentages of all the other elements (except for MgO) gradually increased. With this observation it can be concluded that the chemistry of SFCA phase even in one iron ore pot-grate sinter is highly variable and it was not possible to classify them into various groups.

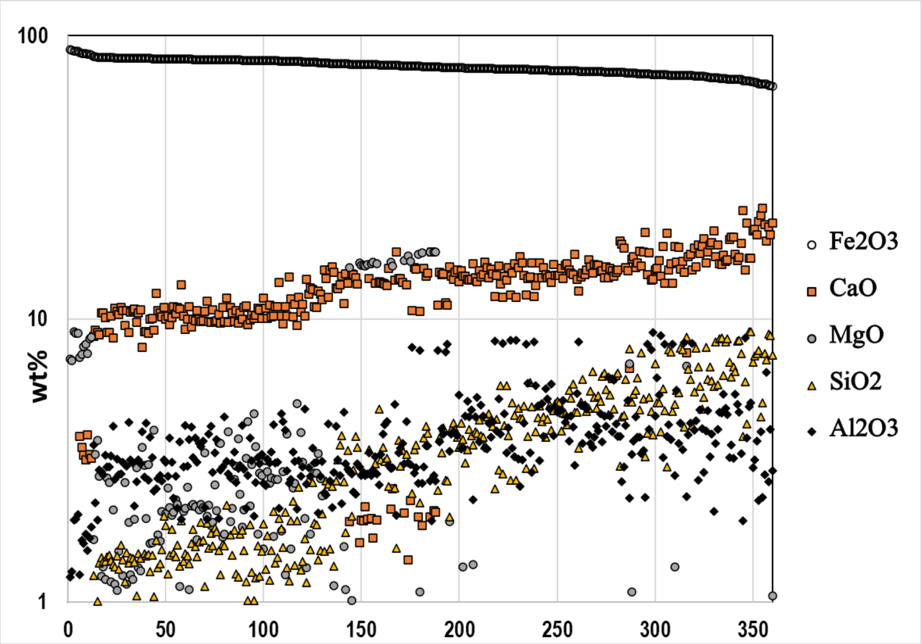

FIG 9 – Comparison of Fe_2O_3, CaO, MgO, SiO_2 and Al_2O_3 data in 360 SFCA particles in a pot-grate sinter sample. (note the Y axis in logarithmic scale).

Figure 10 shows a comparison of the measured Fe_2O_3, CaO, SiO_2 and Al_2O_3 data from the EPMA conducted on large number of SFCA particles (irrespective of their particle size, morphology, or texture and neglecting whether they are SFCA-I or SFCA) in a variety of pot-grate sinter samples. The SFCA particles were mainly separate SFCA particles which either can be SFCA-I or SFCA. The plot in Figure 10 displays a comparison of other elements such as CaO, SiO_2 and Al_2O_3 against Fe_2O_3 content (wt. per cent). The EPMA data indicated the existence of vast range of SFCA compositions varying with Fe_2O_3:60.0–89.0 wt. per cent, CaO: 8.0–20.0 wt. per cent, SiO_2:0–10 wt. per cent and Al_2O_3:1.5–16 wt. per cent. All SFCA analysis displayed minor concentrations of TiO_2 and MnO_2.In general, with decreasing Fe_2O_3 content the weight percentages of all the other elements gradually increased. With this observation it can be concluded that the chemistry of SFCA phases in iron ore pot-grate sinter is highly variable and it was not possible to classify them into various groups based on EPMA chemistry alone.

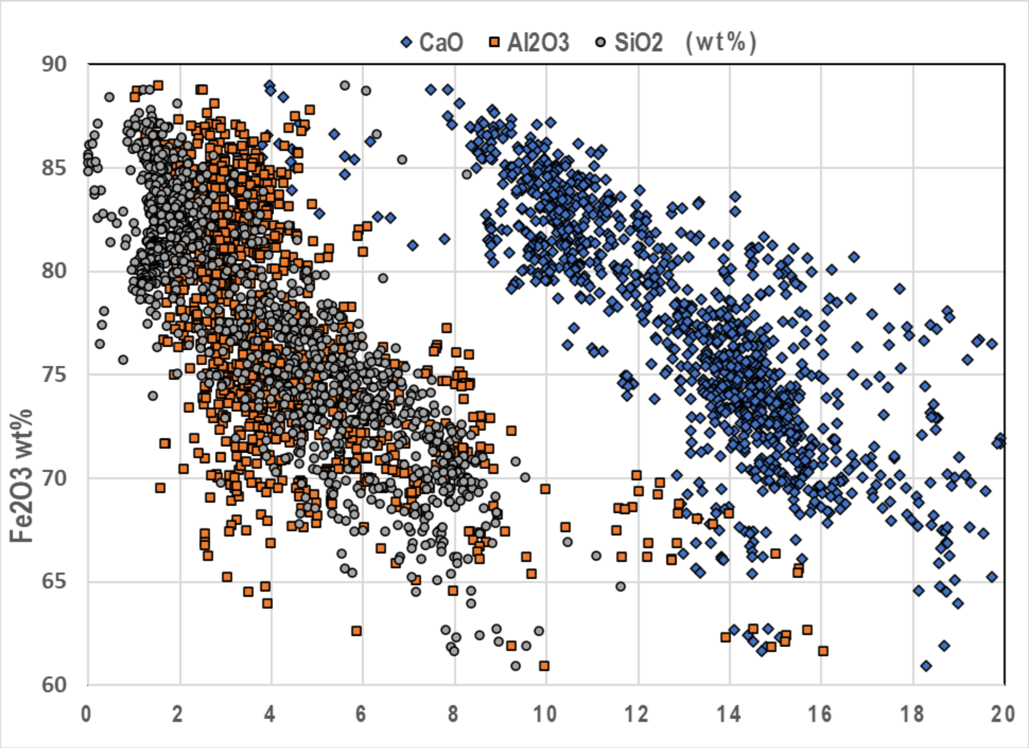

FIG 10 – Variation of Fe_2O_3, CaO, SiO_2 and Al_2O_3 EPMA analysis data in SFCA in iron ore pot-grate sinters.

A summary table showing the average EPMA compositional data for the various types of SFCA particle in several pot-grate sinter samples (samples are made of representative -1 mm sinter particles), one compact sinter analogue, a pot-grate sinter lump sample and SFCA from a slag iron sample is presented in Table 3. Particles or areas with different SFCA morphologies and the association of SFCA with other sinter phases such as magnetite or glass etc were selected and several spots on SFCA particles in a particular particle or an area were analysed under EPMA. The main SFCA morphologies analysed were, fine micro-platy SFCA (similar to SFCA-I (S1) in Figure 2a), coarse flaky or platy (similar to SFCA in Figure 2b area S2, 2c, 2e, 2f and 2g areas marked as S2), coarse-tabular prismatic (similar to the SFCA in Figure 2p and 2q and mostly associated with magnetite and glass), coarse platy-thin acicular (similar to the SFCA in Figure 2t) and dense SFCA (similar to the SFCA in Figure 3c). Particles with a similar morphology and chemistry were added together and then it was possible to recognise some chemical differences in separate morphologies or within the same SFCA morphological type. For example, there were clear chemical differences between fine SFCA with coarse SFCA (in the same sample) and chemical differences within the same SFCA morphological type. As well, in the sinter from Blend1 (basicity 2.1), two clusters of coarse plates (flaky) SFCA, three clusters of fine microplaty SFCA and three clusters of coarse tabular-prismatic SFCA were identified. There were clear chemical differences within the same SFCA morphology such as fine microplaty SFCA with higher contents (Fe_2O_3 wt. 83 per cent), medium (Fe_2O_3 wt. 75 per cent) and low (Fe_2O_3 wt. 69 per cent). MnO_2 and TiO_2 contents in majority SFCA were very low, MnO_2 ranging from 0.01–0.8 wt. per cent and TiO_2 contents varying from 0.0–0.6 wt. per cent. Generally, in all samples a variety of coarse flaky (platy) SFCA has shown the Fe_2O_3 contents above 80 wt. per cent.

Magnesium ferrite was difficult to recognise optically in sinter samples, however, based on the EPMA data magnesium ferrite compositions were clearly identified in sinter from several blends. In Blend5, magnesium ferrite exhibited a morphology like dense microplaty SFCA and had characteristically high Fe_2O_3:80 wt. per cent, MgO: 16 wt. per cent, CaO: 2wt. per cent, Al_2O_3:3 wt. per cent, low SiO_2 whereas in the form of coarse flaky (platy) SFCA it had high Fe_2O_3:88 wt. per cent, MgO:10 wt. per cent, CaO: 2 wt. per cent, Al_2O_3:2.3 wt. per cent, low SiO_2. In Blend11 sinter, the magnesium ferrite had a texture similar to fine microplaty SFCA with high Fe_2O_3:84 wt. per cent, MgO:10 wt. per cent, CaO: 5 wt. per cent, Al_2O_3:1.8 wt. per cent, low SiO_2 and in Blend8 the magnesium ferrite appeared similar in appearance to coarse flaky (platy) SFCA with high

Fe_2O_3:86 wt. per cent, MgO:9.8 wt. per cent, CaO: 4.7 wt. per cent, Al_2O_3:1.3 wt. per cent, low SiO_2. From these observations it can be concluded that magnesium ferrite can form similar morphologies to dense fine microplaty SFCA, coarse flaky (platy) SFCA or coarse tabular-prismatic SFCA and therefore may very likely be confused with the identification of SFCA.

Based on the EPMA data in Table 2 following observations can be made. SFCA compositions with high Fe_2O_3 (>80 wt. per cent), was reported in majority of SFCA averages (in thirteen samples) in spot measurement on coarse platy SFCA morphologies. Three samples had fine microplaty SFCA with high Fe_2O_3 (>80 wt. per cent). One sample had high Fe_2O_3 (>80 wt. per cent), coarse tabular-prismatic SFCA and another one sample had coarse acicula SFCA with high Fe_2O_3 (>80 wt. per cent). Coarse tabular-prismatic SFCA in thirteen samples had low Fe_2O_3 in the range of 62–73 wt. per cent. However, there were several low Fe_2O_3 (below 70 wt. per cent), medium Fe_2O_3 (between 70–80 wt. per cent) and high Fe_2O_3 (over 80 wt. per cent) average SFCA compositions were reported as all forms of SFCA morphologies irrespective of whether they were fine microplaty SFCA, coarse flaky (platy) SFCA, dense SFCA, coarse prismatic SFCA or coarse acicular SFCA.

Webster *et al* (2012) found that SFCA in industrial sinter was comprised of 60–76 wt. per cent Fe_2O_3, 3–10 wt. per cent SiO_2, 13–16 wt. per cent CaO, 0.7–1.5 per cent MgO, 4–10 wt. per cent Al_2O_3, while SFCA-1 contained 84.4 wt. per cent Fe_2O_3, 12.8 wt. per cent CaO, 0.9 wt. per cent SiO_2, 2.2 wt. per cent Al_2O_3. When comparing the measured EPMA data of pot-grate sinter in this study and industrial sinter described by Webster *et al* (2012), several compatible compositions can be seen. However, SFCA-I/SFCA classification based on size and texture is still questionable as both fine/coarse versions had similar compositional range based on EPMA results.

TABLE 2

Average EPMA analysis data for various SFCA-I and SFCA types identified in pot-grate sinter, compact sinter and in a slag iron sample.

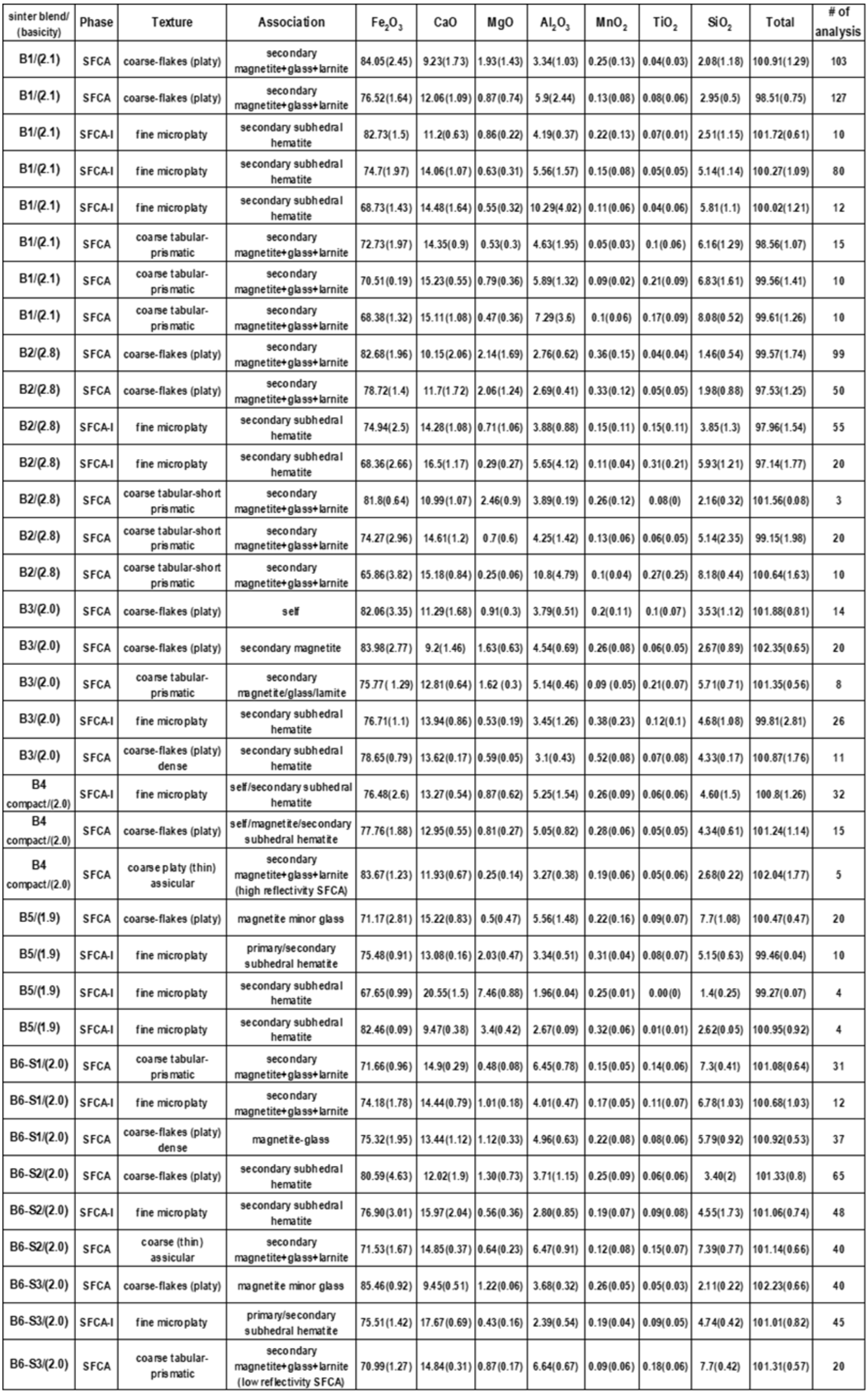

sinter blend/ (basicity)	Phase	Texture	Association	Fe_2O_3	CaO	MgO	Al_2O_3	MnO_2	TiO_2	SiO_2	Total	# of analysis
B1/(2.1)	SFCA	coarse-flakes (platy)	secondary magnetite+glass+larnite	84.05(2.45)	9.23(1.73)	1.93(1.43)	3.34(1.03)	0.25(0.13)	0.04(0.03)	2.08(1.18)	100.91(1.29)	103
B1/(2.1)	SFCA	coarse-flakes (platy)	secondary magnetite+glass+larnite	76.52(1.64)	12.06(1.09)	0.87(0.74)	5.9(2.44)	0.13(0.08)	0.08(0.06)	2.95(0.5)	98.51(0.75)	127
B1/(2.1)	SFCA-I	fine microplaty	secondary subhedral hematite	82.73(1.5)	11.2(0.63)	0.86(0.22)	4.19(0.37)	0.22(0.13)	0.07(0.01)	2.51(1.15)	101.72(0.61)	10
B1/(2.1)	SFCA-I	fine microplaty	secondary subhedral hematite	74.7(1.97)	14.06(1.07)	0.63(0.31)	5.56(1.57)	0.15(0.08)	0.05(0.05)	5.14(1.14)	100.27(1.09)	80
B1/(2.1)	SFCA-I	fine microplaty	secondary subhedral hematite	68.73(1.43)	14.48(1.64)	0.55(0.32)	10.29(4.02)	0.11(0.06)	0.04(0.06)	5.81(1.1)	100.02(1.21)	12
B1/(2.1)	SFCA	coarse tabular-prismatic	secondary magnetite+glass+larnite	72.73(1.97)	14.35(0.9)	0.53(0.3)	4.63(1.95)	0.05(0.03)	0.1(0.06)	6.16(1.29)	98.56(1.07)	15
B1/(2.1)	SFCA	coarse tabular-prismatic	secondary magnetite+glass+larnite	70.51(0.19)	15.23(0.55)	0.79(0.36)	5.89(1.32)	0.09(0.02)	0.21(0.09)	6.83(1.61)	99.56(1.41)	10
B1/(2.1)	SFCA	coarse tabular-prismatic	secondary magnetite+glass+larnite	68.38(1.32)	15.11(1.08)	0.47(0.36)	7.29(3.6)	0.1(0.06)	0.17(0.09)	8.08(0.52)	99.61(1.26)	10
B2/(2.8)	SFCA	coarse-flakes (platy)	secondary magnetite+glass+larnite	82.68(1.96)	10.15(2.06)	2.14(1.69)	2.76(0.62)	0.36(0.15)	0.04(0.04)	1.46(0.54)	99.57(1.74)	99
B2/(2.8)	SFCA	coarse-flakes (platy)	secondary magnetite+glass+larnite	78.72(1.4)	11.7(1.72)	2.06(1.24)	2.69(0.41)	0.33(0.12)	0.05(0.05)	1.98(0.88)	97.53(1.25)	50
B2/(2.8)	SFCA-I	fine microplaty	secondary subhedral hematite	74.94(2.5)	14.28(1.08)	0.71(1.06)	3.88(0.88)	0.15(0.11)	0.15(0.11)	3.85(1.3)	97.96(1.54)	55
B2/(2.8)	SFCA-I	fine microplaty	secondary subhedral hematite	68.36(2.66)	16.5(1.17)	0.29(0.27)	5.65(4.12)	0.11(0.04)	0.31(0.21)	5.93(1.21)	97.14(1.77)	20
B2/(2.8)	SFCA	coarse tabular-short prismatic	secondary magnetite+glass+larnite	81.8(0.64)	10.99(1.07)	2.46(0.9)	3.89(0.19)	0.26(0.12)	0.08(0)	2.16(0.32)	101.56(0.08)	3
B2/(2.8)	SFCA	coarse tabular-short prismatic	secondary magnetite+glass+larnite	74.27(2.96)	14.61(1.2)	0.7(0.6)	4.25(1.42)	0.13(0.06)	0.06(0.05)	5.14(2.35)	99.15(1.98)	20
B2/(2.8)	SFCA	coarse tabular-short prismatic	secondary magnetite+glass+larnite	65.86(3.82)	15.18(0.84)	0.25(0.06)	10.8(4.79)	0.1(0.04)	0.27(0.25)	8.18(0.44)	100.64(1.63)	10
B3/(2.0)	SFCA	coarse-flakes (platy)	self	82.06(3.35)	11.29(1.68)	0.91(0.3)	3.79(0.51)	0.2(0.11)	0.1(0.07)	3.53(1.12)	101.88(0.81)	14
B3/(2.0)	SFCA	coarse-flakes (platy)	secondary magnetite	83.98(2.77)	9.2(1.46)	1.63(0.63)	4.54(0.69)	0.26(0.08)	0.06(0.05)	2.67(0.89)	102.35(0.65)	20
B3/(2.0)	SFCA	coarse tabular-prismatic	secondary magnetite/glass/lamite	75.77(1.29)	12.81(0.64)	1.62 (0.3)	5.14(0.46)	0.09 (0.05)	0.21(0.07)	5.71(0.71)	101.35(0.56)	8
B3/(2.0)	SFCA-I	fine microplaty	secondary subhedral hematite	76.71(1.1)	13.94(0.86)	0.53(0.19)	3.45(1.26)	0.38(0.23)	0.12(0.1)	4.68(1.08)	99.81(2.81)	26
B3/(2.0)	SFCA	coarse-flakes (platy) dense	secondary subhedral hematite	78.65(0.79)	13.62(0.17)	0.59(0.05)	3.1(0.43)	0.52(0.08)	0.07(0.08)	4.33(0.17)	100.87(1.76)	11
B4 compact/(2.0)	SFCA-I	fine microplaty	self/secondary subhedral hematite	76.48(2.6)	13.27(0.54)	0.87(0.62)	5.25(1.54)	0.26(0.09)	0.06(0.06)	4.60(1.5)	100.8(1.26)	32
B4 compact/(2.0)	SFCA	coarse-flakes (platy)	self/magnetite/secondary subhedral hematite	77.76(1.88)	12.95(0.55)	0.81(0.27)	5.05(0.82)	0.28(0.06)	0.05(0.05)	4.34(0.61)	101.24(1.14)	15
B4 compact/(2.0)	SFCA	coarse platy (thin) assicular	secondary magnetite+glass+larnite (high reflectivity SFCA)	83.67(1.23)	11.93(0.67)	0.25(0.14)	3.27(0.38)	0.19(0.06)	0.05(0.06)	2.68(0.22)	102.04(1.77)	5
B5/(1.9)	SFCA	coarse-flakes (platy)	magnetite minor glass	71.17(2.81)	15.22(0.83)	0.5(0.47)	5.56(1.48)	0.22(0.16)	0.09(0.07)	7.7(1.08)	100.47(0.47)	20
B5/(1.9)	SFCA-I	fine microplaty	primary/secondary subhedral hematite	75.48(0.91)	13.08(0.16)	2.03(0.47)	3.34(0.51)	0.31(0.04)	0.08(0.07)	5.15(0.63)	99.46(0.04)	10
B5/(1.9)	SFCA-I	fine microplaty	secondary subhedral hematite	67.65(0.99)	20.55(1.5)	7.46(0.88)	1.96(0.04)	0.25(0.01)	0.00(0)	1.4(0.25)	99.27(0.07)	4
B5/(1.9)	SFCA-I	fine microplaty	secondary subhedral hematite	82.46(0.09)	9.47(0.38)	3.4(0.42)	2.67(0.09)	0.32(0.06)	0.01(0.01)	2.62(0.05)	100.95(0.92)	4
B6-S1/(2.0)	SFCA	coarse tabular-prismatic	secondary magnetite+glass+larnite	71.66(0.96)	14.9(0.29)	0.48(0.08)	6.45(0.78)	0.15(0.05)	0.14(0.06)	7.3(0.41)	101.08(0.64)	31
B6-S1/(2.0)	SFCA-I	fine microplaty	secondary magnetite+glass+larnite	74.18(1.78)	14.44(0.79)	1.01(0.18)	4.01(0.47)	0.17(0.05)	0.11(0.07)	6.78(1.03)	100.68(1.03)	12
B6-S1/(2.0)	SFCA	coarse-flakes (platy) dense	magnetite-glass	75.32(1.95)	13.44(1.12)	1.12(0.33)	4.96(0.63)	0.22(0.08)	0.08(0.06)	5.79(0.92)	100.92(0.53)	37
B6-S2/(2.0)	SFCA	coarse-flakes (platy)	secondary subhedral hematite	80.59(4.63)	12.02(1.9)	1.30(0.73)	3.71(1.15)	0.25(0.09)	0.06(0.06)	3.40(2)	101.33(0.8)	65
B6-S2/(2.0)	SFCA-I	fine microplaty	secondary subhedral hematite	76.90(3.01)	15.97(2.04)	0.56(0.36)	2.80(0.85)	0.19(0.07)	0.09(0.08)	4.55(1.73)	101.06(0.74)	48
B6-S2/(2.0)	SFCA	coarse (thin) assicular	secondary magnetite+glass+larnite	71.53(1.67)	14.85(0.37)	0.64(0.23)	6.47(0.91)	0.12(0.08)	0.15(0.07)	7.39(0.77)	101.14(0.66)	40
B6-S3/(2.0)	SFCA	coarse-flakes (platy)	magnetite minor glass	85.46(0.92)	9.45(0.51)	1.22(0.06)	3.68(0.32)	0.26(0.05)	0.05(0.03)	2.11(0.22)	102.23(0.66)	40
B6-S3/(2.0)	SFCA-I	fine microplaty	primary/secondary subhedral hematite	75.51(1.42)	17.67(0.69)	0.43(0.16)	2.39(0.54)	0.19(0.04)	0.09(0.05)	4.74(0.42)	101.01(0.82)	45
B6-S3/(2.0)	SFCA	coarse tabular-prismatic	secondary magnetite+glass+larnite (low reflectivity SFCA)	70.99(1.27)	14.84(0.31)	0.87(0.17)	6.64(0.67)	0.09(0.06)	0.18(0.06)	7.7(0.42)	101.31(0.57)	20

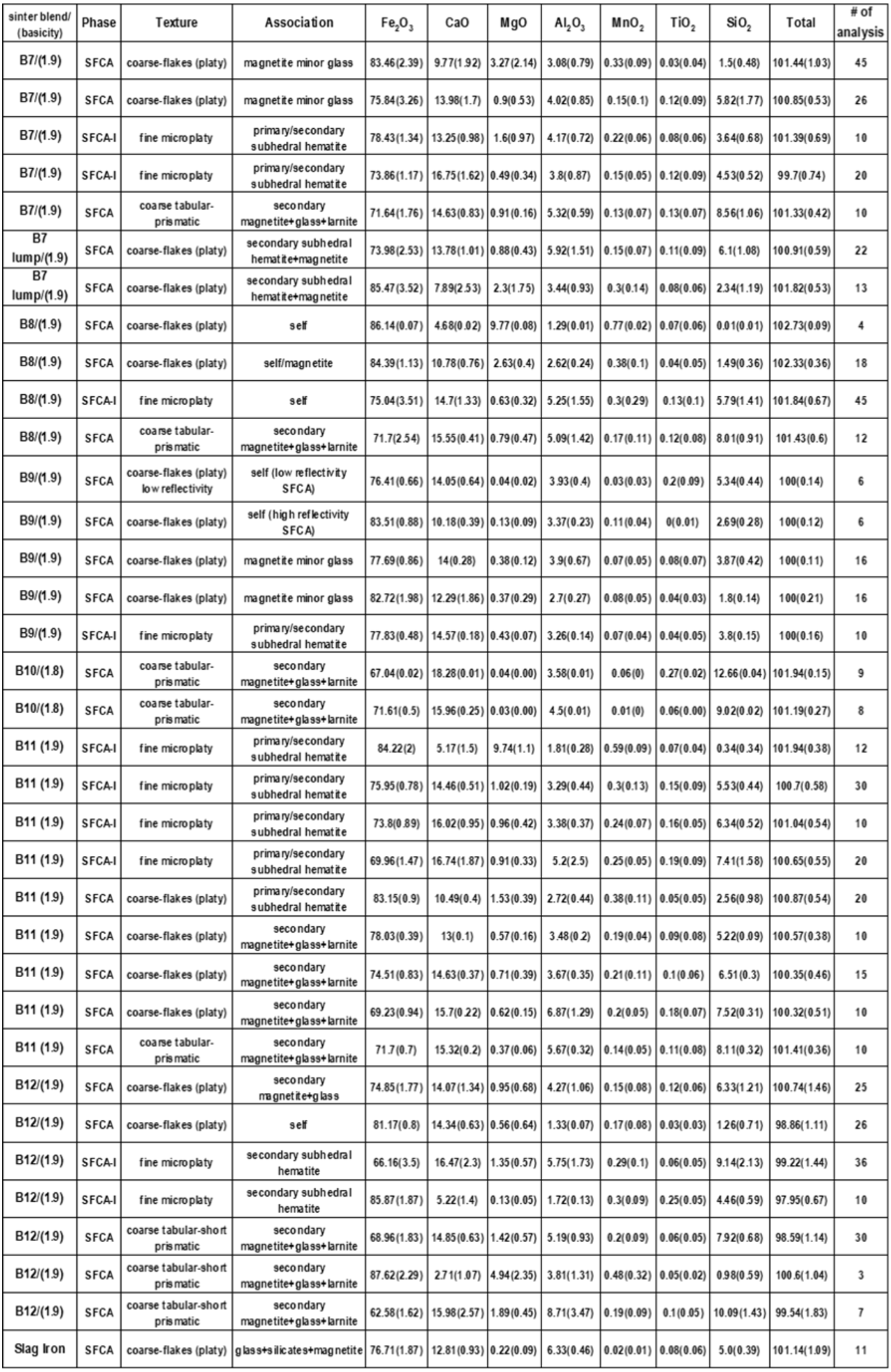

sinter blend/ (basicity)	Phase	Texture	Association	Fe_2O_3	CaO	MgO	Al_2O_3	MnO_2	TiO_2	SiO_2	Total	# of analysis
B7/(1.9)	SFCA	coarse-flakes (platy)	magnetite minor glass	83.46(2.39)	9.77(1.92)	3.27(2.14)	3.08(0.79)	0.33(0.09)	0.03(0.04)	1.5(0.48)	101.44(1.03)	45
B7/(1.9)	SFCA	coarse-flakes (platy)	magnetite minor glass	75.84(3.26)	13.98(1.7)	0.9(0.53)	4.02(0.85)	0.15(0.1)	0.12(0.09)	5.82(1.77)	100.85(0.53)	26
B7/(1.9)	SFCA-I	fine microplaty	primary/secondary subhedral hematite	78.43(1.34)	13.25(0.98)	1.6(0.97)	4.17(0.72)	0.22(0.06)	0.08(0.06)	3.64(0.68)	101.39(0.69)	10
B7/(1.9)	SFCA-I	fine microplaty	primary/secondary subhedral hematite	73.86(1.17)	16.75(1.62)	0.49(0.34)	3.8(0.87)	0.15(0.05)	0.12(0.09)	4.53(0.52)	99.7(0.74)	20
B7/(1.9)	SFCA	coarse tabular-prismatic	secondary magnetite+glass+larnite	71.64(1.76)	14.63(0.83)	0.91(0.16)	5.32(0.59)	0.13(0.07)	0.13(0.07)	8.56(1.06)	101.33(0.42)	10
B7 lump/(1.9)	SFCA	coarse-flakes (platy)	secondary subhedral hematite+magnetite	73.98(2.53)	13.78(1.01)	0.88(0.43)	5.92(1.51)	0.15(0.07)	0.11(0.09)	6.1(1.08)	100.91(0.59)	22
B7 lump/(1.9)	SFCA	coarse-flakes (platy)	secondary subhedral hematite+magnetite	85.47(3.52)	7.89(2.53)	2.3(1.75)	3.44(0.93)	0.3(0.14)	0.08(0.06)	2.34(1.19)	101.82(0.53)	13
B8/(1.9)	SFCA	coarse-flakes (platy)	self	86.14(0.07)	4.68(0.02)	9.77(0.08)	1.29(0.01)	0.77(0.02)	0.07(0.06)	0.01(0.01)	102.73(0.09)	4
B8/(1.9)	SFCA	coarse-flakes (platy)	self/magnetite	84.39(1.13)	10.78(0.76)	2.63(0.4)	2.62(0.24)	0.38(0.1)	0.04(0.05)	1.49(0.36)	102.33(0.36)	18
B8/(1.9)	SFCA-I	fine microplaty	self	75.04(3.51)	14.7(1.33)	0.63(0.32)	5.25(1.55)	0.3(0.29)	0.13(0.1)	5.79(1.41)	101.84(0.67)	45
B8/(1.9)	SFCA	coarse tabular-prismatic	secondary magnetite+glass+larnite	71.7(2.54)	15.55(0.41)	0.79(0.47)	5.09(1.42)	0.17(0.11)	0.12(0.08)	8.01(0.91)	101.43(0.6)	12
B9/(1.9)	SFCA	coarse-flakes (platy) low reflectivity	self (low reflectivity SFCA)	76.41(0.66)	14.05(0.64)	0.04(0.02)	3.93(0.4)	0.03(0.03)	0.2(0.09)	5.34(0.44)	100(0.14)	6
B9/(1.9)	SFCA	coarse-flakes (platy)	self (high reflectivity SFCA)	83.51(0.88)	10.18(0.39)	0.13(0.09)	3.37(0.23)	0.11(0.04)	0(0.01)	2.69(0.28)	100(0.12)	6
B9/(1.9)	SFCA	coarse-flakes (platy)	magnetite minor glass	77.69(0.86)	14(0.28)	0.38(0.12)	3.9(0.67)	0.07(0.05)	0.08(0.07)	3.87(0.42)	100(0.11)	16
B9/(1.9)	SFCA	coarse-flakes (platy)	magnetite minor glass	82.72(1.98)	12.29(1.86)	0.37(0.29)	2.7(0.27)	0.08(0.05)	0.04(0.03)	1.8(0.14)	100(0.21)	16
B9/(1.9)	SFCA-I	fine microplaty	primary/secondary subhedral hematite	77.83(0.48)	14.57(0.18)	0.43(0.07)	3.26(0.14)	0.07(0.04)	0.04(0.05)	3.8(0.15)	100(0.16)	10
B10/(1.8)	SFCA	coarse tabular-prismatic	secondary magnetite+glass+larnite	67.04(0.02)	18.28(0.01)	0.04(0.00)	3.58(0.01)	0.06(0)	0.27(0.02)	12.66(0.04)	101.94(0.15)	9
B10/(1.8)	SFCA	coarse tabular-prismatic	secondary magnetite+glass+larnite	71.61(0.5)	15.96(0.25)	0.03(0.00)	4.5(0.01)	0.01(0)	0.06(0.00)	9.02(0.02)	101.19(0.27)	8
B11 (1.9)	SFCA-I	fine microplaty	primary/secondary subhedral hematite	84.22(2)	5.17(1.5)	9.74(1.1)	1.81(0.28)	0.59(0.09)	0.07(0.04)	0.34(0.34)	101.94(0.38)	12
B11 (1.9)	SFCA-I	fine microplaty	primary/secondary subhedral hematite	75.95(0.78)	14.46(0.51)	1.02(0.19)	3.29(0.44)	0.3(0.13)	0.15(0.09)	5.53(0.44)	100.7(0.58)	30
B11 (1.9)	SFCA-I	fine microplaty	primary/secondary subhedral hematite	73.8(0.89)	16.02(0.95)	0.96(0.42)	3.38(0.37)	0.24(0.07)	0.16(0.05)	6.34(0.52)	101.04(0.54)	10
B11 (1.9)	SFCA-I	fine microplaty	primary/secondary subhedral hematite	69.96(1.47)	16.74(1.87)	0.91(0.33)	5.2(2.5)	0.25(0.05)	0.19(0.09)	7.41(1.58)	100.65(0.55)	20
B11 (1.9)	SFCA	coarse-flakes (platy)	primary/secondary subhedral hematite	83.15(0.9)	10.49(0.4)	1.53(0.39)	2.72(0.44)	0.38(0.11)	0.05(0.05)	2.56(0.98)	100.87(0.54)	20
B11 (1.9)	SFCA	coarse-flakes (platy)	secondary magnetite+glass+larnite	78.03(0.39)	13(0.1)	0.57(0.16)	3.48(0.2)	0.19(0.04)	0.09(0.08)	5.22(0.09)	100.57(0.38)	10
B11 (1.9)	SFCA	coarse-flakes (platy)	secondary magnetite+glass+larnite	74.51(0.83)	14.63(0.37)	0.71(0.39)	3.67(0.35)	0.21(0.11)	0.1(0.06)	6.51(0.3)	100.35(0.46)	15
B11 (1.9)	SFCA	coarse-flakes (platy)	secondary magnetite+glass+larnite	69.23(0.94)	15.7(0.22)	0.62(0.15)	6.87(1.29)	0.2(0.05)	0.18(0.07)	7.52(0.31)	100.32(0.51)	10
B11 (1.9)	SFCA	coarse tabular-prismatic	secondary magnetite+glass+larnite	71.7(0.7)	15.32(0.2)	0.37(0.06)	5.67(0.32)	0.14(0.05)	0.11(0.08)	8.11(0.32)	101.41(0.36)	10
B12/(1.9)	SFCA	coarse-flakes (platy)	secondary magnetite+glass	74.85(1.77)	14.07(1.34)	0.95(0.68)	4.27(1.06)	0.15(0.08)	0.12(0.06)	6.33(1.21)	100.74(1.46)	25
B12/(1.9)	SFCA	coarse-flakes (platy)	self	81.17(0.8)	14.34(0.63)	0.56(0.64)	1.33(0.07)	0.17(0.08)	0.03(0.03)	1.26(0.71)	98.86(1.11)	26
B12/(1.9)	SFCA-I	fine microplaty	secondary subhedral hematite	66.16(3.5)	16.47(2.3)	1.35(0.57)	5.75(1.73)	0.29(0.1)	0.06(0.05)	9.14(2.13)	99.22(1.44)	36
B12/(1.9)	SFCA-I	fine microplaty	secondary subhedral hematite	85.87(1.87)	5.22(1.4)	0.13(0.05)	1.72(0.13)	0.3(0.09)	0.25(0.05)	4.46(0.59)	97.95(0.67)	10
B12/(1.9)	SFCA	coarse tabular-short prismatic	secondary magnetite+glass+larnite	68.96(1.83)	14.85(0.63)	1.42(0.57)	5.19(0.93)	0.2(0.09)	0.06(0.05)	7.92(0.68)	98.59(1.14)	30
B12/(1.9)	SFCA	coarse tabular-short prismatic	secondary magnetite+glass+larnite	87.62(2.29)	2.71(1.07)	4.94(2.35)	3.81(1.31)	0.48(0.32)	0.05(0.02)	0.98(0.59)	100.6(1.04)	3
B12/(1.9)	SFCA	coarse tabular-short prismatic	secondary magnetite+glass+larnite	62.58(1.62)	15.98(2.57)	1.89(0.45)	8.71(3.47)	0.19(0.09)	0.1(0.05)	10.09(1.43)	99.54(1.83)	7
Slag Iron	SFCA	coarse-flakes (platy)	glass+silicates+magnetite	76.71(1.87)	12.81(0.93)	0.22(0.09)	6.33(0.46)	0.02(0.01)	0.08(0.06)	5.0(0.39)	101.14(1.09)	11

An attempt was made to plot the measured EPMA compositions in triangular plots (Figure 11). Figure 11a is a comparison of Fe_2O_3, CaO and Al_2O_3 average mole-fraction data in SFCA in all pot-grate sinters. The SFCA (exp), SFCA-I (exp) and SFCA-II (exp) are from Mumme, Clout and Gable (1998) and Mumme (2003). SFCA-I, SFCA-C and SFCA-P compositions are distributed in a wide area indicating that SFCA can be formed as complex solid solution series. Oxide wt. per cent data for the SFCA is plotted (Figure 11b) on CaO-SiO_2-Fe_2O_3, ternary diagrams which were proposed by Lister and Glasser (1967) showing the compositional relationship between SFCA and SFCA-I. The area in Figure 11b shown as SFCA and SFCA-I is the region where most SFCA compositions are formed in iron ore sinters. MgO, TiO_2 and MnO_2 concentrates were added to the CaO concentrations and Al_2O_3 concentrates were added to the Fe_2O_3.

Figure 11b display the sub triangle showing the same SFCA-I, SFCA-C and SFCA-P compositions in relation to industrial sinter SFCA and SFCA-I compositions (compositional zones are from Scarlett *et al*, 2004b). Some of the measured SFCA compositions in this study are plotted in the SFCA industrial iron ore sinter region with few outliers. As discussed earlier the SFCA-I, SFCA-C and SFCA-P identification was based on the size, crystal morphology and texture of SFCA. As shown in Figure 11b the measured SFCA very few SFCA-I analyses are plotted on the proposed SFCA-I zone. There was no clear discrimination between three SFCA types. This was another observation to support that SFCA compositions are highly variable and are difficult to categorise based on EPMA compositional data.

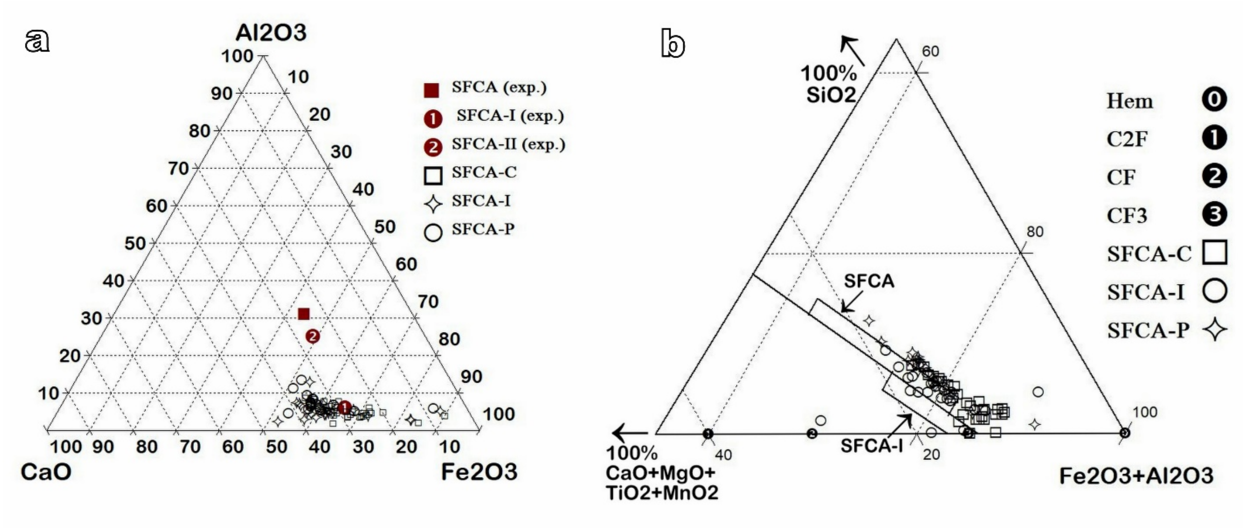

FIG 11 – Triangular plots of measured EPMA data. a) display measured EPMA mol concentrations on part of the Fe_2O_3-Al_2O_3-CaO system with experimental data of (Mumme, Clout and Gable, 1998; Mumme, 2003) SFCA, SFCA-I and SFCA-II. b) Schematic diagrams showing the compositional relationship between SFCA and SFCA-I compositions in relation to industrial sinter. Area shown as SFCA is the region where most SFCA compositions are formed in iron ore sinters (Scarlett *et al*, 2004b).

SUMMARY AND CONCLUSIONS

Two main types of silico ferrites of calcium and alumina (SFCA) are widely described in iron ore sinter. These are SFCA with fine-microplaty type morphology characterised by high Fe_2O_3 (~84 wt. per cent), low SiO_2 (~ 1 wt. per cent) and low Al_2O_3 (~2 wt. per cent) and a coarse prismatic type SFCA with low Fe_2O_3 (~75 wt. per cent) and high Al_2O_3 (4–8 wt. per cent). The fine variety is typically referred to as SFCA-I and the coarse variety is named SFCA. In this study, detailed optical microscope observations of several pot grate and compact sinter samples revealed the presence of a variety of fine, coarse and dense forms of both types of SFCA phase type. The observations indicated the presence of several texturally and chemically different SFCA types namely fine-microplaty SFCA, coarse-flaky/platy SFCA, tabular/short-prismatic SFCA, thin-acicular SFCA and dense verities of SFCA in iron ore sinter. Fine microplaty SFCA was mainly associated with primary and secondary subhedral hematite, coarse flaky/platy was mainly associated with subhedral hematite and secondary magnetite and tabular/short prismatic SFCA was mainly associated with magnetite and glass. In several cases optical point counting and XRD quantification of SFCA-I/SFCA showed some differences.

Comparison of optical point counting results and XRD analysis of the same sinters revealed that the total SFCA measurements from both techniques were comparable however, the separation of SFCA into two categories as SFCA-I/SFCA was variable. This indicates that using optical microscopy to separate the different SFCA types based on crystal size, shape and texture may not accurate.

The controlled cooling tests revealed that cooling rate has an impact on the form and size of SFCA crystals with slow cooling generally producing greater SFCA formation and the development of large crystal sizes. Nonetheless, at slow or fast cooling rates, both SFCA-I and SFCA can develop fine or coarse crystal morphologies. The basicity level also has a direct impact on the SFCA formation as the higher basicity levels favour higher levels of SFCA formation. EPMA analysis data of SFCA types from a variety of pot grate and compact sinter samples showed that the SFCA types exhibit a broad range of complex compositions within the system $Fe_2O_3/CaO/SiO_2/Al_2O_3/MgO/TiO_2/MnO$. Although SFCA-I and SFCA are known to be crystallographically distinct and with different, well-defined ranges in composition, there was considerable overlap in compositions of the experimental sinter samples. There is a high possibility that both SFCA-I/SFCA can form as fine or coarse platy crystals and therefore difficult to distinguish. Based on optical/SEM imaging the development of SFCA textures depend on several parameters including the local chemistry and conditions including the maximum temperature attained and the cooling rate, within the sinter bed, there by suggesting that SFCA identification and classifying them into SFCA or SFCA-I types based on size, morphology and texture alone may be erroneous.

ACKNOWLEDGEMENT

The authors wish to thank CSIRO Mineral Resources for supporting this research. The external reviewers are thanked for their valuable comments and improvements to the paper. Dr Nathan Webster, CSIRO is acknowledged for providing quantitative XRD analysis. The authors acknowledge the facilities and the scientific and technical assistance of the Centre for Microscopy and Microanalysis (CMM) at University of Queensland.

REFERENCES

Ahsan, S N, Mukherjee, T and Whiteman, J A, 1983. Structure of fluxed sinter, *Iron making, Steel making*, 10:54–64,

Bristow, N J and Waters, A G, 1991. Role of SFCA in promoting high temperature reduction properties of iron ore sinters, *Trans, Institute, Min, Metall*, 100:C1-C10.

Dawson, P R, Ostwald, J and Hayes, K M, 1985. Influence of alumina on development of complex calcium ferrites in iron-ore sinters, *Transactions of the Institution of Mining and Metallurgy Section C-Mineral Processing and Extractive Metallurgy*, 94(1985):C71-C78.

Gan, M, Fan, X, Ji, Z, Chen, X, Yin, L, Jiang, T, Li, G and Yu, Z, 2015. High Temperature Mineralization Behaviour of Mixtures during Iron Ore Sintering and Optimizing Methods, *ISIJ International*, Vol. 55 (2015), No. 4, pp. 742–750.

Hancart, J, Leroy, V and Bragard, A, 1967. A study of the phases present in blast furnace sinter, Some considerations on the mechanism of their formation, *CNRM Metall, Rep*, 14:3–7.

Hapugoda, S, Lu, L, Donskoi, E and Manuel, J, 2016. Mineralogical quantification of iron ore sinter, *Mineral Processing and Extractive Metallurgy (Trans, Inst, Min, Metall, C)*,125(3):156–164.

Hapugoda, S, Lu, L, Donskoi, E, Han, H, Manuel, J and Yu, Y, 2019, Characterization of Iron Ore Sinter by Optical Microscopy and EPMA, *AusIMM Iron Ore 2019*.

Honeyands, T J, Manuel, Matthews, L, O'Dea, D D, Pinson, D J, Leedham, J B, Monaghan, B H, Li, H J, Chen, J P C, Hayes, P C E, Donskoi, E and Pownceby, M I, 2017. Characterizing the Mineralogy of Iron Ore Sinters – State of the Art in Australia, *Iron Ore Conference, AusIMM*.

Hsieh, L H and Whiteman, J A, 1989. Effect of oxygen potential on mineral formation in lime-fluxed iron ore sinter, *ISIJ Int*, 29:625–634.

Kitamura, K, 1985. Studies and operation of high reducibility sinters, *AIME Ironmaking Proc*, 44:405–414.

Lister, D H and Glasser, F P, 1967. Phase relations in the system $CaO–Al_2O_3$–iron oxide, Br,Ceram, *Soc, Trans*, 66(1967):293–306.

Loo, C E, Wan, K T and Howes, V R, 1988. Mechanical Properties of Natural and Synthetic Mineral Phases in Sinters having varying Reduction Degradation Indices', *Ironmaking Steelmaking*, 15:279–285.

Lu, L, Manuel, J R, Holmes, R J, Smyth, R, Adam, M, Edenton, A, Ware, N and Raynlyn, T, 2009. Characteristics and Sintering Performance of Iron Ore Sinter Fines, *Proceedings, Iron Ore 2009*, pp 259–267.

Mežibrický, R and Fröhlichová, M, 2016. Silico-ferrite of Calcium and Aluminum Characterization by Crystal Morphology in Iron Ore Sinter Microstructure, *ISIJ International*, 56(6):1111–1113.

Mumme, W G, 2003. The crystal structure of SFCA-II, Ca$_{5,1}$Al9,3Fe3+ 18,7 Fe2+ 0,9 O48 a new homologue of the aenigmatite structure-type and structure refinement of SFCA-type, *Neues Jahrb Mineral Abh*, 178, 307.

Mumme, W G, Clout, J M F and Gable, R W, 1998. Thecrystal structure of SFCA-I, Ca$_{3,18}$Fe$_{14,663}$+Al$_{1,34}$Fe$_{0,822}$+O$_{28}$, a homologue of the aenigmatite structure type and new crystal structure refinements of beta-CFF, Ca$_{2,99}$Fe$_{14,303}$+Fe$_{0,552}$+O$_{25}$ and MG-free SFCA, Ca$_{2,45}$Fe$_{9,043}$+Al$_{1,74}$Fe$_{0,162}$+$_{\mathrm{Si}0,6}$O$_{20}$, *Neues Jahrbuch fuer Mineralogie – Abhandlungen*, 173(1):93–117.

Nicol, S, Chen, J, Pownceby, M I and Webster, A S, 2018. A review of the chemistry, structure and formation conditions of Silico-Ferrite of Calcium and Aluminium ('SFCA') phases, *ISIJ International*, 58(12):2157–2172.

Ostwald, J, 1981. Mineralogy and micro-texture of Australian iron ore sinters, *BHP Technical Bulletin*, 25(1981):13–20.

Patrick, T R C and Pownceby, M I, 2001. Stability of Silico-Ferrite of Calcium and Aluminum in Air-Solid Solution Limits between 1240°C and 1390°C and Phase Relationships within the Fe_2O_3-CaO-Al_2O_3-SiO_2 (FCAS) System, *Metallurgical and Materials Transactions B*, 32B:79–89.

Pimenta, H, P and Seshadri, V, 2002, Characterization of structure of iron ore sinter and its behavior during reduction at low temperatures, Ironmaking and Steelmaking, Vol, 29 No, 3, pp 169–174.

Pownceby, M I and Clout, J M F, 2003. Importance of fine Ore chemical composition and high temperature phase relations: applications to iron ore sintering and pelletizing, *Transactions of the Institution of Mining and Metallurgy Section C – Mineral Processing and Extractive Metallurgy*, 112:C1-C10.

Pownceby, M I, Webster, N A S, Manuel, J R and Ware, N, 2015. Iron Ore Geometallurgy-Examining the Influence of Ore Composition on Sinter Phase Mineralogy and Sinter Strength, *Iron Ore Conference*, pp 579–586.

Sasaki, M and Hida, Y, 1982. *Tetsu-to-Hagané*, 68:563–571 (in Japanese).

Scarlett, N V Y, Madsen, I C, Pownceby, M I and Christensen, A N, 2004a. In situ X-ray diffraction analysis of iron ore sinter phases, *Journal of Applied Crystallography*, 37:362–368.

Scarlett, N V Y, Pownceby, M I, Madsen, I C and Christensen, A N, 2004b. Reaction Sequences in the Formation of SFCA and SFCA-I in Iron Ore Sinter, *Metallurgical Transactions B*, 35B:929–936.

Shigaki, I, Sawada, M and Gennai, N, 1986. Phase formation, In situ synchrotron XRD, During the iron ore sintering process, *Trans, Iron Steel Institute, Japan*, 26:503–511.

Stenlake, R M, Pepper, M and Ostwald, J, 1981. 3rd Int, Symp, Agglomeration—Eine Veranstaltung den Reihe Partikel Technologie, Nurnberg and 242 Veranstaltung der Europaeischen Foederation, fuer Chemie-Ingenieur-Wesen, NMA Nuremberg Fair and Exhibition, Society, I71.

Tonzetic, I and Dippenaar, A, 2011. An alternative to traditional iron-ore sinter phase classification, *Minerals Engineering*, 24:1258–1263.

Umadevi, T, Rameshwar, S and Mahapatra, P C, 2014. Influence of sinter basicity (CaO/SiO2) on low and high alumina iron ore sinter quality, *Mineral Processing and Extractive Metallurgy*, 123(2):75–85, DOI: 10.1179/1743285514Y.0000000052

Webster, A S, Pownceby, M I, Madsen, I C and Kimpton, J A, 2012. Silico-ferrite of Calcium and Aluminum (SFCA) Iron Ore Sinter Bonding Phases: New Insights into Their Formation During Heating and Cooling, *Metallurgical and Materials Transactions B*, 43B:1344–1357.

Webster, A S, Pownceby, M I, Madsen, I C, Studer, A J, Manuel, J R and Kimpton, J A, 2014. Fundamentals of Silico-Ferrite of Calcium and Aluminum (SFCA) and SFCA-I Iron Ore Sinter Bonding Phase Formation: Effects of CaO: SiO_2 Ratio, *Metallurgical and Materials Transactions B*, 45B:2097–2105.

Webster, N A S, Pownceby, M I and Madsen, I C, 2013. In situ x-ray diffraction investigation of the formation mechanisms of silico-ferrite of calcium and aluminum-I-type (SFCA-I-type) complex calcium ferrites, *ISIJ International*, 53(8):1334–1340, doi:10.2355/isijinternational.53.1334

Yang, L X and Loo, C E, 1997. Structure of Sinters Formed from Complex Chinese Iron Ores, *ISIJ Int*, 37(5):449–457.

Zhang, Z, An, S, Luo, G and Wang, Y, 2012. Effect of Basicity and Alumina-Silica Ratio on Formation of Silico-Ferrite of' Calcium and Aluminum, *Journal of Iron and Steel Research, International*, 19(4):01–05.

Influence of the occurrence state of Al_2O_3 on the metallurgical performance of product sinter

J Pan[1], C C Yang[2], D Q Zhu[3], Z Q Guo[4], Q H Li[5] and X Wang[6]

1. Professor, Central South University, Changsha, Hunan 410083, China.
   Email: pjcsu@csu.edu.cn
2. PhD, Lecturer, Central South University, Changsha, Hunan 410083, China.
   Email: smartyoung@csu.edu.cn
3. Professor, Central South University, Changsha, Hunan 410083, China.
   Email: dqzhu@csu.edu.cn
4. Associate professor, Central South University, Changsha, Hunan 410083, China.
   Email: gzqcsu@126.com
5. Professor, Central South University, Changsha, Hunan 410083, China.
   Email: liqihou@csu.edu.cn
6. PhD student, Central South University, Changsha, Hunan 410083, China.
   Email: gangtiexiwangxin@csu.edu.cn

ABSTRACT

Al_2O_3 in natural iron ores generally occurs in goethite, kaolinite, gibbsite, hematite and iron carbonate. When the content of alumina in sinter increases from 1.11 per cent to 3.50 per cent, the reducibility of sinter decreases with the addition of four different types of alumina. When gibbsite and kaolinite are added, the low temperature reduction disintegration ($RDI_{+3.15\ mm}$) of sinter increases with the increase of Al_2O_3 content in the range of 1.5 per cent to 3.5 per cent. Furthermore, when adding pure reagent alumina, the increase of Al_2O_3 content in the range of 1.5 per cent to 3.0 per cent will increase the $RDI_{+3.15\ mm}$ of sinter. The addition of ferric oxide–alumina spinel with the Al_2O_3 content in the range of 1.5 per cent to 2.5 per cent, also increases the $RDI_{+\ 3.15\ mm}$ of sinter. The influence difference is results from the change of the mineral composition and microstructure of sinter because of the occurrence state of Al_2O_3. Under the condition that Al_2O_3 content of sinter is 2 per cent, the porosity of sinter with kaolinite is 37.26 per cent, and the shape is irregular. When gibbsite and ferric oxide–alumina spinel are added, the porosity of sinter is about 16 per cent, and the pores are round. When pure reagent alumina is added, the porosity of sinter is 17.49 per cent, and the pores are regular and small. When kaolinite, gibbsite and ferric oxide–alumina spinel are added, platy calcium ferrite is mainly formed in the sinter, and some of it is columnar calcium ferrite. On the other hand, when pure reagent alumina is added, in addition to platy columnar calcium ferrite, acicular calcium ferrite is also formed in the sinter.

INTRODUCTION

With the continuous consumption of high-quality iron ore resources, the iron grade of iron ore for sintering production is gradually decreasing combined with a continuous increase in the Al_2O_3 content (Umadevi *et al*, 2010; Li *et al*, 2017; Chai *et al*, 2018). Moreover, for the purpose of reducing production cost, more and more iron ore types with high Al_2O_3 content is used for sinter production in recent years (Chai *et al*, 2018; Zhu, D Q, 2020a). Al_2O_3 in natural iron ores generally occurs in goethite, kaolinite, gibbsite, hematite and iron carbonate, and the occurrence state and content of Al_2O_3 are diverse for different types of iron ore (Zhu *et al*, 2020b). Therefore, it is of great significance to investigate the influence of alumina content and occurrence state on the metallurgical performance of iron ore sinter.

The effects of Al_2O_3 on the metallurgical performance of product sinter have been investigated by many researchers. Due to the different occurrence states of Al_2O_3 in the experimental raw materials, the conclusions obtained by different scholars are even contradictory. The research results of some researchers (Umadevi *et al*, 2010; Gan *et al*, 2003) show that within a certain range of Al_2O_3 content, the increase of Al_2O_3 content will lead to deterioration of the reduction disintegration index (RDI) and increases in reduction index (RI), while the opposite conclusion is found by some other researchers (O'Dea and Ellis, 2015; Dong *et al*, 2015; Yu *et al*, 2013; Guo *et al*, 2013), namely that an increase of Al_2O_3 content can improve the low temperature reduction disintegration index of sinter and deteriorate the reduction index. Umadevi *et al* (2010) used Indian high-alumina iron ore as the experimental raw material and found that when the Al_2O_3 content of sinter ranged from 2.00 per cent to 5.46 per cent, the reduction index of sinter increased by approximately 5 per cent, and the low temperature reduction disintegration index ($RDI_{+3.15\ mm}$) decreased by about 16 per cent. As for the reasons for the deterioration of the reduction disintegration index caused by increasing the Al_2O_3 content of product sinter, the current research conclusions mainly focus on the decrease in the fracture toughness of the sintered glass phase (Yang and Qiu, 1999; Guo *et al*, 2013); the massive development of flake hematite, flake calcium ferrite and continuous crystal magnetite (Hu, 2011; Wang and Qi, 1997), which results in stress concentration during the reduction process, and the ability of the sinter to resist crack propagation decreases. O'Dea and Ellis (2015) used BHP fines as raw material for iron ore, and the results showed that, when the Al_2O_3 content ranged from 1.65 per cent to 2.7 per cent, the reduction degree and low temperature reduction disintegration index ($RDI_{+2.8\ mm}$) of sinter increased slightly with the increase of Al_2O_3 content. Dong *et al* (2015) found that when the bauxite type Al_2O_3 content of sinter increased from 2.67 per cent to 3.47 per cent, the low temperature reduction disintegration index ($RDI_{+3.15\ mm}$) of sinter first decreased and then increased, while the trend for the reduction index was opposite to that for the reduction disintegration index.

In contrast to the previous research about the influence of Al_2O_3 on the metallurgical properties of sinter only considering a single occurrence state of alumina, in this work, a series of Al-containing additives such as alumina (AR), gibbsite (AR), kaolinite and ferric oxide-alumina spinel are used to adjust the Al_2O_3 content of product sinter in order to simulate the main occurrence of Al_2O_3 in natural iron ore fines. The influence of different aluminium occurrence states on the metallurgical properties of sinter is systematically studied in this paper. Furthermore, in order to explain the effect of aluminium content and occurrence state on the metallurgical performance, the sinter mineralogy is also investigated.

MATERIALS AND METHODS

Materials

Raw materials

The raw materials used in this research mainly included Brazilian Carajas fines (IOCJ), limestone, quicklime, dolomite, coke breeze, silica sand, and return fines. The main chemical compositions and particle size compositions of these materials are shown in Tables 1 and 2, respectively. The Brazilian Carajas fines, assaying 65.42 per cent Fe, 1.00 per cent Al_2O_3 and 2.05 per cent SiO_2, and especially less than 0.05 per cent for both S and P, are quite suitable for sintering production. In term of the particle size distribution, the average particle size of IOCJ is 2.69 mm, which is distributed across all particle size, and the content of particles above 0.5 mm is about 75.37 per cent.

TABLE 1

Chemical compositions of raw materials (wt %).

Element	TFe	FeO	SiO_2	CaO	Al_2O_3	MgO	P	S	LOI*
IOCJ	65.42	0.25	2.05	0.06	1.00	0.11	0.046	0.010	1.74
Limestone	0.20	-	1.51	51.78	0.45	2.53	0.004	0.006	42.32
Dolomite	0.56	-	0.75	33.50	0.17	22.29	0.010	0.010	44.28
Quicklime	0.22	-	4.20	82.07	1.18	1.81	0.009	0.091	10.42
Coke	0.53	-	5.36	1.04	3.96	0.11	0.040	0.750	88.08
Silica Sand	0.07	-	98.86	0.06	0.82	0.12	-	-	0.25
Return Fines	56.68	6.06	4.82	9.40	1.96	0.68	0.060	-	0.29

LOI*: Loss on ignition

TABLE 2

Size distributions of raw materials (wt %).

Particle size/mm	IOCJ	Limestone	Dolomite	Quicklime	Coke	Silica sand	Return fines
+8	8.57	-	-	-	0.97	-	-
6.3~8	4.13	-	-	0.63	0.51	-	-
5~6.3	5.96	0.94	0.10	1.75	6.62	-	-
3~5	17.48	8.60	41.66	21.26	15.74	-	41.40
1~3	25.64	45.01	37.09	20.11	35.61	-	31.26
0.5~1	13.59	23.68	10.37	5.19	12.68	-	8.49
0.25~0.5	9.94	9.68	1.63	2.96	16.81	-	5.44
-0.25	14.69	12.09	9.15	48.10	11.06	100.00	13.41
average*	2.69	1.53	2.51	1.51	2.00	0.13	2.38

average* is characterised by the weighted average particle size of the raw material

The X-ray diffraction (XRD) pattern of IOCJ and the distributions of aluminium in the mineral phases in the IOCJ sample are presented in Figure 1 and Table 3. The Brazilian Carajas fines mainly consist of hematite together with a small amount of quartz and goethite, while the aluminium is contained in gibbsite, kaolinite, earthy goethite and vitreous goethite, with proportions of 45.85 per cent, 28.30 per cent, 15.10 per cent and 10.75 per cent, respectively.

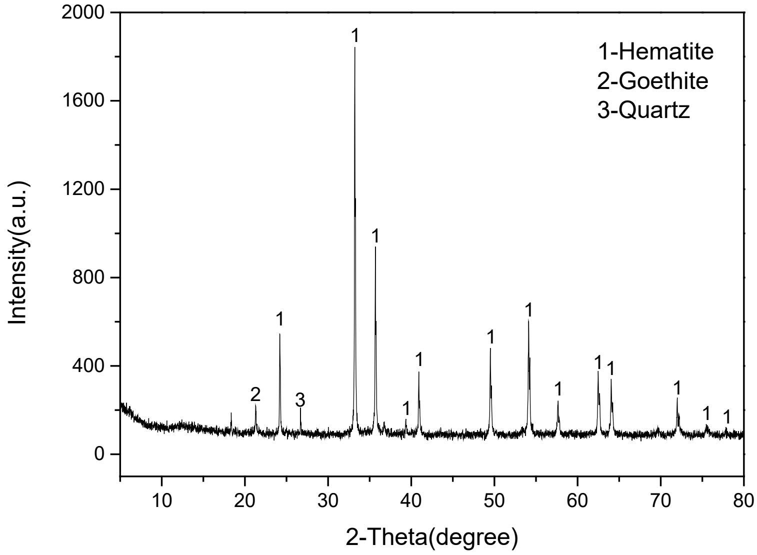

FIG 1 – XRD of Brazilian Carajas fines.

TABLE 3

The distributions of aluminium in mineral phases in the IOCJ (wt %).

Minerals	Gibbsite	Kaolinite	Earthy goethite	Vitreous goethite	Al_2O_3 (total)
Content	0.46	0.28	0.15	0.11	1.00
Fraction	45.85	28.30	15.10	10.75	100

Al-containing additives

In order to simulate the main occurrence of Al_2O_3 in natural iron ore fines, there are four main Al_2O_3 additives used in the research, including alumina (Al_2O_3), gibbsite ($Al(OH)_3$), kaolinite ($Al_2O_3{\cdot}2SiO_2{\cdot}2H_2O$), and ferric oxide-alumina spinel ($FeO{\cdot}Al_2O_3$). Among them, alumina (Al_2O_3) is an aluminium oxide (AR) to study the influence of free Al_2O_3 on sinter, and the gibbsite ($Al(OH)_3$) is replaced by aluminium hydroxide (AR). The chemical composition of the Al_2O_3 additives is shown in Table 4.

TABLE 4

Chemical compositions of additives containing alumina (wt %).

Additives	TFe	FeO	SiO_2	CaO	Al_2O_3	MgO	P	TiO_2	LOI*
Aluminium oxide (AR)	0.01	-	-	-	94.42	-	-	-	5.00
Aluminium hydroxide (AR)	-	-	-	-	64.07	-	-	-	33.84
Kaolin	1.02	-	44.80	0.01	36.20	0.03	0.022	0.20	15.76
ferric oxide–alumina spinel	34.25	20.94	0.96	0.12	48.38	0.99	0.170	0.65	-3.32

LOI*: Loss on ignition

The content of Al_2O_3 in the analytical grade of alumina (AR) and aluminium hydroxide (AR) is 94.42 per cent and 64.07 per cent, respectively; the contents of Al_2O_3 and SiO_2 in kaolin are 44.80 per cent and 36.20 per cent, and the content of impurity elements is relatively low; and the content of Al_2O_3 in the ferric oxide–alumina spinel is 48.38 per cent, and it contains 20.94 per cent FeO.

All four aluminium-bearing additives have small particle sizes of 100 per cent passing 0.074 mm.

Methods

This research was carried out in a pilot-scale laboratory equipment, and mainly included proportioning, mixing, granulation, sintering, and characterisation of sinter products. During the experiment, the target sinter composition was set as follows: sinter basicity of 1.8, 5.0 per cent SiO_2 (adjusted with quartz sand), and 1.5 per cent MgO. The burnt lime was fixed at 2.0 per cent. The Al_2O_3 content of the base case sinter was 1.11 per cent, while higher Al_2O_3 (1.5 per cent, 2.0 per cent, 2.5 per cent, 3.0 per cent and 3.5 per cent) was achieved by adding different aluminium-bearing additives, including pure alumina, bauxite, kaolinite and ferric oxide-alumina spinel in reagent form. The sinter with the return fines balance between 0.95 and 1.05 can be obtained by adjusting the amount of water and coke breeze.

The characterisation of the resultant sinter products was in accordance with GB/T 13241–2017 and GB/T 13242–2017 standard measurements of metallurgical properties, including reduction index (RI) and low temperature reduction disintegration index (RDI).

The chemical compositions of raw materials were determined by using a chemical titration method. A Leica DMLP optical microscope, an Advance D8 X-ray diffractometer from the German Bruker Company, and a TESCAN MIRA3 Scanning Electron Microscope from the Czech Taskin Company were used for the investigation into the microstructure and phase composition of sinter products. The porosity of sinter were obtained by area statistical calculation from a series of mineral phase photos.

RESULTS AND DISCUSSION

Metallurgical properties of product sinters

Reduction index (RI)

In this research, four aluminium-containing additives (alumina, gibbsite, kaolinite and ferric oxide–alumina spinel) were used to adjust the Al_2O_3 content of the sinter. With increasing Al_2O_3 content, the change of the reduction index of the product sinter is shown in Figure 2. When the alumina pure reagent is added to increase the Al_2O_3 content of the sinter feed, as the Al_2O_3 content increases from 1.11 per cent to 2.0 per cent, the reduction index of the product sinter slightly increases first from 82.28 per cent to 82.94 per cent. However, with the Al_2O_3 content exceeds 2.0 per cent, the reduction index of the product sinter begins to decrease continuously. When gibbsite is added, the degree of reduction begins to decline after the sinter Al_2O_3 content exceeds 1.5 per cent. In contrast, the reduction index of the sinter continuously decreases as the Al_2O_3 content increases by adding kaolinite and ferric oxide-alumina spinel separately.

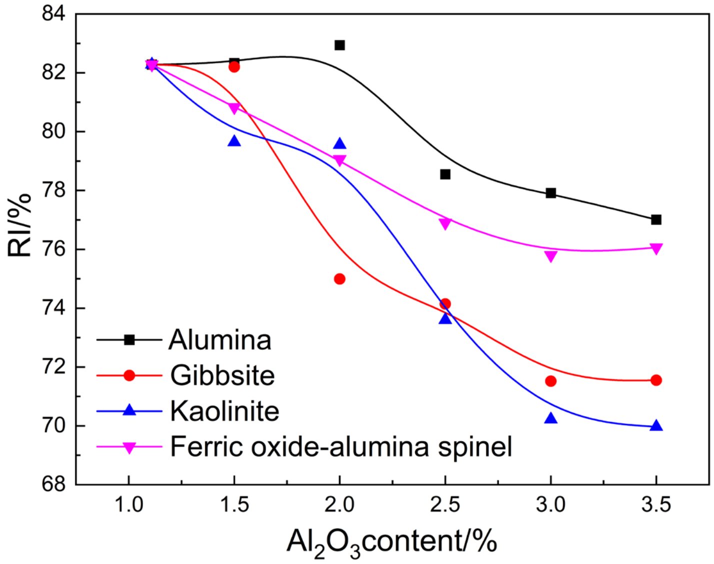

FIG 2 – Effects of different types of Al_2O_3 on reduction index of sinter.

Judging from the decrease in the reduction index, the deteriorating effect of gibbsite and kaolinite on the reduction index is significantly higher than that of alumina and ferric oxide-alumina spinel.

Reduction disintegration index (RDI)

The low temperature reduction disintegration index ($RDI_{+3.15\ mm}$) of the sinter samples was tested according to national standard GB13242–2017, and the results are shown in Figure 3. After adding different types of Al_2O_3 additives, the low temperature reduction disintegration index ($RDI_{+3.15\ mm}$) of sinter decreases first and then increases when the content of Al_2O_3 is 1.11 per cent to 2.50 per cent. When gibbsite and kaolinite are added, the low temperature reduction disintegration index ($RDI_{+3.15\ mm}$) of sinter increases with increasing Al_2O_3 content in the range 1.5 per cent to 3.5 per cent, while increasing Al_2O_3 content in the range 1.5 per cent to 3.0 per cent by adding pure reagent alumina increases the $RDI_{+3.15\ mm}$ of sinter. When ferric oxide-alumina spinel is added to increase the Al_2O_3 content in the range 1.5 per cent to 2.5 per cent, the $RDI_{+\ 3.15\ mm}$ of the sinter is also increased.

Compared with the other three aluminium additives, alumina in the form of kaolinite has the most significant improvement effect on the low temperature reduction disintegration index ($RDI_{+3.15\ mm}$) of product sinter. Although the sinter has the lowest low temperature reduction disintegration index ($RDI_{+3.15\ mm}$) at low dosages of gibbsite, with further increases in the addition amount (Al_2O_3>2 per cent), the low temperature reduction disintegration index ($RDI_{+3.15\ mm}$) is greatly improved and the effect at an Al_2O_3 content of 3.5 per cent is the same as that for adding kaolinite.

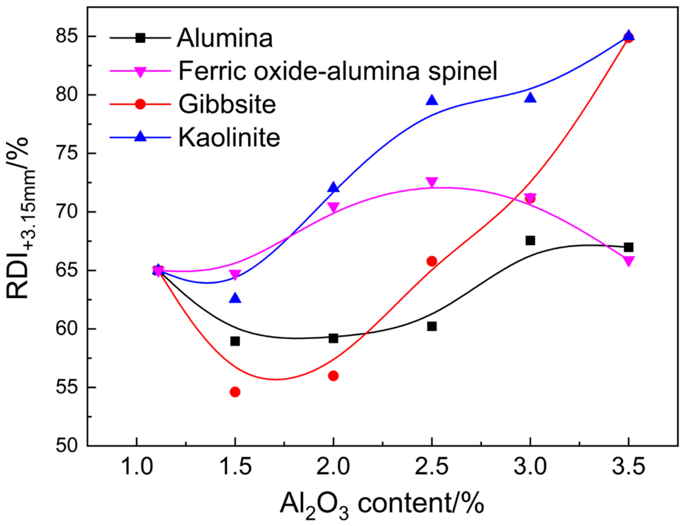

FIG 3 – Effects of different types of Al_2O_3 on reduction disintegration index of product sinter.

Mineralogical properties of product sinters

In this research, optical microscopy is used to analyse the influence of different occurrence states of Al_2O_3 on the microstructure and phase distribution of product sinter, and the phase composition and average pore diameter are statistically analysed.

The effects of different types of Al_2O_3 on the microstructure, phase composition and pore characteristics of product sinter are shown in Figures 4, 5 and 6. When the content of Al_2O_3 in sinter is increased to 2.00 per cent by adding different forms of aluminium-containing additives, the quantity of calcium ferrite in the sinter is reduced from 43.00 per cent for the raw ore to 36.62 per cent (alumina), 30.44 per cent (gibbsite), 25.61 per cent (kaolinite) and 28.30 per cent (ferric oxide-alumina spinel), respectively. In addition, when kaolinite, gibbsite and ferric oxide–alumina spinel are added, platy calcium ferrite is mainly formed in the sinter, and some of it is columnar calcium ferrite. However, when pure reagent alumina is added, in addition to platy columnar calcium ferrite, acicular calcium ferrite is also formed in the sinter. The formation of more silicate and less reducible phases is believed to be the decisive factor responsible for the low sinter reducibility with the addition of kaolinite and ferric oxide-alumina spinel. The results agree well with some earlier studies (Zhang and Andrade, 2016).

From Figure 5, in terms of the shape and pore size of sinters, the sinter without any aluminium additive (1.11 per cent Al_2O_3) has less pores, and its average pore size is about 388 μm. When Al-containing additives are added to Increase the Al_2O_3 content to 2.00 per cent, the quantity of pores in the product sinter increases significantly, with the average pore size being 152 μm (alumina), 343 μm (gibbsite), 523 μm (kaolinite), and 476 μm (ferric oxide-alumina spinel). Moreover, the pores in the sinter with different types of alumina show circular structure (raw ore; ferric oxide-alumina spinel), small pore structure (alumina), oval structure (gibbsite) and irregular structure (kaolinite), respectively. Figure 6 shows the porosity of resultant sinters in which the Al_2O_3 content is increased to 2.00 per cent by adding different aluminium-containing additives. The porosity of sinter is 37.26 per cent, 17.49 per cent, 16 per cent, 16 per cent and 12.34 per cent for the various Al-containing additives as kaolinite, alumina, gibbsite, ferric oxide-alumina spinel and natural raw ore, respectively. Combining the porosity and pore size in combination with the results with the RDI results, it can be seen that higher porosity and larger pore size generally contributes to better resistance to reduction disintegrate, leading to higher $RDI_{+3.15\ mm}$ of sinter products with kaolinite addition.

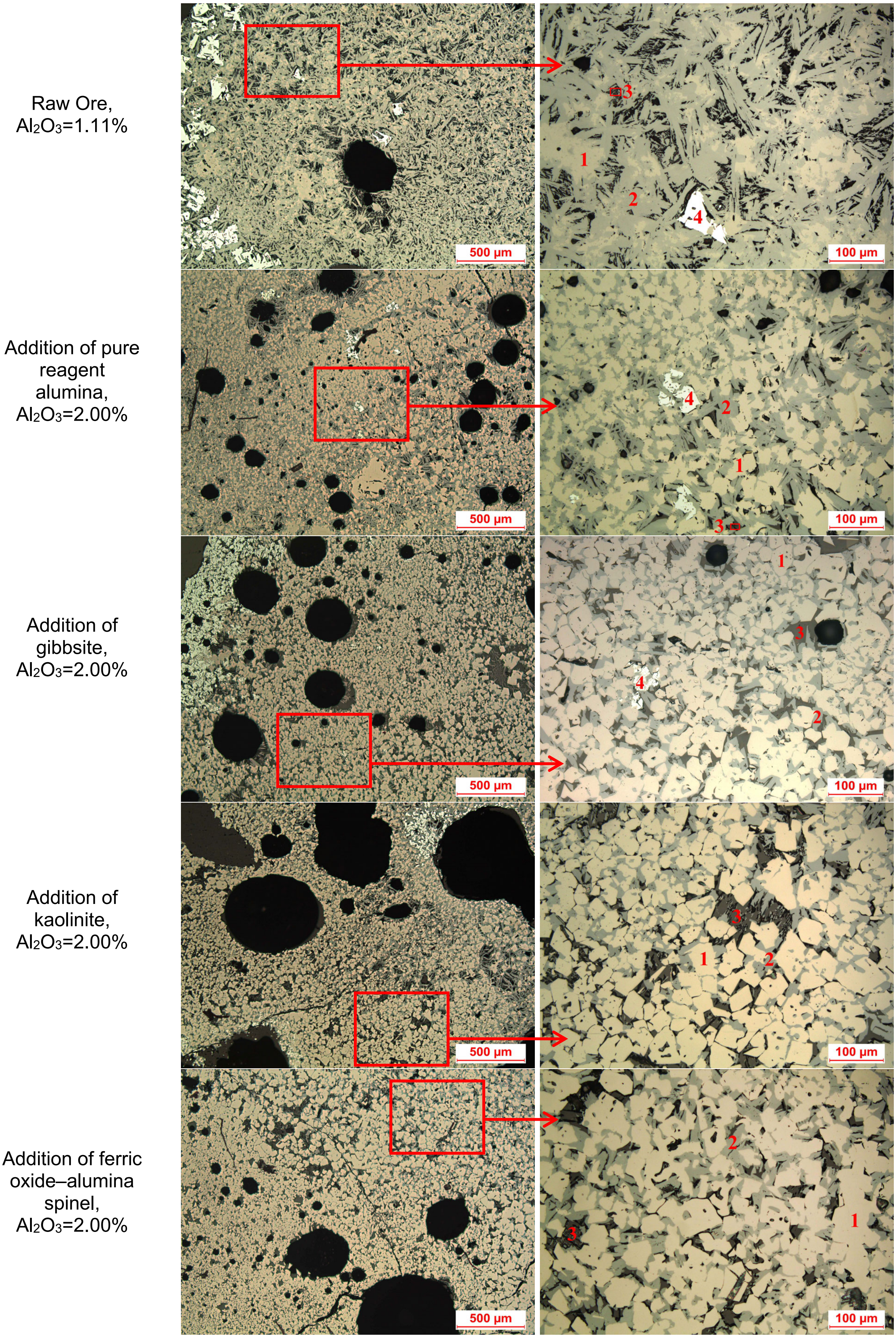

FIG 4 – Effects of different types of Al_2O_3 on the microstructure of product sinter.
NB: 1 – Magnetite, 2 – SFCA, 3 – Silicate, 4 – Hematite.

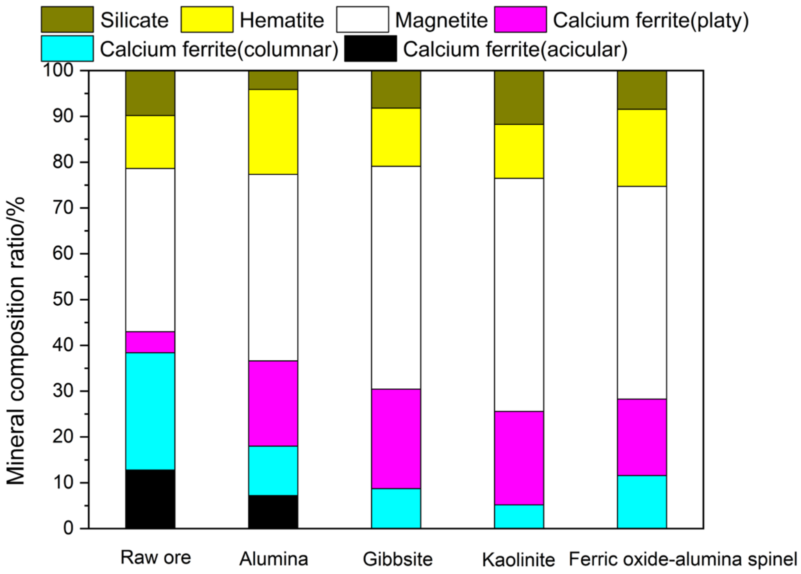

FIG 5 – Effects of different types of Al_2O_3 on mineral compositions of sinter (Al_2O_3=2.0 per cent).

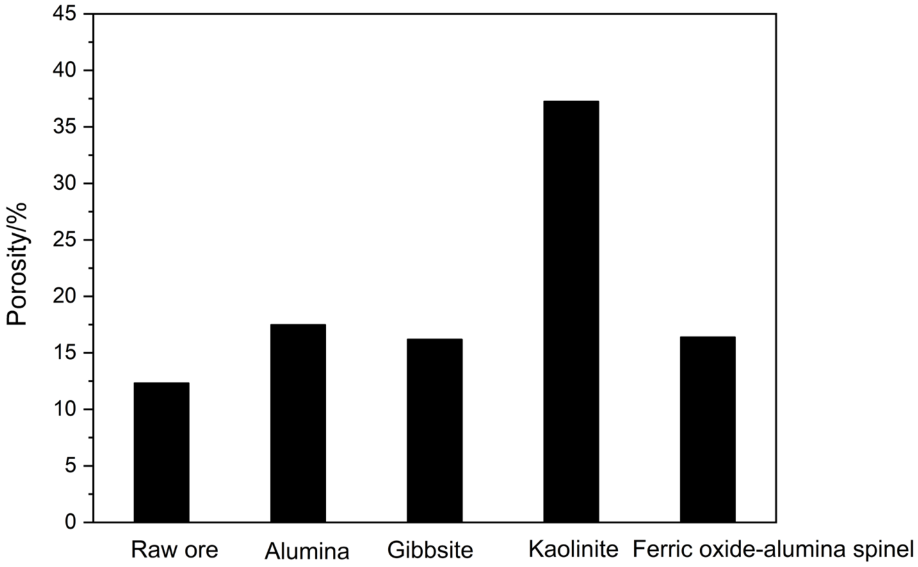

FIG 6 – Sinter porosity for different types of aluminium-bearing additives (2 per cent Al_2O_3).

CONCLUSIONS

Based on the analysis of aluminium occurrence on the metallurgical performance of product sinter with different content of Al_2O_3, it has been clearly shown that the reduction index and the reduction disintegration index ($RDI_{+3.15\ mm}$) of sinter with different forms of Al_2O_3 occurrence states change with the content of alumina. The following conclusions are drawn:

- Increasing the Al_2O_3 content from 1.11 per cent to 3.50 per cent results in a decrease in the sinter reducibility for all aluminium-bearing additives.
- Different aluminium occurrence states result in different impacts on the RDI of sinter products. When gibbsite and kaolinite are added, the $RDI_{+3.15\ mm}$ of sinter increases with increasing Al_2O_3 content from 1.5 per cent to 3.5 per cent. When adding pure reagent alumina, an increase in Al_2O_3 content in the range 1.5 per cent to 3.0 per cent increases the $RDI_{+3.15\ mm}$ of sinter. Moreover, the addition of ferric oxide-alumina spinel also improves the $RDI_{+3.15\ mm}$ of sinters, but in the range of 1.5 per cent to 2.5 per cent Al_2O_3.
- The occurrence state of Al_2O_3 largely affects the mineral composition and microstructure of sinters. At the same Al_2O_3 content, the sinter made with kaolinite addition is likely to produce higher sinter porosity, while gibbsite, ferric oxide–alumina spinel and reagent alumina addition leads to low sinter porosity. Sinters with higher porosity and larger pore size tend to display

better RDI. The addition of kaolinite, gibbsite and ferric oxide-alumina spinel tends to promote the formation of platy calcium ferrite and less reducible silicates, resulting in lower RI.

REFERENCES

Chai, Y F, Yu, W T, Zhang, J L, An, S L, Peng, J and Wang, Y Z, 2018. Influencing mechanism of Al_2O_3 on sintered liquid phase of iron ore fines based on thermal and kinetic analysis, *Ironmaking & Steelmaking*, 46(5):1–7.

Dong, J J, Wang, G, Gong, Y G, Guo, Q and Wang, S J, 2015. Effect of high alumina iron ore of gibbsite type on sintering performance, *Ironmaking & Steelmaking*, 42(1):34–40.

Gan, Q, He, Q, Li, J M, Yuan, T Y and Wang, Z D, 2003. Study on the behavior of Al_2O_3 in vanadium and titanium sinter, *Steel*, 38(1):1–4.

Guo, Q F, Li, J L, Ren, W and Li, Y R, 2013. Study on the effect of high Al_2O_3 iron ore on the metallurgical properties of Angang sinter, China Metal Association, *Proceedings of the 9th China Iron and Steel Annual Conference*, pp 323–326 (Metallurgical Industry Press: Beijing).

Hu, L, 2011. *Study on the Influence of Al_2O_3, SiO_2 on the Sintering of Iron Ore and Its Mechanism,* Doctoral dissertation, Central South University.

Li, T I, Sun, C Y, Liu, X Y, Song, S and Wang, Q, 2017. The effects of MgO and Al_2O_3 behaviours on softening–melting properties of high basicity sinter, *Ironmaking & Steelmaking*, 45(2):1–9.

O'Dea, D and Ellis, B, 2015. New insights into alumina types in iron ore and their effect on sintering, *10th China Iron and Steel Annual Conference and 6th Baosteel Academic Annual Conference*.

Umadevi, T, Deodar, A V, Mahapatra, P C, Prabhu, M and Ranjan, M, 2010. Influence of alumina on iron ore sinter properties and productivity in the conventional and selective granulation sintering process, *Steel Research International*, 80(9):686–692.

Wang, S T and Qi, F, 1997. Study on the Causes of Enhancement of Low Temperature Degradation of Sinter by Al_2O_3, *Sintering Pellets*, 22(2):1–4.

Yang, H M and Qiu, G Z, 1999. Effect of Al_2O_3 on RDI of sinter, *Research on steel and iron*, 11(1):1–4.

Yu, W T, Zuo, H B, Zhang, J J and Zhang, T, 2013. Study on metallurgical properties of high Al_2O_3 sinter, China Metal Association, *Proceedings of the 9th China Iron and Steel Annual Conference*, pp 352–356 (Metallurgical Industry Press: Beijing).

Zhang, M M and Andrade, M W, 2016. Effect of MgO and Basicity on Microstructure and Metallurgical Properties of Iron Ore Sinter, *Characterization of Minerals Metals & Materials*, pp 167–174.

Zhu, D Q, Xue, Y X, Pan, J, Yang, C C and Guo, Z Q, 2020a. An investigation into aluminum occurrence impact on SFCA formation and sinter matrix strength, *Journal of Materials Research and Technology*, 9(5):10223–10234.

Zhu, X L, Qin, C X, Qin, L N and Wang, C H, 2020b. Study on the occurrence state of a high alumina limonite in foreign countries, *Modern Mining*, 36(09):139–141.

Alternative fuel sources for ironmaking

Replacement of Pulverised Coal Injection (PCI) with hydrogen and its impact on blast furnace internal conditions

N Barrett[1], P Zulli[2], D O'Dea[3], S Mitra[4] and T Honeyands[5]

1. AAusIMM, PhD candidate, Centre for Ironmaking Materials Research, Newcastle Institute for Energy and Resources, University of Newcastle, Callaghan NSW 2308. Email: nathan.barrett@uon.edu.au
2. Director, ARC Research Hub for Australian Steel Manufacturing, Faculty of Engineering and Information Sciences, University of Wollongong, NSW 2522. Email: paul_zulli@uow.edu.au
3. Principal Technical Marketing, BHP Marketing Iron Ore, Brisbane, Qld 4000. Email: damien.p.odea@bhp.com
4. Research Associate, Centre for Ironmaking Materials Research, Newcastle Institute for Energy and Resources, University of Newcastle, Callaghan NSW 2308. Email: subhasish.mitra@newcastle.edu.au
5. FAusIMM, Associate Professor, Centre for Ironmaking Materials Research, Newcastle Institute for Energy and Resources, University of Newcastle, Callaghan NSW 2308. Email: tom.a.honeyands@newcastle.edu.au

ABSTRACT

The steel industry continues to explore and demonstrate technologies that decrease its greenhouse gas emissions, especially in blast furnace ironmaking where alternate operating conditions will be required. As the furnace has been optimised over many years, it is approaching the minimum fuel rate possible with coke and Pulverised Coal Injection (PCI). Alternative operating conditions are therefore required to further decrease greenhouse gas emissions. Because of this, hydrogen has been proposed as a reducing agent in the blast furnace. Injection of hydrogen through the tuyeres was assessed using a comprehensive 2D blast furnace global model. The model was calibrated to a blast furnace operating with PCI as a base case and various approaches to hydrogen injection assessed, with a particular focus on displacing PCI. The maximum hydrogen injection rate of 19.5 kg H_2 per tonne of hot metal was predicted, limited by decreases in the raceway adiabatic flame temperature and top gas temperature. Internal blast furnace conditions, such as gas composition and reduction degree were also predicted. Holistic analysis was performed to estimate the effectiveness of hydrogen injection on reduction of greenhouse gas emissions. Based on these results, the changes in blast furnace operation and emissions under hydrogen injection are discussed.

INTRODUCTION

Over recent decades, the steel industry has made significant reductions in greenhouse gas emissions (GHG) through practices that improve energy efficiency and material utilisation and implementation of new technologies. This has been and will remain the case for blast furnace ironmaking, particularly with new technologies being considered to enable a transition towards a lower overall carbon footprint in steel manufacturing. With blast furnaces expected to maintain the high demand of the steel industry in the near future, hydrogen has been proposed as a supplementary reducing agent in the blast furnace to transition ironmaking to lower carbon consumption (Thyssenkrupp, 2019).

The blast furnace process is inherently dependant on coke. Combustion of coke and other injectants like pulverised coal provide heat and reducing gases in the raceway/lower zone of the furnace; however, coke must also provide a gas-permeable internal structure at high temperature. This structure is critical in maintaining gas flow-through the furnace and limits the extent of coke replacement with hydrogen. The thermodynamics and kinetics of reduction of iron ores with hydrogen are also significantly different to those of carbon monoxide. The most obvious difference is that indirect reduction with hydrogen is endothermic, as opposed to exothermic reduction with carbon monoxide (Spreitzer and Schenk, 2019). The extra heat required will therefore need to be supplied by other means.

The injection of pure and cold hydrogen into the tuyeres is considered a feasible method of enriching the blast furnace with hydrogen (Chen and Zuo, 2021). To date, Thyssenkrupp have achieved an injection rate of 90 kg/h of H_2 into one tuyere of a blast furnace, with plans to increase the injection rate to all tuyeres (Thyssenkrupp, 2021). However, it remains a challenging issue to determine the upper limits of hydrogen injection in the blast furnace under various operating conditions. Typically, injection of hydrogen into the tuyeres of the blast furnace is constrained by a decrease in the Raceway Adiabatic Flame Temperature (RAFT), as the hydrogen does not react in the raceway and is simply heated up (Spanlang, Wukovits and Weiss, 2020; Yilmaz, Wendelstorf and Turek, 2017). If the RAFT is maintained through oxygen enrichment, a decrease in the Top Gas Temperature (TGT) is seen (Nogami, Kashiwaya and Yamada, 2012; Tang *et al*, 2021). Because of these effects, the limit of hydrogen injection into the blast furnace is dependent on the baseline operating conditions of the system, as well as constraints applied to the RAFT and TGT. In addition to constraints on the operation conditions, previous studies have typically constrained the bosh gas rate, allowing the productivity to increase (Nogami, Kashiwaya and Yamada, 2012).

Numerical modelling is an important tool in estimating the impact of injecting hydrogen on the blast furnace operation. When assessing cold hydrogen injection through the tuyeres, the injection rate can be normalised per tonne of hot metal produced (denoted t-HM) for comparison. Using hydrogen injection (in kg-H_2/t-HM and Nm^3/t-HM) the replacement of coke (in kg-coke/t-HM) has been estimated by various investigations: 10.8 kg-H_2/t-HM (120 Nm^3-H_2/t-HM) replaces 45 kg-coke/t-HM (Tang *et al*, 2021); 18 kg-H_2/t-HM (200 Nm^3-H_2/t-HM) replaces 54 kg/t-HM of coke (Spanlang, Wukovits and Weiss, 2020); 20.25 kg-H_2/t-HM (225 Nm^3-H_2/t-HM) replaces 27 kg-coke/t-HM (see Case 2 of appropriate study) (Castro, Takano and Yagi, 2017).

In previously reported studies, hydrogen has been used exclusively to replace coke. Coke rates in modern blast furnaces are close to the minimum and Pulverised Coal Injection (PCI) already replaces a significant amount of coke. As well as this, the coke ovens gas is used for heating and for power generation in an integrated steelworks. For these reasons, in this study it was decided to swap auxiliary injectants and replace PCI with hydrogen to have the least impact on the whole operation. This study estimates the maximum hydrogen injection possible based on the blast furnace thermal balance and calculates the impact of hydrogen injection on the furnace internal conditions. The impact of hydrogen injection on the greenhouse gas emissions of the blast furnace is also discussed.

METHODOLOGY

Determining hydrogen injection limits

A two-stage heat and mass balance model of the blast furnace was used to determine the limits of hydrogen injection (Mathieson *et al*, 2011). The base case scenario was an operating blast furnace without any hydrogen injection, to which the model was calibrated. The operating conditions of the base case scenario are presented in Table 1.

TABLE 1

Operating parameters – Maximum hydrogen injection scenario (19.54 kg-H_2/t-HM).

Parameter	Base case	Hydrogen injection
RAFT (°C)	2250	2050
Top Gas Temperature (°C)	138	118
Productivity (t-HM/day)	7748	7748
Blast Rate (Nm^3/t-HM)	899	790
Oxygen Enrichment (%)	2.71	4.66
Slag Rate (kg/t-HM)	313	307
Coke Rate (kg/t-HM)	364	364
PCI Rate (kg/t-HM)	140	102.5

System constraints

Previous studies have constrained hydrogen injection through either a constraint on the RAFT (Spanlang, Wukovits and Weiss, 2020; Yilmaz, Wendelstorf and Turek, 2017), or if the RAFT is maintained through oxygen enrichment, a decrease in the TGT (Long *et al*, 2016; Nogami, Kashiwaya and Yamada, 2012; Tang *et al*, 2021; Wang *et al*, 2017). In this study, both the RAFT and TGT were constrained in a stagewise fashion. Initially, the RAFT was maintained through oxygen enrichment until the TGT was decreased to 118°C. This maintained the TGT above the acid dew point of the gas. Following this point, with increasing hydrogen injection the RAFT was allowed to decrease. A maximum decrease of 200°C was considered appropriate for the RAFT.

In all cases, the blast flow rate and thus the bosh gas flow rate, was adjusted to maintain the production rate of the furnace. The bosh gas flow rate refers to the reducing gas generated in the raceways, which continues to rise through the furnace. As well as this, the coke rate was maintained constant, allowing the hydrogen to replace PCI. Note that the productivity of the blast furnace was constrained in consideration of the designed capacity of downstream processes.

Internal conditions of blast furnace

The heat and mass balance model outputs were used as inputs to a comprehensive 2D blast furnace global model. This model is a 2D steady state, multifluid model which approximates spatial distribution of parameters inside the blast furnace (Abhale, Viswanathan and Saxén, 2020; Chew, Zulli and Yu, 2001).

RESULTS AND DISCUSSION

Limits of hydrogen injection

Shown below in Figure 1 are the constrained parameters (RAFT and TGT) determined from the heat and mass balance model for increasing hydrogen injection rates.

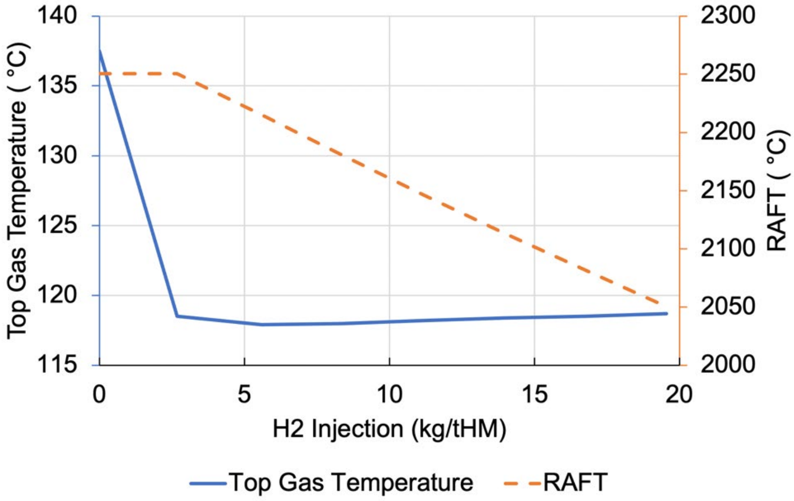

FIG 1 – Constrained operation parameters with increasing hydrogen injection.

From Figure 1, the stage-wise constraint of the system is evident, with the initial constraint to the top gas temperature being met at 2.7 kg/t-HM of hydrogen injection, with an increase in oxygen injection to maintain the RAFT constant. Following this point, the RAFT is allowed to decrease, as further oxygen injection would violate the TGT constraint. The RAFT decreased by the acceptable amount of 200°C at 19.54 kg/t-HM of hydrogen injection. Thus, this was determined to be the maximum hydrogen injection for the system. It is worth noting that to inject this amount of hydrogen would require approximately 151 t-H_2/day.

The operating conditions of the simulated blast furnace under the maximum hydrogen injection are shown in Table 1. As seen through comparison of the operating parameters for the base case and hydrogen injection case, the maximum hydrogen injection of 19.54 kg-H_2/t-HM reduces the PCI rate by 37.5 kg-PCI/t-HM.

Emission reduction through hydrogen injection

Emissions are typically categorised into three types – Scope 1 emissions refer to emissions which are directly produced from a process, Scope 2 emissions refer to emissions produced from purchased electricity and Scope 3 emissions refer to those generated indirectly, upstream and downstream of the process. Assuming the replacement of PCI with hydrogen has little impact on other processes in an integrated steelworks (and thus limited effect on the Scope 2 emissions), the resulting decrease in emissions can be approximated through the emissions attributed exclusively to the PCI and hydrogen. World Steel Association (2021) provides approximate emission factors for direct emissions from blast furnace materials. Using these values, the total direct blast furnace emissions were calculated to be 1.163 t-CO_2/t-HM for the base case scenario and 1.053 t-CO_2/t-HM for the maximum hydrogen injection case. This was a decrease in direct blast furnace emissions of 9.46 per cent.

This value is based on the assumption that the hydrogen injected produced no emissions. However, when considering the upstream emissions related to hydrogen production (Scope 1 if generated on-site, Scope 3 if purchased (World Steel Association, 2021)), it is clear that the source of hydrogen is critical to achieve a net decrease in emissions. Shown in Table 2 is the change in emissions attained when accounting for emissions from hydrogen production, depending on the source of hydrogen used. Green hydrogen refers to hydrogen produced using renewable energy, blue hydrogen refers to hydrogen produced through natural gas reforming with CO_2 sequestration and grey hydrogen refers to hydrogen produced through natural gas reforming without CO_2 sequestration.

TABLE 2

Net emission decrease based on source of hydrogen.

Hydrogen source	Emissions factor* (t-CO_2/t-H_2)	Net change in emissions (%)
Green hydrogen	0	-9.5
Blue hydrogen	1.8	-6.4
Grey hydrogen	19.8	23.8

*(World Steel Association, 2021).

From Table 2, it is clear that the use of grey hydrogen is not a feasible method for a net decrease in emissions around the blast furnace. Blue hydrogen, while providing a significant reduction in emissions, is dependent on the development of carbon sequestration technology to be adopted on a large scale. It is therefore desirable to use green hydrogen in the blast furnace. At present, the largest green hydrogen electrolyser has a capacity of 8.2 t-H_2/day (Air Liquide, 2021), so multiple electrolysers would be required to supply the theoretical demand of 151 t-H_2/day for the modelled blast furnace. As electrolyser technology improves, the scale and cost of green hydrogen is expected to improve significantly.

From the determined values of 19.54 kg-H_2/t-HM replacing 37.5 kg-PCI/t-HM and reducing emissions by 110 kg-CO_2/t-HM, an approximate break-even pricing for the utilisation of hydrogen can be determined. The economics of hydrogen usage are dependent on two factors, namely the cost of hydrogen and the potential offset for decreased carbon emissions. With today's prices roughly US$165/t-PCI (Li, 2021), the breakeven price of hydrogen would be approximately US$317/t-$H_2$. At today's green hydrogen prices of US$5000/t-$H_2$ (Bade, 2021), the carbon subsidy required to break even would be US$832/t-$CO_2$. With projected cost decreases to as low as US$1000/t-$H_2$ within the decade (Bade, 2021; Chevrier, 2020) the carbon subsidy required to break even would be US$121/t-$CO_2$.

Flow modelling – determining blast furnace internal conditions

The internal conditions of the blast furnace were simulated using a comprehensive 2D blast furnace global model, details of which are provided elsewhere (Chew, Zulli and Yu, 2001; Liu *et al*, 2018). Three cases were evaluated: Base case (0 kg-H_2/t-HM), an intermediate case (9.77 kg-H_2/t-HM) and maximum hydrogen injection (19.54 kg-H_2/t-HM). The internal conditions are displayed on a contour plot representing the conditions on a 2D section of the blast furnace.

In Figure 2, the spatial distribution of the reduction degree of the burden is shown, as a function of hydrogen injection rate.

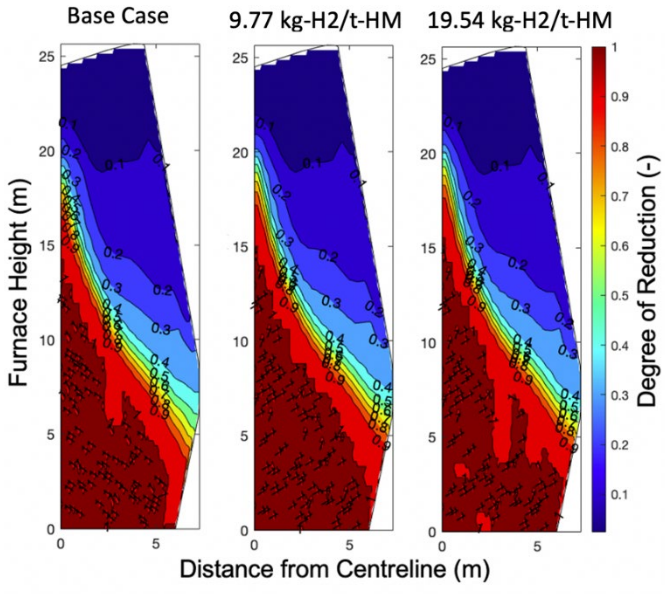

FIG 2 – Degree of reduction contour plot (Left: Base case, Middle, 9.77 kg-H_2/t-HM injection, Right: 19.54 kg-H_2/t-HM injection).

As seen in Figure 2, the reduction degree progresses quickly from 40 to 100 per cent. The rate of progress or change in these isopleths is most rapid for the maximum hydrogen injection case and occurs at higher locations (with reference to the furnace baseline) in the furnace.

Shown below in Figure 3 is a comparison of the spatial distribution of the hydrogen volume fraction in the gas inside the furnace with increasing hydrogen injection rates. The concentration of hydrogen in the bosh gas for the Base case is approximately 7 per cent. At the maximum hydrogen injection, the bosh gas is approximately 20 per cent hydrogen. The region over which the hydrogen concentration decreases is seen to be significantly smaller in the maximum hydrogen injection case when compared to the base case.

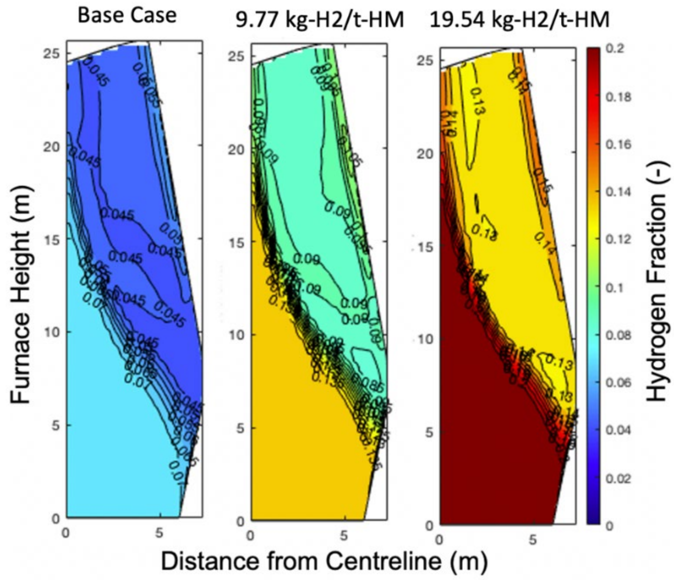

FIG 3 – Hydrogen concentration contour plot (Left: Base case, Middle, 9.77 kg-H_2/t-HM injection, Right: 19.54 kg-H_2/t-HM injection).

When comparing Figures 2 and 3, it is evident that the region over which the hydrogen concentration decreases correspond to the region in which the majority of the reduction of iron oxides occurs. This implies that the increased hydrogen concentration leads to enhanced reduction conditions, especially in the cohesive zone (the calculated position of the cohesive zone is not depicted in the figures).

It is worth noting that the utilisation efficiency of hydrogen in the modelling was assumed to be proportional to the carbon monoxide utilisation efficiency during modelling. The ratio used was based on data from an operating blast furnace to which the model was calibrated. What is evident from Figure 3 is that this utilisation (around 50 per cent) results in significant hydrogen leaving the furnace unreacted with the top gas. Previous operational trials have indicated that in practice, the utilisation of hydrogen may be even lower at approximately 38–42 per cent (Matsuzaki *et al*, 2012; Watakabe *et al*, 2013). While blast furnace top gas is typically utilised in other processes within the steelworks, the value of future green hydrogen and the best way to deploy such a commodity must be considered. To optimise the use of hydrogen in the blast furnace, alteration to the blast furnace process may be required, such as the introduction of top gas recycling.

CONCLUSIONS

Numerical models were used to estimate the theoretical limits of hydrogen injection with an aim to assess changes in furnace internal conditions with reference to a base case involving PCI. The hydrogen injection limits were primarily constrained by a decrease in the top gas temperature and raceway adiabatic flame temperature. In these simulations, the productivity of the furnace was maintained constant. Based on the modelling results, the maximum hydrogen injection for the system was determined to be 19.54 kg-H_2/t-HM, replacing 37 kg-PCI/t-HM. The maximum hydrogen injection was noted to decrease the direct emissions of the blast furnace by 9.46 per cent if green hydrogen was used. Under the maximum hydrogen injection condition, the reduction of ferrous burden was determined to progress more rapidly, indicating enhanced reduction conditions in the cohesive zone.

Some key considerations for the feasibility of hydrogen injection were identified. The source of hydrogen is critical in achieving a net decrease in emissions around the blast furnace; however, there is insufficient green hydrogen to support the high demand of the steel industry. As well as this, hydrogen is not expected to reach high utilisations in the blast furnace, resulting in much of the injected hydrogen leaving the system through the top gas stream. This low utilisation may require modification to the blast furnace operation with new measures such as top gas recycling in order to make best use of the highly valuable green hydrogen in the future.

ACKNOWLEDGEMENTS

The authors acknowledge the funding of the Australian Research Council in supporting the ARC Research Hub for Advanced Technologies for Australian Iron Ore and BHP for their financial support and permission to publish this paper. The authors also thank BlueScope Steel for valuable discussions on the numerical modelling.

REFERENCES

Abhale, P B, Viswanathan, N N and Saxén, H, 2020. Numerical modelling of blast furnace – Evolution and recent trends, *Mineral Processing and Extractive Metallurgy, 129*(2):166–183. doi:10.1080/25726641.2020.1733357

Air Liquide, 2021. Air Liquide inaugurates the worlds largest low-carbon hydrogen membrane-base production unit in Canada, https://www.airliquide.com/mainland-china/air-liquide-inaugurates-worlds-largest-low-carbon-hydrogen-membrane-based-production

Bade, D, 2021. US Department of Energy announces green hydrogen cost-cutting goal, https://ieefa.org/us-department-of-energy-announces-green-hydrogen-cost-cutting-goal/#:~:text=The%20DOE%20estimates%20hydrogen%20from,currently%20costs%20about%20%245%2Fkg.

Castro, J A d, Takano, C and Yagi, J-I, 2017. A theoretical study using the multiphase numerical simulation technique for effective use of H2 as blast furnaces fuel, *Journal of Materials Research and Technology*, 6(3):258–270. doi:10.1016/j.jmrt.2017.05.007

Chen, Y and Zuo, H, 2021. Review of hydrogen-rich ironmaking technology in blast furnace, *Ironmaking & Steelmaking*, 1–20. doi:10.1080/03019233.2021.1909992

Chevrier, V, 2020. Ultra-Low CO2 Ironmaking: Transitioning to the Hydrogen Economy, https://www.midrex.com/tech-article/ultra-low-co2-ironmaking-transitioning-to-the-hydrogen-economy/

Chew, S, Zulli, P and Yu, A, 2001. Modelling of Liquid Flow in the Blast Furnace, Application in a Comprehensive Blast Furnace Model, *ISIJ International,* 41(10):1122–1130. doi:10.2355/isijinternational.41.1122

Li, A, 2021. COKING COAL DAILY: PCI prices up slightly amid continuous supply tightness, https://www.metalbulletin.com/Article/3995674/COKING-COAL-DAILY-PCI-prices-up-slightly-amid-continuous-supply-tightness.html

Liu, X, Honeyands, T, Evans, G, Zulli, P and O'Dea, D, 2018. A review of high-temperature experimental techniques used to investigate the cohesive zone of the ironmaking blast furnace, *Ironmaking & Steelmaking*, 1–15. doi:10.1080/03019233.2018.1464107

Long, H M, Wang, H, Zhao, W, Li, J X, Liu, Z and Wang, P, 2016. Mathematical simulation and experimental study on coke oven gas injection aimed to low carbon blast furnace ironmaking, *Ironmaking & Steelmaking,* 43(6):450–457. doi:10.1080/03019233.2015.1108480

Mathieson, J, Rogers, H, Somerville, M, Ridgeway, P and Jahanshahi, S, 2011. *Use of biomass in the iron and steel industry – An Australian perspective*.

Matsuzaki, S, Higuchi, K, Shinotake, A and Saito, K, 2012. Possibility of hydrogen reduction in iron-making process: Course 50 Programs in Japan, 2:977–983.

Nogami, H, Kashiwaya, Y and Yamada, D, 2012. Simulation of Blast Furnace Operation with Intensive Hydrogen Injection, *ISIJ International,* 52(8):1523–1527. doi:10.2355/isijinternational.52.1523

Spanlang, A, Wukovits, W and Weiss, B, 2020. Development of a Blast Furnace Model with Thermodynamic Process Depiction by Means of the Rist Operating Diagram, *BHM Berg – und Hüttenmännische Monatshefte,* 165(5):243–247. doi:10.1007/s00501–020–00963–6

Spreitzer, D and Schenk, J, 2019. Reduction of Iron Oxides with Hydrogen—A Review, *Steel Research International,* 90.(10. doi:10.1002/srin.201900108

Tang, J, Chu, M, Li, F, Zhang, Z, Tang, Y, Liu, Z and Yagi, J, 2021. Mathematical simulation and life cycle assessment of blast furnace operation with hydrogen injection under constant pulverized coal injection, *Journal of Cleaner Production,* 278:123191. doi:10.1016/j.jclepro.2020.123191

Thyssenkrupp, 2019. World first in Duisburg as NRW economics minister Pinkwart launches tests at thyssenkrupp into blast furnace use of hydrogen [Press release].

Thyssenkrupp, 2021. Injection of hydrogen into blast furnace: thyssenkrupp Steel concludes first test phase successfuly [Press release].

Wang, H, Chu, M, Bi, C, Liu, Z and Dai, W, 2017. *Effects of Hydrogen-Enriched Reduction on Metallurgical Properties of Iron-Bearing Burdens Under BF Operation with COG Injection*.

Watakabe, S, Miyagawa, K, Matsuzaki, S, Inada, T, Tomita, Y, Saito, K, … Wikstrom, J-O, 2013. Operation Trial of Hydrogenous Gas Injection of COURSE50 Project at an Experimental Blast Furnace, *ISIJ International,* 53(12):2065–2071. doi:10.2355/isijinternational.53.2065

World Steel Association, 2021. *CO2 Data Collection*, https://www.worldsteel.org/en/dam/jcr:9dd44705–6b4a-496e-8f8f-14cc1158752d/CO2_User_Guide_V10.pdf

Yilmaz, C, Wendelstorf, J and Turek, T, 2017. Modeling and simulation of hydrogen injection into a blast furnace to reduce carbon dioxide emissions, *Journal of Cleaner Production,* 154:488–501. doi:10.1016/j.jclepro.2017.03.162

Utilisation of energy sources other than coke in the sintering process

Y Iwami[1], T Higuchi[2], K Takehara[3], S Fujiwara[4] and K Fukada[5]

1. Senior Researcher, JFE Steel Corp, Fukuyama Hiroshima 721–8510, Japan.
   Email: yu-iwami@jfe-steel.co.jp
2. Senior Researcher, JFE Steel Corp, Fukuyama Hiroshima 721–8510, Japan.
   Email: ta-higuchi@jfe-steel.co.jp
3. Senior Researcher, JFE Steel Corp, Fukuyama Hiroshima 721–8510, Japan.
   Email: ke-takehara@jfe-steel.co.jp
4. Senior Researcher, JFE Steel Corp, Fukuyama Hiroshima 721–8510, Japan.
   Email: sh-fujiwara@jfe-steel.co.jp
5. Senior Researcher, JFE Steel Corp, Fukuyama Hiroshima 721–8510, Japan.
   Email: k-fukada@jfe-steel.co.jp

ABSTRACT

Following the Paris Agreement adopted in 2015 and the SDGs, reduction of CO_2 emissions has been taken up as an issue worldwide, and the steel industry, which has a particularly large emission, is required to significantly reduce it. Most of the CO_2 generated in the steel industry is generated from the ironmaking process, due to the use of coke and its raw material coal in the ironmaking process.

JFE Steel Corporation has been considering the use of hydrocarbon-based gaseous fuels and liquid fuels as a partial alternative to coke breeze used in the sintering process since 2006, immediately after the Kyoto Protocol came into effect in 2005. In a laboratory study, a pot test was used to investigate the effect of the type of fuel, its amount and its injection method on the heat pattern in sinter bed. As a result, the authors developed a technology, in which a predetermined amount of gas fuel or liquid fuel was injected from the surface of sintering bed to extend the holding time of 1200°C or higher at which liquid phase sintering occurs in the layer, to improve the sinter strength while reducing the amount of coke breeze. The authors succeeded in putting this technology to practical use using hydrocarbon-based gas fuel in 2009 and achieved a maximum annual reduction of 60 000 tons of CO_2 per sintering machine.

In this report, the authors introduce the results of laboratory studies on the use of various energy sources, the practical application of the technology for injecting hydrocarbon-based gaseous fuel into the sintering machine, and the operational results.

INTRODUCTION

In recent years, there is an urgent need to develop technology to reduce CO_2 emissions as a concrete measure against climate change. Approximately 60 per cent of the emissions in the steel industry are generated in the sintering and blast furnace processes (Hanmyo, 2007), so the reduction of coke breeze ratio used in sintering machine (hereinafter, bonding agent ratio, BAR) and the carbon materials ratio used in the blast furnace (hereinafter, reducing agent ratio, RAR) has been strongly demanded.

It is generally known that the improvement of sinter strength and reducibility is an effective method for reducing BAR and RAR (Kajikawa *et al,* 1982). Improvement of sinter strength makes the generation ratio of return fines decrease and the BAR can be reduced. Improvement of sinter reducibility makes RAR reduce in the blast furnace. Therefore, the production of high strength and high reducibility sintered ore is important for decreasing CO_2 emissions in ironmaking process.

The temperature in the sintering bed must be kept between 1200°C and 1400°C to produce high strength sintered ore. Generally, when BAR increases, the sinter strength improves, because more melt is generated. If BAR increases excessively, the sinter strength decreases by the formation of glassy silicate with over melting.

In the past, some technologies have been proposed, in order to improve the sinter strength without increasing BAR. For example, it was reported that the main exhaust gas recirculation system in sintering machines decreases the cooling rate with its sensible heat (Sato *et al*, 1985). On the other hand, it was pointed out that the sinter productivity decreases due to the lower O_2 concentration and higher humidity in the main exhaust gas (Yasumoto *et al*, 1978). Moreover, preheated air injection methods were suggested (Ishimitsu *et al*, 1962; Tashiro *et al*, 1980). However, it was difficult to control the temperature zone over 1200°C, because the preheating air temperature was low about 300°C. It also deteriorated the permeability with the increase in actual velocity. Therefore, each technology is not widely applied to sintering machines.

Then the hydrogen-based gaseous fuel (hereinafter, gaseous fuel) injection technology was developed and installed to Keihin No. 1 sinter plant in JFE Steel Corporation. This technology can produce high strength sintered ore without increasing BAR by changing the heating/cooling rate in the sintering process (Oyama *et al*, 2011). The fundamental research was carried out at laboratory scale to clarify the effect of gaseous fuel injection on the temperature distribution in the sintering bed. Operational tests were also performed at commercial plants to verify the principle of this technology.

Furthermore, the combustion speed control by oxygen enrichment and the utilisation of liquid fuel as an alternative to gaseous fuel were examined.

CONCEPT OF THIS TECHNOLOGY

Effect of temperature on iron ore sintering process

The iron ore sintering process proceeds by bonding the ores to each other with the melt produced by the reaction between the ore and the flux as the temperature rises. Figure 1 shows the schematic diagram of the sintering process. Raw materials start to melt above 1200°C, after that SFCA (silico ferrite calcium and aluminium) texture forms from this melt. This SFCA texture excels in the strength (Kissin and Litvinova, 1960). However, it decomposed into a low-strength glassy silicate at 1400°C.The authors aimed to control the holding time of temperature between 1200°C and 1400°C to maintain the SFCA texture.

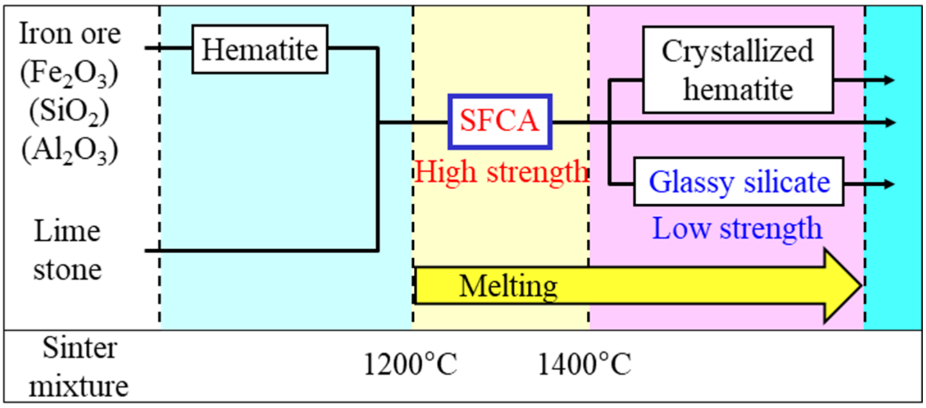

FIG 1 – Schematic diagram forming mineral composition in the sintering process.

Increasing coke breeze rate is a conventional method to extend the holding time of temperature over 1200°C. However, this method causes overheating and temperature exceeding 1400°C. Therefore, authors focused on phenomenon that the combustion position of gaseous fuel is different from coke breeze in the sintering bed. If these combustion points are controlled properly, it'll enable to extend the holding time of optimum temperature between 1200°C and 1400°C.

EXPERIMENTAL METHOD

Sintering pot test

Figure 2 shows the measurement method for the temperature distribution in the sintering bed. Transparent quartz glass pot (300 mmφ × 400 mm height) was used. After charging the sinter mixture (42 kg/charge) into the pot and igniting it, liquefied natural gas (hereinafter, LNG; $CH_4/C_2H_6/C_3H_8$ = 89/5/6 vol per cent) and air were injected from the top of sintering bed for 60 sec after ignition. LNG was injected for the duration of the sintering time. The sintering test was performed at the constant suction pressure of 6.9 kPa and the hearth layer thickness of 20 mm. Video camera and infrared thermography were set in front of the glass pot and R type sheathed thermocouples (1.6 mmφ × 200 mm length) were used to compensate the temperature data acquired by thermography. The three thermocouples were inserted 150 mm into pot side holes, which were installed at intervals of 100 mm in height.

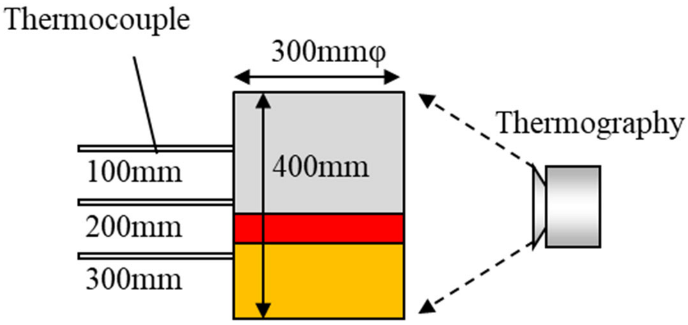

FIG 2 – Measurement method for temperature distribution in the sintering bed.

The blending ratio of limestone and silica sand were adjusted to obtain a SiO_2 content of 4.8 mass per cent and basicity (CaO/SiO_2) of 1.9 in the sinter, and return fine ratio was set at 20 mass per cent.

Table 1 shows the experimental heat conditions in the sintering pot test. In the conventional method, coke breeze ratio was set at 5.0 mass per cent of the sinter mixture. In the LNG injection method, LNG concentration was set at 0.4 vol. per cent versus suction air. When LNG concentration was more than 0.5 vol. per cent, the improvement effects were saturated. Based on this preliminary evaluation a safe LNG concentration was decided upon. When LNG was injected with a coke breeze ratio of 5.0 mass per cent, over melting was caused and the sinter strength decreased. Therefore, coke breeze ratio was reduced to 4.6 mass per cent to match equal combustion heat amount and avoid over melting. Here, the combustion heat of coke breeze is higher heating value of 27.1 MJ/kg and LNG has lower heating value of 41.6 MJ/Nm^3. The average suction air volume was 1.5 m^3/min measured with the orifice flowmeter.

TABLE 1

Experimental heat conditions in the sintering pot test.

	Conventional method	**LNG injection method**
Coke (mass%)	5.0	4.6
LNG (vol.%)	0.0	0.4

In these tests, shatter strength, degree of reduction (hereinafter, JIS-RI) and reduction disintegration index (hereinafter, JIS-RDI) were measured. Quantitative analysis of hematite, SFCA, magnetite and glassy silicate was performed by the powder X-ray diffraction method in the same way as previous reports (Oyama *et al*, 1996).

Sintering test using hot stage X-ray CT scanner

The pore structure has a major effect on the sinter quality and permeability in the sintering bed (Kasama, Inazumi and Nakayasu, 1992), because the pores in the sinter cake are simultaneously structural defects and also function as air passages. Therefore, a sintering test was performed with an X-ray CT scanner (Oyama *et al*, 1998), which had been remodelled to enable LNG injection and observe the changes in the pore structure in the sinter cake directly. First, the sinter mixture was charged into a carbon pot (100 mmφ × 100 mm height), and the suction gas volume was set at 0.2 Nm^3/min measured by the pitot tube flowmeter located under the pot. The LNG concentration was set at 0.4 vol. per cent (relative to the suction air volume) and then LNG was injected from the surface 180 sec after ignition. The X-ray tube voltage was 130 kV, the tube current was 200 mA, and it took 2.8 sec to photograph one cross-sectional image. The resolution of the CT images was 1 mm.

Commercial sintering machine test

The operational tests were carried out at Keihin No. 1 sinter plant to confirm the effects observed in the laboratory. Table 2 shows the experimental conditions in the operational test. The LNG injection volume was set at 250 Nm^3/h (0.5 $Nm^3/t\text{-s}$, combustion heat amount: 20 MJ/t-s). The BAR was reduced from 5.3 mass per cent to 5.0 mass per cent (heat amount 80 MJ/t-s). Therefore, the reduced heat amount was approximately four times as large as the injected LNG heat amount. The LNG was injected at the initial one-third length of the sintering machine, where the flame front existed in the upper layer. The sinter strength of the upper layer tends to be weaker than that of the lower layer.

TABLE 2

Experimental conditions in the operational test at Keihin No. 1 sinter plant.

	Conventional method	**LNG injection method**
Coke (mass%)	5.3	5.0
LNG (Nm^3/h)	0.0	250

The granulation moisture was set at 7.6 mass per cent and the bed height was set at 650 mm. The pallet speed was controlled so that BTP (burn through point; end point of sintering) were constant. In this test, R type thermocouples (3.2 mmφ × 1000 mm length) were inserted 500 mm into the sintering bed through the holes on the sidewall. Moreover, tumble strength, JIS-RI and JIS-RDI were measured to determine sinter quality.

EXPERIMENTAL RESULTS AND DISCUSSION

Effect of gaseous fuel injection method on sintering characteristics

Figure 3 shows a comparison of the combustion behaviour, sinter productivity and quality between the conventional method and the LNG injection method in the middle layer of the sintering bed. The observation results confirmed that the red-hot region, in which the combustion/melting zone existed, was greatly expanded by the LNG injection method.

On the other hand, the sinter strength improved, and the generation rate of return fines decreased remarkably, while the sintering time extended slightly. Although JIS-RI and JIS-RDI normally tended to be inversely related to sinter strength, they also improved with the LNG injection method.

	Coke 5.0mass% (Conventional method)	Coke4.6mass% and LNG0.4vol.% (LNG injection method)
Macroscopic image of red-hot region with quartz glass pot	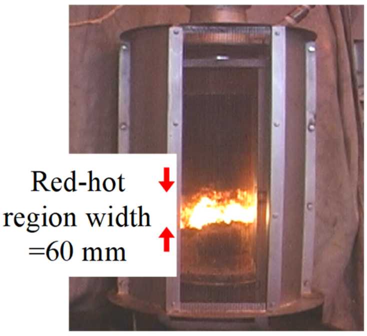	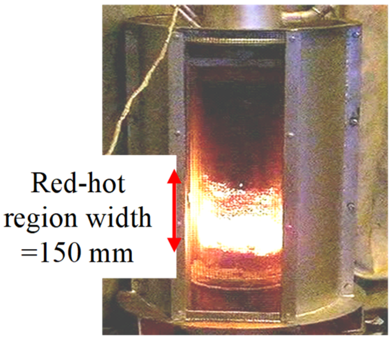
Sintering time (min.)	16.0	16.7
Sinter yield (%)	69.0	72.8 (+3.8)
Productivity (t/h・m^2)	1.56	1.64 (+0.8)
Shatter index (%)	70.7	72.9 (+2.2)
JIS-RDI (mass%)	36.1	28.3 (-7.8)
JIS-RI (%)	64.5	70.4 (+5.9)

FIG 3 – Comparison of the combustion behaviour in the sintering bed, sinter productivity and quality between the conventional method and the LNG injection method.

Effect of gaseous fuel injection method on sintering characteristics

Figure 4 shows the effect of the gaseous fuel injection method on temperature distribution measured by thermography in the sintering bed. In this figure, the temperature zone over 1200°C was expanded in upper direction with the LNG injection. The combustion positions of the LNG and coke breeze were different in the direction of bed height, because the LNG was injected from the top of sintering bed and burned before reaching at the coke breeze combustion position with the temperature 650–750°C Here this temperature was the ignition temperature of CH_4 composing approximately 90 per cent of LNG. Therefore, the temperature zone over 1200°C was expanded in upper direction with the low cooling rate by the combustion positions difference.

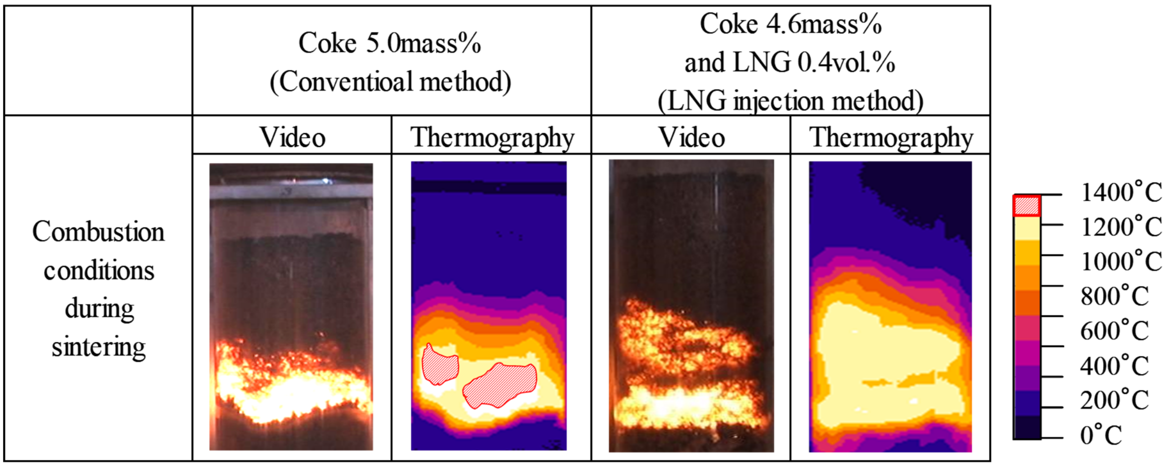

FIG 4 – Effect of the gaseous fuel injection method on temperature distribution measured by thermography in the sintering bed.

Figure 5 shows the changes in the temperature distribution measured by the infrared thermography with the LNG injection method. From these results, the temperature zone over 1200°C was narrow and the maximum temperature was over 1400°C in the conventional method. In contrast, the maximum temperature decreased, but the temperature zone over 1200°C was greatly expanded with the LNG injection method. Moreover, the holding time over 1200°C measured by the thermocouples was extended from 144 sec to 376 sec at 200 mm height from the top of sintering bed.

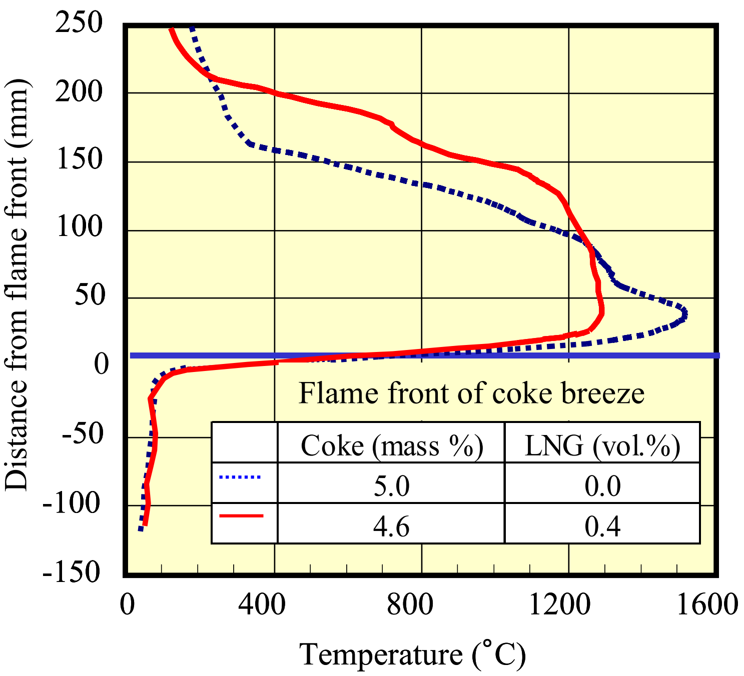

FIG 5 – Changes in the temperature distribution measured by infrared thermography with the gaseous fuel injection method.

Effect of gaseous fuel injection on pore structure in sintering bed

Figure 6 shows the comparison of X-ray CT image in the sinter cake between the conventional method and the LNG injection method. In this figure, the solid parts are shown in white and pores in black. From these results, the pores over 5 mm increased and the pore (1–5 mm) decreased by the LNG injection method in comparison with the conventional method. The extension of the holding time over 1200°C increased liquid phase ratio. As a result, the increase in liquid phase ratio promoted the combination of pores (1–5 mm) and improved the sinter strength (Oyama *et al*, 1998).

	Coke 5.0mass%	Coke 4.6mass% and LNG 0.4vol.%
CT images	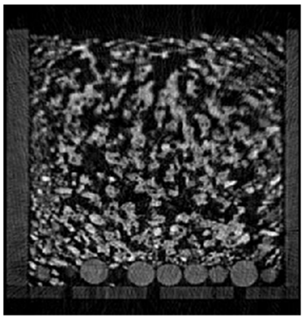	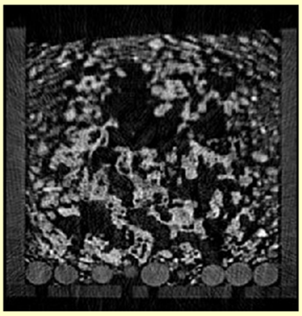

50mm

FIG 6 – Comparison of X-ray CT image between conventional method and LNG injection method.

Effect of gaseous fuel injection on formation of mineral texture

Figure 7 shows the change of mineral composition with the LNG injection method in the sintering pot test. From these results, LNG injection method increased the SFCA ratio by 1.6 times and decreased in the glassy silicate ratio. The extension of holding time between 1200°C and 1400°C supressed the decomposing SFCA texture into glassy silicate texture. As a result, the SFCA ratio increased, and the glassy silicate ratio decreased with the LNG injection method. Kissin and Litvinova (1960) reported that the SFCA texture was excellent strength and reducibility, and the glassy silicate texture was inferior in these two properties. Therefore, the increase in the SFCA ratio and the decrease in the glassy silicate ratio were part of the reason that the LNG injection method improved sinter strength and reducibility.

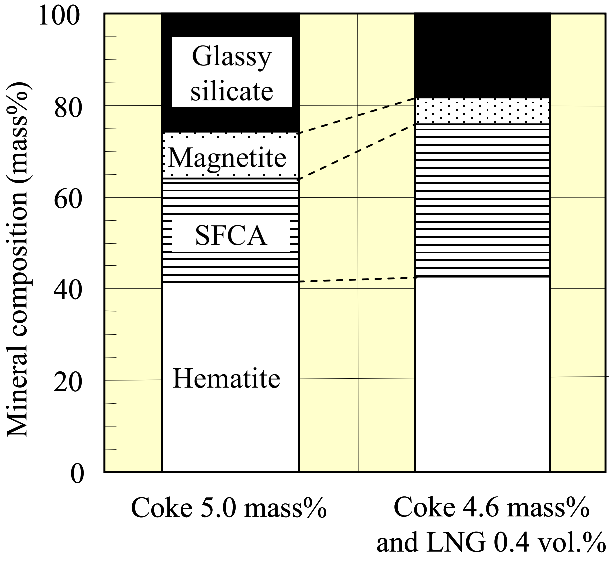

FIG 7 – Change of mineral composition by LNG injection method in the sintering pot test.

Effect on operational condition at actual plant with gaseous fuel injection

At first, the effect of the gaseous fuel injection on the temperature distribution was evaluated at Keihin No. 1 sinter plant. Figure 8a shows the temperature distribution in the upper layer, while (b) shows that in the lower layer. As shown in Figure 8a, the holding time over 1200°C was extended from 134 sec to 258 sec without the maximum temperature rising by the LNG injection method. On the other hand, Figure 8b shows that the maximum temperature decreased from 1437°C to 1370°C with the LNG injection method. The decrease of the maximum temperature was caused by the decrease of bonding agent consumption in 3.0 kg/t-s. Therefore, it was thought that is why the sinter strength at the upper weak layer was improved by the LNG injection and JIS-RI at the lower layer was improved by the decrease of bonding agent consumption.

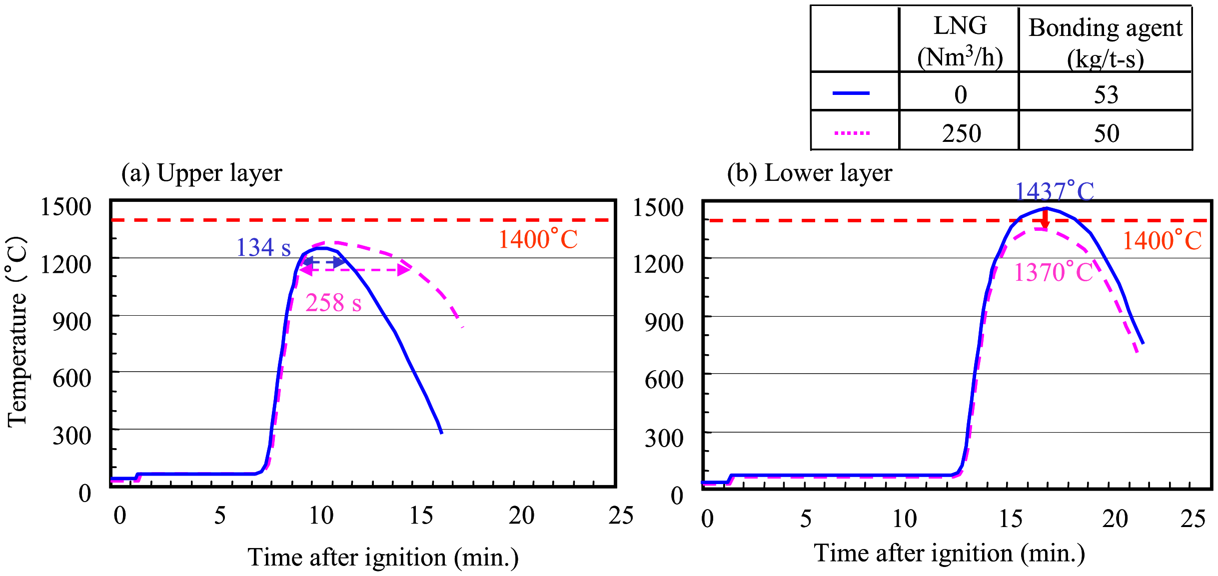

FIG 8 – Effects of LNG injection on the temperature in the sintering machine at Keihin No. 1 sinter plant.

The temperature distribution without increase on the maximum temperature and with extension of the holding time over 1200°C formed by the LNG injection method was considered to be the 'Type C sintering process' (Sasaki and Hida, 1982).

Figure 9 shows the changes in the operational result and quality between LNG injection method and conventional method. In this figure, the tumble strength increased by approximately one per cent with the same sinter production in the LNG injection method. Therefore, the bonding agent consumption was reduced with this increase in the tumble strength. Bonding agent consumption was reduced by 3.0 kg/t-s and CO_2 emissions were reduced by a maximum of approximately 60 000 t/a at Keihin No. 1 sinter plant. JIS-RI also gradually increased, and finally, a four per cent improvement effect was confirmed.

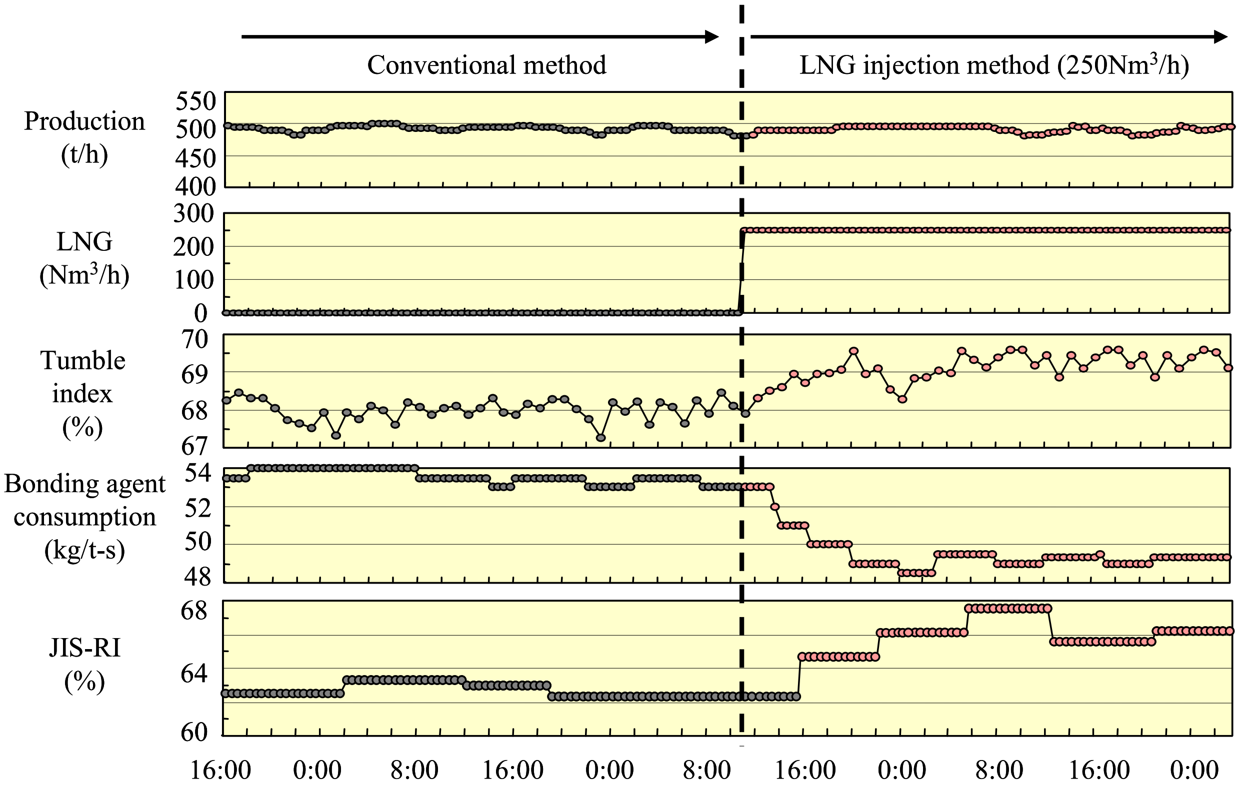

FIG 9 – Effects of LNG injection on sintering operation and quality at Keihin No. 1 sinter plant.

Table 3 shows the comparison of heat balance and sinter quality at Keihin No. 1 sinter plant. In the calculation for the heat balance, the heat inputs consisted of combustion heat of coke oven gas in the ignition furnace, combustion heat of coke breeze and LNG. From this table, the unit heat consumption decreased by approximately 60 MJ/t-s with the LNG injection method in comparison with the conventional method. Here, combustion heat of coke oven gas was 17.6 MJ/Nm^3, coke breeze was 27.1 MJ/kg and LNG was 41.6 MJ/Nm^3. However, the unit heat consumption decreased with the LNG injection method, and sinter quality improved by one per cent in tumble strength and four per cent in JIS-RI in comparison with the coke method at the same sinter production facility.

TABLE 3

Comparison of heat balance and quality of sintered ores at Keihin No. 1 sinter plant.

		Conventional method	**LNG injection method**
Heat input	Combustion heat of coke-oven gas (MJ/t-s)	39	39
	Combustion heat of coke breeze (MJ/t-s)	1505	1420
	Combustion heat of LNG (MJ/t-s)	0	22
Total	(MJ/t-s)	1544	1481
Operational result	Tumble index (mass%)	68	69
	JIS-RI (mass%)	63	67
	Production (t-s/h)	500	500

Introduction of additional technology development

Gaseous fuel and oxygen injection technology

As described above, holding temperature in the sintering bed between 1200°C and 1400°C is effective for formation of SFCA texture which has high strength and reducibility. Gaseous fuel injected from the surface of sintering bed combust at upper position of coke combustion position, and gaseous fuel injection technology can extend the time holding temperature between 1200°C and 1400°C. The effects are caused by the behaviour that gaseous fuel combust in 650°C to 750°C in the atmosphere.

The authors also studied the method to control the ignition behaviour of gaseous fuel and extend the holding time between 1200°C and 1400°C by oxygen and gaseous fuel injection at the same time (Iwami *et al*, 2013).

At first, the behaviour of the red-hot region was investigated in gaseous fuel and oxygen injection conditions. Table 4 shows experimental conditions. Ordinary condition (Case A), LNG injection (Case B), Oxygen injection (Case C) and LNG and Oxygen injection (Case D) were carried out.

TABLE 4

Experimental condition of gaseous fuel and oxygen injection.

	Case A	**Case B**	**Case C**	**Case D**
Coke (mass%)	5.0	4.6	5.0	4.6
LNG (vol.%)	0.0	0.4	0.0	0.4
O_2 (vol.%)	21	21	28	28

Figure 10 shows the observations of the red-hot region. In the Case B, the red-hot region was wider than that of Case A. Moreover, the red-hot region of Case D was wider than that of Case B. On the other hand, the red-hot region of Case C was narrower than that of Case A.

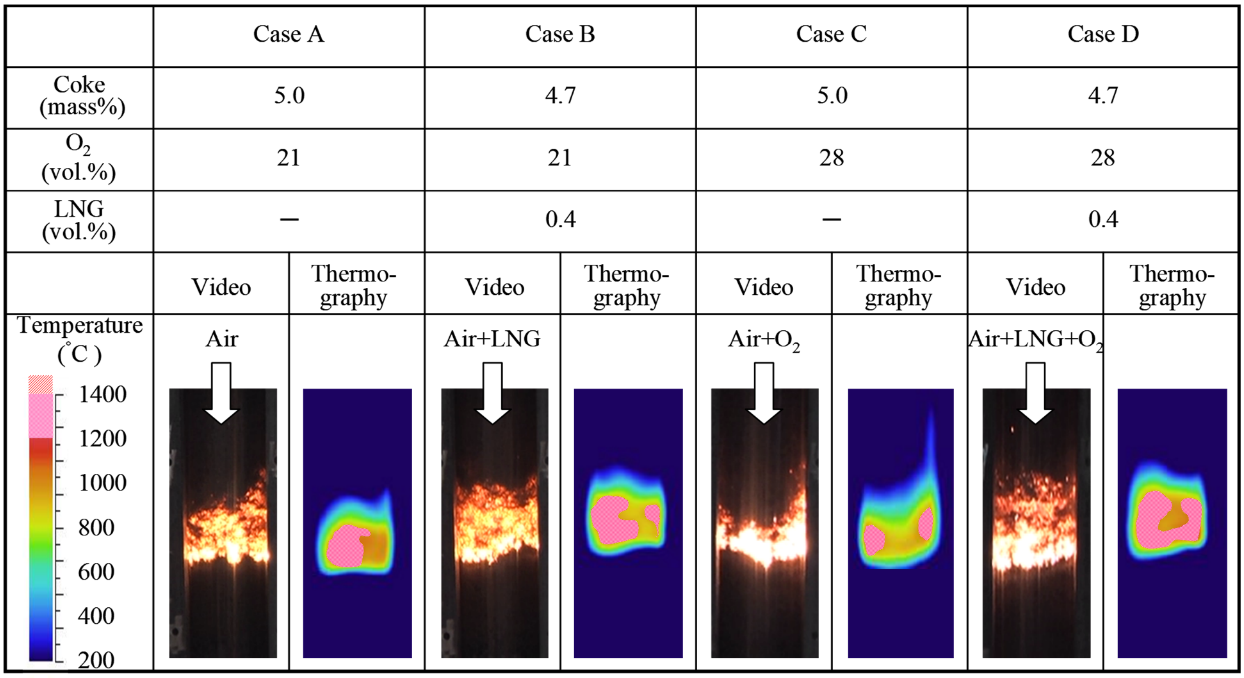

FIG 10 – Observation result of red-hot region with each condition.

In general, the oxidation rate of coke and LNG (CH_4) are described as follows (Hasatani *et al*, 1986; Kasai, Taketomi and Omori, 1984; Taketomi, Kasai and Omori, 1983).

$$R_C^* = n_C 4\pi r^2 k_C [O_2] \tag{1}$$

$$R_{CH4}^* = k_{CH4}[CH_4]^a [CH_3]^b [CH_2O]^C [CO]^d [H_2]^e \cdots\cdots [O_2]^X \tag{2}$$

R_C^*	Reaction rate (mol/s)
k_C	Reaction rate constant (m/s)
n_C	Total number of carbon particles in the system (-)
r	Radius of carbon particle (m)
$[O_2]$	Oxygen concentration (mol/m^3)
R_{CH4}^*	Reaction rate (mol/s/m^2)
k_{CH4}	Reaction rate constant (m/s)
$[i]^I$	Concentration of element i (mol/m^3)
$[O_2]$	Concentration of oxygen (mol/m^3)
I, X	Order in reaction equation (-)

Each equation is expressed as a function of temperature and oxygen concentration and increase of temperature and oxygen concentration increases oxidation rate. As noted before, LNG combusts in 650°C to 750°C in atmosphere (O_2: 21 vol. per cent). In other words, oxidation rate reach at the value to combust in 650°C to 750°C. In here, if oxygen concentration is higher than 21 vol. per cent, the temperature that oxidation rate reach at the value to combust is lower than 650°C to 750°C. Therefore, coke and LNG start to combust at lower temperature with high oxygen concentration.

Figure 11 shows schematic image of forming red-hot region. Coke and LNG start to combust with low temperature due to oxygen injection. As a result, coke combustion commences at a lower position in the bed and LNG combustion begins higher in the bed. Due to this shift of each combustion position the red-hot region is expanded.

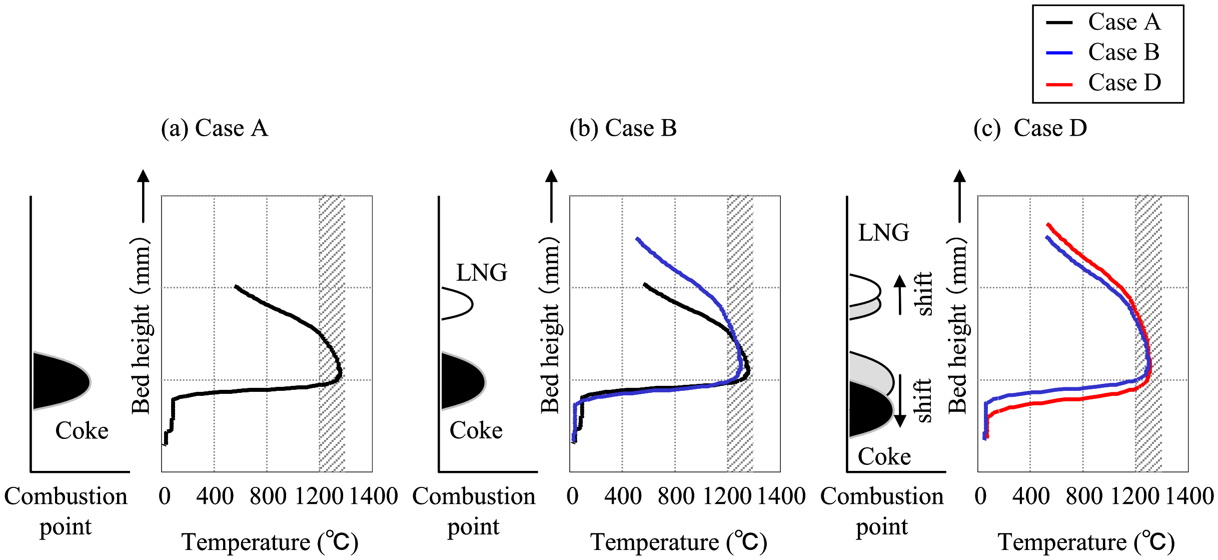

FIG 11 – Schematic image of forming red-hot region.

Figure 12 shows relationship of strength and productivity. LNG and oxygen injection extends the time between 1200°C and 1400°C and improves sinter strength. Moreover, the increase of oxygen concentration shortens sintering time and improves productivity. Further, sinter strength and productivity improved in Case D compared with Cases B and C due to the synergistic effect by simultaneous usage of LNG and oxygen.

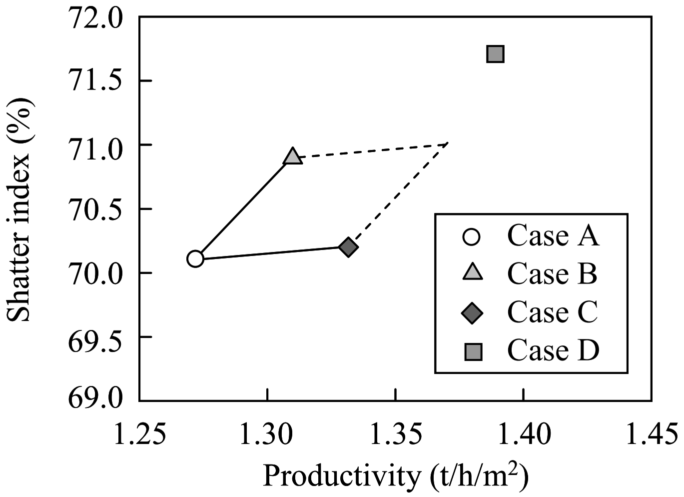

FIG 12 – Relationship between productivity and cold strength in pot test.

Liquid fuel injection technology

There are some plants without infrastructure for safe usage of gaseous fuel like LNG, consequently discussions about usage of liquid fuel were carried out as alternative heat sources to LNG.

The combustion mechanism of liquid fuel in the sintering bed is shown in Figure 13. Liquid fuel combustion is carried out by combustion of flammable gas generated from vapourisation of liquid fuel. Therefore, it is considered that control of combustion behaviour of liquid fuel makes a possible to achieve the same effects with gaseous fuel injection technology. To that end supply of the liquid fuel to the high temperature zone in the sintering bed is required.

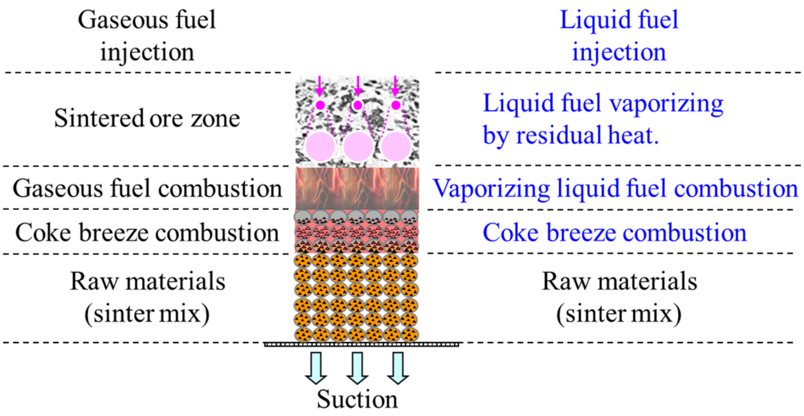

FIG 13 – Mechanism of liquid fuel combustion in the sintering bed.

Then, injection was carried out with misty liquid fuel by spray nozzle and pot test was carried out. Figure 14 shows the schematic image of pot test with liquid fuel injection. The silica glass pot (150 mmφ – 400 mm) was used and the combustion behaviour was observed by video camera. Table 5 shows the list of liquid fuels injected in this test. Injection rate of liquid fuel was controlled to be equal in heat amount to LNG injected as previously explained and coke ratio was set at 4.6 mass per cent.

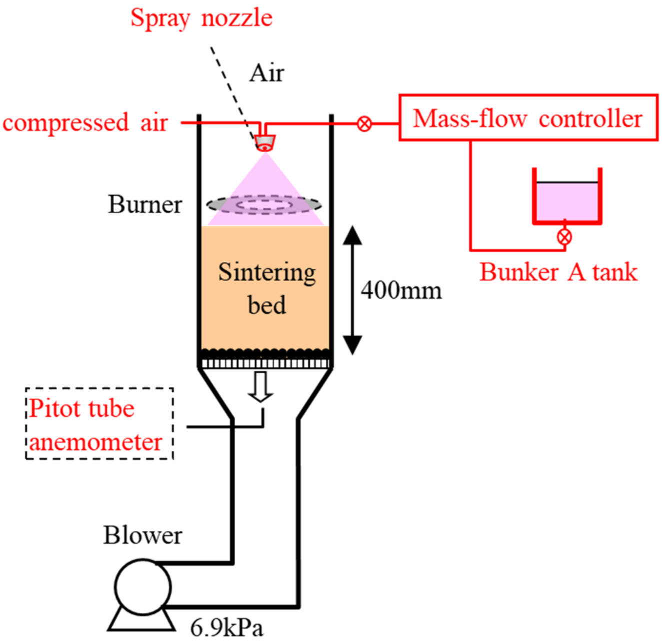

FIG 14 – Schematic image of pot test with liquid fuel injection.

TABLE 5

List of liquid fuel injected in pot tests.

	Bunker A	**Heating oil**	**Sesame oil**
Heat value (MJ/kg)	45.3	46.4	40.3
Viscosity (Pa.s)	0.06	0.03	0.05
Density (kg/m^3)	0.86	0.79	0.92

Figure 15 shows experimental results of liquid fuel injection tests. Red-hot regions were expanded in every case of liquid fuel injection. Therefore, shatter strengths were increased by more than three per cent in each injection condition compared with base condition. Moreover, there were few differences between these conditions. Productivity was increased by more than four per cent in each injection condition.

	Base	Bunker A	Heating oil	Sesame oil
Red-hot region	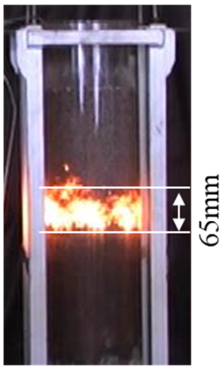 65mm	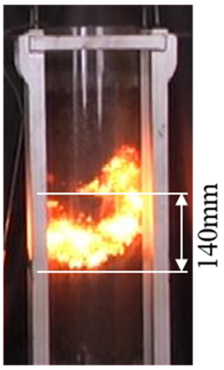 140mm	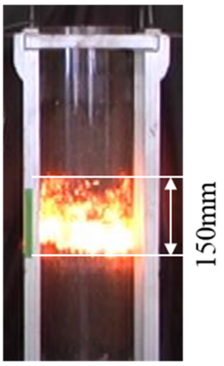 150mm	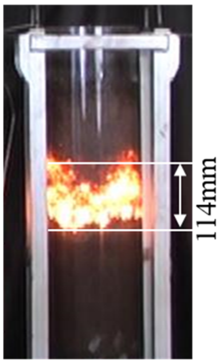 114mm
Shatter strength (%)	73.4	78.6	77.7	76.7
Sintering time (min)	17.8	17.6	17.6	17.8
Productivity (t/h·m²)	1.33	1.44	1.41	1.39

FIG 15 – Experimental results of liquid fuel injection tests.

But remaining liquid fuel in the sintered ore resulted in the smell of liquid fuel from sintered ore. Then, the amount of liquid fuel remaining in the sintered ore was measured with bunker A injection condition. At first, sintered ore was dipped in 80°C acetone and bunker A attached to sintered ore solved into the acetone. After that its solution was volatilised and amount of remaining bunker A was measured. As the result, it was confirmed that nine per cent of injected bunker A remained in sintered ore as unburnt fuel.

Oil remaining in sintered ore is not good for sintering operation. Oil in the sintered ore has possibility to be cause of fire hazard in the electrostatic dust collector and cool and reduce handling performance of equipment. Therefore, hot air injection was discussed for inhibition of oil remaining in sintered ore.

Bunker A and hot air (160°C, 200°C) injection was carried out through the pot tests. Figure 16 shows the experimental results. The remaining ratio of oil in the sintered ore was decreased by hot air injection. Especially, oil was not detected with 200°C hot air injection. Moreover, shatter strength increased. But sintering time increased and productivity did not increase.

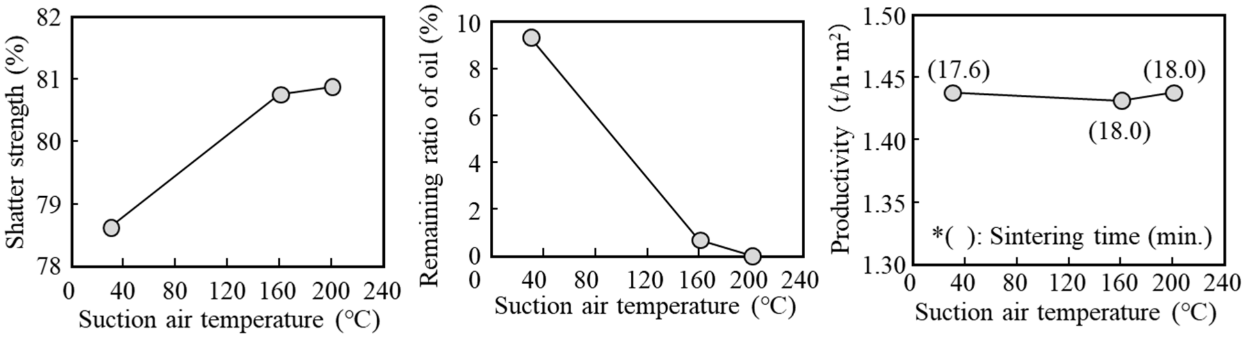

FIG 16 – Experimental results of pot tests with bunker A and hot air injection.

Next, a pot test with only hot air injection to isolate the effect of liquid fuel injection and hot air injection was conducted. Figure 17 shows experimental results. Hot air injection increased shatter strength of sintered ore. However only hot air injection decreased productivity. On the other hand, bunker A and hot air injection maintain productivity. It was considered that this difference of effect was liquid fuel injection effect.

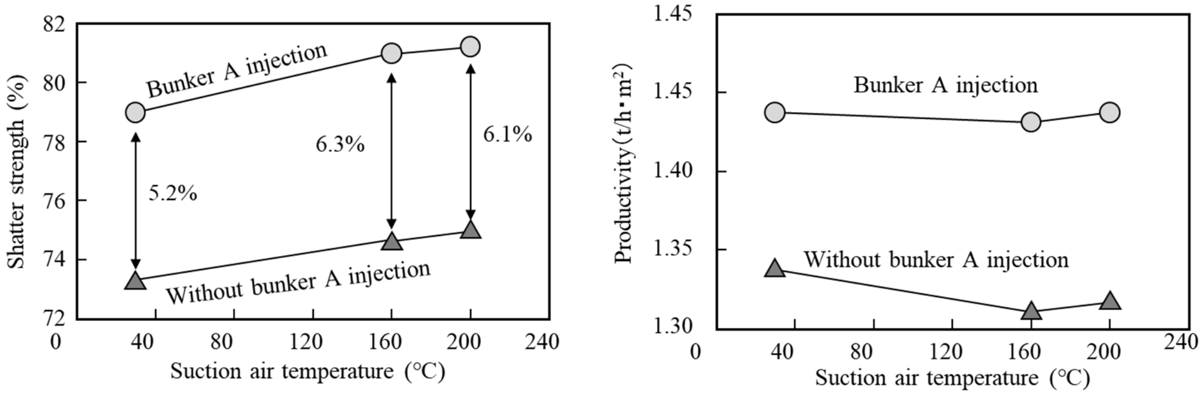

FIG 17 – Isolation of bunker A injection and hot air injection.

CONCLUSIONS

A fundamental study was carried out in the laboratory experiment to confirm the effect of the gaseous fuel injection technology on the temperature distribution, the sinter texture, pressure drop and the pore structure in the sinter cake. The effects of this technology were also quantified by performing operational tests at the commercial plant.

1. The temperature zone between 1200°C and 1400°C was expanded in upper direction without increasing the maximum temperature in the sintering bed with the gaseous fuel injection method, because the gaseous fuel was injected from top of sintering bed and burned before reaching the coke breeze combustion position with the temperature 650–750°C.
2. The increase in SFCA ratio and decrease in glassy silicate ratio were caused with the extension of holding time between 1200°C and 1400°C in the sintering bed with the gaseous fuel injection method. The increase in SFCA ratio and the decrease in the glassy silicate ratio were part of reason that the LNG injection technology improved sinter strength and reducibility.
3. The bonding agent ratio was decreased with the gaseous fuel injection method and the maximum temperature decreased in the sintering bed. As a result, the iron ore self-densification was depressed and the large number of micro pores under one µm remained in the unmelted ores with the gaseous fuel injection method. This also improved reducibility.
4. The gaseous fuel injection technology enabled production of high strength and high reducibility sinter while maintaining the same level of sinter production at commercial sinter plant. Moreover, it has achieved a decrease in the bonding agent consumption by 3.0 kg/t-s and reduction of CO_2 emissions by a maximum of approximately 60 000 t/a at Keihin No. 1 sinter plant.
5. LNG and oxygen injection method was discussed in the recent research. Increase of oxygen concentration increased the oxidation rate of coke and LNG, and extended the time holding temperature between 1200°C and 1400°C. As a result, strength and productivity improved more than LNG injection method alone.
6. The red-hot region was expanded and holding time over 1200°C was increased by misty liquid fuel injection just like gaseous fuel injection. It was considered that vapourising liquid fuel has similar combustion behaviour with gaseous fuel. But unvapourised liquid fuel was remaining in the sintered ore at normal temperature.
7. Liquid fuel and hot air injection can inhibit the liquid fuel remaining in the sintered ore and increase strength of sintered ore. But sintering time was expanded and productivity did not increase.

REFERENCES

Hanmyo, M, 2007. Development of Environmentally Conscious Steelmaking Technology and its Vision for the Future, *Bull Iron Steel Inst Jpn*, 12(7):456.

Hasatani, M, Kimura, J, Arai, N and Sato, A, 1986. *Fundamentals and applications of combustion*, Kyoritsu publishing house, Tokyo, :22.

Ishimitsu, A, Wakayama, S, Tomura, S and Sato, K, 1962. Use of Preheated Air for Sintering Iron Ores, *Tetsu-to-Hagané*, 48(11):1266–1267.

Iwami, Y, Yamamoto, T, Higuchi, T, Nushiro, K, Sato, M and Oyama, N, 2013. Effect of Oxygen Enrichment on Sintering with Combined Usage of Coke Breeze and Gaseous Fuel, *ISIJ Int*, 53(9):1633–1641.

Kajikawa, S, Yamamoto, R, Nakajima, R, Kishimoto, S and Fukushima, T, 1982. Phenomena in a Blast Furnace Operated at the Low Fuel Rate, *Tetsu-to-Hagané*, 68(15):2361–2368.

Kasai, E, Taketomi, H and Omori, Y, 1984. Study on Combustion Rate of Coke in Bed Packed with Alumina Spheres, *Bull Res Inst Miner Dressin Metal,* 40(6):61.

Kasama, S, Inazumi, T and Nakayasu, T, 1992. Development of an Evaluation Method for the Pore Structure of Sinter Cake and Its Application to the Permeability Analysis, *Tetsu-to-Hagané*, 78(7):1069–1076.

Kissin, D A and Litvinova, T I, 1960. Mechanism of Mineral Formation in Sintering Fluxed Sinter, *STAL IN ENGLISH*, (5):318–323.

Oyama, N, Iwami, Y, Yamamoto, T, Machida, S, Higuchi, T, Sato, H, Sato, M, Takeda, K, Watanabe, Y, Shimizu, M and Nishioka, K, 2011. Development of Secondary-fuel Injection Technology for Energy Reduction in the Iron Ore Sintering Process, *ISIJ Int*, 51(6):913–921.

Oyama, N, Nushiro, K, Igawa, K and Sorimachi, K, 1998. Investigation of Sintering Phenomena by Direct Observation using Hot Stage X-ray CT Scanner, *57th Ironmaking Conference Proceedings*, Toronto, pp 109–114.

Oyama, N, Nushiro, K, Konishi, Y, Igawa, K and Sorimachi, K, 1996. Influence of Matrix Strength and Pore Structure on Sinter Cake Strength, *Tetsu-to-Hagané*, 82(9):719–724.

Sasaki, M and Hida, Y, 1982. Consideration on the Properties of Sinter from the Point of Sintering Reaction, *Tetsu-to-Hagané*, 68(6):563–571.

Sato, T, Nakano, K, Kurosawa, S, Nozawa, M and Sawada, T, 1985. Main exhaust gas circulation system at Ohgishima No.1 Sintering Plant of Nippon Kokan KK, *Tetsu-to-Hagané*, 71(4):S38.

Taketomi, H, Kasai, E and Omori, Y, 1983. Combustion rate of coke in packed beds of alumina-coke mixture, *Tetsu-to-Hagané*, 69(12):S723.

Tashiro, K, Soma, H, Shibata, J, Konno, N and Hosotani, Y, 1980. Mechanism and Effects of Sintering Method with Previous Preheating Raw Mix, *Tetsu-to-Hagané*, 66(12):1603–1611.

Yasumoto, S, Fukudome, M, Yamada, T, Kodama, T, Tamei, A, Imai, Y, Haitani, M and Kitazawa, K, 1978. *Tetsu-to-Hagané*, 64(11):S483–S484.

Fundamental study for biomass char utilisation at sintering process in view of combustion property

M Matsumura[1], R Muroi[2] and T Takayama[3]

1. Visiting Professor, Tohoku University, Chiba 293–8511, Japan.
   Email: masaru.matsumura.d6@tohoku.ac.jp
2. Master's student, Tohoku University, Chiba 293–8511, Japan.
   Email: yuki.konno.r7@dc.tohoku.ac.jp
3. Researcher, Materials Characterization Research Laboratory, Advanced Technology Research Laboratories, Nippon Steel Corporation, Chiba 293–8511, Japan.
   Email: takayama.9fy.toru@jp.nipponsteel.com

ABSTRACT

The steel industry occupies 14 per cent of CO_2 emissions in Japan, and the sintering process is one of the major emitters. Since most of CO_2 released from the sintering process comes from coke fine combustion, replacement of coke fines with biomass char as bonding agent is a potential countermeasure.

In order to explore the effective use of biomass char, we chose char made from Palm Kernel Shell (PKS) as a sample.

First, the char's combustion behaviour was examined with varying the char's particle size by means of admixing the char in alumina ball packed bed placed in an electric furnace. As a result, the finer the PKS char the faster the burning rate and reaching a higher temperature compared to coke fine. In addition, it is also concluded that the optimum size of PKS char was larger than coke fines.

Next, the effect of different heat profiles on sinter structure was examined by sintering tablet made of chemical reagents. In this experiment, the chemical composition is designed based on sinter composition. By this sintering test, even at high temperature, rapid cooling is effective to make fine sinter matrix and fine pores, which has possibility for high sinter reducibility.

Based on these two experiments, using PKS char as a sinter fine source has the possibility to improve sinter reducibility.

INTRODUCTION

Most of the CO_2 emitted in the sintering process comes from coke fine used as a heat source to aid in formation of the bonding agent. It is effective to replace coke fines with low oxidised iron or biomass as a bonding agent. Regarding the former, Fujino, Murakami and Kasai (2017a) examined a method for promoting oxidation of ferrous (Fe^{2+}) oxide (Fujino, Murakami and Kasai*,* 2017b). They concluded that magnetite ore must be located separately from coke and limestone because the liquid phase suppresses magnetite oxidation at sintering. This suggestion was confirmed by sintering test (Matsumura *et al*, 2019).

Regarding the latter, Kawaguchi, Hara and Kasai (2013) examined utilisation of biomass by sinter pot test. They found biomass has effect of rapid sintering speed and increasing biomass particle size improves sinter product yield. However, biomass combustion rate is not clear and the relationship between heat profile and sinter mineral structure must be examined for sinter quality. In other words, due to the fast combustion rate of biomass char, it is expected to adversely impact sinter quality via the sinter heat profile.

In this study, small scale combustion tests were conducted to understand the combustion characteristics of the carbon materials, and then the impact of the maximum sintering temperature and cooling rate on the sintered structure were examined by sintering tablets in an electric resistance furnace.

EXPERIMENTAL

Characteristics of carbon materials

In order to evaluate the combustion characteristics of coke fines and Palm Kernel Shell (PKS) char as biomass char during the sintering process, it is extremely important to understand the basic carbon material characteristics in advance. Therefore, we carried out cross-sectional structure observation and combustion testing of the carbon materials. A description of the combustion test is given below.

PKS char and coke fine were used as the bonding agent. The particle size was sieved into six size fractions, 1.0–2.0, 2.0–2.8, 2.8–4.0, 4.0–5.0, 5.0–6.7, and 6.7–8 mm. PKS char was obtained by keeping PKS in an air atmosphere at 900°C for 1 hour for carbonisation.

Figure 1 shows the outline of experimental apparatus. The furnace temperature is controlled by electric heating up to a predetermined temperature. The reaction tube has a double wall structure, and its inner diameter is 37 mm. Air is supplied from the upper part, and combustion exhaust gas flows towards the lower part. The exhaust gas was turned back at the bottom of the double pipe, and the NOx, CO, and CO_2 concentrations were measured by an infrared continuous gas analyser. The packed bed was formed by placing a bed (about 20 mm depth) of 50 g of alumina balls on the grate, setting the sample layer (alumina balls 50 g + carbon material) on it, and laying 200 g (about 80 mm depth) of alumina balls as a preheating layer on it. In the experiment, the sample layer was heated to 900°C with N_2 gas at a flow rate of 21.5 NL/min, and then switched to air to start the combustion of the sample layer. Table 1 gives the condition of the combustion experiment.

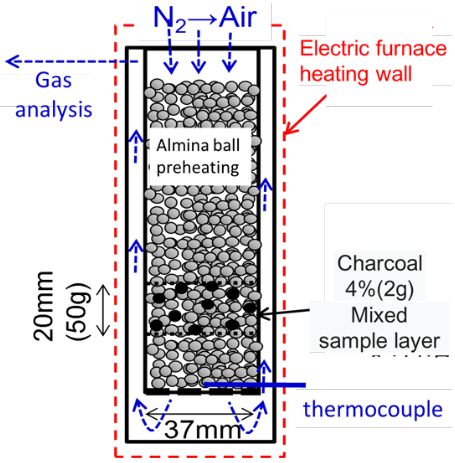

FIG 1 – Experimental apparatus for combustion test.

TABLE 1

Test condition and sample properties.

Sample	Preheating temperature (°C)	Material amount (g)	Fixed Carbon (%)	N_2 gas (%)
Coke	700	2.30	84.9	1.1
	900	2.30	84.9	1.1
PKS char	700	3.06	73.8	0.72
	900	3.06	73.8	0.72

Effect of different heat profiles on sinter structure

We expected a large difference in heat profiles (the maximum temperature, cooling rate etc) between coke fines and PKS char, resulting in a great difference in the sinter structure therefore, we observed the changes in the structure by optical reflected light microscope and electron microprobe analyser (EPMA), and analysed the pore structure with an image analyser.

Reagents were mixed in the ratio shown in Table 2 and mixed in a mortar. A 20 mmφ × 14 mmH cylindrical tablet sample, which had been prepared by compacting under pressure in a vertical direction, was then heated from room temperature to maximum temperature in a box-type electric resistance furnace. The temperature settings were six profiles in total with three types of maximum temperature and two types of cooling rate as shown in Figure 2.

The heated samples were analysed by an optical microscope, EPMA and XRD, and the pores were investigated by cross-sectional image analysis.

TABLE 2

Reagent mix ratio.

Reagent	**Mixing ratio (%)**
Fe_2O_3	81.5
CaO	10.0
SiO_2	5.0
Al_2O_3	1.5
MgO	1.0

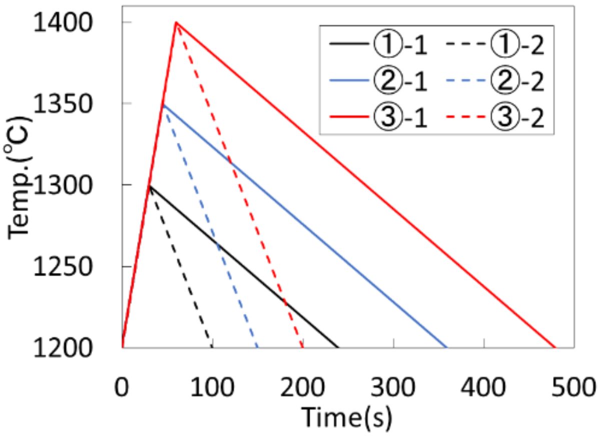

FIG 2 – Experimental heat profile.

RESULT AND DISCUSSION

Characteristics of carbon materials

Figure 3 shows cross-section images of each carbon material. The coke fines samples have large pores, and the PKS char has many small pores, which suggests high combustion rate.

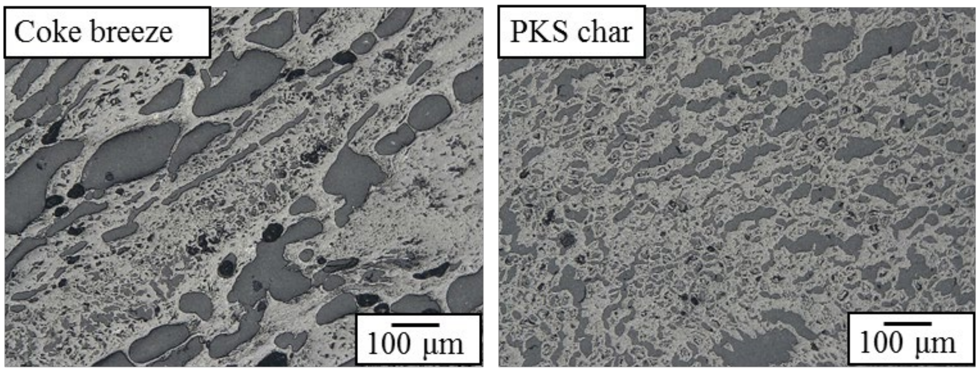

FIG 3 – Cross-section images of carbon materials.

The combustion heat profile of each carbon material is shown in Figure 4.

PKS char except diameter of 2.8–4 mm showed a sharp heat profile with a higher maximum temperature and higher cooling rate compared with coke fines.

Even coarse PKS (4–5 mm diameter) showed a high maximum temperature. On the other hand, it is suggested that optimum diameter for coke is 1–2 mm and 2–2.8 mm based on maximum temperature.

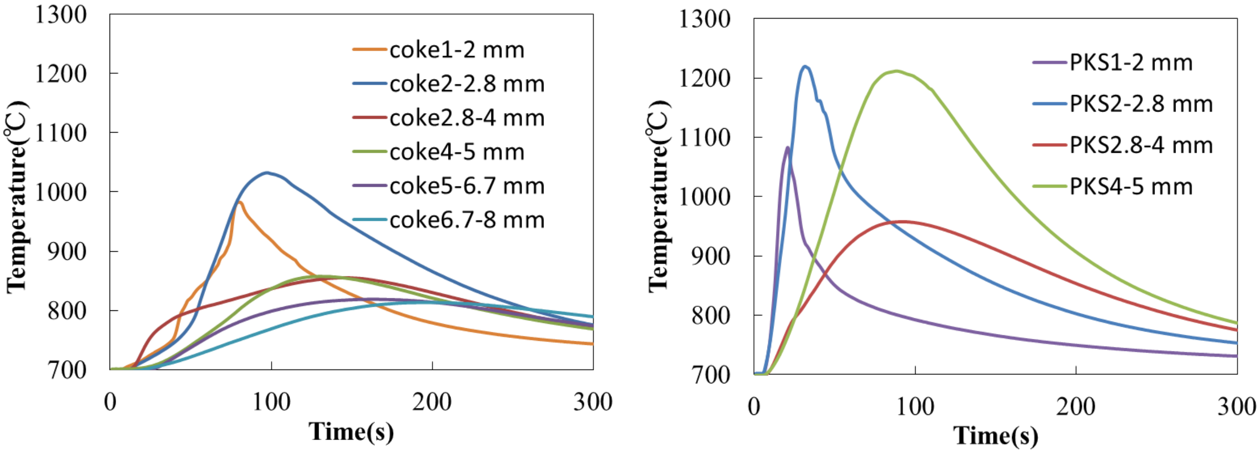

FIG 4 – Combustion heat profile.

Effect of different heat profiles on sinter structure

Figure 5 shows a cross-section observation photograph taken with an optical microscope. The pore size and the skeletal hematite (secondary hematite, white) particle size increase as the maximum temperature rises (1300 ⇒ 1400°C). It is considered that promoting melt formation with increasing temperature results in pores consolidation and crystal growth of skeletal hematite. On the other hand, focusing on the cooling rate, the higher cooling rate tended to have a finer structure. It is considered that when the cooling rate is high, assimilation is restricted due to short high temperature time. In other words, the sample is cooled before the pores and the matrix are consolidated by the movement of the melt and before the coarsening of the skeletal hematite occurs.

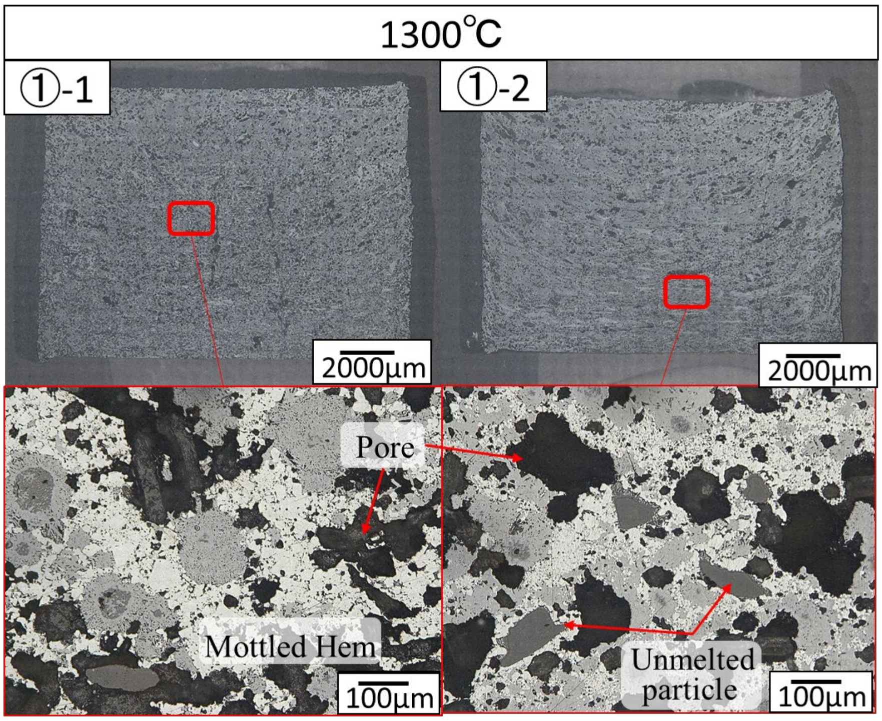

(slow cooling) (rapid cooling)

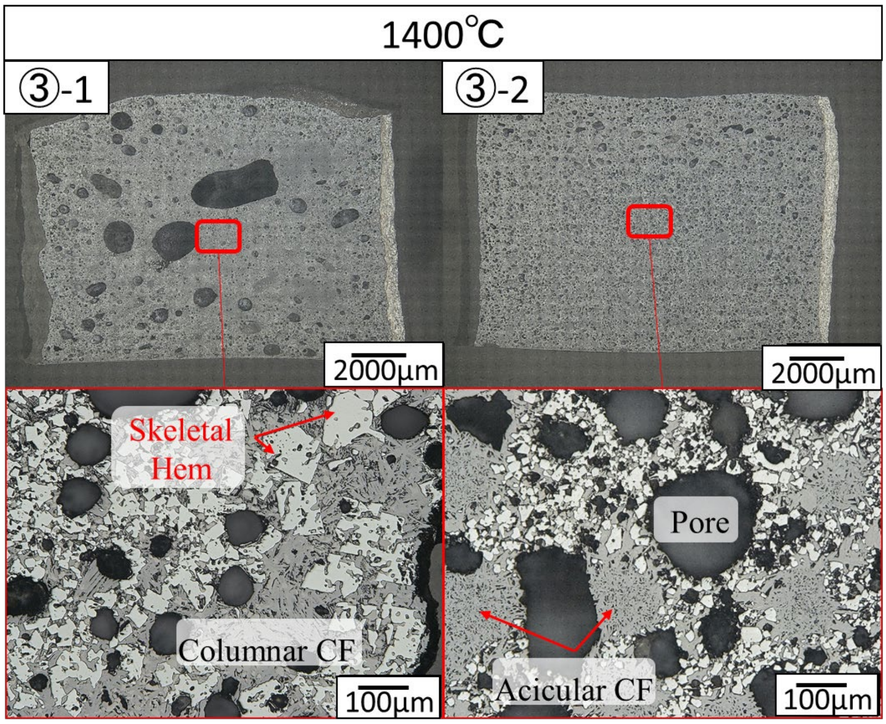

(slow cooling) (rapid cooling)

FIG 5 – Cross-section observation by optical microscope.

Figure 6 shows the pore circularity distribution. In the slow cooling case, the pore shape circularity increases, and the number of pores tends to decrease as the temperature rises (Figure 6). On the other hand, in case of rapid cooling at 1400°C, the pore circularity was high, but the number of pores was large.

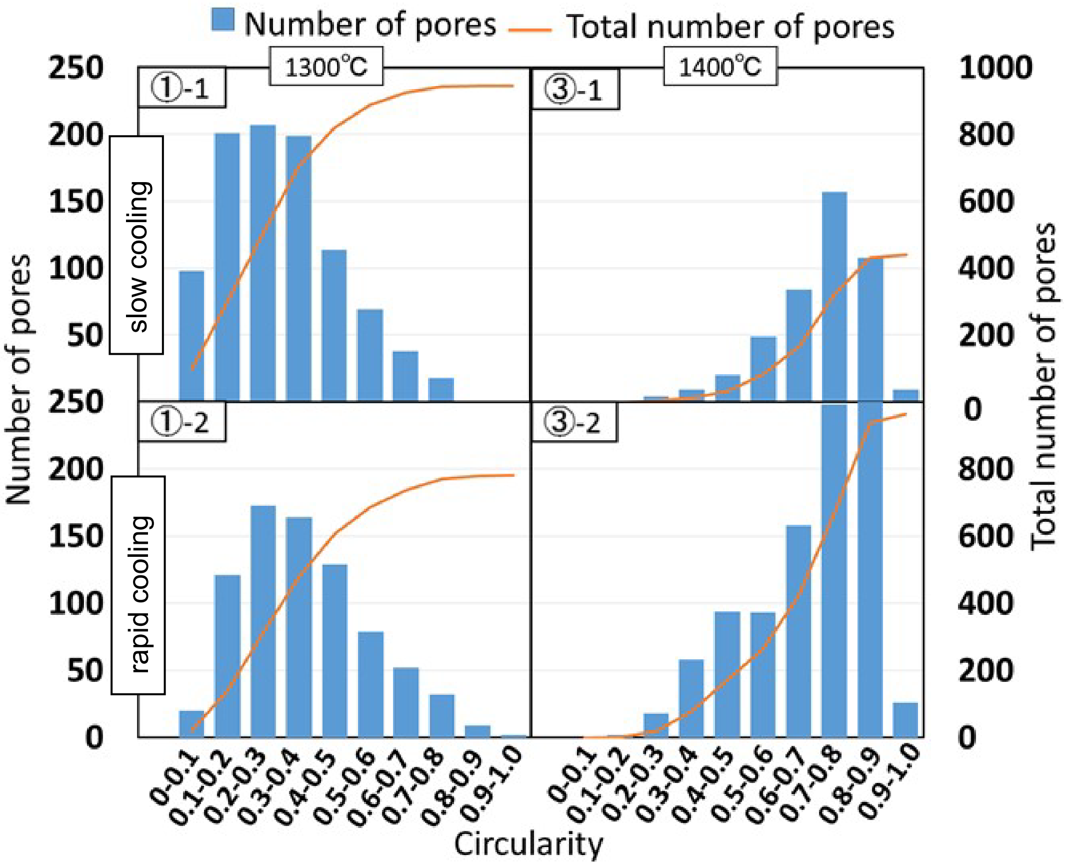

FIG 6 – Circularity distribution.

CONCLUSIONS

Characteristics of carbon materials

In order to clarify the characteristics of the carbon material, property observation and combustion tests were conducted. PKS char had a smaller pore size and a porous structure compared to coke fine. PKS char combustion showed a sharp heat profile, a higher maximum temperature and faster cooling compared with coke fine.

Effect of heat profiles on sinter structure

The higher the maximum temperature, the more the melt formation proceeded, and the consolidation of pores and calcium ferrite proceeded. On the other hand, as the cooling rate increased, the consolidation of pores was suppressed and generated finer matrix structure. It is considered that when the cooling rate is high, assimilation is restricted due to short high temperature time.

Pore structure analysis showed that the circularity increased, and the number of pores decreased with increasing temperature. The pore circularity was high, but the number of pores was the high in the case of rapid cooling at high temperature (1400°C). This suggested that rapid cooling remained fine but many pores in sintered tablet.

Based on both experiments (Characteristics of carbon materials; and Effect of heat profiles on sinter structure), PKS char combustion indicate high maximum temperature and rapid cooling profile. And at sintering such a heat profile, sintering matrix and pore structure of sintered tablet were fine, which has advantage for sinter reducibility.

REFERENCES

Fujino, K, Murakami, T and Kasai, E, 2017a. Promoting Effect on Oxidation Reaction of Iron-bearing Agglomeration Agent by Melt Formation, *Tetsu-to-Hagane*, 103:348–356 (The Iron and Steel Institute of Japan, Tokyo).

Fujino, K, Murakami, T and Kasai, E, 2017b. Oxidation Characteristics of Metallic Iron and Magnetite Concentrate with Coke in Sintering Bed, *Tetsu-to-Hagane,* 103:365–371 (The Iron and Steel Institute of Japan, Tokyo).

Matsumura, M, Takayama, T, Hara, K, Yamaguchi, Y, Ishiyama, O, Higuchi, K, Nomura, S, Murakami, T, Hayashi, M and Ohno, K, 2019. Improvement of Sinter Strength and Reducibility through Promotion of Magnetite Ore Oxidation by Use of Separate Granulating Method, *ISIJ International,* 59:768–777 (The Iron and Steel Institute of Japan, Tokyo).

Kawaguchi, T, Hara, M and Kasai, E, 2013. Utilization of Biomass for Iron Ore Sintering, *ISIJ International*, 53:1599–1606 (The Iron and Steel Institute of Japan, Tokyo).

Acceleration of the oxidation reaction of iron-bearing materials by using biomass char in the sintering bed

T Murakami[1], Y Konno[2], D Maruoka[3] and E Kasai[4]

1. Associate Professor, Graduate School of Environmental Studies, Tohoku University, Sendai, Miyagi 980–8579, Japan. Email: taichi@material.tohoku.ac.jp
2. Graduate Student, Graduate School of Environmental Studies, Tohoku University, Sendai, Miyagi 980–8579, Japan. Email: yuki.konno.r7@dc.tohoku.ac.jp
3. Assistant Professor, Graduate School of Environmental Studies, Tohoku University, Sendai, Miyagi 980–8579, Japan. Email: daisuke@material.tohoku.ac.jp
4. Professor, Graduate School of Environmental Studies, Tohoku University, Sendai, Miyagi 980–8579, Japan. Email: kasai@material.tohoku.ac.jp

ABSTRACT

The iron ore sintering process produces approximately three per cent of carbon dioxide emission in Japan because a large amount of coke breeze is used as the main agglomeration agent. Therefore, its suppression has been required. A promising method is to replace the coke breeze with biomass char and iron-bearing materials. In this study, the effect of the utilisation of metallic iron with coke or palm kernel shell char (PKS char) as an agglomeration agent on its oxidation behaviour was examined by a series of experiments using a sintering simulator. The use of PKS char leads to a larger decrease in the pressure drop difference of the sintering bed compared to the case using coke. Furthermore, the oxidation rate of metallic iron was larger in the case using PKS char together than that using coke. It was considered that the oxidation of metallic iron was promoted because the bed-temperature increased at a faster rate and achieved a higher temperature.

INTRODUCTION

Iron ore sinter, which is produced using iron ore, limestone, coke breeze provides the main burden for the blast furnace and reducing the amount of coke breeze in sintering is required to reduce the amount of carbon dioxide emissions. Many investigations have been reported on this issue such as the utilisation of biomass char and iron-bearing materials to replace a part of coke breeze. Lowering the coke consumption in the sintering process is also in demand from the viewpoint of energy consumption. Millscale (Kaimoto *et al*, 2017), steel can chips (Fujimoto, Inazumi and Okuno, 1994) and partially reduced iron (Nakano *et al*, 1998) were focused on as an alternative agglomeration agent of coke. However, studies on the utilisation of partially reduced iron ore and steel can chips resulted in a considerably decreased productivity due to the significant decrease in the permeability of the sintering bed. This decrease in the bed permeability occurred mainly at the bottom of the sintering bed.

Other workers have demonstrated that an increase in the replaced ratio of coke to biomass char results in an increase in the productivity of sinter because of an increase in the permeability of sinter bed which leads to a reduction in the sintering time (Lovel, Vining and Del'Amico, 2007; Zandi, Martinez-Pacheco and Fray, 2010). However, a decrease in the yield of sinter was also reported (Kawaguchi and Hara, 2013) and may also lead to increasing return fines generation. A possible reason may be that the density of biomass char is lower than that of coke breeze and it therefore leads to an increase in the porosity of the sinter.

In this study, the sintering process using a combination of iron-bearing material and carbonaceous materials such as biomass char and coke breeze was focused on. The effect of the replaced ratio of carbonaceous materials to metallic iron on the oxidation of iron-bearing materials was examined to understand the effect of using metallic iron as the agglomeration agent.

EXPERIMENTAL

Metallic iron (purity 99.9 per cent), coke breeze (86.6 mass% fixed carbon (FC), 12.2 mass% Ash, 1.2 mass% volatile matter (VM), and palm kernel shell char (PKS char), 60.5 mass% FC, 32.8 mass% Ash, 6.7 mass% VM), of which the particle size was 1.0–2.0 mm, were used in this study. Model granules called alumina cored pellets (ACP) were prepared (Figure 1), which consisted of alumina balls (2 mmϕ) as nuclei, and a fine mixture of hematite and calcium carbonate reagents as adhering layers (0.1–0.2 μm in thickness) (Fujino, Murakami and Kasai, 2013). Table 1 shows the composition of ACP and mixing ratio in the sample bed. The CaO content in the ACPs was controlled from 20 mass% to 30 mass% in order that the CaO content in sinter sample was 15 mass%. The replaced ratio was defined as the ratio of metallic iron to agglomeration agent based on the heat equivalent.

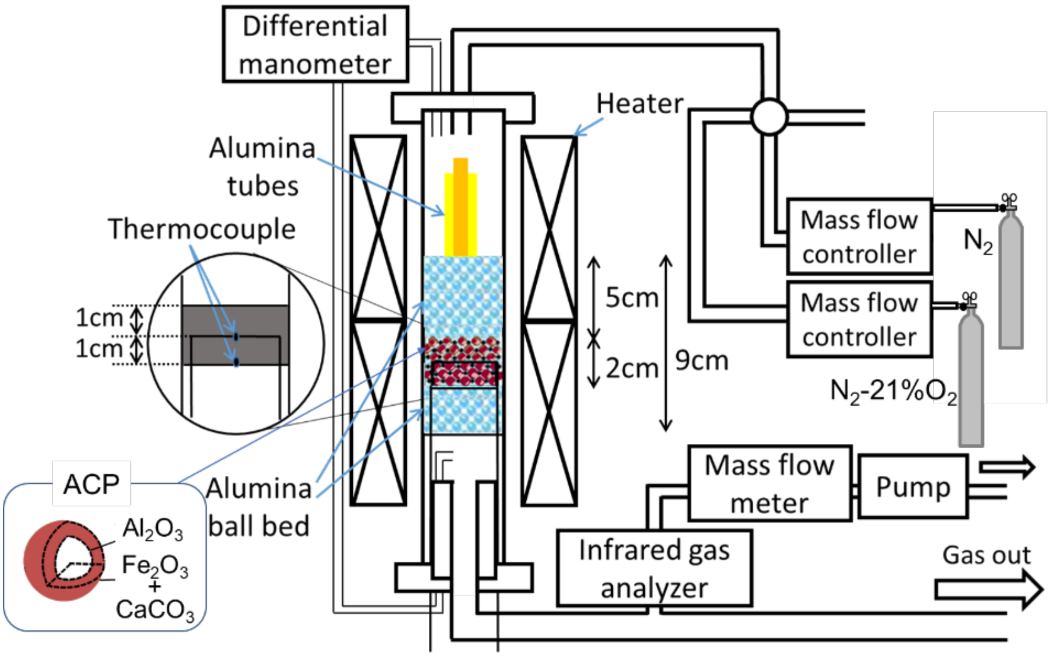

FIG 1 – Schematic diagram of the sintering simulator and cross-section of an alumina cored pellet (ACP).

TABLE 1

Composition of ACP and mixing ratio in the sample bed.

Sample	Ratio of CaO : Fe_2O_3 in ACP	ACP (g)	Carbonaceous materials (g)		Metallic iron (g)
Coke-Fe25	20 : 80	29	Coke	1.00	1.4
Coke-Fe50	25 : 75	26	Coke	0.75	2.9
Coke-Fe75	30 : 70	23	Coke	0.40	4.4
PKS-Fe25	20 : 80	29	PKS	1.10	1.4
PKS-Fe50	25 : 75	26	PKS	0.83	2.9
PKS-Fe75	30 : 70	23	PKS	0.50	4.4

Sintering experiments were carried out using a differential type sintering simulator (Fujino, Murakami and Kasai, 2013) as shown in Figure 1. An alumina tube with a 35 mm inside diameter was used as the reaction tube. The height of the sample bed was set at 20 mm. Packed beds of alumina balls (2 mmϕ) were placed at 50 mm above and 20 mm below the sample bed. After packing the sample and alumina balls into the reaction tube, they were heated up to the specified temperature under a N_2 stream to prevent reaction of the agglomeration agent with oxygen. When the bed-temperature reached 900°C, the gas flow rate was controlled at 0.45 Nm/s. After the gas flow became steady, the gas was changed to N_2–21 per cent O_2 gas mixture which simulated dry air. The oxidation reaction of the agglomeration agents mixed in the sample generated heat and the generated the temperature profile in the bed. The bed-temperature at the centre of the sample bed, the border-temperature between the sample bed and the lower alumina ball layer (lower border), the concentration of CO, CO_2 and O_2 of outlet gas, and the pressure drop of the bed were all measured with time. Using the change in the gas concentration, the reaction ratio of metallic iron was calculated.

RESULTS AND DISCUSSION

The temperature measured at the centre of the sample bed using PKS char as the agglomeration agent was approximately 100ºC higher than that measured using coke breeze (Konno *et al*, 2021). The effect of the replaced ratio of metallic iron on the maximum temperature difference between using PKS char and coke breeze was very small. The average heating rate of the sample bed was calculated from the preheating and the maximum temperature measured. The effect of the replaced ratio of metallic iron on the heating rate is shown in Figure 2. The average heating rate using PKS char decreases with increasing replaced ratio of metallic iron. This value is higher than that using coke breeze, and this difference decreases with increasing the replaced ratio. This difference between carbonaceous materials is caused by the difference of combustion rate (Kawaguchi and Hara, 2013). There was no significant difference of the temperature at the lower border between these two carbonaceous materials. The pressure drop difference before and after sintering using PKS was approximately twice as large as that using coke breeze (Konno *et al*, 2021). These are the average values of duplicate experiments conducted at each condition and the data indicates that the permeability of the sinter bed was significantly improved when using PKS char. The reason is that the apparent density of PKS char is lower than that of coke breeze (Zhou *et al*, 2020), leading to a higher porosity of sinter.

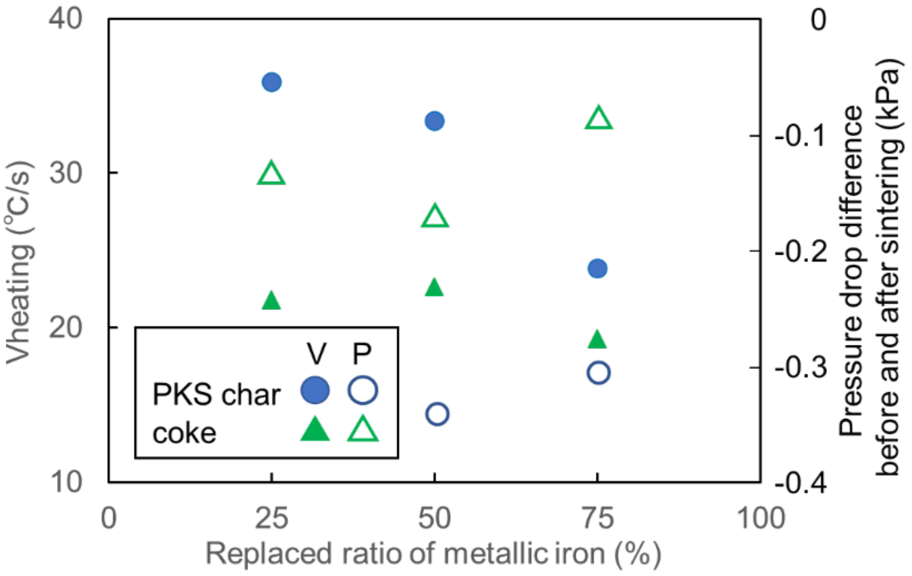

FIG 2 – Effect of replaced ratio of metallic iron on the average heating rate and pressure drop difference before and after sintering. Each data point represents an average value from duplicate experiments.

To compare the reaction behaviour of metallic iron with coke breeze and PKS char, the reaction ratios of metallic iron during the heating and cooling stages are shown in Figure 3. Coke-Fe25 means that the replaced ratio of metallic iron is 25 per cent and the carbonaceous material is coke breeze. At all conditions, the total reaction ratio of metallic iron does not reach 100 per cent indicating that the oxidation of metallic iron to Fe^{3+} does not complete and Fe^{2+} remained in the sample (Fujino, Murakami and Kasai, 2013). The total reaction ratio using coke breeze increases during heating with increasing replaced ratio of metallic iron. On the other hand, the reaction ratio during cooling decreases. It seems that progress of the oxidation reaction decreases the driving force for further oxidation. The reaction ratio using PKS char during heating decreases with increasing the replaced ratio of metallic iron because the amount of metallic iron increases. A trend observed however is that both the total reaction ratio using PKS char and the reaction ratio during heating are always higher than when coke breeze was used (except for experiment PKS-Fe75). The reason is that the temperature of the sample bed using PKS char increased faster and higher than that using coke breeze as shown in Figure 1. Accordingly, an acceleration of the oxidation reaction of metallic iron can be possible when using PKS char over a wider range of replaced ratio of metallic iron.

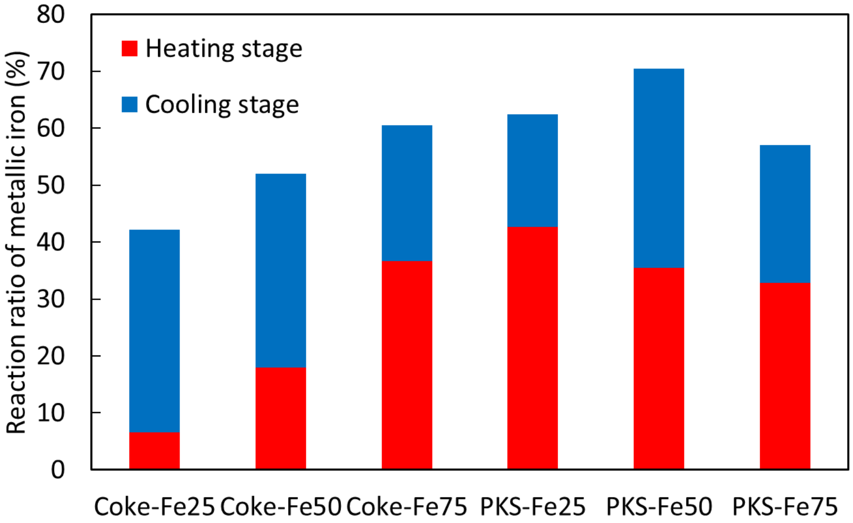

FIG 3 – Reaction ratio of metallic iron with different amounts of coke breeze and PKS char during heating and cooling of sintering.

CONCLUSIONS

The pressure drop difference before and after sintering using PKS char with metallic iron was approximately twice as large as that measured using coke breeze because the apparent density of PKS char is lower than that of coke breeze. The average heating rate of the sinter bed using PKS char with metallic iron is larger than that using coke breeze because the combustion rate of biomass char is larger than that of coke breeze. The reaction ratio of metallic iron with PKS char is larger than that with coke breeze because the heating rate of the sinter bed is large. The results mean that the utilisation of biomass char accelerates the oxidation of metallic iron in the sinter bed.

REFERENCES

Fujimoto, M, Inazumi, T and Okuno, Y, 1994. Investigation of sintering process using steel-can chip, *CAMP-ISIJ, Materials and Processes*, 7(1):143.

Fujino, K, Murakami, T and Kasai, E, 2013. Effect of Utilization of Metallic Fe Particles as an Agglomeration Agent on the Permeability of Sintering Bed, *ISIJ International*, 53:1617–1624.

Kaimoto, K, Shiozaki, R, Matsuyama, K, Sassa, Y and Chiba, H, 2017. Improving of Productivity on Sinter Operation by Preparatory Granulation Method in High Blending Ratio of Mill Scale, *Tetsu-to-Hagané*, 103:272–279.

Kawaguchi, T and Hara, M, 2013. Utilization of Biomass for Iron Ore sintering, *ISIJ International*, 53:1599–1606.

Konno, Y, Maruoka, D, Murakami, T and Kasai, E, 2021. Acceleration of Oxidation Reaction of Iron-bearing Materials Co-existed with Carbonaceous Materials in Iron Ore Sintering Bed, *Tetsu-to-Hagané*, 107:439–446.

Lovel, R, Vining, K and Del'Amico, M, 2007. Iron Ore Sintering with Charcoal, *Mineral Processing and Extractive Metallurgy*, 116:85–92.

Nakano, M, Yamakawa, Y, Hayakawa, N and Nagabuchi, M, 1998. Effects of Metallic Iron Bearing Resources on Iron Ore Sintering, *ISIJ International*, 38:16–22.

Zandi, M, Martinez-Pacheco, M and Fray, T A T, 2010. Biomass for iron ore sintering, *Minerals Engineering*, 23:1139–1145.

Zhou, M, Zhou, H, Cheng, Y and Xing, Y, 2020. Investigation on the combustion behaviors of coke and biomass char in quasi-granule with CuO-CeO$_2$ catalysts in iron ore sintering, *Journal of the Energy Institute*, 93:1934–1941.

Exploration and geology

Exploration advances – MinEx CRC's mission

A C Bailey[1] and D Giles[2]

1. Chief Executive Officer, MinEx CRC, Perth WA 6000. Email: andrew.bailey@minexcrc.com.au
2. Chief Scientific Officer, MinEx CRC, Perth WA 6000. Email: david.giles@unisa.edu.au

ABSTRACT

In the first 20 years of the 21st century, just over 20 per cent of Australian mineral exploration expenditure was dedicated to iron ore, totalling >A$8 billion and >30 million metres of drilling (Australian Bureau of Statistics, 2021). Improvements in the cost, efficiency, safety, reliability and data quality of drilling have the potential to deliver significant productivity improvements, increasing the probability of discovery and reducing the time from discovery to mining. Currently in its third year of research, Mineral Exploration Cooperative Research Centre (MinEx CRC) is focused on a new set of exploration tools and new ways to deploy those tools which recognise the fundamental importance of collecting quantity and quality data from the subsurface, to enable exploration success for all minerals, including iron ore.

MinEx CRC is focused on developing more productive, safer and environmentally friendly drilling methods to discover and drill-out deposits. This includes pioneering work on Coil Tube (CT) drilling technology and innovations in Diamond and Reverse Circulation (RC) drilling techniques aimed at improved drilling optimisation and automation. In parallel, MinEx is developing new technologies for collecting data whilst drilling. This is being undertaken in four separate industry-led projects utilising geophysical, seismic, downhole analytical and 3-dimensional (3D) modelling improvements. A National Drilling Initiative (NDI) is also underway, with two drilling programs completed in 2020. The NDI is a world-first collaboration of Geological Surveys, researchers and industry, which undertakes drilling in under-explored areas of potential mineral wealth in Australia and provides a test-bed for new mineral exploration technologies.

INTRODUCTION

The Perth-based MinEx CRC, with a 10-year program (2018–2028) and A$220M in resources, is the world's largest mineral exploration research centre. The MinEx CRC mission is to address the threat of declining mineral inventory, acknowledging that current exploration methods would be unable to discover and define the quantity of new iron orebodies needed to sustain the Pilbara's iron ore output (Knight, 2015).

Currently in its third year of research, MinEx CRC is developing a novel set of drilling and sensing tools to measure the subsurface, explore new ways to deploy those tools and seek new methods to assess the resultant data and inform mineral exploration decisions. In combination, these techniques and methods help kick off a virtuous cycle of exploration activity leading to discovery. MinEx CRC currently supports approximately 100 researchers across universities, CSIRO, Geoscience Australia, state geological survey organisations and our industry partners in both iron ore and other mineral commodities. This effort is augmented by 28 PhD and Masters' students, with an aim to graduate 50 higher degree by research students by 2027.

The Australian government's Cooperative Research Centres (CRC) Program has been supporting research for 30 years. The CRC Program provides government grant funding to support industry-led collaborative research partnerships, with matching contributions from partners. Mineral exploration research has been the subject of previous CRC's, including the Australian Geodynamics CRC, Predictive Mineral Discovery CRC, the CRC for Landscape Evolution and Mineral Exploration and Deep Exploration Technologies CRC (DET CRC).

MinEx CRC builds on the legacy of its predecessors by combining a mineral systems approach to exploration geoscience – acknowledging the importance of scale-appropriate data collection and decision-making, with the development of technologies that are geared to the challenge of exploration and mine-development. These technologies include more efficient drilling (faster, cheaper, safer, low energy and water consumption, environmentally friendly, high sample quality), in-field measurement of critical rock properties (chemistry, mineralogy, petrophysics, texture) and rapid integration of data into 3D geological models. In addition, MinEx CRC is trialling new exploration technologies and testing geology and mineral systems concepts through a multiyear, continent-scale drilling program, referred to as the National Drilling Initiative (NDI).

RESEARCH SCOPE

MinEx CRC research is organised into three concurrent programs: Drilling technologies, Data from Drilling and the NDI.

PROGRAM 1 – DRILLING TECHNOLOGIES

MinEx CRC is undertaking two projects to develop innovative drilling technology. We are extending the capability, and potential market reach, of Coil Tube (CT) drilling so that it can drill deeper, is steerable and delivers the highest quality sampling. CT technology promises drilling at 1/5th the cost of conventional diamond drilling and thus has the potential to drive a revolution in mineral exploration (Soe *et al,* 2018). Despite the potential for CT drilling, we recognise that many drilling tasks will still be best suited to existing techniques and we are directing significant resources to develop technologies for optimising performance and increasing productivity of Diamond and RC drilling, which dominate iron ore exploration and definition drilling expenditure.

Project 1 – drilling optimisation and automation

Industry partners: BHP, South 32, Geotec Boyles, Imdex, Mackay, Sandvik

Conventional rotary and percussive drilling, including Diamond and RC drilling, are used extensively in iron ore exploration, with 14 per cent of Australian exploration expenditure being on iron ore, totalling $103M, in the March quarter of 2021 (ABS, 2021). Performance continues to rely heavily on the skill, experience and intuition of individual drillers. The collection of key drilling parameters is still not standardised or routine, the extent to which those parameters reflect drill, rock and fluid interactions in the hole is not well-understood, and there is little concerted effort to utilise drilling measurements to optimise performance.

In this project, we are improving the productivity of diamond and RC drilling, aiming for a 50 per cent improvement by 2028, and ultimately paving the way for automated drilling by: (1) gaining understanding in the key drill, rock and fluid interactions that control drilling efficiency; (2) collecting multiparameter drilling and drilling fluid data from the surface and downhole; (3) analysing those data in real-time; and (4) developing algorithms to optimise the drilling operation and predict drilling problems. Initially, drilling optimisation is being conducted under the supervision of drillers to codify and standardise driller performance, but longer-term research is developing optimisation algorithms as an important component of fully automated drilling control systems.

Our research commenced with controlled laboratory experiments, leveraging unique drilling research infrastructure at Curtin University, Perth. This includes an instrumented flow loop, in which to test drilling fluid properties and fluid/rock interactions, and an instrumented drilling simulator with the capacity to accommodate bottom-hole assemblies from a range of drilling methods (eg positive displacement motors, turbines, air and water hammers, percussion bits, diamond drill bits). In collaboration with drillers and drilling operators, the project has undertaken field experiments in the Pilbara. Drilling rigs undertaking routine iron ore exploration drilling have been instrumented with sensors and dedicated monitoring systems based on the results of laboratory experiments. The field experiments have gathered significant commodity-specific data and are being used to validate the laboratory research, test the implementation and reliability of the sensors and software and trial optimisation procedures.

Project 2 – coil tube drilling for definition of mineral deposits

Industry partners: Anglo American, Epiroc, BHP, LKAB Wassara, Minerals Research Institute of Western Australia (MRIWA), South 32

The DET CRC (2010–2018) built and tested a prototype CT drill rig, the RoXplorer®, delivering an initial platform for low-cost, rapid, safe and environmentally-friendly drilling, meeting key technical challenges of: (1) coil durability; (2) drilling hard rocks with low weight-on-bit; and (3) sample fidelity (Figure 1). The RoXplorer® represented a significant technical breakthrough and the emergence of new, potentially disruptive technology in the hard rock mineral drilling market. The RoXplorer® was specifically designed for greenfields exploration applications at depths of <500 m, and at the closure of DET CRC in 2018, initial field trials and early commercialisation discussions had taken place.

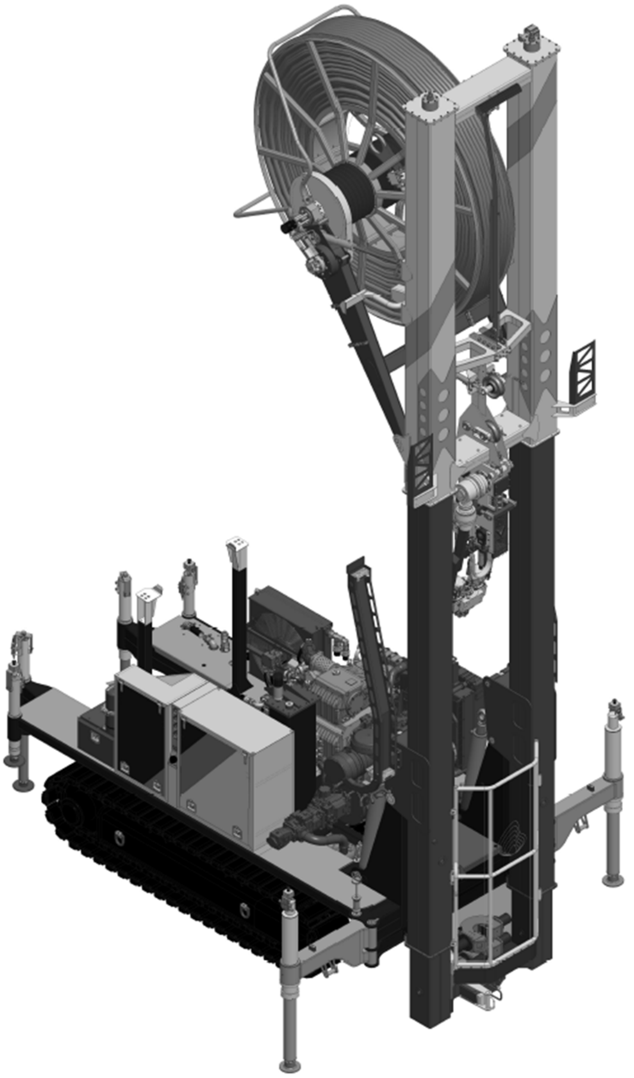

FIG 1 – RoXplorer® Coil Tube drill rig design, with 500 m coil.

The CT Rig has been further enhanced since the commencement of MinEx CRC in 2018, under the sole control of MinEx CRC. Integrated projects have seen the development of a second CT rig capable of drilling to 1000 m depth, and work is ongoing on an accurate steering system and the delivery of samples rivalling the quality of diamond drilling. To this end, an integrated Hydraulic Processing System (HPS) has been designed and constructed, and the HPS and 500 m CT rig are drilling in South Australia on behalf of the Geological Survey of South Australia. Learnings are also being applied from technology being developed using underground coil tube drilling taking place in iron ore mining in Sweden (Moore, 2018).

The ultimate CT drill rig will drill multiple deviated holes in hard rock environments, including for iron ore, of up to 1000 m reach from a single pad, landing within 10 m of target at end-of-hole, surveyed within 1 m and with sample quality comparable to diamond drilling but at a fraction of the cost. The research is delivering this ambitious target via a series of connected modules: (1) technologies for ensuring sample fidelity, including tracing algorithms; (2) improved drilling fluids to inhibit fluid loss in the hole and facilitate sample transport; (3) real-time surveying of bottom hole position with communications to surface for steering; (4) hole steering with surface control; (5) technologies (including downhole motors, bits and spot coring) to enable deviated and horizontal drill holes up to 1000 m; and (6) a rig platform for low-footprint CT drilling to 1000 m. New technologies have been developed in the laboratory (Chen *et al*, 2020) and are continuously rolled out to be trialled in the field during National Drilling Initiative (NDI) drilling campaigns.

PROGRAM 2 – DATA FROM DRILLING

This program is developing technologies for capturing geochemical, petrophysical and seismic data during drilling and within the drilling workflow in four separate projects.

Project 3 – real-time downhole assay

Industry partners: Anglo American, South32, Imdex, Sandvik

Numerous downhole tools are being researched and utilised for downhole assays. For iron ore, the near real-time assay with downhole assay tool (FastGrade 100) is becoming more widely used, but is restricted to larger-diameter drill holes, and is applied in iron ore blasthole environments in Australia (Chi *et al,* 2017). The MinEx real-time downhole project is developing a Laser Induced Breakdown Spectroscopy (LIBS) tool for measuring downhole geochemistry while the hole is being drilled, and in a narrow-diameter (~65 mm) setting (Figure 2).

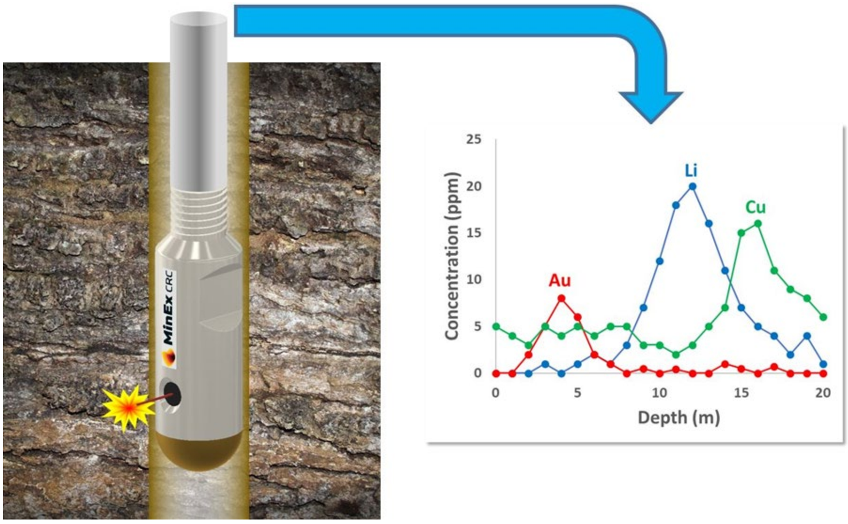

FIG 2 – Conceptual Laser Induced Breakdown Spectroscopy (LIBS) analysis tool.

Despite the potential benefits of downhole assay (real-time data, reliable depth registration, no reliance on representative sample return to surface) and a number of previous attempts to build a downhole assay tool, there is no existing technology which can satisfy the needs of deep slimline exploration drilling. The desirable features of a downhole assay tool for exploration is that it; would fit into a narrow gauge exploration borehole; would operate reliably in a wet, hot, high pressure, vibrating environment; is safe and can be operated by the driller; is environmentally friendly; would take measurements whilst moving past the target rocks; provide data at sub ppm level for a wide selection of elements, and; can be easily calibrated to its environment of operation.

Competing and emerging technologies have been reviewed, and it has been concluded that LIBS analysers are robust, safe, relatively easy to use and amenable to miniaturisation. To date the team has built two laser-labs and a prototype tool, which has been proved to be capable of undertaking LIBS analysis on moving and wet surfaces with extremely encouraging results.

Project 4 – petrophysical logging while drilling

Industry partners: South32, Imdex, MRIWA

This project has two linked components: (1) development of new sensors for real-time logging of multiple petrophysical properties while drilling; and (2) rapid, automated imaging of the volume around drill holes, such as to inform steering toward targets during drilling (geo-steering). Routine collection of downhole petrophysical data is the missing link between drilling and geophysics.

Broad acreage geophysical data sets (eg magnetics, gravity, electromagnetic and increasingly seismic) collected at the surface or from the air are primary exploration targeting tools. Such data sets are useful because the surface measurement provides an indication of the subsurface geology and because they can be collected in a systematic fashion to produce a (pseudo) continuous 2D coverage – effectively a map of variations in the chosen parameter. These maps are amenable to geological interpretation and can be used to generate 3D models and inversions which seek to produce plausible subsurface distributions of petrophysical properties with which to target drilling (Le *et al*, 2019). The drawback of this approach is that the geophysical models are non-unique and generally measure proxies for mineralisation rather than mineralisation itself. In addition, a poor understanding of rock properties and failure to measure them during drilling, results in many drill holes for which the target geophysical anomaly is never adequately explained. This situation can be dramatically improved if the collection of multiparameter downhole petrophysical data becomes a routine part of drilling.

To date, this project has researched and built a sensor and prototype deployment platform compatible with slimline CT drilling, producing a tool small enough to be adapted to a range of other drilling techniques and for numerous commodities.

Project 5 – seismic in the drilling workflow

Industry partners: Anglo American, BHP, HiSeis, MRIWA

This project combines the relatively new concept of low-cost fibre optic cables deployed as seismic sensors in drill holes with low-cost seismic sources in order to develop a seismically instrumented drill site. Borehole seismic data offers significant benefits. Sources and receivers can be located below heterogeneous cover rocks providing a clearer picture of the deep search space. Reliable velocity profiles, which are critical to depth correction, can be obtained and compared to geological and petrophysical logs. They provide acquisition geometries which enable imaging of complex and steeply dipping structures. To date borehole seismic has been little used in the minerals industry because it is technically demanding, expensive and access to drill holes subsequent to drilling is limited.

This project has now researched and deployed an optimal fibre-optic cable configuration in various scenarios, including over Pilbara iron ore terrains, to test Distributed Acoustic Sensing (DAS) methods for borehole hard rocks and the integration with surface seismic techniques (Urosevic *et al*, 2019) (Figure 3).

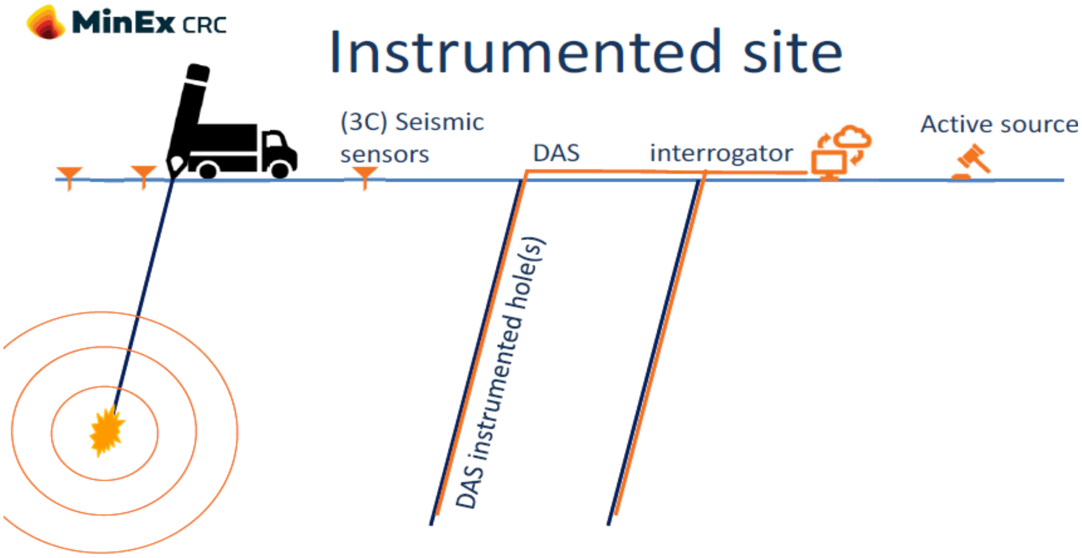

FIG 3 – Distributed Acoustic Sensing (DAS) trials for surface and borehole applications in hard rock environments are being trialled.

The new generation of DAS seismic receivers holds great promise in the borehole because they are cheap, easy-to-deploy and can deliver data of comparable or better quality than conventional alternatives. The outcomes of this work have already: (1) shown what the optimal acquisition design and methodology in order to reduce the footprint and time of seismic acquisition and maximise the value of the data is; and (2) developed processing and imaging software to allow full waveform analysis and visualisation of the resultant data. In addition to the identification of seismic reflectors, the latter provides a 3D image of P-wave velocity, shear modulus and density around the drill hole.

Project 6 – automated 3D modelling

Industry partners: Anglo American, BHP, Micromine, GSWA

Even with closely spaced drilling, it remains a challenge to extrapolate geology in the spaces between drill holes. Exploration companies seek methods by which data collected in drill holes can be integrated with regional geological and geophysical data sets in order to model the entire 3D search space. Current techniques rely on subjective, end-user guided forward modelling or inversions based on limited geophysical parameters. These techniques are time-intensive, do not allow rapid updating and incorporation of new data and fill the 3D volume with inferred geology based on what the model defines it to be, rather than what it might be.

A new approach is thus being researched and implemented to enable probabilistic outputs and objective methodologies, is less time-intensive and can be readily updated as new data comes to hand. In addition to identifying specific targets, probabilistic modelling prioritises volumes for drilling based on the value of acquired data to understanding the entire search space. It therefore enables successive reduction of search space toward volumes with the most chance of success.

This project is developing automated 3D geological mapping software to reduce the time taken from receiving drilling data to constructing a probabilistic and objective geological model from weeks to hours at the mine-scale and to a week at the regional-scale. It is developing techniques for the rapid integration and first-pass interpretation of geological and geophysical drill hole data (Giraud *et al,* 2020). The software is being trialled using a Pilbara iron ore deposit data set and output being developed is an open-source software package.

PROGRAM 3 – NATIONAL DRILLING INITIATIVE (NDI)

Primary partners: Geoscience Australia, Geological Survey of New South Wales, Geological Survey of South Australia, Geological Survey of Western Australia

MinEx CRC is deploying both conventional and CT drilling technologies in collaboration with Australia's geological surveys to map the deep cover search space and determine its mineral prospectivity. Application of CT drilling will allow the subsurface to be sampled at a density never before economically possible, and the samples will be subjected to a suite of cutting-edge analytical techniques which will allow 3D geological reconstructions.

Whilst the NDI is not designed to discover mineral deposits in its own right, it is already providing significant data to de-risk areas of previously unknown geology and guide mineral explorers toward areas with the greatest chance of exploration success, as illustrated in the recent NDI campaigns carried out in the Northern Territory (Pitt and Manison, 2021).

The NDI is managing and delivering drilling programs in multiple case study areas proposed by MinEx CRC's partner geological survey organisations. The NDI involves drilling multiple holes in a region to map the regional geology and architecture and define the potential for mineral systems in 3D. A range of drilling methods are being used however it is intended that there will be a significant component of CT drilling and associated sensing technology to maximise the number of drill holes and the volume of data collected in upcoming programs.

MinEx CRC manages the NDI in a matrix structure in which responsibility for implementation aspects of the research program lies with Geoscience Australia and the state geological survey organisations, whereas exploration geoscience aspects of the program, comprising three research projects, are managed by CSIRO and university research groups.

Implementation aspects of the NDI are organised on a chronological basis, centred on: (1) preparation; (2) drilling and sampling; and (3) analysis and access.

The preparation and planning required to deliver the NDI includes determining the location and purpose of each drill hole; preparing an environmental protection and rehabilitation plan; determining the logistics of access; and initiating stakeholder engagement. In designing the drill plans we utilise the repository of existing data and samples that are stored by the geological surveys, including logging and re-analysing legacy samples if required. This theme informs the location of NDI drilling, contributes to the NDI database, and delivers a training set of samples for the new analytical technologies to be developed.

The drilling and sampling stage of the NDI campaigns is critical to the success of MinEx CRC with logistics, management of multiple internal and external stakeholders and heightened levels of risk. Key tasks include drill site management, safety and environmental compliance, stakeholder liaison, logging, and in-field data collection. MinEx CRC works closely with our partners, researchers, drilling contractors, geological survey organisations, government departments, landholders and aboriginal custodians to ensure best practice in our drilling activities.

The post drilling stage of the NDI involves analyses of in-field data and logging, sampling for downstream analyses, management and distribution of drill samples and data to researchers, sample storage and storage and delivery of data. MinEx CRC and the partner surveys publicly release all data collected by the NDI as pre-competitive data as soon as practical. This release comprises rapid delivery of in-field NDI data, systems to apply quality control, collate, cross reference and store the NDI data (including laboratory analyses conducted at some later time after drilling), and to provide a single point of access for viewing, interrogating and downloading the NDI data.

MinEx CRC has developed a single point of access to digital data and data analytics delivered by the NDI program (including legacy sampling and analyses) through the NDI portal, which can be accessed at <www.minexcrc.com.au>. The portal allows visualisation and interrogation of a range of exploration relevant data in a 3D spatial context with ability to download data by spatial search or database query. The NDI portal has been designed to incorporate advanced geospatial data analytics providing users with online access to cutting-edge decision-making software tools.

The geological architecture and evolution project aims to provide new geoscience data and knowledge of the geology in NDI campaign areas via integration of geophysics and petrophysics, regolith and hydrogeology, alteration signatures, basin analysis, and igneous and metamorphic analysis. These new geoscience data and knowledge are aimed to inform the 3D geology and 4D geological evolution of the case study areas and aid in the identification of known and potential mineral systems. New technologies and methodologies are being developed and leveraged to change practices in under-cover exploration-targeted mapping.

Our mineral systems targeting project aims to create a new generation of multiscale (province, district and camp scale) exploration targeting models for the NDI campaign areas, that represent and quantify the spatial variations in architectural, stratigraphic, geophysical, geochemical, mineralogical and isotopic (collectively geological) characteristics of potential mineral systems in the area. The project integrates temporal and spatial geoscientific data for the NDI campaign areas with our existing understanding of mineral systems to create maps of mineral potential, using data – and knowledge-driven prospectivity mapping techniques.

CONCLUSIONS

At the end of the first of three three-year phases, MinEx CRC has delivered encouraging results comprising aspects of a new set exploration tools which have been trialled in numerous field settings and for numerous commodities, including in the Pilbara for iron ore exploration. In addition, new ways to deploy those tools for collecting quantity and quality data from the subsurface is emerging. The pioneering work on CT drilling technology is emphasising its productivity, safety and environmental benefits. Conventional drilling techniques are also being improved through drilling optimisation and automation. The new technologies for collecting data while drilling is being developed in parallel in four separate industry-led projects covering geophysical, seismic, downhole analytical and 3D modelling. The drilling and technology improvements are being applied to the NDI, with two drilling programs completed in 2020 and a further nine programs being planned in under-explored areas of Australia. In addition, this research is contributing to addressing the threat of declining mineral inventory resulting from current exploration methods that are not able to discover and define the quantity of new iron orebodies needed to sustain the Pilbara's iron ore output.

ACKNOWLEDGEMENTS

This work has been supported by MinEx CRC whose activities are funded by the Australian Government's Cooperative Research Centre Program. This is MinEx CRC Document 2021/35.

REFERENCES

Australian Bureau of Statistics (ABS), 2021. Mineral and Petroleum Exploration, Australia, Quarterly statistics on mineral and petroleum exploration expenditure by private organisations in Australia, Reference period March 2021. <https://www.abs.gov.au/statistics/industry/mining/mineral-and-petroleum-exploration-australia/mar-2021>.

Chen, G, Fox, S, Lancaster, D G and Soe, S, 2020. Temperature-compensated interferometric torque sensor with bi-directional coiling, *Journal of Lightwave Technology*, 8 p.

Chi, B, Maddever, R A M, Mahanta, A and Dominguez, O, 2017. Near real-time assay with downhole assay tool (FastGrade 100), In *Proceedings Eighth World Conference on Sampling and Blending*, pp 137–144 (The Australasian Institute of Mining and Metallurgy: Melbourne).

Giraud, J, Lindsay, M, Jessell, M and Ogarko, V, 2020. Towards plausible lithological classification from geophysical inversion: Honouring geological principles in subsurface imaging, *Solid Earth*, 11(2):419–436.

Knight, J, 2015. Address at the AusIMM Iron Ore Conference, Perth, reported in The Australian, 14 July 2015. <https://www.theaustralian.com.au/business/mining-energy/iron-ore-miners-unprepared-for-challenges-warns-bhp/news-story/dfb3d38406fea04c6c74430bbc4f1dba>

Le, C V A, Harris, B D and Pethick, A M, 2019. New perspectives on Solid Earth Geology from Seismic Texture to Cooperative Inversion, *Scientific Reports*, vol 9(1), Article number 14737.

Moore, P, 2018. LKAB Wassara celebrating 30 years. Available at <https://im-mining.com/2018/10/18/lkab-wassara-celebrating-30-years/>

Pitt, K and Manison, N, 2021. A joint ministerial release from The Hon Keith Pitt MP, Minister for Resources, Water and Northern Australia and The Hon Nicole Manison MLA, Northern Territory Minister for Mining and Industry. Available at <https://www.minister.industry.gov.au/ministers/pitt/media-releases/national-drilling-initiative-reveals-golden-opportunity-northern>

Singh, B, Malinowski, M, Hlousek, F, Hellwig, O, Buske, S, Koivisto, E and Heinonen, S, 2019. Benefits of Depth Imaging in 3D Seismic Mineral Exploration: Case Study from the Kylylahti Mine, Finland. *81st EAGE Conference and Exhibition*, Finland.

Soe, S, Lagat, C, Evans, B, Mostofi, M and Fox, S, 2018. The Coiled Tubing Drilling Rig for Mineral Exploration, *SPE/ICoTA Coiled Tubing and Well Intervention Conference and Exhibition*, March 2018, paper: SPE-189918-MS.

Urosevic, M, Bona, A, Ziramov, S, Pevzner, R, Tertyshnikov, K, Martin, R, Dwyer, J, Felding, D, Guarin, C and Foley, A, 2019. Seismic exploration of mineral resources in Western Australia with Distribute Acoustic Sensing, in *25th European Meeting of Environmental and Engineering Geophysics*, September.

A new look at detrital iron deposit geology of the Hamersley Province of Western Australia

J M F Clout[1], G Plummer[2] and C Simpson[3]

1. Principal, Clout Mining, Nedlands WA 6009. Email: John@cloutmining.com
2. Senior Geometallurgist, Fortescue Metals Group Ltd, East Perth WA 6004.
   Email: gplummer@fmgl.com.au
3. Geology Manager, Fortescue Metals Group Ltd, East Perth WA 6004.
   Email: csimpson@fmgl.com.au

ABSTRACT

Detrital iron deposits (‘DID’) in the Hamersley Province of Western Australia have been successfully mined and processed as small quantities of saleable standalone or blended lump and fine ore products over many decades. Despite their past, present, and potential future exploitation, they have received far less geological attention than the economically more significant higher grade bedded iron deposits (BID) or channel iron deposits (CID).

DID are composed of Pliocene to Quaternary unconsolidated colluvial/alluvial hematite gravels with minor sand, silt, and ferruginous clay, as well as minor iron rich hematite clast conglomerates. DID mineralisation at Solomon has been subdivided into six distinct stratigraphic units, DID-5 (lowermost) to DID-0 (uppermost) based on differences in clast and matrix textures and mineralogy, degree of consolidation/lithification, particle size distribution and replacement textures. The most significant accumulations of DID-1 to DID-5 are in tributary valleys that have been cut through the Joffre Member of the Brockman Iron Formation on either side of the main Kings-Queens valley which contains the CID.

DID-5 and DID-4 are ferruginous conglomerate, referred to as canga, with four subtypes recognised. DID-4 is composed of BID hematite clasts cemented by hematite or goethite. DID-5 is characterised by partial to complete replacement of BID hematite clasts and matrix by the yellow ochreous and brown to black vitreous forms of goethite. DID-3 to DID-0 are unconsolidated hematite detritals composed of largely (>80 weight per cent) fine to coarse gravel, minor sand and little silt or clay. The gravel clasts are largely composed of hematite and hydrohematite that replace BID, micro-nanoplaty hematite-martite-ochreous goethite (m-nplH-M-oG) BID, reworked canga, hematite pisoids, siliceous hematite BID (micro-nanoplaty hematite-martite-quartz, m-nplH-M-quartz), chert (~10–20 per cent) and minor (<5 per cent) Banded Iron Formation (BIF). Hematite abundance decreases from DID-3 to DID-0 whilst siliceous hematite BID is highest in abundance in DID-0 and lowest in DID-3.

A key finding of the study is that >90 per cent of mineralised detrital clasts are derived from hypogene altered BID micro-nanoplaty hematite-martite with subsequent later supergene ochreous goethite mineralisation hosted by the Joffre Member. The DID genesis model entails interpreted Palaeoproterozoic siliceous hematite hypogene microplaty BID mineralisation of the Joffre Member undergoing Cenozoic supergene leaching of quartz and replacement by ochreous goethite to form low phosphorous BID micro-nanoplaty hematite-martite-ochreous goethite clasts. BID martite-nanoplaty hematite-martite-ochreous goethite clasts and detritus eroded from hill slopes were deposited in the valleys as an initial single DID-5-DID-4 unit over a weathered pre-CID basal conglomerate. DID-5 and DID-4 underwent goethite cementation of the matrix followed by replacement by hydrohematite, hematite, and maghemite. DID-3 formed during subsequent periods of erosion of largely DID-4 hematite clasts and pisoids. Groundwater flow-through hematite canga resulted in partial to complete hydration replacement of DID-4 hematite clasts and matrix by ochreous and vitreous goethite to form DID-5. Deposition of DID-2 to DID-0 was via reworking and deposition of DID-5 to DID-4 canga and DID-3 as clasts and pisoids/ooids, as well as siliceous hematite and BIF sourced from the Joffre Member in the hill slopes.

INTRODUCTION

The Hamersley Province in the Pilbara region of Western Australia contains five styles of iron mineralisation:

1. Unenriched banded iron formation (BIF)
2. BIF-hosted high-grade bedded iron deposits (BID), including:
   - microplaty hematite-martite (mplH-M)
   - supergene martite-goethite (M-G) styles
3. Mid-late Miocene goethite-pisolite dominant channel iron deposits (CID)
4. Pliocene–Quaternary colluvial-dominant hematite detrital iron deposits (DID) (Morris and Kneeshaw, 2011; Kneeshaw and Morris, 2014).

Of these BID is estimated to account for ~75 per cent of current mine production with CID accounting for ~20 per cent.

Cenozoic DID in the Hamersley Province of Western Australia have been successfully mined and processed but only as smaller quantities of saleable standalone or blended lump or fine iron ore products. Despite their past, present, and potential future exploitation, they have received far less geological attention than the massive resources of banded iron formation (BIF) hosted high-grade microplaty hematite-martite and martite-goethite BID, and CID.

Previous work

The earliest published work on Pilbara DID was by McKenna and Harmsworth (1998) who described the geology of the Brockman 2 detritals (B2D) deposit, which lies 55 km NW of Tom Price township (Figure 1). The B2D deposit comprised a measured Mineral Resource of 38 Mt of ore averaging 62 per cent Fe (60 per cent Fe cut-off) and consisted of four discrete lenses downslope of hills composed of mineralised Brockman Iron Formation. The authors described a vertical sequence through the deposit with a basal hydrated hematite conglomerate (>60 per cent Fe) overlain by a hematite conglomerate (>60 per cent Fe), then unconsolidated hematite detritals (>60 per cent Fe), lower grade hematite detritals (55 per cent – 60 per cent Fe) and an uppermost siliceous detritals unit (<55 per cent Fe). Butt, Hawke and Flis (2002) established the *in situ* bulk density characteristics and gravity Bouguer Anomaly signature of the B2D deposit.

In the northern central Hamersley Ranges, Dalstra *et al* (2010) briefly described the geology of DID mineralisation which overlies the flanks of extensive CID at the Caliwingina deposit (Figure 1). Kepert *et al* (2010) described the discovery of significant CID and lesser BID and DID at the Solomon and Serenity deposits associated with the Solomon Miocene palaeochannel. The DID at Solomon is thought to be derived from Pliocene erosion of supergene martite-goethite (M-G) BID mineralisation and local deposition overlying the CID. Simpson *et al* (2011) documented the DID geology at the Solomon deposits, including a basal canga and three unconsolidated units: mature (lowermost); semi-mature; and immature (uppermost). McDonald (2011), Petts, McDonald and Corlis (2011) and Tylkowski *et al* (2013) described the DID geology of the Blacksmith deposit (Delta, Eagle, Champion and Blackjack), located to the SSE of Caliwingina, and document four discrete DID units (DID1–4) located immediately above CID in tributary valleys to the west of the main channel of the Serenity CID.

Kneeshaw and Morris (2014) provided the most comprehensive review of Cenozoic DID geology and stratigraphy of all previous workers across the Hamersley Province, recognising an older Eocene DID (CzD1) composed of mainly alluvial with minor pisoids underlying mid-late Miocene CID (CzD2) and a younger Pliocene–Quaternary DID (CzD3) which comprises coarse alluvial and colluvial gravels and minor pisoids. The authors considered the DID clasts (gravel-size fraction) to be derived from and largely retaining the original textures of supergene martite-goethite BID, hard cap or variably ferruginised surface BIF. They interpreted the alluvial/colluvial DID matrix as a 'ferroan-aluminous soil' and, where replaced by goethite, the resulting ferruginous conglomerate is referred to as canga. The DID canga goethite matrix may in turn be dehydrated to hematite, in part due to interpreted exposure at surface.

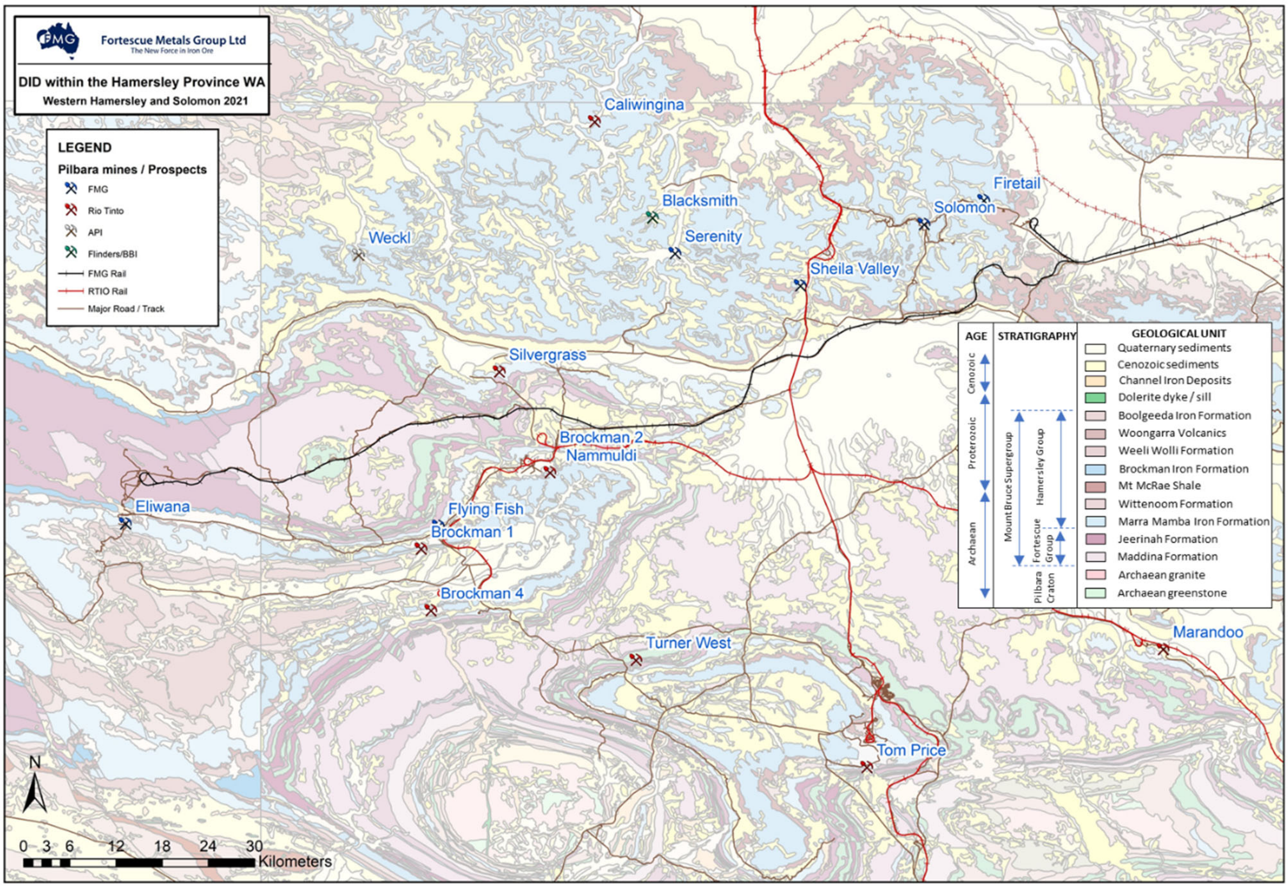

FIG 1 – Regional geology of the NE Hamersley Province, adapted from GSWA 1:250 000 geology.

Aims

This paper documents recent work on DID at the Solomon hub based on extensive pit exposures and drilling (both diamond core and reverse circulation (RC) drilling). The aim of the work was to provide a clearer understanding of DID stratigraphy, particle size distribution, clast type textures and implications for DID ore genesis in the northern Hamersley Province.

Sampling methods

DID samples were obtained by excavation of 13 bulk sample from pit faces at Solomon (Kings deposits), followed by stockpiling and subsampling into multiple 1 tonne bulk bag lots. Bulk samples were analysed for particle size distribution, chemical assay by the typical iron ore industry fused bead X-ray fluorescence (XRF) and thermogravimetric loss on ignition methods, and geometallurgical characterisation. A large rotary sample divider was used to obtain representative 100 kg subsplits for subsequent dry sizing down to 1 mm followed by wet screening the undersize and chemical analysis of all size fractions. Care was taken to avoid adhering silt and clay being retained on the gravel size fractions during dry screening. Uncrushed natural size fractions and hand specimens were at first classified by eye aided by a hand lens and hand sorted, weighed to determine clast type per cent by weight, with selected representative specimens sectioned using a diamond saw before photographing. Polished and thin sections were prepared from crushed -10 mm size fractions and hand specimens for observation using a petrographic optical microscope under plane polarised reflected light and cross polarised reflected light.

The sectional interpreted DID geology is based on closed spaced RC drill hole chip geological logging and assays, diamond drill core geological logging and photography as well as pit face exposures.

SOLOMON HUB GEOLOGY

The Solomon hub, located in the NE Hamersley Province of Western Australia, comprises a basement of Neoarchean to Palaeoproterozoic Mount Bruce Supergroup, with the lowest unit exposed within the valleys being the Dales Gorge Member of the Brockman Iron Formation (Figure 1) (Simpson *et al*, 2011; Clout, Simpson and Counsell, 2017). The Joffre Member of the Brockman Iron Formation is typically exposed in the higher portions of the hills (Figure 2). A younger Cenozoic colluvial to Quaternary alluvial cover sequence occurs within broad open valleys 1 to 2 km in width that are incised into bedrock geology belonging to the Dales George Member. The Kings-Queens main valley is continuous, extending for 30 km of strike trending generally east to west, with modern drainage crossing these valleys draining predominantly south to north (Kepert *et al*, 2010) (Figure 2).

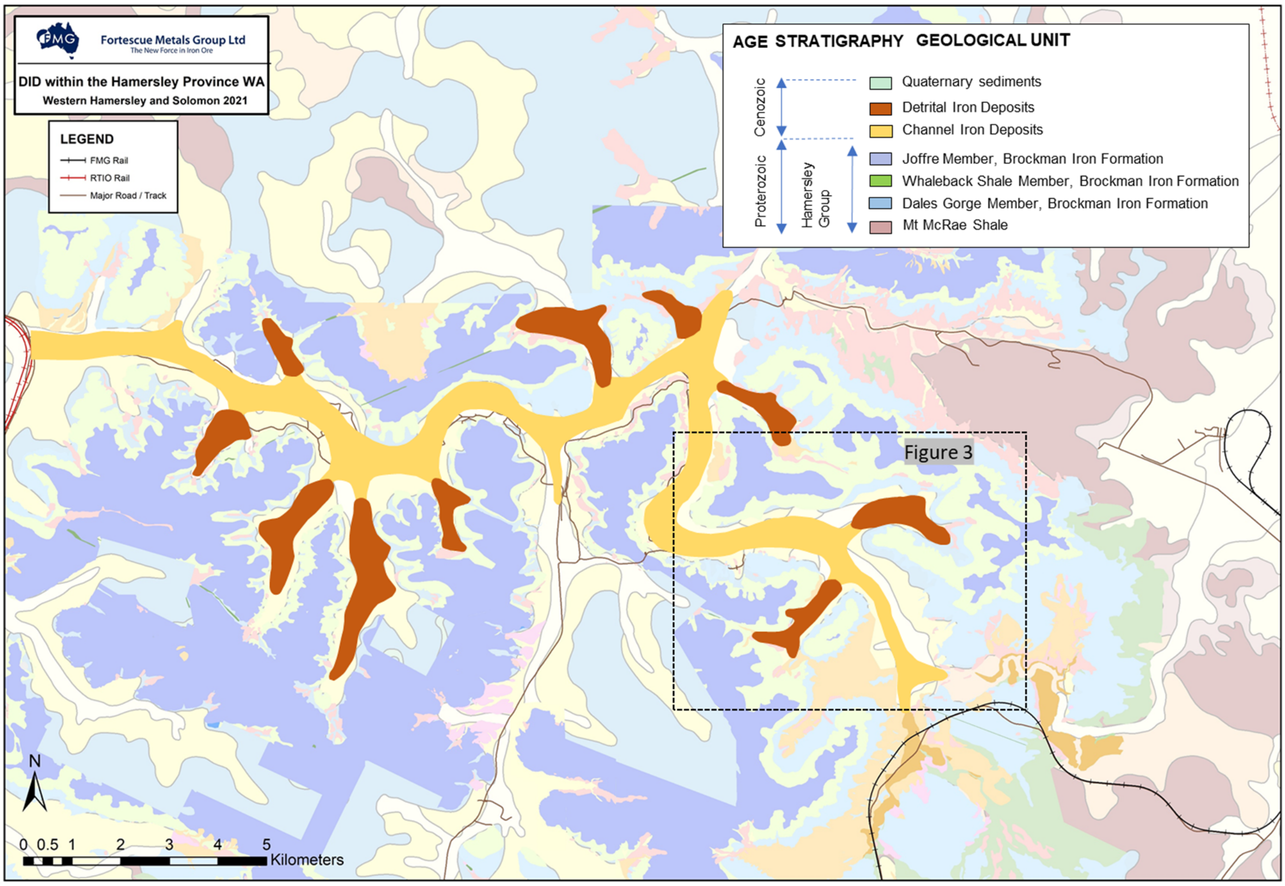

FIG 2 – Solomon CID and DID geology, modified after Simpson *et al* (2011).

Iron mineralisation at Solomon consists of BID hosted within the Dales Gorge and Joffre Members (eg Firetail), Miocene CID deposits in the Kings and Queens main valley and minor DID. The greater Solomon area also includes undeveloped CID with minor DID mineralisation including Serenity and Sheila Valley deposits (Figure 1).

Economic mineralisation at the Kings and Queens deposits is comprised of largely CID, and to a far lesser extent DID. The CID deposits occur predominantly below a younger Cenozoic alluvial cover sequence within broad open valleys (Figure 3). Thickness of the total CID varies throughout the valley system, being thin (<20 m) in the eastern, outcropping portion of the valley, to greater than 50 m in the central Kings and Queens deposits. The CID are vertically zoned with a conglomeratic to semi-consolidated clay and ochreous goethite basal sequence (lower CID), transitioning to a progressively harder brown goethite-rich lithified upper sequence (upper CID). This is in turn unconformably overlain by a hard silcrete to siliceous clay and calcrete horizon called the Oakover Formation, as well as poorly consolidated clay, silt, and gravel. Various thicknesses of iron rich detrital clast conglomerates and unconsolidated colluvial/alluvial DID overlie the Oakover Formation. The DID consists of a basal ferruginous conglomerate overlain by unconsolidated hematite gravels with minor ferruginous sand, silt, and clay. Overlying the dominantly colluvial DID is Quaternary alluvium consisting of ferruginous clays, silt, quartz sand, water-worn subrounded BIF clasts and minor thin (<75 mm) beds of maghemite-hematite ‘pea’ gravel.

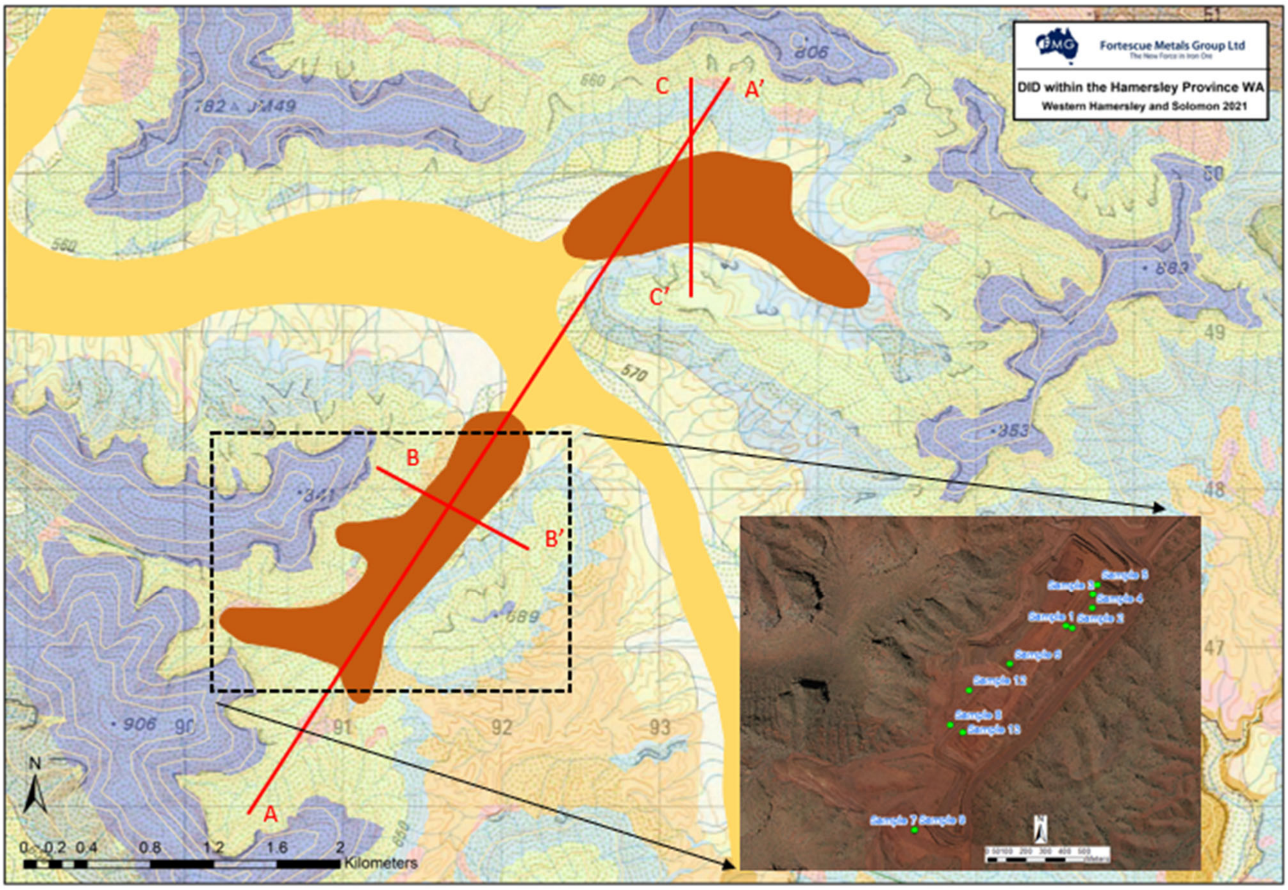

FIG 3 – Location plan geology of Kings DID and CID, and location of sections A-A', B-B' and C-C' in Figure 4.

DID GEOLOGY

DID stratigraphy

Kneeshaw and Morris (2014) defined detrital stratigraphy across the Hamersley Province starting with a lowermost Oligocene DID unit (CzD1), a mid-late Miocene CID unit (CzD2) and a Pliocene dominantly colluvial DID (CzD3) unit, which is overlain by Quaternary alluvial sediments. Kneeshaw and Morris (2014) compiled a lithostratigraphic correlation across the province for various companies, including work by Simpson *et al* (2011) for the Solomon Hub (Table 1). Between four and seven Pliocene CzD3 DID stratigraphic units are recognised across the Hamersley Province, with some broad correlations possible between the various units, including a basal hematite conglomerate (canga) overlain by unconsolidated hematite-pisolith rich detritals and an uppermost unconsolidated detrital unit comprising siliceous gravels in a silt-sand matrix.

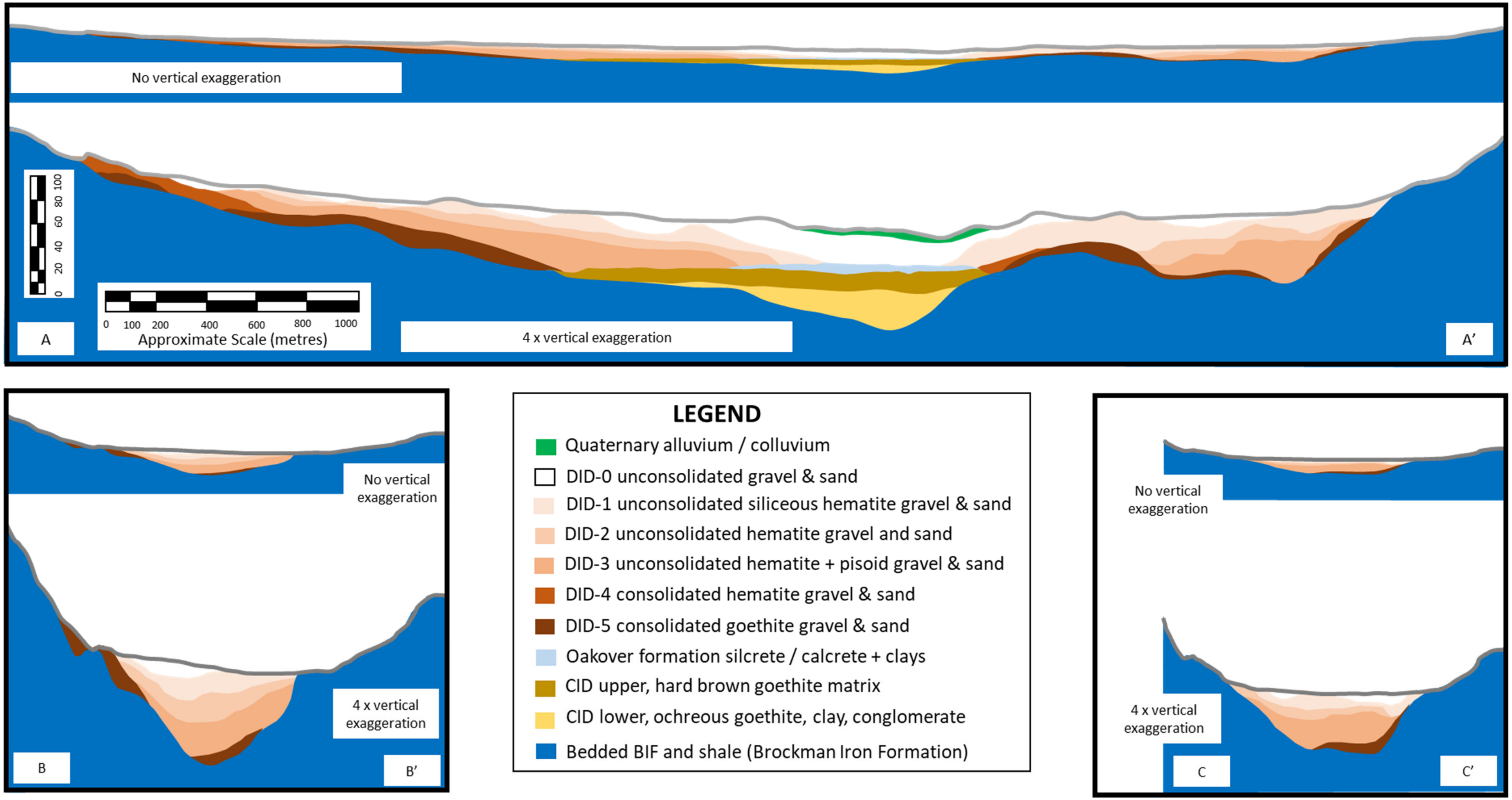

FIG 4 – Interpreted longitudinal and cross-sections depicting DID sequences over basement weathered BIF, CID, and Oakover Formation. Section locations as per Figure 3.

TABLE 1

Comparison of the various company CzD3 DID and CzD2 CID classification systems and Cenozoic litho-stratigraphic similarities across the Hamersley Ranges and Fortescue Valley. From Kneeshaw and Morris (2014).

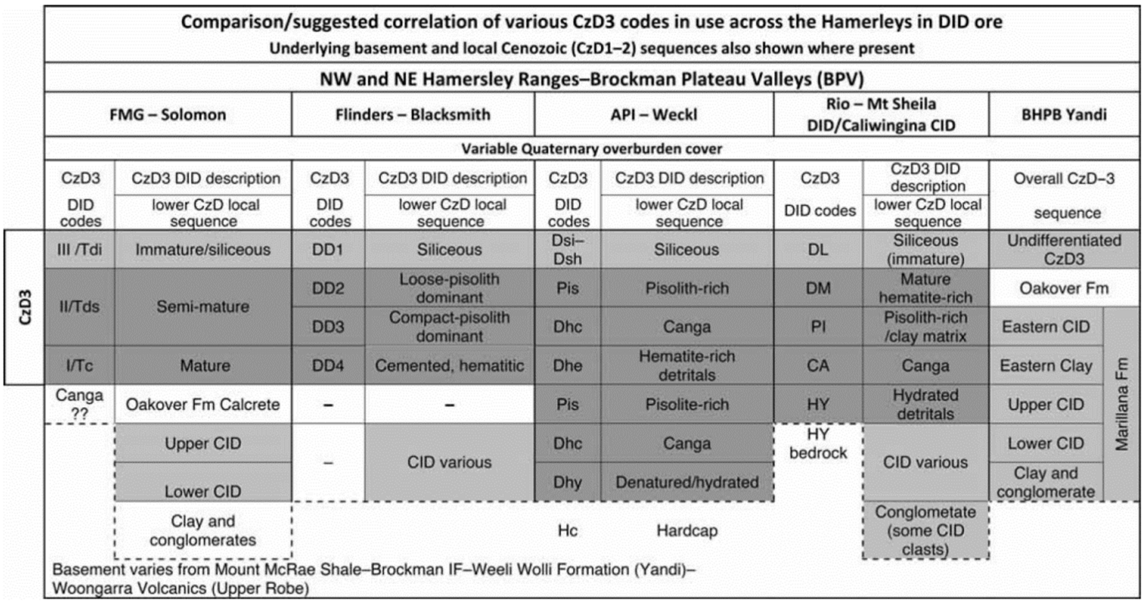

	Comparison/suggested correlation of various CzD3 codes in use across the Hamerleys in DID ore **Underlying basement and local Cenozoic (CzD1–2) sequences also shown where present**									
	NW and NE Hamersley Ranges–Brockman Plateau Valleys (BPV)									
	FMG – Solomon		**Flinders – Blacksmith**		**API – Weckl**		**Rio – Mt Sheila DID/Caliwingina CID**		**BHPB Yandi**	
	Variable Quaternary overburden cover									
	CzD3 DID codes	CzD3 DID description lower CzD local sequence	CzD3 DID codes	CzD3 DID description lower CzD local sequence	CzD3 DID codes	CzD3 DID description lower CzD local sequence	CzD3 DID codes	CzD3 DID description lower CzD local sequence	Overall CzD–3 sequence	
CzD3	III /Tdi	Immature/siliceous	DD1	Siliceous	Dsi–Dsh	Siliceous	DL	Siliceous (immature)	Undifferentiated CzD3	
	II/Tds	Semi-mature	DD2	Loose-pisolith dominant	Pis	Pisolith-rich	DM	Mature hematite-rich	Oakover Fm	
			DD3	Compact-pisolith dominant	Dhc	Canga	PI	Pisolith-rich /clay matrix	Eastern CID	Marillana Fm
	I/Tc	Mature	DD4	Cemented, hematitic	Dhe	Hematite-rich detritals	CA	Canga	Eastern Clay	
	Canga ??	Oakover Fm Calcrete	–	–	Pis	Pisolite-rich	HY	Hydrated detritals	Upper CID	
		Upper CID	–	CID various	Dhc	Canga	HY bedrock	CID various	Lower CID	
		Lower CID			Dhy	Denatured/hydrated			Clay and conglomerate	
		Clay and conglomerates			Hc	Hardcap		Conglometate (some CID clasts)		
	Basement varies from Mount McRae Shale–Brockman IF–Weeli Wolli Formation (Yandi)–Woongarra Volcanics (Upper Robe)									

As part of more recent work, the original three CzD3 DID units recognised at the Solomon hub (Table 1) and the current five-unit codes used in logging have since been re-subdivided into six units (DID-0 to DID-5) based on logging of diamond drill holes, RC drill chips, pit floor and face mapping at Kings and Queens (Table 2). In keeping with an existing DID classification at the nearby Blacksmith deposit, the western extension of the Serenity DID, the units have been numbered from the top down, for RC drill hole logging convenience, rather from the bottom up by stratigraphic convention. The six DID units for Solomon broadly correlate with those presented by Kneeshaw and Morris (2014) (Table 2) and show a clear stratigraphic position overlying CID and the Oakover Formation in the main Kings-Queens channel and above a basal unconformity with weathered-goethitic and hard capped Dales Gorge Formation to the south (Figure 4).

TABLE 2

Solomon DID and CID stratigraphy and codes.

Age	**Kneeshaw and Morris (2014) codes**	**Current FMG codes**	**Proposed FMG codes**	**Dominant clast and matrix/cement descriptions**	
Qa		Qa	QA	Quaternary colluvium/alluvium, clay, silt, BIF clasts	
Pliocene – CzD3	DM	Ta	DID-0	Highly siliceous clasts (<45 per cent Fe), unconsolidated	
	DS	Tdi	DID-1	Siliceous hematite clasts, unconsolidated	
	DHs/DSh/DH	Tds	DID-2	Hematite clasts, unconsolidated	
	DP/DPh	Tdm	DID-3	Hematite pisoid clasts, unconsolidated	
	DH-Ca	Tdc	DID-4	Canga – Fe conglomerate	Hematite clasts, hematite, or goethite cement
	DY	Tdc	DID-5		Goethite replacement of hematite, cemented
Miocene - CzD2		To	Ok FM	Silcrete, calcrete and siliceous clays	
		UCID	CIDu	Brown goethite pisolite	
		LCID	CIDl	Ochreous dominant goethite pisolite	
		CIDb	Basal	Clay and conglomerates	

DID colluvium geometry and particle size distribution

DID is developed at the sides of the main Kings-Queens channel above the CID but is most extensive in the NE-SW striking tributary valleys which have eroded through the Joffre Member down through the Whaleback Shale Member and into the Dales Gorge Member (Figure 3). The DID in longitudinal and cross-section (Figure 4 section, A-A', and B-B' and C-C') has an apparent colluvial fan geometry but when viewed without vertical exaggeration it is more like a channelised sheet prograding downslope across and over the Oakover Formation. Of note is the presence in the main Kings-Queens channel of a significantly thicker DID-0 unit overlain by a very thin sequence of Quaternary clay-rich alluvium and colluvium.

DID occurrences at Solomon are largely located above the current water table, although some DID-5 is in perched water tables and the deepest portions of DID-0 to DID-3 can occur below water table.

Little evidence was found of bedding in the DID units although some weak imbrication of elongated clasts was noted in some locations. The contacts between DID-0 through to DID-2 are gradational, whereas there are sharp contacts between DID-2 and DID-3, as well as between DID-3 and DID-4. The contact between DID-4 to DID-5 is less discrete.

Particle size analysis of thirteen bulk samples reveals the unconsolidated DID to be composed of largely (>80 weight per cent) fine to coarse gravel, minor sand and little silt or clay (Figure 5). The particle size distribution for DID-1 to DID-3 is largely between 1 and 20 mm (Figure 6). DID-3 is moderately to well sorted with low levels of silt and clay compared to the higher levels of clay and lower levels of sorting in DID-0 to DID-2. DID-3 shows a slightly finer gravel and less sand-silt whilst DID-0 has more of the coarser gravel. DID-3 lacks the bimodal peak between 10 and 40 mm seen in the other DID units (Figure 6). The coarse clasts have a bi-modal size distribution.

Clast particle shapes in the 5 to 80 mm size range typically have aspect ratios of 3:2:1–0.5 (length:width:thickness), typical of 'biscuity' to platy fragmentation of Joffre Member microplaty hematite-ochreous goethite mineralisation, controlled by breakage along bedding and orthogonal joint planes. Above 80 mm, mineralised clast shapes are more likely to be either subangular to subrounded and less biscuity. Clasts from 1 to 5 mm are more dominated by near-spherical hematite/hydrohematite pisoids and subangular to subrounded hematite/hydrohematite/maghemite clasts.

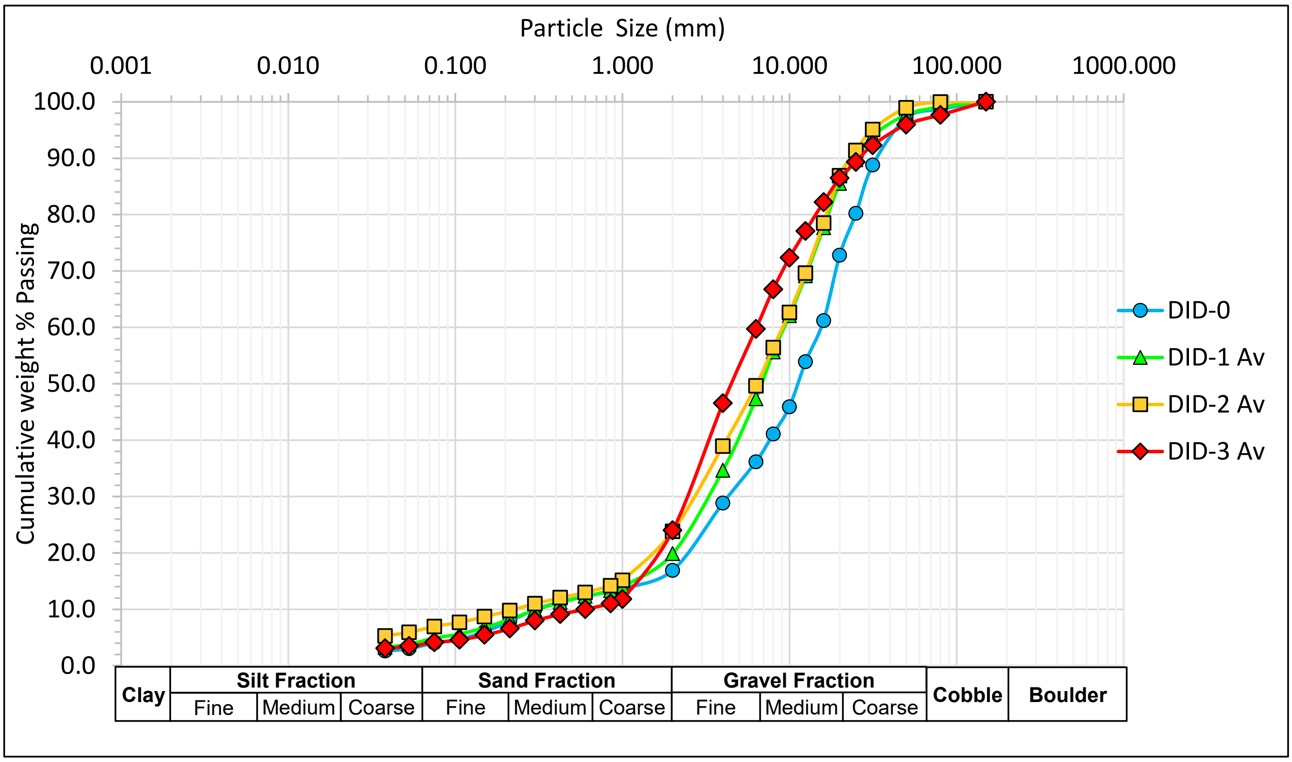

FIG 5 – Typical DID-0, DID-1, DID-2, and DID-3 particle size distributions.

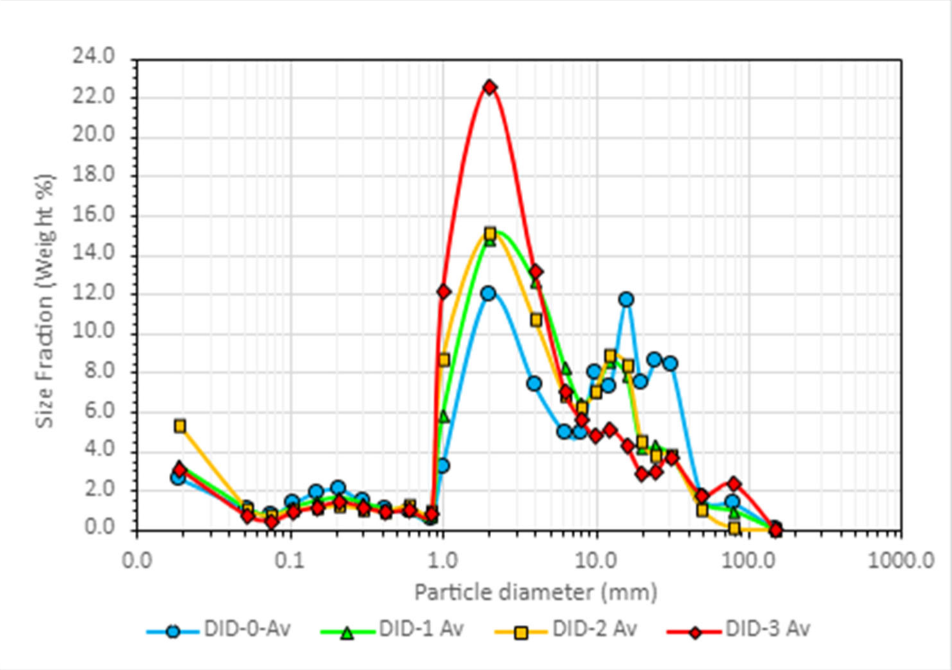

FIG 6 – DID retained size fraction data for FIG 5 samples.

DID unit descriptions

The DID unit clast and matrix petrography are summarised as a stylised vertical profile in Figure 7 and in more detail below, from oldest (DID-5) to youngest (DID-0).

DID Vertical Profile	Zone	Description	Mineralogy	Approximate Thickness
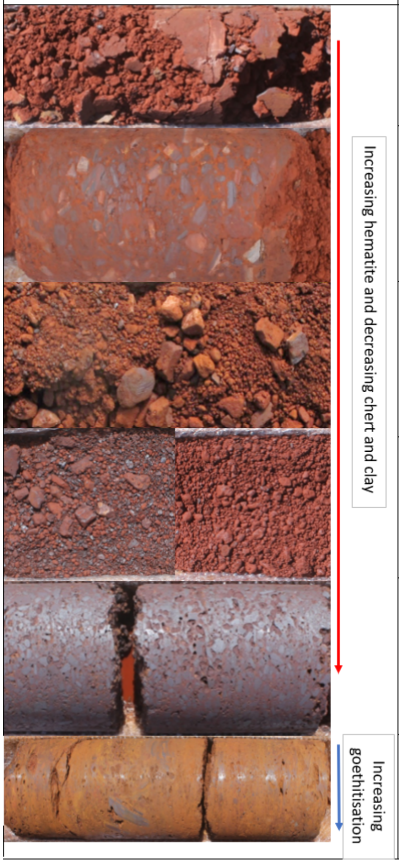	DID-0	Massive, fine gravel to cobble sized clasts in a fine to coarse sand matrix. Friable to rheologically stiff	Comprised mainly of pebble to cobble sized clasts of chert and siliceous hematite with abundant ferruginous kaolinite. Occasional, discrete hydrohematite and maghemite particles present	5 to 25 metres
	DID-1	Composed of poorly sorted fine gravel to cobble sized, angular to sub angular clasts in a fine to coarse sand matrix. Friable to rheolgically stiff.	Comprised primarily of medium gravel to cobble sized, discrete chert, siliceous hydrohematite grains, reworked canga, with minor to moderate maghemite. Moderate amount of fine silt to kaolinite clay and fine quartz sand	5 to 25 metres
	DID-2	Moderately sorted, coarse gravel to very coarse sand sized, subrounded clasts that can be clast supported or in a fine to coarse sand matrix. Friable	Comprised primarily of fine to coarse gravel sized hematite, hydrohematite, reworked canga, and maghemite clasts. Particles can show a hard goethite ferricrete cutan. Discrete, coarse medium to coarse gravel sized chert grains present	5 to 15 meters
	DID-3	Moderately to well sorted coarse sand to medium gravel sized clasts that are subrounded BID to well rounded hematite pisoids (pea gravel). Can be either clast supported or present within a fine to coarse sand matrix. Very friable to mostly granular	Largely coarse sand to medium gravel sized hematite, reworked canga, hydrohematite, and maghemite clasts and pisoids with very little chert or BIF gangue and low clay levels. Particles may show a hard goethite or hydrohematite replacement ferricrete cutan.	5 to 20 metres
	DID-4	Fine to medium gravel sized clasts that can be clast supported or less frequently matrix supported. Matrix typically hematite or goethite partially dehydrated to hematite. Clasts angular to subrounded. Network of 2-5 mm macropores lined with goethite	Typically comprised of coarse sand to medium gravel sized hydrohematite and hematite clasts within a matrix of hydrohematite after goethite or goethite. Occasional patches of red ferruginous clay matrix with Al-rich goethite.	5 to 10 metres
	DID-5	Medium to coarse gravel remnant hematite clasts and matrix showing partial to complete replacement by ochreous-vitreous goethite. Occasional irregularly sized vugs surrounded by colloform vitreous goethite.	Dominated by brown goethite with occasional patches of vitreous (glassy) goethite present. Replacement of clasts by goethite can create pseudoclasts of original material.	5 to 15 metres

Please note, this is a theoretical vertical profile and not all zones may be present

FIG 7 – Summary of typical DID drill core samples (left), particle size and clast mineralogy.

Canga – DID-4 and DID-5

The term 'canga' was originally applied to BIF-derived hematite-rich fragmentals forming a superficial cover over erosional surfaces (Jackson, 1997; Ramanaidou, 2009; Kneeshaw and Morris, 2014). However, the term in the Pilbara refers to ferruginous cemented hematite conglomerate which often have a deeper non-surficial occurrence (Kneeshaw and Morris, 2014). McKenna and Harmsworth (1998) describe four types of conglomerate: rice bubble canga composed of subrounded hematite clasts and hematite cement; welded canga with tightly packed hematite clasts that have been partially or completely replaced by goethite, with a goethite-clay-quartz matrix; cemented red matrix canga comprising hematite clasts cemented by a ferruginous kaolinitic matrix; and goethitic canga consisting of hematite clasts supported in a hard brown goethite matrix with minor clay-quartz.

DID-5 sits immediately above basement of weathered and hard capped Dales Gorge Member, interpreted as the Hamersley Surface (Kneeshaw and Morris, 2014). DID-5 has a gradational upper contact with DID-4. DID-5 is characterised by partial to complete replacement of BID hematite clasts and matrix by yellow ochreous goethite and vitreous goethite (Figures 8a and 8b) and contains high (>0.3 per cent) TiO_2 levels compared to the underlying weathered BIF (<0.1 per cent TiO_2). However, in RC drill chips compared with diamond core, it can be more difficult to distinguish visually DID-5 from weathered BIF or supergene enriched martite-ochreous goethite (M-oG) mineralisation. The contact between DID-5 and DID-4 is often visible in-pit faces due to colour differences between DID-5 (yellow-brown) versus DID-4 (red-brown) (Figure 9). Clasts of chert tend to be more easily discernible than the goethite replaced hematite clasts in DID-5 (Figure 8a, upper right). DID-5 is equivalent to the welded canga variety of McKenna and Harmsworth (1998).

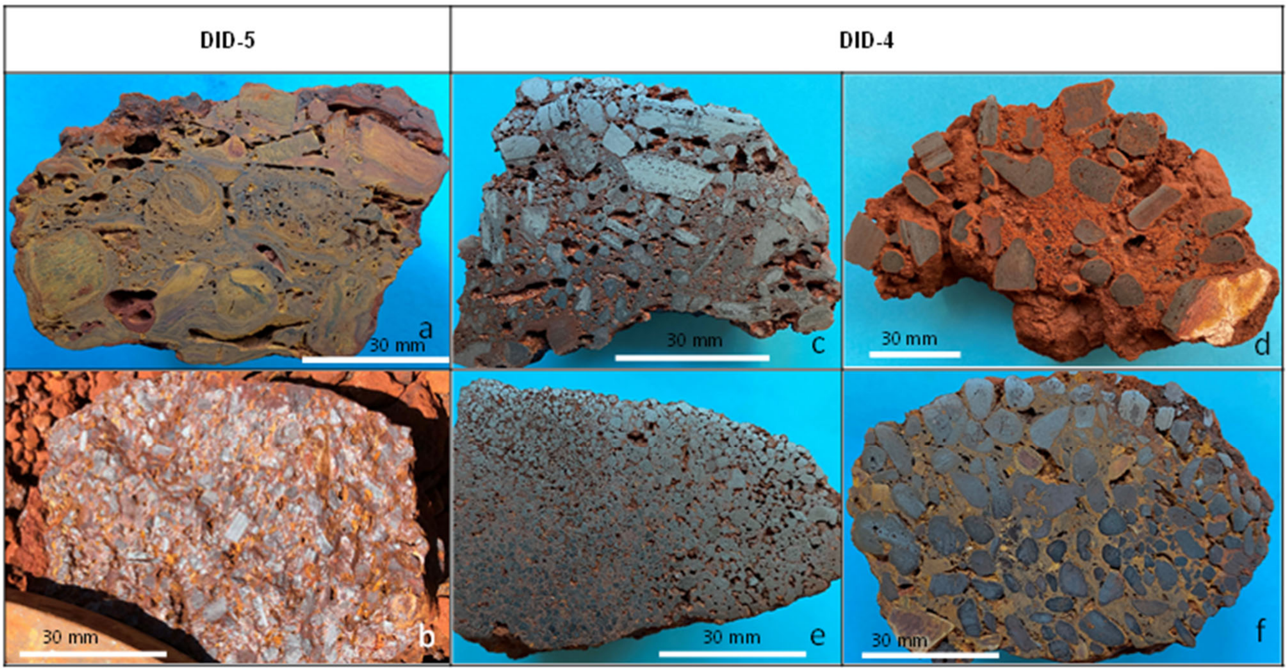

FIG 8 – Typical textures present in DID-5 (a and b, left hand column) to DID-4 canga (c, d, e and f, right hand 2 columns).

DID-4 canga is often high-grade (>60 per cent Fe) and includes a wide variety of subtypes based on clast and matrix relationships and mineralogy which are described below from most abundant to least abundant.

Hematite canga, the most common subtype, varies from clast to matrix supported, dominated by angular to subangular BID hematite clasts and with little or no BIF or goethite, with the original goethite matrix largely or completely replaced by secondary hematite (Figure 8a). Clasts are typically angular to subangular with clast aspect ratios of 3:2:1–0.5 (length:width:thickness) and 5–30 mm length. Dissolution macropores, often circular in cross-section, cross-cut both clasts and matrix, and are typically lined with a thin (<1 mm) coating of vitreous goethite and clay. In many cases the original porous goethite matrix can be seen under reflected light microscopy to have been completely replaced by massive secondary hydrohematite (with internal dehydration cracks) or steely blue maghemite, with destruction of the original BID microbanding. Occasional 1–4 mm hematite replacement fossilised hardwood can be found cemented within the hematite matrix.

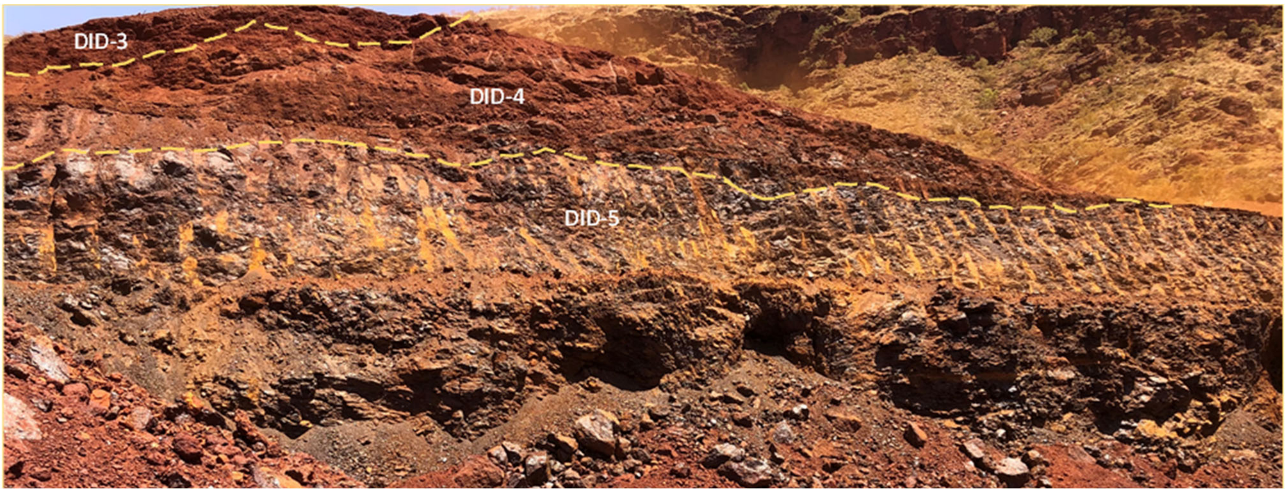

FIG 9 – Face (8 m height) showing DID-3 to DID-5. Bottom left corner of image shows rill from higher benches.

Red clay cemented hematite canga is composed of subangular to subrounded hematite BID clasts in a matrix of ferruginous clay with minor goethite and fine (<0.2 mm) detrital quartz sand grains. Minor subangular BIF may be present (Figure 8b, lower left column).

Hematite pisolite canga consists of varying proportions of rounded hematite pisoids (2–10 mm), ooids (0.25–2 mm) and granules in a matrix of hematite. In some locations at Solomon, the subrounded to near-spherical hematite 'pelletoids' were examined after sectioning and found to be granules of dense to microporous BID and not pisoids. In the example in Figure 8c, there is a higher percentage of hematite-maghemite ooids and fine matrix. This unit is equivalent to the 'rice bubble canga' unit at the nearby B2D DID (McKenna and Harmsworth, 1998).

Goethite cemented hematite canga is composed of BID hematite clasts cemented within a matrix of hard brown goethite matrix cement that contains minor yellow ochreous goethite and 0.1–0.25 mm quartz sand grains. This canga subtype can be either matrix or clast-supported and clasts vary from the subrounded hematite in Figure 8d, to more typically subangular hematite clasts. Occasional angular to subrounded slightly weathered chert clasts may also be present.

Overall, the Solomon canga subtypes clasts and matrix relationships are similar to those observed at the B2D DID (Figure 10) (McKenna and Harmsworth, 1998), the Blacksmith DID (Petts, McDonald and Corlis, 2011) and more generally by Kneeshaw and Morris (2014).

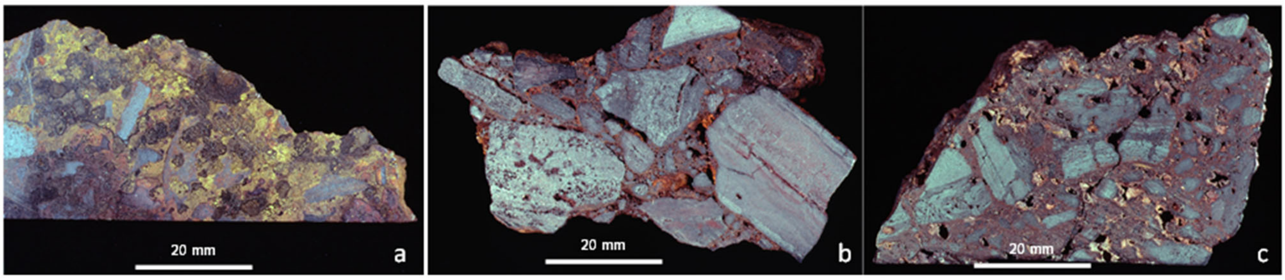

FIG 10 – Typical DID canga clast textures in hand specimens. Canga types from B2D – (a) goethitic/welded canga; (b) hematite clast-supported canga; and (c) goethite cemented hematite canga.

DID-0 to DID-3

DID units 0–3 can be distinguished by their iron grade (eg Petts, McDonald and Corlis, 2011) but more importantly by the abundance of type of the clasts present as well as a progressive increase in the amount of sand, silt and ferruginous clay going vertically upwards from DID-3 to DID-0 and down the slope of the tributary valleys heading towards the main Kings-Queens channel. All four DID units are largely (>75 per cent) composed of hematite/hydrohematite with low (<20 per cent) to very low (<12 per cent) total abundance of goethite, with goethite abundance highest (~20–40 per cent) in size fractions below 1 mm.

Descriptions of DID-0 to DID-3 typical clast and matrix relationships and mineralogy are summarised in Figure 7. Reworked clasts of DID-4 hematite and goethite cemented canga occur in decreasing abundance vertically upwards from DID-3 to DID-0 and laterally from the tributary valley headwaters going towards the main Kings-Queens channel.

Using the clastic sediment definitions for colluvium and alluvium used by Kneeshaw and Morris, 2014), DID units 0–3 are largely interpreted as colluvium, since the coarse (>25 mm diameter) clasts, which are more susceptible to abrasion, predominantly contain friable accretionary coatings of cemented hematite pisoids or 0.1–2 mm rims of brown goethite or hydrohematite replacement of goethite. Towards the uppermost portion of DID-0, there can be minor (<5 weight per cent) subrounded and water worn BIF clasts, interpreted to be of alluvial origin, or they may represent recent reworking of DID-0. In contrast, the Quaternary to Recent unconsolidated clastic sediments within the main Kings-Queens channel are of mixed dominant alluvial-minor colluvial material with the coarser clasts, mainly of BIF and chert, lacking accretionary coatings and have a smooth water worn surface.

Clast textures

Mineralised clasts account for 70–85 per cent of all clasts (Figures 11a to 11h and 11j) whilst the remainder mainly (10–20 per cent) are of chert (Figure 11l) and minor (5–10 per cent) unmineralised BIF (Figures 11i and 11k). The key mineralised textures are detailed below.

Disseminated microplaty hematite in a microporous to dense matrix of hydrohematite (HH-mplH-M) (Figures 11c and 11d). The coarser grained microplaty hematite can be identified by eye using a standard field hand lens. The hydrohematite has a lower reflectivity than hematite and shows microcracking indicative of volume loss from dehydroxylation of primary goethite to hydrohematite (Figure 12a). The microcracking and dull steel grey colour of hydrohematite is easily distinguished from hematite using a hand lens. The hydrohematite replacement texture often retains some of the original BID microbanding (Figure 11d). The hydrohematite-disseminated microplaty hematite texture is most common in DID-3 and less common in DID-1 and DID-0.

The second most common clast texture is microplaty hematite-disseminated martite within a microporous matrix of red to yellow brown nanoplaty hematite-ochreous goethite (mplH-nplH-oG-M) (Figures 11a and b) and is most abundant in DID-2 and DID-1 but is absent from DID-3. The texture also contains locally minor disseminated martite and kenomagnetite after primary BIF magnetite (Figure 12b). In some examples disseminated nanoplaty hematite may be present with disseminated microplaty hematite and martite (Figure 12c).

DID-0 to DID-2 contain clasts with the texture composed of microplaty hematite with minor martite and moderate (10–15 per cent) quartz (mplH-M± quartz) (Figure 12d) which is gradational to the common DID-0 to DID-1 siliceous hematite comprising disseminated microplaty hematite and martite in a largely (>50 per cent) matrix of chert/quartz (quartz-mplH-M) (Figures 11j and 12d).

Pelletoids composed of concentrically banded hematite/hydrohematite/maghemite pisoids (2–10 mm) and ooids (0.25–2 mm) (Figure 12f), the so called ‘pea gravel’, is most common in DID-3 and less common in DID-0 to DID-2.

Clasts of subrounded to angular canga are present in DID-0 to DID-3 and account for most of the clasts textures in the -150 +50 mm size fraction. The clasts of canga include hematite canga (Figure 11f and 11h), clasts of heavily replaced and variably microporous hydrohematite/maghemite (HH/Mh) canga (Figures 11e and 11g), goethite cemented canga (Figure 12g), hydrohematite cemented reworked canga clasts with inclusions of white to red clay (Figure 11g) and hematite pisolite canga with hematite/hydrohematite pisoids and ooids (Figure 11a, upper right and Figure 12h). DID-5 canga clasts were only found within DID-0. In one case, fine (<0.5 mm diameter) plant roots were found to have colonised the macropore surfaces within larger (>80 mm diameter) hematite canga (Figure 13).

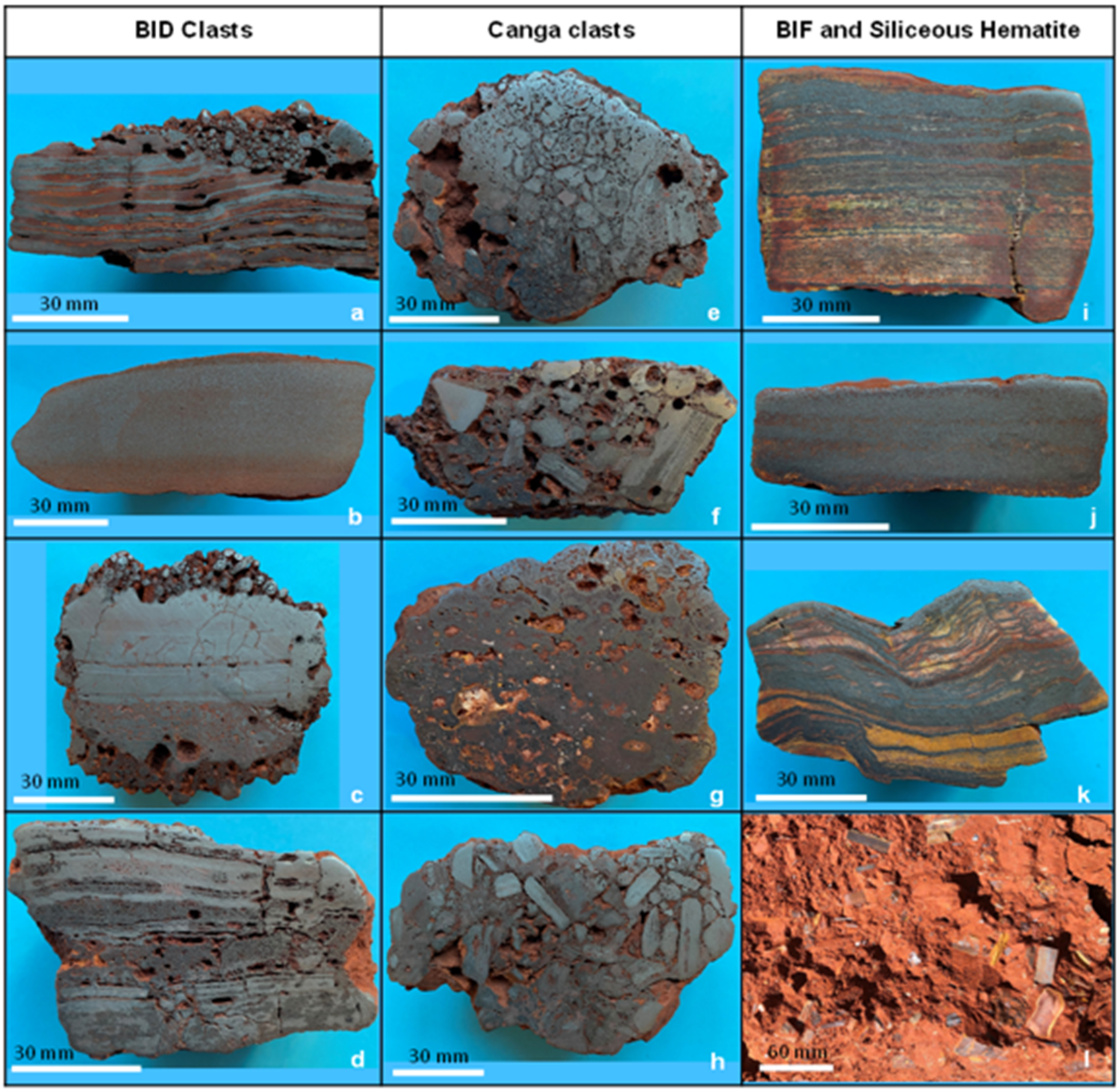

FIG 11 – Typical textures present in DID-0 to DID-3 clasts.

Some BID and canga clasts contain an outer 5–10 mm wide rim of maghemite and some internal rims of pisoids may also be of maghemite. The replacement maghemite is often asymmetrically distributed around a particle rim, with the clast example in Figure 11a only containing maghemite in the pisoids (upper right) and along just the 5 mm left rim of the clast. Some clasts contain a 0.1–2 mm rim/cutan of brown goethite or hydrohematite replacement of goethite.

The main gangue clast texture is chert (10–30 per cent of total DID), often fresh to only slightly weathered (Figure 11i) or displaying micropores along quartz-quartz grain boundaries that are interpreted as weak dissolution from incipient supergene leaching. Typically, the BIF clasts are far less common than expected and are composed of quartz microbands and minor stilpnomelane-rich microbands alternating with either disseminated microplaty hematite (Figure 11i), nanoplaty hematite or martite (Figure 11k).

Examination of the sand and silt size fraction under a petrographic microscope indicates it is composed of fine chert and quartz sand (10–40 area per cent), goethite (5–40 area per cent), hydrohematite and hematite ooids (0.25–2 mm apparent diameter, 20–60 area per cent). The finest (<0.038 mm) size fractions are dominated by ferruginous clay with minor aluminous vitreous goethite and hematite/hydrohematite. There is an increasing abundance of ferruginous clays going stratigraphically upwards from DID-2 to DID-0, whilst clays are almost frequently absent from DID-3.

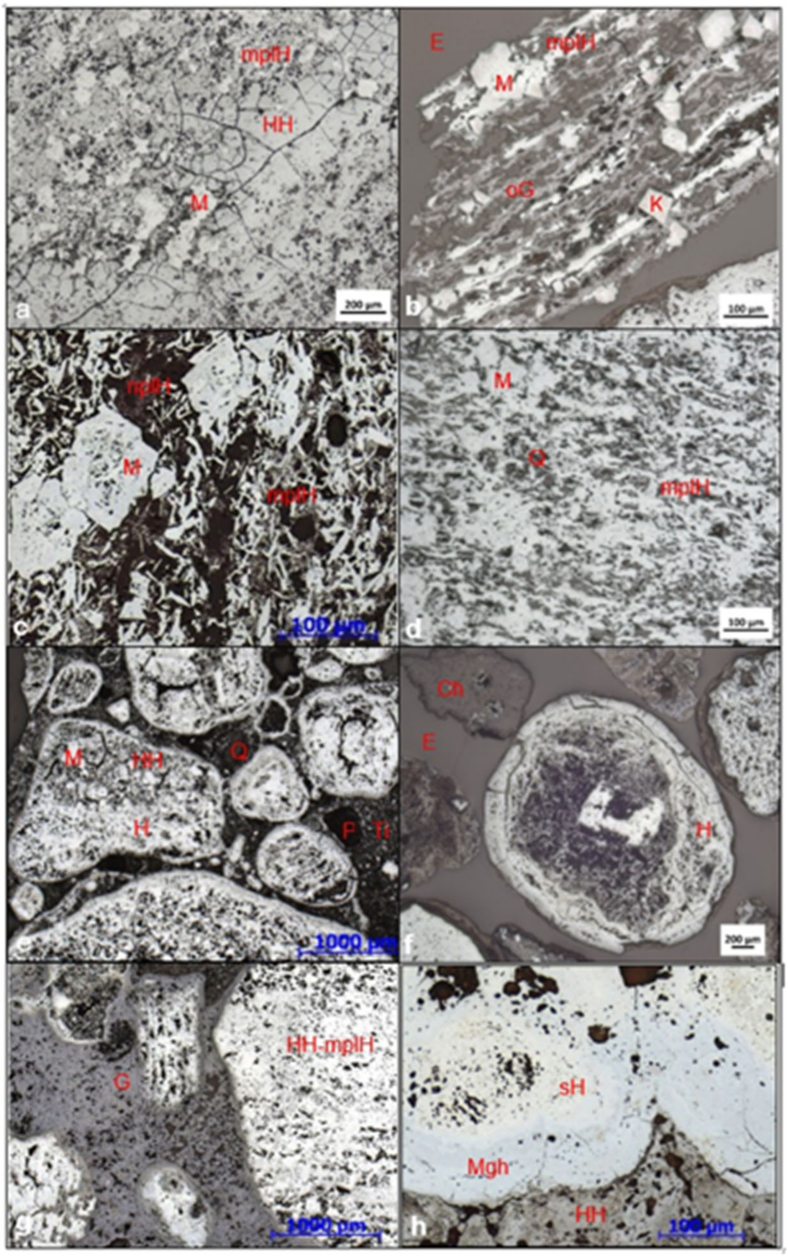

FIG 12 – Photomicrographs of typical DID-0 to DID-5 clast textures. Reflected plane polarised light. mplH = microplaty hematite, H = hematite, HH = hydrohematite, M = martite, E = epoxy resin, K = kenomagnetite, oG = ochreous goethite, Q = quartz, nplH = nanoplaty hematite, Ch = chert, G = brown goethite, Mgh = maghemite, sH = secondary hematite.

FIG 13 – Large DID-1 canga cobble of biscuity (>10 mm) hematite clasts and 2–5 mm hematite pisoids cemented by goethite-hematite-ferruginous clay. White plant rootlets colonised on matrix, macropore and clast surfaces.

DISCUSSION

Previous DID genesis models

McKenna and Harmsworth (1998) suggested the hematite-rich ferruginous carapace of the Hamersley surface as the source of the B2D DID and together with Morris (1994) interpreted the hematite canga as being derived from unconsolidated hematite detritals by cementation during hiatuses in deposition. The NW Hamersley area around Solomon consists of a Brockman Iron Formation plateau environment of broad folds and long sinuous valleys floored by Brockman Iron Formation, referred to as 'Brockman IF Plateau Valleys' by Kneeshaw and Morris (2014). Regional stripping of the Hamersley surface (HS3) during the mid – to late-Miocene is believed by Kneeshaw and Morris (2014) to have produced the CID and exposed Brockman BID which during a Pliocene-Quaternary period of major renewal of exposure and erosion resulted in the deposition of extensive CzD3 DID iron gravels. The final history is thought to involve stripping of BIF ridges to produce BIF-dominant scree in most valleys followed by current erosion cutting down through CzD3 DID to produce the deep gorges in BIF of the Hamersley Ranges, including the northern range-front areas.

For the B2D deposit, model Morris (1994) and Kneeshaw and Morris (2014) defined three stages of DID ore accumulation and nine detailed stages in the genesis model summarised as:

1. Goethitisation of the valley floor as part of pre-CID HS2 and post-CID weathering.
2. Shallow carapace and hydrated zone developed over outcropping BID ore which was partially stripped and transported to form the basal low-P proximal accumulation of CzD3 followed by ferruginisation of the detritals matrix in the vadose zone of the deposit to form canga.
3. Erosion and stripping of loose surficial detrital sediment with partial dehydration of the upper level of the cemented zone.
4. Erosion of bedrock ore and slow accumulation of mimetic-textured loose detritals.
5. Shallow ferruginous cementation from run-off waters from above along the base of the hardened zones as they formed. Stripping and exposure of detrital material and dehydration.
6. Period of accumulation followed by a new cementation phase.
7. Erosion from outcrop to complete the main ore sequence.

8. Erosion of outcrop reaching down to the primary M-G ore and then into BIF, giving rise to increasing goethitic ore and BIF in the upper non-commercial detrital accumulations.
9. Thick siliceous hardpan development in the upper BIF-rich detritals sequence.

Dalstra (2011) presented a similar but more comprehensive six stage genetic model for DID.

Simpson *et al* (2011) presented a simplified DID genetic model for DID involving three cycles of deposition with each having an intervening hiatus and erosional period.

DID Genesis model

Key observations of the DID at Solomon that impact on ore genesis constraints in the NW Hamersley Province include:

- The most significant accumulations of DID-0 to DID-5 are located in tributary valleys that have been cut through Joffre Member, Whaleback Shale Member and down into the Dales Gorge Member.
- The majority (>90 per cent) of the mineralised clasts in DID-4 to DID-0 are of Joffre Member BID interpreted Palaeoproterozoic hypogene microplaty-nanoplaty hematite-disseminated martite in a matrix of later supergene Mesozoic replacement ochreous goethite or microplaty hematite-disseminated martite in a matrix where the ochreous goethite matrix has been completely dehydrated to hydrohematite. In contrast, the expected Mesozoic–Palaeocene BID martite-goethite supergene style of mineralisation (eg B2D deposit, McKenna and Harmsworth (1998)) is only present in DID-4 to DID-1 in low (<5 per cent) levels or is absent.
- Hematite and hydrohematite clasts, pisoids, ooids and reworked hematite canga clasts predominate in DID-3, where minor (<15 per cent) goethite is present.
- The longitudinal section provides key evidence to support the mid- to late-Miocene CID being directly overlain by younger Pliocene to Quaternary DID-0 to DID-4, consistent with evidence presented for the Caliwingina North CID-DID by Dalstra *et al* (2010).

The interpreted genesis model for Solomon DID invokes the involvement of initial hypogene Palaeoproterozoic microplaty-nanoplaty hematite-disseminated martite mineralisation, along structurally controlled faults, hosted by the Joffre Member followed by (as outlined in the steps of Figure 14):

1. Mesozoic to Palaeocene supergene leaching of earlier microplaty-nanoplaty hematite-disseminated martite mineralisation (m-nplH-M) with replacement of remaining BIF quartz and carbonate matrix by ochreous goethite to form microplaty-nanoplaty hematite-disseminated martite-ochreous goethite mineralisation (m-nplH-M-oG) in the Joffre Member. Supergene leaching has also resulted in removal of phosphorus. Active weathering and erosion to form the pre-Miocene valley topography and weathered and hard capped Dales Gorge Member basement.
2. Stripping of the Miocene surface to deposit goethite pisoids and ooids, derived from weathering of the BID micro-nanoplaty hematite-martite-ochreous goethite mineralisation (Figures 11a and 15), and transport to the main CID channel, followed by transport of sediment into the channel and formation of the Oakover Formation. Formation of a Pre-Pliocene basal conglomerate over the weathered Dales Gorge Member basement.
3. Erosion of the valley walls and deposition of detrital clasts and matrix material (DID-5 and DID-4) over the basal conglomerate.
4. Transport and deposition of BID micro-nanoplaty hematite-martite-ochreous goethite clasts and matrix material with subsequent downward percolation of groundwater resulting in goethite cementation of DID-4 clasts followed by hematite and minor maghemite replacement of goethite matrix, ochreous goethite-nanoplaty hematite in clasts and goethite pisoids-ooids. Results in formation of hematite cemented canga. Potentially DID-5 may have formed by the same process as DID-4, but with later secondary ochreous goethite replacing earlier hematite replacements of in situ canga clasts and matrix. The BID micro-nanoplaty hematite-martite-ochreous goethite mineralisation is preferentially eroded due to being softer than the outer halo

of Palaeoproterozoic primary m-nplH-M-quartz mineralisation which has not undergone later supergene replacement of quartz and carbonate gangue by supergene ochreous goethite. The goethite pisoids-ooids derived from weathering of BID micro-nanoplaty hematite-martite-ochreous goethite mineralisation are transported, deposited then replaced by hematite, hydrohematite and maghemite.

5. Initial erosion and transport of DID-4 hematite cemented canga as clasts and hematite pisoids, to form the initial well sorted base of DID-3 followed by continued erosion of valley walls with unconsolidated detritus covering most of DID-4. DID-3 also has extensive dehydration of goethite in clasts and goethite pisoids to hematite/hydrohematite and lacks consolidation, but DID-3 dehydration may have been coeval with dehydration of DID-4.
6. Erosion from the harder Joffre Member siliceous hematite (m-nplH-M-quartz) and minor BIF includes mixed detritus from the erosion of the underlying DID-5 to DID-3 and remnant BID m-nplH-M-oG clasts to form DID-2.
7. Continued erosion of the valley walls and reworking and transport of earlier DID with an increasing Joffre Member siliceous hematite mineralisation and BIF as well as clays derived from weathering of Al-silicates in the BIF. Quartz sand is potentially derived from supergene grain boundary leaching of chert quartz grains at the site of BID micro-nanoplaty hematite-martite-ochreous goethite mineralisation followed by erosion and transport into the valley. The final deposition of Quaternary colluvium is channelised and cross-cuts DID-4 near the base of the hills (Figure 11l) but forms a thin sheet of ferruginous clays and BIF-rich clast detrital material along the valley floors.

New work is needed on age dating of the goethite and palynology to better constrain absolute timing and DID genesis. Examination of fossilised and hematised hardwood in DID-4 may also help constrain timing along with recognition that ancient to modern plant roots have colonised the highly microporous and groundwater-permeable DID.

Kneeshaw and Morris (2014) attributed the presence of kenomagnetite in DID to formation from heating during surface bush fires, followed by slow oxidation to maghemite followed by final inversion to hematite. In this study kenomagnetite and maghemite were found to have replaced specific microbands within pisoids and for a kenomagnetite-maghemite boundary to cut across cemented canga clasts and matrix over several centimetres. An alternative interpretation is that kenomagnetite may have formed by a nonredox reaction (Equation 1; via addition of Fe^{2+}), as proposed by Ohmoto (2003), or as part of a local slightly acidic and reducing environment (Equation 2; redox reaction) due to the presence of weak organic acids generated from breakdown of organic matter that was growing within the DID profile (eg Figure 13).

$$Fe_2O_{3(hm)} + Fe^{2+} + H_2O \rightarrow Fe_3O_{4(mt)} + 2H^+. \tag{1}$$

$$3Fe_2O_{3(hm)} + 2H^+ + 2e^- \rightarrow 2Fe_3O_{4(mt)} + H_2O. \tag{2}$$

The weak organic acids carried by groundwater may also be responsible for the irregular vermicular-shaped network of macropores (Figures 8c, 9c,11a and 11f), which cross-cut all BID microbanding, DID clasts and hematite matrix, through interpreted localised dissolution of hematite and goethite followed by transport of iron in solution and deposition elsewhere as goethite. The likely mechanism for dissolution of hematite and goethite requires further investigation.

It is recommended that experimental research is required to prove or disprove the nonredox theory of Ohmoto (2003) for Pilbara DID kenomagnetite formation and the mechanism for the replacement of goethite matrix and clasts by hydrohematite/hematite and maghemite within thick (>5 m) contiguous sequences of DID-4.

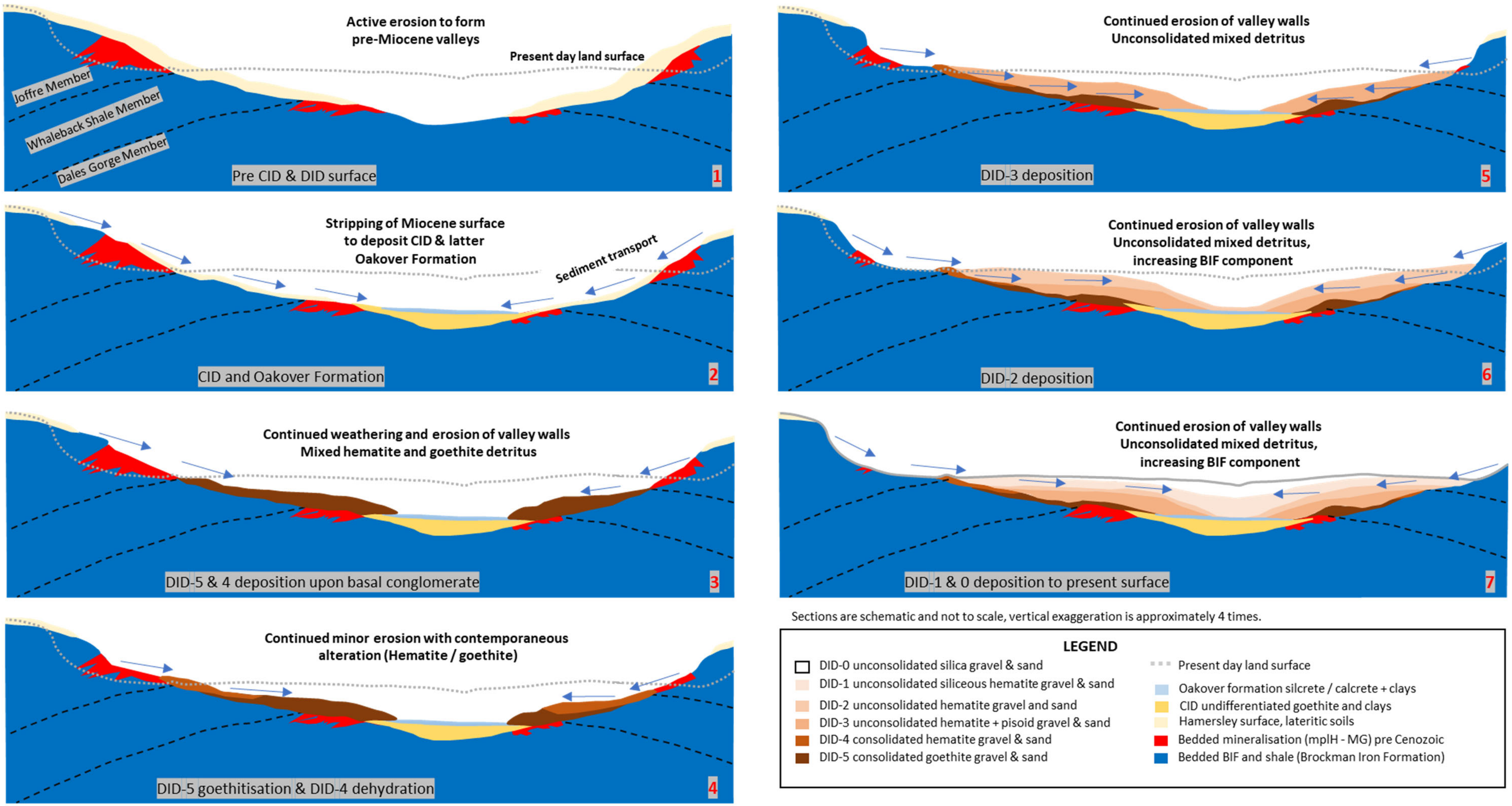

FIG 14 – Conceptual schematic for DID genesis.

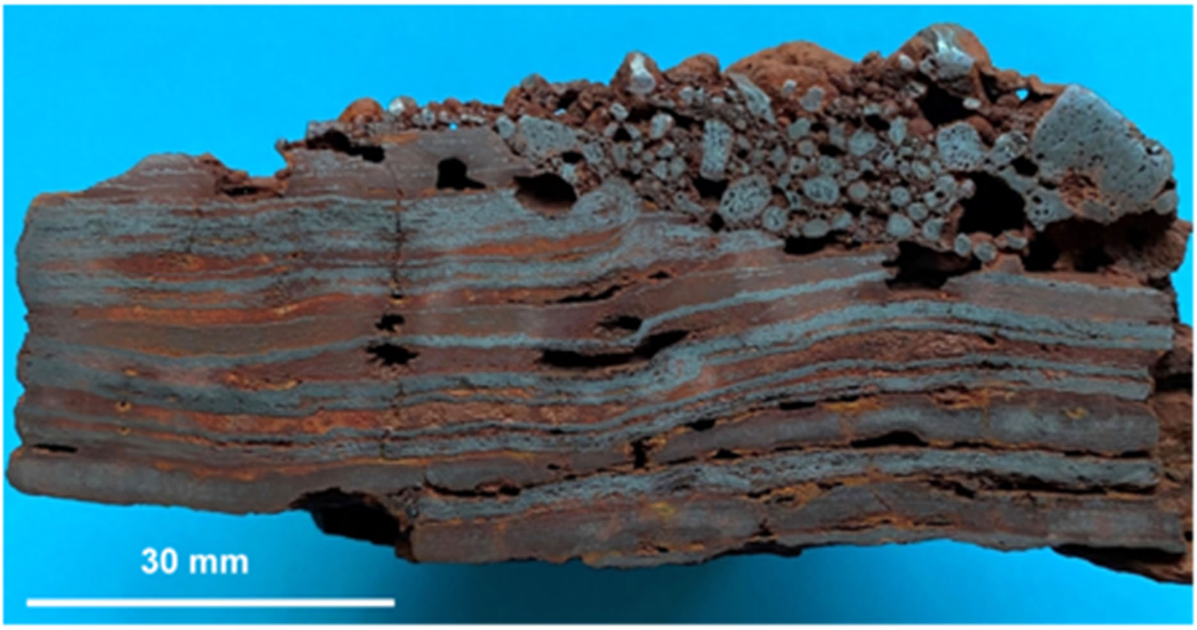

FIG 15 – BID Microplaty hematite with disseminated martite microbands (grey) in a microporous matrix of nanoplaty hematite-ochreous goethite (red). Note BID microbands are cross-cut by later dissolution macropores and hematite-maghemite replaced goethite pisoids (upper right).

CONCLUSIONS

The DID mineralisation at Solomon can be subdivided into six distinct stratigraphic units (DID-0 to DID-5) based on differences in clast and matrix types, degree of consolidation/lithification and replacement textures. The most significant accumulations of DID-1 to DID-5 are all located in tributary valleys that have been cut through the Brockman Iron Formation.

Palaeoproterozoic siliceous hematite (m-nplH-M-quartz) hypogene mineralisation of the Joffre Member then underwent Mesozoic to Palaeocene supergene leaching of quartz and replacement by ochreous goethite to form BID m-nplH-M-oG mineralisation followed by erosion and transport as clasts and detritus as the main source rocks for the DID. Very little of the DID source rock is of martite-goethite supergene mineralisation. Subsequent goethite cementation and lithification of DID-4 clasts and matrix was followed by replacement of goethite by hematite and hydrohematite.

Subsequent periods of erosion of DID-4 as hematite clasts and pisoids initially formed DID-3, followed by deposition of DID-2 to DID-0 through reworking of older DID units and deposition of DID-5 to DID-3 clasts and pisoids/ooids, as well as siliceous hematite and BIF derived from Joffre Member in the hills and slopes.

ACKNOWLEDGEMENTS

We wish to thank Fortescue for the permission to publish information within this paper. There was also significant contribution from many employees with respect to figures, images and conversations for the information contained in this paper. Especially, Robert Walker is acknowledged for his petrology images, and Robyn Clout for her photography of the hand specimens.

We would also like to acknowledge the late Mal Kneeshaw and the late Dick Morris for their papers which has instigated much more discussion on the Cenozoic geology of the Pilbara.

REFERENCES

Butt, A L, Hawke, P J and Flis, M F, 2002. Of detritals, derivatives and determination – an example of detrital iron discovery, in *Proceedings Iron Ore 2002*, pp 67–70 (The Australasian Institute of Mining and Metallurgy: Melbourne).

Clout, J M F, Simpson, C and Counsell, C, 2017. Chichester and Solomon bedded and channel iron deposits, In *Australian Ore Deposits* (Ed. G N Phillips), Monograph 32, pp 351–358 (The Australasian Institute of Mining and Metallurgy: Melbourne).

Dalstra, H J, 2011. From Banded Iron Formation to Iron Ore—Genetic models and their application in iron ore exploration in the Hamersley Province, Western Australia, in *Proceedings Iron Ore 2011*, pp. 73–82 (Australasian Institute of Mining and Metallurgy: Melbourne).

Dalstra, H J, Gill, T, Faragher, A, Scott, B and Kakebeeke, V, 2010. Channel iron deposits, a major new district around the Caliwingina Creek, central Hamersley Ranges, Western Australia. *Transactions of the Institutions of Mining and Metallurgy, Applied Earth Science* 119, B12–B20.

Jackson, J A, 1997. *Glossary of Geology*, 4th Edition. American Geological Institute, Alexandria, Virginia USA.

Kneeshaw, M and Morris, R C, 2014. The Cenozoic detrital iron deposits of the Hamersley Province, Western Australia. *Australian Journal of Earth Sciences*, 61, 513–586.

Kepert, D, Clarke, N, Simpson, C and Edwards, D, 2010. Discovery of the Solomon Iron Deposits, Hamersley Province, Western Australia, *Transactions of the Institution of Mining and Metallurgy, Applied Earth Science*, 119: B21-B27.

McDonald, G D, 2011. Geochemical characterisation of Flinders Mines' Pilbara Iron Mineralisation. *Proceedings of Iron Ore 2011*, pp. 301–313 (The Australasian Institute of Mining and Metallurgy: Melbourne).

McKenna, D M and Harmsworth, R A, 1998. Brockman No.2 detritals (B2D) iron ore deposit, in *Geology of Australian and Papua New Guinean Mineral deposits* (Eds. D A Berkman and D H Mackenzie), pp 375–380 (The Australasian Institute of Mining and Metallurgy: Melbourne).

Morris, R C, 1994. Detrital iron deposits of the Hamersley Province, CSIRO Division of Exploration and Mining, restricted report 76R (unpublished).

Morris, R C and Kneeshaw, M, 2011. Genesis modelling for the Hamersley BIF-hosted iron ores of Western Australia—a critical review. *Australian Journal of Earth Sciences* 58, 417–451.

Ohmoto, H, 2003, Nonredox transformations of magnetite-hematite in hydrothermal systems: *Economic Geology*, v. 98, p. 157–161.

Petts, A E, McDonald, G D and Corlis, N J, 2011. Channel and detrital iron deposits of the Flinders Mines Pilbara Iron Ore, *Proceedings of Iron Ore 2011*. pp. 125–132 (The Australasian Institute of Mining and Metallurgy: Melbourne).

Ramanaidou, E R, 2009. Genesis of lateritic iron ore from banded iron formation in the Capanema mine (Minas Gerais, Brazil). *Australian Journal of Earth Sciences* 56, 605–620.

Simpson, C, Storey, D, Kepert, D, Boyd, R and Nitschke, N, 2011. Solomon Iron Deposits – continued growth and development, in *Proceedings Iron Ore 2013*, pp 649–660 (The Australasian Institute of Mining and Metallurgy: Melbourne).

Tylkowski, L N, Corlis, N J, McDonald, G D, Petts, A E, Jennings, M F and Thomas, B J, 2013. The hunt for hydrous bedded iron deposits—an investigation into Flinders Mines' Blacksmith tenement, in *Proceedings of Iron Ore Conference 2013*, pp. 121–126 (The Australasian Institute of Mining and Metallurgy: Melbourne).

Preliminary 3D geological model and structural analysis of the Neoarchean to Palaeoproterozoic Hamersley Basin, Pilbara, Western Australia

A Piechocka[1], M Jessell[2], D McB Martin[3], M Lindsay[4] and E Ramanaidou[5]

1. Senior Research Scientist, Commonwealth Scientific and Industrial Research Organisation, Kensington WA 6151. Email: nishka.piechocka@csiro.au
2. Professor, University of Western Australia, Crawley WA 6009. Email: mark.jessell@uwa.edu.au
3. Manager State Geoscience, Geological Survey of Western Australia, East Perth WA 6004. Email: david.martin@dmirs.wa.gov.au
4. Principal Research Scientist, Commonwealth Scientific and Industrial Research Organisation, Kensington WA 6151. Email: mark.lindsay@csiro.au
5. Commodity Research Leader, Commonwealth Scientific and Industrial Research Organisation, Kensington WA 6151. Email: erick.ramanaidou@csiro.au

ABSTRACT

The Hamersley Basin of Western Australia, approximately 500 km long by 200 km wide, is recognised globally for its rich endowment of iron ore resources. Two types of bedded iron ore mineralisation are recognised: the Proterozoic hypogene martite-microplaty hematite ores; and the more recent Cenozoic supergene martite-goethite ores. Exploration strategies depend on the style of mineralisation being targeted; however, stratigraphy and structure are fundamental controls on both ore types. Therefore, the ability to visualise the 3D geology of the entire basin is critical for the understanding of iron ore occurrences and their relationship to ore genesis of bedded iron ore mineralisation. However, due to the large size of the basin, generating a 3D geological model of the regional stratigraphy and structure has not been possible, or prioritised, primarily due to software limitations. Recent advances in implicit automated geological modelling presents an ideal opportunity to develop a 3D model of the entire Hamersley Basin. The innovative *Loop* software was used to model open source geological data (ie geological mapping, outcrop orientation data, and fault data) sourced from the Geological Survey of Western Australia. In addition to generating a 3D geological model, information such as stratigraphic thickness and fault offset information was extracted using the *map2loop* module and demonstrated its application to exploration targeting. This study demonstrates how a basin-wide 3D geological model was used to conduct a regional structural analysis of the Hamersley Basin. The results of this study provide opportunities for other prospective regions to be rapidly modelled in order to enhance the understanding of the geology and improve exploration targeting.

INTRODUCTION

Generating a basin-wide 3D geological model can be challenging due to software limitations, time constraints and data availability. One example is the well-endowed and extensively explored and mined 500 km long by 200 km wide Hamersley Basin, of the Pilbara Craton, Western Australia (Figure 1). Although, the iron ore mining and exploration companies produce deposit-scale geological models for resource estimation purposes, no regional scale basin-wide geological model currently exists. Furthermore, access to these company models is rare due to confidentiality; however, there are several publications that show examples of modelled deposits across the Hamersley basin (eg Bodycoat, 2010; Crowe, 2012; Egglseder *et al*, 2017; Perring, Crowe and Hronsky, 2020) utilising different modelling packages.

The Hamersley Basin banded iron formations (BIF) (ie the Brockman Iron Formation and Marra Mamba Iron Formation (Figure 1) are host to ~50 Gt of iron ore mineralisation (Knight *et al*, 2018) and is recognised as the world's largest source of banded iron formation hosted iron ore mineralisation (Clout and Simonson 2005; Hagemann *et al*, 2016). The two styles of bedded iron ore mineralisation are the localised martite-microplaty hematite ores which account for <5 Gt and the widespread martite-goethite ores making up close to 50 Gt (Knight *et al*, 2018). The martite-microplaty hematite deposits were the first to be mined and are represented by the well-known Mt Tom Price, Mt Whaleback and Paraburdoo mines, opened in 1966, 1968, and 1972 respectively

(Perring, Crowe and Hronsky, 2020). Although Figure 1 only shows the locations of known martite-microplaty deposits/mines hosted within the Brockman Iron Formation, there are significant occurrences of martite-microplaty minerastalition hosted in the Marra Mamba Iron Formation in the Chichester Range (Thorne *et al*, 2014). The more abundant but less studied bedded ore is the martite-goethite iron ores. Examples of martite-goethite mines in the Hamersley include Brockman, Marandoo, West Angelas, Mining Area C, South Flank and Jimblebar (Figure 1). Despite there being strong support for two different genetic models (eg Morris, 1980; Powell *et al*, 1999; Taylor *et al*, 2001; Perring, Crowe and Hronsky, 2020) resulting in two styles of bedded iron ore mineralisation, it is unequivocal that faults play a fundamental role in both styles (eg Morris, 1985; Powell *et al*, 1999; Clout and Simonson, 2005; Dalstra, 2006, 2014; Bodycoat, 2010; Perring, Crowe and Hronsky, 2020). Furthermore, structures play an important role in targeting for iron ore (martite-microplaty or martite-goethites ores) and are used as critical exploration criteria for regional scale target generation (Hannon *et al*, 2005).

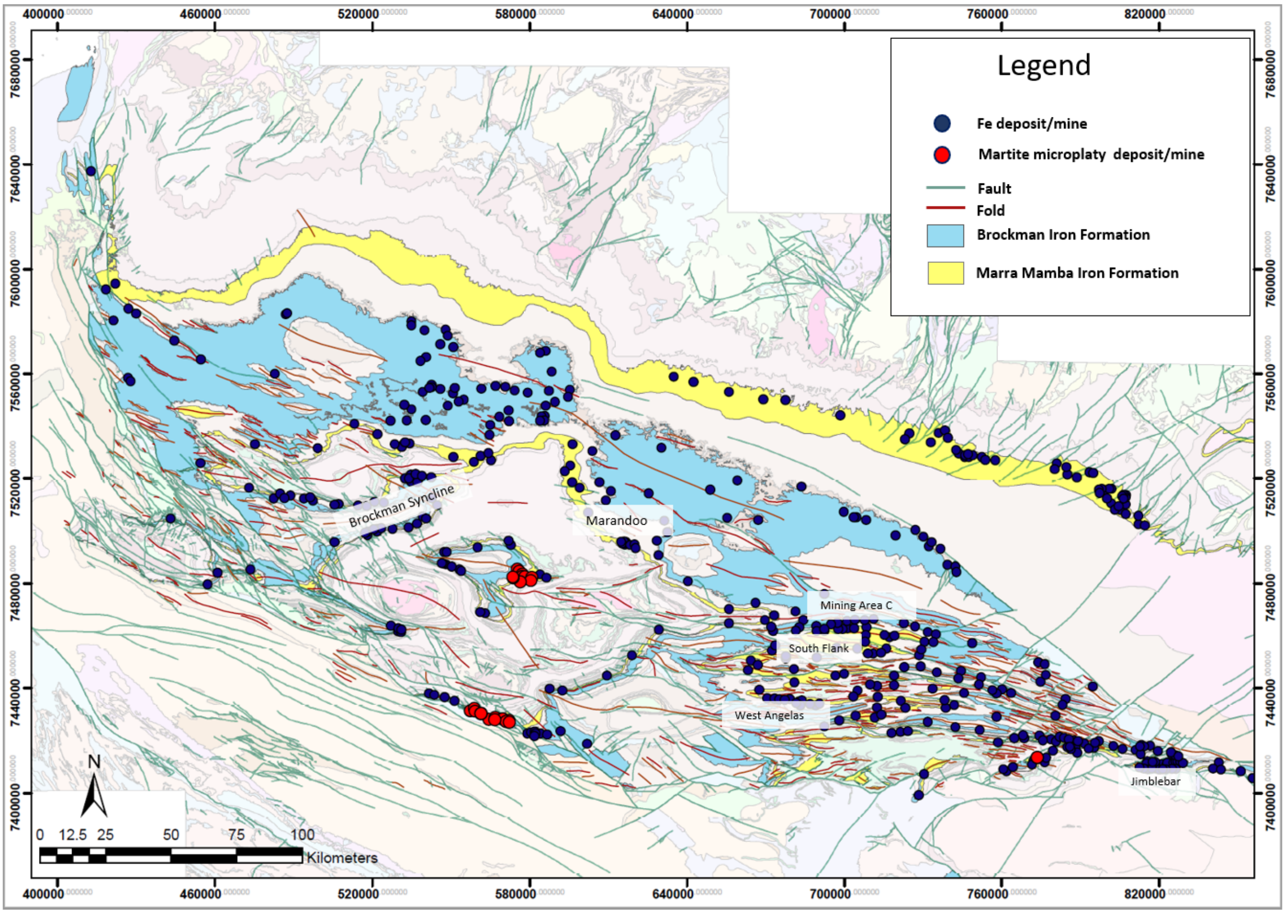

FIG 1 – Basin-wide outcrop map highlighting the occurrence of the Brockman Iron Formation and the Marra Mamba Iron formation with the locations of key mines and deposits. Only the key iron formations are shown in the legend, for full stratigraphic references refer to Fortescue-Hamersley (2018). Fe deposit/mine refers to martite-goethite bedded iron ore mineralisation and only the Brockman Iron Formation hosted martite-microplaty mines are shown on the map.

The availability of basin-wide geological mapping (GSWA, 2016a; Fortescue-Hamersley, 2018) presents the ideal opportunity to produce a regional 3D geological model and to study the relationships between the faults and known bedded iron ore mines and deposits. Here we present a new methodology of implicit modelling using the Hamersley Basin as an example. The implicit modelling presented here is based on recent advances generated as part of the *Loop* Consortium (eg Grose *et al*, 2020; Jessell *et al*, 2021). Despite the economic significance of the iron ores of the Hamersley Basin their origin remains equivocal. This study utilises a regional 3D model to provide new knowledge to assist in future studies relating to the genesis of the martite-microplaty and martite-goethite iron ores the relationship between faults and iron ore deposits.

METHODOLOGY

To generate the 3D geological model of the Hamersley Basin the python library *map2loop* (Jessell *et al*, 2021) was used to deconstruct the map and provide the data inputs to *LoopStructural* (Grose *et al*, 2020) to build the geological model. *Map2loop* and *LoopStructural* are part of the larger Loop consortium; however, the work presented here relates to the functions of *map2loop* and *LoopStructural.* Specifically, the relevant functions of *map2loop* that were used in this study will be presented here, for the detailed methodology refer to Jessell *et al* (2021). The *map2loop* library uses the Geopandas library to load data from several persistent formats (ESRI shapefiles, MapInfo tab files, JavaScript Object Notation (JSON) format files) and can also load data from Web Feature Services (WFS). Geospatial data can be in any standard coordinate reference system (assuming a European Petroleum Survey Group (EPSG) code is supplied, http://epsg.io). In the example we present here, we use the 2016 1:500 000 Interpreted Bedrock Geology map of Western Australia (GSWA, 2016a), the Fortescue-Hamersley (2018) Geological Mapping and the WAROX outcrop database (Compilation of WAROX data, 2016) as sources of the data needed to build a first-pass model of the Hamersley Basin, Pilbara, Western Australia. The below discussion will be structured according to the input data and the subsequent outputs.

Data inputs

The following is an outline of the input data (polygons, polylines and point data) used to build the Hamersley Basin 3D geological model (Figure. 2):

- Chronostratigraphic polygon and multipolygon layer: this vector layer describes the chronostratigraphic information that underlies the complete geological map. To ensure entire basin coverage multiple geological mapping layers were used in this study including the GSWA 100K, 250K and 500K Geology mapping (Fortescue-Hamersley, 2018; GSWA, 2016a).
- Fault polyline and multipolyline layer: this vector layer describes the location, orientation and displacement information on mapped faults or narrow shear-zones at the surface. The fault data used in this study was sourced from the GSWA 100K and 250K Pilbara faults and folds layer (Fortescue-Hamersley, 2018; GSWA, 2016b).
- Fold axial trace polyline layer: this vector describes the location and polarity (anticline versus syncline) information on mapped fold axial traces, defined by the intersection of the fold axial surface and the surface of the Earth. The fault data used in this study was sourced from the GSWA 100K and 250K Pilbara faults and folds layer (Fortescue-Hamersley, 2018; GSWA, 2016b).
- Bedding orientation point layer: this vector layer describes the local orientation of bedding, and is often missing from map packages, but can be found in the separate databases, or original field notebooks. The orientation data used here was sourced from the GSWA WAROX database (Compilation of WAROX data, 2016).
- Reference stratigraphy: this data is extracted from a stratigraphic database (if available) that allows access to detailed stratigraphic information at the formation-level and above. The data in this study was sources from the Geoscience Australia's Australian Stratigraphic Units Database (Geoscience Australia, 2017).
- Digital terrain model (DTM): this grid layer, usually derived from the SRTM (Shuttle Radar Topography Mission; Farr *et al*, 2007) or GDEM (Aster Global Digital Elevation Map; NASA/JPL, 2009) data sets, or a fusion of both, provides a uniform coverage of surface topography measurements over most of the continents. The *map2loop* library uses the Geoscience Australia server for 90 m coverage in Australia (Geoscience Australia, 2017), the 1 km global coverage offered by the Pacific Islands Ocean Observing System (https://pae-paha.pacioos.hawaii.edu/thredds/dem.html?dataset=srtm30plus_v11_land) or the topography.org server for 90 m or 30 m coverage outside Australia.

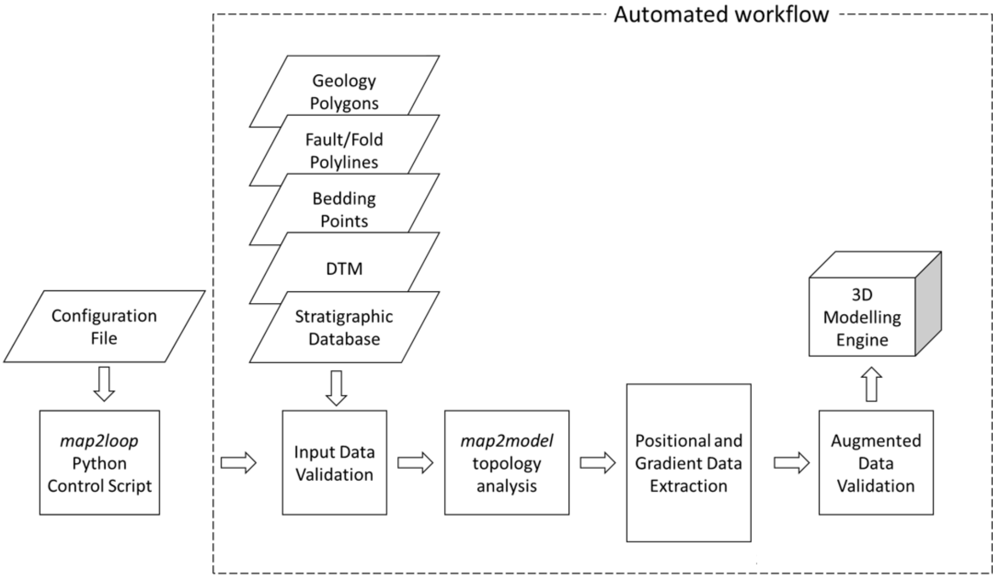

FIG 2 – Diagram highlighting the automated workflow used to generate the 3D Hamersley model in *map2loop*. The steps in the dashed rectangle are fully automated, with no manual intervention. These automated steps are described in Jessell *et al* (2021).

Data outputs

The *map2loop* library combines the inputs described above in different combinations to produce a series of minimum necessary outputs as csv, geotif and gl format files that can be used directly by the target 3D geological modelling systems, or as sources of analysis for 2D studies. Outlined below is a summary of how the different inputs are combined to produce information needed by the target 3DGM systems, grouped by type: positional outputs; gradient outputs; and topological outputs For a detailed account of the process refer to Jessell *et al* (2021). However, the specific positional, gradient and topological outputs are in most cases calculated by combinations of their inputs, and therefore the ordering below does not in general reflect the order in which these augmented data are produced by the *map2loop* library.

Positional outputs provide information on the location and shape of features and include DTM; basal contacts; fault position and dimensions; fold axial trace position and dimensions; local unit thickness; and local fault displacement (Figure 2). Features refer to contacts between units, faults, fold axial traces and bedding measurements. Gradient outputs provide information on the orientation of features and include bedding orientations; fold orientation; fault orientation; and interpolated orientation field. The third class of modelling constraints derived by the *map2loop* algorithms use the spatial and temporal topology of the map layers. Specifically, it creates network diagrams showing the stratigraphic relationships between units in the region of interest (Burns, 1988; Perrin and Rainaud, 2013; Thiele *et al*, 2016), network diagrams of the relationships between faults, and relationship tables showing whether a particular fault cuts a unit or group. Topological outputs that provide information on the spatial and temporal relationships between features and include local stratigraphy; fault-fault relationships; and fault-stratigraphy relationships (Figure 9 in Jessell *et al*, 2021).

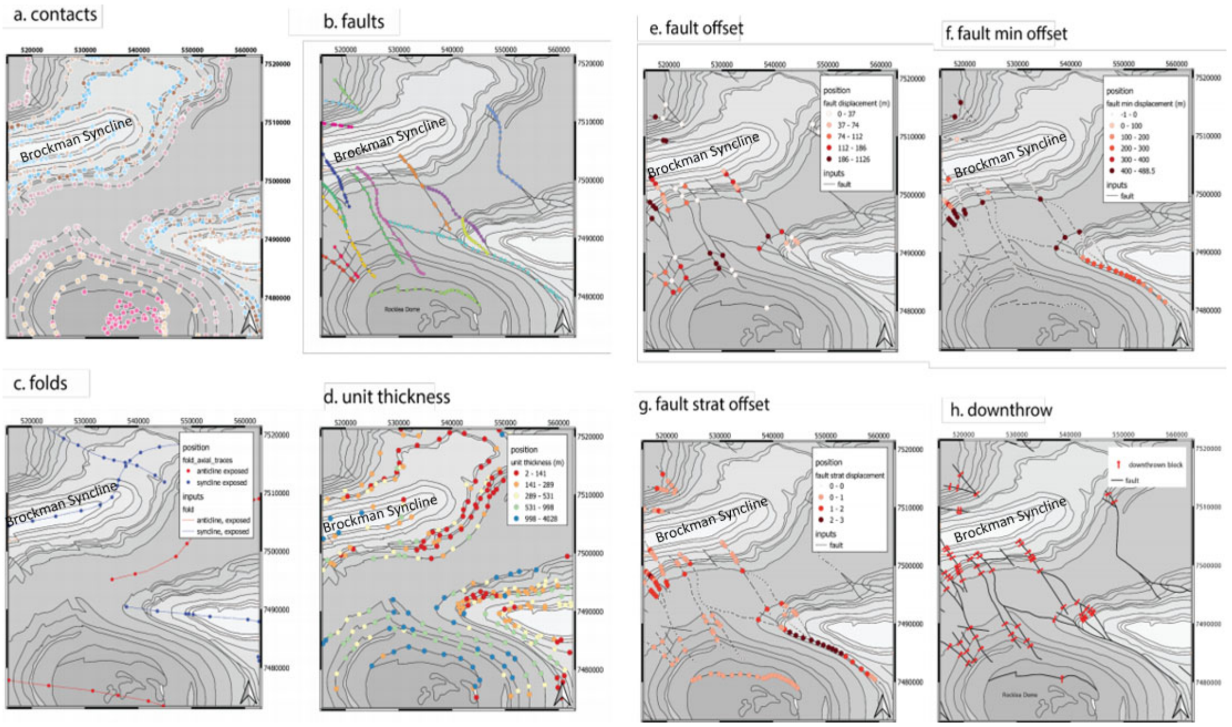

FIG 3 – Positional information derived from map: a) Basal contacts of stratigraphic units, b) Fault traces, colours randomly assigned to each fault, only faults longer than a defined length, in this case 5 km, are processed, c) Fold axial traces, d) Local unit thicknesses, e) Fault offset, assuming down-dip displacement, f) Fault offset derived from minimum stratigraphic offset, g) Stratigraphic fault offset, and, h) Fault downthrown block direction (from Jessell *et al,* 2021).

Once the augmented data types have been calculated by *map2loop*, a final validation of the data is performed. Validation checks include ensuring that there are no ‘orphan’ data, for example orientation data for units that will not be modelled, and a unit in the stratigraphy for which we have no contacts or orientations. Although this can happen in nature, current modelling systems struggle with this concept, so we need to ensure that the model will actually build by removing unresolvable data. To generate the Hamersley model the *map2loop* output data was imported into *LoopStructural* 3D modelling engine for the implicit interpolation. *LoopStructural* is a new open source 3D modelling engine connecting python libraries such as *pandas*, *numpy* and *scipy* and allows for six different interpolation algorithms to be used (Grose *et al*, 2020). One of the key features of *LoopStructural* relevant for this study is the direct link to map2loop for automated 3D implicit geological modelling, for the full methodology refer to Grose *et al* (2020).

Faults and relationship to mines/deposits

To investigate the relationship between the faults and known mines and key bedded iron ore deposits we used a two-part statistical approach using the faults _and the Fe deposit/mine layer (as shown in Figure 1) as data input files. The first is the Berman test (Berman, 1986) and tested the dependence of the deposit location intensity (number of deposits per unit area) with fault locations. The resulting p-value for the test is close to zero (3.2e-06). Figure 4A shows that the observed distribution (solid line) has higher cumulative probability values at distances proximal to the fault than would be expected if random (dashed line). While the deposit location density displays a strong dependence on locations proximal to faults, the effect of the fault location could still be weak.

The second test evaluates the discriminatory power of distance from a fault with the Receiver Operator Characteristic (ROC) curve, and the area under that curve (AUC). Figure 4B shows that using distance from a fault is a reasonable measure to evaluate dependence of deposit location with faults. If no discriminatory power was observed, the ROC curve would not deviate from dashed diagonal bisecting the chart. The curve lies away from the diagonal which indicates moderate discriminatory power with 60 per cent of deposits lying in ~35 per cent of area proximal to faults, and 80 per cent of deposits within ~62 per cent of area proximal to faults. Accordingly, the AUC value can be between 0 and 1, with 0 being lowest.

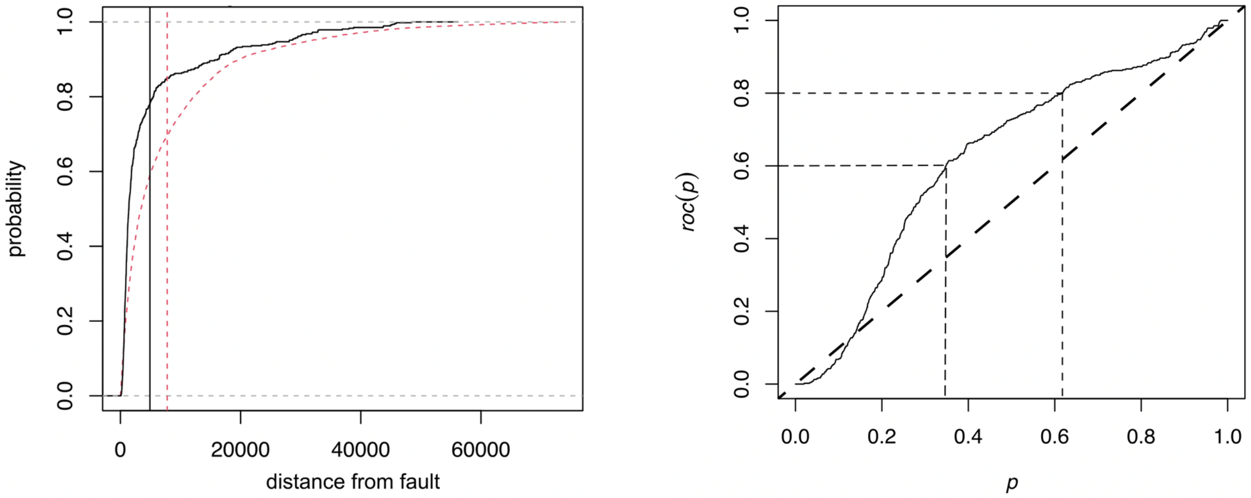

(a)

(b)

FIG 4 – (a) Berman test displaying a strong association of deposit intensity with locations proximal to mapped faults (*p* value = 3.2e-06). (b) Receiver Operating Characteristic (ROC) curve showing moderate discriminatory power of using distance from mapped faults as a measure to find association between fault and deposits. Area under curve (AUC) = 0.62.

DISCUSSION

In this study we have demonstrated a novel approach to basin-wide implicit 3D geological modelling using the Hamersley Basin as a test case (Figure 1). The results of this study provide the first 3D geological model of the entire Hamersley Basin (Figure 5). The stratigraphy was modelled at either the Group or Formation level to match the data inputs from the geological mapping. For instance, the Brockman and Marra Mamba Iron Formations were not subdivided into their respective members as the geological mapping is published at Formation or Group level. Most of the modelled faults were assigned a vertical orientation purely due to the lack of available orientation data. Some orientation data was available in the GSWA polyline layer and we obtained further fault orientation data via literature searches and some company data from drill hole televiewer data. Furthermore, any faults that were less than a 5 km in length were excluded from the modelling process.

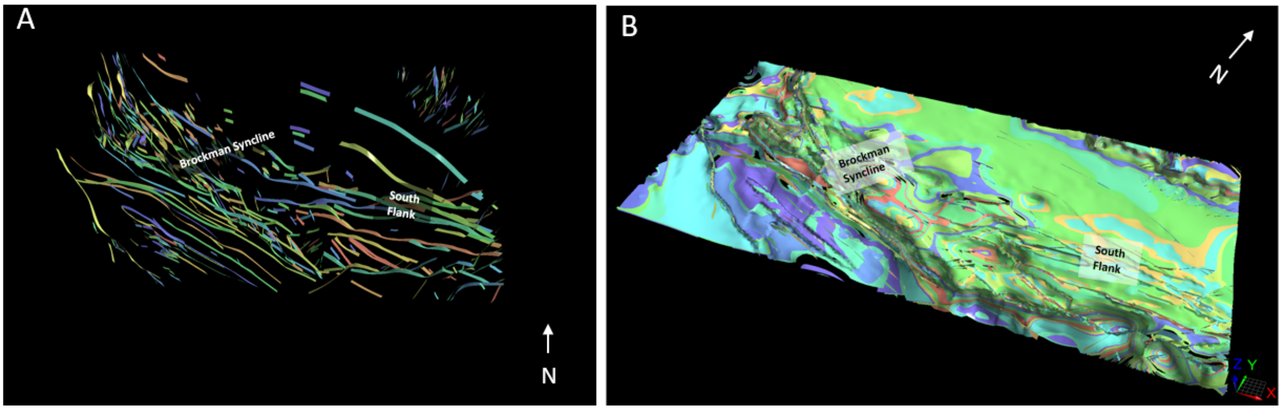

FIG 5 – (a) modelled faults. (b) modelled basin stratigraphy displayed in Geoscience Analyst.

Since the 3D model relied heavily on the open source data (bedding orientation data, geology mapping and fault data) a level of upscaling was performed. For instance, in cases where the data density was high (eg orientation data at member level) the orientation data was decimated to match the Formation to Group (c.a. 1:250 000 map) input scale. High density localised data would be suitable for modelling at deposit scale; for instance deposit scale (Jimblebar area) implicit modelling was recently conducted by Yang, Achtziger-Zupančič and Caers (2021). In contrast our aim was to generate a basin-wide geological model with well distributed data to provide an understanding of the broader structural architecture of the basin. Although there is the risk of information loss when upscaling data, appropriate decimation of data were applied to ensure that the resulting 'augmented' data points (Jessell *et al*, 2021) are representative of the higher resolution data set. Reduction via grid cell averaging is possible; however, the resulting orientations are not field measurements, but modelled approximations. At regional scales, grid cell averaging may be entirely appropriate, but this depends on how comfortable the modeller is with using modelled points to constrain another model. More sophisticated methods, such as those using the Kent Distribution (Kent, 1982; Carmichael and Ailleres, 2016) are also possible. Figure 6 shows data density maps highlighting areas of dense data and limited data. In future, we hope to obtain further fault orientation data, and bedding orientation data in areas of sparse data from sponsor companies to enable a more accurate structural representation of the Hamersley Basin to be generated.

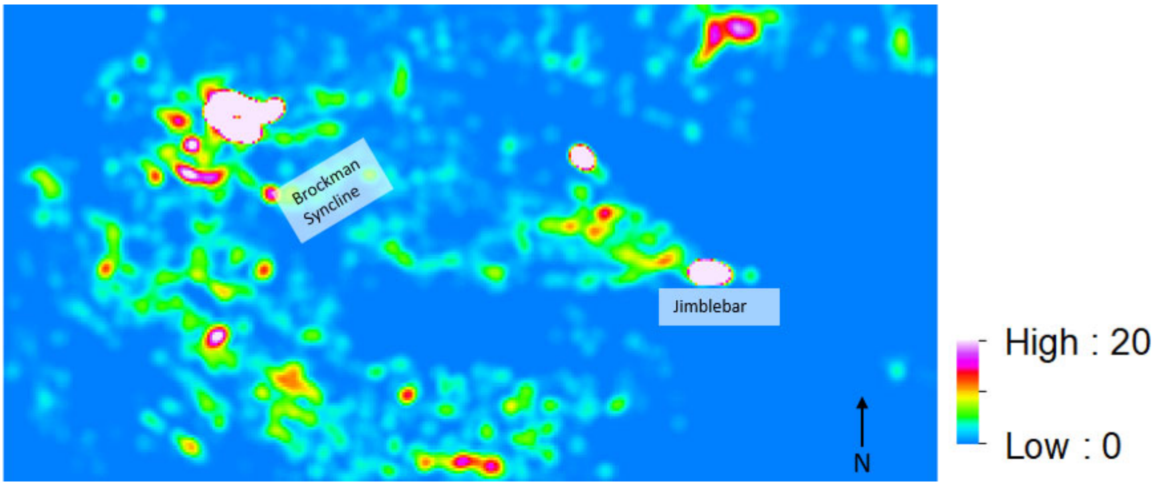

FIG 6 – Spatial bedding data density (observations per square km) for the whole basin.

The 3D geological model presented here is a regional structural and stratigraphic model generated from mostly open source data. We compared our model to two published geological cross-sections (where closely spaced drill hole data was used to produce the model): one from the western extents and the second from the eastern extents (representing two distinct structural domains in the Hamersley Basin). Figure 7a is an example from the South Flank area with our model (left) showing a broad anticline; however, the detailed cross-section (Perring, Crowe and Hronsky, 2020) exhibits a more complex fold and thrust structural setting. The difference here is largely attributed to the complex nature of the South Flank area that is difficult to resolve relying on bedding orientations alone. In the second example (Figure 7b) from the western Hamersley's Brockman Syncline deposit our model is a closer representation, showing the limb of a broad anticline, of the detailed model in Sommerville *et al* (2014). These examples demonstrate that the quality (or accuracy) of a model will only be as good as the data input into the model. Although our model does not capture local structural complexities it provides a regional framework for future geological investigations into the Hamersley Basin. Moreover, the ability to generate all necessary input data for a geological model from a set of source layers in a matter of minutes demonstrates the potential for this approach to reduce the entry barrier for geologists who wish to make 3D models as part of their exploration or research programs. However, it must be noted that the quality of the product relies on the quality of the input data and in instances of deep cover different approaches (such as using geophysical inputs) need to be considered.

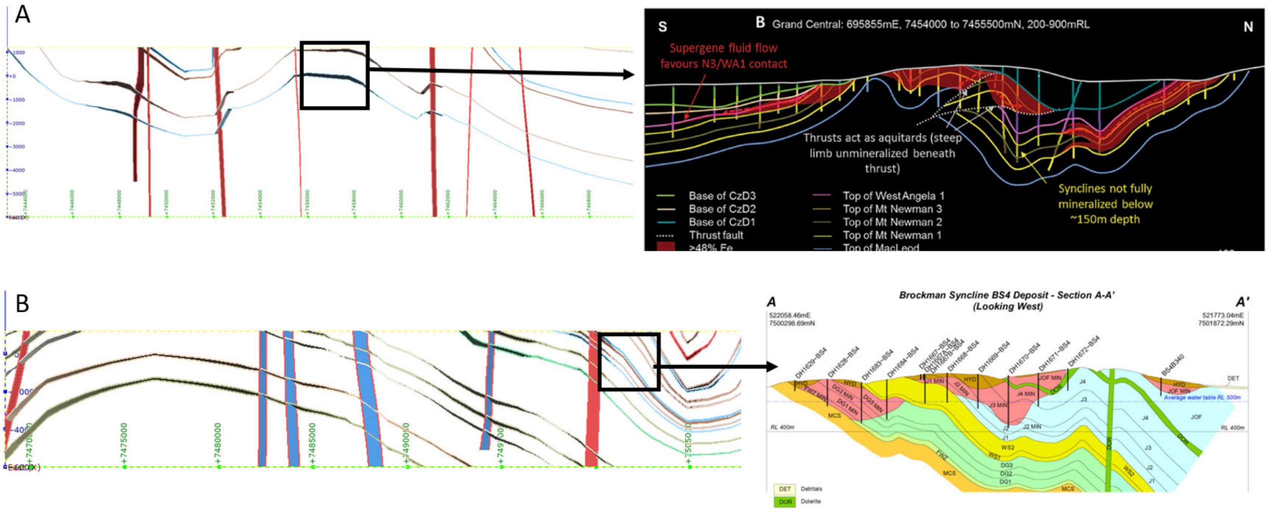

FIG 7 – Comparison of our regional 3D model against local deposit scale geological cross-sections. A. South Flank (eastern Hamersley) our model (left) and model in Perring, Crowe and Hronsky (2020) (right). B. Brockman syncline (western Hamersley) our model (left) and model from Sommerville *et al* (2014) (right).

Despite there being two accepted genetic models for the formation of iron ore mineralisation (Morris, 1980; Powell *et al*, 1999; Taylor *et al*, 2001; Perring, Crowe and Hronsky, 2020) both processes result in a significant reduction of stratigraphic thickness. For instance, in the case of martite-goethite ores the BIF to ore transition results in a ~35 per cent reduction in thickness compared to a ~45–50 per cent reduction in thickness for martite-microplaty ores (Morris and Kneeshaw, 2011). Being able to identify zones of reduced stratigraphic thickness in the Brockman Iron Formation and Marra Mamba Iron Formations would be a very useful exploration targeting tool. One of the outputs from *map2loop* is a stratigraphic thickness estimate which shows areas of stratigraphic thinning (Figure 3d). This output combined with other exploration tools (such as airborne or ground geophysics (gravity) would assist in delineating prospective bedded iron ore deposits. Furthermore, it is well established that structures play a fundamental role in promoting both styles of bedded iron ore mineralisation. Deep seated faults are favourable for the hypogene mineralisation (Taylor *et al*, 2001) whereas thrust faults are an important targeting criterion for the martite-goethite mineralisation (Powell *et al*, 1999; Perring, Crowe and Hronsky, 2020). Regional fault displacement (amount of displacement and direction of displacement) information would provide further knowledge for exploration targeting. Additional outputs from *map2loop* include the apparent and inferred true fault offset, fault stratigraphic offset (mismatch in stratigraphic level across two sides of fault) and downthrow information (Figure 3e–3h).

Our statistical analysis confirms the relationship of faults to known mines and deposits. In particular, the results of the Berman test yielded a p-value close to zero (3.2e-06) which suggests strong evidence for dependence of deposit location with fault location. Furthermore, the results of the ROC test show that the AUC is 0.62, indicates a favourable relationship of deposits/mines to the faults. These results are probably unsurprising for the exploration geologist as faults have long been recognised as important exploration vectors for martite-microplaty hematite and martite-geothite ores. What this analysis does provide is rigorous statistical support for the selection of these faults as input for the purpose of generating a geological model relevant for the mineralisation style under study.

CONCLUSIONS

The Hamersley Basin is recognised as the world's largest iron ore basin and although it has been extensively mined and explored many questions around the genesis of the iron ores remains equivocal. Producing a regional scale structural and stratigraphic model will provide a publicly available starting framework for future genesis/exploration related studies. This study demonstrates a new methodology of implicit modelling with three main input data requirements: geological mapping, outcrop bedding information and where applicable fault polylines. However, it must be noted that the quality of the model will reflect the quantity and quality of the input data. Furthermore, our statistical analysis demonstrates a strong correlation between faults and known mines and deposits, confirming that structure plays a fundamental role in the bedded iron ore genesis process. Additionally, the stratigraphic thinning and fault displacement outputs generated as a product during the modelling process can be used (in combination with other exploration tools) to aid in the target generation and delineation of prospective areas for bedded iron ore mineralisation.

ACKNOWLEDGEMENTS

This research is supported by the Minerals Research Institute of Western Australia as project M0557. We also acknowledge the support from the ARC-funded Loop: Enabling Stochastic 3D Geological Modelling consortia (LP170100985) and DECRA (DE190100431). The work has been supported by the Mineral Exploration Cooperative Research Centre whose activities are funded by the Australian Government's Cooperative Research Centre Programme. This is MinEx CRC Document 2021/43. Source data provided by GSWA and Geoscience Australia. DM publishes with the permission of the Executive Director Geological Survey and Resource Strategy.

REFERENCES

Berman, M, 1986. Testing for spatial association between a point process and another stochastic process. *Applied Statistics*, 35: 54–62.

Bodycoat, F M, 2010. Stratigraphic and structural setting of iron mineralisation at E Deposit (East), Area C, Hamersley Province, Western Australia, *Applied Earth Science*, 119(1): 49–55.

Burns, K L, 1988. Lithologic Topology and Structural Vector Fields Applied to Subsurface Prediction in Geology, GIS/LIS'88, *Proceedings 3rd Annual International Conference, Exhibits and Workshops*, Volume 1, San Antonio, Texas, 950 November 30-December 2, 26–34.

Carmichael, T and Ailleres, L, 2016. Method and analysis for the upscaling of structural data, *Journal of Structural Geology*, 83: 121–133.

Clout, J M F and Simonson, B M, 2005. Precambrian iron formations and iron formation-hosted iron ore deposits, *Economic Geology 100th Anniversary Volume*, 643–679.

Compilation of WAROX data, 2016. Geological Survey of Western Australia.

Crowe, M, 2012. The Wheelarra Fault – Structural evolution and influence on ore forming processes, Master's Thesis (unpublished), Centre for Exploration Targeting, University of Western Australia.

Dalstra, H J, 2006. Structural controls of bedded iron ore in the Hamersley Province, Western Australia–an example from the Paraburdoo Ranges. *Applied Earth Science*, 115(4):139–145.

Dalstra, H J, 2014. Structural evolution of the Mount Wall region in the Hamersley province, Western Australia and its control on hydrothermal alteration and formation of high-grade iron deposits. *Journal of Structural Geology*, (67): 268–292.

Egglseder, M S, Cruden, R C, Dalstra, H and Nicholas, L, 2017. The role of deformation in the formation of banded iron formation – hosted high-grade iron ore deposits, Hamersley Province (Australia), *Precambrian Research*, (296):62–77.

Farr, T G, Rosen, P A, Caro, E, Crippen, R, Duren, R, Hensley, S, Kobrick, M, Paller, M, Rodriguez, E, Roth, L and Seal, D, 2007. The shuttle radar topography mission. *Reviews of geophysics*, 45(2):1–33.

Fortescue-Hamersley, 2018. Geological Information Series. Geological Survey of Western Australia.

Geological Survey of Western Australia (GSWA), 2016a. 1:500 000 State interpreted bedrock geology of Western Australia, 2016: Geological Survey of Western Australia, digital data layer, www.dmp.wa.gov.au/geoview.

Geological Survey of Western Australia (GSWA), 2016b. 1:500 000 State linear structures of Western Australia, 2016: Geological Survey of Western Australia, digital data layer, www.dmp.wa.gov.au/geoview.

Geoscience Australia and Australian Stratigraphy Commission, 2017. Australian Stratigraphic Units Database. https://asud.ga.gov.au/.

Grose, L, Ailleres, L, Laurent, G and Jessell, M, 2020. LoopStructural 1.0: time-aware geological modelling, *Geoscientific Model Development*, (1)4:3915–3937.

Hagemann, S G, Angerer, T, Duuring, P, Rosière, C A, Figueiredo e Silva, R C, Lobato, L, Hensler, A S, Walde, D H G, 2016. BIF-hosted iron mineral system: A review, *Ore Geology Reviews*, 76: 317–359.

Hannon, E, Kepert, D A and Clark, D, 2005. From target generation to two billion tonnes in 18 months – the re-invention of the Chichester Range. In *Australasian Institute of Mining and Metallurgy,* pp 73–77.

Jessell, M, Ogarko, V, Lindsay, M, Joshi, R, Piechocka, A, Grose, L, de la Varga, M, Ailleres, L and Pirot, G, 2021. Automated geological map deconstruction for 3D model construction. *Geoscientific Model Development Discussions*,1–35.

Kent, 1982. The Fisher-Bingham distribution on the sphere. *J R Statist Soc B,* 44:71–80.

Knight, J, Perring, C, Stephens, D and Crowe, M, 2018. Discovery, Geologic setting and controls on iron mineralisation, South Flank, Western Australia, Society of Economic Geologists Special Publication, 21:321–347.

Morris, R C and Kneeshaw, M, 2011. Genesis modelling for the Hamersley BIF-hosted iron ores of Western Australia: a critical review, *Australian Journal of Earth Sciences*, 58: 417–451.

Morris, R C, 1980. A textural and mineralogical study of the relationship of iron ore to banded iron-formation in the Hamersley iron province of Western Australia. *Economic Geology*, *75*(2):184–209.

Morris, R C, 1985. Genesis of iron ore in banded iron-formation by supergene-metamorphic process – a conceptual model, in *Handbook of Strata-Bound and Stratiform Ore Deposits (ed: K H Wolf),* Vol 13, pp 73–235 (Elsevier: Amsterdam).

Perrin, M and Rainaud, J F, 2013. Shared Earth Modelling: Knowledge Driven Solutions for Building and Managing Subsurface 3D Geological Models (Editions Technip).

Perring, C, Crowe, M and Hronsky, J, 2020. A New Fluid-Flow Model for the Genesis of Banded Iron Formation-Hosted Martite-Goethite Mineralization, with Special Reference to the North and South Flank Deposits of the Hamersley Province, Western Australia. *Economic Geology*,115(3):627–659.

Powell, C M, Oliver, N H, Li, Z X, Martin, D M and Ronaszeki, J, 1999. Synorogenic hydrothermal origin for giant Hamersley iron oxide ore bodies. *Geology*, *27*(2):175–178.

Sommerville, B, Boyle, C, Brajkovich, N, Savory, P and Latscha, A-A, 2014. Mineral resource estimation of the Brockman 4 iron ore deposit in the Pilbara region, *Applied Earth Science*, 123(2):135–145.

Taylor, D, Dalstra, H J, Harding, A E, Broadbent, G C and Barley, M E, 2001. Genesis of high-grade hematite orebodies of the Hamersley Province, Western Australia. *Economic Geology*, 96(4):837–873.

Thiele, S T, Jessell, M W, Lindsay, M, Ogarko, V, Wellmann, F and Pakyuz-Charrier, E, 2016. The topology of geology 1: Topological analysis, *Journal of Structural Geology*, 91:27–38.

Thorne, W S, Hagemann, S G, Sepe, D, Dalstra, H J and Banks, D A, 2014. Structural control, hydrothermal alteration zonation and fluid chemistry of the concealed, high-grade 4EE iron orebody at the Paraburdoo 4E deposit, Hamersley Province, Western Australia. *Economic Geology*, 109(6): 1529–1562.

Yang, L, Achtziger-Zupančič, P and Caers, J, 2021. 3D Modeling of Large-Scale Geological Structures by Linear Combinations of Implicit Functions: Application to a Large Banded Iron Formation. *Natural Resources Research*, 1–25.

Maximising resource utilisation in South Africa – the BIF story

A Singh[1] and C Da Corte[2]

1. MAusIMM, Senior Technical Specialist: Physical Separation, Mintek, Randburg, 2194, South Africa. Email: ashmas@mintek.co.za
2. Senior Engineer, Mintek, Randburg, 2194, South Africa. Email: carlad@mintek.co.za

ABSTRACT

Banded Iron Formations or more commonly known as BIF are sedimentary rock formations with alternating silica-rich layers and iron-rich layers that are typically composed of iron oxides (hematite and magnetite), iron-rich carbonates, and/or iron-rich silicates. Considering the depletion of high-grade iron ore reserves in South Africa, there is a need to maximise resource utilisation through the exploitation of sterile resources in particular BIF material which makes up greater than 65 per cent of current reserves. BIF, like most resources, is non-renewable and the deposition of BIF is thought to have come about by the reaction of Fe^{2+} ions in the ocean water with dissolved oxygen billions of years ago. BIF ore derived from the Limpopo region in South Africa (SA) located in the Penge Iron Formation is according to Cairncross, Kramers and Villa (2018) equivalent to that contained within the Asbestos Hills Iron Formation of the Transvaal Supergroup in the Northern Cape, SA. Considering that these are one of the largest iron ore deposits in SA, the case study involved mineralogical characterisation followed by beneficiation of BIF from these two regions to ascertain the comparability.

Coarse and fines gravity separation comprising of Heavy Liquid Separation/Dense Media Separation on the +1.18 mm size fraction and shaking table on the -1.18 mm size fraction was conducted to ascertain whether an on-grade product or blended feedstock could be produced. The Limpopo mixed and Northern Cape conglomerate BIF samples achieved similar overall responses due to the conglomerate sample containing 15.3 per cent additional -1.18 mm fines. A combined coarse and fines product grading at 60 per cent Fe could be achieved at a yield and recovery of 43.9–53.0 per cent and 62.2–63.8 per cent respectively. Increasing the grade to 63 per cent Fe reduces the overall recovery by 13.3 per cent. At the higher target grade, the contaminant specifications could be achieved for both samples.

The Northern Cape laminated BIF sample is the most promising of the three samples studied. At the two iron target grades overall yields and iron recoveries of 72.9–65.4 per cent and 85.2–80.2 per cent was achieved. In both instances the silica grade exceeded the product specification, however if the silica content is the driver the target iron grade should increase to 63.32 per cent. This will result in a minimal decrease in recovery of 0.4 per cent.

The promising results of this study indicate that coarse beneficiation of BIF material is possible. These ore types could be blended with superior grade products to improve overall yields and recoveries or sold directly at a 63 per cent Fe product grade whilst sacrificing 0.4–13.3 per cent recovery.

INTRODUCTION

Ferrous Minerals (eg iron ore, manganese, chrome etc) is one of the four most important commodity sectors for South Africa's economy with iron ore alone accounting for about 12 per cent of the total mineral sales. It is primarily used by the construction, engineering, automotive, and machinery industry, often as the main raw ingredient in steelmaking. Approximately 98 per cent of the world's mined iron ore is used for making steel, as such the demand for iron ore closely follows that of the metal (Garside, 2020). Thus, the importance of iron ore mining in the South African economy cannot be underestimated and the sustainability and future of the industry needs to be supported.

Iron ore deposits are known to occur in sedimentary, hydrothermal and magmatic environments. At present about 90 per cent of iron ore mined in the world comes from high-grade hematite deposits hosted by Precambrian BIF (Cairncross, 1997). Considering the depletion of high-grade material in South Africa, the need to research and exploit abundantly available BIF is investigated.

SOUTH AFRICAN IRON ORE CHALLENGES

The South African iron ore mining sector is facing a confluence of challenges some of which entail depletion of high-grade reserves, high operational costs, market competition, lack of innovation and skills shortage with instability and volatility in commodity prices exacerbating the crisis in the industry.

Depletion of high-grade reserves

Kumba Iron Ore (KIO) a subsidiary of global miner Anglo American and Assmang a JV of Assore and African Rainbow Minerals (ARM) are South Africa's primary iron ore producers accounting for greater than 80 per cent of iron ore production within the country. Their life-of-mine (LOM) forecast suggests that their high-grade lumpy material will be depleted within the next two decades (average life of approximately 12–13 years) in the absence of further exploration and discoveries (Anglo American, 2011).

There exists potential to unlock value from sterile fines, low-grade stockpiles and Banded Iron Formation (BIF) lithology which would further extend mining operations for another two decades. Seeing that BIF is projected to make up greater than 65 per cent of current reserves, the study undertaken focused in particular on exploiting this resource. The highest-quality and most important iron ores for steelmaking are hematite and magnetite. Hematite is the more sought-after ore accounting for about 95 per cent of South Africa's iron ore production and is the preferred raw material in efficient steelmaking mills. Thus, the future of iron ore processing in South Africa will be fines processing involving predominantly hematitic material in order to extend LOM and deliver on high quality (premium) feedstock requirements to iron and steel producers.

Market competition

Globally, the iron ore industry is dominated by major producers Vale, Rio Tinto, BHP Billiton and Fortescue Metals. It is important to note, that the operating costs of the top four iron ore producers are the lowest in the world, and the barriers to entry (upfront capital cost) for suppliers to the iron ore market are high (Nortje, 2018; Singh, Lydall and Bungane, 2019). Figure 1 captures the cost curve for iron ore production in 2019 (Bodley *et al*, 2013) relative to the spot price of iron ore reporting ~US$167/ton as at end March 2021.

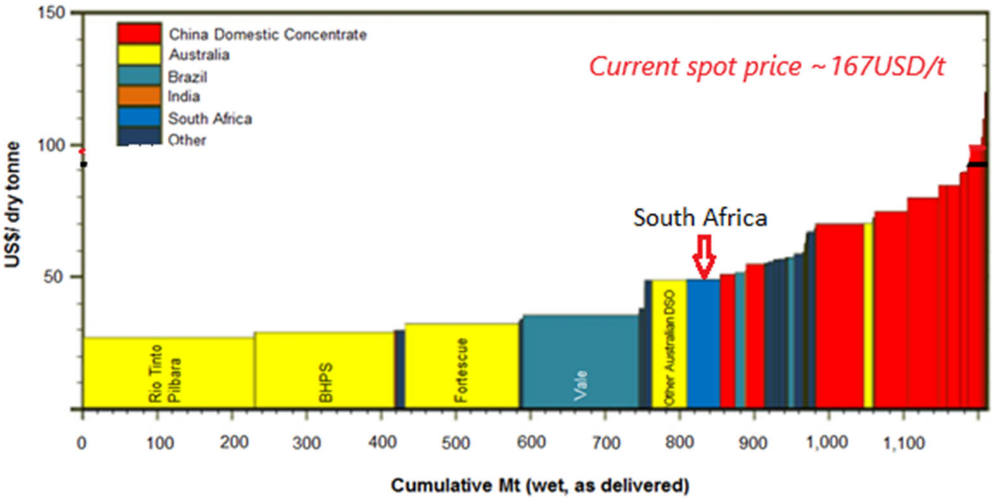

FIG 1 – Global production cost curve (Metalytics, 2019).

The prevailing volatility in commodity prices have ensured that only the largest and lowest-cost producers survive, thus mines in South Africa and globally are experiencing continued pressure resulting in mine closures and production cuts. Although the iron ore market is dominated by Australia and Brazil who produce high-grade products, the raw material acquired from South Africa offers a different trace element mix that is highly sought after for complementing the concentrates from major producers. Some of the benefits derived include:

- High average iron content of 64.1 per cent Fe (Creamer Media, 2018)

- Contains less deleterious elements
- High competence and less friable resulting in minimum product breakdown and fines generation.

The steady rise in mining costs and escalating electricity prices have resulted in the higher production cost curves and necessitated South Africa to explore innovative ways of mining and downstream beneficiation to resolve the aforementioned challenges with the objective of growing and sustaining the iron ore reserves aimed at reduced operational and capital costs, improved energy efficiency and utilisation of unexploited reserves (Creamer Media, 2019).

Volatility in commodity prices

The fluctuation of the price in iron ore over the years is presented in Figure 2 and shows that the highest price achieved for one dry metric ton unit (dmtu) of iron ore was US$168 in 2011. The price dramatically decreased to US$55 per dmtu in December 2015 with a promising increase to US$167 per dmtu as of end March 2021 (Statista, 2019).

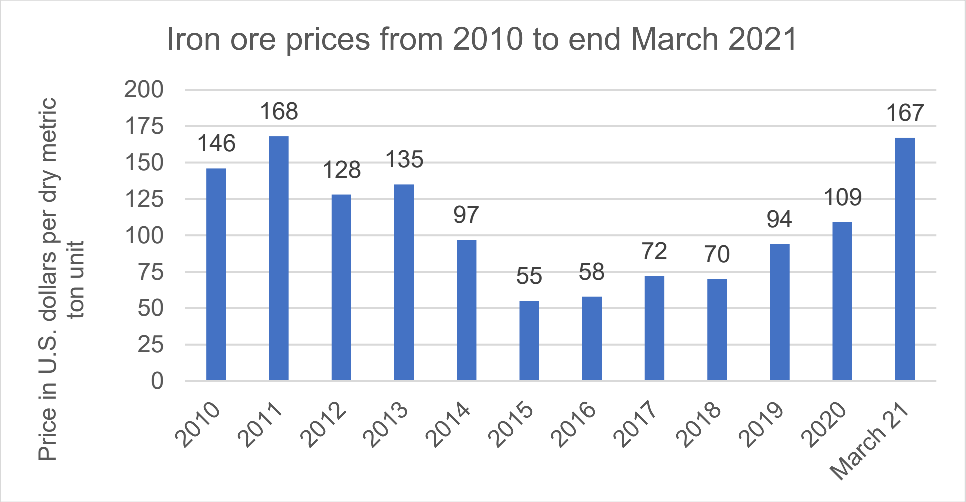

FIG 2 – Iron ore price from 2010 to March 2021 (Statista, 2021).

In addition, the coronavirus (Covid-19) pandemic has had a noteworthy impact on iron ore prices (Figure 3). The impact of Covid-19 on the global iron ore industry is apparent from the decline in the average year-to-date price of iron ore as of May 2020 (US$83.50 per metric ton) as compared to the average price in 2019 (US$94 per metric ton). The pandemic continues to impact negatively on economic activity in South Africa and globally and hence is a major concern to the mining industry (Godongwana, 1943; Economic Transformation Committee (ETC), 2020). Compared to other metals, however, iron ore prices have stayed relatively resilient, and are expected to recover further during 2021 once China's demand increases further, currently reporting at approximately US$167/t in the first quarter of 2021. Steel production however in SA has become less attractive due to high cost of production, aging plants, inefficiencies as well as lack of maintenance and upgrade and global oversupply. South Africa's steel industry has been in constant decline since 2010 and this is evident across the value chain from mining to primary steel mills and domestic manufacturers struggling to compete, sustain jobs and investment.

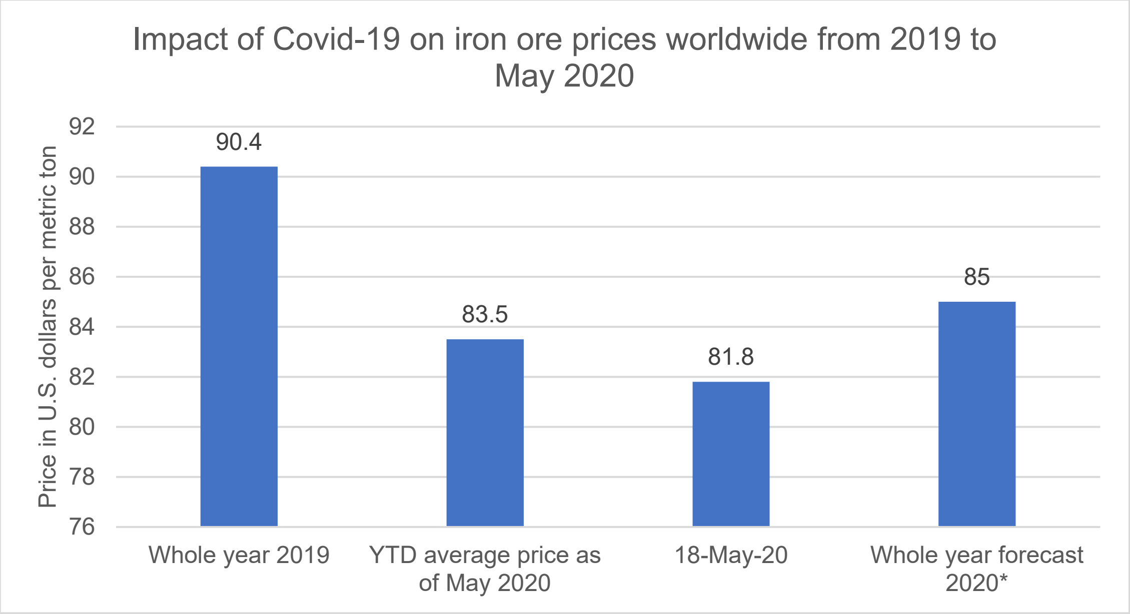

FIG 3 – Impact of Covid-19 on Fe ore prices (Statista, 2020).

Research capability and skills shortage in SA

The current economic downturn, price instability, high operational costs, imminent depletion of high-quality reserves amongst others has forced iron ore producers to re-evaluate their business strategy. Kumba Iron Ore is only second to government as the largest employer in the Northern Cape Province. Thus, the importance of iron ore mining in the South African economy cannot be underestimated and the sustainability and future of primary industries need to be supported (Anglo American, 2011). Research into fines, low-grade stockpiles and BIF material resides predominantly at Mintek due to historical work conducted on iron ore deposits across SA and globally. With a drive to maximise resource utilisation through beneficiation of fine and BIF material, collaboration with iron ore producers have been sought with work underway. This paper captures in part some of the research undertaken to evaluate beneficiation potential of South African BIF material.

DOMINANT IRON ORE RESERVES IN SOUTH AFRICA

Figure 4 represents the primary South African iron ore deposits (excl titaniferous-magnetite) with Table 1 representing the volume of raw material produced as recorded by Creamer Media (2019, 2020). Kumba is the largest iron ore producer at 43.1 million tons with only 13.9 per cent being fines followed by Assmang. Iron ore lump premiums have dropped significantly (almost by 70 per cent) as steel mills reduced the usage of lump material in response to thinner steel margins. The need exists to exploit unutilised fine stockpiles and BIF to increase production capacity, which will inevitably be the future of iron ore processing in South Africa.

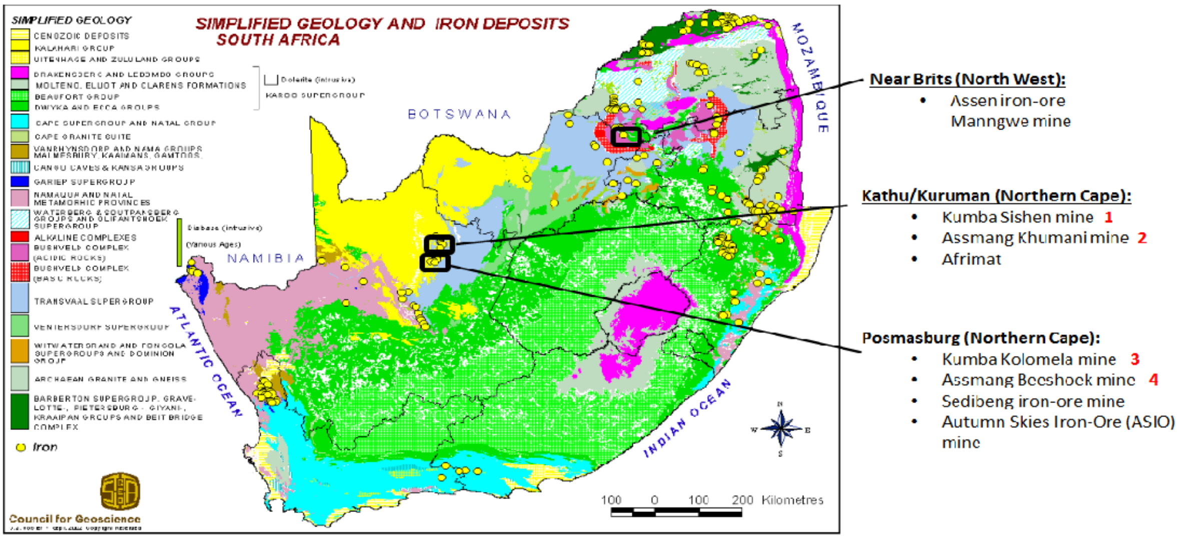

Near Brits (North West):
- Assen iron-ore Manngwe mine

Kathu/Kuruman (Northern Cape):
- Kumba Sishen mine 1
- Assmang Khumani mine 2
- Afrimat

Posmasburg (Northern Cape):
- Kumba Kolomela mine 3
- Assmang Beeshoek mine 4
- Sedibeng iron-ore mine
- Autumn Skies Iron-Ore (ASIO) mine

FIG 4 – Primary iron ore deposits in South Africa (1–4 order of abundance).

TABLE 1

Key South African iron ore producers (Creamer Media, 2019).

Producer	**Kumba**	**Assmang**	**Afrimat**	**Aquila Resources**	**Autumn Skies Resources and Logistics**	**Manngwe Mining**
Mines	Sishen; Kolomela mine	Khumani; Beeshoek mine	Demaneng	Meletse deposit	Autumn Skies Iron-Ore (ASIO) mine	Assen iron-ore mine
Lump (Million Tons)	29.17					
Fines (Million Tons)	13.93					
Total (Million Tons)	43.1					
Individual mine production (Million Tons)	Sishen mine (64.5% Fe): 29.25	Khumani mine (62.2% Fe): 14.70				
	Kolomela mine (64.5% Fe): 13.86	Beeshoek mine (64.85% Fe): 3.88				
Total Production (Mt/yr)	**43.1**	**18.58**	**1**	**2.5**	**0.504**	**0.72**

The statistic in Figure 5 shows the mine production volume of iron ore in South Africa from 2009 to projected end 2021. In 2019, South Africa's production of iron ore amounted to an estimated 75 million metric tons. The trend mirrors the iron ore pricing data (Figure 2) showing the potential for iron ore production increase as projected in 2021.

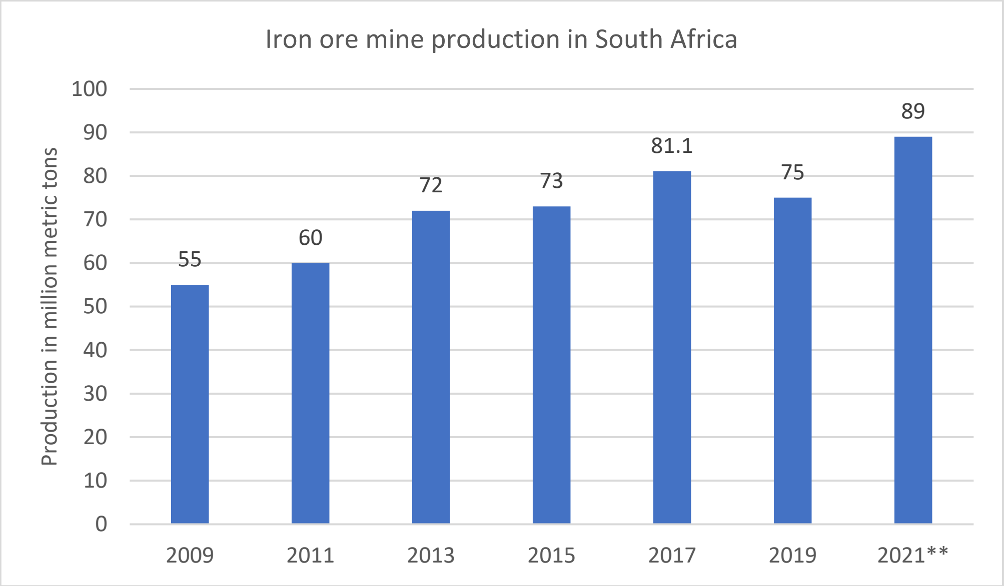

FIG 5 – Iron ore production volumes over a ten-year period (Statista, 2021; Minerals Council of SA 2019).

BANDED IRON FORMATION (BIF)

Banded iron formations (also known as BIF or banded ironstone formations) are distinctive units of sedimentary rock consisting of alternating layers of iron oxides and iron-poor chert/gangue which are often red in colour of similar thickness. Almost all of these formations are of Precambrian age, with most deposits dating to the late Archean period (2500–2800 Ma) (Gross, 1965; Condie, 2011).

Banded iron formations are thought to have formed in sea water (during times of oxygen deficiency in the Earth's atmosphere) as a result of oxygen production by photosynthetic cyanobacteria. This oxygen combined with the dissolved iron in the ocean to form insoluble iron oxides, which precipitated out, forming a thin layer on the ocean floor. BIF's tend to be extremely hard, tough and dense thus making them resistant to erosion (Trendall, 2002). Banded iron formations account for greater than 65 per cent of primary iron ore reserves in South Africa, thus representing the future of iron ore mining. The two most important BIF ore districts in South Africa being the Northern Cape Province and Limpopo Province is discussed within this paper with test work undertaken on material from both regions as represented in Figure 6.

FIG 6 – Geographical location of BIF material investigated within the Republic of South Africa.

GEOLOGY OF NORTHERN CAPE (NC) IRON ORE

The Transvaal Supergroup or Griqualand West Supergroup as it is referred to where it occurs in the Northern Cape Province of South Africa is the largest known resource of high-grade hematite (Eriksson, Hattingh and Altermann, 1995; Carney and Mienie, 2013). The Transvaal sedimentation began with predominantly fragments of sedimentary rocks followed by carbonate bearing rocks and banded iron formation (Eriksson, Hattingh and Altermann, 1995). The Asbestos Hills Subgroup is considered to be a superior type BIF that can be up to 500 m thick (Figure 7). The upper portion of the BIF tends to be enriched to ore grade (Fe>60 per cent) (Kumba Iron Ore, 2020).

Hematite ore is currently being beneficiated at Sishen, Khumani, Kolomela and Beeshoek. The two latter mines represent the Sishen South deposits which are located approximately 65 km south of the Sishen mine. Sishen and Kolomela are owned by Kumba Resources Limited (a subsidiary of Anglo American) with Khumani and Beeshoek being owned by Assmang (a joint venture between African Rainbow Minerals and Assore).

Carney and Mienie (2013) explains that the Sishen and Sishen South deposits located in the vicinity of the western perimeter of the Kaapvaal craton have both been subjected to structural deformations such as folding, faulting and thrusting. The deformations occurring approximately 2400–1700 million years ago is suggested to be a reason for the formation and preservation of the ores from erosion.

According to Carney and Mienie (2013), four iron ore occurrences have been identified in both deposits with each ore occurrence created from depositions under specific environmental conditions yielding physical, chemical and metallurgical properties unique to that occurrence. The first and second occurrence is the bulk of the high-grade hematite comprising of laminated and massive ores located in the upper region of the Asbestos Hills Subgroup. The second is the brecciated ore of medium to lower grade preserved in sinkholes developed within dolomites from the Campbell Rand Subgroup. The last are lower grade conglomeratic and gritty ores which are also located in conglomerates, shales and quartzites from the Gamagara Subgroup.

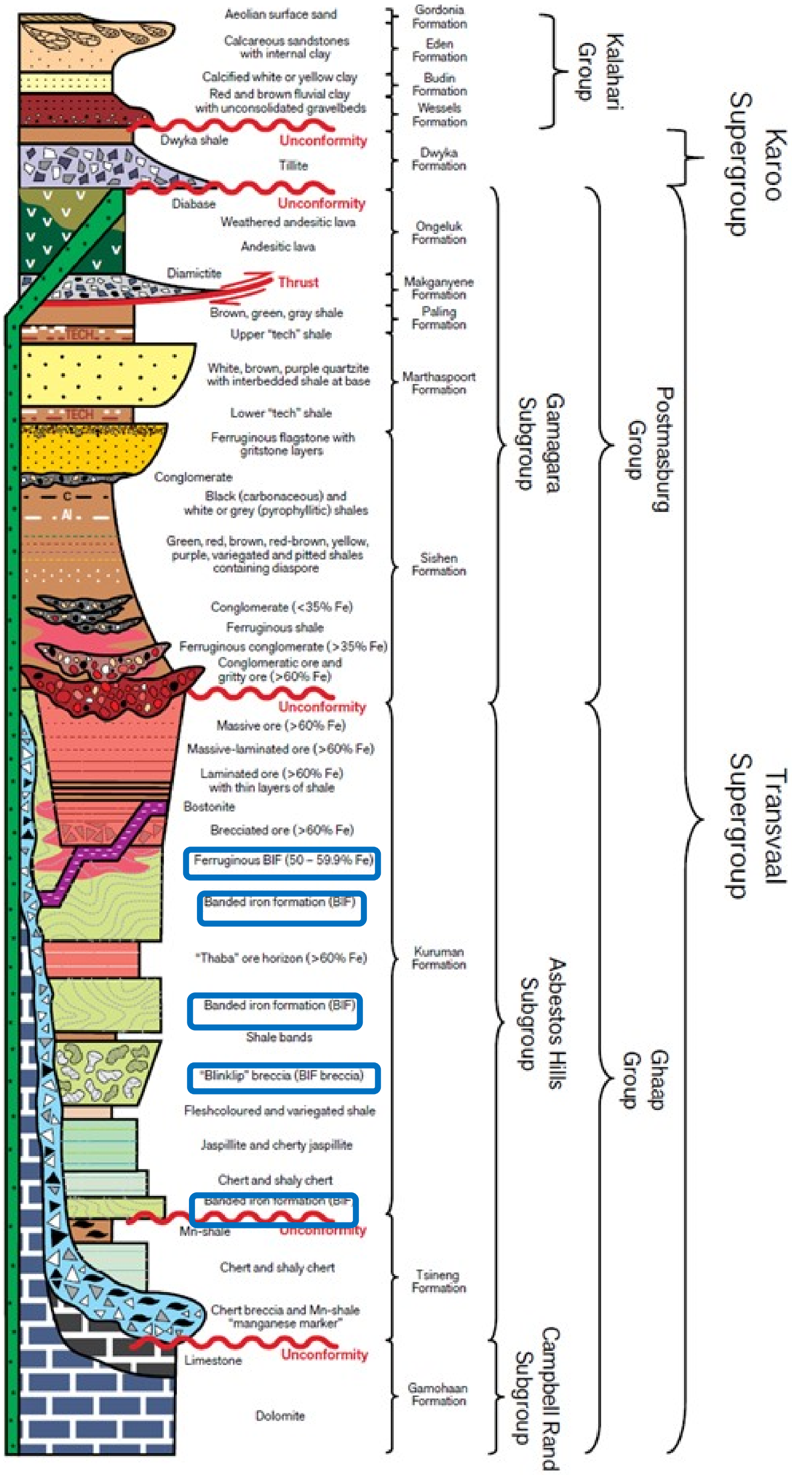

FIG 7 – Simplified stratigraphic column depicting the Sishen-NC local geology (Kumba Iron Ore, 2020).

The research study undertaken focused on two BIF ore types from the Northern Cape Province namely laminated and conglomerate ore represented in Figure 8. The laminated ore has alternating hematite (dark grey) and chert (orange and light grey) laminations. The thickness of these laminations vary between 0.2–2.0 cm. The conglomerate material displays rounded/elongated pebble-like hematite inclusions. Both samples exhibit marginal to moderate ferruginisation.

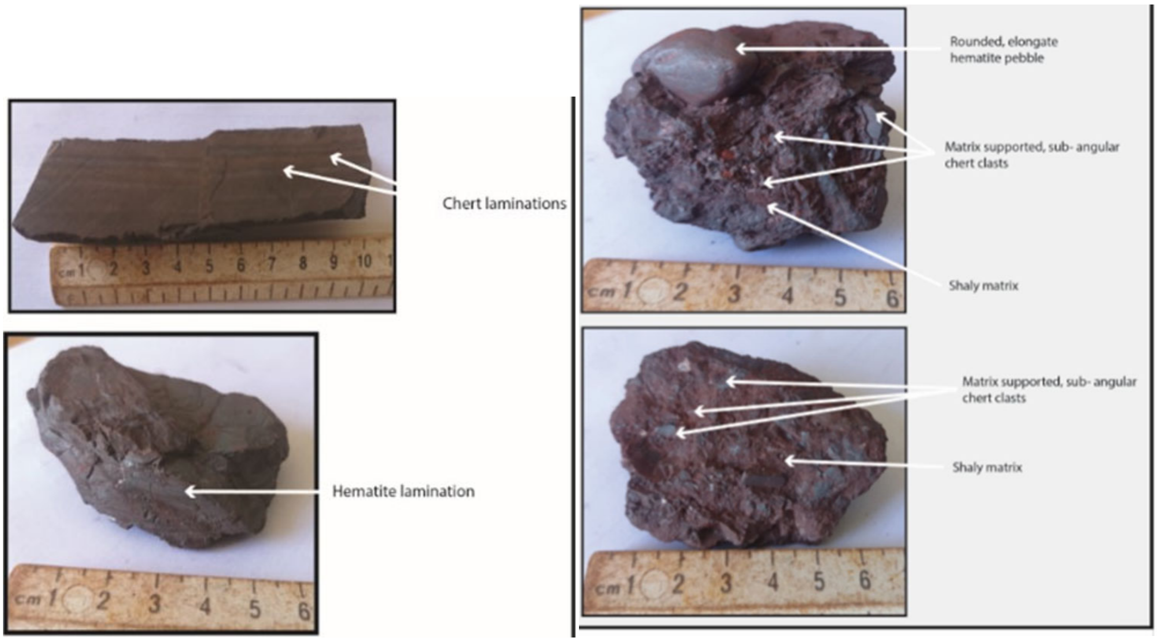

FIG 8 – Image of BIF ore types from the Northern Cape Province tested at Mintek; (left): laminated ore; (right): conglomerate ore.

GEOLOGY OF LIMPOPO IRON ORE

Iron ore mining occurs about 260 km north-west of Johannesburg in the Waterberg District of the Limpopo province. To the east are hills that consist of Transvaal Supergroup comprising dolomite and Penge Iron Formation lithologies that host these iron ore deposits (Mining Data Online, 2019). According to Cairncross (2011) the deposit is believed to be the lateral equivalent of the Asbestos Hills Iron Formation of the Transvaal Supergroup in which the Sishen and Sishen South Deposits are located in the Northern Cape.

The Penge Iron Formation consisting predominantly of BIF material lies in between chert poor dolomites of the Malmani Subgroup and the siliciclastic sedimentary rocks of the Pretoria Group with the latter forming the uppermost layer (Beukes, 1986 as cited by Cairncross, 2011). According to Gutzmer *et al* (2005 as cited by Cairncross, 2011) the high-grade hematite ores (~65 per cent Fe) occur predominantly at the base of the Penge Iron Formation.

Interesting to note is that BIF contained within the Thabazimbi region is similar in stratigraphic setting to that of the major BIF hosted hydrothermal high-grade hematite ore deposits of Western Australia (Taylor, Dalstra and Harding, 2001).

The Penge Iron Formation created approximately ~2.48 billion years ago preceded the formation of the Bushveld Complex (2.06 billion years) and the setting in place of the Bushveld Complex caused the Transvaal Supergroup strata to dip steeply (45–55°) to the south below the Bushveld Complex (Cairncross, 2011) as illustrated in Figure 9.

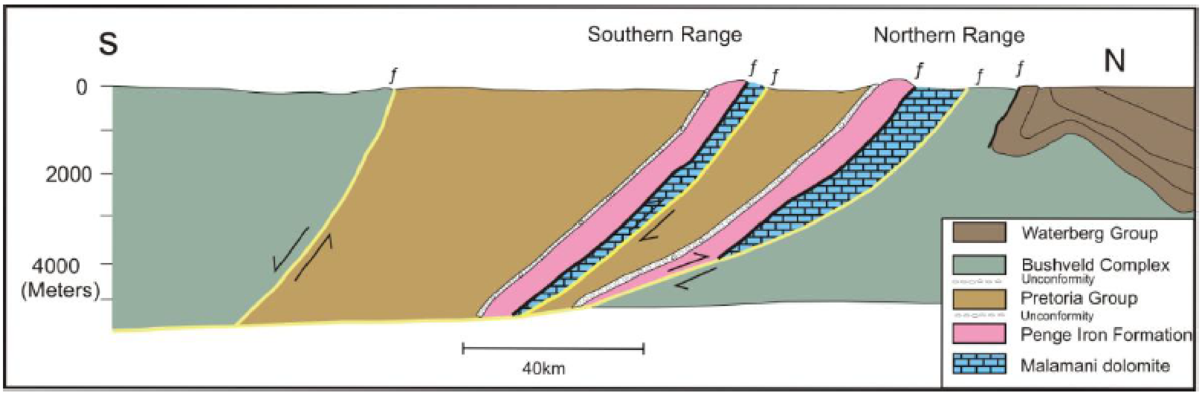

FIG 9 – Simplified geological cross-section through the Thabazimbi region (Cairncross, 2011).

The research study undertaken focused on a mixed BIF stockpile from the Limpopo Province as represented in Figure 10. The texture of the BIF sample reflect laminated and finely intergrown hematite within chert layers. The study therefore focused on upgrade potential of the orebody at discrete sizes.

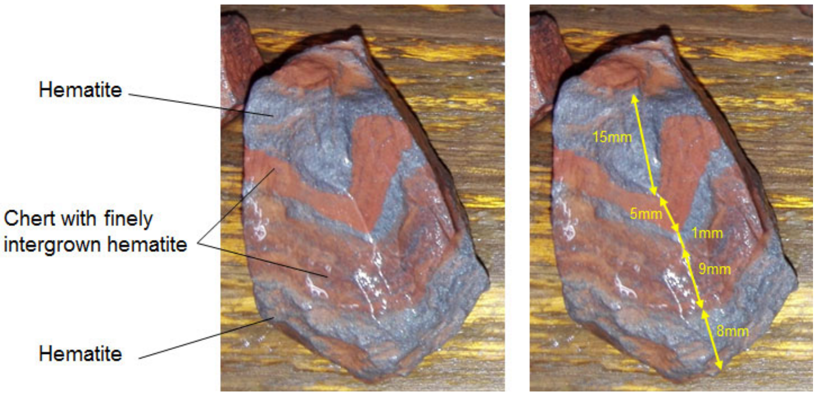

FIG 10 – Image of mixed BIF material from the Limpopo Province tested at Mintek.

METHODOLOGY

Samples

One BIF sample from the Thabazimbi region in Limpopo and two BIF samples from the Northern Cape Province in South Africa at top sizes ranging between 20–40 mm and grading at 43–52 per cent Fe as shown in Table 2, were used in this study. The BIF sample originating within the Limpopo region has a mixture of lithologies, with 15.2 tons received, whilst the conglomerate and laminated BIF ore types were separately received from the Northern Cape Province and each weighed under 100 kg. It is important to note that since the BIF ore types in the Northern Cape are not currently being mined it was difficult for the iron ore producers to provide Mintek with sample masses exceeding 100 kg. BIF is the dominant lithology for the Limpopo source material and stockpiles of this material was readily available and thus a large sample mass was feasible.

TABLE 2

Feed head grades of the three BIF samples.

Source Material	BIF Ore Type	Top Size Received	Mass Received	Grades (%)											Total (XRF)
				Fe	Si	Al	K_2O	Na_2O	CaO	TiO_2	MgO	P	Mn	LOI	
Product				**Targets**	**< 3.5**	**<1.50**					**<0.075**				
Limpopo	Mixed	-40mm	15.2 tons	42.61	16.90	0.56	0.00	0.01	0.16	0.10	0.17	0.03	0.21	1.05	98.86
Northern Cape	Conglomerate	-20mm	86.4 kg	51.48	10.27	1.30	0.54	0.07	0.02	0.16	0.02	0.04	0.20	0.81	99.98
	Laminated	-20mm	93.4 kg	51.08	11.05	1.02	0.07	0.02	0.05	0.11	0.02	0.05	0.04	0.96	99.93

* S&P Global Platts (2020)

The Northern Cape samples have similar iron grades with low phosphorus and alumina content at elevated potassium content for the conglomerate BIF ore type. The Limpopo BIF is lower in iron and alumina content compared to the Northern Cape BIFs, although both regions contain silica as the dominant gangue element.

The product specifications for a seaborne lumpy ore at 62.5 per cent Fe is included in Table 2. The alumina and phosphorous content in the feed is below the product specifications, indicating good beneficiation potential for the three BIF samples.

Sample preparation

Previous coarse test work conducted on iron ore (Da Corte *et al,* 2021) indicated reducing the top size reduced the contaminant levels to below the target specifications, and thus a top size of -12 mm was selected. The Limpopo sample was mechanically blended and five tons removed via cross-cutting. The five ton aliquot was subjected to the same procedure until a 150 kg aliquot was obtained. The 150 kg aliquot for the Limpopo sample and the ‘as-received; Northern Cape samples were stage crushed to -12 mm using a jaw crusher. The -12 mm material was wet screened at 8 mm, 3.35 mm and 1.18 mm. The wet screening mass splits and associated Fe deportment is presented in Figure 11. The Fe deportment closely follows mass pull indicating no preferential upgrading to either size fraction for all the BIF samples. The mass and thus Fe deportment for each size fraction varies across the samples with similarities observed between the Limpopo and Northern Cape laminated samples.

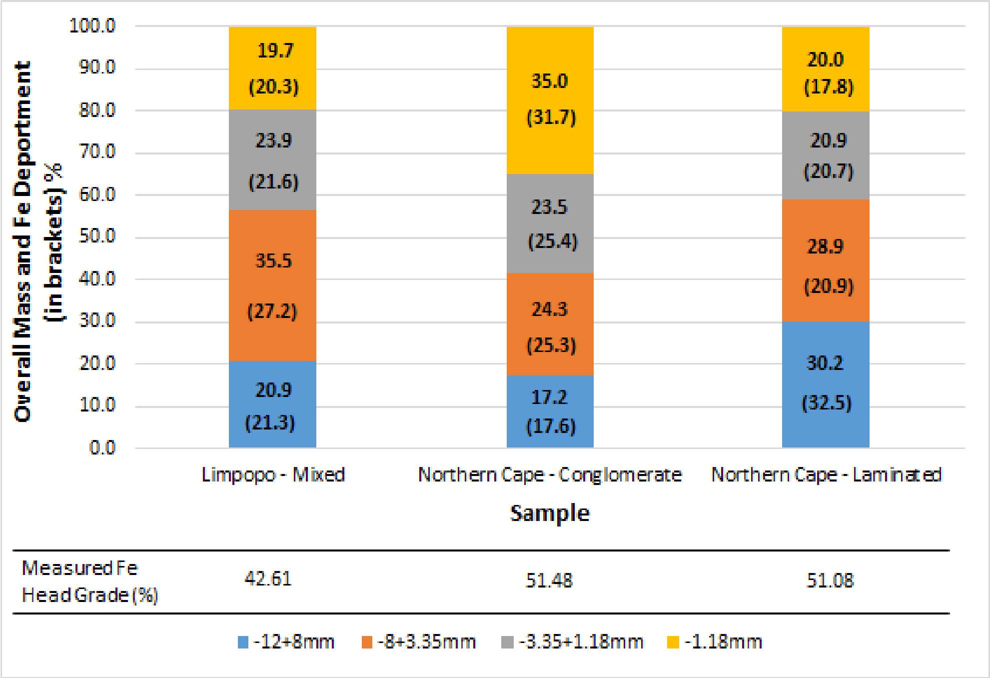

FIG 11 – Wet screening mass splits and iron deportment (in brackets) for all three BIF samples.

The -12+8 mm, -8+3.35 mm, -3.35+1.18 mm size fractions generated for each sample was subjected to Heavy Liquid Separation (HLS). The natural -1.18 mm size fractions were independently subjected to shaking table test work 'as-is' (without de-sliming) to determine the beneficiation potential of this material and allowing for an overall mass balance to be generated. The natural -1.18 mm was also subjected to size-by-assay to determine the iron and gangue deportment across size, particularly to the slimes. Gravity separation was considered for these BIF samples in order to ensure low OPEX costs are attained. HLS and shaking tables were selected for two reasons, firstly these methods are typically used to benchmark what can be achieved on Dense Media Separators and spirals respectively. Secondly, the limited mass available for the Northern Cape material necessitated those methods with small mass requirements be utilised.

Heavy liquid separation

HLS utilises the differences in particle density to concentrate material into various density classes. The ore is introduced to the fluid medium and the density gradient results in particles that are heavier than the medium to sink, while particles lighter than the medium float. Separation is facilitated by a separation medium as follows:

- For densities less than 2.96 g/cm³ TBE and Acetone are used to prepare the mixture.
- For densities between 2.96 g/cm³ and 3.7 g/cm³, Tetrabromo-Ethane (TBE) and Atomised Ferrosilicon are used.
- For densities at and greater than 3.8 g/cm³, Tetrabromo-Ethane (TBE) and Tungsten Carbide are used.

Densimetric (HLS) test work was conducted on -12+8 mm; -8+3.35 mm and -3.35+1.18 mm size fractions for all the BIF samples. Approximately 8–15 kg of each size fraction was separated in the HLS laboratory at six density cut points namely 3.8, 3.9, 4.0, 4.2, 4.4 and 4.7 g/cm^3. The HLS procedure employed for this study is outlined in Figure 12.

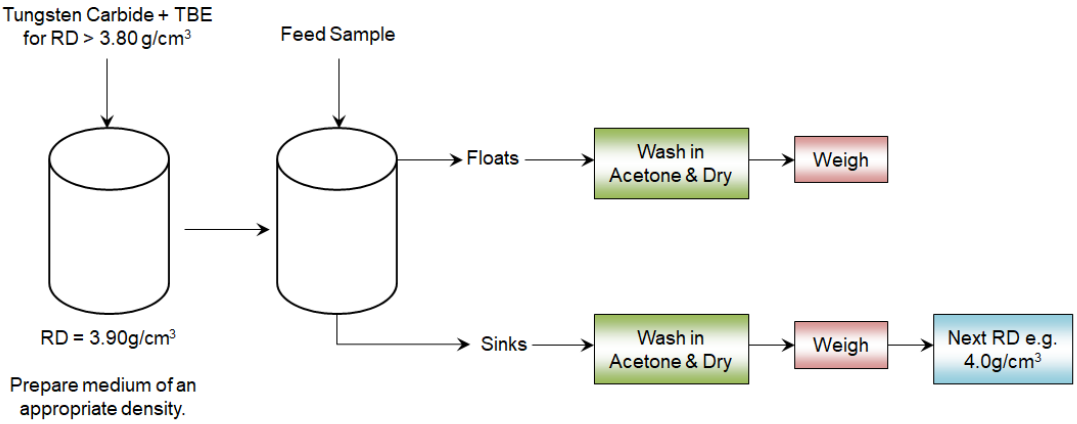

FIG 12 – Overview of the HLS procedure.

The resulting densimetric fractions (six floats and one sink) for each size fraction was dried, weighed and a subsample removed for quantitative chemical analysis to generate washability data and determine the presence of near density material at the cut point that achieves the target grades of 60 per cent Fe and 63 per cent Fe.

Predicted partition curves for dense media separation

Utilising the washability characteristics obtained during HLS test work, partition curves were constructed to predict Dense Media Separation (DMS) performance. An empirical Weibull function, derived by Rao (2004), is used to represent the partition surface of gravity concentrators in terms of size and density attributes as illustrated in Equation 1.

$$Y = 100\left(1 - exp\left(-\left(\frac{1}{1-Y_P}\right)\right)\left(\frac{\rho}{\rho_P}\right)^{pd^q}\right) \qquad (1)$$

Where:

Y	is the Partition number, a function of particle size and density
Y_P	is the Pivot partition number, representing the fraction of bypass in gravity concentrators
ρ_p	is the Pivot density (in kg/m^3)
p	captures viscosity effects
q	represents flow conditions (turbulence) of the separator
d	represents particle size (in mm)

The Weibull model is used in the Mintek Model to predict the performance of DMS operations. The effect of particle size and difference in performance of DMS are built into the Mintek Model. The Mintek Model is therefore able to predict efficiency of separation (Ecart Probable, Ep) at various density cut points for DMS plants. The predicted product yield, iron grade (and main contaminant grades silica and aluminium), iron recovery with the predicted Ep at several density cut points were determined.

The parameters used in the Mintek Model include the Geometric mean size, Y_P, ρ_p, p and q. Each of these parameters is related to the particle size, density cutpoint and Ep of the separation. Sets of values for these parameters were derived based on test work done in the past on DMS operations. These parameters are used as the basis on which the Mintek Model predicts the performance in DMS plants.

Shaking table on the natural -1.18 mm size fraction

Shaking tables operate on the principle of separating the ore according to density using water. The table is inclined at an angle and particles of high specific gravity move slower than lighter particles.

Particle size plays a very important role in table separations. The wider the size ranges in the feed, the lower the efficiency of separation.

The separation process of a shaking table is dependent mainly on the difference in specific gravity between the minerals and to a lesser degree on the shape and size of the particles. As the water flows over the table the heavy materials are not affected as they collect in the riffles along which they move to the end of the table. The lighter material rides above the heavy minerals and tend to be washed over the riffles to the diagonal side of the table. Suitable launders are placed at the end of the table to collect the various products as they are discharged. These launders are provided with movable dividing devices to separate concentrates, middlings and tailings product fractions. Shaking tables are used to benchmark performance of the ore in gravity units. Grades and recoveries achieved on a spiral circuit can thus be compared to this performance.

Approximately five kg of the natural -1.18 mm (not deslimed) for all three BIF samples were processed over a standard one-eighth Wilfley Shaking Table unit, the separation of which can be observed in Figure 13.

FIG 13 – The one-eighth Wilfley Shaking Table at Mintek with the Limpopo BIF sample separating across the shaking table.

RESULTS AND DISCUSSION

Heavy liquid separation

The unit cumulative iron grade-recovery curve for the individual size fractions and mathematically combined -12+1.18 mm size fraction for the Limpopo BIF sample is presented in Figure 14. At iron grades of 60 per cent and above all the size fractions have a similar recovery profile with the exception of the -12+8 mm size fraction which achieved significantly higher iron recoveries. At a product grade of 63 per cent Fe the unit iron recovery ranges from 50.2–61.2 per cent with 10.8–14.2 per cent additional recovery available should the iron product grade decrease to 60 per cent Fe.

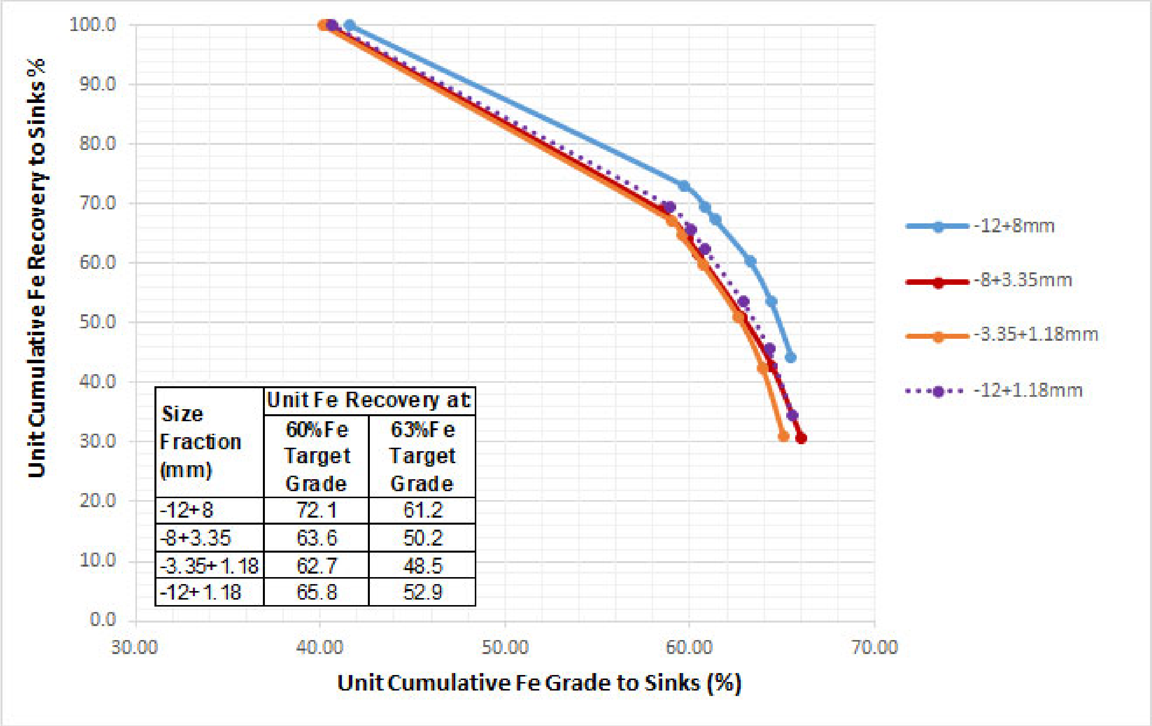

Size Fraction (mm)	Unit Fe Recovery at: 60%Fe Target Grade	63%Fe Target Grade
-12+8	72.1	61.2
-8+3.35	63.6	50.2
-3.35+1.18	62.7	48.5
-12+1.18	65.8	52.9

FIG 14 – Iron grade-recovery curve for the Limpopo mixed BIF sample.

The HLS unit cumulative iron grade-recovery curve for the individual size fractions and mathematically combined -12+1.18 mm size fraction for the Northern Cape BIF samples are presented in Figures 15 and 16. The conglomerate sample shows improved grade-recovery response as the particle size decreases whilst the laminated sample has a similar response for the +3.35 mm size fractions and slightly improved response in the -3.35+1.18 mm size fraction.

The conglomerate sample can achieve unit iron recoveries of 74.3 per cent to 91.1 per cent at a product grade of 60 per cent Fe with significant iron losses of 10.3 to 21.0 per cent observed with an increase in the product grade to 63 per cent Fe. The -12+8 mm size fraction has the highest losses at the elevated product grade and a reduced top size of -8 mm should be considered for this sample. The impact of the target product grades on the unit iron recovery is marginal (2.0 per cent to 3.8 per cent difference) for the laminated sample with this sample achieving the highest unit recoveries of 88.6 per cent to 92.3 per cent at a product grade of 63 per cent Fe.

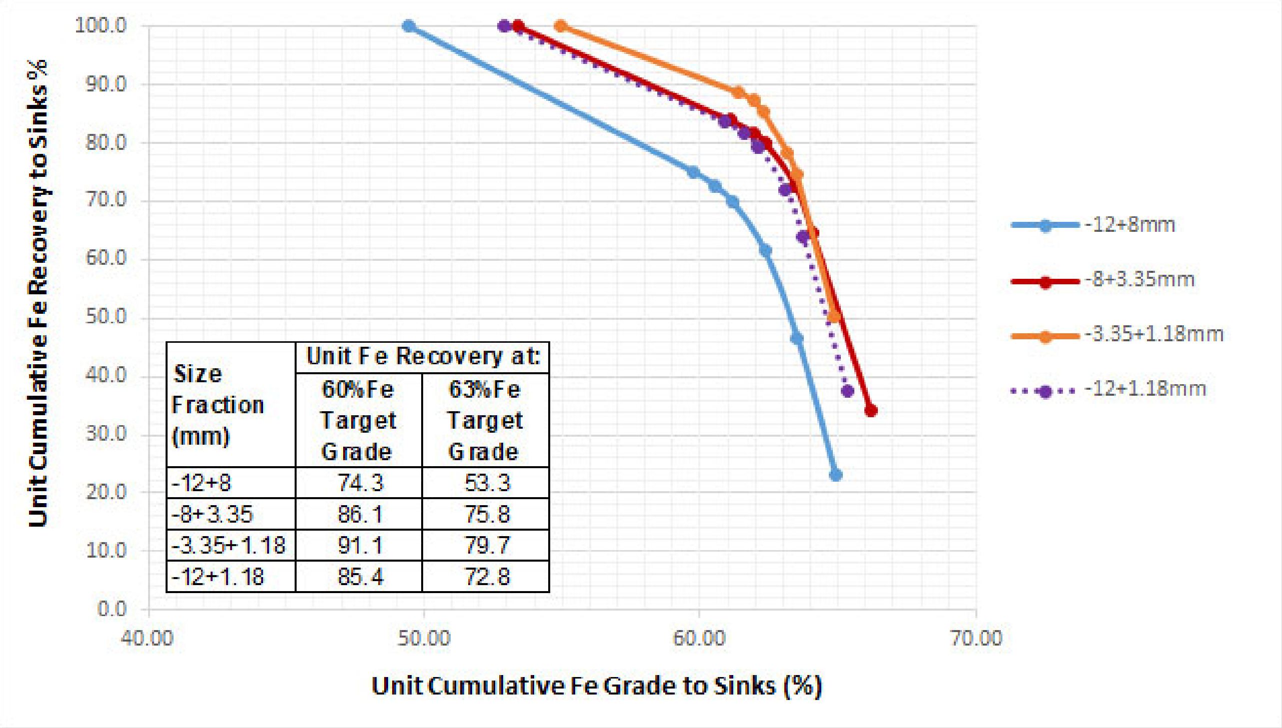

Size Fraction (mm)	Unit Fe Recovery at:	
	60%Fe Target Grade	63%Fe Target Grade
-12+8	74.3	53.3
-8+3.35	86.1	75.8
-3.35+1.18	91.1	79.7
-12+1.18	85.4	72.8

FIG 15 – Iron grade-recovery curve for the Northern Cape Conglomerate BIF sample.

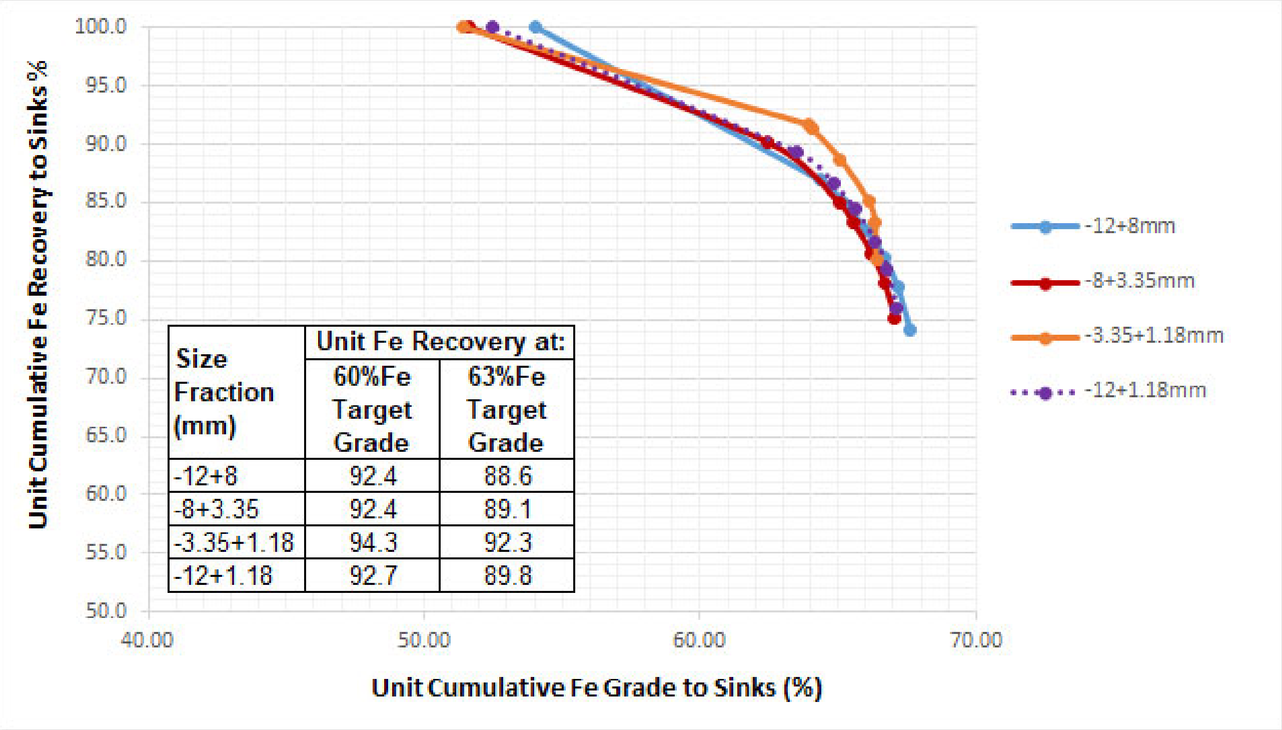

Size Fraction (mm)	Unit Fe Recovery at:	
	60%Fe Target Grade	63%Fe Target Grade
-12+8	92.4	88.6
-8+3.35	92.4	89.1
-3.35+1.18	94.3	92.3
-12+1.18	92.7	89.8

FIG 16 – Iron grade-recovery curve for the Northern Cape Laminated BIF sample.

The discrete washability data for the mathematically combined size fractions (-12+1.18 mm) for the Limpopo and Northern Cape BIF samples respectively are presented in Figure 17 along with the HLS cut density required to achieve the two target product grades. Tom (2015) defines near density material as material that lies within 0.05 to 0.1 relative density intervals on either side of the cut density, and further suggests near density material in excess of 15 per cent as very difficult to beneficiate. Figure 17 indicates that at both target iron grades the proportion of near density material within a 0.1 RD interval ranges from 6.3 per cent to 7.3 per cent indicating this material would be amenable to dense media separation.

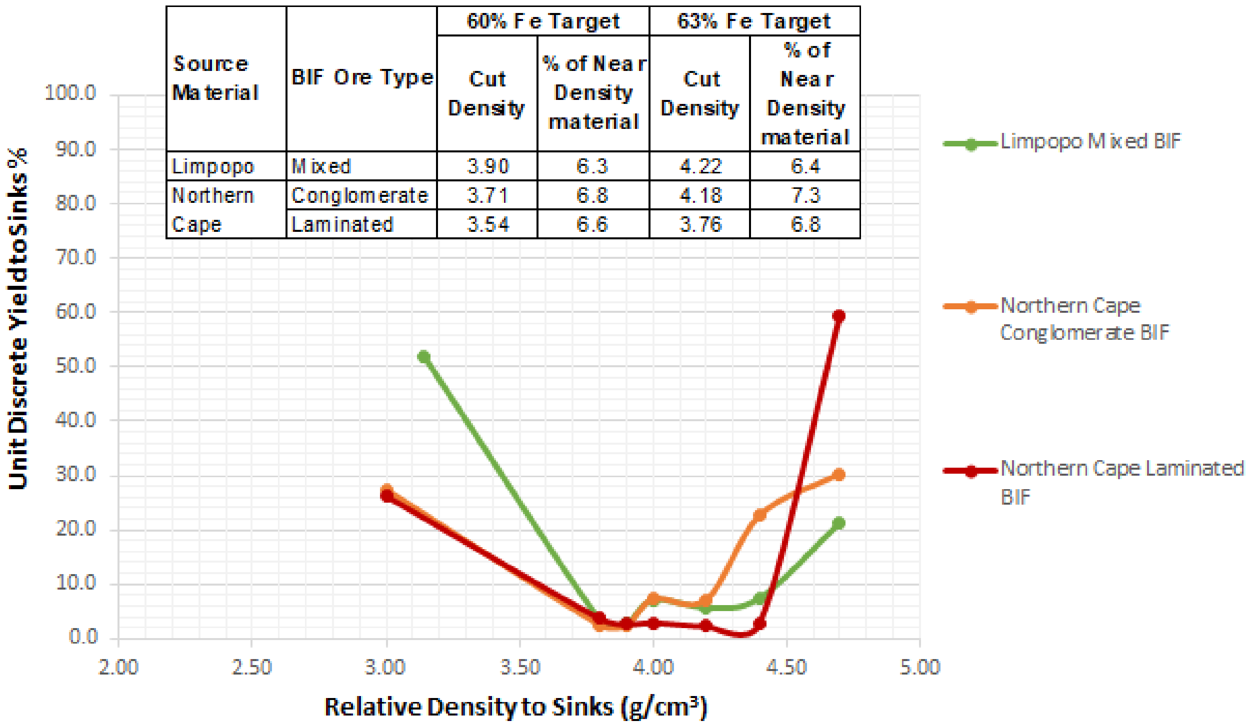

Source Material	BIF Ore Type	60% Fe Target		63% Fe Target	
		Cut Density	% of Near Density material	Cut Density	% of Near Density material
Limpopo	Mixed	3.90	6.3	4.22	6.4
Northern Cape	Conglomerate	3.71	6.8	4.18	7.3
	Laminated	3.54	6.6	3.76	6.8

FIG 17 – Discrete washability profiles for the -12+1.18 mm size fraction for all three BIF samples.

Predicted partition curves for dense media separation

The predicted DMS iron grade recovery curve for the three BIF samples are compared to the HLS results in Figure 18 which indicates similar responses were achieved, with the DMS results superimposed on the HLS results. At the target iron grades the DMS achieves unit recoveries 0.3 per cent to 0.78 per cent lower than HLS, the similar response can be attributed to the low proportion of near density material around the cut point. At the higher target grade a significant drop (13.1 per cent to 14.4 per cent) in the iron unit recovery is observed for the mixed and conglomerate BIF. Increasing the target iron grade has a negligible impact on the unit iron recovery (2.8 per cent difference) for the laminated BIF sample.

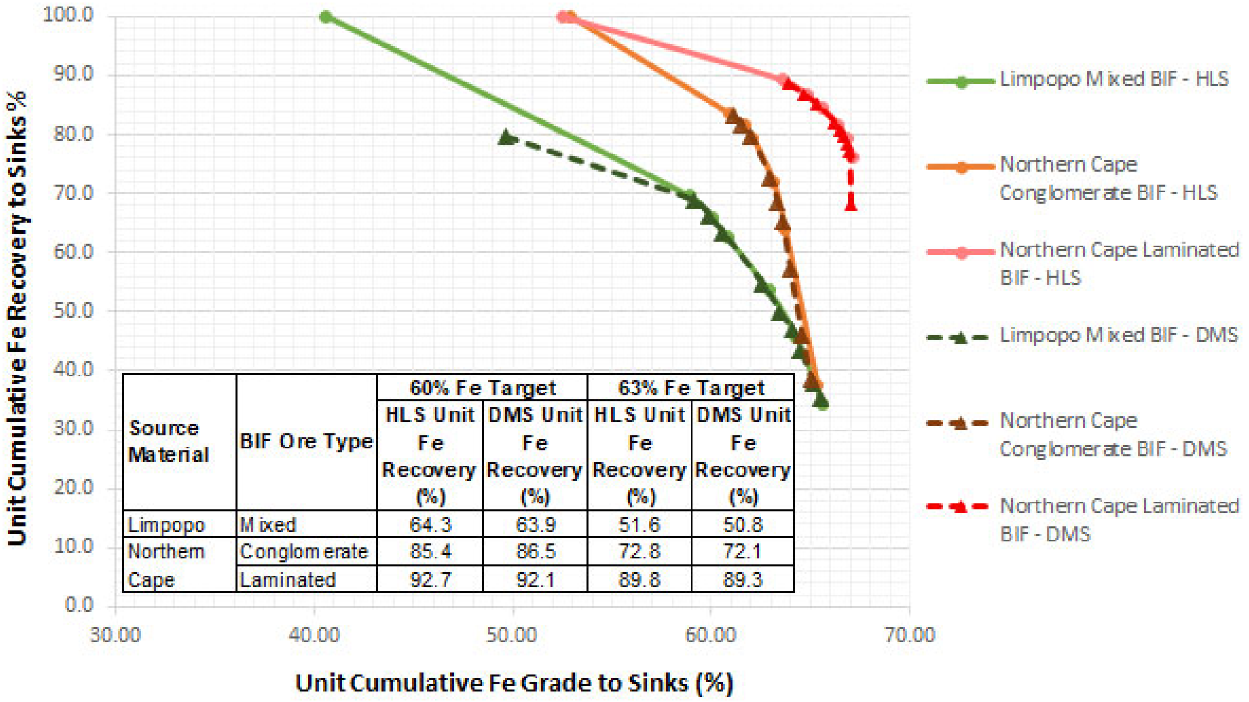

Source Material	BIF Ore Type	60% Fe Target		63% Fe Target	
		HLS Unit Fe Recovery (%)	DMS Unit Fe Recovery (%)	HLS Unit Fe Recovery (%)	DMS Unit Fe Recovery (%)
Limpopo	Mixed	64.3	63.9	51.6	50.8
Northern Cape	Conglomerate	85.4	86.5	72.8	72.1
	Laminated	92.7	92.1	89.8	89.3

FIG 18 – Predicted iron grade-recovery curve for DMS in comparison to HLS.

The comparison between the DMS performance at an Ep of 0.05–0.07 is compared to the HLS results at a target iron grade of 60 per cent and 63 per cent in Table 3. At 60 per cent Fe product grade the DMS cut density ranges from 3.57 g/cm^3 to 3.92 g/cm^3 at overall yields and overall recoveries of 35.7–64.7 per cent and 51.9–75.3 per cent respectively. Although the head grade of the conglomerate sample is higher than the mixed BIF sample similar overall recoveries are achieved due to the high proportion of fines in this sample necessitating the beneficiation of this fraction to improve overall recoveries. Increasing the product grade to 63 per cent Fe results in a 5.1–10.2 per cent and 2.8–14.4 per cent drop in the overall yield and overall recovery respectively.

For all three samples at the two target iron grades the alumina specification is met, however only the mixed and conglomerate BIF samples are able to achieve the silica specification when a target grade of 63 per cent is targeted. Due to the low alumina and phosphorus content an elevated silica specification could be negotiated, or these ore types could be blended with superior grade products to improve overall yields.

TABLE 3

Predicted DMS performance for the -12+1.18 mm size fraction at a target iron grade of 60 per cent and 63 per cent.

Source Material	BIF Ore Type	Size Fraction (mm)	Target Fe Grade: 60% Fe and 63% Fe									
			Process	Ep	D50	Unit Mass (%)	Overall Mass (%)	Grade [%]			Unit Recovery (%)	Overall Recovery (%)
								Fe	Si	Al	Fe	Fe
			Product Specifications*					Targets	< 3.5	<1.50		
Limpopo	Mixed	-12+1.18	**HLS/DMS Feed Grade**			**100.0**	**80.3**	**40.64**	**40.64**	**40.64**	**100.0**	**79.3**
			HLS	0	3.90	43.8	35.8	60.00	4.55	0.50	64.3	52.2
					4.22	33.5	27.4	63.00	2.54	0.50	51.6	41.9
			DMS	0.06	3.92	43.6	35.7	60.00	4.56	0.50	63.9	51.9
				0.07	4.25	33.0	27.0	63.00	2.53	0.50	50.8	41.3
Northern Cape	Conglomerate	-12+1.18	**HLS/DMS Feed Grade**			**100.0**	**65.0**	**52.91**	**8.84**	**0.98**	**100.0**	**67.2**
			HLS	0	3.71	75.7	49.2	60.00	4.27	0.68	85.4	57.3
					4.18	67.9	44.1	63.00	2.36	0.55	72.8	48.9
			DMS	0.05	3.57	76.2	49.5	60.00	4.29	0.69	86.5	58.1
				0.06	4.21	60.5	39.3	63.00	2.37	0.55	72.1	48.4
	Laminated	-12+1.18	**HLS/DMS Feed Grade**			**100.0**	**80.0**	**52.49**	**10.28**	**0.76**	**100.0**	**81.8**
			HLS	0	3.54	82.2	65.7	60.00	5.59	0.66	92.7	75.9
					3.76	75.1	60.0	63.00	3.72	0.63	89.8	73.5
			DMS	0.06	3.63	80.92	64.7	60.00	5.59	0.66	92.1	75.3
				0.07	3.76	74.56	59.6	63.00	3.71	0.63	89.3	73.0

* S&P Global Platts (2020)

Shaking table on the natural -1.18 mm size fraction

The iron grade and recovery response as a function of yield for the shaking table test work on the natural -1.18 mm fines is presented in Figure 19. A similar iron grade and recovery profile is observed across all three samples with the conglomerate sample achieving lower purity concentrates and unit recoveries at yields below 37 per cent and 70 per cent respectively. At the target product grades of 60 per cent Fe and 63 per cent Fe the laminated sample achieved the best unit recoveries of 52.4 per cent and 39.1 per cent at unit yields of 40.6 per cent and 28.7 per cent respectively. Unlike the coarse size fraction increasing the target grade has a significant impact on iron recovery for the laminated BIF sample.

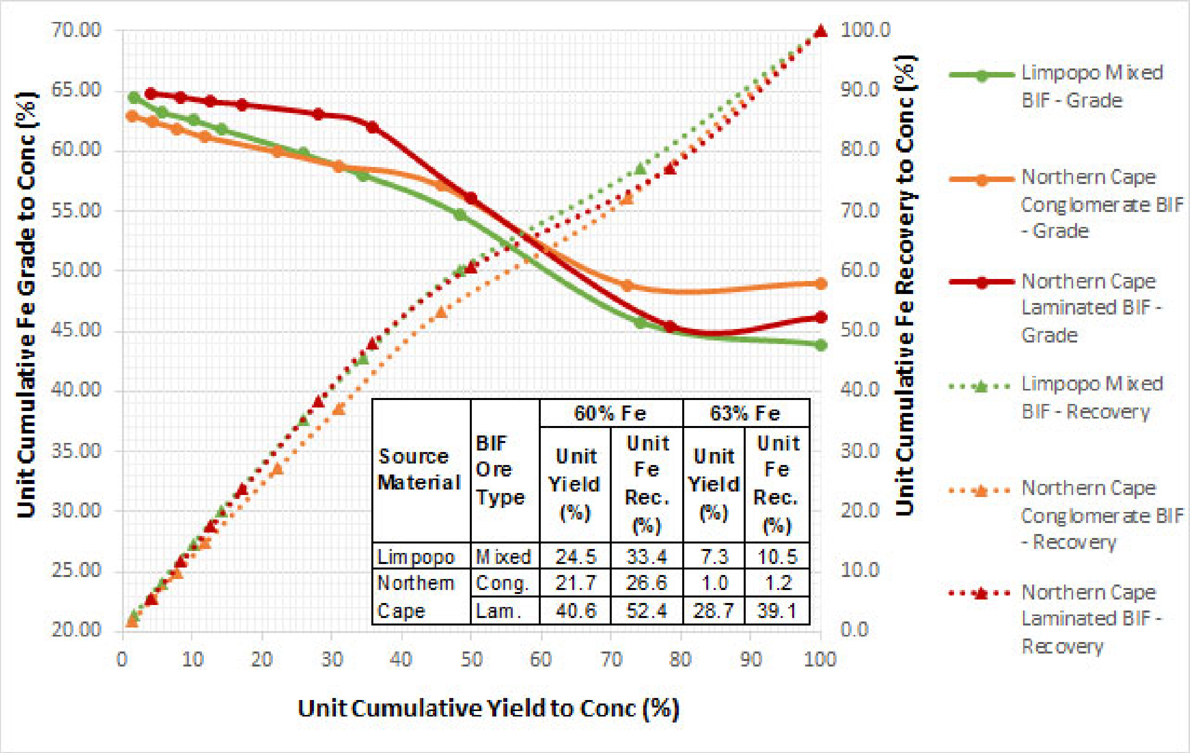

Source Material	BIF Ore Type	60% Fe		63% Fe	
		Unit Yield (%)	Unit Fe Rec. (%)	Unit Yield (%)	Unit Fe Rec. (%)
Limpopo	Mixed	24.5	33.4	7.3	10.5
Northern Cape	Cong.	21.7	26.6	1.0	1.2
	Lam.	40.6	52.4	28.7	39.1

FIG 19 – Iron grade and recovery as a function of yield for the shaking table test work on the natural -1.18 mm fines.

The unit iron recoveries on the fines are significantly lower than that of the coarse (+1.18 mm) material for all three samples. The particle size distribution and iron deportment of the shaking table feed for all three BIF samples is presented in Table 4 and indicate that the conglomerate and mixed BIF samples are finer than the other samples containing 10.5–21.0 per cent additional slimes (-38 µm material). The Fe deportment closely follows mass per cent with 24.3–36.7 per cent reporting to the -38 µm size fraction and is thus not recoverable by gravity separation. Magnetic separation on these slimes could improve the overall iron recoveries.

TABLE 4

Size-by-assay of the Shaking Table feed.

Size Fraction (µm)	Limpopo Mixed BIF			Northern Cape Conglomerate BIF			Northern Cape Laminated BIF		
	Discrete Mass (%)	Fe Grade (%)	Fe Deportment (%)	Discrete Mass (%)	Fe Grade (%)	Fe Deportment (%)	Discrete Mass (%)	Fe Grade (%)	Fe Deportment (%)
-1180+850	7.7	42.47	7.3	6.5	58.35	7.6	6.4	47.29	6.6
-850+600	14.1	43.70	13.8	11.8	57.96	13.8	16.4	48.55	17.4
-600+425	9.4	43.39	9.1	9.3	56.72	10.6	13.0	48.52	13.8
-425+300	8.5	44.27	8.4	7.9	55.50	8.9	10.9	48.53	11.5
-300+212	6.3	46.32	6.6	5.7	49.97	5.8	7.7	47.14	7.9
-212+150	5.4	46.76	5.7	4.9	47.70	4.8	6.3	44.57	6.1
-150+106	4.8	49.01	5.2	4.5	37.43	3.4	4.5	40.68	4.0
-106+75	4.8	51.15	5.5	6.8	28.25	3.8	4.6	37.75	3.8
-75+53	3.7	50.77	4.2	4.2	31.35	2.6	2.9	39.64	2.5
-53+38	3.7	48.58	4.0	2.9	36.01	2.1	2.3	42.60	2.1
-38	31.5	42.67	30.1	35.6	51.11	36.7	25.1	44.47	24.3
Total	**100.0**	**44.68**	**100.0**	**100.0**	**49.61**	**100.0**	**100.0**	**45.84**	**100.0**

Overall mass balances and comparisons

The summary of the overall mass balance with respect to the concentrates at a target product grade of 60 per cent Fe and 63 per cent Fe is presented in Tables 5 and 6 respectively. Additional iron recovery from the -1.18 mm is minimal and ranges from (0.5 per cent to 12.0 per cent), although it is observed that at a 63 per cent Fe product grade the shaking table concentrates meets the silica target specification. The iron recoveries of the final concentrate for the mixed and conglomerate BIFs are similar despite the difference in head grades and yields. The laminated BIF sample achieved the best recoveries and yields with minimal impact on the overall recovery when higher iron product grades are targeted.

TABLE 5

Overall mass balance summary at an iron target grade of 60 per cent Fe.

Source Material	**BIF Ore Type**	**Product**	**Overall Yield (%)**	**Conc Grade (%)**			**Overall Fe Recovery (%)**
				Fe	**Si**	**Al**	
Product Specifications*				**Targets**	**< 3.5**	**<1.50**	
Limpopo	Mixed	***Relative Error (%)***		***3.11***	***1.04***	***15.52***	
		Measured Head		***42.61***	***16.90***	***0.56***	
		Calculated Head	***100.0***	***41.29***	***16.73***	***0.64***	***100.0***
		DMS Conc	35.7	60.00	4.56	0.50	51.8
		ST Conc	8.3	60.00	4.32	0.50	12.0
		Final Conc	**43.9**	**60.00**	**4.52**	**0.50**	**63.8**
Northern Cape	Conglomerate	***Relative Error (%)***		***0.56***	***3.60***	***2.00***	
		Measured Head		***51.48***	***10.27***	***1.30***	
		Calculated Head	***100.0***	***51.19***	***10.64***	***1.27***	***100.0***
		DMS Conc	49.5	60.00	4.29	0.69	58.0
		ST Conc	3.5	60.00	4.01	1.01	4.1
		Final Conc	**53.0**	**60.00**	**4.27**	**0.71**	**62.2**
	Laminated	***Relative Error (%)***		***0.50***	***0.50***	***8.09***	
		Measured Head		***51.08***	***11.05***	***1.02***	
		Calculated Head	***100.0***	***51.33***	***10.99***	***1.10***	***100.0***
		DMS Conc	64.7	60.00	5.59	0.66	75.7
		ST Conc	8.1	60.00	4.38	1.34	9.5
		Final Conc	**72.9**	**60.00**	**5.45**	**0.74**	**85.2**

* S&P Global Platts (2020)

TABLE 6

Overall mass balance summary at an iron target grade of 63 per cent Fe.

Source Material	BIF Ore Type	Product	Overall Yield (%)	Conc Grade (%)			Overall Fe Recovery (%)
				Fe	Si	Al	
Product Specifications*				**Targets**	**< 3.5**	**<1.50**	
Limpopo	Mixed	***Relative Error (%)***		***3.11***	***1.04***	***15.52***	
		Measured Head		***42.61***	***16.90***	***0.56***	
		Calculated Head	***100.0***	***41.29***	***16.73***	***0.64***	***100.0***
		DMS Conc	27.0	63.00	2.53	0.50	41.2
		ST Conc	6.1	63.00	2.15	0.50	9.3
		Final Conc	**33.1**	**63.00**	**2.46**	**0.50**	**50.5**
Northern Cape	Conglomerate	***Relative Error (%)***		***0.56***	***3.60***	***2.00***	
		Measured Head		***51.48***	***10.27***	***1.30***	
		Calculated Head	***100.0***	***51.19***	***10.64***	***1.27***	***100.0***
		DMS Conc	39.3	63.00	2.37	0.55	48.4
		ST Conc	0.4	63.00	1.69	0.76	0.5
		Final Conc	**39.7**	**63.00**	**2.36**	**0.55**	**48.9**
	Laminated	***Relative Error (%)***		***0.50***	***0.50***	***8.09***	
		Measured Head		***51.08***	***11.05***	***1.02***	
		Calculated Head	***100.0***	***51.33***	***10.99***	***1.10***	***100.0***
		DMS Conc	59.6	63.00	3.71	0.63	73.2
		ST Conc	5.7	63.00	2.99	0.88	7.0
		Final Conc	**65.4**	**63.00**	**3.65**	**0.65**	**80.2**
		DMS Conc	59.0	63.36	3.49	0.62	72.8
		ST Conc	5.7	63.00	2.99	0.88	7.03
		Final Conc	**64.8**	**63.32**	**3.45**	**0.64**	**79.8**

* S&P Global Platts (2020)

Since the recovery for the laminated BIF sample is high at a 63 per cent Fe product grade, a second option was explored in which the DMS concentrate product grade was driven by a silica content of 3.49 per cent (just below the target product specification). In this option (highlighted orange in Table 6) the overall iron recovery drops by 0.4 per cent indicating this sample lends itself to economic beneficiation and is very promising.

CONCLUSIONS

- South African high-grade iron ore reserves are in depletion, hence there is a need to exploit alternative resources in particular BIF which makes up greater than 65 per cent of current reserves in order to maximise resource utilisation and extend life-of-mine.
- Research undertaken was based on the hypothesis that BIF contained within the Asbestos Hills Iron Formation of the Transvaal Supergroup in the Northern Cape, South Africa is equivalent to BIF derived from the Limpopo regions in South Africa located in the Penge Iron Formation and thus beneficial potential for one can be extrapolated for the other.
- The Limpopo mixed and the Northern Cape conglomerate BIF samples responded similarly with overall iron recoveries of 62.2–63.8 per cent and 48.9–50.5 per cent achieved at target iron grades of 60 per cent Fe and 63 per cent Fe respectively despite the difference in head grades and yields. This includes both coarse processing via Dense Media Separation (DMS) and shaking table on the natural -1.18 mm fines. For these two samples the silica target specification could be achieved at target grades of 63 per cent Fe, however with low alumina and phosphorus content, a relaxed silica specification could be negotiated. Alternatively, these ore types could be blended with superior grade products to improve overall yields and recoveries.
- The Northern Cape laminated BIF sample achieved the best metallurgical results of all three samples with overall yields and iron recoveries of 72.9–65.4 per cent and 85.2–80.2 per cent respectively. In both instances the silica grade exceeded the product specification, however if the silica content is the driver the target iron grade increases to 63.32 per cent with a minimal decrease in recovery of 0.4 per cent. This sample lends itself to economic beneficiation and is very promising.

- The promising results of this study indicate that coarse beneficiation of BIF material is possible. These ore types could be blended with superior grade products to improve overall yields and recoveries or sold directly at a 63 per cent Fe product grade whilst sacrificing 0.4–13.3 per cent recovery.
- For all the samples tested the fines concentrate contributes 0.5 per cent to 12.0 per cent to the overall iron recovery and thus a simplified flow sheet comprising solely of Dense Media Separation could be used and the -1.18 mm fines stockpiled for later processing.

ACKNOWLEDGEMENTS

The authors would like to acknowledge Mintek for funding the research project and for providing the necessary facilities and resources to successfully complete the study.

REFERENCES

Anglo American, 2011. *Section 2: Creating a growing and sustainable iron and steel value chain in South Africa*, The South African Iron and Steel Value Chain report.

Bodley, D, Bruch, S, Ralijaona, A and Sithole, R, 2013. The South African Iron Ore Cluster: Potential unrealized, 38 p.

Cairncross, B, 1997. *The manganese adventure: The South African manganese fields*, 235 p (Thorold's Africana Books).

Cairncross, B, 2011. The Thabazimbi Mine Cave, Limpopo Province, South Africa: Assessment of the Cave and its Speleothems, 20 p.

Cairncross, B, Kramers, J D and Villa, I M, 2018. Unusual speleothem formation in the Thabazimbi mine cave, Limpopo Province, South Africa, and its chronology, *South African Journal of Geology*. doi: 10.25131/sajg.121.0020

Carney, M D and Mienie, P J, 2013. A geological comparison of the Sishen and Sishen South (Welgevonden) iron ore deposits, Northern Cape Province, South Africa, *Applied Earth Science*, 112:81–88. Available at: https://www.tandfonline.com/doi/abs/10.1179/0371745032501171

Condie, K C, 2011. *Earth as an Evolving Planetary System,* 2nd ed (Elsevier). doi: 10.1016/C2010-0-65818-4

Media, C, 2018. Iron-Ore, *Published by: Creamer Media's Research Channel, Africa (May 2018)*

Media, C, 2019. Iron-Ore, *Published by: Creamer Media's Research Channel, Africa (April 2019)*

Media, C, 2020. A review of Souths Africa's Iron-ore sector, *Published by: Creamer Media's Research Channel, Africa (June 2020)*

Da Corte, C, Singh, A, Manuel, M, Thakurdin, Y and Mmamakoko, M, 2021. Phase 1: Mineralogical and Density Characterisation of three Fe ore Pit samples from an undisclosed source, External report no 8250. South Africa: Mintek.

ANC's Economic Transformation Committee (ETC), 2020. *Discussion document: Reconstruction, Growth and Transformation: Building a new, inclusive economy.* Available at: https://cisp.cachefly.net/assets/articles/attachments/82688_etc_document_final_8_july_2020.pdf

Eriksson, P G, Hattingh, P J and Altermann, W, 1995. An overview of the geology of the Transvaal Sequence and Bushveld Complex, South Africa, *Mineralium Deposita*, 30(2):98–111. doi: 10.1007/BF00189339

Garside, M, 2020. Iron ore – Statistics and Facts [online], Statista. Available from: https://www.statista.com/topics/1919/iron-ore/

Godongwana, C E, 1943. 'Economic reconstruction', *Nature*, 151(3830), pp 343–346. doi: 10.1038/151343a0

Gross, G A, 1965. Origin of precambrian iron formations, *Economic Geology*, pp 1063–1065. doi: 10.2113/gsecongeo.60.5.1063

Kumba Iron Ore, 2020. Ore Reserve (and Saleable Product) and Mineral Resources 2020, December.

Metalytics, 2019. Iron, Available at: https://investiv.co/category/investiv-daily/iron/

Minerals Council Of South Africa, 2019. 'Facts and Figures | 2018 EDITION', (September), pp. 1–47. Available at: https://39k5cm1a9u1968hg74aj3x51-wpengine.netdna-ssl.com/wp-content/uploads/2019/07/2018_NHPCO_Facts_Figures.pdf.

Mining Data Online, 2019. Major Mines & Projects | Thabazimbi Mine, Mining Data Solutions. Available at: https://miningdataonline.com/property/1513/Tapira-Mine.aspx

Nortje, P G, 2018. The Impact of Supply and Demand Drivers on the Iron Ore Price and Cycle. Thesis. Wits Institutional Repository environment on DSpace (WIReDSpace). https://wiredspace.wits.ac.za/handle/10539/24186

Rao, B V, 2004. Weibull partition surface representation for gravity concentrators, *Minerals Engineering*, 17:953–956.

Singh, A, Lydall, M and Bungane, T, 2019. Roadmap of the Iron and Steel Value Chain. External report no: 43174. South Africa: Mintek

Statista, 2019. Iron ore prices from 2003–2019. Available at: https://www.statista.com/statistics/282830/iron-ore-prices-since-2003

Statista, 2020. Impact of Covid-19 on iron ore prices worldwide from 2019 to May 2020. Available at: https://www.statista.com/statistics/1125574/impact-of-covid-19-on-iron-ore-price/

Statista, 2021. Iron ore mine production by country 2010-2020. Available at: https://www.statista.com/statistics/267380/iron-ore-mine-production-by-country/

Taylor, D, Dalstra, H J and Harding, A E, 2001. Genesis of high-grade hematite orebodies of the hamersley province, Western Australia, *Economic Geology*, 96(1):pp 837–873. doi: 10.2113/gsecongeo.97.1.174

Tom, P, 2015. Optimisation of dense media cyclone plant for the beneficiation of low grade iron ore with associated high proportion of near-density material at Sishen Iron Ore Mine. MSc. University of the Witwatersrand.

Trendall, A F, 2002. The Significance of Iron-Formation in the Precambrian Stratigraphic Record, *Precambrian Sedimentary Environments*, pp 33–66. doi: 10.1002/9781444304312.ch3

Geophysics

Challenges in designing a magnetic resonance logging-while-drilling tool for iron ore exploration

K T O'Neill[1], S Mukkisa[2], M L Johns[3] and T A J Hopper[4]

1. Research Associate, University Western Australia, Crawley WA 6009.
   Email: keelan.oneill@uwa.edu.au
2. Mechanical Engineer, RIG Technologies International, Midvale WA 6056.
   Email: sravani.mukkisa@rigtechnologies.com.au
3. Winthrop Professor, University Western Australia, Crawley WA 6009.
   Email: michael.johns@uwa.edu.au
4. Managing Director, RIG Technologies International, Midvale WA 6056.
   Email: timothy.hopper@rigtechnologies.com.au

ABSTRACT

Technological advances the sensor design and performance for logging while drilling (LWD) instrumentation offer considerable opportunities in iron ore exploration. Here we focus on the development of a nuclear magnetic resonance (NMR) LWD tool. NMR is an advanced geotechnical logging technology capable of providing *in situ* measurements of the porosity, pore size and permeability of the formation of interest. The ability to provide real-time characterisation of iron-ore systems is beneficial to both drilling operations as well as real-time formation evaluation.

The development of an NMR LWD tool for mineral exploration drilling has previously not been achieved due to the significant technical and environmental challenges associated with the design and operation of such a tool. The tool outlined in this work is designed to work in reverse-circulation (RC) drilling systems. As such, the tool needs to be compatible with the RC drill-string, as well as being highly robust to survive the shocks and vibrations experienced during RC drilling operations. The magnetic physics of the probe must be capable of measuring at the appropriate depth into formation whilst being subject to the array of motions experienced during drilling operations. Furthermore, conducting accurate NMR measurements in an iron ore formation is challenging and the measurement methodology must be tailored to characterise the magnetic environment. The tool also requires high-powered electronics capable of operating the necessary pulse sequences for excitation and acquisition. The resultant tool design must therefore optimise the inherent trade-offs which exist between the physical components (ie mechanical structure, magnetic components and electronic hardware) in order to operate appropriately whilst not hindering RC drilling operations.

Current experimental analysis of the prototype indicates that the current probe design exhibits the required measurement specifications and is nearing field testing. Future work will look towards commercialisation of the instrument.

INTRODUCTION

The current development of advanced instrumentation and sensors is enabling a greater array of data to be captured across resource industries. For example, in the oil and gas industry, there has been a significant uptake in 'whilst-drilling' metrology. These technologies measure operational and geophysical data from instruments located behind the drill-bit in tool bottom-hole assemblies (BHAs) (Simpson, 2017). Such real-time measurements provide critical information which can be used to monitor and manage operations. Measurement-whilst-drilling (MWD) systems focus on monitoring the drilling operations using performance factors such as the rate of penetration and the force-on-bit (Gearhart, Moseley and Foste, 1986). More advanced logging-whilst-drilling (LWD) systems are used to measure and examine geophysical properties of the surrounding formation (Zhang, Wang and Guo, 2006). For example, induction and ultrasonic LWD sensors can be used to measure the resistive and acoustic properties of the geology of interest. Such information provides real-time formation characterisation which support live resource management decisions and operations. MWD and LWD have seen very minimal application in the mining industry; primarily due to the high shock and rugged environment experienced during mineral exploration drilling (Hopper *et al*, 2019). Recent advances in technology however are enabling the development of robust MWD and LWD systems for mining.

Low-field NMR is renowned in the oil and gas industry for its application in well logging enabling effective reservoir characterisation (Kleinberg, 2001). The NMR logging tools operate as ‘inside-out‘ NMR measurements in the sense that the measured sample (ie the formation) is external to the measurement probe. NMR is particularly advantageous as it is able to perform *in situ*, non-invasive measurement of rock properties to provide valuable information on; total porosity, free and bound fluid quantification, permeability and wettability state (Coates, Xiao and Prammer, 1999; Kleinberg and Jackson, 2001). NMR is not widely used in other resource industries, however recent advances in NMR tool design towards mobile, lower cost well-logging tools is allowing measurements to be performed across a variety of geo-resource industries (Hürlimann and Heaton, 2015). For example, NMR has been successfully applied towards determining water content in iron ore (Hopper, Trofimczyk and Birt, 2017), hydrogeological characterisation of groundwater aquifers (Woods *et al*, 2019) and evaluation of coal seam gas deposits (Hopper, Neville and O’Neill, 2018).

In this work, we outline the design of a novel NMR LWD tool which is designed for application in reverse circulation (RC) drilling. The tool is intended to measure the porosity, free and bound fluid volumes and estimate the permeability. This information is crucial to the geophysical evaluation of iron ore resources during exploration and development. Major challenges in designing the tool predominantly involve ensuring the tool is robust to drilling operations. This includes designing the mechanical structure of the tool to be considerably durable to the harsh environment of mineral exploration drilling. Furthermore, we must ensure the NMR signal is not significantly impacted by drilling motion. In this work, we will first outline the background to designing an NMR LWD tool, including: anticipated drilling motion and relevant NMR theory. We will then outline the proposed tool design being utilised for the prototype tool being constructed. Finally, we will present the results of motion simulations, which will examine the performance of the tool under anticipated motion.

BACKGROUND

Drilling motion

In this work, we are focused on developing an NMR LWD tool towards for RC drilling, which is one of the primary drilling methods utilised in mineral exploration within Australia. It is thus important to understand the design and operations of a RC system and the resulting motion experienced by the tool during drilling. In RC drilling, high pressure air is pumped down through outer tubes to the drill-bit and is then returned through the inner tube drawing the rock cuttings back to the surface without contacting the formation (Marjoribanks, 2010). This enables on-depth sampling of uncontaminated drill cuttings for further analysis. A pneumatic reciprocating piston drives the drill bit to impact the rock and crush the formation. The drill bit movement against the rock surface, rotation and percussion, generate axial and lateral vibrations through the drill rod. To quantify the shocks and vibrations in the drill-string, preliminary testing was done with 3-axis vibration data logging sensors built into an adaptor rod connected directly behind the 4.5’ hammer. An example of the 3-axis vibration test results are presented in Figure 1. The accelerometers were mounted on radially (Y and Z directions) damped chassis – thus the axial shocks (X direction) are more prominent.

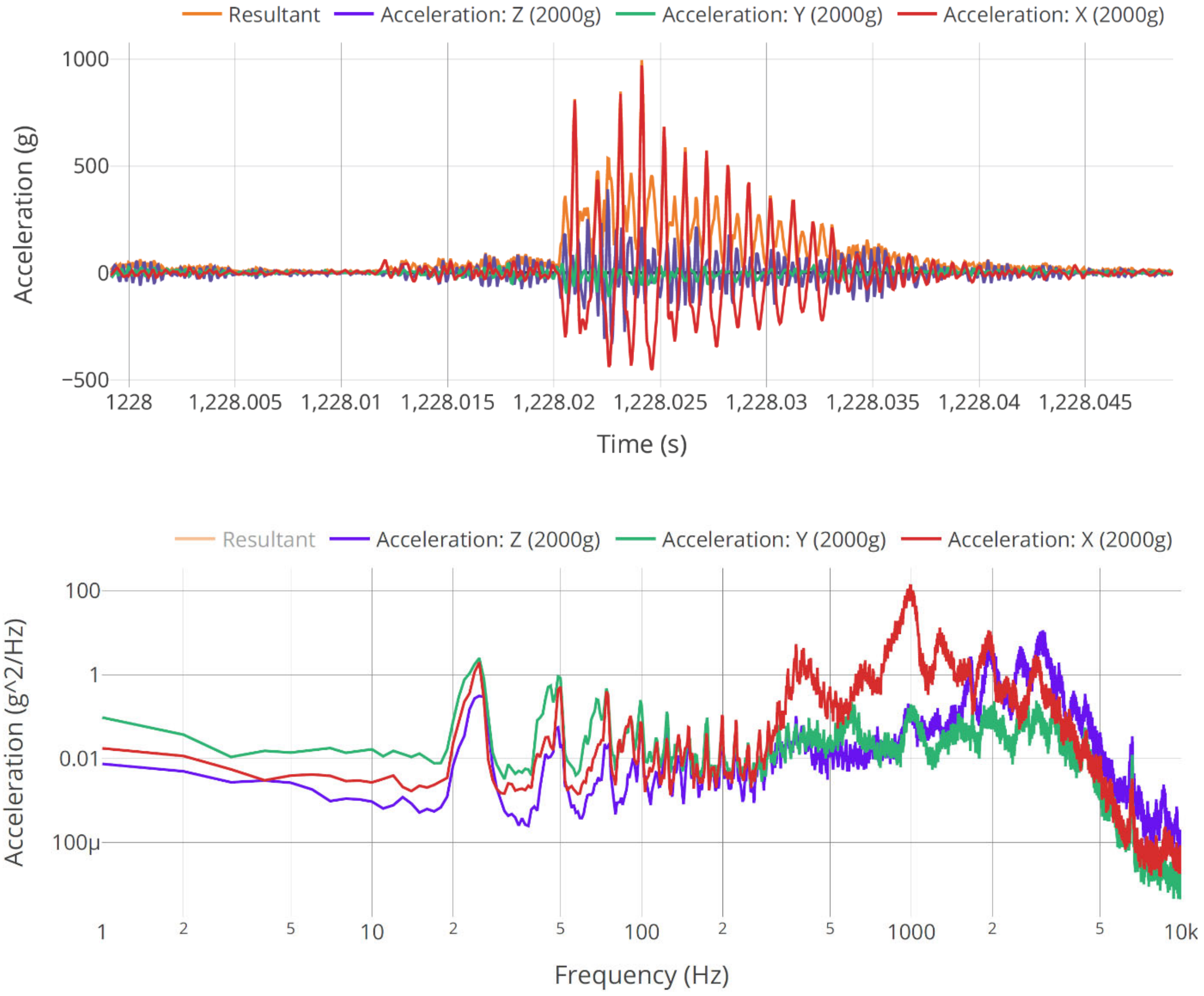

FIG 1 – Example 3-axis accelerometer measurements of shocks and vibrations experienced in RC drilling. Note that the accelerometers are damped in radial directions (Y and Z).

Test results indicated significant shocks at the hammer frequency at 15–40 Hz (with harmonics observed at higher frequencies). Vibrations at even higher frequencies (>400 Hz) also present significant shocks (up to 100 g^2/Hz) on the system.

Nuclear magnetic resonance

This section provides a brief introduction to NMR and the aspects fundamental to this work, however for a more detailed description of NMR, the reader is directed towards the extensive literature on the subject (Callaghan, 1993; Levitt, 2001). NMR involves the interaction between nuclei of atoms and an external magnetic field. Hydrogen atoms (^{1}H) are the most commonly measured atoms in NMR and are the atoms of interest in this work. A static magnetic field (B_0) is used to align hydrogen nuclei in the direction of the external magnetic field. Radio frequency (r.f.) pulses at the appropriate frequency are then used generate an oscillating electromagnetic field (B_1) to excite atoms from a ground state to a higher energy. Atoms return to the ground state via relaxation processes which are used to quantify and characterise physical information about the materials present.

NMR measurements utilise pulse sequences that depict the application of r.f. pulses to appropriately excite the species of interest. For example, the commonly applied Carr-Purcell-Meiboom-Gill (CPMG) sequence is utilised to capture T_2 relaxation within a material (Carr and Purcell, 1954; Meiboom and Gill, 1958). This involves a single 90° pulse to excite the signal followed by a series of 180° pulses to refocus the signal for detection.

In NMR logging, tool motion influences the spin dynamics experienced by the nuclei throughout the duration of a measurement (Deng *et al*, 2013; Edwards, 1997; Akkurt, 1991). The effect of tool motion on the measurement can be considered with respect to the measurement during both the signal polarisation and acquisition stages. In general, the impact of motion is relatively insignificant on the polarisation stage (Coman *et al*, 2015), therefore in this work we focus on NMR signal attenuation in the acquisition stage.

The influence of the tool motion experienced during drilling on the measurement dynamics during the acquisition stage is deconvoluted into two key components (Coman, Thern and Kischkat, 2018; Blanz, Thern and Coman, 2017); (i) the flow effect, and (ii) the dephasing effect. Flow effects are a consequence of the position of the tool at the refocusing r.f. pulses and NMR echo acquisition relative to the position when the nuclei where initially excited. The dephasing effect is a consequence of nuclei experiencing a changing magnetic field during acquisition. The effect is analogous to the diffusion effect normally observed during CPMG sequences with stationary measurements (Hürlimann, 2001).

Two of the key factors which can be controlled in the tool design influencing the motion are the tool magnetic field gradient (G) and the echo spacing (T_E) (Heaton *et al*, 2012). A low gradient has a two-fold benefit to the sensitivity of the tool to motion. Firstly, the lower gradient results in a thicker slice of the sensitive volume being excited. This results in lower signal attenuation due flow effects; a larger slice means that there is less of the initially excited volume leaving the sensitive volume relative to a thinner slice; resulting in improved robustness to lateral motion (Borghi *et al*, 2005). The second benefit of a low magnetic field gradient is the reduced impact of signal dephasing (Blanz *et al*, 2010). The low field gradient means that excited nuclei experience a smaller change in magnetic field during tool motion relative to a higher gradient. Reducing the echo spacing (T_E) considerably reduces the degree of signal attenuation due to dephasing (Blanz *et al*, 2010; Coman *et al*, 2014) and also improves the data sample rate in NMR measurements.

TOOL DESIGN

Concept

In terms of the tool components relevant to generating a signal, an NMR logging probe usually consists of permanent magnets, magnetic cores and a coil (attached to the electronics). The permanent magnets are usually materials such as NdFeB or SmCo that generate the strong static magnetic field (B_0). An oscillating current is passed through the coil in order to produce an electromagnetic field (B_1) field used to excite nuclei. Magnetic cores produced from high magnetic permeability materials (eg iron, ferrites) concentrate the magnetic field in the core material. The coil is wrapped around the electromagnetic cores in the shape of a solenoid to create an inductor.

One of the most common configurations utilised in the majority of LWD tools as well as many wireline NMR tools is the Jasper-Jackson design (Burnett and Jackson, 1980; Jackson, Burnett and Harmon, 1980; Cooper and Jackson, 1980). The design consists of two cylindrical magnets placed with magnetic poles opposing each other (Jackson, 1984). The antenna inductor (cores and coil) are then placed in the region between the two magnets. The resulting interaction of the static field produced by the permanent magnets and the oscillating electromagnetic field produced by the coil results in a axisymmetric, cylinder-shaped sensitive region around the tool in the formation (schematically shown in Figure 2. This region has a low magnetic field gradient which enables a sufficiently large sensitive volume to be measured (Jachmann, Yang and Chen, 2013). Finally, the Jackson design offers a simple geometry which provides ease of manufacturing. The design can be contained in a diametrical section of the tool (ie it does not need to use the centre of the tool) allowing it to be compatible with RC drilling operations.

The Jackson design has been selected for the NMR LWD tool outlined in this work.

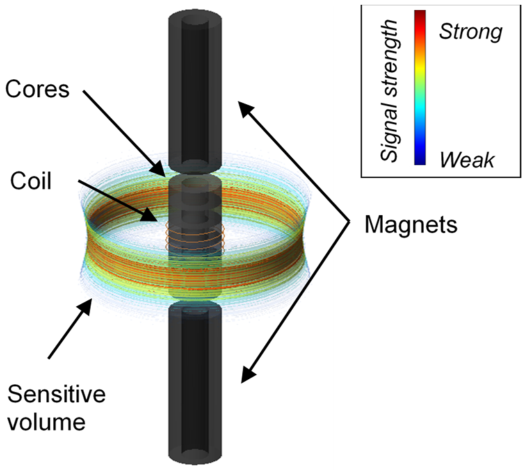

FIG 2 – Illustration of the Jackson logging tool design, with the position of the sensitive volume indicated.

Mechanical and electronic design

The tool is designed to be used in a 4.5’ RC drilling system operating in iron ore exploration environments up to depths of 250 m. The RC drill-string uses dual-wall drill rods with inner and outer tubes. The outer tubes supply air at pressures from 35–70 bar to operate the pneumatic hammer, with a maximum operating temperature of 130°C. The air supply will vary depending on the compressor and the formation being drilled. The mechanical design for the probe will need to ensure the airflow is not significantly impacted and that the operational lifetime of the components is reasonable. The Jackson design means that the NMR components (magnets, cores and coil) need to be housed within an axisymmetric section in a very constrained space between the outer rod and the housing.

A medium size RC rig has a torque capacity of 10 kN-m and an overpull capacity of 200 kN. Tool joint connections and the mechanical components of the tool that are part of the drill string need to handle the drilling torques, shocks, vibrations and overpull loadings of the drill string with an adequate safety factor.

A major challenge in the choice of material to use in the antenna section. This material is required to be non-magnetic and non-conductive in order to be able to perform electromagnetic measurements. Furthermore, the material must be robust to survive the abrasion and wear experienced in mineral exploration drilling environments. The selected material is a high strength thermoplastic composite which meets the above criteria. The remainder of the housing (away from the antenna) as well as other key mechanical sections (ie core chassis and drill rods) will use high strength austenitic stainless steel for strength and abrasion performance. The cylindrical cores are assembled directly onto the chassis followed by cylindrical magnet subassemblies. The antenna is to be potted (using epoxy) to minimise any movement between the magnets and cores to avoid signal loss.

The operation of a NMR probe requires a high voltage (2800 V) power supply system in a constrained spatial environment. A modular electronics system has been designed to achieve the specific operational requirements of the NMR system. A power buffer is included to provide energy storage to allow for the short bursts of pulses required by the probe. A high voltage power supply system manages the application of power from the buffer to the probe. The transmission system is designed to generate the appropriate pulse sequence transmitted by the NMR coil in order to produce a measurable signal. A receive (acquisition) system captures the measured signal and applies appropriate initial processing (eg filtering) to enable data communication. Finally, the communications system manages the control (eg input settings and parameters) as well as measured data (ie output signal) to external interfaces.

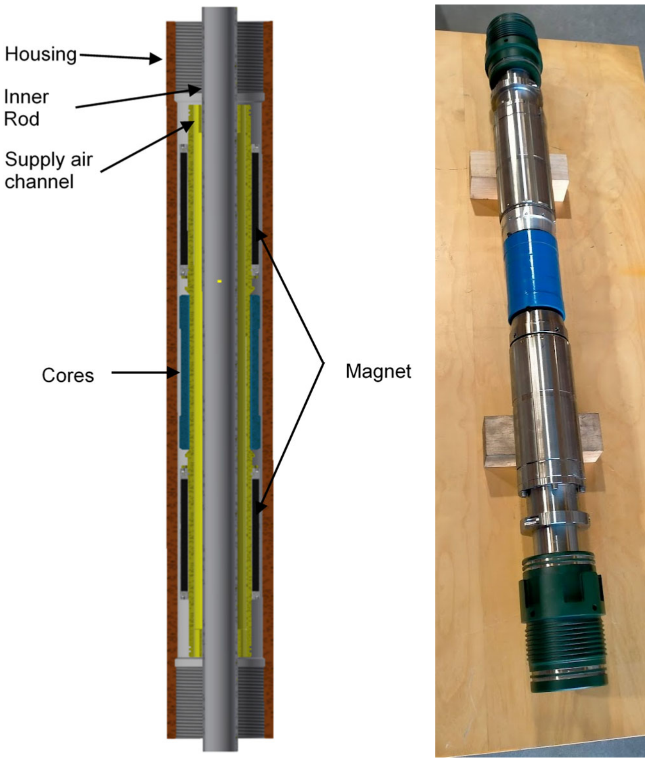

FIG 3 – (a) Cross-section of the antenna assembly with the key components indicated, and (b) a photo of the prototype tool.

MEASUREMENT SIMULATIONS

In order to understand and quantify the performance of relative tool designs, the tool measurement has been reproduced using electromagnetic simulations. Finite element method magnetics (FEMM) is used to perform NMR tool simulations. A given tool design (eg component sizing, materials and geometric arrangement) is input into the simulation. A magnetostatic simulation is initially performed to determine the B_0 field which is the permanent magnetic field generated by the permanent magnets. The magnetic field strength at the desired diameter of investigation (doi:) is determined and the appropriate operating frequency for ^{1}H is calculated. This frequency is input into a time-dependent magnetic field simulation to quantify the B_1 field. Both the B_0 and B_1 fields are determined in an axisymmetric manner across radial (r) and axial (z) dimensions. The calculated B_0 and B_1 fields are then input into the subsequent spin dynamic calculations (outlined in Hürlimann and Griffin, 2000). These calculations consider a standard CPMG sequence which is commonly utilised in logging.

Here, we focus on the impact of drilling motion on the NMR signal measurement. Motion profiles are introduced into the spin dynamic simulations to adjust the position of the tool with respect to the initially excited fluid volume during a signal acquisition. Simple harmonic motion profiles are introduced to represent drilling shocks and vibrations; whilst not as complex as true drilling motion, however the application of harmonic profiles will enable easier identification of the factors influencing signal attenuation. A harmonic profile with an amplitude of 1 mm, a frequency of 20 Hz and a phase of zero is considered to approximately reflect the anticipated drilling motion. We examine the impact of the two key parameters discussed in the Background section: the echo spacing (T_E) and the magnetic field gradient (G).

We first consider the impact of echo spacing. The base harmonic profile is introduced in the axial direction (ie vertical vibrations). This profile is imposed during the spin dynamic calculations and the resulting signal attenuation over the duration of the CPMG sequence (0.5 s) is monitored. The echo spacing is varied across typical values (0.2–2 ms). The resulting attenuation is plotted in Figure 4(a) and the residual signal (at t = 0.5 s) is plotted against the echo spacing in Figure 4(b). Note that for a stationary tool, we would observe zero attenuation at all echo times, such that the signal attenuation plot would be a flat line at one for the entire acquisition.

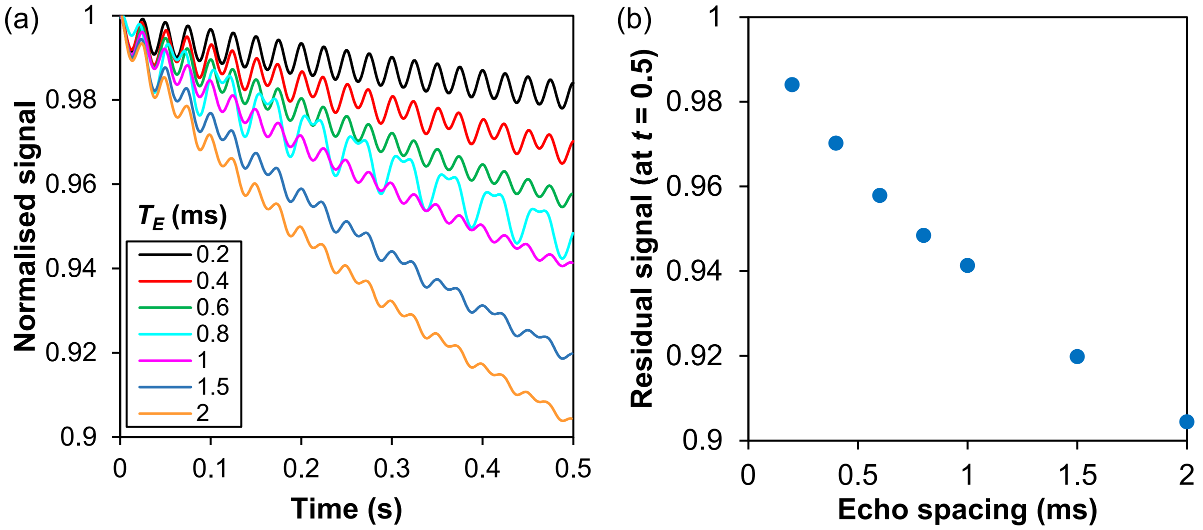

FIG 4 – Impact of echo time on the signal attenuation under motion. An axial harmonic motion profile (amplitude = 1 mm, frequency = 20 Hz) is imposed on the tool during the NMR acquisition. (a) The signal attenuation during acquisition for each echo spacing, and (b) the residual signal (at t 0.5 s) as a function of echo spacing.

The degree of signal attenuation due to motion is observed to increase as a function of echo spacing. This is in agreement with the anticipated behaviour: longer echo spacing's allow more time for excited nuclei to dephase as they move through an inhomogeneous magnetic field before they are refocused. This leads to an overall loss is signal across the excited nuclei, ie increased signal attenuation. The exact dynamics of the signal decay can be more complex than a simple harmonic oscillation: for example, at T_E = 0.8 ms, there is enhanced fluctuations across the duration of the acquisition. This is suggested to relate to the signal interference patterns between the harmonic motion (at 20 Hz) and the CPMG acquisition sequence (at 1250 Hz for T_E = 0.8 ms). For NMR measurement's with echo spacing's which do not resonate with the harmonic motion, more complex wave interference patterns can occur.

The second parameter examined is the magnetic field gradient. The radial gradient is far more significant relative to the axial gradient in the static magnetic field. This is as the opposing poles of the cylindrical permanent magnets result in the axial field negating at the measurement volume, whereas the radial field is pointing outwards and away from the tool. The radial gradient is strongly influenced by the distance between the two magnets, termed the 'magnet spacing'. A small magnet spacing results in a stronger magnetic field as well as a stronger radial gradient at the measurement volume, whereas a larger distance between magnets results in a weaker magnetic field and weaker magnetic field gradient at the measurement volume. This concept will be illustrated via electromagnetic simulations. Signal attenuation will be influence by radial motion due to the direction of the gradient. Thus radial harmonic motion with an amplitude of 1 mm and a frequency of 20 Hz and an initial phase of zero is imposed on the tool. The magnet spacing is varied from 160–300 mm (in 20 mm steps). The measured signal attenuation profile (as a function of CPMG time) is shown in Figure 5(a) whilst both the measured radial gradient (G_r) and final signal attenuation (at t = 0.5 s) are plotted with respect to magnet spacing in Figure 5(b).

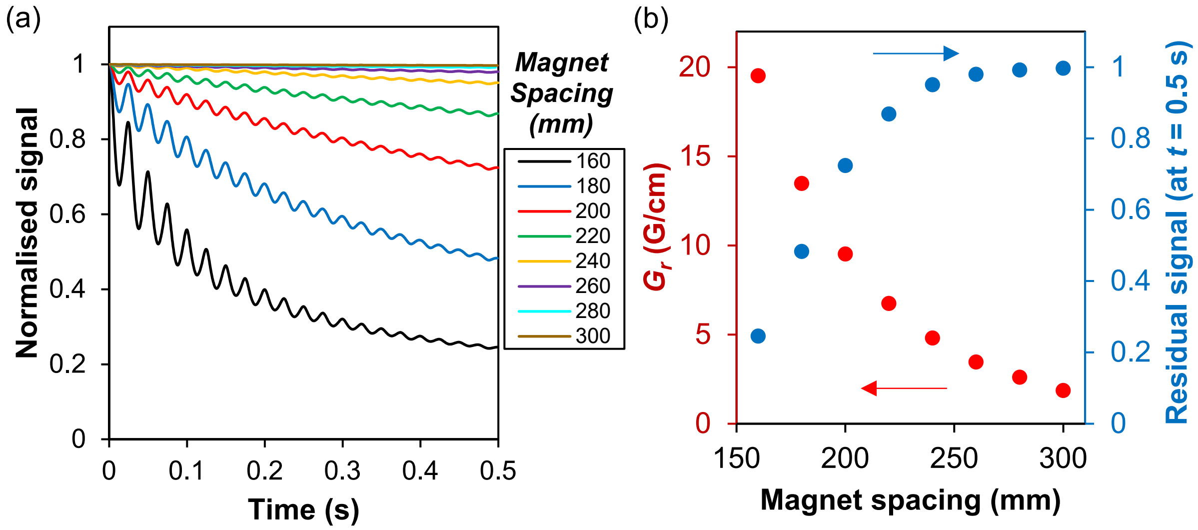

FIG 5 – The impact of the magnet spacing on the signal attenuation due to motion. (a) Signal attenuation across a CPMG measurement for different magnet spacing's from 160–300 mm, and (b) the measured radial gradient (G_r) as well as the final signal (at t = 0.5 s) as a function of magnet spacing.

From Figure 5, we can observe that a lower magnet spacing results in significantly greater signal attenuation. This can be seen in Figure 5(a), where the measured signal attenuation curve decays more rapidly for lower magnet spacing's whilst in Figure 5(b) the final signal is significantly reduced for lower magnet spacing's. This is a consequence of the increasing radial gradient with reduced magnet spacing. A higher gradient has a two-part impact on the signal attenuation due to motion. Firstly, the radial thickness of the measurement volume is inversely proportional to the radial gradient, thus at higher radial gradients, a thinner measurement volume is excited. This results in increased attenuation due to the flow effect: nuclei which are initially excited may not be fully refocused due to the relative position of the tool between excitation and refocusing pulses. This effect is more prominent with thinner excited volumes. Secondly, the increased gradient results in increased signal dephasing between echoes. Signal dephasing is proportional to the field gradient which the excited nuclei move through, thus increasing the gradient results in a greater degree of attenuation due to dephasing. These results demonstrate that the radial gradient (controlled by the magnet spacing) is critical to minimising the influence of signal attenuation induced by motion. The gradient should ideally be kept below 10 G/cm to minimise signal attenuation: although this will also depend on other parameters such as the echo spacing and the anticipated motion.

The results presented here demonstrate an example of how NMR logging tool design can be tailored to reduce sensitivity to motion. The tool design must also account for a range of other key tool performance characteristics (eg signal-to-noise ratio, power consumption). However, understanding the influence and sensitivity towards motion is a key component of logging tool performance.

CONCLUSIONS

In this work, we have discussed the challenges in designing a NMR LWD tool targeted towards the mineral exploration industry. The purpose of the tool is to measure the porosity, free and bound fluid volumes and give an estimate of permeability. The key challenge is ensuring the tool is robust to the harsh environment experienced in reverse circulation drilling. The tool uses the Jackson design for the NMR probe: consisting of two permanent magnets with opposing poles facing each other and an inductor (magnetic cores wrapped with a coil) situated between the two magnets. This design ensures a measurement volume which is axisymmetric and of appropriate size such that it is robust to drilling shocks and rotational movement. The mechanical structure of the tool is designed such that it is sufficiently robust to abrasion and wear across all sections. Furthermore, an appropriate material has been selected such that the electromagnetic NMR measurements are not impacted by the tool housing. Finally, electromagnetic simulations have been performed to assist the geometric design of the tool. This includes understanding the impact of drilling motion on NMR measurements. The echo spacing and magnetic field gradient where identified as having the most significant influence on motion induced attenuation. Simulations have quantified the relative impact of these parameters, allowing informed design decisions to be made in conjunction with other key performance parameters. A prototype probe is currently under construction and the system is anticipated to undertake field trials in the next year. Future work involves extending the measurement capabilities of the probe, including: incorporating more advanced pulse sequences to account for internal gradient attenuation in iron ore, as well as designing a multifrequency system in order to be capable of performing measurements at multiple depths of investigation. We are looking towards the commercialisation of the NMR LWD probe in the coming year.

ACKNOWLEDGEMENTS

This work is funded by CRC-P grant CRCPSIX000068.

REFERENCES

Akkurt, R, 1991. *Effects of motion in Pulse NMR logging.* Colorado School of Mines.

Blanz, M, Kruspe, T, Thern, H F and Kurz, G, 2010. Nuclear Magnetic Resonance Logging While Drilling (NMR-LWD): From an Experiment to a Day-to-Day Service for the Oil Industry.

Blanz, M, Thern, H F and Coman, R, 2017. *T2 inversions with reduced motion artifacts*. US patent application.

Borghi, M, Porrera, F, Lyne, A, Kruspe, T and Krueger, V, 2005. Magnetic Resonance Logging While Drilling Streamlines Reservoir Evaluation. *SPWLA 46th Annual Logging Symposium.* New Orleans, Louisiana: Society of Petrophysicists and Well-Log Analysts.

Burnett, L J and Jackson, J A, 1980. Remote (inside-out) NMR. II. Sensitivity of NMR detection for external samples. *Journal of Magnetic Resonance (1969)*, 41, 406–410.

Callaghan, P T, 1993. *Principles of Nuclear Magnetic Resonance Microscopy*, Clarendon Press.

Carr, H Y and Purcell, E M, 1954. Effects of diffusion on free precession in nuclear magnetic resonance experiments. *Physical review*, 94, 630.

Coates, G R, Xiao, L and Prammer, M G, 1999. *NMR logging: principles and applications*, Houston, Haliburton Energy Services.

Coman, R, Thern, H and Kischkat, T, 2018. Lateral-Motion Correction of NMR Logging-While-Drilling Data. *SPWLA 59th Annual Logging Symposium.* London, UK: Society of Petrophysicists and Well-Log Analysts.

Coman, R, Tietjen, H, Thern, H and Blanz, M, 2014. New Large-Hole Magnetic Resonance Logging-While-Drilling Tool with Short Inter-Echo Time and Improved Vertical Resolution. *SPWLA 55th Annual Logging Symposium*. Society of Petrophysicists and Well-Log Analysts.

Coman, R, Tietjen, H, Thern, H, Blanz, M and Christensen, S A, 2015. Improved NMR Logging Approach to Simultaneously Determine Porosity, T2 and T1. *SPE Annual Technical Conference and Exhibition.* Houston, Texas, USA: Society of Petroleum Engineers.

Cooper, R K and Jackson, J A, 1980. Remote (inside-out) NMR. I. Remote production of region of homogeneous magnetic field. *Journal of Magnetic Resonance (1969)*, 41, 400–405.

Deng, F, Xiao, L, Liu, H, An, T, Wang, M, Zhang, Z, Xu, W, Cheng, J, Xie, Q and Anferov, V, 2013. Effects and Corrections for Mobile NMR Measurement. *Applied Magnetic Resonance*, 44, 1053–1065.

Edwards, C M, 1997. Effects Of Tool Design And Logging Speed On T2 Nmr Log Data. *SPWLA 38th Annual Logging Symposium.* Houston, Texas: Society of Petrophysicists and Well-Log Analysts.

Gearhart, M, Moseley, L M and Foste, M, 1986. Current State of the Art of MWD and Its Application in Exploration and Development Drilling. *International Meeting on Petroleum Engineering.* Beijing, China: Society of Petroleum Engineers.

Heaton, N, Jain, V, Boling, B, Oliver, D, Degrange, J-M, Ferraris, P, Hupp, D, Prabawa, H, Ribeiro, M, Vervest, E and Stockden, I, 2012. New Generation Magnetic Resonance While Drilling. 5.

Hopper, T, Neville, T and O'Neill, K, 2018. Quantifying Gas Content in Coals Using Borehole Magnetic Resonance. *In:* Engineers, S. O. P. (ed.) *SPE Asia Pacific Oil and Gas Conference and Exhibition.* Brisbane.

Hopper, T, Schubert, M, Joldes, G, Moran, B, Kalisch, P, Crumby, M, Buters, N, Ott, K-U, Rogozinski, K, Morgan, Q, Neville, T, Shanmugam, H, Zaeper, R, Lowe, J and Prince, A, 2019. Downhole geophysical data acquisition during reverse circulation drilling for mining. *Australian Exploration Geoscience Conference*, 2–5 September 2019 Perth.

Hopper, T, Trofimczyk, K and Birt, B, 2017. Development of a slimhole downhole nuclear magnetic resonance tool for iron ore – some applications and limitations. *Iron Ore 2017*. (The Australasian Institute of Mining and Metallurgy: Melbourne).

Hürlimann, M and Griffin, D, 2000. Spin dynamics of Carr–Purcell–Meiboom–Gill-like sequences in grossly inhomogeneous B0 and B1 fields and application to NMR well logging. *Journal of Magnetic Resonance*, 143, 120–135.

Hürlimann, M D and Heaton, N J, 2015. NMR well logging. *In:* Johns, M. L, Fridjonsson, E. O, Vogt, S. J and Haber, A. (eds.) *Mobile NMR and MRI.* Cambridge: Royal Society of Chemistry.

Hürlimann, M D, 2001. Diffusion and Relaxation Effects in General Stray Field NMR Experiments. *Journal of Magnetic Resonance*, 148, 367–378.

Jachmann, R, Yang, J and Chen, S 2013. New Data Processing with new Generation Magnetic Resonance While Drilling Tool. *SPWLA 54th Annual Logging Symposium.* New Orleans, Louisiana: Society of Petrophysicists and Well-Log Analysts.

Jackson, J A, Burnett, L J and Harmon, J F, 1980. Remote (inside-out) NMR. III. Detection of nuclear magnetic resonance in a remotely produced region of homogeneous magnetic field. *Journal of Magnetic Resonance (1969)*, 41, 411–421.

Jackson, J, 1984. Nuclear magnetic resonance well logging. *The Log Analyst*, 25.

Kleinberg, R L and Jackson, J A, 2001. An introduction to the history of NMR well logging. *Concepts in Magnetic Resonance*, 13, 340–342.

Kleinberg, R L, 2001. Well logging overview. *Concepts in Magnetic Resonance*, 13, 342–343.

Levitt, M H, 2001. *Spin Dynamics: Basics of Nuclear Magnetic Resonance*, Wiley.

Marjoribanks, R, 2010. *Geological Methods in Mineral Exploration and Mining*, Berlin, Heidelberg, Springer.

Meiboom, S and Gill, D, 1958. Modified spin-echo method for measuring nuclear relaxation times. *Review of scientific instruments*, 29, 688–691.

Simpson, D. 2017. *Practical Onshore Gas Field Engineering*, Elsevier Science.

Woods, R, Bothwell, T, Birt, B J, Hopper, T A J and O’Neill, K T. 2019. Optimising Well Injection Rate for a Managed Aquifer Recharge Project Through the Use of Magnetic Resonance Logging. *FastTimes*, 24, 95–102.

Zhang, X-Y, Wang, J-N and Guo, Y-J. 2006. Advances and trends in logging while drilling technology. *Well Logging Technology*, 30, 10.

Improving drill productivity and delivering better geophysical data faster

D Palmer[1], T A J Hopper[2], K-O Ott[3] and S Mukkisa[4]

1. General Manager, RIG Technologies, Perth WA 6056.
   Email: darren.palmer@rigtechnologies.com.au
2. Managing Director, RIG Technologies, Perth WA 6056.
   Email: timothy.hopper@rigtechnologies.com.au
3. R&D Manager, RIG Technologies, Perth WA 6056. Email: kai-uwe.ott@rigtechnologies.com.au
4. Sustaining Engineering Manager, RIG Technologies, Perth WA 6056.
   Email: sravani.mukkisa@rigtechnologies.com.au

ABSTRACT

RIG Technologies has developed new technology that can successfully acquire high quality natural gamma ray (GR) and hole deviations, downhole while drilling, on reverse circulation drills. This technology survives the hostile downhole environment with shocks of between 400–2500 g for 7–10 days at a time. The Logging While Drilling (LWD) service eliminates the need to run in-rod surveys, either by the driller or by wireline trucks and crews. This time saving is in the middle of the drilling process, thus enabling drills to keep drilling and increase their productivity.

Additional to the natural GR and directional survey, the downhole tool is equipped with sensors to measure the downhole dynamic response of the drilling system providing insights into rock hardness, density and potentially clay types. These parameters have never been acquired behind the hammer before and coupled with surface measurements from the drills themselves, form a rich data set for trainable machine learning algorithms shortening the time to receive advanced geophysical answer products from sometimes months, to live feeds directly from drills (Hopper, 2019).

Alive, high speed, two-way data link between surface data acquisition systems and downhole geophysics tools has been established and incorporates calibrated surface measurements of dynamic forces directly on the drill string to match up with those measured downhole. Receiving live streams of natural GR and hole deviation surveys as the drill is drilling allows true remote decision-making with live data available anywhere in the world. The combined data from surface and downhole dynamics builds a data set that could begin to enable true optimisation of autonomous drilling processes.

INTRODUCTION

Over the last ten years the mining industry has begun to show an interest in obtaining data from behind the drill bit. This was initially done on coring rigs for drilling optimisation, but then expanded to include geophysical measurements. RIG Tech provided some of the first ever behind the hammer geophysical measurements in 2018 and has continued to build on this since then.

With the dominance of Reverse Circulation (RC) drilling in the iron ore industry, there is a significant economic benefit to being able to obtain real-time geophysical data with this drilling technique. These benefits are varied and include:

- reduction of wireline geophysical logging runs and increase drill productivity,
- improved rate of penetration (ROP)/increase in metres drilled,
- rock hardness estimates,
- density while drilling,
- drilling depth optimisation via updated mine models,
- big data analytics on drilling efficiency,
- predictive maintenance on drilling rigs, and
- driller/contractor performance management.

In addition to the above benefits, the use of LWD tools is an enabler for mine sites to progress towards full automation.

ENVIRONMENT

The drilling systems use a pneumatically driven reciprocating hammer operating at around 30 Hz to crush rock and penetrate the ground. This generates significant amounts of shock and vibration in the drill string. This shock and vibration environment in the locations behind the drilling bit and hammer has been characterised to understand the design requirements and rating of the equipment designed. Given the nature of the environment with intense shock events at 30 Hz from the hammer, the shock component is examined.

The shock component is characterised using a Pseudo Velocity Shock Response Spectrum (PVSS) which defines how a system will respond to a given shock impulse for a range of natural frequencies (Figure 1). This gives us a peak pseudo velocity, used in military standards to qualify the likelihood of causing damage. Typically shocks that induce velocities greater than 2540 mm/s are classified as ‘Severe Shocks’ and are likely to cause damage. Damage is probable with velocities greater than 7620 mm/s.

Based on the measured environment, a peak pseudo velocity of greater than 10 000 mm/s would be expected for systems with low natural frequencies, and above 5000 mm/s for systems with a natural frequency around 1000 Hz. This far exceeds the severe shock threshold driving the need for damping and mitigation.

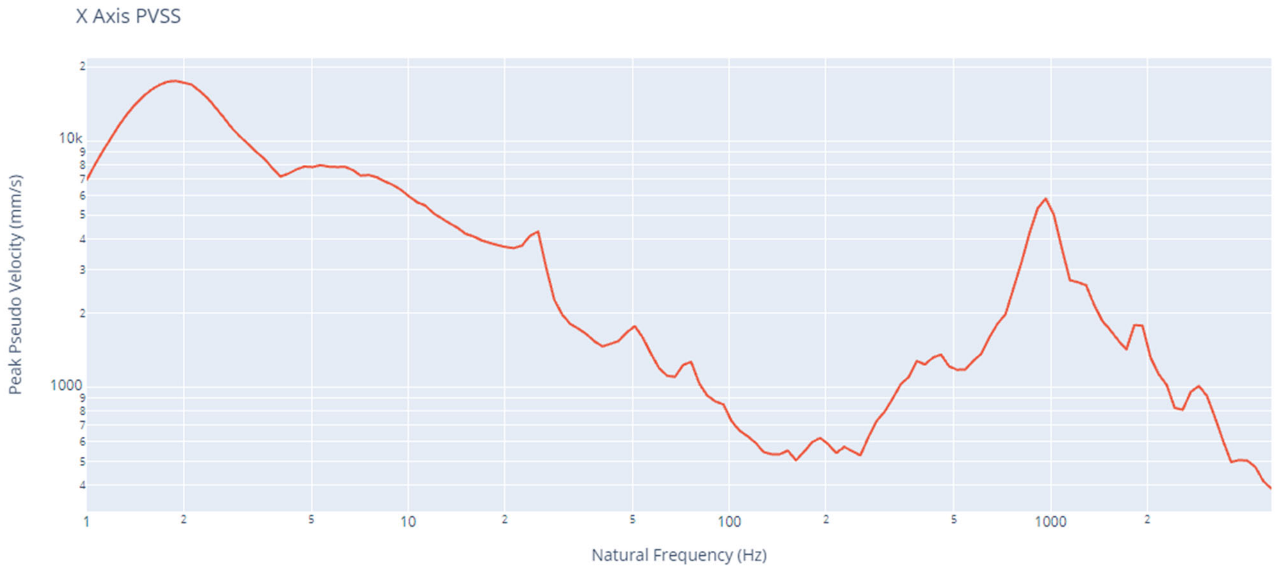

FIG 1 – Pseudo Velocity Shock Response Spectrum for systems located behind an RC pneumatic hammer.

From this analysis a shock rating or test standard was created. Given the behind the hammer geophysics system has been successfully acquiring data, this gives a current shock rating to the system of at least 30 shocks @ 3500 gn/0.4 msec.

One more familiar method of understanding the shock environment is the peak acceleration experienced by the system. Note that while familiar, this measurement does not talk to the energy involved with the shocks, nor the response across potential natural frequencies. In this frame the general peak acceleration for the shocks was >400 G with peak shocks saturating sensors at >2000 G.

PERFORMANCE

The behind the hammer geophysics system drillMAX has been operating successfully now since September 2020 acquiring over 60 000 m in iron ore areas of the Pilbara region of Australia. This system operates in concert with a drill-based sensor hub and edge computing platform drillHUB and a cloud-based data processing, quality control (QC) and delivery system drillINFO. This system acquires the required geophysical information without impacting drilling operations or sampling, and significantly reducing the time spent acquiring data.

Alongside surviving the hostile shock environment, the drillMAX system is designed such that it does not interfere with the reverse circulating sample return path ensuring the quality of physical samples collected at surface is not impacted. A further feature is the ability to allow high-rate air to pass through the tool without inducing any noticeable pressure drop in the pneumatic system driving the hammer. These two features ensure that the drilling process is not impacted when the drillMAX tool is installed on the string.

The system is powered by lithium-ion batteries with advanced firmware to ensure low power draw while acquiring data, and ultra-low power while on standby. Typically, the batteries deliver three or four days of continuous operations before requiring charging, which can be done overnight, without removing the tool from the string.

Our recent experience has enabled us to compare the time taken for drills to deliver the drillMAX service, with the time taken on drills using driller run GR and hole deviation tools, or calling in wireline trucks to acquire in rod surveys (Figure 2). On average drills spend 6–10 minutes per day on the drillMAX system, while spending 40–110 minutes using other methods of acquiring the same data. This is a significant reduction seriously improving drill productivity. Across a fleet of ten drills, operating the drillMAX system effectively provides the same boost in productivity as contracting an additional drill.

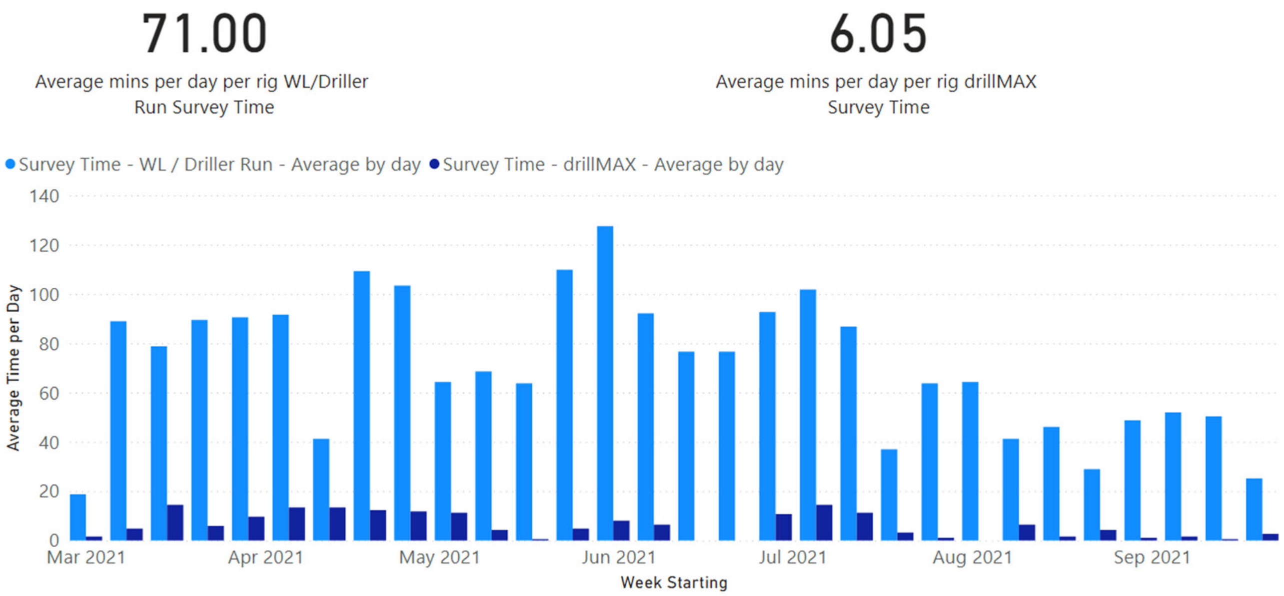

FIG 2 – Survey times for the LWD GR + gyro versus the wireline or driller deployed tools across multiple drills in multiple areas.

DATA DELIVERY

The delivery of high-quality natural GR and hole deviations is the primary purpose of the drillMAX system and being located on the drilling system enables this data to be available quickly and directly to customer data management systems.

The data delivery workflow makes two products available for various internal customers. A raw data product is available at the drill immediately on the tool returning to surface directly via the drillHUB local wi-fi allowing field geologists first look interpretation and decision-making. This product can be downloaded directly to customers devices allowing transfer of information without the use of flash drives or external devices. A final QC'd product is made available via the web based drillINFO portal typically within 24 hrs and certainly within 48 hrs. Outputs from drillINFO can be configured for direct loading on QC into customer database management systems via email, FTP or other mechanisms.

Alongside the natural GR and hole deviations, the data acquired from drillMAX includes the following channels:

- Total Natural GR – [cps/API]
- Hole Azimuth [DEG]
- Hole Angle [DEG]
- Acceleration: Axial, Lateral, Frontal [G]
- Weight on Bit [kN]
- Torque at bit [Nm]
- Hammer Frequency [Hz]
- Temperature [degC].

The standard measurements provided from the drill include:

- Depth [m]
- Force on String [kN]
- Rate of Penetration [m/min]
- Drillhead Torque [Nm]
- Drillhead Rotation Rate [rev/min].

The drill measurements are time synced with the downhole data to ensure that everything can be accurately converted to depth. The modern drills typically require very little modification to get these, however the older drills can be retrofitted to ensure this data is acquired.

When these surface and downhole measurements are combined, it allows advanced geophysical answers to be calculated. For example, we can calculate Density based on the energy loss into the rock and also an Unconfined Compressive Strength (UCS). The calculated density (live, whilst drilling) has a strong correlation (R^2 of 0.75) with the wireline density in the orebody (Figure 3).

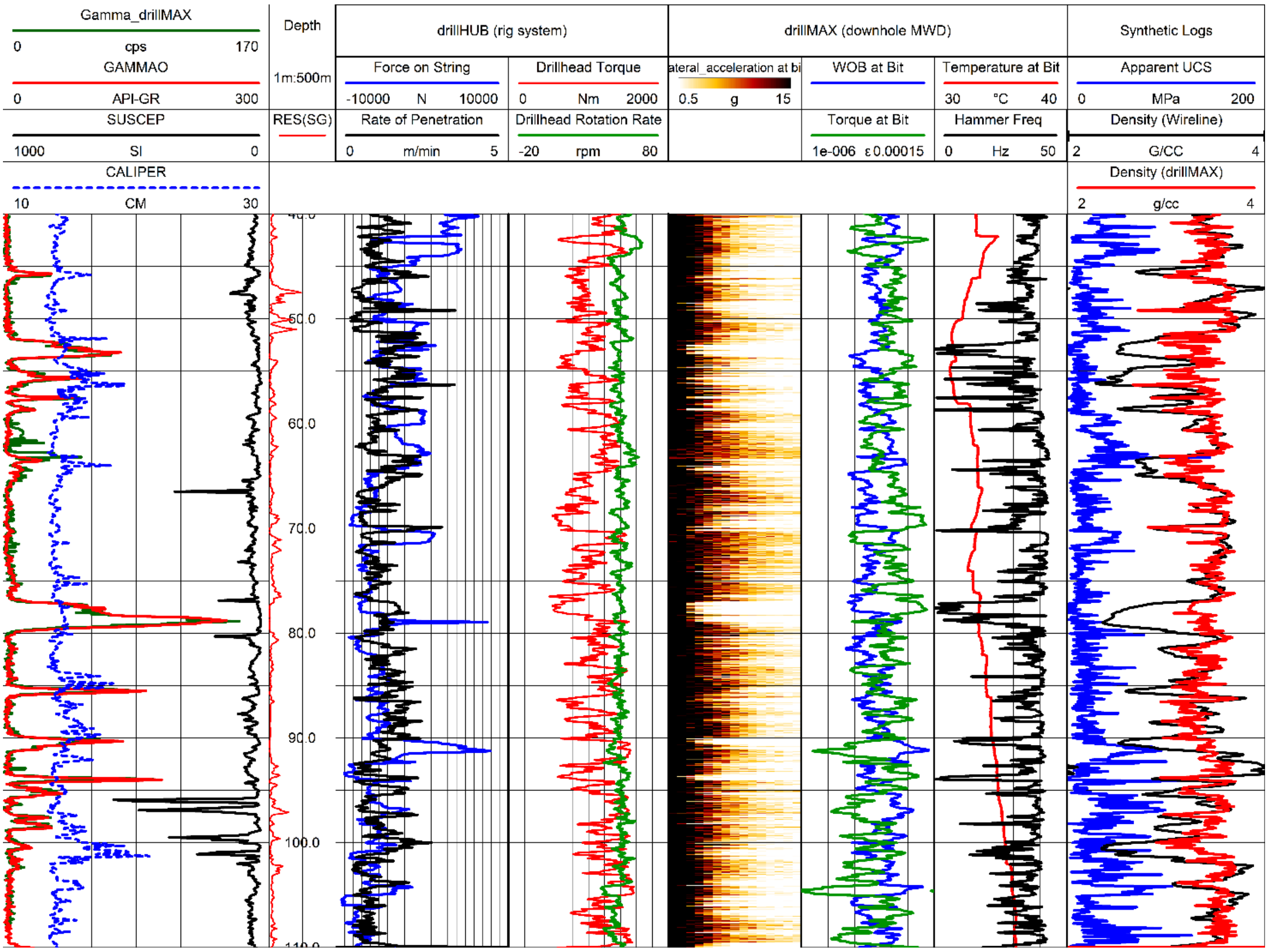

FIG 3 – Log composite with Wireline data and LWD GR on far left. Then the rig sensor network track shows the 4 key outputs of the rig. The next set of tracks are from the downhole instrument. The far-right track shows the calculated Density compared to WL density, and UCS.

The ability for the clients to access this data in real-time to near real-time has helped to enable the use of 24 hr mine model updates, that can be used to change the following days drilling plan for both depth of hole and location.

Most recently, a live, two-way data link between surface and the drillMAX tool downhole has been deployed that enables true real time delivery of geophysics. Prior versions of the system acquired data on memory that was available at the end of hole for analysis and interpretation. The live two-way link streams data directly to the cloud allowing monitoring and decision-making from remote operations centres – anywhere in the world. This not only drops the time required to operate the drillMAX system on the drill even further, it enables remote decision-making and monitoring for improved efficiency, cost of operations and risk reduction.

CONCLUSIONS

Downhole, behind the hammer, logging while drilling continues to roll out across the mining industry. The lifetime of the tools continues to increase, and we are now starting to see reliability come to the point where it can replace conventional wireline deployed GR and Gyro. The additional data acquired behind the hammer is opening up new and exciting pathways for analysis of drilling dynamics. The ability to stream the data live to the client enables time savings and associated productivity improvements for each drill.

ACKNOWLEDGEMENTS

We would like to thank Wallis Drilling for continued support on their drilling rigs.

REFERENCES

Hopper, T, Schubert, M, Moran, B, Kalisch, P, Crumby, M, Buters, N, Ott, K, Rogozinski, K, Joldes, G, Morgan, Q, Neville, T, Shanmugam, H, Zaeper, R, Lowe, J and Prince, A, 2019. Downhole geophysics sensors for reverse circulation drilling in iron ore, in *Proceedings Iron Ore 2019* (The Australasian Institute of Mining and Metallurgy: Melbourne).

Geophysical blasthole sampling

C Simpson[1] and J Market[2]

1. MAusIMM, Geology Manager, Fortescue Metals Group, Perth WA 6019.
   Email: csimpson@fmgl.com.au
2. Geophysics Manager, MPC Kinetic, Kewdale WA 6105. Email: jennifer.market@mpckinetic.com

ABSTRACT

The process of sampling blasthole cones utilising personnel to manually shovel material into sample bags is a long-standing industry accepted process. However, this method has several drawbacks, including the safety issues around having personnel performing manual sampling in a harsh environment and the variability involved in getting a human to repeatedly get a ‘shovel full of dirt’, and make it always representative.

Geophysical blasthole sampling, or utilising a Downhole Assaying Tool (DHAT) has been tested and has now begun implementation at many iron ore sites throughout the Pilbara region, Western Australia. This method uses a geophysical tool to capture data within blastholes, and together with a semi-autonomous logging platform to minimise risks around manual handling, delivers a multielement proxy-assay which can be utilised by the mine geology team to accurately domain the orebodies.

Logistically, the combination of a specially designed tool and semi-autonomous truck are the way forward for a safer and more data-robust blasthole sampling practice. The method utilises a neutron-generating geophysical tool and linked elemental spectroscopy sensor, which measures the response of the material surrounding an open hole. This delivers results at submetre intervals. These results are then utilised, similar to blasthole sample results, to map out areas within the blast pattern that are ‘ore’, ‘waste’, or ‘other suitable grade’.

This paper outlines a project that has been in ‘proof of concept’ at selected Fortescue sites over the last few years with testing of these tools carried out on reverse circulation (RC), diamond drill and blastholes. The method is now being implemented at operational hematite mine sites. Fundamentally, the method adds more than enough value to justify its implementation.

The aim is that these learnings will enable the greater industry to adapt, implement and improve their mining practices. Ultimately, the outcome will be greater value in mining for the industry by having a larger volume of good quality data to make reliable decisions on material movements, minimising ore-loss and dilution, and maximising the value of our current and future orebodies.

INTRODUCTION

Iron ore mining within the Pilbara region of Western Australia is considered a bulk mining activity. The simple outlook on how a mine is developed is that it is initially explored and ‘proven up’ by a team of geoscientists, who define it into a 3D Mineral Resource. A feasibility study (by a greater team of geoscientists, engineers, and approval teams) ensures that the deposit meets suitable economic criteria, and if ‘all the stars align’ then an Ore Reserve is declared, and the mine can progress to construction and development. Eventually mining begins, and the iron ore can be extracted, suitably processed, railed, or trucked to port, and shipped for sale traditionally to overseas markets.

All this activity is hinged around the initial delineation of the Mineral Resources that constitute the mining hub. In most circumstances for Australian developments, this utilises RC drilling rigs to extract samples of a certain vertical length (usually between 1–3 metres) which are subsampled and analysed at laboratories, traditionally for >20 elements by X-ray Fluorescence (XRF) analysis. For exploration activities, RC holes are generally widely spaced, with the spacing gradually reduced (infill holes) during the resource definition stage ahead of mining. The infill drilling better delineates the variability within the orebodies and increases the confidence in the mining schedule to be ‘on tonnes and grade’ during certain periods as analysed by the mine planners.

A further step to increase confidence in the grade variability (and therefore reduce risk) is the process of traditional blasthole sampling. This simple process involves the taking of a sample 'after the fact' when a blasthole drilling rig has completed its principal purpose of 'drilling a hole' for it to be loaded with explosives. Activating the explosives will fragment the ground, enabling mining equipment to efficiently dig the material. Unfortunately, the focus whilst drilling blastholes is not on sample quality, but on productivity (getting as many holes drilled in a shift as possible) and the resultant material to be sampled (Figure 1) is commonly just a 'pile of dirt' around the drill collar, from which a qualified person will collect a subsample of material from the cuttings of the entire drilled hole (varying 500 to 1500 kg in size depending on hole dimensions and depth). The results of this blasthole sample, once received from the laboratory, represent a full-bench composite sample used to predict grade-zones within the mining sequence.

FIG 1 – Blasthole cone, representing common drilling practices where a sample bias can be created by the drilling process.

There have been several papers presented on analysing the quality of blasthole samples (eg Pitard, 2008), with the majority outlining the shortcomings of this sampling method. Being that, unless within a very homogeneous material type, then the variability within the sample presented is often greater than the precision for the result required.

The greatest benefit for blasthole samples, is that 'data is king' and because you can quickly (and cheaply for mining operations) collect and analyse a sample from a hole that is 'already drilled'. Then you can get an indicative sample on the short-scale spacing between blastholes and essentially map out the greater 'ore' versus 'waste' domains within the bulk mining environment. Any anomalous results generated by poor sampling practices are 'smoothed out' by the large volume of samples generated. For bulk mining activities, the delivered average grades within selected zones are suitable for planning and reconciliation purposes.

Just like with the introduction of RC face-sampling hammers to the drilling process in the 1970s (Harlsan, 2021), which improved sample quality, there must be an improved way of doing the blasthole sampling process. Hence, the minerals industry looked to the petroleum industry about what could be done better 'down the hole'. A method that has been utilised for more than 50 years was intelligently investigated by CSIRO Australia (in the early 2000s), and in partnership with Sodern (a French company), BHP Australia and Kinetic logging services, they adapted neutron activation geophysical technology to onshore mineral operations (Sodern, 2021).

The 6-metre-long petroleum industry probes (engineered to withstand high pressures and temperatures in holes more than 1000 metres deep) utilise a neutron radiation generator and a spectral scintillometer to measure and report on the response for the *in situ* material surrounding boreholes. These tools are generally called 'Litho-scanners' (Schlumberger, 2021), and are designed to map the relative variability between 'high silica' sandstones, compared to 'high iron' basalts, and 'high carbon + oxygen' shales or other suitable formations. These tools are designed to analyse to as high a penetration into the formations as possible, so therefore they log very slowly and often run multiple passes over the most interesting horizons to get 'quality over quantity'.

Current practices within the onshore mineral industry are less about getting highly accurate data from a single deep hole, rather obtaining a lot of data quickly and cheaply over short holes provides greater value.

The resultant 'FastGrade^{TM}' tools that were developed, utilising Pulsed Fast and Thermal Neutron Activation Analysis (PFTNA) technology, are shorter (3 metres) and designed for fast data capture and reporting. Combined with semi-autonomous logging trucks, this method can log a 13-metre-deep blasthole in under 10 minutes.

AIM OF THIS PAPER

This paper presents a discussion around implementing new technology into the iron ore industry. Specifically, around improving the data quality and quantity around blasthole sampling, which ultimately leads to 'more data = better decisions' for our mine geology and quality teams. Geophysical blasthole sampling is presented as that option.

BASIS OF WHY WE NEED A WAY FORWARD

The practice of sampling blastholes has had many industry reviews about how to improve the system (McArthur, Jones and Murphy, 2010; Abzalov *et al*, 2007; Crawford *et al*, 2005; Bitencourt *et al*, 2002, to name a few). The fundamentals are that a blasthole drilling rig has the sole purpose to 'drill a hole' and load this cavity with explosives to fragment the ground (Hartman, 1968). There has been little change in thinking over the last 60 years for this industry practice, and realistically why change something that is not broken (and if the ground is not broken enough, just increase the drill density and add more charge!).

The iron ore industry is ultimately progressing to maximising value from our orebodies by mining not just direct shipping ores (DSO) but also the marginal ores that can be upgraded through beneficiation or blended to reach optimal product grades and optimise mine life. This not only benefits the economic sustainability of the company extracting the resources, but there are countless further benefits to the associated economic communities linked to mining (federal, state, and local governments, traditional owner communities, local and national suppliers to mining companies to name just a few).

More and better-quality data is required on the ultimately lower grade deposits that future miners are going to have to deal with. More data equals better decisions, which penultimately means that our processing facilities are fed better ore and less waste, meaning lower dilution and better mine-output grade compliance.

Utopia, here we come….

CURRENT INDUSTRY PRACTICE

Iron ore deposits in Australia are mapped out within a 3D model via the use of drill holes (being RC, diamond core, or a combination of both), which ultimately capture a sample interval of between 1–3 metres vertical resolution within a drill hole. Subsamples are taken of this material and analysed at either on-site or off-site laboratories, the results of which drive the planning of mining activities.

As the level of data driven by drilling upon a deposit increases, the confidence in the (less) variability of the deposit increases, and as per the JORC code (JORC, 2012) a Mineral Resource can be classified at a rating reflecting increasing confidence (eg from Inferred, to Indicated, to Measured). One of the main drivers for increasing the Mineral Resource level of confidence is drilling density. Within the Australian deposits, the Inferred Resource level is generally exploration stage (200–400 metre spaced holes), and the Measured Resource level is generally close spacing (25–50 metres spacing), with Indicated Resource level somewhere in between.

Mining of orebodies generally occurs at the highest level of confidence (Measured Mineral Resources, converted to Proved Ore Reserves) reflecting the ability for the mine to rail (or truck) out the iron ore within the acceptable grade variance.

The block model as defined during the creation of the Ore Reserves is utilised by the mine planning team (generally mining engineers) to schedule which portions of the pits will be mined and in what sequence, allowing for the blending of higher and lower-grade areas to reach the target mine-production grades.

The practice of blasthole sampling (Figure 2) is an added benefit (and often a required process) to better understand the short-scale grade variability within the deposit. As blastholes are often 6–9 metres apart, and a blast pattern at least 200 by 100 metres in dimension, there can be around 700 blasthole cones available for sampling. This is a large amount of extra data to enable definition of the many different grade zones. It also comes at a reasonable cost for the extra personnel, equipment, flights, accommodation, and laboratory costs. It would not be unreasonable for any significant mine site, sampling around 500 blastholes per day, to have an on-site team of four to six samplers and additional crew for an on-site laboratory to process the samples (Fortescue, 2020). Estimated total costs to obtain and analyse these samples can be AU$ millions per annum per site. Additionally, the turnaround time at the laboratory (depending upon the efficiency of the laboratory) can be two to four days after the last samples are taken.

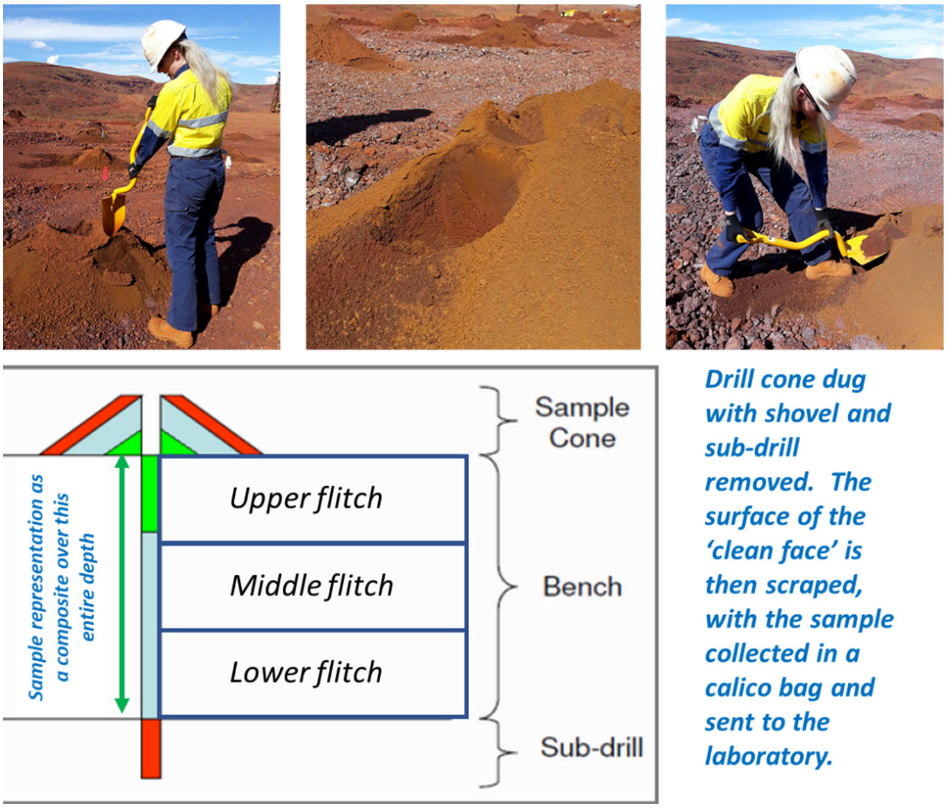

Drill cone dug with shovel and sub-drill removed. The surface of the 'clean face' is then scraped, with the sample collected in a calico bag and sent to the laboratory.

FIG 2 – Current (common) industry practice of blasthole sampling involving manual labour. Sample quality can vary with the method of drilling and the level of training for personnel to performing the task (Fortescue, 2020).

The main disadvantage for the blasthole sampling method is the sample quality, being subjective to the drilling quality (wet or dry drilling, and environmental conditions after drilling). Plus, the methodology for removal of the subdrill material (before sampling) and then ensuring all sections of the blast cone are sampled evenly. Thankfully, there are good training practices for the personnel that are performing this task (Fortescue, 2020). There is however undoubtedly a large subjective error in where and how the samples are taken on the blast cone (Figure 1).

The blasthole sampling results, after laboratory analysis, are then fed into industry databases, verified through standard Quality Assurance and Quality Control (QAQC) processes, and then interpreted through mining software, creating either a visual-coloured trace (high to low-grade) of drill holes or local block models (termed grade-control models).

The ore-categorisations by the mine geologist have a large economic impact on the outcome of the quality of the ore-tonnes (tracked on a weekly or monthly basis). Their decision allocates each mining block to be within a specific grade variance, commonly classed as DSO or material to be blended (or beneficiated) to meet the final product grades. The other alternative is material sent to the long-term low-grade stockpiles, or ultimately the waste dump.

Finding areas of previously undefined economic ore (upgrades) adds large economic benefit to the mine, however better defining areas of poor economic material that would otherwise have been fed to the process plant (downgrades) can be argued to provide greater economic value. This being that then this material does not ‘dilute’ the grade through the process plant (if not upgradeable). Consequently, the process plant when fed the material grades within its design criteria is running optimally and therefore delivering the best cost-value to the business.

ALTERNATIVE METHOD, GEOPHYSICS DEFINING ORE GRADE HORIZONS

Geophysics involves the methodology of measuring the natural (or instigated) response of rocks within the earth, most commonly using engineered equipment (for example a compass indicates the direction of the earth’s magnetic field).

The 20th and 21st centuries have seen the rapid evolution and implementation of geophysics, specifically in the petroleum exploration and development environment, where deep (greater than 1000 m) drill holes are very expensive, and the maximum amount of information is required for deposit evaluation.

The onshore minerals industry has similarly implemented geophysical technology, however within the iron ore environment it has traditionally been a focus on ‘just get a large amount of information quickly and cheaply’. The results from these campaigns are utilised to map out domains of the orebodies and assign appropriate results for orebody modelling. For example, natural gamma is utilised to define shale bands and geological domains, with source-gamma utilised to define the *in situ* dry density of geological units (Jones, Walraven and Knott, 1973).

Measuring the spectral response of elements which are activated by a neutron radiation source is not a new methodology to petroleum science (Tittman and Nelligan, 1960), but can be considered relatively new to the minerals industry, especially iron ore (Borsaru and Charbucinski, 1997; Borsaru *et al*, 2002). There has however been a rapid evolution for implementing this method to the mineral industry over the last few years, specifically around its highest value-in-use being gathering quantitative data on blastholes.

Neutron activation technology has evolved considerably over the last 60 years, with the improvement of both the engineered equipment and the computational technology being able to refine the spectral signatures obtained into more accurate results. The history of testing neutron tools within iron ore was first documented before the start of the last iron ore boom, with a trial completed within blastholes at Mt Whaleback by BHP and CSIRO (Bitencourt *et al*, 2002). More refined tools have subsequently been tested and results recently published (Jeanneau, Flahaut and Maddever, 2017; Market *et al*, 2019).

The proposed ‘new’ implementation methods utilise a specially designed probe, together with advanced semi-autonomous logging units (Figure 3). This method collects and stores the geophysical responses, and then interprets and presents a proxy-assay at submetre intervals for every blasthole surveyed. There is simply just a lot more extra data gathered compared to a traditional blasthole sampling, giving greater resolution for flitch mining (several mining passes within a bench), especially in the vertical extent.

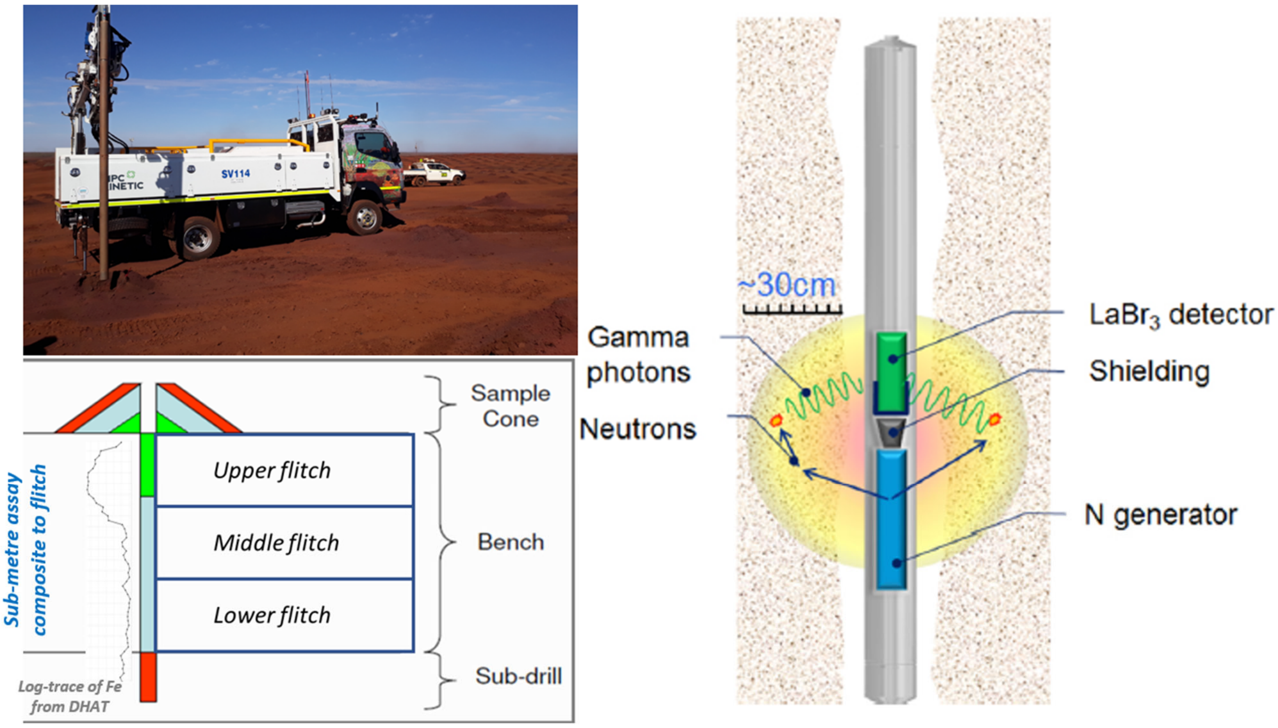

FIG 3 – Geophysical blasthole sampling (DHAT) methodology with semi-autonomous trucks. Giving submetre proxy-assays that can be composited to mining intervals. Tool image adapted from Jeanneau, Flahaut and Maddever (2017).

One of the main safety benefits with the evolution of these PFTNA tools in the mineral industry, was the integration of electrical induced neutron radiation (rather than a permanent radioactive source). Essentially radiation is only produced when power is supplied to the neutron generator (Jeanneau, Flahaut and Maddever, 2017; Chi *et al*, 2017), and due to safety protocols, this only occurs when it is at depth within a drill hole. This dramatically reduces the radiation risks associated with handling of these tools. In addition, if a tool is lost within the mining area, it does not ‘sterilise’ a large zone from future mining.

The simple justifiers

Every business case in mining usually looks at some simple metrics and evaluates the risk-payback on each of them (accountants usually put cost at the top, however the authors disagree with this and put it as an outcome of other metrics).

The four main metrics and comparisons between traditional blasthole sampling and DHAT are summarised here:

Safety:

- Current blasthole sampling methods involve personnel walking around uneven blast patterns and physically shovelling material into sample bags, often in extreme heat conditions (+40°C).
- Geophysical methods engineer out manual handling with robotics and efficiently lower the probes into the hole to gather the data. The operator rarely needs to leave the air-conditioned cab of the truck, but rather tracks data collection via computer screens. In this sense, with appropriate lighting and risk reviews, night shift operations can be carried out, doubling effective use of the equipment.

Quality:

- Current methods collect a subsample representing a composite whole hole assay (usually 6–15 metres vertical depth). As noted in later sections of this paper, this is less than 1 per cent by volume representative and is subjective to the quality of the drilling conditions and training of the samplers to ensure reliability.

- Geophysical methods are measuring the *in situ* material surrounding the drill hole which excludes all bias in subsampling. Vertical resolution is submetre (Fortescue is implementing at 0.2 m intervals) rather than composite, meaning for an example 13 m blasthole there is more than 50 times more data points in each blasthole. This vertical resolution data can readily be applied to the changing grade observed between upper and lower flitches (for this mining method), improving grade-domain assignment.

Schedule:

- Current methods rely on the turnaround of manual samplers to collect and bag the sample (admittedly very fast with 2 minutes per hole for a team not unreasonable), however the bottleneck is the capacity of the site laboratory (commonly 1 to 4 days to report a result) and even higher turnaround if an off-site laboratory is used (5 to 14 days not uncommon).
- Geophysical methods have the capacity to report and use data within hours after logging the hole, as essentially once the data is collected it just needs to be uploaded (over the network) to an appropriate computing system and undergo conversion from spectral to usable data. Several QAQC checks should also be completed before being extracted and utilised by the end user (the mine geologist). The timing of data delivery is restricted not necessarily by the equipment, but by the systems and user requirements.

Cost:

- Without presenting actual budget numbers, most of the costs for blasthole sampling revolve around labour and support equipment for the on-site crews and site laboratory. If starting up a new mine, the capital cost of setting up a new on-site laboratory can be prohibitive, and therefore many mines allow for the increase in turnaround time for an off-site (or mine site within the region) laboratory.
- Simple estimates demonstrate that the vendor costs to have qualified and experienced equipment and personnel collect and report the data are comparable to laboratory running costs (without the capital input). If accountants put a dollar figure on safety, quality, schedule (more important than cost in the authors opinion) then geophysics is a clear winner in this comparison.

Statistics of RC, blasthole and geophysical sampling methods

Although taking a subsample of drilled material for analysis is a well-accepted industry practice, there is definite potential for sample errors or bias in this process. Any improvement within the system should be adequately reviewed and implemented if appropriate.

A RC sample bit diameter is commonly 140 mm and using volume × density of rock we can end up with a total weight of sample being 40 kg per metre drilled (Figure 4).

FIG 4 – DHAT trucks operational on near-mine RC drill holes for testing and calibration. The tool measures a larger volume of material surrounding the borehole and has no subsampling resulting in (theoretically) less bias. (Tool zone of investigation adapted from Jeanneau, Flahaut and Maddever (2017)).

Current best industry practice utilises cone (or rotary cone) sampling systems on RC drilling rigs, these systems take a nominal 10 per cent by volume (or as designed) split of the sample into a sample bag. This is then sent off for laboratory analysis, commonly by fused bead XRF analysis, where the ~4 kg sample is crushed, milled and subsampled with under 1 g of material going into the fused bead. The final sample (to the XRF machine) represents only 0.003 per cent of the original ~40 kg sample, which is even a lower representation if the RC vertical sample interval is greater than 1 metre. However, common industry knowledge is that the greatest sample bias exists in the RC sampling system (Pitard, 2005), with the laboratory having robust sample-hygiene practices.

As a comparison, a blasthole sample, which is commonly a bagged 'shovel of material' from a blast cone, represents a ~4 kg sample from a common size of 230 mm diameter and 13 m deep blasthole. This first sample represents a non-mechanised sample taken from approximately 1400 kg of material within the blast cone (ie. a 0.3 per cent sample split), which as above is then further subsampled at the laboratory. Eventual representation being 0.00007 per cent from the original blast cone material.

Please note that the industry has evolved, hopefully for all current and future iron ore companies, to ensure the highest quality of sample presentation from the RC drilling rig or blasthole sample to the laboratory. Many papers have been presented on this (for example Pitard, 2005, 2008). Ultimately, the accuracy within the mining models generated from the drilling or sampling can be heavily compromised by the variability within the sampling method presenting the data to be estimated.

Geophysical sampling (DHAT), when run within drill holes, is looking at the *in situ* material *surrounding the borehole*. The neutron radiation penetration of ~300 mm within this 'doughnut of material' represents ~800 kg of material per metre (Figure 4), and most importantly has *no sample subsplits* potentially causing error and bias in the sample. Volumetrically there is an additional 10 to 20 times more available material representing a single assay on a per-metre basis.

Risks are associated with how representative geophysical sampling can be as there is a potential for uphole contamination (clay coatings) within the borehole. Given that coatings are generally less than 10 mm, it can be considered negligible compared to the volume of neutron penetration and analysis (3 per cent). Ultimately, the sample volume (and therefore representation of analysed material) is considerably different between RC, blasthole and DHAT sampling. We should not expect exact correlation between all the results, but rather accept that all should show the same trends withing their own data without bias.

Consideration of data used in short-term plans.

Although the data from RC samples almost wholly drives the medium-term plans, most mines utilise the larger volume of blasthole sample results to create short-term or grade control models used by the mine geologists. The higher level of data (derived from closer spaced drill holes) enables better definition of the localised grade variance within the blast blocks. These short-term models will drive the stockpiling strategy and the weekly to monthly reconciliation against shipping grades.

Geophysical sampling (for Fortescue commonly termed DHAT) presents a more quantitatively aligned data set than what the traditional blasthole cone sampling practices deliver. Specifically for bench mining where multiple passes (flitch mining) are carried out and the extra detail in vertical resolution is highly beneficial above the composite sample delivered by a blasthole sample.

Blasthole sampling is still highly valuable!

Please do not consider extinguishing all the blasthole sampling teams and site laboratories. This would be a sub optimal economic decision. These crews will (and even after the implementation of DHAT) be required for quality checks and sampling of areas where DHAT trucks are not able to gain access (for example steep sloping contour shots where single bench mining is generally carried out).

A smarter decision is to decide what size and reliability these future sampling teams and laboratories need to ensure operational requirements after implementation of DHAT. Or the fact that if the deposit is homogeneous enough to not flitch mine, then the current blasthole sampling (or alternative) practices may be adequate.

DATA INTEGRITY FOR THIS STUDY

Fortescue acknowledges that the development of this technology for the iron ore industry has been ongoing for decades, mostly without its direct involvement. When the technology evolved sufficiently, and became commercially available, it was then viable to 'jump in' to test this technology. It has been a three-year journey for Fortescue to get involved in this technology, however the 'fast moving' attitude of the company has enabled a rapid integration to operational mine sites.

Calibrations are extremely important for geophysics, and although many FastGrade^{TM} tools can be quickly implemented with a 'factory calibration' (Market *et al*, 2021), there are shortcomings in the accuracy for each element. It is essential to spend extra time building up *a robust calibration* model for each tool to meet the data accuracy requirements for each mine site.

The proof-of-concept journey for Fortescue involved testing several tools across many sites, and correlation of DHAT results against almost 100 000 metres of RC samples and collecting more than 300 000 metres of production (blasthole) samples. The proxy-assay results demonstrate acceptable grade accuracy in all environments, and productivity upon blast patterns was also within acceptable limits.

During the testing period there has also been a continual evolution of the technology, with the original 'demonstration' tools (termed the FG740 series) evolving into a faster and more robust tools (the FG100d series). Additionally, the trial of a larger tool (the FG170 series) was carried out for a period. In total nine tools were tested and calibrated across four operational Fortescue hematite mine sites (Solomon, Cloudbreak, Christmas Creek and Eliwana).

Each of these tools has its own dedicated data set utilised to build robust calibrations (on RC holes), plus continual repeat-runs on dedicated RC holes as a QAQC measure. All data once reported is captured within Fortescue's acQuire database, including relevant data fields such as date, tool name and model version to ensure the ability to report on the increasing data confidence involved with the implementation of this method.

CURRENT RESULTS SHOWING CONFIDENCE IN DHAT RESULTS

Data analysis has shown that the elemental analyses of iron (Fe), manganese (Mn), silica-oxide (SiO2), titanium oxide (TiO2), and to a lesser extent aluminium oxide (Al2O3) plus Loss on Ignition (LOI at variable temperatures) have demonstrated adequate robustness. However, it has also been shown that some of the minor elements, such as phosphorus (P), sulfur (S), magnesium oxide (MgO), potassium oxide (K2O), chlorine (Cl), and sodium oxide (Na2O), have their current limitations showing high variability. As the elements of ‘major economic concern’ are deemed to be robust, DHAT is now considered an adequate method for geological domain and grade prediction.

Figure 5 demonstrates data for one of the trials at a particular mine site, the results include the data set utilised to build a single tool calibration. The scatter plots (sample pairs by depth in each drill hole), although showing a widespread in ‘twin results’, show no bias of concern. The lack of bias is backed up by the Quantile-Quantile (Q-Q) plots in Figure 5, which involve sorting the two separate paired data sets (DHAT and RC) separately in ascending order of results. A large trend away from the 45° trend line indicates a bias. In this instance, the variability is less than 0.2 per cent absolute for any element shown (within the range of economic interest).

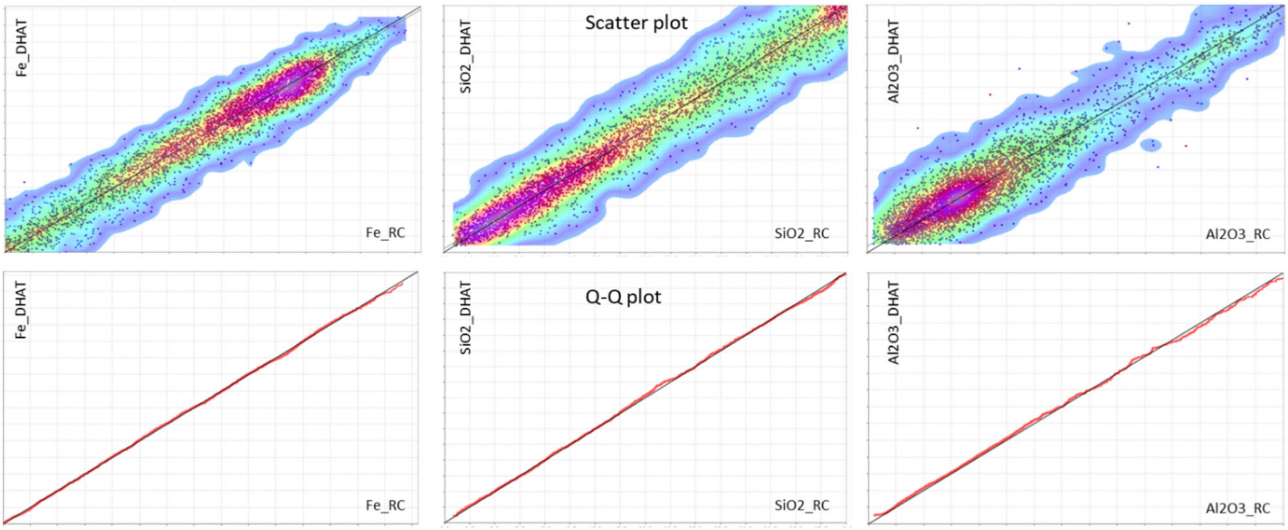

FIG 5 – RC versus DHAT results on calibration drill holes. Scatter and Q-Q plots of major elements at one of Fortescue sites for a single tool calibration. Heat map indicates zones of greater data density. Axis labels not shown for confidentiality purposes.

To understand the existing variability of sampling within the deposits, current Quality Assurance (QA) practices were investigated. RC and blasthole sampling duplicates (where two samples are taken at the RC splitter or blasthole cone at the same time) are presented as scatter plots on Figure 6. For comparison the variability of RC to DHAT results (within the same hole) are also presented. Although the samples presented here are for different holes (and therefore different geology) and different time periods, the data population is considered comparable (approximately 5000 data points for each set) and therefore geostatistically sound.

Interestingly, because the DHAT is calibrated against the RC samples, which have their own variability within the sampling method, the fact that the DHAT variability is ‘just outside’ that of which it is calibrated against is considered a very good result. Users should not expect the precision of the tools to be smaller than the variability currently existing within the calibration method (RC or similar).

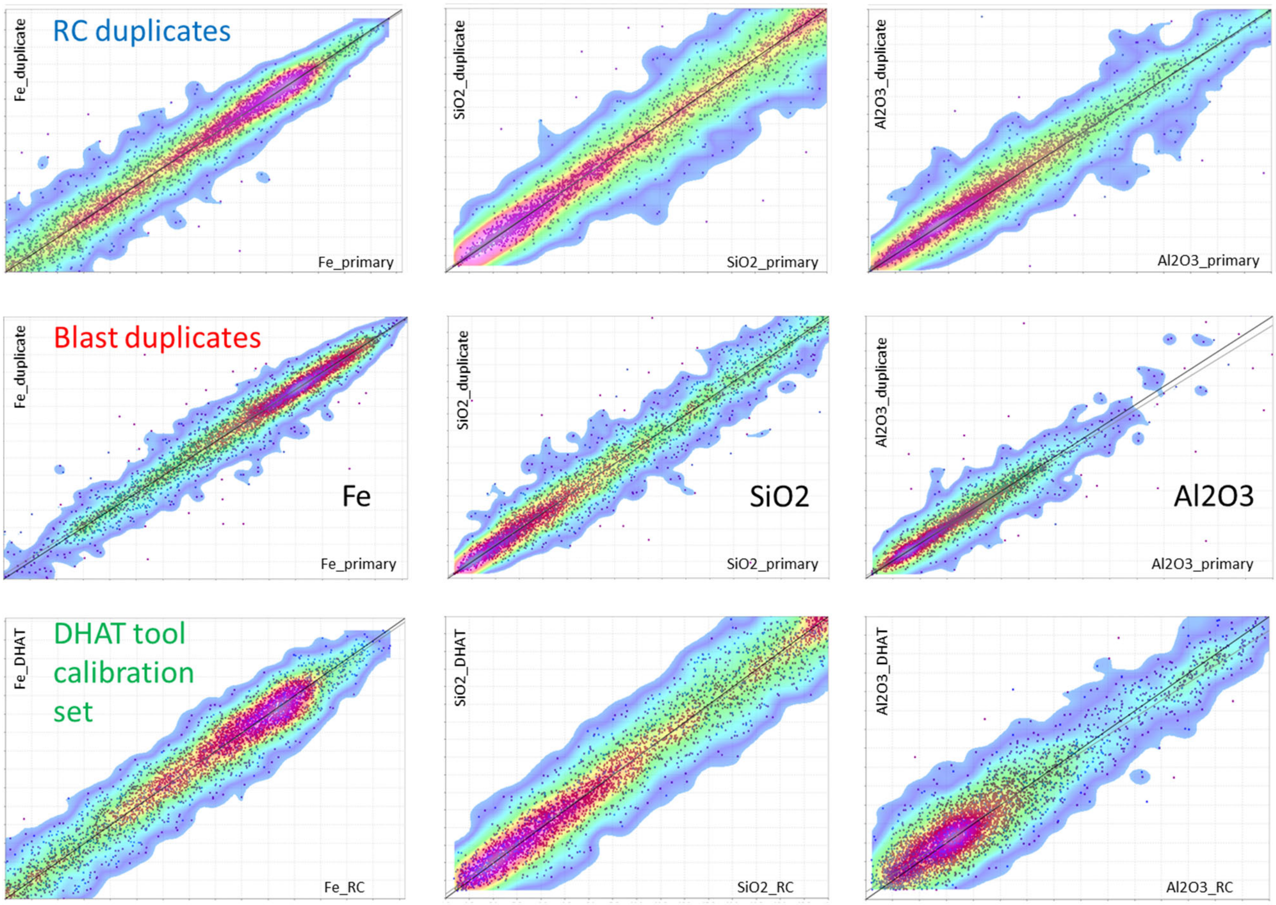

FIG 6 – Comparison of variability within sampling methods. RC duplicates, Blasthole duplicates and a single tool DHAT calibration set. Results from the same mining hub with similar sized data sets. Axes not shown for confidentiality purposes.

A comparative method (downhole) of demonstrating variance

In addition to performing extensive work on calibrating the DHAT tools on RC samples (the largest volume and quickest way to obtain representative coverage of a project area), a program of diamond core sampling was undertaken at all mine sites where DHAT was tested.

Comparing the DHAT to diamond core has the added benefit that both the DHAT and core samples have a resolution that is below 1 metre. Therefore, small-scale geological variances (such as clay or shale bands) can be correlated well at this sampling resolution. Combined with spectral scanning of the core (Corescan, 2021), this has assisted in defining the truthfulness of the 'high anomalies' that come out during statistical analysis (see Figure 7).

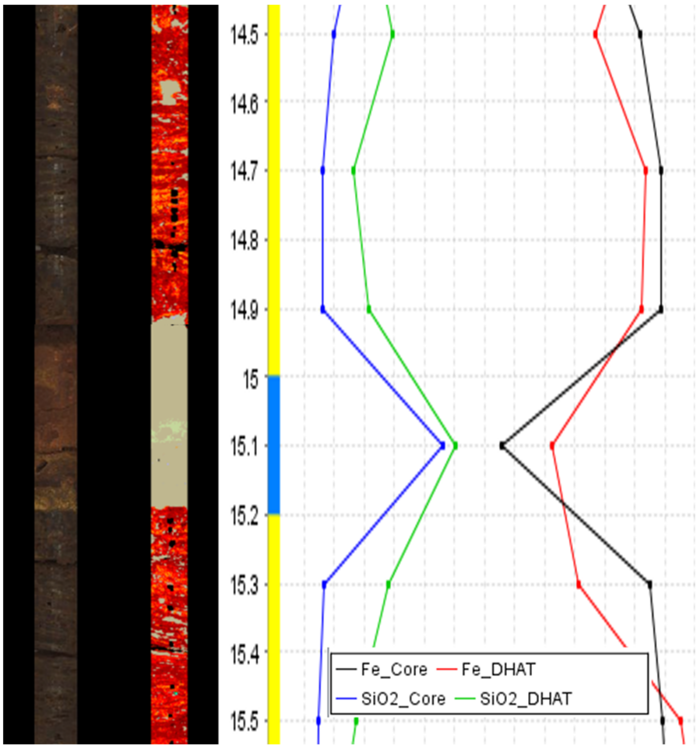

FIG 7 – Diamond core photography and spectral mineral trace, with correlation of 'clay bands' to diamond core and DHAT measurements at 0.2 m vertical resolution. Axis labels not shown for confidentiality of results.

For many purposes in mining, all data is binned to a minimum of 1 metre resolution (this averaged data having fewer anomalies), and in most cases is binned even further to the flitch mining level (3–6 metres). As per Figure 8, a comparison between the three types of sampling methods for iron ore mines (diamond core, RC twin and now DHAT) shows that all three methods can depict the 'ore' versus 'waste', upper and lower contacts, and blendable zones. Each of them has some minor variance at the ~1 m vertical resolution from each other, which possibly is due to the different sampling volumes and in the case of the RC twin, the ~5 metre lateral change in geology.

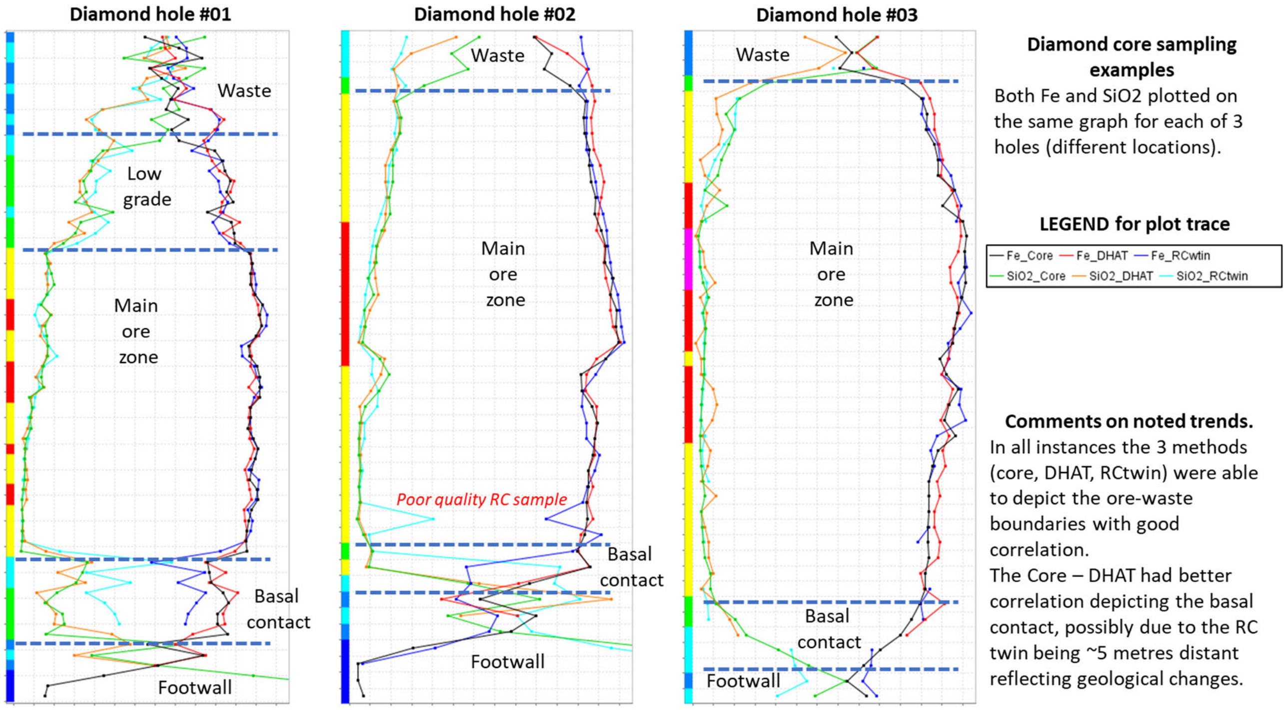

Diamond core sampling examples

Both Fe and SiO2 plotted on the same graph for each of 3 holes (different locations).

Comments on noted trends.

In all instances the 3 methods (core, DHAT, RCtwin) were able to depict the ore-waste boundaries with good correlation.

The Core – DHAT had better correlation depicting the basal contact, possibly due to the RC twin being ~5 metres distant reflecting geological changes.

FIG 8 – Downhole plots on three separate diamond holes at one of the Fortescue sites. Comparison of three sampling methods (Core samples, DHAT, RC twin) which all depict the overall grade trends with little to no bias.

USE IN THE MINING ENVIRONMENT

Due to confidentiality of the results, little can be presented here in detail, so it can only be discussed as a conceptual implementation. There is undoubtedly the capability for another paper to be written solely on this subject. Hopefully, some of the people utilising this method going forward will be able to write and present the positive outcomes that are recognised in years to come.

Flitch mining is the main benefit for the implementation of DHAT. This is a method of mining benches, where due to the likelihood of large changes in grade (horizontally or vertically), the mining method (via excavator) takes several ‘passes’ (of 3–6 metre vertical extent) to complete the full bench (commonly 10–15 metre vertical extent) as shown in Figure 9. This allows for greater selectivity in mining (compared to full bench mining), and ultimately better grades going to the process plant and waste going to the waste dump.

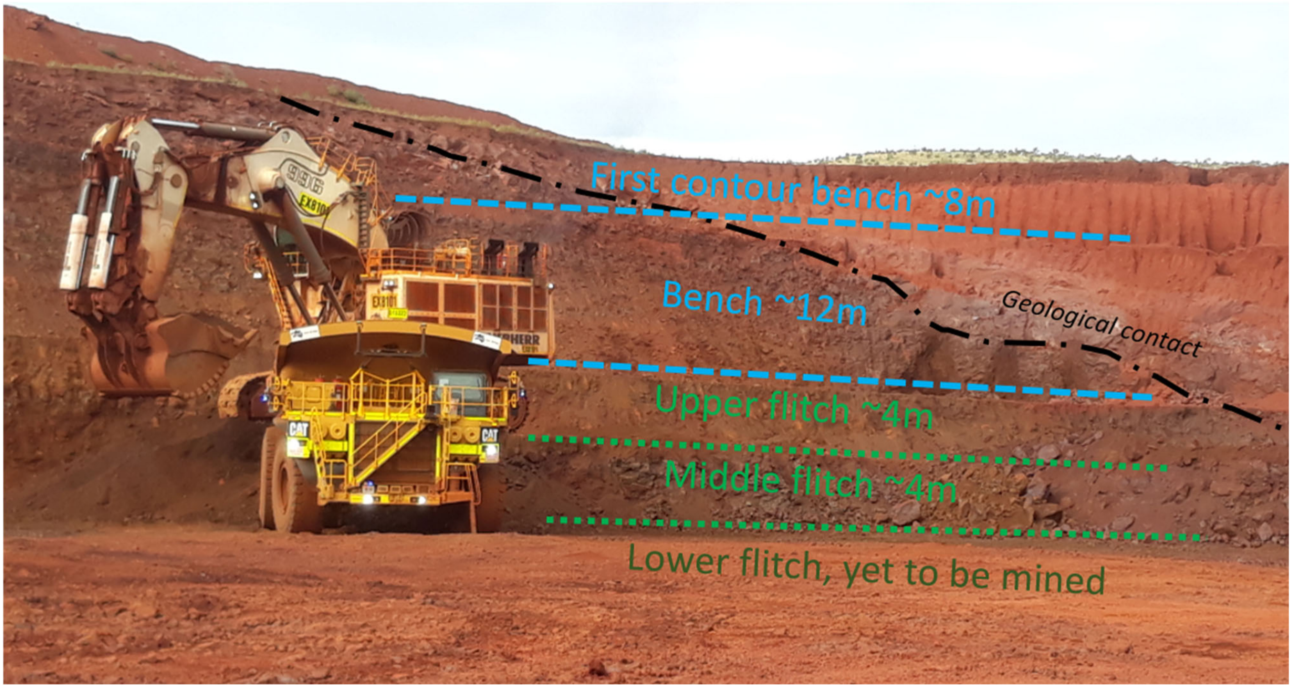

FIG 9 – Example of flitch mining operations, where an excavator takes several ~3 metre 'passes' to complete the full bench. Having high resolution of grade variance within each flitch adds greatly to optimising mining grades.

The definition of which portions of the mining block are ore versus waste is defined by the mine geologist, traditionally utilising either the mining block model (1–5 metre vertical block sizes), or blasthole sampling (full bench 10–15 metre composite sample), or a combination of both.

The mining block model has its limitation, as it is by definition an estimate and therefore 'smooths' out the anomalously high and low-grade data. The smoothing factor is compounded if the RC drill spacing (the data source) is much wider than the required mining resolution due to topography, infrastructure, or budget cuts to the drilling activities in previous years. The vertical resolution of the blocks created is usually limited by the vertical sampling of the drilling rig (commonly up to 3 metres).

Blasthole sampling has its limitations (as discussed previously) of having few alternatives to take multiple samples from the drill hole (McArthur, Jones and Murphy, 2010). Most commonly it is a single sample representing the entire bench, which represents less than 1 per cent by volume (as per previous section). It would have to be a very homogeneous deposit to ensure that this sample is proven to be reliable. The single sample result per hole, if utilised to represent each flitch, would then just be duplicated downhole across each flitch. For example, in a three-flitch situation, the upper flitch will have the same grade as lower flitch (Figure 10), even though their centroids could be greater than 8 metres apart.

However, DHAT provides the largest amount of vertical data points (samples can be presented at 0.2 m resolution), and therefore the greatest confidence in the variability of grades within each flitch. This includes being able to define the 'base of pit' and 'final-dig surfaces' more accurately. If logging every blasthole on a pattern (nominally 6–9 metre spacings), then the lateral resolution, combined with the vertical resolution, gives a large amount of data to more accurately define the 'ore blocks' within the mining sequence. In many instances this leads to appropriate 'upgrades' of material (ore previously defined as waste, now reclassified as ore), which adds value to the mine (Figure 11).

When material is 'downgraded' (ore recategorised as waste) this is still an advantage as it costs almost the same to truck the material from the digger to the waste dump as it does to the stockpiles in front of the processing plant. It however then costs more to process this material, which may not upgrade (if beneficiating) and therefore ultimately cause dilution of grades through to the train loadout or shipping stockpiles.

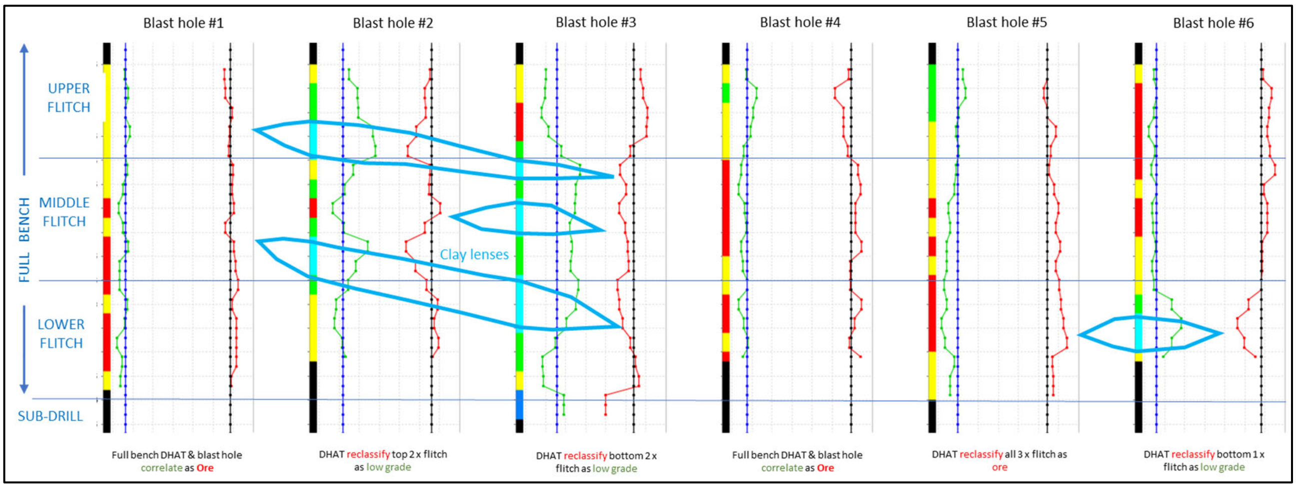

FIG 10 – Representation of DHAT versus blasthole samples within a row of blastholes (widely separated) along a bench. Trace legend: – red = DHAT Fe, black = blast Fe, green = DHAT SiO2, blue = blast SiO2.

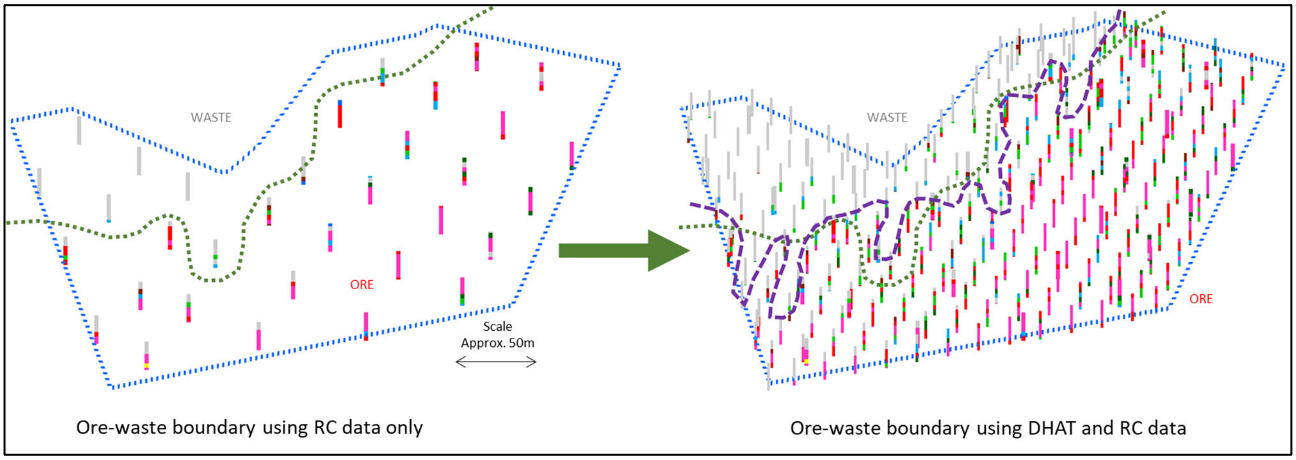

FIG 11 – demonstration of the adjustment in mining boundary resolution utilising the much larger amount of data available from DHAT than from RC data alone. Drill hole colour traces indicate grade variance. ie grey = waste, blue-green = low-grade, red-pink = high-grade.

CONCLUSIONS AND RECOMMENDATIONS

Geophysical blasthole sampling (termed here as the Downhole Assay Tool or DHAT) is a new method being instituted to iron ore mining operations as it can deliver a multielement proxy-assay which has adequate accuracy and repeatability for grade definition within bulk mining operations.

The process involves utilising a semi-autonomous logging truck to lower a geophysical probe into open blastholes after drilling. Neutron radiation then instigates a response in the material surrounding the blasthole (to almost a 1-metre diameter ‘sample’), which is measured by a scintillation crystal and delivers a digital result which is used as a proxy-assay.

As this process measures the in situ response of the material surrounding the borehole, there is no subsampling and therefore minimised the potential for sample inaccuracies and bias. The extensive calibration methodology on each tool has improved over time (with more data), and the accuracy of results are now at an acceptable level for implementation throughout mining operations.

Ultimately, the process delivers an adequate result for defining mining domains used for grade scheduling. It however delivers this in a safer, higher quality (vertical resolution), faster schedule, and at costs comparative to existing blasthole sampling practices.

Fortescue has spent almost three years to test and prove this technology and is now implementing this technology at selected mine sites in the Pilbara region of Western Australia.

ACKNOWLEDGEMENTS

The authors wish to thank the supporting companies of Fortescue Metals Group Ltd and MPC Kinetic for the permission to use information to publish this paper. The previous companies (Sodern, Kinetic, BHP, CSIRO) that have been involved in leading the development of this technology (conversion from petroleum industry technology) into the mineral industry over the last approximately 20 years are also thanked.

Acknowledgement is also given to the large site-based and Perth office Fortescue teams that have been working on the proof of concept and implementation of this technology at multiple sites around the Pilbara. There is nothing like testing new technology right within the production environment to 'see what breaks' as that way the bugs can be sorted out sooner. Although frustrating at times, it is the best way to 'fix it quickly', or just 'fail fast' and 'move onto something else', which is the entrepreneurial way to quick and strong success of new projects.

Thanks also go to the many reviewers of the drafts to this final paper who helped re-shape some late-night written and badly worded paragraphs into a more comprehensive and readable paper.

The authors are passionate about this technology and believe that is has a high economical payback to the industry. There is still effort required to prove this technology at each chosen mine site, with some sites likely not being suitable to uptake the technology. Every journey starts with a beginning though, so I suggest that those that are contemplating this new technology should 'give it a go'.

REFERENCES

Abzalov, M Z, Menzel, B, Wlasenko, M and Philips, J, 2007. Grade control at the Yandi iron ore Mine, Pilbara region, Western Australia – comparative study of the blastholes and reverse circulation holes sampling, In *Proceedings, Iron Ore Conference 2007*, pp 37–43, (The Australasian Institute of Mining and Metallurgy: Melbourne).

Bitencourt, R, Mackenzie, B, Gordon, J and Morey, B, 2002. High grade optimization and improved grade control practices Mount Tom Price. In *Proceedings Iron Ore Conference 2002*, pp 261–277 (The Australasian Institute of Mining and Metallurgy: Melbourne).

Borsaru, M, and Charbucinski, J, 1997. Nuclear borehole logging techniques developed by CSIRO – exploration and mining for in situ evaluation of coal and mineral deposits, In *Proceedings, International Conference on Isotopes 1997*, pp 178–183, Australian Nuclear Association.

Borsaru, M, Rojc, A, Ronaszeki, J and Smith, C, 2002. The determination of Fe, Si and Al content in iron ore blastholes by nuclear logging. In *Proceedings Iron Ore Conference 2002*, pp 171–176 (The Australasian Institute of Mining and Metallurgy: Melbourne).

Chi, B, Maddever, R A M, Mahanta, A and Dominguez, O, 2017. Near real-time assay with downhole assay tool (FastGrade 100). In *Proceedings Eighth World Conference on Sampling and Blending*, pp 137–144 (The Australasian Institute of Mining and Metallurgy: Melbourne).

Corescan web site, 2021. Information leaflet on Hyperspectral scanning and mineralogical interpretations. https://corescan.com.au/services/hyperspectral-mineralogy/ (accessed 31/03/2021)

Crawford, D, Leevers, P, Parsons, S, Solly, G and Nielsen, S, 2005. Grade control in the Southern Middleback Ranges – A case study. In *Proceedings Iron Ore Conference 2005*, pp 271–280 (The Australasian Institute of Mining and Metallurgy: Melbourne).

Fortescue, 2020. Standard work instruction, blasthole sampling procedure. Internal report (confidential).

Harlsan web site, 2021. What is reverse circulation drilling. Information article https://www.harlsan.com.au/what-is-rc-drilling/ (accessed 01/08/2021).

Hartman, H L, 1968. *Principles of Drilling*. The American Institute of Mining, Metallurgical, and Petroleum Engineers.

Jeanneau, P, Flahaut, V and Maddever, R A M, 2017. Iron ore benefits from neutron pulsed geochemical tools. In *Proceedings Iron Ore Conference 2017*, pp 387–395 (The Australasian Institute of Mining and Metallurgy: Melbourne).

Jones, H, Walraven, F and Knott, G, 1973. Natural gamma radiation as an aid to iron ore exploration in the Pilbara region of Western Australia. In *Proceedings Australasian Institute of Mining and Metallurgy Conference 1973*, pp 53–60 (The Australasian Institute of Mining and Metallurgy: Melbourne).

JORC, 2012. The JORC code 2012 edition http://www.jorc.org/docs/JORC_code_2012.pdf (accessed 14/04/2021).

Market, J, Bryne, C, Robinson, D, Jeanneau, P and Rossiter, H, 2019. Downhole assays in the Pilbara. In *Proceedings Iron Ore Conference 2019*, pp 366–386 (The Australasian Institute of Mining and Metallurgy: Melbourne).

Market, J, Simpson, C, Rossiter, H and Jeanneau, P, 2021. Advances in downhole assay measurements and calibration techniques. In *Proceedings Iron Ore Conference 2021*, pp 351–373 (The Australasian Institute of Mining and Metallurgy: Melbourne).

McArthur, G, Jones, C and Murphy, M, 2010. Blasthole cone sampling experiments for Iron ore flitch mining. In *Proceedings Sampling Conference 2010*, pp 131–136 (The Australasian Institute of Mining and Metallurgy: Melbourne).

Pitard, F F, 2005. Sampling correctness – a comprehensive guideline. In *Proceedings Second World Conference on Sampling and Blending 2005*, pp 55–66 (The Australasian Institute of Mining and Metallurgy: Melbourne).

Pitard, F F, 2008. Blasthole sampling for grade control – the many problems and solutions. In *Proceedings Sampling 2008*, pp 15–21 (The Australasian Institute of Mining and Metallurgy: Melbourne).

Schlumberger web site, 2021. Information on Lith scanner. https://www.slb.com/reservoir-characterization/surface-and-downhole-logging/wireline-openhole-logging/litho-scanner-spectroscopy (accessed 14/04/2021).

Sodern web site, 2021. Information leaflet on FastGrade logging tool: Pulsed Neutron Technology https://www.sodern.com/website/docs_wsw/RUB_325/tile_702/FastGrade_Leaflet_SODERN.pdf (accessed 31/03/2021).

Tittman, J and Nelligan, W B, 1960. Laboratory Studies of a Pulsed Neutron-Source Technique in Well Logging. *Journal of Petroleum Technology,* 12 (issue 07): pp 63–66.

Geophysical log applications to geological and geotechnical assessment

B Zhou[1]

1. Senior Principal Research Scientist, CSIRO Minerals, Pullenvale Qld 4019.
   Email: binzhong.zhou@csiro.au

ABSTRACT

Geophysical borehole logging, which measures various *in situ* petrophysical parameters, can be used not only for qualitative interpretation such as strata correlation, but also for geotechnical assessment through quantitative data analysis. It can play an important role for safe and productive mining operations. Here we provide various applications of geophysical logs such as the estimation of the strength of intact rock or unconfined (or uniaxial) compressive strength (UCS), automated lithological/geotechnical interpretation, geophysical strata rating and orebody delineation and grade estimation. These derived parameters could provide input to control of geological and geotechnical models. This could assist site geologists and planning and production geotechnical engineers to predict and manage mining conditions on an ongoing basis. Both conventional logs such as density, natural gamma and sonic, and less common logging data such as full waveform sonic and televiewer data are examined for different applications. Although the examples used here are mainly for coal mining applications, but they can be equally applied to hard rock metalliferous mining such as iron ore mining.

INTRODUCTION

Geophysical borehole logging is an established and very cost-effective exploration method and can play an important role in establishing reliable geological and geotechnical models required for safe and productive mining operations. It is an alternative way to provide the required information from non-cored boreholes. This provides for either a substitution of diamond drilling or an extension of drilling programs within the same budget, as non-cored holes are cheaper to drill.

Geophysical logging measures various *in situ* petrophysical parameters such as the acoustic, radiometric and electric properties of the rocks down boreholes and is carried out routinely in mineral exploration and mining. The logs provide a rich source of rock property information from a drilled borehole and can be used for strata correlation (Kayal, 1979; Hofman, Jordan and Wallis, 1982; Hatherly, 2013), litho-stratigraphic interpretation (Fullagar and Fallon, 1997; Fullagar, Zhou and Fallon, 1999), orebody delineation and grade estimation (Fallon, Fullagar and Zhou, 2000; Zhou and O'Brien, 2016) and geotechnical and rock mass characterisation (McNally, 1990; Guo *et al*, 2000; Zhou *et al*, 2001, 2005; Hatherly, 2002; Medhurst, Hatherly and Zhou, 2010; Guo and Zhou, 2011; Kitzig, Kepic and Kieu, 2017).

In this paper, we present various applications of geophysical logs such as the estimation of the strength of intact rock or the unconfined (or uniaxial) compressive strength (UCS), geophysical strata rating and orebody delineation. These derived parameters could provide input to modelling, control geological and geotechnical models. Geophysical logs such as density, natural gamma, sonic, resistivity, full waveform sonic, and televiewer are examined for different applications. Most of examples in this paper are published (eg Zhou and Guo, 2020) and mainly from coal mining applications, but they can be equally applied to hard rock metalliferous mining such as iron ore mining where the mentioned geophysical logs are often acquired. Therefore, they are presented here as the broader mining industry could use their acquired geophysical logs to extract more information to maximise the value of their drill holes.

GEOTECHNICAL CHARACTERISATION FROM GEOPHYSICAL LOGS

Geotechnical assessments such as rock strength estimation and rock mass characterisation are the most attractive applications of geophysical logs, as it is critically important to have a proper understanding and accurate estimation of the strength and characteristics of the various rock types present for mine design and production. Rock strength properties are often affected by, for example, porosity, mineral bonding type, quality of the solid particles, the internal structure of the rock skeleton, and water content (Schön, 2015). The complexity of rock strength influences (porosity, mineralogy and water content) and dependencies (bonding type and quality of solid particles, and internal structure of the rock skeleton) makes estimation of rock strength difficult. Rock strength can be determined in various ways but most approaches require an understanding of the properties of the intact rock and of the defects within it. Geophysical logs can be used to estimate both of these properties, which will be illustrated in the next section.

Estimation of uniaxial compressive strength by sonic logs

UCS estimation from acoustic logs – the McNally method

Uniaxial Compressive Strength (UCS) is one of the most important parameters for ground control design in mining. For this rock strength estimation, sonic logs are more useful parameters than neutron, gamma ray and density logs as identified by McNally (1990). McNally (1990) proposed an exponential relationship between the UCS and the sonic log. The McNally method for UCS estimation from a sonic log is widely accepted as a conventional approach in the Australian coal industry (Oyler, Mark and Molinda, 2010). Based on the UCS test results on 1004 core samples from 40 boreholes in the coal measures of the Sydney and Bowen basins, McNally (1990) derived the following relationship:

$$UCS = 1000e^{-0.035t} \tag{1}$$

where t is the sonic transit time (P-wave) measured in microseconds per foot (μs/ft) and the UCS is measured in mega Pascals (MPa).

The McNally method is an empirical first order estimate of rock UCS. It often has a broad data scatter and a high uncertainty in derived relationships due to the fundamental difference between static (UCS) and dynamic (sonic log or the seismic velocity) (Hatherly, 2002; Schön, 2015). At many mines, it has been found that a local relationship is required to enable UCS to be estimated with sufficient accuracy or as an alternative approach, a UCS – sonic transit time correlation based on lithological variations should be used (Lawrence, 1999). For example, the German Creek Mine derived their own local formula (Ward, 1998):

$$UCS = 3330e^{-0.0499\Delta t} \tag{2}$$

where the UCS is in MPa while the sonic log transit time Δt is measured in μs/ft. Zhou *et al* (2001) computed the UCS from the sonic log using this site-specific formula and compared the results with those from laboratory UCS tests for two boreholes from German Creek Mine. They found that the UCSs derived from the sonic transit times generally matched the laboratory tests although there was some scatter in the data. This provides confidence in using the sonic-derived UCSs for mine design.

To improve the rock strength estimation, Roland Turner suggested it would be useful to incorporate a bed resolution density log (BRD) with sonic log (Δt) with the following alternative formula (Chatfield, 2016):

$$UCS = 1500000\frac{BRD}{\Delta t^2} \tag{3}$$

The term $\frac{BRD}{\Delta t^2}$ is essentially equivalent to the P-wave modulus ρV^2 in which ρ is density and V is the P-wave velocity. Based on the laboratory data published by Azimian and Ajalloeian (2015), we compared the correlations of UCS with P-wave velocity and P-wave modulus as shown by Figure 1. Both methods produce very similar results in terms of correlation coefficients in soft rocks, which was also demonstrated by Chatfield (2016). But, in hard rock settings, where sonic logs tend to plateau in high density iron rich formations, it is hoped that the incorporation of density improves the analysis, as well as log resolution.

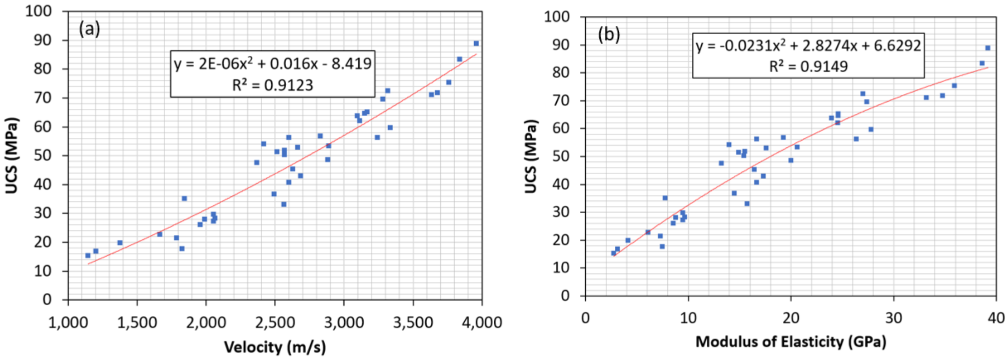

FIG 1 – Correlation Relationships: (a) UCS and P-wave velocity; (b) UCS and P-wave modulus.

Rock strength evaluation from acoustic scanner logs

Acoustic teleview scanner data measures two parameters: the two-way interval transit time from the transducer to the borehole wall; and the reflected amplitude of the signal from the borehole wall. The recorded scanner amplitude measures the contrast of the acoustic impedance (the product of velocity and density) between the drilling mud and borehole wall and indicates the variation of the rock strength and rock unit boundaries. In addition, the low amplitudes are normally associated with fractures. Therefore, acoustic televiewer scanner images provide rich information regarding the rock strength and rock defects. The usefulness of the acoustic scanner data can be easily demonstrated by the scanner amplitude image from a borehole at Kakatiya Khani (KTK) Coalmine (India) in Figure 2. From this plot, we can qualitatively identify the strong (yellow), moderately strong (light brown), weak (dark brown) and very weak (dark blue) rock units. From this, we can easily interpret the major bedding planes. We can also recognise fractures and joints in the coal seams. Note that the coal has relatively high strength at this mine, similar to the weak rock units, which is consistent with the actual lab tests.

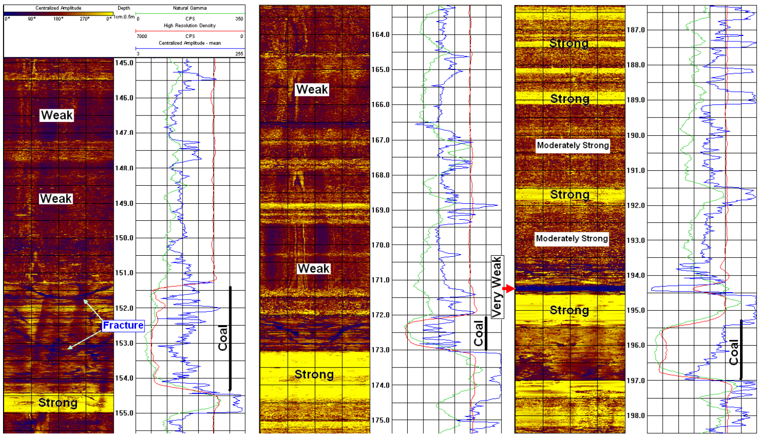

FIG 2 – The acoustic scanner amplitude image from a Kakatiya (India) borehole plotted along with the raw density counts (red), gamma ray (green) and average amplitude (blue). The colour of the image indicates the rock strength: dark colour for weak strata and light colour for strong strata.

As demonstrated by Zhou and Guo (2020), the acoustic scanner data can also be used to determine breakouts and *in situ* stress (direction and magnitude). The principle of stress determination from borehole breakouts can be found in MacGregor (2003) and Chang (2004). The breakouts occur due to overstressing of the borehole wall. Borehole breakout, depending on the *in situ* stress magnitude, rock strength, drilling mud weight and pore pressure, is a shear failure in the direction of the minimum horizontal (minor) stress and can be used as a high-quality indicator of stress direction. In addition, we can also estimate the stress magnitude using the Kirsch solution based on the rock strength, breakout angle and depth, pore pressure and drilling mud pressure.

Rock integrity assessment from full-waveform sonic and acoustic scanner data

A fully cored hole from the Illawarra area, New South Wales, Australia, along with comprehensive geophysical logs, has provided a unique opportunity for the assessment of full waveform sonic data. A core photograph and corresponding acoustic scanner and full waveform sonic data are shown in Figure 3. The logs in this case were obtained by a single receiver at a separation of 4 feet (1.22 m) from the source.

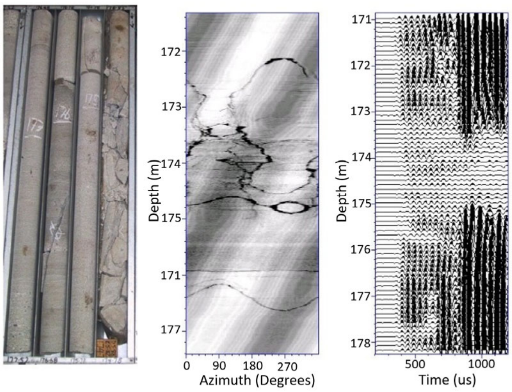

FIG 3 – Core photograph (left), acoustic scanner log (middle) and full waveform sonic log (right) from the same section of a cored borehole.

The striking features of this part of the full waveform sonic log is the decline in P-wave energy between 173.2 m and 175.8 m and the loss of Stoneley wave energy between 173.5 m and 175.2 m. No S-wave is evident in this log but it is probable that interference from the tail of the P-wave event from 400 to 800 microseconds is masking the S-wave arrival.

The core photograph and the scanner image show that the zone of P-wave and Stoneley wave attenuation encompass a zone of fractured rock (sandstone) containing strong vertical fractures. Their vertical orientation presumably explains why there is no significant decline in P-wave velocity through the zone but the losses in the Stoneley-wave and S-wave are clear indicators of the presence of significant permeable fractures. Note also that neither the horizontal fracture at 175.9 m nor the dipping fracture between 176.1 m and 176.6 m, which are evident in the core and scanner image, produce attenuation anomalies on the full waveform sonic log. Similarly, there is no full waveform sonic anomaly for the fracture seen on the scanner image between 172.1 m and 172.8 m.

An indication of the severity of the fracturing present within a borehole is possible through consideration of full waveform sonic data. Figure 4 shows another example for identification of integrity of the rock by the full waveform sonic logs. The left plot is a full waveform sonic log. There are two distinguishable waves marked as P and S-wave. The S-waves are the Stoneley waves travelling along the borehole wall. The right plot shows the rock quality designation RQD index from the core. The strength of the Stoneley wave is well matched with low RQD. This suggests that the Stoneley wave can be used to identify the rock fractures.

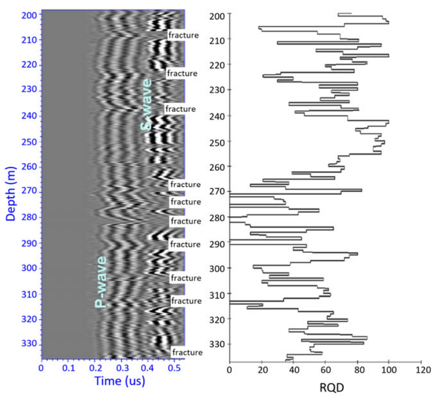

FIG 4 – The Full waveform sonic log (left) and the RQD (right).

Geophysical Strata Rating

Although UCS is an important geotechnical parameter, it only applies to the intact rocks that do not have defects. To overcome this limitation, Hatherly *et al* (2003), Hatherly, Medhurst and MacGregor, (2008) and Hatherly, Medhurst and Zhou (2016) have developed a new scheme designed specifically for clastic rocks – the geophysical strata rating (GSR). This scheme combines separate ratings for the intact rock mass and defects. GSR values are similar to those obtained through the Coalmine Roof Rating (CMRR) (Molinda and Mark, 1994), a scheme that is similar to the Rock Mass Rating (RMR) (Bieniawski, 1989). It generally delivers a value for rock quality between 10 and 100, whereby rock quality improves with increasing value of GSR. To calculate the GSR, a quantitative analysis of geophysical logs is undertaken to determine the porosity (from density or neutron logs), the shaliness (from gamma ray, neutron or resistivity logs) and the effective stress. The P-wave velocity provides a strength score that underpins the GSR. Adjustments are then made to this according to the porosity, the shaliness, the amount of bed cohesion and inferred defects (fractures and bed boundaries). The details of the GSR computation can be found in Hatherly, Medhurst and Zhou (2016).

Figure 5 presents an example of the GSR estimation for a borehole from Kakatiya Khani (KTK) Coalmine, India. The first column shows the porosities calculated from the density log with a matrix density of about 2.66 g/cc and the clay contents computed from the gamma ray log with a sand gamma ray of 20–30 cps and the clay gamma ray of 300–320 cps. The second column is the clay contents from the resistivity log with the shale resistivity of 125–180 ohmm and water resistivity of 20–30 ohmm. The estimated sonic velocities based on the porosities and clay contents in the first two columns, along with the measured sonic log, are shown in the third column. It is clear that the estimated velocities are well matched with measured sonic velocities. This demonstrates the validity of the estimation of the porosities and clay contents.

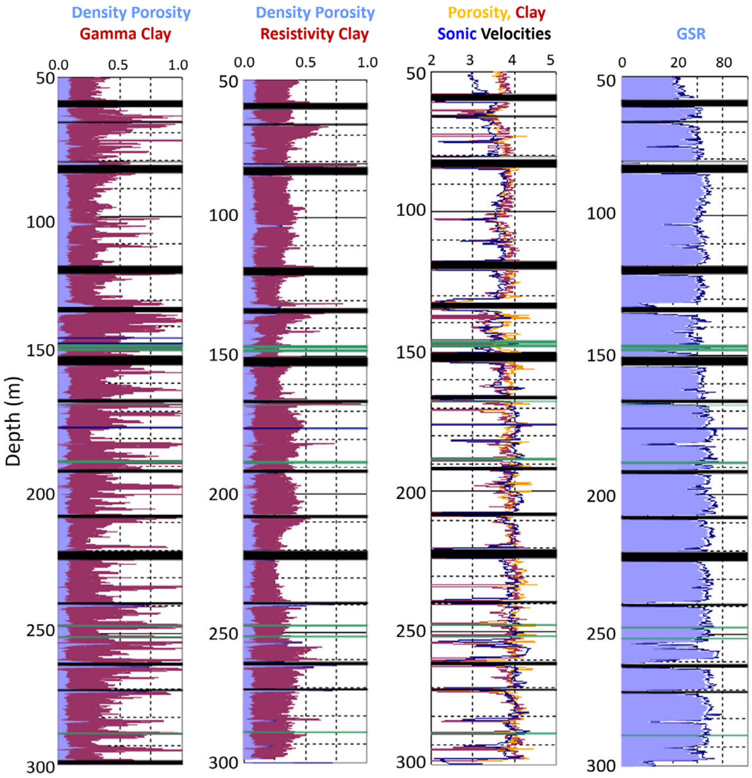

FIG 5 – GSR estimation based on estimated clay content and sonic logs for a KTK borehole. First column: the estimated porosity (light blue) from density and clay (maroon) from natural gamma logs; Second column: the estimated porosity (light blue) from density and clay (maroon) from resistivity; Third column: comparison of the calculated sonic velocities (brown and maroon) from estimated porosity and clay content in the first and second columns with the measured sonic velocities (blue); Fourth column: the estimated GSR based on the porosities and clay contents in the second column and the measured sonic velocities in the third column. The black bands are coal seams.

The column on the right displays the estimated GSR based on the porosities and clay content in the second column and the measured sonic velocities for the three boreholes are given in the third column. The GSR is quite uniform with an average estimated value of about 60 for all three boreholes, although there are some thin bands with low GSR. Therefore, we can conclude that the rock at KTK longwall block is very strong and competent. The estimated GSR data allows geotechnical engineers to better assess roadway stability and longwall caving behaviour and improve design ground support for longwall mining (Medhurst, Hatherly and Zhou, 2010).

Automated lithological and geotechnical interpretation

The strength of the rock is usually related to the rock type: well cemented sandstones are stronger than mudstones, claystone and siltstone. Therefore, lithological interpretation of geophysical logs and its spatial distribution of lithologies will greatly improve our understanding of the effects of overburdern sediments in relation to mining activities. The prediction of lithology from conventional geophysical logs is well established and automatic geophysical interpretation programs such as LogTrans have been developed (Fullagar, Zhou and Fallon, 1999). Figure 6 shows an example of the LogTrans lithotype interpretation for an independent hole based on the training parameters from five control boreholes at Century Mine (Fullagar, Zhou and Fallon, 1999). The geophysical logs used in this auto log interpretation are Natural gamma, focused electric resistivity, magnetic susceptibility, gamma-gamma, and sonic velocity logs. The result is extremely encouraging: 98 per cent of the 143 'ore' points (Units 2 – sphalerite in shale + Pb and Unit 4 – sphalerite in shale) and 97 per cent of the 1542 'rock' (waste) points were correctly interpreted. The overall success rate for ore-waste discrimination was 97 per cent.

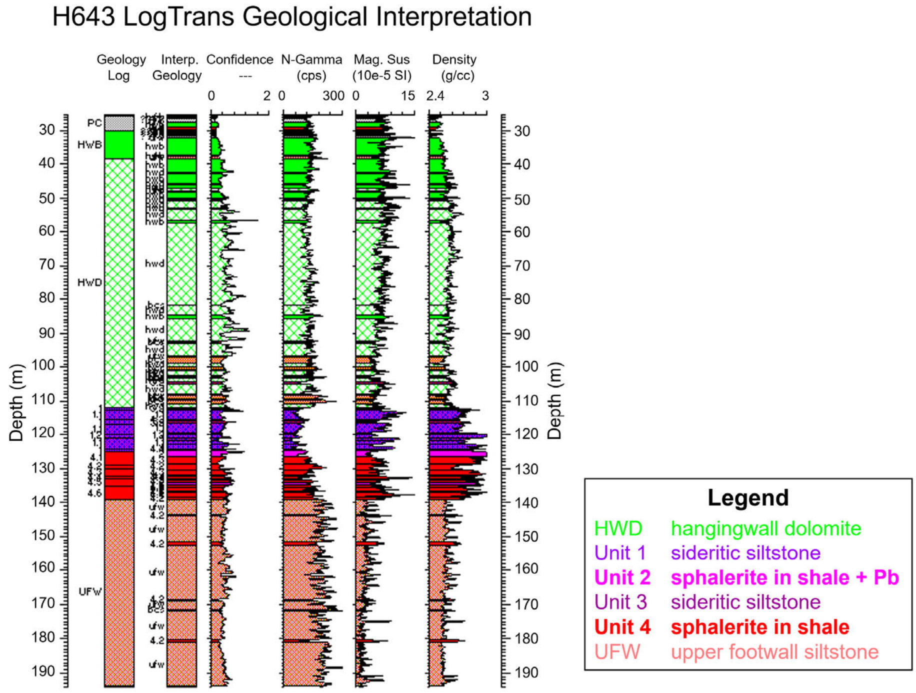

FIG 6 – Lithology-based Logtrans interpretation of logs from an independent hole based on five training holes. A fault has been correctly interpreted within the Century mineralised sequence, where Unit 1 (sideritic siltstone) and Unit 4 (sphalerite in shale) are juxtaposed.

Although this purpose-drilled hole was intended to pass through the entire mineralised sequence, it unexpectedly encountered a fault. The truncated sequence (Units 2 and Unit 3 – sideritic siltstone – missing) has been correctly interpreted by LogTrans. These results suggest that it may be possible to interpret stratigraphy from percussion holes using geophysical logging. Replacement of diamond drilling with percussion drilling + logging is potentially the most cost-effective approach for mapping the fault systems.

In a similar way, Borsaru *et al* (2006) demonstrated that the prompt gamma neutron activation analysis (PGNAA) – measuring the elemental composition of rocks – logging data can be used for lithology prediction while Zhou and Guo (2020) demonstrated that SIROLOG spectrometric natural gamma logging data can also be the inputs to LogTrans for recognition of sugar sands at Callide Mine in Queensland.

In addition to the lithological interpretation, we can also predict geotechnical strata units directly from geophysical logs. This can be illustrated using an example from Southern Colliery, Queensland, Australia, where the main purpose of the study was to understand and predict the caving behaviour caused by longwall mining in the area. In this study, we classified the rocks as geotechnical strata units in terms of coal, and strong (sandstones), moderately strong (sandstones and siltstones) and weak strata (siltstones and mudstones). The type of geotechnical strata was derived from density, gamma ray and UCS (from the sonic log) logs by using LogTrans software. Figure 7 presents the LogTrans result for the drill hole DD0412. LogTrans successfully interpreted the geotechnical strata units with an overall success rate of 85 per cent. The comparison of the interpretation with the core photographs on the right of Figure 7 is very favourable. These geophysically-derived geotechnical units can be used as input to digital mine to generate a 3D geotechnical block model for mine design purposes (Guo *et al*, 2000).

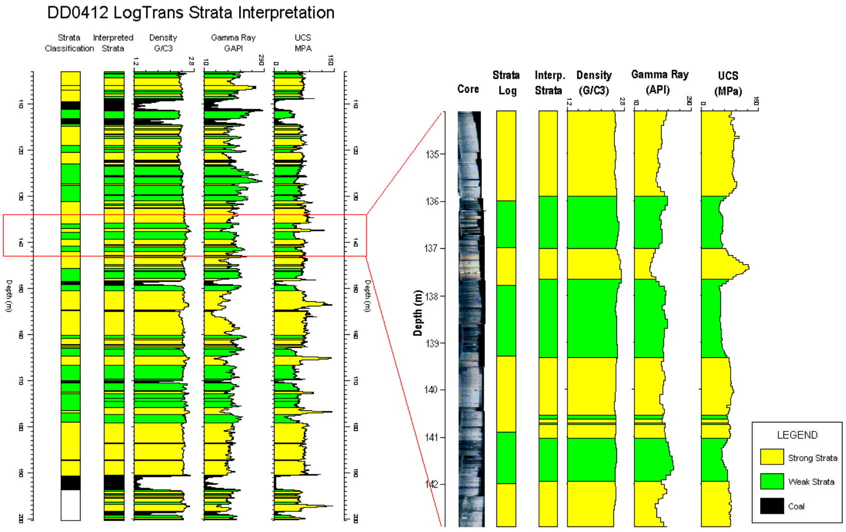

FIG 7 – Strata interpretation for control hole DD0412. The first column is the geotechnical strata classification determined from core photos. The second column is the LogTrans interpretation from the geophysical logs presented in the other columns. The left plot shows the comparison of LogTrans interpretation with core photographs for part of the hole.

Ore grade estimation from geophysical logs

Knowledge of the accurate spatial distribution of orebody and its grade is fundamental to planning, design, extraction and beneficiation, through to utilisation, for both coal and metalliferous mining. As illustrated above, geophysical borehole logging measurements can be used for lithology identification and correlation and geotechnical rock mass characterisation. They can also be used for specific coal-quality assessment (Fallon, Fullagar and Zhou, 2000; Dong *et al*, 2001; Charbucinski and Nichols, 2003; Zhou and Esterle, 2008; Zhou and O'Brien, 2016). Based on our previous work (Fullagar, Zhou and Fallon, 1999), here we present an example on a grade-based LogTrans interpretation of geophysical logs from Rosebery Mine. The available geophysical logs include natural gamma (n-Gamma), gamma-gamma (GG – inversely related to density), magnetic susceptibility (susc), and conductivity. Visual inspection of the logs indicated that the n-Gamma and GG logs exhibited the strongest correlations with grade. This observation led to introduction of a derived parameter, the reciprocal gamma product (RGP) 1/(n-Gamma*GG), which closely related to the density-gamma quotient introduced by Wanstedt (1993). The LogTrans interpretation for four control holes is based on GG, n-gamma, and $\log_{10}$(susc), $\log_{10}$(conductivity) and $\log_{10}$(RGP) logs – the use of the logarithmic values of the logs is to reduce the skewness of data distribution. Figure 8 shows the 'rock-ore' interpretation by LogTrans for one of the four control boreholes. Only intervals interpreted as medium or high-grade are regarded as 'ore'. The visual impression is very encouraging, since a finite number of ore and waste intervals have been inferred. The success rates for the four control holes were as follows: 76 per cent of the 'ore' zones were correctly interpreted as ore, and 87 per cent of the 'rock' were successfully classified as rock. The result is very satisfactory, especially in view of the variability of Rosebery ore.

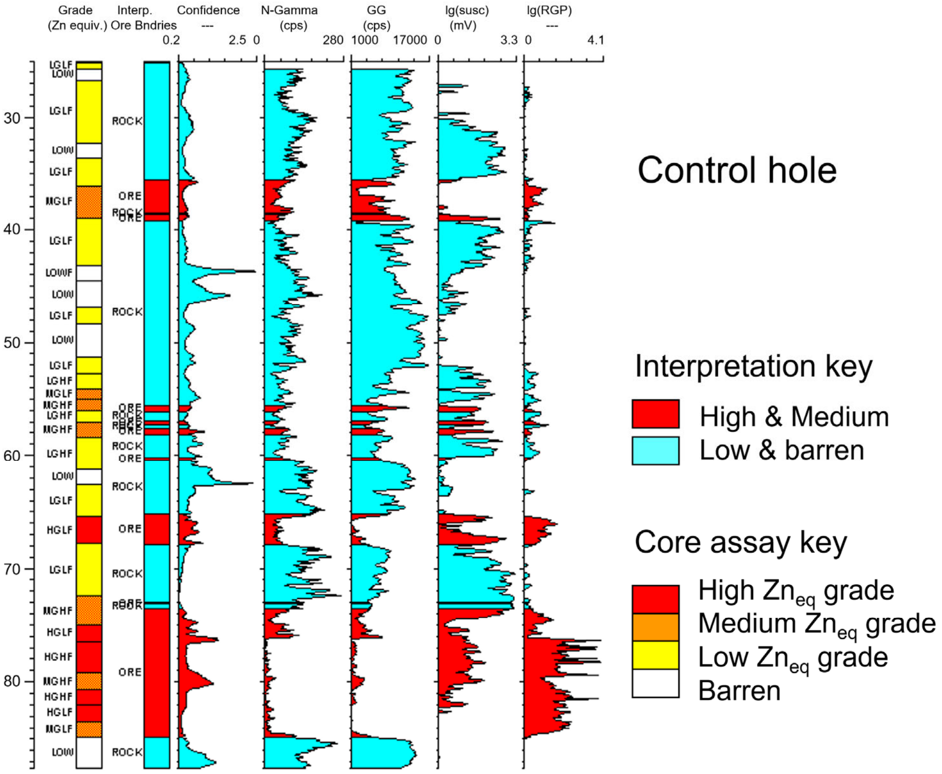

FIG 8 – Grade-based LogTrans interpretation of control hole data for a borehole at Rosebery Mine. Medium and high-grade material regarded as 'ore' zones interpreted as low-grade or waste are labelled 'rock'.

CONCLUSIONS

Geophysical borehole logs can be used for automated lithology interpretation, UCS estimation, rock mass characterisation through GSR and ore grade estimation. This allows generation of improved geological and geotechnical models for safe, productive and beneficial mining operations, and demonstrates the usefulness and effectiveness of geophysical logs for geotechnical characterisation. These applications include quantitative analysis of geophysical borehole logging data and require the geophysical logging data to be of high quality. A pre-requisite for any form of quantitative analysis is the consistency of the borehole logs, from hole to hole, from year to year and from one service provider to another, while absolute accuracy of the log itself is, in general, less important. Log-data quality improvement and control can be achieved by establishing calibration boreholes for checking the logging equipment and developing log quality control procedures and criteria for newly-acquired data as illustrated by Fullagar, Zhou and Turner (2005).

ACKNOWLEDGEMENTS

The author would like to cordially acknowledge the professional contributions and support to the work reported here offered by the following colleagues Peter Fullagar, Peter Hatherly, Gary Fallon, Hua Guo, Terry Medhurst, Joan Esterle, Graham O'Brien, Uday Bhaskar, Peter Chern, Greg Poole, Mark Biggs, Andy Willson, Doug Dunn, Ken Preston, Wes Nichols, and Roland Turner.

REFERENCES

Azimian, A and Ajalloeian, R, 2015. Empirical correlation of physical and mechanical properties of marly rocks with P wave velocity. *Arab J Geosci*, 8, 2069–2079.

Bieniawski, Z T, 1989. *Engineering Rock Classifications, a Complete Manual for Engineers and Geologists in Mining, Civil and Petroleum Engineering*. Wiley, New York.

Borsaru, M, Zhou, B, Aizawa, T, Karashima, T and Hashimoto, H, 2006. Automated lithology prediction from PGNAA and other geophysical logs. *Applied Radiation and Isotopes*, 64, pp. 272–282.

Chang, C, 2004. Empirical rock strength logging in boreholes penetrating sedimentary formations. *Geology and Earth Environmental Sciences*, Chungnam National University, Daejeon, Vol. 7, No. 3, p. 174–183.

Charbucinski, J and Nichols, W, 2003. Application of spectrometric nuclear borehole logging for reserves estimation and mine planning at Callide coalfields open-cut mine. *Applied Energy*, 74, 313–322.

Chatfield, M, 2016. Overview of Geotechnical Issues, *Wireline Workshop*, No. 16, 1–6.

Dong, H, Hou, J, Li, N, and Wang, H, 2001. The logging evaluation method for coal quality and methane: *Geophysical & Geochemical Exploration*, 25, 138–143.

Fallon, G, Fullagar, P K and Zhou, B, 2000. Towards grade estimation via automated interpretation of geophysical borehole logs. *Exploration Geophysics*, 31, 236–242.

Fullagar, P K and Fallon, G N, 1997. Geophysics in metalliferous mines for orebody delineation and rock mass characterisation: in *Proceedings of Exploration'97 — Fourth Decennial International Conference on Mineral Exploration 1997*, A G Gubins (ed.), 573–584.

Fullagar, P K, Zhou, B and Fallon, G N, 1999. Automated interpretation of geophysical borehole logs for orebody delineation and grade estimation. *Mineral Resources Engineering*, 8, 269–284.

Fullagar, P, Zhou, B and Turner, R, 2005. Quality appraisal for geophysical borehole logs. *Proceeding of Bowen Basin Symposium*, 12–14 October 2005, Yeppoon, Queensland, pp 141–150.

Guo, H and Zhou, B, 2011. Geotechnical characterisation from geophysical logs for longwall coal mining. *73rd EAGE Conference & Exhibition incorporating SPE EUROPEC 2011*, Vienna, Austria, 23–26 May 2011.

Guo, H, Zhou, B, Poulsen, B and Biggs, M, 2000. 3D overburden geotechnical characterization for longwall mining at Southern Colliery. *Proceedings of Bowen Basin Symposium*, Rockhampton, Queensland, Australia, 22–24 October, 2000, pp 67–72.

Hatherly, P, 2002. Rock Strength Assessment from Geophysical Logging. *Proceedings of the 8th International Symposium on Borehole Geophysics for Minerals, Geotechnical and Groundwater Applications*, Toronto, Ontario, Canada, August 2002.

Hatherly, P J, 2013. Overview on the application of geophysics in coal mining. *International Journal of Coal Geology*, 114, 74–84.

Hatherly, P, Medhurst, T and MacGregor, S, 2008. Geophysical Strata Rating. *Final Report ACARP Project C15019*.

Hatherly, P, Medhurst, T and Zhou, B, 2016. Geotechnical evaluation of coal deposits based on the Geophysical Strata Rating. *International Journal of Coal Geology*, 163, 72–86.

Hatherly, P, Sliwa, R, Turner, R and Medhurst, T, 2003. Quantitative geophysical log interpretation for rock mass characterisation. *Final Report ACARP Project C11037*.

Hofman, G L, Jordan, G R and Wallis, G R, 1982. *Geophysical Borehole Logging Handbook for Coal Exploration*; Edmonton, Alberta: The Coal Mining Research Centre; ISBN 0969104804.

Kayal, J R, 1979. Electrical and gamma-ray logging in Gondwana and Tertiary coalfields of India. *Geology and Exploration*, 17, p. 243–258.

Kitzig, M C, Kepic, A and Kieu, D T, 2017. Testing cluster analysis on combined petrophysical and geochemical data for rock mass classification. *Exploration Geophysics*, 48, 344–352.

Lawrence, W, 1999. Interpreting and understanding strata behaviour. *The 2nd Annual Longwall Mining Summit*, Yeppoon, Australia, 25–26 February 1999.

MacGregor, S, 2003. Maximising In-Situ Stress Measurement Data from Borehole Breakout using Acoustic Scanner and Wireline Tools. *Final Report for ACARP Project C1009*.

McNally, G H, 1990. The prediction of geotechnical rock properties from sonic and neutron logs. *Exploration Geophysics*, 21, 65–71.

Medhurst, T, Hatherly, P and Zhou, B, 2010. 3D geotechnical models for coal and clastic rocks based on the GSR. *Proceedings of the 2002 Coal Operators' Conference*, 11–12 February, 2010, University of Wollongong.

Molinda, G M and Mark, C, 1994. Coal mine roof rating (CMRR). A Practical Rock Mass Classification for Coal Mines 9387. United States Department of the Interior, Bureau of Mines, *Information Circular*, p. 34.

Oyler, D C, Mark, C and Molinda, G M, 2010. In situ estimation of rock strength using sonic logging. *International Journal of Coal Geology*, 83 (4), 484–490.

Schön, J H, 2015. *Physical properties of rocks: Fundamentals and principles of Petrophysics*, 2nd ed.; Elsevier Science Ltd.

Wanstedt, S, 1993. An overview of recent research on geophysical logging in underground mines in Sweden. *Pmc. 5th Mineral and Geotechnical Logging Society Symp,* Tulsa, Paper D, 1–7.

Ward, B, 1998. German Creek Mines Rock strength from velocity logs. *Unpublished* report for Capricorn Coal Management Pty Ltd.

Zhou, B, Fraser, S, Borsaru, M, Aizawa, T, Sliwa, R and Hashimoto, T, 2005. New approaches for rock strength estimation from geophysical logs. *Proceeding of Bowen Basin Symposium*, Yeppoon, Queensland, Australia, 12–14 October 2005, pp 151–164.

Zhou, B and Guo, H, 2020. Coal mining application examples of geophysical logs. *Resources*, 9(2), 11.

Zhou, B, Guo, H, Hatherly, P and Poulsen, B, 2001. Automated geotechnical characterisation from geophysical logs: Examples from Southern Colliery, Central Queensland. *Exploration Geophysics*, 32, pp. 336–339.

Zhou, B and O'Brien, G, 2016. Improving coal quality estimation through multiple geophysical log analysis. *International Journal of Coal Geology*, 167, 75–92.

Zhou, B and Esterle, J, 2008. Toward improved coal density estimation from geophysical logs. *Exploration Geophysics*, 39(2), 124–132.

Machine learning, big data and automation

Bulk carrier vessel tracking automation – the Dalrymple Bay use case

J Franke[1], P Wighton[2] and W Russell[3]

1. CEO, Frontier Automation, Perth WA 6007. Email: jochen.franke@frontierautomation.com.au
2. Technical Director, Frontier Automation, Perth WA 6007.
   Email: paul.wighton@frontierautomation.com.au
3. Electrical Manager, Dalrymple Bay Infrastructure, Hay Point Qld 4740.
   Email: wayne.russell@dbinfrastructure.com.au

ABSTRACT

Recent advances in ruggedised industrial control system technology and architecture in combination with latest technologies in the fast-evolving 3D LiDAR sensor sector becoming available have enabled the implementation of sophisticated automation algorithms for mining equipment such as bucket wheel reclaimers, as published by the authors in the peer reviewed AusIMM 2019 Iron Ore conference proceedings. This paper provides an overview of a second use case for such automation technology in bulk material ports integral to iron ore operations.

The real-time 3D machine-vision based port automation system described in this paper was originally developed for the BHP-Mitsubishi Alliance's (BMA) Hay Point port. The system has seen deployment at other major mining and general ports in Australia, such as at Dalrymple Bay Terminal (DBT) (shown in Figure 1) managed by Dalrymple Bay Infrastructure Management (DBIM), Hay Point, Queensland. It has the following use cases:

- docking aid for pilots
- port traffic control on-site and at remote operations centres
- vessel loading safety assurance
- port/berth infrastructure safeguard, particularly fenders being impacted excessively, and for loading infrastructure
- vessel breaking mooring safeguard
- commercial port management tool to manage demurrage fees
- berth to berth voyage planning, or port planning management.

FIG 1 – DBT wharf consisting of two double berths capable of hosting a total of four large bulk carriers at any given time. BHP-Mitsubishi Alliance's (BMA) neighbouring Hay Point wharf hosting three berths is visible in the background.

In order to deliver the above functionality, the system automatically tracks in real-time and records in a historical database not only vessel approach and departure data in form of speed, angle, and individual fender distances of vessel bow and stern, but while the vessel is moored also all six degrees of freedom (6 DoF) vessel motions surge, sway, heave, roll, pitch and yaw for all attending vessels during their mooring cycle.

This paper details the specific use case of the system at DBT's continuous wharf featuring four berths. It also details the potential for using it as the basis for increasing berth access for required

tasks during a vessel mooring cycle, considering such access is traditionally categorically denied because of the potentially fatal risk of mooring line snap back.

INTRODUCTION

The first section of this paper provides an overview of the generic use cases of vessel tracking systems, including the specific one applicable to DBIM. The Docking Aid use case includes a summary of the types of marine vessel tracking systems that can be used to track bulk carriers as in use by DBT at their Hay Point port operation in Queensland, Australia. Since a shore-based LiDAR has distinct advantages over on-board vessel tracking system types as described therein, DBIM opted to implement a shore based, permanently installed LiDAR system. The second section of this paper provides an overview of the main components of that system, including descriptions of the LiDAR sensors utilised and associated performance characteristics that are required to make the vessel tracking system fit for purpose.

The third and last section of the paper provides a comprehensive breakdown of requirements that DBIM were looking to satisfy with the system, complemented with explanations on how these requirements were met. Whilst DBIM had a range of site specific needs to meet, these are certainly very much representative of and applicable to the majority of other global ports, including Western Australia's iron ore export operations.

SYSTEM USE CASES

Docking aid

Port and pilot operations of major ports with large vessels including bulk carriers in attendance have two options to provide real-time information for use as a docking aid. The first one is to use Global Navigation Satellite System (GNSS) or Global Positioning System (GPS) data collected by either dedicated antennas and their receivers or the existing on-board systems integrated into a pilot's Portable Pilot Unit (PPU) and ideally its other navigation software. All associated equipment has to be brought on-board and set-up prior to use for every vessel approach.

The second option is to use laser-based LiDAR sensors based onshore. Perkovič *et al* (2020) provide a good summary and practical insights on these options in their recent publication Laser-Based Aid Systems for Berthing and Docking. The World Association for Waterborne Transport Infrastructure (PIANC) – Maritime Navigation Commission (2020) published a review of current shore-based and ship-based berthing velocity measurement technology options in its Berthing Velocity Analysis of Seagoing Vessels Over 30 000 DWT report.

On-board GNSS docking aid systems

In order to enable ship heading to become aligned well to the docking aid system, two or more dedicated high accuracy GNSS or GPS antennas need to be set-up on-board with a long baseline in-between them, otherwise the determination of the heading offset will be inaccurate, potentially prohibitively so. This is often impractical to achieve at accessible locations on-board, hence pilots may resort to short baselines, thereby already introducing an error into the docking aid system.

As Perkovič *et al* (2020) highlight, satellite-based positioning systems can only function to any acceptable accuracy when their antennae are not physically obstructed, and when the pilot has enough time to properly set-up the PPU system by entering antenna positions and identifying the ship's gyro heading offset, if that is even possible. PIANC Working Group 145 (The World Association for Waterborne Transport Infrastructure (PIANC) – Maritime Navigation Commission, 2020) suggests that 'the mounting location of the primary (position) GNSS antenna relative to the vessel's bow/stern and port/starboard sides should be accurately established.' We would argue that this is in practice impossible to achieve without introducing a significant error to the coordinate system in use.

The reason why aligning the on-board high accuracy GNSS antennas with the ship's coordinate system is problematic is because that firstly requires valid and accurate knowledge of the applicable offsets of the ship's coordinate system to the antenna mounting position, which is at best difficult but in reality likely impossible to obtain and pre-plan to have at hand *in situ*. Secondly, even if such offsets can be established, there is always an error between design and as-built dimensions of a vessel's features that the antenna is mounted on. These are likely in excess of several cm or more, depending on where exactly the antennas are placed. This may appear a small error, but it will result in significantly larger errors regarding the tracked position of a vessel's bow or stern relative to fenders, potentially in excess of several metres.

Further compounding the problem, the total error budget of on-board GNSS docking aid systems consists of a number of additional components that are explained below. A comprehensive explanation is also available in the Guideline for Control Surveys by GNSS, published by the Intergovernmental Committee on Surveying and Mapping (ICSM, 2020).

At many port locations, the approaching and berthing pilotage phase is short, so there often is not enough time to set-up an advanced PPU system. Regardless of timing, the biggest issue with these systems is manual error, which they are highly prone to in the high-pressure process of docking a large vessel, where many other tasks and considerations have to be taken care of by the pilot and any other support crew. This leads to distractions and the potential for erroneous on-board system set-up, which is worse than not having a docking system at all, since it may provide a false sense of security for the docking manoeuvre that in actual fact may lead to an unanticipated collision.

Additional obstructions other than the highest portion of the vessel itself frequently come into play in constrained ports in form of port infrastructure such as ship loaders, cranes, buildings, and even other vessels, all of which result in much more inaccurate determination of the antenna positions placed on the vessel than sufficiently accurate Real-Time Kinematic (RTK) or Differential GPS (DGPS) systems are capable of providing otherwise. Any change in direction of the vessel during approach changes the horizon obstructions which can lead to further or changes to degradations and time delays to regaining signal accuracy, which is unacceptable when seconds count during a berthing process.

It is also pertinent to point out that even latest generation survey grade RTK equipment and antennas are limited to horizontal positional Survey Uncertainty (SU) of <4 cm, which is only achievable if best practice in RTK specific survey data collection is observed. As advised by the ICSM (2020) such best practice requires recording and averaging of positions for an absolute minimum of 1 minute after the rover has successfully initialised, ie after ambiguity resolution. Averaging of positions to minimise survey error requires the antenna to remain stationary. This is impossible to achieve in a dynamic application such as tracking moving vessels with an on-board GNSS system and means that horizontal positional accuracies of an on-board RTK vessel tracking system are by default worse, potentially much worse than 4 cm for each of the antennas installed on-board, leading to combined baseline inaccuracies and misalignments much worse than advertised.

Table 1 summarises all factors affecting on-board GNSS docking aid system accuracy described in the preceding paragraphs as a list of error budget items. Rather than quantifying these errors at the source such as the PU of antennas for example, their effective magnitude is expressed as the resultant potential difference between actual and displayed distance of vessel bow or stern sections to fenders, since that is the truly relevant criterion when using docking aids.

TABLE 1

Error budget summary of relevant factors negatively impacting on-board GNSS docking aid system accuracy, expressed as the difference between actual and displayed vessel bow or stern section distances to fenders, which is the relevant criterion for docking aids.

Error description	Magnitude
Short on-board antennas' baseline	Up to metres
Coordinate system offsets	Up to metres
Berth (chart) reference generalisation	Up to metres
Vessel 2D display generalisation	Up to metres
Antenna horizon obstructions	Up to metres
RTK antenna never static for >1 min	Up to metres
RTK signal degradation	Up to metres

Perkovič *et al* (2020) investigated berthing data of a large vessel in order to quantify the magnitude of actual inaccuracies of on-board docking aid systems. For a ship of the large size investigated, the authors state that such an orientation error could mean a deviation of up to ten metres from where the pilot and captain think the bow of the vessel is. This matches what has been expressed in the error budget summary in Table 1 and all but renders this method a prohibitively inaccurate docking aid tool.

More anecdotally but nevertheless highly relevant for real-life scenarios, Perkovič *et al* (2020) report that marine pilots have observed sudden jumps of the vessel or tug in certain areas on their monitoring equipment, which in effect shows the ultimate outcome of signal degradation in GNSS or GPS positioning devices or other detrimental effects as listed in Table 1 and described in preceding paragraphs. Whilst the severity varies between locations, it does mean that unfailing reliability is never achievable if this data is to be used to mitigate to a satisfactory extent potentially catastrophic events caused by such large vessels.

Shore-based LiDAR docking aid systems

Shore based LiDAR docking aid technology can be divided into mobile and permanently installed systems. Mobile systems have been proposed in the past on the basis of perceived cost advantages, as described by the European Union (2015) in their DockingMonitor project report. A single mobile LiDAR docking aid system is intended to be deployed to multiple berths as needed, thereby reducing the capital cost to a single rather than multiple systems. In reality, this is not only impractical for multiple berth and busy ports where several vessels may need to be tracked at the same time, leading to a logistical planning overhead, but more importantly, the deployment of such mobile systems requires operational personnel. Not only would this involve training to ensure system accuracy and be prone to manual error regardless just the same as GNSS based systems are, it also constitutes an ongoing operational cost. This negates the additional capital cost to install multiple but permanently mounted systems in a short amount of time.

Permanently installed LiDAR docking aid systems are intended to be a set and forget solution. They fully autonomously track every single mooring cycle of all attending vessels, without the need for any error prone manual input and therefore any operational personnel, and without the need for any equipment to be brought on board the vessel.

PIANC collated available vessel velocity data from Berthing Aid Systems (BAS) for its report on berthing velocities of sea-going vessels published in 2020. The authors state that ‘although not yet adopted for BAS, rotating or oscillating head lasers (Lidar) offer the ability to scan the ship profile in 2D or 3D. Lidar has the potential to better identify hull curvature and features.’ This indicates that none of the 14 ports that collected vessel approach velocity data sets for this report had such superior 3D data available. Hence this paper provides an update on this statement in that such a superior 3D system is now available.

For the system implemented at DBT, all vessel tracking occurs remotely, with vessel ranges, speeds, and approach angles numerically reported in real-time, and visualised in a 3D viewer. It is important to note that unlike GNSS docking aid systems relying on charts to define the distance of the vessel relative to berth, which risks overlooking the potential for collisions with actual berth elements such as fenders which are typically not shown in required detail, the DBT shore and 3D LiDAR based system measures and has in its field of view all actual berth infrastructure near the water line, including fenders. It can therefore report on actually applicable critical distances between all portions of the vessel and all portions of the berth. Critical distances are automatically selected and displayed.

All approach events are recorded in a database that can be searched and recalled to identify any collision featuring excessive vessel speeds during berthing. This system is unique in that it is the only commercially available docking aid that is fully functional and therefore reliable at all times under any conditions as explained in subsequent sections below. DBIM ruled out the use of alternative shore based, permanently installed offerings on the basis of their intermittency of tracking, caused by inferior tracking sensors not collecting 3D data, and/or their lack of software capability in providing tracking data in real-time. This aspect is detailed further in the DBIM Requirements and Deliverables chapter below.

Port traffic control

Many modern mining operations including all of Western Australia's established Iron Ore producers have implemented remote operation centres to coordinate the entire production chain from a central location. Generic rather than mining ports have similar central control centres. The system presented lends itself to be used for traffic control and therefore to become an integral tool for planning purposes on the basis of tracking and visualising actual vessel movements in real-time and in 3D for locations potentially thousands of kilometres away. This can extend to highly detailed task planning and management such as tide and loading dependent mooring line pattern allocation.

Crucially, this system is not affected by adverse weather conditions such as fog or night-time darkness that affect standard CCTV cameras. Such 2D sensors cannot provide any 3D tracking either. Whilst radar technology can maintain measurement robustness in adverse weather conditions, such systems have to date no capability to provide high resolution 3D visualisation data rivalling LiDAR based vessel tracking output.

Port/berth infrastructure safeguard

Very rapid cargo volume growth often exceeding port capacity, and vessel size increase to a point where port facilities can no longer serve larger vessels were listed as major challenges for existing ports in the Masterplans for the Development of Existing Ports report by The World Association for Waterborne Transport Infrastructure (PIANC) – Maritime Navigation Commission (2014).

This is a fundamental industry trend that has been ongoing for centuries but has accelerated into significant civil engineering challenges more recently. It poses the potential risk for significant berth infrastructure damage, particularly to fenders, if vessel speeds and approach angles during approach and berthing exceed prescribed limits as set by The World Association for Waterborne Transport Infrastructure (PIANC) – Maritime Navigation Commission (2020) for example. If any excess speed results in a collision force induced by the vessel onto the fender or other berth infrastructure larger than it is rated for, then permanent damage may be the outcome. Rectifying such damage is very costly and it is in the asset owner's interest to identify the specific event that caused it, so that accountability can be established.

The berth infrastructure safeguard use case of this system is to fully autonomously track every single mooring cycle of all attending vessels, without the need for any error prone manual input, and without the need for any equipment to be brought on board the vessel. As per Docking Aid use case, all vessel tracking occurs remotely, with vessel ranges, speeds, and approach angles numerically reported in real-time, and visualised in a 3D viewer. All such events are recorded in a database and in the event that any berth or infrastructure damage is noticed at any time after the event, the database can be searched, and matching incidents recalled to identify and quantify any collisions during berthing. This has proven to be a compelling business case for port asset owners who don't themselves operate the terminals to install the tracking system.

We note that in its very recent report on all aspects of bulk port operations, The World Association for Waterborne Transport Infrastructure (PIANC) – Maritime Navigation Commission (2019) recommends that approach velocity limits of 0.1 m/sec and 0.15 m/sec should be applied to modern large bulk carriers berthing in protected harbours or at offshore berths respectively to ensure berth infrastructure is not damaged. This requires that the system measuring vessel velocity is commensurately accurate.

The accuracy of reported system vessel approach data as installed at DBT has been thoroughly and independently tested by Curtin University of Technology's Spatial Sciences and reported on by the department's domain expert Dr. David Belton (2021) in extensive vessel approach scenarios including a large range of unlikely ever to occur but nevertheless relevant edge cases, and has been proven to meet the most stringent tracking accuracy requirements as summarised in Table 2. This is essential to assure not only continuity without intermittency, but also quality of vessel tracking under all circumstances, considering that even minor precision or time synchronisation errors between multiple sensors can have a detrimental impact on overall system accuracy.

TABLE 2

3DPortGuard vessel tracking system accuracy as reported by Curtin University (Belton, 2021) in an independent accuracy assessment.

	Mean	Lower 5%	Upper 5%
Distance Error [m]	-0.0065	-0.0127	-0.0002
Speed Error [m/sec]	0.0000	-0.0062	0.0062
Orientation Error [deg]	-0.0076	-0.0160	-0.0020

Validity for finding unequivocal root causes for infrastructure damage in the tracked database of the system presented is therefore ensured, should its data ever be needed for any legal court cases where potentially tens of millions of dollars in contested infrastructure repair costs are at stake.

Vessel loading safety assurance

Bulk carrier vessels such as the ones listed in Table 4 Vessel Classes attending DBT and their sizes, are subjected to the elements of wind, tide, current, and wave motion when moored at exposed wharves, causing the vessel to move within the limits that the mooring arrangement permits. Similar motions are induced even in more protected ports through windage or where surges can be caused by wave reflections off port enclosures. Passing large vessels can also cause berthed vessels to surge.

Such vessel motions can lead to retractable portions of ship loaders to collide with bulk carrier hatch openings, which can lead to ship loader or vessel damage, or both. This has occurred in industry (Perkovič *et al,* 2020) and constitutes a considerable financial burden for replacement, not to mention disruptions to operations. Offshore oil and gas loading at Floating Production Storage and Offloading (FPSO) facilities is subject to similar risks, either when a tanker is loaded alongside the FPSO as occurs at Shell's Prelude operation in Western Australia, or if it a tanker is loaded behind a FPSO, which can lead to jack-knifing and associated strain of loading infrastructure.

Other vessels such as container and cruise ships are subjected to just the same motions when moored as bulk carriers, with similar hazards affecting their core operations in port. Cranes loading container vessels must stack containers on top one another inside the cargo hold within very tight placement tolerances (The World Association for Waterborne Transport Infrastructure (PIANC) – Maritime Navigation Commission, 2012), which becomes unsafe if the vessel is moving under the suspended crane load.

Current crude practice is for stevedore crews to station a sentry near the vessel to visually observe how much it is moving. Needless to say this is difficult to visually judge and impossible to visually quantify to any degree of certainty, particularly at vessel sections relative to berth distant to the sentry's own location. Yet PIANC (Permanent International Association of Navigation Congress (PIANC), 1995; The World Association for Waterborne Transport Infrastructure (PIANC) – Maritime Navigation Commission, 2012) actually quantifies what these motions should not exceed in its dedicated reports on this subject matter.

Vessel breaking mooring safeguard

The world's largest bulk material export port (Pilbara Ports Authority, 2021), with exports including primarily iron ore, but also lithium and salt is located at Port Hedland in Western Australia. It is utilised by three of Australia's top four iron ore miners, BHP Group, Fortescue Metals Group (FMG), and Roy Hill. As summarised in a Pilbara Ports Authority (PPA) Port of Port Hedland Marine Safety Bulletin from January 2021, mooring line failures and parted mooring line incidents pose a significant risk to personnel, infrastructure, and operations in the port. Over the past few years, a significant number of mooring line incidents were reported in the Port of Port Hedland. These form approximately 20 per cent of all marine incidents in the port. The Australian Maritime Safety Authority (AMSA, 2015) reported in their special bulletin on mooring safety that this issue caused two fatalities in 2015 alone. The World Association for Waterborne Transport Infrastructure (PIANC) – Maritime

Navigation Commission (2014) also reports that mooring snap back poses an ongoing risk to maritime personnel with potentially fatal consequences.

In the context of stringent safety considerations by all Australian iron ore and other mining operations, this kind of concentration of a specific safety hazard not least because it has the potential to cause fatalities warrants a concerted effort to mitigate the risk.

This problem has indeed been recognised as a major issue for the maritime sector, evidenced by the 2020 Austmine facilitated BHP Challenge titled Safely Enabling Port Access for Personnel During Vessel Mooring Cycle (Austmine, 2020), which states that risk presented by rapid energy release or snap-back is an industry issue at multiple port operations presenting an opportunity to establish a new industry benchmark.

The following activities are directly impacted by the mooring line energy release (snap-back) risk:

- Provisioning vessels
- Accessing vessels
- Carrying out maintenance activities with vessels alongside (above and below deck)
- General access to the berths.

Weather conditions including wind and open ocean conditions are major impact factors with total closure of berthing areas required during mooring and during any high-risk scenarios.

Like other industries, Australian iron ore port operations have considered the implementation of automated mooring systems to replace mooring lines entirely. Whilst this technology has been in use for specific scenarios for a range of vessels in a select number of other ports for over a decade, it has to date not been universally adopted in large Australian bulk material ports.

As instructed in the Port of Port Hedland Handbook (Pilbara Ports Authority, 2020), a lines boat is required to run ships lines to the wharf on all berths. In 2010, Cavotec Moormaster, an automated suction mooring system was installed on berth PH4, which provides the primary means for vessel mooring operations this berth. The handbook states that traditional mooring lines are also to be run ashore at head and stern at PH4, but to remain slack. They are referred to as ‘comfort lines’. Tightening of ‘comfort lines’ must only be undertaken on specific instruction from PPA Operations staff or marine pilot.

The World Association for Waterborne Transport Infrastructure (PIANC) – Maritime Navigation Commission (2019) reported in its coverage on Specialist Mooring Systems that the vast majority of terminals for any type of shipping rely on traditional mooring lines. As a result, large vessel operations not having universally adopted vacuum or other automated mooring systems to replace the use of traditional mooring lines have an ongoing need to mitigate the risk of mooring lines parting, and with it the risk of mooring line snap back. The system described in this paper delivers the fundamental tracking data to do so in that it is the only type of system on the market that provides actually measured data on all six degrees of freedom of vessel motions:

- Surge
- Sway
- Heave
- Roll
- Pitch
- Yaw.

Alternative systems commercially available invariably only track a portion but not all six degrees of freedom. The reason for this is further explained in DBIM Requirements and Deliverables below.

The above aspects on mooring lines directly affect the risk of vessels breaking mooring. The 3D tracking system installed at DBT automatically switches from approach mode, which can be used as a docking aid, to drift mode, tracking data when the vessel is moored to determine vessel drift.

Excessive vessel drift outside normal parameters is automatically alarmed on to various operations personnel, such that immediate action for bulk carrier retrieval can be instigated in order to prevent damage to the vessel and port infrastructure.

Large vessels have not only broken mooring in generic maritime settings but specifically Cape Size carriers in bulk material ports have also broken moorings in the past. This last occurred at the DBT wharf specifically in 2008 (Daily Mercury, 2008; Feary, 2008). These events are relatively rare but have potentially catastrophic consequences in regards to infrastructure or vessel damage or both. As is evident in the description by the Australian Maritime Safety Authority (AMSA, 2020) of another Cape Size carrier breaking mooring at Hay Point in 2019, every second counts in these circumstances.

The drift mode functionality of the vessel tracking system described in this paper was the key use case that DBIM determined it needed to implement with the intention of mitigating the risk of a vessel breaking mooring. Like other Australian east coast bulk material ports, DBT's wharf is not located in any protective harbour, but exposed to the elements. The chapter DBIM Requirements and Deliverables below provides further detail on what had to be considered to achieve this outcome.

SYSTEM FEATURES

System Equipment

All system components are installed permanently at a stable and unobtrusive location at the DBT wharf, predetermined by accounting for all relevant criteria such as attending vessel types, sizes and shapes, tides, potential wave effects, loading effects, impeding (obstructing) infrastructure, available mounting locations, and any other relevant factors.

As for all other installations, robustness of the system providing reliable and accurate output in all scenarios is dynamically tested in real-time using a dedicated 3D port simulator and a 3D digital twin of the wharf in question that can assess scenarios that are impossible to test *in situ*.

Aside from the sensors themselves, the following system equipment is provided:

- Enclosure fitted with:
  - Fibre optic network equipment
  - AC power rail
  - Embedded high performance industrial PC.
- Real time industrial network protocol inter-faces
- Twin-CAT database server.

3D LiDAR

The vessel tracking system presented uses 3D LiDAR machine vision technology in order to meet the stringent accuracy requirements to track all required lateral and longitudinal vessel motions. The software system is sensor agnostic and hence can use any 3D point cloud data as input. Whilst that could in theory include 3D radar data as available from a range of radar sensor OEMs on the market, tests by the authors of such sensors have not yielded satisfactory data quality. Neither in signal to noise ratio, nor range or particularly spatial resolution, all of which are very poor.

Therefore, LiDAR sensors are most certainly the preferred choice for a vessel tracking system at this time, but 3D radar data can be considered as input again should its quality improve in the future. 3D LiDAR system specifications are as follows:

Real time 3D

The presented LiDAR system does not require a turntable to collect 3D point cloud data. Instead, it captures up to 1 million data points per second (configurable) in a wide instantaneous field of view. Measurement speed per frame can be configured to tens of Hz by reducing point resolution to a still more than adequate level.

Long range

The 3D LiDAR sensors used have an unambiguous range of 260 m, 200 m measurement range to 10 per cent reflective targets and 90 m to a 3 per cent reflective target. Vessel hulls and dark paints have reflectivity as low as 3 per cent. The laser return intensity is also greatly affected by the object incidence angle. The author's experience is that sensor range is a key success factor for applications with potentially low reflective targets.

High spatial resolution and accuracy

The 3D LiDAR sensors of the presented system provide very high spatial resolution of up to 0.037 degrees in the horizontal and 0.015 degrees in the vertical direction. Compared to traditional time of flight sensors, the 3D LiDAR in use maintains distance accuracy over a wider range and with lower reflectivity targets. Real-time 3D high resolution facilitates feature detection for tracking of vessel movements. Individual LiDAR point range precision is significantly improved by extracting planes and features of the vessel covered by typically thousands or tens of thousands of individual 3D points. Actual accuracies achieved by the entire system accounting for all system errors including those of the LiDAR sensors are presented in Table 2.

3D image processor

Multiple 3D LiDAR sensors with high resolution and wide field of view inherently require efficient image processing software which is designed for modern processor architectures in order to yield real-time output. The presented system's proprietary 3D Image Processor provides a High-Performance Computing (HPC) software platform with advanced image processing capability to meet the demands of both current and future high-resolution 3D sensors.

The software is designed to take full advantage of the latest high core count processors and Intel AVX instruction sets. It features the following:

- 3D LiDAR image processing software application
- 3D computer graphics, image processing, and visualisation based on open-source software
- Extensive image point cloud processing capability
- Coded to support high core count processors and the latest Intel High Performance Compute Libraries
- Multithreaded image processing pipelines
- Designed with capacity to handle future high-resolution 3D sensor technologies (>1M points/second per sensor)
- Hosted on Windows 10 LTSB platform
- High bandwidth interface to PLC.

DBIM REQUIREMENTS AND DELIVERABLES

The system functions DBIM were looking to implement were a subset of the total system functional capability as described in the previous section System Use Cases. In other words, the overall system caters for a range of needs, with users setting different priorities on which of the functions they require. Existing users other than DBIM have selected different functions as their priority, all of which can be met.

All subchapters in the following sections of this paper first identify what DBIM stated as their key requirement for the vessel tracking system, and then provide details on how these requirements are met by the 3DPortGuard system that was chosen by DBIM for site implementation in a competitive tender process.

Drift detection

Drift detection was identified by DBIM as a key requirement in order to mitigate the risk of vessels breaking mooring as indicated earlier.

Lateral drift detection

The system must be able to reliably differentiate between vessel drift away from the berth, and normally expected ship movement. Vessel drift is considered to be a movement of 2 m or more of the vessel bow or stern away from the dolphins.

3DPortGuard vessel lateral tracking is based on full 3D measurements that are processed in real time by dedicated proprietary 3D image processing software modules. Alternative systems are known to be unreliable including the lateral measurement because unless full 3D measurements covering sufficient portions of the vessel are continuously covered by the sensor field of view and are processed in real-time, reliable and robust vessel tracking in the lateral direction particularly for the stern and bow sections featuring curved hull shapes is not possible.

This is particularly true when large tidal movements and loading variations in the vertical direction apply, which is the case for DBT at Hay Point, and very much also applies to all iron ore ports in Western Australia. 3DPortGuard lateral vessel movement is accurate and reliable under any tidal and loading condition because of its 3D detection and processing capability. The drift detection tracking algorithm automatically commences once a vessel is fully moored.

All subsequent lateral vessel movements are reported as distances of the straight portion of the vessel bow and stern sections relative to the closest dolphins. Otherwise, any slight longitudinal vessel movement along the berth that naturally occurs for any moored vessel would result in a large lateral movement being reported for any curved hull portions on the bow and stern, resulting in false vessel drift alarms. It can therefore be argued that this lateral drift algorithm as described is the only way to achieve meaningful tracking of actual lateral vessel drifts.

Figure 2 illustrates this issue. Tracking this vessel relative to the fender along the red line as shown would result in unusable values because of the curved shape of the bow in this case. Secondly, the system separately reports on bow and stern positions such that any vessel breaking mooring lines only at one of these locations as has occurred in industry is still alarmed on. Any integrated vessel alarm reporting on the movement of the vessel centre point for example may not be effective in such a scenario where only a portion of mooring lines break. Any integrated vessel position difference relative to a berth reference would potentially suggest overly optimistic or overly pessimistic summary values and would make the system unreliable.

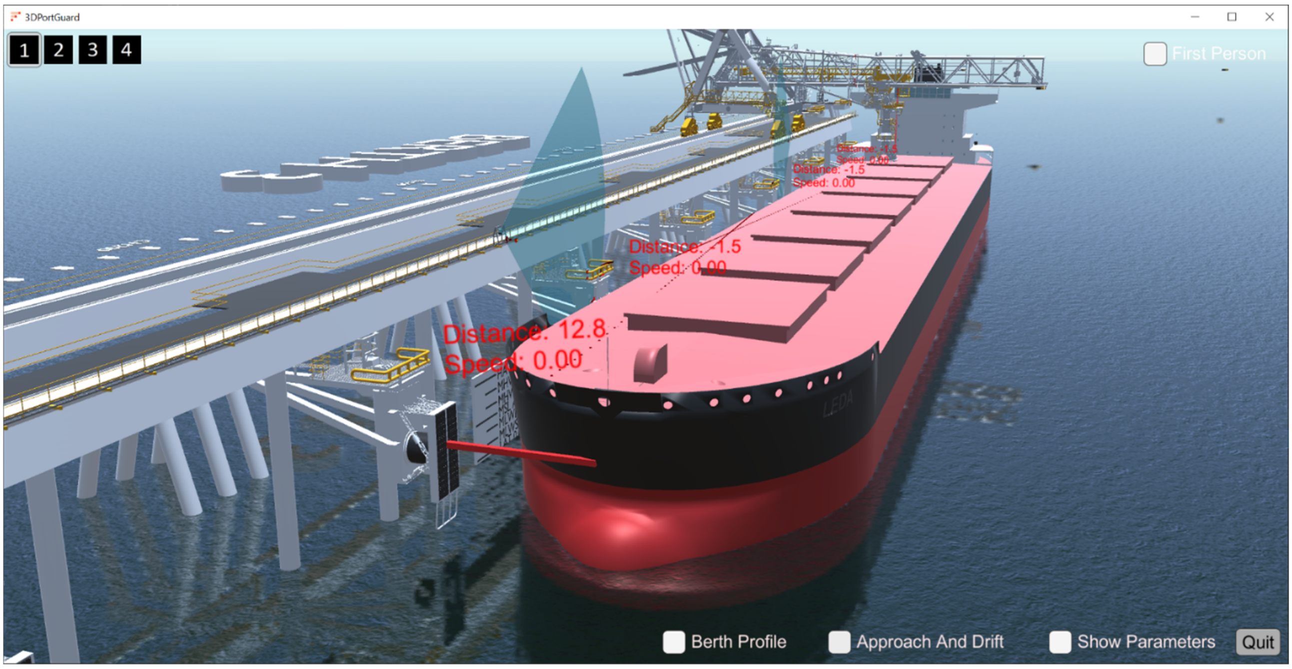

FIG 2 – 3DPortGuard showing a wharf digital twin and the vessel tracking system’s lateral drift vector relative to a fender opposite the curved vessel bow section. Such drift vectors are excluded from the vessel tracking system because they would lead to false drift alarming on what are in fact natural vessel motions during a mooring cycle.

3DPortGuard is designed to be set-up to utilise and track vessel movement against for example PIANC or in this case DBIM site determined vessel movement guidelines for safe loading, un-loading, and detection of vessels breaking mooring. This includes acceptable lateral movement detection of up to 2 m of bow and stern sections away from dolphins as defined by DBIM for berthed vessels, albeit allowing for greater lateral variation during mooring/un-mooring when mooring lines are tightened or slackened as part of the process. Any lateral movement exceeding 2 m is alarmed on in internal control systems.

Longitudinal drift detection

The system must be able to reliably differentiate between vessel drift along the berth and normally expected ship movement. Vessel drift is considered to be a movement of 1.5 m or more of the vessel along the berth.

As for lateral vessel tracking, 3DPortGuard vessel longitudinal tracking is based on full 3D machine vision measurements collected at tens of Hz over the entire sensor field of view. The data is processed in real-time by dedicated proprietary 3D image processing software modules. As per comments in the preceding *Lateral Drift Detection* section, other systems are known to be unreliable, particularly for the longitudinal measurement, because unless full 3D measurements covering sufficient portions of the vessel are continuously covered by the sensor field of view and are processed in real-time, reliable and robust vessel tracking in the longitudinal direction is not possible because of the vessel hull and deck feature shapes. In most scenarios only the flat side of vessels is in the field of view of 1D or 2D sensors, which makes it impossible to reference any feature for longitudinal tracking. 3DPortGuard's 3D system always has distinctive identifiable features in its field of view, which ensures reliable longitudinal tracking.

This issue is particularly relevant when large tidal movements and loading variations in the vertical direction apply, which is the case for DBT at Hay Point, and all iron ore ports in Western Australia as shown in Figure 3.

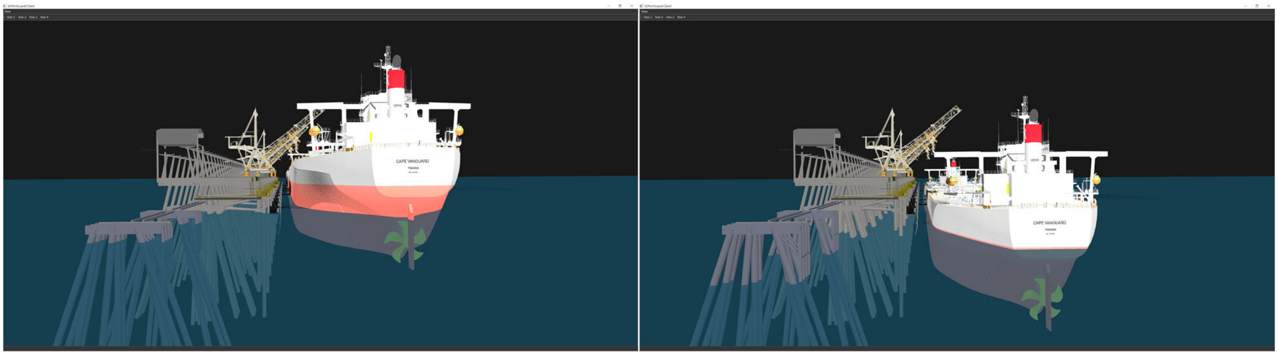

FIG 3 – 3DPortGuard showing to scale an empty bulk carrier at high tide against the wharf (left), and a fully laden equivalent at low tide as applicable to DBT (right).

In such scenarios it is critical for the sensors to track identical features of the vessel in 3D over time because of the drastic change in field of view content, and for the software algorithm to have the capability to process such varying scan cloud data to arrive at accurate drift detection results. In effect, what the 3D sensors view at the beginning of a mooring cycle of a vessel may bear very little resemblance to what they see from the same mounting point towards the end of a mooring cycle when tidal and loading changes caused the vessel to be positioned in excess of 20 m higher or lower relative to the key line at the Hay Point wharf. 3DPortGuard's longitudinal vessel movement is accurate and reliable under any tidal and loading condition because of its 3D detection and processing capability.

As per the preceding section on *Lateral Drift Detection*, 3DPortGuard is designed to be set-up to utilise and track vessel movement against for example PIANC or in this case DBIM site determined vessel movement guidelines for safe loading, un-loading, and detection of vessels breaking mooring. This includes acceptable longitudinal movement detection of up to 1.5 m along the berth as defined by DBIM for berthed vessels, albeit allowing for greater longitudinal variation during mooring and un-mooring when mooring lines are tightened or slackened as part of the process.

Operating conditions

It is important to note that unless operating conditions are taken into account, any shore-based vessel tracking system is destined to fail because it is not fit for purpose as has occurred regularly in industry. This led to the development of 3DPortGuard and to its first installation on all three berths at BHP-Mitsubishi Alliance's (BMA) Hay Point port. A previously installed simplistic shore-based vessel tracking system had fallen into disuse on-site because it was not providing tracking parameters reliably, accurately, or in a timely fashion during the entire mooring cycle. Such systems are not only impractical, but potentially dangerous, because they may provide a false sense of security.

Tidal movement

The system must be able to operate with tidal variation of up to 7 m.

As explained in detail in the section above on how we track longitudinal and lateral vessel movement, it is critical that a sophisticated 3D and not 2D or 1D machine vision sensor array is used to capture usable spatial point cloud data for vessel drift tracking such that large tidal movements of up to 7 m and Vessel freeboard variations in excess of 20 m and any combination thereof does not prevent any or accurate vessel drift being reported.

Secondly, a dedicated and highly sophisticated 3D virtual digital twin simulator has been developed for our port systems, which caters for testing sensor positioning and orientation in the actual berth environment detecting vessels in question. This ensures vertical vessel variations induced by tides and loading can be accounted for before anything is installed or used *in situ*. Any extreme cases of vessel tracking that are impossible to account for through *in situ* testing can be tested in the simulator.

The simulator emulates all actual sensor specifications, tidal movements, loading effects on vertical vessel positioning, opening and closing of hatches, ship loader and access ladder motions, vessel positions and orientations along the continuous DBT berth, and wave motions, therefore replicating the actual system as closely as possible to ensure it achieves maximum reliability and accuracy.

Vessel freeboard

The system must be able to operate with vessel freeboard variation of between 6 m and 29 m at LAT (Lowest Astronomical Tide). This requirement is covered in the *Tidal Movement* section above.

Vessel size and position

The system must be able to operate with vessel length indicated in Table 3.

TABLE 3

Vessel classes attending DBT wharf and their sizes

Vessel class	Length overall (LOA)	Beam (width)
HandyMax	179 m	32.25 m
Panamax	225 m	32.25 m
Japmax	225 m	40 m
Cape	290 m	45 m
VLC	320 m	55 m

The DBT wharf is continuous for each dual berth pair and allows for vessels to berth at varying locations along each pair. This is different to fixed length berths, where the position of berthed vessels does not vary much. Secondly, the varying sizes of vessels as listed in Table 3 introduces an additional variation in the location and size of 3D data coverage required by the combined sensor fields of view of the drift detection system. These two factors above combined – continuous berth pairs and varying vessel sizes in attendance and their location along the berth – require careful design of the location and orientation of individual array 3D sensors such that all size vessels are detected and tracked at all times. The smallest size vessels listed to attend DBT berths (HandyMax class) determine the sensor spacing along berth in that regard, the smaller the vessel size the closer the spacing between individual 3D sensors must be.

Frontier Automation carefully designed the sensor array layout in 3D space, that is to say not only longitudinal and lateral, but also tide and loading induced vertical considerations must be accounted for in this process to arrive at the required number of sensors and their position and orientation as provided in the layout screenshot in Figure 4. Sensor numbers are set at six per berth pair, or twelve for the entire wharf. The exact location and orientation was finalised in the 3D simulator using 3D DBT wharf digital twin data as described earlier and shown in images throughout this paper.

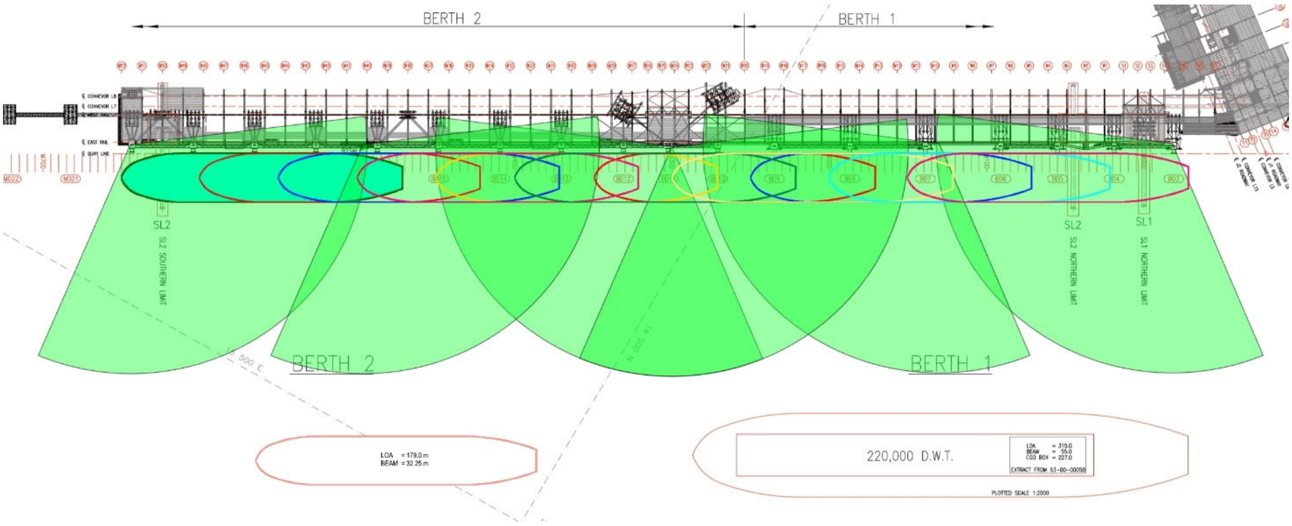

FIG 4 – Sensor array superimposed as green sensor field of view and range arcs over DBT's double berth 1 and 2. This graph is amended by outlines of the smallest attending vessel hulls (HandyMax class) every 50 m along the double berth to showcase possible berthing locations. The diagram illustrates that no matter where along a berth a HandyMax vessel is moored, the planned sensor array will always capture sufficient portions of the vessel by a sufficient number of sensors to provide accurate drift detection. The largest vessel in attendance (VLC class) is also shown to highlight that any sensor array coverage of the smallest vessel automatically also works for any larger vessel.

On average the system covers one DBT berth with three sensors, which is one more per berth than is typically required. The reason why one more sensor per berth is needed for the DBT wharf is that single berths of discrete length feature very little vessel mooring location variation, whereas DBT vessels attending with varying sizes as defined can be moored anywhere along the berth pair as described in the section *Vessel Size*. Figure 4 illustrates these possible vessel variations showing the smallest size vessel outline at 50 m spacings and showing the selected 3D LiDAR locations and their field of view in green along one of the berth pairs. The second berth pair arrangement is identical to the one shown.

Number of vessels and berth length

The system must be able to detect drift of up to two vessels on each berth pair of Berths 1 and 2, or Berths 3 and 4 respectively. Each berth pair is 650 m long, making the wharf approximately 1.3 km long. The system should be able to detect drift of a vessel located anywhere along the length of a berth pair.

Frontier Automation's sensor array layout as per Figure 4 ensures that up to two vessels per berth pair can be tracked for vessel drift. It is relevant to note that a large field of view and long-range 3D point cloud data coverage is important or spacing between individual 3D sensors may have to be prohibitively short.

The reason this becomes prohibitive is because the system needs to be able to distinguish between the two vessels by detecting sufficient continuous data coverage for each vessel regardless of sizes of vessels in attendance and their location along the berth pair to facilitate robust classification of which point cloud data belongs to which vessel. This is at best difficult or at worst impossible to achieve with a larger number of individual point clouds from a larger number of sensors, because their respectively limited coverage may not contain sufficiently unambiguous features for vessel-by-vessel classification. This issue is further compounded by tidal and loading induced variations in vertical vessel positioning, which over time during the vessel mooring cycle results in a significant change to what the sensors see from their fixed mounting location.

Aside from technical aspects, a larger number of perhaps lower cost sensors with inferior specifications still results in a comparable or even higher total sensor and auxiliary equipment cost because more sensors are needed than for the technically superior option.

Large swells

The system must be able to operate reliably with vessel movements caused by large swells.

Since 3DPortGuard reports vessel drift in real-time on the basis of 3D machine vision sensors, and subsecond image processing of raw data and output of lateral and longitudinal movement values, large swell induced vessel motion will not distort reported drift values through motion blurring of the 3D data set. This cannot be achieved with scanning motion type sensors that collect 3D data by sweeping across the scene to achieve horizontal data coverage, because the time it takes to collect a full scan cloud is too slow to avoid motion blurring. Real-time image processing of large 3D scan clouds is not trivial to achieve and sits at the heart of the system installed at DBT.

Any actual and real swell induced vessel motion will contribute to overall longitudinal and lateral vessel drift reported by 3DPortGuard as it should but provided the DBIM site defined motion thresholds of 1.5 m for longitudinal movement and 2 m for lateral movement are representative to account for acceptable moored vessel motion at berth including the effect of large swells, then alarming for any movement above these thresholds is fit for purpose.

If large swell results in moored vessel motions to exceed these original DBIM thresholds without the risk of vessels breaking mooring, then 3DPortGuard's alarming thresholds can be adjusted to more representative values. 3DPortGuard provides moving average drift data to detect whether a vessel has remained at an excessive distance from the dolphins that is not wave induced. Alarming is tuned to account for motion at swell intervals such that wave induced false alarms are avoided.

Vessel orientation

The system must be able to function with a vessel berthed facing either north or south.

The system's 3D image processing software fully automatically determines vessel drift regardless of whether berthed vessels are facing north or south because the algorithms works on feature recognition and matching between measured point cloud epochs that are independent of such vessel orientation. Although available, it therefore doesn't require the vessel orientation data of the existing DBT vessel reporting system as input, in other words it can operate independently of it and doesn't rely on it. The visualisation viewer automatically shows vessels with their correct orientation in 3D.

Site infrastructure

The system must not be adversely affected by the movement of other site infrastructure such as mobile ship loaders, movable ship access ladders, and berth access ladders.

The 3D sensors array system design as shown in the Figure 4 ensures sufficient point cloud coverage on berthed vessels even if parts of individual sensor fields of view are obstructed by mobile site infrastructure like ship loaders or ship access ladders. All associated obstruction scenarios were extensively tested in the 3D Simulator and DBT's Digital Twin using actual site infrastructure 3D data reconstructed from CAD documentation, and all potential vessel sizes and their variable location along a berth pair, as well as vertical variations caused by tides and loading effects.

This process confirmed that selected sensor locations and orientations always work with no or minimal field of view obstruction in regard to fixed infrastructure on the wharf, and that any obstruction of any individual sensor's field of view by mobile wharf infrastructure like ship loaders or ship access ladders is fully mitigated by ensuring sufficient 3D data coverage by other (neighbouring) sensors. As is self-evident in these descriptions, if the process of fully accounting for obstructions in

3D is not pre-planned, any such shore-based LiDAR vessel tracking system will not be providing output data reliably all the time, as has occurred in industry with unrelated installations.

Whilst removing fixed infrastructure data coverage from point clouds to isolate only vessel data for further data processing is relatively simple and only needs to be set-up once for each 3D sensor to facilitate automated data processing, culling coverage of mobile equipment potentially protruding into a sensor's field of view is more complex. The 3DPortGuard system features a sophisticated automatic true 3D point cloud culling algorithm that can utilise existing motion data input from ship loaders, access ladders, or any other relevant mobile equipment if available, as is the case for DBT, to determine which scan cloud portions need to be culled because they cover portions of such equipment at their applicable position and orientation. If such erroneous point cloud coverage is not culled it will distort vessel tracking data. On the other hand, the culling algorithm cannot be too aggressive or it may prohibitively reduce vessel data coverage. All point cloud data collected of the water surface is automatically filtered by using tide data as input.

System functions

Real-time view/measurement of vessels' position at all berths

The system must use field mounted instrumentation to measure and map vessels on an ongoing real-time basis, and provide a visual representation to Logistics, Controllers, Supervisors, Ship loader Operators, and any other stakeholder of the actual 3D position of vessels at berth.

Visualisation of the 3DPortGuard system data and all associated tracked vessels is provided in real-time, with each vessel displayed at its actual position along the berth, and its actual tide and loading induced vertical position. The system can also provide a combined simultaneous real-time view of all vessels at all berths as shown in Figure 5 in a port. This is akin to a traffic control system and is an attractive feature for remote operations centres where real-time visibility of all vessel activities in a port is a highly useful tool.

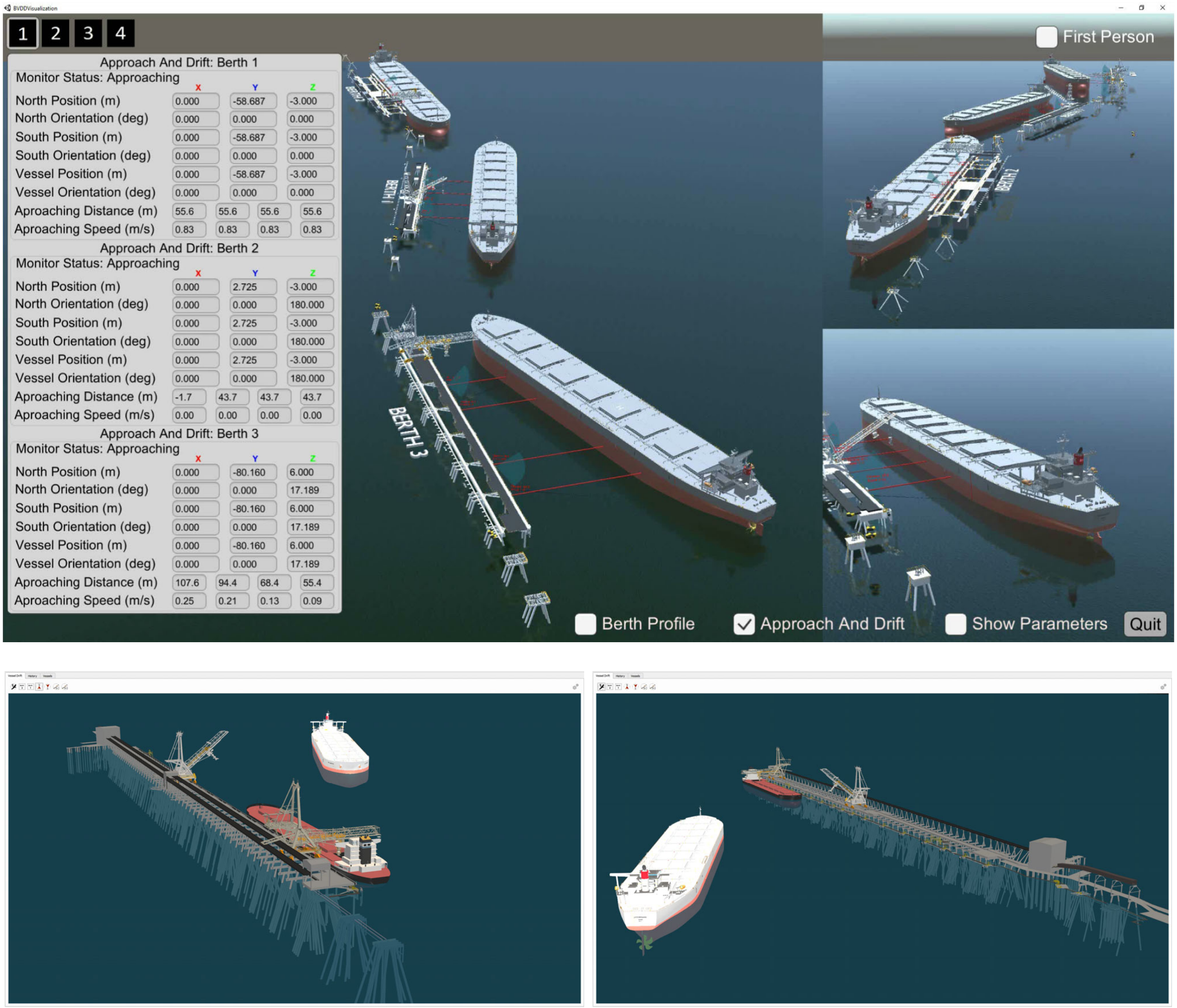

☐ First Person

Approach And Drift: Berth 1

Monitor Status: Approaching

	X	Y	Z	
North Position (m)	0.000	-58.687	-3.000	
North Orientation (deg)	0.000	0.000	0.000	
South Position (m)	0.000	-58.687	-3.000	
South Orientation (deg)	0.000	0.000	0.000	
Vessel Position (m)	0.000	-58.687	-3.000	
Vessel Orientation (deg)	0.000	0.000	0.000	
Aproaching Distance (m)	55.6	55.6	55.6	55.6
Aproaching Speed (m/s)	0.83	0.83	0.83	0.83

Approach And Drift: Berth 2

Monitor Status: Approaching

	X	Y	Z	
North Position (m)	0.000	2.725	-3.000	
North Orientation (deg)	0.000	0.000	180.000	
South Position (m)	0.000	2.725	-3.000	
South Orientation (deg)	0.000	0.000	180.000	
Vessel Position (m)	0.000	2.725	-3.000	
Vessel Orientation (deg)	0.000	0.000	180.000	
Aproaching Distance (m)	-1.7	43.7	43.7	43.7
Aproaching Speed (m/s)	0.00	0.00	0.00	0.00

Approach And Drift: Berth 3

Monitor Status: Approaching

	X	Y	Z	
North Position (m)	0.000	-80.160	6.000	
North Orientation (deg)	0.000	0.000	17.189	
South Position (m)	0.000	-80.160	6.000	
South Orientation (deg)	0.000	0.000	17.189	
Vessel Position (m)	0.000	-80.160	6.000	
Vessel Orientation (deg)	0.000	0.000	17.189	
Aproaching Distance (m)	107.6	94.4	68.4	55.4
Aproaching Speed (m/s)	0.25	0.21	0.13	0.09

☐ Berth Profile ☑ Approach And Drift ☐ Show Parameters

FIG 5 – Examples for a 3D traffic control type display suitable for remote operations centres in use by the West Australian iron ore producers.

Vessel visualisation

The system must include an integrated visualisation system that supports pan and zoom functionality around all sides of all vessels.

3DPortGuard provides real-time vessel visualisation in the wharf coordinate system including berth infrastructure adjacent to the quay line and caters for rotating, panning, and zooming functionality. As shown in images throughout this paper, vessels are displayed in rendered 3D graphical form, derived from the merged scan clouds of sensor stations.

Historical data and playback

The system must be capable of displaying the vessel view at any point in time over the last four weeks.

All 3DPortGuard data is recorded in a database and historical data can be interrogated retrospectively. This is critical for root cause analysis of any incidents or accidents, such as retrospectively discovered damage to berth infrastructure. Whilst not applicable to DBIM specifically, owners of older port assets with infrastructure now subjected to larger than originally intended attending vessels can use this tool to hold operational entities accountable for such damage. Historical data and playback can also be used as a business or safety improvement tool because it facilitates identification and analysis of previously hidden or inaccessible operational scenarios or processes.

It is key for such a historical database not only to be recorded at a sufficiently detailed and accurate level, which needs to be carefully managed because of the large amounts of 3D data involved, but to also be made accessible through meaningful search criteria and an associated user-friendly interface as shown in Figure 6.

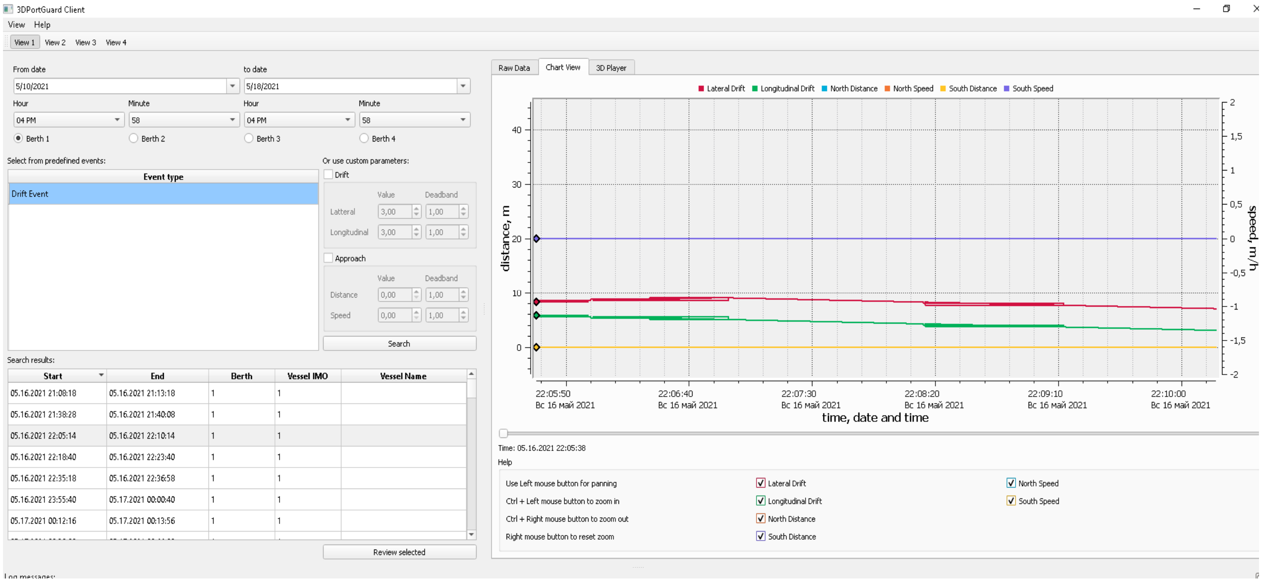

From date: 5/10/2021
to date: 5/18/2021
Hour: 04 PM
Minute: 58
Hour: 04 PM
Minute: 58

● Berth 1 ○ Berth 2 ○ Berth 3 ○ Berth 4

Select from predefined events:

Event type
Drift Event

Or use custom parameters:

☐ Drift

	Value	Deadband
Latteral	3,00	1,00
Longitudinal	3,00	1,00

☐ Approach

	Value	Deadband
Distance	0,00	1,00
Speed	0,00	1,00

Search results:

Start	End	Berth	Vessel IMO	Vessel Name
05.16.2021 21:08:18	05.16.2021 21:13:18	1	1	
05.16.2021 21:38:28	05.16.2021 21:40:08	1	1	
05.16.2021 22:05:14	05.16.2021 22:10:14	1	1	
05.16.2021 22:18:40	05.16.2021 22:23:40	1	1	
05.16.2021 22:35:18	05.16.2021 22:36:58	1	1	
05.16.2021 23:55:40	05.17.2021 00:00:40	1	1	
05.17.2021 00:12:16	05.17.2021 00:13:56	1	1	

Time: 05.16.2021 22:05:38

Help

Use Left mouse button for panning
Ctrl + Left mouse button to zoom in
Ctrl + Right mouse button to zoom out
Right mouse button to reset zoom

☑ Lateral Drift
☑ Longitudinal Drift
☑ North Distance
☑ South Distance
☑ North Speed
☑ South Speed

FIG 6 – 3DPortGuard Graphical User Interface (GUI) for identifying historical drift events from all automatically recorded vessel mooring cycles in the database.

System operator clients

The system must support a minimum of twenty clients with at least ten able to utilise the system concurrently.

The facilitation of multiple concurrent users of vessel tracking users is important to make it accessible to different stakeholders such as different groups of operational personnel, any third parties, or remote operations centres for example. Yet such concurrent use of a real-time system requires an appropriate system architecture that goes beyond traditional approaches. It involves the use of a visualisation server aggregating the data from multiple image processors to provide efficient 3D content distribution. It also links to the database storage and retrieval from a centralised management and access point. This server architecture can be either on premise or virtualised depending on whether dedicated on-site hardware under the user control and management, or outsourcing these elements to a cloud based provider is preferred. Communication links between all system elements including the image processor, the server, and the visualisation clients utilised at the end user location are via secure encrypted internet protocols.

The 3DPortGuard visualisation client provides a composite view of all berths in the wharf coordinate system. Multiple remote visualisation systems can consume high network bandwidth. 3DPortGuard minimises this bandwidth by careful design of the client interface and all associate data structures. This in effect leads to no real limitation in the number of concurrent users of the real-time system. Concurrent access to the historical database is theoretically limited by inherent generic SQL database constraints, that can however in any case be mitigated by increasing hardware performance.

Continuous function during all environmental conditions

The system must continuously operate during periods of heavy rain, fog, wind, sea spray, daylight, and night-time.

3D LiDAR sensors adopted from the autonomous vehicle sector feature superior technical specifications over conventional 3D LiDAR, yet neither are supplied by their respective Original Equipment Manufacturers (OEM) in an appropriately industrialised embodiment that lends itself for direct exposure to the harsh environments of a port berth. DBT's sensor installation features a third-generation sensor protection system as shown in Figure 7 that allows it to function continuously under all such environmental conditions.

FIG 7 – Photographs of a vessel tracking system LiDAR sensor station installed along the DBT wharf.

It was specifically developed and engineered for this purpose because ready-made off-the-shelf solutions are either not available or not fit for purpose. 3DPortGuard sensors are deployed in housings that are air purged incorporating the following components:

- An industrial grade air purge fan
- Air intake pre-cleaning
- Pre-cleaned air intake filtration
- Air flow sensors
- Passive cooling.

which maximises 3D LiDAR sensor preventative maintenance intervals to nominally between 12 and 24 months, depending on the environment specifics. Such long preventative service intervals are achieved by maintaining constant and significant positive air pressure inside the custom sensor head housings such that no dust, moisture or other obscurant can reach or settle on the sensor window. All sensors can be diagnosed remotely from the office so as to only schedule maintenance checks if and when required.

Control system integration – PLCs

The system must be able to interface with existing control system PLCs to send and receive data. All interfacing to the PLC shall be via ethernet TCP/IP.

3DPortGuard features alarming against user defined lateral and longitudinal vessel movement thresholds as per previous sections. These alarm signals are provided through interfacing with existing DBT control system PLCs via ethernet TCP/IP. Any data input interfacing such as usage of moored vessel data to augment 3D vessel views with their name and ID also occurs in this way.

3DPortGuard supports all major industrial ethernet protocols. Interfaces to existing control systems can be implemented through PLC and/or OPC-UA interfaces.

Durability and longevity

Maintenance

The system should be maintainable by suitably qualified DBT personnel with relevant training.

Sensor mounting locations on the DBT wharf are primarily selected to deliver best possible data coverage of vessels to achieve reliable and accurate vessel tracking. The exact mounting location does however also take into consideration accessibility for maintenance. At DBT this was implemented by mounting all sensor stations next to a walkway, taking care to utilise anchor points not subject to any operational vibrations or deformations as this would distort tracking data. As shown in Figure 7, sensor stations are attached to large and rigid structural beams of the wharf, avoiding contact with the much less stable walkway and handrail, yet providing safe sensor station access without the need for scaffolding, mobile cranes, or any other access aids.

Preventative maintenance itself is facilitated through a system maintenance and operations manual, which enables technical personnel to complete tasks such as filter changes with no or minimal training. Spare sensors can be interchanged with any malfunctioning sensor in minutes in the unlikely event that this should be required.

Support

The system must be actively supported by its supplier.

Whilst this aspect is not strictly essential to keep the system operational in the short to medium term, it becomes relevant in the medium to long-term, because IT and automation infrastructure at any industrial port site including at DBT naturally undergoes regular and ongoing upgrades and updates which exposes any system that is not supported to keep according pace to the risk of failing interfaces or other malfunctions and therefore disuse.

3DPortGuard uses appropriate hardware and automation products such as Dell High Performance computer platforms, NVIDIA GPUs and Beckhoff automation components and software designed for real-time 3D applications. Image processing is based on the latest Intel HPC libraries, which are engineering visualisation libraries in a Microsoft Visual Studio development environment. The system is developed as a product rather than as a bespoke custom development, resulting in economic long-term maintainability from a vendor point of view.

Mean time between failure (MTBF) of the sensor equipment

MTBF of the main sensor equipment must be fit for purpose.

MTBF – or in other words the average lifespan or reliability of sensors is a noteworthy aspect of any vessel tracking system, because it is designed to be operating every day of the year, 24 hours a day, and hence sensor wear and tear may become relevant in terms of equipment life expectancy. 3DPortGuard utilises 3D machine vision sensors that do not feature a scanning motion using turntables to collect a full 3D field of view. Aside from data collection speed advantages this also significantly reduces mechanically moving parts that are subject to long-term wear and tear, which in turn significantly increases sensor longevity.

The current 3DPortGuard LiDAR sensor generation deployed at DBT has been designed and manufactured with an automotive application at its core. Associated high-reliability components from the automotive and telecommunications sectors were tested by the OEM for reliability using accelerated lifetime testing. MTBF was determined to be greater than 40 years after more than 35 unit-months of accelerated testing.

System maturity

The proposed system must be in use in other shipping terminals.

As is the case for many major industrial organisations, DBIM opted not to be an early but rather a later adopter of this technology implementation so as to mitigate technical risk. 3DPortGuard has a proven track record in industrial wharf installations and was originally developed as a product for BHP-Mitsubishi Alliance's (BMA) Hay Point operation in very close proximity to DBIM's port, therefore confirming it is fit for purpose in the site conditions such as tidal ranges, exposed berths, and weather conditions experienced by DBT.

SUSTAINABILITY CONSIDERATIONS

DBIM has adopted a comprehensive sustainability strategy aligning with the United Nations Sustainable Development Goals (SDG) that were formulated in 2015. Sustainable Development Goal number 9 specifically targets the creation of resilient infrastructure, promotion of sustainable industrialisation, and fostering of innovation, all applicable to this project.

DBIM has refined the broad United Nations goals to a more specific application at its industrial facilities for a range of themes including people, environment, and business performance that it proactively pursues in its day-to-day operations. This vessel tracking project forms part of the overall portfolio of such strategic activities in that it addresses the sustainability aspects detailed in Table 4.

TABLE 4

DBIM sustainability considerations addressed by this vessel tracking project.

Theme: People	
Key strategic actions	**Alignment and commentary**
Safety	The project demonstrates a proactive approach to managing operational safety issues
Theme: Environment	
Key strategic actions	**Alignment and commentary**
Managing terminal footprint	Project focuses on proactively managing potential impacts from operations – in the sensitive marine environment
Clean and safe shipping	Project clearly improves shipping safety for vessels alongside at the terminal
Theme: Business performance	
Key strategic actions	**Alignment and commentary**
Change and risk management	Project clearly demonstrates a robust approach to risk identification and responsive management.
Asset management	Project clearly demonstrates a commitment to carefully managing and improving assets to reduce potential infrastructure impacts – and consequent environmental and financial impacts and potentially significant operational outages.

CONCLUSIONS

Whilst site specific needs and solutions to DBIM's vessel tracking system scope have been the focus, a range of broader use cases and technical considerations have also been presented in this paper with the aim of providing readers with a more holistic view of all associated relevant aspects.

Considerable design, planning, soft – and hardware development has gone into the implementation of this latest generation vessel tracking system that has overcome previous failings of such systems by others that fell into disuse. A key enabler to do so has been the recent advances in 3D LiDAR machine vision sensors originally developed for autonomous vehicles that have now been adopted for industrial use such as this.

The sophistication of the features and technical specifications described presents the opportunity to address long standing operational shortcomings and safety risks during the mooring cycle of vessels in port. It does so on the basis of genuine automation technology that eliminates the influence of manual error and eliminates operational effort and expenditure otherwise applicable.

ACKNOWLEDGEMENTS

The authors would like to acknowledge Dalrymple Bay Infrastructure Management (DBIM) for the kind permission to publish all site and company related content in this paper.

We would also like to acknowledge all personnel at Dalrymple Bay Terminal involved in this project for their professional contributions to the design, installation, and commissioning of the vessel tracking system at DBT Hay Point port during challenging times when the global Covid-19 pandemic caused severe disruptions not only to operations but also to supply chains.

Lastly, acknowledgement goes to the technical team at Frontier Automation, who have tirelessly and diligently resolved the technical challenges involved.

REFERENCES

Austmine, 2020. BHP Challenge – Safely Enabling Port Access for Personnel During Vessel Mooring Cycle, Expression of Interest document.

Australian Maritime Safety Authority (AMSA), 2015. Shaping Shipping for People – Thinking Mooring Safety, Maritime Safety Awareness Bulletin, Issue 2, September 2015.

Australian Maritime Safety Authority (AMSA), 2020. Warren Bath recipient of 2019–20 Australian Vessel Traffic Services Award [online]. https://www.amsa.gov.au/news-community/newsletters/warren-bath-recipient-2019–20-australian-vessel-traffic-services-award.

Belton, D, 2021. Vessel Monitoring System: Accuracy Assessment Report, Curtin University.

Daily Mercury, 2008. Coal Carrier Breaks Free, Clips Hay Point Mooring, *Daily Mercury*, 13 February.

European Union, 2015. DockingMonitor – development of automated combined berthing aid and drift monitoring system for large ships, particularly oil and LNG gas tankers [online]. https://cordis.europa.eu/project/id/315423

Feary, C, 2008. More Bad Weather Leads to Runaway Ship, *Mining Monthly*, 13 February.

Intergovernmental Committee on Surveying and Mapping (ICSM), 2020. Guideline for Control Surveys by GNSS, Geodesy Working Group (GWG) Special Publication 1, Version 2.2.

Perkovič, M, Gucma, L, Bilewski, M, Muczynski, B, Dimc, F, Luin, B, Vidmar, P, Lorenčič, V and Batista, M, 2020. Laser-Based Aid Systems for Berthing and Docking, Journal of Marine Science and Engineering, May-2020:1–21.

Permanent International Association of Navigation Congress (PIANC), 1995. Criteria for Movement of Moored Ships in Harbours, Report of Working Group no. 24.

Pilbara Ports Authority, 2020. 2020 Port Handbook Port of Port Hedland, 4.5 Mooring, 4.6 Mooring Lines, 4.7 Line Running, 4.8 Mooring Line / Cavotec Failure, p 26–27.

Pilbara Ports Authority, 2021. Mooring Line and Mooring Systems Management, Port of Port Hedland Marine Safety Bulletin 01/2020.

The World Association for Waterborne Transport Infrastructure (PIANC) – Maritime Navigation Commission, 2012. Criteria for the (Un)loading of Container Vessels, Report No. 115.

The World Association for Waterborne Transport Infrastructure (PIANC) – Maritime Navigation Commission, 2014. Masterplans for the Development of Existing Ports, Report No. 158.

The World Association for Waterborne Transport Infrastructure (PIANC) – Maritime Navigation Commission, 2019. Design Principles for Dry Bulk Marine Terminals, Report No. 184.

The World Association for Waterborne Transport Infrastructure (PIANC) – Maritime Navigation Commission, 2020. Berthing Velocity Analysis of Seagoing Vessels Over 30,000 DWT, Report No. 145.

Implementing condition-based wear surface management

P Velletri[1] *and N Gaylard*[2]

1. Global Product Manager – WearSense™ and Fasteners, Metso Outotec, Perth WA 6000.
   Email: piero.velletri@mogroup.com
2. Product Development Engineer, Metso Outotec, Perth WA 6000.
   Email: nigel.gaylard@mogroup.com

ABSTRACT

The management of wear surfaces in mining operations has remained largely unchanged since the inception of mining. Sacrificial wear liners are installed on the inside of chutes, hoppers and other equipment used to transfer bulk ore to protect the asset from abrasive wear caused by the flow of material. These liners are generally replaced at fixed intervals which may be determined based on historical wear rates or may be driven by other maintenance requirements for that asset. This approach does not always yield satisfactory results, especially for critical assets where the impact of downtime on production can be substantial. For such assets, a condition-based maintenance strategy has the potential to significantly increase productivity and reduce the total cost of ownership associated with the asset. However, for such a strategy to be successful, timely information on the actual condition (remaining thickness) of the wear liners is essential.

This paper describes the development and implementation of a wear monitoring system that can be used to remotely and continuously report on remaining liner material thickness in real time. It details some of the challenges that were overcome when developing the system, including the design of a patented thickness measuring system that can be used in a variety of liner materials and is tolerant to the presence of ore on the wear surface. The paper also explains how a cloud-based approach enables data from the wear sensors to be integrated into external systems such as a data historian, which has been demonstrated through a collaborative project with one of the largest iron ore producers in the Pilbara. This ability to combine real time liner thickness information with other data sources, such as throughput, provides the foundation for the transition to a condition-based maintenance strategy.

INTRODUCTION

Over the past few decades there has been a growing interest in moving away from traditional schedule-based maintenance methodologies towards a proactive maintenance strategy based on monitoring the condition of the asset in real-time. This type of maintenance strategy, known as condition-based maintenance (CBM), is particularly valuable in assets that are highly utilised, difficult to access, expensive to maintain or have a high cost to shutdown. CBM, and the broader field of predictive maintenance, has the potential to significantly reduce the operational downtime due to both scheduled and unscheduled maintenance in addition to minimising the cost (and associated wastage) of spare parts.

Despite the benefits of CBM, the reality is that it has gained little acceptance in the mining industry due to the interdependence of equipment in the supply chain, meaning it is generally not practical to plan individual asset maintenance independently of other equipment. While CBM might reduce the downtime (increasing availability) for each asset considered in isolation, it could negatively impact the availability of the overall processing plant. Notwithstanding, there are assets within mining and mineral processing operations where adopting parts of a CBM strategy, such as condition monitoring (CM), adds value. Monitoring the condition of an asset can inform the extent of maintenance to be undertaken during the next scheduled outage or provide warning of unexpected circumstances (positive or negative) that require planned maintenance to be brought forward or allow it to be delayed.

The management of wear surfaces on assets, such as chutes and hoppers, is an area that would benefit from a CBM strategy, as these surfaces generally consist of individual liners that can wear at different rates. Even if the asset is maintained on a fixed schedule (to align with other maintenance being carried out on the system), the ability to selectively change only those liners that will not last until the following shut can not only yield a cost and time saving, but also reduce wastage. The difficulty in implementing a CBM approach to liner maintenance is the requirement to monitor the remaining material thickness to be able to make an informed decision as to which of the liners should be changed during the next shut. Recently, however, the introduction of real-time monitoring systems for liner wear has enabled a condition-based approach to wear surface management.

This paper describes a system that is capable of continuously and remotely monitoring the remaining thickness of wear liners and explains how this information can be used to assist in the management of these wear surfaces. It details some approaches that can be used to integrate the wear data with information from other data sources to better predict the end of life for the liners. Examples are provided of how the implementation of a wear monitoring system has led to reduced total cost of ownership for the assets in which they are installed, as well as minimising the risk of unplanned maintenance due to uncertainty in the performance of the wear lining material.

MONITORING WEAR IN LINERS

Wear plates or liners are sacrificial elements that are installed on the inside of chutes and other equipment within mineral processing operations to protect the underlying asset from abrasive wear caused by flowing ore. This practice dates to the industrial revolution, when it was recognised that removable plates could be fitted to high wearing surfaces on an asset to avoid the need to continually repair or replace the equipment. The effectiveness of this philosophy relies on the ability to know when to replace the wear plates; if they are replaced too often, the business incurs unnecessary costs due material wastage, labour, and equipment downtime. Replace a liner too late and it can wear through allowing the ore flow to damage the asset surface below, potentially leading to an unplanned shut and expensive repairs.

Ultrasonic testing

The traditional approach to monitoring the wear in liners is to utilise ultrasonic testing (UT) to measure the remaining thickness of the material. UT measurements need to be made directly on the material being tested which means either shutting down the equipment to access the wear surface of the liner (leading to lost production) or incorporating inspection holes in the chute wall to expose the back surface of the wear material. While using UT through holes in the backwall of the chute can minimise disruptions to operations it can be problematic with some liner materials (such as chromium carbide overlays) as there are multiple internal reflective layers leading to false thickness measurements.

3D laser scanning

More recently, 3D laser scanning has proven to be a popular method for assessing and monitoring the wear on large surfaces. This technology can deliver very accurate measurements of wear (and impressive heat maps highlighting problem areas) but it requires the surfaces to be free from material build-up and needs to be performed from inside the chute, usually with the equipment shutdown. Both laser scanning and UT can introduce safety risks for the personnel conducting the measurements as they often need to access confined spaces or work at heights to complete their tasks. Furthermore, neither of these techniques is particularly well suited to the continuous or remote monitoring of wear liners (although remote monitoring systems based on UT are now starting to be seen).

Sensor monitoring

The concept of monitoring wear in liners using a sensor is not new, indeed the idea which led to the development of the WearSense™ system (to be described in this paper) was patented more than ten years ago (Davies, 2010). However, to gain acceptance, wear monitoring systems need to be easy to install, provide broad coverage across the wear surface, have the ability to be fitted to existing assets and all liner types, be low cost, non-invasive and provide the ability to remotely monitor the asset. Over the past few years, wear monitoring systems which fulfill most of these criteria are starting to become commercially available, with a few different technologies being implemented to measure the wear.

Ultrasonic sensors

Some of the commercially available systems utilise UT sensors (or sensors based on similar penetrating radar technology) which are embedded on the back surface of the liner. These systems are completely non-invasive and have the advantage of enabling multiple measurement points without disrupting the wear surface of the liner. However, they can be complicated to implement, high in power consumption and may require the supply of purpose-built wear liners.

Probe sensors

Due to the limitations of UT sensors, by far the majority of the wear monitoring systems currently available on the market (including WearSense) rely on a physical probe that penetrates (or is implanted in) the liner and wears with the liner. Electrical elements or circuits are embedded in the probe and as the probe wears the sensor detects changes in the circuit and converts this to a corresponding probe length, or liner thickness. Wear monitoring sensors which utilise probes based on optical fibre technology are also available, however these tend to be more expensive and have higher power requirements than those based on electrical circuits.

One of the challenges of using a probe with conductive elements to measure thickness is that as the probe wears the electrical circuit becomes exposed to the ore. Damage to the probe in combination with the fact that some minerals (such as iron ore) are conductive can lead to false measurements. To overcome this issue, a patented probe design and sensing algorithm was developed which can reduce the risk of incorrect thickness reports resulting from an electrical short circuit at the probe tip. The WearSense probe was incorporated into a self-contained sensor that is inserted through the liner to the wear surface as shown in Figure 1, with data from the sensors being wirelessly transmitted to a nearby receiver and gateway. This sensor design makes the system very simple to implement and means that it is completely independent of the liner system being used.

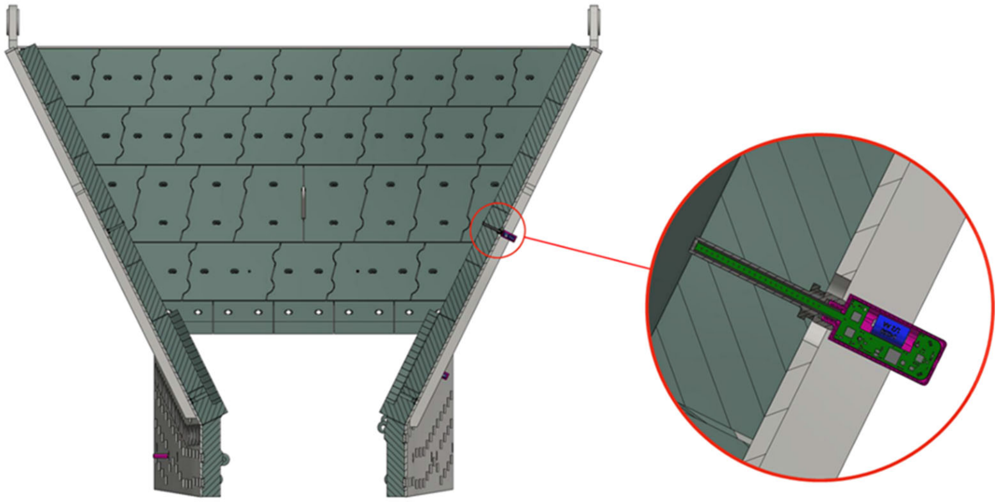

FIG 1 – Cross-section of a chute showing an installed wear sensor.

As the sensor probe penetrates through the liner, the diameter of the probe has been deliberately kept as small as possible to minimise the risk of preferential wear caused by what is essentially a hole on the wear surface.

Patented design

For wear plates that are secured using bolts that pass through the liner (such as tapered, or oval head bolts) it is also possible to incorporate the sensor probe into the fastening system, as shown in Figure 2, which can simplify the sensor installation even further. The idea of incorporating the wear monitoring sensor into the mechanical element used to fasten the liner is patented (Davies, 2010) and therefore only available to the WearSense system. This wear sensor design has been successfully installed in chutes processing several different ore types as well as a variety of different wear liner materials including ceramics, quenched and tempered (Q&T) plate, chromium carbide weld overlay (CCO), and cast white iron.

FIG 2 – Wear sensors incorporated into the mechanical fasteners used to secure the wear liner.

Table 1 provides a comparison of some of the alternative methods available for monitoring wear in liners, indicating some of the benefits of each system.

TABLE 1

Comparison of methods for monitoring wear in liners.

	Embedded WearSense probe	Manual UT inspection	3D laser scanning	Embedded UT sensor	Embedded conductive probe	Embedded optical fibre probe
Continuous real-time measurement	✓	✗	✗	✓	✓	✓
Provides a remote monitoring solution	✓	✗	✗	✓	✓	✓
Measures full surface wear profile	✗	✗	✓	✗	✗	✗
Low power (can be battery powered for life of liner)	✓	✗	✗	✗	✓	✗
Can be embedded in liner fastener	✓	✗	✗	✗	✗	✗
Non-invasive (does not penetrate to wear surface)	✗	✓	✓	✓	✗	✗
Measurement can be taken with equipment running	✓	✓	✗	✓	✓	✓

APPLICATION OF IOT TO WEAR PLATE MONITORING

The physical sensor used to measure the remaining thickness of a wear liner forms only one part of a wear monitoring solution. For the information from the wear sensor to be useful, it needs to be available in a timely manner, and preferable without requiring personnel to access the site. The internet of things (IoT), or more specifically industrial IoT (IIoT), provides the framework for completing the end to end wear monitoring solution. Figure 3 provides an overview of an IoT system that can be used to monitor wear in liners.

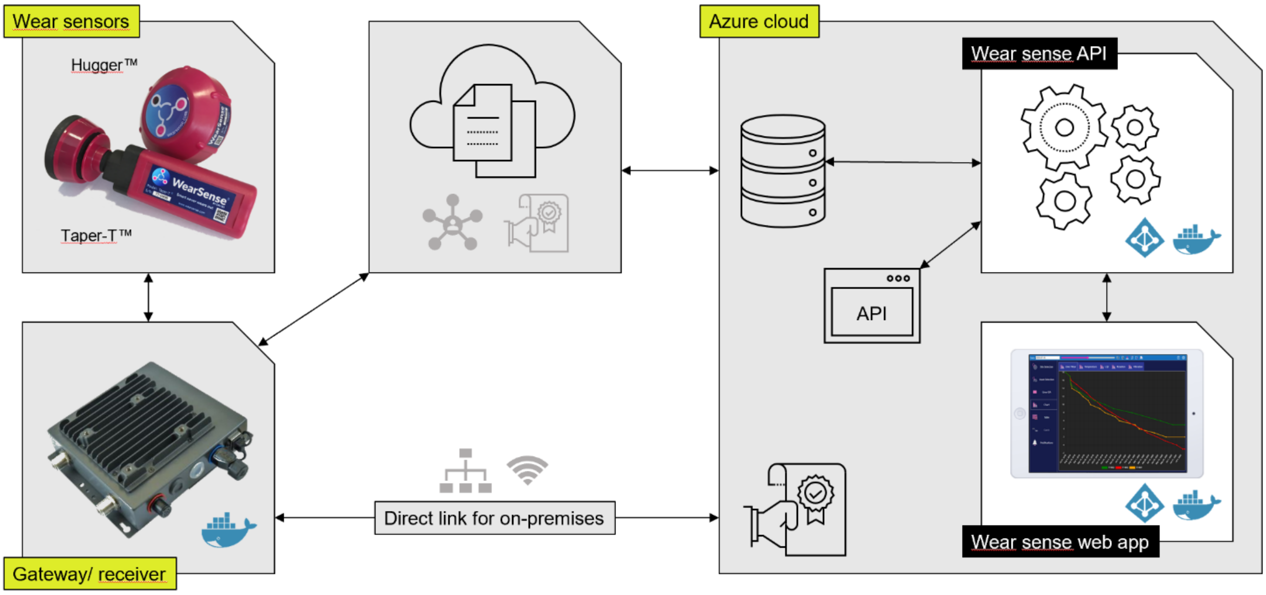

FIG 3 – Components of the WearSense IoT system for monitoring wear.

Gateway

In addition to the wear sensors themselves, a wear monitoring IoT system will typically incorporate a gateway which acts as a bridge between the sensor local area network, typically a low power wireless network, and the wide area network for connection to the cloud. While the primary purpose of the gateway is to transfer sensor data into the cloud, it may also be used to aggregate the data and perform other edge processing tasks that can reduce the bandwidth requirements.

Most standard IoT gateway computers are not robust enough to withstand the harsh conditions experienced in a mining environment as they are targeted at industrial automation and factory environments. Mechanical, electrical, and environmental requirements need to be considered to survive the installation conditions. Physical and remote access to the gateway and sensors can be limited, requiring robust hardware and software implementations. Integration can be a challenge as IoT sensing is typically implemented by operational teams rather than information technology (IT) technicians despite requiring significant IT expertise. With modern connected devices, emphasis is often placed on deploying updates frequently to maintain the most current version. However, operational teams and plant have a different risk profile and a stable system that has minimal change is preferred. When integrating an IoT system one of the challenges is ensuring that both requirements are met.

One means of implementing a monitoring system is to ensure that it is fully decoupled from the IT system and the process control system. This partitioned approach is facilitated using technologies such as existing telecoms infrastructure using 4G networks for the back-haul and cloud computing to manage the IoT system independent of the main infrastructure. Client access to the data can be enabled through an application programming interface (API) which manages the communication between the IoT system and client. The API provides a read-only interface to the client for data retrieval. Using delta queries ensures that data is retrieved efficiently and enables access to both current and historic data. As the API forms the interface to the client system it should be stable and sufficiently documented for ease of integration and to prevent breaking the interface when software changes are made to the IoT system (Uddin and Robillard, 2015).

User interface

While the sensors and gateway are essential in order to be able to gather the data related to liner wear, the benefits of condition monitoring can only be realised if this data is readily accessible and presented in a way that is easy to interpret and actionable. The user interface should clearly highlight any critical areas on the asset that require immediate attention, preferably with the ability to send automated alerts if the level of wear passes pre-set thresholds. Having near real time visibility of the current condition (remaining material thickness) of the liners is already a significant improvement over traditional monitoring techniques, however the true value of collecting this data is the ability to predict the future condition. By continuously monitoring the remaining thickness of the liners it is possible to fit trendlines to the data and calculate wear rates which can then be used to estimate the end of life.

Figure 4 shows two screenshots of the user interface for the WearSense wear liner monitoring system. The first image displays the current remaining liner thickness at various points on the asset with alerts highlighting areas which have worn below pre-set levels. The second image shows the ability to plot historical wear profiles at any of the sensor locations and extrapolate these to estimate the end of liner life (the chart shown correlates to the six sensors highlighted in the main image). It should be noted that the wear liners being monitored in this example are chromium carbide overlay (CCO) and the reported thickness corresponds only to the overlay, so at the estimating end of life ('zero' wear surface remaining) the thickness of the backing plate material would still remain.

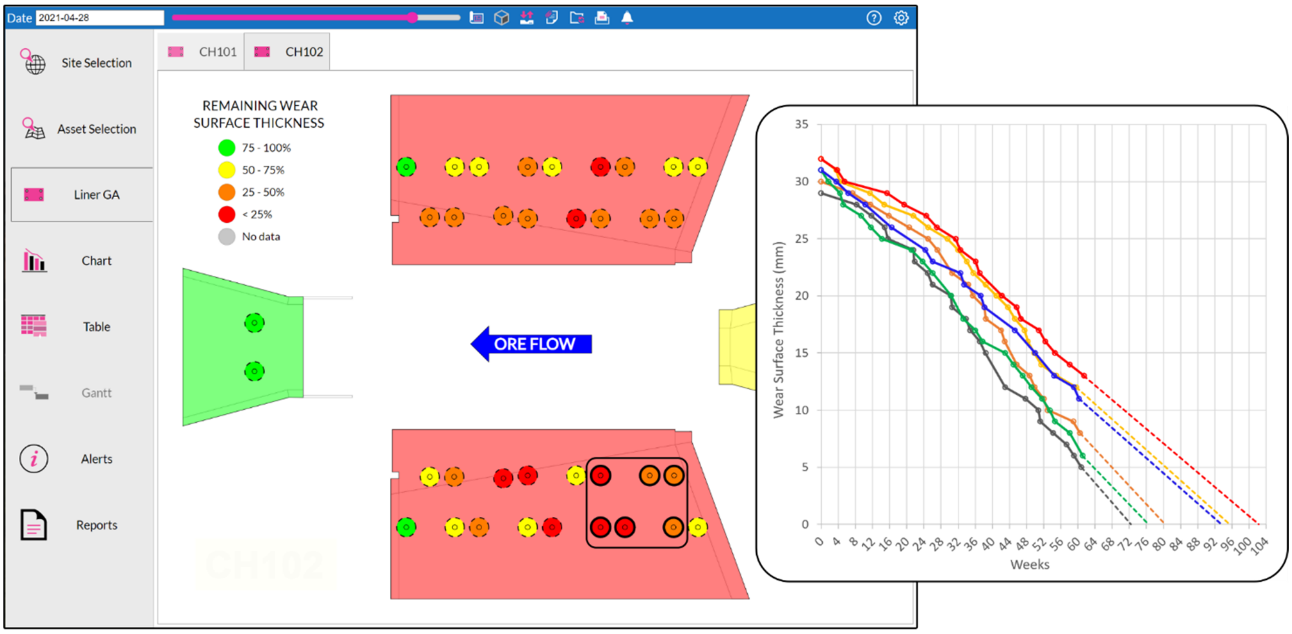

FIG 4 – User interface for the WearSense liner monitoring system.

CONDITION-BASED WEAR SURFACE MANAGEMENT

The introduction of a wear monitoring system, such as WearSense, provides information regarding the current state of the liners as well as data that can be used to predict the future condition, which forms the basis for a CBM strategy. However, one of the challenges with adopting a true CBM strategy to individual assets within a mineral processing plant is that while it may locally optimise the availability of that piece of equipment and reduce the maintenance costs, it would generally be at the expense of total supply chain throughput. The interdependence of assets within mineral processing operations has led to the common practice of schedule-based block maintenance which considers both upstream and downstream buffers (ore stockpiles) to try and minimise loss of throughput resulting from equipment downtime due to maintenance. In effect, scheduled maintenance aims to optimise the total plant availability despite inefficiencies in the maintenance of individual assets.

Imperfect maintenance

The availability of wear data enables an alternative, hybrid, maintenance strategy to be implemented that combines scheduled maintenance with CM. With the knowledge of actual asset health provided by CM, the amount of maintenance conducted can be optimised to reduce both the equipment downtime and direct costs (labour and material) associated with the scheduled shut. This approach represents the practical implementation of an imperfect maintenance model where, rather than restoring the condition of the asset to 'as good as new', it is only partially restored with reduced costs but also with high confidence that the equipment will continue operating until the next scheduled maintenance interval. In the context of wear surface management, this means that only selected liners are identified for replacement during the next scheduled shut which reduces the inventory costs, minimises material wastage and eases the requirement for resources during the shut. To assist with this process, the WearSense user interface can highlight all liners that will last until the next planned shut but not the following one. These liners are automatically selected and added to a list that the shutdown planners can use when ordering replacement liners for the next shut.

Comparing material options

Another way in which wear monitoring can be used to reduce costs without altering fixed maintenance schedules is by helping to build an understanding of the performance of alternative liner materials. Asset managers have many options available to them with regards to the selection of liner materials which include ceramics, CCO, quenched and tempered plate, cast (chrome white iron), bi-metallics, rubber, polyurethane and hybrid materials (such as rubber with ceramic inserts). Many of these materials will also have numerous options available in terms of the wear surface thickness. While the characteristics of each type of liner (such as performance when subject to impact) will have an influence on its suitability for a specific application, multiple choices will normally exist. By continuously monitoring and comparing the performance of wear liners when different materials are used, it is possible to optimise the selection of the liner to match to desired maintenance schedule. WearSense provides the ability to superimpose the wear profile from multiple installations which enables a direct comparison between different liner materials to be made.

Selecting maintenance intervals

Despite the prevalence of schedule-based maintenance, there will always be situations where it is extremely difficult to decide on the correct maintenance interval for wear surfaces. In new projects, for example, the wear rates of liners will be unknown making it difficult to select a suitable maintenance schedule, especially if the material or equipment design varies significantly from similar existing operations. In addition, most mineral processing operations will always contain some wear surfaces which are designed to have very long maintenance intervals (often in excess of three to five years). These are typically installed in assets where the cost associated with replacing the wear surface can be extremely high, such as the hoppers located underneath stockpiles. For these types of assets, the value of liner thickness monitoring systems, such as WearSense, is unquestionable. The data collected provides a way of estimating the next maintenance interval as well as providing confidence that the performance of the chosen liner material is meeting expectations.

THE BENEFITS OF INTEGRATION

The challenge with implementing any type of condition monitoring system is to ensure that the data is readily available and presented in a way that facilitates its use in the decision-making process. Ideally the information from a wear monitoring system should be integrated with other data sources, such as throughput, so that (for example) the prediction algorithms can be based on production schedules rather than elapsed time. The reality is that some companies do not have the resources or capability to deal with the sheer volume of data that is typically being generated in most modern mineral processing plants. The user interface should therefore, as a minimum, provide sufficient information to enable site-based personnel to immediately use it to enhance their decision-making processes. It should, however, also allow for the possibility of integration with other software and data management systems.

The development of the WearSense user interface has followed a continuous evolution based on direct feedback from the users, who are typically site-based personnel responsible for the management of wear surfaces on assets. Basic features, such as visualisation of the current condition of the liners and historical trends in wear have evolved into more advanced features such as automated condition monitoring reports and alerts which can be emailed to users. The integration of wear data into other systems is another key focus at Metso Outotec, with several collaborative projects initiated in 2020 to facilitate this (both with the end-users as well as third-party solution providers).

Sharing operational data

One of the leading iron ore producers in the Pilbara region of Australia has an ongoing project to integrate data from multiple sources into a common platform in order to help enable data-driven decision-making. Working closely with their development team, access was provided to WearSense data through a secure API enabling them to regularly retrieve wear data and push this into their OSIsoft PI historian system. The result is a common platform that provides access to multiple sources of information, including condition monitoring, production data, and possibly also unplanned maintenance events. This data could eventually become a direct input to the supply chain simulation models that many companies typically use for long-term scenario planning. As these models become more advanced and start to incorporate artificial intelligence and machine learning, it is conceivable that they could one day be used for short-term planning and lead to optimised maintenance across multiple assets while still maximising overall system throughput.

Automating business processes

An additional benefit of condition monitoring systems, such as WearSense, is the potential to use real-time data to automate the procurement process. Planning for a maintenance shut is a complicated process and part of this process is the requirement for spare parts to be sourced from multiple suppliers and delivered to site in a timely manner. During a shut it is not uncommon to discover that the incorrect part was supplied or, indeed, the required part was not even ordered. As confidence grows in the ability of wear monitoring systems to accurately predict the liners that will be required for the next shut, the next logical step would be to pass this information through to the company's enterprise resource planning (ERP) software so that appropriate action can be taken. Such action might include raising a maintenance order and generating a requisition so that appropriate parts can be procured. TOKN technologies (Smith, 2021) have demonstrated the ability to use real-time liner thickness data from WearSense to drive a rule-based decision-making process that can then automatically generate workflows within an ERP system, such as the widely used SAP software.

IMPLEMENTATION RESULTS

Since WearSense was first launched in 2018, the system has been implemented across a range of assets with more than 500 wear sensors installed. Three of these assets have been selected to demonstrate some of the insights obtained from the wear monitoring system.

Case 1 – Apron feeder hoppers

The feed hoppers (Figure 5) that are located underneath the coarse ore stockpiles (COS) were identified by one iron ore company as an ideal application area for a remote wear monitoring system. Access to the wear liners inside these hoppers for inspection or replacement is difficult, as the COS needs to be run down and then dozed to prevent any risk of engulfment. In addition, the hoppers are generally large and the process of replacing the lining can be both time consuming and expensive. The direct cost to replace these liners can exceed several million dollars (without taking into consideration the associated loss of production) so there is a strong drive to fully utilise the liners and maximise the replacement interval. Unfortunately, the difficulty in accurately measuring the remaining thickness had previously resulted in the liners being replaced with a significant amount of usable wear material remaining. For this reason, a decision was made to install the WearSense wear monitoring system with the new liners.

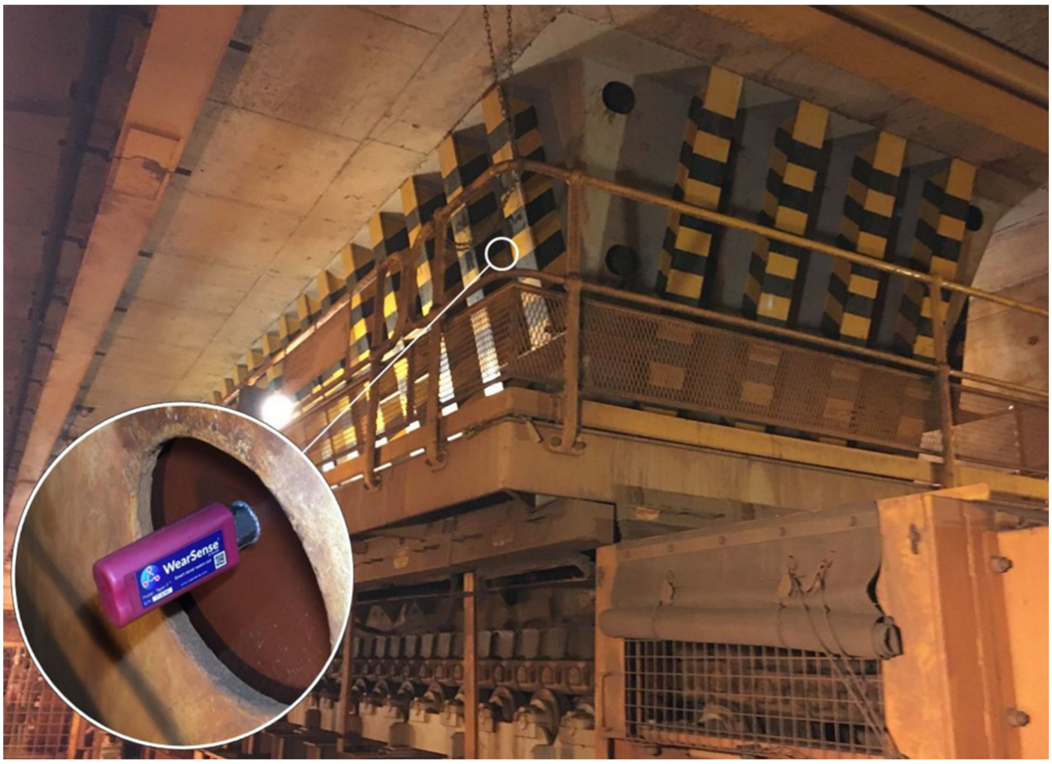

FIG 5 – Apron feeder hopper showing one of the installed wear sensors.

Based on the previous life of the liners, the new liners were anticipated to last in excess of three years, however the data from the WearSense system was indicating a wear rate that was substantially higher than expected. The chart in Figure 6 shows the trend in minimum and maximum thickness for one liner over the first 12 months in service. At this point, the system was predicting that in some locations the wear surface of the liner would be completely worn through in a further five months (less than half the expected liner life). In this instance, the system provided the company with an advanced notice of accelerated wear which would potentially not have been discovered until damage to the hopper had occurred.

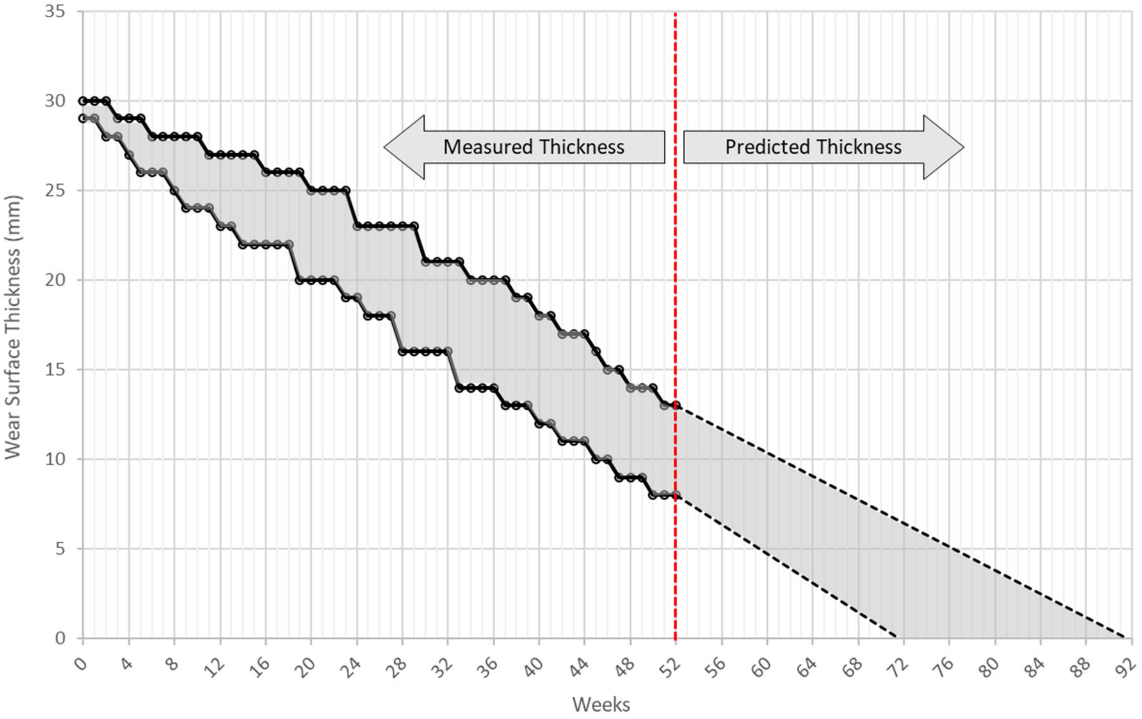

FIG 6 – Minimum and maximum thickness for a selected liner.

Case 2 – Train loadout chute

The second asset was a train loadout (TLO) chute which was being replaced with a new design. The company decided to install the WearSense system due to the critical nature of the asset and the uncertainty in wear rate, which had previously let to the chute being damaged (Figure 7). Information provided by the wear monitoring system enabled the high wearing liners to be identified for targeted for replacement during the next planned shut. The ability to limit the scope of the liner changeout could potentially save around $50k in direct material costs alone (not taking into consideration the reduced duration of the maintenance shut).

FIG 7 – Damage to TLO chute due to wear (left) and new chute with installed wear sensors (right).

As it turned out, the customer was unable to replace any of the liners during the planned shut and concerns grew that the liners would wear through and once again damage the parent metal. The ability to continually monitoring the remaining thickness of the wear liners enabled the asset managers to leave the chute in service with confidence that there would be minimal risk of damage to the underlying asset. In fact, as shown in Figure 8, the wear rate began to decrease slightly, even though the liner material had worn through the weld overlay into the base metal of the liner (as evident by the negative measurements which the WearSense system was able to record). The non-linear wear characteristic of this liner material is one which has been observed in many of the CCO wear plates being monitored by WearSense systems, possibly due to the non-uniform distribution of chromium carbide elements within the weld overlay substrate. The fact that the lower wear rate has continued into the base metal of the liner (which would have been impossible to predict) could be due to changing equipment utilisation or ore type, highlighting the need to integrate wear measurements with other operational data.

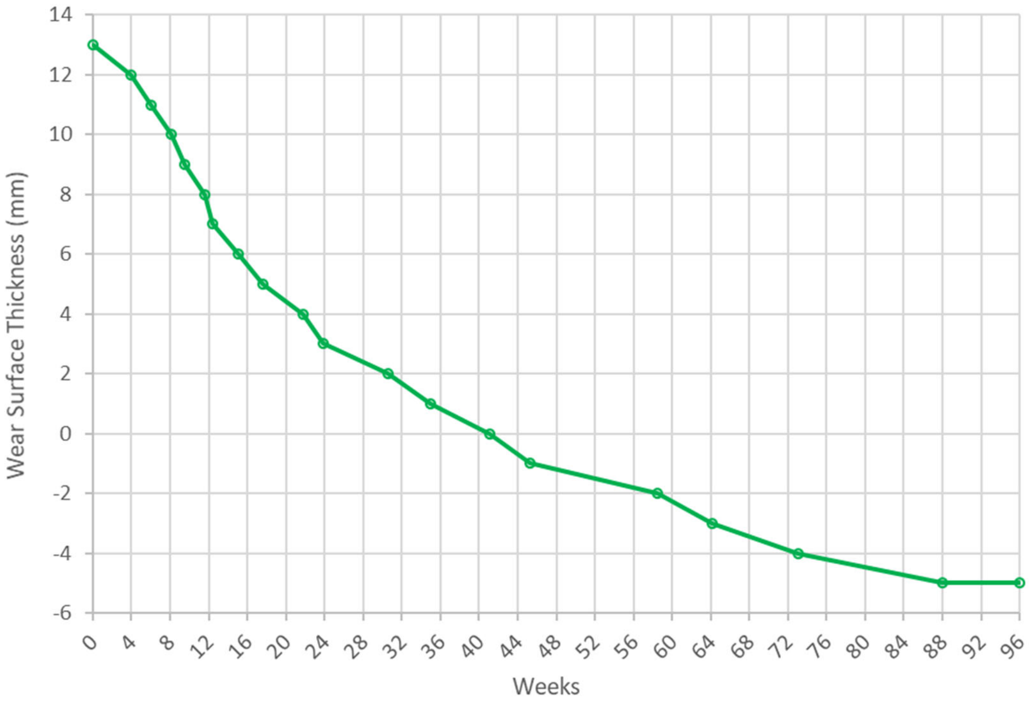

FIG 8 – Liner wear profile showing a decrease in wear rate over time.

Case 3 – Reclaimer spill face

The final asset was a reclaimer spill face in which all of the liners are replaced regularly based on a fixed maintenance schedule. New liners were always installed at each shut (even if some of the existing were only partially worn) as it was felt that there was insufficient material remaining to safely extend the replacement of the liners to the following shut. In this instance, the WearSense system was installed as a trial to determine whether there was any possibility of adjusting the shut schedule to extend the liner life. Data from the WearSense system indicated that there was a potential to save up to $135k annually in direct wear liner materials costs through adjustments to the shut schedule. However, as the maintenance schedule had been selected to align with other equipment in the circuit (and adjustments would have had the potential to negatively impact the overall supply chain availability), it was decided to retain the existing shut schedule for liner replacements. Notwithstanding, the WearSense system also identified the potential to select a lower specification liner material or utilise thinner liners, both with the potential to reduce costs without altering the existing maintenance schedule

CONCLUSION

This paper provides an overview of a wear sensor that can be embedded in a liner and used to continually monitor the remaining thickness of the wear surface. When combined with a IoT system the wear sensor forms part of a complete wear monitoring solution, WearSense, which provides near real-time information through an online user interface. WearSense and other commercially available wear monitoring systems provide a foundation for the implementation of CBM for wear surfaces. However, the schedule-based maintenance strategies adopted by most companies to maximise supply chain availability do not always facilitate the implementation of CBM at an asset level. Notwithstanding, there are several ways in which wear monitoring systems can still be used to add value to the process of wear surface management:

- Reducing the scope of liner maintenance by assisting planners to select for replacement only those liners which will not survive until the following shut (imperfect maintenance).
- Providing guidance for the scheduling of maintenance for long life liners, or liners that are installed in new assets that do not have a wear history.
- Providing a better understanding of the wear profile so that the liner material, or thickness, can be chosen such that all the wear material is fully utilised across the asset.

- Objectively comparing the wear performance of different liner materials to enable, for example, the benefits of using a more expensive material to be weighed against the reduced maintenance costs.

To realise these benefits, data from the wear monitoring system needs to be presented in a way that is clearly actionable. The WearSense user interface provides multiple options for viewing information from the wear sensors. The current thickness at each of the sensor locations is displayed on a liner general arrangement drawing for the asset. If shut schedules are provides, the user interface will suggest which liners need to be changed in the following shut. Alternatively, it can predict an end of liner life, which can be used to set the maintenance time. Wear profiles from multiple liner installations can also be overlaid to compare the performance of different liner materials.

Data from the WearSense system can also be directly integrated into other software platforms such as PI or SAP through an API. The ability to combine CM data with other operational data and use this information to drive supply chain simulation models could potentially lead to the creation of CBM strategies that optimises overall plant availability while at the same time attempting to optimise the maintenance of individual assets within the supply chain.

Results from several WearSense installations have highlighted some of the benefits that can be achieved through the use of a wear monitoring system, which include: 1) forewarning that wear has increased, 2) identifying non-linear wear rates, 3) potential for cost reduction through different material choice.

REFERENCES

Davies, B, 2010. Wear Sensor. International (PCT) Patent, Patent No. WO 2010/096873 A1.

Smith, K, 2021. TOKN Sense: IoT and Preventative Maintenance. [Online] Available at: https://www.tokntechnology.com/tokn-sense-iot-and-preventive-maintenance/ [Accessed: 15 May 2021].

Uddin, G and Robillard, M, 2015. How API Documentation Fails, *IEEE Software*, July/August.

Application of a reinforcement learning AI solution for optimisation of screening shuttles control

B Versiani[1], A Gooch[2], A Höreth[3] and E Duggan[4]

1. Principal Control Systems Engineer, BHP, Perth WA 6000. Email: bruno.versiani@bhp.com
2. Director of Innovation, Andritz Automation Ltd, Richmond BC V6V 2X8, Canada. Email: arthur.gooch@andritz.com
3. Senior Data Scientist, Psiori, Hamburg 20359, Germany. Email: alexander@psiori.com
4. Senior Control Systems Engineer, Andritz Automation Ltd, Richmond BC V6V 2X8 Canada. Email: elise.duggan@andritz.com

ABSTRACT

Iron ore screening plant productivity is strongly affected by the performance of the shuttle operation, with the control system robustness and associated strategies having a direct impact on utilisation and throughput rates. A number of aspects intrinsic to the methods and technologies traditionally applied on the motion control of shuttles are often observed to decrease the efficiency of the ore distribution process across multiple screening modules, which ultimately impacts the plant's production. Those include the number of operational scenarios that are unmanaged by conventional discrete control logics which may intermittently lead to undesired events, such as 'high level alarms' and 'low level interlocks' in the screening bins. This outcome usually demands excessive manual intervention by Control Room Operators.

A Reinforcement Learning (RL) Artificial Intelligence (AI) solution was deployed to control the motion operation of the scalping and products screening shuttles in an iron ore handling plant. The RL algorithm was trained in advance to handle multiple operational scenarios and generate optimised outputs. In nominal operation, the shuttles are moved in a modulating and highly predictive fashion over the whole range of safely reachable bins. When the need occurs, the AI control agent deviates from that modulation behaviour, limiting its travel range or moving to other groups or clusters of available bins by employing 'bin jumping' or 'ore break' strategies. The RL platform capabilities include the ability to learn in real time to account for and auto-adapt to new operational patterns and process changes whilst applying improved strategies for shuttle dwelling times, target setting and speed control.

The deployed Reinforcement Learning AI solution has better managed the existing challenges associated with the shuttle operation and control, and resulted in a more efficient ore delivery process, superior operations stability and increased production rates.

INTRODUCTION

Real time control of process equipment using reinforcement learning artificial intelligence techniques was implemented at BHP's Mount Whaleback Ore Handling Plant 4 (OHP4). The site is in the Pilbara region of Western Australia, roughly six km west of Newman. The scope of the implementation was motion control of two shuttle conveyors, each of which supplies ore to a set of screening modules.

Previous optimisation projects in this process area had successfully applied advanced process control techniques to improve the throughput via better control of upstream reclaim feeders and downstream vibrating feeders. However, the shuttle control presented a set of challenges that could not be addressed using conventional techniques. Multiple areas of improvement were desired, including:

- Improved bin level control performance during normal operations in order to:
    - Avoid starving screens by under-filling bins.
    - Reduce bin 'high high' level events that fault upstream process equipment.
- Implementation of an 'ore break' and 'bin jumping' functionalities to allow the shuttle to traverse out of service bins, keeping more bins operational.
- Decreased number of operators interventions.

A controller based on neural networks was developed off-line and trained using simulated data. Acceptance testing was performed in simulation and the pre-trained controller was transferred to the live plant, where it was commissioned using normal controls acceptance practices. The existing and new control methods are described, including the novel development methods that enabled the successful deployment of this application.

PROCESS AND EXISTING CONTROLS

The scalping and products screening separate coarse ore into oversize for re-crushing and lumps and fines for the outflow operations. As shown in Figure 1, scalping screening receives ore from a Coarse Ore Stockpile (COS), while products screening is downstream of scalping, receiving both scalping discharge and ore from the tertiary crushing circuit.

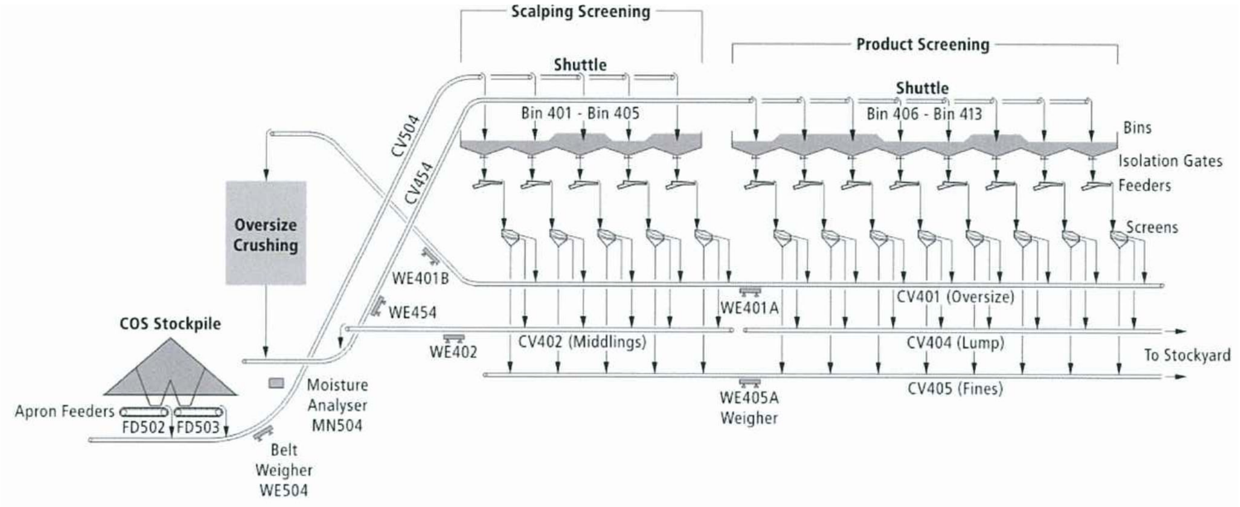

FIG 1 – Screening plant process summary.

The screening sections consist of five modules for scalping and eight modules for products, each oriented in a line with a shuttle conveyor that travels linearly across its row of bins, as shown in Figure 2. Each shuttle is operated by a variable speed drive. Shuttle direction and speed are adjusted to maintain all bin levels within acceptable values.

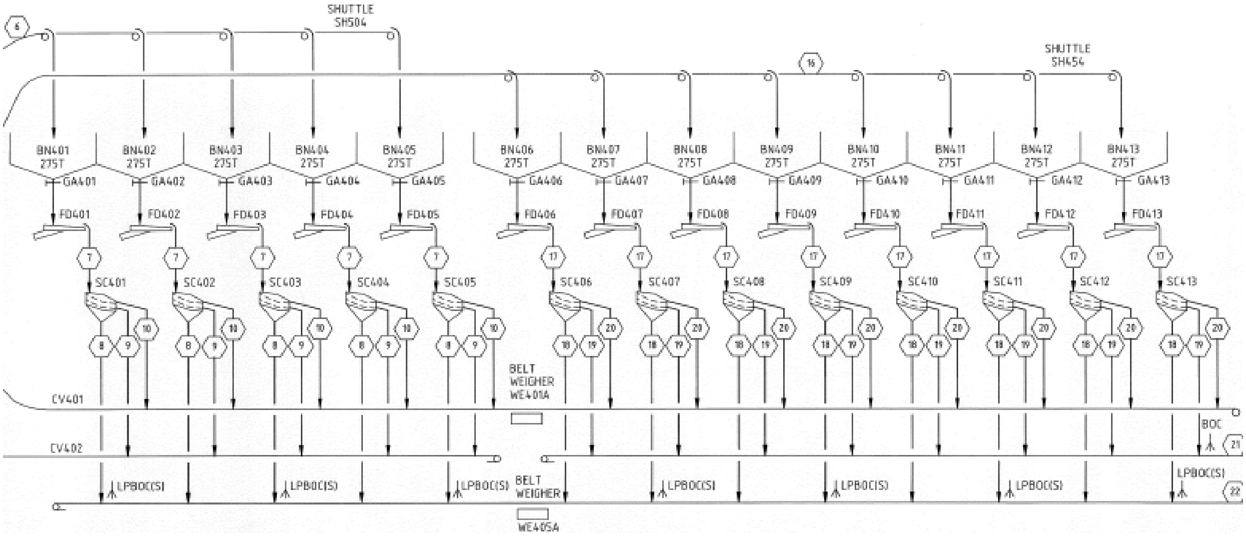

FIG 2 – Scalping and product screening detail.

The existing automatic shuttle controls consist of two basic parts: position target selection and speed control.

Position target selection

Position targets are chosen to create a continuous sweep across all safely reachable bins. Every time the shuttle reaches its destination, the position target is updated to be the bin at the other end from the shuttle's current position. The operator has the ability to intervene by deselecting bins, shortening the extent of travel.

Under normal circumstances, the continuous sweep works well. However, in upset scenarios, operator intervention is required. A plugged chute on a middle screen will stop by interlocking that bin's discharge feeder. As no ore is discharged from a stopped module, the shuttle cannot continue to traverse across all bins without eventually faulting the out-of-service bin on 'high high' level. Frequently operators prevent this outcome by disabling the out-of-service module and any modules beyond it to restrict shuttle travel. For example, stoppage of FD402 would be managed by disabling BN402 and also BN401. The shuttle would then service BN403, BN404, and BN405.

Shutdown of BN403 restricts operation to just two modules, a reduction of 60 per cent throughput. Shutdown of either BN402 or BN404 restricts throughput by 40 per cent, as three bins can continue to operate.

Speed target selection

The speed target of the shuttle is set by considering only the level of the bin that the shuttle is currently feeding. An equation calculates shuttle target speed with the general aim of moving slower when the bin level is low to allow more filling time. While there is no holistic consideration of all bin levels, there are several exceptions that override the calculated speed if end bins have a low level. In that case, the shuttle rushes at maximum speed to the end bin.

While the existing speed control generally performs well during normal operation, the fact that the controller considers only the currently fed bin means that there is no mechanism to address imbalances between bins. For example, the shuttle will attempt to feed more or to a moderately low-level bin even if the adjacent bin is critically low. Without any action to equalise bin levels relative to one another, bin starvation events are common.

Dynamic response

Much of the challenge of dynamic level control arises from the relationship between ore feed rate, transport delay, and bin volume. For the scalping screens, there are roughly 90 seconds transport delay between ore reclaim and discharge into the bins, while filling a bin completely from empty takes only approximately 30 seconds. Feedback control of the level of a single bin using reclaim rate is, therefore, impractical.

The overall feed rate is adjusted to manage total available volume in the screening modules and the role of the shuttle motion controller must be to allocate available feed to appropriate locations.

Compared to scalping, products screening has a much longer retention time, rendering the level control problem much easier. The existing controls perform the level control function adequately under nominal conditions. However, the desire for automatic management of upsets was sufficient to include products screening in the AI control implementation.

AI CONTROL STRATEGY

The Bin Filling AI has two significant components: a cognitive architecture that manages various modular behaviours and the neural network speed controller that manages speed control. This structure mixes both symbolling and machine learning AI techniques to achieve the control objective. By subdividing the overall control task into specific functions with the cognitive architecture, individual behaviours can be modified without impacting or retesting the overall function.

Cognitive architecture

For decision-making, the Cognitive Architecture provides a high-level behaviour arbitration interface. Within this interface, behaviours, as the central abstraction, are defined as self-contained modules, providing checks for whether it can take and retain control given the current state of the plant. Behaviours also contain functionality for generating a new command given the system's state when it is currently in control. By these means, each behaviour can be specialised for specific operating ranges, resulting in an overall easily maintainable and scalable system. Additionally, this separation of behaviours contributes to make control actions more explainable for observers.

Behaviours operate within an overall Belief, Desire, Intention (BDI) architecture, a cognitive concept for modelling intelligent systems (Lauer *et al*, 2010). In this context, the belief is the agent's internal model of the information perceived from the environment. Desires are the overall goals to be achieved by the agent's actions. Intentions are the immediate commands, produced by the currently active behaviour.

Behaviours are ordered in a directed acyclic graph as shown in Figure 3. The graph is constructed by priority. When selecting a behaviour, the graph is traversed from root to leaf to find the behaviour with highest priority willing to commit. Each behaviour in itself can consist of further individual behaviours, resulting in nested structures in the behaviour graph.

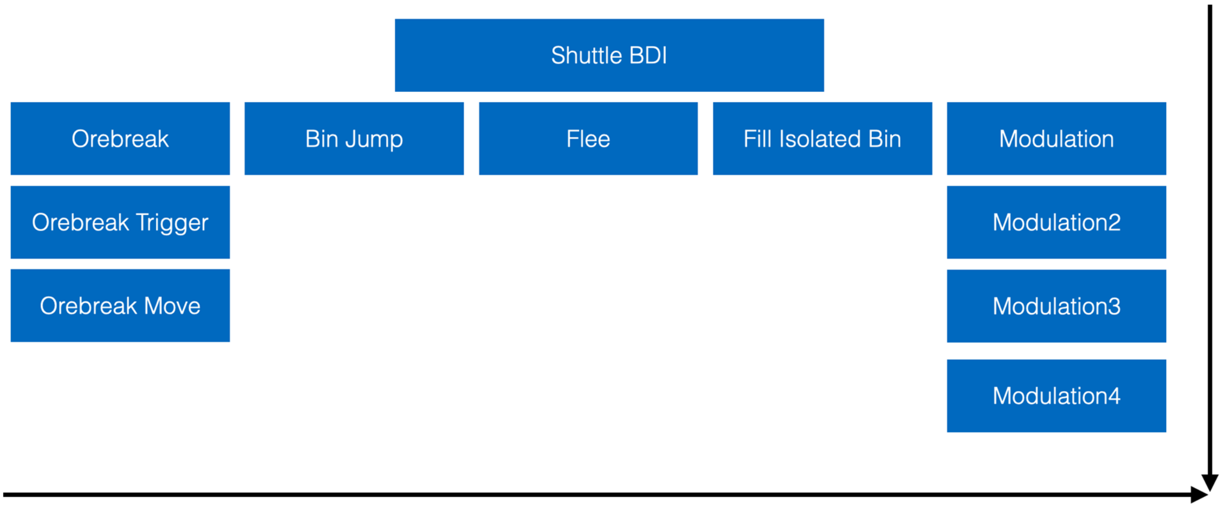

FIG 3 – Shuttle belief-desire-intent hierarchy.

This framework allows for a simple integration of multiple abstractions ranging from hardcoded rules (eg for safety purposes) to statistics based heuristics to machine learning algorithms.

The cognitive architecture transfers the idea of closed-loop control to a variety of applications. By evaluating the graph every cycle and thereby always employing the highest priority behaviour for the current situation, commands are always produced based on the most recent information available. By internally enriching the information using predictions and heuristics or by basing the decision-making itself on data driven algorithms, the overall system is able to produce highly complex behaviour, while still fulfilling the paradigm of closed-loop control. It is even possible to combine multiple agents into a system which either communicates explicitly or shares a single internal model of the world, producing cooperative agents.

Plant representation

The state of the plant is abstracted into clusters. Clusters are defined as continuous ranges of bins that fulfil some condition. A simple example of such a condition would be the 'available' status.

Generally, the agent tries to have the shuttle be located within the most desirable cluster and fill the bins within that cluster evenly. Depending on the system's state, that most desirable cluster might not span all bins, but instead only be the adjacent available bins or, if all bins in the cluster are available but very empty, a subset of those adjacent available bins.

The clusters are adjusted by their available, unavailable and inhibited status as well as by their fill level, both overfull and too low. Using the Behaviour Hierarchy, the agent can move the shuttle to other clusters if those become more desirable.

Behaviour hierarchy

The behaviour hierarchy shown in Figure 3 is defined in terms of priority, where the first behaviour has highest priority and the last, lowest priority. Some behaviours like 'Modulation' or 'Orebreak' are split into multiple sub behaviours, constructing a tree.

The bottom behaviour is 'Noop' (No Operation), which is always true when no other behaviour can commit in the given state. Commitment of this behaviour only ever happens if no bins are available, or the shuttle is stuck. 'Modulation' is a hierarchy of behaviours altering speed and target bin position in order to move the shuttle efficiently within a cluster. 'Fill Isolated Bin' deals with the situation where just a single bin is currently reachable by the shuttle, noting however that this behaviour is different from 'Noop'. In nominal conditions, isolated filling and modulation behaviours are the standard modes of operation. 'Flee', 'Bin Jump', and 'Orebreak', on the other hand, have very specific conditions for triggering commitment based on the current cluster size and fill levels. They have higher priorities since activation deals with infrequently occurring situations where the standard mode of operation is insufficient to maintain efficient plant operation. This hierarchy has the added benefit that it nicely separates the actual goal to distribute ore in a stable manner from edge cases that should occur infrequently.

Ore break

The Ore Break function allows the shuttle to cross an out of service bin by requesting that upstream equipment halt briefly, creating a gap of ore on the belt that the shuttle motion controller can use to cross the out of service bin without depositing any ore into it. This function is only available for the Scalping Shuttle. The Ore Break Function consists of three major components: the ore break trigger that creates gaps, the motion control that moves the shuttle, and the reclaim rate controller that sets the rate of ore on the belt when feeders are on.

The ore break trigger is configured in the PLC and triggers ore breaks whenever there are multiple clusters separated by an inhibited bin. The trigger function is deliberately simplistic: it consists of timers that set a duty cycle for the reclaim feeders. The on and off times of the duty cycle vary according to the cluster sizes Filling time is based on the time to fill the destination cluster at maximum feed rate and the stopped time is based on the maximal time it would take to move the shuttle between clusters.

The ore break move is a straightforward motion control function that detects when there is a sufficiently large gap on the belt with no ore and then moves the shuttle to the cluster with the most available volume.

A reclaim rate controller overrides the normal Model Predictive Control, as the ore breaks happen too fast for feedback control to be possible. The reclaim rate is calculated based on the available volume and calculated ore density. Under most circumstances, the reclaim rate is at or near the maximum tonnage of the upstream process, in order to account for the time spent with no ore on the belt while the shuttle is moving.

Bin jump

Bin jumping is the act of crossing a bin (or multiple bins) that are unavailable, so that the shuttle can fill the bins on the other side of the unavailable bins. The key difference between a Bin Jump and an Ore break is that, for a Bin Jump, the crossing is conducted without a gap of ore on the belt that stops feed. This procedure is risky, as unavailable bins are not expected to be emptied once filled. Therefore, stringent criteria must be met before jumping to validate that the source and destination clusters are valid, there are no high-level bins in the way, and that the shuttle is departing from the shortest logical point with sufficient speed to minimise discharge into any unavailable bins being crossed.

Flee

Fleeing occurs when the agent finds the shuttle over a bin that should not be filled, either currently or in the imminent future. The shuttle immediately proceeds to an available cluster at highest possible speed.

When fleeing, the agent will prefer its current direction of movement (as turn arounds are slow), while also trying to avoid getting stranded in single bins. Therefore, fleeing to a cluster of three bins is greatly preferable to fleeing into a single isolated bin.

Fill isolated bin

Some situations require not leaving the current bin. If the surrounding bins are not available, staying on the current bin is the best option. When FillIsolatedBin is active, the shuttle will attempt to centre itself on the bin at creep speed, and once this position is attained, it will remain stopped. Once a neighbouring bin becomes available, a modulation behaviour will again take over.

Modulation

Modulation is the standard mode of operation, moving the shuttle back and forth over the whole range of a cluster of bins. It is active if the shuttle is in a cluster of at least two bins. As for small clusters the required movement dynamics are very different to moving back and forth over a larger group of bins, there are specialised sub-options for such smaller clusters.

By moving faster in the middle than on the sides, more ore gets distributed to outer than to inner bins. Through filling outer bins to higher levels first, the dangers of overfilling a bin are minimised because an outer bin inhibition is more preferable than an interior bin inhibition. Slowing down before entering starving and speeding up before entering overfull bins will over time make the fill level distribution represent the same shape as the shuttle movement speed's function.

As Modulation2 does not have any centre bins it represents a special case. Handling clusters of two bins, the shuttle moves in a small range around the connecting edge of the two bins very slowly, creeping back and forth, ensuring as equal a fill level as possible.

REINFORCEMENT LEARNING

For the challenging modulation settings of three or more bins, a learned motion control is used. Unlike conventional control methods, the behaviour of a reinforcement learning agent is not explicitly programmed in advance; the agent learns a control policy by evaluating the results of control actions against process response and incrementally improving its own behaviour (Sutton and Barto, 1998). The shuttle speed controllers are optimised to minimise the individual fill levels' deviation from the average fill level of the current cluster. By minimising this deviation, the controllers learn to retain pendulum motion shaped fills and prevent inhibition events of individual bins, as those would be triggered by having outliers from the mean fill level.

Machine learning techniques

The speed modulation controllers are optimised using value-based Reinforcement Learning to train a neural network that executes the policy in the run-time environment. Given a cost function (herein the sum of deviations for a desired targeted level), the algorithm optimises the sum of costs into the future, the so-called expected cost. During training the agent interacts with the environment and by choosing different actions the algorithm learns to minimise those costs and thereby learns to minimise the overall costs experienced during application.

A broad range of Reinforcement Learning approaches and algorithms exist, much as there many algorithms used in Model Predictive Control. Reinforcement Learning agents may learn in a purely online mode (eg Q-learning) or batch learning methods that sample historical data (eg Fitted Q Iteration or Least Squares Policy Iteration). The shuttle agent uses a hybrid approach called Neural Fitted Q-Iteration with Continuous Actions (NFQCA). This algorithm is a form of growing batch learning that mixes aspects of both online and batch learning methods (Riedmiller *et al*, 2009).

Growing batch learning alternates between online exploration and batch learning phases. In the online phase, the agent interacts with the process according to its stored policy. After some number of iterations, a batch learning step updates the policy by sampling the saved set of state transitions. The agent then returns to the exploration phase of online interaction, which adds to the set of available training examples. By cycling between exploration and learning, the set of saved transitions grows, giving rise to the 'growing batch' name. Once subsequent iterations do not produce an appreciable change to the learned policy, the policy has converged and can be deployed to the live application. A diagram of this process is shown in Figure 4 (Hafner and Riedmiller, 2011).

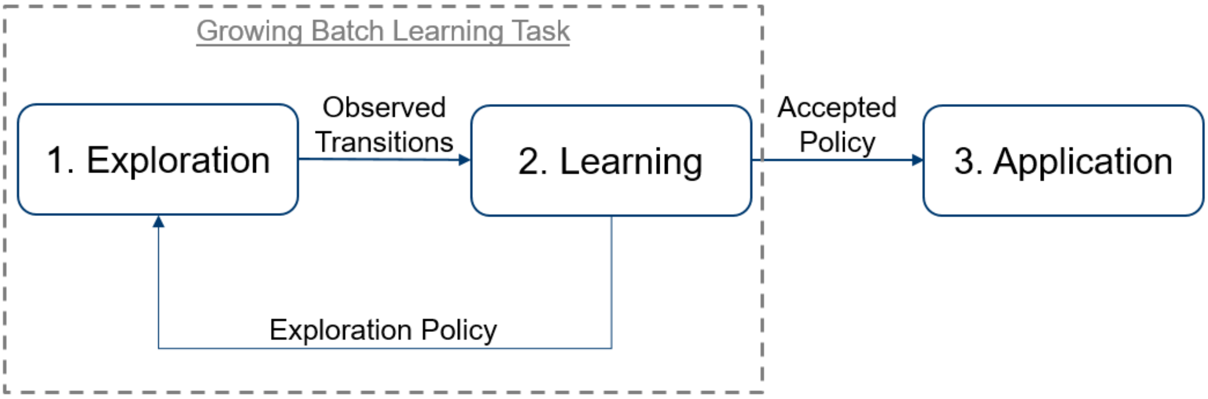

FIG 4 – Growing batch reinforcement learning process.

The goal of the NFQCA algorithm is to find a policy that minimises the expected cost from the current time until an infinite horizon (Hafner and Riedmiller, 2011). There is no terminal goal state, so the agent must maintain the system inside the goals. The cost for being within target bounds is therefore zero, with gradually increasing costs corresponding to increasing error. Because an infinite horizon is considered, proprietary methods are used to enforce stability and bound expected cost to finite values.

NFQCA is a form of model-free reinforcement learning, which aims to learn the value of any possible action in a particular process state. This value is known as the Q-value. The action with the best Q-value in a particular state would be the action with the lowest expected cost. The NFQCA algorithm represents the Q-function as a neural network. Each observed state is stored as a triple with members (state, action, successor state). An iterative function updates the weights of the neural network for all observed states. This loop repeats until a satisfactory policy has been learned (Hafner and Riedmiller, 2011).

Reinforcement learning controller design and development

Designing and developing a reinforcement learning controller required a variety of innovative controls engineering practices, independent of the technology of the AI controller itself. A cluster of process simulations provided synthetic data for machine learning model training, while customised automated test scripts evaluated controller performance over expected test scenarios.

Simulation

Central to the AI development is a dynamic process simulation, modelled using the IDEAS® software platform (Gooch, 2020). The model provides an accurate real time facsimile of the live process that allowed off-line testing and design iteration of the AI to minimise impact to the running process. The model of the scalping screening process is shown in Figure 5.

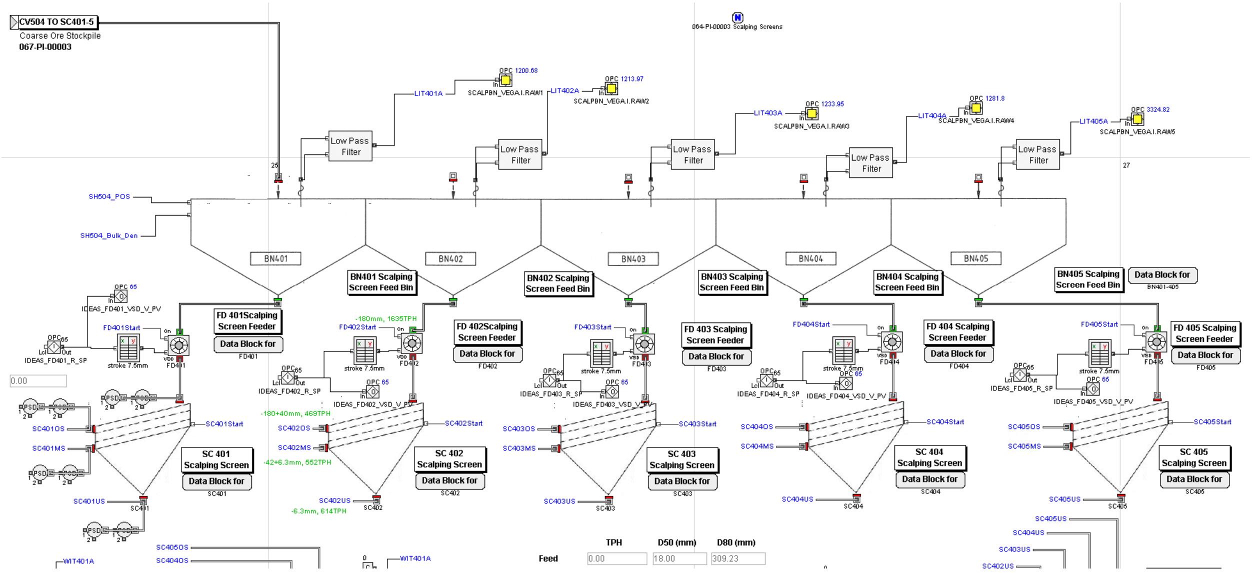

FIG 5 – IDEAS model of scalping screening.

The major challenge in simulating the screening process is accurate representation of the ore volume inside the bins. The shape of the ore is extremely relevant to the control problem as the shuttle discharge is offset from bin midline and bins are not separated from each other so ore can flow from one bin to another. The actual working volume of the bins is significantly less than the measured internal volume and the level measurement point is not aimed at the peak of the ore in any bin.

In order to balance model performance and accuracy, each bin is discretised into 25 sections in the horizontal plane. Scalping having five bins is, therefore, modelled by 125 sections. Each column of ore is able to flow to its immediate neighbours to create an appropriate angle of repose for the ore. Figure 6 shows a graphical representation of the discretised bin ore volumes modelled.

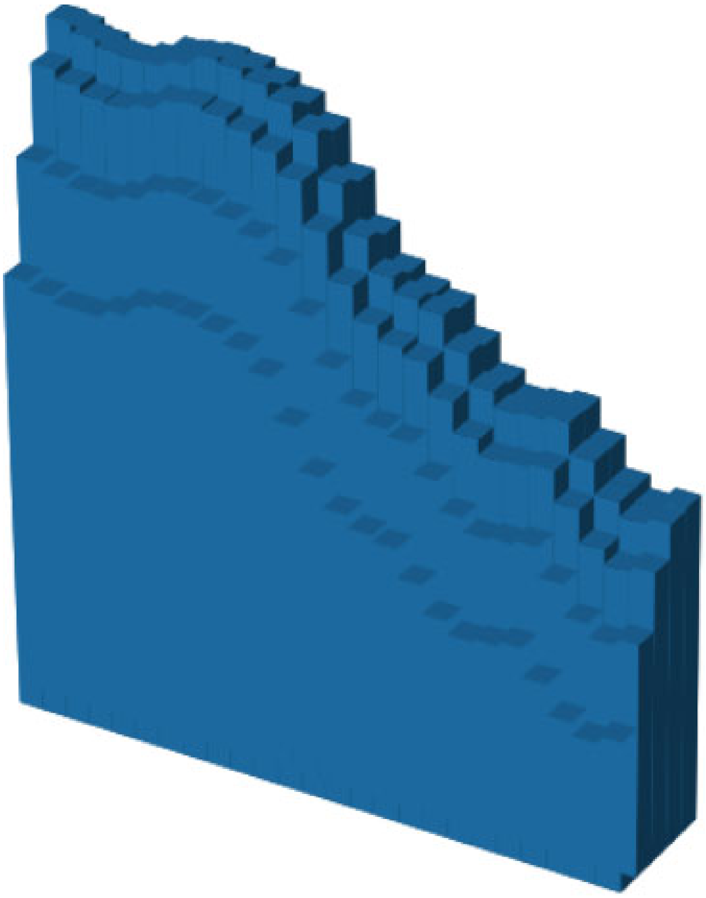

FIG 6 – Representation of discretised bin ore volumes.

AI training

The reinforcement learning algorithm was trained on a cluster of simulations running in parallel in a Microsoft Azure cloud environment. Multiple simulations were used to generate sufficient training data and to evaluate different machine learning models within the implementation's timeline constraints. The development architecture is shown in Figure 7.

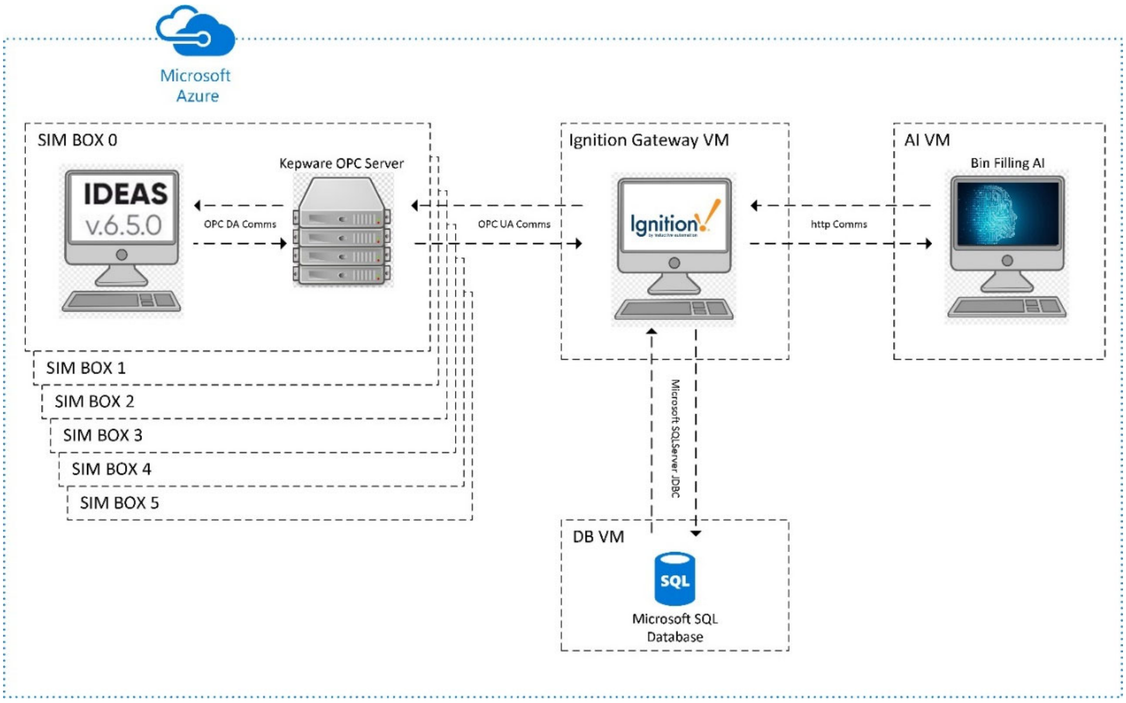

FIG 7 – Cloud development architecture.

In the six months of detail engineering associated with this implementation (January to May 2020), approximately 38 months' worth of simulated time was logged on the development system. Of this time, the Scalping Shuttle had approximately 35 months and Product Shuttle had three months of training time.

Prior to commissioning, the AI was tested exhaustively over various permutations of plant throughputs, ore types, and equipment upsets. In total, the Scalping Shuttle has 440 scenarios, and the Product Shuttle has 500 scenarios. Individual scenarios range in length from ten minutes to one hour. To run all the Scalping Shuttle scenarios takes 78 hours and the Product Shuttle scenarios takes 88 hours.

To manually run each scenario would require excessive human supervision, so a 'Scenario Dispatch' tool was used to automatically execute all the scenarios in sequence. Figure 8 shows the 'Scenario Dispatch' interface utilised where users were able to start a dispatch and let it run continuously until all the scenarios had been executed.

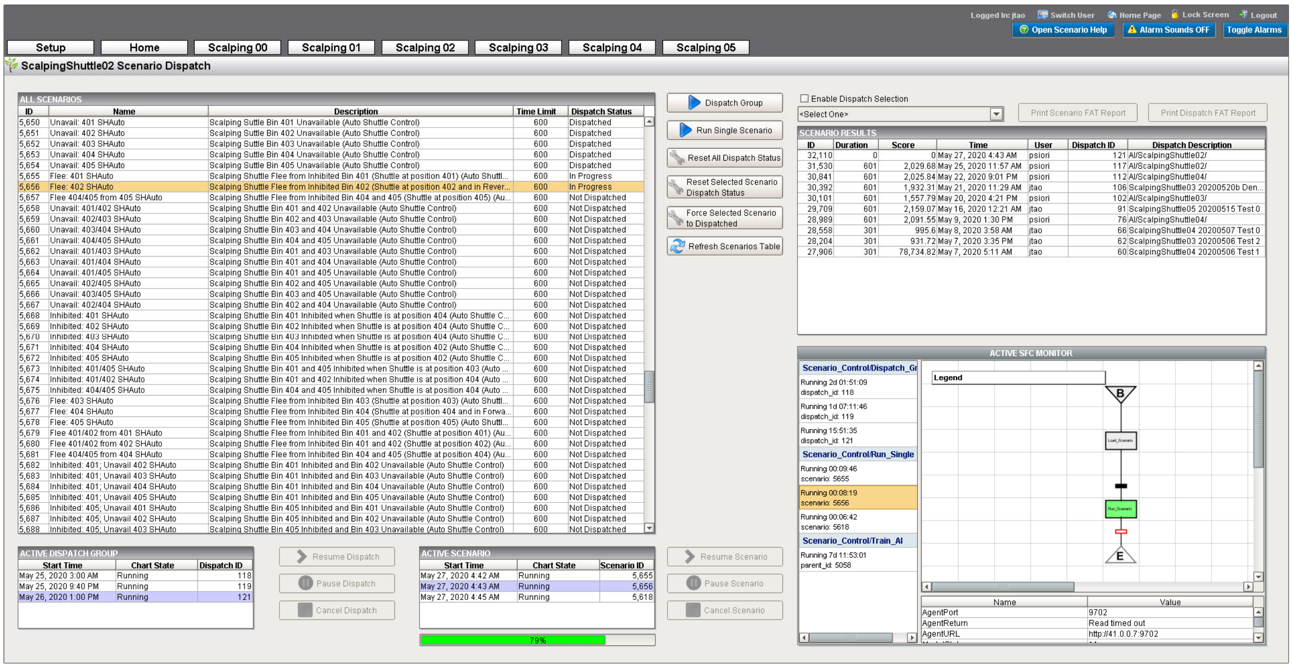

ScalpingShuttle02 Scenario Dispatch

ALL SCENARIOS

ID	Name	Description	Time Limit	Dispatch Status
5,650	Unavail: 401 SHAuto	Scalping Suttle Bin 401 Unavailable (Auto Shuttle Control)	600	Dispatched
5,651	Unavail: 402 SHAuto	Scalping Suttle Bin 402 Unavailable (Auto Shuttle Control)	600	Dispatched
5,652	Unavail: 403 SHAuto	Scalping Suttle Bin 403 Unavailable (Auto Shuttle Control)	600	Dispatched
5,653	Unavail: 404 SHAuto	Scalping Suttle Bin 404 Unavailable (Auto Shuttle Control)	600	Dispatched
5,654	Unavail: 405 SHAuto	Scalping Suttle Bin 405 Unavailable (Auto Shuttle Control)	600	Dispatched
5,655	Flee: 401 SHAuto	Scalping Shuttle Flee from Inhibited Bin 401 (Shuttle at position 401) (Auto Shuttl...	600	In Progress
5,656	Flee: 402 SHAuto	Scalping Shuttle Flee from Inhibited Bin 402 (Shuttle at position 402 and in Rever...	600	In Progress
5,657	Flee 404/405 from 405 SHAuto	Scalping Shuttle Flee from Inhibited Bin 404 and 405 (Shuttle at position 405) (Au...	600	Not Dispatched
5,658	Unavail: 401/402 SHAuto	Scalping Shuttle Bin 401 and 402 Unavailable (Auto Shuttle Control)	600	Not Dispatched
5,659	Unavail: 402/403 SHAuto	Scalping Shuttle Bin 402 and 403 Unavailable (Auto Shuttle Control)	600	Not Dispatched
5,660	Unavail: 403/404 SHAuto	Scalping Shuttle Bin 403 and 404 Unavailable (Auto Shuttle Control)	600	Not Dispatched
5,661	Unavail: 404/405 SHAuto	Scalping Shuttle Bin 404 and 405 Unavailable (Auto Shuttle Control)	600	Not Dispatched
5,662	Unavail: 401/403 SHAuto	Scalping Shuttle Bin 401 and 403 Unavailable (Auto Shuttle Control)	600	Not Dispatched
5,663	Unavail: 401/404 SHAuto	Scalping Shuttle Bin 401 and 404 Unavailable (Auto Shuttle Control)	600	Not Dispatched
5,664	Unavail: 401/405 SHAuto	Scalping Shuttle Bin 401 and 405 Unavailable (Auto Shuttle Control)	600	Not Dispatched
5,665	Unavail: 402/405 SHAuto	Scalping Shuttle Bin 402 and 405 Unavailable (Auto Shuttle Control)	600	Not Dispatched
5,666	Unavail: 403/405 SHAuto	Scalping Shuttle Bin 403 and 405 Unavailable (Auto Shuttle Control)	600	Not Dispatched
5,667	Unavail: 402/404 SHAuto	Scalping Shuttle Bin 402 and 404 Unavailable (Auto Shuttle Control)	600	Not Dispatched
5,668	Inhibited: 401 SHAuto	Scalping Shuttle Bin 401 Inhibited when Shuttle is at position 404 (Auto Shuttle C...	600	Not Dispatched
5,669	Inhibited: 402 SHAuto	Scalping Shuttle Bin 402 Inhibited when Shuttle is at position 404 (Auto Shuttle C...	600	Not Dispatched
5,670	Inhibited: 403 SHAuto	Scalping Shuttle Bin 403 Inhibited when Shuttle is at position 404 (Auto Shuttle C...	600	Not Dispatched
5,671	Inhibited: 404 SHAuto	Scalping Shuttle Bin 404 Inhibited when Shuttle is at position 402 (Auto Shuttle C...	600	Not Dispatched
5,672	Inhibited: 405 SHAuto	Scalping Shuttle Bin 405 Inhibited when Shuttle is at position 402 (Auto Shuttle C...	600	Not Dispatched
5,673	Inhibited: 401/405 SHAuto	Scalping Shuttle Bin 401 and 405 Inhibited when Shuttle is at position 403 (Auto ...	600	Not Dispatched
5,674	Inhibited: 401/402 SHAuto	Scalping Shuttle Bin 401 and 402 Inhibited when Shuttle is at position 404 (Auto ...	600	Not Dispatched
5,675	Inhibited: 404/405 SHAuto	Scalping Shuttle Bin 404 and 405 Inhibited when Shuttle is at position 404 (Auto ...	600	Not Dispatched
5,676	Flee: 403 SHAuto	Scalping Shuttle Flee from Inhibited Bin 403 (Shuttle at position 403) (Auto Shuttl...	600	Not Dispatched
5,677	Flee: 404 SHAuto	Scalping Shuttle Flee from Inhibited Bin 404 (Shuttle at position 404 and in Forwa...	600	Not Dispatched
5,678	Flee: 405 SHAuto	Scalping Shuttle Flee from Inhibited Bin 405 (Shuttle at position 405) (Auto Shuttl...	600	Not Dispatched
5,679	Flee 401/402 from 401 SHAuto	Scalping Shuttle Flee from Inhibited Bin 401 and 402 (Shuttle at position 401) (Au...	600	Not Dispatched
5,680	Flee 401/402 from 402 SHAuto	Scalping Shuttle Flee from Inhibited Bin 401 and 402 (Shuttle at position 402) (Au...	600	Not Dispatched
5,681	Flee 404/405 from 404 SHAuto	Scalping Shuttle Flee from Inhibited Bin 404 and 405 (Shuttle at position 404) (Au...	600	Not Dispatched
5,682	Inhibited: 401; Unavail 402 SHAuto	Scalping Shuttle Bin 401 Inhibited and Bin 402 Unavailable (Auto Shuttle Control)	600	Not Dispatched
5,683	Inhibited: 401; Unavail 403 SHAuto	Scalping Shuttle Bin 401 Inhibited and Bin 403 Unavailable (Auto Shuttle Control)	600	Not Dispatched
5,684	Inhibited: 401; Unavail 404 SHAuto	Scalping Shuttle Bin 401 Inhibited and Bin 404 Unavailable (Auto Shuttle Control)	600	Not Dispatched
5,685	Inhibited: 401; Unavail 405 SHAuto	Scalping Shuttle Bin 401 Inhibited and Bin 405 Unavailable (Auto Shuttle Control)	600	Not Dispatched
5,686	Inhibited: 405; Unavail 401 SHAuto	Scalping Shuttle Bin 405 Inhibited and Bin 401 Unavailable (Auto Shuttle Control)	600	Not Dispatched
5,687	Inhibited: 405; Unavail 402 SHAuto	Scalping Shuttle Bin 405 Inhibited and Bin 402 Unavailable (Auto Shuttle Control)	600	Not Dispatched
5,688	Inhibited: 405; Unavail 403 SHAuto	Scalping Shuttle Bin 405 Inhibited and Bin 403 Unavailable (Auto Shuttle Control)	600	Not Dispatched

SCENARIO RESULTS

ID	Duration	Score	Time	User	Dispatch ID	Dispatch Description
32,110	0	0	May 27, 2020 4:43 AM	psiori	121	AI/ScalpingShuttle02/
31,530	601	2,029.68	May 25, 2020 11:57 AM	psiori	117	AI/ScalpingShuttle02/
30,841	601	2,025.84	May 22, 2020 9:01 PM	psiori	112	AI/ScalpingShuttle04/
30,392	601	1,932.31	May 21, 2020 11:29 AM	jtao	106	ScalpingShuttle03 20200520b Den...
30,101	601	1,557.79	May 20, 2020 4:21 PM	psiori	102	AI/ScalpingShuttle03/
29,709	601	2,159.07	May 16, 2020 12:21 AM	jtao	91	ScalpingShuttle05 20200515 Test 0
28,989	601	2,091.55	May 9, 2020 1:30 PM	psiori	76	AI/ScalpingShuttle04/
28,558	301	995.6	May 8, 2020 3:58 AM	jtao	66	ScalpingShuttle04 20200507 Test 0
28,204	301	931.72	May 7, 2020 3:35 PM	jtao	62	ScalpingShuttle03 20200506 Test 2
27,906	301	78,734.82	May 7, 2020 5:11 AM	jtao	60	ScalpingShuttle04 20200506 Test 1

ACTIVE DISPATCH GROUP

Start Time	Chart State	Dispatch ID
May 25, 2020 3:00 AM	Running	118
May 25, 2020 9:40 PM	Running	119
May 26, 2020 1:00 PM	Running	121

ACTIVE SCENARIO

Start Time	Chart State	Scenario ID
May 27, 2020 4:42 AM	Running	5,655
May 27, 2020 4:43 AM	Running	5,656
May 27, 2020 4:45 AM	Running	5,618

ACTIVE SFC MONITOR

Scenario_Control/Dispatch_Gr
Running 2d 01:51:09
dispatch_id: 118
Running 1d 07:11:46
dispatch_id: 119
Running 15:51:35
dispatch_id: 121
Scenario_Control/Run_Single
Running 00:09:46
scenario: 5655
Running 00:08:19
scenario: 5656
Running 00:06:42
scenario: 5618
Scenario_Control/Train_AI
Running 7d 11:53:01
parent_id: 5058

Name	Value
AgentPort	9702
AgentReturn	Read timed out
AgentURL	http://41.0.0.7:9702

FIG 8 – Scenario dispatch dashboard.

AI PERFORMANCE RESULTS

Long-term operation encompassing a broad variety of ore types is necessary to confirm that the AI application delivers robust performance that exceeds the existing automation. Regardless, preliminary results indicate improved production during normal operations and the availability of the ore break allows a dramatic production improvement when a bin is out of service.

Nominal operations

The AI controller reduces the production losses associated with bin starvation events, in which a bin temporarily runs empty because of poor ore distribution choices by the shuttle. The quantity of starvation events in AI mode is reduced by 17 per cent, compared to control under the pre-existing PLC logic.

Bin level variability is used as a proxy for level control quality. Given that level oscillation is expected, standard deviation is compared between AUTO and AI modes to evaluate controller performance. The overall bin variability improves slightly (approximately 0.4 per cent) from 11.05 per cent in AUTO mode to 10.62 per cent in AI mode. The differences in bin level standard deviation between AUTO and AI modes are shown in Figure 9.

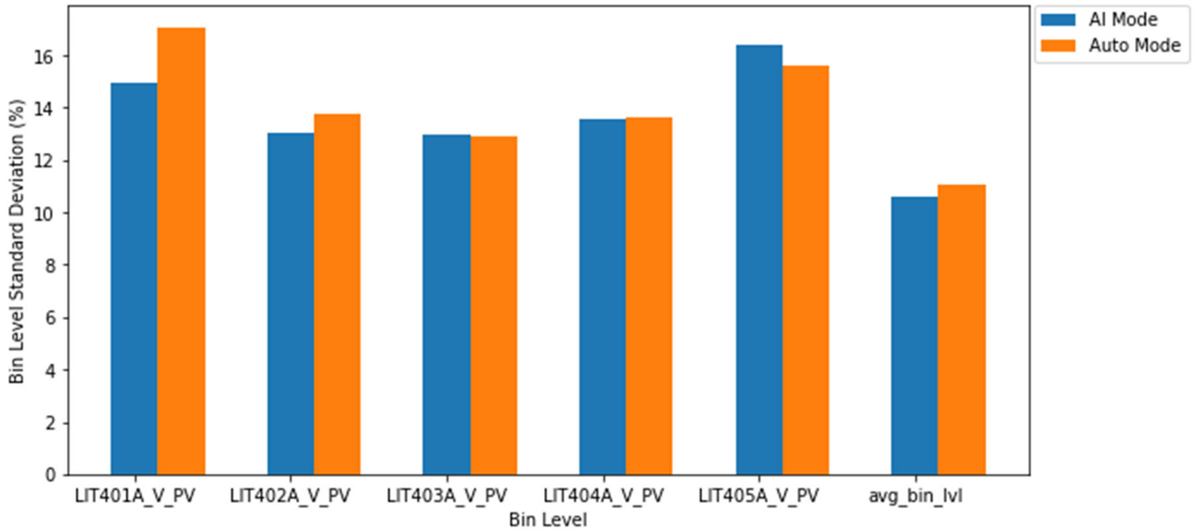

FIG 9 – Scalping bin variability results under AUTO and AI control.

The stability of the controller against overfilling a bin and tripping on high level is also important. The AI has poorer overall stability (0.16 trips per hour, as opposed to 0.12 for Auto). However, the average level of all bins when a trip does occur in AI mode is 95 per cent, compared to 85 per cent when a trip happens in AUTO mode. This statistic indicates that, when a trip happens in AUTO mode, there exists significantly more available volume in bins other than the one that tripped, meaning that the controller made worse choices and overfilled a small region of the bins prior to the trip occurring. However, if that is the case, one expects a lower rate of high-level trips. Further study is required to understand this phenomenon.

Average scalping start-up duration under AI mode (9.09 minutes) has decreased by almost 15 per cent compared to average start-up duration under Auto mode (10.72 minutes).

Ore break

The ore break function shows significantly improved performance in the case where the middle of the five scalping bins is out of service. By being able to cross the middle bin, four screening modules operate instead of two, raising the screening area throughput by 40 per cent for the duration of the module outage.

In the cases where bins 402 or 404 are out of service (creating a cluster of three and a single isolated module), the ore break function does not yet outperform the pre-existing automation. However, work is ongoing to reduce width of ore gaps on the belt and thereby increase overall tonnage.

CONCLUSIONS

This implementation demonstrated that reinforcement learning control can be applied to real time equipment control to improve control performance and enable functions that could not be achieved using conventional control approaches. The results indicate that increased production in nominal operation and in upset scenarios can be achieved by deploying machine learning at the regulatory control layer.

ACKNOWLEDGEMENTS

The authors are grateful to their extended teams for their persistence and ingenuity to execute and commission this technical solution under the additional working constraints imposed by COVID-19 precautions.

The authors wish to thank their respective employers for their support in the creation and publication of this work.

REFERENCES

Gooch, A, 2020. *Industrial Plant Controller* (US Patent No. 11,036,214), US Patent and Trademark Office. http://appft.uspto.gov/netacgi/nph-Parser?Sect1=PTO1&Sect2=HITOFF&d=PG01&p=1&u=%2Fnetahtml%2FPTO%2Fsrchnum.html&r=1&f=G&l=50&s1=%2220200192340%22.PGNR.&OS=DN/20200192340&RS=DN/20200192340

Hafner, R and Riedmiller, M, 2011. Reinforcement Learning In Feedback Control, *Machine Learning*, 84:137–169.

Lauer, M, Hafner, R, Lange, S and Riedmiller, M, 2010. Cognitive Concepts in Autonomous Soccer Playing Robots, *Cognitive System Research*, 11(3):287–309.

Riedmiller, M, Gabel, T, Hafner, R and Lange, S, 2009. Reinforcement Learning For Robot Soccer, *Autonomous Robotics*, 27:55–73.

Sutton, R S and Barto, A G, 1998. *Reinforcement Learning: An Introduction (adaptive computational and machine learning)* (MIT Press: Cambridge).

Mining

Fused sensors for slope deformation monitoring – considerations for iron ore mines

M Elmouttie[1] *and P Dean*[2]

1. Mining Geoscience Research Team Leader, CSIRO Minerals, Pullenvale Qld 4019.
   Email: marc.elmouttie@csiro.au
2. Senior Software Engineer, CSIRO Minerals, Pullenvale Qld 4019. Email: peter.dean@csiro.au

ABSTRACT

Radar monitors are now widely used in surface mining for monitoring slope deformations and predicting failure events. Their introduction has facilitated better management of risk associated with slope failure during mining and therefore protection of personnel and equipment. However, a well-recognised problem is that radar monitors only measure deformation directed towards the detector (line-of-sight bias). This bias can lead to misinterpretation of deformation size, rate and failure mechanism, and therefore miscalculation of failure volume, which can significantly impact safety and productivity.

This paper presents recently completed research and field trials into the feasibility of using low cost vision systems to mitigate this issue. It has been demonstrated that by integrating a computer vision system with an existing slope monitor, high precision tracking of features in the field of view can be performed. Combined with assumptions on the deformation characteristics, the true 3D deformation vector can be estimated. The applicability of using this technique for monitoring iron ore mine slopes is discussed.

INTRODUCTION

Iron ore mining in Australia now utilises state-of-the-art technologies for the monitoring, data assimilation and analysis of slopes (de Graaf and Wessels, 2013). Slope stability radar has had an impressive impact on operational as well as design considerations, particularly when risk-based design methods are used (Haile *et al*, 2020). For the case of typical iron ore mines in the Pilbara region, where quasi-linear walls with long strike lengths of a kilometre or more are possible and radar resources are limited, the scenario of using radars to scan quite oblique angles is a reality. Current methods to compensate for the line-of-sight bias affecting slope deformation monitors make potentially inaccurate assumptions about the failure mechanics and deformation vector relative to the wall/slope orientation. This can lead to significant misunderstanding of both the deformation magnitude as well as the failure mechanics responsible.

Alternatively, using multiple slope monitors to observe the same region can address this problem (Severin *et al*, 2014), but this is rarely done due to the expense associated with deploying multiple monitors for the one sector.

Previous research undertaken by the authors and largely funded by the Australian Coal Association Research Programme (ACARP) has focused on the development of computer vision algorithms for mine site characterisation. Applications have included geotechnical slope characterisation, stability analysis and drill and blast design in surface mining (Poropat and Mamic, 2004; Elmouttie, Poropat and Soole, 2012; Dean, 2015). As algorithm robustness has improved and computational resources become more readily available, the potential to apply computer vision for slope deformation monitoring has become a reality. The authors have therefore been developing fused-sensor approaches, integrating computer-vision with existing mine monitoring sensors such as radar. CSIRO has patented a technology for the integration of a vision-based system with a deformation monitor to allow estimation of the true deformation vector and ACARP has recently funded field trials (Elmouttie, Dean and Van de Werken, 2020; Elmouttie and Poropat, 2015).

The basic scenario is shown in Figure 1. A vision system is combined with a slope deformation radar to resolve the 3D components of the deformation. The vision system may comprise multiple units in an array, and due to their low unit cost, such a configuration would not be prohibitive. However, the field trials and simulations described in this paper assume a single vision sensor is available and co-located with the radar. This configuration is particularly attractive as most of the commercial radar providers already ship vision systems with their radars. Such a system should be capable of providing a more accurate estimation of deformation for slope failures occurring along steeply or obliquely dipping surfaces relative to the radar direction.

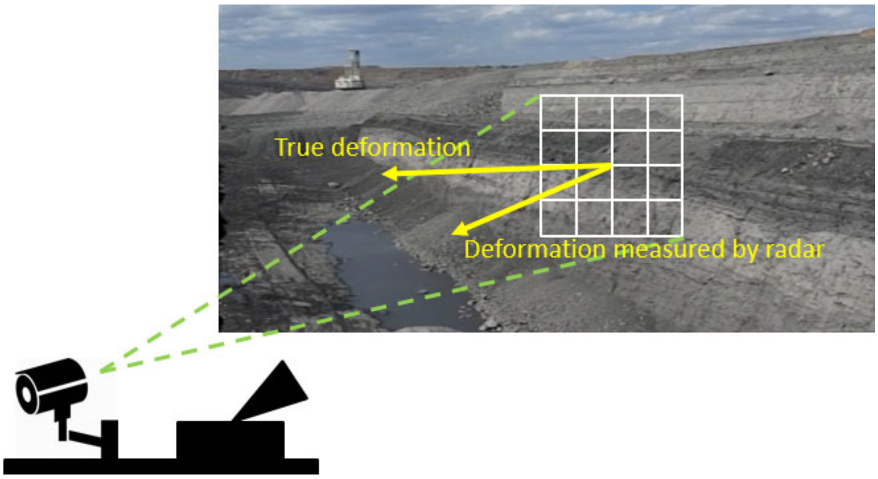

FIG 1 – The approach: computer vision system tracks deformation of the wall in the field of view and, combined with radar data, estimates the true deformation vector.

The following paper describes field trials undertaken to date at two mines and the observed efficacy of the proposed approach. Following this, a semi-synthetic analysis for an iron ore mine is described demonstrating both the potential value as well as special considerations for deployment in these settings.

FIELD TRIALS

This purpose of the field trials was to investigate the feasibility of using the existing, relatively low cost visions systems that are coupled with existing slope monitors, to support high precision tracking of features in the field of view in concert with the line-of-sight radar measurements being undertaken. Combined with assumptions on the deformation characteristics, namely that the surface expression of the deformation is representative of the failure mechanics, the true deformation vector was then to be estimated. Because the proposed system uses the existing radar measurements, a camera and software, the additional costs associated with supporting this sensing mode is expected to be extremely low when compared to the purchase or rental costs of the radar monitoring systems themselves.

Trials at two mines were conducted, labelled Sites A and B.

Site A

Site A is a coalmine located in Queensland, Australia. The wall monitored for this project was a low wall dump and Northern end wall during coal recovery. Similar to many iron ore mines, the wall geometry was quasi linear and a single radar was tasked with surveying deformations across the entire strike length as well an adjacent end-wall. The period of observation used in the project was 11th May 2018 to 5th June 2018.

A GroundProbe SSR-XT slope stability radar was used for this project. The slope monitoring radar comes equipped with a camera system capable of providing panoramic, mosaiced imagery of the entire survey area being monitored. The specifications for this monitor are shown in Table 1. Note that the images analysed in this experiment were not raw camera images but rather the post-processed and mosaiced images, hence a degraded pixel resolution is noted in the table.

TABLE 1

Radar/Vision parameters for Site A.

Parameter	Value
Sensor resolution	3 milli-radians*
Radar resolution	8.7 m @ 1 km or 8.7 milli-radians
Radar deformation sensitivity	Submillimetre

*Effective resolution after mosaic process.

Figure 2 shows one of the deformation events being monitored by the radar, this one being a particularly oblique angle event located approximately 400 m away and showing around 580 mm of (radar) deformation over the observation period. The red rectangle indicates the region of interest and the blue rectangle indicates the stable reference area. Note that similar to radar and other slope deformation monitoring techniques, identification of a stable reference is important for discriminating confounding deformations (such as sensor platform movement and atmospheric effects) from true slope deformation.

Figure 3 shows the results of combining the radar observations with the vision observations, through formal fusion of the data. The green dashed line indicates the line-of-sight deformation (essentially 1-dimensional) data detected by the radar for the region of interest (red rectangle in Figure 2). The blue dashed line indicates the essentially 2-dimensional movement measured by the vision system. Note the significance 'noise' associated with this measurement, partly due to the lower image pixel resolution available at this site, and also partly caused by the ravelling nature of the failure being observed. The solid red line indicates a naïve integration of these two measurements, also displaying significant noise. The solid black line (vectors) indicate the final solution of the fusion algorithm which also takes into account individual sensor noise.

Note that the 3-dimensional deformation deviates significantly from the line-of-sight to the radar. Reconciliation of this result with the local mine geometry and failure being observed shows consistency, indicating the technique has been successful.

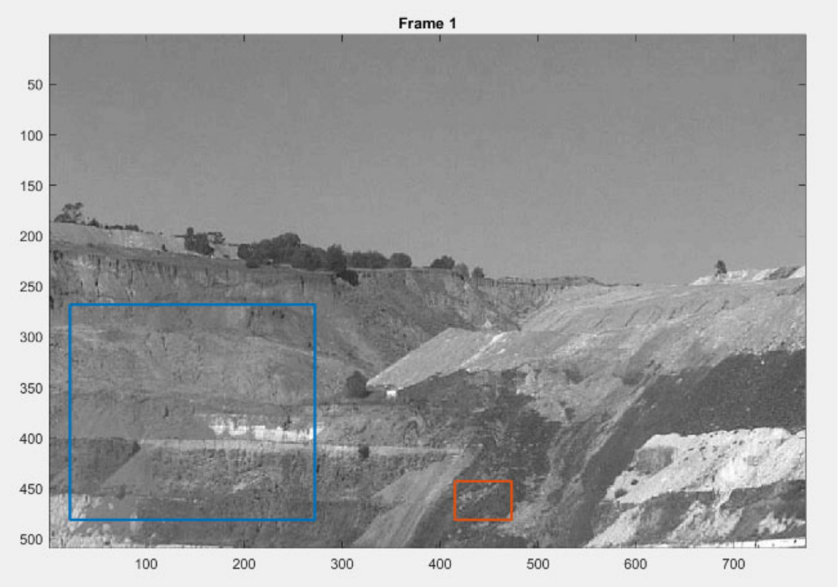

FIG 2 – Region B stable reference area (blue) and region of interest (red).

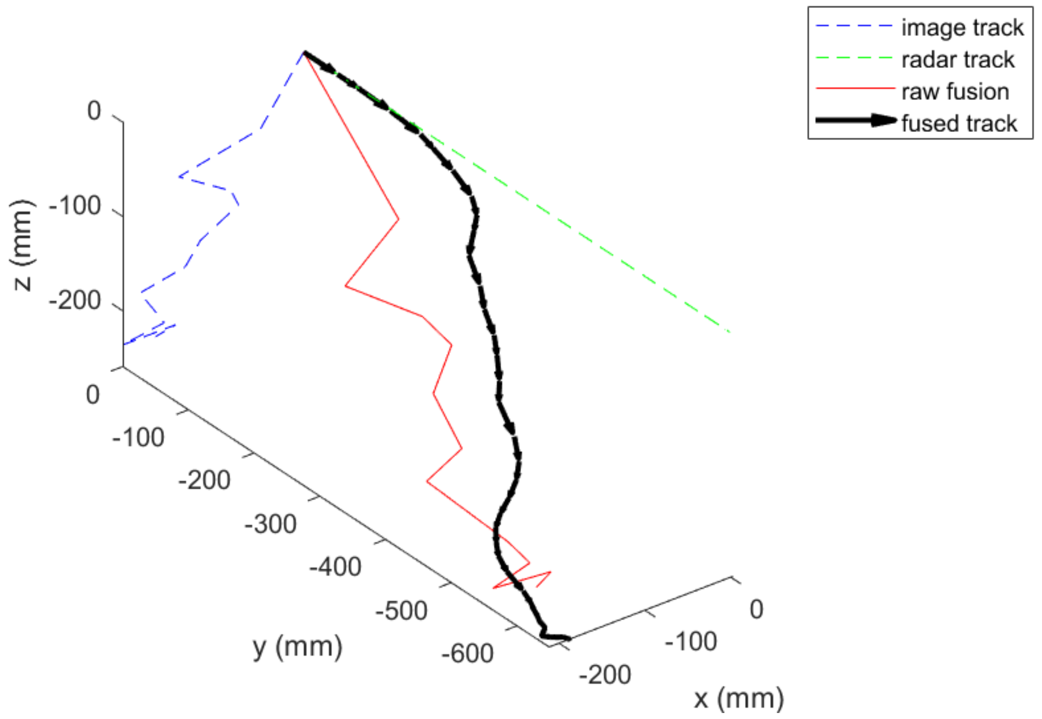

FIG 3 – 3D deformations based on Fusion of image and radar data for deformation vectors for Region B.

Site B

Site B is a gold mine located in New Zealand. The gold deposits are located within a low-angle shear zone. The mine is developed within this regionally continuous shallowly east dipping structure. The zone consists of variably altered, deformed, and mineralised schist. The wall being monitored is the north-east slope of the main pit.

An IDS IBIS-FM radar is the primary monitoring system for this slope and, to support this research, IDS and the mine site kindly set-up an IDS Georadar Eagle Vision camera system. The camera was mounted on the door of the shipping container housing the IBIS-FM. This door was anchored during the image acquisition program. The radar and camera parameters are listed in Table 2.

As for Site A, Site B analysis involved simultaneous monitoring of the failure zone with both vision and radar systems. The deforming slope consisted of a bull-nose located approximately 500 m away from the monitor and obliquely positioned relative to the radar. Around 20 mm of deformation was measured by the radar during the 28-day observation period. Figure 4 shows this zone and the red rectangle indicates the region of interest and the blue rectangle indicates the stable reference area.

Figure 5 shows the results of combining the radar observations with the vision observations, through formal fusion of the data. The solid black line (vectors) indicates the final solution of the fusion algorithm. In this case, one can clearly see that the observed deformation is dominated by that observed by the vision system.

TABLE 2

Radar/Vision parameters.

Parameter	Value
Sensor resolution	36 mm @ 1 km or 0.037 milli-radians*
Radar resolution	<4 m @ 1 km or 4 milli-radians
Radar deformation sensitivity	Submillimetre

FIG 4 – Stable reference area (blue) and region of interest (red).

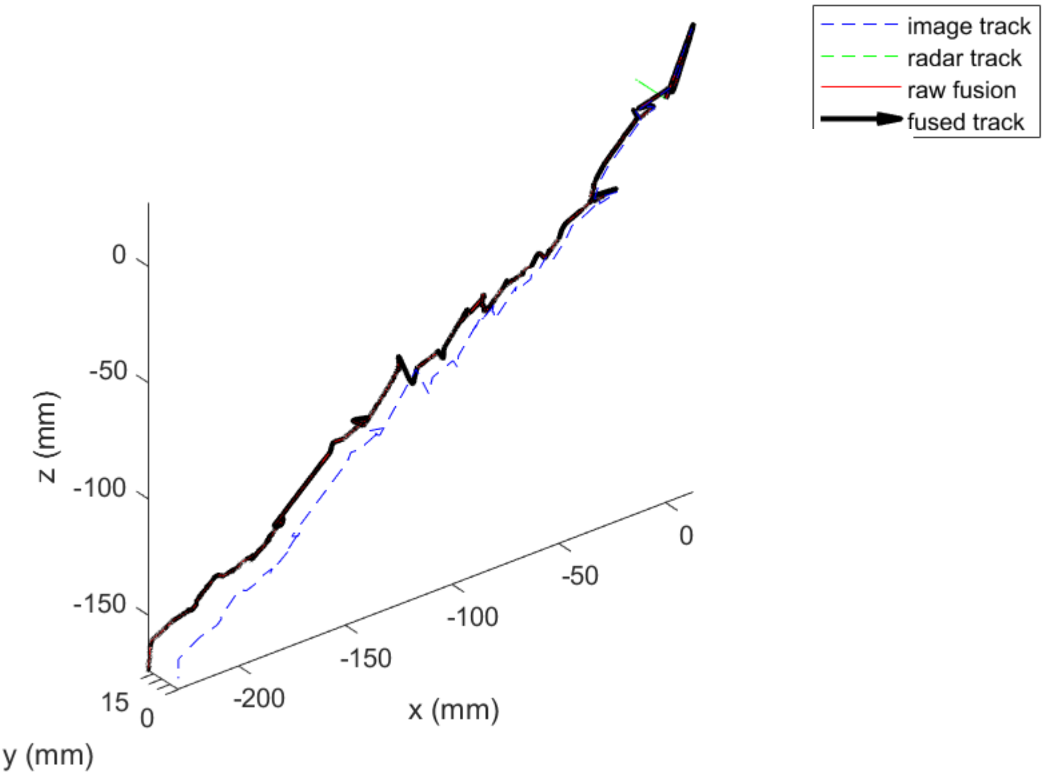

FIG 5 – 3D deformations based on Fusion of image and radar data for deformation vectors.

Figure 6 more clearly shows this effect in plan view. The green line, indicating the radar line-of-sight measurement, is also shown. This result has been validated with the mine staff and, to a certain extent, was expected given the location of the radar and the oblique angle to the deforming bull-nose being monitored.

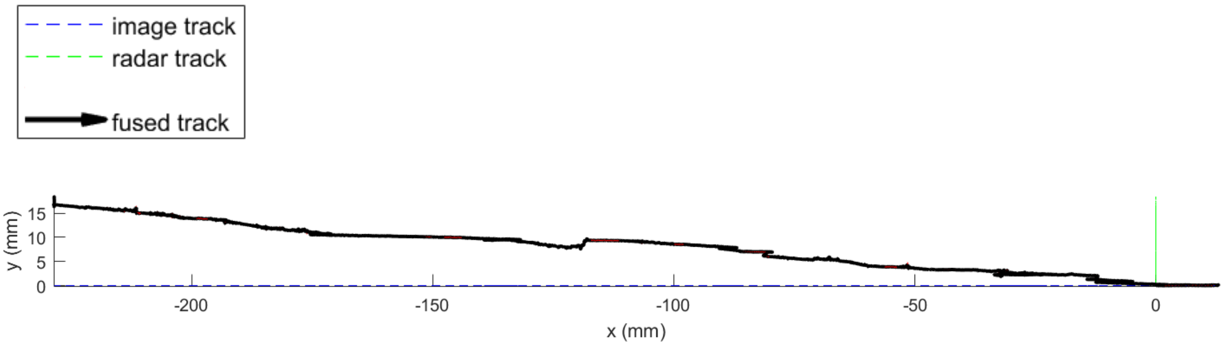

FIG 6 – Plan view of 3D deformation vectors.

APPLICATION TO IRON ORE MINES

As shown in the previous section, field trials and subsequent analysis have demonstrated the potential of the fused sensor system for slope deformation monitoring of surface mines, but notwithstanding the geometrical similarities of the Site A trials to a Pilbara mine, it has yet to be trialled in an iron ore mine. The following section therefore presents a semi-synthetic analysis. Although the analysis is fictional, it is closely based on previously studied Pilbara iron ore pits and uses actual imagery acquired at one such pit. Consider a pit sector undergoing deformation. The instability is structurally controlled and has been caused through a combination of uncertainties in the structural model, including bedding strength estimates, as well as unforeseen structural complexity leading to daylighting structures. The scenario is depicted in Figure 7. The radar/vision monitor system is located on the crest of the opposite wall, approximately 500 m away from the unstable zone. The radar has been tasked with monitoring several other deformation zones, and therefore only an oblique look-angle to our region of interest is available.

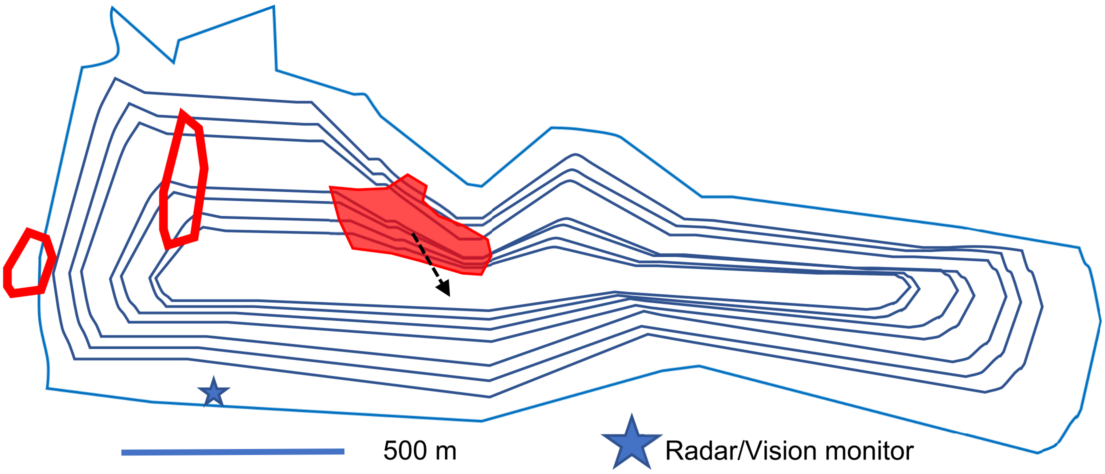

FIG 7 – Plan view of iron ore pit geometry, unstable region of interest for this analysis (red polygon, with dashed arrow showing deformation direction), and radar/vision monitor location. Other deforming zones being monitored by the radar are shown as unfilled polygons.

Figure 8 shows the actual imagery acquired at an iron ore mine at a range of approximately 500 m. The 35 mm lens used provided a wide field of view, dramatically reducing the amount of imagery needing to be acquired to cover the full pit, at the expense of pixel resolution. The radar parameters of the monitoring system are assumed to be identical to those used for the Site B trials and shown in Table 2, with camera details also shown in Table 3. Although the analysis was performed for the 35 mm lens option, details for a 100 mm lens option are also shown as this would also be a practical focal length to use without compromising the field of view too dramatically.

TABLE 3

Radar/Vision parameters.

Parameter	Value
Camera sensor	3872 × 2592 pixels 23.6 × 15.8 mm CCD (DX format)
Sensor resolution	87 mm @ 500 m (35 mm lens) 31 mm @ 500 m (100 mm lens)
Radar resolution	<4 m @ 1 km or 4 milli-radians
Radar deformation sensitivity	Submillimetre

It is assumed that the slope deformation in the unstable zone corresponds to a structurally controlled failure, of approximately magnitude 10 mm/day and directed somewhat obliquely to the radar line-of-sight as shown in Figure 7. To be precise, for this exercise it was assumed that the deformation components were equally distributed along East, South and downwards vectors.

To simulate this slope deformation, the structural features evident in Figure 8 have been used as constraints in an image deformation algorithm. As viewed in the camera frame, the deformation occurs towards the bottom left of the image. That is, there is a component of deformation detectable in the imaging system and therefore orthogonal to the radar. This is shown in Figure 8b.

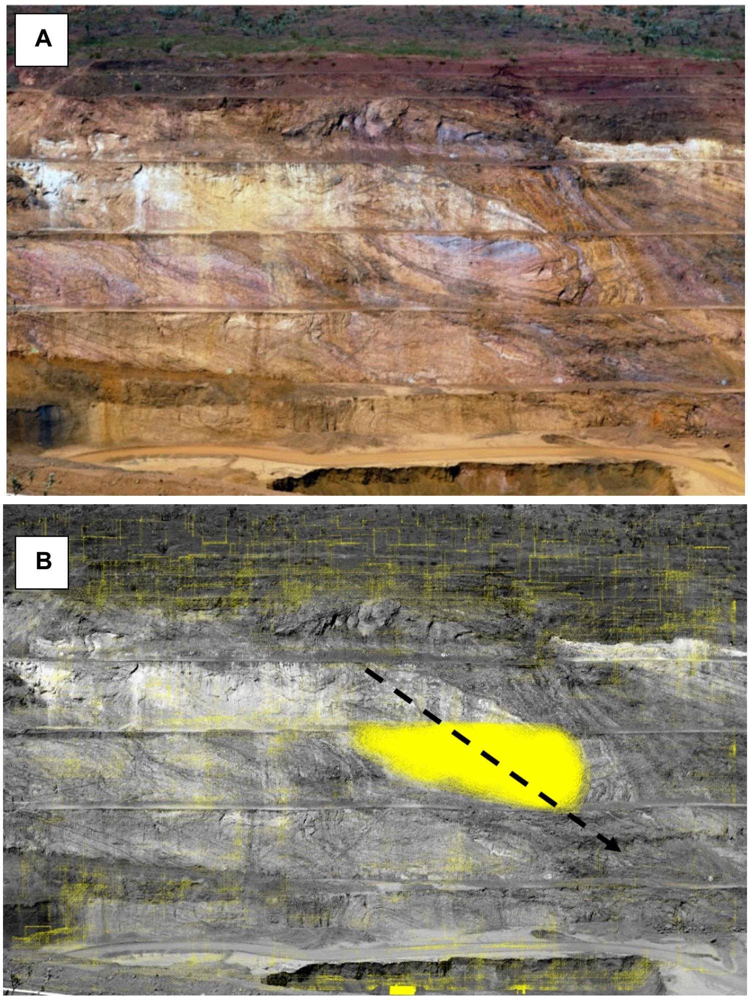

FIG 8 – Image of open pit iron ore mine (a) and visualisation of the synthetic deformation applied to a section of banded formation (b), with the black dashed arrow showing the apparent deformation vector observed by the vision system.

The radar response to this deformation has been simulated based on the radar location and failure geometry, and corresponds to 10 mm/day.

Using these parameters, a predicted response of the individual radar and vision sensors is shown in Figure 9. Even with the wide field of view lens used in this analysis, the deformation trends are clearly discernible in the vision data, albeit with significantly more noise than the radar. Note that due to the geometry of the sensors relative to the deformation, some components are measured as negative deformations (ie directly oppositely to the component basis vector).

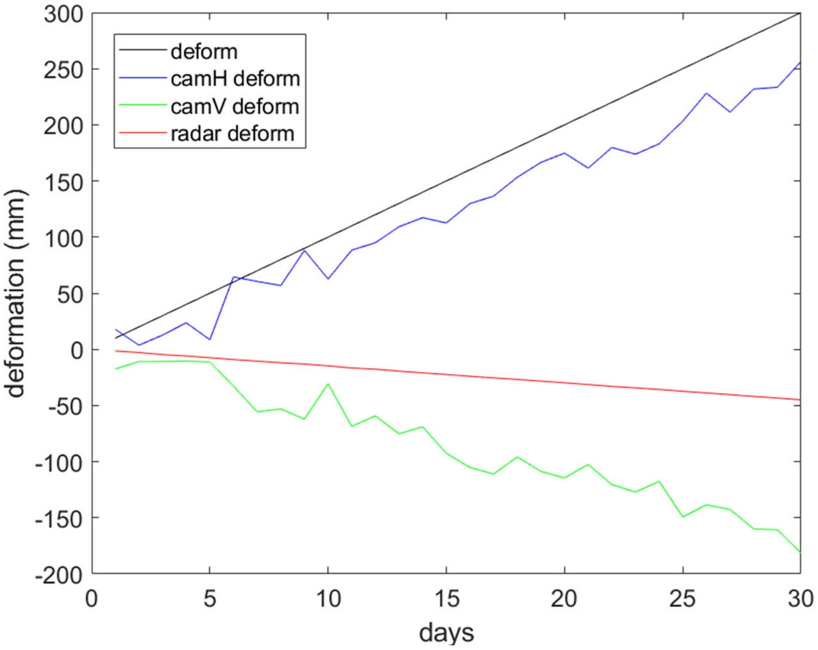

FIG 9 – Deformations as measured by vision and radar sensors, based on fusion of image and radar data for the iron ore slope deformation simulation.

Figure 10 shows the result of fusing the vision and radar measurements. The blue dashed line shows the deformation component observed by the vision sensor, the green dashed line shows the radar component, the red dashed line shows a naïve solution, the magenta solid line is the actual deformation simulated (ground truth) and finally, the solid vectors show the fused result. The fusion model takes into account the precisions of the sensors and the result is a less noisy prediction of 3D deformation than allowed for by the vision sensor alone. One can see that the fusion algorithm takes some iterations to converge on the correct solution, with initial predictions deviating from the groundtruth but steadily converging on the solution. This clearly demonstrates that the fusion algorithm can support 3D deformation monitoring in iron ore mines, with typical surface feature characteristics and mine geometries. In the following section, we describe some qualifications to this statement based on implementation considerations.

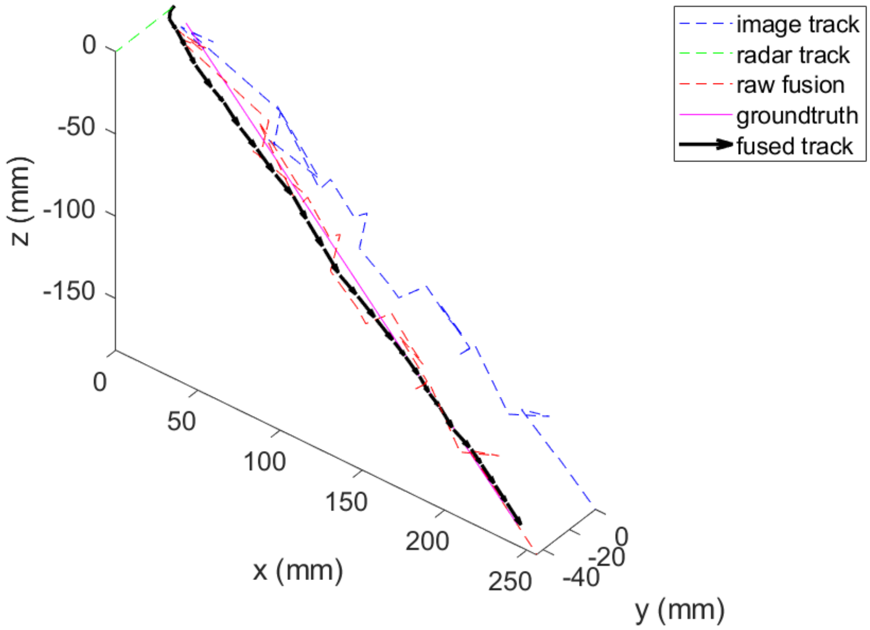

FIG 10 – Fusion of image and radar data for the iron ore slope deformation simulation.

Implementation considerations for iron ore mines

Illumination

Although the computer vision algorithms described in this paper rely on image intensity features which are expected to be prominent in typical iron ore mine benches, they are nonetheless sensitive to scene illumination changes. In the field, the causal factors for this are:

- Position of sun in the sky
- Presence or absence of cloud cover
- Changes in opacity of the intervening air mass (fog, dust etc).

To study these effects, a series of simulations have been performed based on the semi-synthetic data presented in the previous section. Figure 11 shows an example of the effect of illumination change on the scene.

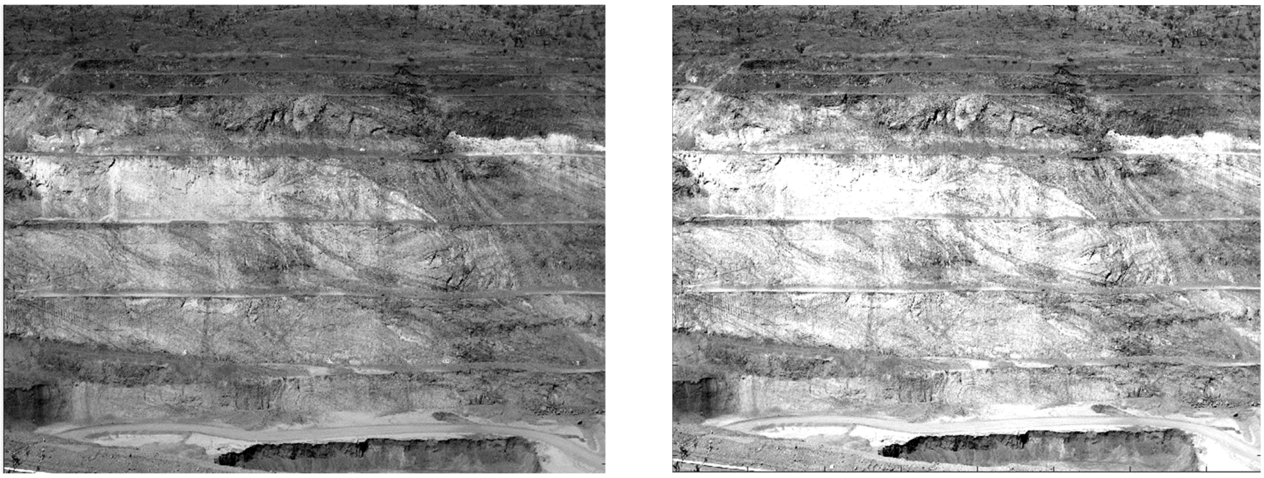

FIG 11 – Example of illumination change for an iron ore mine.

The changes in image intensity were varied randomly in the range of 0.5 to 1.5 times the base image. Without active illumination correction, all methods suffer to varying extents although the general tracking performance is still acceptable.

Stable reference

The use of the stable reference area is critical for quantification of noise due to geometric (eg mount stability) as well as atmospherics. As with radar monitoring, the stable reference area must be associated with a region of the wall known not to be deforming (or with tolerably small deformation) and preferably as close as possible to the region of interest. The need for multiple stable references is also likely for wide area monitoring. In the context of long strike lengths available in iron ore surface mining, stable reference areas should be readily available.

CONCLUSIONS

A newly developed sensor fusion algorithm has been trialled using field and semi-synthetic studies. It has been demonstrated that the new generation of cameras being deployed with radars are capable to support the proposed method. Experiments at Site A demonstrated the efficacy of the approach for monitoring both oblique and transversely oriented failures in a low wall dump. Even using post-processed and compressed imagery, the computer vision algorithms and sensor fusion technique clearly demonstrated 3D vector estimation which was consistent with the surface type failure being observed.

Site B focused on the use of the technique using raw (unprocessed), high resolution imagery to obliquely monitor a deeper-seated multibench failure, in a hard rock environment. The method clearly detected deformation perpendicular to the radar with deformations significantly greater than those measured along the line-of-sight. The derived 3D deformation vectors were consistent with both an understanding of the failure mechanism as well as previous measurements undertaken using a dual-radar system.

Semi-synthetic studies for an iron ore mine have been conducted using actual imagery acquired at a Pilbara site. The results are very encouraging and suggest the sensor fusion approach should be just as successful in these settings as demonstrated in the field trials.

Through fusion of vision and radar data, it has been also demonstrated that at least millimetre precision at a range of around 500 m can be achieved, but it is expected much greater ranges can be supported with suitably chosen optics. This then supports estimation of 3D deformation vectors with equivalent angular precisions. For these precisions to be achieved, the following conditions are required

- A well-designed mount to provide stability of the vision sensor
- Availability of a stable reference area to support further high precision vision frame stabilisation
- Sufficiently high frame rate in image acquisition to support selection of optimal images (from a large sample) and improved vision-based tracking

ACKNOWLEDGEMENTS

ACARP is acknowledged for its funding of this research, and in particular Adrienna Robotham (BHP) and Patrick Tyrell are thanked for their guidance and support throughout the ACARP funded project.

Dave Edwards (Downer) and Andy Winneke (Oceana Gold) have provided significant site support, expertise in site choice, and assistance with data interpretation.

Lachlan Campbell (Ground Probe) and Henri Prevost and Evgeny Shilov (IDS GeoRadar) have been extremely supportive throughout this project with coordination and access to their respective systems and data.

REFERENCES

de Graaf, P J H and Wessels, S D N, 2013. Slope monitoring and data visualisation state-of-the-art – advancing to Rio Tinto Iron Ore's Mine of the Future™, in P M Dight (ed.), *Slope Stability 2013: Proceedings of the 2013 International Symposium on Slope Stability in Open Pit Mining and Civil Engineering*, pp 803–814 (Australian Centre for Geomechanics: Perth), https://doi.org/10.36487/ACG_rep/1308_55_deGraaf

Dean, P, 2015. C23028 Improved Blast Outcomes, Brisbane: ACARP.

Elmouttie, M and Poropat, G, 2015. Monitoring systems and methods. United States of America, Patent No. US10724861B2.

Elmouttie, M, Dean, P and Van de Werken, M, 2020. Estimation of True Deformation Vector from Slope Radar Monitoring, Brisbane: ACARP.

Elmouttie, M, Poropat, G and Soole, P, 2012. Open Cut Mine Wall Stability Analysis Utilising Discrete Fracture Networks, Brisbane: ACARP.

Haile, A, Ross, D, Maldonado, A, Neyaz, M and Rajbhandari, C, 2020. BHP Western Australia Iron Ore geotechnical open cut slope design system: a simple pragmatic process for slope risk decisions, in P M Dight (ed.), *Slope Stability 2020: Proceedings of the 2020 International Symposium on Slope Stability in Open Pit Mining and Civil Engineering*, pp 415–426 (Australian Centre for Geomechanics: Perth), https://doi.org/10.36487/ACG_repo/2025_23

Poropat, G and Mamic, G, 2004. C9036 Highwall Hazard Mapping Project, Brisbane: ACARP.

Severin, J, Eberhardt, E, Leoni, L and Fortin, S, 2014. Development and application of a pseudo-3D pit slope displacement map derived from ground-based radar. *Engineering Geology*, pp 202–211.

Managing continuous improvement of Mine to Mill begins with measurement

J Loeb[1], P Cameron[2], R Ramanathan[3] and H Ingham[4]

1. Senior Consulting Manager, Hexagon, Vancouver BC V6E 3Z3.
   Email: jeffrey.loeb@hexagon.com
2. Business Development Manager (Split Engineering), Hexagon, Brisbane Qld 4000.
   Email: peter.cameron@hexagon.com
3. Business Development Manager, Hexagon, Perth WA 6000.
   Email: rangan.ramanathan@hexagon.com
4. Principal Mining Services Engineer, Hexagon, Denver, Colorado 80014.
   Email: harrison.ingham@hexagon.com

ABSTRACT

Most mining operations, including iron ore, maintain a focus on continuous improvement and asset optimisation in their operations. As all the unit operations in the Mine-to-Mill value chain are inter-dependent, available technologies that address efficiencies across the value chain are once again in the spotlight as companies are driven to improve productivity and maximise mine site profits to increase return on capital invested.

Core to continuous improvement is the need to understand the baseline and impact of changes to the process. In this paper, we discuss some of the critical attributes in the Mine-to-Mill process, including their influence on productivity and cost, the need for direct measurement and areas where they should be applied. Many initiatives can be considered to improve Mine-to-Mill processes.

Mining operations are planned and executed based on designs and models to achieve the operation's objectives. However, there are many variables in the different parts of the value chain, such as blasting, material handling, crushing and screening. Therefore, measurement of the key attributes establishes the baseline for Mine-to-Mill (or Pit to Plant) performance, which is necessary to understand the impact of any proposed improvements to the process design and execution and monitor the outcomes on an ongoing basis sustain the improvements that have been implemented.

This paper focuses on two types of measurement – blast movement and particle size of materials through the Mine-to-Mill process. Several innovative technologies and control loops are readily available to measure these attributes and assist operations to improve productivity and mine site profits.

The size of the tangible benefits, which can flow from measuring and optimising fragmentation and blast movement, provide a remarkable return on the investment. Realising these benefits needs a focus outside conventional operation silos as a successful Mine-to-Mill project requires a multidiscipline approach across all the silos in the value chain. Required technologies are available; adding the necessary ingredients of communication and co-operation by all concerned across the silos will ensure the benefits are realised.

INTRODUCTION

Continuous improvement is a primary focus for most iron ore operations. Unfortunately, many initiatives to identify ways to improve productivity and efficiencies and reduce costs are considered in organisational silos.

There is a case to consider process improvement holistically throughout the Mine-to-Mill value chain, which cuts across the silos in operational management. The impacts of blasting and subsequent size reduction in the processing plants, if well understood, can offer several opportunities for improvement to improve the positive effects, as well as efforts to minimise any undesirable impacts. Most of these are known but must be considered in a Mine-to-Mill context to realise maximum benefit.

Implementation of these opportunities leads to productivity improvement across multiple aspects, including production throughput, product quality, reduction in process downtime, managing energy cost, and reducing maintenance costs. Figure 1 summarises the opportunities for improvements and reduction of undesirable impacts.

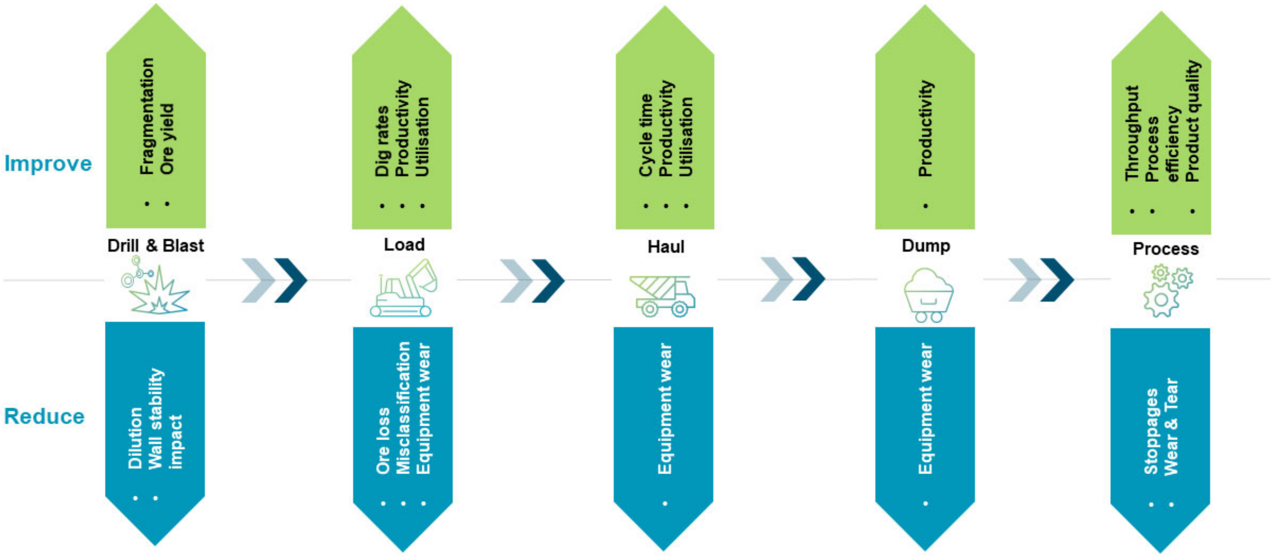

FIG 1 – Opportunities for improvements and reduction of undesirable impacts.

POTENTIAL DRIVERS FOR IMPROVEMENT IN THE MINE TO MILL PROCESS

As shown later in this paper, optimising blast fragmentation can lead to:

- Productivity enhancement by improving dig rates, truckload and cycle times, as well as improving equipment utilisation and reducing maintenance in the load and haul process.
- Increase in throughput by reducing (or even avoiding) blockages at the primary crusher.
- Throughput and process efficiency of the Ore Handling Plants (OHP), specifically crushing and screening capacity and throughput, is critical in iron ore.
- Increase in revenue by increasing lump to fines ratio.

Better knowledge of blast movement can lead to:

- Reduction in misclassification of material, which results in correct downstream allocation and optimisation of blending, in turn increasing ore yield.
- Meeting product chemical specifications, particularly phosphorus.

Measuring and managing fragmentation through Mine-to-Mill can lead to:

- Automatic optimisation of crusher closed side settings to increase throughput in the OHP.
- Early detection of oversize in product streams to indicate screen failure and screen blinding to avoid re-screening of batches of product.

THE ROLE OF MEASUREMENT IN CONTINUOUS IMPROVEMENT

All the above provide continuous improvement opportunities for mining operations through:

- Validation and verification of mining models, blast designs and processing parameters.
- Confirming adherence to process design.
- Making design changes to optimise operating objectives.

For each of these opportunities, the first step is to understand what is currently happening in the operation by measuring some of the critical attributes of the material being processed.

This paper focuses on two key attributes that significantly influence a cost-effective and efficient Mine-to-Mill process – material type and material size.

Measurement of these attributes brings into focus the importance of fragmentation and Particle Size Distribution (PSD) to optimise fragmentation and minimise blast-induced material misclassification which provides:

- Baseline for the operation to determine if it is performing as planned.
- Understanding of the impact of process or design changes for improvements.
- Ability to sustain gains realised from improvements.

BLASTING

Comminution is an energy-intensive process that accounts for a significant proportion of mine site costs. Therefore, effective blasting can improve comminution and significantly reduce mine site unit costs (CEEC, 2016).

Blast Engineers measure fragmentation in ROM ore for feedback to manage energy input in the design of blast patterns to optimise the ROM product size for feed into the primary crusher.

Specific to iron ore:

- Reducing fines in ROM ore can increase lump to fines product ratio (McKee, 2013).
- For mines with semi-autogenous grinding (SAG) treating magnetite to make pellets, increasing fines in ROM ore can increase SAG mill throughput from 8–30 per cent (Cameron, Drinkwater and Pease, 2017).

Improved fragmentation in ROM ore can increase shovel dig rates and truck fill factors, leading to decreased cycle times and reducing maintenance costs on loading and hauling equipment.

Detecting oversize rocks at the ROM muck pile allows diversion to a secondary breakage area to avoid blocking the primary crusher causing downtime and lost production. Better still is to modify the blast design to avoid producing oversize rocks.

Blast design

Effective blast design includes an understanding of:

- Rock structure and rock mechanics where Unconfined Compressive Strength (UCS) and Point Load Index data are complemented by knowledge and measurement of fracture zones.
- Blasthole crushing zone which is a function of hole diameter and explosive energy.
- Detonation timing and sequences.
- Production tonnage.
- Downstream process requirements.

In blast design and simulation software, fragmentation models predict the blast's particle size distribution (PSD) for different rock masses, blasthole geometry, and explosive parameters. Predicted size distributions are used as inputs in the simulation of downstream processes to determine the blast design required to optimise fragmentation and help optimise process throughput. Two fragmentation models used extensively worldwide to predict fragmentation in the blast are Kuz-Ram and Swebrec, which are described respectively in detail by Cunningham (2005) and Ouchterlony (2005).

When a blasthole is detonated, rock breakage occurs in two different stress regions, compressive and tensile:

- Compressive stress waves form a ‘crushing zone’ adjacent to the blasthole, which creates fine particles.
- Tensile stress waves propagate the ‘cracked zone’, outside the crush zone and between blastholes to create coarse particles. The size of these particles is influenced by the characteristic rock fracture zones and rock mass.

Figure 2 which illustrates the formation of a crushing zone, fracture zone and fragment formation zone around the blasthole was developed by Kabwe (2018).

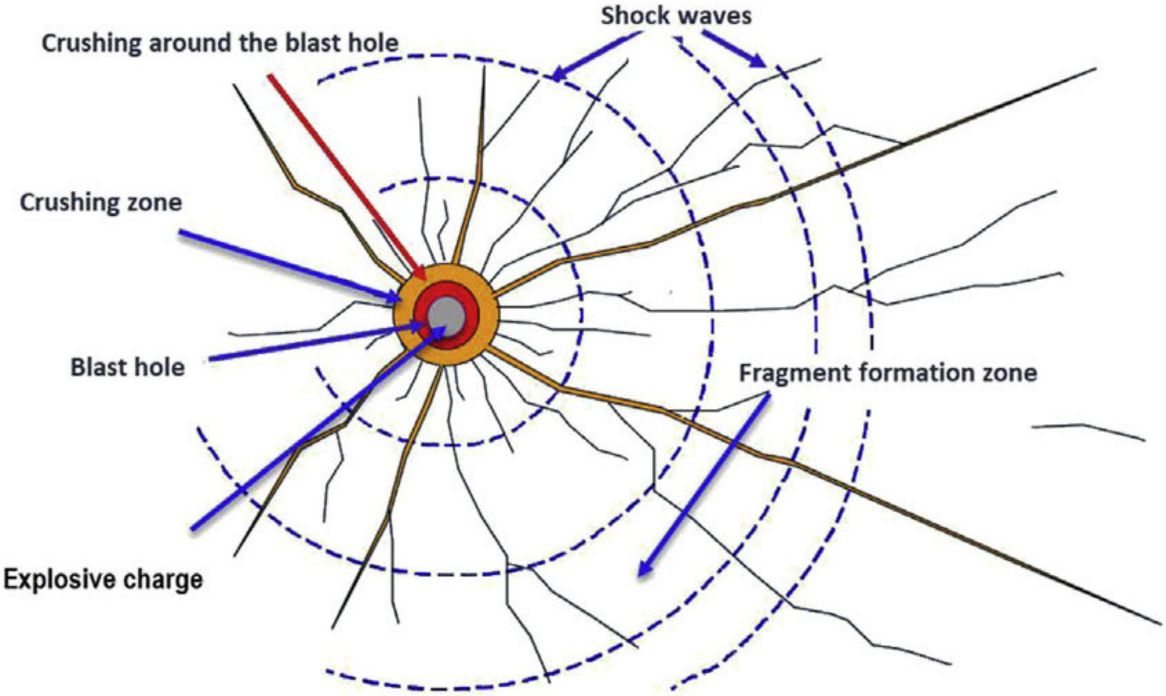

FIG 2 – Rock breakage mechanisms near the blasthole.

When the actual measure of fragmentation does not match predictions, blast engineers can modify their blast designs to manage selected parameters to meet the required PSD, therefore tuning the model to their specific rock type and mine parameters.

The blast 'engineer's options to control the ROM PSD are generally to manage blasthole geometry, explosive type and quantity. It can be almost impossible to change hole diameter in the short-term due to the investment in drilling equipment and explosive supply. Likewise, bench height cannot be changed due to the impacts this would have on mining schedules. Consequently blast pattern parameters (hole spacing, depth, diameter, hole angle), explosives (type, quantity, and position within the hole), and blast initiation (sequence and timing) are the available variables in blast design.

Conditions in blasting that the blast engineer has control over influence aspects of blast movement in different ways; which at times can be in counterbalance with designed targets such as PSD.

- Initiation changes directly influence movement geometries and trends, sending the material in more or less favourable directions and subjecting that material to more or less uniformity in its movement geometries.
- Explosive changes have direct impacts on movement magnitudes and directly impact the variability of those magnitudes.
- Pattern parameters, such as burden and spacing, similarly link into movement geometries as initiation design does, resulting in increased or decreased uniformity of movement.

Holistic approach to the drill and blast process

A holistic approach to drill and blast provides solutions to improve yield, fragmentation and misclassification is shown in Figure 3. Incorporating blast design software, high-precision drilling, sound QA and QC in blast execution, and post-blast analytics empowers blast engineers to optimise fragmentation of the blast.

The ability to tailor fragmentation outcomes and to minimise misclassification through blast movement monitoring are highly sought. In effect, this tailoring acts as another form of preconcentration by mining the ore delineations in the correct post-blast locations and meet product chemical specifications.

A holistic view of the Drill and Blast 'ecosystem' combines key knowledge banks, such as geology behaviour, effects on powder factor, blast design and mine planning, which enables blast engineers to optimise fragmentation, minimise misclassification and solve challenging problems, such as steepening slopes and Mine-to-Mill ore tracking to improve mine site productivity and profits.

Realising these benefits needs a focus outside conventional operation silos as a successful Mine-to-Mill project requires a multidiscipline approach across all the silos in the value chain.

FIG 3 – Holistic process.

MEASUREMENTS IN THE PROCESS

Blast movement measurement

Technology to measure blast movement uses monitors which are placed in the blast block prior to blasting and are subsequently located after the blast is fired. These assist in determining the movement of the *in situ* rock due to the blast. Since the actual movement is measured, it is an accurate measurement for the specific blast, resulting in correct identification of the material post-blast to reduce misclassification.

If blast-induced misclassification of material is minimised, then the geologist's precision in material delineation (pre-blast) is carried through the blasting process to production, resulting in optimal blending and minimal penalties or revenue loss due to off-specification chemistry in the products.

Measuring fragmentation and particle size after the blast

Image-based measurement systems which automatically measure particle size in the mine and throughout the plant, are shown in Figure 4. These can be installed on the loading equipment and at the primary crusher to understand the fragmentation in the pit and at the transfer to the crushing plant. Knowledge of particle size of the blasted muck pile provides feedback to the drill and blast design and execution process. It also detects oversize to reduce or avoid blockages of the primary crusher.

The use of cameras and image processing on conveyors in the crushing and screening process provides measured data on particle size and material flow. This data can be analysed to optimise throughput, proactively manage operational controls such as crusher closed side settings, and provide early indications of blockages and screen damage problems.

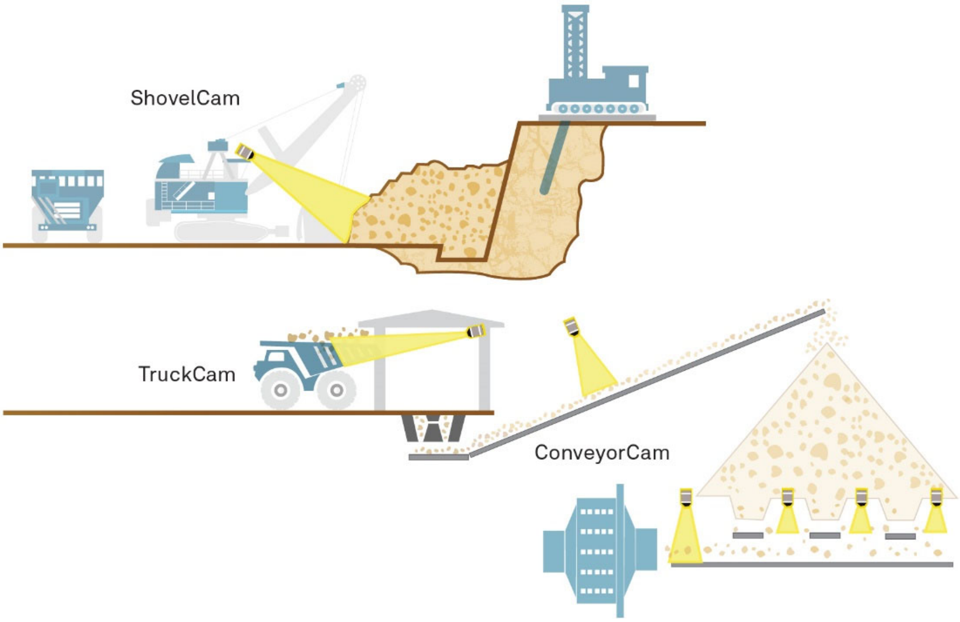

FIG 4 – Fragmentation measurement at different points in the process.

IMPACT OF FRAGMENTATION ON LOAD AND HAUL PERFORMANCE

Many papers confirm blast fragmentation impacts digability and truckload factors, and several field studies have endeavoured to quantify the impact.

Data from fieldwork at Granny Smith gold mine in Western Australia was subjected to rigorous statistical and simulation studies, Brunton *et al* (2003). This study concluded that the P_{80} was the best fragmentation distribution parameter to estimate dig time. For P_{80} values greater than 800 mm, the relationship with dig time was expected to increase, resulting in a more significant change in dig time for any increase in P_{80}.

CASE STUDIES

Business cases for measuring blast movement and PSD at the shovel and truck dump locations can be based on:

- Preventing oversize rocks from entering the primary crusher to decrease the number of bridging incidents and hence downtime of the crusher.
- Feedback to Blast Design Engineers as part of an overall Mine-to-Mill optimisation plan:
  - For hematite iron ore mines, minimising fines in the blast can increase lump to fines ratio, thus increasing revenue.
  - For magnetite iron ore mines, finer material from blasting reduces the specific energy in comminution and increases grinding circuit throughput.

- Increase in shovel or loader digability and truck fill factors.
- Decrease in the maintenance of Ground Engaging Tools and truck bodies.
- Minimise misclassification of material, and optimise blending as a direct result of blast movement.

The following case studies outline how some mines have gone 'back to basics' to measure PSD to manage blast design to improve mine site productivity and measure blast movement to reduce misclassification.

Morenci copper mine, Arizona

PSD data from cameras on shovels was used to increase fragmentation of the blast by tightening the drill pattern. As a result, top size in the ROM ore muck pile reduced from 1300 to 840 mm while 80 per cent passing size (P_{80}) reduced from 700 to 400 mm.

In addition to improving productivity in the downstream value chain, a significant side-benefit from reducing top size and P_{80} in the blast came from an increase in digability with shovel productivity increasing from 30 000 to 70 000 t per day, Lowery, Kemeny and Girdner (2000).

After a year of data analysis of measured fragmentation overall rock types and mining areas, the site employed a zone-specific blast fragmentation optimisation program to identify a target PSD to optimise the next stage in the process, either heap leach (for oxide ore) or feed to the mill (for sulfide ore).

Once targets were identified, Morenci measured fragmentation from shovel mounted cameras to manage fragmentation in the blast to further improve productivity. The outcome is summarised in Figure 5.

Drill Pattern (metres)	P_{80} (mm)	Top Size (mm)	Shovel tons per day
9.1 × 9.1	700	1270	**30 000**
8.2 × 8.2	400	840	**70 000**

FIG 5 – Different blasting parameters yielded better results, person and object for scale in blue circle. (left) Blast pattern 9 × 9 m with 2 m man; (right) Blast pattern 8 × 8 m with 250 mm ball.

Copper mine in the United States

Historically, testing different blast patterns or explosive types was difficult due to the inability to quantify PSD at the ROM muck pile. Camera systems located on shovels provided a continuous measure of fragmentation in the muck pile giving Blasting Engineers direct and accurate feedback on the performance of their blast. The copper mine could manage its blast pattern (burden and spacing) to decrease drilling and blasting costs while maintaining target fragmentation. This site also tested alternative explosive types to justify switching to a cheaper explosive while maintaining fragmentation targets.

African mine

A large copper mine in Africa reports daily downtime at the primary crusher due to oversize rock bridging events. This information is currently used to track the downtime, where the truck came from, the time at which that truck was loaded and the PSD data from the shovel. Fragmentation is monitored and reported as shift and daily PSD data and is a crucial metric in their hour-by-hour and day-to-day operations. Control systems integrated with mine dispatch systems which allow data from camera systems mounted on shovels to divert trucks with oversize rocks to secondary breakage automatically, are in development.

Porgera gold mine, Papua New Guinea

By increasing the fineness of fragmentation at Porgera through blast design and properties of explosives used, the truck payload was increased by 10 per cent, and loader dig time was decreased by 36 per cent. Both positive production increases led to an overall productivity increase in the loading and hauling phases of mining of 12 per cent.

Australian iron ore mine

A trial to minimise the misclassification of material as a direct result of blast movement assessed that by ignoring blast movement there could be as much as 12 per cent of misclassification or ore ending up at the incorrect downstream location. The ability to calculate this parameter improves mine performance and offers a more accurate control for the mining team. Additional updates include the implications of mixing material based on content of Fe, SiO_2, Al_2O_3 and P.

SIZE OF THE PRIZE OR THE VALUE OPPORTUNITY

Modifying blast design can avoid the production of oversize rocks and primary crusher downtime:

- For a 40 Mt/a operation delivering 5000 t/h to the primary crusher at a value of $30 per ton, one hour of downtime reduces revenue by $150 000.

Modifying blast design to decrease the PSD in the blast can increase digability and truckload factors. Decreasing particle size in the blast can reduce load and haul costs by 8 per cent:

- Typically load and haul costs in an iron ore surface mine are ~20 per cent of total costs. If the total mine cost is ~$12 per ton, load and haul would be ~$2.40 per ton. If a 40 Mt/a operation achieved a decrease in load and haul costs of 8 per cent or 20 cents per ton the reduction in costs would be $8 000 000 per annum.

Blast design can be managed to increase the lump to fines ratio, Kojovic *et al* (1998):

- If a 40 Mt/a iron ore operation increases lump to fines ratio by 5 per cent from 20 Mt/a lump to 22 Mt/a lump, with a $10 per ton premium for lump, revenue could increase by $20 000 000.

Measuring PSD on crusher discharge conveyors allows automatic adjustment of the gap or closed side setting (CSS) which avoids downtime for manual measurement and increases safety by removing people from this task.

Measuring PSD on screen discharge conveyors can detect oversize from screen panel wear or holes in screen panels. In some applications, if an oversize particle is detected three times in one minute, the control system shuts the process down to repair the offending hole in a screen panel:

- The cost of re-screening iron ore products is in the order of $5 per t. If two re-screening exercises of 100 000 tons each are encountered each year, costs increase by $1 000 000 per annum.

Cost of automatically measuring PSD by image analysis

For a typical 40 Mt/a iron ore mine with eight shovels, one primary crusher, and three conveyors in the ore preparation plant producing lump and fines, the capital for a 12 camera image analysis system would be in the order of USD700 000, delivering an impressive return on investment.

Benefits of monitoring blast movement

Many mines using blast movement technology report accurately identifying ore movement delivers savings of several hundred thousand dollars per blast.

CONCLUSIONS

There are several opportunities to understand Mine-to-Mill processes at iron ore mining operations by measuring the material's key attributes. This data can lead to initiatives to improve productivity and efficiencies and increase mine site profits. In addition, a holistic approach to the drill and blast process can lead to significant benefits for the operation.

Technologies and methodologies to measure and optimise fragmentation and blast movement are readily available and can be automated to integrate into the mine operation's workflow to deliver significant increases in yield, productivity, and mine site profits.

ACKNOWLEDGEMENTS

The authors acknowledge support from Hexagon to submit this paper for publication.

REFERENCES

Brunton, I, Thornton, D, Hodson, R and Sprott, D, 2003. Fifth Large Open Pit Mining Conference, pp. 39–48.

Cameron, P, Drinkwater, D and Pease, J, 2017. The ABC of Mine-to-Mill and metal price cycles (online), *AusIMM Bulletin*. Available from: https://www.ausimmbulletin.com/feature/mill-operations-the-abc-of-mine-to-mill-and-metal-price-cycles/

CEEC, 2016. *Comminution Energy Factsheet*, Coalition for Energy Efficient Comminution. https://www.ceecthefuture.org/resources/smart-blasting

Cunningham, C V B, 2005. The Kuz-Ram fragmentation model – 20 years on, *Brighton Conference Proceedings 2005,* European Federation of Explosives Engineers.

Kabwe, E, 2018. Velocity of detonation measurement and fragmentation analysis to evaluate blasting efficacy, *Journal of Rock Mechanics and Geotechnical Engineering*, 10(2018):523–533.

Kojovic, T, Kanchibotla, S, Poetschka, N and Chapman, J, 1998. The effect of blast design on the lump to fines ratio at Marandoo iron ore operations. *Proceedings, Mine to Mill Conference*, pp 149–152 (The Australasian Institute of Mining and Metallurgy: Melbourne).

Lowery, M, Kemeny, J and Girdner, K, 2000. Advances in blasting practices through the accurate quantification of blast fragmentation, *2000 SME Annual Meeting*, Salt Lake City, USA.

McKee, D, 2013. *Understanding Mine-to-Mill* (CRC ORE).

Ouchterlony, F, 2005. The Swebrec© function: Linking fragmentation by blasting and crushing, *Mining Technology (Trans. Inst. Min. Metall. A*), 114:A29.

Microseismic monitoring for open pit slope stability and rockfall detection

X Luo[1], Y Duan[2], M Elmouttie[3] and P Dean[4]

1. Senior Principal Research Scientist, CSIRO Minerals, Brisbane Qld 4069. Email: xun.luo@csiro.au
2. Senior Project Research Officer, CSIRO Minerals, Brisbane Qld 4069. Email: yi.duan@csiro.au
3. Senior Physicist, CSIRO Minerals, Brisbane Qld 4069. Email: marc.elmouttie@csiro.au
4. Senior Engineer, CSIRO Minerals, Brisbane Qld 4069. Email: peterdDean@csiro.au

ABSTRACT

Slope instability is one of the major concerns in open pit mining operations. A significant collapse of the pit wall can result in injuries, damage to machinery and interruptions to production. A broadband microseismic monitoring technique has been developed for diagnosing the healthy condition of a target slope area. This technique has been successfully applied to an open pit mine in Chile. Our research has found that this microseismic monitoring technique can be used in open pits for tracking and locating a falling rock that is rolling on a slope, if a dedicated seismic sensor network has been established. In collaboration with other monitoring techniques (radar, laser scan, aerial photography), more accurate determination of rock rolling trajectories can be obtained.

In this paper, an example of using the CSIRO microseismic monitoring technique at an open pit mine is presented. Results from an experiment where we used the microseismic technique for determination of the trajectory of a rockfalling on a slope are also presented.

INTRODUCTION

Slope stability is one of the major concerns in open pit mining, as a significant collapse of the pit wall can injure or even kill personnel, damage mining equipment and cause interruption to production. Microseismic monitoring techniques have been recognised as an efficient tool to map rock fracture network development for assessing slope stability (Hardy and Kimble, 1991; Lynch and Malovichko, 2006). The technique has also been used for identifying potential failure locations (Trifu, Shumila and Leslie, 2008), estimating potential damage scales and unstable volume (Wesseloo and Sweby, 2008), predicting impending failures and improving understanding of how mining affects pit stability (Lynch *et al*, 2005).

Properly interpreted microseismic data can be used to identify potential instability and the associated failure mode. Microseismic monitoring techniques measure seismic signals generated from rock breakage or movement inside the open pit. As microseismic sensors can measure rock fracture events remotely, it can provide data to map the 4D pattern and dynamic development of rock fractures before any deformation on the slope surface can be observed.

Although several technologies, such as radar and laser scan, have the potential to assist with monitoring and the analysis of rockfalls and their trajectories, no effective systems exist (de Graaf and Wessels, 2013). In 2020, we proposed to use microseismic monitoring techniques to monitor rockfalls for determining the trajectory of rocks rolling on a slope. The method intends to combine microseismic monitoring techniques with radar and vision monitoring systems to provide more accurate estimations of precursory of rockfalls and the rolling trajectory. Microseismic monitoring methods applied to the detection of rockfalls in open pit mining operations may improve operational safety, and, importantly, provide quantitative data to justify current standoff designs.

ESCONDIDA SLOPE STABILITY

Escondida mine is the world's largest high-grade copper mine. It is located near Antofagasta in Northern Chile (Figure 1) and it has reached an excavation depth of approximately 800 metres. The final pit design depth is estimated to be approximately 1500 m by the end of the pit's operational life. However, with increasing depth, pit slope stability is a risk that increasingly needs to be monitored and managed. In 2015 a section of the slope collapsed to the north-east of the pit, and the downwards movement of the slope has been in progress since. The mine needs to understand the dynamic changes of geotechnical conditions that control the movement in order to manage the hazard.

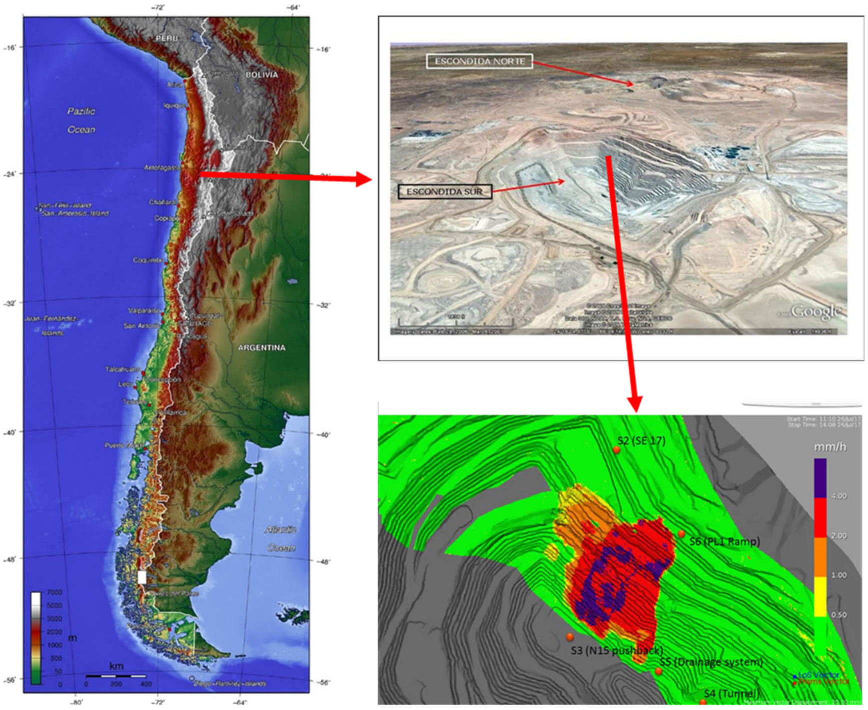

FIG 1 – Location of Escondida mine and unstable pit wall. Left: Map of Chile and the location of the mine (red arrow); Top right: Topology of the mine looking north-east; Bottom right: The north-east (NE) pit movement. Map sources: en.wikipedia.org/wiki/Chile (on the left), Google Maps (top right) and Escondida mine (bottom right).

In December 2017, a microseismic monitoring network was established at the east wall of the pit to investigate the feasibility of using microseismic monitoring techniques for slope stability assessment at Escondida mine (Figure 2). The project mainly aims to install a microseismic network on the pit's north-east (NE) wall to continuously capture 'creep' related microseismic events and investigate the relationship between those weak events and slope displacement.

The microseismic monitoring network comprises four small aperture geophone arrays, A, B, C and D, that are deployed in the NE and east parts of the pit, and at different elevations ranging from 2610 m to 3100 m. The A and B arrays are used for monitoring the unstable section in the NE of the pit. Arrays C and D are designed to enhance event location accuracy and detect any ground instability events adjacent to the processing plant. Each array has three triaxial geophones, spaced at approximately 50 m.

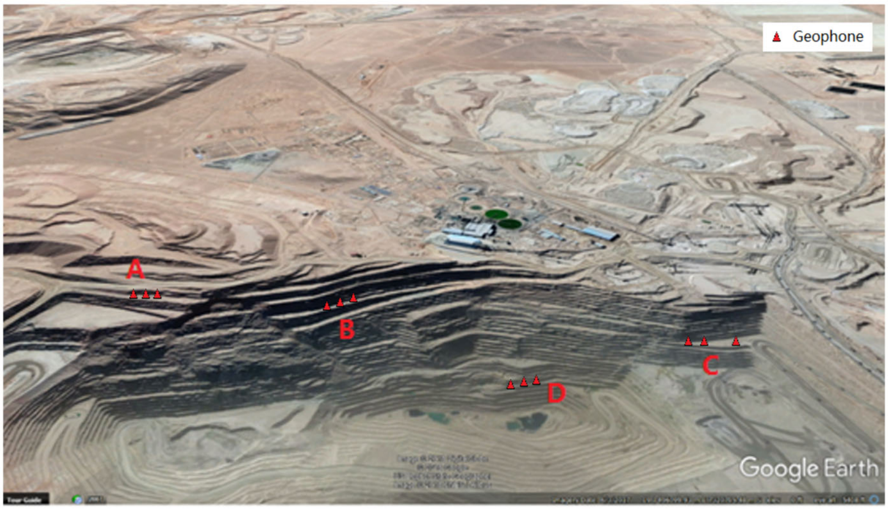

FIG 2 – Plan view of geophone locations at the NE and east walls of Escondida mine, looking eastwards. The microseismic monitoring network is composed of four geophone arrays noted as A, B, C and D. Each of the arrays is equipped with three triaxial geophones. The size of the collapsed slope at the NE wall is clearly seen between arrays A and B. The processing plant is located about 150 m from the top bench. The 3D map is from June 3, 2017 (image of Google Earth).

It is expected that each of the arrays can capturing seismic events adjacent to the pit slope for predicting impending slope movement. The combination of the arrays forms a larger-aperture network, which will be used to capture deeper and stronger microseismic events that may play a controlling role for the development of deep structure.

A number of seismic events recorded presented high frequency (300–350Hz) signals (Figure 3). These events were only recorded by one geophone and they are interpreted as being associated with borehole fractures near the geophone.

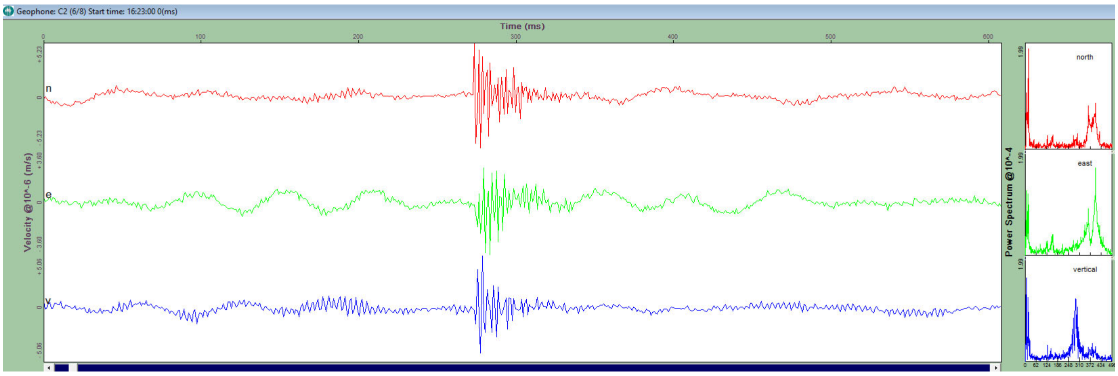

FIG 3 – Left: a typical waveform of a brittle rock fracture near a geophone; Right: the spectra associated with the waveform. The dominant frequency domain is from 300–350 Hz.

As most of the seismic events were recorded by fewer than four geophone arrays and the P-wave arrival times are difficult to pick, the locations of the events were estimated based on the changes of the seismic amplitude and relative arrival times of wave packets observed at different geophone locations. Figure 4 shows three areas (in yellow circles) in the pit where the seismic event locations have been estimated.

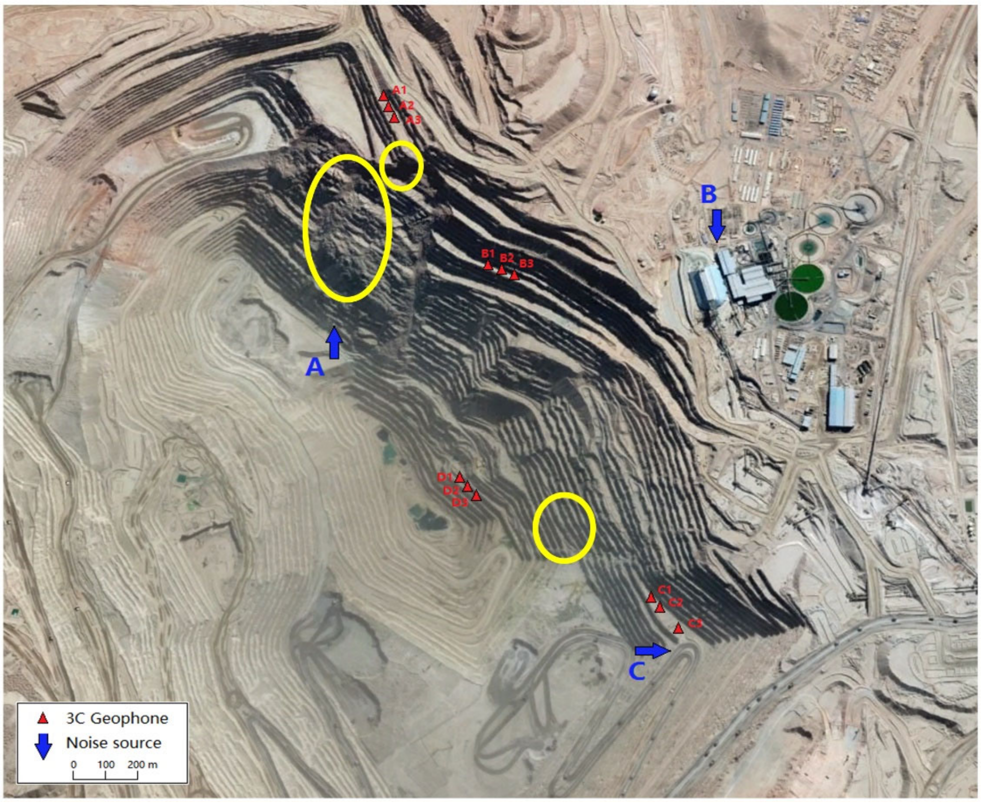

FIG 4 – Three areas (yellow circles) in which the microseismic event locations are estimated.

ROCKFALL DETECTION

To validate the potential of microseismics as a data source for detecting seismic signals induced by small rockfall events, an experiment was conducted at CSIRO Pullenvale, Queensland. A geophone array consisting of four triaxial geophones were installed along the slope from the top to the bottom (Figure 5).

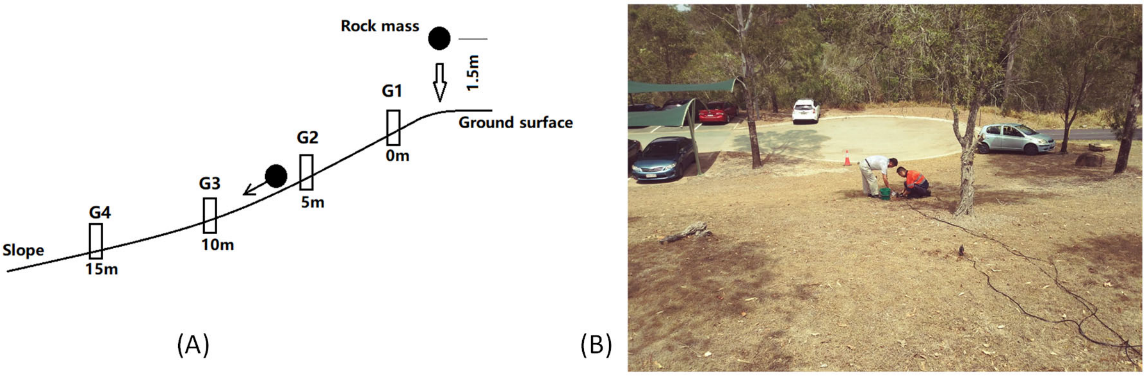

(A) (B)

FIG 5 – Experiment conceptual design (A) and field trial site (B).

Four types of rocks with different rock masses were used in this field trial (Figure 6). The characteristics of the rocks are summarised in Table 1. All rock drops and rolling movements on the ground slope were detected by the geophone array. Figure 7 shows the seismic waveforms responding to three drops of the largest rock on the top of the slope recorded by the four triaxial geophones.

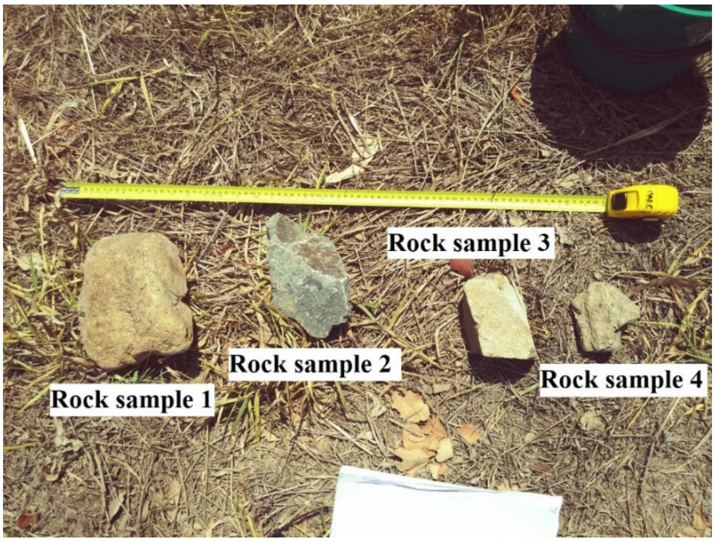

FIG 6 – Rock samples used in the field trial. They were dropped from the largest (left), approximately 20 cm × 20 cm, to the smallest (right), 10 cm × 10 cm.

TABLE 1

Parameters of rock samples used in the field trial.

Rock	Type	Density (g/cm^3)	Rock mass (g)
1	jasper/quartz	2.487	4696.4
2	granodiorite	2.706	2047.2
3	quartz rich sandstone	2.640	1144.6
4	sandy mudstone/low-grade metamorphic mudstone	2.684	536.2

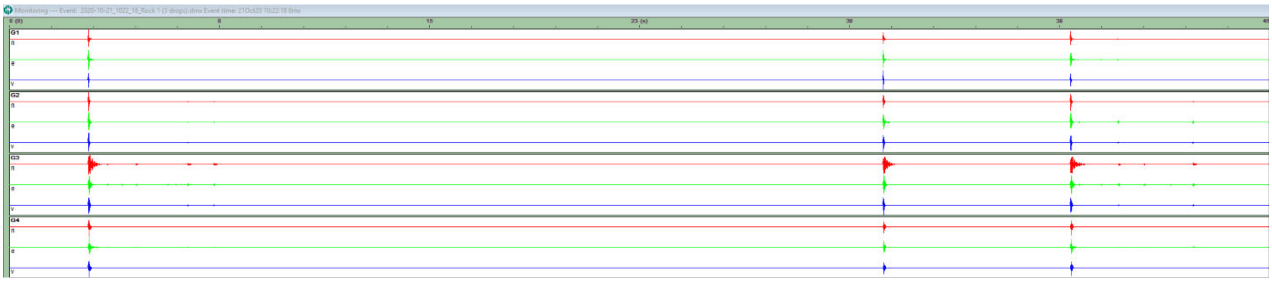

FIG 7 – Seismograms associated with three drops of Rock 1 (the largest rock). The seismic signals are clearly recorded by four geophones. The north, east and vertical components of the triaxial geophones are denoted in red, green and blue traces, respectively.

DATA PROCESSING AND INTERPRETATION

Every landing impact of a bouncing rock on the slope was clearly recorded by all the geophones. Different seismic wave arrival times recorded by the geophone array can be easily differentiated (Figure 8). The arrival time differences can be used to locate landing locations of a bouncing or rolling rock, to assist with 3D trajectory estimation.

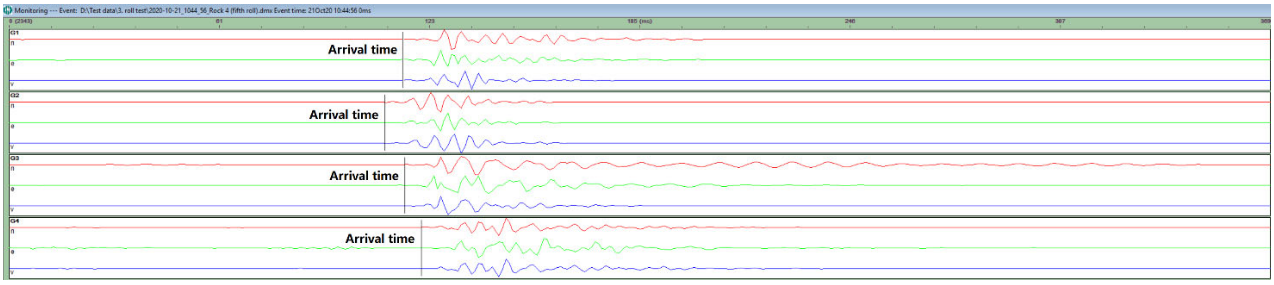

FIG 8 – Seismic waveforms associated with Rock 4, landing near geophone 2 (G2). The arrival-time sequence clearly shows that this landing position is close to G2.

Moreover, different size rocks presented different landing intensities from which, the size of the falling rock may be inferred, if seismic calibration is conducted before monitoring. The peak particle velocity (PPV) with regards to the rock samples are listed in Table 2.

TABLE 2

Seismic amplitude associated with the four sizes of rocks in dropping tests.

Rock size	Rock 1	Rock 2	Rock 3	Rock 4
Amplitude (m/s)	11.5×10^{-4}	8.1×10^{-4}	6.0×10^{-4}	2.5×10^{-4}

The relationship between the peak particle velocity (PPV) and the distance from the dropping location to each geophone is obtained (Figure 9) for seismic energy attenuation interpretation. This relationship can be used to assess the sensitivity of the monitoring network and the seismic amplitude attenuation factor. The background noise level during this experiment is below 0.1×10^{-5} m/s. Therefore, as shown in Figure 9, the maximum detection ranges with respect to the different rock samples can be predicted and are summarised in Table 3.

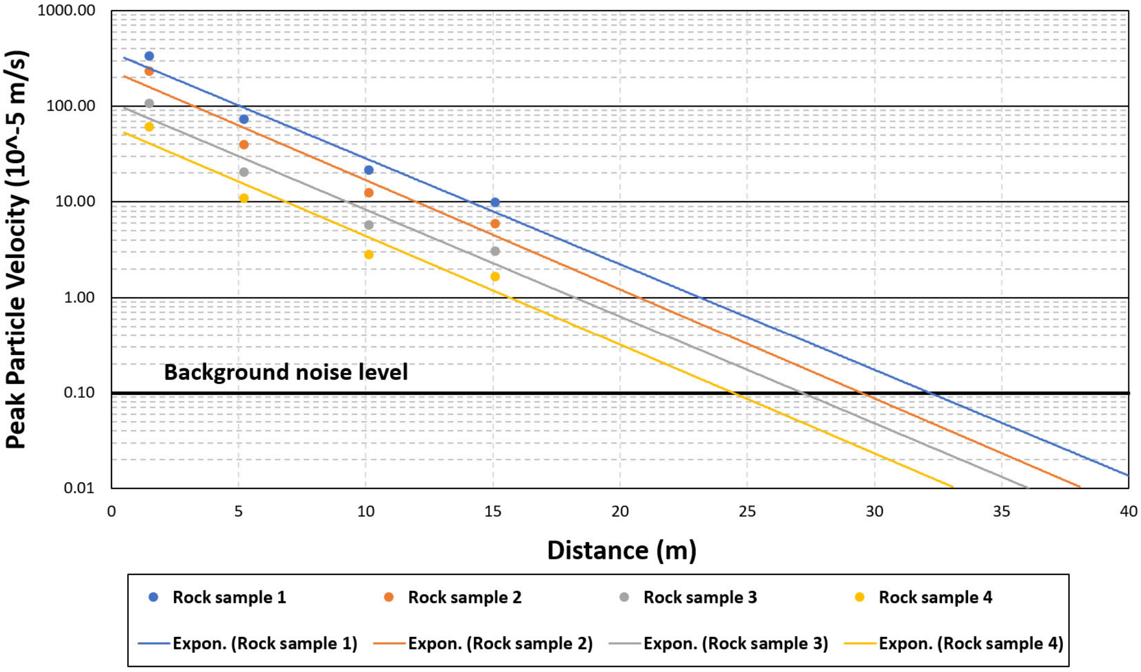

FIG 9 – Relationship between PPV and the travel distance of seismic wave.

TABLE 3

Maximum detection range with respect to rocks.

Rock	Rock mass (g)	Detection range (m)
1	4696.4	32
2	2047.2	29.5
3	1144.6	27
4	536.2	24.5

CONCLUSION

Our study in an open pit mine reveals that the microseismic monitoring system is capable of detecting weak seismic events near the surface of the open pit slope, which can be used to infer instability areas in the open pit. This finding provides the potential for microseismic monitoring to support detection of slope movement and wall collapse.

The rock drop tests were performed at CSIRO's Pullenvale site to investigate microseismic characteristics in response to rock impacts and rocks rolling on the ground. This experiment has shown that microseismicity associated with rocks rolling on slopes can be detected using a well-designed geophone array. In this experiment the maximum seismic detectable distance is more than 30 m. Different seismic wave arrival times recorded by the geophone array can be easily differentiated and used to locate landing locations of a bouncing or rolling rock. From that information, the rockfalling trajectory can be determined.

ACKNOWLEDGEMENTS

The CSIRO Microseismic Research Team would like to thank Pedro Gonzales and Jorge Calderon and Juan Muñoz from BHP Minera Escondida for their strong support in establishing this project. Our thanks also go to Ashley Creighton, Principal Adviser – Geotechnical Engineering, Growth and Innovation Rio Tinto, for his strong recommendation to apply CSIRO microseismic monitoring techniques at Escondida mine. This experiment was supported by Minera Escondida.

The rockfall detection experiment was supported by ACARP (Australian Coal Association Research Program).

Drs Jane Hodgkinson and Binzhong Zhou are thanked for reviewing this paper and their comments to improve it.

REFERENCES

de Graaf, P and Wessels, S, 2013. Slope monitoring and data visualisation state-of-the-art – advancing to Rio Tinto Iron Ore's Mine of the Future^{TM}, in: *Int. Symp. on Slope Stability in Open Pit Mining and Civil Engineering (Slope Stability 2013).* pp. 803–814 (Australian Centre for Geomechanics). https://doi.org/10.36487/acg_rep/1308_55_degraaf

Hardy, H R and Kimble, E J, 1991. Application of high-frequency AE/MS techniques to rock slope monitoring, in: *Proceedings of the Fifth Conference on Acoustic Emission/Microseismic Activity in Geologic Structures and Materials.* Pennsylvania State University, Clausthal-Zellerfeld, Germany, pp. 457–477.

Lynch, R, Wuite, R, Smith, B and Cichowicz, A, 2005. Microseismic Monitoring of Open Pit Slopes, in: *Proceedings of the 6th International Symposium on Rockburst and Seismicity in Mines*. pp. 581–592 (Australian Centre for Geomechanics: Perth). https://doi.org/10.36487/acg_repo/574_65

Lynch, R A and Malovichko, D A, 2006. Seismology and slope stability in open pit mines, in: *International Symposium on Stability of Rock Slopes in Open Pit Mining and Civil Engineering*. Southern Africa Institute of Mining and Metallurgy, Cape Town, pp. 375–390.

Trifu, C, Shumila, V and Leslie, I, 2008. Application of Joint Seismic Event Location Techniques at Chuquicamata Open Pit Mine, Chile, in: Schunnesson, H, Nordlund, E. (Eds.), *Proceedings of the 5th International Conference and Exhibition on Mass Mining*. Luleå University of Technology, Luleå, pp. 943–952.

Wesseloo, J and Sweby, G, 2008. Microseismic Monitoring of Hard Rock Mine Slopes, in: *Proceedings of the First Southern Hemisphere International Rock Mechanics Symposium*. pp. 433–450 (Australian Centre for Geomechanics: Perth). https://doi.org/10.36487/acg_repo/808_179

Improving compliance in mining through an effective geoscientific information management framework

S Mundell[1], A Atkins[2] and S van de Water[3]

1. Director of Product, acQuire Technology Solutions, Applecross WA 6153. Email: s.mundell@acquire.com.au
2. CEO, acQuire Technology Solutions, Applecross WA 6153. Email: a.atkins@acquire.com.au
3. Operations Manager – EnviroSys, acQuire Technology Solutions, Adelaide SA 5000. Email: s.vandewater@acquire.com.au

ABSTRACT

Geoscientific information management enables the capture, management and delivery of the original geoscientific observations and measurements of the earth's natural resources. However, original observations and measurements are worth nothing if the quality and integrity of the data can't be guaranteed. Geoscientific information is one of the fundamental assets enabling miners to make confident and accurate business decisions, whether that is defining a resource model, performing reconciliation, delivering ore reserve reports or meeting environmental compliance requirements. Without access to reliable, validated or verified data it increases the risk of miners using incorrect information for reporting and compliance. Industry codes, such as JORC, or government regulations, such as environmental compliance requirements, must be adhered to and companies should be able to confidently report to these standards.

Without having a robust information management framework in place, it becomes a challenge to make trustworthy decisions, report confidently and reduce the risk of non-compliance. As a key initiative, good data governance should form one part of a miner's information management strategy. Within the mining industry it is common for companies to only consider technology tools as the key focus for compliance whereas a mature information management focus will additionally consider people and process. All three pillars are critical for a miner to have confidence in their data driven decisions.

This paper discusses an industry framework for best-practice geoscientific information management based on the observations gathered from analysing data management practices within the mining industry. It focuses on how the three pillars of people, process and technology are crucial elements to improve operational decisions and ensure companies are compliant.

INTRODUCTION

With growing expectations on the mining industry from a broad range of stakeholders, licence to operate continues to be identified as a top risk for miners (Mitchell, van Dinter and Stall, 2020). While disputes and failures to comply with conditions set for iron ore projects present financial and operational disruption risks, they also impact stakeholder groups' perceptions of an organisation. This can potentially damage its reputation and ongoing support for a project.

Licence to operate has motivated an increasing number of miners to be transparent with respect to Environment, Society, and Governance (ESG) issues to demonstrate they are either 1) compliant with the conditions set out for their operations, or 2) are making positive, conscious contributions to the broader community. While the ESG scorecard is broad and requires input from all parts of the business, demonstration of performance (eg compliance) on many metrics puts a demand on geoscientific information management (GIM). GIM is the discipline concerning the management of geoscientific information, which includes geological drill hole data (eg rock types, assays etc) and environmental data (water, air, noise etc).

For an ESG scorecard, the availability of quality, trusted geoscientific data, and the visibility and confidence in the processes and management of the data, is important for aspects such as environmental compliance, exploration licence compliance, resource reporting and mine closure regulations. From this perspective, it may not only be the data itself which is needed for reporting, but also demonstrating the activities performed to capture the data and the practices in place to manage the data.

A focus on GIM best-practices can help iron ore miners improve compliance and in turn, reduce the risks concerning licence to operate given the direct link between geoscience and ESG issues. This paper presents a best practice approach which includes not only the technology, but also the people and processes component to support compliance requirements. These three components are:

- **People** – the human dimension is core to all activities and knowledge for managing data.
- **Process** – the structured frameworks set to achieve data management objectives.
- **Technology** – the enabling tool to support people and process.

THE ROLE OF GEOSCIENCE IN COMPLIANCE

Geoscience intersects many aspects of compliance and ESG reporting. For example:

- Environmental Compliance.
- Exploration Licence Compliance.
- Resource Reporting Compliance.
- Mine Closure.

The compliance and ESG reporting examples above place different demands on geoscience outlined through the following dimensions:

1. Data: Geoscientific data is a vital asset in all mining organisations, including iron ore, and incorporate both geological and environmental information. Geology provides the foundation on which a mine plan is built, therefore the quality and accuracy of the geologic data is crucial (Holloway and Cowie, 2019). Geoscientific data also underpins reports, models, analysis and decisions for environmental activities. It comprises the original observations and measurements of the in-ground resources (ie ore) and the environment, obtained through drilling, sampling and other forms of testing. These observations and measurements provide control points which describe environmental conditions, and define the size, grade, quality and location of resources.
2. Activities: Activities are the actual tasks performed by an organisation to collect data, such as drilling and/or sampling programs.
3. Practices: Practices are methods put in place to confidently achieve a desired and acceptable outcome in a consistent way. For managing geoscientific information, this includes:
    - QAQC protocols to ensure quality data,
    - sampling techniques,
    - sample security,
    - logging methods.

Table 1 briefly outlines examples of compliance where geoscience plays a part and the risk of getting it wrong.

TABLE 1

Compliance examples where geoscientific information is required, and risks.

Compliance	Description	Demonstrated by	Risk
Planning and Approvals	Ensures planning activities and approval activities are informed and aware of all relevant geoscientific impacts and considerations including baseline environmental conditions, surface and subsurface constructs, and heritage and sensitive land considerations.	Baseline, geophysical and accurate location data with contextual meta-data	• Harm to the environment • Disturbance of heritage and sensitive sites • Lengthy delays in the approvals process
Environmental Compliance	Ensures resource industry activities are designed, operated, closed, decommissioned and rehabilitated in an ecologically sustainable manner, consistent with agreed environmental outcomes and end land uses without unacceptable liability to the State (Department of Mines, Industry Regulation and Safety, 2021).	Monitoring environmental data against guidelines	• Financial • Suspension of operations.
Exploration Licence Compliance	Ensures eligibility for certification and registration to undertake a proposed method of exploration through a detailed program of work (Australian Business Licence and Information Service (ABLIS), 2021)	Listing activities performed	Inability to retain licence
Resource Reporting Compliance	Ensures holders of mining tenements prepare and submit mineral exploration reports that comply with the governmental mining regulations in their operational location. In Western Australia, as defined by section 115A(1) of the Mining Act, a mineral exploration report contains records of the progress and results of: a) programs involving the application of one or more of the geological sciences; b) drilling programs; c) activities involving the collection and assaying of soil, rock, groundwater and mineral samples, that have been carried out in the search for minerals. (Department of Mines, Industry Regulation and Safety, 2019)	Describing practices to ascertain confidence in the data	Suspension of companies securities and/or ASIC investigation
Mine Closure	Mine completion and relinquishment incorporates delivery of a defined post-mining land use rather than just closure when the operational stage of a mine ceases and decommissioning is complete. Also referred to as the mineral resource legacy (Department of Industry, Science, Energy and Resources, 2016)	Providing up to date data	Inability to relinquish land leading to a long-term liability.

In the cases outlined in the table, each relies on reliable and quality geoscientific data. For a business to successfully leverage the full value of its data for compliance and ESG reporting it must be:

- Accurate (correct).
- Accessible (able to be located quickly and easily).

- Trustworthy (consistent within context).
- Contextual (able to be understood for those it is intended for).
- Useable (by appropriate users).
- Secure (protected against loss, theft, fraud and degradation).

‘ARE WE COMPLIANT RIGHT NOW?’

There is a consistent theme and approach to how compliance and ESG reporting is managed today. Managing compliance is commonly a static linear set of relatively unconnected tasks and activities, with lots of work done in isolation that aren’t necessarily feeding the next link in the chain.

What makes the question ‘Are we compliant right now?’ challenging to answer is the nature of the interdependencies of inputs, systems and process. Take, for example, the environmental compliance scenario (Figure 1):

- Approvals, which state the project conditions and guidelines, are provided by authorities in the form of hardcopy documents or pdf.
- The approvals are translated to obligations, which are a list of requirements that need to be managed.
- Sampling and other monitoring data is collected to answer whether the project is compliant or not. The data is collected manually in the field, or by devices, generally in a specialist system.
- Compliance is managed in a separate system with a loose relationship to the monitoring data.

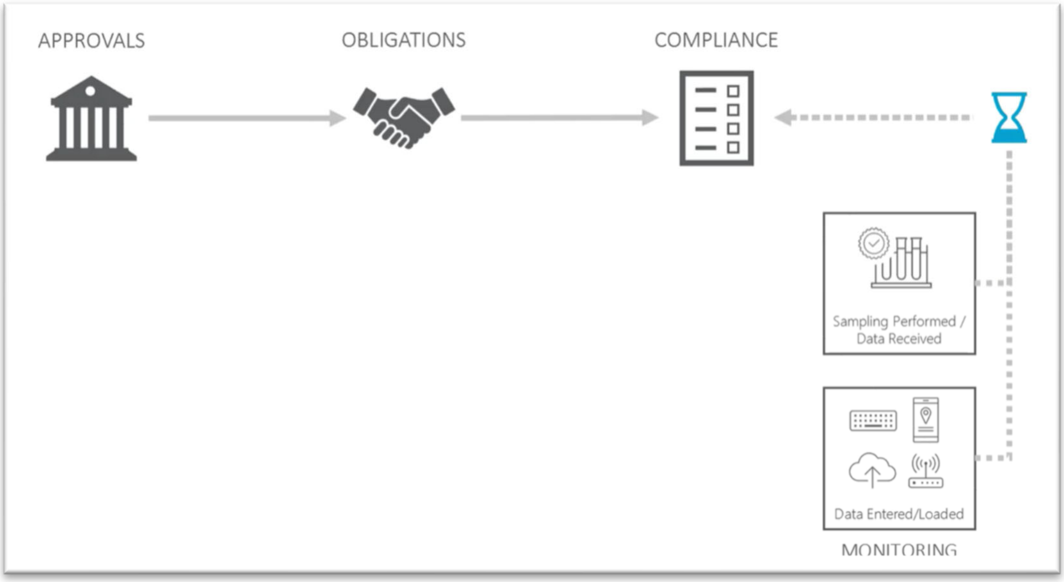

FIG 1 – Environmental compliance scenario and inputs.

Ultimately, it often provides an answer but only after significant effort has been invested into collating, checking, double checking and correcting data.

The implications of this approach when asking the question ‘Are we compliant right now?’ are twofold. First, is the timeliness of providing an answer. It may be days or weeks of work. And second, is the lingering fear or concern whether the right information has been provided and if it is the required quality. Will it stand up to an audit and expectations?

This concern arises because there are several issues with current practices that create risk:

- Data is collected from a number of sources and systems. It can be ingested from the field, laboratories and other data providers. It may be a manual process which is prone to error and is often not timely.

- Regulatory and corporate reporting is managed manually and inconsistently, especially when an organisation has multiple sites.
- Challenges when sharing data across the entire organisation and to other stakeholders.
- Lack of ability to act on, trend, forecast, model and report on potential impacts, events and statistics.

This results in:

- Increased risk across the operation.
- Lack of trust in the data.
- Inability to report and react in a timely manner, which can be crucial for issues that impact our environment.
- Inability to be proactive, so putting in measures to counter an evolving situation.

The ultimate and unfortunate outcome is compromised obligations, communities and the environment in which companies operate, plus a severe impact on the licence to operate.

AN INFORMATION MANAGEMENT FRAMEWORK

With a long-term background in working with geoscientific data across a variety of mining companies, the authors consider a robust information management framework is needed to support iron ore companies to make trustworthy decisions, report confidently and help reduce the risk of non-compliance when operating. Founded on GIM, which is the discipline concerning the management of processes used for the collection and quality control and assurance of geoscientific information, this framework is built upon the three pillars of people, process and technology. It is critical for all three pillars to be considered, rather than just relying on one individual part, such as a software tool or having processes in place but without the right technology or skilled people to support the processes. The multifaceted approach focusing on the interchange between people, process and technology makes it easier for companies to prove their compliance.

People

People are the most important asset a company has (Prodan, Prodan and Purcarea, 2015) and play a vital role in an effective information management framework. Iron ore businesses need to recognise they own the issue of geoscientific information management and to employ the people responsible. The human dimension of the framework needs to have the required information management skills and knowledge to know how and what activities to perform. No technology will improve the situation until people in the organisation have clearly outlined behaviours and accountabilities to deliver data quality goals along with processes to support those goals. The behaviours should be communicated across the organisation and not just maintained by the database geologist or database administrator. Anyone who collects, uses or views geoscientific data needs to be held accountable for maintaining good data management behaviours. People need to be digitally-enabled specialists and data experts to support operational decision-making.

The ‘human dimension’ can be difficult to change particularly within mine operations. Despite its importance, the topic of ‘data management’ still suffers from a lack of profile and frequently fails to capture the attention of mine management, until there is a problem. Even then, the problem is likely to be associated with the tools being used rather than the lack of an overall data management skills and ownership.

Process

The mining industry is continually advancing digital technologies (Barnewold and Lottermoser, 2020). Advances in information technology, such as the collection of larger volumes of data from multiple and varied sources and the need for enterprise-wide software solutions to manage this data compels companies to adopt a structured and system-wide view of data management. For the iron ore industry the key drivers have been:

- The move away from systems that allow users to manage data in siloes as if they own it.

- The need to prevent data errors, such as duplicate information, missing or incomplete data at the point of capture or origin.
- The realisation that many errors do not affect the person or group who created them
- The move to reliable systems that support corporate standards, data governance and data interoperability.

Processes connect people or groups to tasks. For iron ore businesses a good process will enable internal and external groups to establish effective data supplier relationships. With geoscientific information in mind, the processes listed below all benefit from an easy connection between the human dimension (people) and the task:

- Capture of original observations and measurements to reduce error at the point of capture
- Data discovery and access to the collected data
- Differentiation of original data from derivative data
- Identification of metadata (or data about the data)
- Data interoperability – providing the data in variety of standard formats
- Delivery of select data sets to required client systems
- Aggregation and abstraction of data and delivery in desired formats
- Internal data quality alerts and measures.

Redman (2008) estimates that knowledge workers spend on average 30 per cent of their time searching for the data they need and are unsuccessful at least half of the time. In a mining company where skilled workers are at a premium, the business cannot afford for geoscientists to spend this amount of their time using or creating poorly designed data management systems. This is a major opportunity to improve workplace productivity.

Technology

The challenge for the technology pillar is to connect people to the process. This encourages the discovery, access and integration of diverse geoscientific information. A well-designed geoscientific information management solution will provide an architecture that enables field workers and geologists to capture and access high quality information on demand. To achieve this goal, the business must pay at least as much attention to their work practices and organisational structure as they do to the selection of available solutions.

For iron ore companies wanting a comprehensive technical solution that supports their individual business requirements, there are a variety of professionally developed, commercial database solutions. These systems may offer all or some of the following enterprise architecture advantages:

- Professionally designed, developed and maintained
- Database hosted by a server-based Enterprise Level RDBMS (eg Microsoft SQL Server)
- User-friendly software interfaces suitable for multiple device types
- Integrated across desktop, web and mobile
- Open and persistent data models
- Support for geoscientific data types and interoperability with third-party software systems
- Long-term software supportability and development to match digital roadmaps
- Inbuilt business and validation rules to ensure no corrupt or incorrect data gets stored, regardless of where the data is captured and who does it.

WHAT THIS LOOKS LIKE FOR A MINING COMPANY IN PRACTICE

Large mining companies, such as iron ore miners, often suffer from a lack of consistency and cohesion. Each operational site tends to perform data management inconsistently with other sites, including how data is stored and managed, and where the data is sourced from. Often the source of data is unavoidably inconsistent between sites due to local availability of companies and people to perform monitoring and subsequent analysis.

Invariably some sites will perform data management in a superior way to others, making it difficult to compare data sets between sites for internal and external stakeholder reporting. It also makes it very difficult to roll out company-wide initiatives to sites, when the data practices are so variable – meaning some sites will be able to use their data as an asset upon which they make operational decisions, whilst other site will be continually chasing their tails trying to keep up with basic reporting and audit requirements.

A diligent application of the people, process and technology framework can realise a significant improvement to a company's data management practices by reducing such inconsistencies, fostering cohesion and provide a greater level of standardisation and transparency between sites. Standardised monitoring and data categorisation set at the corporate level will help sites manage their data and minimise the need for interpretation of compliance and other stakeholder demands across the business. This does not discount the need for some site-specific adaption, but it will be done in a considered and transparent manner. Such standardisation is backed by training and other learning and educational materials to ensure adoption and adherence is maintained, as people are critical in ensuring the success of the framework. Technology can then be the catalyst to bring it all together and support the processes and people. If can help verify and validate inputs and outputs, help schedule activities, identify and track events, and automate information sharing and dissemination.

Air quality and water management are two critical geoscientific aspects which any iron ore miner faces a challenge to manage. Done well, the data sets can be used as a critical input to inform operational decisions according to changing in-field conditions and against compliance obligations. Timely knowledge of operational conditions and tracking against compliance limits allow miners to optimise activities and mitigate risk, and this can only be done when the data can be trusted and is timely. For example, this would mean being able to avoid an exceedance in abstracting too much water from a bore field or detecting and mitigating dust levels before they become an issue on-site and resulting in a non-compliance to the regulator.

THE RESULT OF A BEST-PRACTICE FRAMEWORK

The original geological observations and measurements form the basis of economic and operational decisions made on the future of mining iron ore resources. This data is also used to support regulatory reporting to ensure compliance. Hence it is a valuable business asset and it should be accepted that geoscientific data is managed like all other significant business asset classes.

For a business to leverage the full value of its data assets to ensure compliance, the information must be accurate, accessible, trustworthy, able to be understood, usable and secure. This can be achieved by investing in the people, process and technology components of your business.

By implementing a sound geoscientific information management framework iron ore companies will benefit from:

- Consolidated data from multiple sources
- A trusted data source with appropriate governance
- Normalising the use of data in operational decisions
- Data experts and mining specialists with data management skills
- Leveraging insights and foresights from data to optimise operations to be more stable and capable
- Reduced risk of miners using incorrect information for reporting and compliance.

These three pillars go hand in hand to ensure the quality of your data and ultimately feed into ensuring companies meet compliance requirements across ESG factors. The value of your data to your business goes beyond the cost of drilling, sampling and assaying – think of the opportunity costs of decisions based on poor quality data.

REFERENCES

Australian Business Licence and Information Service (ABLIS), 2021. Exploration Licence (Onshore Minerals) – Western Australia, Australian Government website (https://ablis.business.gov.au/service/wa/exploration-licence-onshore-minerals-/17053).

Barnewold, L and Lottermoser, B G, 2020. Identification of digital technologies and digitalisation trends in the mining industry, *International Journal of Mining Science and Technology* 30, pp747–757.

Department of Industry, Science, Energy and Resources, 2016. Mine Closure: Leading Practice Sustainable Development Program for the Mining Industry, Australian Government.

Department of Mines, Industry Regulation and Safety, 2019. Guidelines for Mineral Exploration Reports on Mining Tenements, Government Gazette, (Government of Western Australia).

Department of Mines, Industry Regulation and Safety, 2021. Environmental Regulation, Government of Western Australia website (http://www.dmp.wa.gov.au/Environment/Environmental-regulation-8311.aspx)

Holloway, E and Cowie, S, 2019. Mine Planning and the Crucial Role of Geology, *SEG Discovery*, Issue 118, pp16–27.

Mitchell, P, van Dinter, A and Stall, R, 2020. *Top 10 business risks and opportunities for mining and metals in 2021*, Ernst & Young, (https://www.ey.com/en_au/mining-metals/top-10-business-risks-and-opportunities-for-mining-and-metals-in-2021).

Prodan, M, Prodan, A and Purcarea, A A, 2015. Three New Dimensions to People, Process, Technology Improvement Model. In: Rocha A, Correia A, Costanzo S, Reis L. (eds) *New Contributions in Information Systems and Technologies. Advances in Intelligent Systems and Computing*, vol 353. Springer, Cham.

Redman, T C, 2008. *Data Driven*. Harvard Business Press, Boston.

Dealing with uncertainties on mining equipment fleet planning and usage

I R Souza[1]

1. Long-term Planning Engineer, Vale S.A, Belo Horizonte, Minas Gerais, 34.006–200.
   Email: igor.resende@vale.com

ABSTRACT

At the mining industry, there are several uncertainties that may affect the mobile mining equipment fleet sizing and usage, such as commodity supply and demand, which impacts the mineral price, environmental licenses to allow operations and strategic decisions made by the own mining company. Due to that, it may happen to acquire a mobile mining equipment for a specific site and before it finishes the entire forecasted life cycle, the machine gets idle on that operation and a decision must be made regarding this matter. On large mining companies with several sites, equipment transfer provides a good solution to solve this issue and at the same time it provides operational flexibility and allows to use the equipment until the initially planned working hours. This article presents a method to compare technically and financially whether it's more feasible to transfer a used equipment or to buy a new one. In other words, we will compare a brand-new machine versus a used one in terms of safety, net present value (NPV) considering both capital expenditures (CAPEX) and operational expenditures (OPEX), technological obsolescence, risks, equipment maintenance reliability and lead times. Although it's not the main purpose of the paper, it will also be briefly discussed the importance of having a considerable amount of backup equipment to handle low likelihood and high consequence risks that may materialise. This backup equipment portfolio is particularly important to avoid loss of sales and profits in case the production plan changes and it demands further equipment than initially planned to cope with the forecasted production.

INTRODUCTION

On 7 February 2011, the iron ore 62 per cent Fe is exchanged under the impressive price of US$186.92 per ton. Less than five years later, on 8 December 2015 the same commodity is traded for US$43.46 and now, in May 2021 the iron ore is back at US$190 per ton. Commodity price volatility is only one of the variants that impacts mobile mining equipment planning and usage. Walker *et al* (2003) defines uncertainty as any deviation from the unachievable ideal of complete determinism. According to Lanke, Ghodarati and Hoseinie (2016), uncertainties that affect a mining operation can be divided in two categories: internal and external. Some examples of external uncertainties are the market ore price, legislation and political risks. In the other hand, uncertainties regarding equipment, management team and labour force illustrates the internal factors. There are also sources of uncertainties which connects both internal and external factors, such as environmental licenses.

As it can be observed, uncertainty is something inherent to any mining company operation, and therefore it must be handled. Many uncertainties can bring idleness to some equipment of the fleet. As an example, a mandatory environmental license to operate that takes longer than expected to be granted by the authorities can bring idleness for a fleet. In terms of handling and mitigating the impact of uncertainty on the activities of mobile mining equipment planning and fleet sizing, the alternative of transferring equipment among operational sites when severe kinds of uncertainties materialise, can a be a great tool to mitigate the threats of uncertainty.

The main goal of this article is to present a method to compare technically and financially whether it is more feasible to transfer a used equipment or to buy a new one. Technically speaking it will be tackled several topics that must be assessed, such as safety and equipment reliability. From the financial perspective, the applied figure of merit will be the net present value (NPV), as this analysis can be considered as a mutually exclusive investment decision. Another covered topic is the advantages and disadvantages of having an amount of backup equipment available in case that low likelihood and high consequence risks occur. In addition to that, the limitations of this method are also presented.

Thus, the question that this article aims to answer is: should we transfer an idle equipment, or should we acquire a new one to fulfil the needs of the operation?

METHODS

Financial analysis

When deciding between purchasing a brand-new equipment or transferring a used one, it can be considered a mutually exclusive investment decision and the net present value (NPV) is a suitable figure of merit to assess it financially. The NPV can be defined as the discounted net cash flow, which means, subtracting the discounted costs of the investment from the discounted expected benefits (Maravas and Pantouvakis, 2018). In other words, Higgins (2012) defines the NPV as a measure to determine how much richer the enterprise will become if it undertakes the investment. Equation 1 represents the formula to calculate the net present value:

$$NPV = C_0 + \frac{C_1}{1+i} + \frac{C_2}{(1+i)^2} + \cdots + \frac{C_n}{(1+i)^n}, \tag{1}$$

Where i is the discount rate and Cn is the net cash flow at period n.

When evaluating mutually exclusive investments that are complex to determine the amount of revenue generated by them, but there is no doubt about the importance of investing, it should be selected the alternative with the lowest net present cost, using the same formula presented above. This is the case for mobile mining equipment, due to the difficulty to measure the impact of those machines on the revenue streams of a mining company. Another feature of mutually exclusive investments is that technically it does not make sense to approve both investments. As an extreme example, when deciding whether to travel from Berlin to Amsterdam for a one-way trip, it is possible to go by plane or train, but not by both transportation methods.

In addition, purchasing a new equipment or transferring an already owned one can be considered as repetitive projects, which means that, when a machine becomes obsolete, it can be replaced by a new one. That is an important characteristic to fulfill an elementary condition to apply the NPV formula, which is to equalise the time horizon for both options. Thus, it is not correct to simply determine the lowest net present cost from a new equipment that will last for six years versus transferring a used equipment that still have three years of service life. To properly determine the most feasible option from the financial perspective, both time horizons must be matched.

Technical analysis

In order to determine what is the best decision, only assessing the best financial option is not enough, as the technical perspective must be also considered aiming to avoid future issues and decrease risk. The main technical topics analysed on this method are:

1. Safety – To ensure operational safety, it is necessary to evaluate the structural integrity of the used equipment to check if there are any issues, such as cracks, that may block the usage of this machine.
2. Emissions – The greenhouse gas emissions of both alternatives must be assessed.
3. Availability – A new acquisition naturally has a higher reliability and availability than a used one. To decrease the risk of loss of production due to lack of availability, it is recommended to double check if the rest of the equipment fleet is capable to absorb the availability difference.
4. Fleet standardisation – When transferring an equipment that is different from the current fleet, it brings some issues, such as, increasing the amount of spare parts on the site and making the operation and maintenance processes more complex.
5. Productivity – It must be assessed if there are productivity differences between both options. If the transfer alternative has a lower productivity than the acquisition one, it is recommended to evaluate if the rest of the fleet can absorb this gap.
6. Load and haul match – When evaluating loading or haul equipment, it is necessary to ensure that the match of those equipment is correct for both alternatives.

Finally, it can be created a matrix to show the advantages and disadvantages of both alternatives to support the decision-making process.

RESULTS AND DISCUSSIONS

In order to demonstrate the application of this method, the results will be presented of an analysis in an open pit iron ore mine in Brazil, where the comparison has been made for the feasibility of acquiring a new excavator (expected to work for 12 years) or transferring another shovel of the same model that was idle and still had seven years of forecasted useful life.

Financial comparison

The first step of the analysis is to determine the economic data and assumptions, such as taxes, the discount rate and the exchange rate between US$ and the local currency. After that, it must be determined what are the relevant cash flows for the analysis. The *with-without principle* explains that we must imagine two scenarios, one which the investment is made and another where the investment is aborted. All cash flows that are different on both scenarios are relevant to make the decision. In the other hand, all cash flows that appear on both worlds are irrelevant (Higgins, 2012). For instance, the costs to disassemble the idle excavator would just happen if it was decided to transfer the equipment. Therefore, this is a relevant cost and must be accounted for on the cash flow for the transferring alternative.

Figures 1 and 2 represent the cash flow distribution, in terms of percentage, during the 12-year time span considered during the analysis for the new machine acquisition and the transfer of the already owned equipment, respectively.

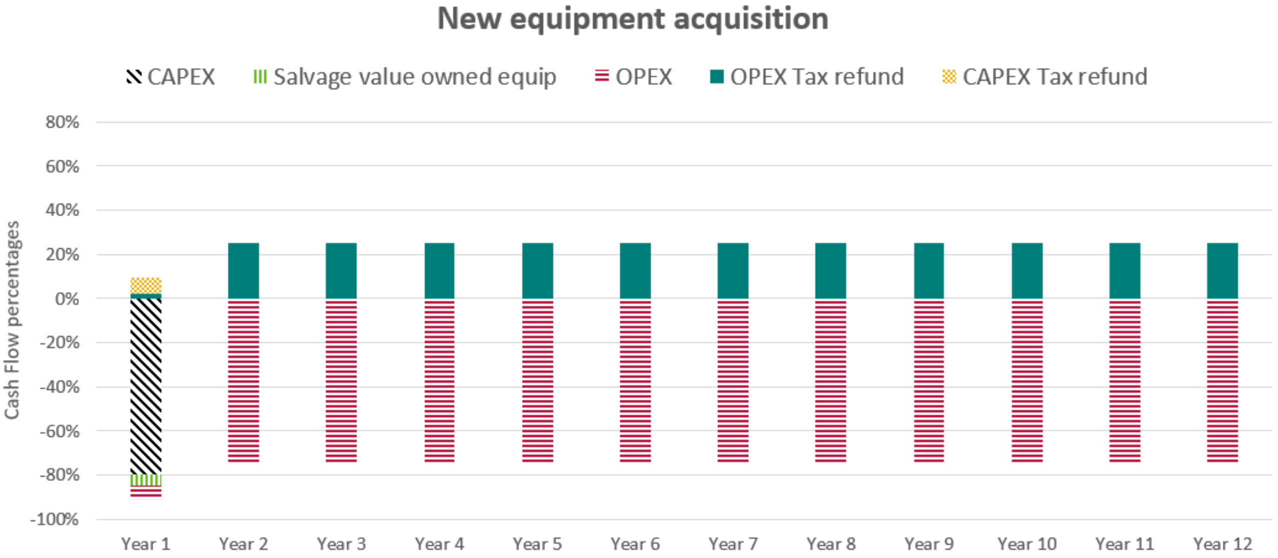

FIG 1 – Considered cash flows for the new equipment acquisition.

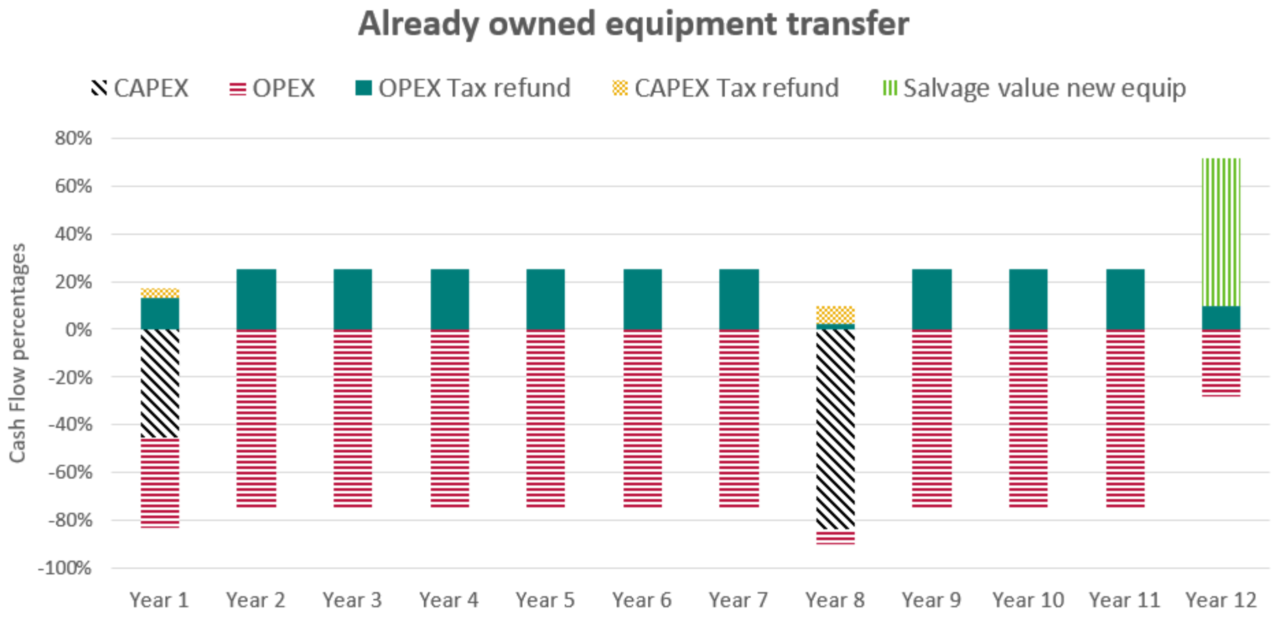

FIG 2 – Considered cash flows for the already owned equipment transfer.

In the scenario considering the acquisition, there is only one capital expenditure cash flow which happens in year 1. Meanwhile, the transfer alternative presents two CAPEX cash flows, the first one related to the costs to retrofit the used equipment and transfer it and another one in year 8, related to the replacement of the used machine when it reaches the end of service life and needs to be replaced by a new shovel. Another difference between the alternatives is that in case of purchasing brand new equipment at year 1, it must be inserted the salvage value cost of the used machine, as it will be disposed prior to reaching its entire fiscal life and therefore there will be a loss of tax refunds for the enterprise. In the other hand, the shovel purchased at year 8 on the transfer scenario will be still productive after year 12. Thus, the salvage value of the equipment on that moment must be included.

Calculating the net present value of both alternatives, the option to transfer the owned excavator has a 17.64 per cent better net present value than the acquisition alternative. Therefore, the best decision from the financial perspective is to transfer the used shovel rather than buying a new one at year 1.

Technical comparison

After discovering that the transfer option is the best decision from the financial side, it must be evaluated if there are any technical issues that could represent a problem to implement this scenario.

1. Safety – The maintenance department of the company has conducted a thorough analysis of the structural integrity of the equipment and have not found any safety issue on it.
2. Emissions – Both alternatives consider equipment with electrical powertrains. Therefore, there is a draw for this criterion.
3. Availability – Figure 3 simulates the forecasted physical availability for the brand-new excavator versus a shovel with five years of operation.

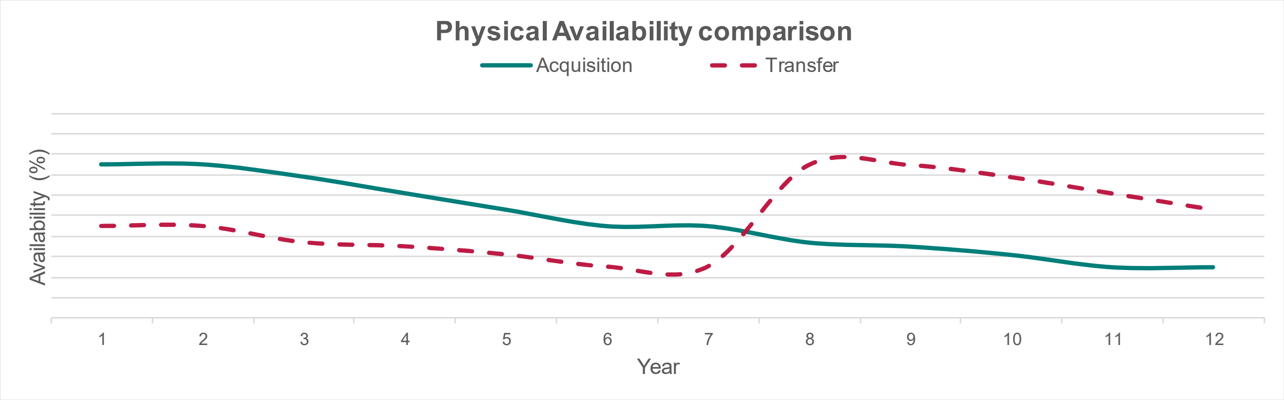

FIG 3 – Availability comparison between the alternatives.

The exhibit above shows that there will be a lower availability of the already owned equipment during the next seven years of operation. After this period, the machine is replaced by a new one and this equipment increases the reliability. The long-term mine planning department has simulated the entire cycle and concluded that the rest of the loading fleet could handle this reliability difference.

- Fleet standardisation – The mining site analysed already have excavators from the same model evaluated. Therefore, both alternatives did not represent any additional complexity for the operations and maintenance processes or increase on spare parts.
- Productivity – Although both scenarios were comparing the same shovel model and in theory, they would have the same productivity, as the already owned machine has a lower reliability, it would also have a lower productivity on the next years. Thus, the long-term mine planning team has simulated the entire cycle and concluded that the rest of the fleet could handle this productivity gap.
- Load and haul match – The haulage trucks used on the analysed mine site were proper for the size of the assessed excavators.

Table 1 summarises the advantages and disadvantages of both alternatives.

TABLE 1

Alternatives advantages and disadvantages summary.

	Transfer already owned equipment	**Acquisition of a new equipment**
Advantages	Better NPV Lower CAPEX Usage optimisation of already owned shovel	Higher reliability Higher technology
Disadvantages	Lower reliability Lower technology	Worst NPV Higher CAPEX Loss of tax refund of the salvage value

Limitations

The main limitation of the current method is that it does not consider the impact of inflation on it. To embed the inflation, it would be necessary to consider a heterogeneous inflation because in the analysis there are cash flows spent in dollars and others in the Brazilian currency, from very different categories, such as considering expenses with maintenance costs and services for seaborne freight.

Another limitation is that the proposed methodology does not consider carbon credits on it. It does not impact the presented case study, as both alternatives evaluated are electrical equipment. This limitation is already under development to be fixed.

CONCLUSIONS

Uncertainties are inherent to any mining operation. Those risks can materialise from both internal and external factors and they impact the process to plan and size the fleet of mining equipment. Under those circumstances, transferring already owned machines that are idle can be a great tool to increase planning flexibility on large mining companies with several sites. To provide the right data for decision-making, it must be considered both the financial and technical topics of the available scenarios. From the financial side, the net present value is the recommended figure of merit to use, as the options can be considered mutually exclusive investments. From the technical perspective, several criteria should be analysed, such as safety, emissions and reliability.

Another interesting strategy is to keep some backup equipment to absorb impacts of low likelihood and high consequence risks that may occur. As an example of this kind of risk, suppose that iron ore is currently exchanged in a very high price and an ongoing environmental licence gets approved faster than expected. In that situation, it would be very hard to react and seize the opportunity to increase the production plan without any backup equipment, as the lead times to purchase a brand-new large mining equipment and make it ready to work is quite long and the process to outsource this kind of machinery is not fast as well. In the other hand, keeping backup equipment provides the disadvantage to increase the costs of the operation and may never be necessary to be used.

ACKNOWLEDGEMENTS

The author is thankful to Vale S.A for supporting and funding this article. The author also thanks Marcos Cunha, Breno Cardozo and the entire long-term mine planning department for the support.

REFERENCES

Higgins, R C, 2012. *Analysis for Financial Management*, 10th edition, pp 247–287 (McGraw-Hill Irwin).

Lanke, A A, Ghodarati, B and Hoseinie, S H, 2016. Uncertainty analysis of production in open pit mines – Operational parameter regression analysis of mining machinery, *Mining Science*, 23:147–160.

Maravas, A and Pantouvakis, J P, 2018. A new approach to studying Net Present Value and the Internal Rate of Return of engineering projects under uncertainty with Three-Dimensional Graphs, *Advances in Civil Engineering*, vol 2018.

Walker, W E, Harremöes, P, Rotmans, J, Van Der Sluijs, J P, Van Asselt, M B A, Janssen, P and Krayer von Krauss, M P, 2003. Defining uncertainty – a conceptual basis ofr uncertainty management in Model-Based decision support, *Integrated Assessment Journal*, 4(1):5–17.

New equipment and processes

Development of a rail-running pipe conveyor for the iron ore industry

M Carr[1], C Wheeler[2], M Lurie[3] and B Chen[4]

1. Senior Mechanical Design Engineer, Centre for Bulk Solids and Particulate Technologies (CBSPT), Newcastle Institute for Energy and Resources, The University of Newcastle, Callaghan NSW 2308. Email: michael.j.carr@newcastle.edu.au
2. Associate Director, Centre for Bulk Solids and Particulate Technologies (CBSPT), Newcastle Institute for Energy and Resources, The University of Newcastle, Callaghan NSW 2308. Email: craig.wheeler@newcastle.edu.au
3. Global Technology, Innovation and Sustainability Manager – Conveyors, thyssenkrupp Industrial Solutions (USA) Inc., Greater Denver Area, Colorado, United States. Email: martin.lurie@thyssenkrupp.com
4. Engineering Manager, TUNRA Bulk Solids, Newcastle Institute for Energy and Resources, The University of Newcastle, Callaghan NSW 2308. Email: bin.chen@newcastle.edu.au

ABSTRACT

The demand for steel products in modern society is prompting the iron ore industry to optimise their operations to ensure sustainability of fines and lump products. One of the key components in the iron ore transportation chain are belt conveyors. The energy consumption of modern belt conveyor systems has reduced considerably over the past few decades, however, there is still significant scope for further reductions, especially when heavily loaded long overland belt conveyors are considered. A new rail based continuous bulk material transportation system has been developed by researchers at the University of Newcastle to reduce the energy consumption of heavily loaded and long overland conveyors. The Rail-Running Belt Conveyor technology is a state-of-the-art continuous belt conveying technology which provides an innovative and novel departure from conventional continuous bulk material transportation systems with significant energy and economic benefits.

This paper presents an overview of a Rail-Running Belt Conveyor variant which considers an enclosed belt. Enclosed belt conveying has the benefits of encapsulating the bulk material, and thereby reducing dust emissions and moisture ingress, in addition to being able to negotiate smaller radius horizontal and vertical curves leading to greater flexibility. To quantify the primary differences between conventional conveying technologies, the Denver office of thyssenkrupp Industrial Solutions (USA) developed a case study for an 11 km long conveyor. The conveyor design throughput was 2750 t/h and included a small net elevation loss of 10 m. When considering CAPEX the Rail-Running Pipe Conveyor equipment supply cost is approximately 45 per cent of the cost of a conventional pipe conveyor, while savings upwards of US$50M emerge for CAPEX combined with five years of OPEX. The savings vary with the topography and density of the bulk commodity, with iron ore generally showing increased savings because the high bulk density increases rubber losses in conventional conveyors.

INTRODUCTION

With increasing pressure on the mining industry to reduce dust emissions (ie the introduction of the new exposure standard for respirable coal dust to 1.5 mg/m^3 from February 2021) (Resources Regulator – NSW Government, 2020) and minimise the cost of transporting products and overburden, new continuous overland transport technologies that fully encapsulate the bulk material need to be developed. Furthermore, there is a need to ensure new transport technologies are flexible in terms of routing and able to negotiate small radius horizontal and vertical curves to reduce the need for transfer points and be able to convey up steeper inclines for potential out of pit transport. While these advantages are achievable, at least to certain degrees with conventional pipe conveyor technology, their application in the Australian mining industry has not eventuated. Despite the significant advantages offered by pipe conveyors their lack of uptake in Australia is primarily due to limitations in throughput and high-power consumption, in addition to their increased cost over conventional troughed belt conveyors.

The significant role belt conveying systems have, and will continue to play, in the iron ore industry is of critical importance. Belt conveyors are by far the most widespread bulk material transportation system used across the mining, mineral processing and power generation industries. Their continuous mode of operation makes them highly desirable for automated mining activities and this continues to drive the technology towards higher capacities and longer transportation distances. Although belt conveyors have significant benefits for automated processes in comparison to alternative technologies such as haul trucks, they still require significant amounts of energy for their operation. The need for reduced energy requirements in the iron ore mining sector is critical when global power demands and the profitability of iron ore mining operations are considered. For example, it is estimated that approximately 23 per cent of the total operating cost for a typical South African mine will be attributed to electricity costs by 2020 (Van der Zee, Pelzer and Marias, 2013). Furthermore, the current initiative for 'green' renewable energy sources will have an increased focus on energy efficient systems as to successfully maintain the supply and demand that the non-renewable fossil fuels currently maintain.

The ongoing development of conventional troughed belt conveyors has been driven by the demand for longer more heavily loaded overland belt conveying systems. The necessity of longer systems will have a resulting increase in belt tension which in effect will also have an associated increase in the energy requirements and demand power of the system. The energy efficiency of belt conveyors can be typically improved through proper equipment selection (Xia and Zhang, 2010). Zhang and Xia (2011) found that the majority of the published literature for the improvement of the energy efficiency of belt conveyors focused on the potential to improve either the operation or equipment of the system, for example the development of low energy idler rolls and specialised low rolling resistant belt compounds (Jansen, 2008). Even with these improvements in mind, the limitations for conventional belt conveyors is the interaction between the rubber covered belt and idler rolls, meaning the efficiency of railway transportation with rolling efficiencies of 0.001 to 0.002 (Saxby and Elkink, 2010), will never be matched by systems supported by conventional idler rolls. With these limitations in mind and to consider the energy efficiency of belt conveyors from a technology optimisation viewpoint, a new rail based continuous bulk material transportation system has been developed by researchers at the University of Newcastle (Wheeler, 2012) to reduce the energy requirements of heavily loaded and long overland belt conveyors. The new technology is aptly named the Rail-Running Belt Conveyor (RRBC) due to its combination of two well-established transportation technologies. The RRBC technology provides an innovative and novel departure from conventional continuous bulk material transportation systems with significant energy and economic benefits.

This paper outlines a new Rail-Running Pipe Conveyor system (Wheeler, Carr and Chen, 2018) that will retain the benefits of existing pipe conveyor technology at significantly lower capital and operating costs, coupled with greater throughput and transport distance capability. These benefits are achievable through increased conveying speeds and reduced motion resistances due to the benefits of supporting the belt by carriages running on rail as opposed to conventional idler rolls. The paper builds upon the novel underlying conveying technology known as the Rail-Running Belt Conveyor. Figure 1 illustrates the troughed RRBC technology that will be adapted to fully enclose the bulk material being transported. Detailed cost analysis indicates combined CAPEX and OPEX savings in the order of 35 to 50 per cent, with OPEX cost savings typically in the order of 50 per cent due to much lower power consumption, with negligible variation between cold and warm conditions because of the elimination of viscoelastic conveyor belt losses.

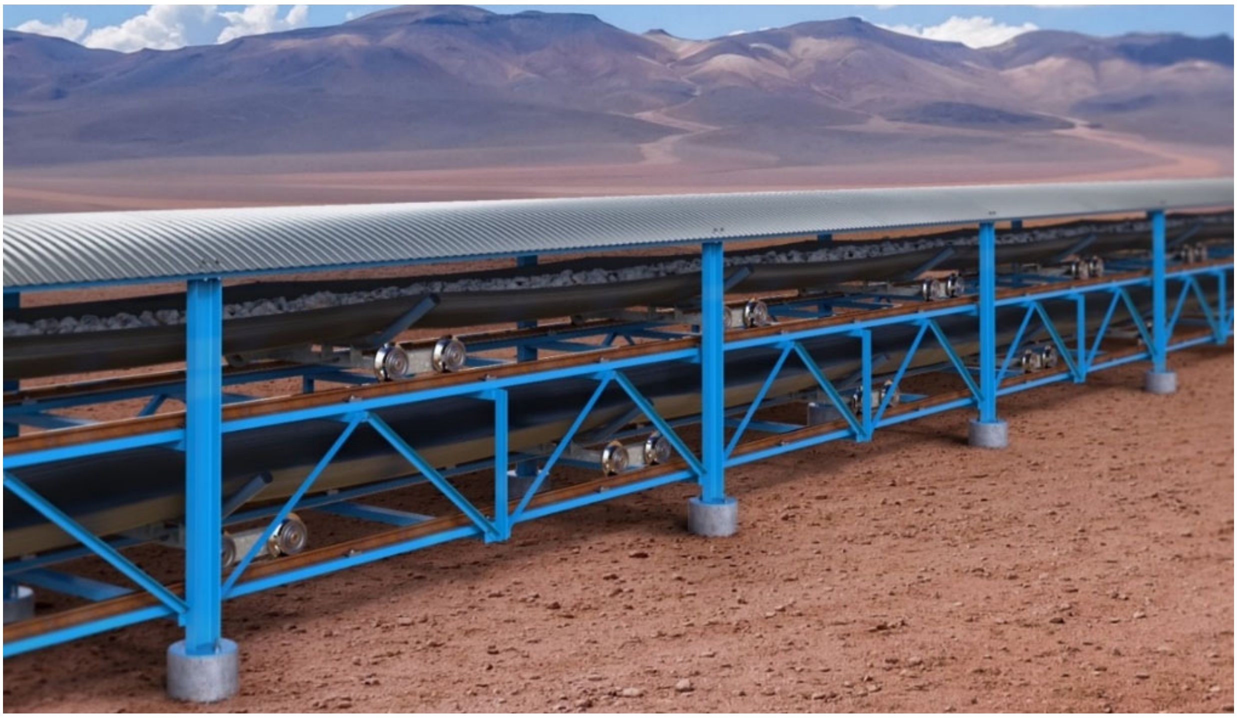

FIG 1 – Rail-Running Belt Conveyor technology.

BACKGROUND

Rail-Running Belt Conveyor technology

The Rail-Running Belt Conveyor technology is a state-of-the-art continuous belt conveying technology that was developed by researchers at the University of Newcastle and licenced globally by thyssenkrupp Industrial Solutions. The RRBC is a novel invention that combines the primary advantages of both belt conveyors and railway systems. The RRBC, illustrated in Figure 2, is a continuous bulk material transportation system that due to steel track wheels running on steel rails shares a rolling resistance similar in magnitude to rail transport, with laboratory tests demonstrating rolling friction values in the range of 0.003 to 0.005, ie less than half of the world's best performing overland belt conveyors. Combining the low rolling resistance benefits of rail with the relatively lightweight nature and continuous operational benefits of belt conveyors is the novel aspect of this invention.

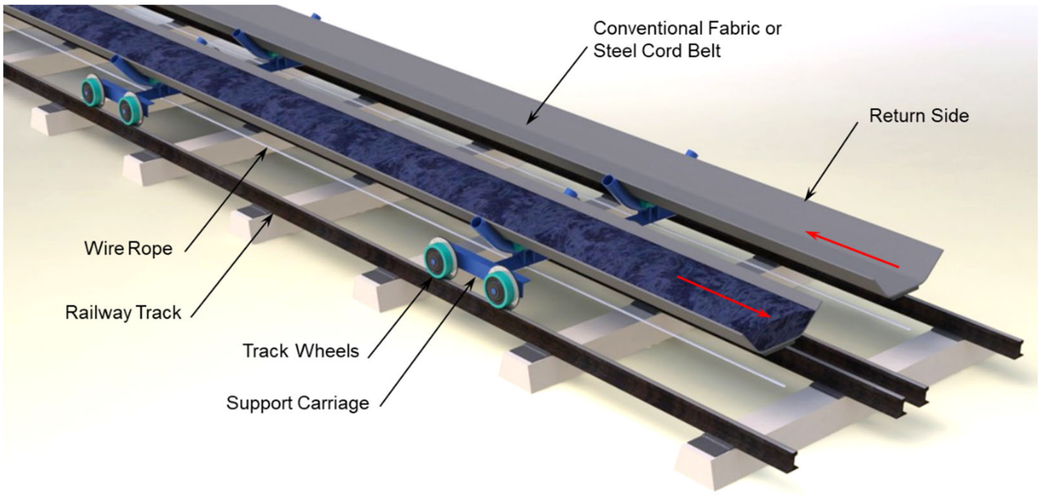

FIG 2 – Rail-Running Belt Conveyor concept (Wheeler, 2017).

Like a conventional belt conveyor, the bulk material being transported by the RRBC is supported by a conveyor belt that is driven by one or more localised drive pulleys, however, rather than being supported by idler rolls the belt is supported by a series of linked carriages. The carriages utilise steel or nylon track wheels that run along light gauge steel railway tracks. The belt is not physically fixed to the support carriages, but drives each carriage by friction developed between the belt and the carriage yoke. The support carriages are attached to an endless wire rope and equally spaced along the length of the system. The support carriages follow a continuous path around the conveying system, supporting the bulk material and belt along the carry side, and the belt on the return side. The system is able to be configured in a side-by-side configuration (as shown in Figure 2), or alternatively, the carry side can be positioned directly above the return side (as shown in Figure 1) to reduce the footprint of the system.

The conveyor belt is driven using conventional belt conveyor technology, incorporating single or dual drive pulleys and a take-up system. The support carriages support the belt until just prior to the discharge point, where the belt then lifts off the carriages and is supported by conventional troughed idler rolls. Bulk material is discharged in the same manner as a conventional belt conveyor, with the belt traveling around a head pulley and belt take-up (tensioning) system before being inverted 180° and guided back on to the support carriages for the return side run. The carriages are able to be turned around at each end using a horizontal turnaround loop as shown in Figure 3, or alternatively, a vertical turnaround wheel as shown in Figure 4. The turnaround systems not only redirect the carriages, but also act as take-up systems for the carriages to allow for the differential stretch between the belt and the cable.

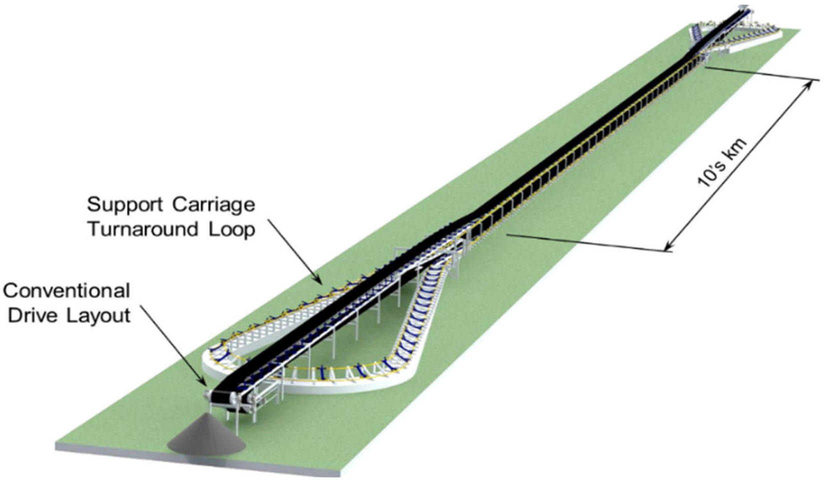

FIG 3 – Horizontal carriage turnaround (Wheeler, 2017).

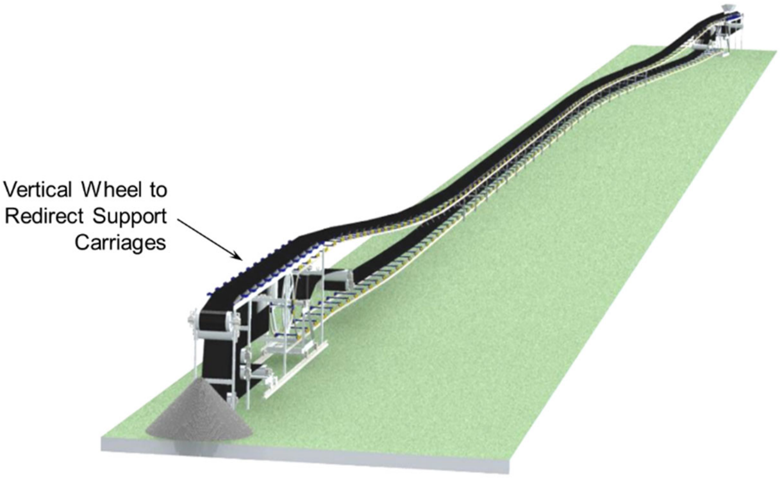

FIG 4 – Vertical carriage turnaround (Wheeler, 2017).

The primary advantage of the RRBC system is that the major resistance components in a belt conveyor are eliminated. Since the belt rests on the support carriages during transportation there is no relative movement between the carriages and the belt, and therefore no indentation rolling resistance or belt and bulk material flexure resistance. The only resistances to motion of the new technology are the rotating resistance and rolling friction of the track wheels, leading to a highly efficient transportation system akin to rail (Carr *et al*, 2020). Figure 5 shows a demonstration RRBC system that is successfully operating in China. The system is 150 m long, has a belt width of 1.2 m and operates at 4 m/s, providing an ideal full-scale test facility.

FIG 5 – Demonstration system operating in China (Wheeler, Carr and Chen, 2017).

To prove the commercial viability of the system, detailed economic modelling of the system has been undertaken in collaboration with thyssenkrupp Industrial Solutions in Germany and the United States, and involved analysing a number of typical long overland conveyors. A case study which explores the characteristics of RRBCs in the context of a long, high-tonnage overland conveyor for iron ore, we sought a potential haulage in the Pilbara that would be too short for heavy rail to be economical, yet beyond the typical length for a conventional high-tonnage overland conveyor. We found such a situation at a mine site whose remote ore deposits are located some 30 km away from the Phase I plant. This is a situation that may quite frequently pertain at iron-ore operations around the world.

The mine tenement that we selected for this study extends onto the alluvial plain of the Fortescue River Valley. This plain provides an attractive path for belt conveyors because of the relatively flat terrain. Though the hills abutting the valley would provide a more direct route, the topography over the hills is much more challenging and the conveyor could interfere with future pit locations. A Google Earth view in Figure 6 shows that the 30 km path requires only large-radius horizontal curves, which are within the curvability of conventional trough conveyors. In Figure 6, the tail of the conveyor is at the left, with the head and the existing processing plant and pit at the right of the frame.

FIG 6 – Google Earth view showing path of 30 km conveyor.

The route traverses a total of approximately 1200 m of flooding channels where we have allowed for elevated structure. This alignment has negligible natural lift between tail and head, but – as would be typical in such applications – the conveyor is arranged to discharge onto a coarse-ore stockpile about 40 m above grade. We selected an operating tonnage of 7500 Mt/h, which would represent the ROM output from a large Pilbara pit. This would give an annual tonnage on the conveyor system of approximately 50 Mt.

A conventional trough conveyor could certainly offer an attractive solution for this duty. The conventional trough conveyor configuration chosen for this study uses a single belt running the full 30 km length, but with a pair of intermediate tripper drives at about two-thirds of the distance from the tail. Such an arrangement reduces the required belt strength to a comfortable ST5000 grade, and the belt-to-belt transfer has advantages with respect to reducing some of the disadvantages of a transfer point. In addition to the intermediate, another two drives at the head and one at the tail give a balanced tension distribution. The total installed power for the conventional trough conveyor outlined above is 18 000 kW. With up to 7200 kW at each drive location, gearless drives would be an attractive – though initially more expensive choice. However, the RRBC for duty requires only 5000 kW of installed drives, so for consistency in comparisons, we chose conventional geared drives for both conveyor types.

Deploying a Rail-Running Belt Conveyor along this route in a Pilbara location means that some conditions increase the differentiation of the new technology compared to standard conveyors, and other conditions reduce the differentiation. It is worth listing these effects.

Conditions that *increase* RRBC differentiation:

- High labour costs in the Pilbara, because the RRBC does not have an intermediate transfer point or idlers that must be inspected and replaced along a 30 km route.
- High power costs play to the RRBC's characteristic of very low frictional losses.
- High tonnage and high ore density produce high rubber hysteresis losses in conventional belt conveyors, but increase the rolling efficiency of the RRBC wheel-on-rail arrangement.
- The relatively small elevation change from tail to head means that most of the power requirement is for losses rather than lift, and this also favours the RRBC technology.

Conditions that *reduce* RRBC differentiation in this case:

- We have taken an aggressively low-friction in design choices for the conventional conveyor, assuming best-in-class components and construction accuracy.
- The route and terrain do not give an advantage for the tight vertical and horizontal curvability that the RRBC can allow.
- There are no significant valleys where the RRBC's tight concave curves would lead to less elevated structure.
- Similarly, the flat terrain in the alluvial plain does not require significant cut-and-fill volumes for the conventional option, which would be significantly reduced for the RRBC.
- The hot ambient temperatures of the Pilbara minimise the rubber hysteresis losses of the conventional belt/idler interaction – cold or very cold temperatures would sharply increase these losses for the conventional conveyor, but the RRBC is essentially unaffected by ambient temperature.
- The RRBC requires drive power to be supplied only at the head of the conveyor – where power is already available – in contrast to the mid and tail drive locations for the conventional option. But for a remote pit as contemplated here, a power line would in any case have to be run to the tail of the conveyor to feed the ROM crusher. Therefore, the power line savings are less significant than cases where a line must be run solely for a remote drive.

Since both the conventional and RRBC options would discharge off a large stacker structure, that structural cost is included in the estimate shown in Table 1. However, the head pulley resultant for the RRBC is only about half the magnitude of that for the conventional option, so the substantial stacker structural weight and cost is likely to be about one third lower than the conventional case. One interesting technical result from the study is that stopping time for the RRBC when applying a modest tail brake is somewhat under three minutes, perhaps shorter than would have been expected with such low friction and high inertia from the moving load.

TABLE 1

Cost comparison for 30 km long iron ore conveyors.

	Units	**Belt Conveyor / Rail-Running Belt Conveyor**	
Design Capacity	mtph	7500	
System	-	***Conventional Troughed Conv.***	***Rail-Running Belt Conveyor***
Warm Season Temp.	°C	30	30
Cool Season Temp. (For Belt Strength)	°C	8	8
Coldest Temp. (For Installed Power)	°C	0	0
Lift	m	65	65
Belt, ST Rating	-	5000	2800
Belt Width	mm	1400	1200
DIN f Equivalent – Warm Season	-	0.0120	0.0025
DIN f Equivalent – Cool Season	-	0.0135	0.0025
DIN f Equivalent – Coldest Operating Temp., High Drag	-	0.0152	0.003
Total Installed Power	kW	18 000	5000
Head Drives	kW	4 × 1800	2 × 2500
Intermediate Tripper Drives	kW	4 × 1800	none
Tail Drives	kW	2 × 1800	none
Power at Design Tonnage, Warm Season	kW	14 900	4010
Power at Design Tonnage, Cool Season	kW	16 600	4010
Power Running Empty, Warm Season	kW	5800	1100

For both conveyor technologies, we have taken construction costs as a percentage of the equipment design/supply price. We have not included earthworks and civils costs, but for this route those costs would be quite similar between the two options. The quantitative results of this case study are shown in Table 1 and Figure 7. For this long, demanding conveyor duty the Rail-Running Belt Conveyor shows very substantial CAPEX and OPEX advantages. This RRBC example uses less power (4000 kW) at design capacity than the power drawn by the empty conventional conveyor (5800 kW). This is an interesting feature of the RRBC technology that emerges in many cases for long, flat overland routes.

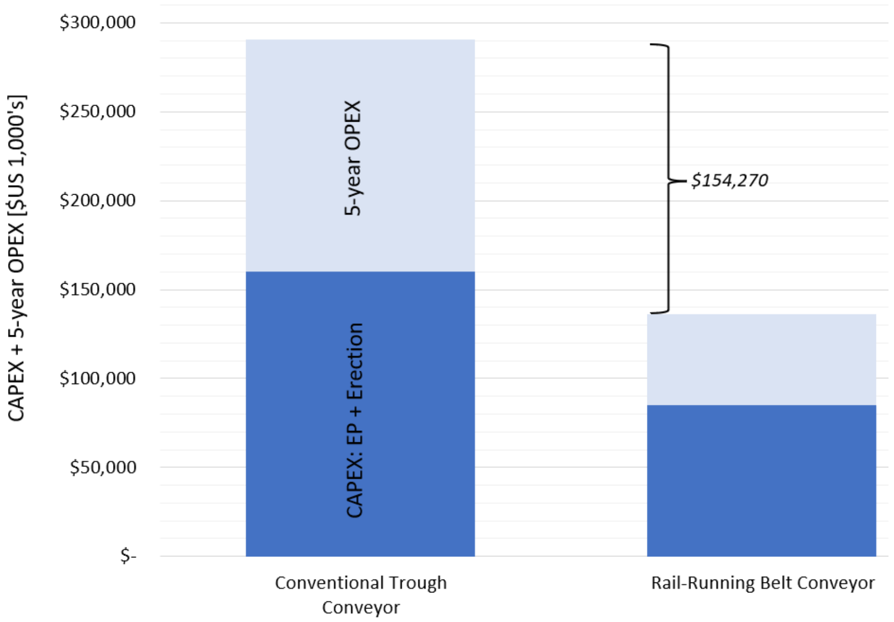

FIG 7 – CAPEX +5year OPEX: 30 km long Conventional Troughed Belt versus Rail-Running Belt Conveyor.

Conventional pipe conveyors

Enclosed belt conveying has the benefits of encapsulating the bulk material, and thereby reducing dust emissions and moisture ingress, in addition to being able to negotiate smaller radius horizontal and vertical curves leading to greater flexibility. Pipe conveyors are the most widely implemented of all enclosed belt conveying technologies and are used extensively throughout the world. They are ideally suited to transporting bulk materials in environmentally sensitive areas where dust and spillage cannot be tolerated, handling bulk materials that must not be contaminated (ie cement, fertiliser etc) or where the conveyor is required to negotiate small radius horizontal curves and/or convey up or down greater angles than troughed belt conveyors. Figures 8 and 9 show a typical pipe conveyor system and cross-sectional profile, while Figures 10 and 11 show the ability of pipe conveyors to negotiate very small radius horizontal and vertical curves, in addition to being able to transport over long distances.

FIG 8 – Conventional pipe conveyor system (Shanghai Ku Qiao Equipment Co., Ltd., 2019).

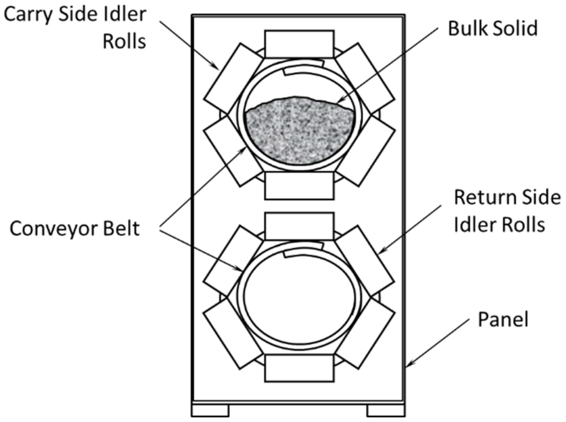

FIG 9 – Cross-section of a pipe conveyor.

FIG 10 – Long overland pipe conveyor (Slurry Master, 2019).

FIG 11 – Tightly curved pipe conveyor (Sdzhongxin, 2019).

Pipe conveyor technology is used extensively throughout the world to ensure mining companies meet stringent safety and environment regulations that dictate the maximum concentration of dust particles in the air. Often these strict safety and environmental limits can only be met with the use of fully enclosed belt conveyor systems that completely eliminate spillage and dust emissions along the transport corridor.

While pipe conveyors have many benefits, they also have several significant drawbacks. The major disadvantages of pipe conveyors compared to conventional troughed belt conveyors are that they are significantly more expensive to build and operate. Pipe conveyors exhibit greater motion resistances due to additional resistances to form and maintain the belt in the pipe shape. This leads to greater motion resistances, and therefore increased belt tensions that requires larger pulleys, drives, take-ups and increased structural requirements. The drawbacks of conventional pipe conveyor technology may be further categorised as follows:

- Very unpredictable and time-varying frictional resistance that often leads Original Equipment Manufacturer (OEM)s to install additional 'redundant' drives as insurance. Overall frictional resistance of conventional pipe conveyors is highly sensitive to:
  - Belt Indentation Rolling Resistance (IRR) through the range of operating temperatures at a particular location. IRR can only accurately be determined through full-scale tests with about fifteen metres of sample belt from the selected manufacturer, which is rarely available at the design stage.
  - Belt transverse stiffness, which varies with belt construction, pipe diameter, ambient temperature and stage of belt 'break-in'.
  - Idler radial misalignment, which determines the degree of flexing imposed on the belt as it passes through each idler station.
  - Idler angular misalignment, which determines the amount of sliding friction between the belt and idlers: the coefficient of friction itself varies significantly between wet and dry conditions.
  - Idler seal friction that makes up a substantial part of the overall resistance: pipe conveyors typically have about 85 per cent more idler rolls per unit length than conventional trough conveyors, so as-built performance is more sensitive to variations from the friction values assumed during design.
  - Losses as the belt presses against idlers in each horizontal or vertical curve: designers seldom have adequate models or enough data to predict this large component of resistance.
- Instability of the pipe form through horizontal curves and over time:
  - The upper portions of a pipe belt may lose contact with the upper or lateral idler rolls if the belt does not have sufficient transverse stiffness, either initially or as a result of stiffness loss over time. This can allow the pipe overlap to turn upside-down in curves, which in turn can cause spillage and serious damage to the belt at the opening station.
- High tensions and special procedures required to install a new belt, because of the resistance in drawing a new, stiff belt through multiple idler stations.

Rail-running pipe conveyor technology

To overcome the disadvantages of existing pipe conveyor systems a Rail-Running Pipe Conveyor system has been developed at the University of Newcastle (Wheeler, Carr and Chen, 2018) in association with thyssenkrupp Industrial Solutions. The Rail-Running Pipe Conveyor system is shown diagrammatically in Figures 12 and 13, and is an extension to the existing Rail-Running Belt Conveyor technology, utilising support carriages to support a belt formed into a pipe shape, effectively encapsulating the bulk material.

The new Rail-Running Pipe Conveyor technology will have the benefits of existing pipe conveyor technology at lower capital and operating cost. These cost savings are achievable due to the reduced motion resistances resulting from the benefits of supporting the belt by carriages running on rail as opposed to conventional idler rolls. Figures 14 to 16 show the 15 m long laboratory demonstration 1:10 scale model which is a test system that has been developed at the University of Newcastle to prove the concept and investigate the minimum radii of horizontal and vertical curves.

FIG 12 – Proposed rail-running pipe conveyor system.

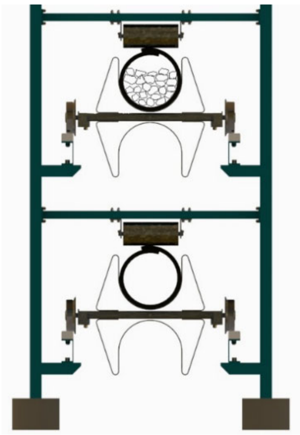

FIG 13 – Cross-section view.

FIG 14 – Rail-running pipe conveyor scale model.

FIG 15 – Tail-end loading point.

FIG 16 – Curvability capability.

Cost analysis for new rail-running pipe conveyor technology

To quantify the primary CAPEX and OPEX differences, the Denver office of thyssenkrupp Industrial Solutions (USA) developed case studies for 1.3 km and 11 km long conveyors operating in the Hunter Valley. The Denver office specialises in long overland and heavy-duty conveyors. Tables 2 and 3 show detailed cost comparisons for each of the respective conveyors outlined above, where all figures are shown in US$1000s.

The first case study considers a 1.3 km coal conveyor operating at a tonnage of 1800 Mt/h. The conveyor alignment included a small net elevation gain of 16 m. The range of operating temperatures were taken as 30°C for the warm season, and 8°C for the cool periods that determine selection of belt fatigue strength (this was considered for both case studies). Table 2 shows the specifications for the 1.3 km long coal conveyor for a conventional troughed conveyor, conventional pipe conveyor and a Rail-Running Pipe Conveyor. When considering CAPEX it can be shown that the Rail-Running Pipe Conveyor cost 59 per cent of the cost of a conventional pipe conveyor, while a saving of $5.7M can be made when considering the CAPEX in addition to five-years OPEX, as shown in Figure 17a.

The second case study considers a 11 km coal conveyor operating at a tonnage of 2750 Mt/h. The conveyor alignment included a small net elevation loss of 10 m. Table 3 shows the specifications for the 11 km long coal conveyor for a conventional troughed conveyor, conventional pipe conveyor and a Rail-Running Pipe Conveyor. When considering CAPEX it can be shown that the Rail-Running Pipe Conveyor cost only 44 per cent of the cost of a conventional pipe conveyor, while a saving of $59.4 M can be made when considering the CAPEX in addition to five-years OPEX, as shown in Figure 17b. A further, and very important observation from both case studies, is that the Rail-Running Pipe Conveyor is less expensive than the conventional trough conveyor in terms of both CAPEX and OPEX.

TABLE 2
Cost comparison for 1.3 km long coal conveyors.

	Units	**Belt Conveyor / Rail Conveyor**		
Design Capacity	mtph	1800		
System	-	***Conventional Troughed Conv.***	***Conventional Pipe Conveyor***	***Rail-Running Pipe Conveyor***
Warm Season Temp.	°C	30	30	30
Cool Season Temp. (For Belt Strength)	°C	8	8	8
Coldest Temp. (For Installed Power)	°C	0	0	0
Lift	m	16	16	16
Belt, ST Rating	-	800	630	500
Belt Width	mm	1400	2250	1800
DIN f Equivalent – Warm Season	-	0.016	0.027	0.003
DIN f Equivalent – Cool Season	-	0.020	0.032	0.003
DIN f Equivalent – Coldest Operating Temp., High Drag	-	0.020	0.032	0.005
Total Installed Power	kW	600	800	400
Head Drives	-	2	2	1
Tail Drives	-	0	0	0
Power at Design Tonnage, Warm Season	kW	295	504	200
Power at Design Tonnage, Cool Season	kW	305	600	200

TABLE 3

Cost comparison for 11 km long coal conveyors.

	Units	Belt Conveyor / Rail Conveyor		
Design Capacity	mtph	2.750		
System	-	***Conventional Troughed Conv.***	***Conventional Pipe Conveyor***	***Rail-Running Pipe Conveyor***
Warm Season Temp.	°C	30	30	30
Cool Season Temp. (For Belt Strength)	°C	8	8	8
Coldest Temp. (For Installed Power)	°C	-5	-5	-5
Lift	m	-10	-10	-10
Belt, ST Rating	-	2000 LRR	1800 LRR	630
Belt Width/Diameter	mm	1350	2200/600	1850/500
DIN f Equivalent – Warm Season	-	0.010	0.021	0.003
DIN f Equivalent – Cool Season	-	0.011	0.023	0.003
DIN f Equivalent – Coldest Operating Temp., High Drag	-	0.013	0.027	0.005
Total Installed Power	kW	2500	6750	900
Head Drives	-	2	2	2
Tail Drives	-	0	1	0
Power at Design Tonnage, Warm Season	kW	1642	3800	495
Power at Design Tonnage, Cool Season	kW	1805	4185	495

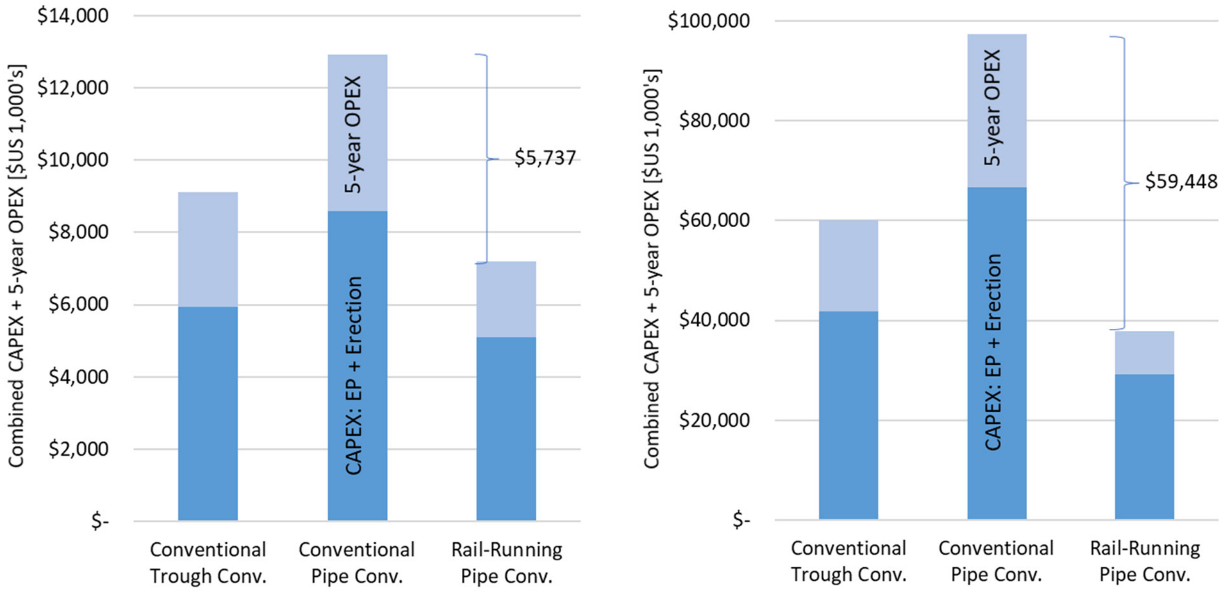

(a) (b)

FIG 17 – CAPEX +5-year OPEX cost comparisons: (a) 1.3 km long coal conveyors; (b) 11 km long coal conveyors.

CONCLUSIONS

This paper has presented a comparison between the Rail-Running Pipe Conveyor system and conventional belt conveyors. The energy consumption of the Rail-Running Pipe Conveyor system was shown to be significantly lower in comparison to conventional belt conveyors. The frictional resistances of both the Rail-Running Belt Conveyor system and conventional belt conveyors can be directly compared when the friction factor of each system is considered. Due to the effective elimination of the indentation rolling resistance and belt and bulk material flexure resistance within the Rail-Running Belt Conveyor system, an approximate reduction of 50 per cent or even greater in energy consumption and cost savings can be achieved. Furthermore, this leads to the reduction in belt tension and therefore capital cost for the Rail-Running Pipe Conveyor system which has been detailed in the presented case study. The cost analysis of the Rail-Running Pipe Conveyor system has been presented where a reduction of approximately 44 per cent in CAPEX and an annual reduction of 28 per cent in OPEX for a 11 km system operating in the Hunter Valley was found when compared to conventional belt conveyors. A further, and very important observation from both case studies, is that the Rail-Running Pipe Conveyor is less expensive than the conventional trough conveyor in terms of both CAPEX and OPEX.

REFERENCES

Carr, M J, Wheeler, C A, Robinson, P W and Chen, B, 2020. Reducing the Energy Intensity of Overland Conveying using a Novel Rail-Running Conveyor System, *International Journal of Mining, Reclamation and Environment,* doi: 10.1080/17480930.2020.1788199

Jansen, M, 2008. The Development of Energy-Optimized Conveyor Belts – A Joint Project of the Conveyor Belt Group of ContiTech AG and RWE Power AG, *World Min*, 60(2):83–7.

Resources Regulator – NSW Government, 2020. Airborne Contaminants and Dust. <https://www.resourcesregulator.nsw.gov.au/safety-and-health/topics/airborne-contaminants-and-dust>. Retrieved 12 December 2020.

Saxby, P and Elkink, J, 2010. Material Transportation in Mining – Trends in Equipment Development and Selection, *Australian Bulk Handling Review*, 15(2):10–14.

Sdzhongxin, 2019. Material Handling Curve Belt Conveyor Pipe Conveyor. <http://www.sdzhongxin.com>. Retrieved 12 March 2021.

Shanghai Ku Qiao Equipment Co., Ltd., 2019. Material Handling Curve Belt Conveyor Pipe Conveyor. <https://ske-slss201911.en.made-in-china.com/product/PZKJpTLyJnhr/China-Ske-Material-Handling-Curve-Belt-Conveyor-Pipe-Conveyor.html>. Retrieved 12 March 2021.

Slurry Master, 2019. Conveyor Products. <http://slurrymaster.co.za/_Documents/Conveyor.pdf>. Retrieved 12 March 2021.

Van der Zee, L F, Pelzer, R and Marais, J H, 2013. The Combined Cost Effect of Carbon Tax, ECS and MYPD3 Tariffs on the Gold Mining Industry of South Africa, in *Proceedings Industrial and Commercial Use of Energy Conference (ICUE)*.

Wheeler, C A, 2012. Rail Conveyor System – International Patent Number; WO 2012/009765 A1, Filed 26 Jan 2012.

Wheeler, C A, 2017. Development of the Rail Conveyor Technology, *International Journal of Mining, Reclamation and Environment,* doi: 10.1080/17480930.2017.1352058

Wheeler, C A, Carr, M J and Chen, B, 2017. The Rail Conveyor – A New Energy Efficient Conveying Technology. *In Proc. Beltcon 19*. IMHC: South Africa.

Wheeler, C A, Carr, M J and Chen, B, 2018. Enclosed Belt Rail Conveyor System – International Patent Number; WO 2019/079859 A1, Filed 26 Oct 2018.

Xia, X and Zhang, J, 2010. Control Systems and Energy Efficiency from the POET Perspective, in *IFAC Conference on Control Methodologies and Technology for Energy Efficiency*.

Zhang, S and Xia, X, 2011. Modeling and Energy Efficiency Optimization of Belt Conveyors, *Applied Energy*, 88(9):3061–3071. doi:10.1016/j.apenergy.2011.03.015

Development of a remotely operated robotic mechanism for accessing and removal of metal tramp from primary gyratory crushers

R Costa[1], A Alves[2], L Ono[3], E Nunes[4], D Jacobson[5], H Lemos[6] and H Delboni Jr[7]

1. Engineer – Service Product Support, Metso Outotec, Sorocaba-SP, Brazil 18087–101. Email: rogerio.costa@mogroup.com
2. Coordinator – Technical Sales Support, Metso Outotec, Sorocaba-SP, Brazil 18087–101. Email: augusto.alves@mogroup.com
3. Application Engineer – Crushing Systems, Metso Outotec, Sorocaba-SP, Brazil 18087–101. Email: lucas.ono@mogrouppartners.com
4. Application Manager – Crushing Systems, Metso Outotec, Sorocaba-SP, Brazil 18087–101. Email: edis.nunes@mogroup.com
5. Director of Process Engineering – Crushing Systems, Metso Outotec, Waukesha, USA WI-53186. Email: dusty.jacobson@mogroup.com
6. Manager – Service Technical Support, Metso Outotec, Sorocaba-SP, Brazil 18087–101. Email: hugo.lemos@mogroup.com
7. Professor – Department of Mining and Petroleum Engineering, University of São Paulo, São Paulo-SP, Brazil 05508–030. Email: hdelboni@usp.br

ABSTRACT

Oversize rock breaking and metal tramp removal are key issues for reducing primary crusher downtime, as well as improving the safety associated with its operation. Remote operation of such tasks would thus not only increase productivity, but also reduce the risks related to work in confined spaces, fall risks, and overhead hazards. These issues are particularly relevant in high-capacity operations such as iron ore mining, where large machines are in continuous operation. This article describes the architecture, construction and advanced testing of a novel remotely operated robotic mechanism for assessment and removal of metal tramp from primary crusher chambers. The system essentially includes a robotic-arm equipped with a hydraulic clamp tool for handling oversize material, as well as an oxy-flame module for cutting metal pieces entrapped within the primary crusher cavity. The first industrial unit was delivered to a large iron ore mine in Brazil, where the installation and testing is scheduled within the coming months.

INTRODUCTION

In recent decades the mining industry has rapidly advanced towards automation and robotics, particularly in areas such as mechanisation of production, remote-control systems, and fully automated equipment to improve safety, productivity, and create an environmentally sustainable process (Li and Zhan, 2018). These advances are well established technologies for coping with increasingly complex and hazardous mine sites, increasing mining and processing costs, and shortage of skilled employees (Lever, 2001 in Boeing and Douglas, 2014). Productivity and safety are thus key issues for the development of safe, efficient, and reliable mining and processing equipment, particularly in the iron ore industry, where both the scale and logistics are driving aspects in new projects.

In a typical high-capacity iron ore operation, the Run-of-Mine (ROM) is dumped in a primary crusher, often a gyratory type, which reduces the size of the ore for handling and further processing. Adequate size rocks will flow-through the crusher chamber according to the equipment capacity and operating conditions. In situations where bridging occurs, relatively simple auxiliary equipment such as slings, hydraulic hammers, and hooks are often used during the crusher operation to reposition the material within the crusher chamber. Conversely, oversize rocks are likely to lodge above the crusher chamber, thus resulting in halting the equipment, together with the upstream operations. In such circumstances, a number of courses of action can be taken, depending upon the available auxiliary equipment, accessibility, and other restrictions. The most common practice involves breaking the boulder by pneumatic or hydraulic hammering, provided the boulder is accessible. Controlling the dump pocket level is thus a key aspect in primary crusher operation for exposing oversized rocks and preventing them to block flow into the crusher chamber. Critical situations involve oversized material sited blocking crusher feed openings while inaccessible due to high level dump pocket. Under such conditions, long periods of equipment shutdown and unsafe work are common (Linares León and Estrella, nd).

Similar problems are due to occur when relatively large pieces of metal obstruct within the crusher chamber. Since compressive crushers are not designed to break solid metal pieces, this creates an obstruction that eventually can stall the machine with the cavity filled with material. In such situations it is not uncommon to manually remove rocks to assess the tramp metal, thus creating high risks to operators that could expose them to hazards, severe injuries, or even to fatalities (Ratliff *et al*, 2014). A mechanised procedure would potentially avoid accidents such as the fatal injury reported in a South Australian quarry during a maintenance procedure to remove tramp metal from a cone crusher in April 2020 (Government of South Australia, 2020).

Depending on the tramp position or alignment inside the chamber, there are different ways to remove it, such as using a rock breaker to push it to the side or pulling it up with a crane. However, frequently, the only way to remove it is by cutting the metal scrap, which usually is carried out by a technician with a thermal lance within a reachable range. This procedure – cutting metal pieces with manual tools – often is performed by inexperienced personnel and may expose the workforce to safety hazards, such as material sliding or metal projectiles. The latter can originate from the rupture and sudden release of the stored energy of the compressed metal when it is weakened by the thermal lance.

Despite a number of different existing methods such as video monitoring and digital image processing are used to prevent tramp metal to reach the primary crusher chamber, the persisting problem has motivated the development of new techniques and associated equipment. One of these initiatives originated from a request by a major iron ore producer to provide a more effective and safer method for one of its larger operations in Brazil.

METHOD

This section initially describes the available procedures for steel tramp removal and associated challenges, followed by describing the development of a remotely operated multitool hydraulic arm designed to reposition or remove oversized rocks and wedged metal, as well as the description of the oxy-flame module.

Available procedures for steel tramp removal at primary crushing station

Detecting and removing tramp metal from a crushing plant is an acknowledged/well-known industry challenge since those metal pieces have the potential to significantly increase downtime and maintenance costs by damaging not only the primary crusher but the downstream equipment as well, such as screens, conveyors, downstream crushers, and High-Pressure Grinding Rolls. To minimise these risks, the industry standard is to apply both magnetic extractors and metal detectors on material handling equipment located downstream from the primary crusher (Helmich, nd), usually starting from the discharge apron/belt feeder. Figure 1 shows a Semi-Mobile Primary Gyratory (SMPG) station displaying its main components and highlighting the magnetic extractor.

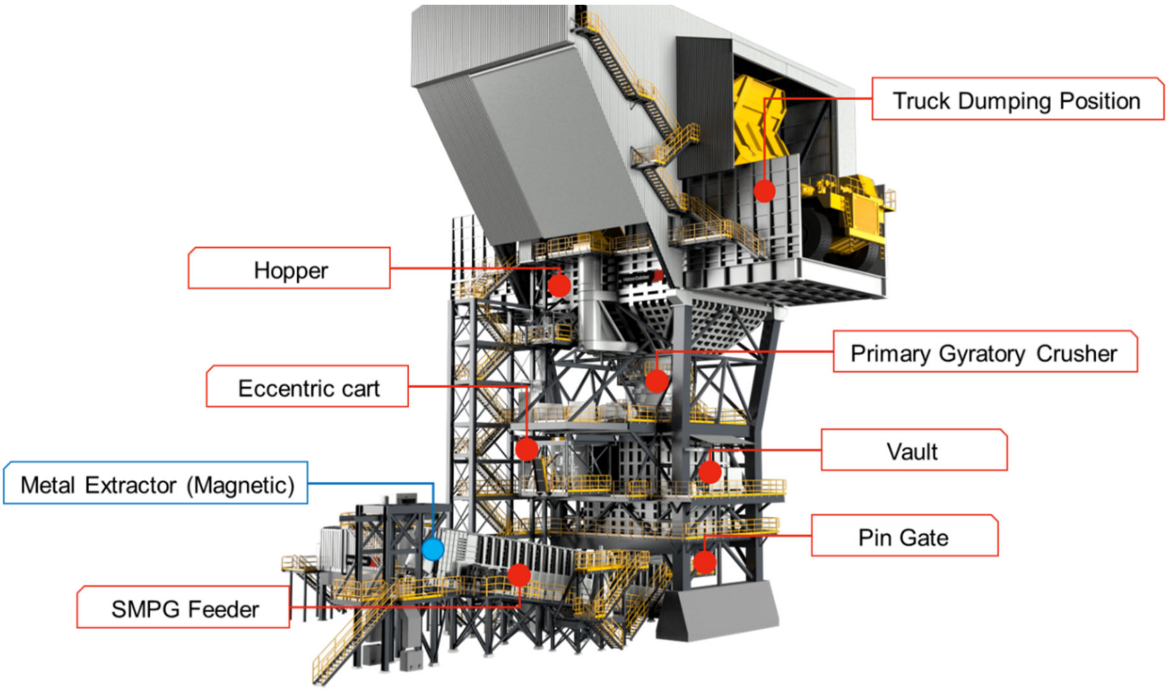

FIG 1 – Semi-Mobile Primary Gyratory (SMPG) station with main structures highlighted.

Metal detectors and magnetic extractors must be placed at limited distance from the material to work efficiently which means that those technologies have an upper limit to both bed depth and particle top size (Shuttleworth and Stipicic, 2011). Moreover, ore properties such as high iron content decrease the efficiency of metal detectors and usually requires customised magnets to be able to extract tramp material without removing fine iron ore particles. In high throughput industrial operations, such as iron ore industry developing an efficient and cost-effective system to extract tramp metal from the stream is still a challenge. Currently there is no reliable method to detect and remove metal pieces such as an excavator tooth from large volumes hauled by mining trucks often including rock blocks larger than 1 m in size. Depending on its size and alignment, an undetected piece of metal may become trapped between the mantle and the concave in the crusher chamber. Given that compressive crushers are not suited to break metal, the tramp material can create an obstruction and eventually stall the machine with the chamber full or partially filled with material.

As newer primary gyratory crushers are equipped with a hydraulic module to adjust the open side setting by raising and lowering the main shaft, such a system is often used in attempting to release the piece of metal from the crusher chamber by dropping the main shaft. Such a procedure is combined with instantly starting (bumping) the crusher – often with reverse polarisation – to help release the tramp. In situations where such a procedure is not effective, different procedures are commonly used to remove the blocks sitting above the tramp, such as using a rock breaker to push the blocks aside, thus making clearance to access the obstruction point. A similar procedure to remove the metal piece from the crusher is using a hydraulic arm or crane, prioritising mechanised methods instead of manual intervention. However, those mechanisms cannot fit the gap at the bottom of the crushing chamber, leading to the metal tramp often being beyond the reach of those mechanisms. If the operation has exhausted the available mechanised means to remove the obstruction from the chamber, manually handled tools may be used to clear the chamber, such as wielding an oxy-fuel cutting tool, also referred to as thermal lance or oxy-flame. To wield a thermal lance or any other manual tool, an operator usually is placed within the crusher chamber in the reachable range of the tramp metal. This procedure exposes the workforce to safety hazards, such as material sliding and high energy projection from the suddenly released metal compressed between the crushing members. Figure 2 shows: (A) an example of a tramp inside a primary gyratory crushing chamber; and (B and C) a manually wielded oxy-fuel cutting tool.

FIG 2 – Example of primary crushing obstruction (A) and manual oxy-flame tool (B and C).

Remotely controlled multi-tool arm

A prototype of a remotely controlled multi-tool arm was developed to essentially enable a safe and reliable procedure for removing tramp material from within primary crusher chambers. The controlled hydraulic arm was designed to aid in the removal of the rocks from the crushing chamber, as well as to operate the thermal lance for cutting pieces of metal within the crusher chamber. Even though the former aspect has been addressed by various authors (Boeing & Douglas, 2014; Wu et al., 2016), the combination with the latter attribute is here considered a novel approach and initiative. The following sections describe in detail the technologies and mechanisms involved in such a system.

Mechanical project

The mechanical project of the hydraulic arm was designed to drive two different devices. The first is a include a dedicated hydraulic clamp designed to remove and relocate rocks from the crushing chamber and hopper. The hydraulic arm provides high degrees of freedom to the clamp tool for reaching and further relocating or even removing large rocks from the crushing chamber. Such a mechanical device was tailored to the specific iron ore operation where it will be installed, in terms of material density and size distribution, as well as the crushing station layout. The apparatus should thus be adapted to each specific operation. The second device driven by the hydraulic arm is the oxy-flame module designed to cut metal pieces in the crushing chamber. Further improvements to the hydraulic arm included a quick coupling system, similar to those commonly used in excavators, in this case to facilitate and speed up the swop between the hydraulic clamp and the oxy-flame modules. A portable controller unit was also incorporated to the system to allow the remote operation of the clamp tool.

Figure 3 illustrates the hydraulic arm with the attached clamp module, together with the schematics of the mechanical mobilities.

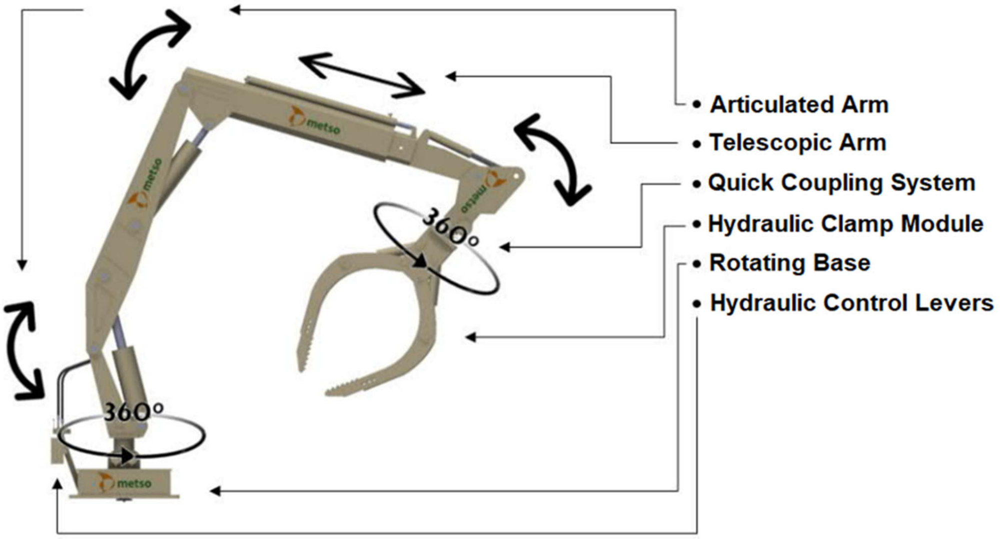

FIG 3 – Robotic-arm diagram equipped with the hydraulic clamp tool.

Figure 4 illustrates the remotely controlled hydraulic arm equipped with the oxy-flame module for piercing the metal tramp.

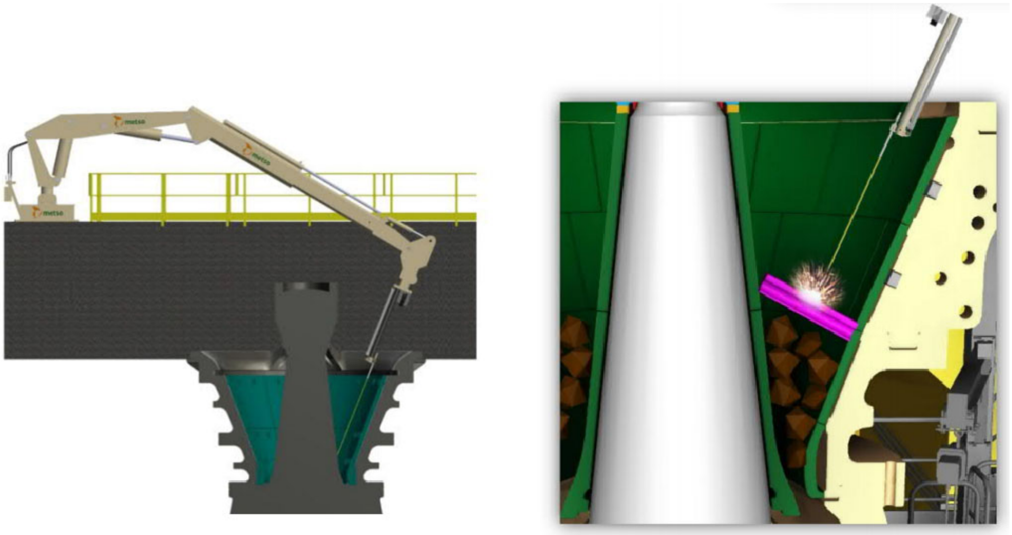

FIG 4 – Remotely-controlled oxy-flame module.

Process monitoring and control

The removal and cut procedures shall be executed remotely by the operators to ensure safety during the entire process. A thermographic camera installed close to the coupling system delivers images in real-time to guarantee precision at those tasks. The control system can use continuous or pulsed commands to reduce the risks of damaging the equipment.

Two control system includes logics for two different functions, depending on which tool is attached to the hydraulic arm. The first dedicated to moving rocks, while the second is designed for cutting metal.

Clamp module

The hydraulic clamp module consisted in double-ended metal pincer, commonly used for transporting and positioning ore in crushers. The clamp features 360° to pivot, it opens, closes, and tilts.

When attached to the robotic arm, the clamp system can be used to maneuver oversized or bridged rocks, therefore resulting in risks to operators in daily basis. The tool can be operated through a portable controller carried by the operator, preferentially in a secure place in the area around the crusher.

Oxy-flame module

As opposed to the clamp module, the oxy-flame module will be used only in situations where the tramp metal is not released by lowering the main shaft, so that metal cutting is absolutely necessary. As a consequence, the oxy-flame tool is equipped with an interlocking system that only allows arm movement to be conducted from a control room. The dedicated cabinet should be located at a safe position, therefore ensuring that the operator is out of the reachable zone of any metal projectile that may be ejected during the cut procedure.

The module comprises of an oxy-flame lance that has a telescopic displacement of 2 m in length, including consumable tubes threaded at the module extremity. As the tool is positioned near the metal piece, the operator can remotely start the industrial oxygen flow-through the tube and ignite the lance through an electric arc device to start the cutting procedure. After igniting the thermal lance, the operator advances the telescopic displacement of the module until it pierces the tramp metal, weakening its structure until it breaks by the pressure exerted by the crusher chamber.

Figure 5 shows photographs of the industrial device taken during the tests carried out at Metso Outotec in Brazil.

FIG 5 – Photographs taken from the industrial equipment during tests carried out at Metso Outotec in Brazil.

Factory test and expected field results

Even though the travel restrictions imposed by the Covid-19 pandemics, have successively postponed the installation in the actual industrial site, the equipment has been tested at a supplier's factory.

The tests were divided in the three major categories, as described in following sections.

Rock removal with the hydraulic clamp

The main purpose of the clamp module is to create access within crusher chamber, to the non-crushable material for the oxy-flame cutting procedure. The tests at the factory aimed to assess the degree of freedom of the mechanism, together with its capacity to grip and elevate weights from different positions. Even though the tests showed suitable results in both aspects, the hydraulic clamp module should be adapted to each individual installation, as the weight of large rocks will vary according to material density and top size. The lifting weight capacity and releasing positions will determine the design of associated components.

The tests also indicated that the hydraulic clamp range will practically eliminate the need for an excavator in the crushing area for boulder removing. It follows that overhead crane will not be necessary to remove rocks that surround the non-crushable element.

Additional tests showed that only the double-ended clamp equipped with a pincer shape could reach the discharge end of the crushing chamber, as opposed to the triple-ended model. However, the double-ended clamp might not be able to grip rocks of particular shapes, albeit it could well reposition and even break some larger rocks.

Replacing clamp and lance modules between operations

Both clamp and lance modules include a quick-coupling system to allow a fast and secure replacement using an Allen wrench to tighten and remove the fixing screw that couples the module to the hydraulic arm. The dedicated tests started by placing both modules onto a container, the latter designed to hold both devices before starting the exchange procedure. Once a module was removed, the hydraulic arm was positioned over the second module with the help of the radio remote control, allowing the operator to closely monitor the alignment of the arm to the locking pins. The actual module exchange operation was carried out at an averaged period of 20 minutes, which was considered adequate. Such a period would thus reduce stoppages for replacement.

Cutting metal pieces

The tests have shown that the remote-controlled oxy-flame operation should not increase the downtime, as compared with the manually wielded cutting procedure. The essential benefit is the safety increase achieved by keeping the operators at a secure location while controlling the entire maintenance procedure assisted by a thermographic camera.

The tests consisted in positioning the thermal-lance coupled to the tip of the arm over the non-crushable element, assisted by real-time images from a thermal camera located near the coupling point of the module. After positioning the oxy-flame near the cutting place, the tests progressed by ignition resulting from the electric arc generated between the lance and a sacrificial plate. After connecting the electric source, oxygen was released into the system while the operator moved the boom backwards and forwards to generate the electric arc until the ignition started. Following the ignition, the operator advanced the oxy-flame lance towards the tramp metal for piercing it. Such a procedure was repeated until the structural resistance of the material was overcome, causing its rupture by applied pressure.

The current design challenge of the thermal lance module is precision to create the electric arc for ignition. This arc is obtained after a few attempts of advancing and retreating the oxy-lance. The tests showed that the use a chemical ignitor facilitates the ignition as it only requires feeding oxygen into the system, therefore not involving a welding source to generate the arc. The tests also indicated that such a method requires a minimum oxygen pressure of 9 to 12 bar, which is not reached in the current boom configuration. Therefore, if such an alternative is considered, further testing with an installed accumulator or compressor is necessary.

CONCLUSIONS

The major motivation for developing the here described remotely operated robotic originated was the request from a major iron ore producer in Brazil for a safer maintenance procedure to remove metal tramps from inside a primary gyratory crusher, as such procedures have recently resulted in injuries and even fatalities worldwide. The prerequisite to Metso Outotec was thus to remove any labourer from the crusher surroundings during any activity associated with tramp metal removal.

When operating the remote-controlled hydraulic arm from a safe position, the worker can use the hydraulic clamp module to relocate the rocks that sit above the obstruction to an adequate position. The same clamp module may be used to pull the tramp metal from the wedged position inside the chamber. In cases where such a procedure fails, the clamp module is replaced by the oxy-flame module, the latter designed to pierce the metal, which results in weakening the metal tramp structure until it collapses due to the pressure applied by the crushing surfaces.

All the above-described procedures can be executed by the workforce from a safe position, where the technicians are either out of reach or shielded from possible sliding rocks or projectiles liberated from the rupture of the tramp metal. Tests performed with a real device showed adequate results in all three stages related to remotely assessing and cutting the metal piece, therefore involving no perceivable risks to the operators and maintenance personnel.

Even though the first unit was developed for a primary gyratory crushing station, the ongoing studies aim to also apply such a technology to primary jaw crushers. Future projects may likewise adapt the design and develop similar mechanisms for other primary crushing stations or downstream crushing stages, such as cone crushers.

REFERENCES

Boeing, A. and Douglas, E, 2014. ‘A remotely controlled robotic rock breaker with collision avoidance for the mining industry'. 2013 Proceedings of the 30th ISARC, Montréal, Canada, IAARC, Montreal, Canada. (August 10th, 2020, https://www.iaarc.org/publications/proceedings_of_the_30th_isarc/a_remotely_operated_robotic_rock_breaker_with_collision_avoidance_for_the_mining_industry.html).

Government of South Australia, 2020, April 30. Clearing metal tramp blockages in cone crushers [online]. Available from: <https://www.safework.sa.gov.au/news-and-alerts/safety-alerts/incident-alerts/2020/clearing-metal-tramp-blockages-in-cone-crushers>

Helmich, T, n.d. The True Value of Magnetic Separators and Metal Detector in Bulk Handling. https://www.eriez.com/Documents/White-Papers/TheTrueValueofMagneticSeparatorsandMetalDetectors_BulkHandling.pdf: Eriez Magnetics Europe Ltd.

Li, J and Zhan, K, 2018. Intelligent Mining Technology for an Underground Metal Mine Based on Unmanned Equipment [online]. *Engineering*, 4(3):381–391. Available from: <https://www.sciencedirect.com/science/article/pii/S2095809917307853> [Accessed: 10 August 2020].

Linares, J, León, C and Estrella, D, nd. Antamina Productivity Increase Through Improvements Implemented In The Primary Crushing. Available from: <https://www.onemine.org/document/abstract.cfm?docid=232445>

Ratliff, B J, Bosley, J H, Rice, R L, Hall, J A and McCabe, P L, 2014. Final Report: Fatality #25 - November 10, 2014. Available form: <https://www.msha.gov/data-reports/fatality-reports/2014/fatality-25-november-10-2014/final-report>

Shuttleworth, T and Stipicic, C, 2011. How industrial plants benefit from apron feeder magnetic separators. Available from: <https://www.eriez.com/Documents/PDFs/ApronFeederMagSepMiningEngineeringJan2011.pdf>

Wu, H, Zhang, X, Zhao, Y and Lou, L, 2016. Simulation and performance testing of the network control system in coal mine automation. In *Proceedings of the 2nd International Conference on Advances in Mechanical Engineering and Industrial Informatics (AMEII 2016)*, pp. 676–682 https://www.researchgate.net/publication/303485802_Simulation_and_Performance_Testing_of_the_Network_Control_System_in_Coal_Mine_Automation

Efficiency improvement of iron beneficiation plant by special fine particle separator

M Lak[1]*, A Haratian*[2]*, S Haji*[2]*, R Amiri*[2] *and M Asghari*[2]

1. Design and Engineering Department, Fakoor Meghnatis Spadana Co., Tehran, Iran. Email: *m.lak@fms-co.com*
2. Design and Engineering Department, Fakoor Meghnatis Spadana Co., Tehran, Iran.

ABSTRACT

Dry magnet separators are used to upgrade and beneficiate a wide variety of minerals such as hematite and magnetite materials. In recent years advances in dry magnetic separators have improved their performance. Fine particle separation is one of the main areas which still remain weak. This paper will present a new design of fine particle drum separators which used for particle size less than 3 mm. A big problem in processing of iron ore is the grade and recovery of mineral values in the fines fraction. The new design high efficiency drum separator is developed to handle fine feeds. In this drum separators both of the drum shell and magnetic yoke rotate in opposite direction. the results showed that when the material feed size was K_{80} = 1298 µm, drum shell speed was 42.5 rev/min, magnetic yoke speed was 100 rev/min and the maximum intensity of magnetic field was at θ = 30° the feed grade increased from 50.87 to 65.67 in concentrate box, increase to 60.45 in middle box and tail grade was 24.44. The total achieved recovery for both concentrate and middle box was 81.89 per cent.

INTRODUCTION

Magnetic drum separators are widely used in mining industry to separate iron concentrate from gangue material by using magnetic properties of minerals. Magnetic drum separators are divided into low and high magnetic field intensity. These drum separators could operate in wet and dry condition. Few papers dealing with dry fine particle separators. This paper proposes a new drum separator model which has both high and low magnetic intensity and used in dry separation. Magnetic drum separator is used to separate materials which are attracted in magnetic field from materials which are not affected by magnetic field. The speed of rotation of drum separators and magnet yoke (core) are in opposite direction. These two parameters and position of gates are adjusted to separate material into concentrate box, middle box and tailing box. Drum rotation speed, magnetic yoke rotation speed, the location of magnetic intensity peak, the gate position and Dedusting system could affect the recovery and grade of concentrate.

By increasing the drum separator rotation speed the feed capacity will increase. Increasing rotation speed of drum separator decrease the recovery of iron and increase the grade of iron in concentrate (Zhang *et al*, 2015). Before the fabrication of new design equipment, the effect of different arrangement of magnet blocks on magnetic field distribution analysed by 2D FEMM software. The FEMM analyses help to obtain the magnetic field distribution through drum separator perimeter. This software uses the finite element method to resolve Maxwell's equations numerically over the 2D generated magnets pattern.

The linear B-H relationship of NdFeB N42 is used to simulate the magnetic field distribution through drum separator surface. Magnet block properties are mentioned in Table 1. Where μ_x is relative permeability, H_c is Coercivity and σ is electrical conductivity.

TABLE 1

Magnet block property.

Block property	μ_x	1.05
	H_c	969969 A/m
	σ	0.667 MS/m

The aim of this paper is to model the magnetic field distribution and optimisation of magnetic separator performance by experiments. A model was developed by Rayner and Napier-Munn (2003) to simulate the effect of operating variable on low intensity magnetic separators performance.

improving the efficiency of wet drum separators has been studied by (Bikbov, Karmazin and Bikbov, 2004). The study results show that wet separation process by magnetic drum separators has low selectivity in separation.

Numerical and experimental (Davis and Lyman, 1983) Studies have focused on the effect of operational parameters on efficiency of separation.

Dry separation has several advantages in comparison with wet separation such as lower water consumption, tailing deposits management etc (Dwari and Rao, 2007).

METHODOLOGY

The magnetic fine particle drum separator of 900 mm diameter and 400 mm length was fabricated in Fakoor Meghnatis Spadana (FMS) factory in Iran. The arc of magnet block pattern was 360°. The dimension of permanent block magnet was 60 × 50 × 20 mm and the material of magnets was NdFeB N40. Both drum and core could rotate with two separate motor gearboxes. Because of reduction of eddy current generation due to rotation of steel in magnetic field, the material of drum shell was changed and composite shell was used instead of steel shell. By using composite shell, the drum rotational speed could increase without any limitation. There is an eccentricity between drum shell centre and centre of core. This eccentricity causes alteration of magnetic intensity through shell perimeter. Mechanical seal was used to minimise penetration of dust and fine particle into the drum shell. Two mechanical gates are designed to separate the concentrate box from middle box and middle box from tail box. The Dedusting system was used to minimise the generated dust because of high rotational speed of drum shell. The suction points are located at feed box, tail box and concentrate box. By adjusting different parameters, the performance of fine particle drum separator could change drastically (Figure 1).

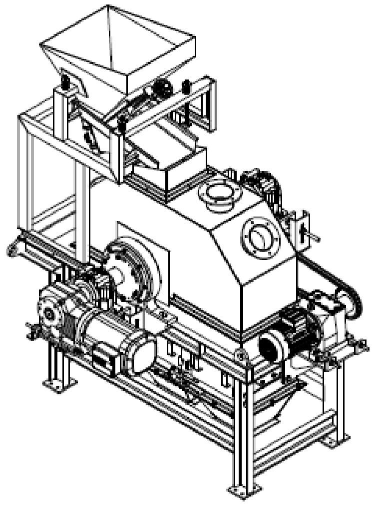

FIG 1 – Fabricated lab scale permanent drum separator.

In this new equipment the alteration of magnetic intensity is from 0.1 T to 0.4 T (Figure 2).

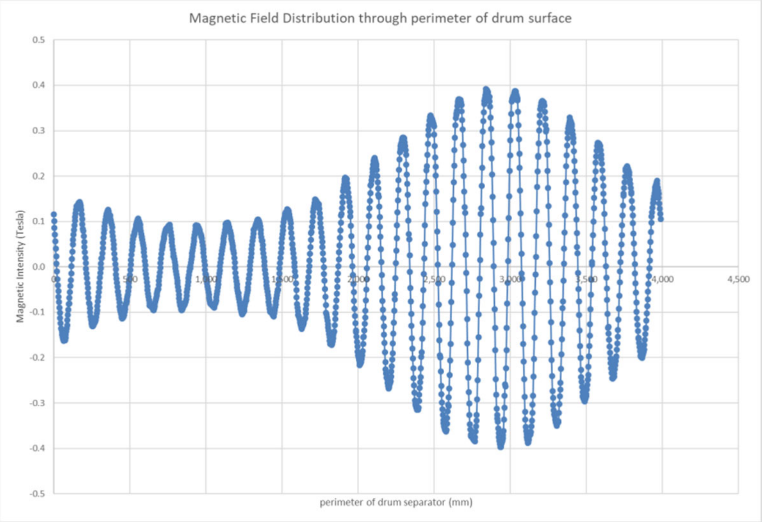

FIG 2 – Magnetic Field distribution through perimeter of drum surface.

VALIDATION OF SIMULATION

By using a gauss metre device, the value of magnetic field intensity in random points was measured. There was a good agreement between the value of magnetic intensity in simulation data and measured data through drum surface at random points (Table 2).

TABLE 2

Comparison of numerical and experimental data.

		Point 1	Point 2	Point 3	Point 4
Magnetic intensity (G)	**Experimental**	2350	1760	3220	3650
	Numerical	2420	1830	3300	3620
	Error (%)	3	4	2.5	1

The simulation of magnetic drum separator was executed using finite element method. Figure 3 depicts the magnetic field distribution and fig shows the field lines.

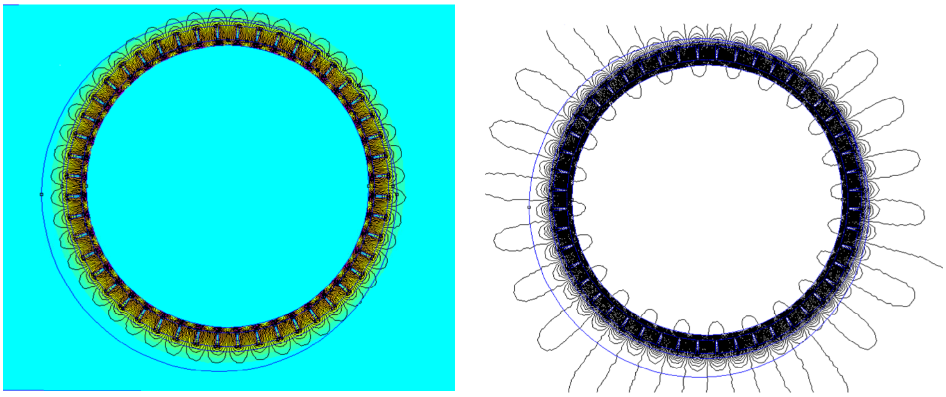

(a) (b)

FIG 3 – Magnetic field distribution (a) flux; (b) field line.

In order to have a better vision of magnetic field distribution on the surface of drum separator Figure 4 was used.

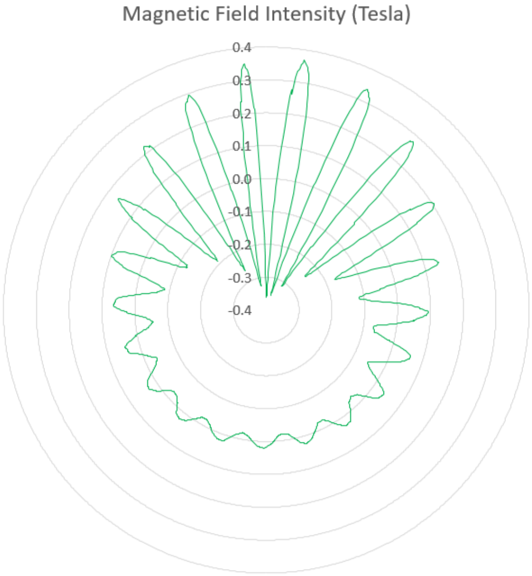

FIG 4 – Magnified magnetic field distribution through drum surface.

Figure 5 represent the fluctuation in magnetic field distribution around the drum perimeter. Through the simulation the highest intensity of magnetic field ensues at the narrow distance between drum and core. The location of peak magnetic field intensity is shown with θ sign.

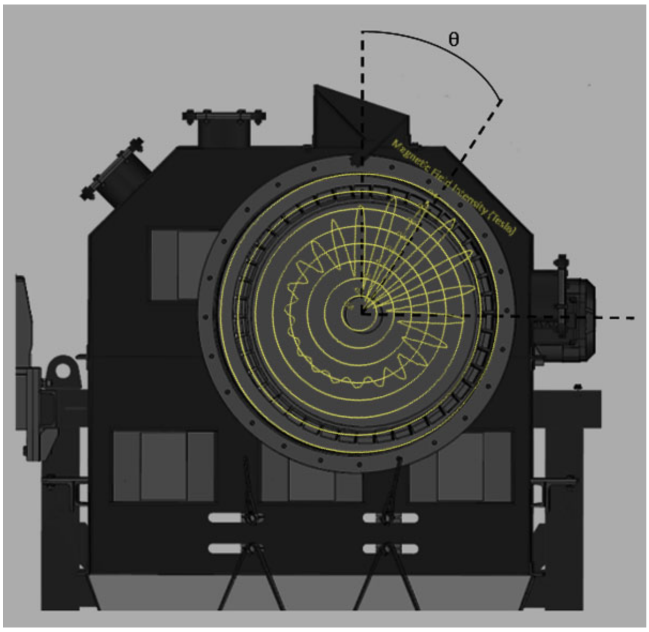

FIG 5 – Fluctuation of magnetic field base on eccentricity between shell and core.

As shown in Figure 6 the construction of new equipment allows separation of feed divided into three fractions. This equipment eliminates the use of re-separation process.

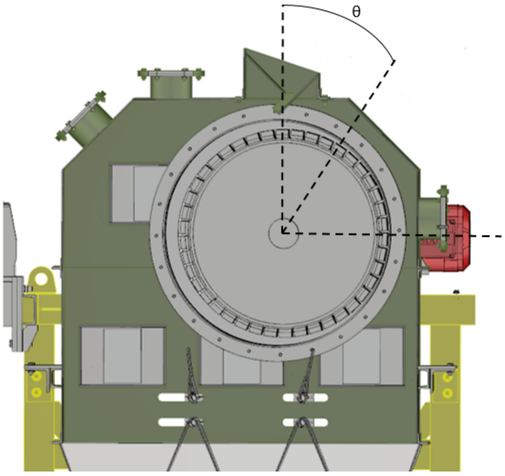

FIG 6 – The location of magnetic intensity peak in fabricated lab drum separator.

There are six variables which can be manipulated to adjust the operation of magnetic separator. Speed of rotation of drum. The magnet yoke speed of rotation. The position of intensity peak, the position of reject gate, the position of middle gate, and Dedusting system.

RESULTS AND DISCUSSION

The iron ore (magnetite) samples are used to test the new equipment performance. Tables 3 to 5 show the results of experimental tests for three stages of drum separators.

TABLE 3

Results of first stage drum separator (1100G).

Test Stage					Rougher
Sample	**Name**	**Wt. kg**	**Wt. %**	**Fe %**	Fe_{Rec} **%**
C31	Concentrate	45.98	77.20	61.57	92.38
T31	Tail	13.58	22.80	17.21	7.62
-	Feed (Calculated)	59.56	100.00	51.45	100.00
F1	Feed (Actual)	60.00	100.00	50.87	100.00

TABLE 4

Results of second stage drum separator (1100G).

Test Stage					Cleaner
Sample	**Name**	**Wt. kg**	**Wt. %**	**Fe %**	Fe_{Rec} **%**
C32	Concentrate	44.08	97.55	61.91	98.92
T32	Tail	1.11	2.45	26.94	1.08
-	Feed (Calculated)	45.19	100.00	61.05	100.00
C31	Feed (Actual)	45.20	100.00	61.57	100.00

TABLE 5

Results of third stage drum separator (1100G).

Test Stage					Final Cleaner
Sample	**Name**	**Wt. kg**	**Wt. %**	**Fe %**	Fe_{Rec} %
C33	Concentrate	42.62	98.71	63.09	99.39
T33	Tail	0.56	1.29	29.70	0.61
-	Feed (Calculated)	43.18	100.00	62.66	100.00
C32	Feed (Actual)	43.38	100.00	61.91	100.00

As shown in Figure 7 by using three stages of LIMS drum separators (1100G) the feed grade increased from 51.45 to 63.09. The linear drum speed is equal to 2 m/s.

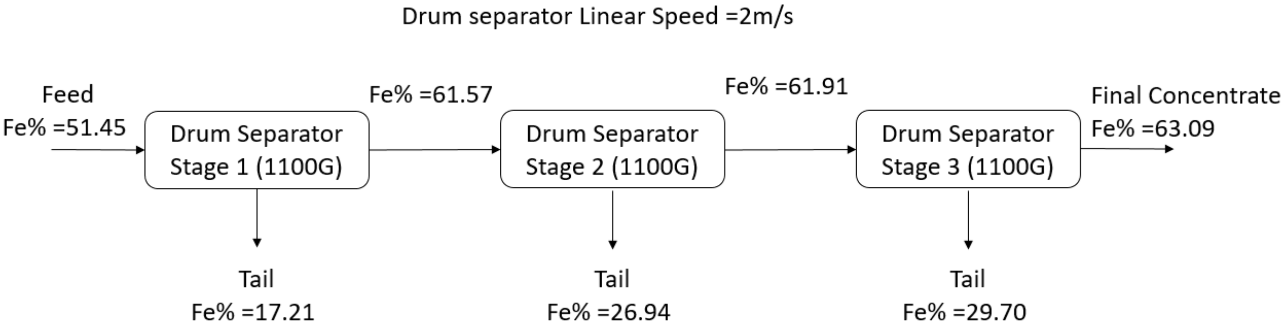

FIG 7 – Results of three stages drum separators.

Tables 6 and 7 show the results for two stages of drum separators while the linear speed of rotation is 2 m/s.

TABLE 6

Results of first stage drum separator (1100G) with 2 m/s linear speed.

Test Stage					Rougher	
Sample	**Name**	**Wt. kg**	**Wt. %**	**Fe %**	Fe_{Rec} %	**FeO %**
C1	Concentrate	40.50	81.33	66.07	93.57	26.83
T1	Tail	9.30	18.67	19.76	6.43	5.32
-	Feed (Calculated)	49.80	100.00	57.42	100.00	22.81
F2	Feed (Actual)	50.00	100.00	56.23	100.00	22.79

TABLE 7

Results of second stage drum separator (1100G) with 2 m/s linear speed.

Test Stage					Rougher	
Sample	**Name**	**Wt. kg**	**Wt. %**	**Fe %**	**Fe_{Rec} %**	**FeO %**
C2	Concentrate	44.08	97.55	67.02	98.99	26.88
T2	Tail	1.11	2.45	27.25	1.01	8.19
-	Feed (Calculated)	45.19	100.00	66.05	100.00	26.42
C1	Feed (Actual)	45.20	100.00	66.07	100.00	26.83

As shown in Figure 8 by using two stages of LIMS drum separators the Fe grade could increase from 56.23 to 67.02. The linear drum speed is equal to 3 m/s. the experimental results show that by increasing drum separator linear speed, the Fe grade of concentrate will increase.

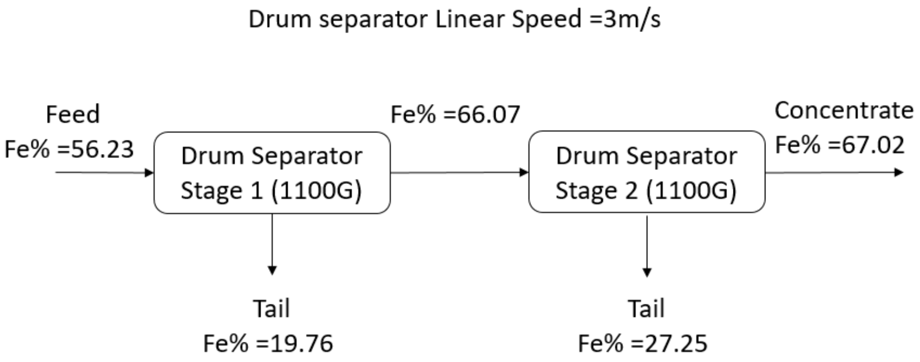
Drum separator Linear Speed =3m/s

FIG 8 – Result of two stages drum separators.

Tables 8 to 10 show the experimental results for new design drum separator to investigate the effect of core speed on grade of concentrate.

TABLE 8

Results of new fine particle drum separator with different core speed (50 rev/min).

Test Stage					Rougher	
Sample	**Name**	**Wt. kg**	**Wt. %**	**Fe %**	**Fe_{Rec} %**	**FeO %**
Step1C	Concentrate	25 400	51.51	64.58	65.89	24.12
Step1M	Middle	9750	19.77	55.73	21.82	17.56
Step1T	Tail	14 160	28.72	21.61	12.29	4.85
	Dust	0	0.00	0.00	0.00	0.00
-	Feed (Calculated)	49 310	100.00	50.49	100.00	17.29
F1	Feed (Actual)	50 000	100.00	50.87	100.00	17.49

TABLE 9

Results of new fine particle drum separator with different core speed (100 rev/min).

Test Stage					Rougher
Sample	**Name**	**Wt. kg**	**Wt. %**	**Fe %**	**Fe_{Rec} %**
Step2C	Concentrate	23 960	48.46	64.80	62.22
Step2M	Middle	10 760	21.76	57.14	24.64
Step2T	Tail	14 720	29.77	22.27	13.14
	Dust	0	0.00	0.00	0.00
-	Feed (Calculated)	49 440	100.00	50.47	100.00
F1	Feed (Actual)	50000	100.00	50.87	100.00

TABLE 10

Results of new fine particle drum separator with different core speed (150 rev/min).

Test Stage					Rougher	
Sample	**Name**	**Wt. kg**	**Wt. %**	**Fe %**	**Fe_{Rec} %**	**FeO %**
Step3C	Concentrate	22 360	45.10	64.31	57.73	24.58
Step3M	Middle	12 260	24.73	58.61	28.85	19.10
Step3T	Tail	14 960	30.17	22.36	13.43	5.06
	Dust	0	0.00	0.00	0.00	0.00
-	Feed (Calculated)	49 580	100.00	50.24	100.00	17.33
F1	Feed (Actual)	50 000	100.00	50.87	100.00	17.49

As shown in Figure 9 there is an optimal core rotation speed. By increase or decrease speed from optimal speed, the grade of Fe in concentrate will decrease.

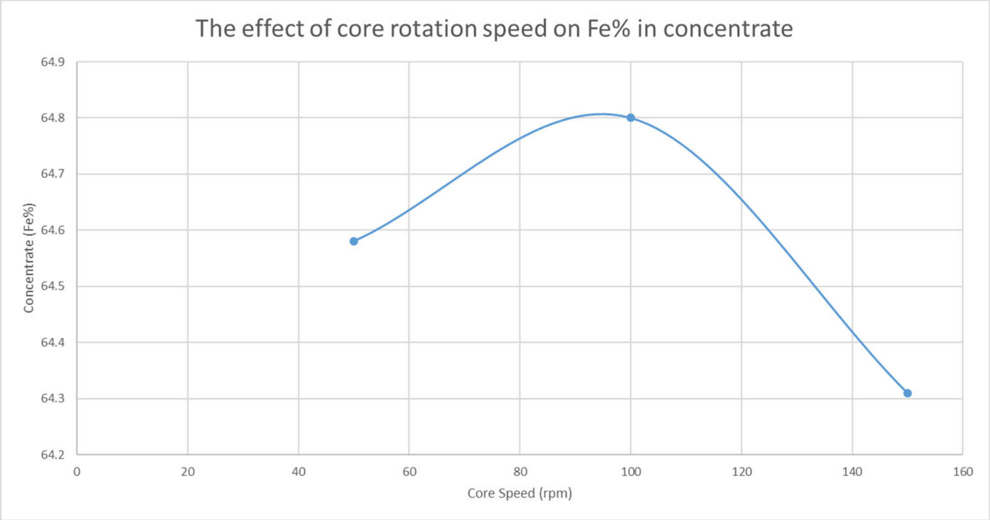

FIG 9 – The effect of core rotation speed on Fe per cent in concentrate.

Tables 11 to 13 show the experimental results to investigate the effect of drum rotation speed on recovery and grade of Fe in concentrate.

TABLE 11

Results of new fine particle drum separator with different drum speed (63.75 rev/min).

Test Stage					**Rougher**	
Sample	**Name**	**Wt. kg**	**Wt. %**	**Fe %**	Fe_{Rec} **%**	**FeO %**
Step4C	Concentrate	24 320	49.41	64.98	63.81	23.81
Step4M	Middle	10 400	21.13	56.86	23.88	17.81
Step4T	Tail	14 500	29.46	21.03	12.31	4.78
	Dust	0	0.00	0.00	0.00	0.00
-	Feed (Calculated)	49 220	100.00	50.31	100.00	16.94
F1	Feed (Actual)	50 000	100.00	50.87	100.00	17.49

TABLE 12

Results of new fine particle drum separator with different drum speed (82 rev/min).

Test Stage					**Rougher**	
Sample	**Name**	**Wt. kg**	**Wt. %**	**Fe %**	Fe_{Rec} **%**	**FeO %**
Step5C	Concentrate	24 160	49.13	65.23	63.24	24.58
Step5M	Middle	10 420	21.19	57.28	23.95	17.97
Step5T	Tail	14 600	29.69	21.85	12.80	5.00
	Dust	0	0.00	0.00	0.00	0.00
-	Feed (Calculated)	49 180	100.00	50.66	100.00	17.37
F1	Feed (Actual)	50 000	100.00	50.87	100.00	17.49

TABLE 13

Results of new fine particle drum separator with different drum speed (42.5 rev/min).

Test Stage					**Rougher**	
Sample	**Name**	**Wt. kg**	**Wt. %**	**Fe %**	Fe_{Rec} **%**	**FeO %**
Step6C	Concentrate	23 080	46.16	64.79	58.79	24.26
Step6M	Middle	9360	18.72	61.34	22.57	19.63
Step6T	Tail	11 360	22.72	23.94	10.69	5.50
	Dust	6200	12.40	32.58	7.94	11.02
-	Feed (Calculated)	50 000	100.00	50.87	100.00	17.49
F1	Feed (Actual)	50 000	100.00	50.87	100.00	17.49

As shown in Figure 10 in new design drum separator by increase the rotation speed of drum separator while the core speed is constant, the grade of iron in concentrate box will decrease.

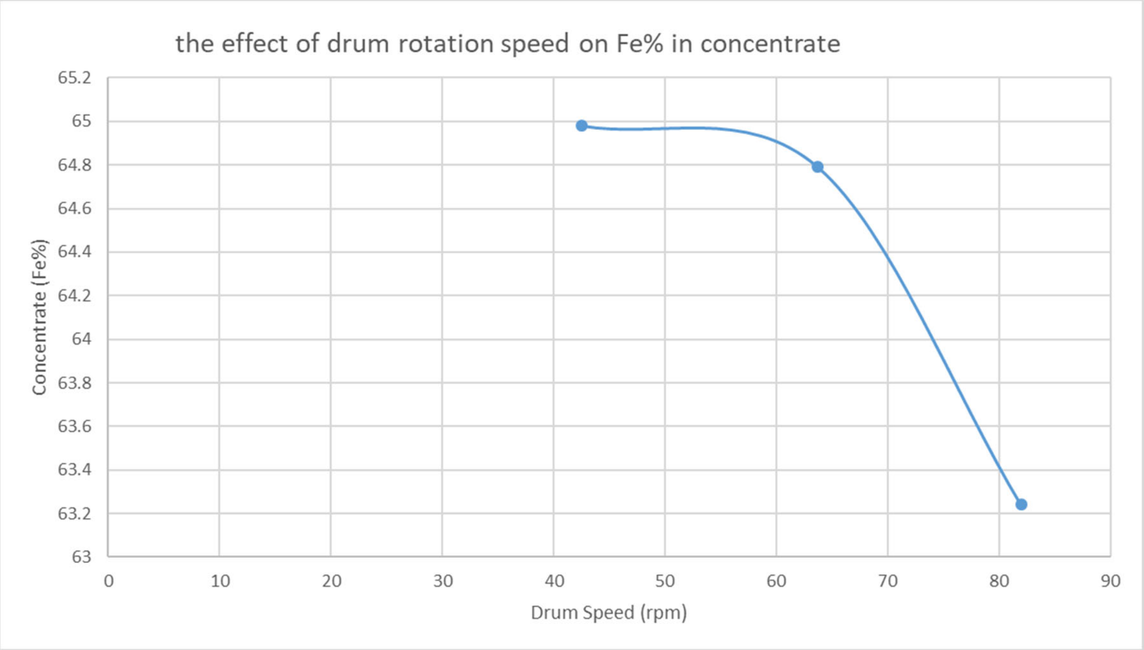

FIG 10 – The effect of drum rotation speed on Fe per cent in concentrate.

Tables 14 to 16 show the experimental results to investigate the effect of Dedusting system effect on Fe grade in concentrate in new design drum separator.

TABLE 14

Results of new fine particle drum separator with different Dedusting position (tail).

Test Stage					**Rougher**	
Sample	**Name**	**Wt. kg**	**Wt. %**	**Fe %**	**Fe_{Rec} %**	**FeO %**
Step7C	Concentrate	23 560	47.12	65.67	60.83	24.62
Step7M	Middle	8860	17.72	60.45	21.06	19.41
Step7T	Tail	12 220	24.44	26.23	12.60	5.96
	Dust	5360	10.72	26.16	5.51	9.25
-	Feed (Calculated)	50 000	100.00	50.87	100.00	17.49
F1	Feed (Actual)	50 000	100.00	50.87	100.00	17.49

TABLE 15

Results of new fine particle drum separator with different Dedusting position (Feed).

Test Stage					Rougher	
Sample	**Name**	**Wt. kg**	**Wt. %**	**Fe %**	Fe_{Rec} **%**	**FeO %**
Step8C	Concentrate	23 660	47.32	65.78	61.20	19.04
Step8M	Middle	9100	18.20	60.36	21.60	5.90
Step8T	Tail	12 360	24.72	25.61	12.45	24.54
	Dust	4880	9.76	24.80	4.76	13.69
-	Feed (Calculated)	50 000	100.00	50.87	100.00	17.49
F1	Feed (Actual)	50 000	100.00	50.87	100.00	17.49

TABLE 16

Results of new fine particle drum separator with different Dedusting position (Concentrate).

Test Stage					Rougher	
Sample	**Name**	**Wt. kg**	**Wt. %**	**Fe %**	Fe_{Rec} **%**	**FeO %**
Step8C	Concentrate	21 500	43.00	65.54	55.41	25.54
Step8M	Middle	9960	19.92	60.23	23.59	19.47
Step8T	Tail	13 600	27.20	20.67	11.05	4.47
	Dust	4940	9.88	51.25	9.95	18.65
-	Feed (Calculated)	50 000	100.00	50.87	100.00	17.49
F1	Feed (Actual)	50 000	100.00	50.87	100.00	17.49

Figure 11 show that the best position for Dedusting system to have minimum effect on reduction of Fe grade in concentrate is on the side of feed opening.

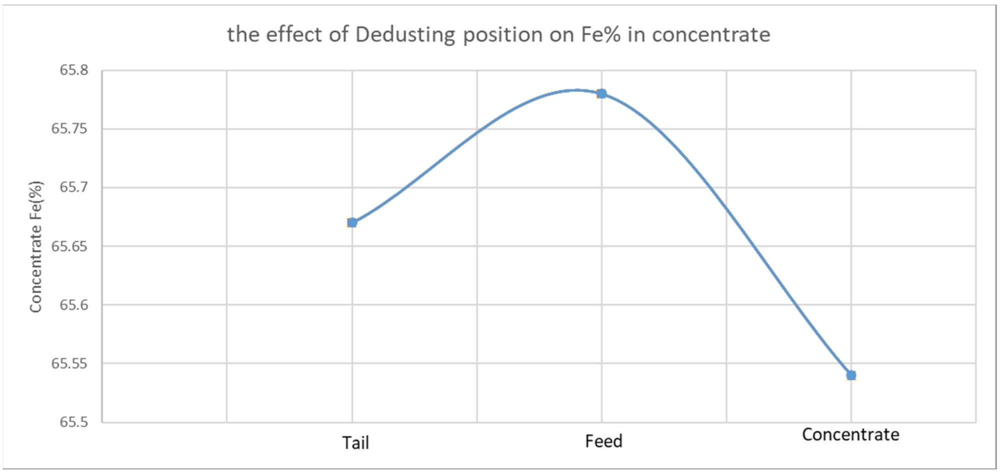

FIG 11 – The effect of Dedusting position on Fe per cent in concentrate.

Tables 17 to 20 show the experimental results to evaluate the effect of location of peak of magnetic intensity through surface of new design drum separator on Fe grade in concentrate box.

TABLE 17

Results of new fine particle drum separator with different location of magnetic field intensity (θ = 30°).

Test Stage					Rougher	
Sample	**Name**	**Wt. kg**	**Wt. %**	**Fe %**	**Fe_{Rec} %**	**FeO %**
Step8C	Concentrate	24 370	49.18	64.75	63.33	24.49
Step8M	Middle	11 520	23.25	55.25	25.54	16.62
Step8T	Tail	13 660	27.57	20.30	11.13	4.58
	Dust	0	0.00	0.00	0.00	0.00
-	Feed (Calculated)	49 550	100.00	50.29	100.00	17.17
F1	Feed (Actual)	50 000	100.00	50.87	100.00	17.49

TABLE 18

Results of new fine particle drum separator with different location of magnetic field intensity (θ = 60°).

Test Stage					Rougher	
Sample	**Name**	**Wt. kg**	**Wt. %**	**Fe %**	**Fe_{Rec} %**	**FeO %**
Step8C	Concentrate	31 600	63.76	65.62	80.86	
Step8M	Middle	4760	9.60	46.37	8.61	
Step8T	Tail	13 200	26.63	20.45	10.53	
	Dust	0	0.00	0.00	0.00	0.00
-	Feed (Calculated)	49 560	100.00	51.74	100.00	0.00
F1	Feed (Actual)	50 120	100.00	50.87	100.00	17.49

TABLE 19

Results of new fine particle drum separator with different location of magnetic field intensity (θ = 90°).

Test Stage					Rougher	
Sample	**Name**	**Wt. kg**	**Wt. %**	**Fe %**	Fe_{Rec} **%**	**FeO %**
C	Concentrate	33 180	67.44	64.40	84.98	
M	Middle	2260	4.59	33.95	3.05	
T	Tail	13 760	27097	21.87	11.97	
	Dust	0	0.00	0.00	0.00	0.00
-	Feed (Calculated)	49 200	100.00	51.11	100.00	0.00
C32	Feed (Actual)	50 000	100.00	50.87	100.00	17.49

TABLE 20

Results of new fine particle drum separator with different location of magnetic field intensity (θ = 75°).

Test Stage					Rougher	
Sample	**Name**	**Wt. kg**	**Wt. %**	**Fe %**	Fe_{Rec} **%**	**FeO %**
C	Concentrate	33 180	66.94	64.85	85.16	23.45
M	Middle	2530	5.10	35.60	3.56	6.51
T	Tail	13 855	27.95	20.57	11.28	4.84
	Dust	0	0.00	0.00	0.00	0.00
-	Feed (Calculated)	49 565	100.00	50.98	100.00	17.39
C32	Feed (Actual)	50 000	100.00	50.87	100.00	17.49

It can be seen in Figure 12 that the best location for peak of magnetic intensity is at θ = 60° which allow getting maximum Fe grade in concentrate box.

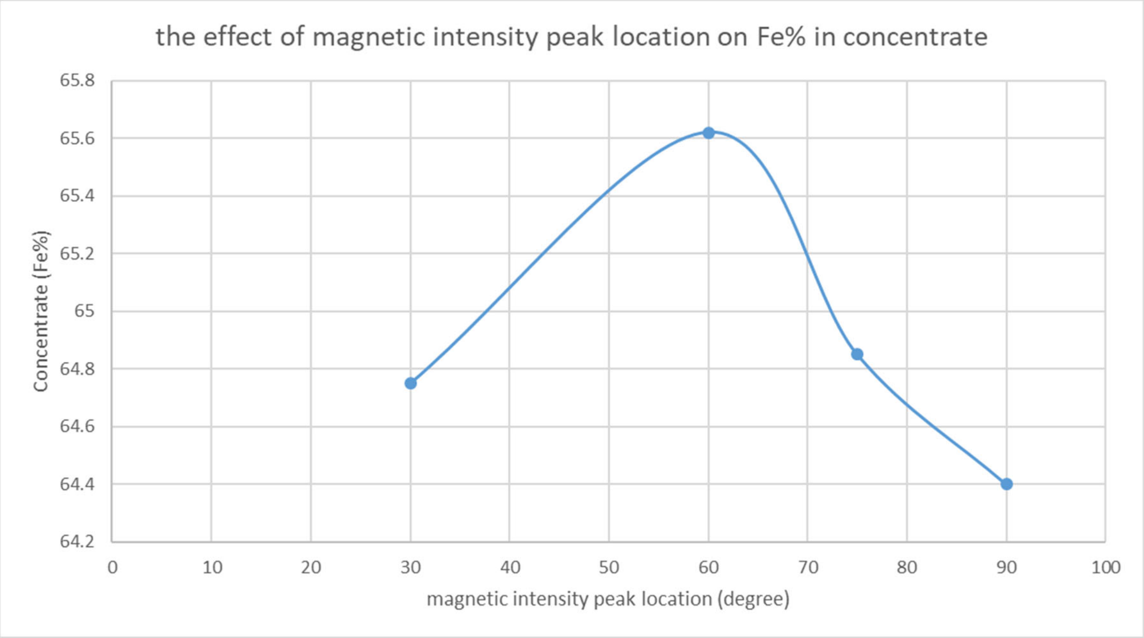

FIG 12 – The effect of location of magnetic intensity peak on Fe per cent in concentrate.

More experimental test has done to comprise the results of new drum separator with traditional drum separators. Tables 21 to 23 are shown the experimental result for traditional drum separators at different condition.

TABLE 21

Results of first stage drum separator (3500G) with linear drum speed 1.5 m/s.

Test Stage					Rougher	
Sample	**Name**	**Wt. kg**	**Wt. %**	**Fe %**	Fe_{Rec} **%**	**FeO %**
C1	Concentrate	42.90	86.35	57.17	96.94	20.05
T1	Tail	6.78	13.65	11.43	3.06	3.42
-	Feed (Calculated)	49.68	100.00	50.93	100.00	17.78
F1	Feed (Actual)	50.00	100.00	50.87	100.00	17.49

TABLE 22

Results of first stage drum separator (3500G) with linear drum speed 2 m/s.

Test Stage					Rougher	
Sample	**Name**	**Wt. kg**	**Wt. %**	**Fe %**	Fe_{Rec} **%**	**FeO %**
C11	Concentrate	41.2	82.97	58.63	95.90	20.63
T11	Tail	8.5	17.03	12.21	4.10	3.52
-	Feed (Calculated)	49.7	100.00	50.73	100.00	17.72
F1	Feed (Actual)	50.0	100.00	50.87	100.00	17.49

TABLE 23

Results of first stage drum separator (1100G) with linear drum speed 2 m/s.

Test Stage					Rougher
Sample	**Name**	**Wt. kg**	**Wt. %**	**Fe %**	Fe_{Rec} **%**
C11	Concentrate	37.9	76.30	61.11	91.54
T11	Tail	11.8	23.70	18.17	8.46
-	Feed (Calculated)	49.7	100.00	50.93	100.00
F1	Feed (Actual)	50.0	100.00	50.87	100.00

Figure 13 show the summary of experimental result of traditional drum separators at different condition.

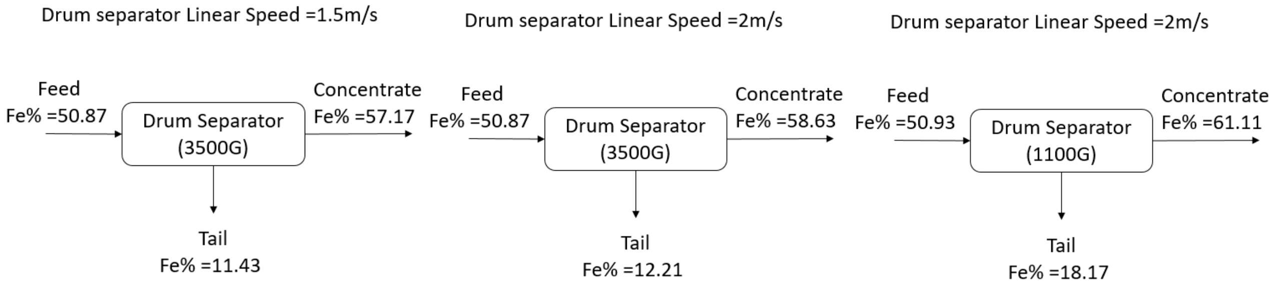

(a) (b) (c)

FIG 13 – Comparison between different type of usual drum separators (a) 3500G with 1.5 m/s speed; (b) 3500G with 2 m/s; (c) 1100 G with 2 m/s.

CONCLUSIONS

The effects of different parameters on fine particle drum separator were investigated. Both experimental and numerical methods are used in this investigation. The FEMM software was used to simulate magnetic field distribution through surface of drum separator. In this new equipment different parameters have effect on efficiency of drum separators. Drum speed, core speed, Dedusting location, gate location and the location of peak of magnetic intensity are the major parameters which have effect on drum separator efficiency. Results show that when drum shell speed was 42.5 rev/min, magnetic yoke speed was 100 rev/min and the maximum intensity of magnetic field was at θ = 30° the feed grade increased from 50.87 to 65.67 in concentrate box, increase to 60.45 in middle box and tail grade was 24.44. The total achieved recovery for both concentrate and middle box was 81.89 per cent.

REFERENCES

Bikbov, M, Karmazin, V and Bikbov, A, 2004. Low-Intensity Magnetic Separation: Principal Stages of a Separator Development – What is the Next Step? *Physical Separation in Science and Engineering,* 13.

Davis, J and Lyman, G, 1983. Magnetite recovery using a wet drum separator, *Australas Inst Min Metall Proc,* 287.

Dwari, R K and Rao, K H, 2007. Dry Beneficiation Of Coal – A Review. *Mineral Processing and Extractive Metallurgy Review,* 28:177–234.

Rayner, J G and Napier-Munn, T J, 2003. A mathematical model of concentrate solids content for the wet drum magnetic separator, *International Journal of Mineral Processing,* 70:53–65.

Zhang, H, Chen, L, Zeng, J, Ding, L and Liu, J, 2015. Processing of Lean Iron Ores by Dry High Intensity Magnetic Separation, *Separation Science and Technology,* 50:1689–1694.

Breakthrough in elliptical motion screen trial delivers significant performance gains

D Teyhan[1] and J Kirsch[2]

1. Product Expert – Screening, Schenck Process Australia, Beresfield NSW 2322.
   Email: d.teyhan@schenckprocess.com
2. Vice President Technology, Schenck Process Australia, Beresfield NSW 2322.
   Email: j.kirsch@schenckprocess.com

ABSTRACT

Traditionally, most Australian iron ore mining operations have been surface-based. Processing plants were designed to handle dry ores. In recent years mining operations in the Pilbara have progressively moved below the water table exposing wet, sticky ores which have caused lost efficiency in screening operations as particles tend to agglomerate and adhere, blinding screening media.

Miners and vibrating screen manufacturers have experimented with a shift from linear motion to elliptical motion screens. Elliptical motion conveys and lifts particles. Effective on flat deck (horizontal and inclined) or sloping decks it can be configured to provide a controlled transport rate, applying pressure in all directions to maximise screening efficiency. In practice, elliptical motion screens have proven to be effective in dislodging sticky particles from screening media, reducing blinding rates and improving screen efficiency.

Moisture and clay content change during the life of a mine. These changes are sometimes the effect of seasonal rainfall, in other cases due to increased groundwater and clay content as mining operations go deeper. To compensate for such changes and optimise screen efficiency, changing the 'shape' of elliptical screen motion is required. This has traditionally required shutting down processing plants and making mechanical screen adjustments. Plant downtime is costly and machine adjustment has been a 'trial and error' practice.

This paper will explore the results of a field trial that is currently underway in Brazil of a next generation elliptical motion screen design that allows operators to make changes to exciter rotational direction, speed and screen stroke angle, through electronic drive phase control. The machine's electronic drive system synchronisation is enhanced for stability with a unique mechanical timing system. Operating at up to 6 g, screen adjustments can be made on the fly without stopping production. Early trial results are showing up to 50 per cent improvement in screen efficiency compared with traditional elliptical motion machines under certain feed conditions.

INTRODUCTION

The earliest form of screening in mineral processing took place in the form of manual sizing. 'Breaker boys' would sit above the product stream and manually sort and size the large lumps as required by the process. Later, static screens were developed where the product was manually manipulated over apertured plate or bars with lateral spacing matching the sizing cut point as required by the process application. Typically, these were aggressively sloped from feed to discharge end to promote the material flow. With the introduction of electric motors to the mineral processing industry, some of the earliest forms of mechanised screening took place in the form of crank driven reciprocating shaker screens and simple spring mounted single shaft circular motion screens which are still used in some applications today (Figure 1). Where shaker screens had significant limitations in terms of capacity and adhesion (having little to no perpendicular acceleration component to the apertured deck), the circular motion mechanised screens facilitate both elevation of the product and transportation of the product from feed to discharge end.

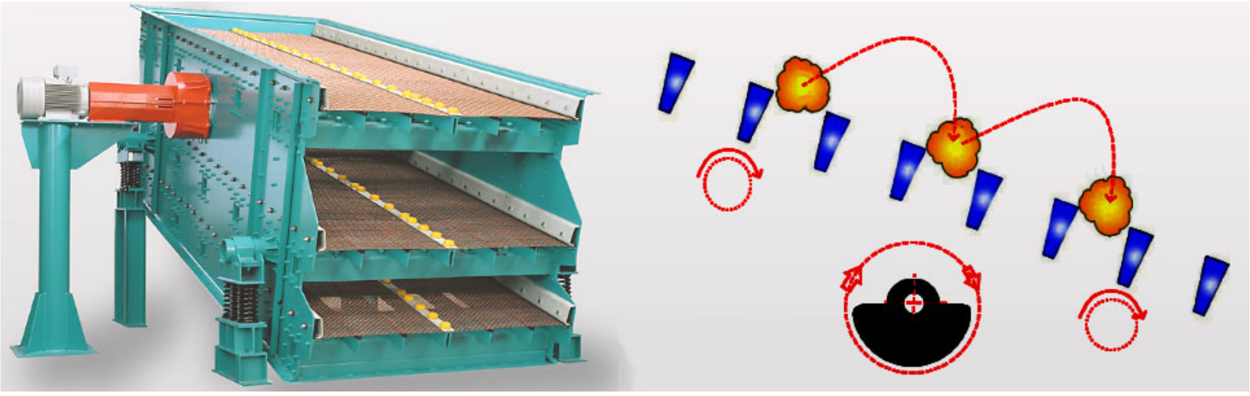

FIG 1 – Single shaft circular motion screen showing motion pattern and particle trajectory.

Circular motion screens are mounted on soft springs and are excited by a forcing function that generates a motion pattern which is essentially an orbital system between the screen body and the counterweight based on momentum principals. Due to the interaction between the particle trajectory of the bed of material and the screen panel apertures on circular motion screens, a very specific range of operating speed and acceleration are required to ensure that the product flow is not over energised resulting in a reduction in probability of separation and reduced overall efficiency, or under energised resulting in retarding the flow of product, increased bed depth, and a reduction in overall efficiency. A typical operating characteristic for circular motion screens would be 3.5 g acceleration at a speed close to 850 rev/min, and the theoretical feed material single particle trajectory from these operating characteristics can be seen in Figure 2. As demonstrated, the feed material particle trajectory with these operating characteristics results in impact with the apertured deck each cycle with the impact occurring somewhere between the maximum velocity of screen vertical motion, and the theoretical point of separation of particles from the apertured deck. It should be noted that particle interaction at the maximum vertical velocity point will result in no horizontal impact component being imparted on the particle, and that interaction at a velocity vector significantly greater than 45° from horizontal will result in under-energisation of the vertical velocity component. For this reason, the operating characteristics selected for circular motion screens need to be highly specific, and the decks need to be inclined to promote material flow. A pegged or adhered particle will however have force components applied in all directions.

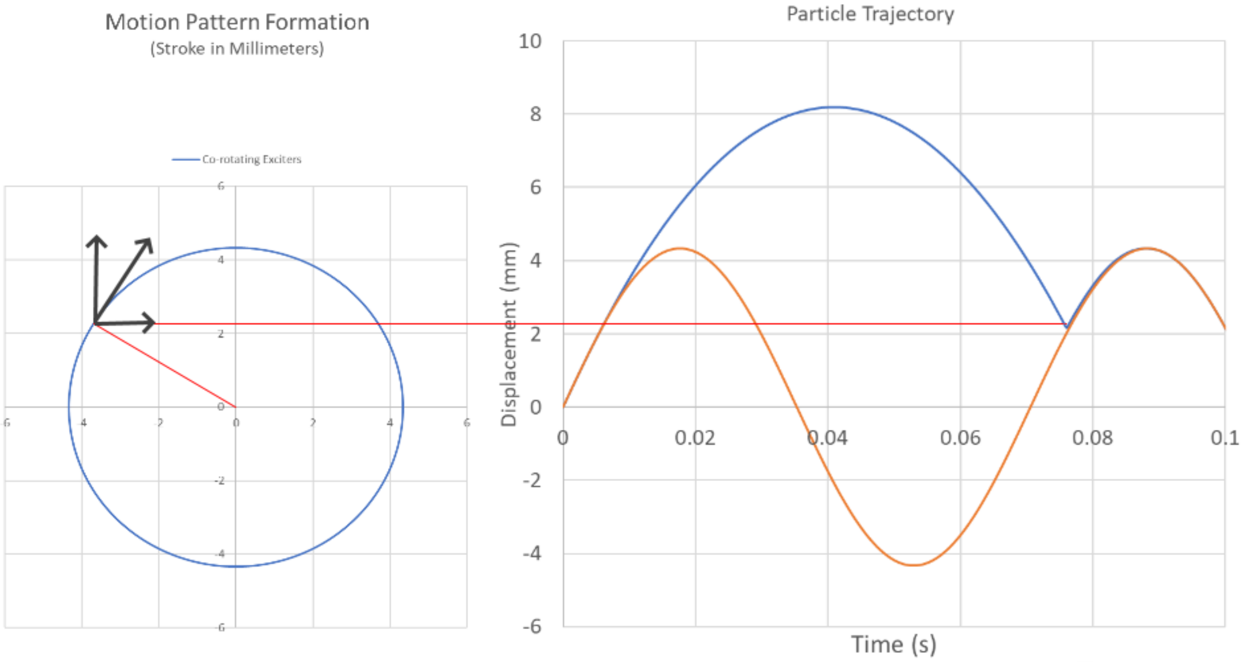

FIG 2 – Theoretical single particle vertical trajectory based on 8.7 mm stroke at 850 rev/min (3.5 g).

One of the benefits of the traditional circular motion screen is the acceleration component imparted on the particle in the plane of the apertured panel. This in plane motion is highly effective at dislodging near size and/or sticky particles when pegged in the apertures. Among the disadvantages are the specific operating characteristic requirements, and the difficulty in controlling flow velocity of larger particles down the deck of the screen. Using simple mathematical models of single particle trajectories to predict probabilities of separation based on operating characteristics of the screen alone, ignores particle on particle interactions and interparticle cohesion (Cleary, Wilson and Sinnot, 2018). A causal link between a simple particle trajectory calculation and material transport velocity and bed depths can be observed in practise. However, this has not necessarily translated to better particle size stratification or process efficiency.

Following from the development of the circular motion vibrating screen was the linear motion flat deck screen (Figure 3). The development of linear motion screening by utilising pairs of counter-rotating eccentric mass shafts addressed some of the issues associated with the requirement for highly specific operating characteristics. This meant that regardless of the speed and stroke length selected, there would always be a velocity component of the screen to lift the particle, and a component transporting the particle from feed to discharge end. Linear motion screens have the advantage of a horizontal velocity component to their stroke which conveniently allowed designers to achieve controlled transport velocities of feed material without needing to incline the screen decks. This facilitated lower overall build heights which allowed for more compact processing plants, and lower overall production power requirements due to the reduction in potential between the feed and discharge points of the screen. Whether appropriate for the application or not, a line of stroke at 45° was assumed as the industry standard as this provided equal vertical and horizontal velocity components.

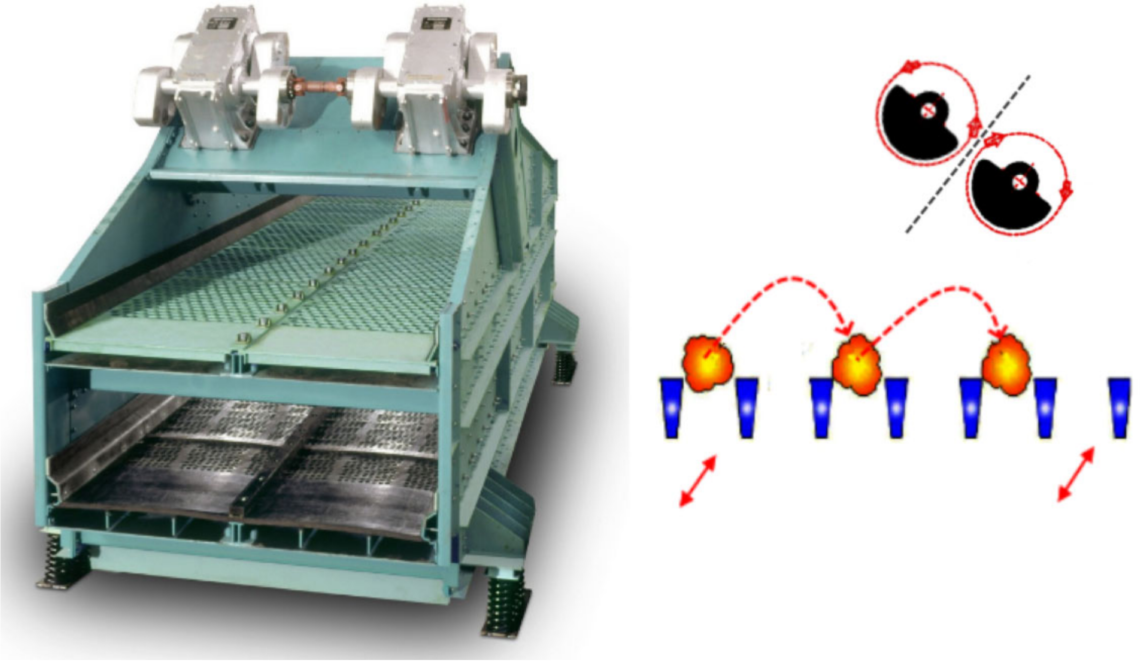

FIG 3 – Counter-rotating mass linear motion screen showing motion pattern and particle trajectory.

Despite having a completely different set of material interaction characteristics to circular motion screens, with the introduction of linear motion screens the nominal speed and maximum acceleration perpendicular to the screening panels of circular motion screens was maintained. For horizontal flat deck screens, this results in a peak acceleration of approximately 5 g along the line of stroke of 45° from horizontal. The theoretical feed material single particle trajectory can be seen in Figure 4.

Alongside the benefits of the new linear motion screening concept was the limitation on structural capacity due to lower deck inclination and lower transport velocities of feed material. Previous studies undertaken on the phenomenon of particle separation using numerical methods (specifically DEM – Cleary *et al*, 2009; Guolang and Tong, 2020) have identified several mechanisms for separation including:

1. energisation of the bed to create interstitial gaps
2. percolation of finer particles through the bed of coarser material
3. particle on particle interactions
4. aperture penetration.

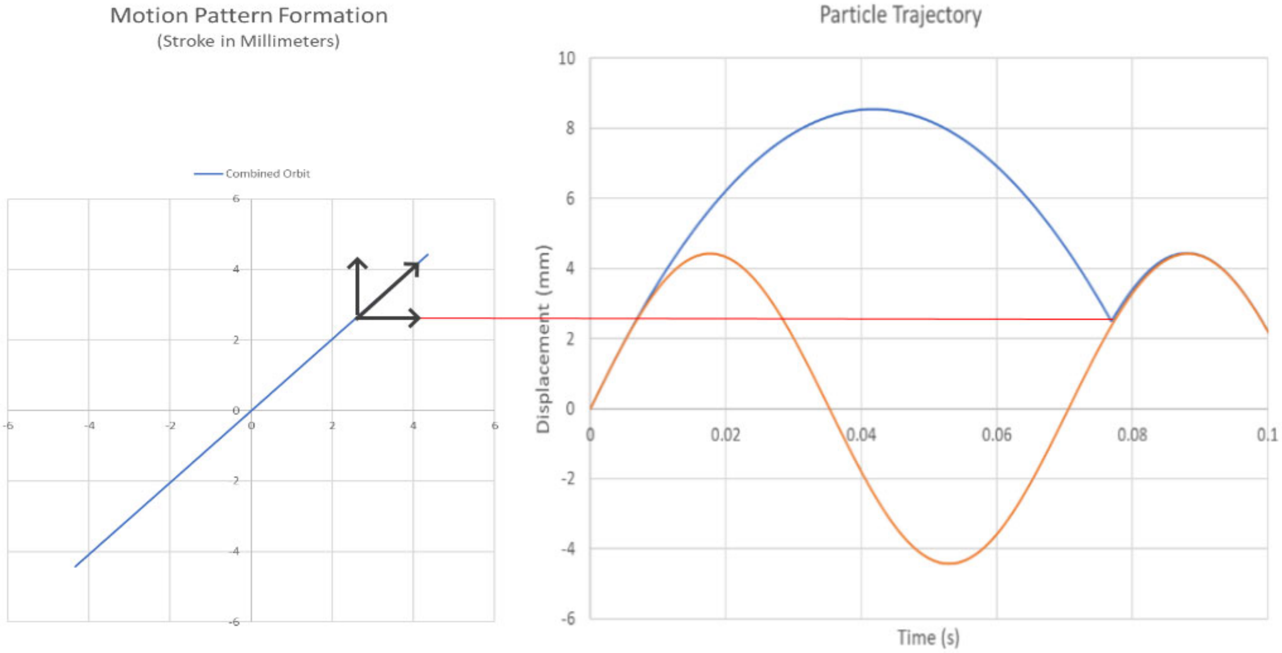

FIG 4 – Theoretical single particle vertical trajectory based on 12.4 mm stroke at 850 rev/min (5 g).

Little information is available in these studies on the segregation phenomenon due to the different levels of mobility of particles in the high velocity feed zone of aggressively sloped screen decks, whereby the higher transport velocity of the larger and less inhibited particles results in segregation, leading to larger particles transporting to the top of the material bed. This contribution to stratification is lost in the feed zone of horizontal flat deck screens. Flat deck screens are sometimes inclined up to 10° from horizontal to circumvent this problem, however in these cases the benefit of low potential between the feed and discharge points of the screen are lost. Pegging of feed material particles in the screening panel apertures of horizontal flat screens with high near size particle fractions in the particle size distribution is also common and strongly related to particle shape and adhesion characteristics. Pegged or adhered particles in linear motion screening only experience forces applied in one direction with fluctuating and completely opposing vectors.

In the last 30 years, the use of multislope 'banana screens' has become increasingly common for high-capacity screening for both wet and dry applications. Banana screens are constructed with an aggressively sloped feed end section which becomes progressively shallower in inclination toward the discharge end. Whilst some circular motion banana screens have been built, banana screens are predominantly driven by the same type of linear motion exciters as flat deck linear motion screens. Curved Banana screen decks introduce the benefit of high ore feed velocity at the feed end of the machine. The elevated transport velocity of the feed material up to 4 m/s results in a thinning of the bed depth, allowing for larger particle spacing of the larger lump fraction which facilitates liberation of more fines. The larger particles being unconstrained from high bed depth pressures are freer to mobilise down the deck at higher transport velocities than the fines fraction, assisting effective stratification at the discharge end. Relatively higher levels of shearing flow at the feed end in comparison to horizontal flat deck screens coupled with progressive reduction in transport velocity due to particle interactions provides an effective means for larger particles to liberate agglomerated fines without relying solely on the machine's operating characteristics. Finally, pressure on the near size particles at the discharge end from the stratified bed with low transport velocity gives higher probabilities of separation.

Wet screening of slurries on banana screens is also effective despite interphase drag having a normalising effect on the particle size related and slurry velocity distributions (Cleary, Wilson and Sinnot, 2018). This effectiveness is due to the ready percolation of fines entrained in slurry through the dilute phase in the feed end bed depth. Despite the high proportion of the fines fraction in the feed material which passes through the apertures in the feed end of the screen, the lower transport velocity of the discharge end and greater number of cycles experienced by the feed material over the discharge stages is important for the screens to achieve the process efficiency target (refer to Figure 5).

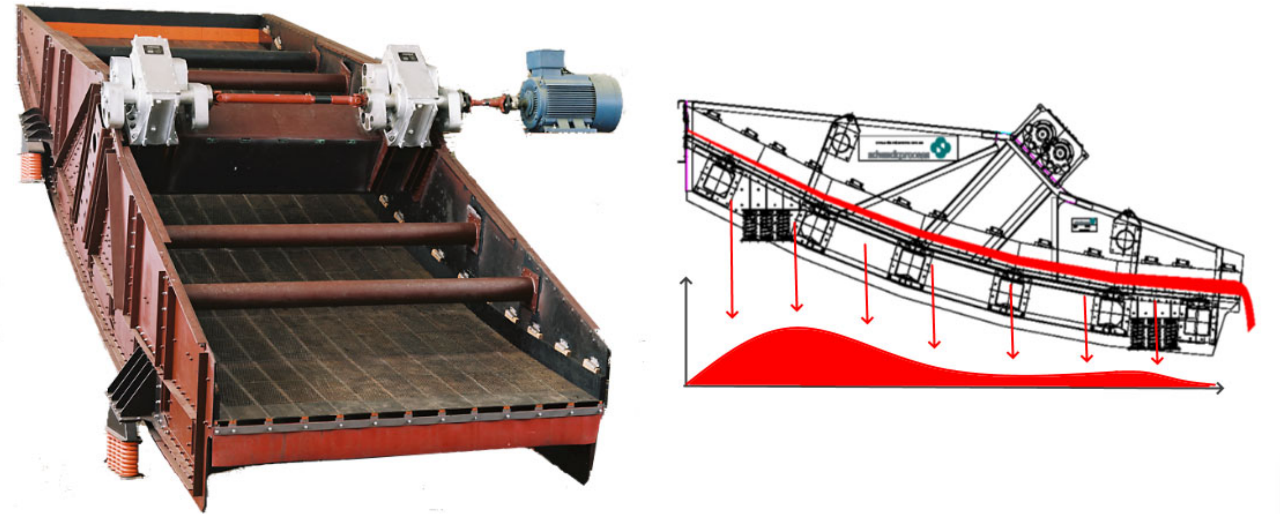

FIG 5 – Counter-rotating mass linear motion banana screen showing typical feed material distribution.

Elliptical motion screen concepts have been in existence since the 1970s but gained market traction over the past two decades as more ore producers have been attempting to mine product below water table or to screen product with natural moisture. The concept of elliptical motion screens is to develop a screen stroke with an orbit path that provides both the reliable transport velocity of a linear motion screen, but with the multidirectional force components of a circular motion screen. The aim is to provide sufficient energisation of the bed of material to maximise stratification by creation of interstitial gaps between larger particles, and to provide a multidirectional excitation to de-peg near size particle blockages of apertures and adherent material. Elliptical motion screens have been built in flat deck designs (both horizontal and inclined), and more recently in multislope banana style designs. Several techniques have been used for generating elliptical motion, including:

- Two counter-rotating single shaft exciters with differing eccentric mass positioned at distances from the screen centre of gravity inversely proportional to the eccentric masses.
- Utilising three single shaft exciters with the same or different eccentric masses, two exciters co-rotating and one counter-rotating.
- Mounting a series of single shaft or double shaft exciters on perpendicular axes and controlling their phase relationship to generate elliptical motion.

In dry coarse sizing, elliptical motion screens have consistently demonstrated the capacity for more efficient separation. Elliptical motion has already been applied to sticky or difficult to screen materials where the empirically derived formulas for screen sizing and efficiency are of questionable validity. This paper presents the findings of a field trial of a 2.5 m × 6.4 m Double Deck Banana Elliptical Motion Screen for natural moisture screening of coarse iron ore.

DESIGN DEVELOPMENT

The Schenck Process Elliptical Motion screen utilised in the trial was developed to fit the existing footprint of a South American Iron Ore producer and was designated the model name SED2564. The screen was designed to be driven by six Schenck Process VZ501 circular motion exciter cells closely spaced about the centre of gravity of the screen and mounted in three laterally opposed pairs connected with intermediate shafts spanning the screen. The screen was designed to be driven by three independent direct drive electric motors via universal shafts, with each motor being independently electronically synchronised. The product designation represents a double deck multislope elliptical machine with a 2.5 m wide and 6.4 m long apertured section, with this particular machine being designed for deck angles from 20° to 8° on the top deck.

The preliminary design stage commenced with the sizing of the screen using traditional proprietary calculation methods by modifying the moisture factor of the material. It should be noted for iron ore with significant fines fraction, feed material with surface moisture content exceeding eight per cent of the product mass will typically suffer from adhesion of fines to the lump fraction. The adhesion of fines makes separation more difficult as the finer particles have a tendency to carry over to discharge from the machine with the coarser particles. Moreover, the particle size distribution (PSD) related transport velocity differential, which aides in stratification, in the feed end of multislope banana screens is present to a lesser extent. Historically, sizing and machine capacities have been determined by an empirically derived formula which treats the process parameters as being independent, for example:

$$C = B \times I \times D \times Sh \times So \times A \times Oa \times W \times Y \times M \times Z \times E \tag{1}$$

Where:

C	is Tonnes / square meter
B	is base capacity
I	is inclination factor
D	is deck number
Sh	is per cent passing half the separation (cut) size
So	is per cent of oversize in feed
A	is the aperture shape factor
Oa	is the Open Area factor of the deck
W	is Bulk density of the feed material
Y	is Wet Screening. Water added as spray or in feed
M	is moisture content of the feed material – If screening is to be dry screening
Z	is Particle Shape factor
E	is Efficiency Factor

Guolang and Tong (2020), identified that under varying material and operating characteristics, there was a noticeable degree of interdependencies between the process application variables. Since at the design stage of this project these interdependencies were unknown, an unmodified traditional application sizing approach was used.

The outputs of the application sizing calculations were required in order to determine worst case retained product loads for the upper and lower deck of the screen. These were dependent on maximum and minimum process efficiencies of the top deck based on both wet and dry season material conditions. The worst case retained deck loads were used for preliminary sizing of the deck components based on hand calculations of cross beam bending stress. Conservative permissible fatigue design stress acceptance criteria were applied according to the recommendations of BS7608–2014 Fatigue design and assessment of steel structures.

Following the basic sizing of the screen components, a bounding envelope for a side plate was defined and a mass estimate developed. Appropriate sizing of the exciters was then conducted to ensure that 6 g of acceleration could be achieved within the bearing capacity limits. At this stage, the screen was modelled in Autodesk Inventor, and Finite Element Analysis (FEA) model produced. Given the primary objective of the screen to be adaptable to the process without shutting the machine down, one aim of the analysis was to achieve a separation between the operating speed and the closest modal frequencies of the screen body structure to permit operation of the screen between

850 rev/min and 950 rev/min. Since acceleration of the screen is a function of the square of the operating speed, with variable speed control in this operating frequency range the screen would be capable of delivering an ellipse with a major axis of between 4.8 g and 6.0 g acceleration without the requirement to change the eccentric mass of the exciter cells. The screen design was extensively analysed with the preliminary FEA focused on the mass and stiffness distribution to ensure the primary flexural natural frequency modes were significantly above the operating frequency so as not to adversely affect the operating characteristics. The FEA then focused on determining the suitability of the component selection under a number of exciter phasing positions and inertia load case combinations. Principal stress load case combinations were used for fatigue design purposes.

In tandem with the screen body structural design, the PLC control logic for phase adjustment between the exciter cells was developed. In order to test the control logic prior to the screen being built, a small-scale workshop test bed weighing 120 kg and driven by three Uras KEE-3-6WK vibrator motors was developed to prove the stroke predictions and test the stability of the control logic. Three operating configurations were tested as detailed in Figure 6.

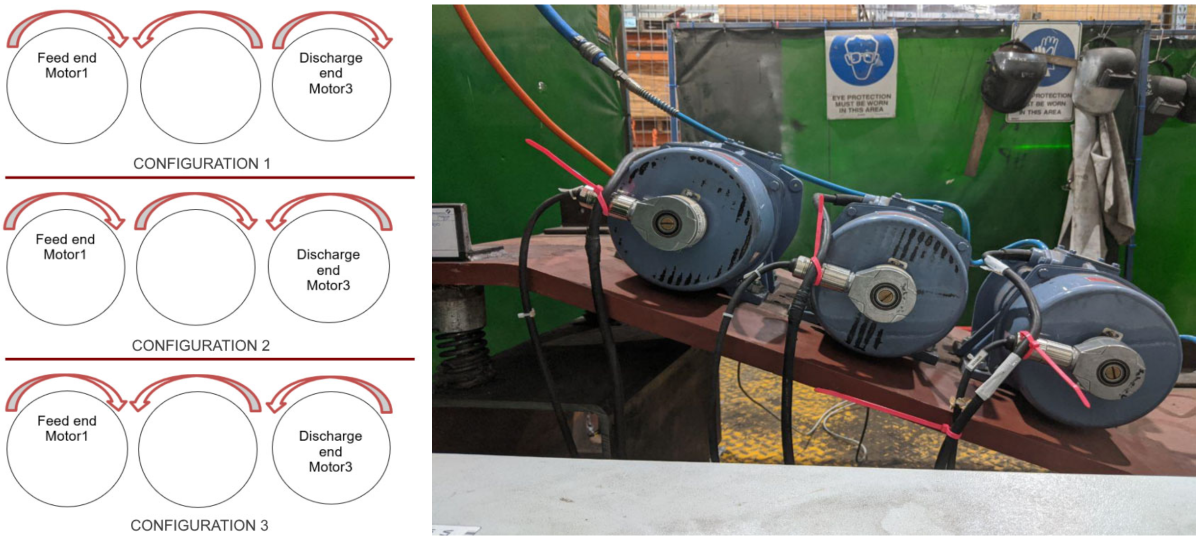

FIG 6 – Operating configurations tested on the scaled test bed.

For each design operating configuration, three intended weights setting (25 per cent, 75 per cent, and 100 per cent) at different phase angles and combinations of rotational directions were tested. For each direction of rotation the Operating Data of speed, torque, and position were recorded and plotted.

Consistent across all test results, design rotation Configuration 1 (both other exciter pairs co-rotating) was shown to be the most stable. It performed better in terms of maximum and minimum possible phase angle adjustment, and synchronisation stability for different parameters of speed and eccentric weights. It was observed that a configuration with a 75 per cent eccentric mass setting and an initial 20° phase angle from horizontal, broke synchronisation stability at 70° phase angle from horizontal. It was further observed at the stability limits of the system that motors 1 and 3, whilst trying to achieve the command velocity, suffered significant signal disturbance in the actual velocity data. There was a torque spike which indicated that the control was suffering some degree of overshoot and a general divergence in the torque demand of motors 1 and 3 as seen in Figure 7. It was not established whether this was due to saturated control, control lag, or inertia torque effects. The same characteristic was not observed on motor 2. This indicated that the development of higher rotational inertia by use of flywheels and developing external synchronisation of co-rotating elements by mechanical means would be effective in eliminating system instability but would still permit complete angular control of the elliptical motion through changing the phasing relationship between co-rotating and counter rotating elements by electronic means. To remove the inertia torque effects from the motor torque demand and make a more stable electronic synchronisation, mechanical connection of motor 3 and motor 1 with a timing belt system was proposed, developed, and tested on the small-scale test bed. A full-scale synchronisation system was developed for the

SED2564 machine and was implemented for the duration of a six month site trial. The synchronisation system development has a Patent Pending.

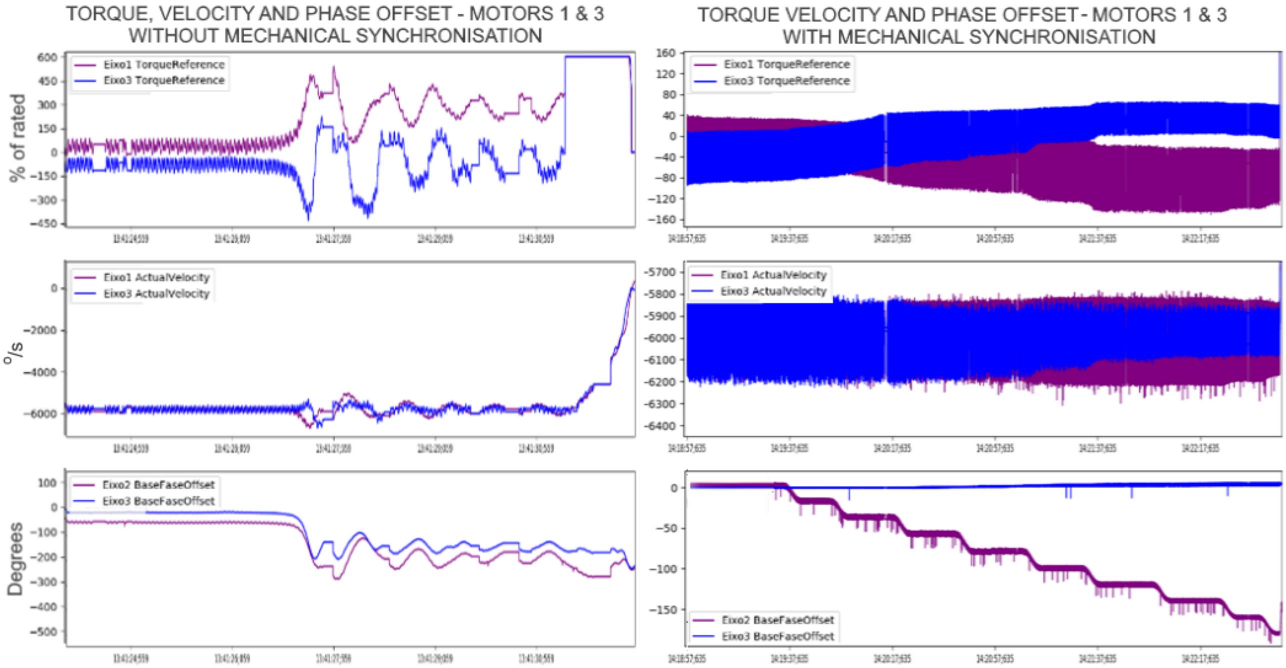

FIG 7 – Torque demand, instantaneous angular velocity, and phase relationship of elliptical test bed with and without mechanical synchronisation between co-rotating elements.

Data collected on the scaled elliptical test bed demonstrated that the system stability was determined by the two outer co-rotating motors due to inertia torque effects. The centre counter-rotating motor appeared not to be affected by inertia torque to the same extent. An actuation of phase angle relationship between the co-rotating and counter-rotating motors resulted in loss of synchronisation at a stroke angle of 70° from horizontal without the mechanical synchronisation system. The same configuration with mechanical synchronisation between co-rotating elements reduced the peak torque demand and permitted full control of the major axis of the ellipse through 180° by electronic synchronisation. Furthermore, a series of tests were run where a step input disturbance was introduced to the scaled test bed by dropping the weighted end of a 4 lb (~1.8 kg) mallet (with parabolic rubber buffer) a distance of 200 mm onto the end of the test bed adjacent to motor 1. In all cases without mechanical synchronisation the system lost synchronisation stability, but with mechanical synchronisation was capable of retaining synchronisation stability at all phasing angles. This indicated that the full-scale system with mechanical synchronisation would be more stable under transient dynamic events, which typically occur under on-feed and off-feed conditions.

The full-scale screen was built in the Schenck Process workshop in Taubate, Brazil, and tested under 6 g acceleration with a series of operating speeds between 850 rev/min and 950 rev/min. Strain gauge data was collected to verify the design, and some fine tuning to the intermediate shafts between exciters was conducted to improve modal separation from torsional resonance of the drive system. The screen was despatched for field trial in a wet season natural moisture iron ore screening application.

APPLICATION OVERVIEW

The scope of the machine development was to design a 2.5 × 6.4 m double deck multislope banana screen capable of screening up to 55 tph/m^2 of high moisture iron ore (up to 13% per cent surface moisture content), but also capable of being adapted to dry screening of ore. The material properties and operating requirements included:

- Bulk Density – 2.7 t/m^3
- Specific Gravity – 4.7

- Maximum Lump size – 120 mm
- 76 per cent of the feed PSD <6 mm (approximately 1/3 the bottom deck cut point)
- Operating acceleration requirement of between 5 g and 6 g.

The high fines content and seasonally high surface moisture content make the application a very challenging process to achieve with a vibrating screen. This is mainly due to adhesion of fines to the lump fraction, but also the cohesion between fines, and the adhesion of the fines to the screening panels. It was understood that this would further be challenged by a significant reduction in stratification caused by the normalising of particle size related transport velocity differences. It was hypothesized that some combination of operating speed between 850 rev/min and 950 rev/min, acceleration between 5 g and 6 g, and some operating angle of the major axis of the ellipse between 20° to 70° from horizontal with operating direction either with material flow or counter material flow at the top of the ellipse, would provide a process efficiency and screen capacity advantage. The exciter configuration to achieve the adjustable elliptical operation can be seen in Figure 8.

The trial of process performance was set at six months to ensure a good seasonal variation of surface moisture content dependent on performance and a target availability. Process performance requirements were measured for the top deck at the discharge, based on the level of fines contaminates (below the cut point) on the top deck, and lump in fines contaminates from the underpan on the bottom deck.

FIG 8 – SED2564 electronic synchronisation testing in Tabaute workshop.

FIELD TRIAL RESULTS

The SED2564 6 g electronically synchronised elliptical motion screen was installed for field trials carried out in the period from 01 December 2020 to 31 May 2021. During the field trial, a significant variation in feed material characteristics was experienced based on differences in surface moisture content. Various operating characteristics of the screen were trialled with each feed material type. Figure 9 demonstrates the operating characteristics with low moisture content (approximately 8 per cent) from data collected between 25–30 November 2020 in the initial commissioning stages of the project. At the time, the screen was operating at a nominal 500 t/h for commissioning purposes, with fines fraction high enough that no appreciable bed depth was forming on the discharge stage. Detail ‘A’ from Figure 9 demonstrates operation with a 6 g acceleration 60° major axis from horizontal with an ellipse aspect ratio of 3:1 with rotation direction of co-rotating exciters with the direction of material flow over top centre. Visual observations of the live operating characteristics clearly demonstrated over energisation of particles with high amplitude particle bouncing, and clearly visible interaction with the screen deck every second cycle. Whilst the general direction of transport was toward the discharge, there were an appreciable number of particles being projected backward during this operating characteristic. It was also evident that the fines carry over at the discharge end was relatively low, and well below the target percentage. Utilising the theoretical particle trajectory as a basis for comparison, the 0.5× subharmonic observed during operation was supported by the theoretical particle trajectory, and the low transport velocity and random particle directions were supported by the theoretical point of interaction with the deck panels having a vector almost vertical in orientation. The opportunity to trial the performance of the screen with these operating characteristics and a more heavily formed bed of material has not yet been provided. Further testing with various operating characteristics is expected to be conducted in the next six months of the trial.

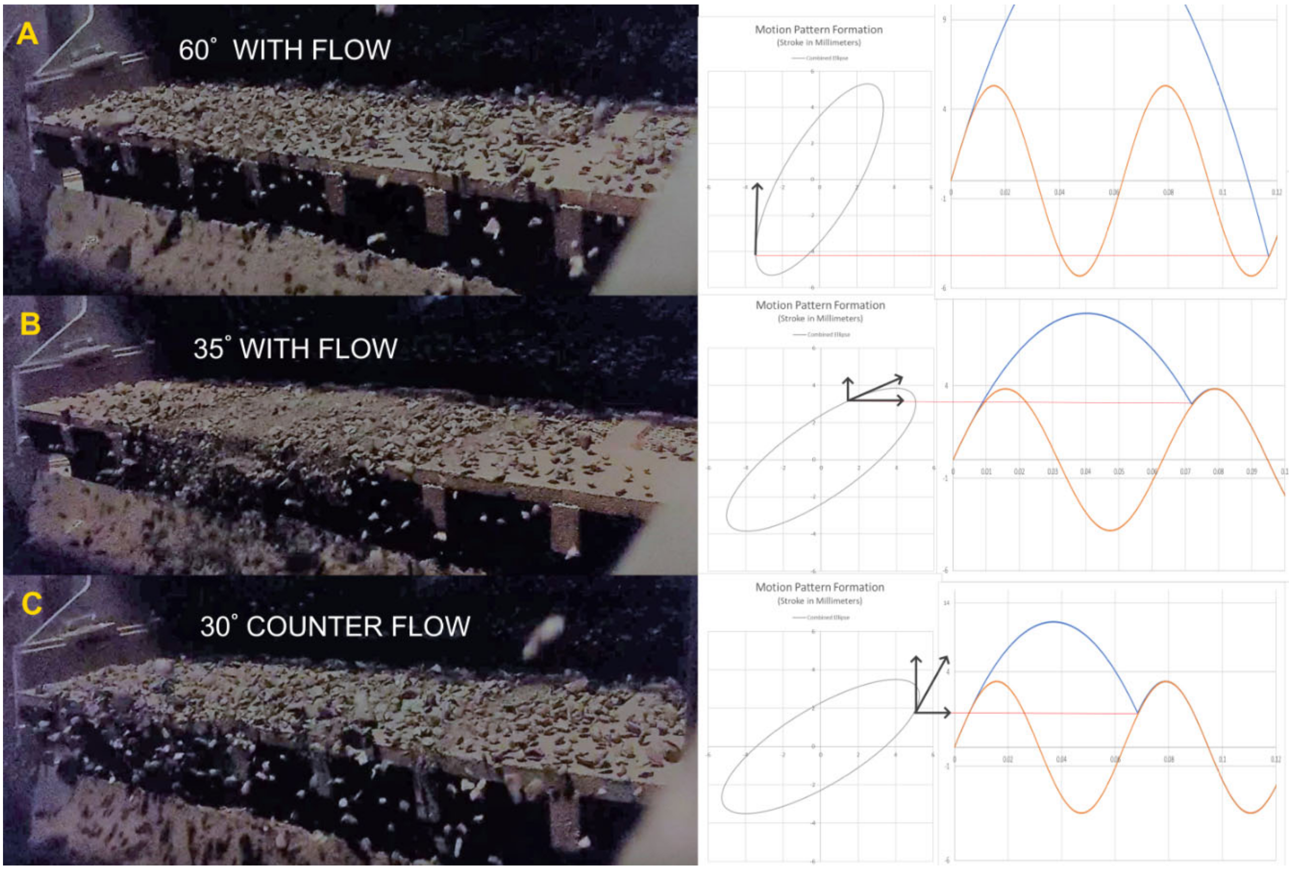

FIG 9 – Observed material conditions and associated theoretical material interaction with the screen deck.

Figure 9 Detail ‘B’ shows the operation with a 6 g 35° major axis from horizontal with an ellipse aspect ratio of 3:1 with rotation direction of co-rotating exciters with the direction of material flow over top centre. The material was visually under energised in the vertical direction resulting in mostly horizontal motion. The transport velocity was high, and fines carry over significantly higher than that seen with operating major axis angle at 60°. The single particle theoretical trajectory also supported the under energisation seen in the actual material flow, and the excessive transport velocity and fines carry over was consistent with the theoretical vector of interaction with the screen deck panels being largely horizontal.

Figure 9 Detail ‘C’ was a trial run with the direction of co-rotating exciters counter flow over top centre with a major axis at 6 g 30° from horizontal. The aspect ratio of the ellipse was again 3:1 and visual observations were characterised by a good well controlled transport velocity, reasonable levels of particle energisation with a regular steady state impact period coinciding with the screen deck every cycle. Fines carry over was low and comparable to that seen with 60° major axis in the co-rotation direction. The main source of fines carry over in this configuration was seen as material tracking along the blank join line between panels. This characteristic was not evident with the higher angle of major axis seen in Detail ‘A’.

Periodic fortnightly bucket samples of product PSD and moisture content failed to capture the true variance of PSD and moisture content observed in the performance of the screen. At times the fines fraction was seen to be a thick, muddy paste indicating surface moisture content at or above 12–13 per cent. Under these circumstances, operation with a low angle of the major axis and counterflow rotation even at 6 g acceleration allowed the bed at the discharge end to form large slabby cakes of agglomerated material. Under these material conditions operation with 60° major axis from horizontal with rotation direction with flow appeared to break up the slabby cakes and allow a significantly larger proportion of fines to pass the bottom deck apertures. Balls of agglomerated fines captured from the undersize fraction during this high moisture operating condition can be seen in Figure 10.

FIG 10 – Agglomerated fines obtained from the undersize of the screen whilst operating with high surface moisture content.

CONCLUSIONS

The development of the elliptical motion for the SED2564 machine demonstrated that phasing stability of the system was limited by the co-rotating exciters. When operating near stability limits, small perturbations to the system caused the scaled screen to lose synchronisation. The development of a mechanical synchronisation system linking the co-rotating exciter cells only, allowed complete phase stability throughout 360° of phasing actuation regardless of eccentric mass, acceleration, or introduced perturbations.

The loss of one of the main mechanisms of stratification with high moisture screening results in significantly restricted tonnage throughput. With surface moisture content between 8–10 per cent, the feed characteristics are such that elliptical motion with a traditional operating angle of 45° results in poor efficiency performance. Two operating characteristics provided beneficial results on efficiency with these feed materials, operation with a 3:1 ellipse at 6 g acceleration and a major axis at 60° from horizontal and direction of rotation of co-rotating exciters with the direction of flow over top centre, and operation with a 3:1 ellipse at 6 g acceleration with a major axis 30° from horizontal and direction of rotation of co-rotating exciters against the direction of feed material flow over top centre. At feed surface moisture content above 10 per cent, the formation of slabby cakes of consolidated fines required the high vertical acceleration of ‘with’ flow rotation and 60° major axis from horizontal to break the material up enough to liberate fines that were capable of passing the bottom deck screen aperture.

ACKNOWLEDGEMENTS

Octavio Leardine Neto – Engineering Co-ordinator, Schenck Process Brazil

Duguai Braga – Technical Director Engineering, Schenck Process Brazil

Alf van Dijk – Head of R&D, Schenck Process Australia

Gordon Ashley – Former Product Expert Vibrating Screens, Schenck Process Australia

REFERENCES

Cleary, P W, Wilson, P and Sinnot, M D, 2018. Effect of particle cohesion on flow and separation in industrial vibrating screens, *Minerals Engineering*, 119(April 2018):191–204.

Cleary, P W, Delaney, G W, Hilden, M and Morrison, R D, 2009. Validation of DEM predictions of granular flow and separation efficiency for a horizontal laboratory scale wire mesh screen, *Seventh International Conference on CFD in the Minerals and Process Industries.*

Guolang, S and Tong, X, 2020. Particle stratification of a vibrating screen with translation-swing composite motion, *Journal of Vibroengineering*, 22(3):498–508.

Online and downhole assay measurement

Real time phosphorus analysis using GEOSCAN on belt analysers at Assmang Khumani Mine in the Northern Cape

L A Balzan[1] *and F Nieuwenhuys*[2]

1. Chief Technology Officer, Scantech International, Camden Park SA 5038.
   Email: l.balzan@scantech.com.au
2. Metallurgist, Assmang Khumani Mine, Northern Cape, South Africa.

ABSTRACT

GEOSCAN on belt analysers have been widely utilised in iron ore for nearly two decades. Since the first installations in 2003, the availability of accurate and reliable grade data has become standardised across iron ore mines in the Northern Cape in South Africa, where various streams are monitored continuously to ensure the optimal functioning of plants. Assmang Khumani has been at the forefront of technology adoption, and has implemented 19 GEOSCANs at various locations throughout the plant, monitoring run-of-mine, stockyard feed, beneficiation plant feeds, and products.

Over the years, collaborative advances in the technology have allowed for numerous benefits and gains to be made. In recent times, there has been a concerted effort on the development of analysis for phosphorus in the material flows, and based on Scantech's experience in the phosphate industry, this element has now been calibrated to achieve statistically acceptable and repeatable accuracies for real time analysis of this element on many of Khumani's GEOSCAN analysers.

This paper provides an overview of GEOSCAN use at Khumani, while focusing on the development of phosphorus analysis. A case study of analysis results is presented for a range of analysers that have been calibrated for this element, as well as a discussion on the benefits obtained as a result of this analysis.

INTRODUCTION

As mining operations continue to move into the 21st century, there is a growing importance placed on access to quality data to enable control of all aspects of an operation. One of these are the increasing importance of knowing in real time what the ore composition of the material is being conveyed is, to enable timely and rapid process control decisions to be made based on actual known material quality and grade information.

Assmang Iron Ore Mining Operations in the Northern Cape Province of South Africa, comprising of the Bruce, King and Mokaning mines, was quick to realise the importance of measuring material grade in real time, and was one of the world's first minerals operations to incorporate real time analysis of conveyed material into its flow sheet.

Scantech's GEOSCAN on belt elemental analysers have been utilised for more than 25 years in the cement and coal industries (Butel *et al,* 1993; Oritz and Harris, 2002; Harris, Smith and Rossi, 2005), and were first utilised in the iron ore industry in 2003 at Assmang's Beeshoek operation, also in the Northern Cape Provence. Based on positive outcomes at that site, when the Assmang BKM project was developed to become Khumani Mine, GEOSCANs were extensively utilised throughout the process to enable real time ore grade information availability at every point throughout the mine's process (Matthews and du Toit, 2011), including classification and sorting of material out of the mines based on grade. Use of Scantech's GEOSCAN in the iron ore industry has become quite widespread, with more than 50 installations in Australia, South Africa, Europe and South America in the industry, with widespread commendation from users of the equipment (Kurth, 2013; Balzan, Beven and Harris, 2015; Balzan and Harris, 2015b; Balzan *et al,* 2018; Balzan *et al,* 2019). Other minerals industries too have benefited from the adaptation of GEOSCAN analysis for different commodities, including manganese (Balzan and Harris, 2015a), copper (Arena and McTiernan, 2011; Balzan *et al,* 2016; Balzan, Harris and Bauk, 2017), lead zinc (Patel, 2014), gold (Bozbay and Moyo, 2019) and phosphates (Balzan, Harris and Bauk, 2018; Balzan and Kalicinski, 2019), with more than 100 installations in the minerals sector now incorporating on belt analysis into their process.

Over time, the technology has continued to adapt and develop as operator requirements becoming increasingly stringent and new areas of focus mature. A key development in recent times has been the use of the technology for bulk sorting and bulk diversion (Kurth and Balzan, 2017, 2018; Nadolski *et al,* 2016*,* 2018), where short analysis increments allow for rapid decisions to be made based on grade or other criteria, with small parcels of material diverted to different process streams or to waste depending on the sorting decisions. Another area of development has been in the application of new elements for analysis. This is most obvious in applications such as nickel, cobalt, lithium, gold and platinum, with all of these commodities now incorporating on belt elemental analysis into their process. Less obvious is the application of certain elements in existing application areas, such as phosphorus measurement in iron ore, which is a key focus for this paper. Building on successes in the aforementioned phosphate industry, it has become possible to measure the small quantities of phosphorus present in iron ores, with Assmang's Khumani Mine benefiting from these measurements as the capability gets rolled out across its GEOSCAN installation base.

This paper presents a background on the operations at Assmang's Khumani Mine, as well as introduces the GEOSCAN analysis technology. It considers the numerous installations at Khumani as a case study, presenting a variety of results, and gives a special treatment to the development of phosphorus measurement, including recent developments and analysis outcomes for the element in the iron ore industry.

ASSMANG KHUMANI MINE OPERATIONS

The Khumani iron ore mine is situated approximately 30 km south of the town of Kathu in the Northern Cape Province of South Africa. The Khumani mine is operated and owned by Assmang Proprietary Limited which is jointly controlled by African Rainbow Minerals Limited and Assore Limited, who each own 50 per cent of the issued share capital and voting rights within the organisation.

The Khumani mine is able to produce in excess of 14 million tons per annum of high-grade iron ore product in the form of both lump and fines. These products are produced at a lump to fines ratio of approximately 54–58 per cent and conform to stringent chemical product specifications, as outlined in Table 1.

TABLE 1

Khumani Final Product are managed Typically to the following specifications.

	% SiO_2	% Al_2O_3	% Fe	% TiO_2	% K_2O	% Mn	% P
Lump	≤ 4.50	≤ 1.80	≥ 65.00	≤ 0.05	≤ 0.28	≤ 0.30	≤ 0.045
Fines	≤ 5.50	≤ 2.30	≥ 64.00	≤ 0.09	≤ 0.35	≤ 0.30	≤ 0.050

In order to achieve the final product grade specifications, the run-of-mine material is beneficiated using a combination of crushing, wet screening, jigging and wet high intensity magnetic separation (WHIMS) technologies. The final product specifications at an overall plant yield to product in excess of 70 per cent, is achieved through the application of a grade control philosophy and procedure which utilises both mass/time based XRF sampling (production/verification/calibration) as well as real time online analysis using Scantech's GEOSCAN on belt elemental analysers. Figure 1 illustrates where the on belt elemental analysers are deployed within the Khumani process as well as the XRF sampling points used to support the grade control procedure.

The extensive use of GEOSCAN on belt elemental analysers in the Khumani process not only allows for short interval grade verification but has also allowed for a reduction in the laboratory sampling load by allowing for high frequency production samples to be replaced by less frequent verification and calibration maintenance sampling instead.

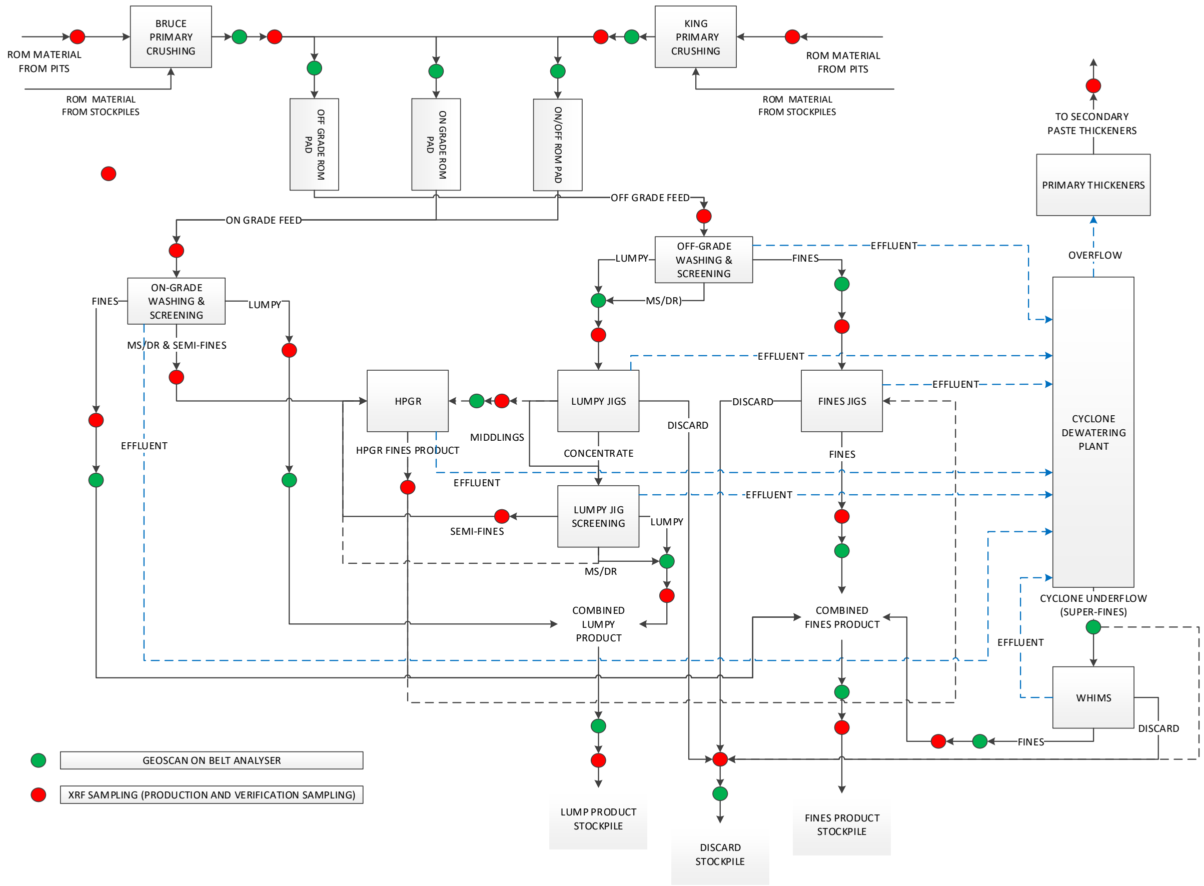

FIG 1 – Khumani process – block flow diagram.

ON BELT ANALYSIS TECHNOLOGY

To be able to benefit from having real-time information about conveyed materials in a process, it is important that the information is a true representation of the material being observed. This is a key objective of good analysis technology, and requires that the analysis technique is accurate and repeatable, and that the measurement being provided is a good estimator of the full material stream. There has been significant research looking at loading profiles, segregation, separation and migration of material on a moving conveyor, suggesting that observing only the surface of the conveyed material or a small section will lead to strong biases in the results. For iron ore, this is particularly important for material streams with a wide particle size distribution, where fines and lump particles constitute different qualities of ore, and for moisture as it migrates as a result of the belt motion.

With a large amount of experience in mineral analysis, Scantech recognises the importance of full material stream and full bed depth analysis, and focuses on technologies that enable fully representative analyses to be obtained in an accurate and repeatable way. Coupled with Scantech's unique tailored calibration methods, designed specifically for a sites' individual requirements, including minimising impacts on production, has allowed Scantech to become a market leader in on-belt analysis for iron ore.

This section highlights two of the key technologies used in the iron ore and steelmaking industries and what results can be produced to allow for enhancements in process control.

GEOSCAN elemental analysis

Scantech's GEOSCAN on-belt analysers utilise thermal neutron capture technology to determine the elemental composition of conveyed bulk materials in real-time. Conveyed material passes through the tunnel of the GEOSCAN, while a californium-252 radioactive source located within the GEOSCAN below the belt passes neutrons through the material. The neutrons are captured in the nuclei of the atoms in the material on the belt, which instantaneously outputs gamma-rays that are energy-specific to the element. The gamma-ray spectrum is captured by an array of detectors located at the top of the GEOSCAN, where Scantech's signal processing algorithms resolve the signal into a set of elemental results.

The measurement technique is completely penetrative and allows for analysis of the full material stream, full bed-depth and full belt-width. It is also independent of particle size and ore mineralogy, allowing for fully representative analysis of the conveyed material. In this way, it does not suffer from sampling errors, such as if a top surface only measurement was taken. Results are produced for a suite of elements calibrated for the specific requirements of the end user, with emphasis on their key elements of interest. The calibration is tailored for their requirements, including incorporation of variation due to changes in the belt load and material composition.

For iron ore and steelmaking, the typical elements of interest include Fe, Mn, and oxides of Si, Al, Ca, and K. Different sites will have varying requirements and may make control decisions based on various criteria; decisions may be made on whether to upgrade or direct-ship or even discard material based on Fe grade, or may make alterations to how the process acts on the material based on the deleterious element content. In steelmaking, the sinter feed is often monitored, with basicity ratios of Ca, Si, Al and Mg observed and lime dosing controlled based on the ratios. Scantech works closely with the end users to ensure a tailored solution for each installation.

Through-belt moisture TBM analysis

The TBM is often coupled together with the GEOSCAN, with both technologies used simultaneously as part of plant QC systems. The underlying principle of moisture measurement requires the transmission of a microwave signal from a transmitting antenna, through the material to be measured, and subsequently received at a receiving antenna. The transmitted signal is known and controlled, and metrics relating to how the signal changes as it passes through the material are observed, subsequently inferring a moisture measurement. Scantech's TBM utilises two orthogonal signal transformation metrics, the absorption of signal power and the delay of the signal transmission through the material, in order to determine the moisture content. A solid understanding of the principles of how the signal is transformed through the material allows the TBM to produce moisture measurements with a high degree of accuracy.

Microwave signals induce oscillations in free water molecules as they transmit through a medium. The oscillation of the water molecules results in signal power loss as well as a reduction in signal velocity, proportional to the complex dielectric of the material, which is itself a linear combination of dielectric of the dry material (usually small) and the moisture (generally large) components. Therefore, there is a strong linear relationship between both the change in signal power and the signal velocity to the amount of moisture in the material. These two metrics are independent and orthogonal measurements of the processed microwave signal. By accounting for other effects such as changing material depth and density, the two metrics can be combined to produce an accurate measurement for moisture.

As well as microwave measurement instruments, there are also surface-measurement devices, using techniques such as near-infrared (NIR), but these do not measure the full bed-depth of material, and are thus potentially subject to inherent inaccuracies in a surface-only measurement. Moisture migration of conveyed materials is a widely known phenomenon, and thus surface-only measurement techniques are not able to accurately measure the true moisture content of conveyed materials.

The use of microwave technology for moisture measurement is well established and accepted in the coal and other industries, though the uptake in the iron ore sector is less mature and has been obscured by devices that do not meet customer expectations. Despite the inherent difficulties of real-time moisture measurement in iron ore, Scantech has been widely successful in providing the TBM device to match every expectation in a large number of installations.

Phosphorus measurement in iron ore

As discussed above, the GEOSCAN is able to independently measure and quantify a range of different elements in the conveyed flow of material. In iron ore, the most common elements of interest include iron, silicon, aluminium and manganese. Phosphorus is another key element for iron ore operators, though typically the concentration is quite low, usually much less than 0.1 per cent, and it had previously been believed that the concentration was below the detection limit for PGNAA due to potential interfering elements in iron ore.

Since 2014, Scantech has become quite involved in the phosphate industry, where the GEOSCAN has been adapted for use measuring phosphorus and other elements for a variety of process control solutions in that industry. As part of this process, a new set of responses was developed for PGNAA analysis in phosphate, and much was learned from the process, including an enhanced ability for measurement of phosphorus in conveyed flows. The learnings gained from this industry have subsequently been applied to Scantech's existing iron ore installations, where it was found that not only could phosphorus be measured, but that the performance calibration ranges were statistically repeatable and accurate within the measuring ranges agreed with the client. The next section of this paper examines phosphorus measurement at Assmang as a case study, presenting a series of recent results.

CASE STUDY OF GEOSCAN ANALYSIS AT ASSMANG KHUMANI MINE

Assmang Khumani Mine operations utilises a vast range of GEOSCAN on belt analysers throughout its process. A selection of these analysers have been chosen for the case study presented below. A summary of the GEOSCAN use is provided, along with a selection of results (where performance is measured by calculating the root-mean-square-deviation, RMSD, a statistical measure of the differences between GEOSCAN and laboratory results), including in phosphorus.

Run-of-mine

The on line elemental analyser at the Bruce Primary Crushing Plant is one of two Run-of-mine analysers installed at Khumani with the second being utilised at the King Primary Crushing Plant. The primary purpose of this analyser is to verify the Run-of-mine material qualities being fed to the plant as they are blended from multiple in-mine sources (pits/stockpiles etc). The hourly analyser output is monitored in conjunction with the current shift average to ensure that the resulting material blend conforms to stringent Run-of-mine specifications. If the material quality is found to be non-compliant to the required specifications, the deviation is communicated to the relevant on shift mining and plant operators, and after collaboration, the required adjustments are made to the blend ratio's in order to correct the observed deviation.

At Khumani they have the option and benefit of In-Pit ROM Bending considerations as well as specialised ROM Yard Staking and Reclaiming equipment to manage to effect the required Grade Control Protocols. Grade Control Protocols are managed against very specific Algorithms aimed at achieving the planed product grade and mass yield objectives.

The GEOSCAN is regularly calibrated, and comparison made between laboratory data and the output results, as it is a critical measurement device in controlling downstream processing of material from the mine. A range of elements are calibrated, and this instrument is arguably the most difficult to calibrate given the relatively higher variation in material composition coming directly from the mine. Despite this, excellent results are regularly observed, as detailed in Table 2. Phosphorus is seen to be performing very well throughout its range of variation. Figure 2 shows comparative results between the laboratory and GEOSCAN for the four key elements discussed. In this and subsequent figures, the x-axis represents sample number and is not shown for clarity.

TABLE 2

Performance results from run-of-mine GEOSCAN.

Element	% SiO_2	% Al_2O_3	% Fe	% TiO_2	% K_2O	% Mn	% P
RMSD	0.79	0.56	1.06	0.06	0.16	0.05	0.006

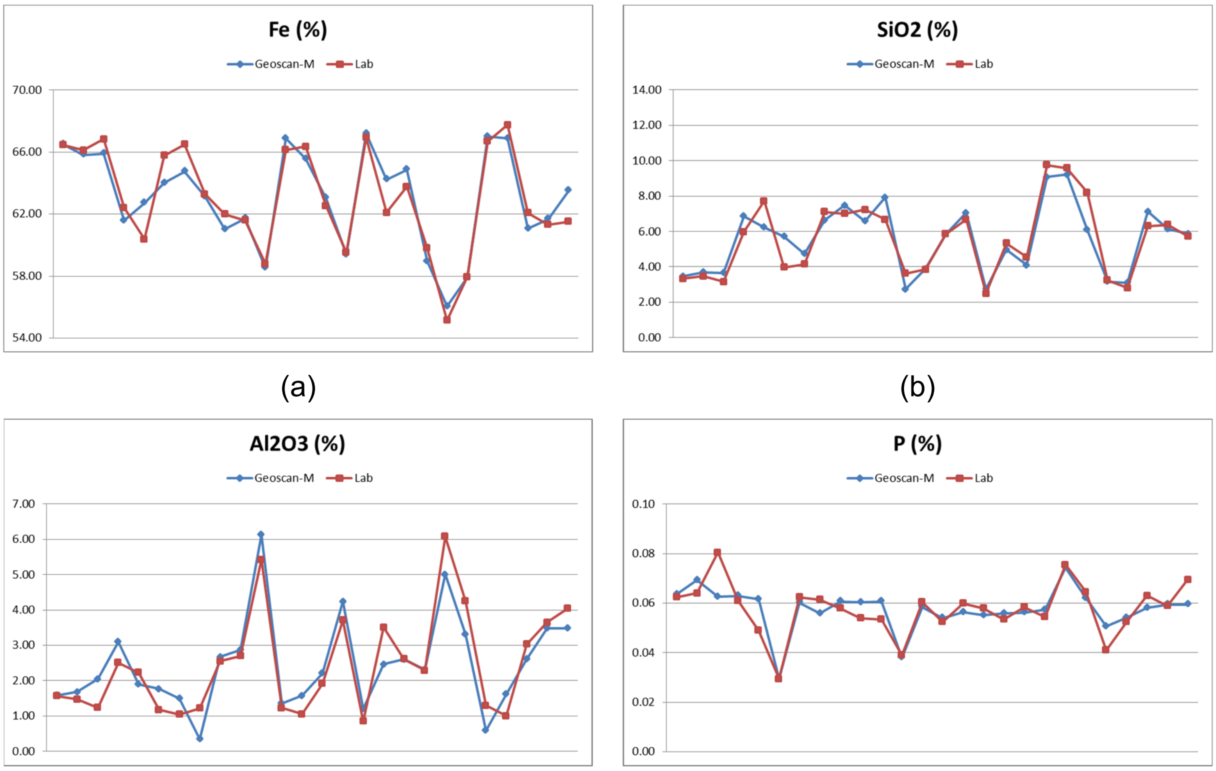

(a) (b) (c) (d)

FIG 2 – Recent results from run-of-mine comparing GEOSCAN (blue) to laboratory data (red) for (a) iron, (b) silica, (c) alumina and (d) phosphorus.

ROM stockpile pad

The purpose of the Run-of-mine stockpile analysers are to verify the quality of the stacked material that results from the practice of simultaneous blending of the Bruce (primarily laminated ore) and King (primarily conglomeratic ore) Primary Crushing Plant materials. The application of the on line elemental analysers at this point in the process allows for the quality of the stacked material blend to be measured and verification of the ROM Stockpile qualities to be achieved. This information is then further used to inform the operational personnel as to the plant blending ratio's from the ROM Pad to be utilised for optimised processing outcomes relating to final product qualities and plant yield to product.

As for the run-of-mine GEOSCAN, comparison between laboratory samples and corresponding GEOSCAN results is regularly made to verify the GEOSCANs performance. There is reasonable variation in the material quality, however it is somewhat more stabilised than for the run-of-mine, and this is reflected in the trends observed in the Table 3 and Figure 3. Again, phosphorus is performing exceptionally well.

TABLE 3

Performance results from a stockyard GEOSCAN.

Element	% SiO_2	% Al_2O_3	% Fe	% TiO_2	% K_2O	% Mn	% P
RMSD	0.75	0.20	0.84	0.02	0.05	0.02	0.003

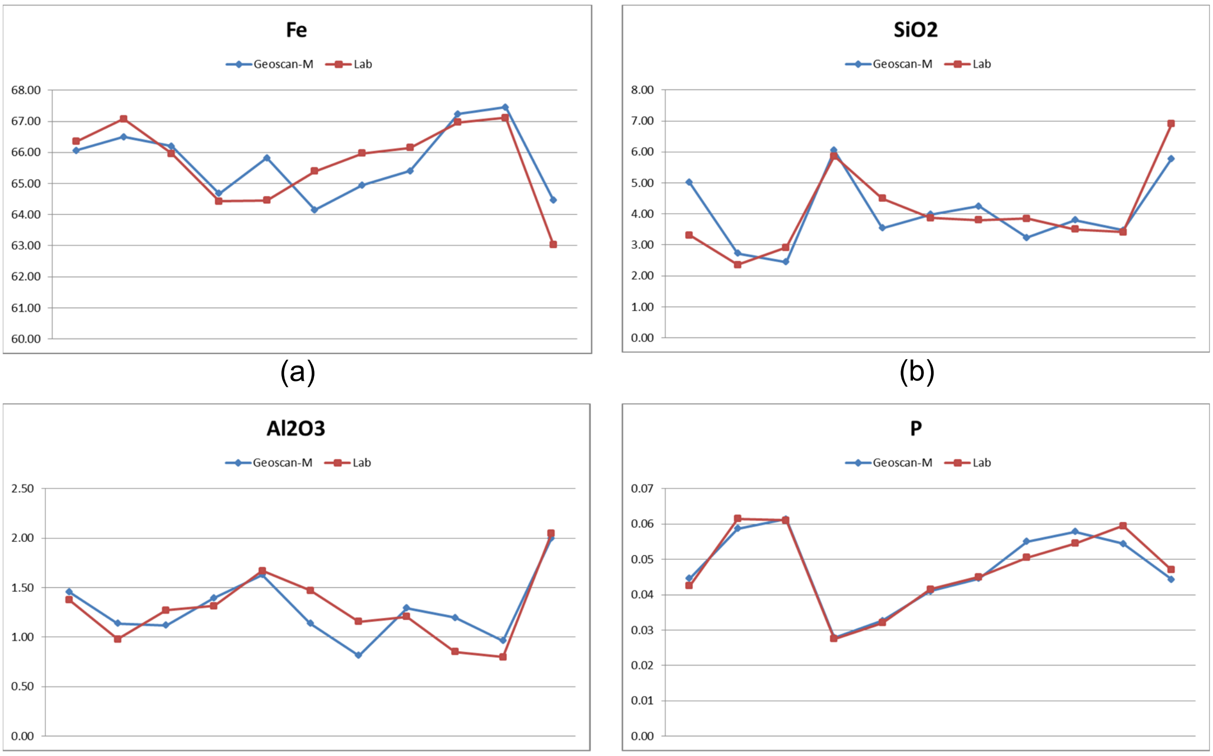

(a) (b)

(c) (d)

FIG 3 – Recent results from a stockyard GEOSCAN, comparing GEOSCAN (blue) to laboratory data (red) for (a) iron, (b) silica, (c) alumina and (d) phosphorus.

Products

The product analysers have been installed on the final lump and fines product belts. The purpose of these analysers are to inform the operational personnel as to the required set-up of the beneficiating processes as well as the plant feed blending ratio's required to achieve optimised processing outputs. The hourly analyser output trends are monitored between four-hourly XRF production sampling (final quality verification) and allows for timeous adjustments to be made to correct deviations with regards to the final product specifications.

Again, regular comparison is made between samples analysed in the laboratory and the GEOSCAN results. The product lines have the most consistent grade, as would be expected, and the GEOSCAN is calibrated across a smaller range accordingly. The results comparing GEOSCAN to laboratory are shown in Table 4 and Figure 4, including again excellent phosphorus results.

TABLE 4

Performance results from a products GEOSCAN.

Element	% SiO_2	% Al_2O_3	% Fe	% TiO_2	% K_2O	% Mn	% P
RMSD	0.38	0.25	0.48	0.01	0.05	0.01	0.007

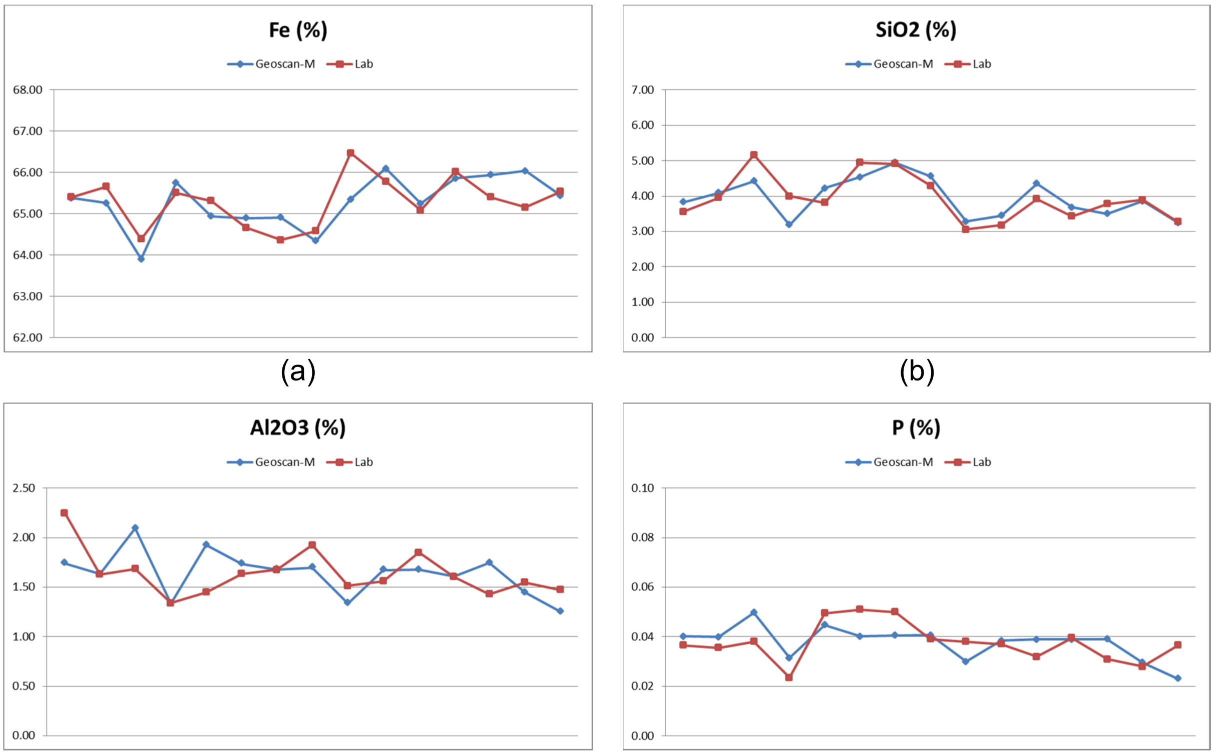

(a) (b)

(c) (d)

FIG 4 – Recent results from a products GEOSCAN, comparing GEOSCAN (blue) to laboratory data (red) for (a) iron, (b) silica, (c) alumina and (d) phosphorus.

CONCLUSIONS

This paper has served as a discussion on continuing enhancements for GEOSCAN analysis capabilities, with a focus on usage at Assmang's Khumani Mining operations. A summary of the Khumani Mine has been given, along with a brief summary of the GEOSCAN analysis technology. A case study of performance and use at Khumani Mine has been discussed, incorporating advances in the ability for measuring phosphorus in iron ore. Benefits of on belt real-time analysis have been provided, concluding the paper.

REFERENCES

Arena, T and McTiernan, J, 2011. On-belt analysis at Sepon copper operation, in *Proceedings MetPlant 2011*, pp 527–535 (The Australasian Institute of Mining and Metallurgy: Melbourne).

Balzan, L and Harris, A, 2015a. Adaptation and performance of GEOSCAN on-belt analysers for manganese ore at Assmang Black Rock, in *Proceedings Africa Australia Technical Mining Conference 2015*, pp 125–130 (The Australasian Institute of Mining and Metallurgy: Melbourne).

Balzan, L and Harris, A, 2015b. Real-time through-belt moisture analysis for iron ore, in *Proceedings Iron Ore 2015*, pp 539–542 (The Australasian Institute of Mining and Metallurgy: Melbourne).

Balzan, L, Beven, B J and Harris, A, 2015. GEOSCAN online analyser use for process control at Fortescue Metals Group sites in Western Australia, in *Proceedings Iron Ore 2015*, pp 99–105 (The Australasian Institute of Mining and Metallurgy: Melbourne).

Balzan, L, Jolly, T, Harris, A and Bauk, Z, 2016. Greater use of GEOSCAN on-belt analysis for process control at Sepon copper operation, in *Proceedings XXVIII International Mineral Processing Congress 2016* (Canadian Institute of Mining, Metallurgy and Petroleum: Quebec, Canada).

Balzan, L A, Harris, A R and Bauk, Z, 2017. Faster Analysis: Recent advances in GEOSCAN on belt analysis techniques allowing for rapid real-time measurement of minerals, in *Proceedings COM2017 The Conference of Metallurgists hosting World Gold and Nickel Cobalt* (Canadian Institute of Mining, Metallurgy and Petroleum: Vancouver, Canada).

Balzan, L, Harris, A and Bauk, Z, 2018. GEOSCAN-M use at a middle eastern phosphate plant, in *Beneficiation of Phosphates VIII, Cape Town* (Engineering Conferences International ECI: New York).

Balzan, L A, Bauk, Z, Kalicinski, M and Lyssyy, M, 2018. Process improvement in iron ore and sinter through real-time on belt analysis, in *Proceedings of the XXIX International Mineral Processing Congress 2018*, pp 105–205 (International Agency of Congress Management MAKO: Russia).

Balzan, L A and Kalicinski, M, 2019. GEOSCAN-M use for process improvement in phosphate plants, in *Symphos 2019, 5th International Symposium on Innovation and Technology in the Phosphate Industry* (Elselvier: Netherlands).

Balzan, L A, Swart, E, Gray, L and Kalicinski, M, 2019. Process improvement at Kumba Iron Ore Sishen and Kolomela mines through the use of GEOSCAN on belt analysis equipment, in *Proceedings of Iron Ore 2019,* pp 649–659 (The Australasian Institute of Mining and Metallurgy: Melbourne).

Bozbay, C and Moyo, P, 2019. Conveyor belt online moisture analyzer at Cortez, in *CIM Convention 2019* (Canadian Institute of Mining, Metallurgy and Petroleum: Montreal, Canada).

Butel, D, Howarth, W J, Rogis, J and Smith, K G, 1993. Coal sorting, in *Coal Preparation*, vol 12, pp 203–214 (Gordon and Breach Science Publishers).

Harris, A, Smith, K and Rossi, F, 2005. On-belt analysis breakthrough, in *International Cement Review*, pp 62–66 (Tradeship Publications Ltd: London, UK).

Kurth, H, 2013. Real time on-belt elemental analysis for advanced process control in iron ore, in *Proceedings 43rd Ironmaking and Raw Materials Seminar, 12th Brazilian Symposium on Iron Ore and 1st Brazilian Symposium on Agglomeration of Iron Ore 2013*, pp 364–373 (Brazilian Association of Metallurgy, Materials and Mining: Brazil).

Kurth, H and Balzan, L, 2017. Assessing bulk sorting suitability at the New Afton Mine, in *Proceedings Metallurgical Plant Design and Operating Strategies (MetPlant 2017)*, pp 315–323 (The Australasian Institute of Mining and Metallurgy: Melbourne).

Kurth, H and Balzan, L, 2018. Ore pre-concentration by bulk sorting using real time elemental analysis, in *Proceedings 50th Annual Canadian Mineral Processors Operators Conference* (Canadian Institute of Mining, Metallurgy and Petroleum: Canada).

Matthews, D and du Toit, T, 2011. Real-time online analysis of iron, validation of material stockpiles and roll out for overall elemental balance as observed in the Khumani Iron Ore Mine South Africa, in *Proceedings Iron Ore 2011*, pp 297–305 (The Australasian Institute of Mining and Metallurgy: Melbourne).

Nadolski, S, Liu, Y, Klein, B, Elmo, D, Scholar, J and Scoble, M, 2016. Investigation into the Implementation of Sensor-based Ore Sorting Systems at a Block Caving Operation, in *Proceedings MassMin 2016 – 7th International Conference & Exhibition on Mass Mining*, pp 393–399 (The Australasian Institute of Mining and Metallurgy: Melbourne).

Nadolski, S, Samuels, M, Klein, B and Hart, D, 2018. Evaluation of bulk and particle sensor-based sorting strategies for the New Afton block caving operation, in *Proceedings 8th International Conference, Sensor-Based Sorting & Control* (RWTH: Aachen, Germany).

Ortiz, C and Harris, A, 2002. Raw mix control, in *World Cement*, February 2005, pp 46–49 (Palladian Publications: Farnham, UK).

Patel, M, 2014. On-belt elemental analysis of lead-zinc ores using prompt gamma neutron activation analysis, in *Proceedings XXVII International Mineral Processing Congress 2014*, ch 17 (Gecamin: Santiago, Chile).

Advances in downhole assay measurements and calibration techniques

J Market[1]*, C Simpson*[2]*, H Rossiter*[3] *and P Jeanneau*[4]

1. Geophysics Manager, MPC Kinetic, Kewdale, WA, 6105.
   Email: Jennifer.Market@mpckinetic.com
2. MAusIMM Geology Manager, Fortescue Metals Group, Perth, WA 6019.
   Email: csimpson@fmgl.com.au
3. Business Development Manager, MPC Kinetic, Brisbane, Qld, 4000.
   Email: Huw.Rossiter@mpckinetic.com
4. Product Marketing Manager, Neutron Technology, Sodern, Limeil-Brévannes, France.
   Email: philippe.jeanneau@sodern.fr

ABSTRACT

Downhole Assay tools are a geophysical method to collect an instigated response from the material surrounding a drill hole and deliver a multielement proxy-assay. They were first tested in the Pilbara at the turn of this century, however since 2011 they have seen a more focused testing and implementation regime with multiple companies across multiple Pilbara mine sites. The increase in the volume of data has led to advances in the measurements and significant improvements to the efficiency of the calibration process.

Pulsed Fast and Thermal Neutron Activation Analysis (PFTNA) downhole assay tools collect gamma photon spectra which are characteristic of elemental signatures. One of the key components of the technique is calibrating the spectral signatures to lab assays. Each tool is slightly different due to the organic nature of the crystal detector and therefore responds slightly differently. Environment and hole conditions as well as ore characteristics are among other external influencing factors. Thus, a unique calibration is required for each tool. In addition, not all elements are measured directly, but some are actually characterised by proxy, meaning that if the signal-to-noise ratio for an element is small, it may be easier to identify the mineral or geology in which that element is found and thus infer the concentration of the element. These proxies may differ for each site or geology type within a site. There is a large advantage to build a unique calibration per tool at each site rather than a universal one to be used across the whole province. This then delivers the accuracy and precision of measurements that mining companies require for modern operations.

Early work with the tool required several thousand metres of calibration data and several weeks of analysis to build each calibration. This process has now been streamlined to significantly reduce the amount of data required and the analysis time to make it much easier to introduce new tools to a site with an existing model or to create new models.

This paper details the calibration process, illustrating the increasing accuracy of the models as training data are acquired as well as the methods for transferring a calibration from one tool to another.

DOWNHOLE ASSAY MEASUREMENTS

The downhole assay tool discussed in this paper is a PFTNA elemental spectroscopy tool which consists of a neutron generator and high-resolution scintillation detector mounted in a 100 mm diameter barrel. A diagram of the tool is shown in Figure 1, and details of the design and operation are given by Smith *et al* (2015) and Jeanneau, Flahaut and Maddever (2017). The neutron generator is designed to operate only while downhole and numerous safety mechanisms ensure that it cannot be inadvertently activated above the surface, making the device adequately safe for mine site operation. The tool can be deployed either by a conventional wireline logging vehicle having a single operator, or as shown by semi-autonomous vehicle logging systems (Figure 2), the latter is preferred in the blasthole environment as it reduces personnel risk around manual handling with the repetitive process of logging shallow holes (under 15 m deep).

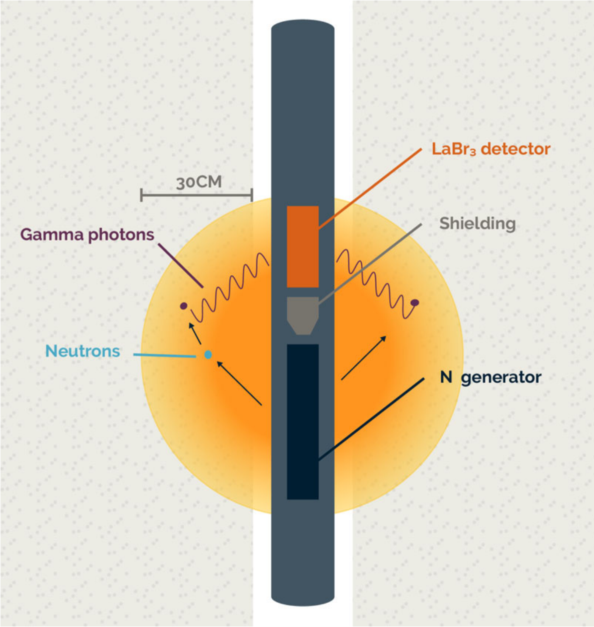

FIG 1 – Diagram of a PFTNA downhole assay tool.

FIG 2 – Downhole assay tool being deployed on a semi-autonomous platform.

As the tool measures the response of the material surrounding the drill hole, the per-metre volume of rock investigated by the tool is larger than that taken from within the drill hole. The additional advantage is that there is no subsampling of the material to gain a sample of suitable size for laboratory analysis, potentially creating sample error or bias in the subsampling process. The sensitive volume of the measurement area is illustrated in Figure 3. Penetration depth varies depending on the host material, with the signal response decreasing with distance into the rock. Typically, the effective investigation depth is in the range of 20–30 cm. Vertical resolution is dependent on the tool's neutron-gamma radiation footprint, logging speed, and rock composition. It is of the order of 20–40 cm, markedly better than that for most Reverse Circulation (RC) assays, which are sampled in the 1–3 m range. It is also dramatically better than a typical iron ore blast-cone sample which composite sample over a 5–15 m vertical whole hole interval. Any thin (<2 metre) layers of highly variable material (higher or lower grade) are blended into the composite blast-cone sample.

Depth control issues that often arise in the collection of physical lab samples are greatly reduced by downhole logging, since measurement depth is well controlled by the wireline logging system.

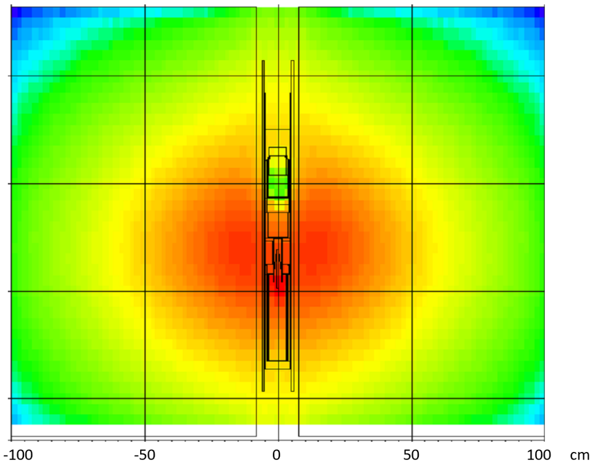

FIG 3 – Zone of investigation for a downhole assay measurement (Jeanneau, Flahaut and Maddever, 2017).

The conversion from spectra to elements (Figure 4) is achieved by combining the theoretical response of the tool to a calibration model, which is trained on conventional laboratory assays from core, RC, or blast cone samples. Further detail on this methodology can be found in Market *et al* (2019).

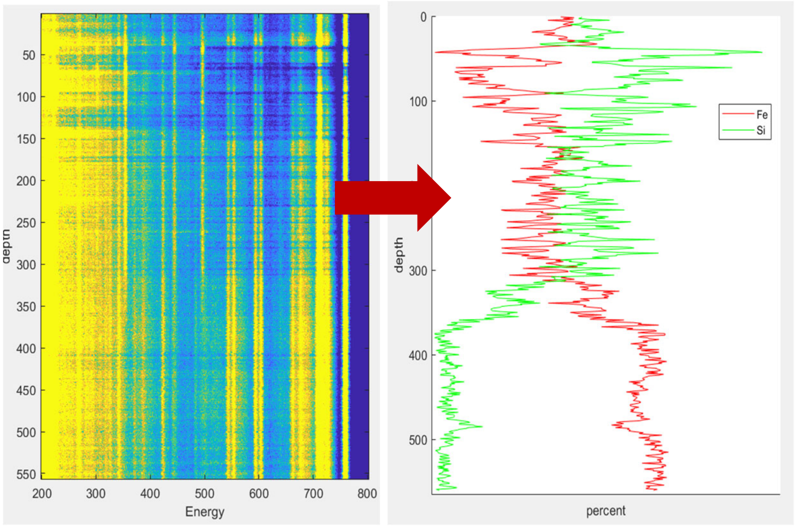

FIG 4 – The calibration process converts spectra (left) into usable elemental curves (right). Assay grades not shown on axes for confidentiality of results.

The range of detection and accuracy of the measurement varies not only by the amount of the element present in a sample, but by the signature of the element itself, the material type (eg the combination of elements in a sample), the environmental conditions (hole condition and moisture), and the quality of the lab assay data used to train the model. Common elements of interest that have high signal-to-noise ratios and can be detected in even very low quantities include Copper (Cu), Nickel (Ni), Silica (Si), Iron (Fe), Aluminium (Al), Titanium (Ti), Manganese (Mn), Calcium (Ca), Hydrogen (H), Oxygen (O), and Potassium (K). Common elements of interest that can be readily characterised when they are in low (>0.1 per cent) quantities include Magnesium (Mg), Phosphorous (P), Sulfur (S), Chlorine (Cl), Sodium (Na), Vanadium (V) and Chromium (Cr). Even if an element is present in extremely small but commercially interesting quantities that are below the direct threshold of detection, such as Gold (Au) in parts-per-million quantities, the tool is able to detect the material type in which gold is found and therefore determine its presence by way of a proxy. Proxy methods are also used for non-elemental quantities such as LOI (Loss on Ignition), which do not have a specific spectral signature.

CALIBRATIONS – TRANSFORMING SPECTRA TO ELEMENTAL COMPOSITIONS

Overview

The PFTNA downhole assay tool records three spectra for each depth sample: Prompt Gamma, Inelastic, and Delayed. These raw spectra are transformed into elemental analysis (assays) for each analysed depth. While the detectors within the tool are built to be very similar in response, they are organically grown and each respond slightly differently to the photon energy as well as to temperature and other environmental factors. New tools are first tested with a built-in factory calibration (developed during the manufacturing process), which works well for elements with high cross-sections (strong signal-to-noise ratios) such as iron and silica and are usable ‘out of the box’ for ore/waste boundaries and stratigraphy delineation. However, to have good definition of minor elements and robustly determine major elements near the threshold of detection, tool-specific calibration models are built before using the tool in full production mode.

The most common method of building a calibration model is to acquire PFTNA downhole assay spectra in a series of RC holes for which the laboratory results from physical samples are available. The laboratory results are then used to train the model such that for future holes, the raw spectra data can be transformed into a reliable proxy-assay. The process is as follows:

Calibration campaign

In the planning stage of a project, the material types in which the tool is intended to be used in production should be considered. This includes determining the elements of interest and the range of interest for each element. Sometimes specific accuracy and repeatability goals are defined at the start of the project. At other times, the performance targets evolve with the project. For example, if, at the outset of a project, the primary purpose of acquiring downhole assays was to determine the ore/waste boundary and then the purpose matured to using the measurements for grade control and then potentially to substitute a portion of the infill RC drilling, then the targeted limits of detection for individual elements may change. Targets may be defined to cover primary and secondary ranges of interest. For example, ‘Aluminium accuracy below 10 per cent should have an RMS error of less than 1.5 but above 10 per cent an RMS error of 1.7 is acceptable’. As part of the planning stage, the thresholds of detection for each element or proxy can be estimated from the available lab assays. Figure 5 illustrates some theoretical responses of elements of interest in a Pilbara project. From this plot it is clear that some elements (such as H, Fe, Si, and Ti) have much stronger responses than elements such as P and Mn. This does not mean that P and Mn are not detectable, but rather that they can be more difficult to detect in very small quantities. Each element (except H) has multiple energy peaks associated with multiple reactions giving them a unique signature.

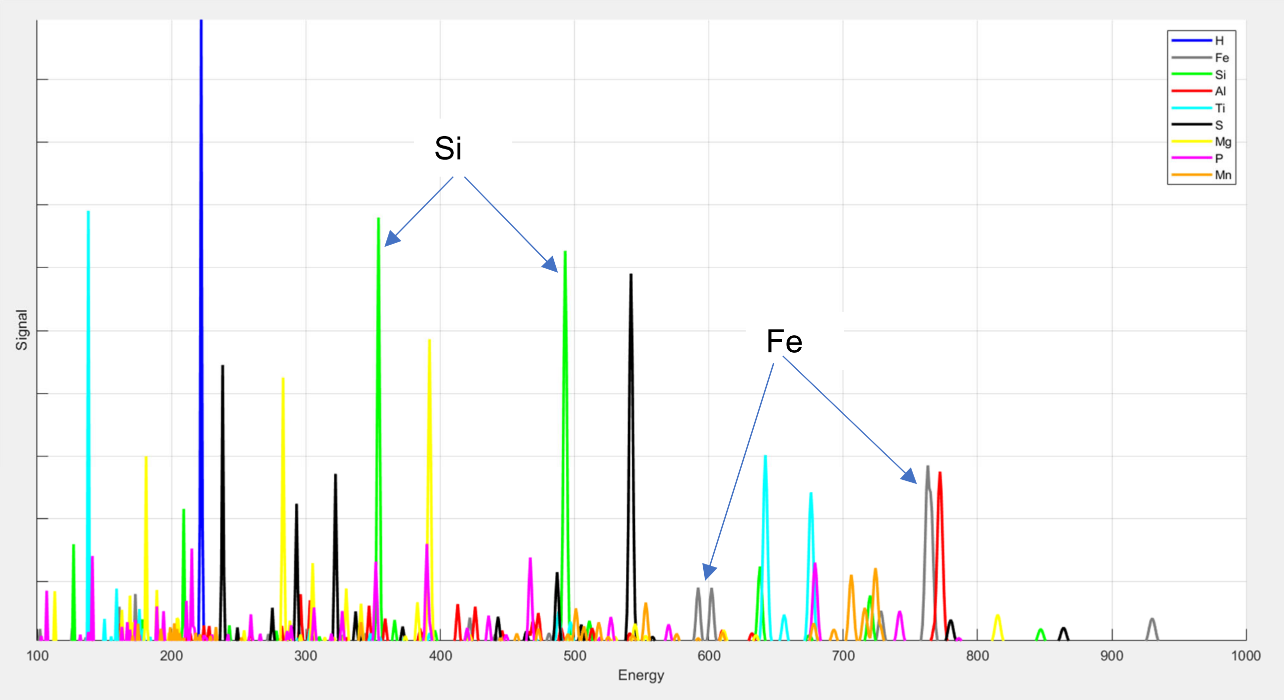

FIG 5 – Theoretical spectral response. This model compares the responses of 100 per cent of each element. Some elements have high cross-sections (signal-to-noise ratios) and are thus easy to detect even when they are present in very small quantities. Others (medium height peaks) are easy to detect in small to large quantities, while others (short peaks) are easy to detect in moderate quantities but may be difficult to detect in very small quantities. Proxy detection techniques can be used to determine the concentration of elements even if there are no high intensity peaks.

Next, laboratory assays are obtained for drill holes which cover the range of material types and grades. Calliper data for these holes is helpful in choosing holes which have the most reliable sampling. When the calliper indicates that the hole is significantly washed out, it is unlikely that the lab assays for those sections will be of good quality or a reliable depth and it is better to remove these samples from the data set. A guide to selecting sufficient data to build a solid calibration model is as follows.

Determine the range of interest for each element. Divide that range into 20 equal bins. For each bin, ensure that there are at least 30 samples. Figure 6 shows an example of assay distributions for a proposed group of holes. The red horizontal lines are at 30 samples. From this set of holes, a good calibration is expected for iron in the middle range with possibly compromised accuracy at the very low and very high ends where there are few training samples. If these extreme ranges are of critical interest, extra sample data within this range should be collected and added to the calibration model. Having little data in a range doesn’t necessarily mean that the model will be very poor in that zone, but the accuracy in those ranges should be considered of lower confidence. S, in the example below, has enough training data to build a solid calibration in the low range and will be able to identify high S samples, but the accuracy in samples with high S may be less than at low concentrations due to the sparsity of training data in this region. When building the model, high accuracy in the zones of primary interest are emphasised without dramatically sacrificing the accuracy dramatically outside the range. A good rule of thumb is to build the model allowing for up to twice as much RMS error outside the range of interest than within.

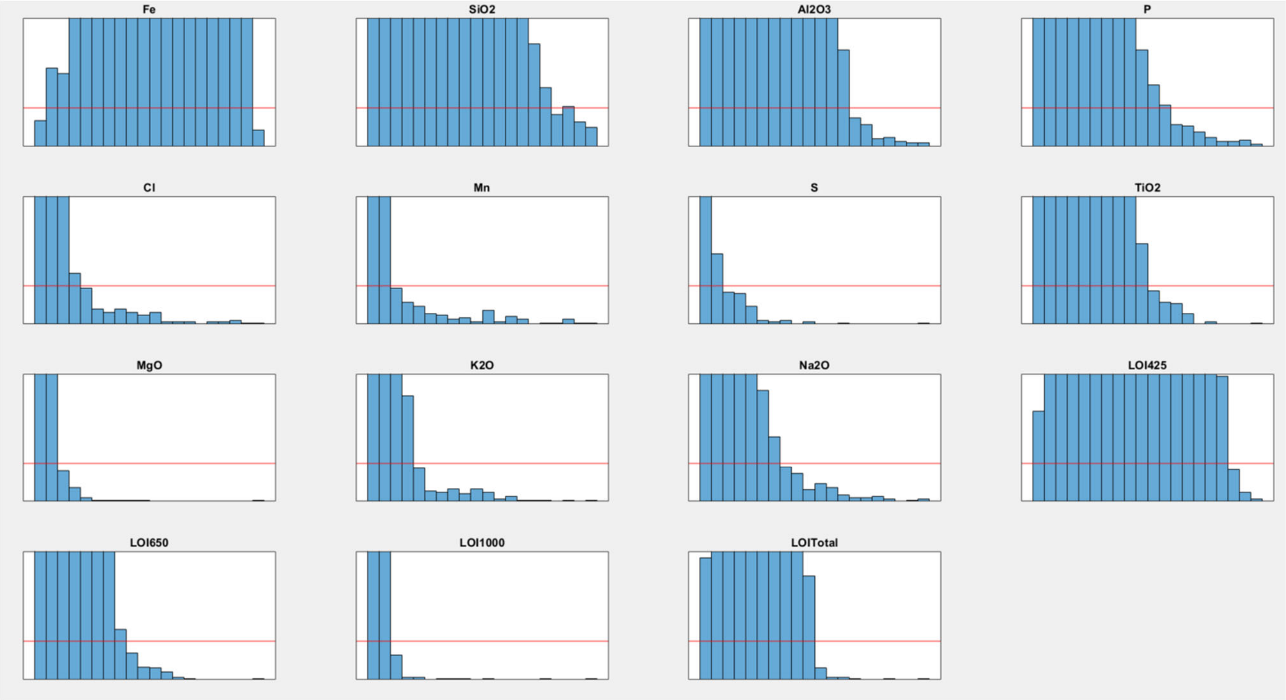

FIG 6 – Example Lab Assay Distribution represented as histograms with grades increasing to the right. Axes labels not shown for confidentiality of results.

To streamline the decision on data-range quantity, software can be used to automatically determine the minimum number of holes required (from the available selection) to meet these criteria. If calliper data is available, additional criteria are applied to select the holes with the best quality lab assays.

In some projects, it is preferred to build one model which works in a wide variety of geologies (even multiple mines in a region) which will require logging more RC holes than if the tool is meant to be used in a more specific geology. Experience shows that having one model per mine (per tool) is a good level of granularity. If a mine has several distinct material types, it will require more training data than a mine with more uniform geology, but it will not necessarily require a specific model for each geology within the mine. A typical number of data points from RC holes required for a relatively simple geological distribution is approximately 3000 samples. For mines which have multiple distinct geologies, such as Channel Iron Deposits (CID) and Bedded Iron Deposits (BID) in the same area, 4000–5000 samples is recommended.

To verify the calibration model, an additional group of holes which cover the geological zones of interest are identified and reserved. These are blind test holes and will not be used in creating the model, but only to test it. A selection of 300–500 data points (around 10 per cent) is usually sufficient for the analysis, as long as they represent the range of interest for all elements.

Once the holes are selected and the lab assays available, logging is carried out with the downhole assay tool. It is recommended to log at whatever vertical resolution will be later used in production – usually either 20 cm (for deposits with significant heterogeneity or fine layers of interest) or 40 cm (most common). Resolution is related to speed of logging, in these examples either 2 or 4 metres per minute. Therefore, a decision on speed (related to volume of data collected on a daily basis) versus precision of results (slower speed gives greater signal to noise results) should also be traded off at this stage of the project.

To evaluate the model, 10–15 per cent of the holes should be logged twice to allow for repeatability analysis. These could be the training holes or the blind holes – either one is suitable for repeatability analysis. Static logs should also be acquired in both ore and waste material. Static logging is a technique where the tool is stationary for 10–15 minutes at one depth to get the best quality data and reduce any variability due to tool movement. This data is used for reference in the statistical analysis.

While the vertical resolution of the tool is in the range of 20–40 cm, it is not necessary (or practical) to acquire lab assay results at such high resolution. Lab assays are usually available at 1–3 m resolution. The 1 m sample interval results have the advantages of not only characterising thin layers better, but also shorten the calibration logging campaign as it takes only half the number of holes to reach the target sampling than it does for 2 m sample intervals. Since the downhole assay data is at higher vertical resolution (typically 20 or 40 cm) than the assays, it is necessary to composite the downhole assay spectra to match the depth sampling range of the lab assay. This is typically done by weighted averaging.

Cleaning the data

To build a robust calibration model with the least number of logs possible, it is necessary to 'clean' the data. The goal is to remove unreliable lab assay measurements, data acquired intervals of poor hole conditions, and that which doesn't align well due to there being sharp stratigraphy changes at finer resolution than the lab assays measure. For every 'bad' point included in the modelling process, roughly three good samples (good hole condition, good depth matching) are needed to reduce its effect on the model – thus, by removing the 'bad' data, less data is needed overall to get robust results. If calliper log data is provided with the lab assay data, it can be used to automatically remove poor quality samples. If it isn't available, the downhole assay tool can be used to estimate the hole size and remove poor quality samples. In a typical 140 mm RC environment, it is best to exclude samples where the calliper is over 160 mm in the interval (ie If drill hole volume error is greater than 15 per cent then it is advised to discard these results). This does not mean that the downhole assay tool doesn't function properly in large holes, it is just that if a hole is enlarged/broken out/washed out more than 20 mm above bit size, then it is likely that the sample depth and quality are likely to be compromised. In addition to removing poor quality data, it also significantly improves the modelling process to remove samples from the training set that don't align well in-depth. This can occur when there are sharp changes in lithology and when there are thin beds. Figure 7 shows an example of cleaning the samples where depth alignment was poor.

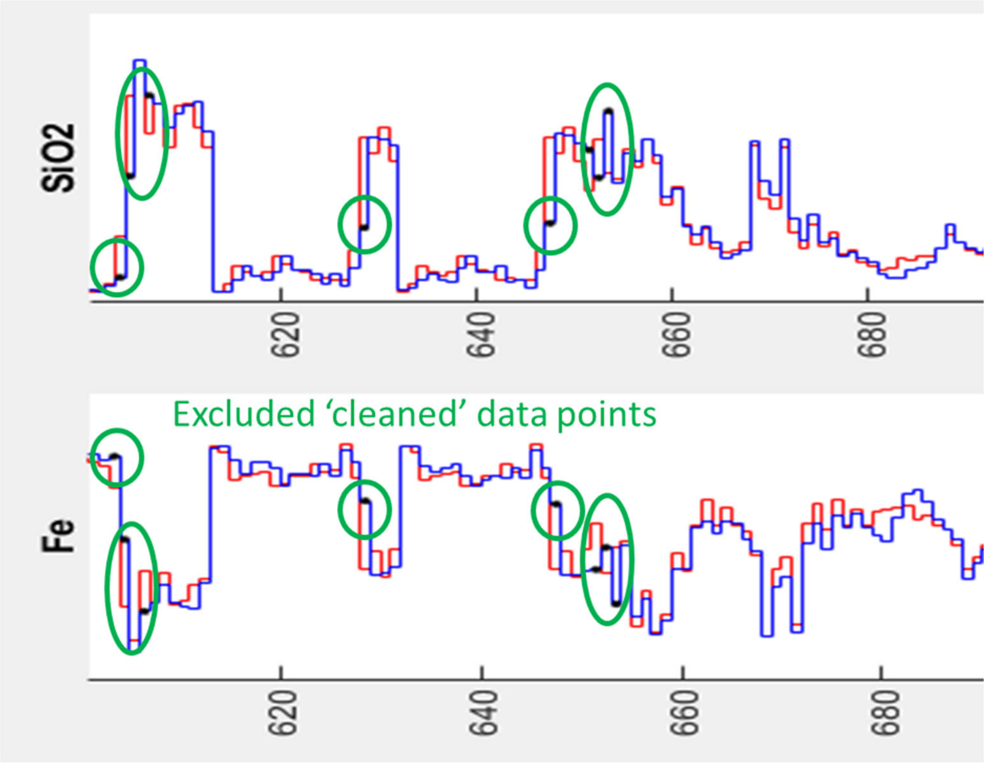

FIG 7 – Data Cleaning – the red curve is the lab assay and the blue curve is the downhole assay results using the factor calibration model. The black dots mark removed depths where the alignment was poor.

Environmental corrections

Before progressing to the machine learning stage, the spectra must be corrected for environmental effects. This allows a model that is built with reference data in one environment (eg an RC hole) to be applied in another environment (eg a blasthole). The most significant environmental effects are temperature and hole size, while bore fluid (air or water) needs to be accounted for as well.

The first effect to consider is temperature, variations of which cause the spectra to shift to higher or lower energy levels. These effects are corrected in the preprocessing stage, ensuring that, regardless of the temperature at which the data was collected, the response will be corrected back to the base thermal response. Figure 8 shows data collected at the same depth for different temperatures – note the shift in the spectral peaks, particularly for iron (680–750 kEV). Figure 9 shows the same data with the peak positions corrected for temperature. The peaks are not only aligned with each other, but also match the 'textbook' responses for the elements. For example, iron has theoretical peaks at 713 and 761 kEV, which can be seen in the corrected figure.

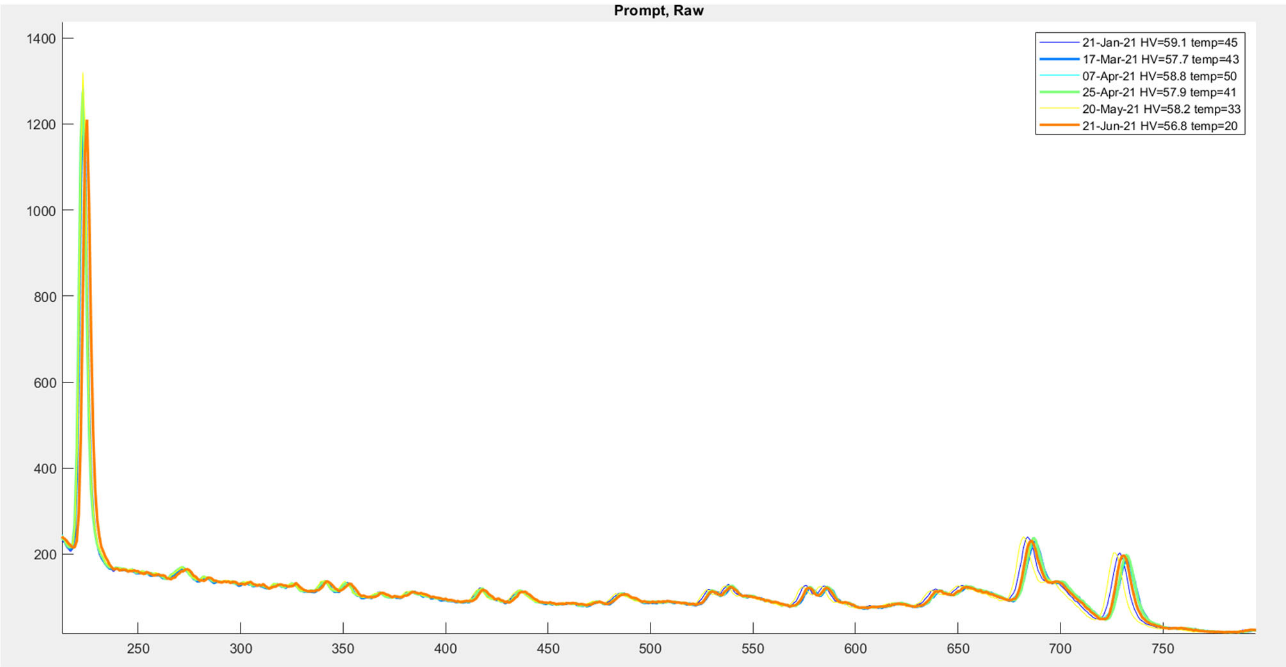

FIG 8 – Variation in the spectra due to temperature variation – uncorrected.

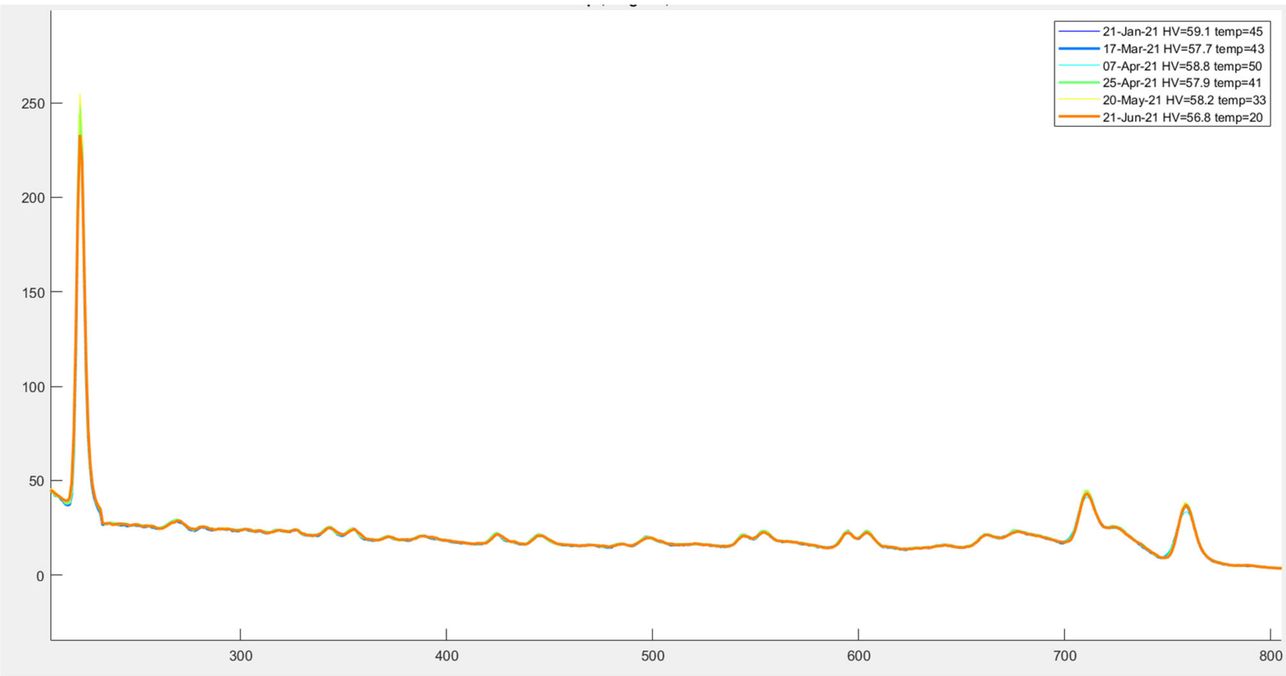

FIG 9 – Variation in the spectra due to temperature variation – corrected.

Once the temperature correction is complete, the hole size effects must be considered. Figures 10 and 11 illustrate the response of the tool in a pair of test blocks. These are two nearly identical concrete blocks with different diameter holes drilled through them to simulate RC and blasthole bit sizes. Figure 10 shows the spectra acquired by running the tool in each block before it is corrected for hole size and Figure 11 shows the spectra corrected for hole size.

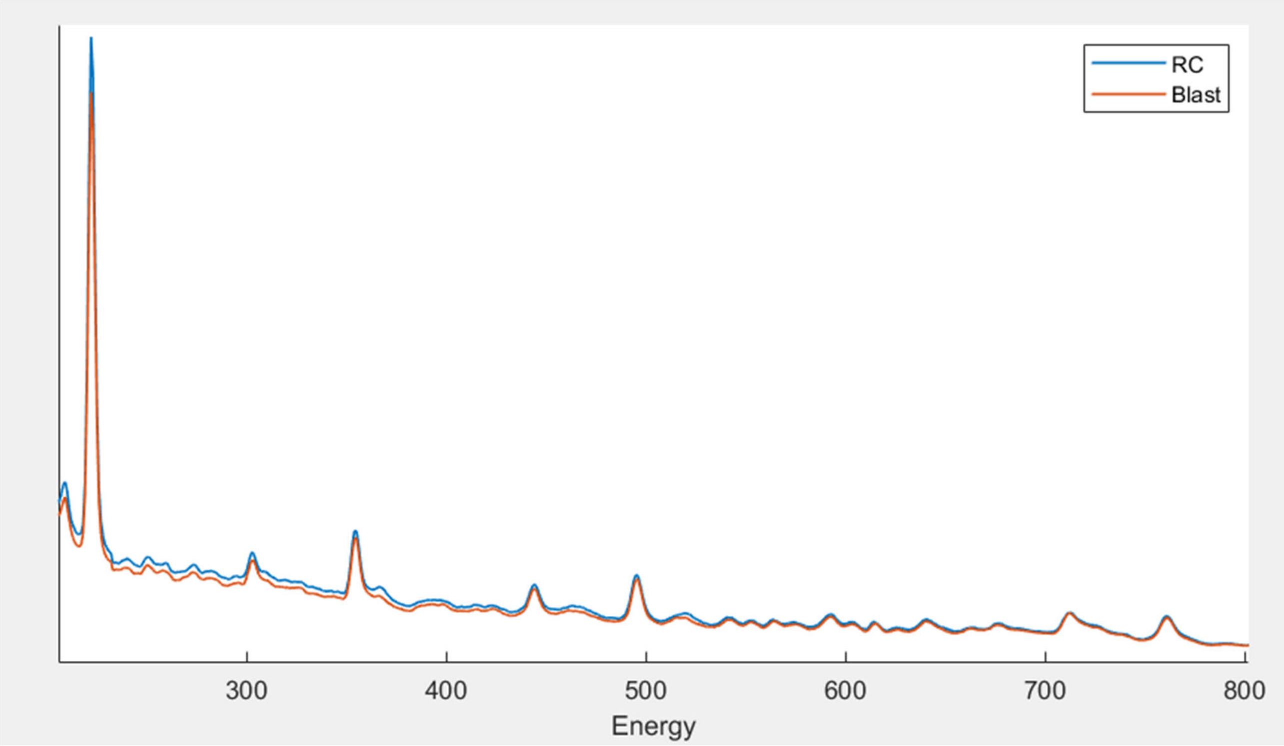

FIG 10 – Spectral response of the tool in a pair of concrete test blocks without a hole size correction applied. Note that the height of the spectra disagrees.

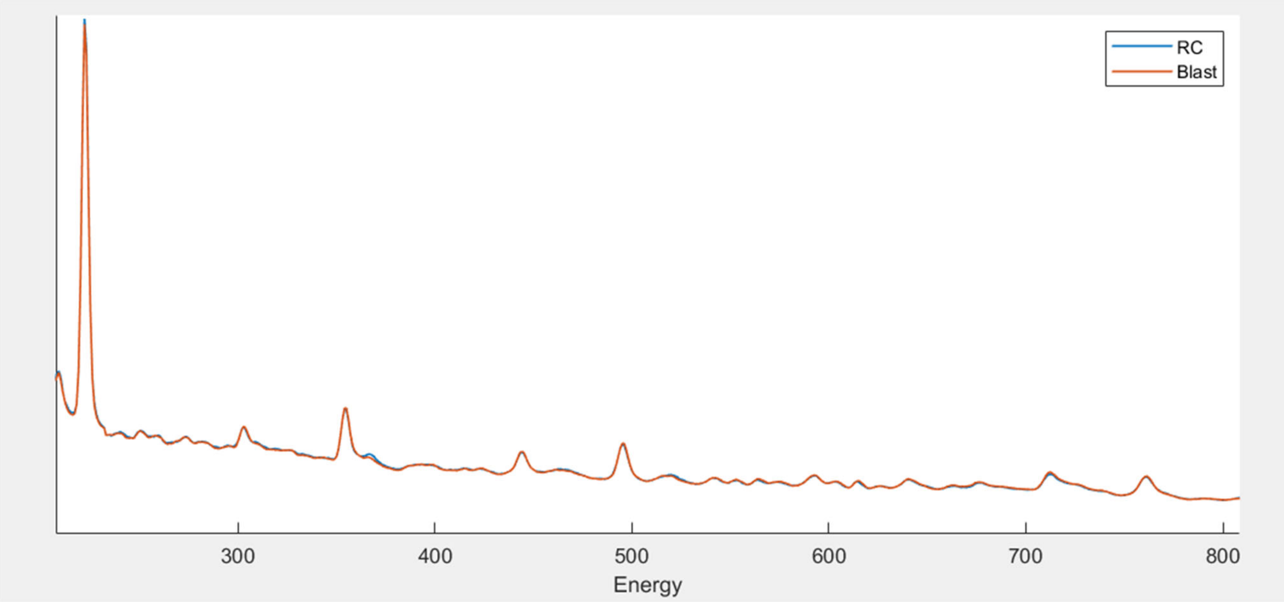

FIG 11 – Spectral response of the tool in a pair of concrete test blocks with a hole size correction applied. Note that the spectra agree well after the environmental corrections.

Fluid in the borehole (such as when the hole is below the water table) can affect the spectral response and should be considered as well. The presence of water in the hole can be detected and the spectra corrected to the dry hole response. Figure 12 shows the spectral data (presented at multiple depths as a Variable Density Log (VDL)) in a hole where the water table was at 49.5 m, noted by a distinct change in the character of the spectrum. The left plot shows the raw data in the energy range encompassing the most dominant iron peaks. Also note the effects of a rugose borehole at 36.5–38 m. The right plot shows the environmentally corrected data.

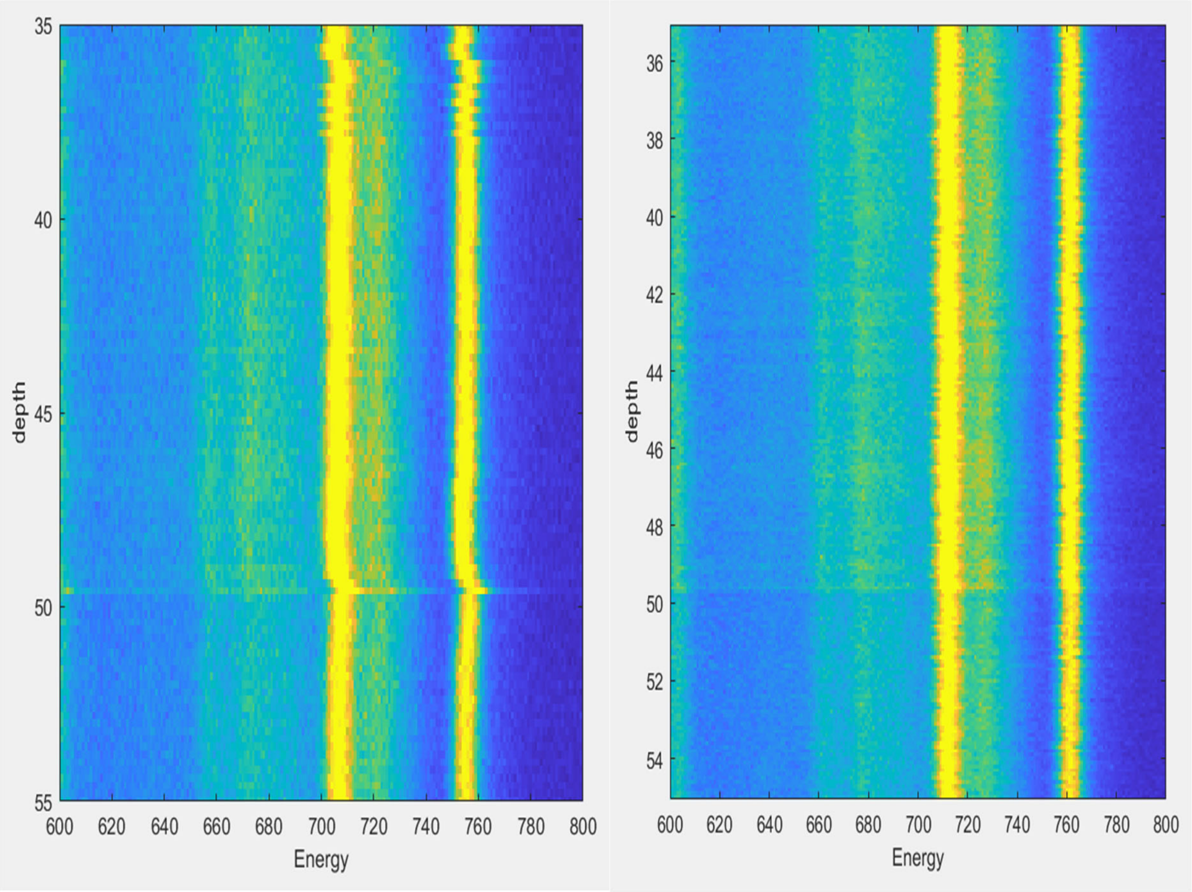

FIG 12 – Left – Raw spectra in a hole where the water table is at 49.5 metres. Right – Spectra corrected for temperature, hole size and fluid in the borehole.

Note that the environmental corrections are not only performed before using the spectra to build a calibration model, but also whenever the model is used. Blasthole data is environmentally corrected before the calibration model is applied.

Machine learning

Using the environmentally corrected spectra and the cleaned lab assays, a combination of machine learning and theoretical tool characterisation is used to obtain a model that transforms spectra into multielement proxy-assays for each depth interval.

Note: The machine learning method reserves a portion -approximately 25 per cent – of the data as test data; eg the machine learning uses approximately 75 per cent of the input data as training data and the remaining 25 per cent as test data. This is integral to machine learning methods and shouldn’t be confused with the blind data, which is additional data held outside the machine learning process for later independent validation.

Once the model is created, the main data set (both the 75 per cent training data and the 25 per cent test data) is processed with the new model to determine the downhole assay performance. The results are compared to the lab assays.

Calibration stages

Next, an example is presented where the progress of building a calibration model is detailed as the calibration campaign progresses.

Factory calibration, week 1

The results shown in Figure 13 were created using the factory ('out-of-the box') calibration for purpose of illustration. The plot shows the downhole tool elemental results versus the lab assay results for the first week (394 samples), processed with the factory calibration. The black dots are those which were identified in the cleaning process to be associated with depth-matching or poor lab assays (due to bad hole condition, sample contamination etc). The green dots are those which are deemed valid lab assays in the cleaning process. The black numbers in the upper left corner are the RMS error value using all the samples (not removing any from cleaning) and the number of valid samples (without cleaning). The green numbers in the lower right corner are the RMS error value and number of remaining points after cleaning is performed. The dark blue diagonal line is the unity line. In this plot display, the slope of the line should be near unity and the bias minimal. As can be seen at first glance, the factory calibration works quite well for Fe and Si) which means the tool can easily detect the ore/waste boundary from the first day. Al, Ti, Mg, K and the Loss on Ignition (LOI) are not bad, but accuracies not robust enough for grade control use. The remaining elements (those that are primarily derived by proxy in low amounts) are not ideal with the factory calibration and thus to have a robust calibration model further targeted RC samples should be collected and used in the next calibration run. Figure 14 shows the Iron and Silica data as logs plots to be easier able to see that, while not perfect, the factory model generates data that are very usable for ore/waste analysis.

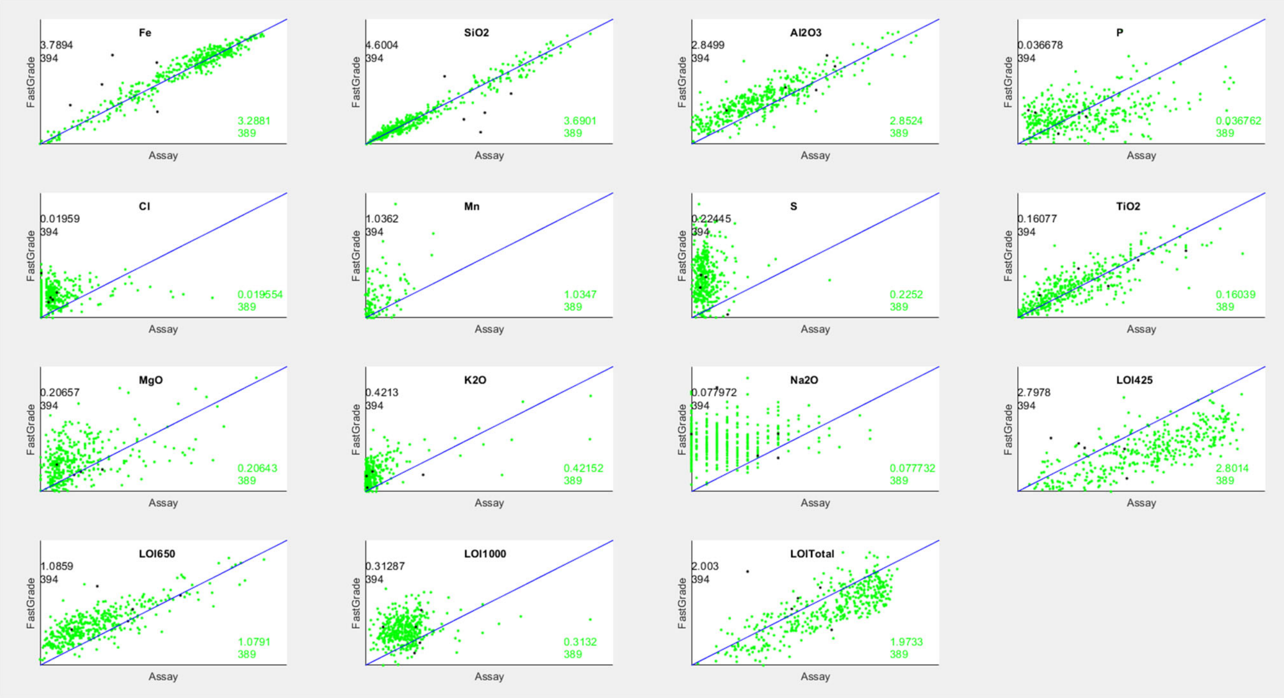

FIG 13 – Calibration Model in Progress – factory calibration.

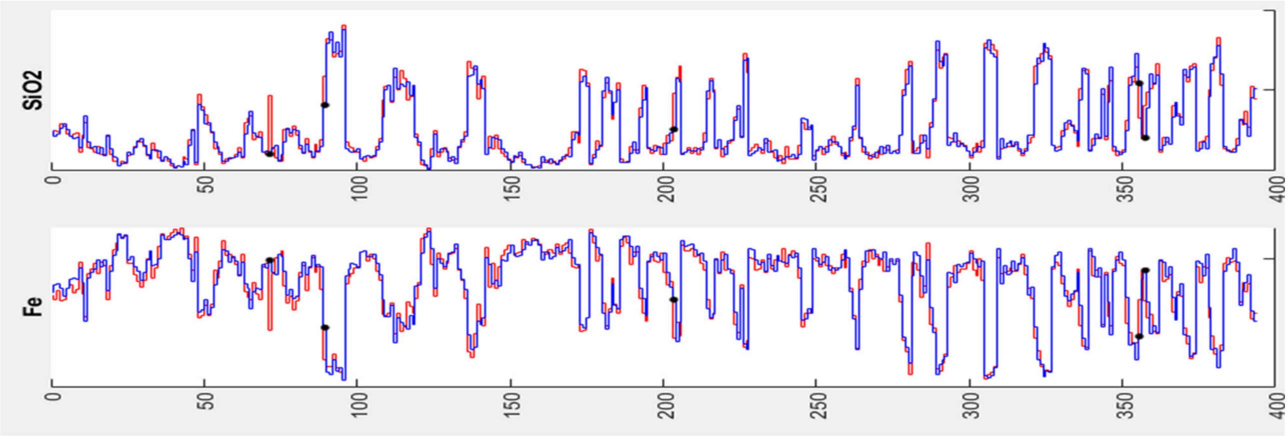

FIG 14 – Factory model performance. The lab assays (reference) are shown in red and the downhole assay data are plotted in blue.

Initial model, week 1

Though it is a small data set, a model can be created from these early data. The 394 samples have an assay distribution as shown in Figure 15. The results from building a model with this small sample are shown in Figures 16–18. The results are improved for most elements, though this model will not be of ideal accuracy for material types not represented in this small training set as any material falling outside the ranges where the histograms of Figure 15 reach above the red line is likely to have reduced accuracy.

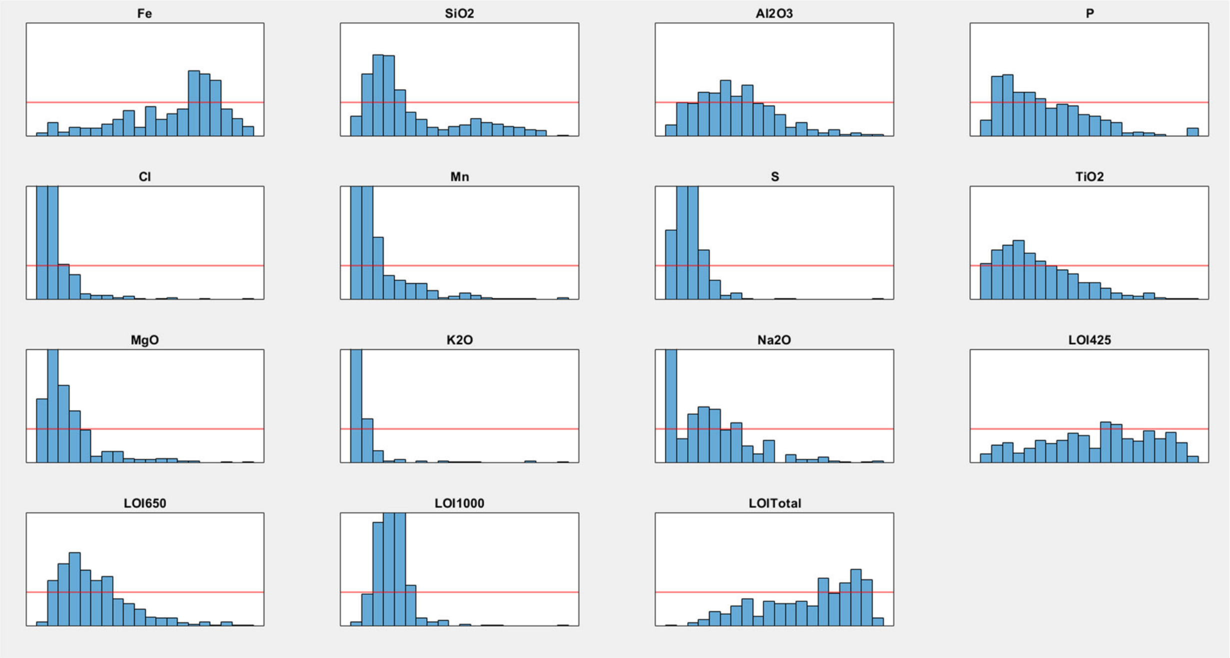

FIG 15 – Lab assay Distribution, first week of logging (394 samples).

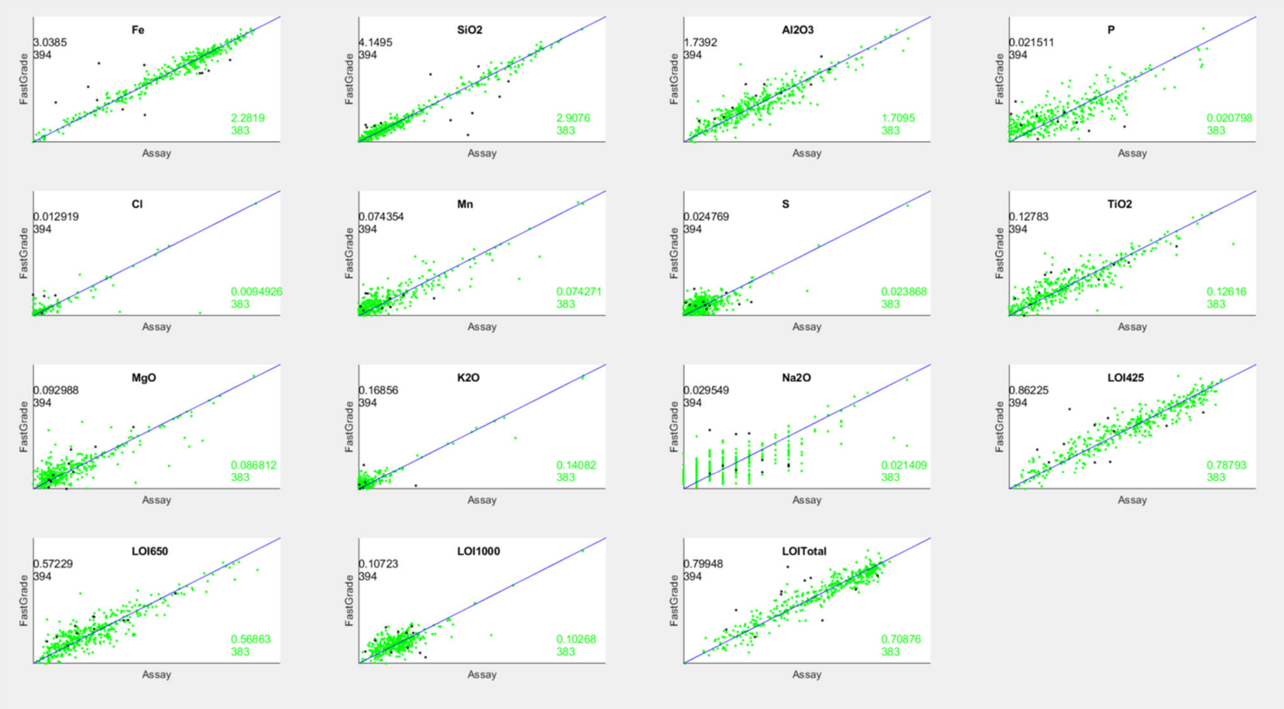

FIG 16 – Performance of model based upon initial 394 samples.

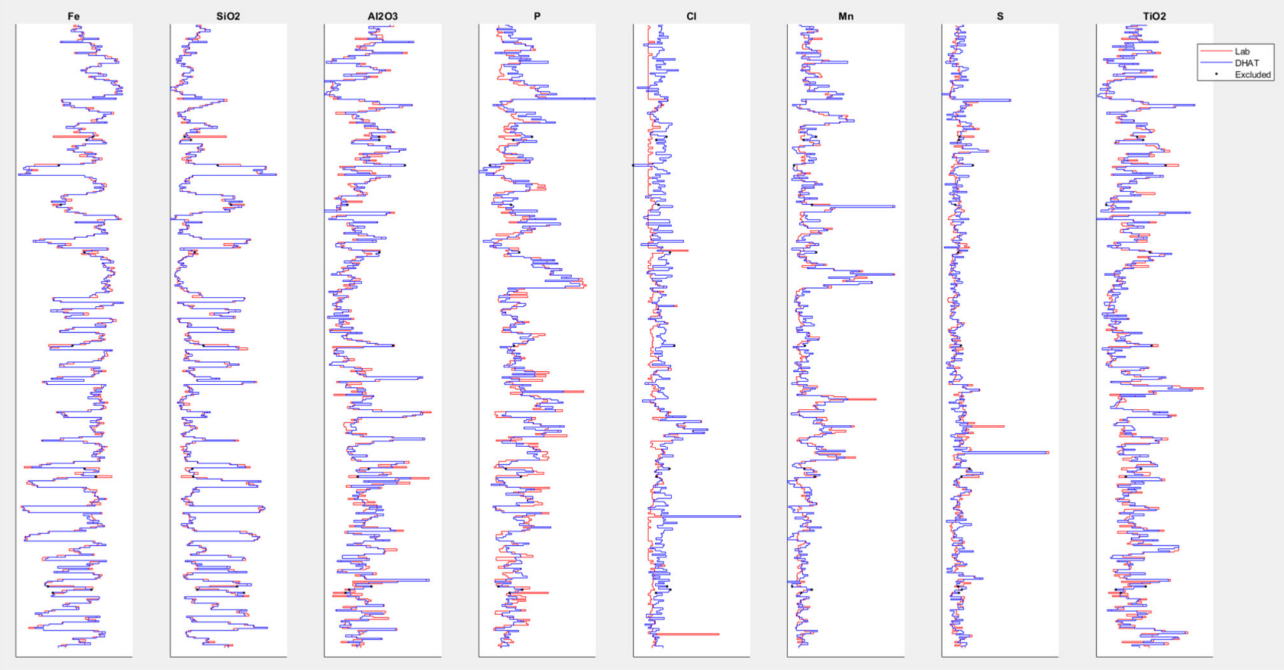

FIG 17 – Calibration model results from initial 394 metres of data. The lab assays (reference) are shown in red and the downhole assay data are plotted in blue.

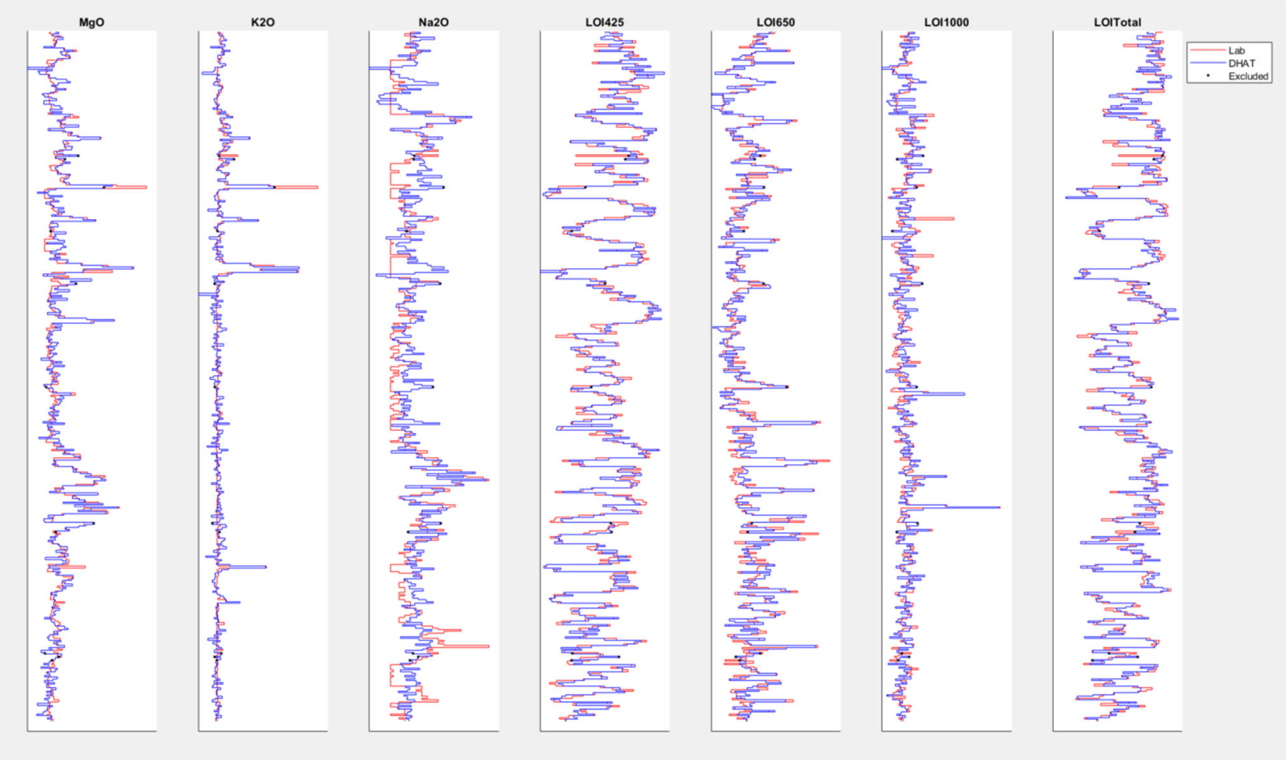

FIG 18 – Calibration model results from initial 394 metres of data. The lab assays (reference) are shown in red and the downhole assay data are plotted in blue.

Refined model, week 2

In the second week, a new area was logged with different geology. An additional 977 samples were collected, bringing the total to 1371 samples. Figure 19 shows the assay distributions for the new area which are significantly different than those of the first area (Figure 15). This is a good example of what happens when a model trained on geology is used on a different geology. Elements such as Fe and Si still perform well but minor elements that were not well represented in the initial data set, such as P, Cl, Mn, and S don't perform well (Figure 20). This is not surprising as the initial data set was very small and quite localised.

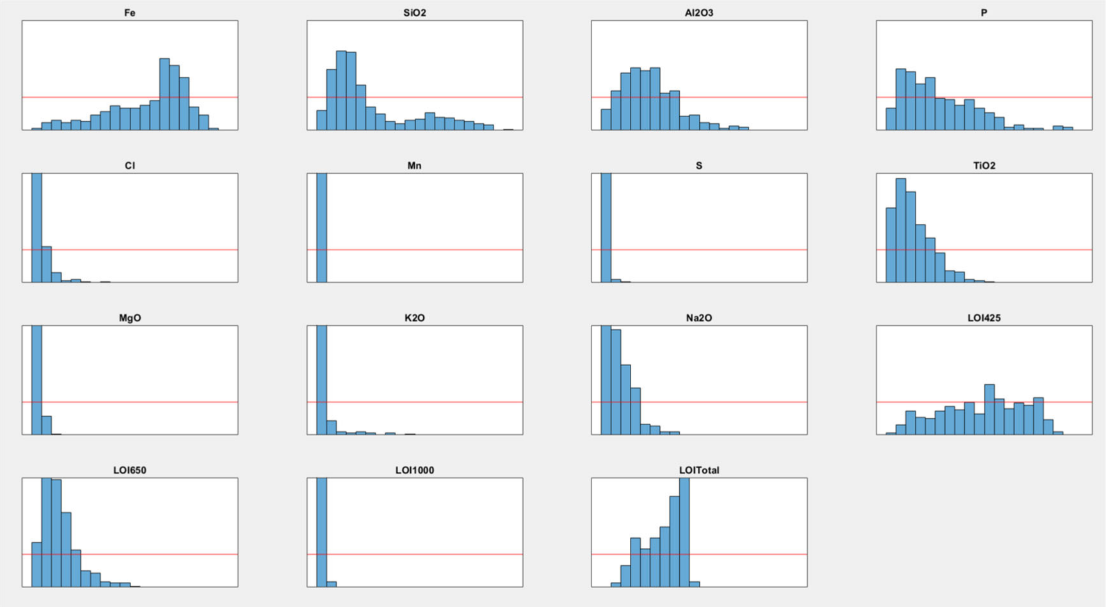

FIG 19 – Assay distributions for week 2 logging.

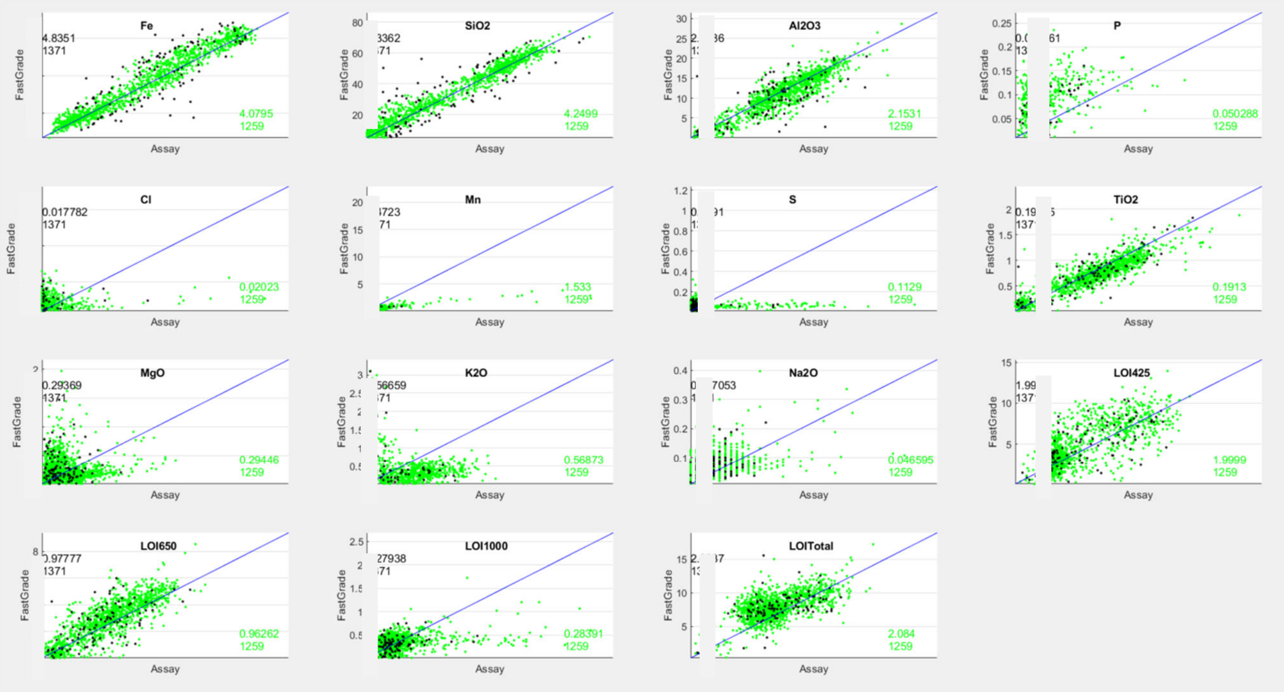

FIG 20 – Calibration model results using the model developed from geological area 1 on area 2.

Next, the calibration model is built using the data from areas 1 and 2 and then applied. Figure 21 shows the assays for the combined regions and Figure 22 shows the calibration performance, which is improved from the one in which only region 1 data was used to build the model.

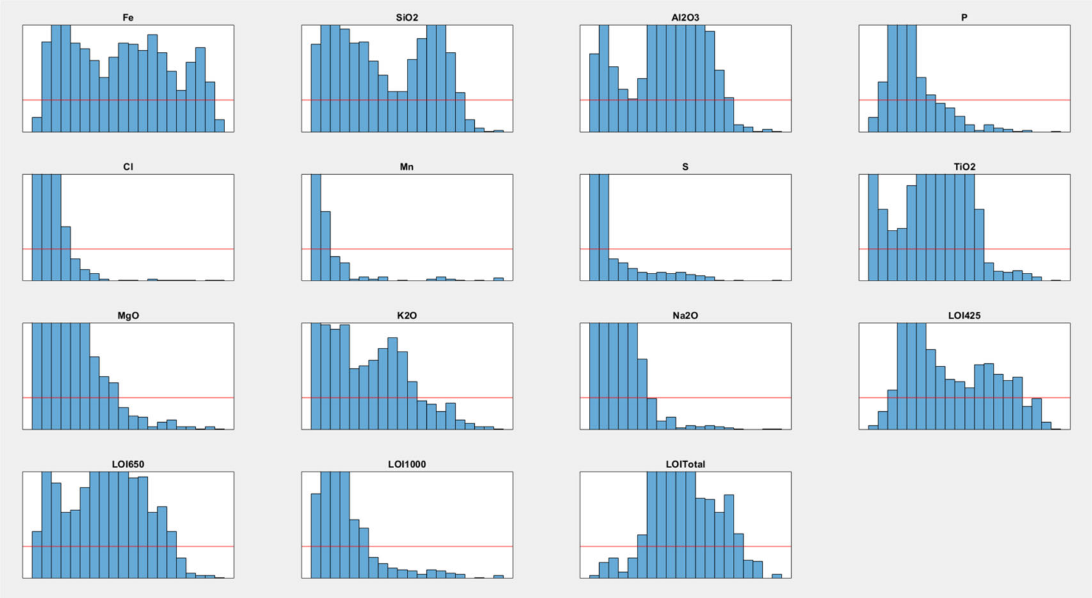

FIG 21 – Assays for combined regions 1 and 2.

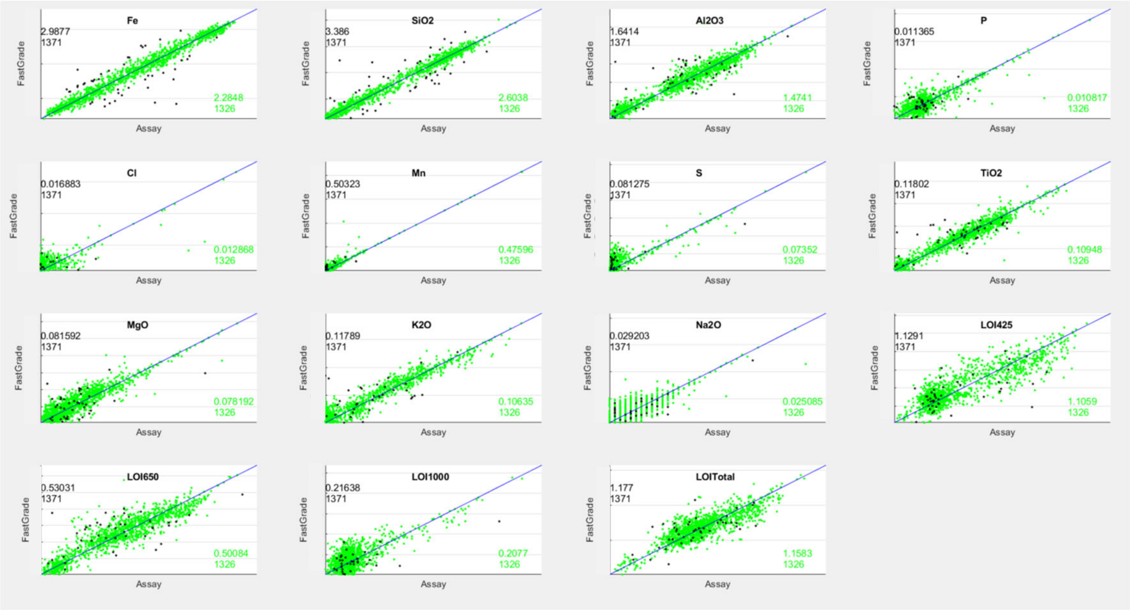

FIG 22 – Calibration model results using the data from 2 geological regions to build a model (and applying it in both regions).

Full calibration model, after more than 3 weeks of data collection

To ensure the final calibrations have enough diversity of material types and grades as possible, additional data was collected to gain the total of 3562 samples. Once this was achieved a combined model was created that works well for all areas. Figure 23 shows the assay distribution for the full RC data set, Figure 24 illustrates the cross-plots of downhole assay versus lab assay, Figure 25 shows the quantile-quantile (QQ) plot and Figures 26 and 27 show the log plots.

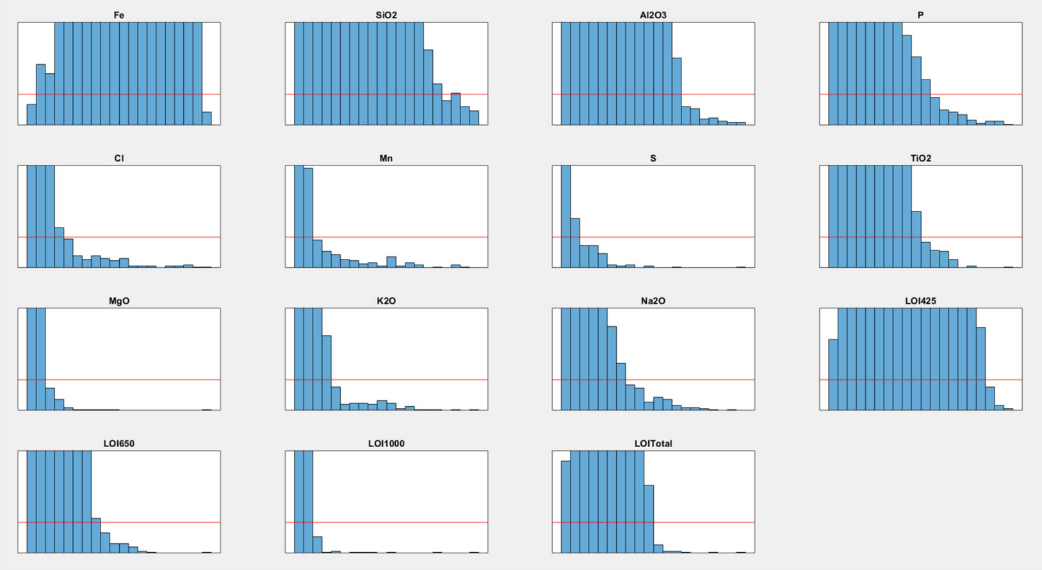

FIG 23 – Assay Distribution for all geological zones in project.

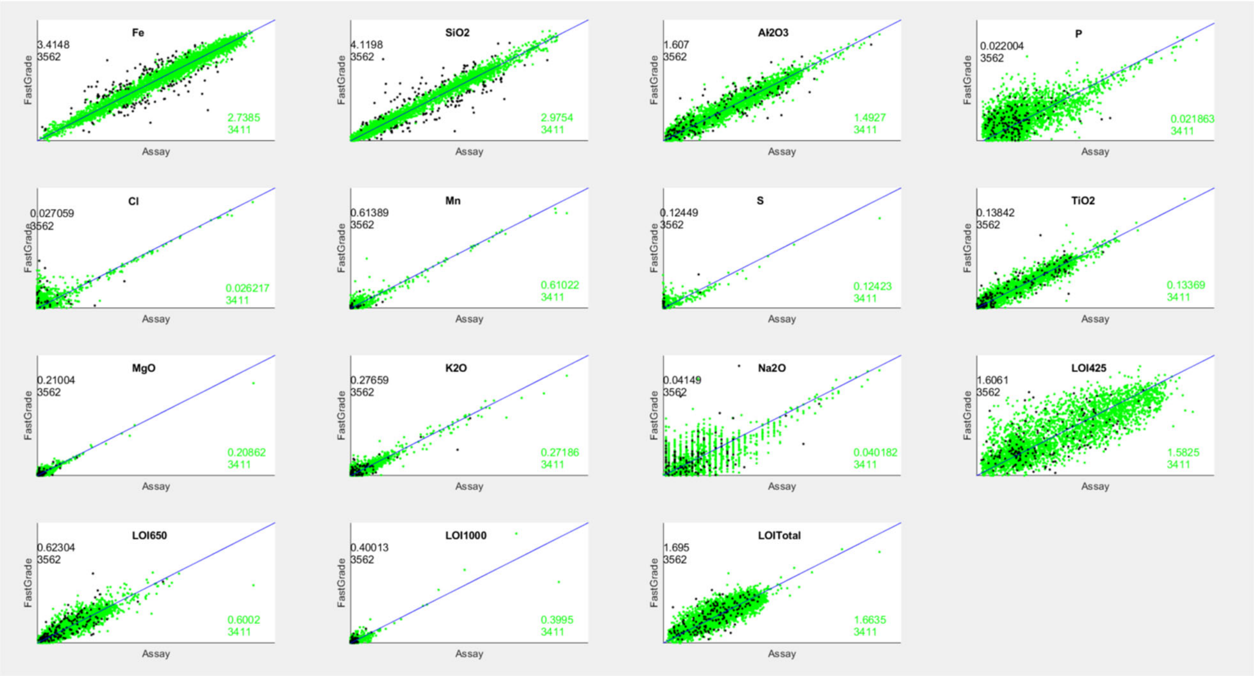

FIG 24 – Cross-plots of the downhole assay versus lab assay.

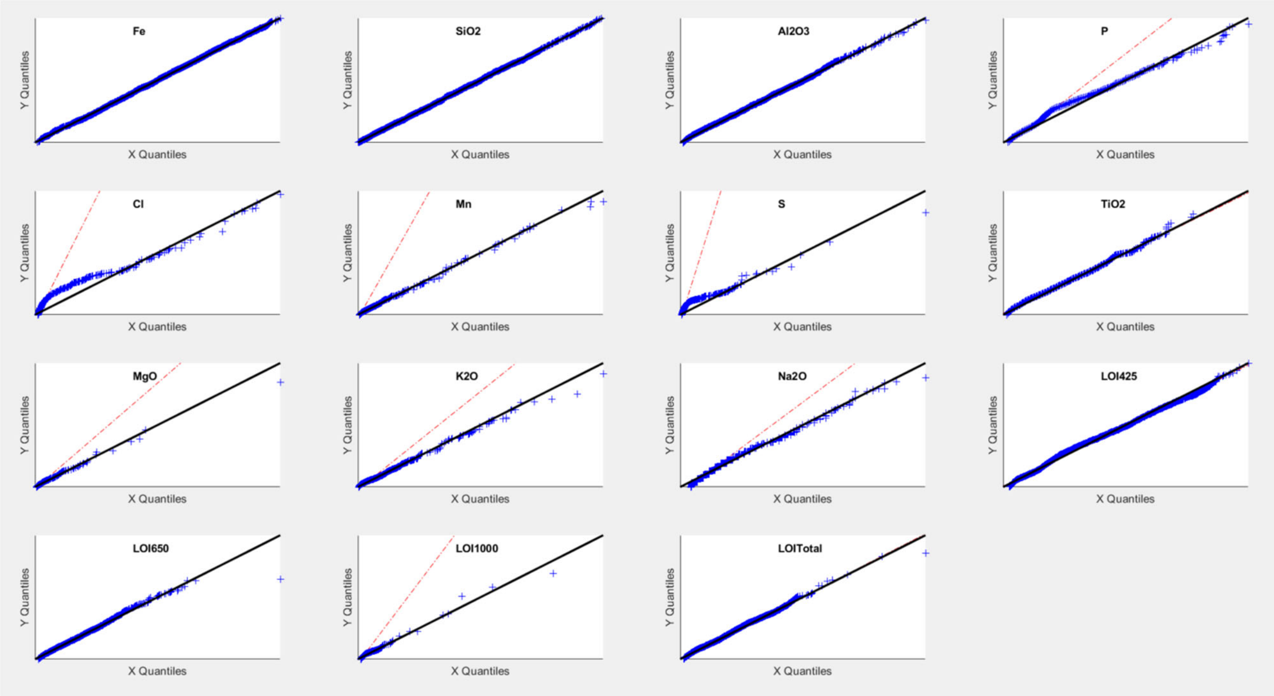

FIG 25 – QQ plots of the performance of the calibration model.

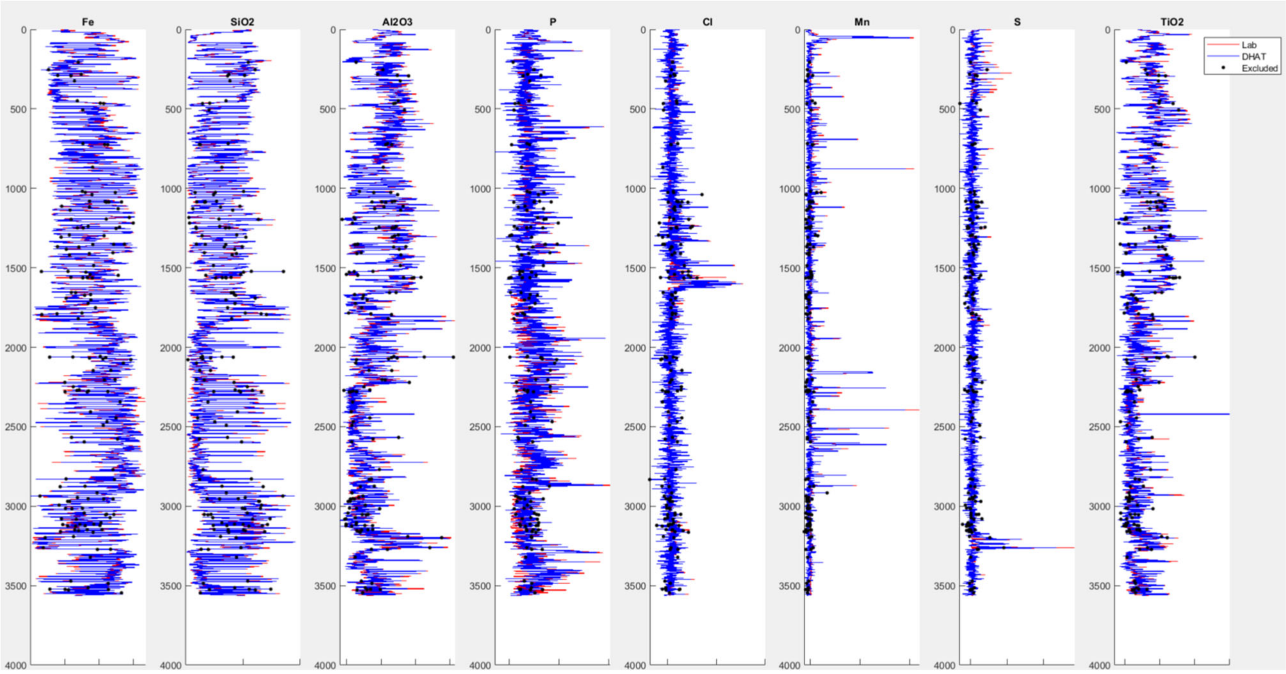

FIG 26 – Log Plots of the performance of the full model. The lab assays (reference) are shown in red and the downhole assay data are plotted in blue.

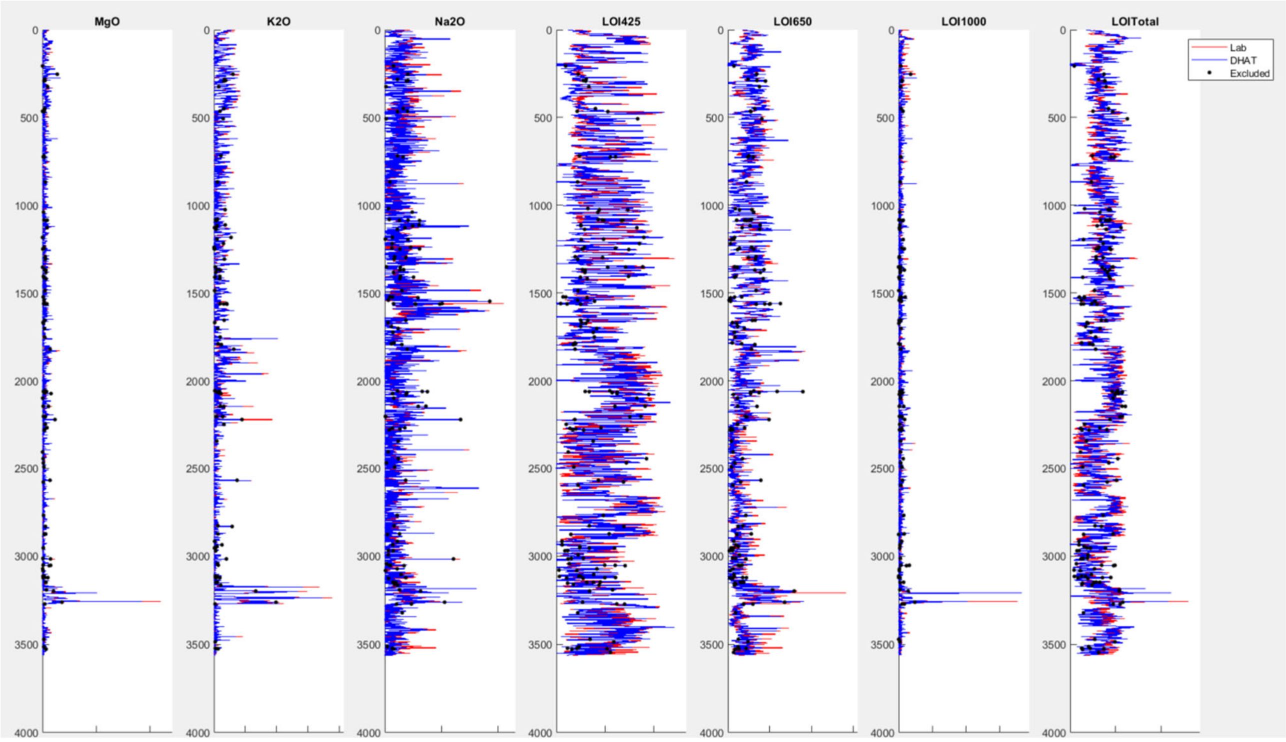

FIG 27 – Log Plots of the performance of the full model. The lab assays (reference) are shown in red and the downhole assay data are plotted in blue.

Evaluating the results

To evaluate the performance of the model and determine if it is ready for production, statistical analysis is performed. The additional data from the blind holes are processed with the model and the results compared with the lab assays. The RMS errors and biases should be similar to the main data set (which includes the training data). This is a check to ensure that the model was not over-trained. Figure 28 shows the blind hole calibration performance which is in line with the performance for the training holes.

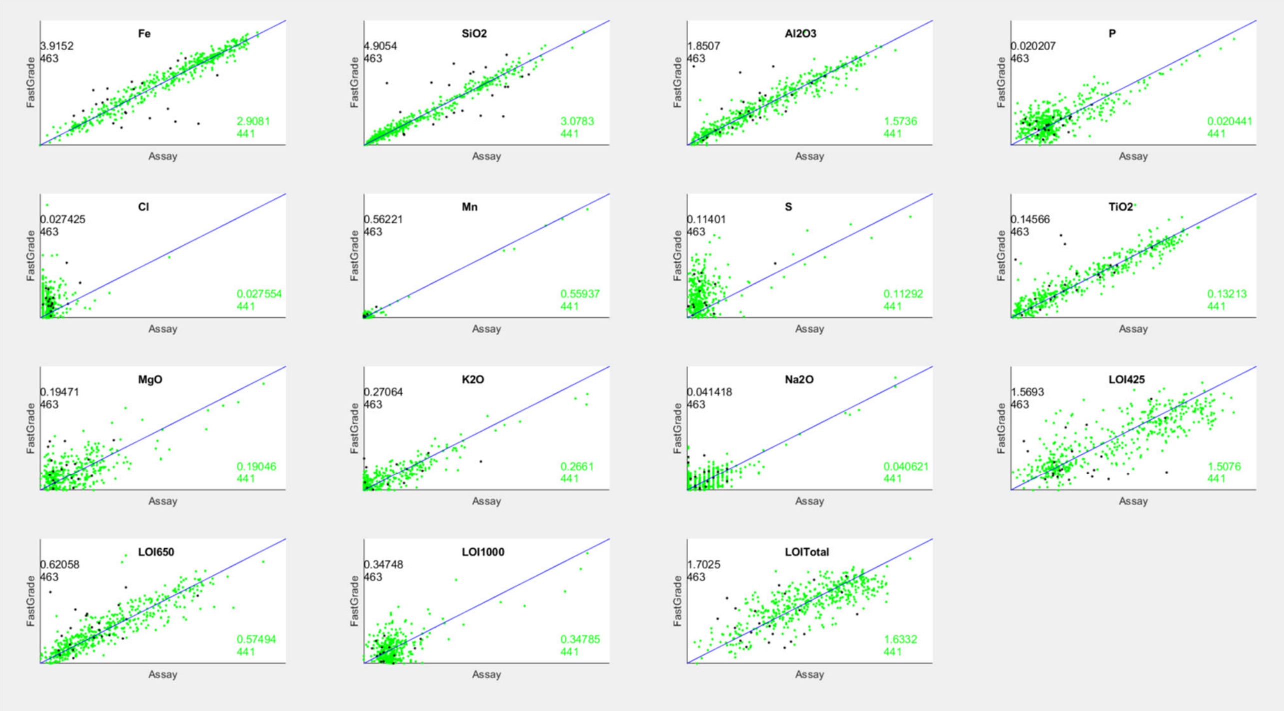

FIG 28 – Blind hole Test performance.

The repeat holes should be processed with the new model and evaluate the repeatability of the model compared to the static performance of the tool. The static repeatability test in where the tool is stationary at a particular depth in a hole and runs for 10–15 minutes. The variation (chatter in the signal) over 1-minute intervals is considered the noise level of the tool. This provides a baseline for testing the repeatability of the model. If the repeatability of running the tool twice in the same hole is less than twice the inherent noise of the system, then the model is considered robust. Figure 29 and Figure 30 show a log plot comparison of repeated holes for each element. Figure 31 shows the performance of the static tests (the baseline noise of the system). Table 1 shows the standard deviation for each element for the static test and the repeat logs. As expected, the repeat logs have a slightly larger error (due to depth control, changes in hole condition etc) but the numbers are within the expected range

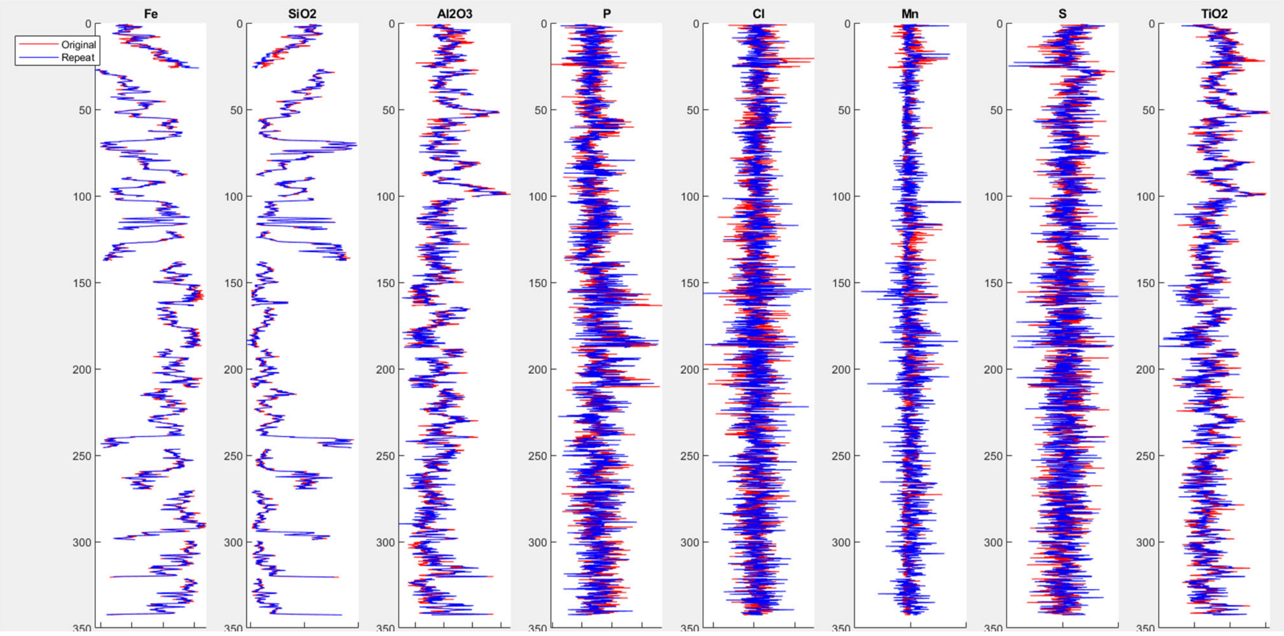

FIG 29 – Repeatability test. A selection of holes was logged twice. The red curves are the original log and the blue are the second pass.

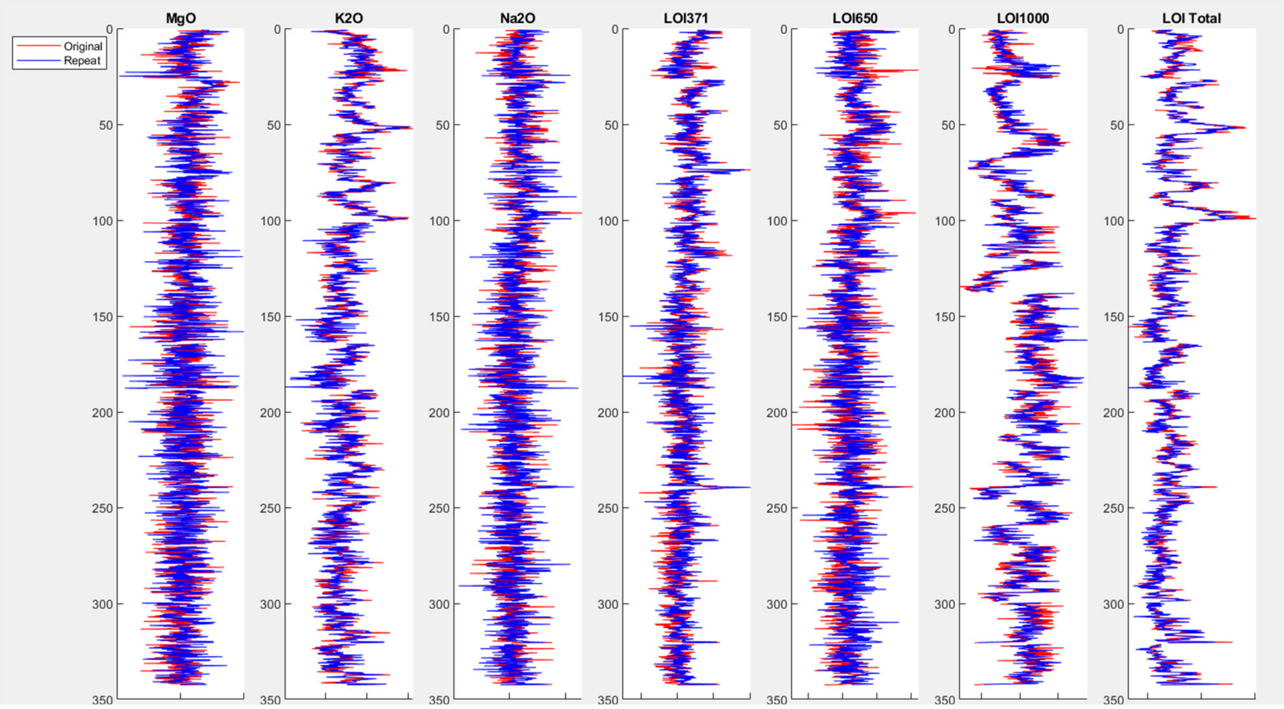

FIG 30 – Repeatability test, additional elements. The lab assays (reference) are shown in red and the downhole assay data are plotted in blue.

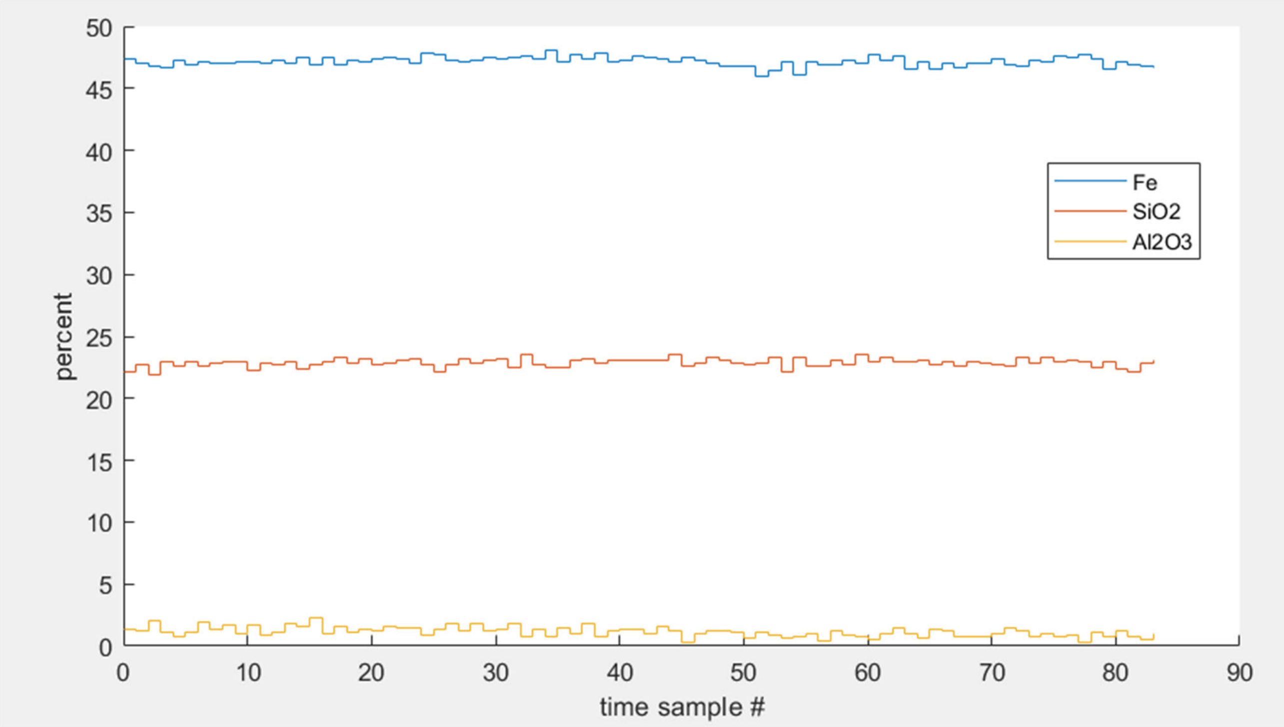

FIG 31 – Static test showing the repeatability of the calibration with the tool in a fixed position in a hole.

TABLE 1

Comparison of static standard deviation and repeated hole standard deviation

	Fe	SiO2	Al2O3	P	Cl	Mn	S	TiO2	MgO	K2O	Na2O	LOI
Std Dev, Repeat Holes	0.518	0.466	0.554	0.012	0.016	0.477	0.116	0.044	0.181	0.133	0.026	0.336
Std Dev, Static Test	0.309	0.355	0.431	0.006	0.010	0.285	0.045	0.038	0.110	0.094	0.013	0.268

If the results satisfy the performance targets, the calibration model is ready to be used to log in future RC, diamond, and blastholes. If not, then it is recommended more RC holes should be selected to add to the model for the elements which do not meet acceptance criteria.

To confirm the effectiveness of the environmental correction, it is recommended to acquire blast cone data in a small selection (approximately 50 holes) that the downhole assay tool has logged to confirm that the model transfers well from the RC environment (140 mm holes) to the production environment (165–300 mm holes). Because of the limitation of blast cone sampling, this comparison is usually only suitable to detect trends – eg., if one or more elements has a bias. If any inconsistencies are present, the environmental corrections can be refined. Figure 32 shows a comparison of the downhole assay data versus the blast cone samples. While a perfect match is not expected (the sample volumes are different and depth resolution in blast cones in very poor), this method is good for checking for biases. In this example, the unity line (black diagonal) is through the centre of the data cloud, which indicates that there is no systematic bias.

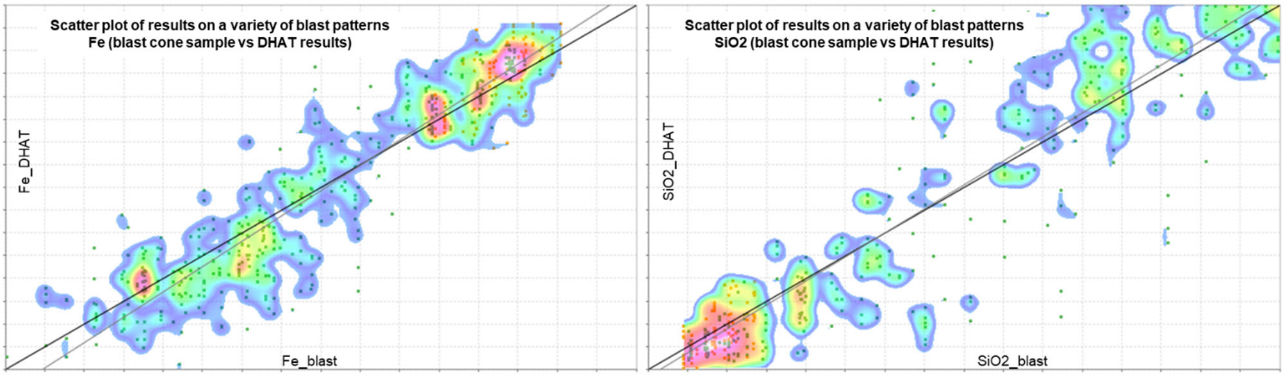

FIG 32 – Comparison of Downhole Assay (DHAT) versus blast cone sampling.

Maintaining the calibration model

For the calibration model to remain valid, the neutron flux generated by the tool must be constant. It is thus essential that the routine flux calibrations be performed and evaluated.

The flux produced by the generator is related to the amount of voltage applied. When the generator (neutron emission module) is new and the target is unused, a high flux is obtained with relatively low voltage. As the generator ages and the neutrons in the target are ‘spent’, it is necessary to increase the voltage in order to keep the flux generated by the module the same. Figure 33 shows the spectra after each routine flux calibration. These tests are performed in a well characterised test system (service rig) that is duplicated at every location that the tools are used. The concept is that the tool is placed in the test block at the same position for each test and the voltage is adjusted until the resultant neutron flux (and thus the spectra) match that of the previous calibration.

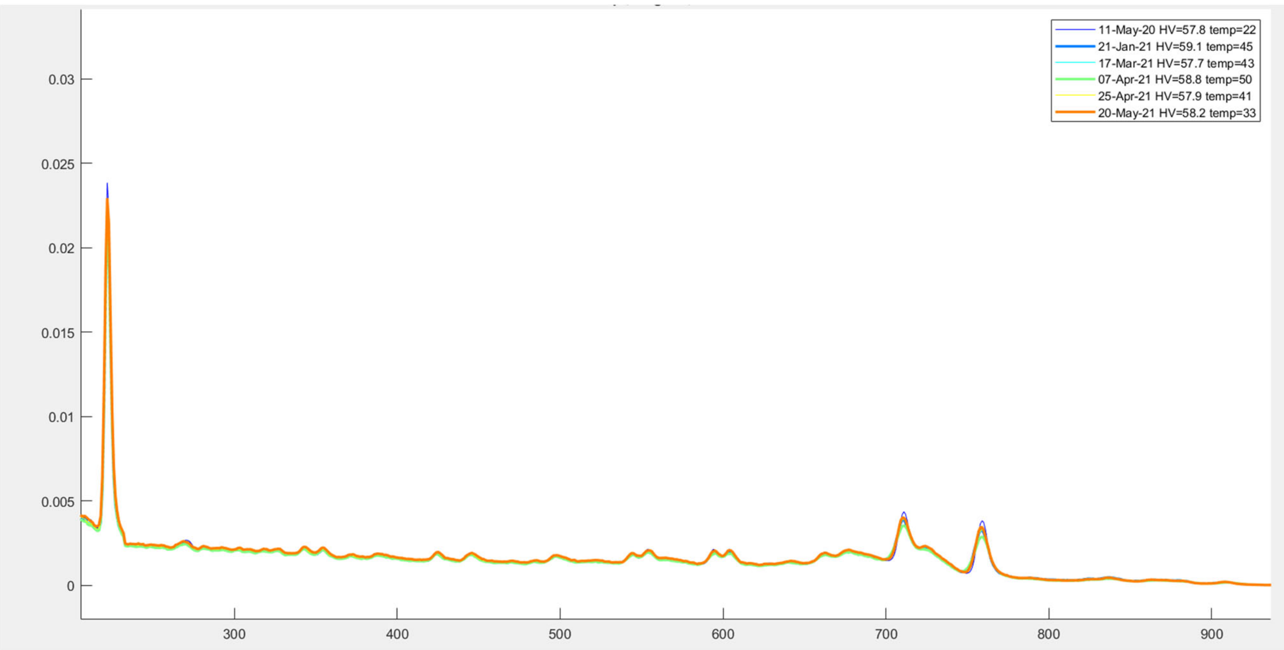

FIG 33 – Routine flux calibrations.

SUMMARY

With the rapid growth of PFTNA downhole assay measurements, the need for more robust and efficient calibration methods has become critical. Recent advances allow for much quicker and cost-effective calibration campaigns. Factory calibrations can be used to enable a tool to be effective in delivering ore/waste boundaries after initial commission if required for production requirements. However, the recommendation is to spend the whole of the initial period on gaining the amount of data required to initiate the building of a robust calibration model for all elements. The time required to build the calibration model (after the data is acquired) has been reduced from weeks to a few days due to the automations in place to refine the calibrations daily throughout the campaign.

These quicker more robust calibration techniques enable the downhole assay service to be introduced effectively into the mining environment, meeting the accuracies and production expectations required by current bulk mining operations.

REFERENCES

Jeanneau, P, Flahaut, V and Maddever, R A M, 2017. Iron ore benefits from neutron pulsed geochemical tools, in *Proceedings Iron Ore Conference*, pp 387–396 (The Australasian Institute of Mining and Metallurgy: Melbourne).

Market, J, Byrne, C, Robinson, D, Jeanneau, J and Rossiter, H, 2019. Downhole Assays in the Pilbara, *Proceedings of Iron Ore Conference 2019*, pp 372-392 (The Australasian Institute of Mining and Metallurgy: Melbourne).

Smith, C P, Jeanneau, P, Maddever, R A M, Fraser, S J, Rojc, A, Lofgren, M K and Flahaut, V, 2015. PFTNA logging tools and their contributions to in-situ elemental analysis of mineral boreholes, *TOS Forum*, 2015(5):157.

Ore characterisation and geometallurgy

Transformation of automated optical image analysis software Mineral4/Recognition4 to Mineral5/Recognition5

E Donskoi[1]*, A Poliakov*[2] *and K Vining*[3]

1. Project Leader, Mineral Processing Modelling, CSIRO Mineral Resources, Kenmore Qld 4069, Australia. Email: eugene.donskoi@csiro.au
2. Senior Experimental Scientist, CSIRO Mineral Resources, Kenmore Qld 4069, Australia. Email: andrei.poliakov@csiro.au
3. Research Group Leader – Carbon Steel Materials, CSIRO Mineral Resources, Kenmore Qld 4069, Australia. Email: keith.vining@csiro.au

ABSTRACT

The automated optical image analysis software Mineral4/Recognition4 (M4/R4) is capable of performing comprehensive characterisation of different materials throughout the iron ore value chain, including ore fines, lump, sinter, pellets and coke. It has been successfully used by CSIRO for industrial and research projects and has been independently licensed to several world leaders in iron ore production and ironmaking. The M4/R4 software was strongly integrated with a Zeiss microscope to make use of the company's powerful AxioVision software. This required users to own both Zeiss microscope hardware and AxioVision software in order to be able to use M4/R4 to its full image acquisition and analysis capacity. Therefore, it was not available to the users of equipment produced by other major microscope manufacturers. In recent times however, Zeiss has indicated that the AxioVision software will no longer be supported.

To overcome this limitation, CSIRO has proceeded with the next generation of this software, Mineral5/Recognition5 (M5/R5). Importantly, the M5/R5 system has been developed without any dependence on a specific microscope hardware/software platform. Furthermore, the image analysis functionality is now based on openCV open access software and has been fully rewritten using state-of-the-art software development tools to allow reading and processing of all major image formats. Although past applications have been specific to iron ore and ironmaking applications, other improvements, such as an increased number of minerals allowing better gangue segmentation, flexible mineral definitions, improved software modules behaviour and refined analysis routines enables the platform independent M5/R5 image analysis system to be used by researchers in any area of mineralogical or materials research.

INTRODUCTION

To meet the growing demand for iron ore, mining companies need to consider lower grade resources compared to those mined only 10–20 years ago. The mineral and textural composition and beneficiation of such ores is becoming more complex. To reflect the increasing complexity of iron ores and their processing, comprehensive characterisation of such ores is needed (Clout, 1998; Donskoi, Poliakov and Manuel, 2015a).

CSIRO's optical image analysis (OIA) software Mineral4/Recognition4 (M4/R4) is capable of performing complicated optical image analysis of ore fines, lumps, pellets, coke and other different commodities. It can provide comprehensive information on mineralogy, porosity, particle size distribution, mineral liberation and association, chemical composition, textural characteristics etc (Donskoi, Poliakov and Manuel, 2015a, Donskoi *et al*, 2015b, 2010). One of the unique features of this software is textural classification of characterised objects based on a textural classification scheme developed by the user. This feature, together with other advanced algorithms for mineral and textural segmentation, comprehensive textural descriptors, convenient reporting etc, enables the software to be a convenient and reliable tool. This allows ore producers/iron makers to improve their resource evaluation and prediction of downstream processing performance, develop waste-management strategies, reduce processing costs and improve productivity. This software is based on Zeiss technology, and its image processing component, Mineral4, requires the Zeiss AxioVision software package to operate. This means that Mineral4 users must have Zeiss software, typically with a Zeiss motorised microscope, to use the automated image acquisition part of Mineral4. Recently Zeiss indicated that AxioVision software would no longer be supported, so CSIRO faced a full redevelopment of the software. This was an opportunity to make it platform-independent and improve its performance.

The new generation of CSIRO OIA software was named Mineral5/Recognition5 (M5/R5). Its analysis functionality is now fully independent of any specific microscope software/hardware platform. It is based on openCV open access computer vision software and is capable of reading and processing images in all major image formats. The increased number of identifiable minerals and its unique textural mineral identification function allow segmentation of different morphologies of the same minerals, such as microplaty hematite and martite in iron ore, or of different types of silico-ferrite of calcium and aluminium (SFCA) in iron ore sinter. The increased number of identifiable minerals also allows for more gangue minerals to be segmented, which can be important for more complex grade ores. The new capability enables the user to change mineral nomenclature making it easier to work with commodities other than iron ore/sinter and to adjust minerals chemical composition according to the ore/commodity. Mineral5/Recognition5 has already been applied to different ore/commodities beyond iron ore, such as: sinter and pellets; manganese ore; and metallurgical coke.

Automated image acquisition, as opposed to analysis, cannot be fully independent and relies on the actual microscopy hardware. As a general rule, all major microscope brands allow, where applicable, automated image collection and saving of images in common formats, eg JPG, BMP, TIF, PNG, which can then be processed by M5/R5. However, to process large and statistically valid sets of data it can be necessary to collect multiple images in a controlled manner. A specific image acquisition routine was created, based on the current Zeiss ZEN software platform, allowing the collection of sets of large, stitched images on a Zeiss microscope. M5 also allows further stitching of images to create larger panorama images for detailed characterisation of mineral/coke lump, pellets and other macroscopic objects. CSIRO considers creating developing similar image acquisition routines for other major microscopy systems such as Leica and Olympus. The ability to process any major image format created an opportunity to use Mineral5 outside of the microscopy field, which was successfully demonstrated during textural studies of pot grate sinter plugs.

After image collection, images are processed in Mineral5. The processing may be comprehensive or simple, depending on the particular task and commodity. The operator is capable of changing processing parameters depending on imaging magnification, object size, peculiarities of the ore etc. The analysis has several major stages which are discussed later. All processing parameters are saved as an ‘analysis profile’ which can be reused for similar samples, without further modification or after necessary adjustments.

Mineral5 has several outputs, one of which is a database of all measured objects containing all mineral/phase/textural information, which is used later by Recognition5 for statistical/textural classification purposes. For other types of analysis, Mineral5 also produces statistical outputs in Excel format, that include comprehensive textural characterisation of materials and characterisation of large continuous objects such as pellets/lump particles. Mineral5 also produces important visual information, such as calculated mineral maps and numbered maps of objects, helping users to connect the information in the database with the original images. The Pellet module can also produce visualisations of spatial phase distributions.

Recognition5 allows its users to develop customised ore textural classification schemes for automated ore and gangue classification of particles/frames. The classification is fully editable and can evolve as the understanding of the commodity increases. Recognition5 can calculate mineral composition, chemical assay, density, dimensional and textural characteristics for every particle, as well as liberation class, ore texture class, or any particle group based on a set of specific mineral, dimensional, textural or chemical criteria. All outputs are in the form of Microsoft Excel and Word graphs and tables, allowing easy integration of analysis data into reports.

Altogether Mineral5/Recognition5 is an even more powerful and user-friendly software than M4/R4 which was commonly used by iron ore mining and ironmaking companies. Now it can be conveniently used for characterisation in other fields.

MINERAL5

In many aspects, Mineral5 OIA software is a direct successor of Mineral4. However there also are significant changes, some of which were driven by the changes to the software on which Mineral4 was built, by customer demand for specific features, and by the developers' vision. The outcome was a software product that is faster, more flexible and less dependent on proprietary software, allowing it to be used outside iron ore/agglomerate studies and Zeiss-based systems. At the same time, Mineral5 retains the benefits of the earlier version, such as the focus on iron ore and related commodities. This section will provide a full overview of Mineral5 with particular attention to the newly added features.

One of the main advantages of Mineral5 is its ability to analyse extensive sets of images and significant numbers of particle sections (tens of thousands) at high resolutions. Such sets often consist of hundreds of images, and that assumes automated image acquisition. Such an automated acquisition requires a significant level of integration between OIA software and the microscope controlling software provided by the microscope manufacturers; the microscopy software also typically offers some image analysis functionality and automation tools. The inclusion of a high-level VBA (visual basic for applications) programming capability into the Zeiss AxioVision software suite was one of the main reasons why Mineral5's predecessor, Mineral4, was fully based on AxioVision, combining image acquisition and analysis in a single product. However, the new Zeiss microscopy software, ZEN, offers less programming functionality, so creating a new generation of highly interactive OIA using ZEN only was not viable. As a result, the image analysis functionality in Mineral5 has been moved away from the Zeiss proprietary platform, and its only ZEN-based component is now Acquisition.

The Acquisition component of the Mineral5/Recognition5 package has been significantly streamlined, in part to accommodate the limitations of the ZEN graphic user interface. Some of the historic set-up and preview functionality, important for older microscopes with low level automation, is no longer relevant for newer fully automated systems, so has been removed. The key functionality, allowing the user to set-up and perform automated image acquisition over a given sample area, fully or partially covering it with individual or tiled images, possibly pre-cropped to reduce edge-effects, is still available to users. Figure 1 gives an example of one of the intermediary screens of Acquisition, where parameters that define the output image, such as tile set-up and camera frame cropping, are set.

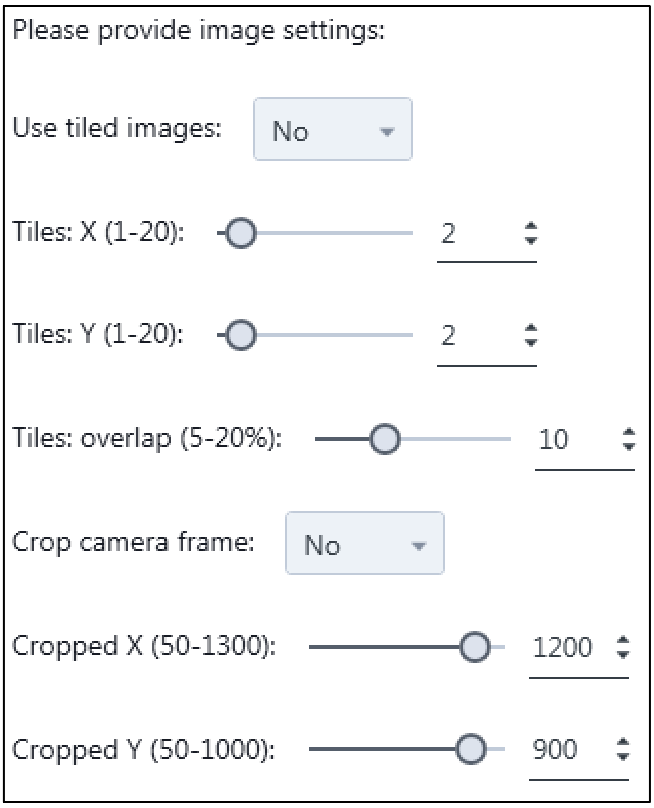

Please provide image settings:

Use tiled images: No

Tiles: X (1-20): 2

Tiles: Y (1-20): 2

Tiles: overlap (5-20%): 10

Crop camera frame: No

Cropped X (50-1300): 1200

Cropped Y (50-1000): 900

FIG 1 – Image settings section in Acquisition.

The result of automated image acquisition in Mineral5 is, in the most typical example, a set of images in Zeiss CZI format, which also allows storage of metadata such as scaling. The so called ‘set file’, containing metadata and the list of files, is also recorded. The images can now be analysed using the Mineral5 program. Apart from the CZI format, Mineral5 also supports the previous Zeiss ZVI image format, making it fully possible to analyse images obtained earlier by Mineral4. Furthermore, common graphic formats such as JPEG, BMP, TIFF or PNG are also fully supported, making it possible to apply Mineral5 to images from virtually any source and, in particular, opening the opportunity to couple Mineral5 with microscopy solutions from other manufacturers. Mineral5 and its libraries are developed in the well-supported Microsoft.NET environment, which ensures extended product life, and its core functionality is based on the widely used openCV libraries. This move also allowed the developers to overcome some of Mineral4’s limitations, such as fixed window sizes; the operator now has full control of their preferred display choices.

The most common analysis type performed by Mineral5 is Particle Analysis. This mode is typically used to process images of ore fines and similar multiple small objects, where every particle section needs to be identified and measured separately to allow subsequent automated characterisation of each particle and of the ore in general. Figure 2 shows the simplified workflow of particle analysis in Mineral5. Each analysis step shown in the workflow performs a number of important operations aimed at identifying, or improving identification of, certain sample features. Operations for each step and corresponding analysis parameters can be accessed via interactive forms, allowing the user to see the results of applying those operations/parameters. The analysis steps rely on those performed earlier (eg porosity identification relies, in many aspects, on particle identification, and mineral correction routines rely on previous mineral identification) so changes performed at an earlier stage will likely require recalculation of the later stages as well. Thus, analysing and subsequent refinement of analysis of an unknown sample may require multiple recalculations; the controls on the Analysis Preview display (see examples in Figures 3b, 4b and 7b) allow the operator to temporarily limit the recalculations to a particular analysis stage and thus save significant time during profile refinement.

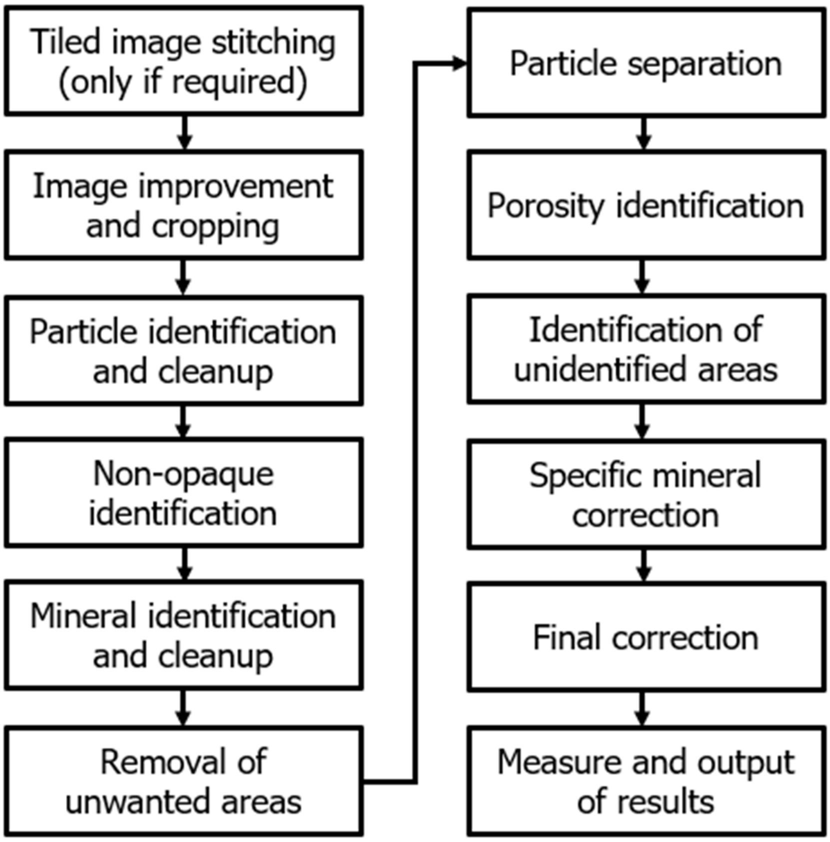

FIG 2 – Mineral5 Particle Analysis workflow.

(a)

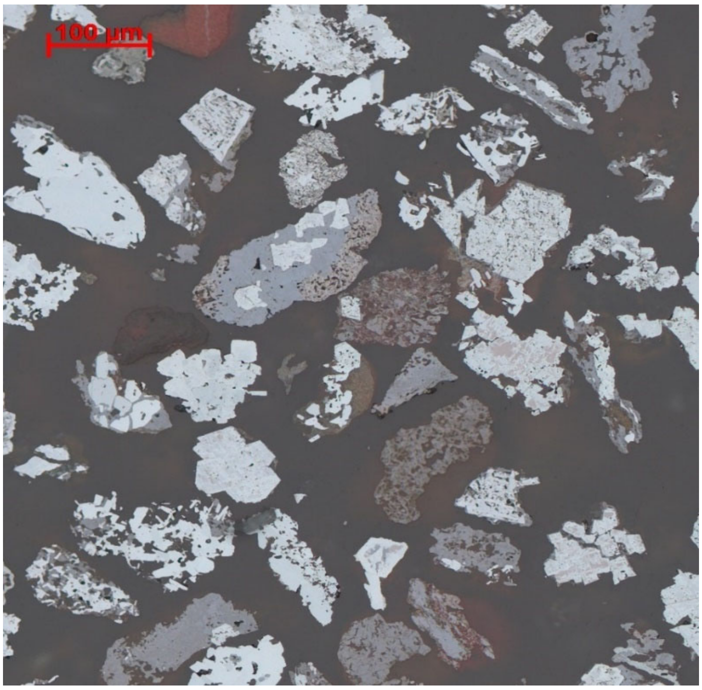

(b)

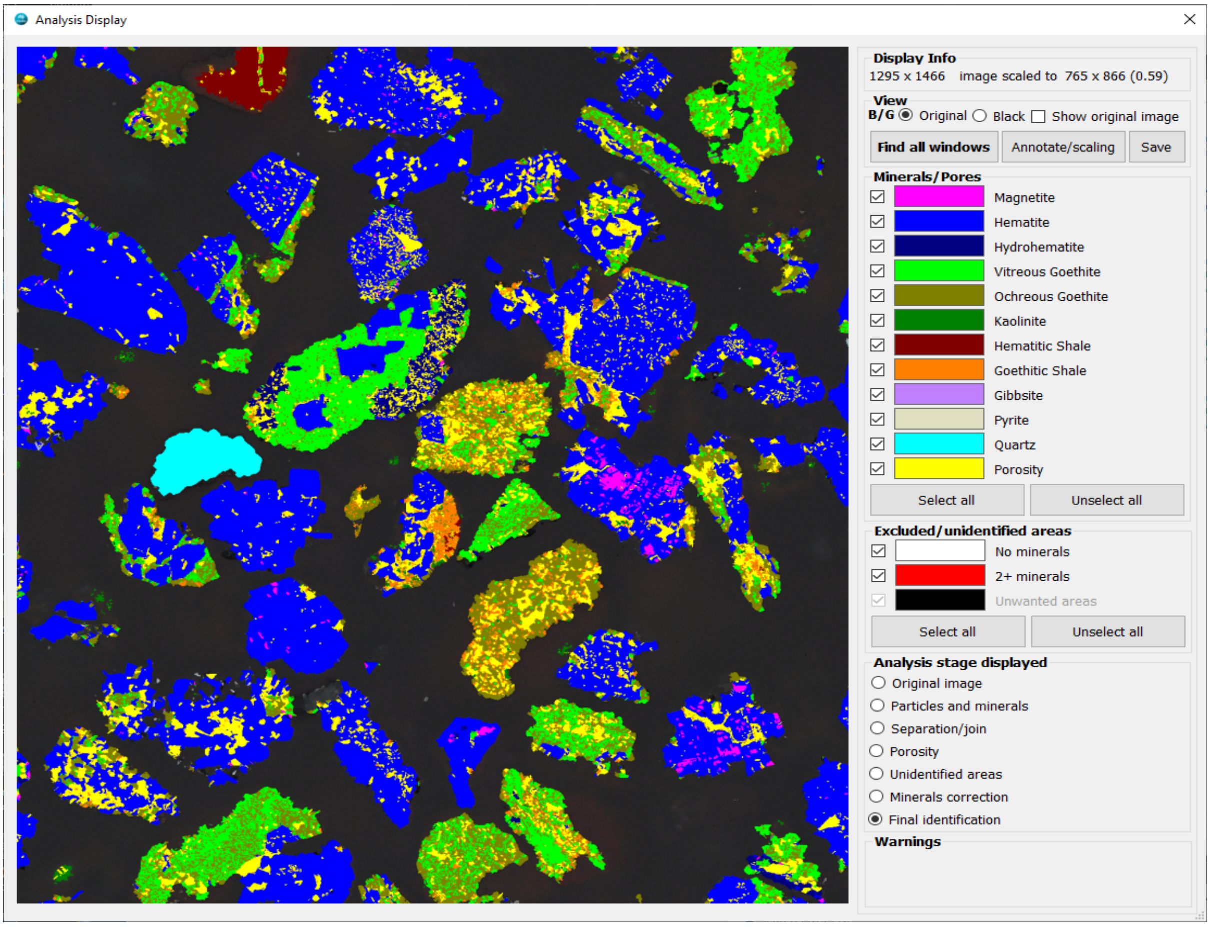

Display Info
1295 x 1466 image scaled to 765 x 866 (0.59)

View
B/G ● Original ○ Black ☐ Show original image

Minerals/Pores
☑ 🟪 Magnetite
☑ 🟦 Hematite
☑ 🟦 Hydrohematite
☑ 🟩 Vitreous Goethite
☑ 🟫 Ochreous Goethite
☑ 🟩 Kaolinite
☑ 🟥 Hematitic Shale
☑ 🟧 Goethitic Shale
☑ 🟪 Gibbsite
☑ ⬜ Pyrite
☑ 🟦 Quartz
☑ 🟨 Porosity

Excluded/unidentified areas
☑ ⬜ No minerals
☑ 🟥 2+ minerals
☑ ⬛ Unwanted areas

Analysis stage displayed
○ Original image
○ Particles and minerals
○ Separation/join
○ Porosity
○ Unidentified areas
○ Minerals correction
● Final identification

Warnings

FIG 3 – Image analysis of iron ore fines in Mineral5: (a) original image; and (b) final mineral/porosity map as it appears in the Analysis Display window.

The analysis settings (the active image analysis operations and corresponding parameters) for a particular sample can be saved in a file, called 'analysis profile' that allows reuse of the analysis settings for processing similar samples (ideally acquired using the same illumination, which is achieved by calibration of the microscope). Once a comprehensive assortment of profiles has been established for a particular commodity, the newly imaged samples can be processed quickly using the suitable profile, although due to the individual peculiarities of each sample, some verification and adjustment may be required.

Also, importantly, in most typical Mineral5 analysis regimes, a whole set of multiple images is processed automatically using the same profile. CSIRO supplies Mineral5 with pre-recorded profiles for certain commodities, making it easy to operate.

The format of this paper doesn't allow for a detailed description of each analysis stage, so special attention will be paid to the new and improved features that distinguish Mineral5 from Mineral4. It is suggested that readers interested in more details refer to the publications referenced throughout this section, in particular, Donskoi, Poliakov and Manuel (2015a).

The very first step in Mineral5 image analysis is stitching of the tile images. In many cases, especially for coarser ore fractions, imaging whole objects at a magnification high enough to accurately register details such as fine porosity, which is very important for characterisation, requires combining individual high-magnification images into stitched, or tiled images. While Mineral4 relied on a Zeiss stitching routine during acquisition, which sometimes resulted in image artifacts, Mineral5 performs this operation at the analysis stage. The results of stitching are recorded so, if the image requires reprocessing, there is no need to repeat the stitching process.

During image improvement the original image can be delineated, which decreases edge effects, and also cropped. Cropping is sometimes required to remove optical aberrations which are strongest near the sides of an image. It is also often used during profile development to speed up the process by focusing on particular areas of interest. Mineral5 allows quicker and easier cropping by dragging the margins to the desired positions.

Particle identification is a very important step as it provides the foundation for many subsequent operations. Mineral5 allows two different methods to be used for that purpose, separately or in conjunction, dynamic thresholding and RGB thresholding. In order to increase the quality of RGB thresholding, two optional extra thresholding operations are offered. During particle 'cleanup', noise objects are removed from the identified particle map, allowing quicker subsequent processing, while a special 'preservation' operation helps to join loose parts of highly porous, friable particle sections together.

Once the particle map is established, it is possible to use advanced Mineral5 routines to identify the non-opaque objects in the sample, some of which are nearly or exactly the same reflectivity as the mounting epoxy resin and are therefore not identifiable by normal thresholding (Poliakov and Donskoi, 2014; Iglesias, Santos and Paciornik, 2019). Quartz is a common example of such a mineral in iron ore and related commodities, and identifying it using optical methods was historically regarded as very challenging. Mineral4 introduced the unique border-based non-opaque mineral identification (Poliakov and Donskoi, 2014), which is now supplemented by a special threshold-based identification routine for improved identification.

The next step of the analysis is identification of individual minerals. One of the major improvements in Mineral5 over Mineral4 is the increased number of available phases, 12 versus 8. For iron ores that means more gangue minerals and, if necessary, more morphologies of ore minerals can now be identified and reported. Even more importantly, the mineral names and definitions are now flexible, so analysis of other commodities such as, for example, manganese ore, iron ore sinter and metallurgical coke can be now performed in a more straightforward manner. Figure 4 gives an example of a manganese ore image processed in Mineral5, showing minerals that are not typically present in iron ores (the same ore processed in Mineral4 would require maintaining a decoding table to translate iron ore mineral names to manganese). The image also shows how abundant non-opaque particles discussed in the previous paragraph are identified.

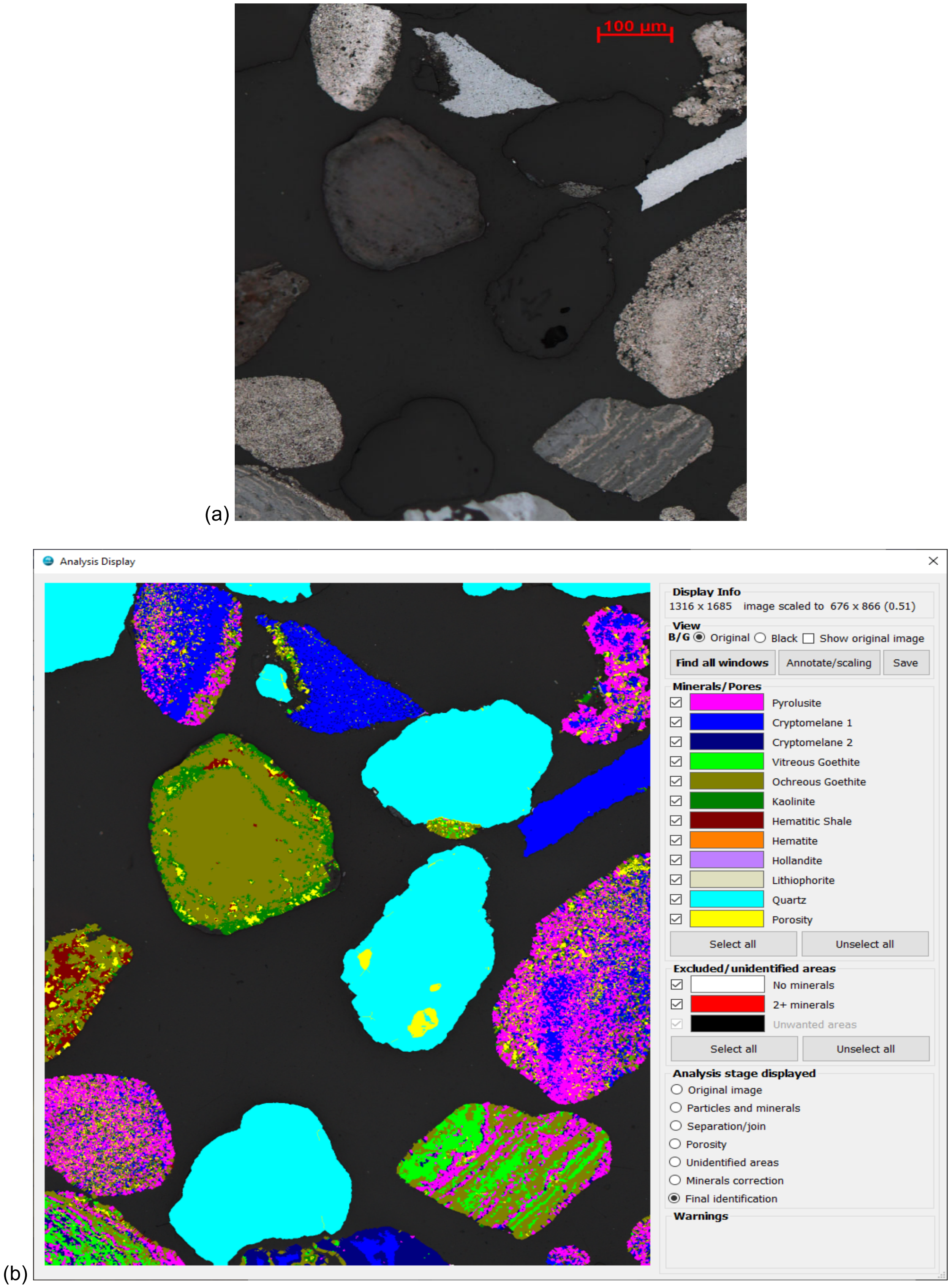

1316 x 1685 image scaled to 676 x 866 (0.51)

B/G ● Original ○ Black ☐ Show original image

☑ 🟪 Pyrolusite
☑ 🟦 Cryptomelane 1
☑ 🟦 Cryptomelane 2
☑ 🟩 Vitreous Goethite
☑ 🟫 Ochreous Goethite
☑ 🟩 Kaolinite
☑ 🟫 Hematitic Shale
☑ 🟧 Hematite
☑ 🟪 Hollandite
☑ ⬜ Lithiophorite
☑ 🟦 Quartz
☑ 🟨 Porosity

☑ ⬜ No minerals
☑ 🟥 2+ minerals
☑ ⬛ Unwanted areas

○ Original image
○ Particles and minerals
○ Separation/join
○ Porosity
○ Unidentified areas
○ Minerals correction
● Final identification

FIG 4 – Image analysis of manganese ore fines in Mineral5: (a) original image; and (b) final mineral/porosity map as it appears in Analysis Display window.

Mineral identification in Mineral5 using existing profiles is simple for the operator. At the same time, it is quite comprehensive, allowing advanced approaches such as extra thresholding (similar to that for particles), separation and selection, and textural identification (see also Donskoi and Poliakov, 2020). However, no matter how advanced the identification of an isolated mineral is, misidentifications or double identifications are still possible. Mineral5 partially mitigates the problem by allowing the user to subtract the maps of minerals identified earlier in the process (these minerals are typically lighter and so easier to identify correctly) from subsequent mineral maps. Still, a number of later steps are aimed at automatically rectifying possible errors and misidentifications, which can significantly improve the overall analysis quality.

After all minerals have been identified, the particle map, updated with the mineral maps, is considered ready for further processing. At this stage Mineral5 can apply its ‘Removal of unwanted areas’ routine to automatically get rid of under-surface particle reflections that can often be mistaken for particles. Such pseudo-particles will be excluded from subsequent analysis. It is also possible to manually edit out other undesired objects, such as bulk sample defects. Nearly every stage of image analysis allows some manual editing facilities, so high quality analysis of complex samples can be achieved by the operator if necessary. Of course, the possibility of using manual editing during high-throughput automated analysis is very limited, and this is where the correction algorithms of Mineral5 described further are of help.

Particle separation allows the user to avoid situations where touching particle sections are reported as one particle, which can distort many aspects of characterisation. Along with the well-established ‘watershed separation’, Mineral5 also offers erosion-based separation first introduced in the latest releases of Mineral4 (Poliakov and Donskoi, 2019).

Porosity is one of the most important characteristics of many materials, and Mineral5 pays particular attention to correct identification of porosity by a variety of methods, which include ‘pores associated with background’ (or open porosity) often omitted by other image analysis packages.

As it has already been mentioned, some misidentifications are quite possible after identifying individual minerals. The ‘unidentified areas’ step allows for the user to account for particle areas that are not assigned to any minerals or have been identified as belonging to more than one mineral. Such areas can be identified based on their proximity to known minerals, either spatial or by reflectivity; unidentified porosity can also be identified with this step.

Mineral correction is a particularly important step, especially in the presence of bright highly porous minerals such as hematite, which is one of the major iron ore minerals. In such cases, phases can be challenging to be segmented properly due to the interference, which can report false complex mineralogy during optical analysis (Donskoi *et al*, 2010, 2015b). To rectify this, the iron mineral correction function was introduced. Importantly, compared to Mineral4 which applied this particular set of correction operations to a pre-defined set of iron minerals, Mineral5 extends the concept to any mineral which, in conjunction with flexible naming, allows Mineral correction to be used with any minerals where it is applicable. Figure 5 demonstrates a section of the mineral editing window showing how a particular ‘feature’ (that is, a specific behaviour in conjunction with other minerals) can be assigned to a particular mineral. Such mineral editing, including adding, removing, renaming (note shorter name versions are used for reporting in Recognition5) and defining features, can be performed by the Mineral5 operator at any time without unnecessary recalculations and will then be recorded with the analysis profile for future use.

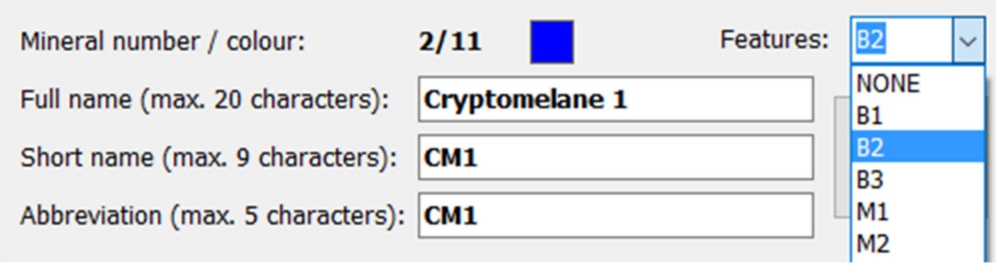

Mineral number / colour: 2/11 🟦

Features: B2

Full name (max. 20 characters): Cryptomelane 1

Short name (max. 9 characters): CM1

Abbreviation (max. 5 characters): CM1

FIG 5 – Fragment of Mineral Definition screen (feature selection shown).

The ‘final correction’ step is used to rectify the mineral map for non-specific issues such as misidentification on borders between minerals and with epoxy. Final manual editing of any image features is also available on this stage. The workflow then proceeds to comprehensive measuring of the resulting particle/mineral maps and output of results. The standard output can be read by Recognition5, which performs subsequent characterisation and reporting as described in the next section. Mineral5 also allows extended, highly adjustable textural measurement of different minerals and phases, including porosity, and the connectivity between phases, which can provide valuable insights into the strength and reactivity of the studied material. Figure 6 shows the Extra Measure screen of Mineral5 with its variety of settings. The results of Extra Measurement, which include extensive data sets such as mineral grain and porosity size distributions, are output in the convenient Excel format. The most important Extra Measure results can be also seen while working with an individual image as shown in Figure 6.

One particular strength of Mineral5 is its ability to segregate different phases not only by their reflectivity, but also their textures (Donskoi and Poliakov, 2020). Based on the existing knowledge of those textures and their association with other minerals in the studied samples Mineral5 allows the operator to build rules to reliably distinguish those phases, which can possibly have the same mineralogy and/or reflectivity but importantly different processing behaviour. Iron ore sinter is a good example of a product where the presence of primary and secondary hematite, as well as different types of silico-ferrite of calcium and aluminium (SFCA), can define its behaviour in terms of strength and reactivity. Figure 7 shows an example of an iron ore sinter sample where Mineral5 has successfully identified two types of hematite and three types of SFCA, along with other challenging phases such as glass and larnite.

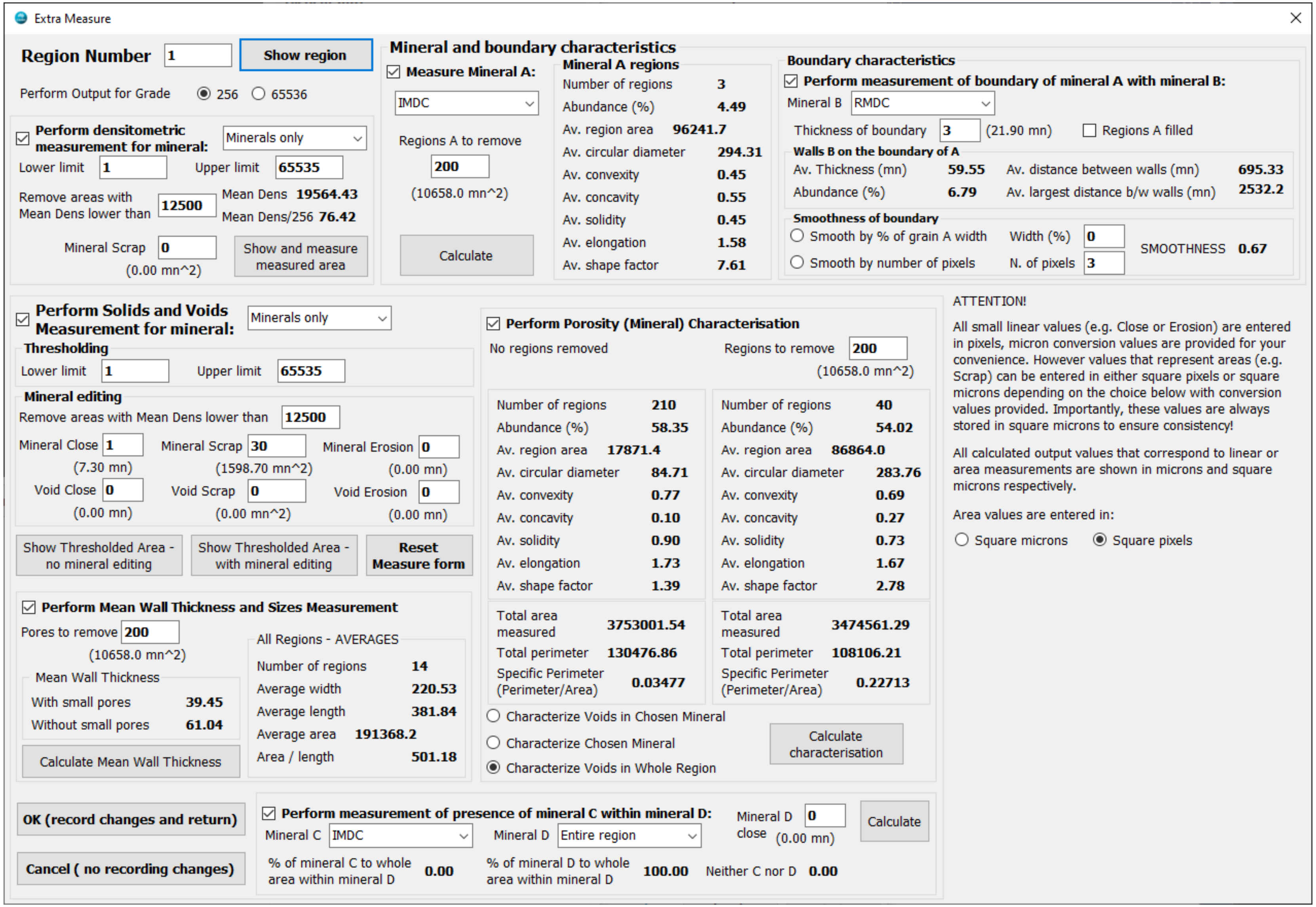
Extra Measure

Region Number 1 **Show region**

Perform Output for Grade ● 256 ○ 65536

☑ **Perform densitometric measurement for mineral:** Minerals only

Lower limit 1 Upper limit 65535

Remove areas with Mean Dens lower than 12500

Mean Dens **19564.43**

Mean Dens/256 **76.42**

Mineral Scrap 0 (0.00 mn^2)

Show and measure measured area

Mineral and boundary characteristics

☑ **Measure Mineral A:** IMDC

Regions A to remove 200 (10658.0 mn^2)

Calculate

Mineral A regions

Number of regions	**3**
Abundance (%)	**4.49**
Av. region area	**96241.7**
Av. circular diameter	**294.31**
Av. convexity	**0.45**
Av. concavity	**0.55**
Av. solidity	**0.45**
Av. elongation	**1.58**
Av. shape factor	**7.61**

Boundary characteristics

☑ **Perform measurement of boundary of mineral A with mineral B:**

Mineral B RMDC

Thickness of boundary 3 (21.90 mn) ☐ Regions A filled

Walls B on the boundary of A

Av. Thickness (mn)	**59.55**	Av. distance between walls (mn)	**695.33**
Abundance (%)	**6.79**	Av. largest distance b/w walls (mn)	**2532.2**

Smoothness of boundary

○ Smooth by % of grain A width Width (%) 0

○ Smooth by number of pixels N. of pixels 3

SMOOTHNESS **0.67**

☑ **Perform Solids and Voids Measurement for mineral:** Minerals only

Thresholding

Lower limit 1 Upper limit 65535

Mineral editing

Remove areas with Mean Dens lower than 12500

Mineral Close 1 (7.30 mn) Mineral Scrap 30 (1598.70 mn^2) Mineral Erosion 0 (0.00 mn)

Void Close 0 (0.00 mn) Void Scrap 0 (0.00 mn^2) Void Erosion 0 (0.00 mn)

Show Thresholded Area - no mineral editing | Show Thresholded Area - with mineral editing | **Reset Measure form**

☑ **Perform Mean Wall Thickness and Sizes Measurement**

Pores to remove 200 (10658.0 mn^2)

Mean Wall Thickness

With small pores	**39.45**
Without small pores	**61.04**

Calculate Mean Wall Thickness

All Regions - AVERAGES

Number of regions	**14**
Average width	**220.53**
Average length	**381.84**
Average area	**191368.2**
Area / length	**501.18**

☑ **Perform Porosity (Mineral) Characterisation**

No regions removed

Regions to remove 200 (10658.0 mn^2)

Number of regions	**210**	Number of regions	**40**
Abundance (%)	**58.35**	Abundance (%)	**54.02**
Av. region area	**17871.4**	Av. region area	**86864.0**
Av. circular diameter	**84.71**	Av. circular diameter	**283.76**
Av. convexity	**0.77**	Av. convexity	**0.69**
Av. concavity	**0.10**	Av. concavity	**0.27**
Av. solidity	**0.90**	Av. solidity	**0.73**
Av. elongation	**1.73**	Av. elongation	**1.67**
Av. shape factor	**1.39**	Av. shape factor	**2.78**
Total area measured	**3753001.54**	Total area measured	**3474561.29**
Total perimeter	**130476.86**	Total perimeter	**108106.21**
Specific Perimeter (Perimeter/Area)	**0.03477**	Specific Perimeter (Perimeter/Area)	**0.22713**

○ Characterize Voids in Chosen Mineral

○ Characterize Chosen Mineral

● Characterize Voids in Whole Region

Calculate characterisation

ATTENTION!

All small linear values (e.g. Close or Erosion) are entered in pixels, micron conversion values are provided for your convenience. However values that represent areas (e.g. Scrap) can be entered in either square pixels or square microns depending on the choice below with conversion values provided. Importantly, these values are always stored in square microns to ensure consistency!

All calculated output values that correspond to linear or area measurements are shown in microns and square microns respectively.

Area values are entered in:

○ Square microns ● Square pixels

OK (record changes and return)

Cancel (no recording changes)

☑ **Perform measurement of presence of mineral C within mineral D:**

Mineral C IMDC Mineral D Entire region

Mineral D close 0 (0.00 mn) Calculate

% of mineral C to whole area within mineral D **0.00**

% of mineral D to whole area within mineral D **100.00**

Neither C nor D **0.00**

FIG 6 – Extra Measure screen of Mineral5.

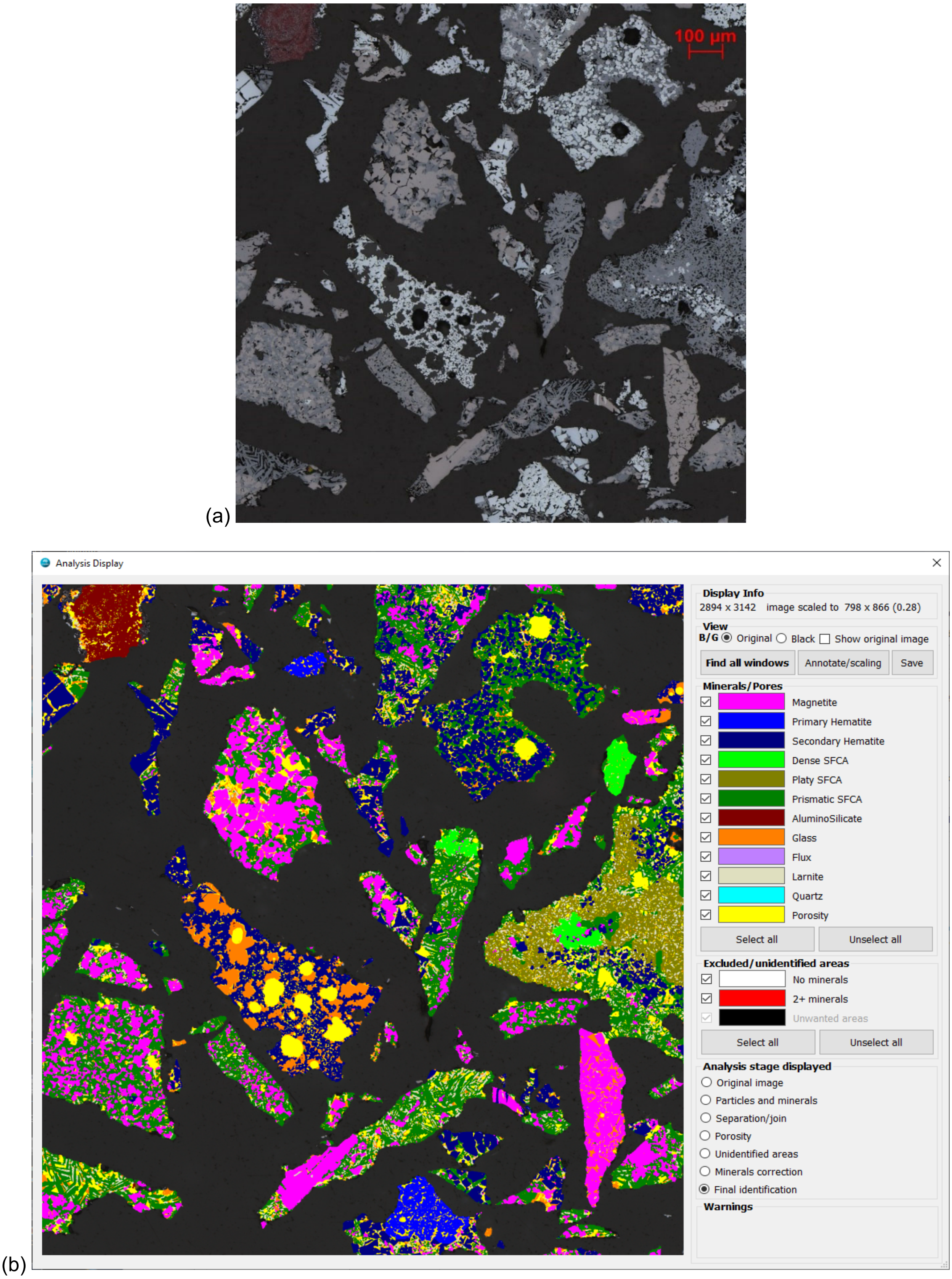

Display Info
2894 x 3142 image scaled to 798 x 866 (0.28)

View
B/G ● Original ○ Black ☐ Show original image

Minerals/Pores
- ☑ 🟪 Magnetite
- ☑ 🟦 Primary Hematite
- ☑ 🟦 Secondary Hematite
- ☑ 🟩 Dense SFCA
- ☑ 🟫 Platy SFCA
- ☑ 🟩 Prismatic SFCA
- ☑ 🟥 AluminoSilicate
- ☑ 🟧 Glass
- ☑ 🟪 Flux
- ☑ ⬜ Larnite
- ☑ 🟦 Quartz
- ☑ 🟨 Porosity

Excluded/unidentified areas
- ☑ ⬜ No minerals
- ☑ 🟥 2+ minerals
- ☑ ⬛ Unwanted areas

Analysis stage displayed
- ○ Original image
- ○ Particles and minerals
- ○ Separation/join
- ○ Porosity
- ○ Unidentified areas
- ○ Minerals correction
- ● Final identification

Warnings

FIG 7 – Image analysis of crushed iron ore sinter in Mineral5: (a) original image; and (b) final mineral/porosity map as it appears in Analysis Display window.

Other analysis modes available in Mineral5 include Frames, used to analyse continuous samples (possibly dividing them into 'virtual' particles), and Pellets, used for macroscopic objects such as iron ore pellets and lump ore particles (Poliakov *et al*, 2017). In Pellets mode, the individually processed high resolution images (often tiled elementary images) can be combined into large Panorama images of the whole object; it also allows the user to visualise spatial phase distributions within the object and, where applicable, calculate radial distributions. Figure 8 provides an example of an iron ore pellet analysed with Mineral5.

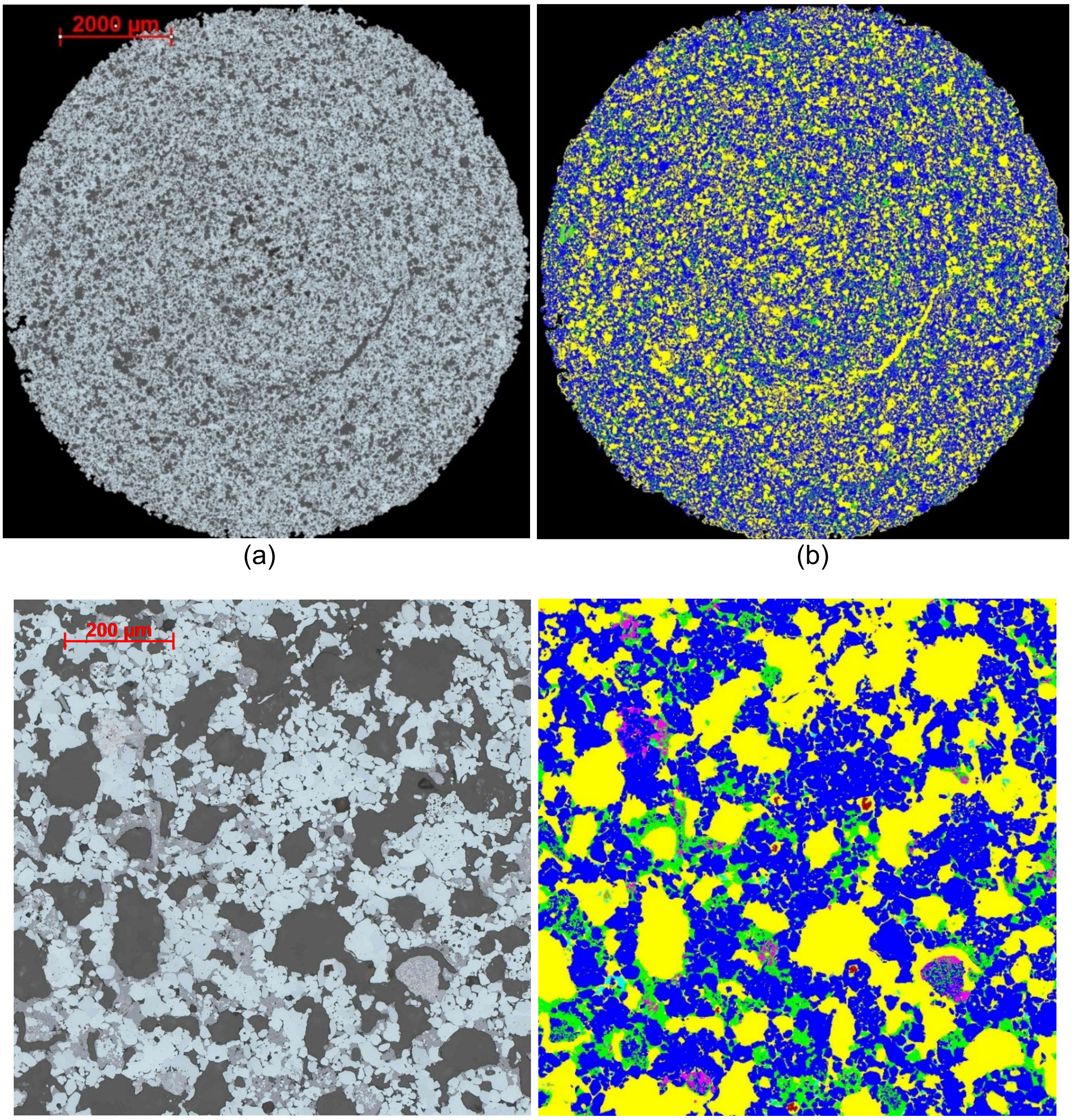

(a) (b)

(c) (d)

FIG 8 – Pellet analysis in Mineral5: (a) Panorama image of a high basicity iron ore pellet; (b) overall minerals/porosity map; (c) an example of an individual processed image; and (d) minerals/porosity map for that image (magenta – magnetite, blue – hematite, green – SFCA, dark brown – flux, cyan – glass, yellow – porosity).

Finally, an important advantage of Mineral5 is its ability to perform unsupervised processing of large sets of images. Importantly, this is not limited to individual sets. It is possible to automatically analyse multiple sets of images within a single session. Related sets (eg taken from multiple polished blocks of the same sample) can be, if necessary, grouped together; in this case Extra Measure reports will not only describe individual blocks, but also provide valuable aggregate statistical data for the whole sample.

Future planned developments for Mineral5 will include automated image collection for Leica and Olympus microscopes, and also further improvement of automated object separation, textural characterisation and mineral correction.

RECOGNITION5

As mentioned in the Introduction, Recognition5 (see Figure 9) reads the database of particle information created by Mineral5. After the database is loaded, Recognition5 automatically classifies all objects in the database according to its current classification scheme (Figure 10). That classification scheme can be edited or changed to a more appropriate one, particularly if the commodity with which the operator works with has changed. Recognition5 provides convenient tools for creation and editing of quite complex classification schemes with up to eight levels of the logical tree. The classification results can be output to Word as tables, which provide information for each textural class on: abundance (particle numbers, area % and weight %), average total iron, density, a particle's area with variability, shape factor and elongation, average mineral composition and porosity (Donskoi, Poliakov and Manuel, 2015a; Donskoi *et al*, 2015b).

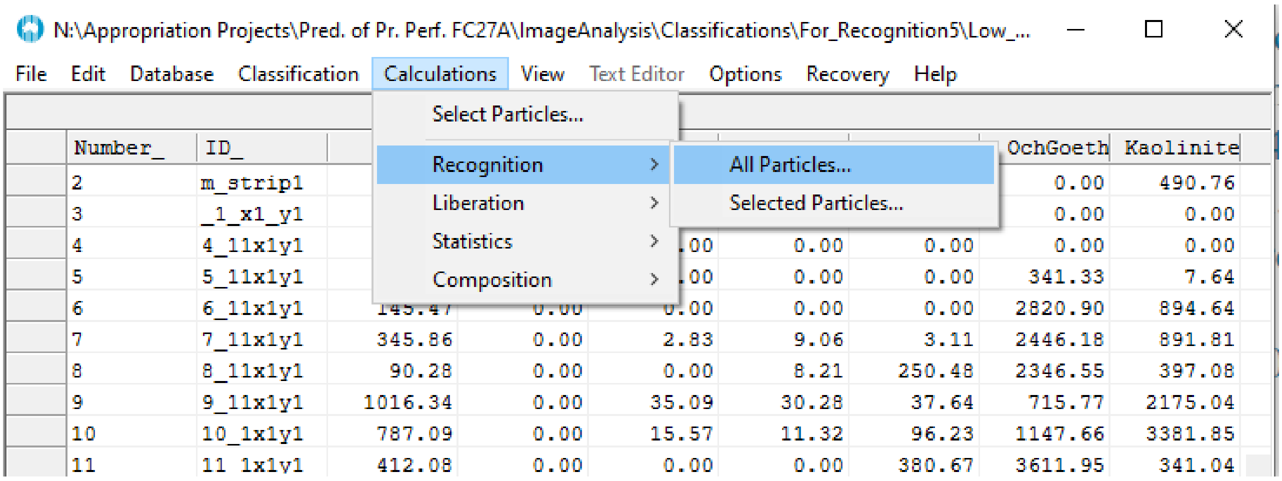

Number_	ID_						OchGoeth	Kaolinite
2	m_strip1						0.00	490.76
3	_1_x1_y1						0.00	0.00
4	4_11x1y1			.00	0.00	0.00	0.00	0.00
5	5_11x1y1			.00	0.00	0.00	341.33	7.64
6	6_11x1y1	145.47	0.00	0.00	0.00	0.00	2820.90	894.64
7	7_11x1y1	345.86	0.00	2.83	9.06	3.11	2446.18	891.81
8	8_11x1y1	90.28	0.00	0.00	8.21	250.48	2346.55	397.08
9	9_11x1y1	1016.34	0.00	35.09	30.28	37.64	715.77	2175.04
10	10_1x1y1	787.09	0.00	15.57	11.32	96.23	1147.66	3381.85
11	11 1x1y1	412.08	0.00	0.00	0.00	380.67	3611.95	341.04

FIG 9 – Recognition5 software: invoking textural classification of all particles in the database.

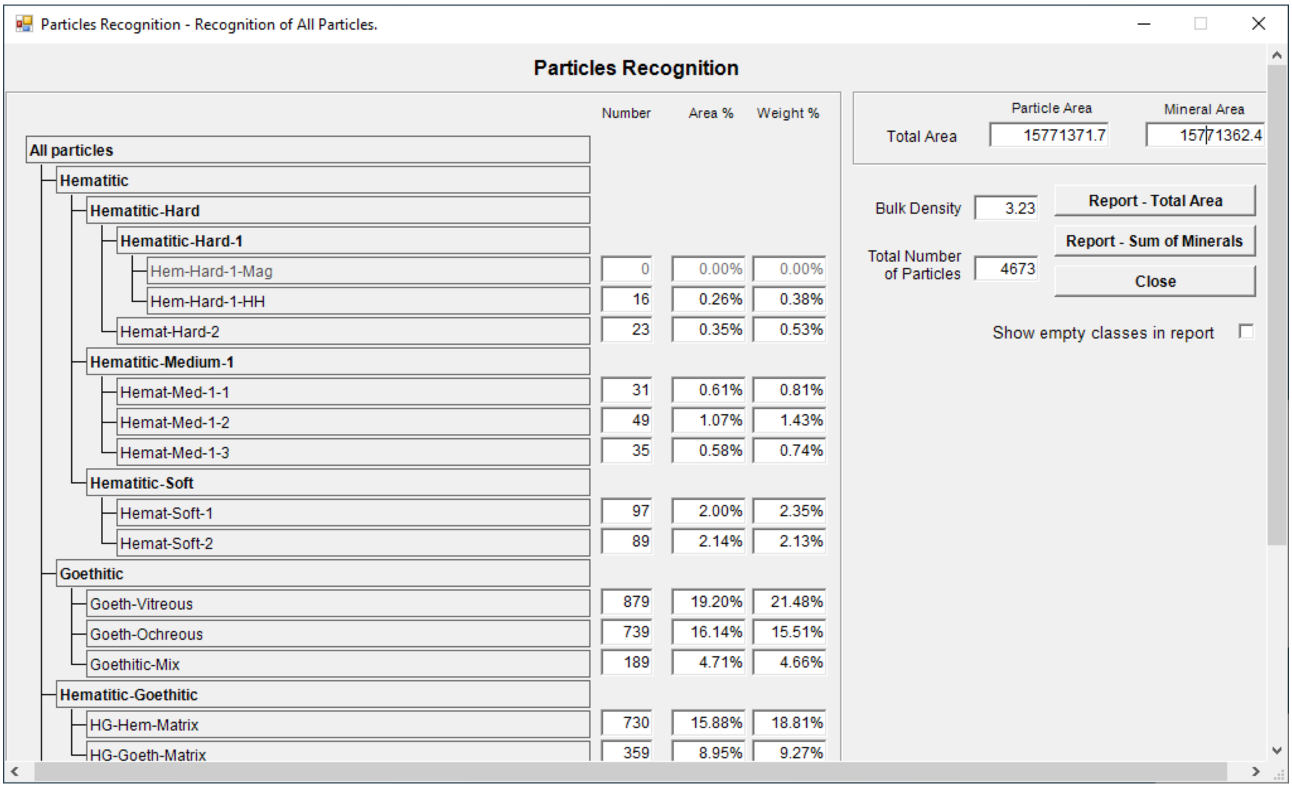

	Number	Area %	Weight %
All particles			
Hematitic			
Hematitic-Hard			
Hematitic-Hard-1			
Hem-Hard-1-Mag	0	0.00%	0.00%
Hem-Hard-1-HH	16	0.26%	0.38%
Hemat-Hard-2	23	0.35%	0.53%
Hematitic-Medium-1			
Hemat-Med-1-1	31	0.61%	0.81%
Hemat-Med-1-2	49	1.07%	1.43%
Hemat-Med-1-3	35	0.58%	0.74%
Hematitic-Soft			
Hemat-Soft-1	97	2.00%	2.35%
Hemat-Soft-2	89	2.14%	2.13%
Goethitic			
Goeth-Vitreous	879	19.20%	21.48%
Goeth-Ochreous	739	16.14%	15.51%
Goethitic-Mix	189	4.71%	4.66%
Hematitic-Goethitic			
HG-Hem-Matrix	730	15.88%	18.81%
HG-Goeth-Matrix	359	8.95%	9.27%

	Particle Area	Mineral Area
Total Area	15771371.7	15771362.4

Bulk Density 3.23

Total Number of Particles 4673

Show empty classes in report ☐

FIG 10 – Example of Recognition5 textural classification for a low-grade iron ore.

Another of Recognition5 capabilities is calculation of chemical composition and density of the whole sample or of a group of selected particles (Figure 11). Calculation of chemical composition is specifically very useful when the concentration of certain element is below XRF detection limit, or when the user requires data for a certain portion of the whole sample, eg characteristics of a particular textural class, mineral composition class or specific density subsample for downstream processing optimisation (Donskoi *et al*, 2006, 2008).

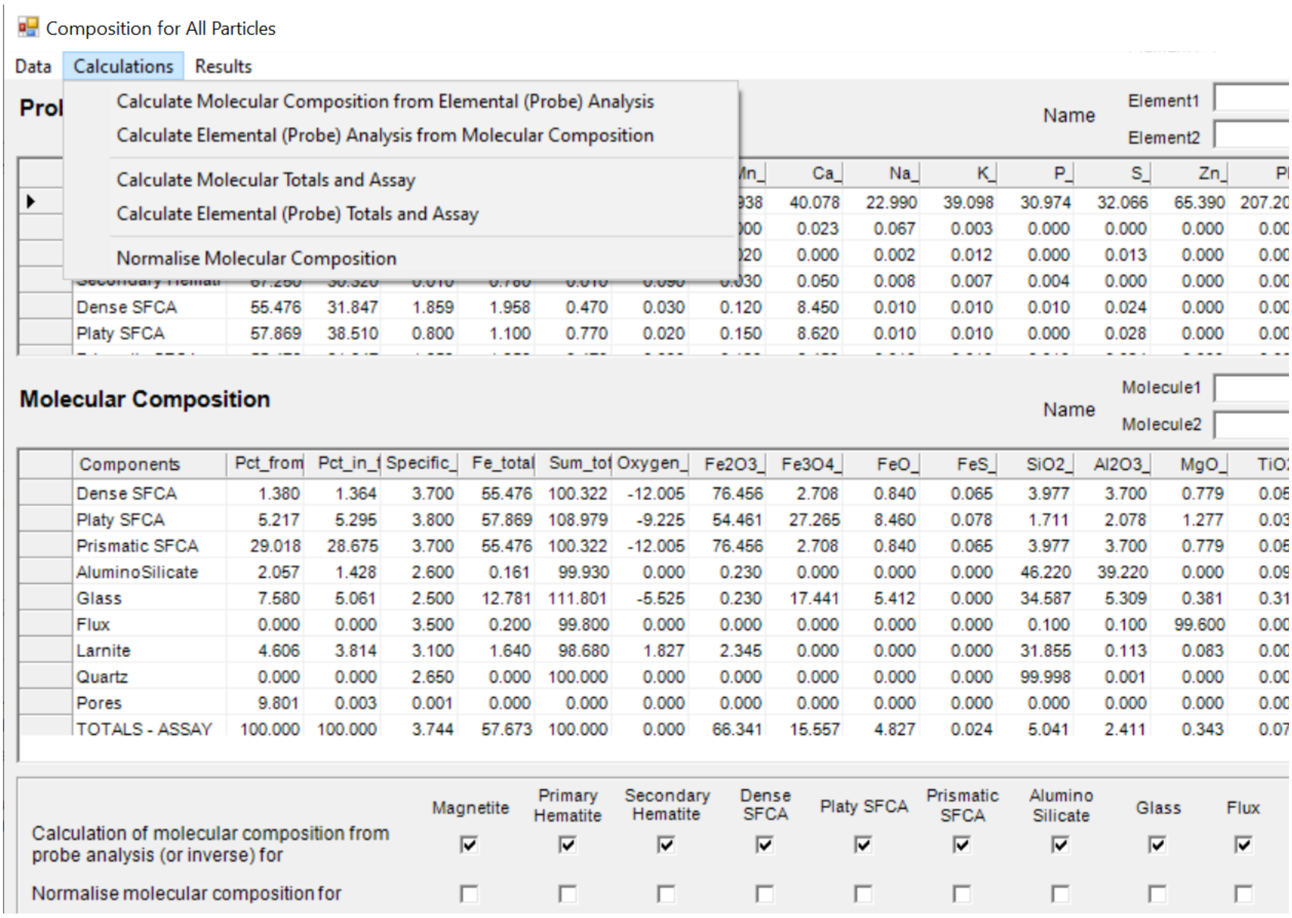

							n_	Ca_	Na_	K_	P_	S_	Zn_	P
							938	40.078	22.990	39.098	30.974	32.066	65.390	207.20
							000	0.023	0.067	0.003	0.000	0.000	0.000	0.00
							020	0.000	0.002	0.012	0.000	0.013	0.000	0.00
							030	0.050	0.008	0.007	0.004	0.000	0.000	0.00
Dense SFCA	55.476	31.847	1.859	1.958	0.470	0.030	0.120	8.450	0.010	0.010	0.010	0.024	0.000	0.00
Platy SFCA	57.869	38.510	0.800	1.100	0.770	0.020	0.150	8.620	0.010	0.010	0.000	0.028	0.000	0.00

Molecular Composition

Components	Pct_from	Pct_in_t	Specific_	Fe_total	Sum_tot	Oxygen_	Fe2O3_	Fe3O4_	FeO_	FeS_	SiO2_	Al2O3_	MgO_	TiO
Dense SFCA	1.380	1.364	3.700	55.476	100.322	-12.005	76.456	2.708	0.840	0.065	3.977	3.700	0.779	0.05
Platy SFCA	5.217	5.295	3.800	57.869	108.979	-9.225	54.461	27.265	8.460	0.078	1.711	2.078	1.277	0.03
Prismatic SFCA	29.018	28.675	3.700	55.476	100.322	-12.005	76.456	2.708	0.840	0.065	3.977	3.700	0.779	0.05
AluminoSilicate	2.057	1.428	2.600	0.161	99.930	0.000	0.230	0.000	0.000	0.000	46.220	39.220	0.000	0.09
Glass	7.580	5.061	2.500	12.781	111.801	-5.525	0.230	17.441	5.412	0.000	34.587	5.309	0.381	0.31
Flux	0.000	0.000	3.500	0.200	99.800	0.000	0.000	0.000	0.000	0.000	0.100	0.100	99.600	0.00
Larnite	4.606	3.814	3.100	1.640	98.680	1.827	2.345	0.000	0.000	0.000	31.855	0.113	0.083	0.00
Quartz	0.000	0.000	2.650	0.000	100.000	0.000	0.000	0.000	0.000	0.000	99.998	0.001	0.000	0.00
Pores	9.801	0.003	0.001	0.000	0.000	0.000	0.000	0.000	0.000	0.000	0.000	0.000	0.000	0.00
TOTALS - ASSAY	100.000	100.000	3.744	57.673	100.000	0.000	66.341	15.557	4.827	0.024	5.041	2.411	0.343	0.07

	Magnetite	Primary Hematite	Secondary Hematite	Dense SFCA	Platy SFCA	Prismatic SFCA	Alumino Silicate	Glass	Flux
Calculation of molecular composition from probe analysis (or inverse) for	☑	☑	☑	☑	☑	☑	☑	☑	☑
Normalise molecular composition for	☐	☐	☐	☐	☐	☐	☐	☐	☐

FIG 11 – Partial view of Recognition5 chemical composition module (calculations correspond to Figure 7)

The information is calculated based on mineral abundances measured by Mineral5, and the average chemical composition and density of each mineral obtained from EPMA or another chemical analysis. When a particle database is loaded by Recognition5, the software seeks the chemical composition information from a separate database, which contains data for the major minerals occurring in iron and manganese ores and iron sinter. Recognition4 did not have such a database, so it was necessary to modify mineral chemical composition data within Recognition4 itself; this capability is also available in Recognition5. The chemical composition database can be extended or changed depending on ore/commodity, so if the operator works with new commodities/ores the mineral compositions and densities of necessary minerals can be added to this database.

All types of calculations/analysis in R5 can be performed for the whole set of particles, or for a certain subsection of it, selected from the whole sample based on a set of criteria determined by the operator. Criteria can include the area-based data transferred directly from Mineral5 or specific information calculated within Recognition5 itself. In particular, the ‘Selection’ form provides mineral abundances by area or by weight for each particle, percentages of different chemical components including loss on ignition (LOI), densities and different textural characteristics. The dimensional characteristics of particles measured in Mineral5 also can be used as criteria for selection. The same functionality is used for building classification schemes.

Following the changes in Mineral5, the entire Recognition5 functionality has been extended to accommodate the increased number of minerals. Mineral Liberation (ML) analysis is one of the major calculations in Recognition5. ML analysis can be performed for any subset of minerals, calculating classes with a different abundance of a subset of minerals (possibly consisting of just one mineral) within those classes. Figure 12 shows the analysis for liberation of primary/secondary hematite and magnetite (forming one phase) from all other phases for the sinter image in Figure 7. Together with liberation for all particles, liberation for selected particles with primary/secondary hematite + magnetite >55 per cent by weight was calculated for this demonstration. It is evident that for classes with the presence of the chosen phases >55 per cent the distributions (if normalised for those classes only) are the same. Apart from the choice of the subset of minerals of interest, the operator can choose to report between 11 or 12 liberation classes. There also are options for liberation calculation (eg total weight of particles versus sum of selected minerals, calculated by Weight/Area versus Number of particles, classified by area versus weight), for cumulative or density distribution, and for graph representation (see Figure 12). The Word output table includes calculated averages for each class by area %, weight %, grade of chosen phases, iron grade and density. It also presents the distribution by total Fe, recovery of chosen phases, cumulative recovery, cumulative yield and the number of particles in each class.

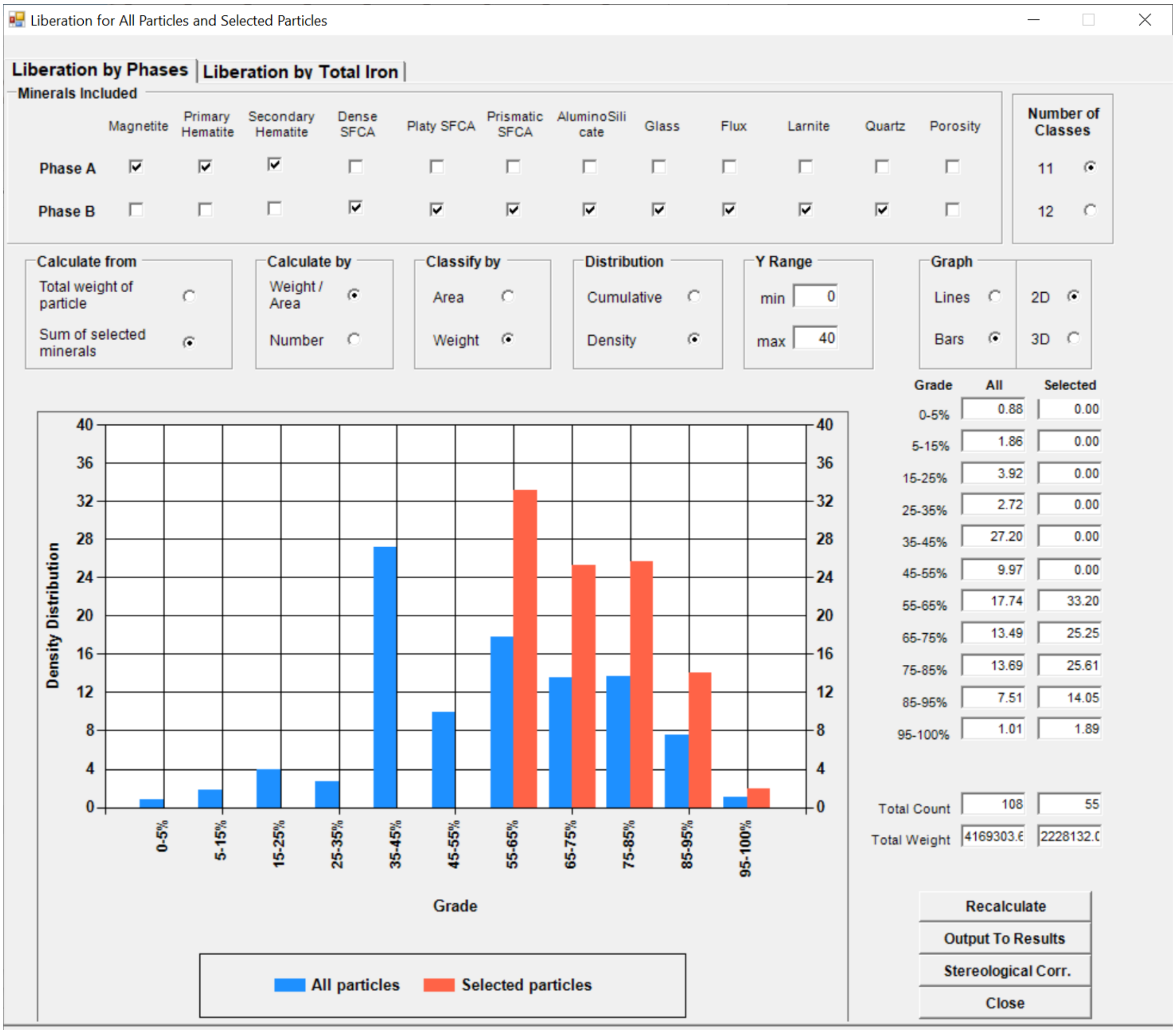

Minerals Included

	Magnetite	Primary Hematite	Secondary Hematite	Dense SFCA	Platy SFCA	Prismatic SFCA	AluminoSilicate	Glass	Flux	Larnite	Quartz	Porosity
Phase A	☑	☑	☑	☐	☐	☐	☐	☐	☐	☐	☐	☐
Phase B	☐	☐	☐	☑	☑	☑	☑	☑	☑	☑	☑	☐

Number of Classes
11 ●
12 ○

Calculate from
Total weight of particle ○
Sum of selected minerals ●

Calculate by
Weight / Area ●
Number ○

Classify by
Area ○
Weight ●

Distribution
Cumulative ○
Density ●

Y Range
min 0
max 40

Graph
Lines ○
Bars ●
2D ●
3D ○

Grade	All	Selected
0-5%	0.88	0.00
5-15%	1.86	0.00
15-25%	3.92	0.00
25-35%	2.72	0.00
35-45%	27.20	0.00
45-55%	9.97	0.00
55-65%	17.74	33.20
65-75%	13.49	25.25
75-85%	13.69	25.61
85-95%	7.51	14.05
95-100%	1.01	1.89
Total Count	108	55
Total Weight	4169303.	2228132.

FIG 12 – Liberation analysis form in Recognition5 corresponding to image (sinter image)

In the 'Liberation by Total Iron' part of the liberation analysis (the other tab in Figure 12), Recognition5 also can calculate classes with different presence of iron in particles. Reporting and adjustments are similar to the mineral liberation part of the liberation module.

Recognition5 also performs comprehensive statistical analysis (Donskoi, Poliakov and Manuel, 2015a). It can perform calculations for all or selected particles, including for any textural class or several textural classes combined together. The results of such calculations can be output to Word or Excel; the output covers a broad range of statistical data grouped in several sections and tables, and so will be described further in more detail. Each of the sections is optional and the reports can be generated for individual textural classes, or for a selection of classes, or for the entire particle database.

The first statistical analysis table, Particle Dimensions, gives the major statistical figures such as mean, variance, standard deviation, coefficient of variation, coefficient of dispersion, the five-number summary (the smallest observation, the first quartile, median, the third quartile and the highest observation) and the number of particles/cases for the following parameters: particle area, equivalent circle radius, maximum length, maximum breadth, shape factor and elongation.

The next output table is Modal Analysis. For each mineral in the sample, it gives the number of occurrences in particles, total area of the mineral, volume abundance, abundance on particle surfaces, density (transferred from the Composition module) and weight abundance (based on density). Also, in this section, the Specific Gravity, Total Iron and Mineral Presence Variability table gives the occurrence and all statistical data described earlier in the Particle Dimensions table for each mineral and porosity, and also for density and total iron. Also located here, the Molecular Composition table gives the details for each mineral and the assay of the sample/selected group of particles.

The next section consists of three different tables of Mineral Association Analysis. The first table provides for each mineral and porosity the percentages of its association with other minerals/porosity (porosity here is considered as one of the association phases). The second table recalculates mineral associations without porosity. The third table gives association figures for each mineral subdivided into fully liberated particles, binary and ternary associations, and complex associations where the mineral is associated with more than two other minerals.

The last set of tables is liberation analysis for each mineral. The output is similar to that of the Mineral Liberation Analysis discussed above, but the calculations are performed for each mineral separately, without grouping them into phases.

A wholly new part of the Statistics module in Recognition5 is the calculation of the Pair Distribution Function. It calculates the probability of finding two particles/grains within a certain distance from each other in the material under investigation. It is very useful for studies of regular structures when distancing between similar features is investigated. For example, when attempting to quantify average distance between pores within a particle.

Further developments in Recognition5 will include: the option to utilise EPMA data for certain minerals, or their molecular composition, or both for calculation of chemical composition; improvement of classification scheme development, and improved output of calculated information to Word and Excel. Independence from any proprietary software platform should allow in the future to combine both Mineral5 and Recognition5 components of the software into one program for more streamlined analysis and reporting.

CONCLUSIONS

During the redevelopment required to transfer the Mineral4/Recognition4 OIA software package to the new Mineral5/Recognition5 software, a number of significant improvements and changes were made. Mineral5/Recognition5 is now independent of a particular microscope platform and is based on openCV open access software and.NET technology. This provides the opportunity for its utilisation by companies/operators without the need to invest in Zeiss hardware and software. The new package supports all major image formats. The newly added features allow Mineral5/Recognition5 to be used with a wide range of commodities, such as different ores, sinters and coke, and with different size fractions, starting from 5–10 µm up to lump ore particles and pellets. Images of macroscopic objects (eg sinter cake) also can be processed.

The software has a sophisticated textural identification capability which, together with multiple thresholding, allows for better identification of minerals and identification of different morphologies of the same mineral, eg primary and secondary hematite, or different morphologies of SFCA in sinter. The increased number of identifiable phases compared to Mineral4/Recognition4, enables better characterisation of an ore/commodity, for example, by allowing the user to segment more gangue materials, which is a very important function for complex and low-grade ores. Its ability to display different analysis stages, to adapt processing to the properties of studied objects (size, magnification, texture etc), the ease of reuse of previously developed analysis algorithms (profiles), convenient graphical user interface, the options for image improvement and removal of under-surface reflections, comprehensive processing routines, the possibility for unsupervised processing and convenient data output make Mineral5 a versatile and reliable tool for image analysis of different commodities.

Other features include: a capability to easily develop new classification schemes (or use a pre-existing classification), automatic classification of the imaged objects, extensive liberation and association analysis, and calculation of sample (or any subsample) chemical composition and density. The enhanced functionality facilitates efficient prediction of downstream processing performance, resource evaluation, development of waste-management strategies and other tasks demanded by iron ore and other minerals industries. This demonstrates that the new M5/R5 OIA package is an exemplary tool for characterisation of ores/sinters and other commodities.

ACKNOWLEDGEMENTS

The authors wish to thank CSIRO Carbon Steel Materials group staff for valuable suggestions and help during this work. We would like to acknowledge Mike Peterson for valuable suggestions and correction of this article. We would also like to express our gratitude to the internal and external reviewers for useful corrections and comments.

REFERENCES

Clout, J M F, 1998. The effects of ore petrology on downstream processing performance: A review, in *Proceedings Mine to Mill 1998 Conference*, pp 43–50 (The Australasian Institute of Mining and Metallurgy: Melbourne).

Donskoi, E, Holmes, R J, Manuel, J R, Campbell, J J, Poliakov, A, Suthers, S P and Raynlyn, T, 2008. Utilization of Iron Ore Texture Information for Prediction of Downstream Process Performance, in *Proceedings 9th International Congress for Applied Mineralogy (ICAM)*, pp 687–693 (The Australasian Institute of Mining and Metallurgy: Melbourne).

Donskoi, E, Suthers, S P, Campbell, J J, Raynlyn, T and Clout, J M F, 2006. Prediction of hydrocyclone performance in iron ore beneficiation using texture classification, in *Proceedings XXIII International Mineral Processing Congress*, pp 1897–1902.

Donskoi, E and Poliakov, A, 2020. Advances in Optical Image Analysis Textural Segmentation in Ironmaking, *Applied Sciences*, 10(18), Article 6242.

Donskoi, E, Poliakov, A and Manuel, J R, 2015a. Automated Optical Image Analysis of Natural and Sintered Iron Ore, in *Iron Ore: Mineralogy, Processing and Environmental Sustainability* (ed: L Lu), pp 101–159 (Elsevier Inc: Cambridge).

Donskoi, E, Poliakov, A, Manuel, J, Peterson, M and Hapugoda, S, 2015b. Novel developments in optical image analysis for iron ore, sinter and coke characterisation, *Transactions of the Institutions of Mining and Metallurgy, Mining Technology, Applied Earth Science,* 124(4):227–244.

Donskoi, E, Poliakov, A, Manuel, J R and Raynlyn, T, 2010. Advances in optical image analysis and textural classification of iron ore fines. In *Proceedings 25th International Mineral Processing Congress*, pp 2823–2836 (The Australasian Institute of Mining and Metallurgy: Melbourne).

Iglesias, J C Á, Santos, R B M and Paciornik, S, 2019. Deep learning discrimination of quartz and resin in optical microscopy images of minerals, *Minerals Engineering*, 2019, p 138, pp 79–85.

Poliakov, A and Donskoi, E, 2014. Automated relief-based discrimination of non-opaque minerals in optical image analysis, *Minerals Engineering*, 55:111–124.

Poliakov, A and Donskoi, E, 2019. Separation of touching particles in optical image analysis of iron ores and its effect on textural and liberation characterization, *European Journal of Mineralogy*, 31(3):485–505.

Poliakov, A, Donskoi, E, Hapugoda, S and Lu, L, 2017. Optical image analysis of iron ore pellets and lumps using CSIRO software Mineral4/Recognition4, in *Proceedings Iron Ore 2017*, pp 583–591 (The Australasian Institute of Mining and Metallurgy: Melbourne).

Liberation characteristics of comminuted ore types of the Per Geijer iron-oxide apatite deposits

P Krolop[1,2]*, K Niiranen*[3]*, S Gilbricht*[4] *and T Seifert*[5]

1. Research Scientist, TU Bergakademie Freiberg, D-09599 Freiberg, Germany. Email: patrick.krolop@mineral.tu-freiberg.de
2. Research Engineer, LKAB, SE-981 86 Kiruna, Sweden. Email: patrick.krolop@lkab.com
3. Advanced Specialist in Process Mineralogy, LKAB, SE-981 86 Kiruna, Sweden. Email: kari.niiranen@lkab.com
4. Technician, TU Bergakademie Freiberg, D-09599 Freiberg, Germany. Email: sabine.gilbricht@mineral.tu-freiberg.de
5. Professor, TU Bergakademie Freiberg, D-09599 Freiberg, Germany. Email: thomas.seifert@mineral.tu-freiberg.de

ABSTRACT

The Per Geijer iron oxide apatite deposits (IOA) display significant potential mineral resources for Luossavaara-Kiirunavaara AB (publ), known as LKAB. LKAB continuously mines magnetite/hematite ores in northern Sweden for almost 130 years. The Per Geijer deposits reveal a high phosphorus content and vary from magnetite-dominated to hematite-dominated ores, respectively. Furthermore, they show a large variation in texture, mineral composition, and relation to wall rocks. The high phosphorus concentration of these ores results from highly elevated content of apatite as gangue mineral. Reliable, robust, and qualitative characterisation of the mineralisation is required as these ores inherit complex mineralogical and textural features. For this purpose, comminution tests at laboratory scale in combination with scanning electron microscopy-mineral liberation analysis (SEM-MLA) were carried out. Based on this work, significant information on the modal mineralogy and degree of liberation of minerals of economic interest (eg magnetite, hematite, and apatite) were obtained. Results show that there is a difference in the degree of liberation of magnetite and hematite between ore types. This seems to be dependent both on the size fractions and the dominance of each iron oxide in the individual ore type. The amount of gangue minerals seems to have no significant impact on the degree of liberation after comminution. Apatite is generally best liberated in ore types associated with silicates, regardless of magnetite or hematite dominance. Based on the results of this study it can be inferred that a high degree of liberation of the minerals of economic interest can be achieved. However, results need to be verified with further beneficiation steps such magnetic separation, apatite flotation and possibly reverse silicate flotation.

INTRODUCTION

The Per Geijer iron ore deposits in the Kiruna district display important exploration targets for the Swedish mining company Luossavaara-Kiirunavaara Aktiebolag (publ), known as LKAB. LKAB continuously exploits iron ore in several locations in northern Sweden for almost 130 years. Nevertheless, decreasing resources of their main operations require the reassessment of the Per Geijer deposits. Although the Per Geijer deposits constitute the same type of iron-oxide apatite (IOA) mineralisation significant amounts of hematite and apatite in mineralogically, and texturally complex ore distinguish them from the nearby and well-known Kiirunavaara deposit. In 2018, a scoping study was started as an internal project at LKAB to reassess the Per Geijer deposits for future exploitation. One of the main targets of this study was the detailed process mineralogical characterisation of the deposits. This part of the project in question combines geological, mineralogical, geochemical and process mineralogical investigations from five orebodies, consolidated as the so-called Per Geijer deposits. An important part in the characterisation of the deposits is the process mineralogical framework based on in situ ore description and several beneficiation stages in the laboratory scale such as comminution of ore types and wet low intensity magnetic separation. Comminution test works were carried out to obtain preliminary information about their amenability for mineral processing. However, there is a considerable challenge based especially on the mineralogical variations of ores in the deposits. As reported by Lamberg *et al* (2013), Wright *et al* (2013), Tøgersen *et al* (2018) and França *et al* (2020) those variations may be the cause of varying process performance. LKAB like many other mining companies faces increasing challenges with variations in ore quality and more complex mineralogy resulting in internal projects that have been successfully developed in recent years (Lund, 2013; Aupers, 2014; Niiranen, 2015; Töyrä *et al,* 2017; Niiranen, Töyrä and Krolop, 2018; Niiranen and Töyrä, 2019; Niiranen and Rutanen, 2019). The importance of comminution test works originates from the high level of energy consumed in the processing chain. To achieve a desirable iron grade in the concentrate with low content of impurities the ore must commonly be fine-grinded (McNab *et al,* 2009; Norgate and Haque, 2010; Reichert *et al,* 2015).

A crucial part of the characterisation of an ore for mineral processing has always been mineral liberation analysis (eg Lamberg, 2010; Liipo *et al,* 2012; Niiranen, 2015). For this purpose, a series of analytical methods can be used to study the degree of liberation and the intergrowth of valuable minerals and gangue. For this study, the process mineralogical approach was a liberation analysis with a focus on modal mineralogy and mineral associations in the pre-defined ore types of the Per Geijer iron ore deposits in combination with particle size distribution (fractions) after comminution test works. These can be regarded as important characteristics in a process mineralogical point of view based on their relation to the degree of liberation and behaviour of different ore types in the beneficiation process. In the present study, liberation characteristics of economically important mineral such as magnetite, hematite, and apatite of 13 pre-defined ore types of the Per Geijer iron-oxide apatite deposits are presented. The degree of the liberation of those minerals was examined by Scanning Electron Microscopy-based Mineral Liberation Analysis (SEM-MLA).

The Per Geijer deposits

The Per Geijer deposits are located adjacent to the East and NE of the well-known Kiirunavaara and Luossavaaara deposits. Five orebodies are comprised as the so-called Per Geijer deposits and constitute iron-oxide apatite mineralisation. The Per Geijer deposits were first identified in the late 1800s and mined in four separate orebodies, eg Nukutus, Henry, Rektorn and Haukivaara. They were exploited mainly during the 1960s, 1970s and 1980s. Geophysics and exploration drilling inferred a fifth buried orebody named Lappmalmen. Basic knowledge of the Per Geijer deposits was established by Geijer (1910, 1931, 1950) and could be intensified during the main operation periods of the Per Geijer deposits. These orebodies are more complex than those currently mined by LKAB. The complexity is induced by large variations in texture and mineralogy (Martinsson, 2015). Most of the IOA deposits in northern Sweden display almost pure magnetite ores with minor impurities in the form of gangue minerals like apatite, quartz, calcite, actinolite and pyrite (Aupers, 2014; Niiranen 2015). The Per Geijer deposits differ mainly in their relatively high phosphorus content (three to five per cent P) and iron contents (40 and 60 per cent Fe) with varying proportions of magnetite and hematite. These variation in mineral ratios of iron oxides resulted in the subdivision into hematite-dominated, magnetite-dominated, magnetite/hematite-mixed and low-grade ore types for the Per Geijer deposits (Krolop *et al,* 2019a). Magnetite and hematite are the two main ore minerals of economic relevance although minor abundances of sulfides occur in the ore. The final close-down of production in 1987 arose primarily because of the high content of apatite as gangue minerals (Geijer, 1950; Martinsson, 2015; Krolop *et al,* 2019a), responsible for the high phosphorus grade of these ores. Other main gangue minerals are carbonates and quartz. They can be found as rounded to irregular aggregates in some parts of the ore. Veins ranging from mm to m of almost pure apatite or rich in carbonate and quartz intersect the ore.

METHODS

Sampling for comminution test works

Sampling for comminution tests works was conducted on rejects that was excess material after chemical assays of exploration drill cores of the Per Geijer deposits. The sample intervals range between several metres of each ore type based on the frequency in the core. In addition, a second batch of each ore type was sampled if enough material was available leading to a total number of 69 samples. Two to three rejects were selected for each ore type representing a drill core interval of two to four metres. These were combined and homogenised to a sample. Samples were split into three subsamples of 2 kg at LKAB's laboratory for physical testing used for comminution test work.

Comminution circuit

Comminution tests were carried out using a laboratory mill with steel rods and balls as grinding media at LKAB's laboratory for mineral processing in Kiruna. All selected samples were first grinded for ten min in the rod mill (A). After drying and homogenisation two samples of each ore type were grinded in the ball mill for 25 min (B) or 35 min (C), respectively (Figure 1). In addition, screen analyses with material of each ore type were carried out after grinding stages A, B and C. For the grinding tests all material (69 samples) was weighted to match exactly 2 kg ± 100 g. In the primary grinding step, the rods were counted and measured to match the criteria of LKAB's Malmberget method. For comminution, steel rods with two kg feed material and one litre water were placed into the mill. After ten min of primary grinding all material was collected in a bucket placed beneath the mill. After 24 hours all the material was settled to the bottom of the bucket and most of the water were removed. The material was filtered with a filter press and dried in the oven at 104°C for at least 12 hours. In the last step the material was sieved and homogenised. The same procedure accounts for secondary grinding with steel balls. Running time of the mills of 25 and 35 minutes, respectively were applied for 23 samples each. The feed used for secondary grinding had undergone primary grinding in advance. According to the Malmberget method, steel balls as grinding media was used for each secondary grinding circuit. The grinding media was weighted each day before the grinding process. Particle size classes analysis after grinding was performed at LKAB's laboratory for physical testing and chemical analysis (XRF) of each particle size class was carried out at LKAB's chemical laboratory.

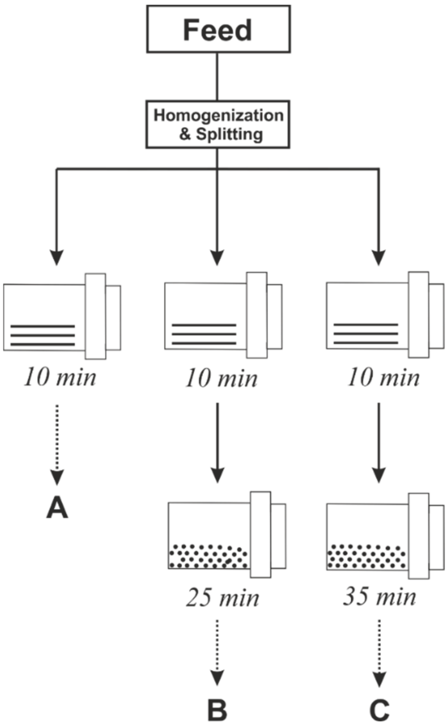

FIG 1 – Flow sheet of performed comminution test works at LKAB's laboratory for mineral processing in Kiruna (modified after Drugge, 2009).

MLA measurement and data processing

For Mineral Liberation analysis 52 grain mount samples were prepared by the sample preparation laboratory of the Helmholtz Institute Freiberg for Resource Technology. Prior to grain mount preparation samples had to be manually deagglomerated. The particle size classes of <63 µm, <45 µm, <38 µm and <20 µm were selected for analysis representing each ore type. All samples were studied with the Scanning Electron Microscope (SEM) including a mineral liberation analyses (MLA) software on a Quanta 650 FEG-MLA650F (FEI©). The analyses were carried out both at the Geometallurgy Laboratory of the Division of Economic Geology and Petrology at TU Bergakademie Freiberg and the Helmholtz Institute Freiberg for Resource Technology. Energy-dispersive X-ray spectroscopy (EDS) was performed with two Nano Dual X-Flash 5030 detectors (Bruker©). An accelerating voltage of 25 kV and a working distance of 12 mm was used. Mineral Liberation Analysis

(MLA) with GXMAP-mode was performed for each grain mount sample. The false-coloured mineral maps (GXMaps) were created with a defined net of EDS-spectra per mm^2 of minerals with specific grey values. For image and data processing collected X-ray spectra were classified. Therefore, the spectrum matching threshold were set to 80 per cent. However, the X-ray spectra and the backscattered electron (BSE) grey levels of the different iron oxides, eg hematite and magnetite are very similar. The effect that similar average atomic numbers results in similar BSE intensities (BSE grey values) requires modification in the data processing stage. Consequently, the results from MLA were checked against the results from optical microscopy and manual correction was applied. BSE ranges of magnetite and hematite and spectrum windows for Ti-rich hematite and apatite were defined. Based on the heterogeneity of the samples with regards to sample surfaces, beam current fluctuations and variation in mineralogy, processing was manually refined by further steps. Further, the touch-up tool was used to remove small unknowns and other noise from the image. Several BSE overlay and touch-up functions had to be applied. Furthermore, automatic deagglomeration was used, since not all agglomerates were destroyed during sample preparation. Finally, databases were created comprising information about the modal mineralogy, particle properties and the degree of liberation of minerals, especially magnetite and hematite. By manually re-defining wrong classified areas the validity for the samples was improved.

RESULTS

The following results are based on the ore type characterisation scheme introduced by Krolop *et al* (2019a). Geological logs and sampling intervals for geochemistry of exploration drill cores were merged to pre-define ore types based on the iron grade, the magnetite/hematite ratio (<0.4, 0.4–4, >4), the phosphorous and silica contents (Figure 2).

			P low		P high	
			SiO_2 low	SiO_2 high	SiO_2 low	SiO_2 high
Fe > 50%	Mag/Hem > 4	Magnetite-dominated	M1a	M1b	M2a	M2b
	Mag/Hem 0.25 - 4	Magnetite-Hematite mix		HM1b	HM2a	HM2b
	Mag/Hem < 0.25	Hematite-dominated	H1a	H1b	H2a	H2b
Fe < 50%				P1		P2

FIG 2 – Scheme for ore type classification based on geological and bulk geochemical data of drill core from the Per Geijer iron-oxide apatite deposits (Krolop *et al,* 2019a).

Modal mineralogy of magnetite-dominated ore types

In the magnetite-dominated ore types magnetite comprises generally above 60 wt per cent of the modal mineralogy, except for the ore type M2b in the particle size class finer than 20 µm (Figure 3). In the low SiO_2 ore types M1a and M2a the content of magnetite is above 80 wt per cent. The content of hematite is commonly below 8 wt per cent. It can be noted that for the ore types M1b (particle size class <45 µm) and M2b (particle size class <20 µm), the hematite content increases up to 28 wt per cent for the former. The finest fractions of the SiO_2-rich ore types M1b and M2b commonly have the highest SiO_2 contents being above 30 wt per cent. The content of apatite is up to 10 wt per cent in the finest fraction of ore type M2a. In the P-poor ore type M1b apatite is enriched up to 4 wt per cent in the particle size class finer than 45 µm. Noteworthy, the content of carbonates in the SiO_2-rich ore types increase from coarser to finer fractions. They constitute up to 10 wt per cent of the modal mineralogy in the particle size class finer than 20 µm of ore type M2b.

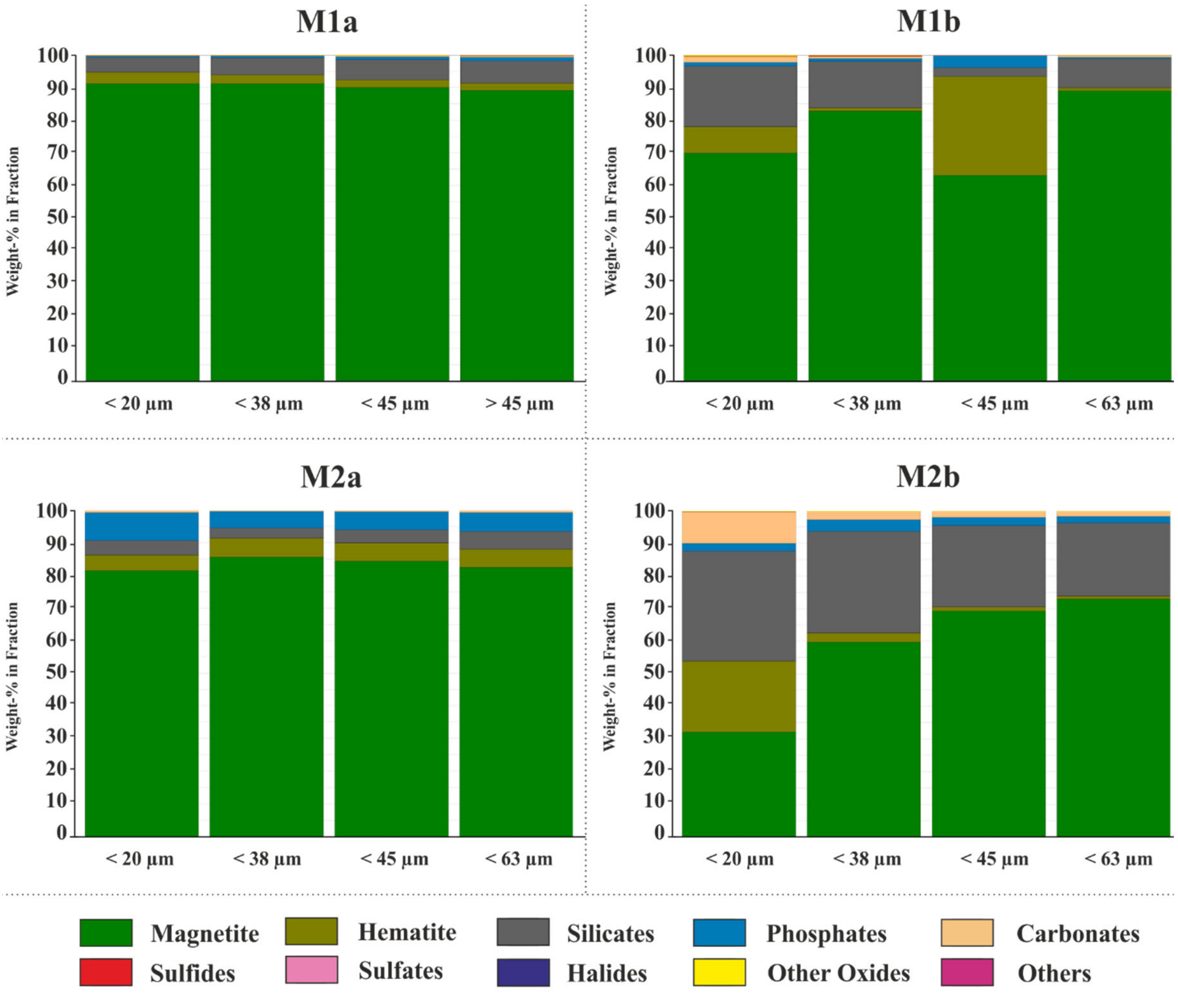

FIG 3 – Modal mineralogy of magnetite-dominated ore types of the Per Geijer iron ore deposits. Except for magnetite, minerals have been consolidated to mineral groups.

Modal mineralogy of hematite-dominated ore types

In the hematite-dominated ore types hematite comprises generally above 65 wt per cent of the modal mineralogy, except for ore type H2a (Figure 4). In the low SiO_2 ore type H1a the content of hematite is above 92 wt per cent. The content of magnetite is commonly <4 wt per cent. However, in the ore type H2a the magnetite content increases up to >70 wt per cent in the finest size fraction. The SiO_2 content in the SiO_2-rich ore types H1b and H2b is commonly >20 wt per cent. The content of apatite is up to 8 wt per cent in the finest size fraction of ore type H2b. Noteworthy, the content of carbonates and sulfides increases with decreasing size fraction when occurring in the SiO_2-rich ore type H2b (Figure 3).

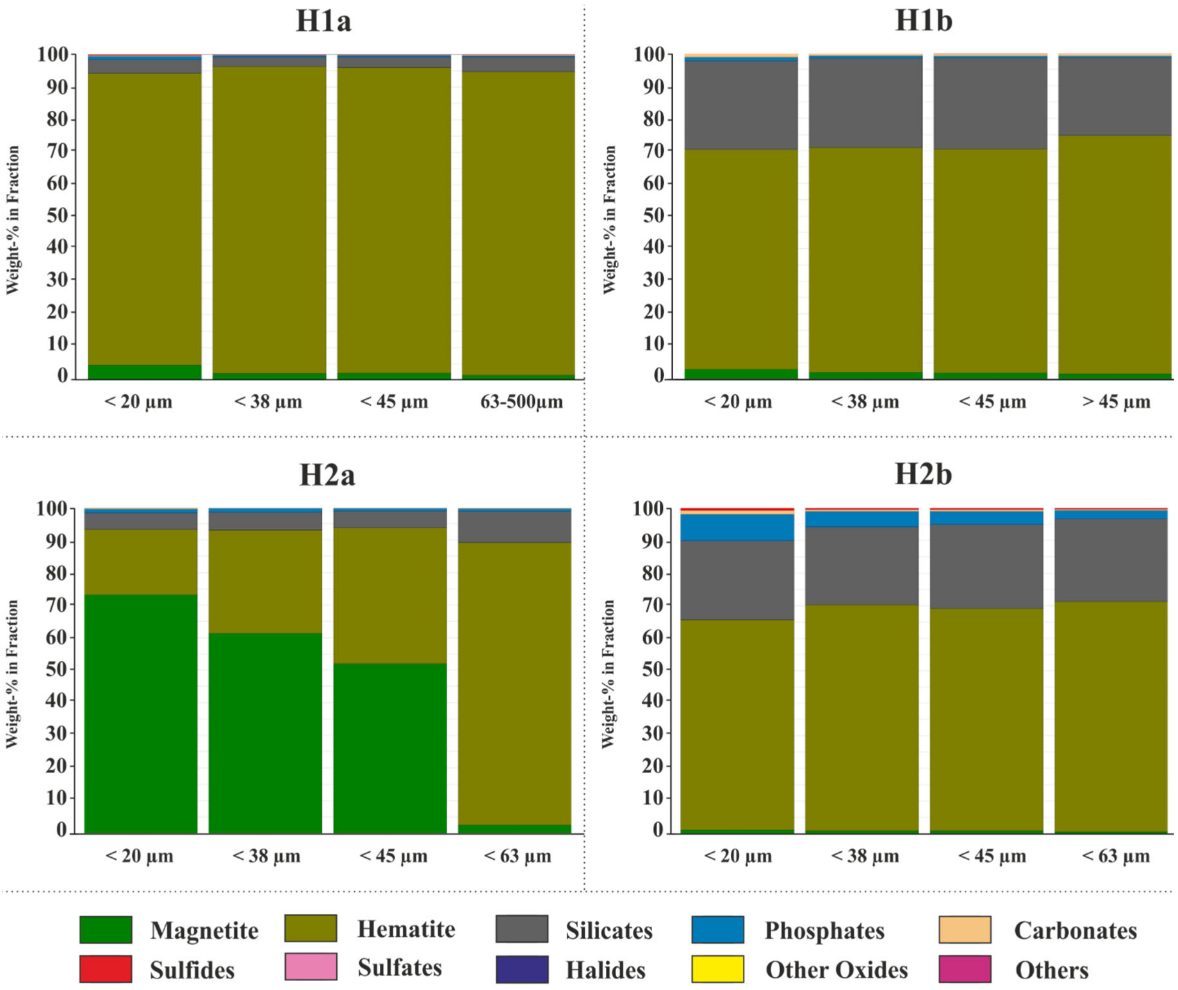

FIG 4 – Modal mineralogy of hematite-dominated ore types of the Per Geijer iron ore deposits. Except for magnetite, minerals have been consolidated to mineral groups.

Modal mineralogy of magnetite/hematite-mixed ore types

In the magnetite/hematite-mixed ore types the content of magnetite and hematite is variable (Figure 5). Generally, the content of hematite increases in the finer particle size classes although that trend is not clear in ore type HM1b. The SiO_2 content in the SiO_2-rich ore types HM1b and HM2b is commonly above 10 wt per cent. The content of apatite is up to 12 wt per cent in the finest size fraction of the ore type HM2a. However, in the same ore type apatite seems to be absent in the particle size class finer than 45 µm. Noteworthy, the content of carbonates seems to increase from coarser to finer size fractions in all ore types.

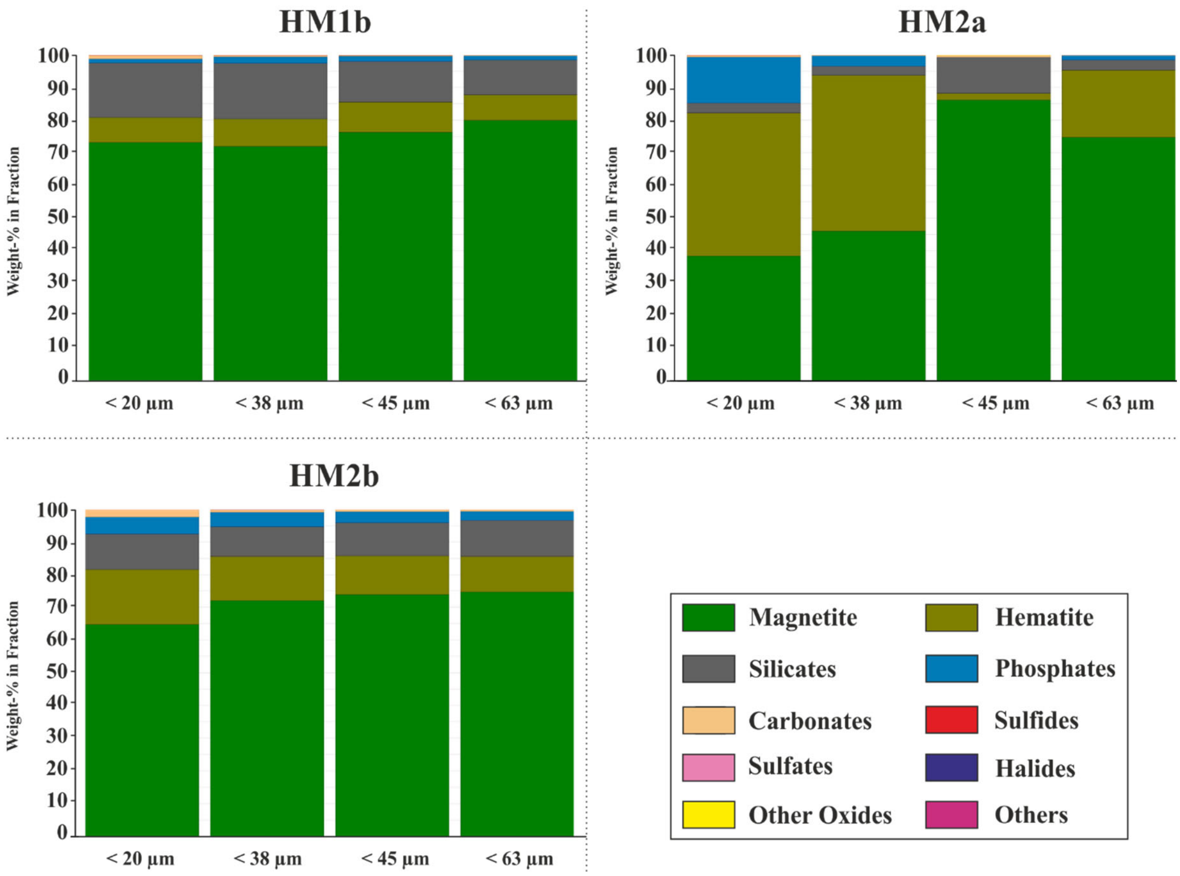

FIG 5 – Modal mineralogy of magnetite/hematite-mixed ore types of the Per Geijer iron ore deposits. Except for magnetite, minerals have been consolidated to mineral groups.

Modal mineralogy of low-grade ore types

In the low-grade ore types the content of magnetite and hematite is variable (Figure 6). Generally, the content of magnetite increases in the finer particle size classes, although that trend is the most apparent in ore type P2. The hematite content either increases or decreases in the finer particle size classes depending on the presence or absence of apatite. The SiO_2 content seems to follow a contrarian trend. The content of apatite is up to 10 wt per cent in the finest size fraction of the ore type P2. The content of carbonates varies from 1 to 3 wt per cent in the P-rich ore type P2.

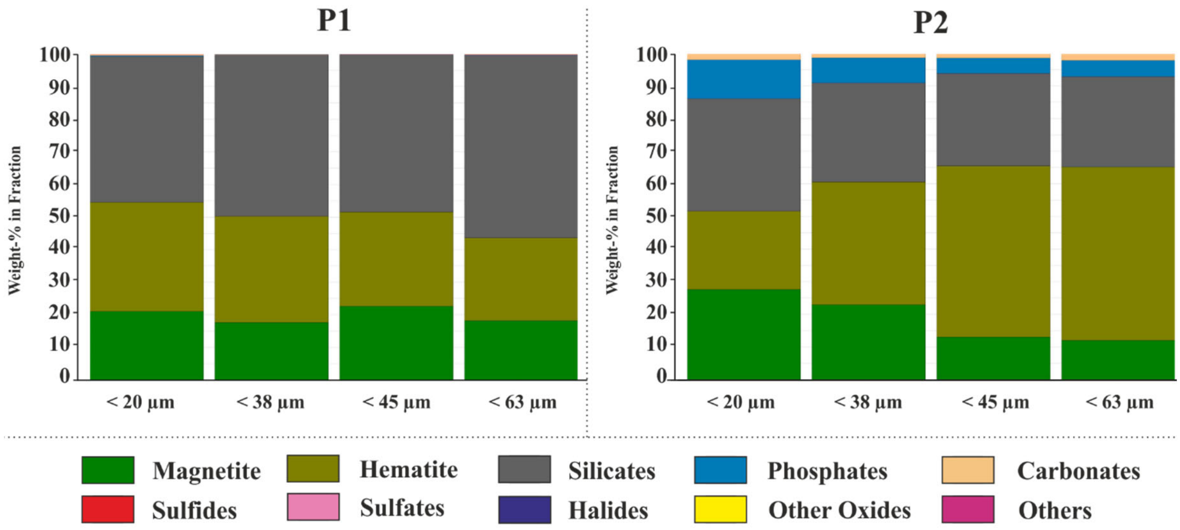

FIG 6 – Modal mineralogy of the minor and accessory minerals present in the different low-grade ore types. (a) All minerals except iron oxides, apatite, and quartz. (b) Like A, but without biotite, chlorite, muscovite.

Liberation analysis of magnetite, hematite, and apatite

It should be noted that the degree of liberation of iron oxides based on data obtained with SEM-based mineral liberation analysis (SEM-MLA) depends on multiple factors such as measurement conditions, sample surfaces and off-line-processing steps (Krolop *et al,* 2019b) and has been described challenging in other publications (eg Figueroa *et al,* 2012; Wartbichler, Böhm and Niiranen, 2014; Tonzetic, 2015). Although, to the best knowledge of the authors, all necessary steps for increasing the validity of the samples have been applied a conservative way of processing was chosen. Thus, it can be assumed that based on the data treatment that actual degree of liberation exceeds the numbers that are presented in the following.

Magnetite-dominated ore types

In the magnetite-dominated ore types the degree of liberation of magnetite is generally above 90 per cent, except for the finest fraction (<20 µm) of ore type M2b (Table 1). Degree of liberation of hematite seems to be variable between ore types and between the size fractions. In the finest size fractions, ie finer than 20 µm hematite is mostly best liberated in each ore type, although a general increasing degree of liberation from coarser to finer fractions is not observable. However, the modal abundance of hematite in magnetite-dominated ore types is generally low <10 wt per cent. The degree of liberation of apatite is generally above 76 per cent. It seems that apatite is generally best liberated in ore type M2b.

TABLE 1

Degree of liberation of magnetite, hematite, and apatite for magnetite-dominated ore types and corresponding particle size classes. Sample abbreviations account for particle size classes and are given in µm. Total particles correspond to all particles measured within the sample.

Ore type	Sample	Total particles	Magne-tite	lib. Mgt	Hema-tite	lib. Hem	Apa-tite	lib. Apa	% lib. Mgt	% lib. Hem	% lib. Apa
M1a	<20 µm	158963	140626	131318	4068	1774	404	330	93.4	43.6	81.7
	<38 µm	214982	189886	174846	5654	2208	1056	807	92.1	39.1	76.4
	<45 µm	144948	127445	120103	2836	1282	843	708	94.2	45.2	84.0
	>45 µm	132970	119156	112916	2109	903	949	776	94.8	42.8	81.8
M1b	<20 µm	81495	52386	49506	2207	1853	657	583	94.5	84.0	88.7
	<38 µm	86229	61294	59197	597	386	777	708	96.6	64.7	91.1
	<45 µm	59251	49297	46927	3803	2215	3011	2731	95.2	58.2	90.7
	<63 µm	96490	80124	77079	819	497	301	265	96.2	60.7	88.0
M2a	<20 µm	81010	64626	62077	1727	1122	5520	4671	96.1	65.0	84.6
	<38 µm	102564	89235	86003	1882	1043	4585	3543	96.4	55.4	77.3
	<45 µm	99804	84372	81063	2082	1255	4948	3933	96.1	60.3	79.5
	<63 µm	98013	77905	74544	2015	1320	4857	4106	95.7	65.5	84.5
M2b	<20 µm	129677	32177	15944	61472	44798	1592	1353	49.6	72.9	85.0
	<38 µm	93169	42373	38075	650	353	2902	2698	89.9	54.3	93.0
	<45 µm	87625	49795	45549	442	278	1992	1839	91.5	62.9	92.3
	<63 µm	92023	55800	51789	593	376	1922	1764	92.8	63.4	91.8

Non-liberated magnetite is partially locked in or bound most often to hematite, quartz and carbonate as shown in Figure 7a–7b. Iron oxides (ie magnetite and hematite) occur closely intergrown with each other, predominantly characterised by hematite replacing magnetite (Figure 7a). The shape of magnetite particles can be characterised as angular to subrounded with high to medium sphericity. Notably, fully liberated magnetite particles are more coarse-grained in relation to hematite. Furthermore, non-liberated hematite is intergrown with magnetite, quartz, carbonates, rutile, and apatite (Figure 7c). The shape of hematite particles can be characterised as rounded to subrounded with high sphericity. Non-liberated apatite is generally bound to magnetite, carbonates, and quartz (Figure 7d). It needs to be highlighted that apatite hosts fine-grained inclusions of magnetite. Alternatively, it can occur as inclusions in hematite (Figure 7e). The shape of apatite particles is subrounded with medium to high sphericity.

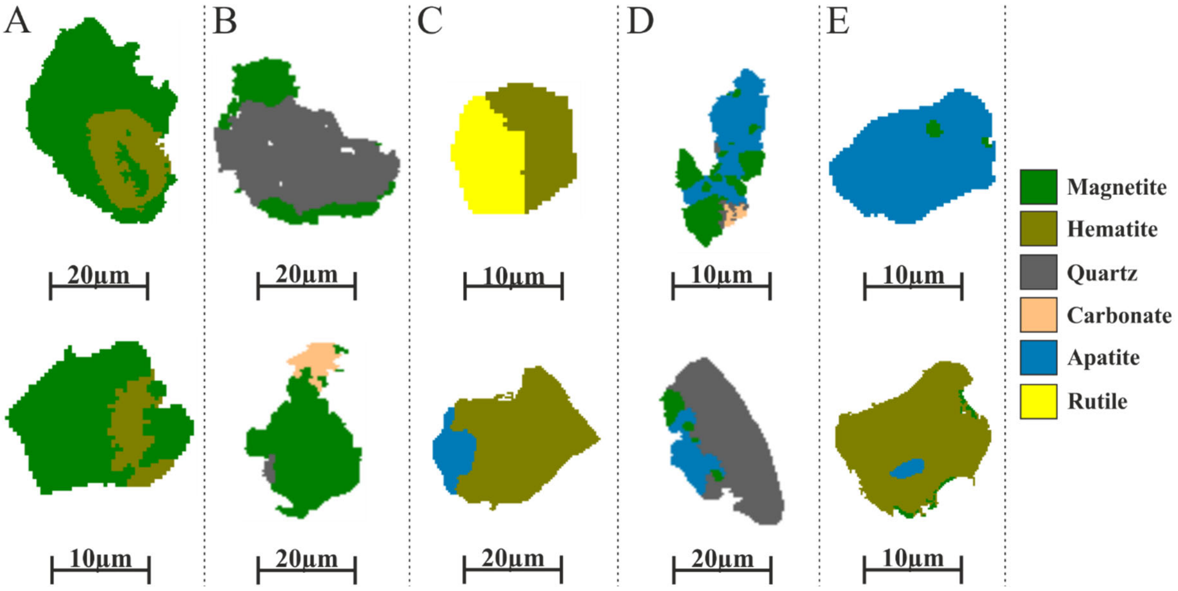

FIG 7 – Particle intergrowths of magnetite-dominated ore types. (a) Intergrowth of magnetite and hematite. (b) Intergrowth of magnetite and quartz (binary) and additionally with carbonates (ternary). (c) Binary intergrowth of hematite and rutile and hematite and apatite. (d) Apatite particle intergrown with magnetite, quartz, and carbonate. (e) Apatite hosting inclusion of magnetite and apatite locked in hematite.

Hematite-dominated ore types

For the hematite-dominated ore types the degree of liberation of hematite is generally above 83 per cent, except for ore type H2a (Table 2). This corresponds with the high content of magnetite in this ore type. The degree of the liberation of hematite is highest in the coarser particle size classes reaching up to 93 per cent in the ore type H1a. It seems that in the absence of apatite (ie the ore types H1a and H1b) the degree of liberation of hematite decreases in the finer particle size classes. The degree of the liberation of magnetite is variable between ore types being generally highest in the coarsest size fractions (63–500 µm and >45 µm) when apatite is absent. In the P-rich ore types H2a and H2b the degree of liberation of magnetite is highest in the finest size fraction (<20 µm). However, the content of magnetite in hematite-dominated ore types is generally lower than 5 wt per cent, except in the ore type H2a. The degree of liberation of apatite is variable between the ore types but commonly above 86 per cent, except for ore type H2a. Apatite is generally best liberated in ore type H2b. The degree of the liberation of apatite is highest in the coarser particle size classes and decreases in finer size fractions.

TABLE 2

Degree of liberation of magnetite, hematite, and apatite for hematite-dominated ore types and corresponding particle size classes. Sample abbreviations account for particle size classes and are given in µm. Total particles correspond to all particles measured within the sample.

Ore Type	Sample	Total particles	Magnetite	lib. Mgt	Hematite	lib. Hem	Apatite	lib. Apa	% lib. Mgt	% lib. Hem	% lib. Apa
H1a	<20 µm	35423	14014	11354	15756	13295	367	317	81.0	84.4	86.4
	<38 µm	27508	7416	5802	14418	12896	390	353	78.2	89.4	90.5
	<45 µm	23944	6975	5727	11834	10677	301	277	82.1	90.2	92.0
	63–500 µm	27280	6698	5668	13540	12575	239	224	84.6	92.9	93.7
H1b	<20 µm	50246	10945	7696	12657	10594	659	586	70.3	83.7	88.9
	<38 µm	47942	8774	5937	13316	11246	664	594	67.7	84.5	89.5
	<45 µm	43989	8372	5971	11180	9564	474	422	71.3	85.5	89.0
	>45 µm	39620	6825	5120	10760	9496	422	390	75.0	88.3	92.4
H2a	<20 µm	78815	69832	66488	3474	1452	672	455	95.2	41.8	67.7
	<38 µm	65030	54404	51181	3820	1782	865	682	94.1	46.6	78.8
	<45 µm	76152	64961	60478	5802	2719	716	487	93.1	46.9	68.0
	<63 µm	42309	18116	14999	15507	13016	491	427	82.8	83.9	87.0
H2b	<20 µm	41138	6851	5228	9447	8496	2956	2782	76.3	89.9	94.1
	<38 µm	40329	7446	4868	11448	9639	2921	2762	65.4	84.2	94.6
	<45 µm	36957	6460	4280	10285	8711	2088	2001	66.3	84.7	95.8
	<63 µm	29533	4286	2770	8860	7776	1293	1239	64.6	87.8	95.8

Non-liberated hematite is partially bound to other minerals such as magnetite, quartz, apatite, and rutile as shown in Figure 8a–8b. Iron oxides (ie magnetite and hematite) occur closely intergrown with each other (Figure 8a). The shape of hematite particles can be characterised as subangular to subrounded with high sphericity. Notably, grain size of the liberated hematite particles is coarser in relation to magnetite particles in the samples. Non-liberated magnetite is intergrown with other minerals such as hematite, quartz, carbonates, and apatite (Figure 8c). The shape of magnetite particles can be characterised as rounded to subrounded with high to medium sphericity. Non-liberated apatite is generally bound to hematite, magnetite, quartz and carbonates (Figure 8d). The shape of apatite particles is subrounded to angular with medium to low sphericity.

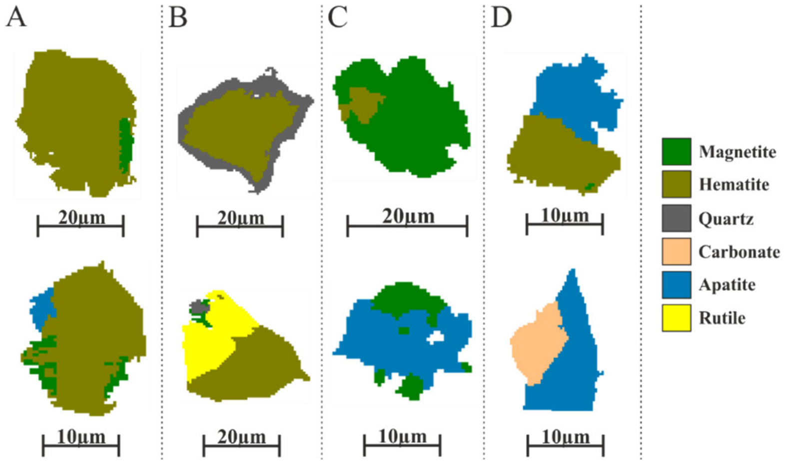

FIG 8 – Particle intergrowths of hematite-dominated ore types. (a) Intergrowth of hematite and magnetite (binary) and hematite with magnetite and apatite (ternary). (b) Intergrowth of hematite and quartz (binary) and hematite and rutile. (c) Binary intergrowth of magnetite and hematite and magnetite and apatite. (d) Apatite particle intergrown with hematite locking magnetite, and apatite intergrown with carbonate (binary).

Magnetite/hematite-mixed ore types

In the magnetite/hematite-mixed ore types the degree of liberation of magnetite is above 92 per cent (Table 3). Notably, the content of magnetite is higher than hematite in ore types HM1b and HM2b, exceeding 65 per cent. Incorrect classification can be ruled out due to verification with optical microscopy. Ore type HM2a has variable proportions of hematite and magnetite. The degree of liberation of hematite is relatively homogeneous between ore types and particle size classes. In the finest size fraction finer than 20 μm the degree of liberation of hematite is highest for each ore type lying above 76 per cent. The degree of liberation of apatite is variable between the ore types being commonly above 84 per cent, except for the particle size class finer than 45 μm of ore type HM2a. Apatite is generally best liberated in ore type HM2b and in the size fraction finer 38 μm in ore type HM2a. The degree of the liberation of apatite seems not to be related to a specific particle size class.

TABLE 3

Degree of liberation of magnetite, hematite and apatite for magnetite/hematite-mixed ore types and corresponding particle size classes. Sample abbreviations account for particle size classes and are given in μm. Total particles correspond to all particles measured within the sample.

Ore type	**Sample**	**Total particles**	**Magne-tite**	**lib. Mgt**	**Hematite**	**lib. Hem**	**Apatite**	**lib. Apa**	**% lib. Mgt**	**% lib. Hem**	**% lib. Apa**
HM1b	<20 μm	74066	53660	50790	3515	2787	552	466	94.7	79.3	84.4
	<38 μm	91367	65056	60794	4538	3515	1702	1488	93.4	77.5	87.4
	<45 μm	65649	51274	49581	1980	1542	1085	999	96.7	77.9	92.1
	<63 μm	111059	90665	86225	5446	4228	1112	916	95.1	77.6	82.4
HM2a	<20 μm	56911	39595	36922	6619	5093	6702	6044	93.2	76.9	90.2
	<38 μm	45234	35040	32272	5862	3519	1702	1601	92.1	60.0	94.1
	<45 μm	86759	69683	66387	1623	1023	99	75	95.3	63.0	75.8
	<63 μm	82608	72849	70455	2911	1757	1214	1033	96.7	60.4	85.1
HM2b	<20 μm	65142	44022	41771	3406	2676	2686	2456	94.9	78.6	91.4
	<38 μm	63293	46703	44682	2465	1730	3045	2807	95.7	70.2	92.2
	<45 μm	64748	48274	46481	2115	1473	2533	2374	96.3	69.6	93.7
	<63 μm	63128	48054	46357	1896	1317	1961	1823	96.5	69.5	93.0

Non-liberated magnetite particles are preferentially intergrown with hematite, apatite and quartz as shown in Figure 9a–9c. Iron oxides (ie magnetite and hematite) occur closely intergrown with each other, predominantly characterised by hematite replacing magnetite (Figure 9a–9b). The shape of magnetite particles can be characterised as subrounded, seldom subangular with high to medium sphericity. Non-liberated hematite particles are intergrown preferentially with magnetite and quartz, subordinately with carbonates (Figure 9d). The shape of hematite particles can be characterised as subrounded to subangular with medium to low sphericity. Non-liberated apatite is generally bound to magnetite and hematite (Figure 9e), subordinately to carbonates and quartz. The shape of apatite particles is angular to subrounded medium to low sphericity.

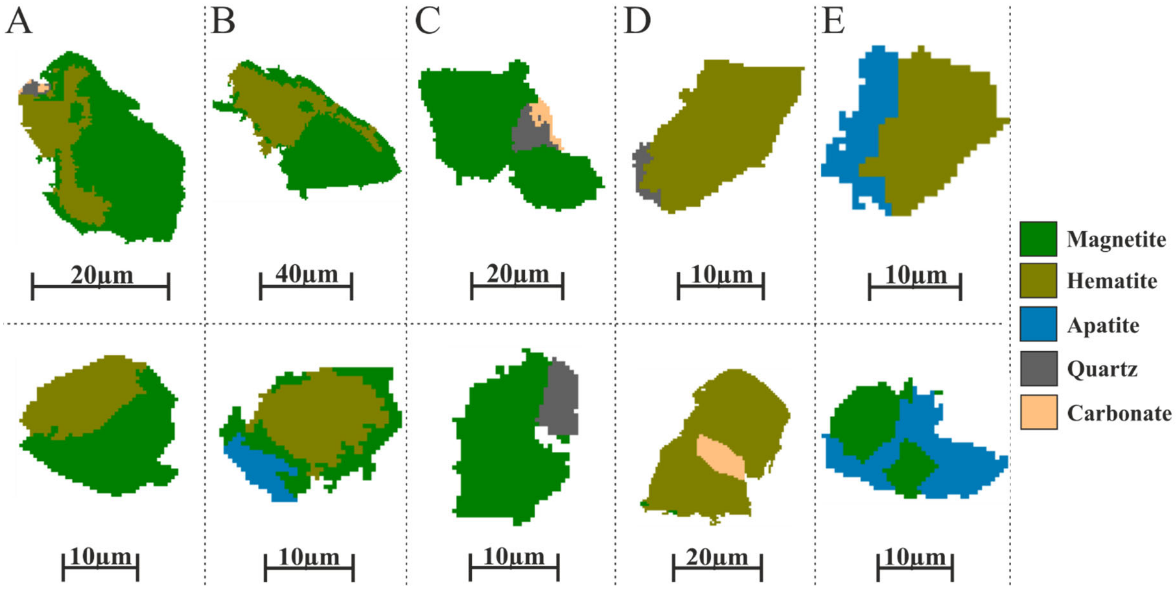

FIG 9 – Particle intergrowths of magnetite/hematite-mixed ore types. (a) Intergrowth of hematite with magnetite and quartz (ternary) and magnetite and hematite (binary). (b) Intergrowth of hematite and magnetite (binary) and hematite rimmed by magnetite intergrown with apatite. (c) Intergrowth of magnetite with quartz and carbonates (ternary) and magnetite with quartz (binary). (d) Hematite particle intergrown with quartz (binary) and hematite intergrown with carbonates and magnetite and the rim (ternary). (e) Apatite intergrown with hematite (binary) and apatite intergrown with magnetite particles.

Low-grade ore types

In the low-grade ore types the degree of liberation of magnetite is above 80 per cent (Table 4). The content of hematite seems to be higher than magnetite in both ore types P1 and P2. Notably, in the ore type P1 the content of silicates is above 60 wt per cent, whereas P2 is more enriched in silicates in finer particle size classes. Incorrect classification can be ruled out due to data verification with optical microscopy. The degree of liberation of hematite is relatively homogeneous in ore type P1. In the ore type P2 the degree of liberation varies from ~74 per cent to ~84 per cent depending on particle size classes. It needs to be highlighted that the highest degree of liberation of hematite in the ore type P2 occurs in particle size class finer that 63 µm. The degree of liberation of apatite is variable between the ore types but above 90 per cent in ore type P2. The low degree of liberation of apatite in ore type P1 of below 76 per cent corresponds with the low modal abundance of apatite in this ore type. The degree of the liberation of apatite seems not to be related to a specific particle size class in both ore types.

TABLE 4

Degree of liberation of magnetite, hematite, and apatite for low-grade ore types and corresponding particle size classes. Sample abbreviations account for particle size classes and are given in µm. Total particles correspond to all particles measured within the sample.

Ore type	Sample	Total particles	Magnetite	lib. Mgt	Hematite	lib. Hem	Apatite	lib. Apa	% lib. Mgt	% lib. Hem	% lib. Apa
P1	<20 µm	50723	15753	13891	5028	4469	48	35	88.2	88.9	72.9
	<38 µm	46138	14502	12724	3854	3375	100	75	87.7	87.6	75.0
	<45 µm	44488	15383	13940	3280	2855	60	43	90.6	87.0	71.7
	<63 µm	48092	15315	13667	3395	3001	41	31	89.2	88.4	75.6
P2	<20 µm	78637	27114	23051	4747	3716	6051	5462	85.0	78.3	90.3
	<38 µm	72185	25724	22182	5467	4040	6036	5574	86.2	73.9	92.3
	<45 µm	76475	24740	20419	8778	7187	3835	3510	82.5	81.9	91.5
	<63 µm	81893	22994	18809	9394	7851	4056	3728	81.8	83.6	91.9

Non-liberated magnetite particles are intergrown preferentially with hematite and quartz (Figure 10a–10b), subordinately with carbonates and rutile. Iron oxides occur closely intergrown with each other, predominantly characterised by hematite replacing magnetite (Figure 10a). Furthermore, magnetite occurs locked in other minerals such as quartz (Figure 10c). The shape of magnetite particles can be characterised as subangular to subrounded with high to medium sphericity. Non-liberated hematite particles are partially locked in or bound to other minerals preferentially quartz as shown in Figure 10d. The shape of hematite particles can be characterised as subrounded to subangular with medium to low sphericity. Non-liberated apatite is generally bound to hematite (Figure 10e) and magnetite, subordinately to carbonates and quartz. The shape of apatite particles is angular to subrounded with medium to low sphericity.

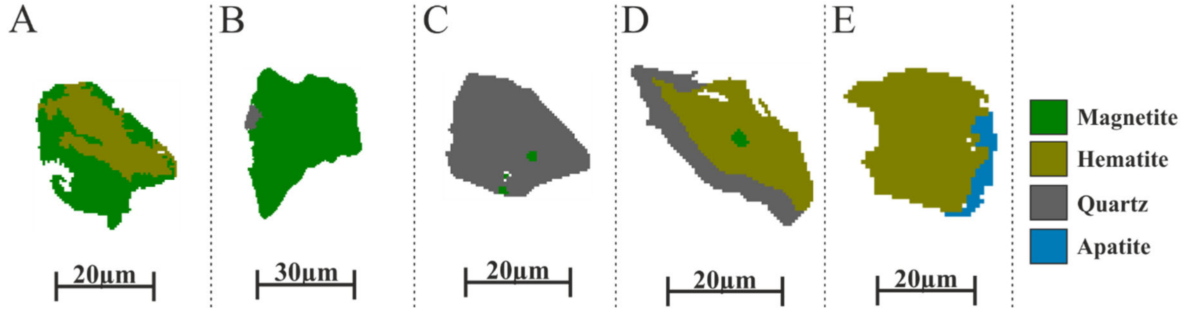

FIG 10 – Particle intergrowths of low-grade ore types. (a) Intergrowth of magnetite and hematite (binary). (b) Intergrowth of magnetite and quartz (binary). (c) Fine-grained magnetite inclusions in quartz. (d) Hematite particle intergrown with quartz hosting fine-grained magnetite inclusion. (e) Apatite intergrown with hematite (binary).

DISCUSSION AND CONCLUSIONS

Observations from 13 ore types of the Per Geijer iron ore deposits after comminution reveal that the modal mineralogy reflects on the pre-definition of ore types reported in Krolop *et al* (2019a) and particle size classes. However, some size fractions differ from expected modal mineralogy in terms of the content of present mineral phases. In the magnetite-dominated ore type M1b the amount of hematite in the particle size class finer than 45 µm is above 20 wt per cent. This is in accordance with microscopic examination. The amount of hematite in the ore type M1b seems to be linked to a decreased degree of liberation of hematite in the size fraction finer than 45 µm. Nevertheless, this does not reflect on the degree of liberation of magnetite. Similar variations in modal mineralogy were observed in the ore types H2a and HM2a. The magnetite content in the hematite-dominated ore type H2a is significantly enriched up to 73 wt per cent in the finest fraction (<20 µm). In general, magnetite becomes enriched from coarser to finer particle size classes in that ore type at concurrent decreasing hematite contents. This is potentially caused by the dominance of coarse-grained hematite particles in that sample. In the magnetite/hematite-mixed ore type HM2a a general trend of decreasing magnetite content is prevalent from coarser to finer particle size classes. This is presumably caused by the fact that hematite replaces magnetite and needs finer grinding to be liberated. Thus, hematite particles become proportionally enriched in finer size fractions. However, the amount of magnetite in the particle size class finer than 45 µm is above 80 wt per cent being highest in this fraction. From this it can be concluded that this enrichment effect of hematite in finer particle size classes occurs below 38 µm. Mineral associations of the *in-situ* ore are an important factor in understanding the behaviour during processing and the influence on the final product as reported in Krolop *et al* (2019a). Niiranen (2015) has shown that very fine-grained inclusions and intergrowth of eg, actinolite and magnetite can result in an increased SiO_2-grade in the concentrate. The iron ores of the Per Geijer deposits, especially magnetite is also host to many different inclusions of varying size. Vice versa, magnetite is partly incorporated as small inclusions in other minerals, especially apatite. This can have an impact on the quality of the iron ore concentrate after magnetic separation process resulting in higher P_2O_5 contents. On the other hand, some magnetite will not be extracted and remain in the waste. From the results it can be assumed that magnetite-dominated ore types do not need fine grinding below 45 µm for magnetite to reach a high enough degree of liberation. In fact, it seems to have a negative effect in magnetite liberation in the presence of both silicates, phosphates, and carbonates (ore type M2b) when samples undergo overgrinding. Similar conclusions can be drawn for the magnetite/hematite-mixed ore types. Magnetite/hematite-mixed ore types do not need very fine grinding below 45 µm for magnetite to achieve a high degree of liberation. However, for hematite the opposite trend is observed with significantly increased degree of liberation in the finest size fraction regardless of the presence of phosphates and silicates in the ore type HM2b or only accompanied phosphates in the ore type HM2a. This trend of decreased degree of liberation can also be observed in the hematite-dominated ore type H2b. Notably, in the absence of apatite in hematite-dominated ore types H1a and H2b fine grinding below 63 µm is not required for hematite to be well liberated. Furthermore, it can be concluded that low-grade ore types do not require very fine grinding below 45 µm to achieve a high degree of liberation of magnetite, when only silicates are present with iron oxides. However, in the presence of apatite and carbonates in the ore type P2 grinding to finer than 38 µm increases the degree of liberation of magnetite to over 86 per cent. However, it should be tested after magnetic separation if grinding to finer than 38 µm is necessary to obtain the required quality of the magnetite concentrate. Knowledge of the degree of liberation of apatite is required since apatite can be regarded as a potential by-product of the Per Geijer iron ores in the future. The degree of liberation of apatite seems generally not to be related to particle size classes, except for hematite-dominated ore types. Here, the highest degree of liberation is achieved in coarser size fractions. From that it follows that overgrinding should be omitted. Furthermore, it can be concluded that the degree of liberation of apatite is highest in the presence of silicates regardless of the dominant iron oxide. It needs to be mentioned that the maximum content of apatite does not exceed 15 wt per cent in the grinded samples. It is envisaged to test the comminution behaviour of apatite-rich *in situ* ore zones, which can locally be up to 20 wt per cent in drill core sections. In addition, comminution tests need to be performed in enlarged laboratory scale and further in pilot scale to verify the results of this study. This is especially important since the number of samples used for this study were restricted by the number of core drillings at the stage of investigation. Many recent core drillings have been conducted by LKAB which led to a significantly enlarged number of samples for mineral processing test works. Furthermore, magnetic separation tests, apatite flotation tests and possibly reverse silicate flotation tests both in laboratory and pilot scale need to be carried out to study liberation degrees of final concentrates. It can be concluded that the information gained from this study is of major importance for further process mineralogical analysis and enlarged beneficiation test work of the Per Geijer deposits. Furthermore, it provides an improved understanding of the behaviour of ore types during comminution at laboratory scale.

ACKNOWLEDGEMENTS

We gratefully thank the reviewers for constructive comments that improved the manuscript. The authors thank the preparation laboratory personnel of the Helmholtz Institute Freiberg for Resource Technology, especially Michael Stoll and Roland Würkert for assistance during grain mount preparation and deagglomeration. LKAB colleagues, especially personnel of the laboratory for physical testing and chemical analysis are admiringly thanked. The main author gratefully acknowledges LKAB for funding this research and for approval of publication.

REFERENCES

Aupers, K, 2014. *Gangue mineralogy and deportment of deleterious elements in the iron ore of the Kiirunavaara deposit, Sweden,* MSc thesis, TU Bergakademie Freiberg, Germany, 167 p.

Drugge, L, 2009. Validering av metod för simulering av framtida anrikningsresultat, LKAB Utredning 09–775 (Internal Report in Swedish), 65 p.

Figueroa, G, Moeller, K, Buhot, M, Gloy, G and Haberla, D, 2012. Advanced discrimination of hematite and magnetite by automated mineralogy, in *Proceedings of the 10th International Congress for Applied Mineralogy (ICAM)*, pp 197–204.

França, J R, Barrios, G K, Turrer, H D and Tavares, L M, 2020. Comminution and liberation response of iron ore types in a low-grade deposit, *Minerals Engineering*, 158.

Geijer, P, 1910. Igneous rocks and iron ores of Kiirunavaara, Luossavaara and Tuollavaara, *Economic Geology,* 5(8):699–718.

Geijer, P, 1931. *The iron ores of Kiruna type: geographical distribution, geological characters and origin*, Ser C (367), 39 p (Sveriges geologiska undersökning).

Geijer, P, 1950. *The Rektor ore body at Kiruna*, 20 p (Sveriges geologiska undersökning).

Krolop, P, Jantschke, A, Gilbricht, S, Niiranen, K and Seifert, T, 2019b. Mineralogical imaging for characterization of the Per Geijer apatite iron ores in the Kiruna District, Northern Sweden: a comparative study of mineral liberation analysis and raman imaging, *Minerals*, 9(9):544.

Krolop, P, Niiranen, K, Gilbricht, S and Seifert, T, 2019a. Ore type characterization of the Per Geijer iron ore deposits in Kiruna, Northern Sweden, in *Proceedings Iron Ore 2019 Conference*, pp 343–353 (The Australasian Institute of Mining and Metallurgy: Melbourne).

Lamberg, P, 2010. Structure of a property based simulator for minerals and metallurgical industry, in *Proceedings of the SIMS, The 51st Conference on Simulation and Modelling*, Oulu, Finland, p 5.

Lamberg, P, Rosenkranz, J, Wanhainen, C, Lund, C, Minz, F, Mwanga, A and Parian, M. 2013. Building a geometallurgical model in iron ores using a mineralogical approach with liberation data, in *Proceedings of the Second AusIMM International Geometallurgy Conference*, pp 317–324 (The Australasian Institute of Mining and Metallurgy: Melbourne).

Liipo, J, Lang, C, Burgess, S, Otterström, H, Person, H and Lamberg, P, 2012. Automated mineral liberation analysis using INCAMineral, in *Proceedings of the Process Mineralogy '12*, Cape Town, South Africa, pp 7–9.

Lund, C, 2013. *Mineralogical, Chemical and textural Characterisation of the Malmberget Iron Ore Deposit for a geometallurgical Model*, Luleå University of Technology, Doctoral Thesis, 97 p.

Martinsson, O, 2015. Genesis of the Per Geijer Apatite Iron Ores, Kiruna Area, Northern Sweden, in *Abstract volume, SGA biennial meeting,* pp 23–27.

McNab, B, Jankovic, A, David, D and Payne, P, 2009. Processing of magnetite iron ores–comparing grinding options, in *Proceedings Iron Ore 2009 Conference*, pp 27–29 (The Australasian Institute of Mining and Metallurgy: Melbourne).

Niiranen, K and Rutanen, H. 2019. Gangue mineralogy of titanium (Ti) in the Kiirunavaara iron ore deposit, northern Sweden, in *Proceedings Iron Ore 2019*, pp 491–499 (The Australasian Institute of Mining and Metallurgy: Melbourne).

Niiranen, K and Töyrä, V, 2019. Gangue mineralogy of titanium (Ti) in the Kiirunavaara iron ore deposit – a challenge for the mineral processing?, *Mineral Engineering 2019 Conference* (Luleå University of Technology).

Niiranen, K, 2015. *Characterization of the Kiirunavaara iron ore deposit for mineral processing with the focus on the high silica ore type B2*, PhD Thesis, Montanuniversitaet Leoben, Austria, 195 p.

Niiranen, K, Töyrä, V and Krolop, P, 2018. Reverse cationic flotation – a possibility to reduce silicate content in magnetite concentrate in LKAB's beneficiation plants in Kiruna, *IMPC 2018 – 29th International Mineral Processing Congress*, pp 1136–1147.

Norgate, T and Haque, N, 2010. Energy and greenhouse gas impacts of mining and mineral processing operations, *Journal of Cleaner Production*, 18(3):266–274.

Reichert, M, Gerold, C, Fredriksson, A, Adolfsson, G and Lieberwirth, H, 2015. Research of iron ore grinding in a vertical-roller-mill, *Minerals Engineering*, 73:109–115.

Tøgersen, M K, Kleiv, R A, Ellefmo, S and Aasly, K, 2018. Mineralogy and texture of the Storforshei iron formation and their effect on grindability, *Minerals Engineering*, 125:176–189.

Tonžetić, I Ž, 2015. Quantitative analysis of iron ore using SEM-based technologies, in *Iron Ore,* pp 161–189.

Töyrä, V, Niiranen, K, Niva, E and Rosendal, O, 2017. increasing Silicate Content in the Kiruna Ore – a Challenge for Mineral Processing, *Mineral Engineering 2017 Conference,* pp 149–159 (Luleå University of Technology, Preprints).

Wartbichler, M, Böhm, A and Niiranen, K, 2014. Comparison of Chemical, Physical and Optical Methods to Distinguish between Magnetite und Hematite. Case Study Kiirunavaara Deposit Sweden, in *Preprints Conference in Minerals Engineering*, Luleå Tekniska Universitet, Mineralteknik, Luleå, pp 181–193.

Wright, B, Carroll, T, Flanagan, M, Sua, T and Van Dijken, B, 2013. BHP Billiton West Australian Iron Ore Geometallurgy – Past, Present and Future, in *Proceedings of the Second AusIMM International Geometallurgy Conference*, pp 105–110 (The Australasian Institute of Mining and Metallurgy: Melbourne).

Mineral chemistry of iron oxides in the Leveäniemi iron ore deposit in Northern Sweden

A Larsson[1] *and K Niiranen*[2]

1. Research Engineer in Process Mineralogy, Process and Product Development, LKAB, SE-98186 Kiruna, Sweden. Email: adrian.e.larsson@lkab.com
2. Advanced Specialist in Process Mineralogy, Process and Product Development, LKAB, SE-98186 Kiruna, Sweden. Email: kari.niiranen@lkab.com

ABSTRACT

The Palaeoproterozoic Leveäniemi iron oxide apatite (IOA) deposit of the so-called Kiruna type is currently mined by Luossavaara-Kiirunavaara AB (publ.), commonly known as LKAB. The mineralogy of iron oxides, ie magnetite, hematite, maghemite, and goethite is more complicated compared to the neighbouring and more famous IOA deposits of Kiirunavaara and Malmberget. Furthermore, the mineral chemistry of the iron oxides in the Leveäniemi deposit is also slightly different. Especially, the information about the deportment of titanium and vanadium in iron oxides and distribution in the deposit is essential since they can have an impact in the steelmaking process. For this study 50 samples were selected from exploration drill cores and investigated by optical microscopy, FE-SEM-EDS and EPMA at LKAB and the Geological Survey of Finland. Investigations revealed that magnetite is the predominant iron oxide mineral with secondary hematite being the second most abundant mineral. Primary hematite, maghemite, and goethite seem to be less abundant. It should be noted, however, that this investigation focused on magnetite which currently is the only mineral with economic value. Vanadium occurs as a substitution element in the crystal lattice of iron oxide minerals in the Leveäniemi deposit and not as discrete stochiometric vanadium minerals. In the investigated samples vanadium concentration in magnetite ranges from 0.12 to 0.32 wt per cent V_2O_3 with higher concentration in the southern part of the deposit. Contrary, titanium does not substitute for iron in the crystal lattice of magnetite or secondary hematite (less than 0.018 wt per cent TiO_2). It either occurs as tiny inclusions of titanium oxide minerals or as exsolution lamellae of ilmenite in magnetite. The spatial distribution for titanium in the deposit, however, remains unknown. Furthermore, results of this study indicate that alteration of primary magnetite to secondary hematite has had no significant effect on the trace element chemistry of these minerals in the Leveäniemi deposit.

INTRODUCTION

IOA deposits are locally an important source of iron ore based on the modal abundance of magnetite >90 vol per cent. Luossavaara-Kiirunavaara AB (LKAB) operates an iron ore mine, a beneficiation plant, and a pelletising plant in Svappavaara, Northern Sweden. The current methods of separation in the beneficiation plants are wet low intensity magnetic separation (WLIMS) and reverse apatite flotation. LKAB operated Leveäniemi open pit in Svappavaara from 1964 to 1983 producing approximately 57 Mt crude ore. In 2010 an internal project at LKAB was started to reassess the Leveäniemi deposit and to evaluate the deposit for future exploitation that than happened in 2015. It is understandable that the mineralogical and geochemical characterisation of the Leveäniemi iron ore deposit was insufficient in the early years. Therefore, more specific information about the mineralogy of the deposit, especially information about the iron oxides and their mineral chemistry is needed, especially as the deposit has more complex mineralogy and geology than those IOA deposits currently mined by LKAB in Kiruna and Malmberget.

In the present study, mineralogy and the mineral chemistry of the iron oxides, especially of magnetite and hematite were of interest which are the main iron oxide minerals in the Leveäniemi IOA deposit. Today, magnetite (Fe_3O_4) is the only ore mineral of economic value in the deposit. However, it should be noted that hematite may be an essential part of production for LKAB in the future, thus research must not be solely on magnetite. Within this context the information about the distribution and deportment of titanium (Ti) and vanadium (V) in the iron oxides is of particular importance, which potentially can have a negative impact in the product quality of the iron ore pellets and further on in the steelmaking process. Furthermore, the deportment of some other trace elements such as nickel

(Ni), chromium (Cr), copper (Cu) and cobalt (Co) in the iron oxides can also be of importance because their presumed negative impact in the product quality not only of the iron ore pellets, but also in the special products in the future (LKAB, 2019).

Currently manual extraction of samples for grade control is conducted from the cones of blasthole drill cuttings in the Leveäniemi open pit to obtain additional information for production planning to fill a sparse pattern of diamond drilling (Engström, 2018). Until recently this material was analysed using an X-ray fluorescence spectrometer (XRF) and Saturation Magnetisation Analyser (SATMAGAN) or alternatively wet chemical analysis of Fe^{2+}. The latter is regarded as the most reliable and sensitive method to determine the amount of magnetite if there is no other source of Fe^{2+} in the samples. The results of these methods of analysis were compared in order to estimate the composition and ratio of magnetite and hematite in the crude ore (feed). This information is crucial especially for production planning for estimation of Fe grade and tonnage, but also for understanding the process behaviour of the crude ore and mass balancing in the downstream. Currently only magnetite can be utilised in the process (dry magnetic separation before and wet low intensity magnetic separation after milling) while other iron oxide minerals are regarded as waste. However, often a comparison of analysis data from SATMAGAN and wet chemical analysis has shown that they are not consistent with each other. For this reason, it could be assumed that several iron bearing minerals besides magnetite and hematite may be simultaneously present in the crude ore. Therefore, the second objectives of this study were to get sufficient mineralogical information about modal mineralogy and abundance of different iron oxides in the Leveäniemi deposit.

DEPOSIT GEOLOGY AND MINERALOGY

Leveäniemi IOA deposit is located in the northern part of Norrbotten county in Sweden which is an important mining district in Europe hosting some IOA and Cu-Au deposit of world-class. Economically most important in the area are IOA-deposits of Kiirunavaara and Malmberget, Tapuli iron deposit, and Aitik porphyry Cu-Au deposit (eg Boyd *et al*, 2016; Martinsson *et al*, 2016; Bergman and Hellström, 2020). Furthermore, close to the Leveäniemi deposit locate IOA deposits of Gruvberget (mined by LKAB between 2010 and 2018) and Mertainen (pilot mining during the 2010s with limited production planned in 2021). Gruvberget, Leveäniemi, and Mertainen constitute so called Svappavaara ore field.

The Svappavaara ore field locates in the geological Norrbotten province within the northern part of the Fennoscandian Shield. The Norrbotten province consists of Karelian rocks (mostly greenstones) and Svecofennian supracrustal units of Palaeoproterozoic age inclusive several units of intrusive rocks that unconformably lies upon an Archaean basement. Noticeably the Norrbotten province seems to be more mineralised in the Palaeoproterozoic rocks than the in the Archaean rocks (eg Bergman, Kübler and Martinsson, 2001; Martinsson *et al*, 2016). The local geology in Svappavaara area is dominated by felsic to mafic metavolcanic and metasedimentary rocks. The metavolcanic rocks probably belong to so called Porphyrite group. They are mainly of andesitic composition with plagioclase phenocrysts. The wall rock at the Leveäniemi deposit consists mostly metavolcanic rocks overlain by metasedimentary rocks. There are also some intrusive dykes ranging in composition from pegmatite to diabase (Bergman, Kübler and Martinsson, 2001).

Leveäniemi deposit is the third largest exploited IOA deposit of so-called Kiruna type first defined by Geijer (1910, 1931) in the northern part of Norrbotten county. The deposit was first discovered in magnetic ground surveys in 1897. An initial drilling program was conducted between 1899 and 1907 to investigate the deposit. The Leveäniemi orebody which nearly aligns with the geographic north–south extends for approximately 1300 metres and is at widest 600 metres with a depth of at least 500 metres. The contacts between the deposit and the wall rock are often sharp. Historically six different geological ore types have been classified by Parák and Espersen (1965) based on their mineralogy as follow: massive magnetite ore (black ore), magnetite/hematite-mixed ore (martite ore), calcareous magnetite ore, magnetite breccia ore, apatite rich magnetite veins, and hematite ore (red ore). In the deposit the contacts between the massive ore and the ore breccia are mostly distinct. Besides apatite, the Leveäniemi deposit contains various amounts of biotite, feldspar, amphibole, quartz, and plagioclase as main gangue minerals (Parák and Espersen, 1965; Bergman, Kübler and Martinsson, 2001).

For purpose of this study, especially the magnetite/hematite-mixed ore is of special interest. Traditionally the mixed ore containing secondary hematite is called martite ore formed probably through extensive alteration of magnetite to hematite (martitisation). The contacts between massive magnetite and martite ore are often gradual over a few metres. (Parák and Espersen, 1965). In addition to secondary hematite, the deposit also contains another type of hematite defined as primary hematite based on the information from this study (see description under chapter Mineralogy of iron oxides).

SAMPLING AND METHODOLOGY

In this study optical microscopy, electron probe microanalyser (EPMA), and field emission scanning electron microscope with an attached energy dispersive spectrometer (FE-SEM-EDS) were used to investigate the mineralogy and mineral chemistry of the selected samples in thin sections. In addition, existing data from drill cores such as lithological logging reports and whole rock assays has also been used as background information. Data from various measurements was also available which have been carried out in the production in the several steps from mine (crude ore) to final products (iron ore pellets). For this study, the most usable were the chemical assays carried out by XRF and measurements of magnetite concentration carried out SATMAGAN.

Sampling

Sampling was conducted on diamond drill cores originated from 12 drill holes along a pre-defined profile in north–south direction in the deposit. Between two and seven samples from each drill core were selected representing various depths between four and 402 metres. However, it should be noted that as the sampling profile followed a north–south profile spatial variation of characteristics could only be investigated along that direction. For this study 50 polished thin sections have been prepared by the preparation laboratory of Erzlabor Advanced Solutions GmbH in Germany. For the analysis with either EPMA or FE-SEM-EDS 21 thin section samples were coated with a layer of carbon at the Mineralogical laboratory at Geological Survey of Finland (GTK).

Optical microscopy

Optical microscopy was performed with a Nikon Eclipse LV100POL microscope at LKAB, Kiruna using both reflected and transmitted light. The microscope also had an attached camera for optical image capturing. Optical microscopy focused on iron oxide minerals, their abundance, relative abundance of different iron oxides, and the textural variations. Limited resources were put into investigating gangue minerals in the samples to get some information about the modal mineralogy. The optical microscopy records were used to the select samples for EPMA and FE-SEM-EDS analysis.

Microanalytical tools

At the Mineralogical laboratory at Geological Survey of Finland (GTK) a Cameca SX 100 electron microprobe analyser (EPMA) was used for measurement of 14 elements, Na (K_α), Mg (K_α), Al (K_α), Si (K_α), K (K_α), Ca (K_α), Ti (K_α), V (K_α), Cr (K_α), Mn (K_α), Fe (K_α), Co (K_α), Ni (K_α), and Zn (K_α). Accelerating voltage and current were set to 15 kV and 60 nA respectively. For hematite and magnetite, the same instrument settings were used resulting in identical detection limits. However, for goethite measurements a slight tweak on the EPMA measurement was implemented resulting in small differences in detection limits compared to the hematite and magnetite measurements. At the same mineralogical laboratory, a JEOL JSM 7100F Schottky field emission scanning electron microscope (FE-SEM) with an attached Oxford instruments energy dispersive spectrometer (EDS) was used to capture elemental distribution maps for Fe, V, and Ti. Simultaneously backscattered electron (BSE) images were captured. The element distribution maps are of semi-quantitative quality showing relative but not absolute concentration of elements.

RESULTS

Mineralogy of iron oxides

Magnetite was investigated in all 50 samples by optical microscopy whilst hematite, maghemite, and goethite only occurred in some samples. The most abundant iron oxide mineral is magnetite, follow by secondary hematite in the Leveäniemi deposit. The other iron oxide minerals, ie primary hematite, maghemite, and goethite seem to be significantly less abundant. Magnetite appears mostly fine-grained (<100 µm) in all samples (Figure 1a). However, some larger magnetite grains (up to 1 mm) occur, commonly at the edges to cavities (Figure 1b). Some samples seem to contain a lot of magnetite grains with triple junctions indicting a granoblastic texture. On the other hand, these samples also contain magnetite grain boundaries without triple junctions. Furthermore, most magnetite grains appear to be anhedral with poor crystal shapes.

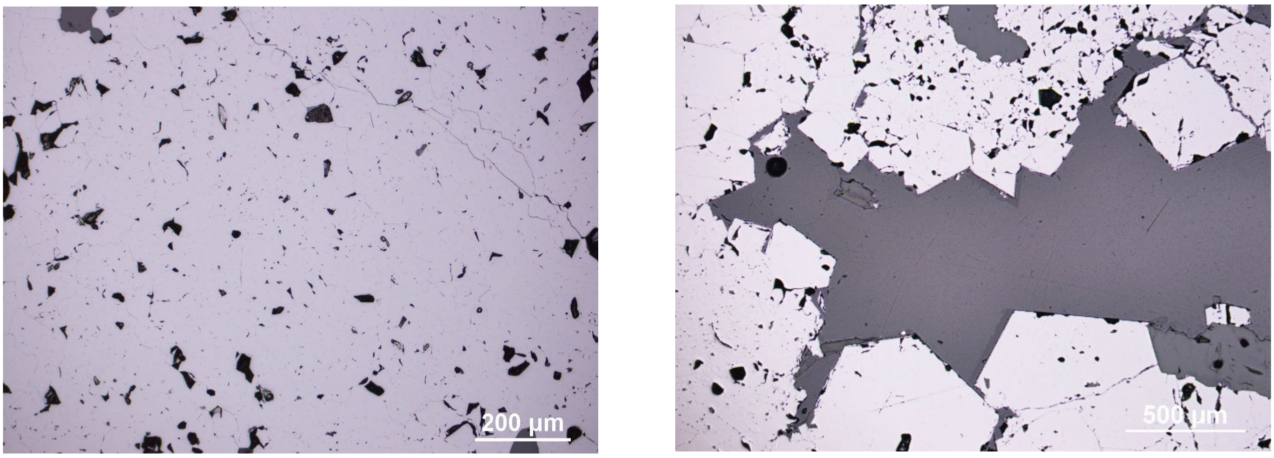

(a) (b)

FIG 1 – (a) Massive fine-grained magnetite, (b) Coarser euhedral magnetite crystals bordering a cavity.

Two distinct types of hematite have been identified in the Leveäniemi deposit. The first type is intergrown with magnetite and to lesser extent with goethite and maghemite. This type has been classified as secondary hematite. The second type of hematite seems not to be intergrown with other minerals consisting of distinct defined grains. This type has been classified as primary hematite and may show porphyroblastic texture. Similar type of porphyroblastic hematite is reported by Lund (2013) from the IOA deposit in Malmberget. Among the high-grade samples (>50 per cent Fe, n = 4046) in the geological database of drill core assays there are no samples containing less than 1 per cent Fe^{2+}.The interpretation of the results is that all samples representing high-grade ore invariably contain ferrous iron minerals. It seems that hematite only occurs mixed with other iron oxides, most likely magnetite. Maghemite was conclusively identified in two samples (81791–083 and 81791–092) only by optical microscopy. Maghemite occurs intergrown with both magnetite and hematite in connection with a possible magnetite-maghemite-hematite zonation (Figure 2).

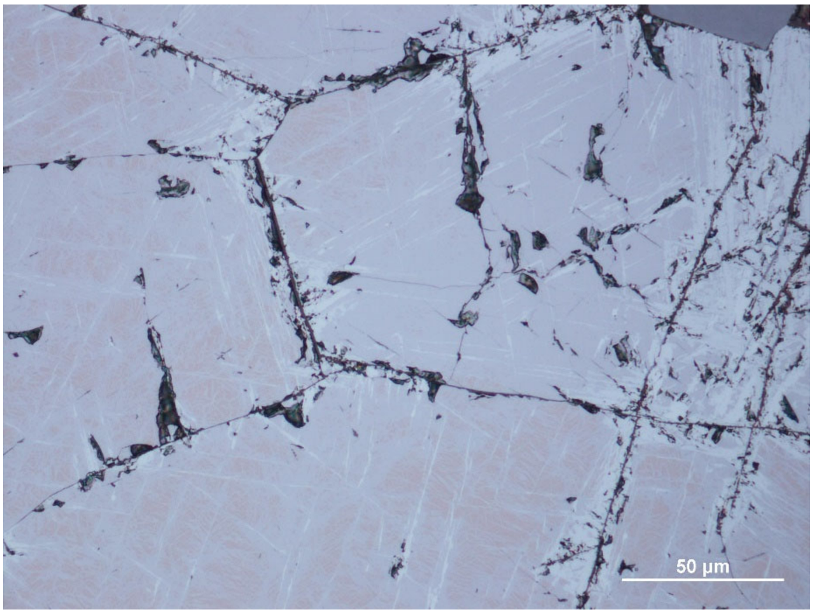

FIG 2 – Coarser magnetite (brownish) crystal partly altered to maghemite (dark grey) and hematite (light grey).

According to Colombo *et al* (1965) alteration of magnetite to maghemite is favoured in the absence of hematite. In presence of hematite, epitaxial growth of hematite is favoured instead of formation of maghemite. Furthermore, maghemite is thermally instable and transforms to hematite at higher temperature. The transition temperature is reported to vary from 250°C to 900°C (Liu *et al*, 2010; Özdemir and Banerjee, 1984). With regards to this information, it is possible that maghemite exists as an intermediary between magnetite and hematite in the Leveäniemi deposit. In addition, it should also be noted that other factors than temperature may affect the stability of the different iron oxide minerals. Goethite was mainly investigated in the samples also containing secondary hematite. Goethite seems to occur mostly associated with fractures and other deformation structures. Along these structures a zonation of goethite-secondary hematite-magnetite seems to be common. Furthermore, quantitatively goethite is far less abundant than secondary hematite. Even though the focus of this study was on the mineralogy of iron oxides some records on gangue mineralogy were also done. Quartz, hornblende, actinolite/tremolite, and biotite were the most common gangue minerals identified in the samples. Furthermore, scapolite and apatite were also identified in most samples, but they are less abundant.

Mineral chemistry of iron oxides

Magnetite

Magnetite was identified and subsequently measured in all 15 samples prepared for EPMA analysis. Between eight and 14 magnetite grains were measured in each sample. In total 180 measurements were conducted on 157 different grains. The use of an instrument set-up including time allocation per measurement and a narrow beam diameter (1 µm) led to relatively high detection limits. As a result, most or all measurements for several elements were below the detection limit (bdl). Results for the measurements of magnetite are presented in Table 1.

TABLE 1

Results of EPMA measurements of trace elements in magnetite and detection limits (ppm).

Compound	**Na_2O**	**MgO**	**Al_2O_3**	**SiO_2**	**K_2O**	**CaO**	**TiO_2**	**V_2O_3**	**Cr_2O_3**	**MnO**	**CoO**	**NiO**	**ZnO**
Maximum	*bdl*	6066	1891	*bdl*	*bdl*	734	657	3176	*bdl*	2597	*bdl*	475	*bdl*
Minimum	*bdl*	*bdl*	*bdl*	*bdl*	*bdl*	*bdl*	*bdl*	1194	*bdl*	*bdl*	*bdl*	*bdl*	*bdl*
Det. limit	859	441	419	471	247	185	180	234	427	452	369	256	997

Vanadium was the only trace element measured above the detection limit in all samples. Six elements (Mg, Al, Ca, Ti, Mn, and Ni) were measured above the detection limit in part of samples whilst the remaining measured elements (Na, Si, K, Cr, Co, Zn) were below the detection limit in all samples. Variance of trace element concentrations in a single sample were investigated by calculating the relative standard deviation (RSD) for each element measured above the detection limit. Low RSD values indicate that the concentration of an element in question is relatively homogenous at minor scale, ie a few centimetres. On the other hand, high RSD values indicate heterogeneity at minor scale. It should also be noted that RSD calculations included some measurement uncertainty. Variance for vanadium is low, (<10 per cent RSD) in all samples indicating low variations and homogeneity of vanadium concentration in magnetite at least in a single sample. For trace elements Mg, Al, Mn, and Ni the RSD is larger, over 30 per cent in some samples indicating heterogeneity of these elements in magnetite. For Ca and Ti no useable RSD could be calculated as most analyses were below the detection limit. As vanadium is of critical importance for the quality of the iron ore in the Leveäniemi deposit EPMA results were compared to whole rock assays from drill cores. It should be noted that a filter is applied for construction in the geological database selecting only samples containing >68 per cent Fe and >20 per cent Fe^{2+} (corresponding to approximately 94 wt per cent magnetite). In this kind of selected samples, the V_2O_3 concentration ranges from 1180 to 3680 ppm (n = 245). The range of vanadium concentration in magnetite measured with EPMA seems to be similar with chemical assays from drill cores.

Hematite

In contrary to magnetite, there were difficulties in identifying hematite in the EPMA measurements, of all samples. Therefore, hematite was measured in fewer samples. Hematite grains were classified prior to measurement as either primary, porphyroblastic hematite or secondary, altered hematite. Thirteen primary hematite grains in a total of eight samples were measured. Further, 19 secondary hematite grains were measured in a total of six samples. Results are presented in Table 2. It should be noted that there was a risk of mix spectra analysis when measuring the fine-grained intergrowth of secondary hematite with magnetite.

TABLE 2

Results of EPMA measurements of trace elements in primary and secondary hematite and detection limits (ppm).

Primary hematite

Compound	**Na_2O**	**MgO**	**Al_2O_3**	**SiO_2**	**K_2O**	**CaO**	**TiO_2**	**V_2O_3**	**Cr_2O_3**	**MnO**	**CoO**	**NiO**	**ZnO**
Maximum	*bdl*	1604	1787	794	*bdl*	284	86 910	3259	*bdl*	4143	*bdl*	442	*bdl*
Minimum	*bdl*	*bdl*	*bdl*	*bdl*	*bdl*	*bdl*	*bdl*	1230	*bdl*	*bdl*	*bdl*	*bdl*	*bdl*

Secondary hematite

Compound	**Na_2O**	**MgO**	**Al_2O_3**	**SiO_2**	**K_2O**	**CaO**	**TiO_2**	**V_2O_3**	**Cr_2O_3**	**MnO**	**CoO**	**NiO**	**ZnO**
Maximum	*bdl*	5324	1160	1880	*bdl*	514	*bdl*	1936	*bdl*	2430	*bdl*	518	*bdl*
Minimum	*bdl*	*bdl*	458	*bdl*	*bdl*	*bdl*	*bdl*	1279	*bdl*	*bdl*	*bdl*	*bdl*	*bdl*
Det. limit	859	441	419	471	247	185	180	234	427	452	369	256	997

Based on the results there are noticeable differences in mineral chemistry between primary and secondary hematite, especially for titanium. The highest measured titanium concentrations were approximately 87 000 ppm TiO_2 in the primary hematite. By contrast, in the secondary hematite all measurements were below the detection limit (<180 ppm TiO_2). Lund (2013) suggested that titanium preferentially partitions into hematite during recrystallisation in the Malmberget IOA deposit. The elevated concentrations of titanium in primary hematite is the result of similar formation process taking place in the Leveäniemi deposit. Generally, there are more variations in mineral chemistry of primary hematite compared to secondary hematite. The variation of mineral chemistry of primary hematite may indicate that at least two different generations occur in the deposit. Although not presented as a table in this paper it can be noted that there seems to be a correlation between trace element chemistry in magnetite and secondary hematite in the same samples. This correlation was observed especially for Mg, Al, and V. However, same kind of observation has not been noted between magnetite and primary hematite.

Maghemite and goethite

Due to the presumed rarity of maghemite in the samples and the difficulty of conclusively distinguish it from hematite under BSE conditions no maghemite grains could be measured with EPMA. In contrast, ten goethite grains could be measured in three samples. Results are presented in Table 3.

TABLE 3

Results of EPMA measurements of trace elements in goethite and detection limits (ppm).

Compound	**Na_2O**	**MgO**	**Al_2O_3**	**SiO_2**	**K_2O**	**CaO**	**TiO_2**	**V_2O_3**	**Cr_2O_3**	**MnO**	**CoO**	**NiO**	**ZnO**
Maximum	*bdl*	5946	10 402	64 357	326	5692	*bdl*	384	*bdl*	4920	*bdl*	*bdl*	*bdl*
Minimum	*bdl*	1740	8393	60 339	*bdl*	910	*bdl*	*bdl*	*bdl*	1345	*bdl*	*bdl*	*bdl*
Det. limit	830	466	418	464	229	183	175	222	415	443	343	242	976

The results reveal that goethite contains higher levels of most measured trace elements, especially Al and Si compared to other measured iron oxides, ie magnetite and hematite. On the contrary the concentration of V is significantly lower in goethite compared to magnetite and hematite. Furthermore, there is also large variations in concentration of some trace elements such as Mg and Mn.

FE-SEM-EDS elemental distribution maps

Elemental distribution maps of iron, vanadium, and titanium were created by processing 450 to 550 individual partial elemental maps per sample. The individual elemental maps were combined using a montage technique with ten per cent overlap. A similar process was used to create BSE images over the same samples (Figure 3a). This operation was kindly performed by the personnel at GTK.

These elemental maps were used to investigate the element associations among the measured elements and distribution of the elements in question. As mentioned earlier the information about the distribution and deportment of Ti and V in the iron oxides, most of all in magnetie, is of particular importance, which potentially can have a negative impact on the product quality of the iron ore pellets and further on the steelmaking process. As magnetite is the dominating iron oxide in all samples every elemental distribution map of iron is obviously affected by the strong signal of iron from magnetite (Figure 3b).

Based on the vanadium elemental maps, it can clearly be observed that no stochiometric vanadium minerals occur in the samples (Figure 3c). Because vanadium only is present at a low background level it can be concluded that is occurs as a trace element in the crystal structure of other minerals. In magnetite, vanadium typically occurs mainly as V^{3+} replacing Fe^{3+} in the crystal structure (Bowles *et al*, 2011).

It can be noted that there seems to be an iron-vanadium correlation as higher concentrations of vanadium spatially coincide with high concentrations of iron when comparing the iron and vanadium elemental maps (Figure 3d). The observed correlation is interpreted as that the iron signal contributor, ie magnetite is the primary mineral in which vanadium occurs. However, based on the elemental distribution maps of vanadium and iron small amounts of vanadium can also incorporate in other minerals (Figure 3c).

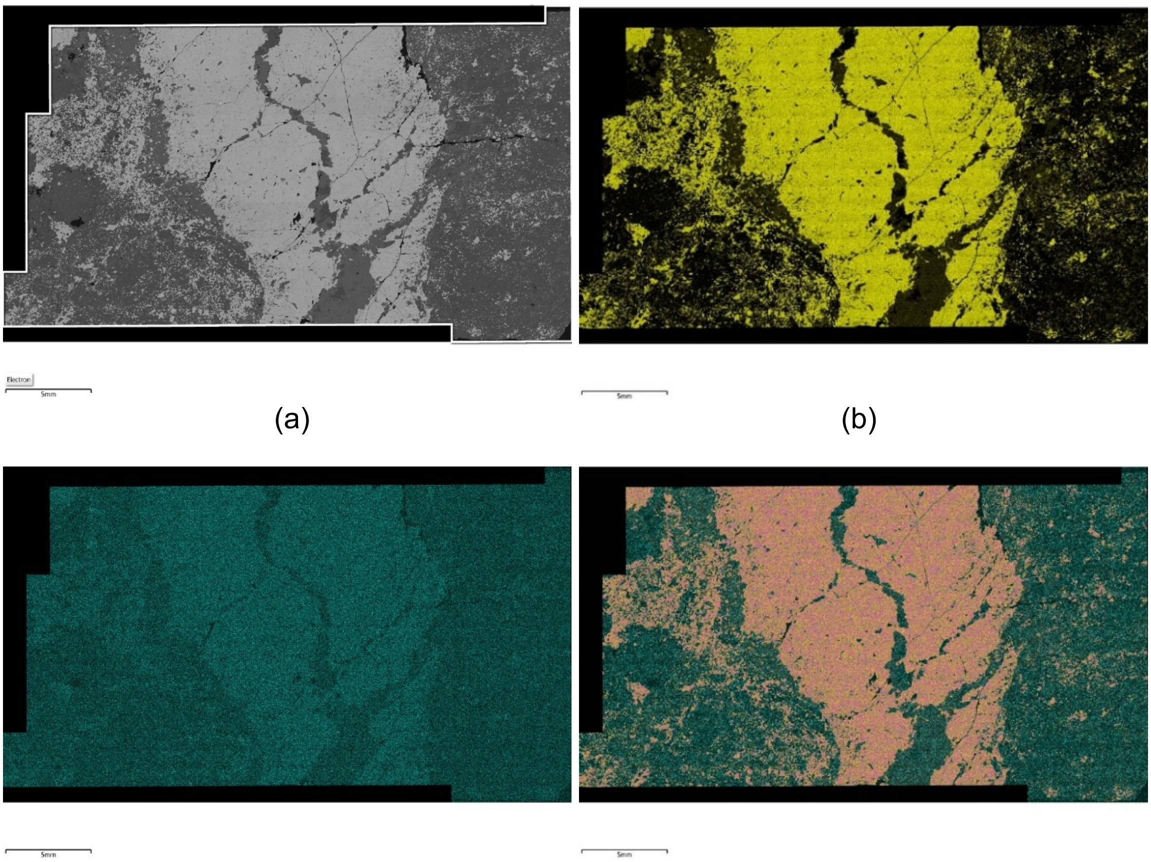

(a) (b)

(c) (d)

FIG 3 – BSE image and elemental distribution maps created by FE-SEM-EDS (scale = 5 mm). (a) BSE image over entire thin section, (b) Elemental distribution map of iron (yellow), (c) Elemental distribution map of vanadium (turquoise), (d) Combined elemental map of iron and vanadium (pink).

Based on the measurements it can be concluded that titanium seems to occur in two different modes throughout the samples. In four of the samples, titanium occurs both at a low background level and at a high level in spot locations (Figure 4a). It is interpreted that the high levels in spot locations correspond to stochiometric titanium minerals, being most probably ilmenite and rutile based on the investigations with optical microscopy. By combining the titanium and iron elemental maps a further observation can be made. The assumed ilmenite and rutile grains seem to occur in association with magnetite and not in association with other gangue minerals (Figure 4b). However, in two samples titanium seems to occur at background levels only. That can be interpreted that titanium is incorporated in other minerals instead of occurring as stochiometric titanium minerals in those samples.

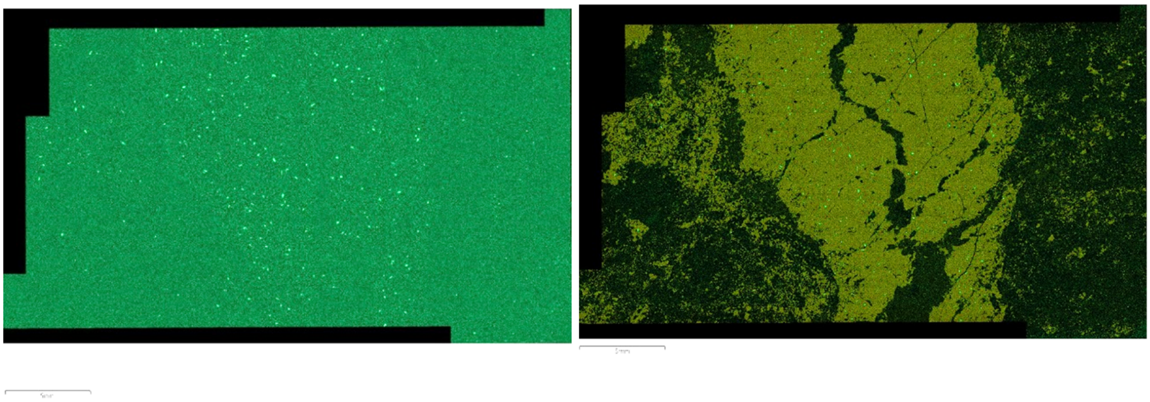

(a) (b)

FIG 4 – Elemental distribution maps created by FE-SEM-EDS (scale = 5 mm). (a) Elemental distribution map of titanium (green), (b) Combined elemental distribution map of iron (yellow) and titanium (green).

DISCUSSION AND CONCLUSIONS

This study had two objectives, both which are directly related to the production of crude ore and iron ore pellets at the Leveäniemi site. Especially the presence and coexistence of multiple iron oxide minerals, ie magnetite, hematite, maghemite, and goethite can be regarded as a clear challenge for mining operations.

Based on the results of optical microscopy there are two different generations of hematite classified as primary and secondary hematite in this study. Of which secondary hematite is much more abundant which can be regarded as an alteration product of magnetite. This can be expected to support the fact that the mineral chemistry of trace elements is similar in magnetite and secondary hematite. Secondary hematite occurs as fine-grained or very fine-grained intergrowth with magnetite often growing inwards from the edges of precursor magnetite grains. Furthermore, the mineral chemistry of trace elements is similar in magnetite and secondary hematite. The alteration process of magnetite to hematite has not been investigated in detail in this study. However, it can be noted that both non-redox and redox (oxidation) processes have been proposed by different authors such as Ohmoto (2003) and Mücke and Cabral (2005).

As mentioned earlier magnetite currently is the only mineral of value in the deposit, while hematite is regarded as waste. Therefore, the liberation and separation of magnetite and hematite is challenging for the mineral processing, because of the fine-grained intergrowth of these minerals. However, it should be noted that also hematite may become a valuable mineral for production in the future. Therefore, there in an obvious need to carry out more process mineralogical test work and liberation analyses both in laboratory, pilot, and full scale to study the separation of magnetite and hematite. This information will be crucial in the case of developing a new concept for the beneficiation process or applying additional beneficiation steps in the current process in the concentration plant.

Maghemite was first identified in this study in the Leveäniemi deposit. However, it is still unclear how much maghemite the deposit contains because maghemite cannot be quantified with the analytical methods currently used in the mining operations for grade control. Future improvements including the introduction of regular X-ray diffraction spectrometry (XRD) analyses are expected to improve the more detailed quantification of different iron oxide minerals resulting in better process monitoring and quality control. In particular, maghemite can be expected to cause problems in quality monitoring mineral processing. Maghemite is like magnetite ferrimagnetic holding a net magnetic moment (Bowles *et al*, 2011). This is believed to cause problems as maghemite will be concentrated by magnetic separation processes ending up in the magnetite concentrate. The problem may be further expanded during the thermal treatment step of pelletisation. In contrast to magnetite, maghemite does not undergo exothermic oxidation to hematite as the minerals share the same chemical formula, Fe_2O_3. Further, this difference in behaviour may cause disturbances in the energy balance during the thermal treatment having adverse effects on the quality on the finished pellets.

Not only the iron grade but also the concentration and deportment of impurities in the crude ore such silica, phosphorus, and alkali (Na + K) are becoming increasingly important. Essential within this context is especially the information about distribution and deportment of vanadium and titanium in the Leveäniemi deposit as they can have impact on steelmaking process. In addition, also some other trace elements such as chromium, cobalt, nickel, and copper can be of importance, especially for specialised iron ore products in the future.

Internally it has been known that the vanadium is the most problematic trace element for the quality of the iron ore pellets. Until now, there has been sparse information about the distribution and deportment of vanadium in the Leveäniemi deposit. Based on this study it can be concluded that there are no stochiometric vanadium minerals in the deposit. Most of vanadium is incorporated in the crystal structure of magnetite, minor amounts of vanadium occur especially in titanite. Therefore, vanadium can be problematic for production because it is enriched with magnetite in the beneficiation process ending up in the magnetite concentrate (pellet feed). The target value of V_2O_3 in iron ore pellets lies between 0.16 to 0.21 wt per cent depending on the type of pellets (LKAB, 2019). Furthermore, an important result of this study was that the concentration of vanadium varies in different parts of the deposit needing enlarged and more detailed investigations in the future.

As in the case of vanadium there is also a target value of 0.18 wt per cent TiO_2 in the iron ore pellets (LKAB, 2019). In contrast to vanadium there are stochiometric titanium minerals in the Leveäniemi deposit of which ilmenite and rutile are the most common. In addition, especially primary hematite contains significant concentrations of titanium. Even though there are low concentration of titanium in the crystal structure of magnetite the very fine-grained intergrowth of magnetite with ilmenite and rutile is a clear challenge for mineral processing to remove Ti-bearing minerals during beneficiation process. When conducting process mineralogical test work as recommended special attention should be taken to the separation and liberation of Ti-bearing minerals and magnetite.

Moreover, enlarged process mineralogical test work and future investigative studies are recommended to use microanalytical tools with lower detection limits. Which allows the distribution and deportment of more trace elements of importance can be studied.

ACKNOWLEDGEMENTS

The authors would like to acknowledge LKAB for supporting this research and for the opportunity to present this paper. The authors would also like to thank Mr Michael Stoll for preparing the polished thin sections at Erzlabor Advanced Solutions GmbH. The authors would also like to send special thanks to Dr Marja Lehtonen and Mr Lassi Paakkonen at the Mineralogical laboratory at Geological Survey of Finland (GTK) for analysing the samples with FE-SEM-EDS and EPMA and for processing the data and, in particular for their valuable comments.

REFERENCES

Bergman, S, Kübler, L and Martinsson, O, 2001. Description of regional geological and geophysical maps of northern Norrbotten county (east of the Caledonian orogen), 110 p (SGU – Geological Survey of Sweden).

Bergman, T and Hellström, F, 2020. Inventory of mineral resources in northeastern Norrbotten County, Sweden, SGU Report 2020–09, 161 p with Appendices (SGU – Geological Survey of Sweden).

Bowles, J F W, Howie, R A, Vaughan, D J and Zussman, J, 2011. *Non-silicates: Oxides, Hydroxides and Sulphides, Rock-forming minerals*, vol 5A (second edition), 920 p (The Geological Society: London).

Boyd, R, Bjerkgard, T, Nordahl, B and Schiellerup, H, (eds) 2016. *Mineral Resources in the Artic*, 482 p (NGU – Geological Survey of Norway).

Colombo, U, Gazzarrini, F, Lanzavecchia, G and Sironi, G, 1965. Magnetite oxidation: A proposed mechanism. *Science*, 147(3661):1033–1033.

Engström, K, 2018. *Sampling in iron ore operations: Evaluation and optimisation of sampling systems to reduce total measurement variability*. PhD-thesis, 280 p with 7 papers, University of Aalborg, Denmark.

Geijer, P, 1910. *Igneous rocks and iron ores of Kiirunavaara, Luossavaara och Tuolluvaara*. Scientific and practical researches in Lapland arranged by Luossavaara-Kiirunavaara Aktiebolag, Stockholm, 278 p.

Geijer, P, 1931. The iron ores of Kiruna type: geographical distribution, geological characters and origin, *Sveriges Geol Unders, Ser C (367),* 39 p.

Liu, X, Shaw, J, Jiang, J, Bloemendal, J, Hesse, P, Rolph, T and Mao, X, 2010. Analysis on variety and characteristics of maghemite, *Science China Earth Sciences*, 53(8):1153–1162.

LKAB, 2019. Products 2019. LKAB handbook, 86 p.

Lund, C, 2013. *Mineralogical, chemical and textural characterisation of the Malmberget iron ore deposit for a geometallurgical model*, PhD-thesis 190 p with 4 papers, Luleå University of Technology, Sweden.

Martinsson, O, Billström, K, Broman, C, Weihed, P and Wanhainen, C, 2016. Metallogeny of the northern Norrbotten ore province, northern Fennoscandian Shield with emphasis on IOCG and apatite-iron ore deposits, *Ore Geology Reviews*, 78:447–492.

Mücke, A and Cabral, A R, 2005. Redox and nonredox reactions of magnetite and hematite in rocks, *Geochemistry*, 65(3):271–278.

Ohmoto, H, 2003. Nonredox transformations of magnetite-hematite in hydrothermal systems, *Economic Geology*, 98(1):157–161.

Özdemir, Ö and Banerjee, S K, 1984. High temperature stability of maghemite (γ-Fe_2O_3). *Geophysical Research Letters*, 11(3):161–164.

Parák, T and Espersen, J, 1965. *Leveäniemi järnmalmsfyndighet*, 85 p (SGU – Geological Survey of Sweden).

Spatial distribution of major, minor and trace elements in iron ores, using micro-XRF technology

N J Potter[1,2], J M F Clout[3] and N W Brand[2,4]

1. Spectral Geologist, Portable Spectral Services, West Perth WA 6005. Email: njpotter@portaspecs.com
2. School of Earth Sciences, The University of Western Australia, 35 Stirling Highway Perth, Crawley, Western Australia 6009.
3. FAusIMM, Principal, Clout Mining, Nedlands WA 6009. Email: john@cloutmining.com
4. Spectral Geologist, Portable Spectral Services, West Perth WA 6005.

ABSTRACT

The increasing demand for iron ore with low concentrations of trace elements, puts increasing pressure on iron ore producers for high-quality material. Understanding the mineralogy, petrography, chemistry, and mineral association of iron ore deposits is becoming increasingly important to provide iron ore products that meet the ever-increasing standards of steel mills. Limited attention has been paid to documenting new orebodies beyond bulk RC drill chip assays and product specification data. Therefore, limited information is known about the spatial distribution of minor and trace elements at the hand specimen scale, and elemental deportment within different ore and gangue minerals. In this study, samples from high-grade microplaty hematite, supergene-enriched martite-goethite and hematite iron ores are examined for their elemental and mineral associations. These samples contain distinctive minor and trace element distributions, with the mapping of deleterious elements (eg Zn, As, Cu) enabling the deportment and abundance within the ore and gangue minerals to be assessed. Results from this study show a diverse range of minor and trace mineralogy that are present in typical iron ore samples, in abundances below the detection limit of routine XRD scans, that host the deleterious elements, including but not limited to, sphalerite (Zn and S), chalcopyrite (Cu and S), xenotime (P and Y), apatite (P and Ca), cryptomelane (K and Mn), barite (Ba and S), alkaline feldspar (K, Al and Si) zircon (Zr and Si) and chromite (Cr and Al). The presence of these minerals and associated deleterious elements, even at low concentrations, has implications for producers, with the ongoing restrictions and tightening of environmental constraints in shipped iron ore products. By understanding the distribution and location of these elements within the iron ore, steps can be considered to maintain increasingly higher quality iron ore supply around the world.

INTRODUCTION

Steel mills have an increasing interest in minor and trace element levels in raw iron ore materials for ironmaking. In addition to environmental concerns, minor and trace elements in iron ores can be concentrated in sinter plant and blast furnace dust streams, blast furnace slag, and in some cases present in the hot metal at the steelmaking stage (Clout and Manuel, 2015). For instance, as shown in Table 1, copper and chlorine in iron ores assists in catalysing the formation of toxic dioxins from carbon derived from coke during the sinter process (Nakano, Morii and Sato, 2009) and so can have a significant environmental impact; and iron ores with elevated Cu also require blending with low Cu iron ores since Cu adversely impacts the physical qualities of finished steel. Steel mills are seeking continuous improvements via a reduction of deleterious minor and trace elements in process dust streams and especially in blast furnace slag and the hot metal. In many cases steel mills have placed upper concentration limits on various elements and their oxides for iron ore concentrates, and fine and lump ores, above which the products are quite likely to be rejected or penalties imposed for use (Table 1). The maximum permissible levels for many trace elements have almost halved over the last 20 years (*cf* Clout, 1998) and this trend of reducing maximum limits is likely to continue as high quality ores diminish.

TABLE 1

Impact of deleterious gangue and minor/trace elements on downstream process performance. Modified from Clout and Manuel (2015).

Deleterious element/mineral	**Exceedance level**	**Geological Control**	**Process Stage ***	**Effects**
Sideritic carbonates	>5%	Carbonate BIF or hydrothermal carbonate alteration, extent of replacement/leaching	Sintering and pelletising	Lowers strength of sinter and pellets due to increased porosity once carbonates are calcined (CO_2 driven off above 1000°C), stabilises more FeO
Clays/Al_2O_3	>6% / >3.2%	Shale bands and Al-silicate content of BIF host	Sintering, pelletising and BF	Lowers strength of sinter and pellets, increases fuel rate and increases BF slag viscosity
Alkalis	K_2O + Na_2O >0.10%	K_2O: BIF micas, Na_2O: hypersaline groundwater, Na-feldspar	Sintering, pelletising, BF	Lowers melt temperature, corrosion of BF refractory bricks, forms scaffolds on upper BF walls
As	>50 ppm	Hydrothermal alteration or black shales	Agglomeration, BF	Concentrates in dust in process waste gas, removal cost, environmental issue
P	>0.10%	Apatite in BIF, extent of supergene leaching of P	Steelmaking	Removal cost, increase in CO_2 emissions
Base and heavy metals (eg Zn, Pb, Hg, Cd)	>50 ppm	BIF host, hydrothermal source	BF, sintering	Removal costs, especially reprocessing or disposal of base and heavy metal-rich dusts
Al_2O_3	>3.2%	Shale bands and Al-silicate content of BIF host	Sintering, pelletising, BF	Higher levels progressively increase melt viscosity hence increase fuel rates
SiO_2	>6%	BIF and shale, extent of supergene leaching	Sintering, BF	Increases the amount of slag through increased use of limestone, since CaO/SiO_2 ratio ~1.8–2.1
Mn	>0.9%	Remobilisation of Mn from impure BIF dolomite above or below mineralisation	Steelmaking	Although some types of steel require Mn, excess levels require dilution with low Mn-bearing ores to maintain steel properties
Cu	>80 ppm	BIF host, hydrothermal source	Sintering, steelmaking	Catalyses dioxin formation during sintering, must be diluted with low Cu ores to maintain steel quality
Cl	>500 ppm	Hypersaline groundwater	Sintering, BF	Increased dioxin (toxic) and NO_x emissions, reduces efficiency of electrostatic dust precipitators and increase BF refractory wear
Se	>30 ppm		Sintering, BF	Concentrates in dusts, removal cost, environmental issue
S	>0.08%	BIF host, organic S in hard cap or near-surface martite-goethite	Sintering, BF	Increased SO_x emissions and higher MgO levels required to partition S into BF slag
Ti	TiO_2 >1.0%	Shale bands, ilmenite from intrusive, or iron sand	Sintering and pelletising	Lower physical strength of pellets and sinter, significantly increases fuel rate for sintering and BF

Major elements assessed during routine assays and product specification data include iron, aluminium, silicon, sulfur and phosphorous to help determine the abundance of typical gangue minerals and deleterious elements within the ore (Table 2). However, not all deleterious elements are routinely analysed by fusion XRF (eg Cd, Hg), or the analytical method detection limits are too high (eg >50 ppm), creating issues for steel makers and manufacturers further down the supply chain. The quality of raw iron ores and its viability in the global market is determined by its chemical composition. Therefore, with the increasing demand for high quality ore the importance of understanding the abundance, association and origin of any deleterious elements cannot be overstated.

TABLE 2

Common iron ore and gangue mineral definitions from Clout and Manuel (2015).

	Chemical Formula	Description
Ore Mineral		
Hematite	Fe_2O_3	Iron oxide
Magnetite	Fe_3O_4	Primary iron oxide
Goethite	$FeOOH$	Most abundant iron oxyhydroxide with three subtypes: yellow ochreous has very high microporosity, very high saturation moisture and chemical impurities; brown, the most common variant is stoichiometric; whilst vitreous is glassy and contains 2–9% SiO_2 + Al_2O_3, either as an impurity or as submicron inclusions of quartz
Maghemite [a]	$Fe^{3+}[Fe^{3+}_{1.67}[]_{.33}]O_4$	Intermediate iron oxide
‘Kenomagnetite’[b]	$Fe_3\text{-}x()xO_4$	Intermediate metal-deficient phase between magnetite and maghemite
‘Martite’	Fe_2O_3	Hematite which has replaced primary magnetite
‘Hydrohematite’[c]	$Fe_{(2-x)/3}(OH)_xO_{3-x}$	A defect solid solution where OH^- ions replace oxygen
Gangue Mineral		
Quartz	SiO_2	Common oxide of silicon
Kaolinite	$Al_4(Si_4O_{10})(OH)_8$	Clay, finely particulate
Gibbsite	$Al(OH)_3$	Clay, often crystalline
Minnesotaite	$(Mg,Fe)_3Si_4O_{10}(OH)_2$	Common Fe-Mg silicate in iron formations
Stilpnomelane	$(K,Na,Ca)_{0.6}(Mg,Fe^{2+},Fe^{3+})_6Si_8Al(O,OH)_{27}.2\text{–}4H_2O$	Common silicate in iron formations
“Chlorite”	$(Fe,Al,Mg)_{12}[(Si,Al)_8O_{20}](OH)_{16}$	Silicate
Berthierine	$(Fe^{2+},Fe^{3+},Al,Mg)_{2\text{–}3}(Si,Al)_2O_5(OH)_4$	Fe silicate
Chamosite	$(Fe^2,Mg,Fe^{3+})_5Al(Si_3Al)O_{10}(OH,O)_8$	Fe silicate
Pyrite	FeS_2	Iron sulfide
Pyrolusite	MnO_2	Manganese dioxide
Siderite	$FeCO_3$	Fe-carbonate
Ankerite	$Ca(Fe, Mg, Mn)(CO_3)_2$	Ca-Fe-Mg-Mn carbonate
Dolomite	$CaMg(CO_3)_2$	Ca-Mg carbonate

() represents cation vacancies. Formulae are from Deer, Howie and Zussman (1992) unless indicated otherwise.

[a] From Waychunas (1991).

[b] From Morris (1985).

[c] From Wolska and Szajda (1985).

[d] From Miyano (1987).

Whilst the levels of many minor and trace elements are generally low to very low in Australian iron ores from the Pilbara, less attention has been paid to documenting new orebodies beyond routine bulk RC drill chip sample XRF assays, loss on ignition and product specification data. Therefore, information on the spatial distribution of minor and trace elements, and elemental deportment within different ore and gangue minerals is limited or unknown at the hand specimen to orebody scale. Understanding the mineralogy and ore textures is important as both parameters can affect the metallurgical process performance during crushing, screening, beneficiation, and agglomeration of fine ores.

In this pilot study we show trace element chemistry, mineralogy and deportment from typical run-of-mine iron-ore deposits. These samples have been analysed using micro-XRF technology as a non-destructive method to rapidly detect deleterious elements, their mineral hosts, texture and deportment and has highlighted previously unidentified or underreported elemental and mineralogy characteristics.

METHODOLOGY

Samples from three banded iron formation (BIF)-hosted iron ore deposits were analysed including:

- high-grade microplaty hematite (mplH) iron ore, interpreted as of hypogene origin,
- Supergene enriched hematite iron ore and,
- Supergene enriched martite-goethite (M-G) iron ore.

The martite-goethite iron ore has been separated into six size fractions (+6.3 mm, -6.3 +4 mm, -2 +1 mm, -600 +300 µm, -125 +63 µm and -38 + 0 µm) to assess how the concentration of gangue minerals and deleterious elements differs with particle size.

Mapped geochemical data were acquired on polished samples using a bench-top BRUKER Nano Analytics 2D-micro-XRF spectrometer (BRUKER M4 TORNADO). The instrument has a 50kV 30-Watt Rh anode target, two simultaneously operating 30 mm^2 XFlash® silicon drift detectors via beryllium windows and poly-capillary optics that can focus a beam spot size down to ~18 µm. The samples were measured under vacuum at 20 mbar using a 30 µm step size with the standard conditions of analysis at 30 ms per pixel, 45 kV acceleration voltage, 600 µA current and no filter.

Elements ranging from sodium (Na) to uranium (U) were simultaneously measured with quantification limits ranging from percentages to parts per million. The two-dimensional element maps are gridded by pixel intensity. The instrument collects an entire X-ray spectrum for each pixel in the grid, with pixel colour intensity proportional to the counts recorded in the X-ray spectrum channel for that element. Evaluation of the data and preparation of mineral distribution maps was undertaken using BRUKER's Advanced Mineral Identification and Characterisation Software (AMICS). For mineral identification, full X-ray spectra are evaluated and compared to a library of known characteristic spectra, using fingerprinting for a best-match mineral classification. Mineral classification is then refined using clustering techniques or manual selection of the X-ray spectral features.

RESULTS

Microplaty hematite ore

The microplaty hematite ore (Figure 1a) is characterised by light martite-rich and darker microplaty hematite micro – and macrobands of varying thickness, with an increasing abundance of microplaty hematite in the right section of the sample. The aluminium (Al) map (Figure 1b) identifies the presence of potential kaolinite-rich microbands (~0.6 per cent), with a gradual increase in the prevalence of these Al-rich microbands towards the right section of the sample and along microfractures. Vanadium is concentrated within the hematite layers in the right section of the sample but does not correlate strongly with either the microplaty hematite or martite-rich bands (Figure 1a, 1c). Small vanadium-rich-bearing grains are disseminated throughout the sample (Figure 1c). Other elements and associated minerals detected in the sample include silica (quartz 0.53 per cent), calcium (calcite 0.075 per cent; Mn-bearing dolomite 0.002 per cent), zinc (sphalerite 0.031 per cent), sulfur (pyrite 0.01 per cent) and, calcium and sulfur (calcium-sulfate 0.004 per cent) along with very low concentrations of deleterious elements including nickel, lead, and copper (Figure 1d).

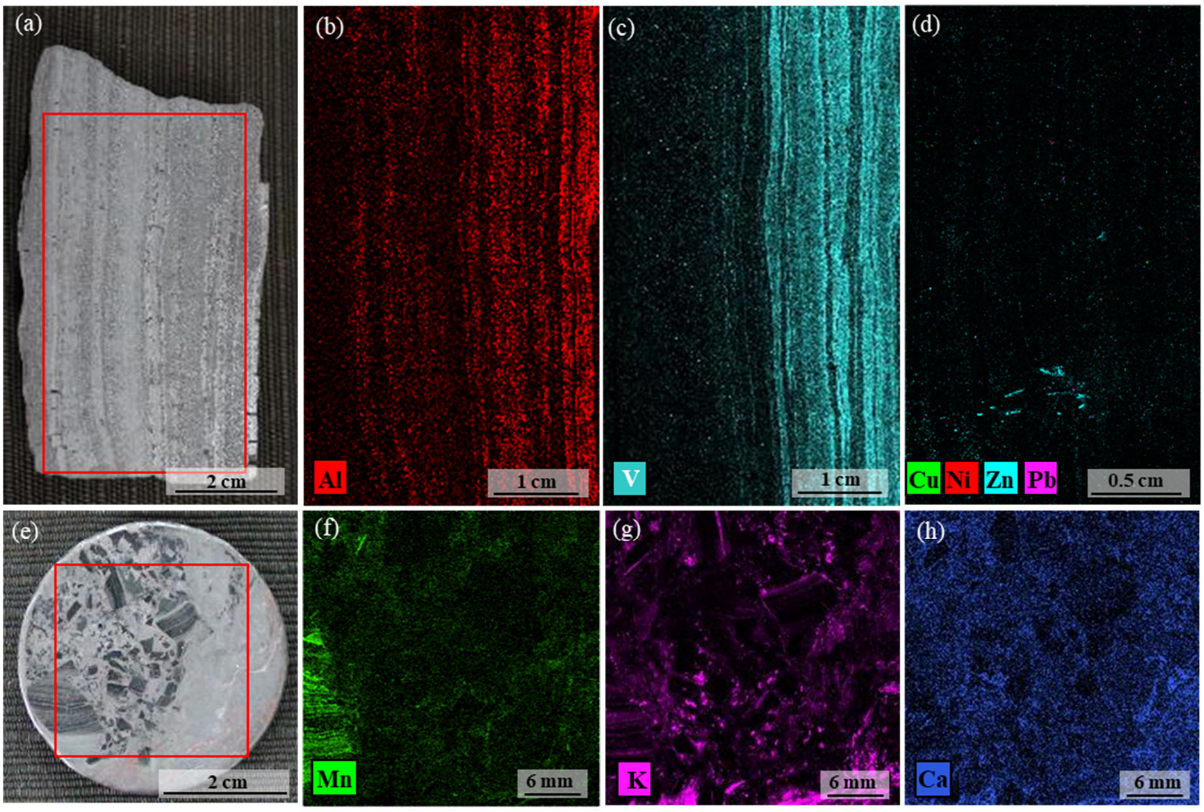

FIG 1 – (a) photograph of micro-platy hematite (b-d) micro-XRF elemental maps, highlighting the presence of base metals (e) photograph of BIF-hosted supergene enriched iron ore (f-h) micro-XRF elemental maps highlighting the presence of feldspar.

Supergene enriched hematite iron ore

The BIF-hosted supergene enriched hematite iron ore sample is composed of angular fragments of laminated and massive hematite iron ore in a fine-grained Fe-rich matrix (Figure 1e). The manganese map (Figure 1f) identifies a block of microbanded martite-hematite from the original BIF that is not visually identifiable. The matrix is composed of supergene hematite along with gangue minerals including a potassic feldspar (2.77 per cent; Figure 1g), quartz (0.5 per cent), Mn-bearing dolomite (0.014 per cent) and gibbsite (0.011 per cent), with trace element concentrations of zirconium, calcium, manganese, copper and nickel. The calcium in the matrix is remanent of the parental dolomitic material (Figure 1h) that was largely replaced during the supergene alteration process. Overall, the matrix has low concentrations of deleterious elements but is slightly high in certain gangue minerals, mainly potassic feldspar (2.77 per cent).

Martite-goethite ore

The various size fractions of martite-goethite ore (+6.3 mm through to -38 μm) represent a typical run-of-mine sample, thus the mineral phases their abundance and overall trace element concentrations will vary. Table 3 shows twenty-four (24) minerals identified within these samples, several of which are not included as well-known gangue minerals in Table 2. We observe that several of the mineral phases are common throughout the size fractions including kaolinite and rutile whilst the deleterious elements and their mineral host preferentially report in the finer size fractions.

TABLE 3

Mineralogy of martite-goethite size fractions.

Size fraction	+6.3 mm	+6.3–4 mm	+2–1 mm	+600–300 µm	+125–63 µm	+63–38 µm	>38 µm
	Area%						
Alkali feldspar	n/d	n/d	0.543	0.169	0.107	0.074	0.010
Kaolinite	3.497	0.146	3.229	0.658	0.306	0.098	0.025
Apatite	n/d	n/d	n/d		0.014	0.031	0.002
Barite	n/d	n/d	n/d	0.037	0.010	0.013	n/d
Calcite	n/d	n/d	n/d	0.203	0.371	0.363	0.118
Mn-bearing dolomite	n/d	n/d	n/d		0.008	0.008	n/d
Chromite	n/d	n/d	n/d	0.001	0.011	0.019	0.007
Cryptomelane	0.006	0.004	n/d	0.023	0.012	0.004	n/d
Cu-bearing phase	0.004	n/d	n/d	0.001	0.001	0.024	0.059
Hematite	74.670	95.095	93.792	94.852	96.343	96.759	99.111
Ti-enriched shale	8.796	n/d	n/d	0.231	n/d	n/d	n/d
Ochreous geothite	5.345	2.522	0.413	2.187	1.739	1.716	0.244
Pyrite	n/d	n/d	n/d	0.005	0.009	0.034	0.005
Rutile	0.094	0.034	0.242	0.370	0.262	0.313	0.166
Mn-enriched iron ore	3.928	0.609	0.490	0.364	n/d	n/d	n/d
Co-bearing phase	0.832	n/d	n/d	n/d	0.003	n/d	n/d
Ni-bearing phase	n/d	n/d	n/d	n/d	n/d	0.008	n/d
Plagioclase	n/d	0.004	0.639	n/d	n/d	n/d	n/d
Pyrolusite	1.895		0.211	0.293	0.479	0.514	0.231
Quartz	0.910	1.577	0.435	0.605	0.293	n/d	n/d
Titanite	n/d	n/d	n/d	n/d	0.010	0.002	0.008
Xenotime	0.002	0.003	0.002	0.002	n/d	0.003	n/d
Zircon	0.020	n/d	n/d	n/d	0.001	0.005	0.004
Zn-bearing phase	n/d	0.003	n/d	n/d	0.020	0.013	0.010

Visual inspection of the >6.3 mm grain size fraction shows the presence of hematite, brown and yellow ochreous forms of goethite, and red and white shale grains (Figure 2a). The geochemical maps show the additional presence of quartz and pyrolusite, and within the large hematite grains are smaller rutile, xenotime (P and Y) and Mn-bearing dolomite grains, along with minor Zr and Cu-bearing grains (Table 3). The pyrolusite grain has Ba-Mn-bearing and Co-bearing microbands running through the grain (Figure 2b). The white shale grain is Ti-bearing and has a smattering of K within the structure (Figure 2c). The presence of Ti, Al, Si, Zr and minor K within the kaolinitic shale grain is consistent with the interpreted composition of an original ash microband (K feldspar-titanomagnetite-pyroxene) in the BIF prior to the supergene enrichment process, with the presence of titanium reflecting the alteration of titanomagnetite and the presence of potassium reflecting the remnants of alkali feldspar fragments within the kaolinite. The red grain (Figure 2a, uppermost) was initially identified visually as shale but geochemical mapping confirmed the grain to be nanoplaty hematite due to the abundance of Fe, extremely fine highly microporosity and lack of Al and Si within the structure (Figure 2c). This highlights the importance of conducting 2D chemical analyses to ensure samples are being accurately characterised. The misidentification of red shale is most likely due to the highly microporous nanoplaty hematite texture, which typically has a brick-red colour (Clout, 2006).

In the -6.3 +4 mm grain size fraction hematite and brown and ochreous goethite are visually identified along with blue-grey hematite/martite (Figure 2d). The presence of plagioclase, cryptomelane (Figure 2g to 2i) and Zn-bearing grains within hematite were identified using geochemical and mineralogy maps (Table 3). Additionally, a recemented DID detrital particle is identified within the grain mount, with the Ti map highlighting the presence of a DID texture with a Ti-rich rim surrounded by recemented smaller DID detrital grains (Figure 3f). Therefore, the use of titanium can assist with fingerprinting samples and the identification of potential sample contamination. Based on the geochemistry and mineralogy maps, the -2 +1 mm particle size fraction has a similar composition to the larger fractions, with the additional identification of alkali feldspar and absence of deleterious base metals (Figure 3; Table 3).

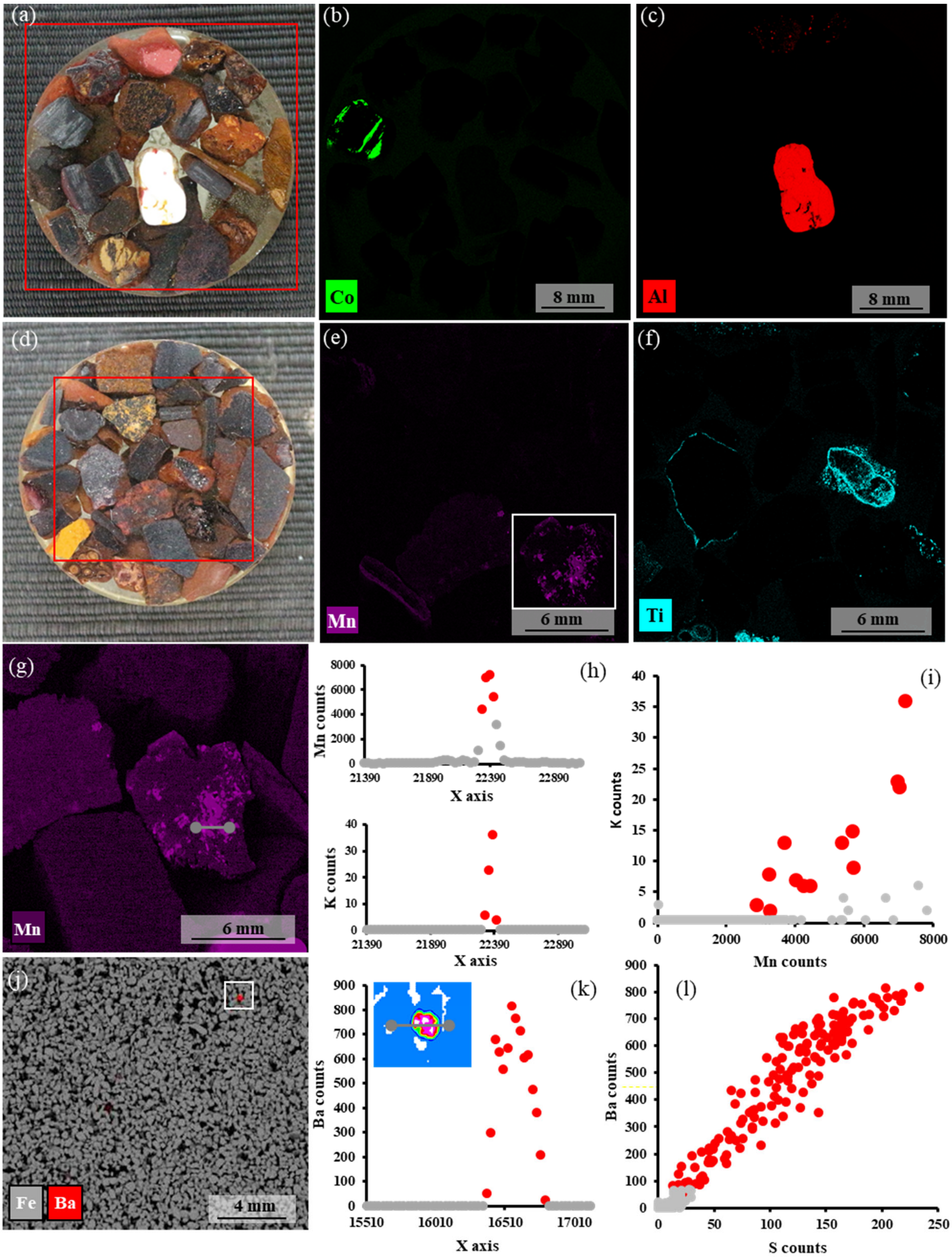

FIG 2 – Micro-XRF element maps of martite-goethite iron ore: (a) photograph of the +6.3 mm grain size fraction, note the appearance of red and white shale; (b, c) micro-XRF maps of the +6.3 mm size fraction highlighting the presence of nano-platy hematite and Ti-bearing shale; (d) photograph of the -6.3+4 mm grain size fraction; (e, f) micro-XRF maps of the -6.3+4 mm size fraction, highlighting the presence of pyrolusite and a recemented DID grain; (g) Mn heat map showing the identification of cryptomelane within the 6.3+4 mm size fraction; (h) cross-section of K and Mn abundance across the cryptomelane grain; (i) K and Mn element plot, supporting the identification of cryptomelane; (j) Ba and Fe heat map showing the identification of barite within the 600–300 µm size fraction; (k) heat map of Ba showing the cross-section; (l) Ba counts across the Ba-rich grain; (m) Ba and P scatter plot, supporting the identification of barite.

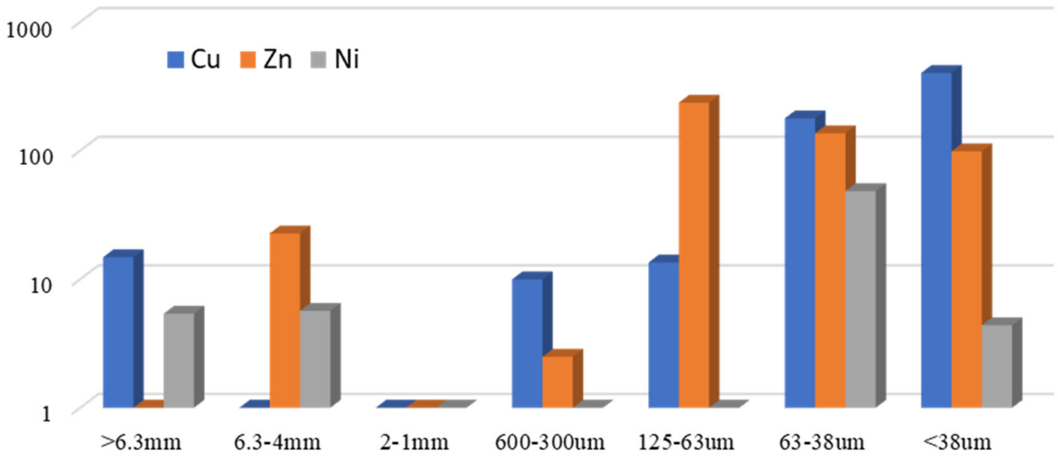

FIG 3 – Abundance of deleterious elements identified in each size fraction of the martite-goethite ore.

There is a distinct shift in composition between the +1 mm particle size fraction and -1 mm size fraction. The -600 +300 μm size fraction is composed of hematite, brown and ochreous goethite, pyrolusite, kaolinite, quartz, rutile, alkali feldspar and xenotime, like the larger grain fractions. However, the addition of calcite, barite (Figure 2j to 2l), pyrite, chromite and chalcopyrite in the smaller size fraction shows a shift in the phases that are preserved at various sizes (Figure 3; Table 3). In finer size fractions, the relative abundance of kaolinite, Mn-enriched hematite, quartz and alkali feldspar decreases, and the presence of rutile, Cu-bearing and Zn-bearing phases increases. In the -125 +63 μm size fraction we observe the addition of Mn-bearing dolomite, titanite, zircon and apatite and a decrease in xenotime. This size fraction also contains a particle of the Co-enriched pyrolusite phase identified in the >6.3 mm size fraction. The size fractions -63 +38 μm and <38 μm have similar mineral phases to -125 +63 μm size fraction, except for the loss of quartz. The main differences between these two samples are the abundances of various gangue minerals (Table 3).

DISCUSSION

Results of this study have mapped the spatial distribution of minor and trace deleterious elements and elucidated on the elemental deportment, host mineralogy and abundance within different run-of-mine iron ore types and gangue minerals. The source of many deleterious elements in iron ore concentrates, fine, and lump ores is believed to often be inherited from the parent BIF mineralogy (Clout and Simonson, 2005; Clout and Manuel, 2015) however may also have been introduced from unrelated hypothermal/hydrothermal fluids via cross-cutting fault systems (eg Cu).

The BIF-hosted supergene enriched hematite iron ore is mostly absent of deleterious elements but has a high proportion of gangue material (3.3 per cent; Figure 2b). In comparison, the microplaty hematite ore has a slightly higher prevalence of deleterious elements but a lower abundance of gangue minerals (1.02 per cent, Figure 1b). The martite-goethite samples have varying abundances depending on the size fraction, with a relatively higher abundance of gangue minerals, predominantly kaolinite and quartz, concentrated in the coarser size fractions and the deleterious elements predominantly concentrating in the finer size fractions (Figure 3; Table 3).

The main deleterious elements in martite-goethite and hematite-rich supergene iron ores are silicon, alumina, sulfur, and phosphorus, with an increasing interest in trace levels of base metals. In the martite-goethite ore these elements are distributed across various minerals, with silicon and alumina concentrated in the larger particle size fractions and sulfur, phosphorous and base metals concentrated in the smaller size fractions. The concentration of these latter elements in the smaller particle sizes is a result of the crushing and screening process concentrating the softer minerals (eg kaolinite) in the finer size fractions. Therefore, a wet process after the dry crushing and screening process may help provide a solution for decreasing the abundance of these low-level deleterious elements in iron ore deposits by removing just the finer fractions (<63 μm).

Several trace elements and minerals have been identified through the study that are not discussed in the literature and are not taken into consideration when determining the upper limits of deleterious trace elements (Table 1). For example, we currently do not know where some of these elements, such as Ba and Y, end up in the processing of ore, eg wet beneficiation slimes, sinter plant dust, blast furnace dust, blast furnace slag, steelmaking slag or hot metal. This might have important implications for steel mills and needs to be taken into consideration when determining the value of iron ore and scope three environmental impacts.

As noted above, unenriched BIF are composed of four facies; oxides, silicates, carbonates and sulfides (James, 1954, 1966; Clout and Simonson, 2005). These BIF minerals include hematite, magnetite, quartz, stilpnomelane, minnesotaite, chlorite, alkaline feldspar, siderite, Mn-bearing dolomite and pyrite. These minerals are the precursor material in the original BIF microbands for any subsequent geological alteration and enrichment processes. An important aspect of ongoing research is to understand how the BIF becomes enriched to economic concentrations, and to identify the enrichment processes we must first understand the mineral phases present within the enriched BIF material.

In the majority of iron ore deposits, the main reported gangue minerals are quartz, Mn-bearing dolomite, dolomite and stilpnomelane/minnesotaite (Table 2), yet during this study we observed phases that are not often identified or expected in iron ore deposits eg barite, rutile and xenotime (Table 3). The identification of these mineral phases and their textural characteristics can have important implications on the genesis of the primary iron ore mineralogy and subsequent enrichment processes. The presence of xenotime in the martite-goethite ore samples indicates that there has been some volcanic contribution to the formation of the deposit, as this mineral phase is not known to precipitate from a sea water column (Table 3; Barley, Sylvester and Pickard, 1997). Additionally, the presence of alkali-feldspar and Ti-rich phases eg rutile (Table 3) in these samples indicates these were more likely to have been derived from ash particles, also supporting the contribution of volcanic material during BIF deposition.

In the microplaty hematite, we observe bands with remanent parental material preserved, which can provide important information about the origin and potential remobilisation of elements during subsequent enrichment. The parental BIF material would not have contained vanadium or base metal elements, and so the addition of these elements into the rock must be associated with the microplaty hematite mineralisation event or later remobilisation. Hematite does not readily substitute other elements into its structure; however, we suggest the presence of vanadium could be due to the development of a solid solution between hematite and karelianite (V_2O_3), which can occur during hematite recrystallisation (Waychunas, 1991). The identification of vanadium-rich layers, base metal enrichment and a calcium-bearing sulfate phase within the microplaty hematite supports the hypothesis of a hypogene brine enrichment process (eg Thorne *et al*, 2008), as these processes often increase the abundance of elements such as V, Cu and Zn within the enriched iron ore. However, it is not the purpose of this paper to provide genetic implications for the minerals identified within the samples, but to highlight the additional benefits of collecting texturally relevant chemical and mineralogical data from iron ore samples.

Routine fusion XRF assay data for the various size fractions of martite-goethite ores show base metal (Cu, Zn, Pb, Ni) concentrations for all samples below the detection limit of 50 ppm. Yet, as we observed, these elements are present at differing concentrations within various mineral phases in the samples (Figure 3). From the XRF assay data for most iron ore deposits, limited information is collected about trace element concentrations and often the limits of detection are higher than the upper limit of the steel mill-imposed limits, which currently sit around 50 ppm (Table 1). The micro-XRF analyses of these samples show the presence of trace elements that are not taken into consideration by assay data as they are either not analysed or are present in concentrations below the detection limit. However, with the lowering of acceptable limits for deleterious elements, it is important that appropriate analytical methods are used that can evaluate these elements at low concentrations to assess the true grade of ore material and to explore options for rejection via selective mineral processing.

CONCLUSION

Understanding the mineralogy, petrography, chemistry and mineralogical associations of iron ore products is of increasing importance to steel mills. This study has shown that the presence of deleterious elements and their host minerals in iron ores can be rapidly mapped and assessed using a non-destructive µXRF technique.

In samples from high-grade microplaty hematite, supergene-enriched martite-goethite and hematite iron ores, trace and deleterious elements were mapped and their mineral host identified including sphalerite (Zn and S), chalcopyrite (Cu and S), xenotime (P and Y), apatite (P and Ca), cryptomelane (K and Mn), barite (Ba and S), alkaline feldspar (K, Al and Si), zircon (Zr and Si) and chromite (Cr and Al); minerals and elements not commonly associated with iron-ore products.

This paper has demonstrated a qualitative and quantitative 'fit for purpose' methodology to determine, in a variety of iron ore deposit types, trace element distributions at or below the detection limit for routine fusion XRF analysis, and mineralogy and mineral associations not visible to the naked eye or detectable by routine XRD.

REFERENCES

Barley, M E, Sylvester, P and Pickard, A, 1997. Emplacement of a Large Igneous Province as a Possible Cause of Banded Iron Formation 2.45 Billion Years Ago. In *Nature*, vol, 385, pp. 55–58.

Clout, J and Manuel, J, 2015. Mineralogical, chemical, and physical characteristics of iron ore. In *Iron Ore,* pp. 45–84.

Clout, J and Simonson, B, 2005. Precambrian iron formations and iron formation-hosted iron ore deposits. In *One Hundredth Anniversary Volume 1905–2005,* pp. 643–679.

Clout, J, 1998. The effects of ore petrology on downstream processing performance: a review. In: *Proceedings of Mine to Mill 1998 Conference*, pp. 43–50.

Clout, J, 2006. Iron formation-hosted iron ores in the Hamersley Province of Western Australia. *Applied Earth Science*, pp. 115–125.

Deer, W, Howie, R and Zussman, J, 1992. *An Introduction to the Rock-Forming Minerals*.

James, H, 1954. Sedimentary facies of iron-formation. *Economic Geology*, 49, pp. 235–293.

James, H, 1966. Chemistry of the iron-rich sedimentary rocks. *U. S. Geological Survey Professional Paper*, Vol. 440.

Miyano, T, 1987. Diagenetic to low-grade metamorphic conditions of Precambrian iron-formations. In *Precambrian Iron-Formations*, pp. 155–186.

Morris, R, 1985. Genesis of iron ore in banded iron-formation by supergene and supergene-metamorphic processes—a conceptual model. In *Handbook of Strata-bound and Stratiform Ore Deposits*, 13, pp. 73–235.

Nakano, M, Morii, K and Sato, T, 2009. Factors accelerating dioxin emissions from iron ore sintering machines. *ISIJ International*, 49–5, pp. 729–734.

Thorne, W, Hagemann, S, Webb, A, Lascelles, D and Clout, J, 2008. Banded Iron Formation-related iron ore deposits of the Hamersley Province, Western Australia, In *Banded Iron Formation-Related High-Grade Iron Ore*, 15, pp. 197–221.

Waychunas, G, 1991. Crystal chemistry of oxides and oxyhydroxides. In: Lindsley, D, (Ed.), Oxide Minerals: Petrologic and Magnetic Significance. In *Reviews in Mineralogy*, vol. 25, pp. 11–68.

Wolska, E and Szajda, W, 1985. Structural and spectroscopic characteristics of synthetic hydrohematite. *Journal of Material Science*, 20, pp. 4407–4412.

Processing and beneficiation

Efficiency improvement of Jalal Abad beneficiation plant by concentrate quality enhancement and tailings recovery

M Asghari[1], A Haratian[2], S Haji[3], R Amiri[4] and M Lak[5]

1. Design and Engineering department, Fakoor Meghnatis Spadana Co., Tehran, Iran. Email: mehrshad.asghari@gmail.com
2. Design and Engineering department, Fakoor Meghnatis Spadana Co., Tehran, Iran. Email: haratian@fms-co.com
3. Design and Engineering department, Fakoor Meghnatis Spadana Co., Tehran, Iran. Email: haji@fms-co.com
4. Design and Engineering department, Fakoor Meghnatis Spadana Co., Tehran, Iran. Email: amiri@fms-co.com
5. Design and Engineering department, Fakoor Meghnatis Spadana Co., Tehran, Iran. Email: m.lak@fms-co.com,

ABSTRACT

In recent years, due to advances in designing of various magnet assemblies, a wide range of magnetic materials with different properties can be concentrated. Jalal Abad iron ore beneficiation plant, which is located in Iran, Kerman province, is currently producing iron ore concentrate with the capacity of 0.8 Mt/a by having medium intensity magnetic separators (MIMS) with rougher and cleaner stages that finally leads to the production of an iron concentrate with the Fe grade of about 65 per cent. In this plant, the rougher tailings directly goes to the thickener as the final tailings and cleaner tailings feeds to the ball mill for regrinding. Since some hematite particles with weak magnetic properties cannot be recovered from only these two stages of magnetic separation, the obtained tailings from this concentration plant has approximately an iron grade of 25 per cent to 27 per cent. Accordingly, laboratory processing tests were conducted on the obtained representative sample of the final tailings. Based on the experimental results performed on final tailings, a new magnetic drum separator with a specific magnetic assembly was designed that could finally lead to product with iron grade range of 58 per cent to 60 per cent with relative and total weight per cent of 8.6 per cent and 3.86 per cent. Finally, it could be concluded that feeding of magnetite particles to the existing drum separators, due to their high magnetic field intensity, cannot efficiently lead to improvement of the grade of concentrate. Therefore, pilot magnetic separation tests were done on the final concentrate for evaluation of product upgrading probability. Consequently, by increasing another stage of cleaning and by decreasing the magnetic field intensity, the final product grade could be enhanced from 65 per cent to 67 per cent.

INTRODUCTION

Iron and steel all over the world have been growing fast in recent years due to significantly increased requests for iron ore trade (Guo and Fu, 2010; Li *et al*, 2010a; Rath *et al*, 2014). High-grade iron ore deposits become rarer through the continuous exhaustion of mineral resources (Mehmet *et al*, 2016). Therefore, some new iron sources are pursued by the main global iron and steel producers instead of the high-grade mines (Li *et al*, 2010b; Suthers *et al*, 2014).

Tailings are produced during the upgradation of run-of-mine (ROM) iron ores and smelting of iron ore concentrate. Most of the tailings is produced during the upgradation of ROM iron ores in mineral processing plants, in which the ROM ore with iron grade of 30–40 per cent is upgraded to a concentrate with iron grade more than 65 per cent (Li *et al*, 2010a). Meanwhile, every year, large amount of iron ore tailings is produced that takes over a large quantity of land and makes pollution of the environment and also gives rise to security risks for the surrounding residents (Zhang *et al*, 2006), for instance, acid mine drainage (AMD) (Das, Kumar and Ramachandrarao, 2000; Ghose and Sen, 2001; Dudka and Adriano, 1997). Therefore, tailings management has a critical importance for iron ore mineral processing plants (Dold, 2008).

So, because of gradual depletion of iron ore reserves, more studies are dedicated to tailings processing (Svoboda and Fujita, 2003; Ersayin, 2004; Das, Kumar and Ramachandrarao, 2000; Ghose and Sen, 2001; Dudka and Adriano, 1997). Several technologies have been employed in this regard including gravity separation, high-intensity magnetic separation and flotation (Batisteli and Peres, 2008; Das *et al*, 2007; Dworzanowski, 2012; Rocha, Caneado and Peres, 2010).

Ghasemi, Behnamfard and Arjmand (2019) used reverse flotation for upgrading of tailings samples with Fe grade of 43.09 per cent from the magnetic separation circuit. In this research, a concentrate of 53.92 per cent Fe at a mass recovery of 60 per cent was obtained at optimum flotation conditions of solid content 20 per cent, pH 12, collector concentration of 1 kg/t, starch as depressant at a concentration of 5 kg/t, Alke/Dirol collector mass ratio of 30/70, conditioning time of 10 min and concentration of Ca^{2+} as activator 1 kg/t (Ghasemi, Behnamfard and Arjmand, 2019).

Praes, Albuquerque and Luz (2013) also applied ultrafine flotation in a column flotation pilot plant installed in the mining facilities with a slime sample, with a view to processing this sludge using the reverse flotation technique. The aim of this experiment was to obtain a final concentrate whose Fe content assayed 66 per cent with a SiO_2 content below 0.8 per cent and P lower than 0.03 per cent (Praes, Albuquerque and Luz, 2013).

Khokhulya, Fomin and Alekseeva (2021) applied magnetic separation and gravity concentration technology for production of iron ore concentrate with total iron content of 65.9 per cent and recovery of 91.0 per cent of magnetite and 80.5 per cent of hematite from tailings containing 20.4 per cent of total iron (Khokhulya, Fomin and Alekseeva, 2021). Magnetic separation is a long-established method for the purification and removal of substances from fluids (Augusto and Martins, 1999; Buck *et al*, 2015; Hoffmann and Franzreb, 2002; Lauda *et al*, 2016; Lindner *et al*, 2010; Podoynitsyn *et al*, 2016; Rashidi *et al*, 2016), mainly in mining processing industries ranging from steel production to coal desulfurisation as commercial technology (Andres and O'Reilly, 1994; Augusto, Augusto and Castelo-Grande, 2002).

High gradient magnetic separation as an effective method for recovering of weak and fine magnetic particles separation has undergone dramatic developments and has also achieved extensive application during this time (Svoboda and Fujita, 1987). Magnetic separation operations can be categorised into high intensity as electrical (up to 20 000 gauss), medium intensity (2000–5000 gauss) and low intensity (less than 2000 gauss) techniques. In recent years, due to advances in designing of various magnet assemblies, a wide range of magnetic materials with different properties can be now concentrated.

This investigation was defined to recovery of material with weak susceptibility and interlocked with gangue such as hematite from tailings of Jalal Abad beneficiation plant. Since this plant does not have any dedicated mine, it will be fed with wide range types of iron ore minerals such as magnetite, magnetite-hematite and hematite. Therefore, for increasing the flexibility of the plant towards the hematite feed, the optimisation of the existing magnetic separation circuit was studied. The magnet assembly of the existing rougher-cleaner magnetic separator in the plant was simulated by ANSYS and FEMM software and then magnetic fluxes in different zones were determined. In the next stage, an innovative high gradient magnet assembly in order to develop a new permanent magnetic separator that is the combination of MIMS and dense medium magnetic separator was applied during lab and pilot scale test work. By this way, a new magnetic separator with high capacity and efficiency was developed as scavenger stage. For concentrate grade improvement, one re-cleaner stage with lower magnetic field intensity was also considered.

MATERIALS AND METHODS

The Jalal Abad iron ore beneficiation plant

Jalal Abad iron beneficiation plant with capacity of 0.8 Mt/a is located 75 km north of Kerman city in Kerman province, Iran. This plant does not have any specific and predetermined iron ore mine and receives its feed from different mines. The main outcome of feed, final concentrate and tailings for the last three months is presented in Table 1.

TABLE 1
The main outcome of feed, final concentrate and tailings of Jalal Abad iron ore beneficiation plant.

Sample	The chemical composition (%)			Particle size (µm)	Yield (%)
	Fe	FeO	SiO_2		
Feed	50	7.45	13.3	<15000	100
Concentrate	<66	11.8	2.72	<120	55
Tailings	<30	2.1	26.23	-	45

The flow diagram of the magnetic separation rougher-cleaner stage is presented in Figure 1.

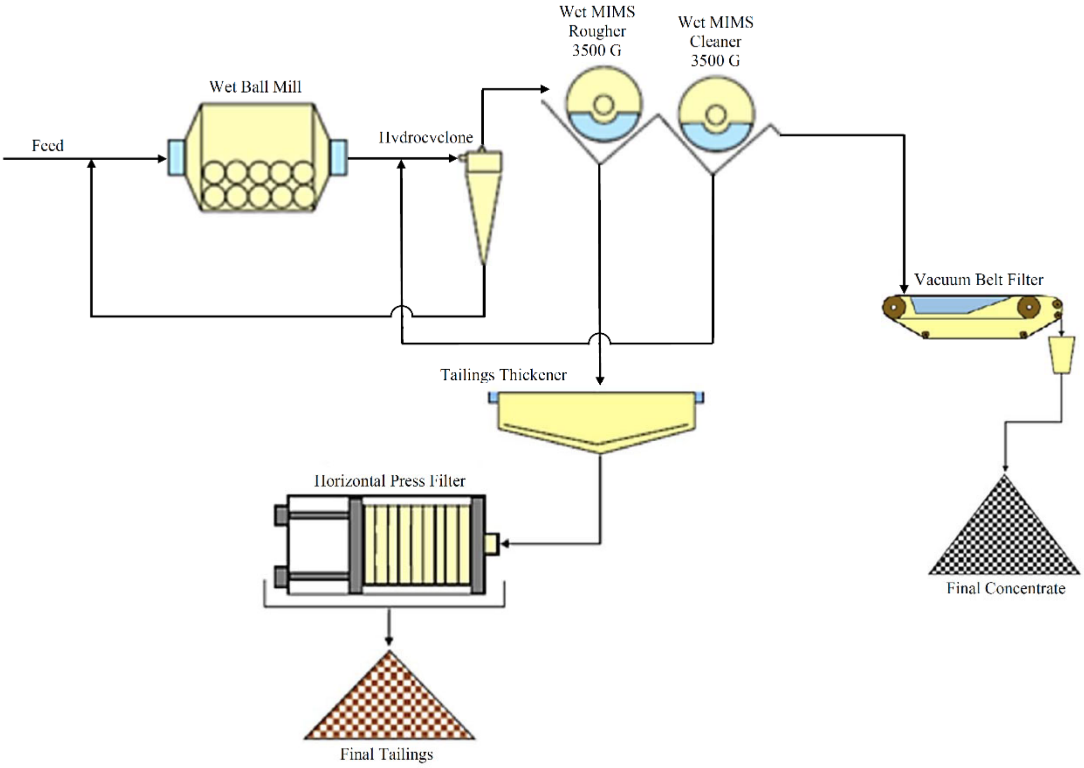

FIG 1 – The rougher-cleaner stage of the magnetic separation circuit of Jalal Abad beneficiation plant.

According to Figure 1, the magnetic separators type in the rougher-cleaner stage of Jalal Abad iron ore plant is wet MIMS. The rougher-cleaner stage has been composed of two stages in two parallel lines. The entire specification of available drum magnetic separators in this stage is presented in Table 2.

TABLE 2

Main data sheet of magnetic drum separators of the rougher-cleaner stage in Jalal Abad iron ore beneficiation plant.

Item	Unit	Data
Type	-	MIMS
Stage	-	Rougher-Cleaner
Magnetic field Strength	G	3500-Permanent
Drum Angular speed	rev/min	21
Feed rate Operation(max)	t/h	115 (for each line)
Feed particle size	µm	<120
Drum diameter	mm	1200
Magnetic effective length	mm	3000
Drum head Material	-	Aluminium
Shield Drum Shell Material	-	NR
Magnetic elements	-	NdFeB
Magnet configuration (assembly)	-	Axial
Tank design	-	Concurrent

Modelling and simulation

In the existing production lines of Jalal Abad, the magnetic field intensity of both magnetic separation stages in rougher and cleaner is 3500 gauss (MIMS) and the tank configuration of all magnetic separators is Concurrent. The simulation results of magnetic field distribution and tank configuration for these wet magnetic drum separators by ANSYS software are presented in Figures 2 and 3.

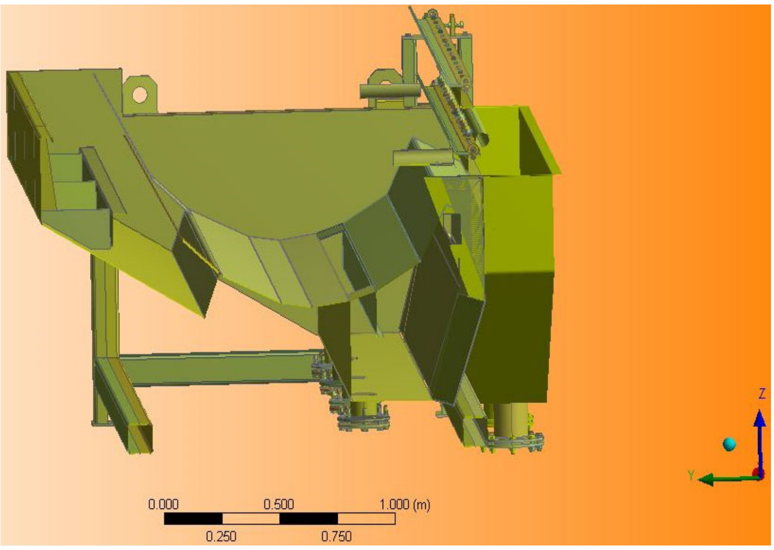

FIG 2 – Drum tank configuration of the rougher-cleaner wet MIMS simulated by ANSYS software.

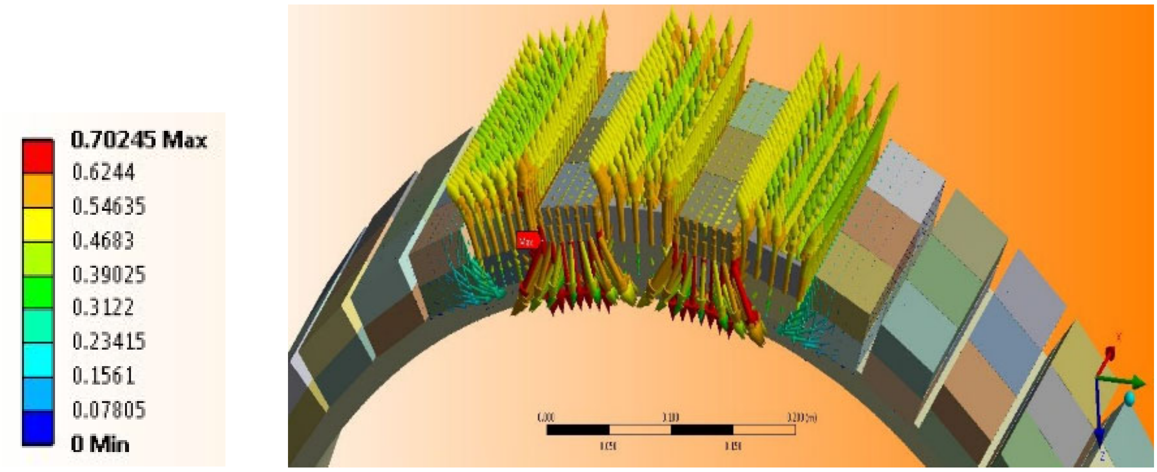

FIG 3 – Magnetic field distribution of the rougher-cleaner wet MIMS simulated by ANSYS software.

The magnetic field distribution was simulated by FEMM software, to evaluate the performance and efficiency of the existing magnetic drum separators and develop new configuration for the magnet assembly to:

- Increase the recovery of hematite particles from final obtained tailings of thickener underflow.
- Increase the grade of final concentrate when magnetite particles with strong susceptibility will be fed.

The simulation is time consuming, user friendly and has industrial benefits. The results are presented in Figure 4.

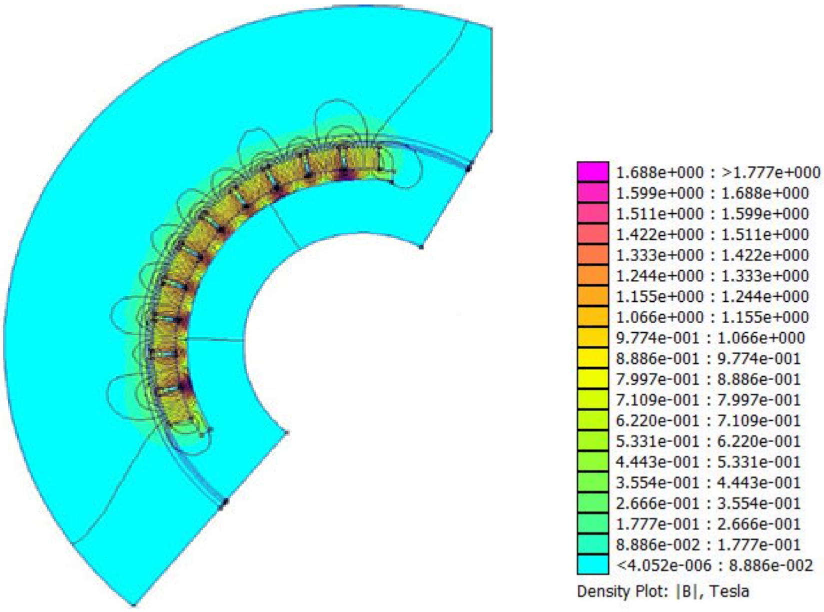

FIG 4 – Magnetic field distribution of the rougher-cleaner wet MIMS simulated by FEMM software.

In order to evaluate the effect of magnetic field intensity and gradient on separation efficiency of the rougher-cleaner stage on the downstream of Jalal Abad plant, a pilot scale wet drum medium intensity magnetic separator, with a diameter of 1200 mm and a working length of 300 mm, was designed and manufactured. In addition, a dense medium tank type was selected for the pilot scale manufactured drum separator.

In this case, one scavenger stage was applied with higher magnetic field intensity and gradient with more powerful permanent rare earth magnet blocks (neodymium, iron and boron (NdFeB)) for iron recovery of final obtained tailings (tailings thickener underflow).

In this pilot drum magnetic separator, by increasing the grade and number of magnetic blocks to 1.5 times the previous one, a new magnetic assembly of high magnetic field intensity and high gradient was obtained. The depth of this new magnetic assembly has also been increased. In this case, the attraction force caused by the magnetic field will be increased. Therefore, the Fe recovery will be increased. This new model of the magnet assembly has been considered for scavenger stage to recovery of weak magnetic material such as magnetite-hematite and hematite particles. Therefore, the new pilot scale model of wet MIMS magnetic separator with specification mentioned in Table 3, was designed and applied in pilot tests.

TABLE 3

Main data sheet of the pilot MIMS.

Item	Unit	Data
Magnetic field Strength	G	4000 to 5000 – Permanent
Feed particle size	μm	<1000
Magnetic elements	-	NdFeB
Magnet configuration (assembly)	-	Axial
Tank design	-	Concurrent-Dense medium
Effective drum dimensions (diameter, width)	mm	1200 × 300

For increasing the recovery of weak magnetic material such as magnetite and magnetite-hematite particles, wet high intensity magnetic separator (WHIMS) was also used for processing of obtained tailings of MIMS to maximise the attraction of iron content material and decrease the amount of achieved final tailings and consequently decrease environmental effects. The specification of applied WHIMS is presented in Table 4.

TABLE 4

Main data sheet of the pilot WHIMS.

Item	Unit	Data
Model	-	Slon-500
Ring diameter	mm	500
Feed particle size	μm	<1000
Feed concentration	% (m/m)	10–40
Slurry throughput	m^3/h	0.25–0.5
Field strength	G	Variable to 10 000

The magnetite separation circuit modification and optimisation procedure

The modification procedure for optimising in the magnetic separation circuit was as follows:

- Sampling underflow from the tailings thickener and determining chemical analysis and characterisation.
- Performing magnetic separation tests by Davis tube tester on representative sample.
- Performing pilot magnetic separation tests by designed wet drum MIMS, based on the most desirable Davis tube results.
- Adding wet drum MIMS with stronger magnetic field intensity as scavenger stage for recovery of iron from final tailings and producing of middle product.
- Adding WHIMS as final scavenger stage for iron recovery of tailings from newly considered MIMS.

- Adding re-cleaner stage with lower magnetic field intensity for increasing the grade of final concentrate from the cleaner stage.
- Performing required modification and optimisation in the magnetic separation circuit of Jalal Abad beneficiation plant and investigating achieved results in industrial scale.

RESULTS AND DISCUSSION

Tailings recovery

Sample characterisation

Comprehensive laboratory and pilot tests were carried out on the received samples from tailings thickener underflow that were prepared by experts of Jalal Abad iron ore beneficiation plant. XRF analysis results on tailings thickener underflow is presented in Table 5.

TABLE 5

XRF analysis results of tailings thickener underflow.

Element	**SiO_2**	**Al_2O_3**	**BaO**	**CaO**	**Fe**	**K_2O**	**MgO**	**MnO**
Unit	%	%	%	%	%	%	%	%
Amount	26.23	2.96	<0.05	9.55	25.3	0.25	10.17	0.16
Element	Na_2O	P_2O_5	SO_3	TiO_2	Cr_2O_3	LOI	Cu	
Unit	%	%	%	%	%	%	%	
Amount	0.16	0.21	0.83	0.17	<0.05	12.98	0.18	

Davis tube test results

In order to investigate the magnetic separation behaviour of the obtained samples from tailings thickener underflow for increasing the circuit iron recovery, individual Davis tube tests were performed on taken samples. The outcome of these samples is presented in Table 6.

TABLE 6

The main outcome of taken samples from tailings thickener underflow.

Chemical composition (%)		**Particle size (μm)**	
Fe	**FeO**	**d97**	**d80**
24.94	2.73	235.2	86.4

Obtained results of magnetic separation tests via Davis tube at field intensity of 5000 gauss performed on representative samples are presented in Figure 5. This magnetic field intensity of 5000 gauss can be reached easily by permanent magnetic blocks.

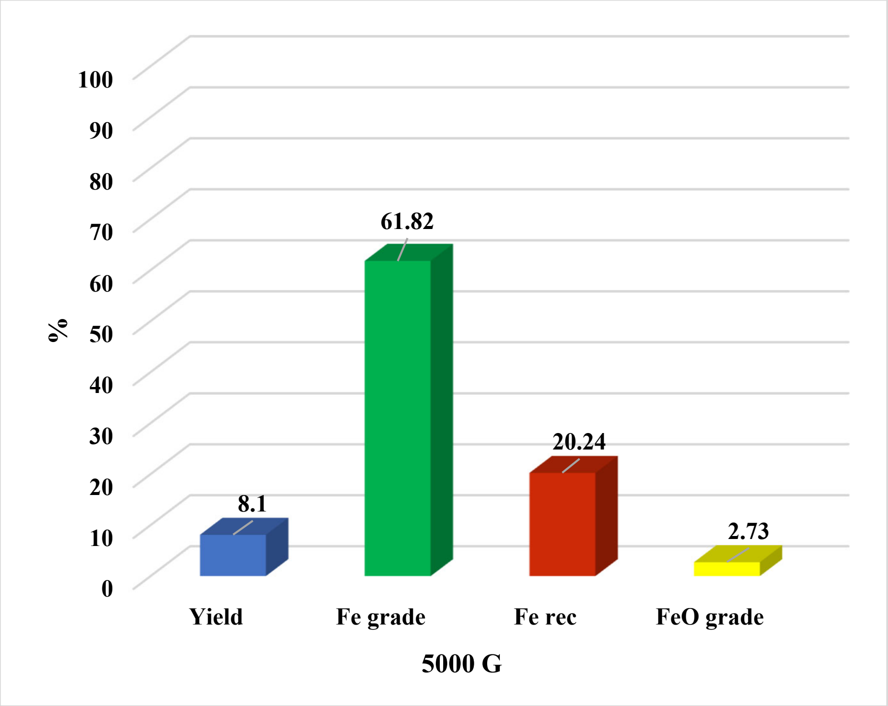

FIG 5 – The results of Davis tube tests on the tailings thickener underflow.

Based on the Davis tube tests, the magnetic field intensity of 5000 gauss resulted in weight recovery of 8.1 per cent for iron recovery from underflow of tailings thickener. In this case, the achieved concentrate has the Fe grade and Fe recovery of 61.82 per cent and 20.24 per cent, respectively.

Pilot wet drum MIMS and WHIMS tests

The conditions and obtained results of magnetic separation tests, which includes MIMS and WHIMS tests of different magnetic field intensity on taken representative sample from tailings thickener underflow in FST lab are presented in Tables 7 and 8. The related flow diagram is presented in Figure 6.

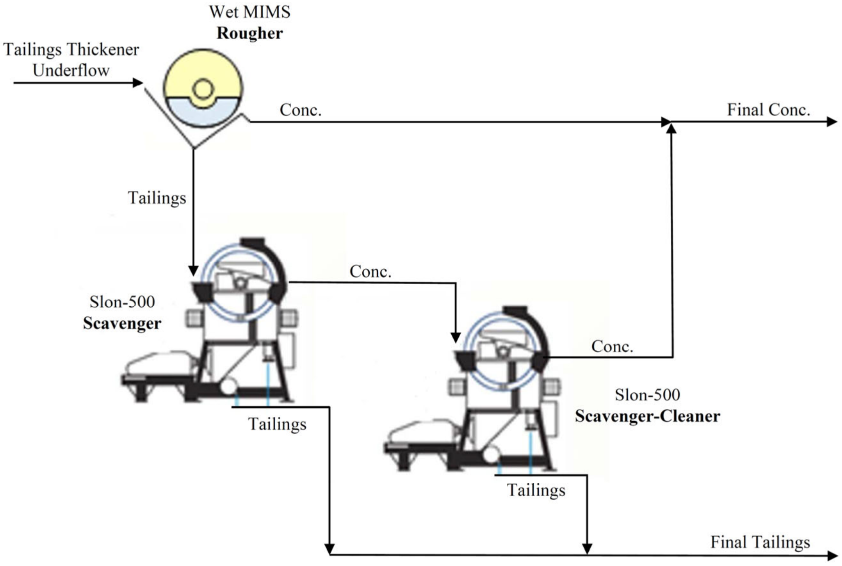

FIG 6 – The flow diagram of pilot magnetic separation tests.

TABLE 7

The condition and results of pilot tests by MIMS 5000 G.

Conditions					Results				
Equipment	**Test stage**	**Magnetic field intensity**	**Drum speed**	**Solidity**	**Product**	**Wt.**	**Fe**	**FeO**	**Fe$_{rec.}$**
		G	**m/s**	**(%)**		**(%)**	**(%)**	**(%)**	**(%)**
MIMS	Scavenger	5000	1.33	17	Concentrate	7.05	58.70	2.95	16.49
					Tailings	92.95	22.55	3.23	83.51
WHIMS	Scavenger	7000	0.09	15	Concentrate	32.76	40.35	2.44	59.51
					Tailings	67.24	13.38	3.45	40.49
WHIMS	Scavenger -cleaner	4000	0.09	13.68	Concentrate	51.59	55.07	2.23	69.47
					Tailings	48.41	25.80	4.31	30.53

TABLE 8

The condition and results of pilot tests by MIMS 4000 G.

Conditions					Results				
Equipment	**Test Stage**	**Magnetic field intensity**	**Drum speed**	**Solidity**	**Product**	**Wt.**	**Fe**	**FeO**	**Fe $_{rec.}$**
		G	**m/s**	**(%)**		**(%)**	**(%)**	**(%)**	**(%)**
MIMS	Scavenger	4000	1.33	17	Concentrate	3.81	64.05	3.79	9.73
					Tailings	96.19	23.53	3.17	90.27
WHIMS	Scavenger	7000	0.09	15	Concentrate	35.20	41.37	2.89	61.70
					Tailings	64.80	13.95	3.43	38.30
WHIMS	Scavenger-cleaner	4000	0.09	13.68	Concentrate	55.55	54.39	2.04	72.78
					Tailings	44.45	25.42	4.02	27.22

The conclusions of these performed tests for each of MIMS 4000 G and MIMS 5000 G are presented in Tables 9 and 10.

TABLE 9

The final results of pilot tests by MIMS 5000 G and WHIMS 7000 G and 4000 G.

Product Name	**Wt. %**	**Fe %**	**Fe $_{rec.}$ %**	**FeO %**
Concentrate Drum 5000 gauss	7.05	58.70	16.59	2.95
Concentrate WHIMS 4000 gauss	15.71	55.07	34.67	2.23
Tailings WHIMS 7000 gauss	62.50	13.38	33.50	3.45
Tailings WHIMS 4000 gauss	14.74	25.80	15.24	4.31
Total Concentrate	22.76	56.20	51.26	2.45
Total Tailings	77.24	15.75	48.74	3.61
Feed	100.00	24.94	100.00	2.73

TABLE 10

The final results of pilot tests by MIMS 4000 G and WHIMS 7000 G and 4000 G.

Product Name	**Wt. %**	**Fe %**	**Fe $_{\text{rec.}}$ %**	**FeO %**
Concentrate Drum 4000 gauss	3.81	64.05	9.68	3.79
Concentrate WHIMS 4000 gauss	18.81	54.39	40.61	2.04
Tailings WHIMS 7000 gauss	62.33	13.95	34.52	3.43
Tailings WHIMS 4000 gauss	15.05	25.42	15.19	4.02
Total Concentrate	22.62	56.02	50.29	2.34
Total Tailings	77.38	16.18	49.71	3.54
Feed	100.00	24.94	100.00	2.73

The results of performed tests in presented tables show that by utilising wet drum MIMS 5000 G, concentrate with Fe grade of 58.7 per cent and weight per cent of 7.05 per cent can be obtained from tailings thickener underflow with Fe grade of 24.94 per cent. The tailings from MIMS 5000 G will be upgraded after two enrichments by WHIMS to produce concentrate with Fe grade of 55.07 per cent and weight per cent of 15.71 per cent. In this order, final concentrate with Fe grade of 56.2 per cent and weigh per cent of 22.76 per cent will be achieved from the tailings thickener underflow. Therefore, it is expected to increase the Fe recovery of Jalal Abad beneficiation plant by utilising medium intensity magnetic separator of 5000 G and two steps of WHIMS in scavenger and scavenger-cleaner stages with magnetic field of 7000 G and 4000 G, respectively. According to the mentioned results in Tables 1 and 9, total amount of middle product with Fe grade of 56.02 per cent will be equal to 10.24 per cent which can be considered separately or can be blended with final concentrate. The Magnetic field distribution of 5000 G was simulated by FEMM software that is presented in Figure 7.

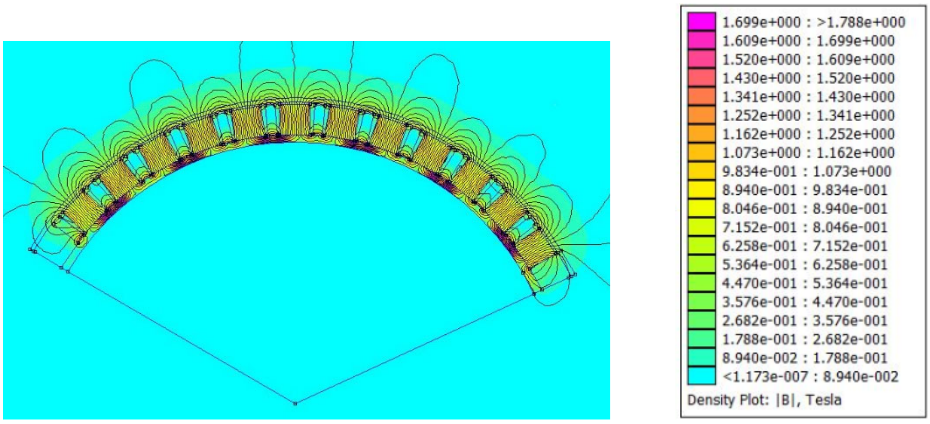

FIG 7 – The magnetic field distribution of wet MIMS 5000 G simulated by FEMM software.

Concentrate quality enhancement

As said before, Jalal Abad beneficiation plant does not have any dedicated iron mine to itself and will receive a wide range of iron ore with different characteristics that results in fluctuation in iron grade of final product. Especially when magnetite with high susceptibility will be fed to the plant since the magnetic field intensity of the existing rougher-cleaner magnetic separators are too strong (3500 G), the Fe grade of the final concentrate will be lower than 65 per cent. Therefore, the existing magnetic separation circuit is needed to be upgraded to increase its flexibility to enrichment of various feed. For this reason, weaker magnetic field intensity of 2500 G was designed by FEMM software and the obtained result is presented in Figure 8. In this order, recleaner wet magnetic separators with magnetic field intensity of 2500 G were considered for the magnetic separation circuit of Jalal Abad beneficiation plant.

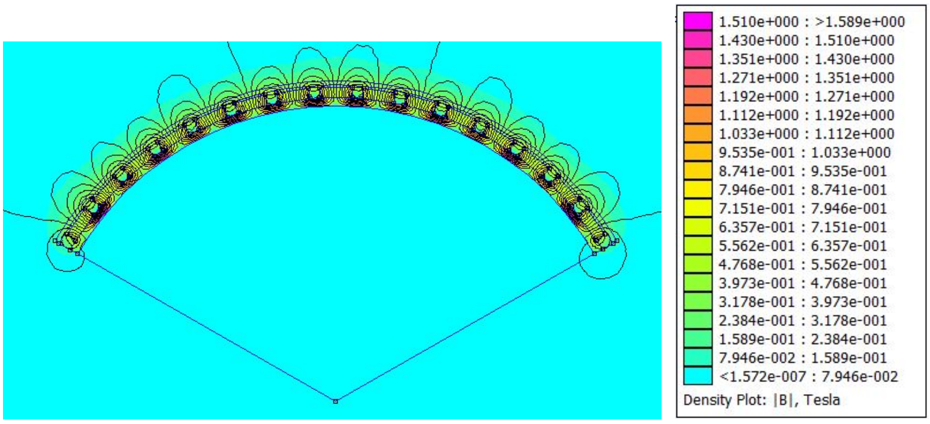

FIG 8 – The magnetic field distribution of wet MIMS 2500 G simulated by FEMM software.

In this order, the flow diagram of the magnetic separation circuit of Jalal Abad beneficiation plant will be as Figure 9.

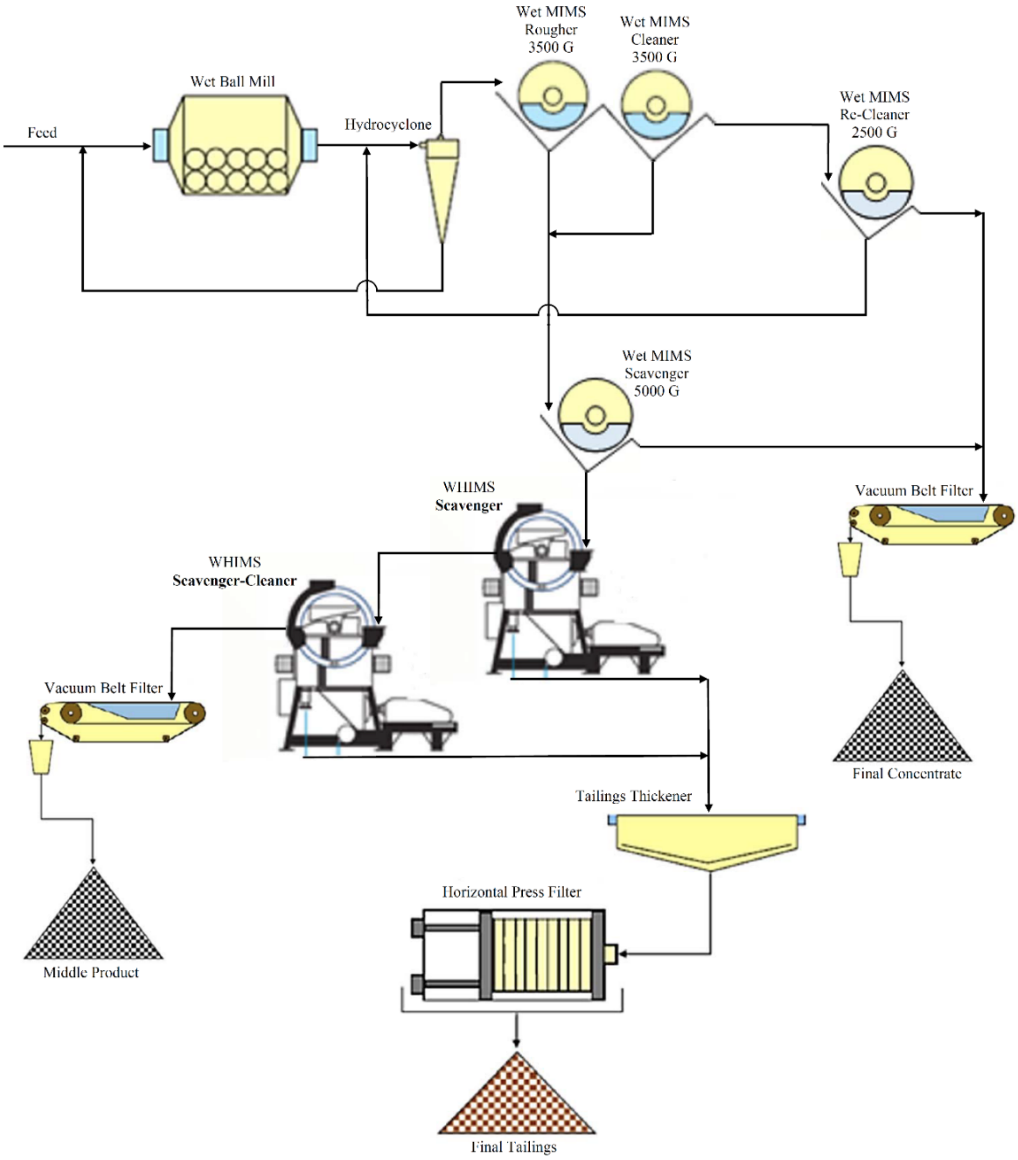

FIG 9 – The modified and optimised of the magnetic separation circuit of Jalal Abad beneficiation plant.

Hence, according to the obtained results of this investigation and gained flow diagram (Figure 6), the desired modifications and optimisation in the magnetic separation circuit of the plant were performed and according to the plant capacity, two MIMS separators with magnetic field of 5000 G were added for iron recovery of tailings from the rougher-cleaner MIMS and two MIMS with magnetic field intensity of 2500 G were added after cleaner separators to improve the iron grade of final concentrate. After reaching steady state conditions, monitoring and controlling of the circuit was performed by taking samples from desired points. In this order, the achieved result of tailings recovery and concentrate enrichment for a recent month of operation of the plant is presented in Table 11.

TABLE 11

The condition and results of industrial tests of the modified magnetic separation circuit.

Conditions				Results				
Equipment	**Test Stage**	**Magnetic field intensity**	**Drum speed**	**Product**	**Wt.**	**Fe**	**FeO**	**Fe$_{rec.}$**
		G	**m/s**		**(%)**	**(%)**	**(%)**	**(%)**
MIMS	Re-cleaner	2500	1.33	Feed	100	65.5	12.25	100
				Concentrate	93	67	13	93.32
				Tailings	7	45	2	4.68
MIMS	Scavenger	5000	1.33	Feed	100	27	2.5	100
				Concentrate	8.57	59	4.6	18.73
				Tailings	91.43	24	2.3	81.27

As shown in Table 11, there is a good and acceptable conformity between pilot and industrial tests results. In this order, Fe grade of the final concentrate of Jalal Abad plant will be upgraded to 67 per cent from 65 per cent and based on Table 1, its total per cent weight will be equal to 51.15 per cent. The product of MIMS 5000 G as a middle product with Fe grade of 59 per cent has a relative and total per cent weight of 8.6 and 3.86 per cent, relatively. If the final concentrate is mixed with this middle product, the amount of final product of Jalal Abad beneficiation plant with Fe grade of 66.43 per cent will be increased to 55 per cent.

In close future the remaining modification that includes the adding of WHIMS for recovery of obtained tailings from MIMS 5000 G will be done.

CONCLUSIONS

- Based on the investigations carried out and pilot tests, – utilising wet drum magnetic separator and WHIMS with more field intensity and gradient was suggested and considered as the most suitable solution for iron recovery of tailings thickener underflow, which is composed from material with weak magnetic properties such as magnetite-hematite and hematite particles.
- Wet drum medium intensity magnetic separation with rare earth permanent magnets block (NdFeB) and field intensities of 2500, 4000 and 5000 gauss on the drum surface was designed and manufactured.
- According to Figure 6 and Table 7, in the best obtained results of the tailings recovery investigation, testing by the model wet drum MIMS 5000 gauss on the taken representative sample from tailings thickener, indicated a scavenger concentrate was achieved with weight recovery of 7.05 per cent and Fe grade of 58.7 per cent from a feed with Fe grade of 25 per cent to 27 per cent. Then the obtained tailings from this MIMS was cleaned and upgraded by WHIMS in two stages as cleaner and recleaner with magnetic field intensities of 7000 G and 4000 G, respectively. In this order, the final achieved concentrate from WHIMS

has a Fe grade of 55.07 per cent and weight per cent of 15.71 per cent. At the end, by blending the concentrate of MIMS and WHIMS, the final achieved concentrate from tailings recovery has Fe grade of 56.2 per cent and per cent weight of 22.76 per cent.

- For upgrading of final concentrate to higher grade when magnetite material is fed, one magnetic separation stage as recleaner with lower magnetic field intensity like 2500 G is also needed to attract the material with stronger magnetic susceptibility and higher grade.
- Based on the obtained results of the investigation and Figure 6, modification of the existing magnetic separation circuit was performed in the plant at industrial scale for the aims of both tailings recovery and concentrate grade improvement. So, one recleaner stage with magnetic field intensity of 2500 G and one scavenger stage with magnetic field intensity of 5000 G were added. According to Table 11, the final concentrate grade was improved to 67 per cent from 65 per cent and a middle product with Fe grade of 59 per cent was gained from tailings recovery, which can be blended with final concentrate or can be considered separately.

REFERENCES

Andres, U and O'Reilly, W, 1994. Selectivity in the magnetic separation of minerals, *Powder Technology*, 79:147–158.

Augusto, P A, Augusto, P and Castelo-Grande, T, 2002. Magnetic classification, *Miner Eng*, 15(2002):35–43.

Augusto, P A and Martins, J P, 1999. A new magnetic separator and classifier: prototype design, *Min Eng*, 12(7):799–807.

Batisteli, G M B and Peres, A E C, 2008. Residual amine in iron ore flotation, *Miner Eng*, 21:873–876.

Buck, A, Moore, R, Christopher, D, Kumar, A, Stroff, C, White, N, Xue, W, Jeffrey, J, Zborowski, M and Magn, J, 2015. *Mat,* 380.

Das, S K, Kumar, S and Ramachandrarao, P, 2000. Exploitation of iron ore tailings for the development of ceramic tiles *Waste Manag*, 20(8):725–729.

Das, B, Prakash, S, Das, S K and Reddy, P S R, 2007. Effective beneficiation of low grade iron ore through jigging operation, *J Miner Mater Char Eng*, 7(1):27–37.

Dold, B, 2008. Sustainability in metal mining: rom exploration, over processing to mine waste management, *Rev Environ Sci Biotechnol*, 7(4):275.

Dudka, S and Adriano, D C, 1997. Environmental impacts of metal ore mining and processing: a review, *J Environ Qual*, 26(3):590–602.

Dworzanowski, M, 2012. Maximizing the recovery of fine iron ore using magnetic separation, *J South Afr Inst Min Metall*, 112(3):197–202.

Ersayin, S, 2004. Low intensity magnetic separator modelling: a pseudo liberation approach, *Miner Process Extr Metall*, 113(3):167–174.

Ghasemi, S, Behnamfard, A and Arjmand, R, 2019. Reprocessing of Sangan iron ore tailings by flotation, *Journal of Mining and Environment (JME)*, 10(3):729–745.

Ghose, M K and Sen, P K, 2001. Characteristics of iron ore tailings slime in India and its test for required pond size, *Environ Monit Assess*, 68(1):51–61.

Guo, Z C and Fu, Z X, 2010. Current situation of energy consumption and measures taken for energy saving in the iron and steel industry in China, *Energy*, 35:4356–4360.

Hoffmann, C and Franzreb, M, 2002. A novel high-gradient magnetic separator (HGMS) design for biotech applications, *IEEE Transactions on Applied Superconductivity*, 12:963–966.

Khokhulya, M, Fomin, A and Alekseeva, S, 2021. Recovery of magnetite-hematite concentrate from iron ore tailings, *E3S Web of Conferences*, 247:01042.

Lauda, M, Füzer, J, Kollár, P, Strečková, M, Bureš, R, Kováč, J, Baťková, M, Baťko, I and Magn, J, 2016. *Mat,* 411:12–17.

Li, C, Sun, H H, Bai, J and Li, L T, 2010a. Innovative methodology for comprehensive utilization of iron ore tailings: part 1 The recovery of iron from iron ore tailings using magnetic separation after magnetizing roasting, *Journal of Hazardous Materials*, 174:71–77.

Li, G, Jiang, T, Liu, M, Zhou, T, Fan, X and Qiu, G, 2010b. Beneficiation of high-aluminium-content hematite ore by soda ash roasting, *Mineral Processing & Extractive Metallurgy Review*, 31:150–164.

Lindner, J, Wagner, K, Eichholz, C and Nirschl, C H, 2010. *Eng Technol*, 1315–1320.

Mehmet, O, Selçuk, S, Durmuş, K and Umit, U, 2016. Searching the fertility potential of iron and steel industry blast furnace slag, *World Journal of Engineering*, 13:482–486.

Praes, P E, Albuquerque, R O and Luz, A F O, 2013. Recovery of Iron Ore Tailings by Column Flotation, *Journal of Minerals and Materials Characterization and Engineering,* 1:212–216.

Podoynitsyn, S N, Sorokina, O N, Kovarski, A L and Magn, J, 2016. *Mat*, 397:51–56.

Rashidi, M M, Johnson, S, Yang, Z and Magn, J, 2016. *Mat*, 398:13–19.

Rath, S S, Sahoo, H, Dhawan, N, Rao, D S, Das, B and Mishra, B K, 2014. Optimal recovery of iron values from a low grade iron ore using reduction roasting and magnetic separation, *Separation Science and Technology*, 49:1927–1936.

Rocha, L, Caneado, R Z L and Peres, A E C, 2010. Iron ore flotation, *Miner Eng,* 23(11–13):842–845.

Suthers, S P, Nunna, V, Tripathi, A, Douglas, J and Hapugoda, S, 2014. Experimental study on the beneficiation of low-grade iron ore fines using hydrocyclone desliming, reduction roasting and magnetic separation, *Mineral Processing and Extractive Metallurgy*, 123:212–227.

Svoboda, J and Fujita, T, 2003. Recent developments in magnetic methods of material separation, *Miner Eng*, 16(9):785–792.

Svoboda, J and Fujita, T, 1987. Magnetic Methods for the Treatment of Minerals, *Developments in Mineral Processing*.

Zhang, S, Xue, X, Liu, X, Duan, P, Yang, H, Jiang, T, Wang, D and Liu, R, 2006. Current situation and comprehensive utilization of iron ore tailings resources, *Journal of Mining Science*, 42:403–408.

An innovative application of gravity separation technology to beneficiate ultrafine iron ore

M Hasan[1], D Pepper[2], J Lyons[3] and C Vadeikis[4]

1. Process Design Metallurgist, Mineral Technologies Pty Ltd, Carrara Qld 4211.
   Email: maruf.hasan@mineraltechnologies.com
2. Lead Design Engineer, Mineral Technologies Pty Ltd, Carrara Qld 4211.
3. Principal Design Specialist, Mineral Technologies Pty Ltd, Carrara Qld 4211.
4. Principal Process Consultant, Mineral Technologies Pty Ltd, Carrara Qld 4211.

ABSTRACT

Processing of large volumes of ultrafine ores has long challenged mineral processing operators because of lower recoveries and increased tailings. This has led to many deposits, or parts of existing deposits, being viewed as uneconomic. As the mining industry can no longer afford to overlook resources that require finer sizes to achieve liberation or result in high tailings losses, the need for technologies to address these issues has increased.

Mineral Technologies (MT) worked with a prominent Australian iron ore producer over five years to implement an innovative gravity separation technology for the beneficiation of ultrafine magnetite. The magnetite mineralisation requires a liberation size of <40 µm and selective rejection of ultrafine silica prior to magnetic separation.

Through collaboration with the client, MT applied their Lyons Feed Control Unit (LFCU) technology for the beneficiation of finely grained magnetite. LFCUs are widely used in the mineral sands and iron ore gravity plants, and in tailings applications, to recover water and provide constant high density process streams. This project was an extension of knowledge gained from these applications.

Test work was conducted on-site, using 1 t/h pilot and 300 kg/hr laboratory scale units. This test work showed that the LFCUs could reject 20 per cent of feed mass to tails whilst recovering >94 per cent of Fe to product. This upgraded the feed from 53.7 per cent Fe and 19.7 per cent SiO_2 to 63.8 per cent Fe and 8.8 per cent SiO_2.

Recovery by size data showed a minimum 88 per cent Fe recovery to product for <8 µm material and up to 98 per cent Fe recovery for the -38+25 µm fraction. The LFCU rejected 70 per cent of <25 µm SiO_2. The information obtained from the test work was utilised in the design of the full-scale units which are due for installation at the project site in 2021.

This paper outlines the results of this laboratory and pilot scale test work and how the data obtained was used to design the full-sized units.

INTRODUCTION

Wet beneficiation processes for the iron ore industry in Australia are becoming a more common practice, due to lower 'run-of-mine' grades because of increases in key impurities such phosphorus, alumina and silica. Further, changes in the mineralogy of non-direct shipped ores have increased the need for grinding ores into fine and ultrafine size fractions to achieve sufficient iron liberation ahead of any separation stages to remove the gangue minerals.

The Western Australia Pilbara iron ore province has a long history of discarding low-grade iron ore fines to the tails. This low-grade iron fines are mostly hydro hematite and goethite verities with rich in alumina and silica (Murthy and Basavaraj, 2012). However, the depletion of direct shipping grade ores and improvements in process technology over the last two decades, combined with societal and shareholder pressure to reduce tailings stockpiles has influenced mining companies to now process these fine particles. As a result, the big four iron ore producers in the Pilbara region (BHP, Rio Tinto, Roy Hill and FMG) have started focusing on ways to beneficiate their fine and ultrafine range hematite-type ores. The Roy Hill (Southway, 2020) and FMG Christmas Creek Mine (Gleeson, 2021) Wet High Intensity Magnetic Separator (WHIMS) plants are examples of fine hematite wet beneficiation processes.

Unlike high-grade hematite, magnetite ore needs to undergo ultrafine grinding, typically below 45 µm, to achieve sufficient magnetite liberation ahead of the separation stages (McNab *et al*, 2009). Treatment of fine, and ultrafine iron ore particles, involves comminution (crushing and grinding), washing, screening, gravity concentration, magnetic separation and agglomeration (Yellishetty *et al,* 2021). Traditionally, gravity separation of particles below 45 µm is considered difficult and only hindered bed type hydraulic separators can work effectively in that size class (Tripathy *et al,* 2015). The Mineral Technologies (MT) Lyons Feed Control Unit (LFCU) is such a type of hindered bed separator that can work effectively in upgrading iron ores in both the fine and ultrafine size ranges.

The LFCU is an established technology and has been used successfully in the mineral sands industry for the last 20 years. It is highly effective in stabilising spiral separator feed flow and density through upstream disruptions, such as the intermittent flow of a dredge (Lyons *et al,* 2009). However, utilising the LFCU to beneficiate and upgrade ultrafine magnetite is a new concept. Therefore, extensive test work had to be completed to validate the concept, before proceeding with a full-scale design.

MT has been working with a prominent Australian iron ore producer for the last five years to introduce LFCU technology for the beneficiation of ultrafine magnetite. The test work was conducted in the producer's pilot facility which included milling, gravity and magnetic separation equipment. MT installed two pilot LFCU units and conducted test work for over three years. MT also undertook test work within their Carrara laboratory on representative samples produced from the pilot work. This paper provides a review of the LFCU technology and covers the development of the rougher magnetic product LFCU (Deslime LFCU) by utilising pilot-scale and laboratory test work data.

WORKING PRINCIPLE

The LFCU is considered as being suitable for magnetite beneficiation due to its ability to elutriate finer, lower density gangue particles from the higher density magnetite particles. The LFCU working principle and mechanisms of magnetite beneficiation are described below.

The magnetite in the feed, consolidates in the LFCU under its own weight (Autogenous) displacing water, forming a dense underflow (u/f) stream. The LFCU is designed to facilitate the formation of an impermeable consolidated layer above the u/f stream which gravitates towards the discharge manifold without blockages. This is achieved through the selection of suitable geometry for the LFCU that promotes mass flow inside the LFCU following Jenike's work (Jenike, 1964). The water released from the consolidated layer flows upwards in the vessel and travels to the overflow (o/f) launder. The velocity of this overflow stream is controlled sufficiently to carry lower density fully, or nearly liberated, gangue minerals with it. '*Autogenous Classification*' is the term MT uses to describe this separation process. This process can be used to classify feed by particle size and/or density.

An LFCU generally operates by varying particle settling flux rate (measured in t/h/m^2) and overflow rise rate (measured in m/h) to control particles rejection rates. The following equations are used to calculate LFCU settling flux and rise rate

$$LFCU\ Settling\ Flux = \left(\frac{Feed\ Rate\ (\frac{t}{h})}{LFCU\ Cylindrical\ Section\ Cross\ Sectional\ Area\ (m^2)} \right)$$

$$LFCU\ Rise\ Rate = \left(\frac{LFCU\ Oveflow\ Stream\ Volumetric\ Flowrate\ (\frac{m^3}{h})}{LFCU\ Cylindrical\ Section\ Cross\ Sectional\ Area\ (m^2)} \right)$$

The LFCU has four operating zones (refer to Figure 1), which are outlined in the following sections.

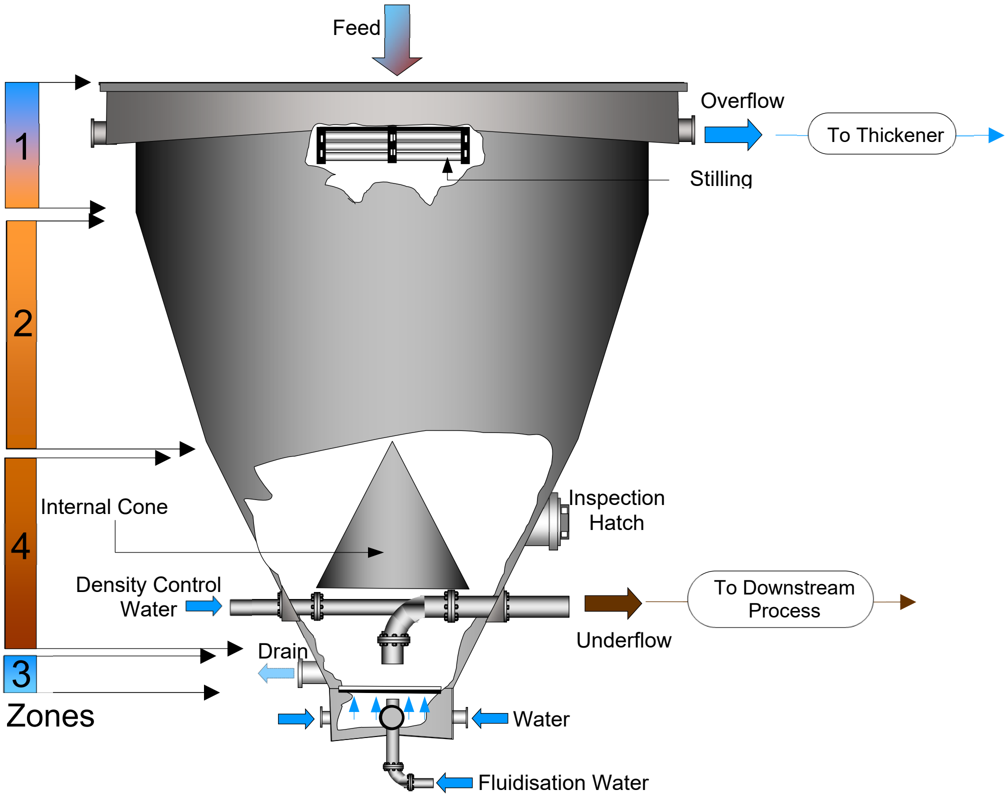

FIG 1 – Schematic of Mineral Technologies LFCU.

- Feed Receival (Zone 1)

  The feed material passes through an energy dissipater and stilling box located just below the water level in the LFCU, which dissipates excess energy and de-aerates the feed. This minimises turbulence and allows the feed slurry to spread out over the full cross-section of the stilling basin.
- Consolidation (Zone 2)

  The consolidation zone occurs in the middle section above the upper internal cone. As the high specific gravity (SG) particles come to rest within this zone, the slurry consolidates to an estimated density of 65–80 per cent solids (w/w) and water, slimes and low SG particles preferentially report to the LFCU overflow at a rate determined by the settling flux rate (t/h/m^2) and overflow rise rate (m/h).
- Fluidisation (Zone 3)

  In the fluidisation zone, at the base of the tank, water is injected through the fluidisation ring outlets to assist material to move horizontally towards the pump suction and vertically to the pipe inlet to be withdrawn from the LFCU. Fluidisation water is added to reduce the density of the consolidated slurry to 50–65 per cent solids (w/w). This water also allows an LFCU to be restarted from the sanded condition after prolonged plant shutdowns.
- Density Control and Discharge (Zone 4)

  The LFCU underflow pump suction line sits below the lower internal cone and draws slurry from the fluidisation zone. A density control water line feeds directly into the underflow pump suction to control the density of material discharged from the LFCU.

ACHIEVING PARTICLE SEPARATION

Particle separation in the LFCU is dependent on the feed characteristics and the key equipment operating principles. Feed characteristics such as particle size distributions and density differences between light and heavy minerals; feed grades and the slimes content affect particle separation. On the other side, equipment operational characteristics such as feed solids density, feed flow rate and underflow flow rate also impact the effectiveness of particle separations. With some material the retention time will be critical to the process; allowing sufficient time for the fine material to consolidate.

The design for the LFCU used in magnetite beneficiation is the result of a comprehensive program of test work in both the laboratory and the on-site pilot facility. The minimum process criteria to design the LFCU was to achieve an approximate ten per cent increase in feed iron grade and remove the maximum amount of ultrafine silica.

Laboratory test work

The laboratory test work was conducted preliminarily to assess particle separation behaviour in a laboratory-scale LFCU and to identify conditions for larger-scale pilot test work. The laboratory unit is 250 mm in diameter and 2240 mm high. The unit is generally operated at 100 kg/h to 300 kg/h of feed and the test work is conducted in 'open-cycle' mode.

During each test run, magnetite ore is pumped into the top of the unit at a constant feed rate and density. Autogenous particle separation occurs in the vertical section of the LFCU. The heavier magnetite settles and consolidates, which displaces water and fine/light gangue minerals upwards towards the overflow. Make-up feed is introduced to the feed sump concurrently to balance the removal of products. Flow-control of the underflow stream is achieved via a peristaltic pump. This sufficiently limits the underflow rate and allows time for particles to settle within the unit. During each test run, feed, overflow and underflow samples are collected and sized using the screen and cyclosizer. The cyclosizer is used to generate test fractions below 38 µm (C1 to C5) to gather information about grade and recovery at ultrafine size fractions. Assays-by-size are completed for the test fractions to assess unit performance (ie iron separation from gangue minerals).

Laboratory test work has shown that the LFCU is capable of separating particles in the ultrafine particles by density, as can be seen in Figure 2. Test conditions pertinent to Figure 2 includes a feed density of 22.2 per cent solids (w/w), flux rate of 1.98 t/h/m^2 and rise rate of 6.25 m/h. Test results are presented in Table 1. Notable results include 94.4 per cent Fe recovery to underflow and a Fe enrichment ratio of 1.2 (approximately). Additionally, approximately 64 per cent of the SiO_2 contained in the feed is rejected to the overflow stream.

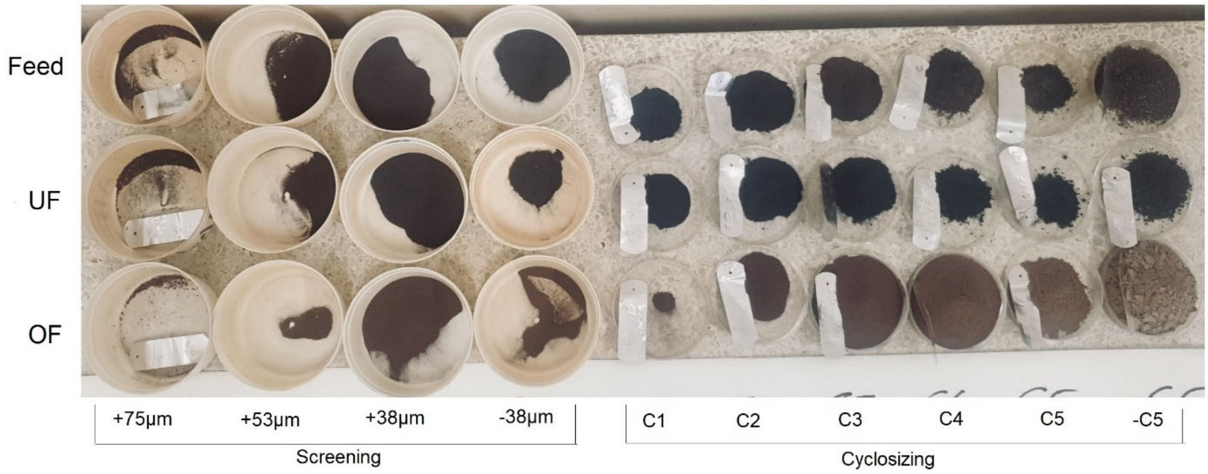

FIG 2 – LFCU particle separation in the different size classes.

TABLE 1

Laboratory LFCU test work result.

Test fraction	**Mass fraction (%)**	**Fe grade (%)**	**SiO_2 grade (%)**	**Fe recovery to underflow (%)**	**SiO_2 recovery to underflow (%)**	**Fe enrichment ratio** (product grade/ feed grade)
Feed	100	53.7	19.7	94.4	36.2	1.2
Overflow	20.2	15.0	61.1			
Underflow	79.8	63.8	8.8			

Assays of the feed, overflow (o/f) and underflow (u/f) samples show that after processing through the LFCU, the iron grade increases from 53.7 per cent to 63.8 per cent whilst SiO_2 grade decreases from 19.7 per cent to 8.8 per cent in the u/f stream. The particle size distribution (PSD) of the feed, o/f and u/f are shown in Tables 2 and 3 where a finer o/f (PSD) is observed in comparison to the feed and u/f streams. The P_{80} size of the feed, o/f and u/f streams are measured as 33 µm, 20 µm and 34 µm respectively.

The assay by size and elemental recoveries by size data of the feed, u/f and o/f streams are shown in Tables 2 and 3. The data shows clearly that the LFCU effectively separates magnetite from silica finer than 10 µm particle sizes. The u/f stream iron grade increase notably below sieve sizes of 25 µm, indicative of the liberation point of the material. The u/f stream SiO_2 grade is significantly lower than the o/f stream SiO_2 grade in all size classes. The elemental recovery by size plots shows that the majority of the iron in the feed reports to the LFCU u/f irrespective of the particle size. The SiO_2 distribution data shows that fine (<30 µm) SiO_2 reports mostly to the o/f stream whereas coarser SiO_2 (>38 µm) preferentially reports to the LFCU underflow.

TABLE 2

Iron grade by size and iron recovery by size data for the LFCU test fractions.

Assay Recovery

size (µm)	**size at 3.8 SG (µm)**	**% wt**			**% Fe**			**% Fe**		
		Feed	**UF**	**OF**	**Feed**	**UF**	**OF**	**Feed**	**UF**	**OF**
38	38	8.6	9.5	4.7	41.2	44.9	11.5	6.6	6.4	0.2
C1	32	12.8	16.0	0.3	70.5	70.7	18.9	16.9	16.8	0.0
C2	24	15.4	17.8	5.7	64.0	67.7	18.9	18.3	17.9	0.4
C3	17	19.4	19.4	19.5	55.4	65.6	15.5	20.0	18.9	1.2
C4	11	14.2	12.9	19.3	51.4	65.3	14.7	13.6	12.5	1.1
C5	8	7.7	6.8	11.5	49.8	65.0	14.5	7.1	6.5	0.6
-C5	-8	21.9	17.5	39.0	42.9	59.2	14.1	17.5	15.4	2.1
Total		100.0	100.0	100.0	53.7	63.6	14.7	100.0	94.4	5.6
Measured					53.7	63.8	15.0			

TABLE 3

SiO_2 grade by size and SiO_2 recovery by size data for the LFCU test fractions.

					Assay			Recovery		
size (µm)	**size at 2.7 SG (µm)**	**% wt**			**%SiO_2**			**%SiO_2**		
		Feed	**UF**	**OF**	**Feed**	**UF**	**OF**	**Feed**	**UF**	**OF**
38	38	8.6	9.5	4.7	33.7	28.8	72.7	14.6	11.0	3.5
C1	41	12.8	16.0	0.3	1.7	1.5	56.3	1.0	0.9	0.1
C2	31	15.4	17.8	5.7	8.6	4.7	56.3	6.7	3.3	3.3
C3	21	19.4	19.4	19.5	18.2	7.1	62.1	17.9	5.5	12.4
C4	14	14.2	12.9	19.3	22.3	7.4	61.9	16.1	3.8	12.3
C5	10	7.7	6.8	11.5	23.7	7.5	61.5	9.3	2.0	7.2
-C5	-10	21.9	17.5	39.0	31.0	13.6	61.8	34.4	9.6	24.8
Total		100.0	100.0	100.0	19.7	9.0	62.0	100.0	36.2	63.8
Measured					19.7	8.8	61.1			

The elemental recovery by size plot (Figure 3), shows that 98 per cent of the iron in the feed is recovered to the LFCU underflow for particles ≥25 µm size. Below this, it gradually reduces to a minimum 88 per cent recovery for particles down ≤8 µm in size. The SiO_2 recovery to the u/f stream is less than 30 per cent for all particles <20 µm after which it increases to 76 per cent at the 38 µm particle size. The coarse SiO_2 is probably not liberated from iron, hence it ends up to the LFCU u/f stream. The result suggests that the LFCU is capable of consistently recovering iron particles at all feed sizes while rejecting fine SiO_2. However, some coarse and unliberated SiO_2 reports to the LFCU product (ie u/f) steam during the particle separation process.

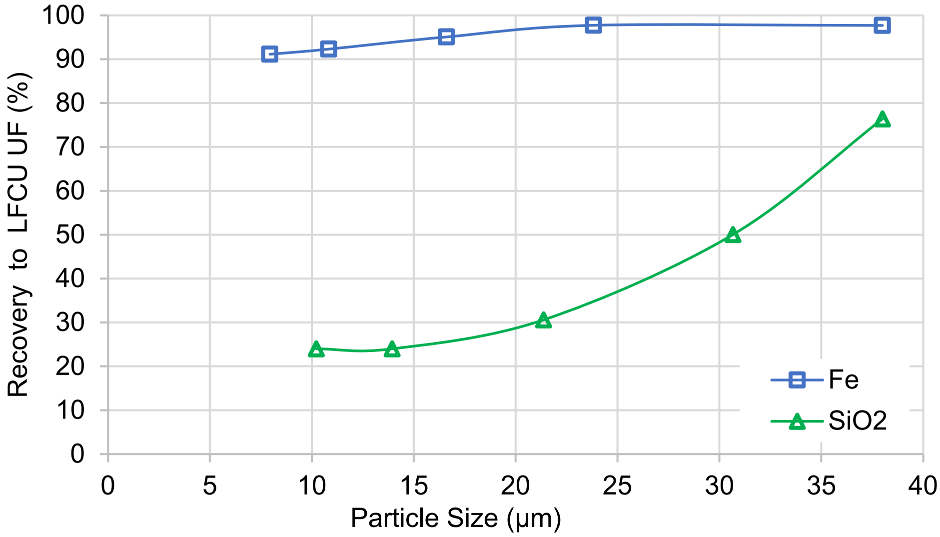

FIG 3 – LFCU Fe and SiO_2 recovery by size data to u/f stream.

Pilot scale testing

The pilot test work was conducted in two LFCUs (700 mm and 400 mm diameters respectively) operating in a rougher cleaner configuration (Figure 4) for a period of over three years in order to generate sufficient data for full scale design. The test work was conducted by keeping the flux rate between 1.1 to 3.5 t/h/m^2; a rise rate between 2.2 to 11.0 m/h and feed solids density between 13.4 to 35.2 per cent. During each test run, control samples were taken to determine the approximate rise rate and feed rate. Once a steady state condition was achieved, survey samples were taken of LFCU feed, o/f and u/f sample points every 30 minutes and analysed to determine particle size and elemental analysis.

FIG 4 – Pilot LFCU rig in the proposed magnetite mine.

Separation efficiency curves (tromp curve or partition curve) were developed for each test run to assist with the definition of particle separation characteristics for the LFCU. Figure 5 shows an example of the efficiency curves that were developed using a pilot test work data. The actual partition curve shows that more than 50 per cent of particles follow the underflow stream without being classified. This is found to be beneficial for the process in a way that for the same particle size class, mostly silica is classified and rejected to the overflow stream whereas heavy magnetite follows the underflow stream. The figure also shows that the LFCU can efficiently classify particles <20 µm. The corrected partition curve that defines particles recovered to the underflow through true classification was developed to compare LFCU separation performance against any particle size separator. The corrected partition curve suggests that the LFCU is not working in the same fashion as a simple particle size separator, such as a hydrocyclone or up-current classifier. The unit instead selectively rejects light minerals and recovers the heavy minerals (ie magnetite) to the underflow stream. This characteristic significantly improves the magnetite recovery in the LFCU and makes the unit ideal for duties of this type.

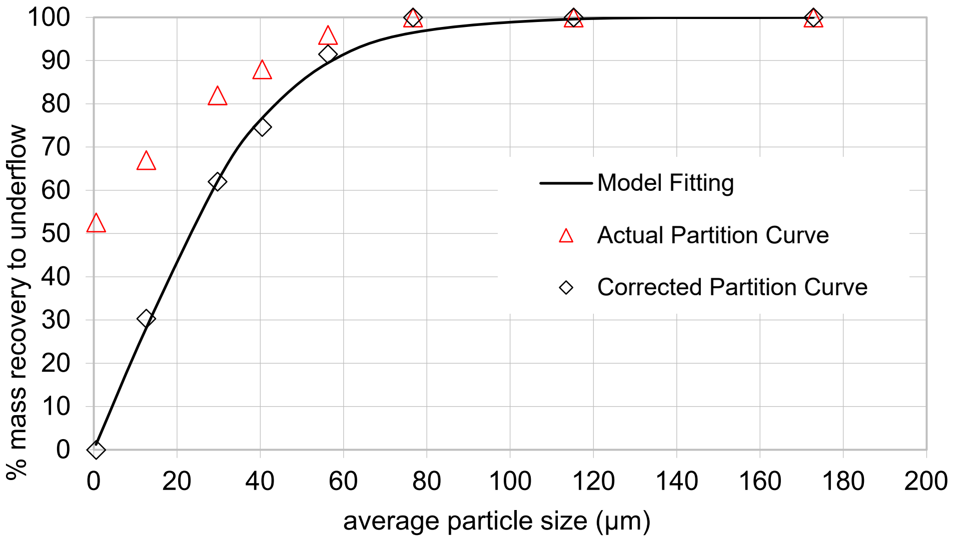

FIG 5 – LFCU particles separation efficiency curves (tromp curve or partition curve).

SCALE-UP ANALYSIS

Mass and mineral balances were determined for each test run by using feed, underflow and overflow mass flows; densities and assay data. Particle settling flux (t/h/m^2), overflow slurry rise rate (m/h), iron recovery to underflow and overflow streams were calculated for each test run using this data.

The combination of data generated from these tests shows that settling flux rate (t/h/m^2) and overflow slurry rise rate (m/h) have a similar influence on the effectiveness of the LFCU. Consequently, the combined effect of settling flux and rise rate is deemed as the critical parameter for scaling up the LFCU. This parameter will be referred to as the LFCU scale-up factor at all other points within this paper and is defined as:

$$LFCU\ Scale\ Up\ Factor = Settling\ Flux\ Rate\ \left(\frac{t}{h.m^2}\right) \times Rise\ Rate\ \left(\frac{m}{h}\right)$$

The effect of the LFCU scale-up factor on Fe recovery (inclusive of both pilot and laboratory testing) is shown in Figure 6. A negative correlation between the LFCU scale-up factor and Fe recovery can be observed. The results also show that increasing either settling flux or rise rate reduce Fe recovery in the LFCU.

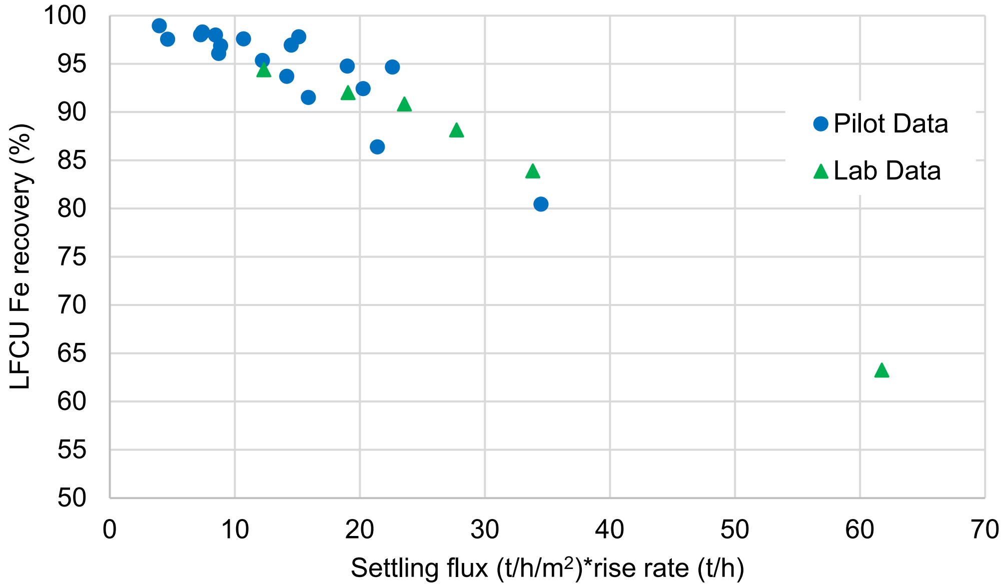

FIG 6 – Primary LFCU scale-up factor versus Fe recovery (%).

The mass split to overflow (%) at different operating conditions is critical for process flow sheet development, particularly with respect to ensuring the LFCU is sufficiently sized. Pilot and laboratory test work results of LFCU scale-up factor versus overflow mass fraction is shown in Figure 7. A clear trend is evident in the figure as the mass loss to overflow increases with increasing LFCU scale-up factor.

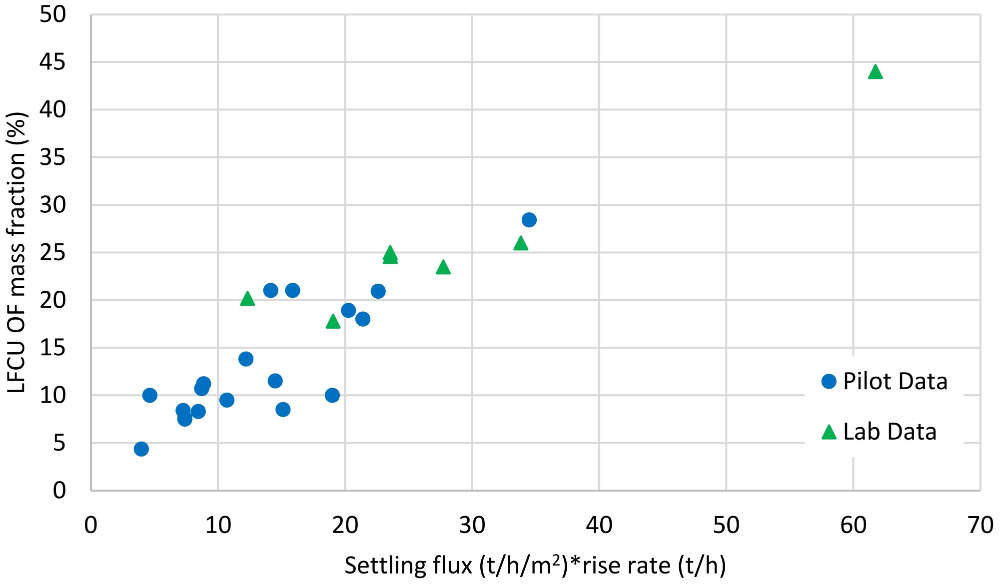

FIG 7 – Primary LFCU scale-up factor versus overflow mass split (%).

The LFCU for the full-scale magnetite processing operation have been designed to handle 4500 t/h (approximately) of finely ground magnetite. The goal of the process is to recover 90 per cent or more iron to the underflow stream, whilst rejecting the maximum amount of SiO_2 from the feed. LFCU product is further processed via magnetic separation to remove any remaining coarse silica. Figure 6 shows that an iron recovery of 90 per cent or more can be achieved by keeping the LFCU scale-up factor below 25. Hence, four 20 m diameter LFCU have been proposed for the duty with an operating flux rate of 3.5 t/h/m^2 and rise rate of 7 m/h. The mass split to the o/f stream has been calculated to 22 per cent with a predicted iron upgrade of 1.15 to 1.2.

CONCLUSIONS

Mineral Technologies has successfully utilised its innovative LFCU technology in a magnetite beneficiation process plant to remove ultrafine entrained silica. Extensive test work in the laboratory and pilot scale LFCUs has been conducted to validate the technology. The test work data showed that the LFCU can recover more than 90 per cent of the iron units within the feed, whilst removing approximately 64 per cent of the silica (primarily ultrafine). The LFCU treated a feed with a P_{80} particle size of 33 µm. The test work data showed that efficient particle separation takes place at particles sizes of less than 10 µm. A reasonable correlation was found between the pilot and laboratory LFCU units, which aided in the development of the scale-up model. Four numbers of 20 m LFCUs were designed to process 4500 t/h (approximately) of magnetite feed at an operating flux rate of 3.5 t/h/m^2 and rise rate of 7 m/h.

LFCU technology provides operators with a cost efficient and proven solution for the removal of ultrafine SiO_2 and Al_2O_3. The application of reverse flotation can provide a similar outcome, but the process will have added operational complexity and higher water requirements. The transition of the LFCU from the mineral sand industry to the iron ore industry is ground-breaking and the equipment should be considered for fine and ultrafine iron ore separation applications in Australia and the rest of the world.

ACKNOWLEDGEMENTS

The authors would like to thank Andrew Sutherland (Process Engineering Manager, Mineral Technologies) and Matthew Gill (Process Engineer, Mineral Technologies) for critically reviewing the paper. The authors also acknowledge that the success of this project would not have been possible without the support and dedication of the site personnel and laboratory staff for the pilot study and laboratory test work. Lastly, the authors would like to thank Mineral Technologies for giving permission to publish the paper.

REFERENCES

Gleeson, D, 2021. Primero completes WHIMS project at Fortescue's Christmas Creek iron ore op [online], *International Mining*. Available from: <https://im-mining.com/2021/02/16/primero-completes-whims-project-fortescues-christmas-creek-iron-ore-op/> [Accessed: 6 May 2021]

Jenike, A W, 1964. Storage and flow of solids, *Bulletin 123 Utah Engineering Experiment Station*, University of Utah, Utah.

Lyons, J, Hill, G, Vadeikis, C and Wiche, S, 2009. Innovative Surge Bin Design for Mineral Sands Processing Plant, *Mineral Processing Plant Design – An update 2009 Conference*, Arizona, USA.

Murthy, A and Basavaraj, K, 2012. Assessing The Performance of a Floatex Density Separator for The Recovery of Iron from Low-Grade Australian Iron Ore Fines – A Case Study, *IMPC 2012*, New Delhi, India.

McNab, B, Jankovic, A, David, D and Payne, P, 2009. Processing of magnetite iron ores–comparing grinding options, in *Proceedings Iron Ore Conference*, pp 277–287 (The Australasian Institute of Mining and Metallurgy: Melbourne).

Southway, K, 2020. Roy Hill: Automation imperative [online], *The Australian Mining Review*. Available from: <https://australianminingreview.com.au/features/roy-hill-automation-imperative/> [Accessed: 6 May 2021].

Tripathy, S K, Bhoja, S K, Kumar, C and Suresh, N, 2015. A short review on hydraulic classification and its development in mineral industry, *Powder Technology*, 270(part A):205–220, ISSN 0032–5910.

Yellishetty, M, Mudd, G, Mason, L, Mohr, S, Prior, T and Giurco, D, 2012. *Iron Resources and Production: Technology, Sustainability and Future Prospects*, Prepared for CSIRO Minerals Down Under Flagship, by the Department of Civil Engineering (Monash University) and the Institute for Sustainable Futures (University of Technology, Sydney), Institute for Sustainable Futures: University of Technology: Sydney, Australia, ISBN 978–1-922173–46–1.

Dry concentration of low-grade magnetic iron ores

J R Kelly[1] *and C S Kelsey*[2]

1. Metallurgical Director, Cyclomag P/L. Email: jrkelly01@optusnet.com.au
2. Operations Manager, Cyclomag P/L. Email: kelsey.eng@optusnet.com.au

ABSTRACT

Australia is presently enjoying the fruits of a booming iron ore market. Expectations are that market strength will be supported in the short to medium term by increasing feedstock demands from steel mills, as world economies rebuild post-Covid-19. However, as cost and environmental pressures increase the longer-term market outlook will be dominated by product quality. The 'flight to quality' will place increasing demands on direct shipping ore miners as they compete to maintain their standing in the iron ore marketplace. China will progressively disengage from its dependence on Australian imports, leaving miners under increasing pressure to boost product quality and diversify outlets globally. Australia has vast deposits of low-grade magnetite ores located mainly in remote and arid regions of the continent. This paper proposes a dry grinding and magnetic separation process to produce premium concentrate grades from the low-grade ores, to assist in meeting future product quality demands. The premium grade concentrates could be either blended with lower quality direct shipping ores or marketed separately. The proposed dry concentration process involves the pairing of Vertical Roller Milling (VRM), a mature technology widely used in the cement industry, and Planar Magnetic Separation (PMS), a new methodology, which has been developed to the threshold of commercialisation by the private Australian company Cyclomag P/L. Two laboratory prototype planar magnetic separators with field strengths of 1800 gauss and 6000 gauss have been built and tested on a range of magnetite ore types over the past three years. In each case, following grinding to liberation sizes, a combination of roughing and cleaning operations has produced pellet grade concentrates. Vertical roller milling has competed successfully with conventional media milling in grinding cement clinker, limestone and blast furnace slags. A key advantage of dry VRM/PMS processing is its potential adaptability to stepwise modular development, which can minimise initial capital investment, while generating early revenue streams to cope with unpredictable market volatility.

INTRODUCTION

Australia's economic recovery post-Covid-19 will depend heavily on maintaining its domination of the seaborne trade in iron ore and concentrates. The current political uncertainties weighing on other major Australian exports heighten the importance of the long-term security of iron ore and concentrate exports. China presently receives around 62 per cent of its steelmaking feedstock from Australia and is actively seeking to establish alternative supply lines. This progressive disengagement will need to take place over a number of years, and Australia must use the breathing space to establish alternative outlets globally and further build on product output and quality.

BACKGROUND

Infrastructure building and allied manufacturing expansion will support the short to medium term global demand for iron ore and steel post-Covid-19, and the market will be buoyed accordingly. However, progressively increasing cost and environmental pressures will accelerate a 'flight to quality' which is already underway. The Australian iron ore industry is not only under long-term threat from rising political tensions but will also be required to effectively deal with competing product quality pressures. Presently Australia's direct shipping iron ore grades, which range from 56 per cent Fe to 64 per cent Fe are on the decline. Over the past 10 years the 62 per cent Fe Pilbara fines spot price has ranged from over \$200/t to \$38/t. Before the recent atypical surge in prices related to demand associated with China's expanding domination of global steel production the price trend was down. Price penalties on some low-grade direct shipping ores have blown out to over 30 per cent. Australia must remain conscious of future risks and move to consolidate its present status as the global leader in sea-born exports. Historically, market volatility has claimed casualties such as US miner Cliffs Resources who exited their mid-West Australian iron ore operations after posting losses in 2017 and in the first half of 2018. Increased price discounting on lower grade ores sounded the death-knell for Cliff's operations, despite a significant increase in bulk commodity pricing. Cliff's bulk shipments averaged around 58 per cent Fe. With Australia poised to expand ore beneficiation investment to meet the increasing product quality demands, the well published financing and cost issues experienced by the giant 'Sino Iron' and 'Karara' projects, should also sound warning bells. The massive scale of these conventional wet processing projects required major plant and infrastructure investment. In addition, long production lead times, compounded by major processing plant capital and operating cost over-runs weighed heavily on working capital, leading to critical debt re-financing issues and forced equity sell-downs. Despite these discouraging past experiences, Australia cannot afford to lose sight of the substantial product quality boost that will be required to maintain and further build on its export market position. The only unassailable defence against future iron ore marketability threats is for Australia to lead the world in the production of premium grade product.

PRESENT DAY MARKET PERCEPTIONS

A widely held view on the security of Australia's long-term seaborne iron ore exports, suggests that Australia will dominate the trade with little significant competition for decades into the future. The Pilbara's remaining iron ore resources consists mainly of Brockman and Marra Mamba ore types. Brockman's is predominantly high phosphorus, which can be up to 1 per cent in goethite associations. Steel producers are now demanding feed-stock phosphorous levels below 0.1 per cent. Ore beneficiation both physical and chemical, to reduce phosphorous comes at a cost. The low alumina Yandi channel iron deposit ores have been depleted and are being progressively replaced with Marra Mamba ore types, high in silica and alumina, which will require beneficiation, Export of these ores target the benchmark Pilbara fines (62 per cent Fe) market. The predominant phase in most Marra Mamba channel iron deposits and detrital iron ore deposits is goethite at 62.9 per cent Fe without impurities. Marra Mamba ores are typically challenging to process due to complex mineralogical associations and fine dissemination of gangue minerals. Marketing pressure on the 62 per cent Fe benchmark are heightening and will continue to increase into the future. Premium high-grade direct shipping lump ores are also being rapidly depleted, and exports will come under increasing pressure from external sources and from beneficiated high-grade magnetite concentrates. Australia's FMG for example are preparing to meet future pressures with the mining and beneficiation of their lower grade Pilbara Iron Bridge magnetite ores, which can be concentrated to premium grades. Further pressure on Australia's iron ore exports will come from the expanding adoption of direct reduction technology (DRI) as an alternative to blast furnace reduction. As this technology expands with the prospect of using hydrogen as the reducing agent in preference to coal, demands for direct reduction grade feed stocks with silica levels at 2 per cent and below will increase substantially. There is vast potential here for dry processing to play the key future role in generating low cost DRI feed grade products from Australia's vast untapped arid region magnetite resources. There is no doubt that at present, Australia is firmly in the seaborne export market driver's seat, but it would be folly to expect this position to remain unchallenged.

CHINA'S IRON ORE TRADE BALANCE

China sources its iron ore from domestic production, overseas rights and overseas imports. Over recent years China's domestic production has been erratic, ranging from less than 100 Mt/a to over 200 Mt/a. Steel mill feed quality demands, production costs and pollution control pressures have been responsible for the erratic domestic production. More recently, China's major steel producers have been pressing the government to support immediate action to increase domestic supplies to at least 25 per cent of total feedstock requirements. Around 50 per cent of China's feedstock supplies from overseas rights and interests, originates from Australia, and China views expansion of supplies from developing countries as a longer-term undertaking. Whilst increasing imports from Brazilian miner 'Vale' will make significant inroads into overall supply in coming years, the question mark hangs over China's domestic production. There is a questionable yet widely held view that any threats from Chinese domestic iron ore and concentrate production will be kept at bay due to the low-grade and wide distribution of ore deposits, as well as the beneficiation difficulties experienced in the past. It is well known that China's iron ore resources are huge, and that China does not intend to remain at the mercy of foreign exporters. It appears that China has no immediate alternative other than to support major expansion of its domestic iron ore and concentrate production. Banded iron formations, account for approximately 64 per cent of China's total identified iron ore resource. A significant proportion of these iron oxides have metamorphosed into coarser grained magnetite. Although head grades are generally low at 20 per cent to 30 per cent total iron, the ores are prime targets for dry magnetic beneficiation. Skarn type deposits hosting higher-grade iron ores are widespread over middle and southern China and are an important resource, which would also respond to dry concentration. In early 2020, the Chinese magnet company 'LONGi' sourced samples of ground magnetite ores from three operating magnetite mines in China. Head grades varied from 20 per cent Fe to 35 per cent Fe. Dry magnetic separation tests through the Cyclomag planar magnetic separator (PMS) at Hope Forest in South Australia, produced saleable concentrate grades from two of the finer ores and a pellet grade concentrate from the higher-grade sample. The LONGi representatives witnessing the tests were impressed with the result and offered to participate in building and testing a commercial prototype PMS. However, negotiations with LONGi were terminated shortly after their visit, due to Covid-19 restrictions. The results of the higher-grade ore sample test are tabulated in the PMS development test work section of the paper. The probability of low-cost dry processing of magnetite ores in China becoming a key concentrate supply source is extremely high.

PLANAR MAGNETIC SEPARATION

During 2017, Christopher George Kelsey the inventor of the Kelsey Centrifugal Jig, turned his innovative talents to the development of a low cost and eco-friendly dry alternative to conventional wet beneficiation of low-grade magnetic iron ores. Kelsey's work was funded by the private Australian company Cyclomag P/L. At the time, it was becoming apparent that magnetite concentrates would feature more prominently in Australia's iron ore export mix. Previous large-scale conventional wet processing operations, which required major outlays of risk capital, had in the past faced significant cost issues. These issues proved to be difficult to manage, particularly during product price downturns. In effect, Kelsey became engaged in a process of risk reduction, which was necessary to encourage future capital investment in the development of Australia's low-grade magnetite resources. The outcome of his work was the planar magnetic separator (PMS), an innovative processing breakthrough, which had the potential to broaden the scope for low-cost dry beneficiation of magnetic iron ores. In 2019, Kelsey received the award of 'Engineering Technologists of the Year' from the prestigious Engineers Australia.

A single cassette PMS is illustrated in Figure 1.

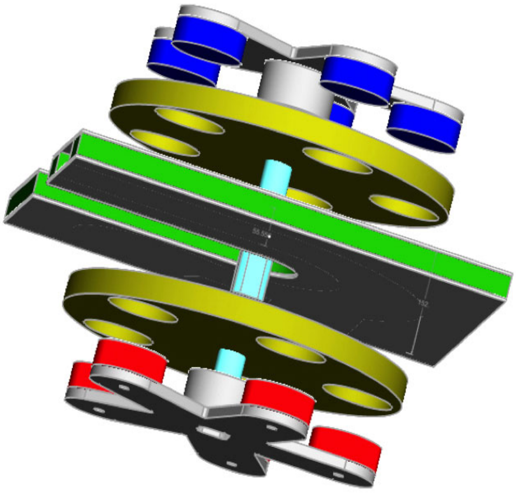

FIG 1 – A single cassette planar magnetic separator.

The PMS is a simple device, consisting of a separation chamber (green) with feed, product and tailings ports. The separation chamber is sandwiched between rotating discs (khaki), with embedded permanent magnets (red and blue). Magnetic particles accumulate on the inside surfaces of the separation chamber as dispersed feed enters the separator in a primary air stream. The magnetic particles are drawn around the semi-circular path to meet the internal partition, which separates the feed port from the product port. The magnetic concentrate disengages from the magnetic field at the internal partition and discharges under gravity. The primary air stream carries non-magnetics to the tailings port, where it is collected in an air cyclone under negative pressure. The dispersion of feed particles in an air stream enables the PMS to selective recovery the full-size range of magnetic particles. The simple and adaptive design of the separator facilitates scaling and has the potential to offer low capital and operating costs. Other advantages of the PMS include full enclosure, which eliminates dusting losses, low entrainment of impurities and high recoveries of values including, ultra-fines. The design configuration of the PMS enables in-line arrangements of multiple cassettes with a common drive shaft. The image in Figure 2 shows a multi cassette separator with one cassette extracted for maintenance.

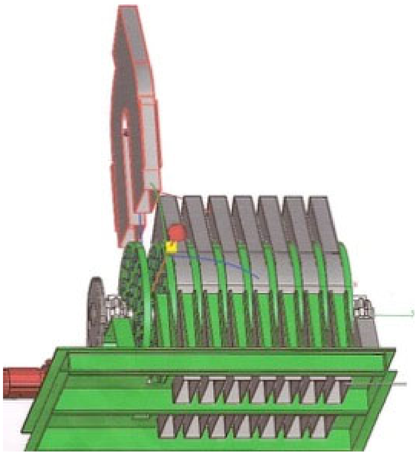

FIG 2 – The multi cassette planar magnetic separator.

The laboratory prototype 1800 gauss PMS 300 and a 6000 gauss PMS 560, shown in Figure 3, have been used for testing and demonstrations over the past three years.

FIG 3 – The PMS 300 and PMS 560 dry laboratory prototype separators.

Cyclomag has also produced detailed workshop drawings for the manufacture of a commercial prototype 6000 gauss PMS 1200. Dimensioned side and end elevation images are shown in Figure 4.

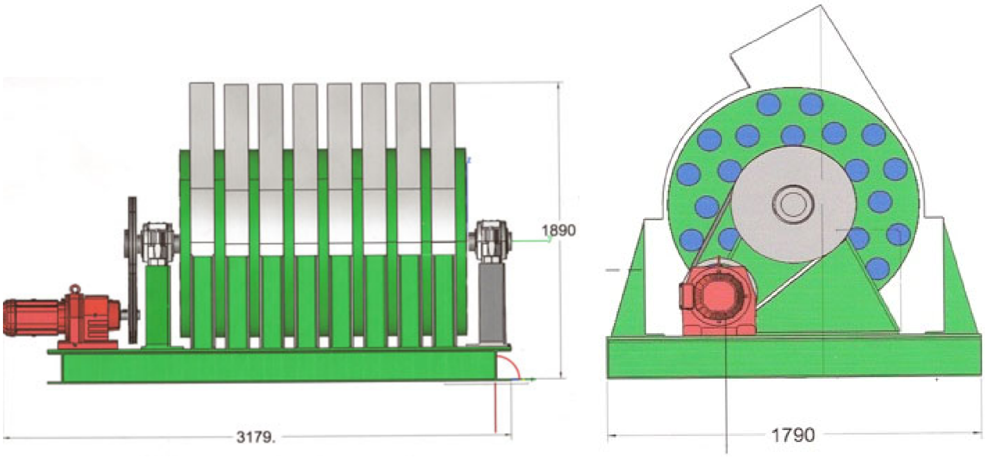

FIG 4 – The proposed eight cassette commercial prototype PMS1200.

Scale-up modelling from laboratory test work data predicts production rates up to 40 t/h from the eight cassette PMS 1200. The separators common drive design can cater for a larger number of cassettes as required. A high field strength (15 500 gauss) PMS 600 laboratory prototype recently built at Cyclomag's engineering facilities in South Australia. is undergoing commissioning trials. The separator is scheduled for magnetite trials, which will aim to further develop commercial designs, with a view to maximising unit processing capacity, in order to minimise the footprint, capital costs and operating costs of a commercial plant. The PMS 600 will also target concentration of paramagnetic iron oxides, including hematite.

PMS DEVELOPMENT TEST WORK

PMS development has primarily focused on dry concentration of low-grade magnetite ores, covering a variety of ore-types. Initial test work with the 1800 gauss PMS 300 consistently demonstrated that pellet grade concentrates could be produced with high iron recoveries from a combination of roughing, scavenging and one or two stages of cleaning. Repeat test work with the advanced 6000 gauss PMS 560 subsequently demonstrated that similar overall performance could be achieved with one roughing and one cleaning stage of processing. The following examples highlight the capabilities of dry PMS technology.

Beneficiation of low-grade magnetite ores

Two samples of low-grade ore with magnetite in associations with siltstone, from the extensive South Australian Braemar formations were processed through the 1800 gauss PMS 300 following super-fine crushing. These ore-types generally show superior values liberation characteristics. The processing results shown in Table 1, demonstrated clean separations, with exceptionally high concentration ratios from a single stage roughing and scavenging separation.

TABLE 1

PMS 300 beneficiation of low-grade Braemar formation magnetite.

Parameter	Unit	Sample 1	Sample 2
Feed Fe grade	%	15	20
Feed size p80	µm	70	54
Concentrate mass yield	%	18	25
Concentrate Fe grade	%	69	69
Fe recovery	%	82.8	86

Comparing dry PMS with wet low intensity magnetic separation

The Table 2 results of comparative studies by Baawuah *et al* (2020) on magnetite ore ground to 80 per cent passing 75 microns, demonstrated that the dry PMS produced a cleaner magnetite concentrates than that of the wet low intensity magnetic separator (WLIMS).

TABLE 2

PMS and WLIMS comparative studies.

Parameter	Unit	Feed	PMS	WLIMS
			Concentrate	**Concentrate**
Mass yield	%	100	45.6	49.5
Fe_3O_4 grade	%	40.8	85.9	78.8
Fe grade	%	41.5	68.4	64.8
Si grade	%	8.84	2.87	3.61
Al grade	%	2.91	1.34	1.59
Ca grade	%	4.74	0.91	1.52

Performance comparison – dry PMS 300 versus operating wet LIMS plant

Samples of magnetite ore feed stock from an operating wet LIMS based plant were processed through the PMS 300 to compare results against plant performances. A typical set of results recorded in Table 3, highlights the potential for significant improvements with dry processing, apparently due to the superior capture of ultra-fine magnetite together with higher levels of fine particle selectivity offered by the PMS.

TABLE 3

Dry laboratory PMS V operating wet LIMS plant.

Parameter	Unit	Dry PMS 300	Wet LIMS plant
Feed size p80	µm	42	38
Feed Fe grade	%	36.2	32
Concentrate Fe grade	%	69	65.5
Concentrate Fe recovery	%	80.1	69.6
Concentrate Mass Yield	%	42	34

Beneficiation of a Chinese banded iron formation magnetite ore

A ground sample of banded iron formation (BIF) magnetite ore from a Chinese mining and processing operation (labelled 32.2 per cent passing 25 microns) was processed through the 6000 gauss PMS 560. Table 4 shows a single pass roughing and cleaning operation producing pellet grade concentrate from a high silica grade feed.

TABLE 4

Ground Chinese magnetite ore beneficiation.

Parameter	Unit	Feed	Rougher concentrate	Cleaner concentrate
Fe grade	%	35.8	65.3	67.1
Si grade	%	37.8	5.1	3.2
Mass yield	%	100	45.3	84.5

PROPOSED DRY PROCESSING METHODOLOGY

IMP Technologies laboratory prototype super-fine crusher (SFC) has been used to generate fine and super-fine feeds for dry laboratory PMS trials and demonstrations at Hope Forest over the past three years. Cyclomag P/L is a sister company of IMP Technologies P/L. The original intention was to combine the SFC and PMS technologies as a prospective low cost, alternative dry processing methodology. However, at that stage the SFC required two further stages of scale-up before it could be considered for commercial applications. Unfortunately, SFC development stalled due to lack of funding and IMP Technologies inability to raise the interest of iron ore miners in providing suitable commercial test facilities. Consequently, over the past two years, Cyclomag and German engineering company Loesche GmbH, have been investigating the prospects of pairing the Loesche vertical roller mill (VRM) with the PMS for possible commercial applications. Loesche have also offered to participate in the commercial development of the VRM/PMS pairing by providing access to their 20 t/h commercial prototype testing facilities. A large-scale vertical roller mill extensively used in the cement industry for grinding of cement clinker, limestone and blast furnace slags is shown in Figure 5.

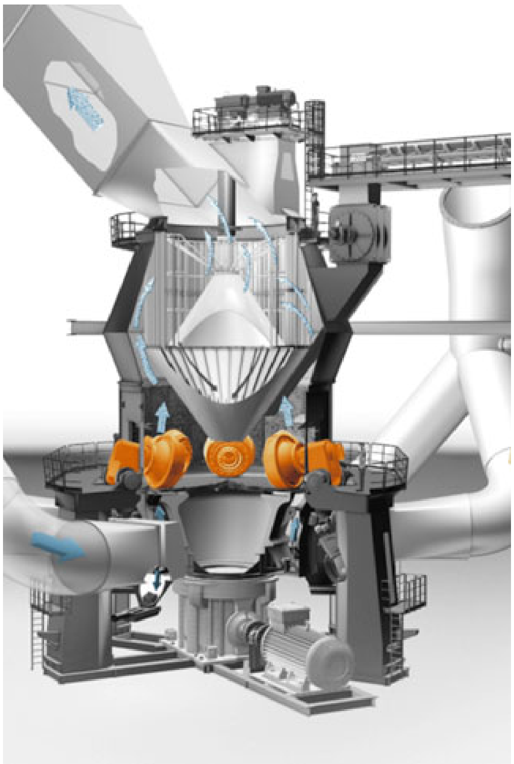

FIG 5 – A large scale vertical roller mill.

The mill has an integrated air classifier, which simplifies the processing circuit. The grinding table rotates under fixed rollers at variable hydraulic pressures, and oversize is recycled within the mill assembly. High particle size reduction ratios, achieved by the mill can eliminate an upstream fine crushing stage. VRM milling trials have achieved size reductions from 40–50 mm top size to 36 microns on hard banded iron formation (BIF) magnetite ore at an economical 21 kWh/t. Costly grinding media is also eliminated. A recently quoted price of a 600 t/h Loesche VRM was US $23 million. The mills are designed for throughputs of up to 1200 t/h.

Modular development

The VRM/PMS pairing is also ideally suited for modular development. The advantages of modular development include the option to minimise initial capital raising and keep debt levels under control, while generating an early revenue stream to reduce working capital risk. Exposure to market downturns could also be more comfortably tolerated and processing can be ‘de-bugged’ ahead of major expansions. Dry processing can also minimise on-site environmental impact and reduce capital and operating costs by enabling the return of agglomerated tailings to the pit as backfill. The elimination of costly and potentially hazardous wet tailings storage adds to the value of dry processing. VRM/PMS processing modules, as outlined in Figure 6, could be sized to meet specific development schedules. The dry modular VRM/PMS concept has the potential to be progressively developed at greatly reduced investment risk in comparison with large – scale conventional wet processing developments.

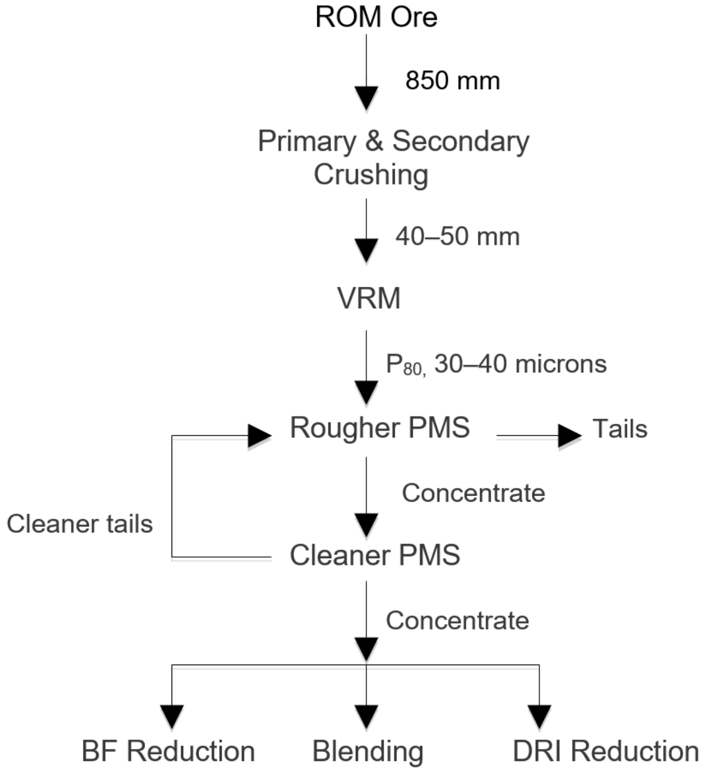

FIG 6 – A proposed VRM/PMS dry processing module.

Six by 1000 t/h modules delivering ≈40 per cent mass yield from feed at ≈36 per cent Fe have the potential to produce around 15 Mt/a of premium grade concentrate.

PMS DEVELOPMENT STATUS

Cyclomag successfully advanced the development of the PMS to the threshold of commercialisation, but unfortunately at that point, development stalled.

Further development to commercial status will require a commercial prototype PMS and access to a proving facility with the necessary infrastructure or to a processing site with bulk materials handling facilities. A single cassette commercial prototype PMS has been designed and could be built at Cyclomag's engineering workshop in South Australia. Despite numerous successful tests and acclaimed laboratory prototype demonstrations on Australian magnetite ores over the past three years, Cyclomag has failed to attract a commitment from any of the potential users to participate in the commercial development of the technology. The only offer to participate in building and testing a commercial prototype PMS has come from the Chinese 'LONGi' magnet company, as previously noted in the paper. Unfortunately, Cyclomag is privately funded and has neither the financial backing nor the operational capacity to advance the technology to commercial status.

COMPETING DRY IRON ORE PROCESSING TECHNOLOGY

Brazilian multinational corporation Vale SA, the world's second largest producer and exporter of iron ore and concentrates, have already adopted and are in the process of expanding dry processing of their magnetic iron ores. The shift to dry processing was in response to catastrophic failures of major wet tailings dams at their iron ore mine sites. The processing technology involves dry grinding and conventional permanent magnet dry rolls magnetic separation, which carries the acronym (FDMS). Vale is presently the world leader in adopting dry iron ore processing and can be commended for successfully applying FDMS technology for the beneficiation of their low-grade ores and tailings from previous operations. Vale invested heavily in acquiring the company 'New Steel', who developed the FDMS technology. The following comments on the FDMS process have been taken from a Cyclomag in-house appraisal, which was based on data submitted with New Steel's US patent 9327292B2 'Process and system for dry recovery of fine and super-fine particles of oxidised iron ore and a magnetic separation unit'. The data submitted related to concentration of dried reclaimed tailings. FDMS has some potential cost and operational issues, which could create significant disadvantages in comparison with dry PMS technology. The configuration of an FDMS plant calls for multiple fractionating and separation units. The fine feed particle mass is cyclone split into six individual size fractions to achieve a more predictable separation response as can be expected from like sized particles under the conventional separators combined influences of gravity, centrifugal force and magnetic fields. The response of the -10 micron particle size fraction was deemed unpredictable and the fraction, which can account for up to 15 per cent of the total mass is discarded. The FDMS process also calls for up to three stages of separation for each size fraction. The accompanying capital, operating and maintenance costs accruing with increasing plant throughputs and lower grade feeds as well as the process control complications, suggests that the economic viability of the process could become severely stressed. Separation selectivity issues with particle sizes finer than 100 microns also raises efficiency doubts. This issue could arise in relation to the processing of the harder banded iron formation ores where fine impurity associations call for finer grinding. On the other hand, the PMS laboratory prototypes have performed efficiently on the entire feed mass including the -10 micron size fraction. In addition, the high field strength laboratory prototype PMS 560 has demonstrated that premium grade concentrates could be produced from one roughing and one cleaning stage of separation.

A WINNING FUTURE AUSTRALIAN IRON ORE MARKET STRATEGY

Australia is uniquely placed to set new dry magnetite beneficiation cost benchmarks and remain ahead of competitors. South Australia has vast untapped deposits of low-grade magnetite ores, located mainly in arid regions of the state, where water availability can become an insurmountable obstacle. The extensive magnetite bearing formations stretch from the Eyre Peninsular to the Mawson province in the north of the state, where the 'Braemar' formation covers some 200 km between Broken Hill and Peterborough. Magnetite ores in this region are commonly hosted in softer siltstones and samples of these ores have been concentrated to premium grades with high iron recoveries, during PMS trials. The Central Eyre Peninsular also hosts major magnetite resources within the states massive 'Gawler' craton. Feasibility studies by prospective developers have shown that the lower grade ores in these regions are commonly coarser grained with magnetite in some cases liberating at sizes, around 100 microns. Magnetic separation of these ores can readily produce premium grade concentrates. A number of resource locations in South Australia, prospectively targeted for development, would each support major mining and processing operations for 30–40 years. There has already been sufficient orebody delineation and feasibility studies undertaken to target premium grade concentrate production rates of up to 50 Mt/a within 10 years, providing the initial development funding can be acquired. South Australia can become a key player in shaping the future of Australia's iron ore industry. Similar potential exists for concentrating low-grade magnetite resources in the Pilbara and central regions of West Australia. Premium grade magnetite concentrates can be blended with lower grade direct shipping ores or directly marketed as high-quality products attracting high price premiums. The concentrates would also provide ideal feedstock for the development of direct reduction processing to produce metallic iron products for export or domestic consumption.

CONCLUSIONS

The Australian iron ore industry can potentially draw major value adding, low risk benefits from the advances in concentration efficiency, offered by planar magnetic separation technology. A synopsis of key factors, which will shape the future of Australia's iron ore industry, could read as follows:

- Australia presently dominates the global seaborne iron ore export trade, but challenges are looming as China actively seeks to establish alternative supply lines outside of Australia.

- China will be pressured into embarking on a major expansion of domestic magnetite ore concentration, which will be facilitated by the availability of low-cost dry processing.
- Australia's high-grade ore reserves are declining and iron ore exports will require a product quality boost, which can come from the concentration of Australia's vast low-grade magnetite ores resources,
- Processed magnetite concentrates will feature more prominently in the iron ore export mix.
- Further product quality pressure will come from the expanding adoption of direct reduction for metallic iron production, as an alternative to blast furnace reduction. The demand for higher-grade iron ore products with silica levels around 2 per cent and below will increase significantly under these circumstances.
- Large scale conventional wet magnetite processing, carrying significant cost and environmental risk will be challenged by the dry combination of vertical roller milling and dry planar magnetic separation, which is potentially the lowest risk and most cost-effective concentration route.

The most important conclusion to draw is that Australia's major revenue earner cannot be expected to look after itself, nor can it rely entirely on major mining companies to get the job done. Decision makers with Australia's interests foremost in mind, must ensure that the iron ore industry adapts to changing demands and remains ahead of the competition as it deals with mounting political pressures, environmental demands and technological change.

REFERENCE

Baawuah, E, Kelsey, C, Addai-Mensah, J and Skinner, W, 2020. Economic and Socio-Environmental Benefits of Dry Beneficiation of Magnetite Ore. Multidisciplinary Digital Publishing Institute (MDPI) Minerals.

Molecular modelling applied to the flotation of iron ores

J Lainé[1,2], C Veloso[3], A C Araujo[4], Y Foucaud[5] and M Badawi[6]

1. PhD Student, Laboratoire de Physique et Chimie Théoriques, UMR CNRS 7019, University of Lorraine, Vandoeuvre-lès-Nancy 54500, France. Email: juliette.laine@univ-lorraine.fr
2. Arcelor Mittal Global Research and Development, Voie Romaine, Maizières-lès-Metz 57280, France.
3. ArcelorMittal Global Research and Development, Voie Romaine, Maizières-lès-Metz 57280, France. Email: carlos.veloso@arcelormittal.com
4. ArcelorMittal Global Research and Development, Voie Romaine, Maizières-lès-Metz 57280, France. Email: armando.correa@arcelormittal.com
5. Laboratoire GeoRessources, UMR CNRS 7359, University of Lorraine, Vandoeuvre-lès-Nancy 54500, France. Email: yann.foucaud@univ-lorraine.fr
6. Associate Professor, Laboratoire de Physique et Chimie Théoriques, UMR CNRS 7019, University of Lorraine, Vandoeuvre-lès-Nancy 54500, France. Email: michael.badawi@univ-lorraine.fr

ABSTRACT

Iron is one of the most exchanged commodities worldwide. Its use for steelmaking explains the growing demand in the metal which remains mainly produced by the mining and the beneficiation of iron ores.

Flotation is the most used mineral separation technique worldwide, processing several billion tonnes (Bt) of ore annually, including, in some cases, hematite and magnetite ores. Based on the physical-chemical properties of mineral surfaces, flotation aims to selectively adsorb molecules that render mineral surfaces either hydrophobic or hydrophilic, known as collectors and depressants, respectively. Hydrophobic particles are then recovered in the froth by the injection of gas bubbles travelling up in the cell and attaching the hydrophobic particles. However, despite the popularity and the good performances of flotation, mining industry faces new challenges of decreasing grades and increased mineralogical complexness in ores. Many flotation variables, especially when related to reagent adsorption, remain poorly understood and it becomes necessary to gain knowledge to enhance the existing processes.

Molecular modelling techniques like the density functional theory or molecular dynamics simulations (ie Classical molecular dynamics or *Ab initio* Molecular Dynamics) currently represent powerful tools for different applications in material sciences, like catalysis or depollution purposes. They have recently been successfully applied in the flotation area, with an increasing number of publications dealing with this topic every year.

These tools provide crucial information on bulk and surface properties as well as on the adsorption mechanisms of reagents on mineral surfaces, key step in the flotation process, and synergetic effect of collector mixtures. A better understanding of the adsorption mechanisms of flotation reagents, provided by molecular simulations, will help to finely choose flotation reagents, and even lead to the development of new reagents formulations.

Overall, these tools enable the discovery of practical and industrial solutions to improve the flotation process, which will undoubtedly help the mining industry to face its future challenges.

INTRODUCTION

Geology of iron ores

Iron is today the second largest commodity exchanged in the world after crude oil. It is mainly used for steelmaking and with demographic and technology growth, its demand constantly increases. Iron recycling is still inefficient, and the main production remains the mining of iron ores.

Iron is the fourth most abundant element of Earth Crust with a content close to five per cent. Almost 300 minerals contain iron but only four are considered as important ore minerals: magnetite, hematite, goethite, and siderite (Ferenczi, 2001). The most important ore minerals being magnetite (Fe_3O_4) and hematite (Fe_2O_3) containing 72.36 per cent and 69.94 per cent of iron, respectively.

Iron ores can be exploited from different types of deposits. Banded Iron Formations (BIFs) which can contain up to 65 per cent of iron (Hagemann *et al*, 2015; Jébrak, Laithier and Marcoux, 2008) are, by-far, the most exploited, followed by other types of deposits like iron skarns, iron-oxide-gold-copper (IOCG) or oolithic deposits. BIFs can be divided into two types namely the Lake Superior-type and the Algoma-type. Their formation occurred 1.9–2.3 and 2.6 billion years ago, respectively in oceanic sedimentary basins. They were chemically formed by the precipitation of iron and silica when oceans became more oxidising (Jébrak, Laithier and Marcoux, 2008) by the presence of dissolved oxygen. BIFs exploitation districts are located in Brazil, Canada, USA, India and Australia with smaller productions in Western and South Africa and Ukraine (Hagemann *et al*, 2015). Iron skarns are formed by metasomatism in a contact metamorphism context. The main iron skarns deposits are located in North Korea and Russia, but other deposits are found in Mexico, Kazakhstan or in the USA, to name but a few (Jébrak, Laithier and Marcoux, 2008). Hydrothermal IOCG are rich in copper, gold, sometimes uranium and iron oxides while magmatic IOCG are magnetite ores. The latter category supplies up to two per cent of the world iron. One important example is the Kiruna deposits which has been exploited since Middle Age (Jébrak, Laithier and Marcoux, 2008). IOCG are widely distributed in the world with deposits in Canada, Lapland, Australia, South America, Eurasia, and Africa. Finally, oolithic iron are formed in shallow ocean basins, they were – before the exploitation of BIFs – the main source of iron in the world with iron contents ranging from 5–35 per cent. Several hundreds of oolithic iron deposits are described in Europe, North America but also in North Africa. A French deposit, in Lorraine (North-East) contained about three Gt of ore (Jébrak, Laithier and Marcoux, 2008). Even if iron deposits are well distributed in the world, nowadays, a small number of countries (Brazil, China, USA, India, and Australia) are the main iron producers with about 1.8–1.9 Bt produced each year (USGS data).

In the different deposits, magnetite and hematite are associated with a certain number of other minerals. Their proportion depend on the type of deposits and on the event that could alter it (ie hydrothermalism). These other minerals, which are mostly discarded in the tailings, form the gangue of the ore. The most common gangue minerals are silicates, such as quartz, kaolinite, epidote and diopside (Araujo, Viana and Peres, 2005; Veloso *et al*, 2018). The presence of the gangue minerals in ore concentrates affects metallurgical processes performance. For steelmaking, particularly routes including furnace and direct reduction, the concentrate's quality must respect strict limits in term of elemental 'pollution': usually concentration less than two per cent for silica, than 0.1 per cent for sulfur, than 0.001 per cent for phosphorus and, than two per cent for aluminium. Thus, these gangue minerals must be removed from the concentrate by different beneficiation treatments.

Froth flotation and treatment challenges

Froth flotation is one the most used mineral separation process today. It represents the treatment of several Bt of ore each year and is found in the beneficiation route of almost all non-ferrous metals world production (Bulatovic, 2007; Fuerstenau, Jameson and Yoon, 2007). In the case of iron ores, flotation is commonly used to remove silicates and purify concentrates (Araujo, Viana and Peres, 2005; Filippov, Filippova and Severov, 2010).

Flotation is based on the physicochemical properties of mineral surfaces. The aim is to selectively adsorb reagents to render the surfaces either hydrophilic – the role of the depressants – or hydrophobic which is the role of the collectors. Gas bubbles (generally air) are then injected at the bottom of the flotation cell and, as they travel up the cell, hydrophobic particles attach to them. These bubble-particle aggregates are collected in the cell in the form of a mineralised froth. Flotation is used for particles with sizes ranging from 10 µm to 300 µm (Foucaud *et al*, 2019a; Fuerstenau, Jameson and Yoon, 2007; Leja, 1981).

Two main routes of flotation exist: a direct flotation where the mineral of interest is floated, and the reverse flotation where only the gangue minerals are floated. The choice of the route depends on the deposit grades, on the overall beneficiation route and on the required selectivity.

The application of flotation for iron ore was first investigated in 1931 and patented for hematite in 1934 (Gaudin, 1934) and for magnetite in 1945 (De Vaney, 1945). However, it was not before 1954 that the first industrial-scaled iron ore flotation has been set-up (Nakhaei and Irannajad, 2018). Hitherto, three flotation routes of flotation have existed or exist: the reverse cationic and anionic flotations of quartz and activated quartz and the direct anionic flotation of iron oxides (Araujo, Viana and Peres, 2005; Zhang *et al*, 2019). Whilst the first installations used the direct anionic route but, they have been replaced over time with the reverse cationic route which have shown better performances (Veloso *et al*, 2018).

However, new ores generally present finer liberation and lower grades (Calvo *et al*, 2016; Mudd, 2007, 2012, 2014). Gangue minerals are more diversified, and the flotation process performances begin to show limitations (Filippov, Filippova and Severov, 2010). The limitations can be of various origins, for example clay minerals can coat certain particles and prevent a correct reagent adsorption; or iron silicates like epidote or chamosite can have surface properties close to iron oxides' and therefore not be efficiently separated. Tailings also contain a non-negligeable content in metal but have highly variable mineralogic compositions and their beneficiation, even if it could represent a large source of iron, remains technologically complicated. For all these reasons and more, a better understanding of the flotation mechanisms is of upmost interest to enhance the existing processes or to propose more efficient ones.

The last decades, modelling tools loaned to chemical sciences have been applied to the flotation of numerous minerals. Some popular ones are based on the Density Functional Theory which has been formulated early in the 20th century. The application of DFT and other molecular simulations for flotation mechanisms is recent but booming with a constant increase of publications sharing the topics each year (see Figure 1) (Foucaud *et al*, 2019a).

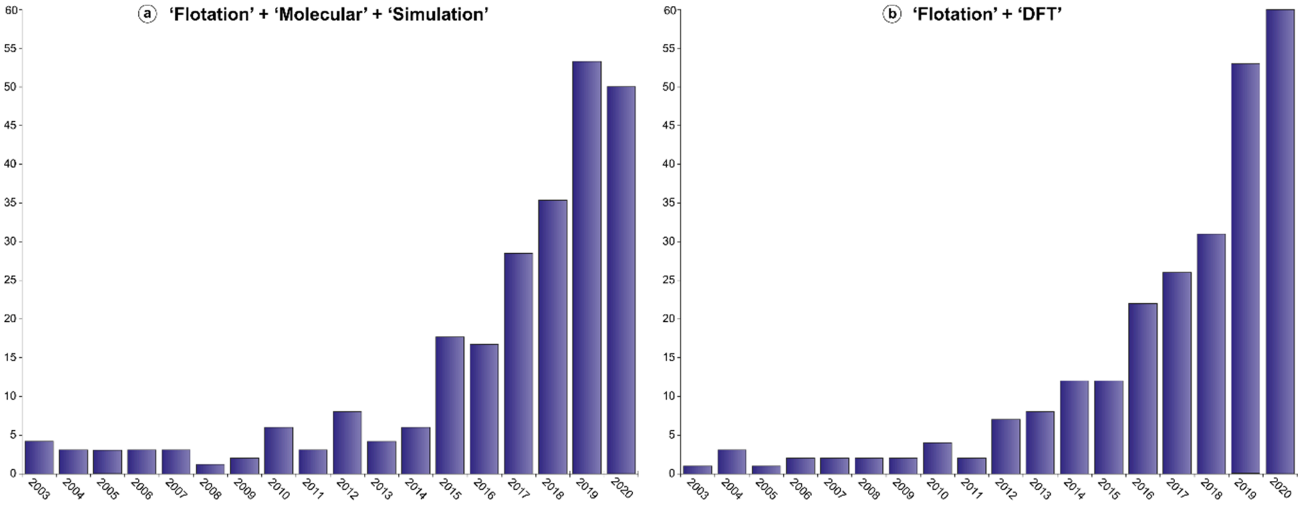

FIG 1 – Number of research articles per annum with the keywords (a) 'Flotation' + 'Molecular' + 'Simulation' and (b) 'Flotation' + 'DFT' (source: Web of Science).

The democratisation of these tools has been made possible by the improvements of the means of computational calculations. Such calculations which would take millions of years to be solved 'by hand' take only a few days or weeks to be realised with supercomputers, offer important perspectives for material science.

In the following, first, some popular modelling tools will be introduced. Then, results and examples from both the literature and the authors work on the topic of iron ore will be presented. It will show how molecular modelling can offer many perspectives for the flotation of iron ores.

MOLECULAR MODELLING METHODS

Density Functional Theory

Density Functional Theory (DFT) was first introduced by Thomas (1927) and Fermi (1927). But the mathematical formalism as it is used today has been developed in the 1960s (Hohenberg and Kohn, 1964; Kohn and Sham, 1965).

The foundation of the overall theory is the solving of the Schrödinger equation (Equation 1) where E is the energy of the system, H a specific operator and Ψ are the wavefunctions describing the system which depends on the nuclei coordinates.

$$H\Psi = E\Psi \quad (1)$$

In the Hohenberg-Kohn formalism, the ground-state energy E_0 is demonstrated as being dependent of the function density of the electrons. And the energy of the system can be expressed as follows (Equation 2).

$$E[\rho] = \mathrm{T}[\rho] + \mathrm{J}[\rho] + E_{XC}[\rho] + \int V_{ne}\vec{r}\,\rho(\vec{r})d\vec{r} \quad (2)$$

In Equation 2, ρ describes the electron density, E[ρ] the energy, T[ρ] the kinetic energy of the electrons, J[ρ] the electron-electron Columbian repulsion, $E_{XC}[\rho]$ the electron-electron exchange-correlation effects and $V_{ne}[\mathbf{r}]$ the electron-nucleus potential where **r** represents the vector of electrons coordinates. To simplify the kinetic energy, the nuclei are considered immobile as they are heavier than electrons, it is the Born-Oppenheimer approximation.

It is first stated that the ground-state energy is a functional of the ground-state electron density (first Hohenberg-Kohn theorem) and then, that the ground-state density minimises the energy density functional (second Hohenberg-Kohn theorem).

The method proposed in 1965 by Kohn and Sham relies on solving the problem working in an imaginary system where electrons do not interact with each other and to set a potential V_{KS} in such way that the electron density is the real one. All the other effects are gathered in the exchange-correlation E_{xc} parameter. This parameter cannot be analytically described by this formalism. Various exchange-correlation functionals have then be proposed to approximate the exchange-correlation energy. The most-common ones are the Local Density Approximation (LDA) functionals and the Gradient Generalised Approximation (GGA) functionals. The LDA approximates the system as an inhomogeneous gas system (Hohenberg and Kohn, 1964) and the GGA takes into account the gradient of electronic density which is more accurate (Grimme, 2006; Perdew, Burke and Ernzerhof, 1996). Nowadays, correction methods have been added to GGA to account for the dispersion interactions representing parts of the van der Waals forces. These interactions are of upmost importance for adsorption on mineral surfaces as they can drive the mechanism. The authors showed that organic molecules like phenol, toluene, oleic acid, or bigger ones like diclofenac adsorb on fluorite or kaolinite solely thanks to dispersion interactions or *via* chain-chain hydrophobic interactions (Dzade, Roldan and de Leeuw, 2014; Foucaud *et al*, 2021; Hounfodji *et al*, 2021). Various exchange-correlation description methods have been developed with different levels of accuracy (Korth and Grimme, 2009). To clarify, DFT allows the relaxation of systems to reach a minimum of potential energy surface in vacuum and at 0 K.

All in all, DFT is a very popular modelling theory with up to 15 000 papers published each year for a wide range of applications and disciplines (Hafner, 2008; Pastore and De Angelis, 2013) as it has already shown very good agreement with high-precision experiments.

Molecular dynamics

Molecular dynamics combines both thermodynamic equilibrium and dynamic properties usually at a finite temperature to describe the evolution of a system with time. Molecular dynamics calculations will depend on the methodology used to describe the forces at each time step (Alder and Wainwright, 1959), the trajectories being then calculated using Newton's equation of motion (González, 2011), see Equation 3 where $\vec{r}$ represents particles coordinates, $\vec{F}$ the force and U the energy.

$$m\frac{d^2\vec{r}}{dt^2} = \vec{F} = -\frac{\partial U(\vec{r})}{\partial \vec{r}} \quad (3)$$

The use of empirical potential for forces in the calculations ('force fields' or FF method) in classical molecular dynamics (CMD) is a popular technique used for a wide range of applications and in particular for biological purposes (Phillips *et al*, 2005). However, classical force fields can show limitations for the study of some properties or for reactivity, the popular method is based on first-principles or *ab initio* calculations (AIMD for *ab initio* molecular dynamics) (Iftimie, Minary and Tuckerman, 2005). The involvement of quantum equations and parameters in AIMD considerably increases the computational cost and therefore is limited to small number of atoms when compared to CMD.

Classical molecular dynamics

Classical molecular dynamics (CMD) is based on interaction potentials called *force fields* (FF method) which are derived from experimental data or electronic structure calculations. Force field development has begun at the early ages of CMD (Benson, Freeman and Dempsey, 1963) but is still ongoing with numerous papers released each year (Brooks *et al*, 2021).

A force field is a set of equations and constants designed for a structure, a molecule, or a system in such way it reproduces molecular geometry and selected properties. The mathematical expressions of FFs show their dependence to the coordinates of particles ($\vec{r}$ in the following). The overall energy can therefore be described with Equation 4 (González, 2011).

$$U(\vec{r}) = U_{bond} + U_{angle} + U_{torsion} + U_{improper} + U_{LJ} + U_{elec} \quad (4)$$

Where U_{bond}, U_{angle}, $U_{torsion}$ and $U_{improper}$ refer to intramolecular and local contributions to the total energy namely bond stretching, angle bending, and dihedral and improper torsions, respectively. U_{LJ} and U_{elec} describe the repulsive and van der Waals interactions (with a Lennard-Jones potential) and the Coulomb interactions which are intermolecular terms.

A force field is described by both the analytical expression displayed in Equation 3 and parameters that are usually derived *via* semi-empirical or first-principles quantum mechanical calculations or by fitting to experimental data (ie neutron, X-ray, and electrons diffraction).

In CMD, the molecules are described by charged points linked by springs representing the atoms and the bonds, respectively. Force fields will then replace the true potential by the simplified model which is valid in the considered region. Numerous force field models are available in the literature (Jalaie and Lipkowitz, 2000).

One main limitation of CMD is that it fails at describing electronic structure and therefore at handling reactions (eg bond breaking and formation), or other phenomena such as electron excitations or charge transfer, that is why force fields specific to reagents like the ReaxFF exist (van Duin *et al*, 2001). Moreover, as it depends on force fields, CMD calculations can only be performed on described systems and hardly transferred to other systems differing from the initial parametrisation. On top of that, as it is based on empirical input, it requires an experimental validation to confirm the results. To overcome these limitations, several teams work on new or hybrid methods. Nowadays, the most popular one is the QM/MM combining quantum mechanical and molecular mechanical potentials (Lin and Truhlar, 2006).

To date, very few papers strictly for the flotation of iron ore has been published using CMD with, nonetheless, a study on the adsorption of oleate on siderite, hematite and quartz published in 2017 (Li *et al*, 2017). However, various other mineral systems have been studied using this method such as micas, clays or carbonates (Chen *et al*, 2019; Liu *et al*, 2017; Tang, Kelebek and Yin, 2020; Xu *et al*, 2013) which shows the perspectives offered by such techniques for iron ores.

Ab initio molecular dynamics

In *Ab initio* molecular dynamics (AIMD) calculations, the forces are calculated at each time steps ('on-the-fly') using DFT which allows combining the precision of DFT with realistic parameters such as temperature or reactivity (Bucko, 2008). It is today one of the most powerful molecular dynamics technique but at an expensive computational cost. It implies that AIMD is restricted to a few hundred atoms and up to hundreds of picoseconds while CMD can allow larger systems of thousands of molecules.

In AIMD calculations, the system is composed of N nuclei and N_e electrons and the Born-Oppenheimer approximation (decoupling of nuclei and electrons movements because of their important mass difference) is considered valid, therefore the nuclei can be strictly treated with classical mechanics on the ground-state electronic surface (Iftimie, Minary and Tuckerman, 2005). The equation of motion can be now written as follows (Equation 5).

$$m.(d^2\mathbf{r}/dt^2) = \mathbf{F} = -\nabla[\varepsilon_0(\mathbf{r}) + V_{NN}(\mathbf{r})] \tag{5}$$

Where ∇ is the Laplacian operator, $\varepsilon_0(\mathbf{r})$ the ground-state energy eigenvalue and V_{NN} the nuclear-nuclear-nuclear Coulomb repulsion. The calculations of the ground-state energy follow the methodology described previously in the DFT presentation.

Anyhow, AIMD is a powerful tool giving access to realistic configurations for a wide range of properties at finite temperature (Iftimie, Minary and Tuckerman, 2005; Rocca *et al*, 2019).

As for CMD, the use of AIMD for the sole purpose of flotation begins to appear (Foucaud *et al*, 2021, 2019b, 2018; Geneyton *et al*, 2020) even if the application for iron ore remains almost inexistant for the moment. However, the perspectives to assess adsorption mechanisms of collectors are important. Amines are small molecules (ie dodecylamine is composed of 40 atoms), modelling their behaviour on mineral surfaces would not require an important computational cost. And, since AIMD simulations can predict reactivity, it is one tool of choice for understanding the phenomena at stake.

Relating molecular simulations to experiments

According the DFT axioms, all atomic properties may be described by the electron densities and therefore molecular properties can be calculated. From these types of calculations many properties can be theoretically predicted such as magnetisation, structure stability or structures vibrations. However, with sole DFT, only the ground-state is considered. Several extensions of the theory have been developed and implemented to access other properties like excitations and vibrational states. One example is the Density Functional Perturbation Theory (DFPT) based on the linear response DFT (Giannozzi *et al*, 1991), it gives the responses of a system to a perturbation (Baroni *et al*, 2001; Giannozzi and Baroni, 1994). In a recent work, the authors compared extensively DFPT infrared spectra of oleate ions adsorbed on fluorite surface to experimental spectra and unravelled the mechanisms of adsorption which were debated for decades (Foucaud *et al*, 2021).

Similar works were proposed for example between water and silica surfaces with the determination of the point of zero charge or infrared (Sulpizi, Gaigeot and Sprik, 2012) and vibrational sum frequency generation spectra (Sulpizi *et al*, 2013), redox potential or acidity constants (Cheng *et al*, 2014) from theoretical calculations. Molecular modelling can actually simulate the responses of almost all the most common experimental techniques like RMN (Fukal *et al*, 2017) or XPS (Duguet *et al*, 2019). The examples are numerous and show the perspectives of combining theoretical calculations to experiments to better appreciate flotation systems.

APPLICATION FOR IRON ORE FLOTATION

Bulk and surface structures

Prior to any adsorption study, DFT is an efficient tool to model bulk phases and surfaces and their magnetic, thermodynamics or even mechanical properties. Surfaces being of upmost importance for flotation being the location of adsorption at the solid/liquid interface. Combinations of DFT calculations and experimentations are often performed together to assess the real structures.

To give an example, the authors would like to discuss magnetite surfaces, and, especially, (111) and (001) surfaces, which are the most exposed cleavage planes of magnetite ($Fe^{III}_{tet}[Fe^{III}Fe^{II}]_{oct}O_4$, where *tet* and *oct* stand for tetrahedral environment and octahedral environment, respectively).

Several terminations have been proposed for the (111) surface. To date, a lot have been discarded and only a few have been estimated as stable (the ½ monolayer (ML) of Fe_{oct} (Cutting *et al*, 2008; Li and Paier, 2016; Santos-Carballal *et al*, 2014) or ¼ ML of Fe_{tet} (Cutting *et al*, 2008; Grillo, Finnis and Ranke, 2008; Li and Paier, 2016; Mu *et al*, 2017). Combination of theoretical calculations with cutting-edge techniques such as STM (Scanning Tunnelling Microscope) enabled the comparison of DFT surfaces with real surfaces (Santos-Carballal *et al*, 2014). As for the (001) surface, several models were proposed to explain the stable (√2x√2)R45° surface reconstruction: The *Bulk Distorted Truncation* (DBT) proposes that the surface results from a lattice distortion coupled to subsurface charge order, while the *subsurface cation vacancy* (SCV) proposes the existence of vacancies within magnetite cation lattice subsurface layers. From DFT calculations, it was shown that the SCV model is thermodynamically more stable than the DBT and is more consistent with the known phase transitions of magnetite. However, other stable terminations of the surfaces have been proposed to which the SCV model is not favourable. The true mechanisms and structures are yet to be proposed, and DFT is indeed an important tool in these investigations (Parkinson, 2016). Bulk and surface defects on magnetite have also largely been investigated and proposed using modelling tools (Parkinson, 2016).

Another modelling application related to magnetite is the investigation of the magnetisation and the spin state of iron atoms. It is made possible thanks to the Hubbard method implemented in DFT codes (called DFT+U) that describes the phenomena of correlation in the *d* and *f* orbitals of some transition metals (in which Fe^{II} and Fe^{III} belong). No actual consensus has actually been reached, but several spin structures have been proposed in the literature which explain insulating or metallic behaviours in certain conditions (Fonin *et al*, 2007; Roldan, Santos-Carballal and de Leeuw, 2013).

Overall, DFT-based tools offer great perspectives for bulk and structures properties determination. It is already used on various materials for different applications (Moreira *et al*, 2015; Rollmann *et al*, 2004) but can also be largely appliable to flotation purposes.

Hydration

During a flotation, minerals are put in a pulp which is a mixture of minerals and water up to 30 to 60 per cent of solid. Therefore, the interaction of minerals with water is of importance prior to any reagent consideration. Interestingly, as water is involved in many other chemical processes like water depollution or catalysis, water on minerals is already quite well studied for numerous iron ore minerals using molecular modelling. This is the case for hematite (Zhang *et al*, 2021), quartz (Rignanese, Charlier and Gonze, 2004; Yang and Wang, 2006), kaolinite (Chen *et al*, 2019; Tunega, 2010; Tunega, Gerzabek and Lischka, 2004; Zhang *et al*, 2014), and magnetite (Li and Paier, 2016; Rustad, Felmy and Bylaska, 2003; Yang *et al*, 2009).

The authors are currently working on the model of hydration of kaolinite using AIMD and DFT. The objective being to confirm or contradict the various studies generally using classical force field modelling. The basal surfaces terminated by aluminol (octahedral surface) or siloxane (tetrahedral surface) groups were simulated with various water coverages from a single water molecule to a fully hydrated system. It was shown that the aluminol surface is more hydrophilic than the siloxane one with the adsorption energy of a single water molecule at 0 K equal to -62.4 $kJ.mol^{-1}$ compared to -37.6 $kJ.mol^{-1}$ on the siloxane surface, both in a molecular form. Interestingly for flotation of kaolinite, the adsorption of water is relatively weak in term of energies compared to other organic molecules like phenol adsorption energies equal to -87.1 $kJ.mol^{-1}$ on the aluminol surface. The adsorption on both surfaces occurring *via* the formation of hydrogen bonds which are smaller or close to two Å-long on the aluminol surface or 2.2 Å-long on the siloxane surface. On both surface, dispersion interactions play a significant role for the adsorption. These results are in agreement with some other studies (Tunega, 2010; Tunega, Gerzabek and Lischka, 2004).

As the number of water molecules in the model increased, the water organised itself on top of the aluminol surface to form a well-structured icelike form. While on the siloxane surface, water is more disrupted, the stabilisation being mainly due to water-water interactions. Then, once the monolayer is reached, each added molecule gathered on less structured layers on top of the aluminol surface to form what seems to be a multilayer adsorption as Chen and co-workers (Chen *et al*, 2019) proposed a three-layered model but, the existence could be discussed as water gets bulkier when the distance with the surface increases and the aspect of the water is disorganised after only two layers (see Figure 2). On the other hand, water is extremely bulky on top of the siloxane surface confirming its less hydrophilic behaviour.

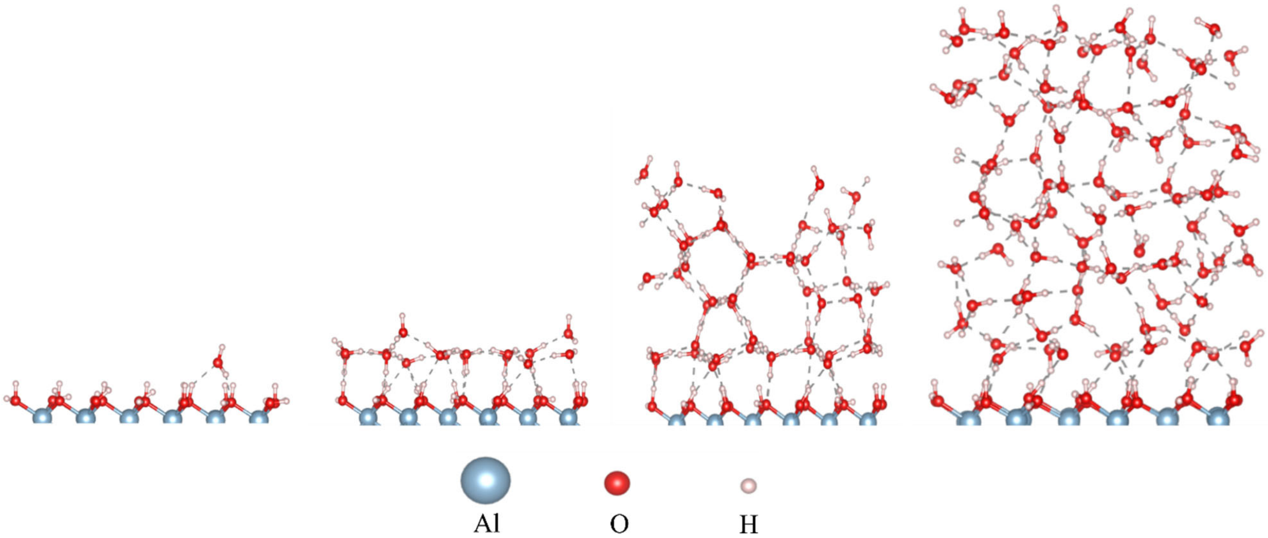

FIG 2 – Hydration of the aluminol surface of kaolinite from one water molecule to a full hydrated model.

On kaolinite basal surfaces, the hydroxyl groups of the aluminol surfaces are available Brønsted acid sites. They render the surface more able to adsorb molecules than the siloxane surface. The difficulty with this material will be to estimate how much both surfaces will influence the overall behaviour of the mineral and that might already explain the difference of flotation between kaolinite and a common silicate such as quartz.

Such study needs to be done on every mineral prior the adsorption of reagents as the presence of hydroxyl groups coming from a dissociation of water will profoundly change the surface properties and reactivity. It was demonstrated on magnetite surfaces that the first water molecules put in contact with magnetite spontaneously dissociates to chemically adsorb on Fe and O atoms and forms surface hydroxyl groups allowing the adsorption of additional molecular water (Mulakaluri *et al*, 2009). Same phenomenon occurs on quartz surfaces (Rignanese, Charlier and Gonze, 2004).

The comparison of water adsorption experiments with theoretical results on kaolinite by comparing the heat of adsorption versus the coverage (Nuhnen and Janiak, 2020) will be useful to propose many perspectives for flotation.

Reagent adsorption

Iron ore flotation reagents

The authors refer the reader to the following reviews for a detailed overview of the flotation reagents used for iron ores (Araujo, Viana and Peres, 2005; Nakhaei and Irannajad, 2018; Papini, Brandão and Peres, 2001). Briefly introduced here are the most important ones.

The most utilised flotation route being the cationic reverse flotation, the collectors are commonly belonging to the amine group. The most common being the mono-etheramines and di-etheramines for low-grade ores. For other types of flotation, for example anionic ones, the common collectors would be hydroxamates or fatty acids (Leja, 1981). They are relatively small molecules, easy to model using DFT and molecular dynamics.

During a cationic reverse flotation, iron oxides are depressed. The most common depressant is starch. Other molecules can be used such as humic acid, dextrin, carboxymethyl cellulose (CMC) or guar gum (Araujo, Viana and Peres, 2005; Veloso *et al*, 2018). They are bigger molecules which can make the DFT or AIMD too heavy or expensive and the use of more classical methods more suitable.

Other reagents or ions can be involved in the flotation of iron ore: dispersants, frothers or activators, the latter being able to change drastically mineral surfaces' properties and influence molecule adsorption (Foucaud *et al*, 2021).

Application of molecular modelling

Interestingly, as the interactions between reagents and surfaces are sole adsorption and involving only the surface of the minerals, molecular modelling techniques are the tools of choice for these systems and can precisely assess the involved mechanisms. Several studies already focused on the interactions of reagents with iron ore using the presented techniques.

In 2014, Huang *et al* (2014) released an article combining flotation tests and DFT calculations of a novel flotation reagent called a Gemini surfactant, they showed that the ethane-1,2-bis(dimethyl-dodecyl-ammonium bromide) is a better collector than dodecylammonium chloride (Huang *et al*, 2014). DFT study of some amines on quartz showed that, ester amines are better quartz collectors than ether amines and primary alkyl amines (Rath *et al*, 2014). Then, quartz was studied with α-Bromolauric acid (see Figure 3), it was concluded that α-Bromolauric acid could not break the hydration shell and adsorb (Zhu *et al*, 2016).

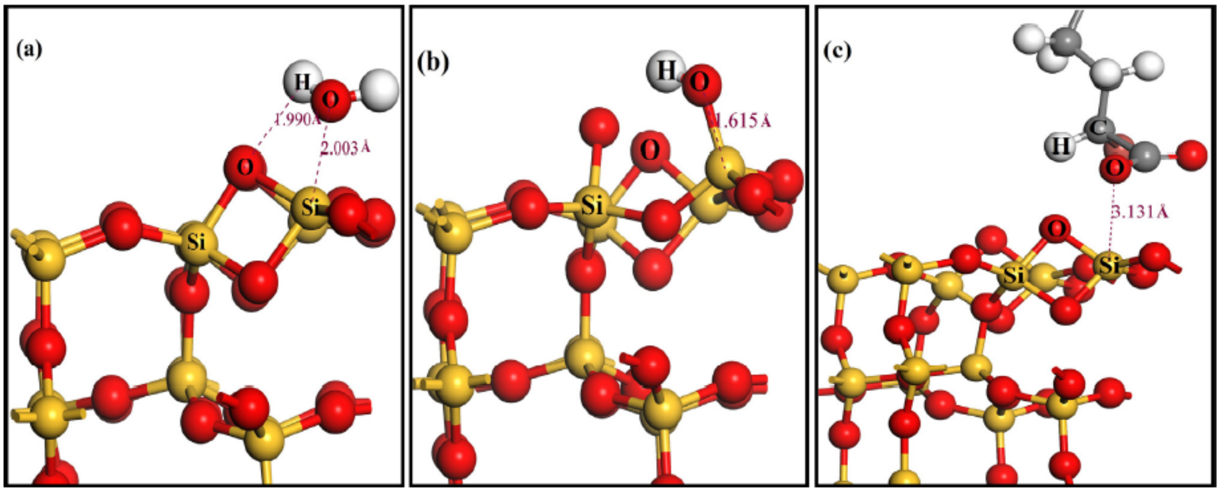

FIG 3 – Adsorption of H_2O (a), HO^- (b) and α-Bromolauric acid (c) on quartz (101) surface from Zhu *et al* (2016).

Using both experiment and DFT, it was shown that cationic polyamine reagents were really efficient in separating kaolinite, silica and alumina from goethite and hematite on iron ore slimes (Patra *et al*, 2018).

In 2019, the depression of hematite was investigated (Li *et al*, 2019) combining AFM and DFT. It was shown that oleate and starch both could form covalent bonds with hematite but that, in presence of starch, the distance between oleate and hematite could not allow the adsorption of the collector. It was also shown that in presence of water, hydrogen bonds could both form between the surface and the water and water and starch favouring the depressing of the iron oxide.

More recently, in 2020, a few studies on the separation of quartz from hematite showed that a newly designed surfactant – the N,N-dimethyl-N′-(2-hydroxyethyl)-N′-dodecyl-1.3-propanediamine or DMPDA – had a selectivity comparable to the ones of N-dodecyl-1,3-propanediamine (NDEA), N,N-Dimethyl-N′-dodecyl-1,3-propanediamine (DPDA). Experimental studies even confirmed the better selectivity of DMPDA over dodecylamine (DDA) predicted by the theoretical calculations. DPDA having a collective ability similar to NDEA but a better selectivity than NDEA and DDA (Liu *et al*, 2020a, 2020b). Then, DDA has been compared with collectors containing iso-propanol substituent groups and it was shown that the presence of these groups could enhance the selectivity of the molecules (Liu *et al*, 2020c).

However, as iron ore minerals can be found in other systems or for other applications (like catalysis), information with modelling tools on the mechanisms of adsorption of molecules close to flotation reagents can be found. For example, Chen *et al* (2020) studied, using DFT, the adsorption of methylamine of kaolinite for agglomeration purposes. They showed that methylamine cations adsorb on kaolinite basal surfaces mainly through electrostatic interactions and that are able to flush out water molecules to stably adsorb (Chen *et al*, 2020).

Other examples can be found for magnetite or hematite which are well-known for catalysis or to produce magnetic nanoparticles. For example, Xue *et al* (2014) studied the adsorption of CO using DFT+U on magnetite defective and non-defective (001) surfaces and showed that both surface can oxidise the molecules and form CO_2, the adsorption being stronger on the defective surface (Xue *et al*, 2014). The adsorption of CO_2 on magnetite happens through covalent bonding and is more favoured on the (111) Fe_{oct} -terminated surface than on the (111) Fe_{tet}-terminated surface (Su *et al*, 2016). A study on the adsorption of benzene on hematite revealed that the adsorption of the molecules occurred via hydrogen-bonding and van der Waals interactions (Dzade, Roldan and de Leeuw, 2014). All this information, even if not directly related to flotation can give precious insights on the reactivity and adsorption behaviour of mineral surfaces and be a good starting point to any investigation related to collectors or depressants.

CONCLUSION

The mining industry is facing new challenges with the increase of ore mineral composition complexity, finer liberation, and grade decrease. The enhancement of existing processes like flotation can only occur by a gain of knowledge of the involved processes. For more than a decade now, density functional theory and molecular dynamics, powerful and popular tools in material sciences have been applied to flotation mainly for assessing the adsorption mechanisms of reagents. Magnetite, kaolinite, quartz or even hematite and surface properties (like pzc or IR spectra) or adsorption mechanisms of many molecules have been successfully modelled and predicted and compared to high precision experiments. The combination of these tools with experimentation will surely offer a better knowledge and new perspectives for flotation like the study of cation bridging of synergetic interactions.

ACKNOWLEDGEMENTS

This work was granted access to the HPC resources of TGCC under the allocations 2020-A0080810169 and 2021-A010081433 by GENCI -EDARI project.

REFERENCES

Alder, B J and Wainwright, T E, 1959. Studies in Molecular Dynamics I, *General Method J Chem Phys*, 31:459–466. https://doi.org/10.1063/1.1730376

Araujo, A C, Viana, P R M and Peres A E C, 2005. Reagents in iron ores flotation, *Minerals Engineering, Reagents'04:*18:219–224. https://doi.org/10.1016/j.mineng.2004.08.023

Baroni, S, de Gironcoli, S, Dal Corso, A and Giannozzi, P, 2001. Phonons and related crystal properties from density-functional perturbation theory, *Rev Mod Phys,* 73:515–562. https://doi.org/10.1103/RevModPhys.73.515

Benson, G C, Freeman, P J and Dempsey, E, 1963. Calculation of Cohesive and Surface Energies of Thorium and Uranium Dioxides, *Journal of the American Ceramic Society,* 46:43–47. https://doi.org/10.1111/j.1151–2916.1963.tb13769.x

Brooks, C L, Case, D A, Plimpton, S, Roux, B, van der Spoel, D and Tajkhorshid, E, 2021. Classical molecular dynamics, *J Chem Phys,* 154:100401. https://doi.org/10.1063/5.0045455

Bucko, T, 2008. Ab initio calculations of free-energy reaction barriers, *J Phys: Condens Matter,* 20:064211. https://doi.org/10.1088/0953–8984/20/6/064211

Bulatovic, S M, 2007. *Handbook of flotation reagents: chemistry, theory and practice*, 1st ed (Elsevier: Amsterdam, Boston).

Calvo, G, Mudd, G, Valero, A and Valero, A, 2016. Decreasing Ore Grades in Global Metallic Mining: A Theoretical Issue or a Global Reality?, *Resources,* 5 :36. https://doi.org/10.3390/resources5040036

Chen, J, Min, F, Liu, L and Jia, F-F, 2020. Adsorption of methylamine cations on kaolinite basal surfaces: A DFT study, *Physicochemical Problems of Mineral Processing,* 56:337–348.

Chen, J, Min, F, Liu, L and Liu, C, 2019. Mechanism research on surface hydration of kaolinite, insights from DFT and MD simulations, *Applied Surface Science,* 476:6–15. https://doi.org/10.1016/j.apsusc.2019.01.081

Cheng, J, Liu, X, VandeVondele, J, Sulpizi, M and Sprik, M, 2014. Redox Potentials and Acidity Constants from Density Functional Theory Based Molecular Dynamics, *Acc Chem Res,* 47:3522–3529. https://doi.org/10.1021/ar500268y

Cutting, R S, Muryn, C A, Vaughan, D J and Thornton, G, 2008. Substrate-termination and H2O-coverage dependent dissociation of H2O on Fe3O4(111), *Surface Science,* 602:1155–1165. https://doi.org/10.1016/j.susc.2008.01.012

De Vaney, F D, 1945. *Beneficiation of magnetite concentrates by flotation*, US2388471A.

Duguet, T, Gavrielides, A, Esvan, J, Mineva, T and Lacaze-Dufaure, C, 2019. DFT Simulation of XPS Reveals Cu/Epoxy Polymer Interfacial Bonding, *J Phys Chem C,* 123:30917–30925. https://doi.org/10.1021/acs.jpcc.9b07772

Dzade, N, Roldan, A and de Leeuw, N, 2014. A Density Functional Theory Study of the Adsorption of Benzene on Hematite (α-Fe2O3) Surfaces, *Minerals,* 4:89–115. https://doi.org/10.3390/min4010089

Ferenczi, P, 2001. *Iron ore, manganese and bauxite deposits of the Northern Territory, Northern Territory Geological Survey* (Government Printer of the Northern Territory: Darwin).

Fermi, E, 1927. Un metodo statistico per la determinazione di alcune propriet`a dell'atomo. *Rendiconti Accademia Lincei*, 6, 602–607.

Filippov, L O, Filippova, I V and Severov, V V, 2010. The use of collectors mixture in the reverse cationic flotation of magnetite ore: The role of Fe-bearing silicates, *Minerals Engineering,* 23:91–98. https://doi.org/10.1016/j.mineng.2009.10.007

Fonin, M, Dedkov, Y S, Pentcheva, R, Rüdiger, U and Güntherodt, G, 2007. Magnetite: a search for the half-metallic state, *J Phys: Condens Matter*, 19:315217. https://doi.org/10.1088/0953–8984/19/31/315217

Foucaud, Y, Badawi, M, Filippov, L O, Barres, O, Filippova, I V and Lebègue, S, 2019b. Synergistic adsorptions of Na2 CO 3and Na2SiO3 on calcium minerals revealed by spectroscopic and ab initio molecular dynamics studies, *Chem Sci,* 10:9928–9940. https://doi.org/10.1039/C9SC03366A

Foucaud, Y, Badawi, M, Filippov, L, Filippova, I and Lebègue, S, 2019a. A review of atomistic simulation methods for surface physical-chemistry phenomena applied to froth flotation, *Minerals Engineering,* 143:106020. https://doi.org/10.1016/j.mineng.2019.106020

Foucaud, Y, Lainé, J, Filippov, L O, Barrès, O, Kim, W J, Filippova, I V, Pastore, M, Lebègue, S and Badawi, M, 2021. Adsorption mechanisms of fatty acids on fluorite unraveled by infrared spectroscopy and first-principles calculations, *Journal of Colloid and Interface Science,* 583:692–703. https://doi.org/10.1016/j.jcis.2020.09.062

Foucaud, Y, Lebègue, S, Filippov, L O, Filippova, I V and Badawi, M, 2018. Molecular Insight into Fatty Acid Adsorption on Bare and Hydrated (111) Fluorite Surface, *J Phys Chem B,* 122:12403–12410. https://doi.org/10.1021/acs.jpcb.8b08969

Fuerstenau, M C, Jameson, G J and Yoon, R-H (Eds), 2007. *Froth flotation: a century of innovation* (Society for Mining, Metallurgy, and Exploration: Littleton).

Fukal, J, Páv, O, Buděšínský, M, Šebera, J and Sychrovský, V, 2017. The benchmark of 31P NMR parameters in phosphate: a case study on structurally constrained and flexible phosphate, *Phys Chem Chem Phys,* 19:31830–31841. https://doi.org/10.1039/C7CP06969C

Gaudin, A M, 1934. *Method of floating hematite*, US1979324A.

Geneyton, A, Foucaud, Y, Filippov, L O, Menad, N-E, Renard, A and Badawi, M, 2020. Synergistic adsorption of lanthanum ions and fatty acids for efficient rare-earth phosphate recovery: Surface analysis and ab initio molecular dynamics studies, *Applied Surface Science,* 526:146725. https://doi.org/10.1016/j.apsusc.2020.146725

Giannozzi, P and Baroni, S, 1994. Vibrational and dielectric properties of C60 from density-functional perturbation theory, *The Journal of Chemical Physics,* 100:8537–8539. https://doi.org/10.1063/1.466753

Giannozzi, P, de Gironcoli, S, Pavone, P and Baroni, S, 1991. Ab initio calculation of phonon dispersions in semiconductors, *Phys Rev B,* 43:7231–7242. https://doi.org/10.1103/PhysRevB.43.7231

González, M A, 2011. Force fields and molecular dynamics simulations, *JDN,* 12:169–200. https://doi.org/10.1051/sfn/201112009

Grillo, M E, Finnis, M W and Ranke, W, 2008. Surface structure and water adsorption on Fe3O4 (111) : Spin-density functional theory and on-site Coulomb interactions, *Phys Rev B,* 77:075407. https://doi.org/10.1103/PhysRevB.77.075407

Grimme, S, 2006. Semiempirical GGA-type density functional constructed with a long-range dispersion correction, *J Comput Chem,* 27:1787–1799. https://doi.org/10.1002/jcc.20495

Hafner, J, 2008. Ab-initio simulations of materials using VASP: Density-functional theory and beyond, *J Comput Chem,* 29:2044–2078. https://doi.org/10.1002/jcc.21057

Hagemann, S, Angerer, T, Duuring, P, Rosière, C, Figueiredo e Silva, R, Lobato, L, Hensler, A-S and Walde, D H G, 2015. BIF-hosted iron mineral system: A review, *Ore Geology Reviews,* 76. https://doi.org/10.1016/j.oregeorev.2015.11.004

Hohenberg, P and Kohn, W, 1964. Inhomogeneous Electron Gas, *Phys Rev,* 136:B864–B871. https://doi.org/10.1103/PhysRev.136.B864

Hounfodji, J W, Kanhounnon, W G, Kpotin, G, Atohoun, G S, Lainé, J, Foucaud, Y and Badawi, M, 2021. Molecular insights on the adsorption of some pharmaceutical residues from wastewater on kaolinite surfaces, *Chemical Engineering Journal,* 407:127176. https://doi.org/10.1016/j.cej.2020.127176

Huang, Z, Zhong, H, Wang, S, Xia, L, Zou, W and Liu, G, 2014. Investigations on reverse cationic flotation of iron ore by using a Gemini surfactant: Ethane-1,2-bis(dimethyl-dodecyl-ammonium bromide), *Chemical Engineering Journal,* 257:218–228. https://doi.org/10.1016/j.cej.2014.07.057

Iftimie, R, Minary, P and Tuckerman, M E, 2005. Ab initio molecular dynamics: Concepts, recent developments, and future trends, *PNAS,* 102:6654–6659. https://doi.org/10.1073/pnas.0500193102

Jalaie, M and Lipkowitz, K B, 2000. Appendix: Published Force Field Parameters for Molecular Mechanics, Molecular Dynamics, and Monte Carlo Simulations, *Reviews in Computational Chemistry*, pp 441–486. https://doi.org/10.1002/9780470125915.ch7

Jébrak, M, Laithier, M and Marcoux, É, 2008. *Géologie des ressources minérales* (Ressources naturelles et faune: Québec).

Kohn, W and Sham, L J, 1965. Self-Consistent Equations Including Exchange and Correlation Effects, *Phys Rev,* 140:A1133–A1138. https://doi.org/10.1103/PhysRev.140.A1133

Korth, M and Grimme, S, 2009. 'Mindless' DFT Benchmarking, *J Chem Theory Comput,* 5:993–1003. https://doi.org/10.1021/ct800511q

Leja, J, 1981. *Surface Chemistry of Froth Flotation* (Springer US: Boston).

Li, L, Hao, H, Yuan, Z and Liu, J, 2017. Molecular dynamics simulation of siderite-hematite-quartz flotation with sodium oleate, *Applied Surface Science*, 419:557–563. https://doi.org/10.1016/j.apsusc.2017.05.069

Li, L, Zhang, C, Yuan, Z, Xu, X and Song, Z, 2019. AFM and DFT study of depression of hematite in oleate-starch-hematite flotation system, *Applied Surface Science*, 480:749–758. https://doi.org/10.1016/j.apsusc.2019.02.224

Li, X and Paier, J, 2016. Adsorption of Water on the Fe3O4(111) Surface: Structures, Stabilities, and Vibrational Properties Studied by Density Functional Theory, *J Phys Chem C*, 120:1056–1065. https://doi.org/10.1021/acs.jpcc.5b10560

Lin, H and Truhlar, D G, 2006. QM/MM: what have we learned, where are we, and where do we go from here?, *Theor Chem Acc*, 117:185. https://doi.org/10.1007/s00214–006–0143-z

Liu, W, Liu, W, Zhao, Q, Peng, X, Wang, B, Zhou, S and Zhao, L, 2020a. Investigating the performance of a novel polyamine derivative for separation of quartz and hematite based on theoretical prediction and experiment, *Separation and Purification Technology*, 237:116370. https://doi.org/10.1016/j.seppur.2019.116370

Liu, W, Liu, W, Zhao, Q, Shen, Y, Wang, X, Wang, B and Peng, X, 2020b. Design and flotation performance of a novel hydroxy polyamine surfactant based on hematite reverse flotation desilication system, *Journal of Molecular Liquids, 301:*112428. https://doi.org/10.1016/j.molliq.2019.112428

Liu, W, Peng, X, Liu, W, Wang, X, Zhao, Q and Wang, B, 2020c. Effect mechanism of the iso-propanol substituent on amine collectors in the flotation of quartz and magnesite, *Powder Technology*, 360:1117–1125. https://doi.org/10.1016/j.powtec.2019.10.060

Liu, W, Wang, X, Xu, H and Miller, J D, 2017. Lauryl phosphate adsorption in the flotation of Bastnaesite, (Ce,La)FCO3, *Journal of Colloid and Interface Science*, 490:825–833. https://doi.org/10.1016/j.jcis.2016.11.016

Moreira, E, Barboza, C A, Albuquerque, E L, Fulco, U L, Henriques, J M and Araújo, A I, 2015. Vibrational and thermodynamic properties of orthorhombic CaSnO3 from DFT and DFPT calculations, *Journal of Physics and Chemistry of Solids*, 77:85–91. https://doi.org/10.1016/j.jpcs.2014.09.016

Mu, R, Zhao, Z, Dohnálek, Z and Gong, J, 2017. Structural motifs of water on metal oxide surfaces, *Chem Soc Rev,* 46:1785–1806. https://doi.org/10.1039/C6CS00864J

Mudd, G M, 2007. Global trends in gold mining: Towards quantifying environmental and resource sustainability, *Resources Policy*, 32:42–56. https://doi.org/10.1016/j.resourpol.2007.05.002

Mudd, G M, 2012. Key trends in the resource sustainability of platinum group elements, *Ore Geology Reviews*, 46:106–117. https://doi.org/10.1016/j.oregeorev.2012.02.005

Mudd, G M, 2014. The future of Yellowcake: A global assessment of uranium resources and mining, *Science of The Total Environment*, 472:590–607. https://doi.org/10.1016/j.scitotenv.2013.11.070

Mulakaluri, N, Pentcheva, R, Wieland, M, Moritz, W and Scheffler, M, 2009. Partial Dissociation of Water on Fe3O4 (001) : Adsorbate Induced Charge and Orbital Order, *Phys Rev Lett,* 103:176102. https://doi.org/10.1103/PhysRevLett.103.176102

Nakhaei, F and Irannajad, M, 2018. Reagents types in flotation of iron oxide minerals: A review, *Mineral Processing and Extractive Metallurgy Review,* 39:89–124. https://doi.org/10.1080/08827508.2017.1391245

Nuhnen, A and Janiak, C, 2020. A practical guide to calculate the isosteric heat/enthalpy of adsorption *via* adsorption isotherms in metal–organic frameworks, MOFs, *Dalton Trans,* 49:10295–10307. https://doi.org/10.1039/D0DT01784A

Papini, R M, Brandão, P R G and Peres, A E C, 2001. Cationic flotation of iron ores: amine characterization and performance, *Mining, Metallurgy & Exploration*, 18:5–9. https://doi.org/10.1007/BF03402863

Parkinson, G S, 2016. Iron oxide surfaces, *Surface Science Reports*, 71:272–365. https://doi.org/10.1016/j.surfrep.2016.02.001

Pastore, M and De Angelis, F, 2013. Intermolecular Interactions in Dye-Sensitized Solar Cells: A Computational Modeling Perspective, *J Phys Chem Lett,* 4:956–974. https://doi.org/10.1021/jz302147v

Patra, A S, Nulakani, N V R, Pavan Kumar, Y, Subramanian, V, Dash, J and Mukherjee, A K, 2018. Design and synthesis of novel polyamine collector to recover iron values from iron ore slimes, *Powder Technology,* 325:180–191. https://doi.org/10.1016/j.powtec.2017.10.045

Perdew, J P, Burke, K and Ernzerhof, M, 1996. Generalized Gradient Approximation Made Simple, *Phys Rev Lett,* 77:3865–3868. https://doi.org/10.1103/PhysRevLett.77.3865

Phillips, J C, Braun, R, Wang, W, Gumbart, J, Tajkhorshid, E, Villa, E, Chipot, C, Skeel, R D, Kalé, L and Schulten, K, 2005. Scalable molecular dynamics with NAMD, *Journal of Computational Chemistry,* 26:1781–1802. https://doi.org/10.1002/jcc.20289

Rath, S S, Sahoo, H, Das, B and Mishra, B K, 2014. Density functional calculations of amines on the (101) face of quartz, *Minerals Engineering*, 69:57–64. https://doi.org/10.1016/j.mineng.2014.07.007

Rignanese, G-M, Charlier, J-C and Gonze, X, 2004. First-principles molecular-dynamics investigation of the hydration mechanisms of the (0001) α -quartz surface, *Physical Chemistry Chemical Physics*, 6:1920–1925. https://doi.org/10.1039/B311842H

Rocca, D, Dixit, A, Badawi, M, Lebègue, S, Gould, T and Bučko, T, 2019. Bridging molecular dynamics and correlated wave-function methods for accurate finite-temperature properties, *Phys Rev Materials*, 3:040801. https://doi.org/10.1103/PhysRevMaterials.3.040801

Roldan, A, Santos-Carballal, D and de Leeuw, N H, 2013. A comparative DFT study of the mechanical and electronic properties of greigite Fe3S4 and magnetite Fe3O4, *J Chem Phys*, 138:204712. https://doi.org/10.1063/1.4807614

Rollmann, G, Rohrbach, A, Entel, P and Hafner, J, 2004. First-principles calculation of the structure and magnetic phases of hematite, *Phys Rev B*, 69:165107. https://doi.org/10.1103/PhysRevB.69.165107

Rustad, J R, Felmy, A R and Bylaska, E J, 2003. Molecular simulation of the magnetite-water interface, *Geochimica et Cosmochimica Acta, Advances in Oxide and Sulfide Mineral Surface Chemistry,* 67:1001–1016. https://doi.org/10.1016/S0016–7037(02)00900–6

Santos-Carballal, D, Roldan, A, Grau-Crespo, R and de Leeuw, N H, 2014. A DFT study of the structures, stabilities and redox behaviour of the major surfaces of magnetite Fe3O4, *Phys Chem Chem Phys*, 16:21082–21097. https://doi.org/10.1039/C4CP00529E

Su, T, Qin, Z, Huang, G, Ji, H, Jiang, Y and Chen, J, 2016. Density functional theory study on the interaction of CO2 with Fe3O4(111) surface, *Applied Surface Science*, 378:270–276. https://doi.org/10.1016/j.apsusc.2016.03.097

Sulpizi, M, Gaigeot, M-P and Sprik, M, 2012. The Silica–Water Interface: How the Silanols Determine the Surface Acidity and Modulate the Water Properties, *J Chem Theory Comput,* 8:1037–1047. https://doi.org/10.1021/ct2007154

Sulpizi, M, Salanne, M, Sprik, M and Gaigeot, M-P, 2013. Vibrational Sum Frequency Generation Spectroscopy of the Water Liquid–Vapor Interface from Density Functional Theory-Based Molecular Dynamics Simulations, *J Phys Chem Lett*, 4:83–87. https://doi.org/10.1021/jz301858g

Tang, Y, Kelebek, S and Yin, W, 2020. Surface chemistry of magnesite and calcite flotation and molecular dynamics simulation of their cetyl phosphate adsorption, *Colloids and Surfaces A: Physicochemical and Engineering Aspects,* 603:125246. https://doi.org/10.1016/j.colsurfa.2020.125246

Thomas, L H, 1927. The calculation of atomic fields. *Mathematical Proceedings of the Cambridge Philosophical Society,* 23, 542–548. https://doi.org/10.1017/S0305004100011683

Tunega, D, 2010. DFT Study of Interactions of Water on Kaolinite and Goethite Surfaces, in: Sih, G C, Naït-Abdelaziz, M, Vu-Khanh, T, (eds), *Particle and Continuum Aspects of Mesomechanics* (ISTE: London), pp 191–198. https://doi.org/10.1002/9780470610794.ch18

Tunega, D, Gerzabek, M H and Lischka, H, 2004. Ab Initio Molecular Dynamics Study of a Monomolecular Water Layer on Octahedral and Tetrahedral Kaolinite Surfaces, *J Phys Chem B*, 108:5930–5936. https://doi.org/10.1021/jp037121g

van Duin, A C T, Dasgupta, S, Lorant, F and Goddard, W A, 2001. ReaxFF: A Reactive Force Field for Hydrocarbons, *J Phys Chem A*, 105:9396–9409. https://doi.org/10.1021/jp004368u

Veloso, C H, Filippov, L O, Filippova, I V, Ouvrard, S and Araujo, A C, 2018. Investigation of the interaction mechanism of depressants in the reverse cationic flotation of complex iron ores, *Minerals Engineering*, 125:133–139. https://doi.org/10.1016/j.mineng.2018.05.031

Xu, Y, Liu, Y-L, He, D-D and Liu, G-S, 2013. Adsorption of cationic collectors and water on muscovite (001) surface: A molecular dynamics simulation study, *Minerals Engineering*, 53:101–107. https://doi.org/10.1016/j.mineng.2013.07.006

Xue, P, Fu, Z, Chu, X, Zhang, Y and Yang, Z, 2014. Density functional theory study on the interaction of CO with the Fe3O4(001) surface, *Applied Surface Science*, 317:752–759. https://doi.org/10.1016/j.apsusc.2014.09.002

Yang, J and Wang, E G, 2006. Water adsorption on hydroxylated alpha-quartz (0001) surfaces: From monomer to flat bilayer, *Phys Rev B*, 73:035406. https://doi.org/10.1103/PhysRevB.73.035406

Yang, T, Wen, X, Cao, D, Li, Y, Wang, J and Huo, C, 2009. Structures and energetics of H2O adsorption on the Fe3O4 (111) surface, *Journal of Fuel Chemistry and Technology*, 37:506–512. https://doi.org/10.1016/S1872–5813(10)60006–0

Zhang, C, Qi, Y-H, Qian, P, Zhong, M-J, Wang, L and Yin, H-Z, 2014. Quantum chemical study of the adsorption of water molecules on kaolinite surfaces, *Computational and Theoretical Chemistry*, 1046:10–19. https://doi.org/10.1016/j.comptc.2014.07.004

Zhang, H, Xu, Z, Chen, D, Hu, B, Zhou, Q, Chen, S, Li, S, Sun, W and Zhang, C, 2021. Adsorption mechanism of water molecules on hematite (104) surface and the hydration microstructure, *Applied Surface Science*, 550:149328. https://doi.org/10.1016/j.apsusc.2021.149328

Zhang, X, Gu, X, Han, Y, Parra-Álvarez, N, Claremboux, V and Kawatra, S K, 2019. Flotation of Iron Ores: A Review, *Mineral Processing and Extractive Metallurgy Review*, 1–29. https://doi.org/10.1080/08827508.2019.1689494

Zhu, Y, Luo, B, Sun, C, Liu, J, Sun, H, Li, Y and Han, Y, 2016. Density functional theory study of α-Bromolauric acid adsorption on the α-quartz (101) surface, *Minerals Engineering*, 92:72–77. https://doi.org/10.1016/j.mineng.2016.03.007

REFLUX® versus hydraulic classifier – a comparative analysis for hematite concentrate cleaning

B Légaré[1], F Lavoie[2], K Bourassa[3] and E Bouchard Marchand[4]

1. Metallurgist, Quebec Iron Ore, Fermont, Quebec, Canada, G0C 1J0.
   Email: blegare@mineraiferquebec.com
2. Technical Marketing Manager, Fermont, Quebec, Canada, G0C 1J0.
   Email: flavoie@mineraiferquebec.com
3. Metallurgist, Soutex Inc., Quebec, Canada, G1N 4K8. Email: kbourassa@soutex.ca
4. Senior Process Engineer, Soutex Inc., Quebec, Canada, G1N 4K8.
   Email: ebmarchand@soutex.ca

ABSTRACT

Quebec Iron Ore (QIO), a subsidiary of Champion Iron Limited (Champion), completed the restart of the Bloom Lake iron ore mine located in the heart of the Labrador Trough region of Northern Quebec, Canada in February 2018. Prior to its restart, the concentrator flow sheet underwent major upgrades which brought the iron recovery to the highest of all Labrador Trough operations.

After two profitable years of production, QIO, supported by Soutex, started to look at technologies to improve its current performance and integrate into its expansion project flow sheet. From the lessons learned while optimising Phase 1, the addition of a scavenger-cleaner processing stage was identified as an improvement opportunity to increase recovery, produce a higher-grade product, and further improve the stability of concentrate quality. In 2019, the NI-43101 feasibility study for the Phase 2 expansion, aiming to double the production of high-grade iron ore concentrate, was published. Based on the metallurgical test work, the hydraulic classifier was selected to perform the scavenger-cleaning duty for its well-established performance and known behaviour at the cleaning step in the Phase 1 plant.

To validate laboratory results, a pilot scavenger-cleaning hydraulic classifier was installed in Phase 1. Although the hydraulic classifier was selected for the feasibility study, metallurgical test work performed with the REFLUX® classifier showed interesting potential. It was thus decided to also install a pilot RC300 Reflux classifier at the scavenger-cleaning stage in Phase 1.

Despite their apparent great similarities, the metallurgical performance was significantly different, and many dozens of sampling campaigns highlighted the different performance of both pieces of equipment considering the feed material particle size. This article presents the pilot plant results in terms of recovery, selectivity and stability for both the Reflux classifier and the hydraulic classifier operated in a scavenger-cleaner stage at the Bloom Lake iron ore concentrator.

INTRODUCTION

Quebec Iron Ore (QIO), a subsidiary of Champion Iron Limited (Champion), completed the restart of the Bloom Lake iron ore mine located in the heart of the Labrador Trough region of Northern Quebec, Canada in February 2018. Prior to its restart, the concentrator flow sheet underwent major upgrades which brought the iron recovery to the highest of all Labrador Trough operations.

Within the framework of Quebec Iron Ore's Bloom Lake Phase 2 expansion project, a new separation stage was proposed to increase recovery and offer better performance when producing a low silica grade concentrate. The initial design, which was tested in a lab-scaled unit and showed promising results, was a standard hydraulic classifier placed downstream of the scavenger spirals, at a scavenger-cleaner stage.

Recent research also demonstrated that Reflux classifiers, an equipment mainly used in the coal industry, had great potential in the recovery of finer iron ore particles. The studies indicated that this equipment showed promising performance in the iron ore industry at a scavenger and/or scavenger-cleaner stage.

Soutex, a mineral and metallurgical consultant, was therefore appointed by Quebec Iron Ore to prepare and carry out scaled-up tests in the Phase 1 separation circuit with the two pilot pieces of equipment mentioned above. Piloting was to be carried within two (2) production scenarios:

- Concentrate with low silica content (less than 2.5 per cent silica).
- Concentrate with standard silica content (less than 4.5 per cent).

This article presents the performance, obtained and projected, of the pilot scavenger-cleaner hydraulic classifier and the pilot Reflux classifier. The results for both individual pilots are then compared to one another to highlight their performance in terms of recovery, selectivity and stability at the Bloom Lake iron ore concentrator (Phase 1).

OBJECTIVES

This comparative study targeted multiple objectives:

- Determine the technical feasibility of producing a low silica concentrate and evaluate the performance associated with this production within the Phase 1 flow sheet.
- Estimate the impact on recovery of adding a separation stage to the usual 4.5 per cent silica concentrate production scenario.
- Accumulate data to pursue the design of the Phase 2 plant process flow sheet.
- Compare the performances of the Reflux Classifier to the hydraulic classifier as a scavenger-cleaner unit.

PILOT UNITS

The pilot units used in this comparative study were a 30” by 30” square sectional area hydraulic classifier and a RC-300 Reflux classifier. Both units were provided by FLSmidth. The pilot Reflux classifier had a total volume of 0.3 m^3 and a sectional area of 0.28 m × 0.27 m, while the pilot hydraulic classifier has a square sectional area of 0.76 m × 0.76 m. These units are presented in Figure 1.

FIG 1 – Pilot hydraulic classifier (left) and pilot Reflux classifier (right).

The pilot units were installed downstream of the current gravity separation circuit. The separation circuit of the Phase 1 concentrator is composed of four main separation steps: rougher spirals, middling spirals, cleaner hydraulic classifier (C-HC) and scavenger spirals. Both pilot units were fed by the concentrate of scavenger spirals. The concentrator circuit as well as the pilot equipment are presented in Figure 2 for the current Phase 1 circuit, and the circuit included each pilot unit.

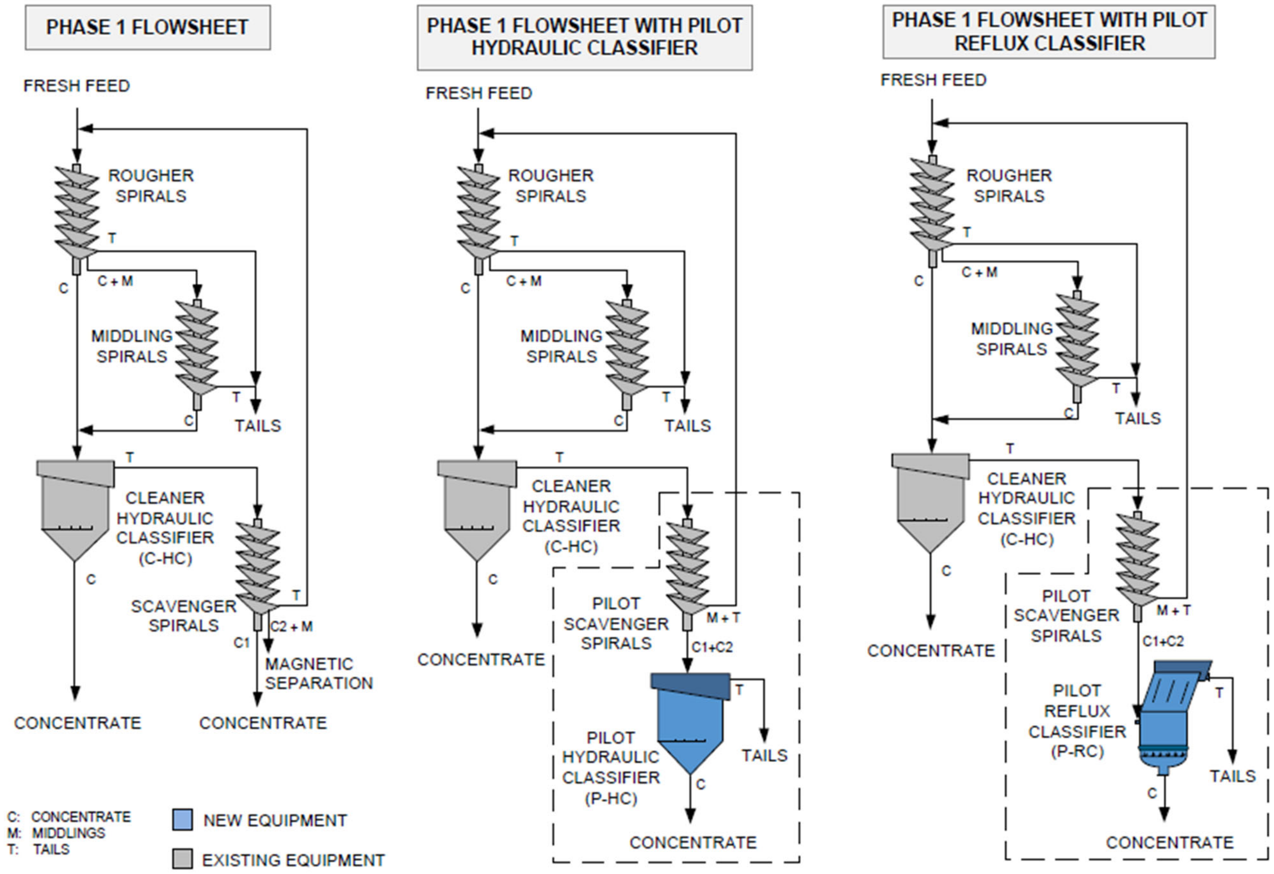

FIG 2 – Simplified flow sheet of pilot units in the separation circuit.

Due to the size of the pilot units, only a small portion of the scavenger spirals from the separation circuit was fed to the pilot units. The concentrate from the cutters and the first splitter of these spiral banks were diverted towards the pilot units while the middlings and tails were returned to the beginning of the separation circuit by changing the piping configuration. These banks were labelled as 'pilot scavenger spirals'. This allowed the operation of pilot units in a selected range of throughputs.

Other spiral banks without piping modifications were used as 'control lines' to obtain operational data of the separation circuit under Phase 1 normal plant conditions. In normal operational mode, only the concentrate from the cutters goes to the final concentrate. The concentrate from the first splitter and middlings is sent to the magnetic separation circuit while tails are sent back to the beginning of the separation circuit. The concentrates from the cleaner hydraulic classifiers (C-HC), scavenger spirals and magnetic separation circuit form the final concentrate.

For the pilot hydraulic classifier (P-HC), the piping configuration of two scavenger spiral banks (out of 32) was modified for use as pilots while two other scavenger spiral banks were defined as control. Upstream, one line made of rougher spirals, middling spirals and a cleaner hydraulic classifier was defined as control. Similarly, two other lines in the upstream separation circuit were used for pilot tests.

For the pilot Reflux classifier (P-RC), the piping configuration of half a spiral bank was modified to be used as pilot while the other half was used as control. Upstream, the same line made of rougher spirals, middling spirals and a cleaner hydraulic classifier was used for both the pilot and the control. This allowed the elimination of inherent variations between two lines even if they were operated under the same conditions.

Testing strategy

The sampling campaigns for both pilot units were carried out in three steps:

1. Identification of the operating ranges of the pilot equipment.
2. Optimisation of operating parameters.
3. Performance comparison with the current process operated under the same conditions for the production of the following final concentrates:
    - low silica grade concentrate, 2.5 per cent
    - standard silica grade concentrate, 4.5 per cent.

The sampling campaigns were performed only when the circuit was under steady state conditions to represent normal mill operations. The piloted lines were set to parameters within normal operating ranges to represent normal conditions while control lines were operated as the rest of the mill.

Assay results from sampling campaigns and process data were reconciled using Bilmat^{TM}.

Sampling campaigns on each pilot were performed in the context of two separate scenarios: a scenario of low silica grade concentrate production (2.5 per cent) and a scenario of standard silica grade concentrate production (4.5 per cent). The target silica grade was to be obtained from the final concentrate made of the cleaner hydraulic classifier concentrate and the scavenger concentrate (scavenger spiral concentrate in the current plant or classifier underflow in the pilot flow sheets).

To reproduce each scenario, modifications to the operating parameters of the upstream pieces of equipment to the pilot and control lines were made. The wash water flow rate as well as the cutters and splitters position of the rougher and middling spirals were modified to obtain adequate feed material to the control and pilot scavenger lines. Similarly, the operating pressure of the cleaner hydraulic classifiers was adjusted.

HYDRAULIC CLASSIFIER RESULTS

A total of 150 sampling campaigns were conducted on the pilot hydraulic classifier at the Bloom Lake Phase 1 concentrator over a period of 2 months. The ore fed to the concentrator was mainly made of silica and iron containing minerals such as hematite, magnetite and, in smaller proportions, limonite and silicates with a feed grade varying between 25 and 33 per cent iron.

The first step of the sampling campaign was to determine the impact of different operating parameters on equipment performance and then to identify the best operating range to optimise equipment performance. The results obtained for both phases are presented in the following sections along with challenges faced during the pilot campaigns.

Identification of equipment operating range

Exploratory sampling campaigns were performed at the beginning of the study to assess the equipment's operating limits allowing to reach reasonable recovery performances. The following operating parameters were tested:

- percent solids
- loading rate
- operating pressure
- fluidisation water flow rate
- rise rate.

At this stage, the performance of the pilot hydraulic classifier was evaluated under different operating parameters without making any changes to the upstream separation circuit stages. These preliminary results allowed the following conclusions on the control of the pilot hydraulic classifier to be drawn:

- The feed per cent solids influence other parameters like rise rate, loading rate and operating pressure but do not show a relationship with silica reduction on its own.

- The relationship between iron recovery and loading rate is weak while the silica reduction ratio is unaffected.
- A higher operating pressure allows for a better silica reduction ratio but lowers recovery as presented in Figure 3. This parameter can therefore be used to move the silica grade versus iron recovery curve in order to reach the required concentrate quality.
- Increasing the fluidisation water flow rate or the rise rate lowers recovery, but the effect on silica reduction was not clearly shown.

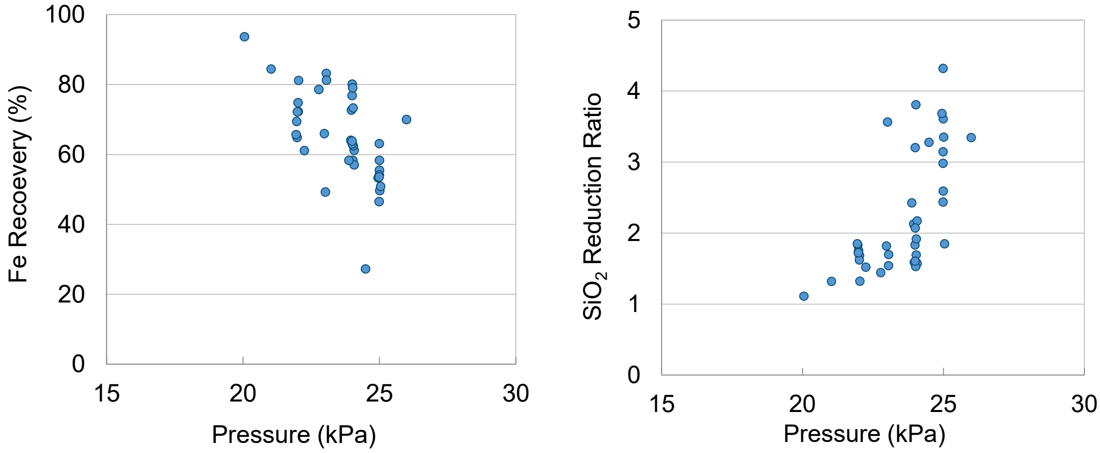

FIG 3 – Effect of pressure on the iron recovery and silica reduction ratio.

These preliminary results confirmed the capacity of the pilot hydraulic classifier to increase the concentrate quality of scavenger spirals, but without further adjustments to the upstream circuit, recovery was low.

Optimisation of operational parameters

To maximise the performance of the pilot hydraulic classifier within the separation circuit, the operating parameters of the whole pilot line were optimised.

The position of the cutters and the wash water flow rates of all spiral stages as well as the pressure and water flow rate of the cleaner hydraulic classifiers were adjusted to maximise overall recovery. These allowed better control over the following parameters:

- feed size distribution
- feed iron grade
- feed tonnage.

The analysis of the particle size distribution of the samples for a few sampling campaigns showed that the iron recovery of the pilot hydraulic classifier is negatively influenced by a coarser feed particle size. Further analysis showed that a coarser feed was also related to the presence of coarse silica particles. Since the coarser silica particles can hardy be separated in the hydraulic classifier, their presence in the feed results in a recovery decrease to maintain constant product quality. A lower feed particle size is obtained by removing the coarser silica particles from the upstream scavenger and middling spirals, resulting in a higher iron recovery in the hydraulic classifier.

While standard silica grade could be achieved with the optimised parameters, low silica grade production was more challenging. The results showed that in order to consistently reach the low silica target, the feed iron grade must be relatively high (>63 per cent).

Lastly, the feed tonnage to the pilot hydraulic classifier was studied to determine possible optimisation of the iron recovery and silica reduction ratio. Results showed no strong correlations between the feed tonnage and the unit's performance.

Challenges faced

During the pilot hydraulic classifier test campaigns, two spiral banks were chosen as control scavenger spirals and two other spiral banks were used as pilot scavenger spirals. Even though these banks received the same material feed and had the same configurations, a systematic bias was observed between the control and pilot lines. This bias could have distorted the comparison between the results.

When the campaigns to produce a standard silica grade concentrate were realised, the control line was producing a lower silica grade concentrate. Thus, the comparison of the recovery is not equivalent for the control and pilot lines since the parameters of the pilot line were modified to produce a standard silica grade concentrate. This also led to a normalisation of results to compare the pilot and control lines under the same conditions. The normalisation involved fixing the circuit feed condition for the control and pilot line. Recovery models were calculated from the sampling campaign results of pilot and control lines at each circuit step. The recoveries were then calculated for the pilot and control lines with the same feed conditions and performance compared on the same basis.

Finally, while laboratory test work showed stable operation, reproducible results and easy obtainment of a low silica grade concentrate, piloting the equipment under plant conditions proved far more difficult. The pilot hydraulic classifier was very sensitive to process variations, feed grind size as well as ore lithology changes.

REFLUX RESULTS

A total of 180 sampling campaigns were conducted on the pilot Reflux classifier at the Bloom Lake Phase 1 concentrator over a period of 4 months. The ore fed to the concentrator was mainly made of silica and iron containing mineral such as hematite, magnetite and, in smaller proportions, limonite and silicates with a feed grade varying between 25 and 36 per cent iron.

The pilot test strategy was the same as in the case of the hydraulic classifier where the impact of the different operating parameters on the equipment performance was determined and the best operating ranges were identified to optimise the performance of the equipment. The results obtained for both phases are presented in the following sections along with the challenges faced during the pilot campaigns.

Identification of equipment operating range

Exploratory sampling campaigns were performed at the beginning of the study to assess the operating limits of the equipment, allowing to reach reasonable recovery performances. The operating parameters tested were the following:

- percent solids
- feed iron grade
- loading rate
- relative density of the fluidised bed
- fluidisation water flow rate
- rise rate.

The relative density of the bed is obtained by the pressure difference and distance between the two pressure probes of the Reflux classifier.

The preliminary results allowed the following conclusions to be drawn regarding the control of the pilot Reflux classifier:

- As with the pilot hydraulic classifier, per cent solids influence other parameters such as rise rate, loading rate and the relative density and, therefore, cannot be considered as a control parameter on its own.

- It was possible to observe a decrease in iron recovery and an increase in the silica reduction ratio at the upper extreme values of the feed volume flow rate. However, there was no correlation between this parameter and the performance of the Reflux classifier for low to high values within a normal operation range.
- The results showed that increasing relative density promotes reduction of silica in the underflow and downwardly affects iron recovery as shown in Figure 4. This parameter can therefore be used to move the silica grade versus iron recovery curve in order to reach the required concentrate quality.
- At high fluidisation flow rates (>2.0 m³/h), a decrease in iron recovery and an increase in silica reduction ratio was observed, while it was not observed at lower values. However, fluidising water flow rate affected other aspects of the Reflux classifier operation:
  - A low fluidising water flow rate caused flow problems at the underflow since it became too viscous. Stabilisation of the process within the equipment then became impossible.
  - Increasing the rise rate resulted in a decrease in iron recovery and an increase in the silica reduction ratio as shown in Figure 5. The effects were particularly marked for high rise rate values.

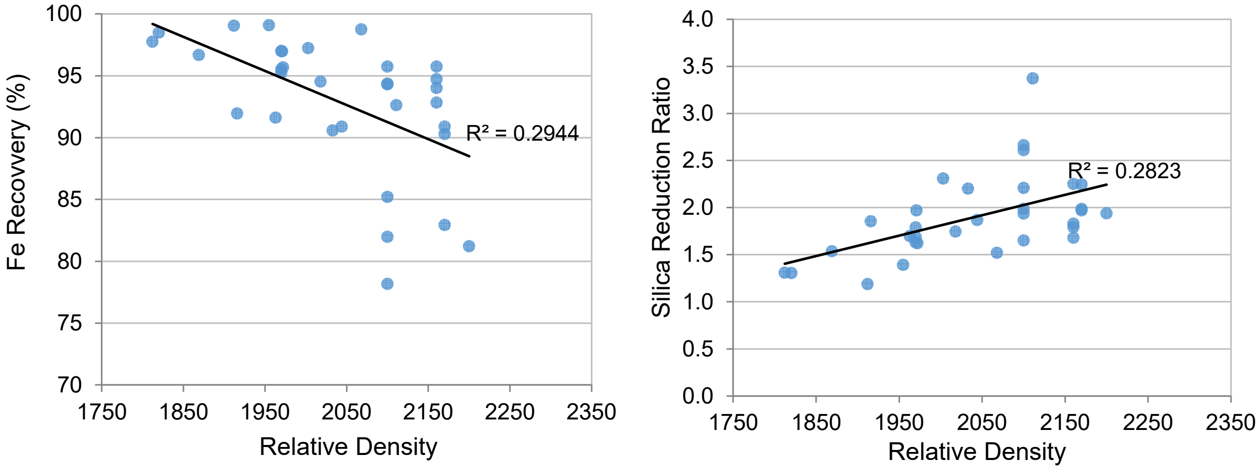

FIG 4 – Effect of relative density on the iron recovery and silica reduction ratio.

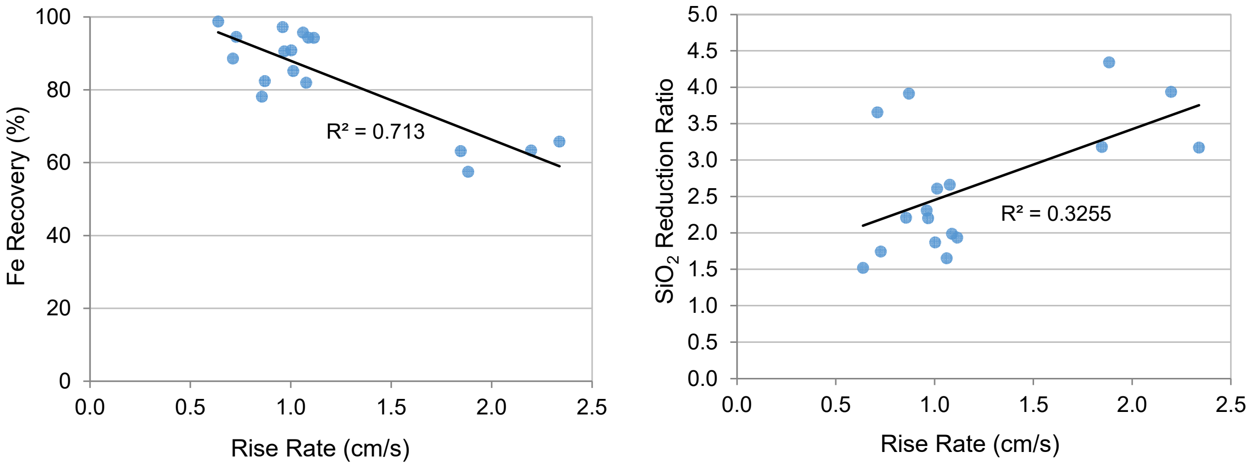

FIG 5 – Effect of the rise rate on the iron recovery and silica reduction ratio.

Optimisation of operational parameters

To maximise the performance of the pilot Reflux classifier, the operating parameters of the whole pilot line were optimised.

The position of the cutters and the wash water flow rates of all spiral stages as well as the pressure and water flow rate of the cleaner hydraulic classifiers were adjusted to maximise global recovery. These allowed better control over the following parameters:

- feed size distribution
- feed iron grade
- feed tonnage
- feed particle size.

Following the experience with the pilot hydraulic classifier, the feed particle size parameter was investigated for the pilot Reflux classifier. It was found that the proportion of particles larger than 212 µm was directly proportional to the feed silica grade. Due to their size, most of these particles were likely to be found in the underflow of the pilot Reflux classifier. Selectivity was low for the +150 and +212 µm particle size ranges: the iron content was low while that of silica was high. Iron recovery, however, remained higher than that of silica. Figure 6 presents the proportion of +212 µm particles in the Reflux classifier feed and the associated concentrate silica grade.

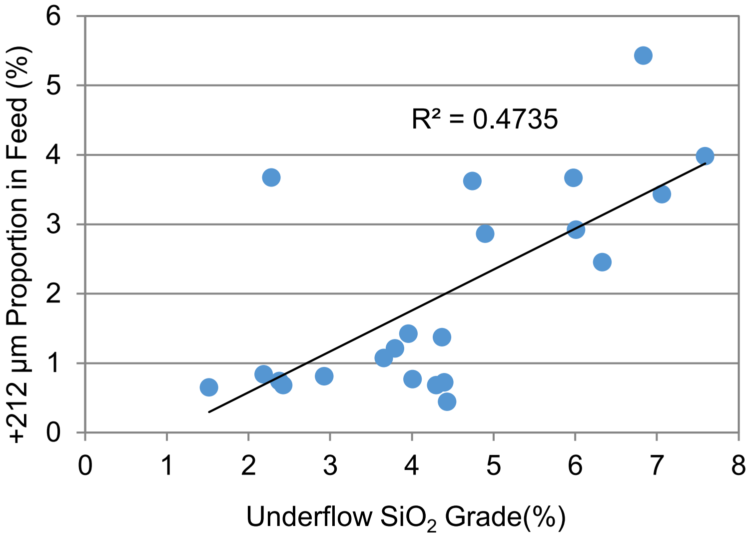

FIG 6 – Proportion of +212 µm particles in the feed and associated concentrate silica grade.

It was also observed that the Reflux classifier recovered fine iron (-75 µm) preferentially to silica with a mass recovery of iron greater than 80 per cent, while only between 20 per cent to 40 per cent of silica was recovered in this same particle size range.

Feed iron grade did not have a significant effect on the performance of the pilot Reflux classifier: feed grades as low as 56 per cent iron showed recoveries higher than 80 per cent while the silica reduction ratio was greater than two.

The feed tonnage to the pilot was studied to determine possible optimisation of the iron recovery and silica reduction ratio from this parameter. Similarly, to the pilot hydraulic classifier results, no strong correlations were found between feed tonnage and unit performance.

Challenges faced

When testing the Reflux classifier under conditions close to the limit of operational parameters, reaching a steady state was challenging. The main parameter showing stability of the pilot was the relative density measured with pressure sensors.

The position of the pilot unit at the end of the separation circuit and lack of feed tonnage control made the pilot equipment vulnerable to upstream perturbations. Unstable mill feed tonnage led to some variations in the discharge flow rates which fluctuated significantly towards either the underflow or the overflow. A volumetric flow rate control system for the equipment feed would improve operational stability. When the feed variations were smooth, the performance of the Reflux, iron recovery and silica grade, were stable and predictable.

COMPARISON BETWEEN THE REFLUX AND THE HYDRAULIC CLASSIFIER

With dozens of reconciled data sets in hand, it was possible to compare the two pilot units in terms of recovery performance, quality performance and operability. Because the plant control line was also sampled systematically, it is possible to compare performance to a reference point and better evaluate the relevance and benefits of adding this scavenger cleaner step, as well as which equipment is best suited for the task. The following section presents the selectivity and recovery performance followed by the equipment operability comparison.

Selectivity and recovery performance

The performance of the pilot Reflux (P-RC) and hydraulic classifier (P-HC) is presented side by side in Figure 7 for different iron grade feed classes for all pilot campaigns. The concentrate silica grade is presented on the left-hand side figure and the iron recovery on the right-hand side figure. The error bars represent the range between the lowest and highest values.

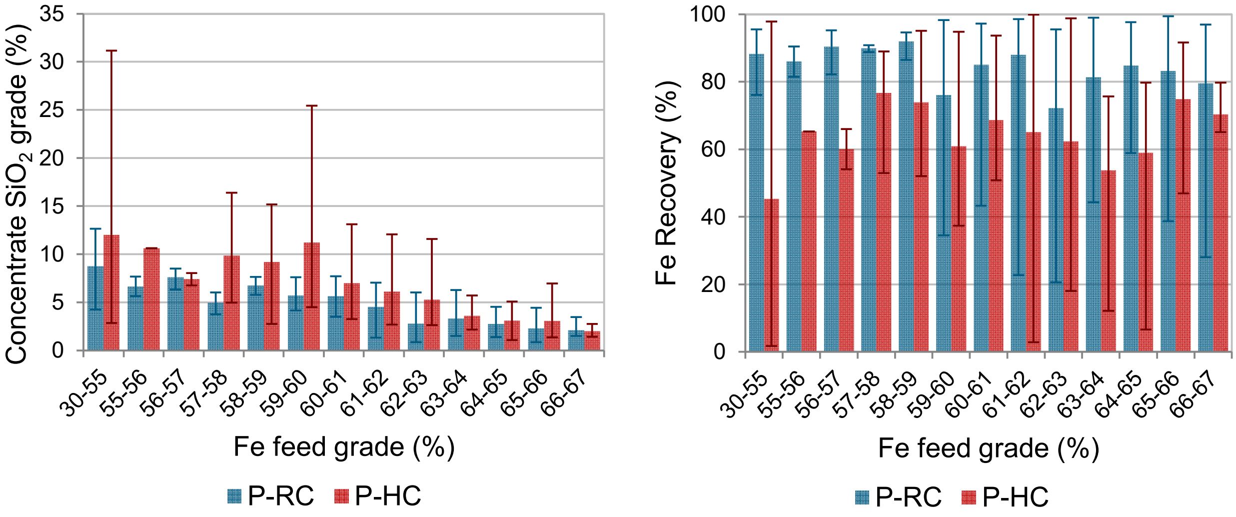

FIG 7 – Recovery performance of the pilot equipment at different Fe feed grade.

The following observations are made:

- The Reflux classifier allows for a significatively higher iron recovery compared to the hydraulic classifier for a similar feed grade.
- The Reflux classifier provided greater and more consistent silica reduction than the hydraulic classifier, regardless of the feed content. A feed iron grade of 61 per cent produced a concentrate under 2.5 per cent silica with values as low as 1.5 per cent silica with the Reflux classifier which proves its higher selectivity compared to the hydraulic classifier. In the case of the hydraulic classifier, the tests that produced 2.5 per cent silica concentrate had a feed iron grade higher than 63 per cent.
- The iron feed grade influences the concentrate iron grade obtained by the Reflux and hydraulic classifiers.
- The iron feed grade does not influence significatively the iron recovery for both the Reflux classifier and the hydraulic classifier.

Figure 8 presents the selectivity of the pilot hydraulic classifier and pilot Reflux classifier obtained for all campaigns carried out during both pilots. The left-side figure shows the recovery of both classifiers for different underflow product silica grades. The right-side figure shows the iron recovery against the silica recovery to illustrate equipment selectivity. The first campaigns were exploratory and do not represent conditions that are optimal for the operation of the equipment. This is mainly what explained the large distribution of iron recovery with the Reflux classifier also observed in Figure 7. Those results are shown in shade while the campaigns that were realised under the right conditions were selected for the determination of the recovery and selectivity models.

Recovery models linking the iron recovery to the silica recovery were developed for each technology in order to predict the performance obtained with the additional equipment.

The goal of these simulations was to allow a normalised comparison of the circuits from the data collected. The model used is based on the following hyperbolic equation:

$$R_{fer} = \frac{a * (R_{Silica} - b)}{(100 - (c - R_{Silica}))}$$

The model is adjusted to represent the asymptotes reflecting maximum and minimum recoveries obtained in the pilot campaigns. The dimensionless parameters a, b and c are calculated from the equipment selectivity data to minimise the root-mean-square error (RSME).

The selectivity models developed from the data are presented in the figure to the right.

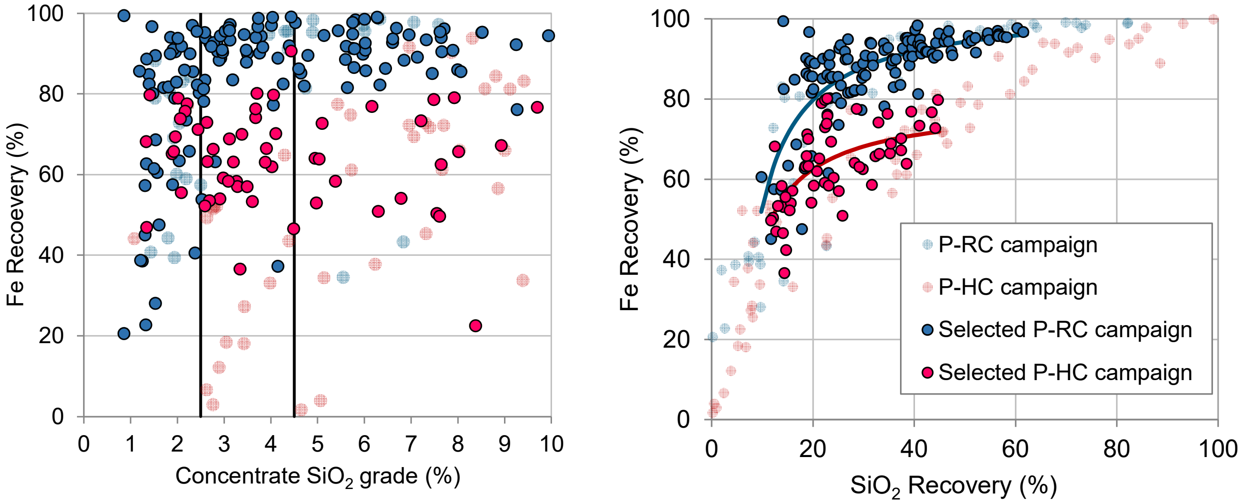

FIG 8 – Recovery performance of the Reflux classifier and the hydraulic classifier.

The main takeaways are:

- The pilot Reflux classifier is more selective than the pilot hydraulic classifier.
- Few sampling campaigns allowed to produce a low silica grade concentrate with the pilot hydraulic classifier. For the samplings where this product quality was reached, the iron recovery was between 45 and 80 per cent.
- Many sampling campaigns allowed to produce low silica grade concentrate below the 2.5 per cent target with the pilot Reflux classifier while maintaining good recovery. The iron recoveries varied between 21 and 99 per cent. When a higher silica grade concentrate was produced, the iron recoveries were between 35 and 99 per cent. However, the majority of the points lay between 80 and 99 per cent.

The models obtained from the pilot campaigns were used to calculate the iron recovery for both pilot classifiers operated under the same plant feed conditions. For the Reflux and hydraulic classifiers, the rougher spiral feed iron grade was 29.3 per cent Fe. Recovery models were also developed for each stage of the gravity separation flow sheet (Phase 1): rougher, middling and scavenger spirals and cleaner hydraulic classifier. An optimisation algorithm was then executed with a recovery maximisation objective while fixing product grade and operating parameters within model calibration boundaries.

The simulations were run for the production of a low silica grade concentrate (2.5 per cent silica) and a standard silica grade concentrate (4.5 per cent silica). The results obtained for the scavenger cleaner step are presented in Figure 9.

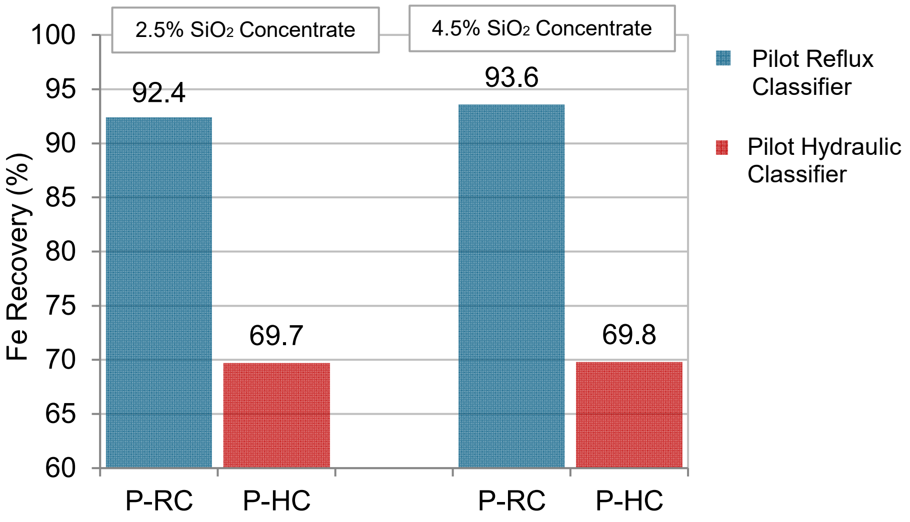

FIG 9 – Recovery of the pilot equipment for the production of low and standard silica grade concentrate.

The results show a significantly higher iron recovery obtained with the Reflux classifier compared to the hydraulic classifier when low and standard silica grade concentrates are produced. The recovery increases slightly with the Reflux classifier when producing a higher silica grade concentrate compared to a low silica grade concentrate. However, the recovery is the same with the hydraulic classifier when producing low or standard silica grade concentrates.

Chemical analyses by particle size classes were performed on some of the test campaigns. Based on the pilot results obtained, the Reflux classifier allows to recover a greater proportion of the fine particles present in the scavenger cleaner stream compared to the hydraulic classifier. As shown in Figure 10, the hydraulic classifier iron recovery decreases for small-size particles while the Reflux classifier iron recovery remains high for all classes. This is especially important as the scavenger-cleaner is exposed to one of the finest concentrate streams of the plant.

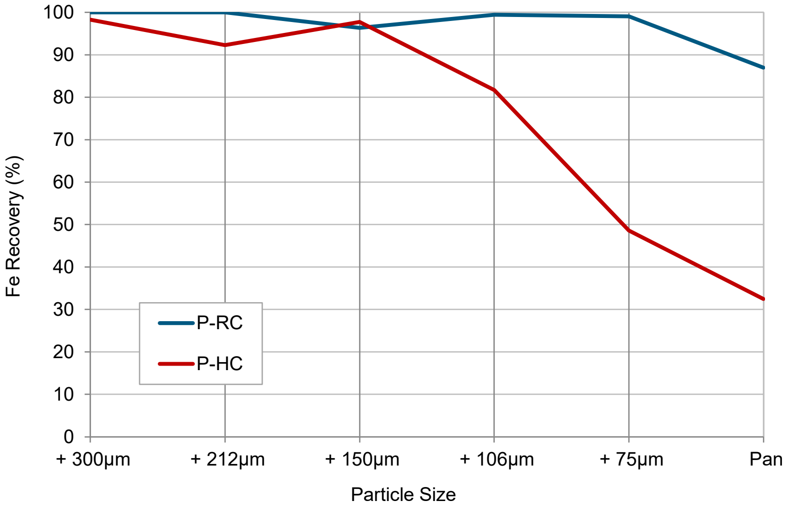

FIG 10 – Recovery performance of the Reflux classifier and the hydraulic classifier.

Operability

In terms of operability, both pilot units had different challenges and operational parameters to control. The operational limits of each parameter were tested for both pilots. These limits are presented in Table 1.

TABLE 1

Tested operational parameters of the hydraulic and Reflux classifier.

Parameter	Units	Pilot Operating Limits			
		Hydraulic Classifier		Reflux Classifier	
		Lower	Upper	Lower	Upper
Feed Solids Concentration	%	39.8	59.0	19.9	61.9
Feed Iron Grade	%	43.5	66.1	45.7	66.9
Feed Silica Grade	%	4.9	35.9	3.9	33.6
Loading Rate	t/h/m²	12.8	42.4	7.9	80.0
Relative Density	-	1240	1470	1800	2400
Fluidisation Water Flow Rate	$m^3/h/m^2$	3.4	23.8	4.0	27.8
Rise Rate	cm/s	0.2	1.6	0.4	2.6
Operating Pressure	kPa	19.0	28.5	28.0	36.0

The hydraulic classifier relative density represents the density of the material from the probe to the overflow while the Reflux classifier relative density represents the density of the material between the two probes located in the dense media.

For the pilot Reflux classifier, most of the sampling campaigns allowed to obtain reasonable iron recovery and silica grades in the concentrate. It was only when the feed throughput to the pilot Reflux classifier was below or above the limits (between 6 and 50 $t/h/m^2$) that the campaigns did not meet the target silica grade.

In the case of the pilot hydraulic classifier, some operating parameters (fluidisation water flow rate and operating pressure) showed an important effect on the iron recovery performance. High values of these parameters led to a low iron recovery performance. Therefore, unsatisfactory sampling results occurred when:

- The fluidisation water flow rate was above 0.9 m^3 per feed t.
- The operating pressure was higher than 26 kPa.

In terms of challenges to operate each unit, the pilot Reflux classifier showed a higher vulnerability to tonnage variations than the pilot hydraulic classifier. However, results showed that the operability of the pilot Reflux classifier at the end of the separation circuit was good with steady state feed to the concentrator. The performances of the pilot Reflux classifier were constant with normal process variability and with different lithologies fed to the concentrator. This was not the case with the pilot hydraulic classifier: results were more affected by the change of lithologies and variability in the concentrator feed.

CONCLUSIONS

Thorough testing of a pilot hydraulic classifier and a pilot Reflux classifier as a scavenger-cleaner alternative under real mill conditions gathered considerable information on the performance and operation of these two pieces of equipment as well as the Phase 1 separation circuit.

The information and experience acquired yielded the following conclusions:

- The iron selectivity of the Reflux classifier is greater than that of the hydraulic classifier.
- The Reflux classifier can reproducibly produce a low silica concentrate with an estimated iron recovery of 92.4 per cent for a silica grade concentrate of 2.5 per cent. The measured silica grade was between 2.5 per cent and 7 per cent and the recovery was varying between 21 and 99 per cent. When a higher silica concentrate is produced, iron recovery varies between 35 and 99 per cent (with most of the points between 80 and 99 per cent).
- The hydraulic classifier can produce a low silica concentrate, but its robustness to circuit variability is poor, and the iron recoveries vary between 45 per cent and 80 per cent for a concentrate silica grade between 2.5 per cent and 7 per cent.

- For the 2.5 per cent and 4.5 per cent silica concentrate production scenarios evaluated, the data accumulated during piloting shows that the circuit with the Reflux classifier performed better or equally with other circuits.
- The actual separation circuit's recovery could be improved at the scavenger stage.

Moreover, recovery models were developed to predict pilot equipment performance in different flow sheets. The following conclusion is drawn:

- When producing low and standard silica grade concentrate, the separation circuit with the Reflux classifier offers the best performance, although closely followed by the actual (Phase 1) circuit.

In sum, for standard silica grade (4.5 per cent) production, both options studied could allow economical production, but recovery gains are limited when compared to the actual circuit. For low silica grade (2.5 per cent) production, higher recoveries can be achieved with the Reflux classifier when compared to the actual circuit.

ACKNOWLEDGEMENTS

The authors are grateful for the assistance of the numerous metallurgists and production staff at the operations of Quebec Iron Ore for providing plant data and their own valuable observations. We also thank many metallurgists at Soutex for their contribution.

Processing options for removal of silica and alumina from low-grade hematite-goethite iron ores

V Nunna[1], S P Suthers[2], M I Pownceby[3] and G J Sparrow[4]

1. Senior Research Project Leader, CSIRO Mineral Resources, Pullenvale Qld 4069. Email: venkata.nunna@csiro.au.
2. Senior Research Project Leader, CSIRO Mineral Resources, Pullenvale Qld 4069. Email: steve.suthers@csiro.au.
3. Senior Principal Research Scientist, CSIRO Mineral Resources, Clayton Vic 3168. Email: mark.pownceby@csiro.au.
4. Honorary Fellow, CSIRO Mineral Resources, Clayton Vic 3168. Email: graham.sparrow@csiro.au.

ABSTRACT

Global demand for iron and steel has increased substantially over the past 20 years and there has been a greater focus on developing suitable processing options to treat low-grade hematite-goethite ores containing higher levels of silica and alumina impurities. The processing applicable to reduce the impurity levels in these lower-grade iron ores depends on their mineralogy and a thorough understanding of the process dynamics associated with the separation technology.

Different separation technologies used to remove silica and alumina from low-grade iron ores were reviewed. The major concentration methods that may be applied to upgrade lower-grade lump iron ores include magnetic separation, wet and dry heavy media separation, and air-pulsed jigging. The technologies applicable to beneficiating iron ore fines include wet and dry gravity and magnetic separation, flotation, and roasting followed by magnetic separation.

It is necessary to investigate the application of separation technologies on a case-by-case basis to select economically viable beneficiation strategies suitable for the particular low-grade iron ore. A commercial flow sheet is expected to involve the implementation of several separation technologies.

INTRODUCTION

Iron ore, the raw material for the steel industry, is critical for the sustainable development of the global economy (Yellishetty, Ranjith and Tharumarajah, 2010). Iron-formation hosted iron ore deposits account for the majority of current world production (Gutzmer and Beukes, 2009) of which there are three subtypes: banded iron formations (BIF) eg Algoma-type BIF and Hamersley-type BIF; granular iron formations (GIF) eg Lake Superior region, Canada, Cockatoo Island, Australia; and Rapitan iron formations (RIF) eg Rapitan, Canada. Of these subtypes, BIF and GIF iron deposits constitute the majority of commercially exploited iron ore deposits worldwide and can be divided into three classes: (1) unenriched primary iron ore formations, containing about 30–45 wt per cent Fe; (2) martite-goethite ore formed by supergene processes with abundant hydrous iron oxides, with 56–63 wt per cent Fe; and (3) high-grade hematite-rich ores of hypogene or metamorphic origin, with 60–68 wt per cent Fe (Clout and Manuel, 2015).

Globally, crude steel production has more than doubled since the beginning of the century, mainly driven by China, resulting in a major expansion in world iron ore production over the past two decades (Holmes and Lu, 2015; World Steel Association, 2021). This expansion along with changes in the nature of iron ore reserves has led to mining or development of new lower-grade ore type deposits such as the hematite-goethite Marra Mamba iron formation, channel iron deposits (CID) and detrital iron deposits (DID) in Australia.

The utilisation of lower-grade deposits has significant implications for the quality and performance of iron ore used in ironmaking as goethite can be a considerable carrier of impurities such as alumina, silica, and phosphorus (Klein and Hurlbut, 1985; Clout and Manuel, 2015; Pownceby *et al*, 2019). Goethite can also generate large amounts of fines during comminution due to its relatively low hardness compared with hematite, increasing the problems associated with processing iron ore fines (Das *et al*, 2010). Ironmaking operations are focused on achieving cost reductions and complying with environmental requirements, which are becoming more stringent. For example, there are strict conditions on acceptable impurity levels in the feed as they can degrade sinter and pellet properties and affect the quality and economics of the blast furnace by increasing slag viscosity and volume, resulting in increasing flux additions and coke consumption, while decreasing blast furnace productivity (Clout and Manuel, 2015). Further, contaminants such as Al and Si increase the carbon emissions of the ironmaking process by 12–80 kg CO_2 per ton of iron ore (Brent, 2019). As a result, there is a greater focus on developing suitable beneficiation flow sheets to treat the lower-grade goethite-rich ores so as to reduce uncertainty with changing feed composition and mineralogy and to increase the resource base while still producing consistent products.

An overview of conventional and novel beneficiation technologies to obtain higher-grade products from low-grade iron ores is presented in this paper with a focus on Australian BIF-derived ore types. Since a beneficiation strategy to increase concentrate grade and recovery will depend on the mineralogy and texture of the ore, options for iron ore lump and fines and the lower-grade hydroxide and carbonate ores are considered separately.

MINERALOGY OF IRON ORES

An understanding of the deposit characteristics and their implications in beneficiation is essential in developing economically viable flow sheets. High-grade iron ores may simply be composed of hematite and quartzite with little or no aluminium-bearing minerals present. Other deposits may contain magnetite as the dominant iron mineral with little or no hematite. Lower-grade deposits contain hydrated hematite (eg goethite or limonite) and iron carbonates (eg siderite), with gangue minerals such as quartzite, complex aluminium silicates (eg kaolinite, chlorite and phlogopite), and aluminium oxides (eg gibbsite). The presence of aluminium-bearing minerals such as ferruginous clay and shale, and quartz veinlets in irregular patches within the ore formations lower the iron ore grade in the various geological formations (DeVaney, 1985).

In Australia, all active mines have their respective commercial product types. The most important BIF ore deposits in the Pilbara region are Premium Brockman, Brockman, Marra Mamba and Channel iron deposits (pisolites) and smaller but locally significant hematite ore deposits (Holmes and Lu, 2015). There are numerous high-grade deposits in the Pilbara region with an iron content of 62 wt per cent Fe or more, but they can vary substantially. These deposits contain massive high-grade zones, which may be exploitable through selective mining and simple beneficiation circuits, such as screening and washing. The unit operations required for upgrading are simple and often involve only sizing to meet the specifications of iron ore products for the blast furnace, so beneficiation cost is minimal for these high-grade deposits. However, ore types being exploited in Australia have moved from hematite Brockman ores to martite-goethite containing Marra Mamba ores, such as the mesas in the Robe Valley and the below water table Yandicoogina channel iron deposit ores. These lower-grade (<60 wt per cent Fe) iron ores in the Pilbara region typically have hematite and goethite as the dominant minerals, characterised by varying amounts of gangue minerals such as quartz, aluminium silicate(s) or carbonate minerals.

The presence of several iron-containing mineral or textural species in an iron ore deposit complicates the beneficiation of the finer particle-sized material. For example, the iron minerals may be anhydrous (hematite pseudomorphs like martite, maghemite after magnetite) in combination with admixtures of hydrous iron minerals (goethite and limonite) and carbonates (siderite) resulting in a range of mineral compositions and properties. These ores require beneficiation to meet the stringent specifications of raw materials for a blast furnace to improve the resource base.

Mineralogical and textural characterisation

Characterisation of the fine and ultrafine material is essential for beneficiation as an intimate knowledge of their mineralogy forms the basis for developing flow sheets for processing complex lower-grade fines. Mineralogical and textural associations of the iron minerals and the liberation size characteristics of individual iron ore deposits are critical to applying the appropriate processing technologies for specific particle size ranges (Murthy and Karadkal, 2011; Donskoi *et al*, 2016). With the advent of automated characterisation technologies, mineralogical associations at micro and macro levels can be quantitatively characterised to address the complex nature of different ore types. These technologies allow the automatic and rapid analysis of the mineralogy of the feed and beneficiated products on a size-by-size and particle-by-particle basis using methods such as optical image analysis (Donskoi, Poliakov and Manuel, 2015; Donskoi *et al*, 2020) and imaging systems using scanning electron microscopy (SEM)-based techniques. Some of the SEM-based technologies are QEMSCAN (Reid *et al,* 1985; Gottlieb *et al,* 2000), the Mineral Liberation Analyser (MLA) (Gu, 2003) and TESCAN Integrated Mineral Analyzer (TIMA) (Hrstka *et al*, 2018). Examples of the utilisation of these technologies to characterise iron ore samples and beneficiation products have been given by Donskoi *et al* (2007, 2008, 2016), Tripathy *et al* (2017b) and Nunna *et al* (2020).

OVERVIEW OF BENEFICIATION STRATEGIES FOR IRON ORES

The growing demand to optimise iron ore operations requires improvements to existing beneficiation plant designs and development of new flow sheets by selection of appropriate unit operations (Figure 1).

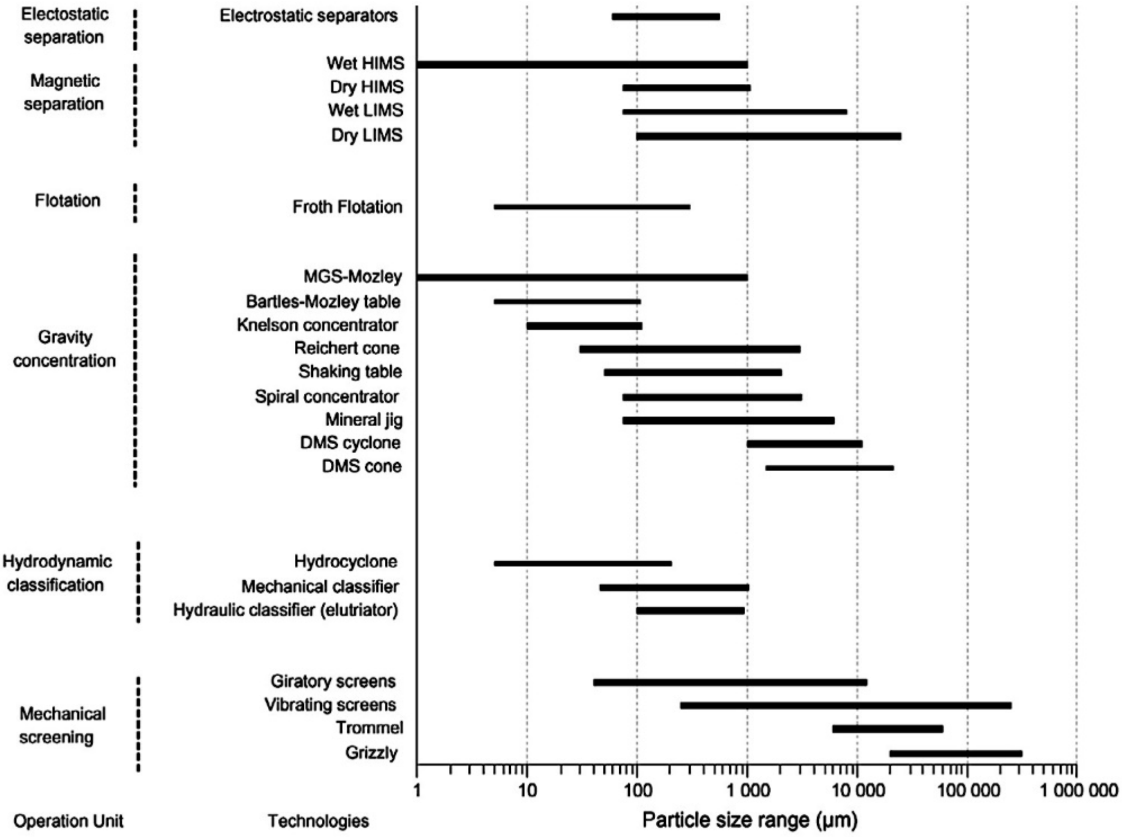

DMS= Dense media separation; HIMS= High intensity magnetic separation; LIMS= Low intensity magnetic separation; MGS= Multi gravity separator

FIG 1 – Feed particle size ranges for various physical separation techniques (after Dermont *et al*, 2008).

The primary raw materials for iron and steelmaking produced from run-of-mine (ROM) iron ore are lump (eg -32+6.3 mm) and fines (eg -6.3 mm), the latter which are converted to agglomerates such as sinter (Lu and Ishiyama, 2015) and pellets (Zhu *et al*, 2015) as shown in Figure 2.

Wet beneficiation plants are required at some iron ore operations to upgrade lower-grade iron ores and produce blast furnace grade iron ore products. However, in iron ore producing countries such as Australia, Brazil, Chile, India and the northern regions of China, where access to water is a problem, there is an increased focus on evaluating dry processing technologies. Consequently, both wet and dry beneficiation techniques have proved beneficial in many complex separation applications. Current commercial beneficiation practices include the use of techniques and equipment such as wet and dry classifiers, heavy (or dense) media separators (HMS), air pulsed water-based or pneumatic (dry) jigs, spirals, hindered settling separators (Maré, Bevan and Crisafio, 2015; Das and Sarkar, 2018), conventional as well as column flotation (Bruckard, Smith and Heyes, 2015; Matiolo *et al*, 2020), wet and dry magnetic separations (Xiong, Lu and Holmes, 2015; Tripathy *et al*, 2017a) and a magnetising roast and magnetic separation (Rath *et al*, 2016; Nunna *et al*, 2021).

It is usually necessary to combine several of these separation technologies in a flow sheet to obtain optimum recovery of a high-grade product. In the following sections, beneficiation options for iron ore lump and fines are discussed.

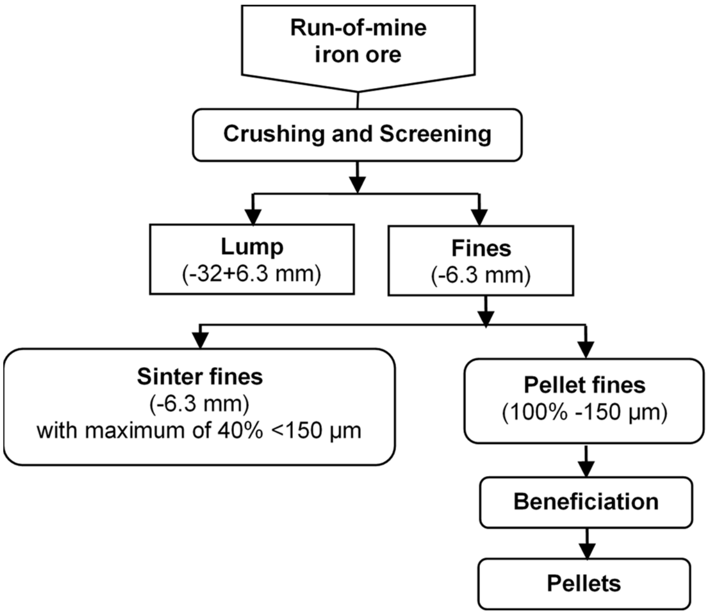

FIG 2 – Simplified flow sheet for upgrading lower-grade iron ores to shipping grade.

BENEFICIATION OF IRON ORE LUMP

Major concentrating methods currently practiced worldwide and applied to upgrade lower-grade lump iron ores to obtain products of acceptable grade and iron recovery include scrubbing and screening, heavy media separation, air pulsed jigging and magnetic separation (Wills and Napier-Munn, 2006; Das and Sarkar, 2018). However, to select beneficiation options that may be economically viable it is necessary to understand the process dynamics and investigate their application on a case-by-case basis. The properties of the feed can have a significant effect on the separation efficiency of iron ore beneficiation.

Friable and soft lateritic particles (ie goethite or clays) present as individual particles adhering to larger ore particles, or within cavities of the ore particles, are usually removed by washing and scrubbing methods. According to Das and Rath (2020), it has been observed in Indian iron ore washing plants that the maximum gangue removal by washing is limited to 25–30 per cent, with free quartz particles being better separated than alumina-bearing minerals.

With gravity separation technologies, ores that have a high proportion of near-gravity material (ie material close to the actual separating density) will be more difficult to process than ores containing very little near-gravity material (Wills and Napier-Munn, 2006). For example, if the iron ore lumps are massive hematite or goethite minerals with a separating cut specific density (SG) requirement of less than 3.8, then using an advanced large coal dense media separator (LARCODEMS) or drum-type heavy media separator (HMS) may be an economical option (Myburgh, 2003; Gent *et al*, 2009). Critical factors for the successful application of this HMS technology to iron ore types include washing ferrosilicon from the sink and float products and recovering the expensive media with minimal losses. Feed preparation and media recovery requirements in HMS flow sheets have been shown by Pretorius and Hoffman (2006) to be expensive.

Gravity separation by jigging to produce higher-grade iron ore products has been practiced for many decades (Miller, 1991, 2003) and is a potential technology for beneficiating difficult-to-treat lower-grade lump iron ores (Mukherjee, Bhattacharjee and Mishra, 2006; Das *et al*, 2007). Jigging uses water as the medium to suspend and separate particles based on the difference in SG between the iron minerals and gangue. Reasons for choosing jigging in preference to other processes include: relatively easy separation; a beneficial trade-off between operating cost and yield when compared with HMS processes; the ability to treat ores requiring cut densities higher than an SG of 4; and physical ore characteristics that make HMS unsuitable (eg unacceptable media loss in macroscopic pores). Mukherjee and Mishra (2006) investigated, experimentally and with numerical simulations, the effects of pulsation amplitude and frequency on particle segregation during jigging. Substantial progress has been made through the development of double-frequency or superimposed jigging pulsation and frequency control. Air-pulsated jig testing equipment is available with advanced pulsating and frequency mechanisms to evaluate, predict and scale-up equipment (Dieudonné, Jonkers and Loveday, 2006).

Dry separation of lump iron ore has been reported using an air dense media separator (Das and Sarkar, 2018). In this separator, iron ore particles are suspended in a gas-solid fluidised bed by upward flowing air. While effective for separating run-of-mine lump ore from gangue, it was found that separation efficiency decreased with decreasing particle size. Oshitani, Franks and Griffin (2010) had previously reported that dry float-sink separation using a heavy medium was not suitable for treating iron ore fines. However, Oshitani *et al* (2013) used a dry fluidised bed without a dense medium to separate iron ore fines in the size range of -500 +250 µm. With the optimum air velocity, density and size separation occurred in the fluidised bed, and it was concluded that a dry density segregation separation has potential for upgrading particulate iron ore.

BENEFICIATION OF IRON ORE FINES

During mining and washing of lump ore, adhering fine clay-like gangue minerals and fines are separated from the large particles. As a result, large quantities of iron ore fines are generated containing iron-bearing minerals such as hematite, martite, goethite and magnetite, along with gangue minerals that are mostly clay, shale and other aluminium silicate minerals in varying proportions (Das and Rath, 2020). The iron ore fines are complex in nature and contain fine-grained or fine-banded intergrowths of hematite, martite, goethite and gangue (Clout, 2003, 2006). Some iron ore minerals may be recoverable in a fine concentrate, but most require fine grinding to liberate the iron minerals from the gangue. Appropriate tests need to be conducted to ascertain the liberation characteristics, mineral properties and most economic beneficiation route.

Commercially, there are several wet and dry beneficiation options available to treat iron ore fines, such as gravity separation, magnetic separation and flotation, all of which have their operational features and limitations concerning particle size (Figure 1). Mineral properties and the size at which separation is required will dictate the selection of suitable beneficiation routes. For example, if there is a sufficient difference in SG, jigging is a possible option for efficient separation down to a particle size of about 0.5 mm (Dieudonné, Jonkers and Loveday, 2006), but some researchers have separated iron ore fines to even more acceptable sizes down to about 150 µm (Mukherjee, Bhattacharjee and Mishra, 2006; Das *et al*, 2007). Based on the weak magnetic properties of hematite iron ore fines, magnetic separation, such as wet high-intensity magnetic separation (WHIMS), has the potential for effective separation of material below 1 mm down to 10 µm.

Beneficiation options for treating low-grade iron ore fines can broadly be grouped based on the operating size range of commercially available equipment, as shown in Figure 3.

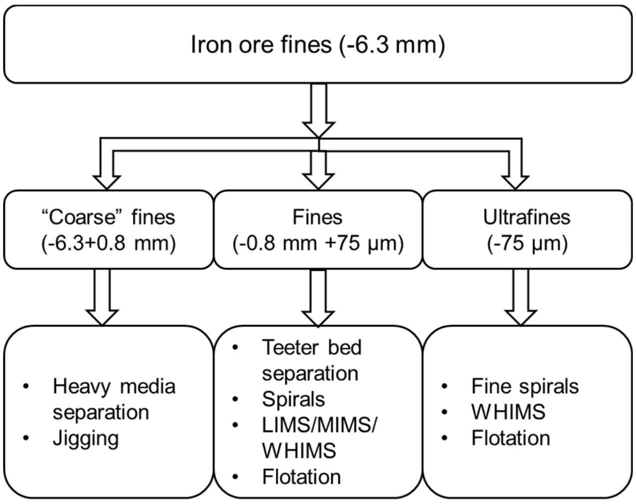

FIG 3 – Beneficiation options for upgrading lower grade iron ore fines (size ranges are indicative and selected to fit commercially available equipment) (modified from Murthy and Karadkal, 2011).

Beneficiation of 'coarse' iron ores fines

The potential beneficiation options for 'coarse' iron ore fines (eg -6.3 +0.8 mm) are similar to those for lump ore where the possible concentrating methods are HMS cyclones and air-pulsed jigging (Wills and Napier-Munn, 2006).

Jigging is an effective and efficient separation technology for beneficiating difficult to treat lower-grade iron ore fines, and jigging machines have been used in many operations (Miller, 1991, 2003; Das *et al,* 2007; Myburgh and Nortje, 2014). However, depending on the nature and complexity of the ore being processed, recoverable iron units are often lost in the tailing streams. Therefore, in some cases there is a need to generate and reprocess middlings, including liberating valuable minerals by further size reduction, which needs to be evaluated on a case-by-case basis.

Air pulsated jigs are an alternative to HMS cyclones, since they have a high capacity and jigging can separate at cut densities up to an SG of 5. Separation inefficiency is usually due to backmixing and fluidisation in the separation chamber when processing a wide range of fine particles (eg -8+0.8 mm), which is addressed by processing close particle size ranges in separate streams (Pretorius and Hoffman, 2006; Myburgh and Nortje, 2014).

Beneficiation of fine and ultrafine iron ore fines

Commercially, the beneficiation techniques available and their application generally depend on the particle size of the feed (Figure 1). Most mineral processing techniques decrease in efficiency as the particle size decreases, particularly with ultrafine material (Wills and Napier-Munn, 2006). To treat material containing particle sizes below 10 µm, hydrocyclones, matrix magnets and froth flotation are possible techniques, although they have several disadvantages that should not be overlooked. For example, due to their high surface area, particles smaller than a threshold size of around 45–75 µm can exhibit electrostatic and van der Waals forces caused by the varying polarisation of nearby particles, adversely affecting the selectivity of beneficiation equipment. Furthermore, most iron ore minerals have inter-granular micropores mainly filled with fine clay-like minerals (eg gibbsite or kaolinite). These impurity minerals are friable in nature and crumble easily, so they tend to report at a greater concentration to the slimes (particles below 10 µm).

Preconcentration

One approach to preconcentrate the valuable components in iron ore fines is to deslime them using hydrocyclones to reject impurity-containing ultrafine slimes (Das *et al*, 1992; Suthers, Clout and Donskoi, 2004; Mohanty and Das, 2010). However, hydrocyclones are inherently inefficient in classifying relatively dense particles of similar size due to misplacement of the heavy iron ore minerals. In most operations, the separation efficiencies of hydrocyclones generally are between 45 per cent and 65 per cent. Improvements including geometry, construction materials, cone angles and vortex finder penetration have improved hydrocyclone performance, although a separation efficiency of 60 per cent is the upper limit in most processing plants (Barrios, 2009).

Hydrocyclones often are used in high flow rate applications in a pod or group of hydrocyclones, with a common feed and overflow compartment. Many pods can be fed through a radial distributor as if they were individual hydrocyclones, thereby enabling large input flow rates. In the laboratory and commercial operations, hydrocyclones can be used to remove ultrafine fractions from iron ore when preparing feed to spirals (Srivastava *et al*, 2001), FLOATEX gravity separators (Sarkar *et al*, 2008), magnetic separation (Mohanty, Nayak and Konar, 2017), flotation (Thella, Mukherjee and Srikakulapu, 2012) or a magnetising roast and magnetic separation (Suthers *et al*, 2014).

Donskoi *et al* (2005, 2006, 2008) have developed a method of classification of iron ore particles that accounts for the decrease in mineral porosity with decreasing particle size to predict hydrocyclone performance and track the mineral content and textural composition of ore particles. This information can be used to predict the performance of downstream processing.

Dry separations are usually carried out on screens, nominally between 0.5 mm and 100 mm. However, dry separations below 1 mm can be problematic in the presence of moisture typically greater than 3 wt per cent in the feed (DeVaney, 1985). When finer particle sizes are present, the capacity and efficiency of the screens decrease substantially as ‘blinding‘ and ‘blanketing‘ increase. (Kelly and Spottiswood, 1982; Wills and Napier-Munn, 2006).

Dry mechanical centrifugal air classifiers have been used to remove slimes from iron ore fines to prepare material for further dry beneficiation. The cut size in an air classifier can be changed by varying the stationary bottom vane configuration and rotational speed of the fan or wheel which changes the strength of the forced vortex created within the classifier to give the preferred cut size and flow profile. When the separation size is too fine for screens (75 µm or finer), or when the throughput is too high (over 800 t/h), circulating air classifiers are a better choice (Jimbo *et al,* 1985; Muscolino, 2010). Depending on the material characteristics, a sharp separation with a cut size as fine as 20–38 µm is achievable with a circulating air classifier. Optimisation studies and numerical modelling of circulating air classifiers have been reported by Karunakumari *et al* (2005), Eswaraiah (2015), Eswaraiah *et al* (2019) and Nunna *et al* (2019).

Suthers *et al* (2019) used an air classifier to deslime goethite-rich iron ore tailings (-2 mm) containing 50.4 wt per cent Fe to obtain a coarse product containing 51.7 wt per cent Fe with removal of about 30 per cent of the silica and 26 per cent of the alumina. However, the performance of the air classifier was not as good as was achieved when the same sample was deslimed with a hydrocyclone (Suthers *et al,* 2014). With the hydrocyclone, about 50 per cent of the silica and alumina were rejected. The poorer performance of the air classifier was considered to be due to the presence of agglomerated particles, including very fine particles coating coarser particles, in the feed to the air classifier.

Concentration by gravity separation

Over the years, various gravity separation techniques have been employed by companies to beneficiate lower-grade iron ore fines. At present, the commercial gravity separation techniques used include heavy media cyclones, spirals and teeter bed separators. However, limitations such as separation size (Figure 1), capacity, footprint and techno-economics need to be evaluated for the mineral properties of the ore deposit of interest.

To evaluate the applicability of gravity separation, three types of particles in the slurry need to be considered: very fast settling heavy particles; relatively heavy particles settling more slowly; and light gangue particles (DeVaney, 1985). Since the SG of common iron minerals, such as hematite (5.1), magnetite (5.17), goethite (4.2) and siderite (3.85), are higher than most of the gangue minerals, such as aluminium silicates and silicate minerals with SG values ranging between 2.65 and 2.85 (John and Edgar, 1985), the objective of gravity separation is to use these SG differences between minerals to separate the faster-settling iron-containing particles from the slower-settling gangue.

Heavy media cyclones are applicable for treating particle sizes down to approximately 212 µm, so additional methods are required for treating and recovering iron ore particles finer than 212 µm in the slurry (Wills and Napier-Munn, 2006). Furthermore, separation and recovery of the expensive heavy media can add substantial cost to the process economics (Pretorius and Hoffman, 2006).

Hence, when treating complex lower-grade iron ore fines, selection of the heavy media cyclone option requires careful investigation to determine whether it is viable.

Gravity concentration using spirals is another option that has been applied to processing iron ore fines (Miller, 1991; Bazin *et al,* 2014). Spirals cannot achieve the desired final product grade in a single stage, so multiple banks of spirals are necessary to obtain the required separations. The basic design of the original 'Humphreys type' spiral has changed over time, with manufacturers now achieving more efficient gravity concentration with banks of spirals using lighter construction materials, improved wash-waterless spirals and feed material distribution systems (Miller, 1991; Palmer and Vadeikis, 2010).

The teeter bed separator (TBS) is a hindered settling classifier in which an upward current of water is distributed across the bottom of the sorting column. The rising current of water creates a 'teeter zone' for the downward settling feed material in the separating tank, which has the effect of enhancing a separation and producing a concentrate based on differences in the size and specific gravity of the minerals, for particle sizes below about 1 mm (Das *et al*, 2009; Nunna, Hapugoda and Raynlyn, 2015; Das and Sarkar, 2018). Developments by manufacturers of TBS have included more advanced design features and control measures for material feeding and product discharge. The application of TBS in processing lower-grade iron ore fines has increased with there being a greater scope for producing a consistent quality product without being greatly affected by feed grade variations. Depending upon the nature and complexity of the feed material, TBS is often integrated with other unit operations to achieve the required overall grade and recovery. This has led to the development of the FLOATEX density separator, ALLFLUX® separator and REFLUX™ classifier. All three units can be used for size classification and density-based concentration of iron ore fines. Their operational principles have been described by Das and Sarkar (2018). The use of TBS in an integrated flow sheet is often a viable option for beneficiating lower-grade iron ore fines due to the technological advantages, operational simplicity, smaller footprint and reduced labour requirements.

Murthy and Basavaraj (2012) used a FLOATEX density separator to reduce the silica and alumina content of a sample of low-grade iron ore fines (-1.0 mm) from the Pilbara region in Western Australia. With a feed of 48.7 wt per cent Fe, a concentrate with a grade of around 57.0 wt per cent Fe (63.0 wt per cent Fe calcined) and an iron recovery of over 77 per cent was obtained, with rejection of over 75 per cent SiO_2 and over 66 per cent Al_2O_3. This result indicated that low-grade iron ore fines and plant rejects containing appreciable amounts of goethite, which were being stockpiled or dumped as waste, could be upgraded to add value.

Clout (2013) described a desand process that recovered a -1.0+0.038 mm higher-grade fraction from -8 mm natural iron ore fines. The fines are initially screened at a nominal cut point of 0.7–1.0 mm and the undersize is processed using a hydrocyclone, with the hydrocyclone underflow fed to an ALLFLUX separator. The ALLFLUX separator further deslimes the hydrocyclone underflow, producing a coarse final concentrate, a deslimed middlings for feeding to spirals, and an overflow (-0.100 mm) for feeding to a residue thickener. The ALLFLUX separator and spiral concentrates are dewatered using vacuum belt filters or fine screens. The ALLFLUX separator provides the spirals with a substantially cleaner feed material than traditional methods. The result is that the spirals do not silt up with slimes and therefore continue to run at their optimum. Potential applications for the process have been exploited in Australia, India and South Africa (Clout, 2013).

Hunter *et al* (2016) used a REFLUX classifier to beneficiate ultrafine iron ore with a nominal top size of 0.106 mm and 59 wt per cent less than 0.038 mm. In a single-stage separation, from a feed of 35 wt per cent Fe, a product containing 66.1 wt per cent Fe was obtained with an iron recovery of 80 per cent.

Enhanced gravity separators, such as the multi gravity separator (MGS), Kelsey centrifugal jig and Falcon concentrator (Das and Sarkar, 2018), have been applied to beneficiate iron ore fines. In these units, a centrifugal force is applied to increase the effect of gravity to achieve the mineral separations. The g-force applied in the Kelsey jig and Falcon concentrator is equivalent to around 100 and 700 g, respectively. Nayak and Pal have demonstrated the use of a Kelsey jig (Nayak and Pal, 2013a) and a Falcon concentrator (Nayak and Pal, 2013b) to beneficiate iron ore fines.

Concentration by magnetic separation

Magnetic separation performance and equipment choice is influenced by a wide range of factors, including particle size, particle shape, magnetic field strength, coercive force and the existence of remanent polarisation of minerals. The overall magnetic separation efficiency depends on the magnetic properties of the iron and gangue minerals and their association. Consequently, variations in the magnetic properties of mineral admixtures can create difficulties in concentrating lower-grade iron ore fines (eg martite-goethite, martite-hematite-goethite and porous natural pisolites) using magnetic separation. Most iron ore minerals exhibit magnetic polarisation that decreases from larger values for coarser grain sizes (eg 100 µm) to zero for 1 µm particles (Svoboda, 1987). This can affect the magnetic separation efficiency.

New types of magnetic separators have been developed making many older style separators obsolete (Svoboda, 1987; Svoboda and Fujita, 2003). The advent of rare earth permanent magnets and superconducting electromagnets, coupled with new construction materials, have changed the scope of magnetic separation. The development of continuous magnetic separators with higher magnetic strength and gradient has made it possible to recover many weakly magnetic minerals and iron-containing minerals down to a few microns in particle size. As each magnetic separation technique has its distinct merits and limitations, often no single technique is applicable to all potential applications (Figure 4).

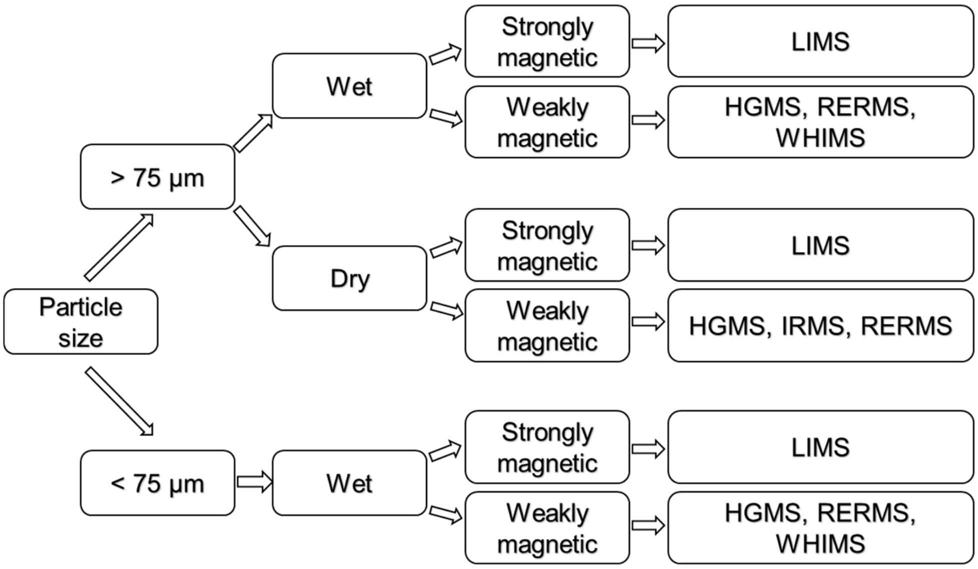

FIG 4 – Magnetic separation processes for treating low-grade iron ore fines (modified from Svoboda, 2004). HGMS = high-gradient magnetic separation; REMS = rare earth roll magnetic separation; IRMS = induced-roll magnetic separation; LIMS = low-intensity magnetic separation; WHIMS = wet high-intensity magnetic separation.

To beneficiate ores containing minerals with strong magnetic properties (eg magnetite and maghemite), wet low-intensity magnetic drum separators (drum LIMS) are usually used. This may be achieved with several stages of separation, or the drum may be used in combination with flotation (Xiong, Lu and Holmes, 2015). The development of wet high-intensity magnetic separators (WHIMS) and wet high-gradient magnetic separators (HGMS), with a matrix in a ring of magnets (Jones, 1960; Yang *et al*, 2018), have enabled iron minerals and admixtures that were considered too fine and too weakly magnetic (eg hematite, goethite, siderite and limonite) to be separated from gangue minerals such as aluminium silicates, quartz, ferruginous clay and shale that are predominantly non-magnetic.

When ore types with variable magnetic properties are processed using HGMS or WHIMS, matrix blockages and mechanical entrainment of non-magnetic particles are likely to be experienced during routine operations. To overcome these problems, the SLON® vertically pulsating high-gradient magnetic separator was developed (Xiong, Liu and Chen, 1998), which features a unique matrix and a vertical ring with a vertical pulsating mechanism. The SLON is used to continuously beneficiate fine weakly-magnetic minerals of sizes from -1.3 mm down to about 10 µm and is claimed to have the advantages of a large beneficiation ratio, high recovery and a matrix that does not clog.

Dry magnetic separation is of increasing interest for upgrading low-grade iron ore fines. The advent of rare-earth permanent magnets has resulted in the construction of magnetic roll separators that generate magnetic forces exceeding those produced by electromagnetic high-intensity separators. Tripathy *et al* (2017b) used a rare earth roll magnetic separator (RERMS) and a dry induced-roll high-intensity magnetic separator (IRMS) to separate hematite from low-grade iron ore fines. They concluded that the RERMS can be used as a rougher unit to achieve maximum recovery while the IRMS can be used as a cleaner unit.

Concentration by flotation

Froth flotation is an efficient method to remove impurities from iron ore when the valuable and gangue mineral particles are liberated. The main objective of iron ore flotation is to upgrade the concentrate by removing quartz, silicate minerals (eg kaolinite) and aluminium-containing minerals (eg gibbsite). The separation is achieved by exploiting differences in the physicochemical properties of the iron and gangue minerals; thus, the floatability of iron ores can differ widely due to the composition of the iron minerals and the nature and association of the gangue. Some of the fine clay-like minerals are reasonably easy to reject (eg chlorite) as they are flaky in nature and easily float in counter-current water even without the addition of flotation reagents. In contrast, other clay-like minerals that exist in veinlets of goethite or limonite may be finely disseminated and can be challenging to separate from the original ore minerals. A wide range of reagents including collectors, depressants, activators, dispersants and frothers are necessary to achieve the required separations (Quast, 2017; Nakhaei and Irannajad, 2018; Rath and Sahoo, 2020; Zhang *et al,* 2021).

Investigations into iron ore flotation commenced in the USA in 1931 and three different flotation processes were developed, namely, direct flotation, reverse anionic flotation and reverse cationic flotation. In direct flotation, the iron ore is floated and collected in the froth product. In contrast, with reverse flotation, the gangue materials are floated into the froth and the tailing is the iron concentrate. Reverse cationic flotation is generally applied in the iron ore industry in the USA, Canada, Brazil, India, Sweden and Russia, while reverse anionic flotation is widely used in China (Bruckard, Smith and Heyes, 2015; Filippov, Severov and Filippova, 2014). Houot (1983) and Zhang *et al* (2021) have presented flow sheets for commercial operations.

Column flotation cells are a pneumatic (non-mechanical) flotation cell with reduced floor space, maintenance and energy requirements. Dey *et al* (2015) studied the effects of column flotation process parameters using Indian iron ore slimes. The application of column flotation makes it possible to extend the size range of particles that can be treated by flotation to about 5–10 µm. Matiolo *et al* (2020) investigated the use of column flotation to recover iron from two different Itabirite iron ore slimes samples without prior desliming, with mixed success.

Beneficiation options for oxyhydroxide and carbonate iron ore types

Hydrated iron ores (goethite and limonite), carbonates (siderite) and their resultant lower-grade mixtures are difficult to beneficiate to produce high-grade concentrates. However, high-grade massive goethite iron ore types may not need any beneficiation and can be directly shipped after crushing and screening. However, the goethite content of the mixed ore types (eg magnetite-hematite-goethite and martite-goethite) is considerably less and goethite can be rejected along with gangue minerals in the beneficiation process. A process involving reduction roasting followed by magnetic separation and pelletising can be applied to these iron ores.

Low-grade non-magnetic iron ores consisting primarily of goethite, limonite or siderite can be converted to synthetic magnetite by a reducing roast and then concentrated using low-intensity magnetic separation (DeVaney, 1985; Uwadiale, 1992). When goethite or limonite ore types are roasted in a reducing atmosphere at 500–550°C, they become strongly magnetic. A siderite ore needs to be roasted in a neutral atmosphere at 700–750°C to make the iron oxides magnetic. After reduction roasting, such ores must be cooled out of contact with air to below 100°C or they will re-oxidise to hematite. However, the processing is relatively expensive and a high proportion of high-grade goethite (>56 wt per cent Fe) in the feed is probably required to make it economical, because a minimum upgrade of 6 wt per cent Fe by the expulsion of the combined water is normally required.

Upgrading low-grade iron ore fines and tailings containing appreciable amounts of goethite using a magnetising roast and magnetic separations have been reported by Jang *et al* (2014), Suthers *et al*

(2014), Rath *et al* (2016) and Nayak *et al* (2019). Reductants have included carbonaceous materials (Rath *et al,* 2016; Nayak *et al*, 2019) and CO/CO_2 gas mixtures (Jang *et al,* 2014; Suthers *et al,* 2014). Yu *et al* (2020) have reviewed the use of conventional roasting techniques such as shaft furnaces, rotary kilns and fluidised beds for magnetising roasts.

There has been a growing interest in investigating microwave-assisted magnetising roasting of low-grade oxyhydroxide iron ore fines to increase the concentrate grade and valuable mineral recovery. Results of microwave roasting followed by magnetic separation for hematite-goethite fines have been presented by Rath *et al* (2016), Nunna*,* Hapugoda and Pownceby (2017) and Nunna *et al* (2021). Carbonaceous materials were used as reductants by Rath *et al* (2016), while CO/CO_2 gas mixtures were used by Nunna*,* Hapugoda and Pownceby (2017) and Nunna *et al* (2021).

Nunna *et al* (2020) processed low-grade hematite-goethite iron ore fines containing 54.5 wt per cent Fe with an air classifier to remove -20 µm fines, followed by microwave-assisted roasting and magnetic separation using IRMS. A high-grade magnetic product of 62.0 wt per cent Fe and around 82 per cent iron recovery, with a rejection of 24 per cent SiO_2 and 23 per cent Al_2O_3, was achieved.

A summary of prospective technologies and application options focusing on Australian BIF for low-grade iron ore beneficiation is presented in Table 1.

SUMMARY

A wide range of beneficiation technologies are essential for treating low-grade iron ores to remove undesirable gangue minerals to lower silica and alumina levels to meet the specifications of ironmaking operations.

When the iron-containing minerals are liberated in lump ore, they may be recovered by magnetic separation with rare earth drums, or gravity methods including wet and dry HMS and air pulsated jigs. On the other hand, for finer size fractions, a more complicated process flow sheet is likely to be necessary, depending on the properties of the iron minerals and associated gangue in the ore.

Most beneficiation flow sheets to treat iron ore fines initially deslime the feed with hydrocyclones, or with air classifiers for dry processing, to reject a large proportion of the silica and alumina present in the slimes fraction of the fines. Gravity processes using HMS, spirals or hindered settling classifiers, are widely used for concentrating iron ore fines. Fines containing natural magnetite, or synthetic magnetite from a magnetising roast of iron oxyhydroxide or carbonate minerals, can be upgraded with LIMS, while WHIMS or HGMS are used for hematite-rich ores. For mixed magnetite-hematite iron ores, LIMS, followed by WHIMS, HGMS or SLON can be used to recover the iron minerals.

For finely disseminated iron ores, particularly when associated with silicate minerals, fine grinding, selective flocculation and cationic reverse flotation has been used widely to recover an iron-rich concentrate. Direct flotation and reverse anionic flotation are also practiced. Numerous reagents, including collectors, depressants, activators, dispersants and frothers are utilised in the flotation process, so extensive testing often is necessary to determine the optimum flotation conditions.

Hydrated iron ores (goethite and limonite), carbonates (siderite) and their resultant lower-grade mixtures can be beneficiated with a magnetising roast followed by magnetic separation. Recently, there has been interest in microwave-assisted heating for the magnetising roasts. Reductants used have included carbonaceous materials and CO/CO_2 gas mixtures.

TABLE 1

Prospective technologies and application options with a focus on Australian BIF for low-grade iron ore beneficiation.

Product (size range)	Technology	Applications	Selection principles
Lump (-31.5+6.3 mm)	Scrubbing or washing	Drum scrubber and log washing	The technology has great potential for desliming porous lower grade Pilbara iron ores, eg., limonite/goethite and hematite-goethite ores, which carry ultrafine clayey kaolin and/or gibbsite minerals in the pores.
	Gravity separation	HMS, LARCODEMS, Tri-Flo separators.	• Processing of some ores may result in slime build-up in the separating suspension, and the medium viscosity may increase to the point where separation efficiency is adversely affected. • The media (magnetite or ferrosilicon), which is lost in the process, maybe difficult or costly to obtain in some regions, for treating low-grade porous ore minerals.
		Jigging	Jigging is a promising technology for upgrading lower-grade Pilbara iron ores, eg., hematite BIF ores and other difficult-to-treat ores. Therefore, the technique should be investigated by conducting tests on selected samples.
	Magnetic separation	RED (Rare Earth Drum) magnetic separators	• Vendors claim that RED magnetic separators can be used to pre-concentrate coarse particles ranging in size up to 75 mm. Established applications include hematite and martite type iron ores. • The possible application of roasting followed by RED magnetic separation technology to low-grade iron ore processing is considered as a prospective option for study and evaluation.
Coarse fines (-6.3+1.0/0.5 mm)	Scrubbing or washing	Attrition scrubbers	• They are used to liberate aggregate minerals from slime coatings, the disintegration of clay agglomerates, high-intensity conditioning and mineral grain cleaning or polishing. • Depending upon the nature of the clayey minerals, attrition scrubbing is generally applicable for particles of -10 mm size. The actual scrubbing time depends on the residence time in the attrition scrubber, which is usually operated at densities of 70–80% solids.
	Gravity separation	HMS, jigging	Similar to Lump processing (see above).
	Magnetic separation	RED/RER (Rare Earth Roll) magnetic separators	Similar to Lump processing (see above).
Ultra-fines (-1.0/0.5 mm+75/45 µm) and Slimes (-75/45 µm)	Sizing/classification/ gravity separation	Hydrocyclones, fine screens	• Supplementary processes like scrubbers, fine screens and cyclones also have potential applications in integrating beneficiation processes. • Separating an aggregate of mixed particles into groups according to size ahead of separation is essential to increase the efficiency of the subsequent gravity/magnetic/flotation separation processes.
		spirals, TBS (Teeter-bed separator)	Spirals and teeter-bed separators (TBS) are widely accepted and used in iron ore processing with additional benefits, including floor space, labour requirements and operational simplicity.
	Magnetic separation	Matrix Magnets WHIMS/HGMS	Although technology might work satisfactorily on specific size fractions that are well liberated, it is unlikely that adequate product grade and recovery would be obtained for lower grade ultrafines and slimes from Pilbara iron ores.
	Flotation	Direct, reverse anionic and reverse cationic flotation. Column Flotation	The separation of kaolinite, gibbsite common alumina containing mineral in iron hydroxides, is challenging due to the similarities in their surface properties.
Dry Beneficiation options (an effective alternative for upgrading low-grade iron hydroxide ores) • A fundamental requirement of feed <3% moisture content is needed.	Sizing/classification	Circulating air classifiers/dust cyclones	Air scrubbing/classification is alternatively can be employed as feed preparation. A sharp separation from -10 mm size with a cut size as fine as 20–38 µm is achievable depending upon the characteristics of the material.
	Roasting followed by magnetic separation	Conventional/Microwave and dry magnetic separators	• Goethite-containing ores have a low magnetic susceptibility compared to hematitic ores. The thermal/advanced microwave-assisted magnetising/neutral air roasting followed by magnetic separation using RED/RER magnetic separators are potential alternative pathways for achieving good separation and recoveries, • Depending upon ore characteristics, the rejection of gangue minerals plus an upgrade of 4 to 6 wt.% Fe by the expulsion of the combined water can be achievable.

Numerous combinations of separation technologies have been incorporated into flow sheets for beneficiating low-grade complex iron ores. Results on the performance of the separation technologies has been reported by many investigators, allowing comparisons between technologies to be made. Flow sheets using several different separation technologies may be applicable for a particular ore, so test work is usually necessary to characterise the ore and evaluate different separation technologies to determine the optimum beneficiation process for an iron ore.

ACKNOWLEDGEMENTS

The authors acknowledge CSIRO Mineral Resources for funding this review.

REFERENCES

Barrios, G F, 2009. Increasing the capacity of the grinding circuits without installing more mills, in *Proceedings Fourth Southern African Conference on Base Metals*, pp 433–444 (The Southern African Institute of Mining and Metallurgy: Johannesburg).

Bazin, C, Sadeghi, M, Bourassa, M, Roy, P, Lavoie, F, Cataford, D, Rochefort, C and Gosselin, C, 2014. Size recovery curves of minerals in industrial spirals for processing iron oxide ores, *Minerals Engineering,* 65:115–123, doi: 10.1016/j.mineng.2014.05.012

Brent, A, 2019. Optimising value – unlocking potential on the revenue side of the value equation, in *Proceedings Iron Ore 2019*, p 2 (The Australasian Institute of Mining and Metallurgy: Melbourne).

Bruckard, W J, Smith, L K, and Heyes, G W, 2015. Developments in the physiochemical separation of iron ore, in *Iron Ore: Mineralogy, Processing and Environmental Sustainability* (ed: L Lu), pp 339–356 Woodhead Publications: Cambridge), doi: 10.1016/B978–1-78242–156–6.00011–3.

Clout, J M F and Manuel, J R, 2015. Mineralogical, chemical, and physical characteristics of iron ore, in *Iron Ore: Mineralogy, Processing and Environmental Sustainability* (ed: L Lu), pp 45–84 (Woodhead Publications: Cambridge), doi: 10.1016/B978–1-78242–156–6.00002–2

Clout, J M F, 2003. Upgrading processes in BIF-derived iron ore deposits: implications for ore genesis and downstream mineral processing, *Applied Earth Science (B)*, 112(1):89–95, doi: 10.1179/0371745032501153

Clout, J M F, 2006. Iron formation-hosted iron ores in the Hamersley Province of Western Australia, *Applied Earth Science (B)*, 115(4):115–125, doi: 10.1179/174327506X138931

Clout, J M F, 2013. Beneficiation of fine iron ores using the desand process, in *Proceedings Iron Ore 2013*, pp 337–347 (The Australasian Institute of Mining and Metallurgy: Melbourne).

Das, A and Sarkar, B, 2018. Advanced gravity concentration of fine particles: a review, *Mineral Processing and Extractive Metallurgy Review*, 39(6):359–394, doi: 10.1080/08827508.2018.1433176

Das, A, Sarkar, B, Biswas, P and Roy, S, 2009. Performance prediction of FLOATEX density separator in processing iron ore fines – a relative velocity approach, *Mineral Processing and Extractive Metallurgy (C)*, 118(2):78–84, doi: 10.1179/174328509X383926

Das, B and Rath, S S, 2020. Existing and new processes for beneficiation of Indian iron ores, *Transactions of the Indian Institute of Metals*, 73(3):505–514, doi: 10.1007/s12666–020–01878-z

Das, B, Mishra, B K, Prakash, S, Das, S K, Reddy, P S R and Angadi, S I, 2010. Magnetic and flotation studies of banded hematite quartzite (BHQ) ore for the production of pellet grade concentrate, *International Journal of Minerals, Metallurgy and Materials*, 17(6):675–682, doi: 10.1007/s12613–010–0373-x

Das, B, Prakash, S, Das, S K and Reddy, P S R, 2007. Effective beneficiation of low grade iron ore through jigging operation, *Journal of Minerals and Materials Characterization and Engineering*, 7(1):27–37, doi: 10.4236/jmmce.2008.71002

Das, B, Prakash, S, Mohapatra, B K, Bhaumik, S K and Narasimhan, K S, 1992. Beneficiation of iron ore slimes using hydrocyclone, *Minerals and Metallurgical Processing*, 9:101–103, doi: 10.1007/BF03402979

Dermont, G, Bergeron, M, Mercier, G and Richer-Laflèche, M, 2008. Soil washing for metal removal: a review of physical/chemical technologies and field applications, *Journal of Hazardous Materials*, 152:1–31, doi: 10.1016/j.jhazmat.2007.10.043

DeVaney, F D, 1985. Iron ore – ore preparation and concentration methods, in *SME Mineral Processing Handbook* (ed: N L Weiss), chapter 20, pp 4–6 (Society of Mining Engineers of the American Institute of Mining, Metallurgical and Petroleum Engineers: New York).

Dey, S, Pani, S, Singh, R and Paul, G M, 2015. Response of process parameters for processing of iron ore slime using column flotation, *International Journal of Mineral Processing*, 140:58–65, doi: 10.1016/j.minpro.2015.04.013

Dieudonné, V, Jonkers, A and Loveday, G, 2006. An approach to confidently predicting jigging performance, Journal of the Southern African Institute of Mining and Metallurgy, 106:733–739.

Donskoi, E, Suthers, S P, Campbell, J J and Clout, J M F, 2005. Prediction of hydrocyclone performance in iron ore beneficiation using virtual modelling, in *Proceedings Iron Ore 2005*, pp 321–330 (The Australasian Institute of Mining and Metallurgy: Melbourne).

Donskoi, E, Suthers, S P, Campbell, J J, Raynlyn, T D and Clout, J M F, 2006. Prediction of hydrocyclone performance in iron ore beneficiation using texture classification, in *Proceedings XXIII International Mineral Processing Congress: IMPC 2006*, vol 3, pp 1897–1902 (International Mineral Processing Council: Istanbul).

Donskoi, E, Suthers, S P, Fradd, S B, Young, J M, Campbell, J J, Raynlyn, T D and Clout, J M F, 2007. Utilization of optical image analysis and automatic texture classification for iron ore particle characterisation, *Minerals Engineering*, 20(5):461–471, doi: 10.1016/j.mineng.2006.12.005

Donskoi, E, Suthers, S P, Campbell, J J and Raynlyn, T, 2008. Modelling and optimization of hydrocyclone for iron ore fines beneficiation — using optical image analysis and iron ore texture classification, *International Journal of Mineral Processing*, 87(3–4):106–119, doi: 10.1016/j.minpro.2008.02.006

Donskoi, E, Poliakov, A and Manuel, J R, 2015. Automated optical image analysis of natural and sintered iron ore, in *Iron Ore: Mineralogy, Processing and Environmental Sustainability* (ed: L Lu), pp 101–159 (Woodhead Publications: Cambridge), doi: 10.1016/B978–1–78242–156–6.00004–6

Donskoi, E, Poliakov, A, Holmes, R, Suthers, S, Ware, N, Manuel, J and Clout, J, 2016. Iron ore textural information is the key for prediction of downstream process performance, *Minerals Engineering*, 86:10–23, doi: 10.1016/j.mineng.2015.11.009

Donskoi, E, Manuel, J R, Hapugoda, S, Poliakov, A, Raynlyn, T, Austin, P and Peterson, M, 2020. Automated optical image analysis of goethitic iron ores, *Mineral Processing and Extractive Metallurgy*, 11 p, doi: 10.1080/25726641.2019.1706375

Eswaraiah, C, 2015. Optimization of process parameters for enrichment of rice bran oil using Box-Behnken experimental design, *Separation Science and Technology*, 50(14):2147–2154, doi: 10.1080/01496395.2015.1020552

Eswaraiah, C, Soni, R K, Tripathy, S K and Filippov, L O, 2019. Particle classification optimization of a circulating air classifier, *Mineral Processing and Extractive Metallurgy Review*, 40(5):314–322, doi: 10.1080/08827508.2019.1643340

Filippov, L O, Severov, V V and Filippova, I V, 2014. An overview of the beneficiation of iron ores via reverse cationic flotation, *International Journal of Mineral Processing*, 127:62–69, doi: 10.1016/j.minpro.2014.01.002

Gent, M R, Menendez, M, Toraño, J, Isidro, D and Torno, S, 2009. Cylinder cyclone (LARCODEMS) density media separation of plastic wastes, *Waste Management*, 29(6):1819–1827, doi: 10.1016/j.wasman.2008.12.026

Gottlieb, P, Wilkie, G, Sutherland, D, Ho-Tun, E, Suthers, S, Perera, K, Jenkins, B, Spencer, S, Butcher, A and Rayner, J, 2000. Using quantitative electron microscopy for process mineralogy applications, *JOM*, 52:24–25, doi: 10.1007/s11837–000–0126–9

Gu, Y, 2003. Automated scanning electron microscope based mineral liberation analysis, *Journal of Minerals and Materials Characterization and Engineering*, 2(1):33–41, doi: 10.4236/jmmce.2003.21003

Gutzmer, J and Beukes, N J, 2009. Iron and manganese ore deposits: mineralogy, geochemistry and economic geology, in *EOLSS: Encyclopedia of Life Support Systems* (eds: B De Vivo, B Grasemann and K Stüwe), pp 43–69 (UNESCO: Paris).

Holmes, R J and Lu, L, 2015. Introduction: overview of the global iron ore industry, in *Iron Ore: Mineralogy, Processing and Environmental Sustainability* (ed: L Lu), pp 1–42 (Woodhead Publications: Cambridge), doi: 10.1016/B978–1-78242–156–6.00001–0

Houot, R, 1983. Beneficiation of iron ore by flotation – review of industrial and potential applications, *International Journal of Mineral Processing*, 10(3):183–204, doi: 10.1016/0301–7516(83)90010–8

Hrstka, T, Gottlieb, P, Skála, R, Breiter, K and Motl, D, 2018. Automated mineralogy and petrology – applications of TESCAN Integrated Mineral Analyser (TIMA), *Journal of Geosciences*, 63:47–63, doi: 10.3190/jgeosci.250

Hunter, D M, Zhou, J, Iveson, S M and Galvin, K P, 2016. Gravity separation of ultra-fine iron ore in the REFLUX™ Classifier, *Mineral Processing and Extractive Metallurgy (C)*, 125(3):126–131, doi: 10.1080/03719553.2016.1155687

Jang, K, Nunna, V R M, Hapugoda, S, Nguyen, A V and Bruckard, W J, 2014. Chemical and mineral transformation of a low grade goethite ore by dehydroxylation, reduction roasting and magnetic separation, *Minerals Engineering*, 60:14–22, doi: 10.1016/j.mineng.2014.01.021

Jimbo, G, Yamamzaki, M, Tsubaki, J and Suh, T S, 1985. Mechanism of classification in a Sturtevant-type air classifier, *Chemical Engineering Communications*, 34(1–6):37–48, doi: 10.1080/00986448508911185

John, L B and Edgar, J M, 1985. Minerals and their properties, in *SME Mineral Processing Handbook* (ed: N L Weiss), chapter 2, pp 10–11 (Society of Mining Engineers of the American Institute of Mining, Metallurgical and Petroleum Engineers: New York).

Jones, G H, 1960. Wet magnetic separation for feebly magnetic minerals, in: *Proceedings 5th International Mineral Processing Congress*, p 717 (Institution of Mining and Metallurgy: London).

Karunakumari, L, Eswaraiah, C, Jayanti, S and Narayanan, S S, 2005. Experimental and numerical study of a rotating wheel air classifier, *AIChE Journal*, 51(3), 776–790, doi: 10.1002/aic.10349

Kelly, E and Spottiswood, D, 1982. *Introduction to Mineral Processing*, 491 p (Wiley: New York).

Klein, C and Hurlbut, C S, 1985. *Manual of Mineralogy*, p 391 (John Wiley and Sons: New York).

Lu, L and Ishiyama, O, 2015. Iron ore sintering, in *Iron Ore: Mineralogy, Processing and Environmental Sustainability* (ed: L Lu), pp 395–433 (Woodhead Publications: Cambridge), doi: 0.1016/B978–1-78242–156–6.00014–9

Maré, E, Bevan, B and Crisafio, C, 2015. Developments in nonmagnetic physical separation technologies for hematite/goethite iron ore, in *Iron Ore: Mineralogy, Processing and Environmental Sustainability* (ed: L Lu), pp 309–338 (Woodhead Publications: Cambridge), doi: 10.1016/B978–1-78242–156–6.00010–1

Matiolo, E, Couto, H J B, Lima, N, Silva, K and de Freitas, A S, 2020. Improving recovery of iron using column flotation of iron ore slimes, *Minerals Engineering*, 158, 106608, 14 p, doi: 10.1016/j.mineng.2020.106608

Miller, D J, 1991. Design and operating experience with the Goldsworthy Mining Limited BATAC jig and spiral separator iron ore beneficiation plant, *Minerals Engineering*, 4(3–4):411–435, doi: 10.1016/0892–6875(91)90145-L

Miller, D J, 2003. Integration of beneficiation process into iron ore resource utilisation, *Mineral Processing and Extractive Metallurgy (C)*, 112(1):2–9, doi: 10.1179/037195503225011376

Mohanty, S and Das, B, 2010. Optimization studies of hydrocyclone for beneficiation of iron ore slimes, *Mineral Processing and Extractive Metallurgy Review*, 31(2):86–96, doi: 10.1080/08827500903397142

Mohanty, S, Nayak, B and Konar, J, 2017. Beneficiation of high-alumina bearing iron-ore slime: a case study from Eastern India, *Mineral Processing and Extractive Metallurgy Review*, 38(6):403–410, doi: 10.1080/08827508.2017.1350955

Mukherjee, A K and Mishra, B K, 2006. An integral assessment of the role of critical process parameters on jigging, *International Journal of Mineral Processing*, 81(3):187–200, doi: 10.1016/j.minpro.2006.08.005

Mukherjee, A K, Bhattacharjee, D and Mishra, B K, 2006. Role of water velocity for efficient jigging of iron ore, *Minerals Engineering*, 19(9):952–959, doi: 10.1016/j.mineng.2005.10.023

Murthy, N and Basavaraj, 2012. Assessing the performance of a FLOATEX density separator for the recovery of iron from low-grade Australian iron ore fines – a case study, in *Proceedings XXVI International Mineral Processing Congress (IMPC 2012)*, pp 3612–3621 (International Mineral Processing Council: New Delhi).

Murthy, N and Karadkal, B, 2011. Alumina reduction challenges in the beneficiation of low-grade haematite iron ores, in *Proceedings Iron Ore 2011*, pp 499–507 (The Australasian Institute of Mining and Metallurgy: Melbourne).

Muscolino, J, 2010. Mechanical centrifugal air classifiers, *Chemical Engineering*, 117(12):48–50.

Myburgh, H A and Nortje, A, 2014. Operation and performance of the Shishen jig plant, *Journal of the South African Institute of Mining and Metallurgy*, 114:569–574.

Myburgh, H A, 2003. The influence of the quality of ferrosilicon on the rheology of dense medium and the ability to reach higher densities, *Mineral Processing and Extractive Metallurgy (C)*, 112(1):133–144, doi: 10.1179/037195503225011448

Nakhaei, F and Irannajad, M, 2018. Reagent types in flotation of iron oxide minerals: a review, *Mineral Processing and Extractive Metallurgy Review*, 39(2):89–124, doi: 10.1080/08827508.2017.1391245

Nayak, D, Dash, N, Ray, N and Rath, S S, 2019. Utilization of waste coconut shells in the reduction roasting of overburden from iron ore mines, *Powder Technology*, 353:450–458, doi: 10.1016/j.powtec.2019.05.053

Nayak, P N and Pal, B K, 2013a. Separation behaviour of iron ore fines in Kelsey centrifugal jig, *Journal of Minerals and Materials Characterization and Engineering*, 1:85–89, doi: 10.4236/jmmce.2013.13016

Nayak, P N and Pal, B K, 2013b. Beneficiation of banded hematite jasper using Falcon concentrator: an alternative to iron ore resources, *Research Open Journal of Mineral and Mining Engineering*, 1(6):8–14.

Nunna, V, Hapugoda, S and Raynlyn, T, 2015. Process amenability studies on goethite-abundant iron ore fines, in *Proceedings Iron Ore 2015*, pp 165–174 (The Australasian Institute of Mining and Metallurgy: Melbourne).

Nunna, V, Hapugoda, S and Pownceby, M I, 2017. Study of microwave-assisted magnetising roasting and mineral transformation of low-grade goethite ores, in *Proceedings Iron Ore 2017*, pp. 575–582 (The Australasian Institute of Mining and Metallurgy: Melbourne).

Nunna, V, Hapugoda, S, Eswarappa, S G, Raparla, S K, Kumar, R and Nanda, N K, 2019. Beneficiation of low-grade iron ore fines by using a circulating-type air classifier, *Mineral Processing and Extractive Metallurgy Review*, 40(5):356–367, doi: 10.1080/08827508.2019.1635468

Nunna, V, Hapugoda, S, Eswarappa, S G, Raparla, S K, Pownceby, M I and Sparrow, G J, 2020. Evaluation of dry processing technologies for treating low grade lateritic iron ore fines [online], *Mineral Processing and Extractive Metallurgy Review*, 17 p, doi: 10.1080/08827508.2020.1837127

Nunna, V, Hapugoda, S, Pownceby, M I and Sparrow, G J, 2021. Beneficiation of a low grade, goethite-rich iron ore using microwave-assisted magnetizing roasting, *Minerals Engineering*, 166, 106826, 14 p, doi: 10.1016/j.mineng.2021.106826

Oshitani, J, Franks, G V and Griffin, M, 2010. Dry dense medium separation of iron ore using a gas-solid fluidized bed, *Advanced Powder Technology,* 21(5):573–577, doi: 10.1016/j.apt.2010.02.014

Oshitani, J, Ohnishi, M, Yoshida, M, Franks, G V, Kubo, Y and Nakatsukasa, S, 2013. Dry separation of particulate iron ore using density-segregation in a gas-solid fluidized bed, *Advanced Powder Technology*, 24(2):554–559, doi: 10.1016/j.apt.2012.11.005

Palmer, M and Vadeikis, C, 2010. New developments in spirals and spiral plant operations, in *Proceedings of the XXV International Mineral Processing Congress (IMPC 2010)*, pp 1099–1108 (The Australasian Institute of Mining and Metallurgy: Melbourne).

Pownceby, M I, Hapugoda, S, Manuel, J, Webster, N A S and MacRae, C M, 2019. Characterisation of phosphorus and other impurities in goethite-rich iron ores – possible P incorporation mechanisms, *Minerals Engineering,* 143, 106022, 10 p, doi: 10.1016/j.mineng.2019.106022

Pretorius, J J and Hoffman, G M, 2006. Utilisation of low-grade iron ore resources to produce new product(s) and the development of the Sishen Expansion Project (SEP), Sishen iron ore mine, South Africa, in *Proceedings DMS and Gravity Concentration Operations and Technology in South Africa*, pp 109–132 (Southern African Institute of Mining and Metallurgy: Johannesburg).

Quast, K, 2017. Literature review on the use of natural products in the flotation of iron oxide ores, *Minerals Engineering*, 108:12–24, doi: 10.1016/j.mineng.2017.01.008

Rath, S S and Sahoo, H, 2020. A review on the application of starch as depressant in iron ore flotation [online], *Mineral Processing and Extractive Metallurgy Review*, 14 p, doi: 10.1080/08827508.2020.1843028

Rath, S S, Dhawan, N, Rao, D S, Das, B and Mishra, B K, 2016. Beneficiation studies of a difficult to treat iron ore using conventional and microwave roasting, *Powder Technology*, 301:1016–1024, doi: 10.1016/j.powtec.2016.07.044

Reid, A F, Gottlieb, P, MacDonald, K J and Miller, R R, 1985. QEM-SEM image analysis of ore minerals: volume fraction, liberation and observational variances, in *Applied Mineralogy* (eds: W C Parks, D H Hausen and R D Hagni), pp 191–204 (TMS-AIME: Littleton).

Sarkar, B, Das, A, Roy, S and Rai, S K, 2008. In depth analysis of alumina removal from iron ore fines using teetered bed gravity separator, *Mineral Processing and Extractive Metallurgy (C)*, 117(1):48–55, doi: 10.1179/174328508X251851

Srivastava, M P, Pan, S K, Prasad, N and Mishra, B K, 2001. Characterization and processing of iron ore fines of Kiriburu deposit of India, *International Journal of Mineral Processing*, 61(2):93–107, doi: 10.1016/S0301–7516(00)00030–2

Suthers, S P, Clout, J M F and Donskoi, E, 2004. Prediction of plant process performance using feed characterisation – an emerging tool for process design and optimisation, in *Proceedings Metallurgical Plant Design and Operating Strategies (MetPlant 2004)*, pp 203–217 (The Australasian Institute of Mining and Metallurgy: Melbourne).

Suthers, S P, Pinto, P, Nunna, V and Nguyen, A V, 2019. Experimental study of dry desliming iron ore tailings by air classification, *Mineral Processing and Extractive Metallurgy Review*, 40(5):344–355, doi: 10.1080/08827508.2019.1635470

Suthers, S P, Venkata, N, Avinash, T, Douglas, J and Hapugoda, S, 2014. Experimental study on the beneficiation of low-grade iron ore fines using hydrocyclone desliming, reduction roasting and magnetic separation, *Mineral Processing and Extractive Metallurgy (C)*, 123(4):212–227, doi: 10.1179/1743285514Y.0000000067

Svoboda, J and Fujita, T, 2003. Recent developments in magnetic methods of material separation, *Minerals Engineering*, 16(9):785–792, doi: 10.1016/S0892–6875(03)00212–7

Svoboda, J, 1987. Industrial applications of high gradient magnetic separation, in *Magnetic Methods for the Treatment of Minerals*, pp 515–529 (Elsevier: Amsterdam).

Svoboda, J, 2004. *Magnetic Techniques for the Treatment of Materials*, p 321 (Kluwer Academic Publishers: Dordrecht).

Thella, S J, Mukherjee, A K and Srikakulapu, N G, 2012. Processing of high alumina iron ore slimes using classification and flotation, *Powder Technology*, 217:418–426, doi: 10.1016/j.powtec.2011.10.058

Tripathy, S K, Banerjee, P K, Suresh, N, Murthy, Y R and Singh, V, 2017a. Dry high-intensity magnetic separation in mineral industry — A review of present status and future prospects, *Mineral Processing and Extractive Metallurgy Review*, 38(6):339–365, doi: 10.1080/08827508.2017.1323743

Tripathy, S K, Singh, V, Murthy, Y R, Banerjee, P K and Suresh, N, 2017b. Influence of process parameters of dry high intensity magnetic separators on separation of hematite, *International Journal of Mineral Processing*, 160:16–31, doi: 10.1016/j.minpro.2017.01.007

Uwadiale, G G O O, 1992. Magnetizing reduction of iron ores, *Mineral Processing and Extractive Metallurgy Review*, 11(1–2):1–19, doi: 10.1080/08827509208914211

Wills, B A and Napier-Munn, T J, 2006. *Wills' Mineral Processing Technology*, 456 pp (Butterworth-Heinemann: Burlington).

World Steel Association, 2021. Total production of crude steel [online]. Available from: https://www.worldsteel.org/steel-by-topic/statistics/annual-production-steel-data.html [Accessed: 19 April 2021].

Xiong, D, Liu, S and Chen, J, 1998. New technology of pulsating high gradient magnetic separation, *International Journal of Mineral Processing*, 54:111–127, doi: 10.1016/S0301–7516(98)00009-X

Xiong, D, Lu, L and Holmes, R J, 2015. Developments in the physical separation of iron ore: magnetic separation, in *Iron Ore: Mineralogy, Processing and Environmental Sustainability* (ed: L Lu), pp 283–307 (Woodhead Publications: Cambridge), doi: 10.1016/B978–1-78242–156–6.00009–5

Yang, C, Li, S, Zhang, C, Bai, J and Guo, Z, 2018. Application of superconducting high gradient magnetic separation technology on silica extraction from iron ore beneficiation tailings, *Mineral Processing and Extractive Metallurgy Review*, 39(1): 44–49, doi: 10.1080/08827508.2017.1324439

Yellishetty, M, Ranjith, P G and Tharumarajah, A, 2010. Iron ore and steel production trends and material flows in the world: is this really sustainable?, *Resources, Conservation and Recycling*, 54(12):1084–1094, doi: 10.1016/j.resconrec.2010.03.003

Yu, J, Han, Y, Li, Y and Gao, P, 2020. Recent advances in magnetization roasting of refractory iron ores: a technological review in the past decade, *Mineral Processing and Extractive Metallurgy Review*, 41(5):349–359, doi: 10.1080/08827508.2019.1634565

Zhang, X, Gu, X, Han, Y, Parra-Álvarez, N, Claremboux, V and Kawatra, S K, 2021. Flotation of iron ores: a review, *Mineral Processing and Extractive Metallurgy Review*, 42(3):184–212, doi: 10.1080/08827508.2019.1689494

Zhu, D, Pan, J, Lu, L and Holmes, R J, 2015. Iron ore pelletization, in *Iron Ore: Mineralogy, Processing and Environmental Sustainability* (ed: L Lu), pp 435–473 (Woodhead Publications: Cambridge), doi: 10.1016/B978–1-78242–156–6.00015–0

Where DEM and SPH collide – wet screening optimisation with numeric tools

J Plinke[1]

1. Consulting Engineer, TUNRA Bulk Solids, The University of Newcastle, Shortland NSW 2307. Email: j.plinke@newcastle.edu.au

ABSTRACT

The imperative to operate sustainably requires all equipment and processes to operate at their maximum possible efficiency. Achieving this ideal state requires a thorough understanding, not only of the process itself, but also of the tools available to design and assess potential improvements. This paper presents a case where the widely employed Discrete Element Method (DEM) toolset proved insufficient to model problematic material flow during the process of optimising wet screening performance. A Smoothed Particle Hydrodynamics (SPH) model was found to more accurately replicate the flow characteristics of the physical system.

Site observations identified biased loading of the screen decks to cause inefficiencies in the wet screening of an iron ore processing circuit. Two numerical modelling approaches were pursued with the aim to select the most suitable one and continue the optimisation process based on that selected model. Selection criteria were established, based on the minimum requirements of being able to replicate the problem, including the main flow dynamics deemed to cause the issue.

The DEM model was found to over-simplify the slurry flow dynamics within the scrubber and no laterally biased flow was introduced by the scrubber's rotation to the otherwise symmetric system. Since DEM was not able to accurately replicate the existing problem, it was deemed an unsuitable method to assess the effect of any changes to the system. The second approach consisted of a SPH model. This model was deemed to map the flow within the scrubber with sufficient accuracy to address the problem, as it produced biased screen loading comparable to that reported from site. Changes to the wet chute, delivering material from the scrubber to the screen, aimed to neutralise the non-centrality introduced via the scrubber, were then successfully designed and assessed using the SPH model.

INTRODUCTION AND PROBLEM DEFINITION

As part of a process optimisation project, a wet screening process was identified as a target for improvements. Site observations indicated a consistent loading bias of slurry onto the northern side of the screens. A more equal presentation of material, utilising the whole available screen area was expected to optimise the screening process, reduce misplacement of particles and improve product moisture contents.

The case study presented here comprises material flow from the scrubber onto the coarse screen deck with the aim to improve material presentation onto the coarse screen. The screening process itself is not modelled. The relevant process geometry is shown in Figure 1 and consists of a wet scrubber followed by a chute discharging onto a wet screen with an aperture of 38 mm × 68 mm.

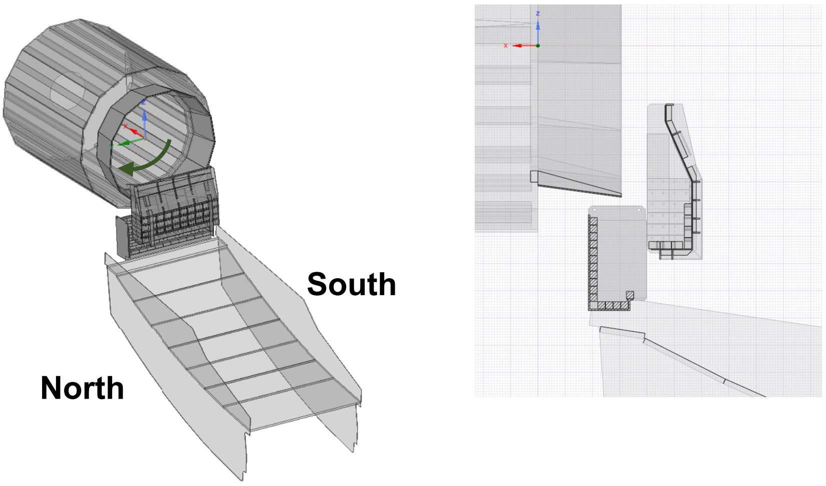

FIG 1 – Scrubber and wet screen.

The scrubber is operated at ~10 rev/min with a slurry throughput approaching 2500 m^3/h at a solids concentration of 35 per cent. Images of the flow pattern within the scrubber are shown in Figure 2. As shown, the rotation adds significant asymmetry to the flow conditions. The main body of slurry within the scrubber is situated south of centre and marked in blue in Figure 2. This volume of slurry itself is relatively slow moving, but it is surrounded by rapid flow driven by the scrubber rotation. The lifters drive some flow underneath the main slurry volume (as indicated as the dotted green arrow in Figure 2) and elevate the slurry along the scrubber wall on the northern side of the scrubber. This flow then reverses after reaching a critical height and cascades back down with rapid velocity.

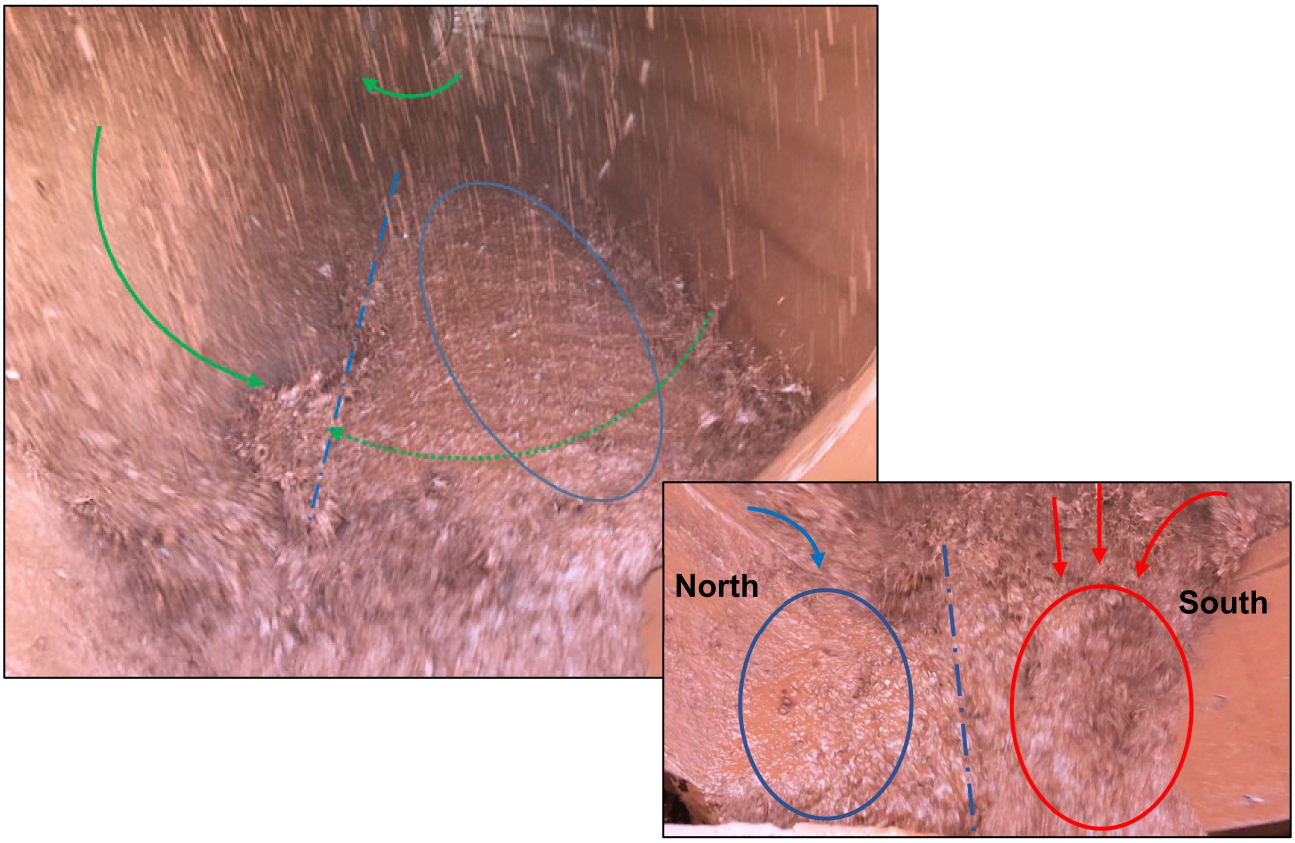

FIG 2 – Scrubber flow pattern.

This rapid downwards flow appears to displace the main slurry volume into the position south of centre, with a distinct boundary line along the length of the scrubber. While difficult to see in the available images, the area marked in blue shows a level surface. This may indicate that some separation of constituents happens within the scrubber, with liquids concentrating in the southern half (blue volume) and solids potentially preferentially accumulating in the northern half and along the circumference of the scrubber.

The circumferential currents within the scrubber, introduced by the rotation into the otherwise symmetric system, introduce non-symmetric slurry outflow across the weir. This is shown in the lower right portion of Figure 2. The outflow is grouped into two regions, with a fast-moving stream on the southern side fed by the main slurry body and a second stream on the northern side which appears to curl around towards the weir from the reversed flow returning along the north side of the scrubber hull.

Owing to the geometry of the chute, the slurry flow-through the wet chute could not be observed past the scrubber overflow. Images of the subsequent screen loading bias were however available and demonstrated a distinct loading bias towards the northern side of the screen deck.

NUMERICAL MODELLING APPROACHES

Appreciating the aphorism that *'all models are wrong, but some are useful'*, attributed to George Box, two numerical approaches were pursued during this project with the intent to determine the most appropriate or useful method during evaluation of a baseline model. The selected model would then be used to assess potential changes in chute geometry aimed at centralising the biased flow.

Given the complexity of the flow dynamics developed during scrubber discharge and the limitations in terms of available site data, neither modelling approach was intended as an absolute predictor of operating performance. Rather, the presented simulations were intended for the development of relative findings between different chute designs operating under otherwise identical conditions. Any investigation of this type needs to be accompanied by a rigorous sensitivity analysis regarding the main material parameters to ensure the numerical model is robust enough to permit any conclusions.

The minimum requirements for any baseline model therefore included the ability to model the undesirable loading bias, as well as observable proxies of the flow dynamics assumed to be the underlying cause of the non-centrality. Baseline models were therefore assessed based on the following qualitative criteria:

- Biased loading outcome comparable to that observed on-site
- Relative velocities at the scrubber weir outlet comparable to those observed on-site
- Flow dynamics within the scrubber comparable to that observed on-site including:
  - one main body with a level surface
  - circumferential flow and lifter interaction characterised by distinct boundaries between slurry bodies.

Discrete Element Method model for fluids

The first modelling approach was based on the Discrete Element Method (DEM). DEM typically finds its application during the modelling of dry granular materials or powders, simulating systems of discrete particles. The DEM software used for the modelling presented here is Rocky 4 which typically uses a hysteretic linear spring model for normal force interactions (Walton and Braun, 1986) and an elastic-frictional force model in the tangential direction. Particle rolling resistance is implemented according to the type C models (Ai *et al,* 2011). In this model the rolling resistance moment is increased linearly with relative motion up to a limiting value, where it becomes constant. A linear cohesion model similar to that described by Singh *et al* (2014) was used to include attractive forces between particles. This method is widely used in industry and one of its main advantages for modelling the presented slurry flow is its ease of application.

DEM has been utilised successfully for a range of fluid modelling projects, highlighting the fact that not all systems require accurate modelling of all aspects of fluid motion for successful assessment of flow. The major shortcomings of DEM when attempting to model liquid flow include the inability to model:

- velocity dependent transfer of shear stress

- surface tension
- incompressibility of the liquid

Velocity dependent damping for example could be simplified to a constant damping or internal friction value, provided the system is not overly dynamic. Surface tension may not play a significant role in governing flow when the liquid volume is sufficiently large to make gravity the major driving force.

In the presented case, to approximate the behaviour of the two-phase slurry, multiple material models were established with frictionless to near frictionless characteristics in both inter-particle and particle-boundary interactions to represent the liquid portion of the slurry. These models were assessed both individually and also coupled with a second phase of high-density particles included to be representative of the lump within the slurry and to indicate how higher density particles may be transported throughout the slurry.

DEM baseline model

The baseline model converged on during calibration and sensitivity analysis is shown in Figure 3. It includes the 'as built' geometry of the scrubber discharge chute and may therefore serve as a means to assess the validity of the computational model by comparison of simulation results with site data.

The simulated flow is more continuous than that observed in the site images. No main body of slurry situated north of centre can be observed in the DEM simulation and no boundary line between north and south flow volumes is established. Rather one continuous angle of repose is formed throughout the scrubber, indicating that the simplifications in terms of shear stress transfer have a significant effect on the flow dynamics within the scrubber. Subsequently the overflow onto the weir is driven by non-realistic flow patterns and the weir flow deviates from site observations. This is highlighted by the opposite locations of fast- and slow-moving streams across the weir when compared to the site images as shown in Figure 3. Even with the extremely non-central weir overflow pattern established in the baseline DEM simulation, the material stream disperses rapidly throughout the upper and lower ledges of the discharge chute, to the point where the coarse screen downstream of the lower ledge is loaded centrally. Based on these observations the model was not pursued any further.

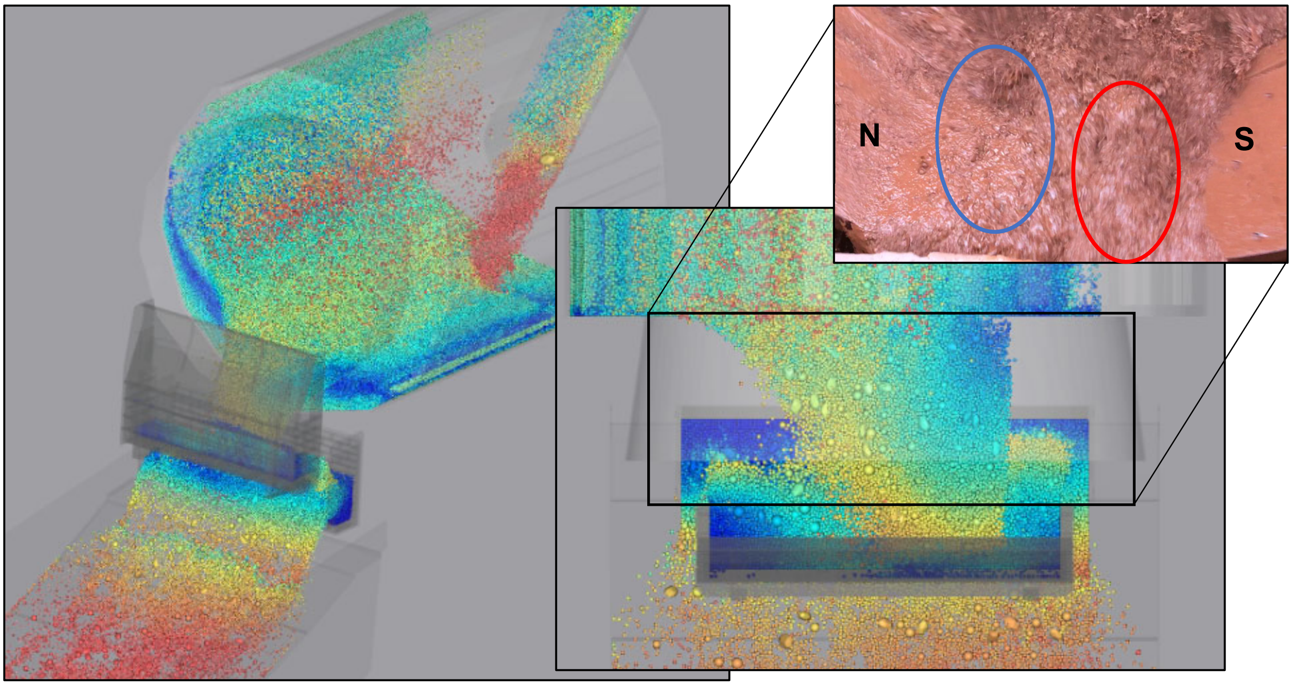

FIG 3 – Baseline DEM scrubber model.

SPH model

The second approach used Smoothed Particle Hydrodynamics as implemented by Crespo *et al* (2015) in the open-source software DualSPHysics. This method is used for simulating the mechanics of continuum media and where DEM solves Newton's equations of motion, SPH utilises the Navier-Stokes equations, which describe the motion of viscous fluids. A two-phase model consisting of water and a sediment phase based on the Herschel-Buckley-Papanastasiou model (Papanastasiou, 1987) was utilised to model the flow behaviour. The water phase is governed by known macro parameters of viscosity and density. The material model of the sediment or 'solids' phase required calibration to derive the material parameters. These included:

- Yield stress (m) to ensure stresses may be transferred when the material is at rest
- Power law index (n), controlling the behaviour of shear stress as a function of shear rate
- Density and viscosity parameters

The shear behaviour model of the sediment phase for various combinations of m and n, as produced by Fourtakas and Rogers (2016), is shown in Figure 4, with m=100 and n=1 being qualitatively representative of the sediment phase in contrast to the liquid phase which is pure Newtonian without any yield stress at zero shear. The resolution or 'particle size' for the SPH model was set to 50 mm, as sensitivity analysis of this parameter showed this to be a good compromise between being able to resolve rapid thin flow (as occurring on the screen deck, along the scrubber wall) and computational cost (read required simulation time).

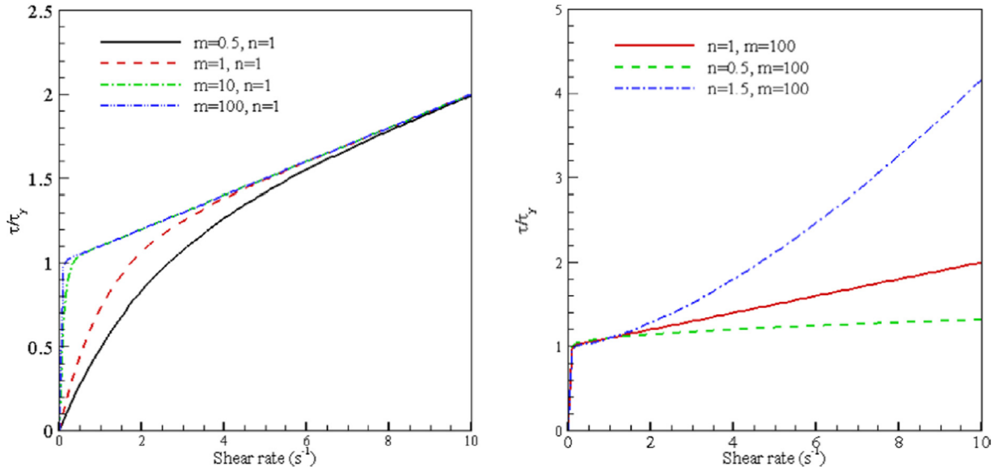

FIG 4 – Shear behaviour model (Fourtakas and Rogers, 2016).

SPH baseline model and corresponding solids biases

The general flow characteristics predicted by the SPH approach are included in Figure 5 and appear to be in good congruence with site observations. The flow effects described in the problem definition can be observed in the simulation and a bias of the solid components of the slurry flow towards the northern side of the screen can be observed. Figure 5 also highlights the comparable flow characteristics observed over the weir in both the physical and simulated cases, with a distinct high velocity, turbulent region on the southern side.

Compared to site images there are two main effects which appear to differ in the SPH model. Firstly, while the lifters appear to lift the main flow up to approximately the correct height within the scrubber, the reverse flow is less established than it appears to be in the site images. Additionally, no droplets are transported past the nine o'clock position and the downward spray of droplets is not captured. Sensitivity analysis showed that both the reverse flow and the droplets could be simulated using finer resolution, although the increase in resolution from the original 50 mm to the 12 mm necessary to resolve these effects posed excessive demands in terms of computational expense.

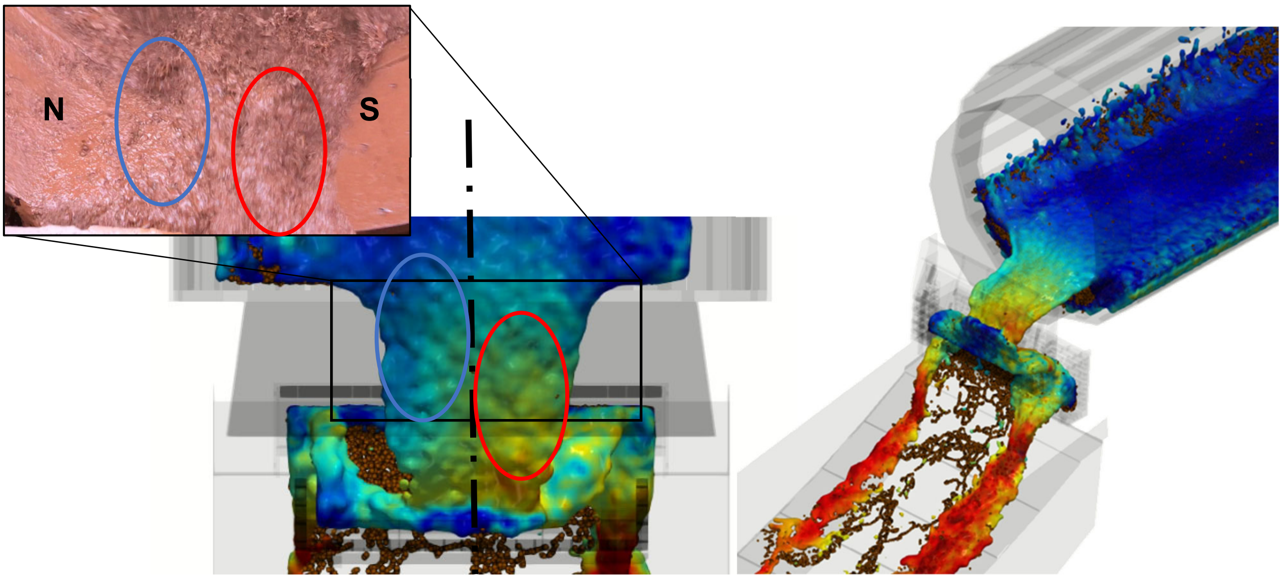

FIG 5 – Baseline SPH scrubber model.

Based on these observations the SPH model was selected to be pursued further and additional analysis was performed in order to form a basis for comparison with any subsequent designs. Figure 6 shows the location of the throughput control volumes used for loading analysis. Here the measuring volumes are indicated in red. The solids mass within these boxes north and south of centre was measured and their ratios were determined. A northern loading bias of 65 per cent was observed through the weir. This bias increased to 85 per cent in the centre control position and then decreased to 60 per cent at the chute exit point.

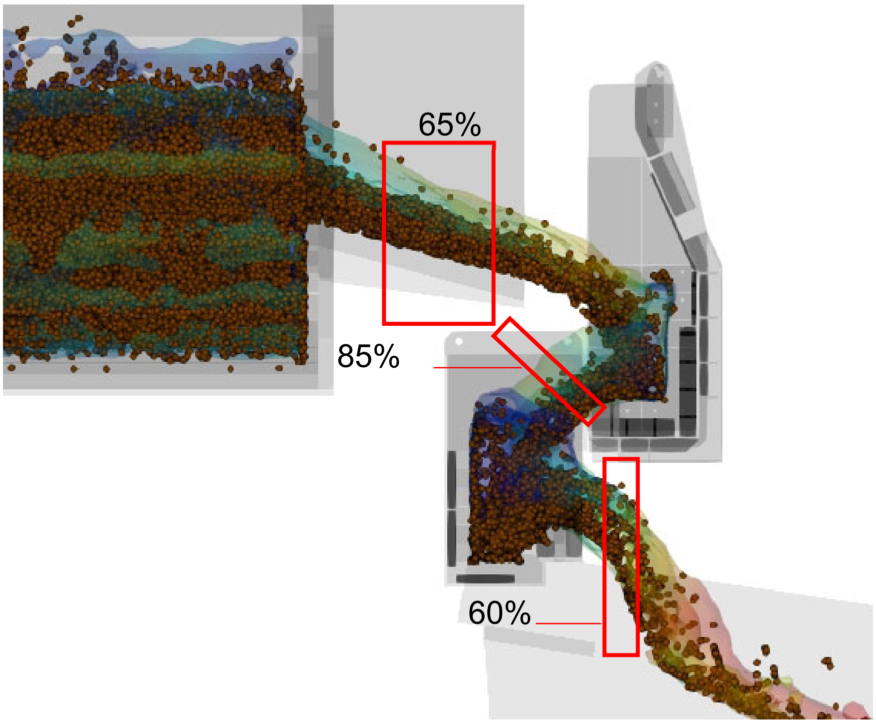

FIG 6 – Location of throughput analysis boxes.

Chute improvements

After assessing the validity of the SPH baseline model, the model was used to assess the effects of changes to the transfer between scrubber and weir aimed at counter-acting the non-central flow conditions. A suitable chute geometry was shown to significantly reduce biased loading throughout the chute and subsequently onto the screen. This improved design was subsequently installed on-site, and positive feedback regarding the effectiveness of the solution has been provided.

CONCLUSIONS

Based on the idea that '*all models are wrong, but some models are useful'*, criteria to assess the usefulness of numerical models to solve an industry problem involving dynamic multiphase flow were developed. Multiple numerical models were then developed and assessed based on their usefulness for the problem at hand. The SPH model was found to map the material flow leading to non-central screen loading with sufficient accuracy to be useful in developing solutions to the problem. After assessing the validity of the SPH baseline model, the model was used to assess the effects of changes to a transfer between a scrubber and a wet screen, aimed at counter-acting the non-central flow conditions. A suitable chute geometry was shown to significantly reduce biased loading throughout the parts of the chute and subsequently onto the screen. Subsequent implementation of the re-designed chute has led to the intended improved screen loading outcomes.

REFERENCES

Ai, J, Chen, J, Rotter, J and Ooi, J, 2011. Assessment of rolling resistance models in discrete element simulations. *Powder Technology*, 206(3), pp. 269–282.

Crespo, A, Domínguez, J, Rogers, B, Gómez-Gesteira, M, Longshaw, S, Canelas, R, Vacondio, R, Barreiro, A and García-Feal, O, 2015. DualSPHysics: Open-source parallel CFD solver based on Smoothed Particle Hydrodynamics (SPH). *Computer Physics Communications*, 187, pp. 204–216.

Fourtakas, G and Rogers, B, 2016. Modelling multi-phase liquid-sediment scour and resuspension induced by rapid flows using Smoothed Particle Hydrodynamics (SPH) accelerated with a Graphics Processing Unit (GPU). *Advances in Water Resources*, 92, pp. 186–199.

Papanastasiou, T, 1987. Flows of Materials with Yield. *Journal of Rheology*, 31(5), pp. 385–404.

Singh, A, Magnanimo, V, Saitoh, K and Luding, S, 2014. Effect of cohesion on shear banding in quasistatic granular materials. *Physical Review E*, 90(2).

Walton, O and Braun, R, 1986. Stress calculations for assemblies of inelastic speres in uniform shear. *Acta Mechanica*, 63(1–4), pp. 73–86.

Testing and modelling of diverse iron ore slurries for pipeline friction and pump head derate

R Visintainer[1], A Sellgren[2], V Matoušek[3] and G McCall[4]

1. VP Engineering and R&D, GIW Industries Inc., Grovetown Georgia, USA.
   Email: Robert.Visintainer@ksb.com
2. Professor Emeritus, Luleå University of Technology, Luleå, Sweden.
   Email: anders.sellgren@telia.com
3. Professor, Institute of Hydrodynamics, Czech Academy of Sciences, Prague, Czech Republic.
   Email: matousek@ih.cas.cz
4. Manager, Hydraulic Laboratory, GIW Industries Inc., Grovetown Georgia, USA.
   Email: George.McCall@ksb.com

ABSTRACT

A 4-component model for settling slurry pipe flow has been previously described by Wilson *et al* (2006) and Sellgren *et al* (2014) to predict pipeline friction loss (hydraulic pressure gradient) over a range of slurry compositions: from fine to coarse particle size, narrow to broad particle size distribution, and low to high solids concentration. The method applies a weighted average of established pipeline models for various settling slurry flow regimes, according to the volume fraction of solids falling within the applicable size range for each model. Further development of the model was undertaken by Visintainer *et al* (2017a, 2017b), based on a comprehensive set of laboratory tests in 203 mm (8 inch) and 103 mm (4 inch) pipelines, and it was also adapted to the modelling of slurry pump performance derates. However, this work was all performed with solids having a specific gravity near 2.65, as is typical for many mineral processing and dredging applications.

The goal of the present work is to test the applicability of these models for settling slurries having a higher solids specific gravity, as may often be seen in the mineral processing of iron ore deposits. To that end, a test program was carried out in a 103 mm (4 inch) pipe loop using various compositions of an iron ore product having a solids specific gravity of 4.75 and containing both coarse and fine solids. By screening and flushing operations, a range of particle size distributions were created having different proportions of the coarse and fine elements. In all, 19 tests were performed with *d50* particle sizes ranging from 50 µm to 3.2 mm and delivered solids concentrations from 10 per cent to 43 per cent by volume. Particle size distributions varied from very narrow to very broad, with *d85/d50* ratios ranging from 1.75 to 26. Pipeline pressure gradient and pump performance data were collected and used to test the applicability of the previously developed 4-component models and to propose improvements to the models for the handling of high-density solids.

INTRODUCTION

The solid-liquid flow of slurry in a pipeline exhibits various regimes according to the mixture velocity, particle size distribution, solids properties, carrier fluid properties and pipeline geometry. Various schemes have been developed to classify and model these (Shook, Gillies and Sanders, 2002; Wilson *et al*, 2006).

A 4-component model was originally proposed and further developed by Wilson *et al* (2006) and Sellgren *et al* (2014) to predict settling slurry pipeline pressure gradient over a range of slurry compositions and flow regimes: from fine to coarse particle size, narrow to broad particle size distribution, and low to high solids concentration (Sellgren *et al*, 2014). The model was further developed by Visintainer *et al* (2017a), based on a comprehensive, settling slurry test program performed in 203 mm (8 inch) and 103 mm (4 inch) pipelines, with particle sizes ranging from <40 µm to 12.5 mm, and delivered solids concentrations from 4 per cent to 38 per cent by volume. Analysis of the data suggested the introduction of two new empirical parameters to account for the interactions between components. The revised model provided good agreement with the experimental data over the entire range of the test program.

Based on the same series of tests, which were driven by GIW 8 × 10 LSA-32 and 3 × 4 LCC-12 slurry pumps respectively, the 4-component concept was adapted by Visintainer *et al* (2017b) to the calculation of centrifugal pump performance derates. By individually accounting for the performance losses contributed by each solids component, improved accuracy over existing mono-sized models was obtained, especially for broad and bi-modal particle size distributions. In this case, empirical parameters to account for the interactions between components were not required.

However, all of the above tests were performed with solids having a specific gravity (S_S) near 2.65, which is typical for many mineral processing and dredging applications. Although the model formulations allow for a variable solids density, and key variables used in the empirical parameters are functions of solids density, their applicability to high density iron ore slurries could not be evaluated without a similar, comprehensive data set on slurries containing higher density solids. Therefore, a series of tests was undertaken in the GIW Hydraulic Lab on slurries composed of coarse and fine magnetite having a solids specific gravity of 4.75.

Summary of the 4-component methodology

Pipeline pressure gradient

In the 4-component methodology, pipeline pressure gradient is calculated by combining a standard Newtonian pipe flow model with weighted values from established settling slurry models for pseudo-homogenous, heterogeneous and fully stratified flow. The solids are partitioned into four volume fractions or 'components' and each is assigned to one of the four submodels based on the characteristic particle sizes which bound their range of application. These are described below and in Figure 1.

- **The 'Carrier Fluid' fraction, *Xf*** includes all particles <40 µm. These solids are assumed to 'combine' with the liquid, and are considered only to the degree that they affect the average density and dynamic viscosity of the resulting mixture. For the purpose of the 4-component model, the term 'liquid' applies to the pure liquid (without solids), while the term 'carrier fluid' applies to the pseudo-fluid mixture of liquid plus *Xf* fraction particles. Losses for this component are modelled according to the Darcy-Weisbach friction factor method. The carrier fluid density is taken as the average mixture density of the liquid plus solids, and its apparent viscosity may be determined according to one of several existing models.
- **The 'Pseudo-homogeneous' fraction, *Xp*** includes all particles >40 µm, up to a limit of 200 µm. These solids are assumed to be fully supported by turbulence in the flow and to behave according to the generalised 'Equivalent Liquid' model for homogenous flow. In applying this model, the carrier fluid properties as determined for the *Xf* fraction are used. An empirical parameter *A″* is applied to account for observed near-wall, hydrodynamic lift effects for particles in this size range.
- **The 'Heterogeneous' fraction, *Xh*** includes all particles larger than the upper limit of *Xp* and smaller than the lower limit of *Xs*. These solids are assumed to be supported by a combination of turbulence and contact forces transmitted through the particles to the pipe wall. The excess pressure gradient Δi_h contributed by these particles is calculated according to the Wilson '*V50*' model. In applying this model, the carrier fluid density is taken as the total mixture density of the preceding fractions and the particle diameter is taken as the average particle size of the *Xh* fraction. An empirical parameter *C″* is multiplied into Δi_h to account for inter-granular support and near-wall lift provided by the preceding fractions. It is expressed as a function of the preceding fraction concentrations and the average slurry velocity.
- **The 'Fully Stratified' Fraction, *Xs*** includes all particles larger than 0.015*D*, where *D* is the pipeline diameter. These solids are assumed to be supported mainly by contact forces transmitted through the particles to the pipe wall. The excess pressure gradient Δi_s contributed by these particles is calculated according to the method proposed by Wilson for fully stratified flows (Wilson and Addie, 1995). In applying this model, the carrier fluid density is taken as the total mixture density of the preceding fractions. An empirical parameter *B″* is multiplied into Δi_s to account for inter-granular support and the associated reduction in mechanical friction of the

coarse particles against the pipe wall provided by the preceding fractions. It is expressed as a function of the preceding fraction concentrations and the average slurry velocity.

The above fractions are defined relative to the total volume of the particles (not the mixture), so that:

$$Xf + Xp + Xh + Xs = 1$$

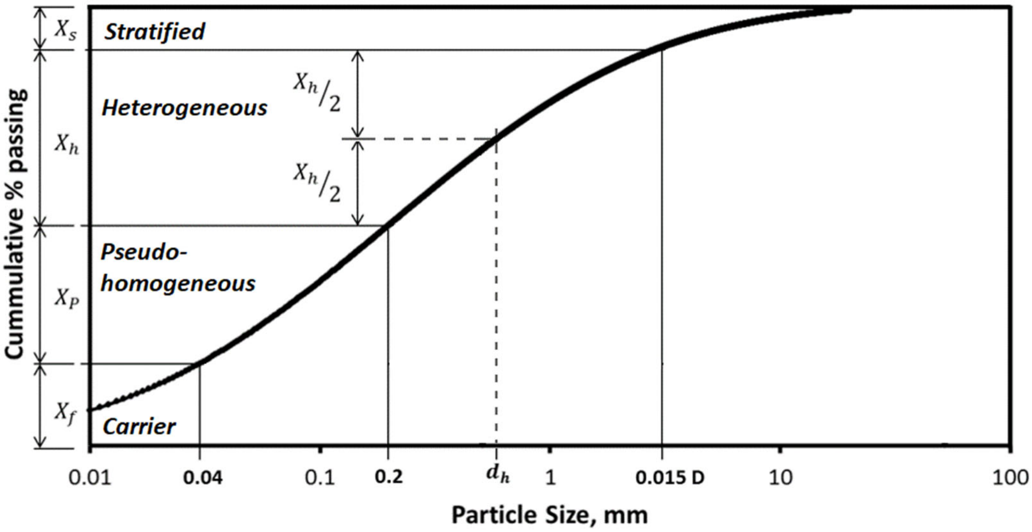

FIG 1 – Representation of the four component fractions and their particle sizes.

The pressure gradient of the combined slurry, expressed as (m water/m pipe), is then calculated as a simple summation of the contributions of each component.

$$i_m = i_f + \Delta i_p + \Delta i_h + \Delta i_s$$

In calculating each of the last three terms, the solids are taken to be running in a fluid with a density equal to the combined fluid and solids of all preceding (finer) fractions. Each term is also weighted (multiplied by) the value of its associated fraction and further adjusted by an empirical parameter to account for the inter-granular support and near-wall lift provided by the preceding fractions. These empirical parameters were an important focus of previous testing and are key to the analysis given below, so they are repeated here for reference.

Pseudo-homogeneous parameter:

$$A'' = 1 - A''_p \cdot X_p$$

Heterogeneous parameter:

$$C'' = 1 - \left(C''_f \cdot X_f + C''_p \cdot X_p\right) \cdot \left(\frac{V_{H1,s} - V_m}{V_{H1,s} - V_{sm,h}}\right)^{n_C}$$

Fully stratified parameter:

$$B'' = 1 - \left(B''_f \cdot X_f + B''_p \cdot X_p + B''_h \cdot X_h\right) \cdot \left(\frac{V_{H1,s} - V_m}{V_{H1,s} - V_{sm,s}}\right)^{n_B}$$

where:

V_m = the average pipeline velocity

$V_{sm,h}$ = the maximum velocity at limit of stationary deposition for the average *Xh* particle size

$V_{sm,s}$ = the maximum velocity at limit of stationary deposition for the 0.015*D* particle size

$V_{H1,s}$ = the pseudo-homogeneous velocity for the 0.015*D* particle size

n_C and n_B are velocity dependence constants which = 0.5 in the standard formulation

and the remaining constant terms are set as follows in the standard formulation:

$$A''_p = 0.25,\ C''_f = B''_f = B''_p = 1.0,\ C''_p = B''_h = 0.5$$

Note that the stationary deposition and pseudo-homogeneous velocities used in these parameters are themselves functions of the solids density.

Detailed descriptions of the 4-component model may be found in the referenced papers, and a complete summary of the most recent formulation can be found in Visintainer (2019). Updates made in this latest reference included the adoption of a fixed upper boundary of 200 µm for the *Xp* fraction, based on the analysis by Matousek *et al* (2018), and an adjusted formulation for the volumetric concentration of each fraction which excludes the solids contained in coarser fractions.

Centrifugal pump solids effect

The 4-component model for centrifugal pump solids effect is an extension of the mono-particle size Hydraulic Institute method from ANSI/HI 12.1–12.6 (2016).

- The effect of the *Xf* fraction is based on the viscosity of the carrier fluid according to ANSI/HI 9.7.6 (2015). This will be small if the carrier fluid viscosity is less than 20 mPa-s.
- The remaining components are calculated according to ANSI/HI 12.1–12.6 (2016) using the average particle size within each fraction and weighted (multiplied) by the value of the associated fraction, (as with the pipeline models). However, the empirical parameters *A″*, *B″* and *C″* have not been used. The formulation is shown below:

$$r_{h,x} = 8(D_{REF}/D_2)^{S1} \cdot (d_{50,x})^{S2} \cdot (S_S\text{-}S_x)/1.65 \cdot (X_x \cdot C_V/0.15)$$

where:

$r_{h,x}$ = the head reduction factor for the selected fraction

X_x = the selected fraction (*Xp*, *Xh* or *Xs*)

D_{REF} = the reference impeller diameter = 1.0 m

D_2 = the actual impeller diameter

$d_{50,x}$ = the average particle diameter for the selected fraction

S1 and *S2* = correlation exponents for the impeller and particle size factors

S_x = the specific gravity of the fluid including all preceding (finer) fractions

A 'root sum of squares' formulation (shown below) is used to combine the component contributions, in order to account for cases where the carrier fluid viscosity is significant. The subscripts *f*, *p*, *h* and *s* identify the carrier fluid (*Xf*), pseudo-homogeneous (*Xp*), heterogeneous (*Xh*) and fully stratified (*Xs*) head reduction factors respectively. When the carrier fluid viscosity is low, the *f* term becomes negligible, and the equation reduces to a summation of the *p*, *h* and *s* terms. Conversely, at high carrier fluid viscosity the solids are better supported by the fluid and the solids effect terms become negligible by comparison. At intermediate viscosities, all four terms contribute to the result.

$$r_h = \sqrt{\left(r_{h,f}\right)^2 + \left(r_{h,p} + r_{h,h} + r_{h,s}\right)^2}$$

A complete summary of the latest formulation can be found in Visintainer (2019). Updates to the model in this latest reference included:

- A simplified correlation for the particle size effect, which is based on the drag coefficient C_d, but does not require direct calculation of its value.
- A revised formulation for the pump size effect parameter selected to better fit the available data. This was of the form: $(D_2/D_{ref})^{-0.5(D2/Dref)}$. The exponent in this formulation varies from -0.2 to -1.0 for impeller diameters of 0.4 m to 2.0 m, which agrees with trends reported for very small and very large pumps by Engin and Gur (2003) and Wolfe (2014) respectively.

DESCRIPTION OF THE EXPERIMENTS

A total of 19 tests were conducted according to a similar methodology, and using a similar range of slurry compositions, as the previous 103 mm (4 inch) tests. Test were carried out in the same pipe loop previously used, but upgraded with a slightly larger pump, to provide more capacity for moving the high-density slurries, and also to provide a new pump size for correlation of the pump solids effect portions of the 4-component model. A schematic of the pipe loop is shown in Figure 2.

The system was driven by a GIW 4 × 6 LCC-16 pump with 150 mm suction, 100 mm discharge and 395 mm impeller. The system volume, including sump, was approximately 1.8 m^3. Slurry was returned to the top of the sump to maximise the active slurry volume, and thus increase the inventory of available solids and reduce particle degradation during testing. This was especially important with the magnetite solids, which were relatively soft and friable compared to silica-based solids. Return flow into the sump was positioned below the water line to avoid introducing air into the slurry. A straight entrance section of 198 pipe diameters was provided upstream of the pressure loss measurement section, which was 59.6 pipe diameters in length (6.1 m).

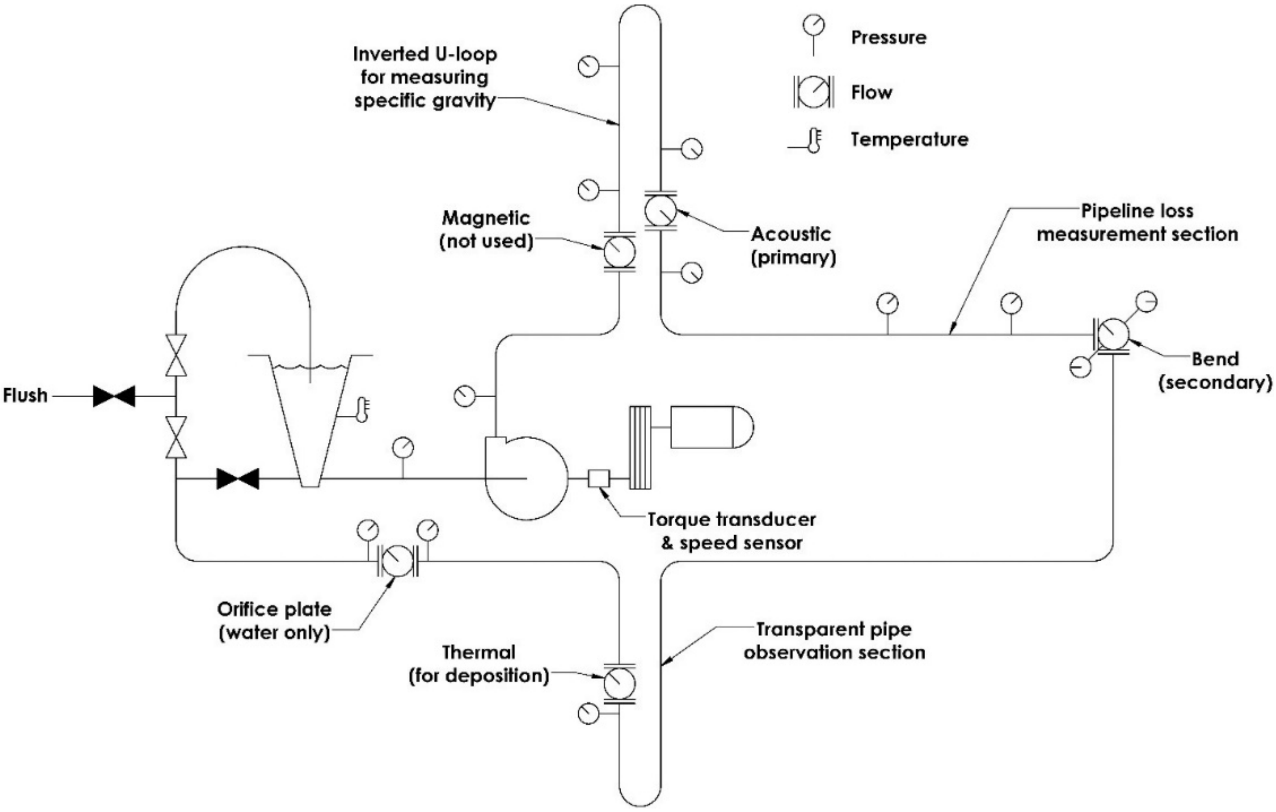

FIG 2 – Schematic representation of the 103 mm pipe loop.

Testing began with the original 'raw' (as delivered) iron ore product at a variety of volumetric concentrations from 9.4 per cent to 43.5 per cent. This product has a relatively broad particle size distribution, with an average *d50* particle size between 1 and 2 mm, a top size of approximately 8 mm and containing 10 per cent to 20 per cent fines smaller than 40 µm. The average fractions as measured for the raw slurry during testing were Xf = 0.17, Xp = 0.18, Xh = 0.17 and Xs = 0.48. A fresh batch of solids was loaded for each test. During flushing after each test, the solids were screened into three fractions of particles corresponding to the Xs, Xh and combined $Xp+Xf$ fraction sizes for this pipe size, ie >1.5 mm, 1.5 mm to 200 µm, and <200 µm. These fractions were then tested individually, and additional slurry compositions were 'constructed' by combining them, and in some cases, by flushing away the <40 µm particles. Volumetric concentrations of the mixtures were selected to maximise the correlation with previous tests and to allow comparisons between fractions in the present tests.

The resulting target matrix of 19 tests is shown in Table 1. Each consecutive integer indicates a fresh loading of solids. Letter versions within an integer series indicate tests where additional material was added to solids already in the pipeline, or fine solids were flushed away.

TABLE 1

Test matrix showing target percentages for volumetric concentration.

Test	1	2	3	4	5	6	7	8	9	10	11a	11b	12	13a	13b	13c	14a	14b	14c
Xf	1.5	2.3	3.0	3.8	5.3	6.8								10			10		
Xp	2.0	3.0	4.0	5.0	7.0	9.0								10	10	10	15	15	15
Xh	1.5	2.3	3.0	3.8	5.3	6.8					10	10	10						
Xs	5.0	7.5	10.0	12.5	17.5	22.5	10	15	20	25		10	10			10			10
Total	**10**	**15**	**20**	**25**	**35**	**45**	**10**	**15**	**20**	**25**	**10**	**20**	**20**	**20**	**10**	**20**	**25**	**15**	**25**

The actual concentrations and fraction contents achieved during testing varied from the target values, in some cases significantly, due to uncertainties in the loading procedure and the fact that adjustments were not made during running, in order to minimise run time and solids degradation. The actual measured concentrations and particle fraction contents based on samples taken during testing were therefore used in the model calculations and analysis. These are shown in Table 2. Note that all solids concentration values cited in this paper, both measured and modelled, represent delivered (not *in situ*) volumetric concentration.

TABLE 2

Actual measured fraction contents and overall volumetric concentrations for each test.

Test	1	2	3	4	5	6	7	8	9	10	11a	11b	12	13a	13b	13c	14a	14b	14c
Xf	.08	.08	.10	.08	.09	.07	.06	.04	.06	.07	.01	.03	.07	.19	.04	.04	.20	.14	.10
Xp	.25	.27	.30	.25	.27	.23	.12	.08	.10	.13	.08	.11	.19	.72	.81	.37	.73	.74	.41
Xh	.18	.16	.17	.18	.16	.14	.15	.16	.16	.14	.85	.37	.41	.07	.14	.12	.07	.10	.10
Xs	.49	.49	.43	.49	.49	.56	.66	.73	.69	.66	.06	.49	.33	.01	.01	.47	.00	.02	.39
%Cv	**9.4**	**14.6**	**20.3**	**25.3**	**33.7**	**43.5**	**10.4**	**15.7**	**21.1**	**26.4**	**11.6**	**22.4**	**23.3**	**21.1**	**10.7**	**21.5**	**26.6**	**16.3**	**27.5**

Once loaded, the pipeline velocity was increased to approximately 6 m/s, which represents a typical maximum operating velocity for industrial slurry systems of this size. All tests were run from the maximum velocity downward until the delivered concentration began to drop and the pressure gradient began to increase, indicating the onset of heavy stratification and eventually, stationary deposition. At this point, the pipe loop system operation often became unstable, which can be seen in some of the data. This instability was most pronounced with tests containing high fractions of *Xs* solids, and these tests often had to be terminated at this stage to avoid system collapse and plugging of the pipe loop (which in any case occurred several times, despite the best efforts of the test engineers to prevent it.)

Prior to tests 11b, 13c and 14c, the solids loaded in the previous tests were bedded out in the pipe loop by reducing the velocity, then an additional portion of *Xs* solids were added to form a new slurry composition.

Prior to tests 13b and 14b, the velocity was lowered to approximately 1 m/s, and the <40 μm solids were flushed out of the system by pulling slurry from the top of the pipe while re-introducing clear water into the sump, creating slurries with a high proportion of *Xp* solids.

The data collected at each velocity included slurry flow rate by acoustic (sonar) flow metre, delivered slurry density by inverted U-loop as described in Wilson *et al* (2006), loss section pressure drop by two independent pressure transducers, and slurry temperature. In addition, pump performance data were collected, including pump suction, discharge and differential pressures, pump rotational speed and shaft power by strain gauge torque bar transducer.

The data were sampled at 100 Hz and averaged over an interval of 10 to 20 seconds, depending on the stability of the system. Whenever possible, data were taken during steady state operation, the exception being at velocities near deposition where the system was inherently unstable. Unstable points near deposition were taken for reference only and were not used in the evaluation of the model.

As is standard for slurry tests in the GIW Hydraulic Lab, a clear section of piping was installed downstream of the measurement section, however, this was of no use for observations, since the finer magnetite solids prevented any visual observations into the pipe, except at the lowest velocities, well below the onset of stationary deposition. For some of the tests, the onset of stationary deposition could be determined by monitoring a set of heated probes placed at the top and bottom of the pipe, as the onset of deposition would interfere with heat transfer from the bottom probe and result in a sudden observable change in the magnitude of the temperature differential between probes. These observations generally confirmed the onset of stationary deposition for these slurries as occurring at a velocity slightly below the onset of increased pipeline pressure gradient and reduced delivered concentration, as the pipeline velocity was reduced during testing.

As with previous tests, slurry samples for measurement of the particle size distributions (PSDs) were taken using a device specifically designed for these experiments. During sampling, a pneumatic linkage was used to lift the sump inflow pipe above the water line by about 0.3 m. A trapezoidal slurry sampler with an opening of 20 × 310 mm was then passed through the flow stream at approximately 0.5 m/s, cutting through the entire cross-section of the 103 mm inflow and collecting a sample of approximately 2 litres in volume. A picture of the device can be seen in Figure 3, just before and during sampling. The slurry sample was taken at a pipeline velocity of approximately 4.5 m/s during each of the 19 tests. This velocity was selected on the criteria of being high enough to ensure good mixing of the various particle sizes, but also representative of the interesting range of velocities for industrial applications. The particle size distributions for each sample were determined by first drying the sample to determine the total weight of solids, then wet sieving down to 40 µm.

A number of clear water tests were also performed throughout the test program to determine the pipe wall roughness, an important parameter for the carrier fluid pressure gradient calculation. Due to the polishing effect of the solids, this was found to be $10^{-5\,\mathrm{m}}$. Water tests were also performed to establish the baseline pump performance for later determination of the pump solids effect derates.

Flow control during the tests was accomplished by varying pump speed. Speeds ranged from 1200 to 2200 rev/min at the higher pipeline velocities, depending on slurry composition, and decreased to the range of 400 to 1200 rev/min at the lower velocities. The flow rates for the collected data ranged between 30 per cent and 70 per cent of the pump best efficiency flow rate (BEPQ).

FIG 3 – Slurry sampling device. Left: before actuation. Right: during sample cutting.

ANALYSIS OF THE DATA

To provide a qualitative overview of the scope of the data set, Figures 4 and 5 show the measured pipeline pressure gradient and pump head derate data for all 19 tests. Each test is labelled with the dominant particle fractions present and the average total solids concentration during testing at velocities above deposition. The 'raw' solids tests refer to the product as delivered. The corresponding measured particle size distributions (PSDs) obtained during sampling for each test are shown in Figure 6.

The pump head derate factor r_h is defined as follows:

$$r_h = (H_w - H_m)/H_w$$

where H_m is the pump head on the slurry mixture and H_w is the pump head on water at equivalent conditions.

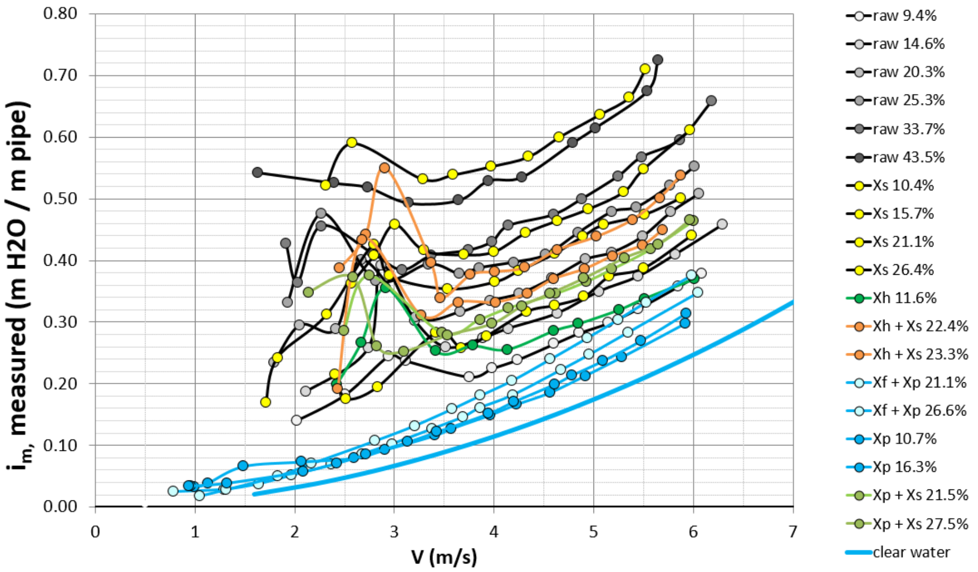

FIG 4 – Measured pipeline pressure gradient for all tests.

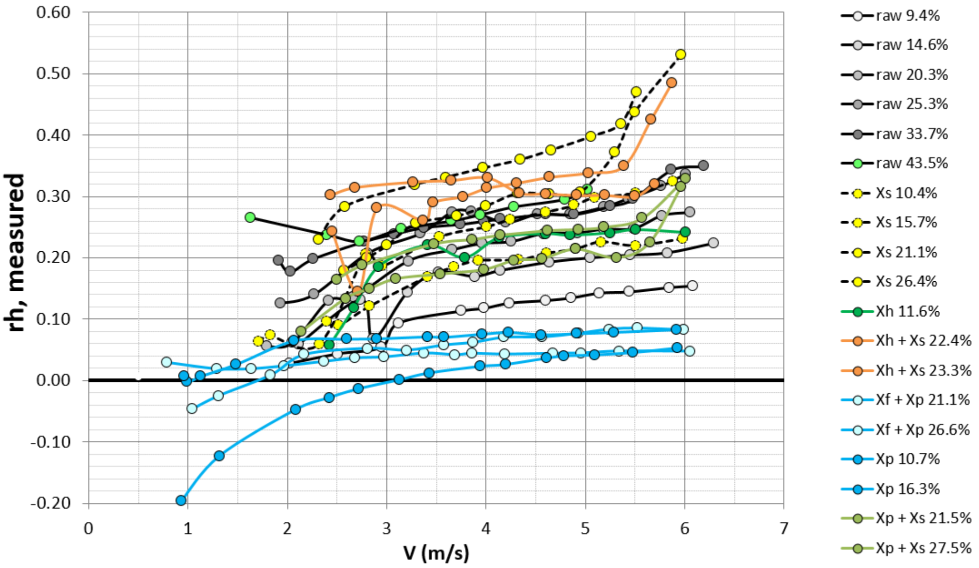

FIG 5 – Measured pump head derate due to solids effect for all tests.

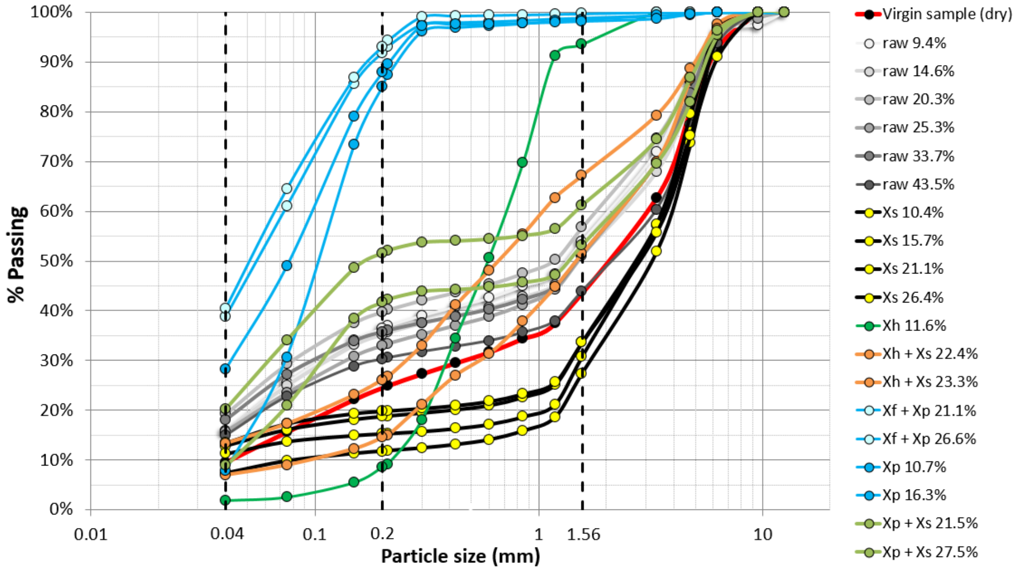

FIG 6 – Measured particle size distributions from the test samples for all tests.

Results of special interest

Due to the scope of the tests, it is not possible to present all of the data within the confines of one paper, nor to examine all of the individual results observed, however, some results of special interest will be considered.

By design, a number of different slurry compositions with different particle size distributions were run at similar values of volumetric concentration ($\%C_v$). For example, Figure 7 shows five tests with different particle size distributions all run near the volumetric concentration of C_v = 20 per cent. As expected, the highest pressure gradient occurs with the coarsest slurry, which is composed of a 0.69 fraction of *Xs* solids. By comparison, the raw slurry, which contains a smaller 0.43 fraction of *Xs* solids, and three times as much of the pseudo-homogeneous *Xp* solids, shows an excess pressure gradient (ie the difference between the water and slurry gradients) that is reduced by approximately 30 per cent.

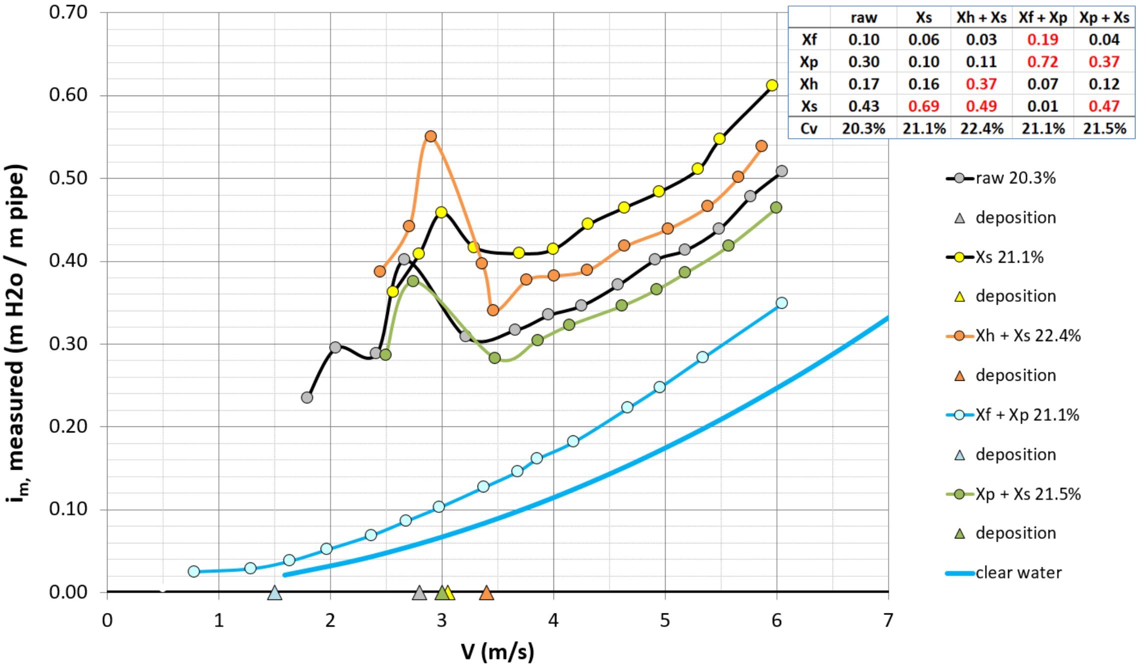

	raw	Xs	Xh + Xs	Xf + Xp	Xp + Xs
Xf	0.10	0.06	0.03	0.19	0.04
Xp	0.30	0.10	0.11	0.72	0.37
Xh	0.17	0.16	0.37	0.07	0.12
Xs	0.43	0.69	0.49	0.01	0.47
Cv	20.3%	21.1%	22.4%	21.1%	21.5%

FIG 7 – Pipeline pressure gradient for tests near C_v = 20 per cent.

Relative to the raw slurry curve, a slurry composed of primarily heterogeneous *Xh* and fully stratified *Xs* solids (*Xh*+*Xs*) shows a 10 per cent to 15 per cent increase in the excess pressure gradient.

Compared to this *Xh*+*Xs* slurry, the *Xp*+*Xs* slurry represents a composition where the relative content of *Xh* and *Xp* fractions are exchanged, and the excess gradient is reduced by about 10 per cent relative to the raw slurry curve. Finally, the *Xf*+*Xp* slurry, which is composed almost entirely of fine particles below 200 µm shows the expected 'equivalent fluid' type behaviour (ie acting like a fluid with density of the slurry and viscosity of the carrier fluid), although as will be shown later in the error analysis, the excess pressure gradient is considerably lower than would be predicted by the current version of the model.

The velocity at the limit of stationary deposition is also shown for each slurry. The *Xh*+*Xs* combination shows the highest deposition velocity and the raw slurry the lowest (aside from the *Xf*+*Xp* fines). The observed deposition velocity increases with increased *Xh* fraction, which represents the worst case particle size for deposition (near 500 µm), but it also decreases with increased *Xf* or *Xp* fines.

In Figure 8, slurries having different particle size compositions and different volumetric concentrations are grouped according to similar pressure gradient. In the first pair with the highest gradient, a slurry of raw solids at C_v = 43.5 per cent shows a similar gradient to a slurry containing a high fraction (0.66) of the fully stratified *Xs* solids, but with a significantly lower overall concentration of 26.4 per cent. Note that due to its higher overall concentration, the volumetric concentration of *Xs* solids in the raw slurry (C_v of *Xs* =24.4 per cent) is actually higher than its paired *Xs* based slurry (C_v of *Xs* =17.5 per cent). A similar result is seen for the second pair of curves, again composed of a higher concentration raw slurry paired with a lower concentration slurry having a higher proportion of fully stratified *Xs* solids. In this case, the ratio of overall volumetric concentration is approximately 3:2.

For both pairs, it may be noticed that the raw slurry has a significantly higher concentration of the pseudo-homogeneous *Xp* solids (3 to 4×), while the relative proportions of *Xf* fines and *Xh* heterogeneous solids are similar. It may be assumed that the increased volume of *Xp* solids provide a particularly effective support to the fully stratified *Xs* solids, reducing their sliding friction and allowing the higher concentration slurry to be transported with the same pressure gradient as the coarser, lower concentration slurry. Similar results were observed during the previous testing with S_S = 2.65 solids (eg Matousek *et al*, 2019).

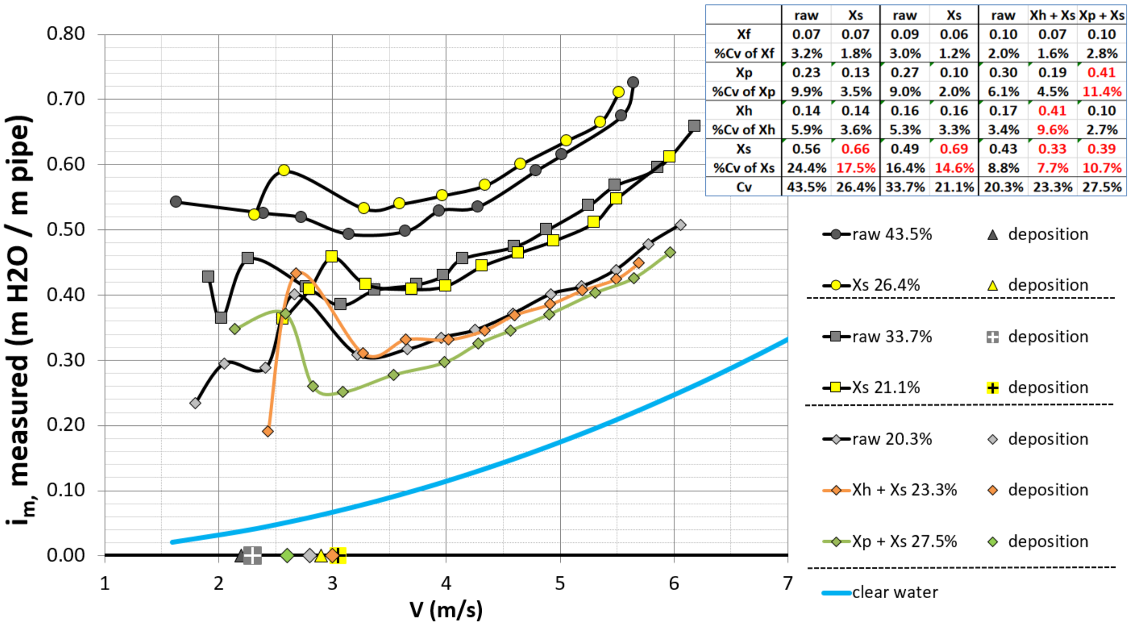

	raw	Xs	raw	Xs	raw	Xh + Xs	Xp + Xs
Xf	0.07	0.07	0.09	0.06	0.10	0.07	0.10
%Cv of Xf	3.2%	1.8%	3.0%	1.2%	2.0%	1.6%	2.8%
Xp	0.23	0.13	0.27	0.10	0.30	0.19	0.41
%Cv of Xp	9.9%	3.5%	9.0%	2.0%	6.1%	4.5%	11.4%
Xh	0.14	0.14	0.16	0.16	0.17	0.41	0.10
%Cv of Xh	5.9%	3.6%	5.3%	3.3%	3.4%	9.6%	2.7%
Xs	0.56	0.66	0.49	0.69	0.43	0.33	0.39
%Cv of Xs	24.4%	17.5%	16.4%	14.6%	8.8%	7.7%	10.7%
Cv	43.5%	26.4%	33.7%	21.1%	20.3%	23.3%	27.5%

FIG 8 – Comparison of various slurries with similar pressure gradients.

The third and lowest grouping shows three different compositions: raw, *Xh*+*Xs*, and *Xp*+*Xs*, with overall volumetric concentrations of 20.3 per cent, 23.3 per cent and 27.3 per cent respectively. The increase in concentration corresponds roughly to the amount of *Xp* and *Xh* solids available to support the fully stratified *Xs* solids, with the lowest percentage seen for the raw slurry (6.1 per cent + 3.4 per cent). The other two slurries have a similar combined volumetric concentration of the *Xp* plus

Xh fractions (about 14 per cent), but the highest overall concentration is achieved by the *Xp+Xs* slurry, where the relative proportion of the most supportive *Xp* fraction is highest.

The observed deposition velocities for these slurries were according to expectations, with the lowest values observed for the high concentration raw slurries, (both near 2.25 m/s), and the highest values for the slurries containing primarily *Xh* and *Xs* solids.

All of the above observations are in accord with the principles and formulation of the 4-component model, so it is expected that the formulation can be successfully adapted to the current data set. This will be examined in the following section.

4-component model error analysis and proposed modifications

Due to the nature of closed loop testing, delivered slurry concentration will change slightly with velocity, and slurry temperature will change with time. Therefore, in comparing the measured data to the predictions of the 4-component model, calculations were made using the individual measured values of flow velocity, slurry concentration, and temperature at each data point.

Pipeline pressure gradient

Figure 9 displays the relative error between the measured data and the 4-component model calculation for all data points above stationary deposition for all 19 tests according to the formulation described in Visintainer (2019). The % error is defined as follows:

$$\% \text{ error} = (i_{m,\ \text{CALCULATED}} - i_{m,\ \text{MEASURED}}) / i_{m,\text{MEASURED}}$$

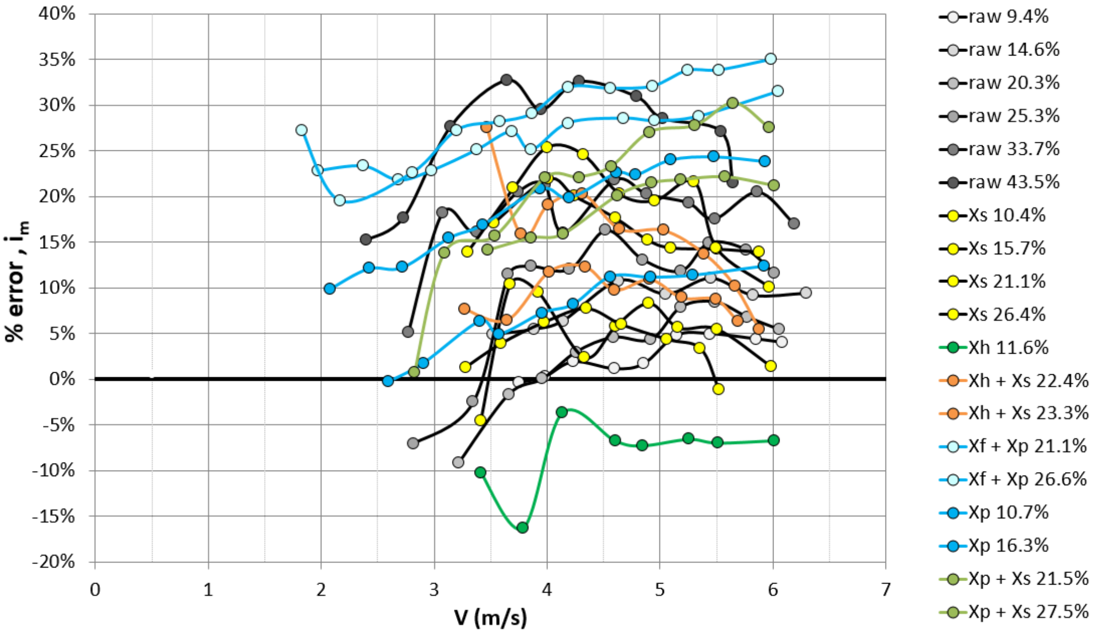

FIG 9 – Pipeline pressure gradient error plot for all tests using previously published model parameters.

As can be seen in the figure, the span of error is relatively large and in most cases the 4-component model over-predicts losses for these slurries, with the largest errors occurring for the highest concentration tests of the raw and *Xs* solids. Surprisingly, there is also a large deviation for the tests containing only the finer *Xf* and *Xp* solids, although the absolute value of the error (in terms of m/m of pressure gradient) is less, since the losses for these slurries are much lower, (see Figure 4). Still, this indicates that the equivalent fluid model is over-predicting losses in this case and that a more aggressive empirical parameter for the *Xp* fraction may be required. Finally, the pressure gradient is somewhat under-predicted for the slurry with a high proportion of *Xh* solids.

In the previous tests on solids with $S_S = 2.65$, the effect of the empirical parameter for the pseudo-homogeneous component *Xp* was found to be virtually negligible. Very little difference was observed for $A''_p = 0.25$ compared with $A''_p = 0$ (giving $A'' = 1.0$), indicating that the *Xp* slurry behaved as pure equivalent fluid. The present tests with high density solids suggest, however, that if suspended by carrier-flow turbulence, then high density *Xp* particles tend to contribute less to fluid-like friction than their S_S = 2.65 counterparts. This reduction of the friction contribution is expressed using *A″* and a much better fit is obtained if this parameter takes on a form similar to the heterogeneous parameter *C″*, namely,

$$A'' = 1 - (X_f + 0.5X_p)$$

which is then used, as before, to calculate the pseudo-homogeneous contribution to the excess pressure gradient *Δip*,

$$\Delta ip = A'' \, X_p \, C_v \, (S_s - S_f) \, i_f$$

where S_f = the specific gravity and i_f the pressure gradient of the carrier fluid. As seen in Figure 10, use of this modified *A″* parameter results in a significant reduction in error, especially for the *Xf* and *Xp* component mixtures. It has, however, little effect on the performance of the model relative to previous tests with lower density solids, and is therefore proposed as a permanent upgrade to the model.

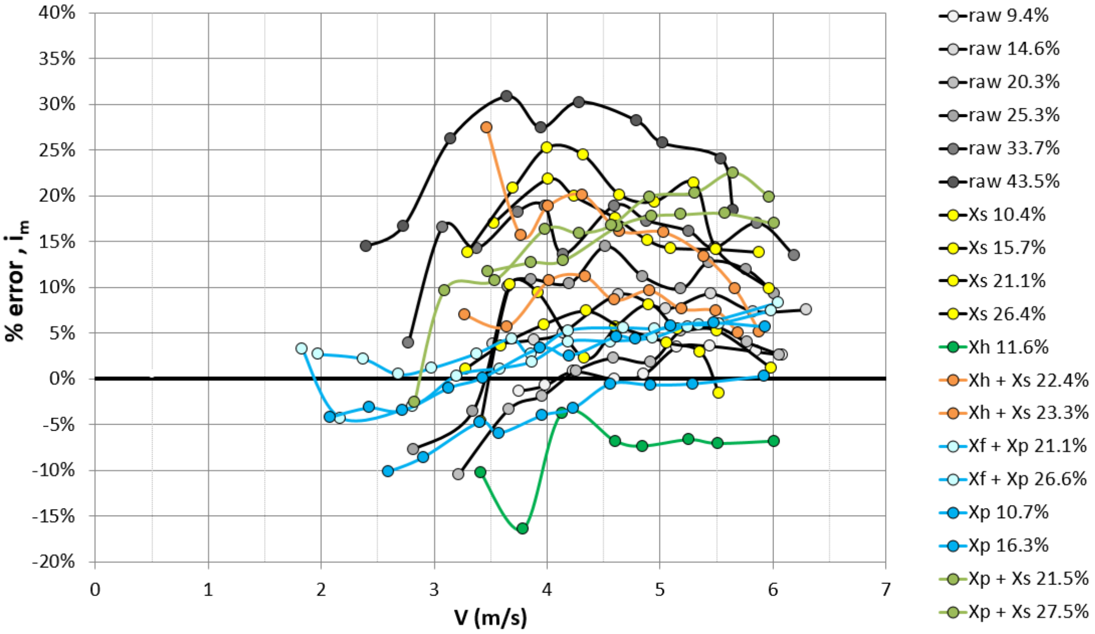

FIG 10 – Pressure gradient error plot for all tests using adjusted *A″* formula.

Some additional model parameter modifications are proposed to account for the observed behaviour of the high density solids. In particular:

1. A lowering of the *Xf* (carrier fluid) particle size boundary to account for the greater ease with which higher density solids will settle and cease to contribute to the carrier fluid properties. For the present tests, a value near 20 µm gives the best fit, and so a variable carrier fluid boundary particle size is proposed that is a function of solids specific gravity (S_S), as follows:

$$Xf \text{ boundary size } (\mu m) = 40 \cdot 2.65/S_s$$

2. An adjustment of the exponent on the solids density term of the 'V_{50}' equation (used in calculation of the heterogeneous *Xh* component of the losses). As mentioned previously, the solids density affects the threshold velocities, such as the velocity at the limit of stationary deposition and the velocity at full suspension. Naturally, it affects also the threshold velocity V_{50} at which one half of solids are transported as contact load and the other half as suspended load. The current tests, particularly those with a dominating proportion of the *Xh* component, indicate that the model under-predicts the pressure gradients for *Xh*-dominated slurries of heavy solids (see *Xh* 11.6 per cent in Figure 9). An improvement of the prediction can be reached by increasing the predicted value of V_{50}. The equation for V_{50} already included a solids-density term but it has not been sufficiently calibrated by experiments with solids of a

density significantly different from 2.65. The current tests reveal that the effect of a higher relative solids density S_S (above 2.65) on V_{50} is considerably stronger than suggested in the original equation. An exponent 1.0 instead of 0.45 in the solids-density term allows for a significantly better prediction of the *Xh*-contribution to the total pressure gradient. Hence,

$$V_{50} = 44.1 \cdot d_h^{0.35} \cdot \left(\frac{S_s - S_{fp}}{1.65} \right)^{1.0} \cdot \nu_r^{-0.25}$$

Finally, for the present magnetite solids, the data indicate that a reduction in the sliding friction factor, (used to calculate the contribution of the pressure gradient from the fully stratified *Xs* component), is required. This is not surprising, considering the more friable nature of these solids, which are more easily degraded and rounded off during transport. A value of 0.4 gives the best fit to the data once the above modifications are applied. The final error result is seen in Figure 11 and compares favourably with previous results for the 4-component model, having an average error of 5 per cent and with the bulk of the predictions between +/-10 per cent.

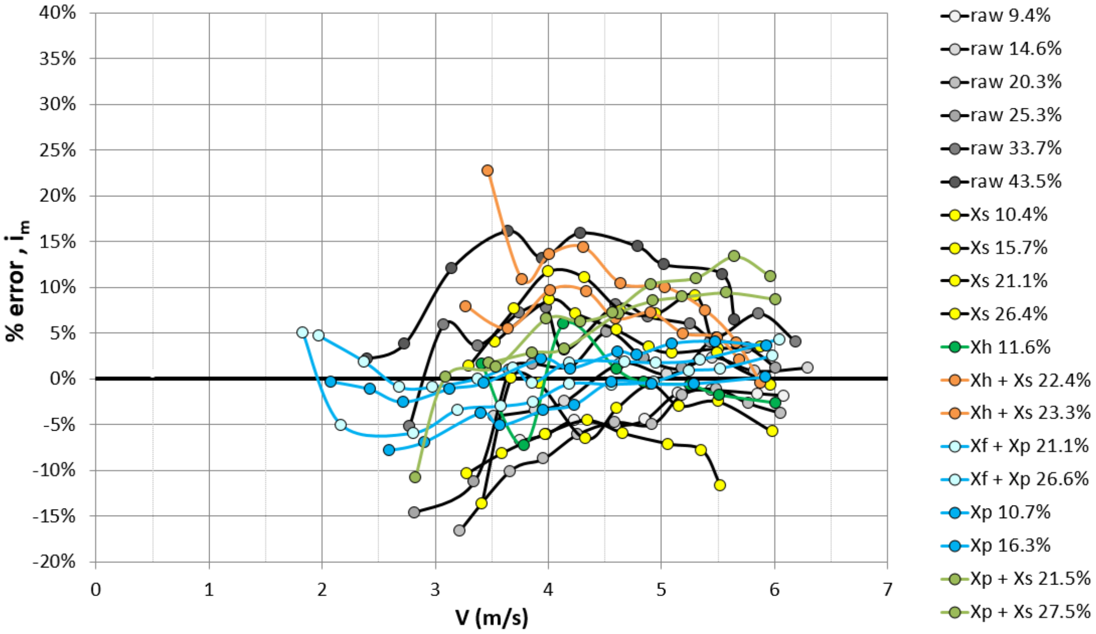

FIG 11 – Final pressure gradient error plot with all proposed model modifications applied.

Centrifugal pump solids effect

For pump solids effect, the resulting error between measured and calculated values is expressed as a percentage, but this percentage represents the absolute difference in the Head Reduction Factor, rather than a relative error, as follows:

$$\text{error} = r_{h,\text{CALCULATED}} - r_{h,\text{MEASURED}} \text{ (expressed as \%)}$$

Therefore, a +1 per cent error indicates a calculated Head Reduction Factor that is one percentage point (ie 0.01) greater than the measured value. This provides a better context for the analysis, since the Head Reduction Factor is already expressed as a percentage and the absolute error is a better measure of model success in actual application. Using a ratio error calculation would magnify the perceived error where solids effects are small and skew a proper understanding of the results.

Figure 12 shows the error analysis for the present tests using the GIW 4 × 6 LCC-16 slurry pump. As with the first analysis of the pipeline pressure gradient, the model is over-estimating the pump solids effect for these high-density solids. Once again, the highest concentration raw slurry test shows the largest overestimate, while with the heterogeneous *Xh* slurry, losses are underestimated. There is also a clear slant to the error plots, indicating an effect of pipeline velocity on the pump solids effect, with increasing losses for increasing velocity.

This general over-estimation of losses and effect of velocity indicate that some degree of friction reducing support is being provided to the coarse solids by the finer solids, reducing losses when they are present and doing so in a way that varies with velocity. A similar effect for pipeline pressure gradient is already included in the 4-componet pipeline model by the addition of the velocity dependent empirical parameters *A″*, *B″* and *C″*. When first developing the pump solids effect version of the 4-component model, the division of losses according to the various components was adopted, but the velocity dependent, empirical parameters did not seem necessary to achieve a good result. However, the similarities of pump solids effect mechanisms to the influence of leading parameters on slurry friction losses in pipelines has been pointed out by Wilson *et al* (2006), Shook, Gillies and McGibben (1995) and others. Presumably there is one set of physical mechanisms involved, and it is desirable to link the solids effect in the pump to that in pipelines. It is therefore proposed to multiply these empirical parameters into the formulae used to calculate the pump head derate (*rh*) contributions for the *Xp*, *Xh* and *Xs* components. In applying this new formulation, the particle size exponent (*S2*) no longer requires a form that is itself particle size dependent, but simplifies to a constant value of 0.4. Otherwise, the formulation is identical to that in previous publications.

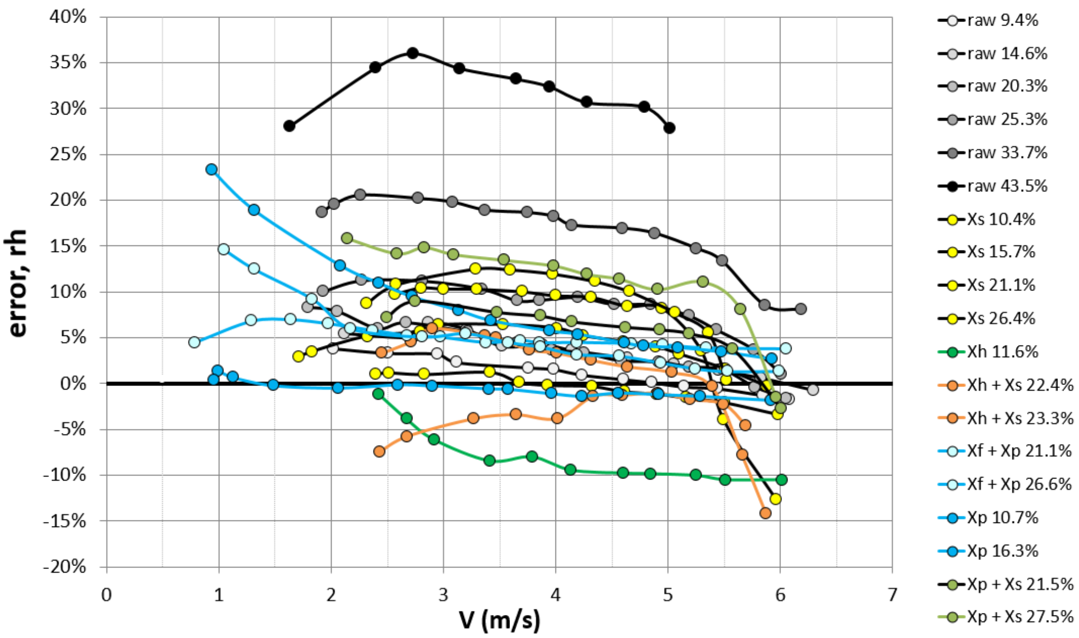

FIG 12 – Pump solids effect on head, error plot for all tests using previously published model parameters.

Applying this new formulation to the present test data gives the error result seen in Figure 13, which is an improvement over the first result seen in Figure 12 in both the magnitude of error and slope of the error curves. The correlation is still not as accurate as with the previous tests for slurries composed of solids with S_S = 2.65, however, the bulk of the error remains within +/-5 per cent, which is not unreasonable considering the difficulties of data collection during these high-density tests and the fact that the absolute value of pump head losses during these tests were rather high (see Figure 5) compared to previous tests on lower density solids.

The highest density (C_v = 43.5 per cent) raw slurry test remains an outlier, but this may represent a case where the concentration has become too high to be accurately described by a settling slurry model. Losses remain under-predicted for the slurries with a high proportion of heterogeneous Xh solids, which is a topic worthy of further study.

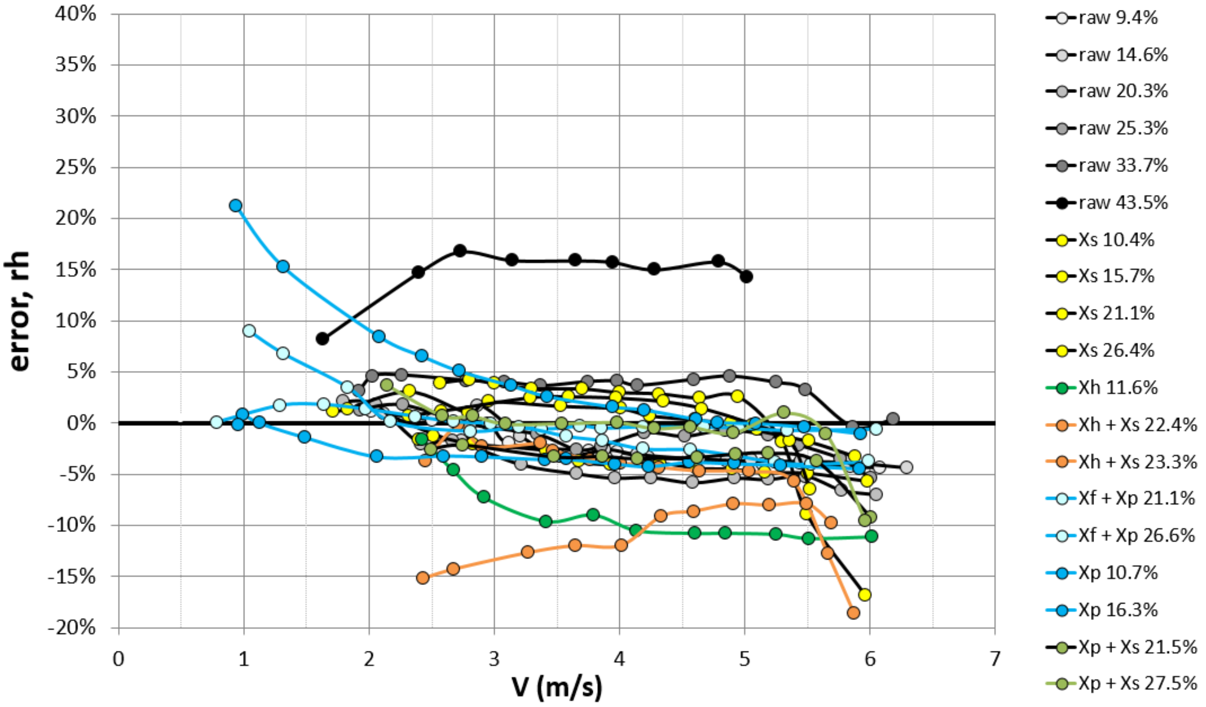

FIG 13 – Pump solids effect on head, error plot after the addition of the empirical parameters *A″*, *B″* and *C″* from the pipeline pressure gradient model.

CONCLUSIONS

- A series of slurry tests was conducted in a 103 mm pipeline using high density iron ore (magnetite) solids with S_S = 4.75 for the purpose of validating the applicability of previously described 4-component settling slurry models for pipeline pressure gradient and pump solids effect derates when handling slurries containing high density solids.
- Solids were screened and flushed to create a range of slurries with particle size distributions divided according to the particle size boundaries of the 4-component model, ie the carrier fluid (<40 µm), pseudo-homogeneous (40–200 µm), heterogeneous (200 µm – 1.56 mm) and fully stratified (>1.56 mm) fractions.
- The pipeline pressure gradient and pump performance data collected demonstrated their dependence on the composition of the slurries and presence (or absence) of the various fractions.
- Based on this data set, modifications to the 4-component models were proposed for improved handling of higher density solids:
  - Modification of the empirical parameter *A″* applied to the pseudo-homogeneous *Xp* component in the pipeline pressure gradient model.
  - Introduction of a variable value for the carrier fluid particle size boundary, based on the solids specific gravity S_S, which reduces the boundary to a smaller particle size when the solids specific gravity is increased.
  - Modification of the exponent for the solids density dependent term of the 'V_{50}' model equation used for the heterogeneous *Xh* component of pipeline pressure gradient.
  - Introduction of the empirical *A″, B″* and *C″* parameters into the pump solids effect model.
- Application of the proposed modifications improved the accuracy of the models when applied to the current, high solids density data set, without reducing their accuracy when re-applied to the previous data sets using lower density S_S = 2.65 solids.
- The data also indicated that a lower sliding friction factor of 0.4 is needed when calculating the heterogeneous and fully stratified pressure gradient components for this magnetite-based slurry. This was attributed to the more friable nature and resulting rounded shape of the solids.

- Note that this may not apply to other high density iron ore solids (for example hematite). For comparison, a sliding friction factor of 0.5 was determined for the S_S = 2.65 silica-based solids (sand and gravel) used in previous testing, and a value of 0.44 has sometimes been used as a default when applying the 'V_{50}' and fully stratified models referenced in this work.

ACKNOWLEDGEMENTS

The authors would like to thank LKAB Minerals (a subsidiary of LKAB Mining) of Sweden for their cooperation in the present tests and permission to publish the data pertaining to the raw slurry compositions. We would also like to acknowledge the contributions of Sr. Test Engineer Travis Basinger, the GIW Hydraulic Lab engineers and staff, and GIW Industries Inc., whose creativity, determination and support made these tests possible.

REFERENCES

ANSI/HI 12.1–12.6, 2016. American National Standard for Rotodynamic Centrifugal Slurry Pumps, pp 50–53, Hydraulic Institute, Parsippany, NJ, USA.

ANSI/HI 9.6.7, 2015. Rotodynamic Pumps – Guideline for Effects of Liquid Viscosity on Performance, Hydraulic Institute, Parsippany, NJ, USA.

Engin, T and Gur, M, 2003. Comparative evaluation of some existing correlations to predict head degradation of centrifugal slurry pumps, *ASME Journal of Fluids Engineering*.

Matousek, V, Visintainer, R, Furlan, J and Sellgren, A, 2018. Threshold criteria for components of predictive model for pipe flow of broadly graded slurry, *ASME Fluids Engineering Division Summer Meeting*, Montreal.

Matousek, V, Visintainer, R, Furlan, J and Sellgren, A, 2019. Frictional head loss of various bimodal settling slurry flows in pipe, *ASME-JSME-KSME Joint Fluids Engineering Conference AJKFLUIDS2019*, San Francisco, USA.

Sellgren, A, Visintainer, R, Furlan, J and Matousek, V, 2014. Pump and pipeline performance when pumping slurries with different particle gradings, *19th International Conference on Hydrotransport*, Colorado, USA.

Shook, C A, Gillies, R G and McGibben, M,1995. Derating of centrifugal pump by large solid particles, pp 144–145, *Proc. Int. Freight Pipeline Soc. Symp,* Pittsburg, PA.

Shook, C A, Gillies, R G and Sanders, R S, 2002. Pipeline Hydrotransport with Applications in the Oil Sand Industry, SRC Publication No. 11508–1E02, SK, Canada.

Visintainer, R, 2019. A New 4-Component Model for Slurry Pump Solids Effect and Pipeline Friction, *Calgary Pump Symposium,* Calgary, Alberta. https://www.calgarypumpsymposium.ca/archive.

Visintainer, R, Furlan, J, McCall, G, Sellgren, A and Matousek, V, 2017a. Comprehensive loop testing of a broadly graded (4-component) slurry, *20th International Conference on Hydrotransport*, Melbourne, Australia, April.

Visintainer, R, Sellgren, A, Furlan, J and McCall, G, 2017b. Centrifugal Pump Performance Deratings for a Broadly Graded (4-Component) Slurry, *18th International Conference on Transportation and Sedimentation of Solid Particles*, Prague.

Wilson, K C and Addie, G R, 1995. Coarse particle transport. Effect of particle degradation on friction, *8th International Freight Pipeline Society Symposium*, Pittsburgh.

Wilson, K C, Addie, G R, Sellgren, A and Clift, R, 2006. *Slurry Transport Using Centrifugal Pumps*, 3rd edition, Springer, New York.

Wolfe, D, 2014. The effect of large particles on oils and hydrotransport slurry pump performance, *19th International Conference on Hydrotransport,* Colorado, USA.

Project development and optimisation

Reproduction of inequality constraint between iron and silica for accurate production scheduling

S Abulkhair[1], N Madani[2] and N Morales[3]

1. Research Assistant, School of Mining and Geosciences, Nazarbayev University, 010000 Nur-Sultan, Kazakhstan. Email: sultan.abulkhair@nu.edu.kz
2. Assitant Professor, School of Mining and Geosciences, Nazarbayev University, 010000 Nur-Sultan, Kazakhstan. Email: nasser.madani@nu.edu.kz
3. Director, Delphos Mine Planning Lab, AMTC and Department of Mining Engineering, University of Chile, 8370451 Santiago, Chile. Email: nelson.morales@amtc.cl

ABSTRACT

Conventional geostatistical algorithms cannot reproduce bivariate complexities such as inequality constraint, nonlinearity and heteroscedasticity. Poor reproduction of these features may decrease the accuracy and reliability of mine planning results. For example, it is not unusual to have an inequality constraint between primary and disturbing elements in a metalliferous deposit. Implementation of traditional methodologies for such complex data sets can lead to the incorrect reproduction of a bivariate relationship, which will affect the validity of NPV results. In this paper, an iron data set containing iron and silica grades with an inequality constraint between variables is introduced as a case study. This study proposes an algorithm based on a hierarchical sequential Gaussian cosimulation integrated with inverse transform sampling. The proposed methodology considers the linear inequation between two variables in the hierarchical cosimulation process to reproduce an inequality constraint. As a comparison, conventional sequential Gaussian cosimulation is also applied to the same data set to demonstrate the difference in bivariate relationships from both models. Unlike the proposed algorithm, the conventional cosimulation cannot reproduce an inequality constraint and slightly overestimates silica grades. The modelled realisations are then used to assess the uncertainty of a plan and generate a stochastic strategy that adapts the destination of the blocks depending on the scenario. Two-stage stochastic long-term production scheduling takes extraction decisions using average information (ie e-type model) and ore/waste destinations based on geostatistical realisations. As a result, the proposed strategy is closer to the upper bound, highest possible NPV for each realisation, than to the lower bound, deterministic strategy that does not manage the risk of sending extracted material to wrong destinations. Furthermore, Comparing production schedules resulting from proposed and conventional geostatistical methodologies shows the importance of inequality constraint reproduction and more accurate long-term mine planning.

INTRODUCTION

The objective of long-term production scheduling in open pit mines is to generate a life-of-mine schedule with defined extraction periods and destinations for each mining block, while maximising net present value (NPV) and respecting operational constraints. Mixed integer programming (MIP) (Gershon, 1983) is a popular production scheduling approach used in the industry. Nevertheless, despite its effectiveness in maximising NPV and producing optimal solutions, it uses a single block model as an input. As a result, such deterministic mine planning methodologies can not control the deviations from production targets, leading to a high risk of not meeting them. Alternatively, using geostatistical realisations produced by simulation/cosimulation methodologies as inputs in MIP leads to suboptimal results (Ramazan and Dimitrakopoulos, 2004). Therefore, stochastic production scheduling approaches are required to effectively minimise the risk of not meeting production targets, maximise NPV and satisfy operational constraints.

Stochastic production scheduling approaches, such as simulated annealing (Godoy and Dimitrakopoulos, 2004) and stochastic integer programming (SIP) (Ramazan and Dimitrakopoulos, 2018), aim to produce optimal solutions with maximised NPV and minimised risks by using multiple unbiased scenarios of the economic block model. Simulated annealing can help to generate a 26 per cent higher NPV than the deterministic method (Leite and Dimitrakopoulos, 2007), but SIP can also make optimal waste removal decisions (Dimitrakopoulos, 2011). However, the integration of uncertainty into stochastic mine planning approaches sometimes leads to a higher number of binary variables. One solution for this issue is replacing some variables with continuous ones and assigning binary variables only to waste blocks (Ramazan and Dimitrakopoulos, 2013). On the other hand, a two-stage stochastic production scheduling (Moreno *et al*, 2017) can be used as a more scalable alternative. In that approach, the first stage produces scheduling based on average information, similar to the deterministic method. The second stage corresponds to resource decisions taken using geostatistical realisations as different equally possible scenarios. According to Moreno *et al* (2017), extraction decisions should be taken in the first stage, while processing decisions – in the second.

Another problem with long-term production scheduling is the limited amount of information that mostly comes from exploration boreholes. Geostatistical resource modelling aims to generate spatially accurate models of mineral grades and geological domains using borehole data (Journel, 1999). In deposits containing multiple sampled elements, the spatial correlation between variables is a crucial source of information. Multivariate geostatistics considers the cross-covariances between variables to produce more valid models (Wackernagel, 2003). Nevertheless, traditional multivariate methods struggle to reproduce bivariate complexities, such as nonlinearity, heteroscedasticity and inequality constraints. It is particularly true for inequality constraints, which are common in mining deposits. Several methods based on the decorrelation of variables have been developed for the specific cases involving inequality constraints (Emery, Arroyo and Peláez, 2014; Arcari Bassani, Costa and Deutsch, 2018; Abildin, Madani and Topal, 2019). Recently, Madani and Abulkhair (2020) proposed a new methodology based on the acceptance-rejection technique integrated into hierarchical cosimulation. However, an acceptance-rejection technique iteratively re-simulates values that are outside an inequality constraint, making this algorithm much slower than traditional cosimulation. Therefore, Abulkhair and Madani (2021) replaced this method with an inverse transform sampling that makes only one iteration to re-simulate faulty values (ie values that are outside an inequality constraint).

This study demonstrates the performance of two-stage production scheduling and updated hierarchical cosimulation integrated with inverse transform sampling. Inverse transform sampling helps to re-simulate values, which do not respect an inequality constraint. Moreover, the proposed production scheduling approach evaluates fixed production periods using an average (ie e-type) resource model in the first stage, and then re-evaluates block destinations based on geostatistical realisations as the second stage decisions.

METHODOLOGY

Hierarchical cosimulation integrated with inverse transform sampling

The proposed cosimulation algorithm is an updated version of hierarchical sequential Gaussian cosimulation (Almeida and Journel, 1994). The basic idea of this algorithm is to simulate coregionalised variables hierarchically: the variable with the most autocorrelation is simulated first and then secondary variables are simulated conditional to the previous simulation results. This study is inspired by hierarchical cosimulation developed by Madani and Abulkhair (2020), in which an acceptance-rejection method integrated into the second simulation helps to model the secondary variable within an inequality constraint. However, an inverse transform sampling approach is used in this study as a faster alternative, while multiple and multicollocated neighbourhood strategies are implemented in the first and second simulations, respectively. For brevity, the readers are referred to both of these papers (Almeida and Journel, 1994; Madani and Abulkhair, 2020) to understand the basic methodology of hierarchical cosimulation, while the whole algorithm is proposed in Abulkhair and Madani (2021). The following steps demonstrate the procedure of an inverse transform sampling in detail:

1. Back transform simulated normal scores of the primary variable $Z_1^n(x_i)$ (ie variable modelled during the first simulation) to the original scale $Y_1^n(x_i)$ for each block i in n realisations.
2. Obtain the maximum max and minimum min truncated thresholds of the secondary variable $Y_2^n(x_i)$ based on the primary variable $Y_1^n(x_i)$. In the case of negative inequation, where $Y_2^n(x_i) \leq a \cdot Y_1^n(x_i) + b$, $[min, max]$ intervals are identified as follows:

$$min^n(x_i) = \min(Y_2) \quad max^n(x_i) = a \cdot Y_1^n(x_i) + b \tag{1}$$

Where:

$\min(Y_2)$	is a minimum value of the secondary variable
a	is a slope
b	is an intercept.

3. Transform $min^n(x_i)$ and $max^n(x_i)$ thresholds into normal scores.
4. Identify values of the secondary variable that are not located within $[min, max]$ interval and store them as $Z_2^m(x_i)$.
5. Generated random numbers within truncated thresholds $V^m(x_i)$ using an inverse transform sampling (Devroye, 1986):

$$V^m(x_i) = F^{-1}\big(F(min^m) + \big(F(max^m) - F(min^m)\big) \cdot U\big) \tag{2}$$

Where:

F^{-1}	is a quantile function
F	is a conditioned cumulative distribution function
U	is a random number generated uniformly between 0 and 1.

6. Re-simulate values $Z_2^m(x_i)$ identified in step 3 using random numbers $V^m(x_i)$ in the following way:

$$Z_2^m(x_i) = Z_{2_{MCCK}}(x_i) + \sqrt{\sigma^2_{2\,MCCK}(x_i)} \cdot V^m(x_i) \tag{3}$$

Where:

$Z_{2_{MCCK}}(x_i)$	is a simple multicollocated co-kriging estimator
$\sigma^2_{2\,MCCK}(x_i)$	is the corresponding estimation variance.

7. Loop to re-simulate all values identified in step 3.
8. Store re-simulated values in $Z_2^n(x_i)$.
9. Back transform simulated values of the primary and secondary variables into the original scale Y_1^n and Y_2^n.

Two-stage stochastic long-term production scheduling

This study implements two-stage stochastic production scheduling that employs average information from e-type models into the first stage, while the second stage decisions are based on geostatistical realisations. Production periods are computed in the first stage and are fixed for all realisations. Alternatively, second stage decisions focus on the re-evaluation of block destinations depending on mineral grades simulated by stochastic geostatistical methods. Integration of uncertainty into the second stage minimises the risk of sending the extracted material to the wrong destinations. The workflow of the proposed production scheduling methodology is the following:

1. Obtain economic block values $EBV(x_i)$ for e-type models and geostatistical realisations accounting on the impurity content of ore as follows:

$$\begin{aligned} EBV_\alpha = \max\,((P - C_S) \cdot R \cdot TON_\alpha * Y_{1_\alpha} - (C_M + C_P) \cdot TON_\alpha - (Y_{2_\alpha} \\ > Y_2^{TH}) \cdot C_I \cdot (Y_{2_\alpha} - Y_2^{TH}) \cdot TON_\alpha, -C_M \cdot TON_\alpha \end{aligned} \tag{4}$$

Where:

P	is a metal price
C_S	is a selling cost
R	is a recovery rate

C_M	is a mining cost
C_P	is a processing cost
TON_α	is a total tonnage for block α
C_I	is cost associated with an impurity content
Y_2^{TH}	is a threshold of the secondary variable, below which no impurity-related cost is applied.

2. Compute ultimate pit limit (UPL) and nested pits from e-type models using a pseudoflow algorithm (Hochbaum, 2008).
3. Define grade blending, mining, processing, reserve and operational constraints for the MIP.
4. Define pushbacks by grouping nested pits from a deterministic model and then selecting groups with similar tonnages.
5. First stage decisions: Compute production periods from e-type models using MIP with the following formulations:

$$\max \sum_{p \in P} \frac{EBV_{\alpha\tau}}{(1+d)^{\tau}} \cdot X_{\alpha\tau} \tag{5}$$

$$\sum_{\alpha \in A} X_{\alpha\tau} = 1 \qquad \forall\, \alpha \in \mathrm{A}, \tau \in \mathrm{T} \tag{6}$$

$$\sum_{\alpha \in A} \left(Y_{1_\alpha} - Y_1^{TH}\right) \cdot OTON_\alpha \cdot X_{\alpha\tau} \geq 0 \qquad \forall\, \alpha \in \mathrm{A}, \tau \in \mathrm{T} \tag{7}$$

$$\sum_{\alpha \in A} TON_\alpha \cdot X_{\alpha\tau} \leq CAP_M^{max} \qquad \forall\, \alpha \in \mathrm{A}, \tau \in \mathrm{T} \tag{8}$$

$$\sum_{\alpha \in A} OTON_\alpha \cdot X_{\alpha\tau} \leq CAP_P^{max} \qquad \forall\, \alpha \in \mathrm{A}, \tau \in \mathrm{T} \tag{9}$$

Where:

d	is a discount rate
$\alpha \in \mathrm{A}$	is a set of blocks
$\tau \in \mathrm{T}$	is set of production periods
$X_{\alpha\tau}$	is an integer variable that is equal to 1 if a block α is extracted in a period τ and 0 if not
Y_{1_α}	is the primary variable
Y_1^{TH}	is a minimum threshold of the primary variable
$OTON_\alpha$	is an ore tonnage

CAP_M^{max} and CAP_P^{max} are maximum thresholds of mining and capacities

Equation 6	is a reserve constraint
Equation 7	is a grade blending constraint

Equations 8–9 are mining and processing scheduling capacity constraints.

6. Re-evaluate tonnages TON_α^n and economic block values EBV_α^n based on n geostatistical realisations.
7. Second stage decisions: Re-evaluate the block destinations BD_α^n using grades from geostatistical realisations.

CASE STUDY

Proposed geostatistical and production scheduling methodologies are tested on a real data set from an iron deposit, which was multiplied by a scale factor to preserve confidentiality. The data set is homotopic and consists of 2137 sample points with coregionalised iron and silica variables. Figure 1a shows the location map of the data set used in this study. A critical feature of this deposit is a sharp inequality constraint between iron and silica (Figure 1b). Inequality constraint has a slope

a of -1.465 and an intercept b of 70.316, meaning that linear inequation for the proposed cosimulation algorithm is as follows:

$$Silica \leq 70.316 - 1.465 \cdot Iron \tag{10}$$

Furthermore, considering that the sampling pattern is slightly irregular (ie samples are mostly taken from the central part), cell-declustering is performed with 50 m × 50 m × 10 m cell dimension (Deutsch, 1989). Table 1 provides declustered statistical parameters of this deposit. Aside from an apparent inequality constraint, the correlation coefficient between variables is high. Therefore, conventional cosimulation is not likely to produce a significant overestimation of silica.

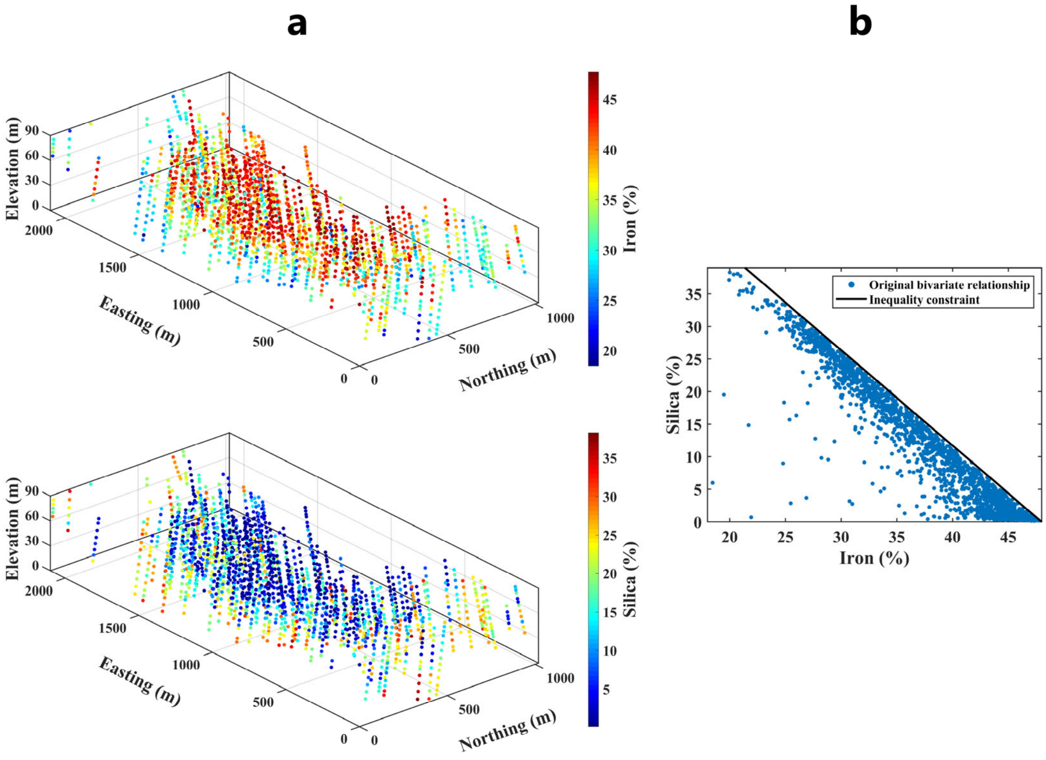

FIG 1 – (a) Location maps of iron and silica; and (b) a scatter plot between variables with a black line representing an inequality constraint.

TABLE 1

Basic declustered statistical parameters.

Statistical parameter	**Iron (%)**	**Silica (%)**
Mean	37.54	11.96
Variance	42.90	96.04
Correlation coefficient	-0.95	

Cosimulation of grade variables

In order to provide unbiased results for this case study, 100 realisations are produced using the proposed hierarchical cosimulation. The grid dimension of a single mining block is 20 m × 20 m × 10, which is used for both geostatistical modelling and production scheduling. Before proceeding to the cosimulation process, variables are transformed into normal scores. Then, direct and cross-variograms are calculated in the horizontal and vertical directions after examining an anisotropy. Finally, the following two-structured linear model of coregionalisation is obtained using a manual fitting:

$$\begin{pmatrix} \gamma_{Iron} & \gamma_{Iron/Silica} \\ \gamma_{Silica/Iron} & \gamma_{Silica} \end{pmatrix} = \begin{pmatrix} 0.25 & -0.17 \\ -0.17 & 0.18 \end{pmatrix} Exp(35m, 35m, 35m) + \begin{pmatrix} 0.65 & -0.66 \\ -0.66 & 0.73 \end{pmatrix} Exp(180m, 180m, 120m) \tag{11}$$

Figure 2 demonstrates e-type models, in which all blocks contain average grades of iron and silica over 100 realisations. Overall, results are compatible with location maps of original borehole data (see Figure 1a). The central part of the deposit contains high-grade iron and low-grade silica, meaning that a negative correlation between variables is reproduced. In fact, the simulated correlation coefficient between iron and silica is -0.93. Moreover, the average grades over 100 realisations are 36.50 per cent for iron and 11.06 per cent for silica, meaning that results are close to the original declustered parameters.

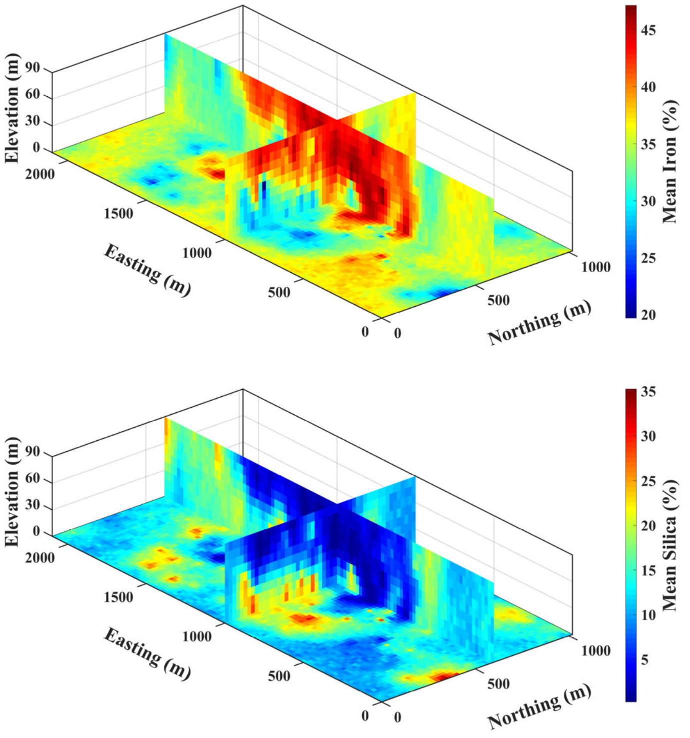

FIG 2 – E-type models over 100 realisations of iron (top) and silica (bottom).

It is of interest to compare the results with models obtained by the conventional methodology. The only difference between the two algorithms is the integration of an inverse transform sampling into the proposed method. Since an inverse transform sampling is implemented on the values computed during the second simulation, iron realisations are identical in both methods. However, the conventional method slightly overestimates silica that has an average grade of 13.40 per cent. Furthermore, the average correlation coefficient in realisations produced by the conventional method is -0.91. Although differences are not critical, it is better to analyse the bivariate relationships. Figure 3 shows how scatter plots between iron and silica are reproduced by two methodologies in realisation No. 1. Simulated bivariate relationships between variables and their marginal distributions are compared to the original parameters in Figure 3a. It should also be mentioned that scatter plots from block models are subsampled to show only 3000 random block values for a more valid comparison. Inverse transform sampling helps to reproduce an inequality constraint perfectly (see Figure 3c), while conventional methodology predictably fails to model this feature (see Figure 3b). Traditional Gaussian-based cosimulation methodologies model the bivariate relationships between coregionalised variables using only their cross-correlation structure. Inverse transform sampling in the proposed algorithm acts as an additional restriction that re-simulates all faulty values to reproduce an inequality constraint. Therefore, the conventional method can show much worse results in deposits with a lower cross-correlation and more skewed marginal distributions (Abulkhair and Madani, 2021).

Another important detail is that the histogram validation of silica realisations demonstrates that the re-simulation of silica values does not negatively affect its marginal distribution. This is because the proposed algorithm only re-simulates values that lie outside the threshold defined by inequation. On the contrary, silica's histogram from the proposed method has a closer resemblance to the original marginal distribution thanks to the re-simulation of overestimated values.

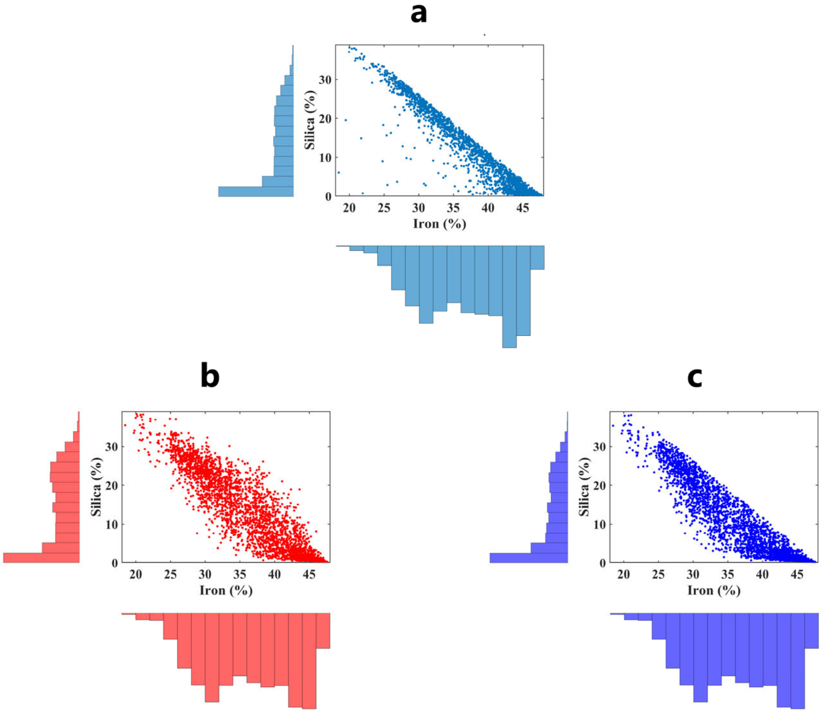

FIG 3 – The bivariate relationship between iron and silica with their corresponding marginal distributions obtained from the original data set (a) and 3000 randomly selected block values from realisation No. 1 simulated by conventional (b) and proposed (c) algorithms.

Production scheduling

This study analyses the performance of hierarchical cosimulation integrated with inverse transform sampling and two-stage stochastic production scheduling. In that regard, production scheduling results produced by the proposed stochastic strategy are compared to the upper and lower bounds. The upper bound is an optimistic and impossible strategy that shows the best NPV for each realisation. It is computed using MIP on each realisation individually. The lower bound is a deterministic strategy obtained from e-type models of iron and silica. It is an inefficient solution because it involves the risk of sending an extracted material to the wrong destinations. For example, if a block is considered as ore in an e-type model but turns out to be waste, both mining and processing costs are applied to this block. Table 2 lists parameters used for long-term production scheduling. This set of parameters is conceptual and not chosen for this particular deposit, and its objective is to provide the same environment for a fair comparison of the three strategies. Finally, three pushbacks are selected based on the deterministic case after grouping pits and ensuring that each group has a similar tonnage.

TABLE 2

Parameters for production scheduling.

Price ($/ton)	80.0	**Penalisation ($/ton)**	1.5	**Mining capacity (ton/day)**	153 000
Mining cost ($/ton)	3.0	**Iron threshold (%)**	30.0	**Processing capacity (ton/day)**	130 000
Processing cost ($/ton)	10.5	**Silica threshold (%)**	5.0	**Slope angle**	50°
Selling cost ($/ton)	30.0	**Recovery rate**	0.8	**# pushbacks**	3

In the proposed mine planning solution, pit limits are identified based on e-type values. As a result, the deposit is planned to produce 457 Mton of ore and 69 Mton of waste. Alternatively, the upper bound strategy demonstrates an average of 476 Mton of ore and 49 Mton of waste. Thus, the proposed solution produces a lower amount of ore and a higher amount of waste than the upper bound, which individually implements MIP on each realisation. This can also be observed in ore and waste tonnages for each production period from the proposed solution (Figure 4c). Both parameters are consistent throughout the life-of-mine, while 95 per cent confidence intervals show fair deviations. However, ore tonnages do not reach the full processing capacity of 47.45 Mton/a, unlike the upper bound (Figure 4a) during the first eight years of production. Furthermore, NPV results after each production period calculated with a discount rate of 10 per cent show consistent growth, and the final NPV is between $458M and $616M based on a 95 per cent confidence interval. On the other hand, the NPV of the lower bound (Figure 4b) is significantly lower, resulting from sending waste material to the processing plant.

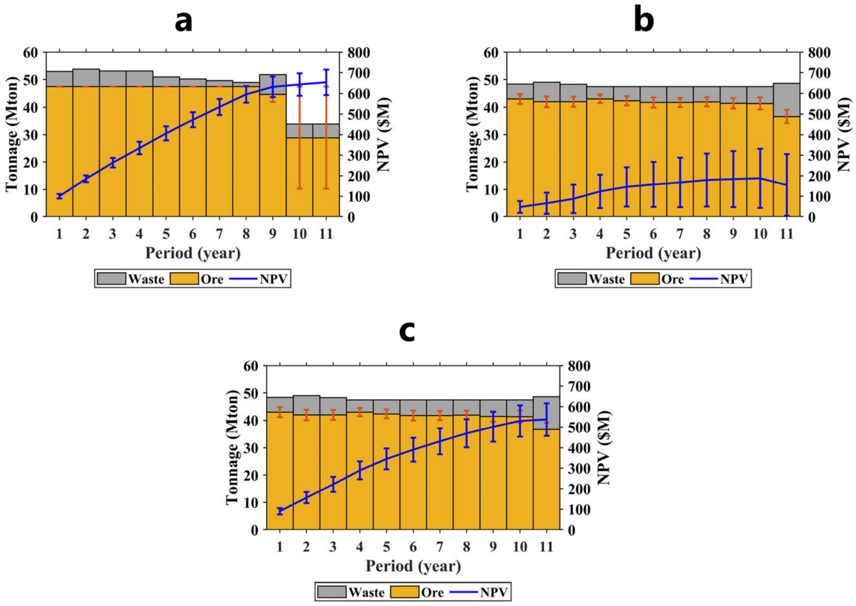

FIG 4 – NPV and tonnage values during each production period with 95 per cent confidence intervals for NPV (blue) and ore tonnage (orange) of the upper bound (a), lower bound (b) and proposed strategy.

NPV results produced by the two-stage stochastic production scheduling are compared to the upper and lower bounds. The average NPV of the upper bound is around $653M, which is the best NPV for this deposit that is impossible to achieve. On the other hand, the lower bound (ie deterministic case) produces only $154M because of losses related to sending waste material to the processing plant. And $537M is reported in the proposed solution. Furthermore, even the worst scenario from the proposed strategy with $443M NPV is considerably better than the best scenario of the lower bound with $389M.

Figure 5 shows plots with NPV for 100 realisations for the proposed mine planning solution, upper and lower bounds, which are normalised to the reference plot of the upper bound (ie 100 per cent). By doing so, deviations from the best possible NPV for each realisation can be analysed. The average plot for the proposed solution is at 83 per cent and the lower bound – 24 per cent. Therefore, the NPV of the proposed solution is 17 per cent lower than the upper bound and 59 per cent higher than the lower bound on average.

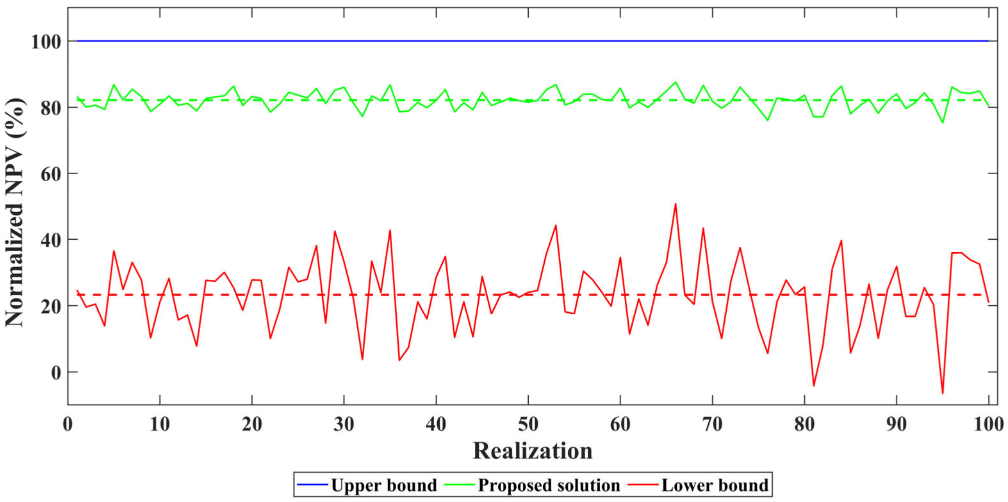

FIG 5 – NPV of the proposed production scheduling strategy compared to the upper and lower bounds for 100 realisations. Plots are normalised to the upper bound (reference case) and dashed lines represent average deviations from the reference plot.

The final analysis is the investigation of the effect of inequality constraint reproduction. Inverse transform sampling prevents the overestimation of silica and increases the economic block values by reducing the cost associated with an impurity content. As a result, optimal pit limits produced using realisations from the proposed cosimulation algorithm contain more profitable blocks. Therefore, NPV increases by 0.76 per cent (Figure 6a) and ore tonnage – by 1.78 per cent (Figure 6b) in comparison to the conventional cosimulation. The absolute benefits from the proposed cosimulation algorithm are 8.39 Mton of ore and $4.08M NPV.

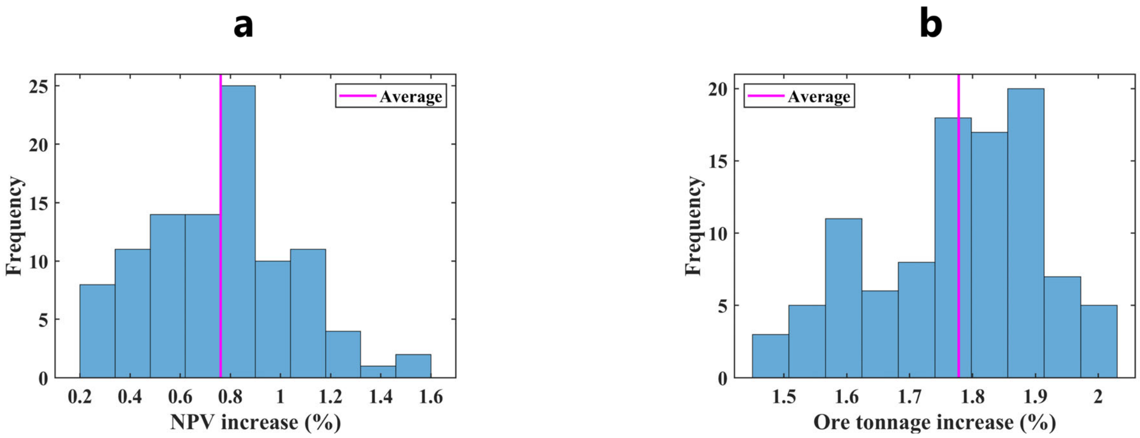

FIG 6 – Histograms of the increase in NPV (a) and ore tonnage (b) in 100 realisations of production scheduling by using the proposed cosimulation algorithm over the conventional one.

CONCLUSIONS

This study shows the economic benefits from inequality constraint reproduction using a case study from an iron deposit composed of iron and silica grades. Poor reproduction of an inequality constraint by the conventional cosimulation methodology leads to an overestimation of silica, which in turn increases losses associated with the impurity content of mined ore. Additionally, although traditional mine planning approaches can maximise NPV, they are unable to manage the risks considering that only a single block model is commonly used as an input. On the other hand, stochastic long-term mine planning approaches generate production schedules with maximised NPV and minimised risks of not meeting production targets.

Iron and silica variables are modelled by the proposed hierarchical cosimulation, which is equipped with an inverse transform sampling to re-simulate faulty values within thresholds from an inequality constraint. Unlike the conventional cosimulation, the proposed methodology perfectly reproduces an inequality constraint, shows better reproduction of silica histogram and produces a higher correlation coefficient between variables.

Two-stage stochastic production scheduling is proposed to introduce grade uncertainty into mine planning. In this study, first stage decisions obtain fixed production periods using average information from e-type models. Second stage decisions adapt the strategy to multiple unbiased geostatistical scenarios by re-evaluating block destinations. Adaptive block destinations help to minimise the risk of sending an actual waste to a processing plant or valuable ore material to a waste dump. Results are compared with the upper and lower bounds, in which the former is the highest NPV strategy that is also impossible to achieve and the latter is the deterministic strategy. The difference between the upper bound and the proposed solution is 17 per cent, while the lower bound is 59 per cent lower than the proposed solution. Furthermore, the reproduction of an inequality constraint increases NPV by 0.76 per cent or $4.08M.

It is recommended to apply the proposed methods to other data sets with inequality constraints between two variables. The NPV benefit from reproducing an inequality constraint can be higher when the overestimation of a disturbing element is more substantial. Moreover, the proposed methodology can also be improved by incorporating lithology modelling. For this, the contact analysis can be considered prior to the co-simulation process.

ACKNOWLEDGEMENTS

The first and second authors are grateful to Nazarbayev University for funding this work via Faculty Development Competitive Research Grants for 2018–2020 under Contract No. 090118FD5336. The authors also would like to thank Delphos Mine Planning Laboratory for giving access to MineLink mine planning library.

REFERENCES

Abildin, Y, Madani, N and Topal, E, 2019. A Hybrid Approach for Joint Simulation of Geometallurgical Variables with Inequality Constraint, *Minerals*, 9(1):24.

Abulkhair, S and Madani, N, 2021. Assessing Heterotopic Searching Strategy in Hierarchical Cosimulation Framework for Modeling the Variables with Inequality Constraints, *Comptes Rendus Géoscience*, 353(1):115–134.

Almeida, A S and Journel, A G, 1994. Joint simulation of multiple variables with a Markov-type coregionalization model, *Mathematical Geology*, 26:565–588.

Arcari Bassani, M A, Costa, J and Deutsch, C V, 2018. Multivariate geostatistical simulation with sum and fraction constraints, *Applied Earth Science*, 127(3):83–93.

Deutsch, C V, 1989. DECLUS: a fortran 77 program for determining optimum spatial declustering weights, *Computers and Geosciences*, 15(3):325–332.

Devroye, L, 1986. *Non-Uniform Random Variate Generation* (Springer: New York).

Dimitrakopoulos, R, 2011. Stochastic optimization for strategic mine planning: A decade of developments, *Journal of Mining Science*, 47:138–150.

Emery, X, Arroyo, D and Peláez, M, 2014. Simulating Large Gaussian Random Vectors Subject to Inequality Constraints by Gibbs Sampling, *Mathematical Geosciences*, 46:265–283.

Gershon, M E, 1983. Optimal mine production scheduling: evaluation of large scale mathematical programming approaches, *International Journal of Mining Engineering*, 1:315–329.

Godoy, M and Dimitrakopoulos, R, 2004. Managing risk and waste mining in long-term production scheduling of open-pit mines, *SME Transactions*, 316:43–50.

Hochbaum, D S, 2008. The Pseudoflow Algorithm: A New Algorithm for the Maximum-Flow Problem, *Operations Research,* 56(4):992–1009.

Journel, A G, 1999. Markov Models for Cross-Covariances, *Mathematical Geology*, 31:955–964.

Leite, A and Dimitrakopoulos, R, 2007. Stochastic optimisation model for open pit mine planning: application and risk analysis at copper deposit, *Mining Technology*, 116(3):109–118.

Madani, N and Abulkhair, S, 2020. A hierarchical cosimulation algorithm integrated with an acceptance–rejection method for the geostatistical modeling of variables with inequality constraints, *Stochastic Environmental Research and Risk Assessment*, 34(10):1559–1589.

Moreno, E, Emery, X, Goycoolea, M, Morales, N and Nelis, G, 2017. A two-stage stochastic model for open pit mine planning under geological uncertainty, in *Proceedings of the 38th International Symposium on the Application of Computers and Operations Research in the Mineral Industry* (Colorado School of Mines: Golden).

Ramazan, S and Dimitrakopoulos, R, 2004. Traditional and New MIP Models for Production Scheduling With In-Situ Grade Variability, *International Journal of Surface Mining*, 18(2):85–98.

Ramazan, S and Dimitrakopoulos, R, 2013. Production scheduling with uncertain supply: a new solution to the open pit mining problem, *Optimization and Engineering*, 14:361–380.

Ramazan, S and Dimitrakopoulos, R, 2018. Stochastic optimisation of long-term production scheduling for open pit mines with a new integer programming formulation, in *Advances in Applied Strategic Mine Planning* (ed: R Dimitrakopoulos), pp 139–153 (Springer: Cham).

Wackernagel, H, 2003. *Multivariate Geostatistics* (Springer: Berlin).

Improved sustainability through WHIMS Plant addition at Roy Hill

C Jenkins[1], S Lozyk[2], J Jasper[3], Y Suryaputradinata[4] and MJ Hartmann[5]

1. Specialist Metallurgical Development, Roy Hill, Perth Airport WA 6105. Email: clinton.jenkins@royhill.com.au
2. Superintendent Metallurgical Improvement, Roy Hill, Perth Airport WA 6105. Email: stefan.lozyk@royhill.com.au
3. Specialist Engineer – Operational Readiness, Roy Hill, Perth Airport WA 6105. Email: justine.jasper@royhill.com.au
4. Principal Study, Roy Hill, Perth Airport WA 6105. Email: yohanes.suryaputradi@royhill.com.au
5. Principal Metallurgist, Roy Hill, Perth Airport WA 6105. Email: thys.hartmann@royhill.com.au

ABSTRACT

The primary objective of mining companies is to function as a profitable business by delivering products that fit customer requirements in a safe and sustainable manner. Optimum resource utilisation is a critical focus area to achieve this objective, and the long-term sustainable business performance of a mining company is determined by the extent to which this is achieved. Technology improvements and/or new technology development could improve resource utilisation. However, adding new projects to a Brownfield operation carries risk. Overall project schedules, tie-in schedules and safety risks normally receive adequate attention, but the introduction and integration of new technology to a Brownfield site also carries the significant risk of failure to achieve design performance (quality or throughput). This risk must be addressed via rigorous design phase risk assessments and piloting. Post commissioning, the effective metallurgical integration of any new technology/circuit/process plant into an existing process plant calls for critical assessment, through circuit performance testing, and optimisation to ensure alignment with design criteria. In addition, this approach provides clear focus areas for further optimisation of the new plant and additional opportunity for overall plant optimisation. Roy Hill recently navigated this process successfully, and this paper provides feedback on the journey that led to improved resource utilisation.

INTRODUCTION

The Roy Hill Iron Ore mine is situated approximately 115 km north of Newman at the eastern end of the Chichester Range within the lower part of the Nammuldi Member of the Marra Mamba Iron Formation. Prior to the commencement of mining operations, the project had a defined mineralisation of more than 2.4 billion tonnes of +55 per cent Fe iron ore with a mine life of more than 20 years. Roy Hill is targeting a production of approximately 60 million tonnes per annum (Mt/a) of Lump and Fines. At a glance, Roy Hill consists of the following distinguishing operational features:

- 60 Mt/a wet processing plant.
- Conventional open pit bulk mining operation from multiple production benches utilising backhoe configured digging equipment and haul trucks.
- Large Run-of-mine (ROM) stockpiles.
- 344 km heavy haul railway linking the mine and port.
- Port stockyard and two berth export facility in Port Hedland.
- Remote Operations Centre based in Perth.

As part of the ongoing optimisation of the mining operation, technical challenges have presented themselves, including variability of physical ore properties.

PROJECT BIRTH

Value creation through optimum resource utilisation is a key driver to minimise waste and improve sustainability in a mining company. At Roy Hill the drive to optimise resource utilisation led to the birth of the Wet High Intensity Magnetic Separation (WHIMS) Project. Expanding the process beneficiation circuit to extract value from an identified waste stream led to increased product throughput through a higher overall mass yield to product.

The original plant design did not cater for the recovery of the majority of iron rich ultrafine iron ore (<106 µm) present in the ROM feed. The inherent size of the material resulted iron losses to tailings streams, this was evident during daily field inspections where ultrafine iron was clearly visible within the Up Current Classifier (UCC) overflow. This resulted in the technical teams further investigating how these losses can be minimised.

Geological modelling and mine planning identified a reasonable amount of High-grade (HG) ultrafine material in plant feed sources. It was predicted that when fed to the original Ore Processing Plant (OPP), the majority of this material would be lost to tailings. Further studies were required to determine if additional iron recovery technologies would be feasible, this included research into the viability of vertical ring WHIMs units which was novel to the Pilbara region at the time.

Ultrafine recovery by WHIMS

WHIMS is a magnetic separation technology that separates material based on its magnetic characteristics and are widely used for processing and recovery of fine-grained ores (-1.2 mm). Hematite is paramagnetic whereas the silica-alumina gangue material is not, therefore the hematite can be effectively recovered by the WHIMS.

The WHIMS units use an excitation coil to generate a high intensity electro-magnetic field. The principle of operation is slurry introduction into the bath of the magnetic separator, with a magnetic ring rotating vertically through the bath while the bath is pulsated to keep the slurry particles in suspension. Wash water is used to wash the magnetic material (product) off the magnified matrix boxes.

A schematic of a WHIMS unit is shown in Figure 1. The slurry enters the feed hopper through the feed pipe and flows through the upper magnetic pole and the rotating ring. The rotating ring comprises of a matrix box which is made of stainless-steel rods. These rods are then magnetised as the ring rotates through the magnetic field. The magnetic particles in the slurry are attracted to the surface of these rods. The slurry is continually being agitated by a pulsating diaphragm which pushes a tympanic membrane to form a pulsating motion within the bath. The pulsating motion keeps the material fluidised assisting with flushing (washing) out the gangue that may be entrained with the magnetic material in the matrix boxes, thereby improving concentrate quality. It also assists to push the magnetic material within the proximity of the magnetised rods. The magnetic materials adhere to the rods and as the ring rotates, they are carried to the non-magnetic field discharge area and are then flushed into the concentrate hopper using flushing water. The non-magnetic particles sink through the gaps of the lower magnetic pole and flow into the tailings discharge (Huate Road, 2019).

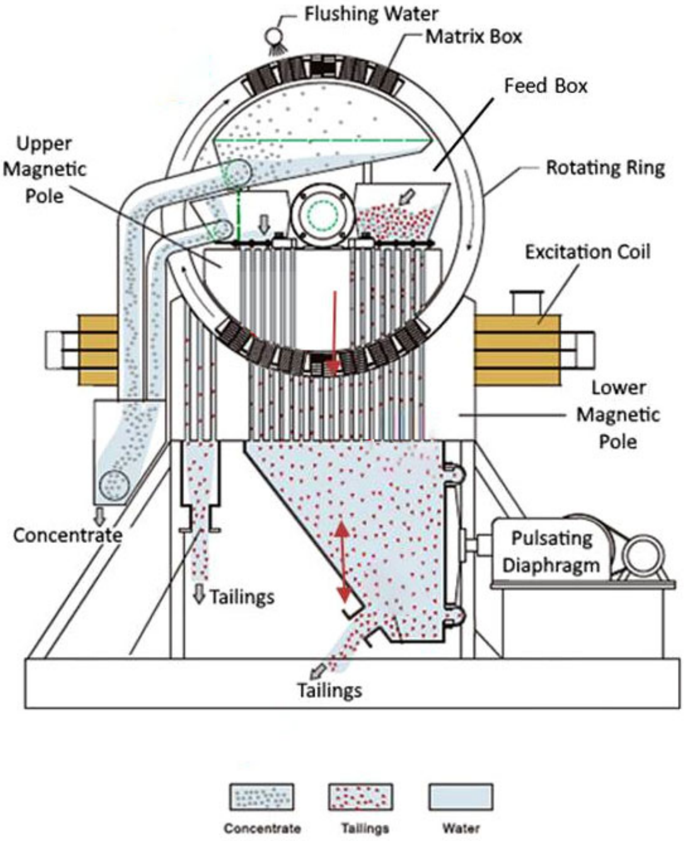

FIG 1 – WHIMS unit (Huate Road, 2019).

TEST WORK PHASES

The test work was conducted in three phases:

1. Concept – Preliminary test work to investigate the treatment of Roy Hill ultrafine tails via WHIMS technology.
2. Variability – Extensive bench scale testing to validate the concept flow sheet and provide additional data for modelling.
3. Bulk – Pilot scale test work to understand equipment scale up and provide engineering design data.

Concept test work

Preliminary WHIMS test work was conducted on tails samples collected in 2017. Two tailings streams were tested:

- The Allflux Classifier Overflow.
- Total Tailings.

The test work identified the Allflux Classifier Overflow stream as displaying superior amenability for treatment by WHIMS with significantly higher mass recoveries and upgrades (Figure 2).

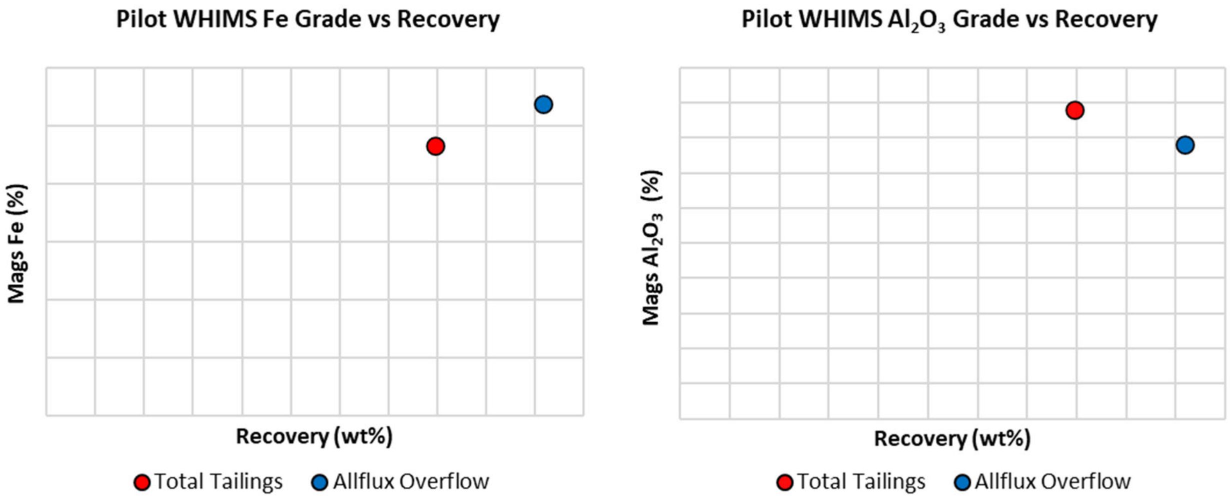

FIG 2 – Concept test work WHIMS results.

Further work has shown that particle size is a primary driver for WHIMS mass recovery (Figure 3). Mass recovery was shown to progressively reduce in size fractions below 32 µm.

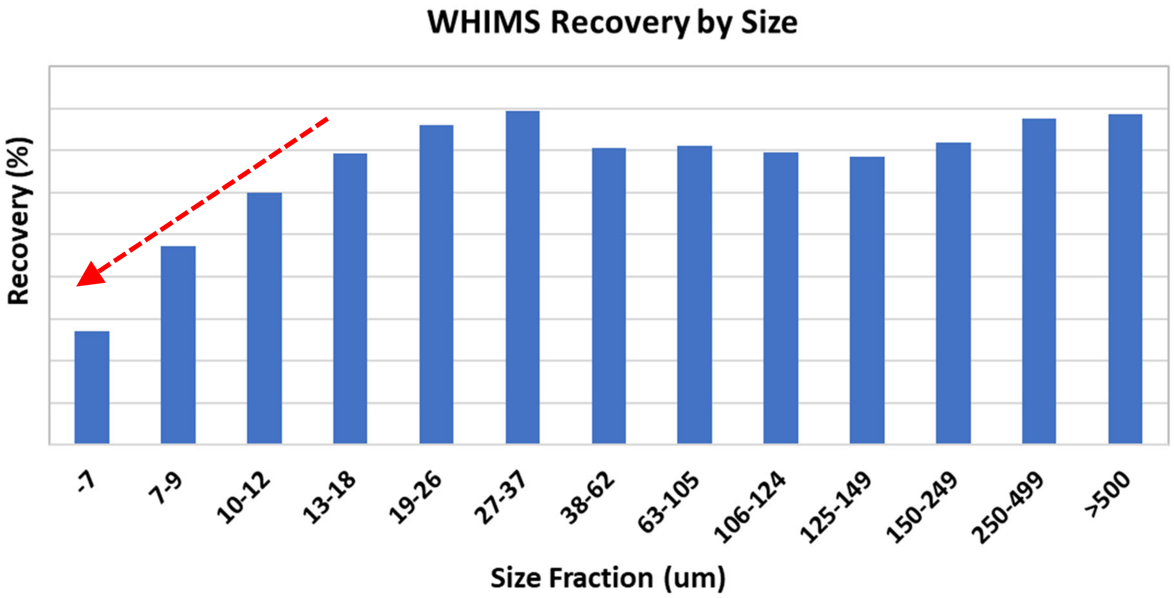

FIG 3 – WHIMS recovery by size fraction.

This reduced mass recovery in finer size fractions has been described in a paper by Forssberg and Kostkevicius (1982). WHIMS effectiveness is reduced due to the increased influence of dynamic forces within the slurry and reduced magnetic attraction for particles less than ~20 µm.

The difference in WHIMS treatability between the two samples can be attributed to the significantly higher proportion of -32 µm material in the Total Tailings stream. For this reason, the project focused on the treatment of the Allflux Classifier Overflow.

The integration of the concept WHIMS plant within the Roy Hill Process Flow sheet is shown in Figure 4.

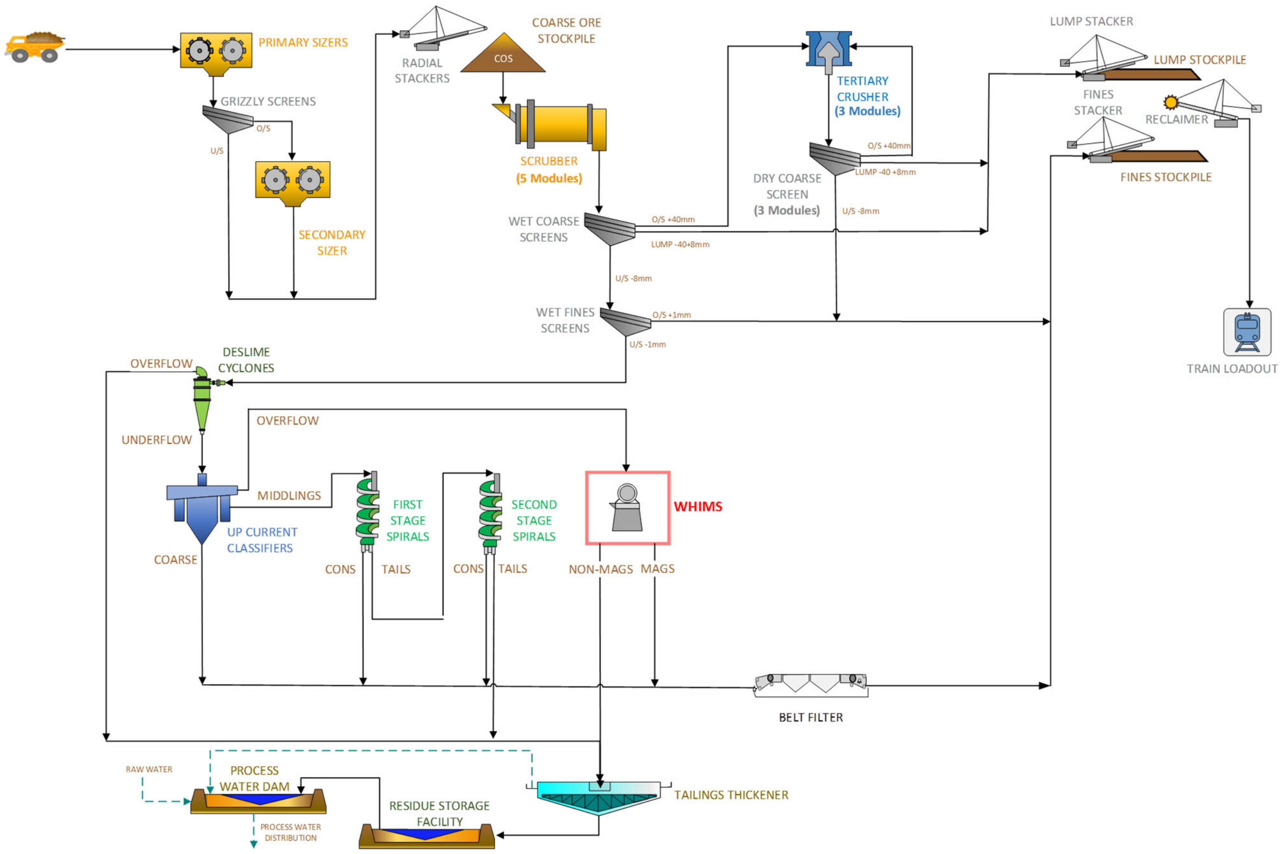

FIG 4 – Roy Hill Process flow sheet with WHIMS.

Given the excellent economics of the project, key processing studies were fast tracked to prove the concept, mitigate risk and support the engineering of the 'Ultrafine Iron Recovery Project/WHIMS Project'. The biggest risk items identified were the impact of recovery of -10 µm ultrafine material over the existing belt filters and the impact on overall fines product quality.

To support the processing studies a detailed sampling and test work program was conducted between September 2017 and January 2018. Samples collected were classified as follows:

- Variability Test work – Daily composite samples of ~20 kg for bench scale WHIMS test work.
- Bulk Test work – Larger composite samples totalling ~8000 kg which were used for Continuous Pilot Scale test work, vendor test work, engineering design and product evaluation.

Variability test work

Daily composite samples were collected from the Allflux classifier overflow stream between October and December 2017 to better understand the day-to-day variability of the stream. Several samples were selected to cover a range of particle size distributions, grades and mineralogy. These samples were tested using the bench scale SLon100 unit at different magnetic intensity (Tesla) settings to generate grade recovery profiles.

The key outcomes from this test work program were:

- The test work confirmed WHIMS suitability to recover Roy Hill ultrafine ore.
- Samples exhibited similar mass recoveries at each magnetic intensity setting (Figure 5).
- Good correlations between the WHIMS feed grade and product grade were obtained at each setting (Figure 6).

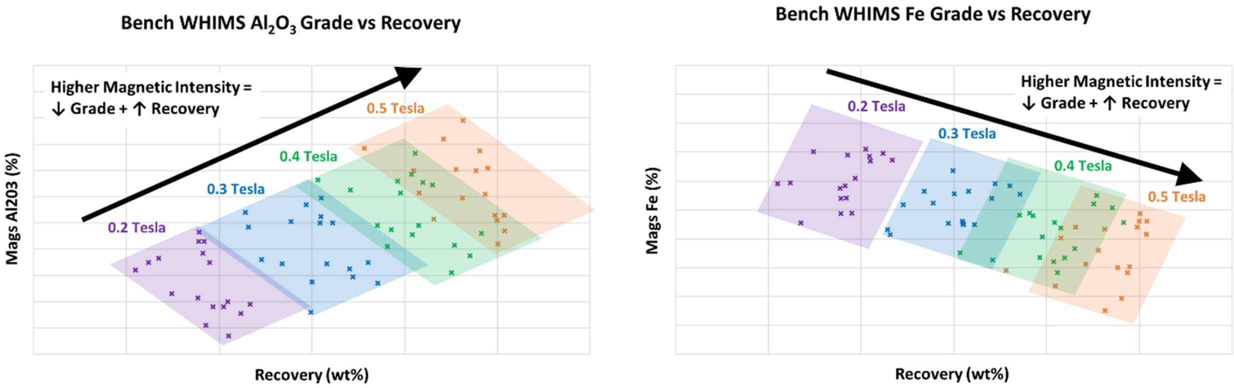

FIG 5 – Mass recovery versus grade of variability samples.

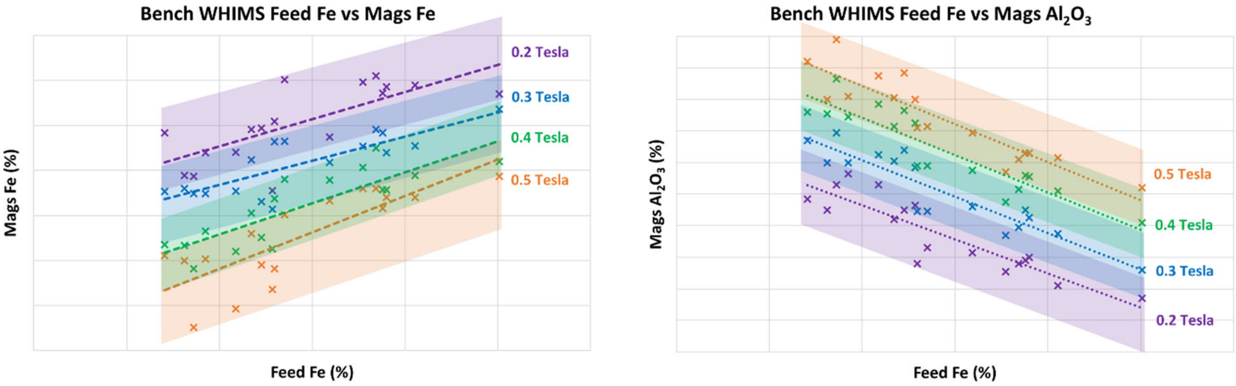

FIG 6 – WHIMS feed grade versus product grade.

As there is a good relationship between plant tails grade and UCC O/F grade, the test work data could be used in conjunction with the mine plan data to estimate the theoretical WHIMS plant concentrate grade. The minimum, average and maximum mass recoveries obtained at each Tesla setting were used for the operational design envelope. This allowed modelling to be conducted to estimate the impact of the WHIMS plant concentrate on the overall Roy Hill Fines Product stream for input into the business case document.

Bulk test work

A bulk sampling campaign of Allflux Classifier overflow was conducted between September and November 2017. This material was used for pilot scale testing to investigate equipment scale up and sizing as well as generating samples for further work. Test work was conducted using a 500 mm diameter pilot unit (Figure 7) at a local laboratory in Australia and at two vendor's testing facilities overseas. All test work was conducted under the supervision of representatives from the Roy Hill Technical Services Development Projects group.

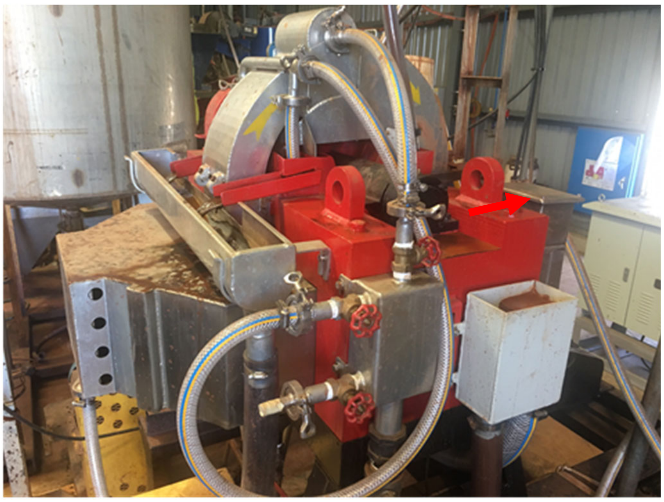

FIG 7 – Pilot scale WHIMS at ALS.

The key outcomes from the test work program were:

- Data showed comparable grade/recovery profile between the Bench scale and Continuous Pilot Scale units (Figure 8).
- Confirmation of the WHIMS technology on pilot scale at multiple independent testing facilities (Figure 9).

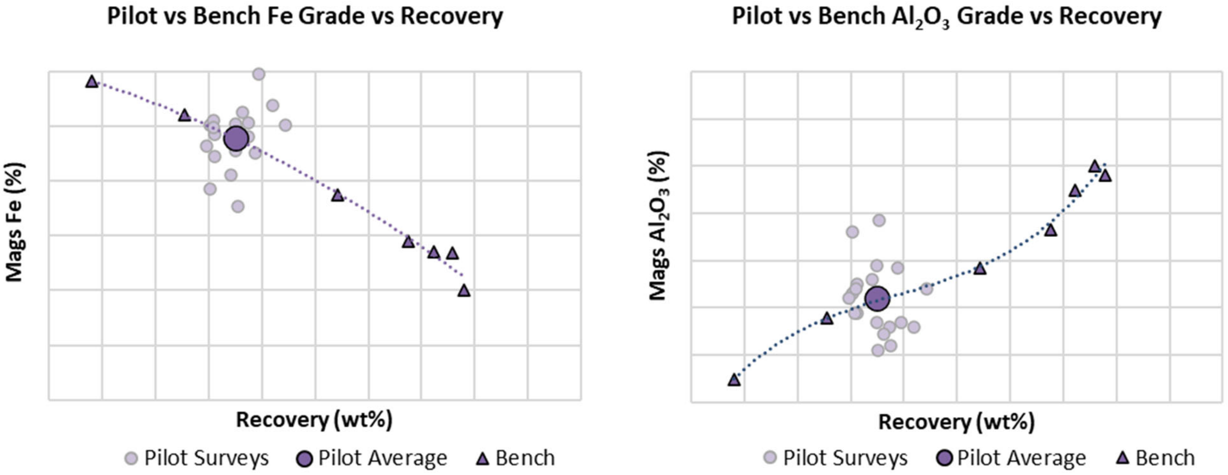

FIG 8 – Bench versus continuous pilot WHIMS grade recovery profile.

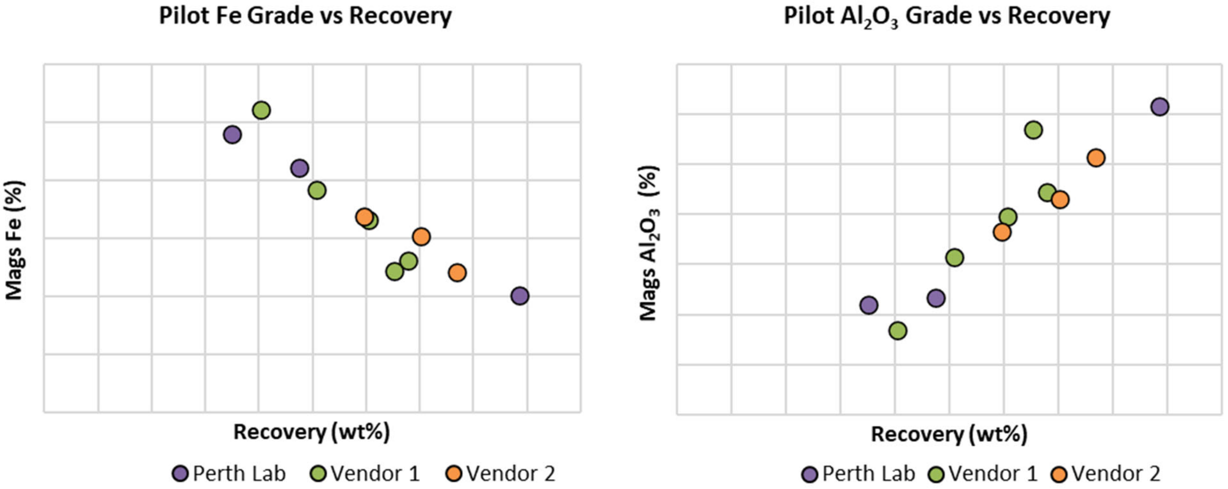

FIG 9 – Pilot WHIMS grade recovery profile between laboratories.

The products from the bulk pilot runs were used for the following programs of work:

- engineering design:
    - rheology
    - tailings characterisation
    - thickening
    - filtration
    - material handling.
- product evaluation (sintering) work at CSIRO.

The simulated blend of existing Roy Hill process streams with WHIMS magnetics was shown to have an acceptable impact on the Roy Hill Fines product stream.

PROJECT TIMELINE

A summary of the project timeline is shown in Figure 10. The total time from concept to execution was approximately 2.5 years. This was an exceptional achievement for the size of the project. The integrated Roy Hill team showed that when people work together to achieve great outcomes their efforts lead to operational excellence.

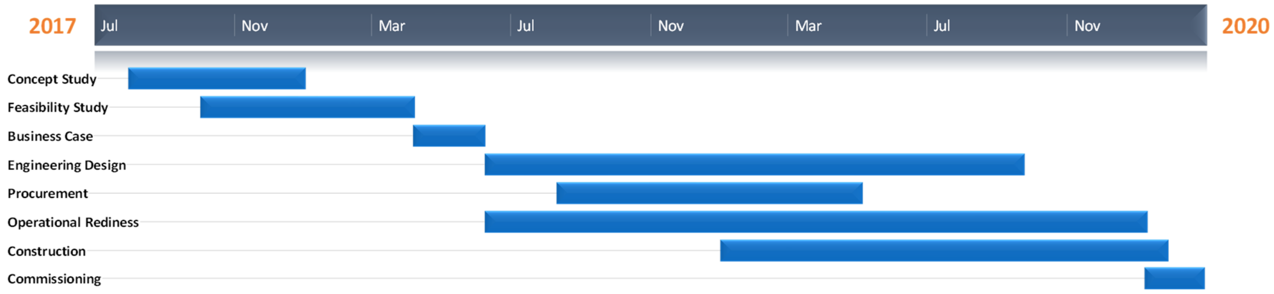

FIG 10 – Project execution timeline.

OPERATIONAL READINESS

The Operational Readiness team at Roy Hill are responsible for preparing both site and Perth based teams including maintenance, operations, and supporting departments to manage new assets within the business. The sole purpose of the team is to ensure that all business functions are fully prepared to receive and operate, safe, high quality, operable and maintainable plant that reaches the set production goals as designed.

The Operational Readiness plan is achieved by establishing collaborative relationships, structure, and work processes to deliver on the following key areas at the time of project handover.

TABLE 1

Operational readiness scope of work.

Focus areas	Project objectives
Recruitment and onboarding	Design the organisational structure, roles, responsibilities, and qualifications necessary to support operations and maintenance functions and recruit the personnel.
Training	Ensure people are suitably skilled and that critical training documentation has been created and integrated within Roy Hill Systems.
Health and safety plan	Ensure new Plant can be safely operated with no risk to people and the environment.
Operations and maintenance readiness	Ensure site operations, maintenance and supporting teams are prepared to manage the new assets and that all critical documents, tools and systems are developed prior to handover. Ensure new plant can be safely and efficiently controlled from the Remote Operating Control Centre (ROC).
Facilities and equipment	Ensure all required facilities and equipment are prepared and ready prior to handover to site team.
Supply chain readiness	Determine requirements for new plant equipment logistics, inventory, sourcing, procurement and warehousing.
Asset management	Ensure the new asset equipment has the system and information well defined to support planned maintenance and reliability activities.

To ensure success of the Operational Readiness program of work the Roy Hill Operational Readiness Manager had a vision of creating a multidisciplinary team from within the current processing plant, incorporating members with a variety of industry experience from within each of the departments: Technical, Mechanical, Electrical, Operations and Training.

The Operational Readiness team were engaged early in the engineering design stages, working as part of the project team to provide key input into the operability and maintainability of the new facility. The final flow sheet for the WHIMS Plant incorporated new technology novel to the Pilbara Iron Ore industry to which limited information was known. To gain firsthand knowledge on this technology the team were given the opportunity to travel to the Huate warehouse in Shandong China where they would walk through the manufacturing process of both the WHIMS and LIMS units. This was a unique learning opportunity which allowed the team to witness all stages of manufacturing whilst also having face time with the technical experts. In addition to visiting the Huate manufacturing warehouse the team also visited two magnetic separation processing plants which utilise both WHIMS and LIMS units within their operations. This experience was extremely valuable and assisted in gaining a better understanding of operational and maintenance practices not commonly known for the equipment. The multidisciplinary structure of the Operational Readiness team, as well as valuable knowledge obtained during the Huate visit, allowed them to develop all critical documentation and systems required for handover of the plant. Throughout the process of design and vendor visits they quickly developed into the subject matter experts and played a key role in providing both the project and operations teams advice on how to maintain and operate the plant. They worked collaboratively with Asset Management to ensure timely development of maintenance plans, and that all capital, commissioning and operational spares were delivered to site in time for ramp-up and commissioning.

The Operational Readiness team became the key interface with the project team on behalf of operations to ensure regular transfer of information to keep key stakeholders informed throughout the process of design, commissioning, and construction. The Operational Readiness function allowed the wider business and processing teams to stay focused on safe operation of existing plant while regular updates allowed them to keep abreast of project progress and activities.

In addition to preparing site teams for handover the Operational Readiness team played a key role in the ramp up and commissioning of the plant, assisting the technical and operational teams with performance test planning and execution, rectification of project defects and optimisation works.

PROJECT RAMP-UP

Ramp-up occurs from the point the processing plant first takes feedstock until it is operating in steady-state with normal production crews. Achieving a fast production ramp-up after cold commissioning is important since time-to-volume in a high-volume commodity business like iron ore directly impact the financial success of the project. The time-to-volume period can have a significant effect on the net present value of the project. Furthermore, being able to respond quickly to favourable market conditions (high demand and high price) can further boost the net present value (NPV) of the project. If the time-to-volume is delayed with respect to the ramp-up performance, revenues are postponed, and NPV is lowered. A shorter ramp-up reduces the payback period for a project and improves financial performance indicators for the business.

Proper pilot test work programs assisted Roy Hill to develop an early learning curve and aided to shorten the WHIMS production ramp-up phase to reach target production throughput at product quality specifications within a period of three months. The planning and execution work of the Operational Readiness team sealed the pathway to success and assisted greatly to achieve the fast ramp-up curve achieved on the WHIMS Plant.

The WHIMS Plant ramp-up curve against the nominal target throughput capacity is provided in Figure 11 and shows that 58 per cent of the target throughput was achieved within the first month after commissioning. In the third month the throughput reached 90 per cent of the target monthly throughput capacity. Due to coarser than expected ROM feed size distributions the feed throughput to the WHIMS varied after this ramp-up period as shown in Figure 11. The mass yield to product reached 77.5 per cent of the target nominal yield during the first month and in the second month the nominal mass yield target was achieved at the required product specification as shown in Figure 12. For some of the months following ramp-up the yield exceeded the nominal yield target and in others it was just below the target. The yield variation is contributed to feed blend variation. Product grade is manipulated by altering the magnetic field strength settings to allow for operation in either grade (lower feed quality) or yield (higher feed quality) operational modes. In general, higher magnetic field strength settings results in a higher mass yield to product but at a lower product quality and vice versa as shown in Figures 5 and 6.

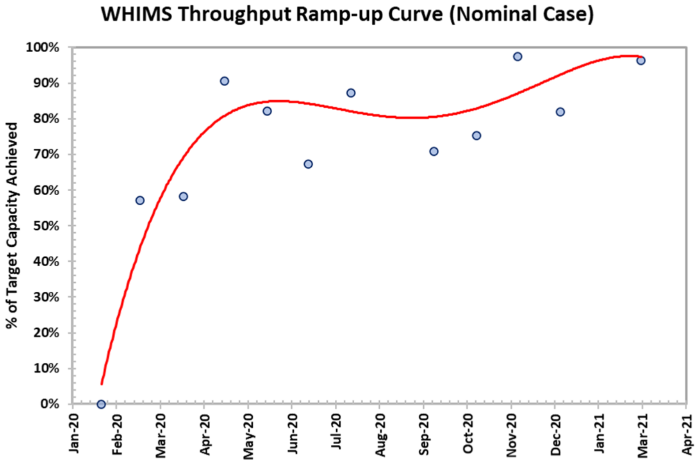

FIG 11 – WHIMS plant throughput ramp-up curve.

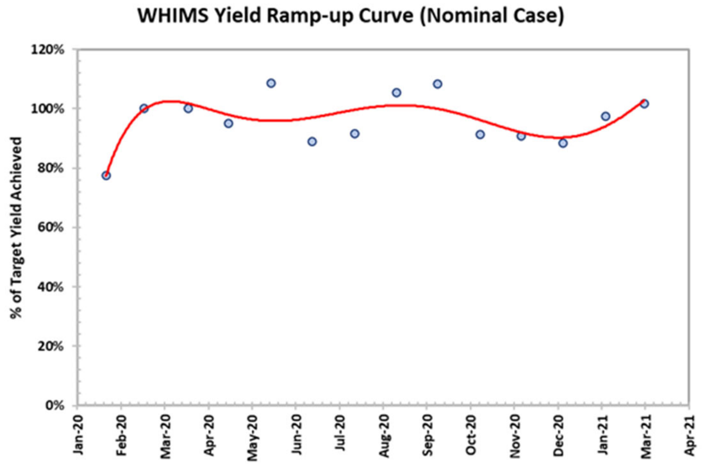

FIG 12 – WHIMS plant yield ramp-up curve.

Early into the ramp-up phase two specific test campaigns were executed:

1. Quality performance testing of the WHIMS Plant at different magnetic field strength settings for different hematite to goethite ratios in the feed blend with the aim to update the preliminary regressions used to predict product grades and mass yield to product.
2. Circuit performance test campaign followed once stable plant performance was achieved and confirmed that the plant met the nominal production throughput and quality objectives.

Overall, the fast WHIMS ramp-up achieved after commissioning provided much needed product capacity into a market experiencing a high demand for iron ore.

Commissioning and optimisation

The processing objectives of WHIMS load commissioning were simple – transport solids from the feed thickener, through each of the units of operations, and produce concentrate and tailings that are integrated back into the existing circuits. Like most projects, load commissioning and ramp up typically does not run smoothly and Roy Hill's WHIMS Plant was no exception. Although all reasonable considerations were taken during design phases, there were two main factors when solids were first introduced into the circuit.

Firstly, the feed and concentrate thickeners experienced issues with the recirculation function due to the feed distributor design in combination with the ultrafine high-density nature of feed and products. Until this was rectified, the thickeners could only operate in recirculation mode for short periods and only under special attention from the control room operator. A few incidences of the thickener ending up bogged ensured a solution was expedited.

The other major challenge during ramp up was the Brownfields tie-in of WHIMS Concentrate into the existing filtration circuit. A new agitated tank was installed to combine the existing Desands Concentrate with the new WHIMS concentrate prior to moisture reduction. The operating philosophy and installed equipment meant that at times of process interruption, both concentrates may not be present (mixed) into the common equipment. This presented functional issues due to the significantly different particle size distributions in each of the products – shown in Figure 13. The agitation and pumping duties differed depending on the mixture. These two issues resulted in very difficult conditions for the Control Room Operators and the field operators during ramp-up.

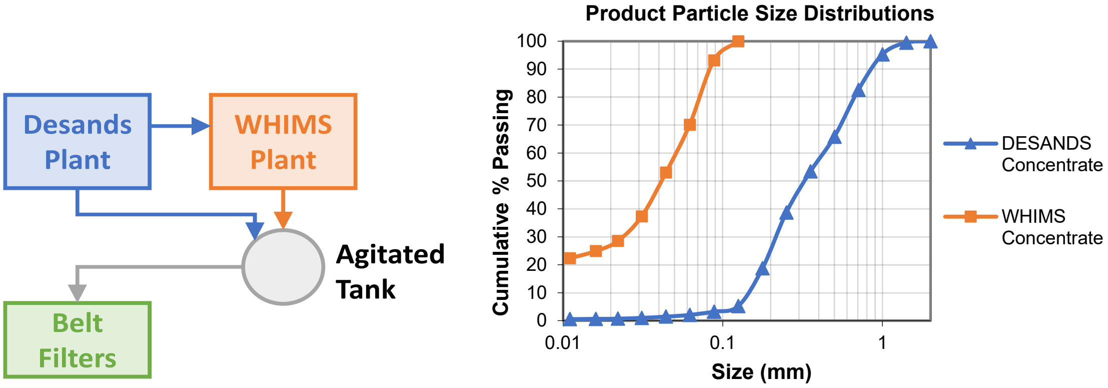

FIG 13 – Brownfield's tie-in diagram and differences in particle size distribution of Desands and WHIMS concentrates.

To mitigate this the agitator was upgraded, pipe sizes changed, and new automatic valving and plumbed flush water were installed to minimise processing risk and improve stability. To assist the Control Room Operators in controlling the added complexity of the circuit, a constraint controller was developed with new logic enabling hands-off control for the tie-in point. This automatically changed set points, constrained upstream flows to suit downstream availability and resulted in better operability.

On completion of ramp-up, the baseline performance of the plant was assessed with a Circuit Performance Test. This test found the plant performed as designed in yield, product quality, availability and utilisation. The focus of the project then quickly moved to further improving the metallurgical performance of the plant.

POST RAMP-UP OPTIMISATION

The primary objective of the WHIMS Optimisation Program was to improve the metallurgical performance of the plant by improving plant yield whilst maintaining or improving product grade. The Optimisation team were deeply involved in concept phases and test work, flow sheet design and commissioning. As this plant was the first of its kind to be used in a hematite environment by a Pilbara iron ore operation the size and scale of Roy Hill, the team were eager to test the capabilities of the plant and try new ideas.

Phase 1

The approach to the first phase of optimisation was to understand the drivers of metallurgical performance for each unit of operation. This was achieved in a series of capacity trials where the system was deliberately fed beyond the original design parameters with the intention to expose relationships of inefficiency.

The method to primarily expose inefficiency, rather than efficiency was necessary as during normal operation the optimal performance was indistinguishable due to confidence in instrument calibration, fluctuations in feed loading and material size, feed lithology and other contributing factors. Analysis of historian data collected from instrumentation during trials effectively exposed limitation of equipment and contrariwise the optimal operating conditions that maximised plant yield. The relationship of overall plant yield against feed tonnage is displayed in Figure 14. This resulted in adjustments to the operating philosophy of the plant and performance notably increased.

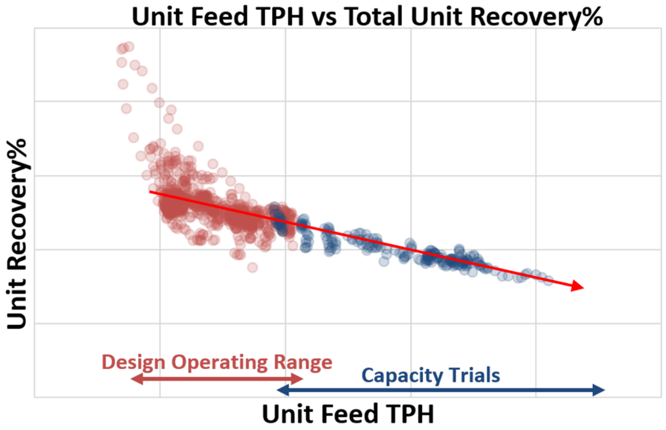

FIG 14 – Relationships developed between feed tonnage and unit yield per cent.

Phase 2

The second phase of the optimisation program targeted each unit of operation in more detail with trials involving changes to feed volume, density and the physical installation were pursued. To assist with metallurgical assessment, the automatic poppet samplers were programmed so metallurgists could execute an instantaneous sampling campaign where multiple streams could be collected in unison supporting the overall accuracy of assessments. This phase identified further efficiency improvements with key changes implemented from the original design.

The optimisation program ran for 8 months and resulted in a plant yield increase of 15 per cent of design without compromising product grade. Along with the improved production benefit it also assisted in building a greater depth of knowledge and experience for Roy Hill employees which has advanced the capability of its workforce.

CONCLUSIONS

The Roy Hill WHIMS project went from concept stage to full operation within a period of two and a half years. Thorough bench and pilot scale test work, combined with integrated teamwork between Study, Project, Operational Readiness, Vendors, Technical Services and Operational team members, made this possible. The success of this project is attributed to the people that worked together and made a difference. The support from executive management showed their belief in the people and the confidence in the robustness of this project. This project showed that when people work together every day to achieve great outcomes their efforts leads to operational excellence. Lastly, Roy Hill named the WHIMS Plant the 'Barry Fitzgerald WHIMS Plant' in recognition of Barry as Roy Hill's Chief Executive Officer (CEO) and his support and contribution to making this project a reality.

ACKNOWLEDGEMENTS

The team of authors would like to acknowledge the following people:

- The Executive Management team for their support during the project and for the opportunity to publish this paper.
- The Project Design and Execution team for their great work and drive to deliver the project in a very short time frame.
- Manjot Singh for his vision and drive to identify and lead the project during the initial study phases.

REFERENCES

Forssberg, K S and Kostkevicius, N R, 1982. Comparative Pilot Scale Tests with Wet High Intensity Magnetic Separators, *Erzmetall*, 35:(6)285–293.

Huate Road, 2019. Ultrafine Iron Recovery Project: Installation, Operation and Maintenance Manuals, pp 21–22.

Positive influence of WHIMS concentrate on the sintering performance of Roy Hill fines

J R Manuel[1], L Lu[2], N A Ware[3], S Hapugoda[4], B D McDonald[5] and X Cao[6]

1. Senior Experimental Scientist, CSIRO Mineral Resources, QCAT, Pullenvale Qld 4069. Email: james.manuel@csiro.au
2. Senior Principal Research Scientist, CSIRO Mineral Resources, QCAT, Pullenvale Qld 4069. Email: liming.lu@csiro.au
3. Experimental Scientist, CSIRO Mineral Resources, QCAT, Pullenvale Qld 4069. Email: natalie.ware@csiro.au
4. Senior Experimental Scientist, CSIRO Mineral Resources, QCAT, Pullenvale Qld 4069. Email: sarath.hapugoda@csiro.au
5. Manager Technical Marketing and Analysis, Roy Hill, Perth Airport WA 6302. Email: brian.mcdonald@royhill.com.au
6. Principal Advisor Technical Marketing, Roy Hill, Shanghai, China. Email: xueming.cao@royhill.com.au

ABSTRACT

Roy Hill is a large iron ore mining, processing, railing and port operation in the Pilbara region of Western Australia. Since delivering its first shipments to customers in December 2015, Roy Hill has quickly achieved a 60 Mtpa production rate of lump and fines products.

The process plant, principally consisting of wet scrubbing, screening and de-sanding unit processes, was expanded from early 2020 to include operation of a Wet High Intensity Magnetic Separation (WHIMS) Plant. The WHIMS Plant treats tailings to recover approximately 4 Mtpa of ultra-fine (nominally -150 µm) high-grade hematitic concentrate which, after dewatering, is blended into the fines product.

Unlike typical hematite concentrates, which consist largely of dense particles with smooth surfaces, the WHIMS concentrate is characterised by very finely microporous hematitic/goethitic particles, reflecting the overall characteristics of the Roy Hill deposit.

Detailed test work has been conducted in collaboration with CSIRO to characterise the WHIMS concentrate in terms of its physical and mineralogical properties, and to determine its influence on the granulation and sintering performance of Roy Hill fines – from fundamental/lab-scale and sinter-pot perspectives. The results demonstrate that blending of the high-grade hematitic Roy Hill WHIMS concentrate into the fines product can maintain overall sinter quality and positively influence granulation and sinter melt formation, as well as Fe grade.

INTRODUCTION

Roy Hill is a large iron ore mining, processing, railing and port operation in the Pilbara region of Western Australia. Since delivering its first shipments to customers in December 2015, Roy Hill has quickly achieved a 60 Mtpa production rate of lump and fines products. The process plant, principally consisting of wet scrubbing, screening and de-sanding unit processes, was expanded from early 2020 to include operation of a Wet High Intensity Magnetic Separation (WHIMS) Plant. The WHIMS Plant treats tailings to recover approximately 4 Mtpa of ultra-fine (nominally -150 µm) high-grade hematitic concentrate which, after dewatering, is blended into the fines product.

The Roy Hill ore is characterised by abundant microplaty hematite, with textures similar to those of Brockman ores (Buswell, Bowman and Batchelor, 2019). Marra Mamba ores are typically dominated by primary (ie after original banded iron formation)/hydrated martite-goethite textures, although microplaty hematite is characteristic of Chichester Range Marra Mamba ores and is most extensively developed in the Nammuldi Formation at Roy Hill (Clout and Fitzgerald, 2011). At Roy Hill, microplaty hematite is typically associated with fine-grained, microporous ore textures and the abundance of ultrafine microplaty hematite generated during wet processing makes the ore amenable to recovery of high-grade hematite from tailings. Changes in demand for iron ore over the last 15 years and a greater awareness of reducing carbon emissions has driven innovation in blast furnace feed and consequently the sintering process. The need for beneficiation of lower grade ores is increasing (Nomura *et al,* 2015) for this reason, as well as due to the gradual decline in grade and quality of direct-shipped ores. There is also an increasing trend in the Asia Pacific to use magnetite and hematite concentrate in blends to either maintain or improve Fe grade (Han and Lu, 2018), to control phosphorus and minimise fuel use and CO_2 emissions (Saito, 2019).

Concentrates improve sinter blend Fe grade, but also affect sintering performance and sinter quality, specifically with respect to granulation characteristics and green bed permeability, as well as sinter productivity, particularly at higher blending levels. Compared with hematite concentrates, magnetite has the advantage of exothermic reaction on oxidation to hematite, but sinter blend proportions of magnetite are limited due to lower reactivity and dependence on oxidation (Han and Lu, 2018). Conversely, ultrafine hematite concentrate has been found to increase ferrite bonding phase formation in sinter, compared with ultrafine magnetite (Yang *et al,* 2019). Smaller blend proportions of magnetite concentrates may improve granule morphology and increase mean granule size, whereas higher proportions can lead to loss of green bed permeability.

In a collaboration between CSIRO and Roy Hill, detailed test work has been carried out to characterise the Roy Hill WHIMS concentrate (RHC) and determine its influence on the granulation and sintering performance of the Roy Hill Fines (RHF) product. This test work involved mineralogical and physical characterisation, pilot scale pot grate sintering and fundamental laboratory-scale evaluation of both sintering and granulating performance.

GRANULATION AND SINTERING TEST WORK

Chemistry, sizing and mineralogy

The Roy Hill fines and WHIMS concentrate chemistry and sizing are summarised in Table 1. Mineralogy was characterised by microscopic point counting of sized ore fractions according to ore group (Table 2), with mass normalised data for individual fractions combined and summarised in Figure 1.

TABLE 1

Chemistry and sizing (wt% per size fraction) of the Roy Hill fines and WHIMS concentrate.

Chemistry (%)	**Fe**	**SiO_2**	**Al_2O_3**	**P**	**TiO_2**	**Mn**	**LOI_{371}**	**LOI_{1000}**
Roy Hill Fines	60.79	4.88	2.26	0.050	0.20	0.65	2.99	4.13
Roy Hill Conc.	64.90	2.78	1.43	0.034	0.15	0.26	1.19	1.92

Size fraction (mm)	-11.2 +9.5	-9.5 +8	-8 +6.3	-6.3 +4	-4 +2	-2 +1	-1 +0.5	-0.5 +0.25	-0.25 +0.15	-0.15 +0.125	-0.125 +0.063	-0.063 +0.038	-0.038
Roy Hill Fines	0.8	1.8	5.6	22.0	23.6	18.4	11.9	5.2	2.7	0.9	2.6	1.5	2.9
Roy Hill Conc.	0.0	0.0	0.0	0.0	0.1	0.3	0.2	0.1	0.1	0.1	22.9	36.2	40.1

The Roy Hill fine ore used in this work was quite coarse, with only 27.9 per cent mass reporting to the -1 mm size fraction. The fines head chemistry showed moderate loss on ignition (LOI) at 1000°C (4.13 per cent) and SiO_2 (4.88 per cent) contents, a relatively high Al_2O_3 content (2.26 per cent) and a moderate Fe grade of 60.79 per cent. Mineralogically, the Roy Hill fines were dominated by fine, microplaty hematite textures, often with hydrohematite/nanohematite (Clout, 2006; Wolska, 1981) and mostly moderately to highly microporous, with less abundant martitic textures. Overall goethite content was intermediate, consistent with the total LOI value of 4.13 per cent. More than 20 per cent goethite-only textures (dense to friable) were present, with slightly less mixed hematite-goethite textures. The proportions of microporous hematite/martite and dense goethite increased with decreasing particle size, with a corresponding reduction in hydrohematite and hematite-goethite textures. Quartz grains and dense martite with silica infill were observed in minor amounts, mainly below 1 mm, with only few shale (aluminosilicate) particles.

TABLE 2

The CSIRO ore classification (N.B. hem. = hematite, goe. = goethite).

Group	Dominant Mineralogy		Subgroup	Hardness	Porosity	Origin
	Matrix	**Infill**				
1	dense hem./ martite			very hard	very low	primary
2	microplaty hematite/ martite		a	hard	medium	primary
			b	medium	medium	
			c	soft/friable	high	
3	martite	goethite		medium	medium	primary
4	goethite	martite		soft	high	primary
5	dense hem./ goethite	hydrohematite	a	hard-very hard	low	dehydration
			b	medium/friable	medium-high	
6	dense martite	goethite		hard		hydration
7	dense goe.	martite		hard	medium	hydration
8	microplaty hematite	goethite	b	medium	medium	hydration
			c	soft	high	
9	ochreous goethite			soft/friable	very high	primary
10	brown/ vitreous goe.		a	medium	low	hydration
			b		medium	

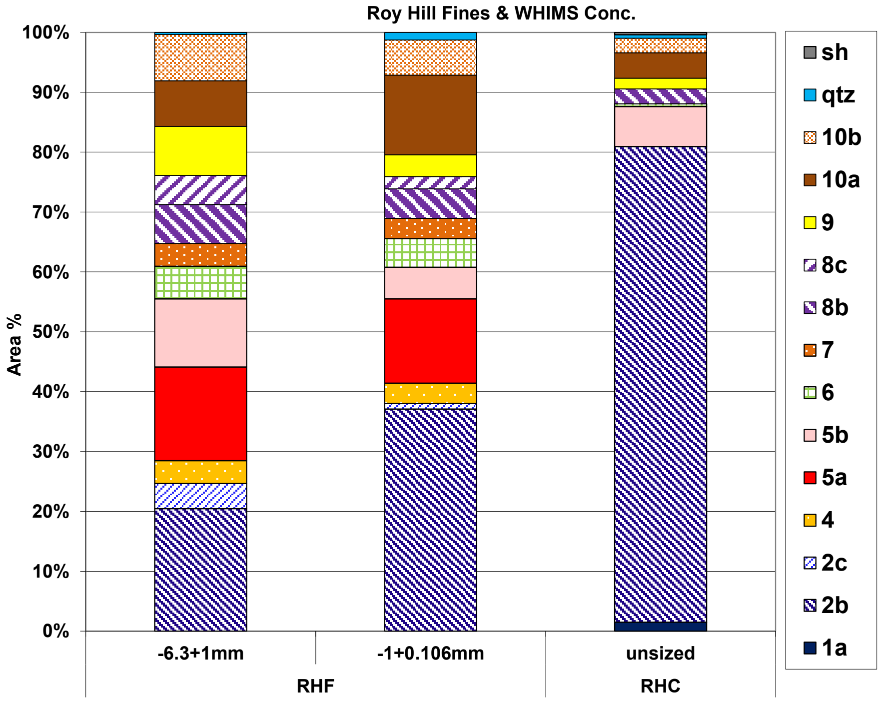

FIG 1 – Ore type abundance for Roy Hill fines and WHIMS concentrate (see Table 2 for description of categories; N.B. qtz = quartz/siliceous, sh = shale).

In comparison, the RHC was extremely fine in sizing, with 99.2 per cent passing 0.15 mm and had a high Fe grade of 64.9 per cent, with 2.78 per cent SiO_2, 1.43 per cent Al_2O_3 and 1.92 per cent LOI. The concentrate was dominated by moderately porous microplaty hematite/martite (80 per cent), followed by porous hydrohematite. It also contained minor amounts (less than 5 per cent) of dense and earthy brown goethite, moderately porous microplaty hematite-goethite and dense hematite. Compared with the +53 µm size fraction, the dense ore groups, particularly dense hematite, significantly increased in the -38 µm fraction, while goethite and hydrohematite decreased.

Pot-grate sintering

An evaluation was carried out to assess the effects of increasing the level of RHC in the Roy Hill composite sample (RHF + RHC) on the granulation and sintering characteristics of a customer blend containing 25 per cent Roy Hill (RH) composite sample and 75 per cent other non-RH blend components. Table 3 lists the proportions and chemistries of the non-RH blend components. Four different blending options for the Roy Hill composite sample were tested, containing 0, 9.6, 13.4 and 16.8 per cent RHC. All blends were fluxed to 5.7 per cent silica, 0.7 per cent MgO and a basicity of 1.85, including addition of 2.3 per cent hydrated lime.

TABLE 3

Chemistry (%) and proportions of non-RH blend components.

Sample	Fe	SiO_2	Al_2O_3	P	TiO_2	Mn	LOI_{371}	LOI_{1000}	% in blend
Ore A	61.01	3.86	2.36	0.101	0.12	0.09	0.80	5.93	2.65
Ore B	61.84	7.75	1.03	0.055	0.07	0.12	0.30	1.99	2.65
Ore C	66.00	4.88	0.31	0.013	0.22	0.03	-0.06	-0.01	4.41
Ore D	57.65	5.71	1.85	0.061	0.14	0.06	0.79	9.56	4.41
Ore E	62.62	5.63	1.56	0.053	0.10	0.37	0.41	2.39	4.41
Ore F	60.85	4.70	2.26	0.093	0.07	0.06	0.77	5.42	4.41
Ore G	65.45	1.47	1.38	0.065	0.10	0.30	0.41	2.74	8.82
Ore H	58.33	4.17	1.48	0.055	0.07	0.04	0.89	10.4	19.42
Ore I	56.33	6.65	1.98	0.040	0.13	0.03	0.95	10.4	23.82

The evaluation of the ore blends was carried out at CSIRO's pilot-scale pot grate testing facility, the only facility in Australia capable of carrying out industry standard iron ore sintering tests, to maximise productivity and yield and minimise fuel rate, to achieve the specified sinter quality as measured by sinter size and strength targets, reduction degradation and reducibility.

The granulation trials were carried out in a small-scale granulation drum of 0.31 m length and 0.50 m internal diameter, using fluxed sinter mixes of 14 kg mass (dry basis), calculated based on an estimated fuel level and targeted sinter chemistries, to determine optimum granulation moisture level.

Results showed that the optimum permeability decreased slightly from 47 to 43 Japanese Permeability Units (JPU) with the increasing level of RHC (Figure 2), due to the decreasing bed voidage of the green granules with increasing blending ratio of WHIMS concentrate. The optimum moisture content, on the other hand, increased slightly from 7.8 to 8.1 per cent with increasing blending ratio of WHIMS concentrate.

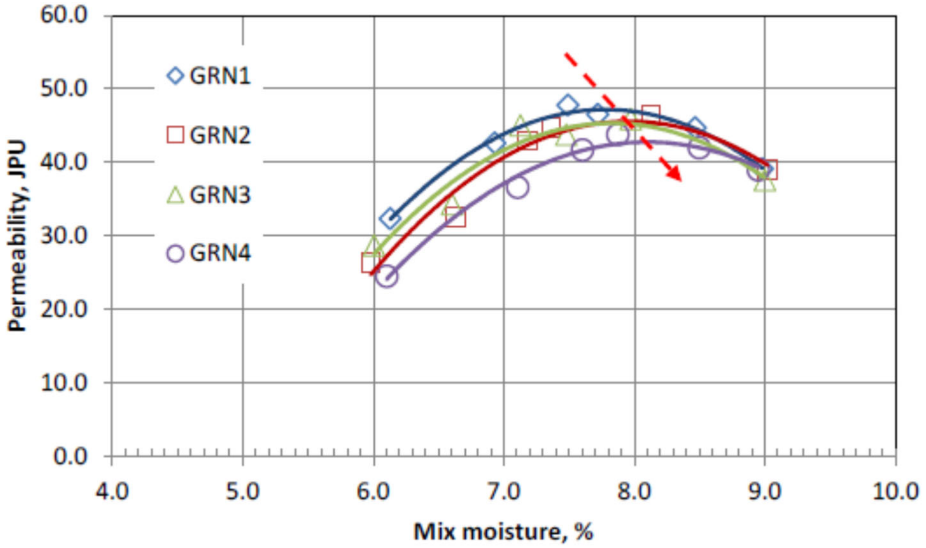

FIG 2 – Green bed permeability as a function of granulation moisture for Blends 1 to 4.

The sintering test procedure involved optimising fuel and moisture levels based on those used in the granulation trials. This optimisation aimed to achieve the targets of acceptable sinter strength and return fines balance, while maximising sinter productivity and yield. Typically, between five and six pot-grate sintering tests per blend are required to establish the optimum sintering conditions. The sintering results show a decrease in fuel rate as the proportion of WHIMS concentrate in the Roy Hill composite sample increased (Figure 3).

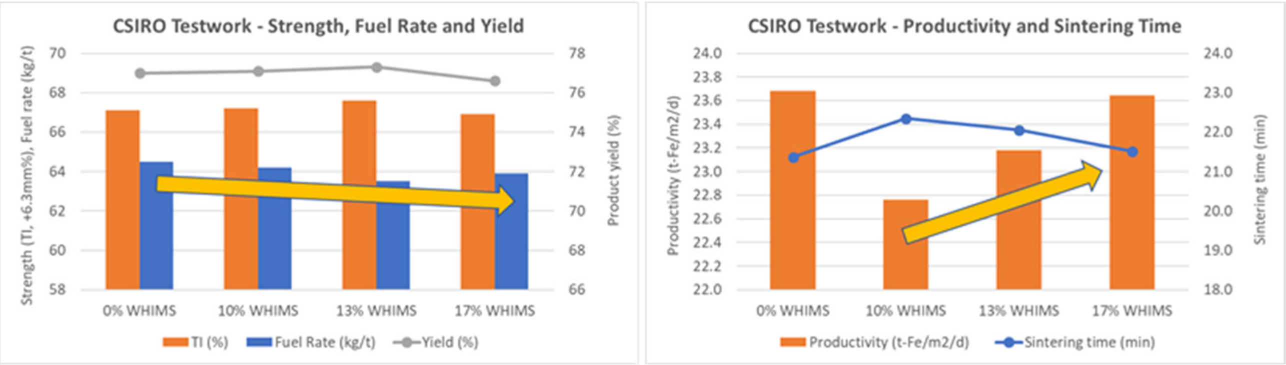

FIG 3 – Trends in sinter quality and performance with increasing RHC proportion for Blends 1 to 4.

Fundamental laboratory scale sintering

Sinter consists of both remnant nucleus particles (nominally, +1 mm) and a sinter matrix formed primarily by melting of the fluxed -1 mm ore fraction present as adhering fines in the granules. The sinter matrix consists of various bonding phases, consisting of SCFA, Ca-rich ferrites, calcium silicates and glass (Pownceby *et al* 2016). The mineralogy and microstructure of this matrix influences sinter parameters including strength and reducibility of the overall sinter product. CSIRO has developed unique laboratory scale sintering test methods (Ware *et al,* 2013; Ware and Manuel, 2015) to provide fundamental information about the behaviour of the -1 mm ore matrix-forming fraction, with a separate nucleus assimilation test for evaluation of coarse nucleus-forming particles. Nucleus assimilation testing was carried out on the Roy Hill fines and indicated generally high reactivity and assimilation, although those results are not further discussed here.

The sinter matrix test was designed to simulate the firing conditions in a sinter plant, specifically the formation of primary sinter melt that occurs in the granule adhering fines. The -1 mm fraction of the ore was fluxed to a SiO_2 level of 5 per cent, a basicity level of 2.4 (correlating with an overall basicity of 1.8) and compacted into 4 g tablets. Samples were fired in duplicate in a horizontal tube furnace at an oxygen partial pressure of 5×10^{-3} atm, under a heating profile designed to simulate the sintering process. The firing temperature was controlled via thermocouple and no solid fuel was used, in order to accurately and reproducibly control temperature. Typically, blends are fired at a series of temperatures and sinter matrix strength is qualified by a laboratory-scale tumble test carried out with a modified Bond Abrasion tester. A sinter strength of 80 per cent +2 mm particles, determined by screening the fired and tumbled sinter samples, corresponds to a pot grate tumble index (TI) of 65 (per cent +6.3 mm) (Clout and Manuel, 2003) and the optimum melt temperature is defined as the lowest temperature required to achieve target fired strength).

Both the RHC and RHF 100 per cent blends were tested using this method as well as a blend simulating the best-performing 13.4 per cent hematite concentrate addition in the composite sample (Blend 3). The results (Figure 4) show that the 100 per cent RHF sample achieved optimum strength at 1300°C, whereas the 100 per cent RHC achieved optimum strength at 1280°C and the composite blend achieved a TI of 80 per cent at 1290°C, ie with intermediate melting characteristics.

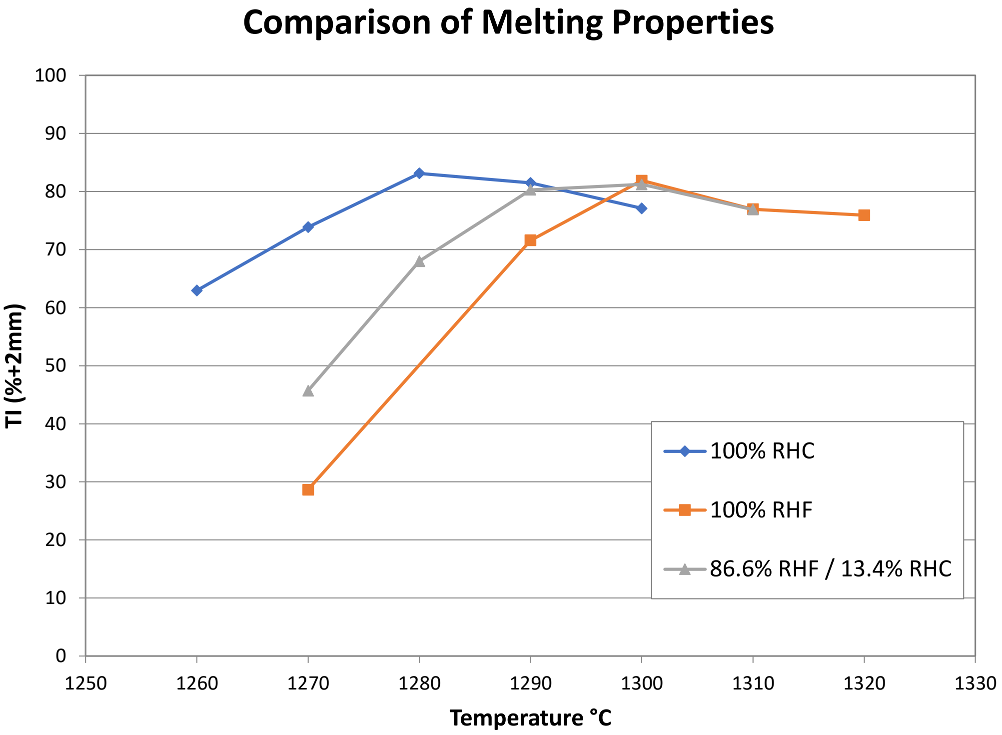

FIG 4 – Melting curves for 100 per cent RHF, 100 per cent RHC and the 13.4 per cent RHC blend.

Laboratory scale granulation

To isolate and further explore the granulation behaviour of the concentrate on a more fundamental level, a laboratory simulation of the granulation process was developed. The method involved using a rock polishing drum with diameter 100 mm as a laboratory scale granulation drum. For each granulation test, nucleus (screened -4+2 mm) and matrix (unsized concentrate ± screened -1 mm fines) components were selected to make up a total sample mass of 100 g, according to the proportions and test conditions in Table 4. The aim was to compare the behaviour of RHC with a commercially traded hematite concentrate. Granulation conditions and the moisture addition method were optimised in trials, so that the cascading motion of the sample visually replicated the pilot scale process. The procedure included mixing the blend components for 1 minute to ensure an even spread of dry sample across the drum, with pre-weighed moisture addition via a syringe and a wet granulation time of 5 minutes. Three moisture levels were selected for each concentrate from trials for each mix (optimum ± 1 per cent for each experimental condition), based on qualitative evaluation of granule development.

The nuclei and -1 mm fines were selected from a goethitic fine ore (Ore H) and tests were run initially with pure concentrate as the adhering fines, then with a combination of goethitic -1 mm fines and concentrate. Identical granulation trials were also carried out substituting a commercially traded Canadian hematite concentrate (CC) for the RHC. The CC was significantly coarser (98.5 per cent -1 mm, 25.5 per cent -125 µm, with ~35 per cent -150 µm) than the RHC (99.2 per cent -150 µm, 40.1 per cent -38 µm).

TABLE 4

Laboratory granulation tests (*AF = adhering fines).

Nucleus wt (g)	Adhering fines 1	*AF 1 wt (g)	Adhering fines 2	*AF 2 wt (g)	Hydrated lime %	Moisture % (aim)
50	RHC	50				10, 11, 12
50	CC	50				5, 6, 7
50	RHC	25	Ore H	25		10, 11, 12
50	CC	25	Ore H	25		5, 6, 7
50	RHC	50			2.3	12, 9
50	CC	50			2.3	10, 7
50	RHC	25	Ore H	25	2.3	12, 9
50	CC	25	Ore H	25	2.3	10, 7

The RHC granulations required a higher moisture level (10–12 per cent) than the CC (5–7 per cent) due to the finer RHC sizing, and consequently greater surface area and void space, also noting the internal microporosity of the RHC particles compared with the dense hematite and magnetite particles characteristic of the CC (Figure 5). Recalibration of moisture levels was also needed for the trials where hydrated lime was introduced as a binder; in this case, only two moisture levels were tested. A size distribution curve was produced from each trial, by freezing the granules in liquid nitrogen, then screening at 6.3, 4, 2 and 1 mm and weighing each fraction, as a method of qualifying the results. Although it is not possible to include plots and microscopy results from these trials within length restrictions here, the results showed that the RHC granules developed consistently higher average size and lower proportions of ungranulated material (-1 mm), compared with the Canadian concentrate granules. Unlike the RHC, the CC required hydrated lime as a binder to produce significant granule growth at all and its granulation performance did not significantly improve when a second adhering fines component (screened -1 mm Ore H at 25 per cent, see Table 4) was used to provide a more realistic range of sizing in the adhering fines.

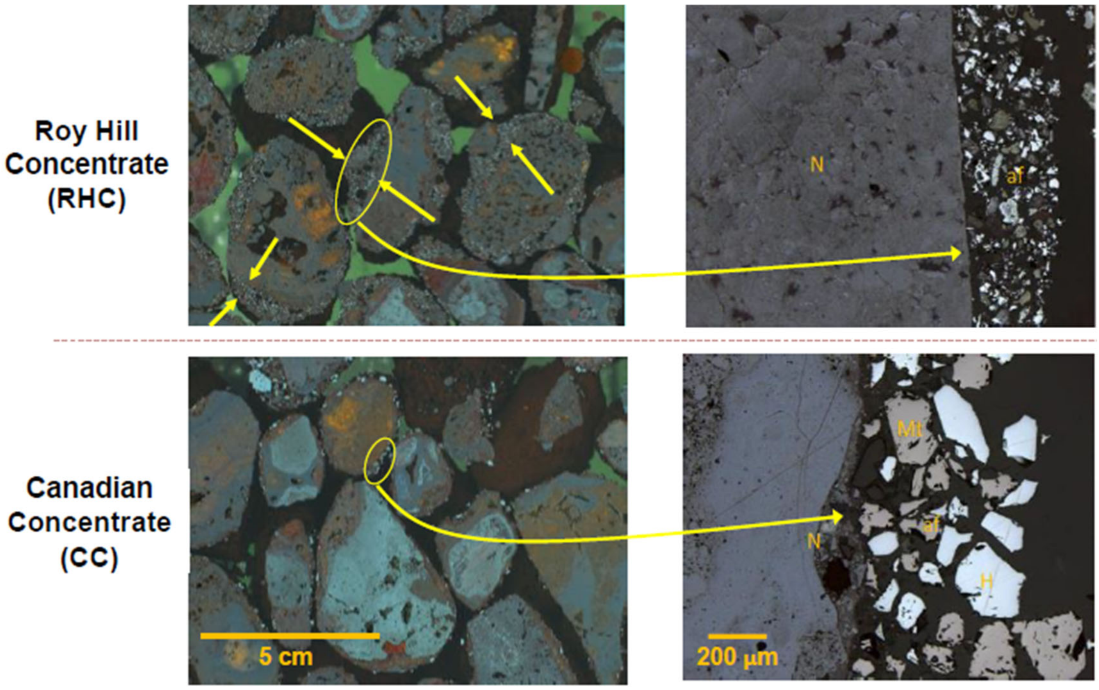

FIG 5 – Granule images from polished sections: left column; incident light, low power stereo microscope and right column; reflected light photomicrographs, showing adhering fines (af) on the surface of nucleus particles, as indicated by arrows (N, goethitic). H = hematite; Mt = magnetite.

The images in Figure 5 illustrate the difference in behaviour between the RHC and CC adhering fines. The granulations in these cases were carried out with the following (actual) moisture addition: 9.9 per cent (RHC), 6.9 per cent (CC), with 2.3 per cent hydrated lime addition in each case. The low magnification images at left show that the RHC granules developed generally thicker and more continuous adhering fines layers. The CC adhering fines, in comparison, only formed locally thicker layers where irregularities or concavities on the surface of the nucleus particles allowed effective particle adhesion and retention. It is reasonable to suggest that the smaller inter-particle voids within the RHC adhering fines layers favoured greater cohesion due to more effective wetting and capillary pressure between adjacent particle surfaces. Note also the greater variety of particle types present within the RHC. Significant magnetite was not present, but ultrafine, microporous (micro – to nano-metre-scale pores) goethite particles (Figure 5, higher magnification) are apparent from their low reflectivity, as well as similar finely microporous hematitic (white to pale grey) particles – many of the particles have surface micro-roughness, as a result, which should also promote adhesion. In contrast, the CC particles lacked internal microporosity and had generally smooth surfaces. In both cases, particles were mostly equigranular. The addition of hydrated lime as a binder assisted granulation for both concentrates. It proved to be necessary for significant adhering fines layer development in the case of the CC and substantially reduced spalling of thick RHC layers.

DISCUSSION

The laboratory sintering tests showed that blending RHC with RHF resulted in a slight lowering in optimum melting temperature, compared with 100 per cent RHF. This is consistent with the trend towards decreased fuel requirement with increasing concentrate level observed in the pot grate sintering tests with Blends 1 to 4 (Figure 3). In the pot grate sintering tests, similar performance was maintained with an increasing level of RHC in the blend, although there was a slight apparent shift in the balance between sinter TI and productivity, while productivity showed an inverse correlation with sintering time. The recovery in productivity with increasing substitution of RHC for RHF from 9.6 to 16.8 per cent was unexpected, however, given that green bed permeability decreased over the same range.

Hseih (2017) pointed out that with coarse (0.1–0.3 mm) concentrates, sinter productivity decreases 5–7 per cent for every 10 per cent concentrate increase, whereas no significant effect on productivity occurs with use of fine concentrates. A -20 µm hematite concentrate favoured granulation and productivity, whereas +45 µm particles had the opposite effect. Fine concentrates were found to decrease the proportion of ungranulated -2 mm fines. Similarly, Oliveira *et al* (2019) confirmed the benefit of pregrinding of Brazilian specularite pellet feed on granulation, due to size reduction and improvement in particle shape factor, improving permeability and productivity while decreasing fuel significantly, and noting the benefits of finer particle sizing on reactivity. Further, Wu, Que and Li (2017) commented on the poor granulation performance of specular hematite concentrates, where loss of permeability and productivity was related to shape factor; ie the typically platy nature of specular hematite particles, as well as contact angle between concentrate adhering fines particles.

Although particle shape was not a major factor in the comparison between RHC and CC granulation characteristics, as both concentrates consisted mainly of relatively equidimensional particles, the improved packing of the finer RHC particles and reduced volume of inter-particle voids do relate to these observations. Results from Yamaguchi *et al* (2020) support Saito's (2019) comments with respect to the benefits of ultrafine concentrate particles on granulation and sintering performance, specifically regarding the ability of ultrafine concentrate particles to fill interparticle voids within the granule adhering fines layer. Saito reported that the addition of a hematite concentrate with very fine sizing (71 per cent -10 µm) into sinter blends increased both permeability and sinter productivity. This may also result in improved distribution of reactive Fe for matrix bonding phase formation, as well as improved adhesion of adhering fines particles to nuclei.

On the above basis, the substitution of Roy Hill WHIMS concentrate in the Roy Hills composite fines showed behaviour expected for a predominantly +45 µm concentrate at the 9.6 per cent level with respect to productivity, but shifting towards that of a -10 µm hematite concentrate at 13.4 and 16.8 per cent. Given that productivity and sintering time (Figure 3) departed from the trend in green bed permeability (Figure 2), this suggests that the influence of RHC may not be due to the physical effect of finer particle sizing on granulation alone. It may be influenced by the very finely microporous nature and significant goethite content of the RHC particles, which both contribute to a higher surface area and capacity to retain moisture, compared with a more typical concentrate consisting mainly of dense particles, with smooth surfaces. Khosa and Manuel (2007) discussed the effects of particle sizing, microporosity and goethite content in adhering fines, and their relationship to granulation moisture, in more detail.

Panigrahy and Rigaud (1988) noted the effect of particle size on reactivity of silica in concentrates (ie lower reactivity when coarse). This may be significant in the case of RHC, due to the association of alumina and silica with goethite in the Roy Hill ore. The comments of Yang *et al* (2019) regarding increased ferrite formation in sinter with ultrafine hematite concentrates, referred to in the introduction, also reflect differences in concentrate reactivity according to mineralogy. This refers back to the unique characteristics of the RHC, specifically micro-/nano-porosity and significant goethite content, compared with typical hematite concentrates, which are dominated by dense particles with smooth surfaces.

Clearly, from the laboratory granulation tests, the finer Roy Hill concentrate particles are more effective in granulation than the coarser particles from the Canadian concentrate. In practice, the range of particle sizes present in the adhering fines for a sinter plant blend will be wider due to the range of blend components present, but the laboratory tests served to highlight differences in the RHC and CC characteristics. It is interesting to note that while addition of an additional -1 mm adhering fines component in the laboratory tests improved granulation for RHC (increased granule size, more uniform adhering fines layers), this was not the case for the Canadian concentrate, which was dependent on hydrated lime as a binder.

The extremely fine microporosity and significant goethite content of the RHC reflect the more general characteristics of the Roy Hill deposit, albeit with higher grade and hematite content, leading to the unique characteristics of the Roy Hill WHIMS concentrate.

CONCLUSIONS

Laboratory and pilot-scale test work was used to evaluate the granulation and sintering influence of a high-grade Roy Hill WHIMS hematite concentrate on Roy Hill fines. Pot grate sintering tests were carried out on a customer sinter blend containing 25 per cent composite Roy Hill fines with RHC substitution for RHF at three levels, from 9.6 to 16.8 per cent. The blends with RHC required slightly higher granulation moisture, due to finer average blend particle sizing, but resulted in a slight decrease in fuel level, while having minimal impact on yield and TI strength. Although sinter productivity decreased slightly with 9.6 per cent concentrate substitution, this recovered at 16.8 per cent and there is therefore potential for further test work at higher concentrate levels. These outcomes were mirrored in laboratory scale sintering results, which showed that substituting 13.4 per cent RHC for RHF decreased optimum melting temperature, correlating with the observed reduction in fuel requirement for balanced sintering.

Novel laboratory granulation tests confirmed the higher moisture level required to produce granules with the Roy Hill WHIMS concentrate, compared with a coarser-grained Canadian hematite concentrate. This is consistent with the finer sizing, goethite content and internal microporosity of the RHC particles. RHC resulted in improved granulation, measured by average granule size and thicker, more continuous adhering fines layers with smaller void spaces, confirmed by polished section microscopy.

ACKNOWLEDGEMENTS

The authors gratefully acknowledge Roy Hill for funding this work, as well as the permission from Roy Hill and CSIRO to publish. Many thanks to the QCAT sintering team for carrying out the pot grate sintering test work, as well as the contributions by the internal and external reviewers.

REFERENCES

Buswell, J, Bowman, D and Batchelor, J, 2019. Use of strength, hardness and abrasion parameters to increase orebody knowledge and characterisation. *Proceedings, Iron Ore 2019, Perth, 22–24 July*, p. 250–263. (The Australasian Institute of Mining and Metallurgy: Melbourne).

Clout, J M F, 2006. Iron formation-hosted iron ores in the Hamersley Province of Western Australia. Applied Earth Science, 115(4), 115–125.

Clout, J M F and Fitzgerald, B, 2011. The Roy Hill Project. Proceedings, Iron Ore 2011, Perth, 11–13 July, p. 3–10. (The Australasian Institute of Mining and Metallurgy: Melbourne).

Clout, J M F and Manuel, J R, 2003. Fundamental investigations of differences in bonding mechanisms in iron ore sinter formed from magnetite concentrates and hematite ores. Powder Technology, 130, 393–399.

Han, H and Lu, L, 2018. Recent advances in sintering with high proportions of magnetite concentrates. Mineral Processing and Extractive Metallurgy Review, 39(4), 217–230.

Hseih, L-H, 2017. Effect of iron ore concentrate on sintering properties. *ISIJ International*, 57(11), 1937–1946.

Khosa, J S and Manuel, J R, 2007. Predicting granulating behaviour of iron ores based on size distribution and composition. *ISIJ International*, 47(7), 965–972.

Nomura, T, Yamamoto, N, Fujii, T and Takiguchi, Y, 2015. Beneficiation Plants and Pelletizing Plants for Utilizing Low Grade Iron Ore. *Kobelco Technology Review*, 33, 8–15.

Oliveira, V M, de Resende, V G, Domingues, A L A, Bagatini, M C and de Castro, L F A, 2019. Alternative to deal with high level of fine materials in iron ore sintering process. *Journal of Materials Research and Technology*, 8(5), 4985–4994.

Panigrahy, S C and Rigaud, M, 1988. Effect of particle size distribution of specularite concentrates on sinter quality and its influence on the formation of calcium ferrites during sintering. *Steel Research*, 59, 153–160.

Pownceby, M I, Webster, N A S, Manuel, J R and Ware, N, 2016. The influence of ore composition on sinter phase mineralogy and strength. *Mineral Processing and Extractive Metallurgy (Trans IMM Section C)*, 125(3), 140–148.

Saito, K, 2019. Recent research and development topics of iron-making technologies in Nippon Steel Corporation. Proceedings Iron Ore 2019, p 19 (abstract). (The Australasian Institute of Mining and Metallurgy: Melbourne).

Ware, N, Manuel, J, Raynlyn, T and Lu, L, 2013. Melting behaviour of hematite and goethite fine ores and its potential impact on sinter quality. Proceedings, Iron Ore 2013, Perth 12–14 August, p. 485–486. (The Australasian Institute of Mining and Metallurgy: Melbourne).

Ware, N and Manuel, J, 2015. Fundamental nucleus assimilation behaviour of hematite – and goethite-containing ores in iron ore sintering. *Proceedings, Iron Ore 2015, Perth, 13–15 July*. (The Australasian Institute of Mining and Metallurgy: Melbourne).

Wolska, E, 1981. The structure of hydrohematite. *Zeitschrift für Kristallographie*, 154, 69–75.

Wu, S-l, Que, Z-g and Li, K-l, 2018. Strengthening granulation behavior of specularite concentrates based on matching of characteristics of iron ores in sintering process. *Journal of Iron and Steel Research International*, 25, 1017–1025.

Yamaguchi, Y, Umemoto, H, Teraji, S, Hara, M, Morita, Y and Matsumura, M, 2020. Improving granulation of sinter materials by using a wet vertical ball mill. *Nippon Steel Technical Report* No. 123, March, p. 33–41.

Yang, C-c, Zhu, D-q, Pan, J and Shi, Y, 2019. Some basic properties of granules from ore blends consisting of ultrafine magnetite and hematite ores. *International Journal of Minerals, Metallurgy and Materials*, 26(8), 953–962.

CITIC concentrate performance in pelletising and sintering

L Y Yang[1] and Z Wang[2]

1. Head of Technical Marketing, CITIC Pacific Mining, Perth WA 6000.
   Email: lisa.yang@citicpacificmining.com
2. Senior Engineer, New Metallurgy Hi-Tech Group, Beijing China, 100081.
   Email: wzh2450@outlook.com

ABSTRACT

This work presents the fundamental properties of CITIC magnetite concentrate and its performance in pelletising and sintering. CITIC concentrate has been widely used in pelletising to produce pellets for blast furnaces. It is also used in sintering to benefit from its sintering performance.

CITIC concentrate has excellent balling properties owing to its size distribution, particle surface properties, large specific surface area and balling index, leading to strong green pellets and product pellets. When used in sintering at appropriate levels, sinter bed permeability improves, productivity is increased while coke consumption reduces, and sinter strength improves.

INTRODUCTION

Generally, magnetite concentrates are used in Russia, Ukraine, China, USA and Sweden for pelletising, while hematite concentrates are used for pellet production in Brazil. A study carried out by Pan *et al* (2017) on the pelletising of an Australian magnetite concentrate revealed that the concentrate had very good induration properties, leading to significant reduction in induration temperature when it was blended with other concentrates. Due to the fine sizing, blending this Australian concentrate with other concentrates improved its preheating performance. This work focuses on the performance of the CITIC's West Australian magnetite concentrate at every stage of the pelletising process.

Concentrate sintering is very common in China for historical reasons and due to the availability of domestic concentrates. The concentrate ratio in sinter blends can be as high as above 90 per cent in some sinter plants, thus, there is abundant experience with magnetite concentrate sintering in China. Steel mills in Japan, Korea and Taiwan have added concentrates in their sinter blends mainly for sinter chemistry adjustment. As the Fe grade in sinter fines deteriorates, an option to increase sinter Fe is to add high-grade magnetite concentrate in sinter blends. However, Iwami *et al* (2017) found that the magnetite they used caused a reduction in sinter productivity. The fact is that every concentrate is different, and their sintering performance is different. Therefore, the impact of the CITIC concentrate on sintering performance was also studied in detail in this work.

FUNDAMENTAL PROPERTIES OF THE CITIC CONCENTRATE

Chemical compositions and size distribution

A few seaborne concentrate samples, collected from the market, and the CITIC concentrate were analysed by XRF and wet chemistry for FeO. Their chemical composition is given in Table 1. It shows that the CITIC concentrate is high in Fe and contains very low Al_2O_3, P and S, but is high in SiO_2.

TABLE 1

Main chemical compositions of concentrates.

Concentrates	Fe	FeO	SiO_2	Al_2O_3	CaO	MgO	P	S
CITIC	65.12	27.0	8.21	0.23	0.15	0.45	0.017	0.003
Magnetite A	64.93	27.8	8.17	0.18	0.15	0.42	0.040	0.040
Magnetite B	66.58	22.3	4.45	1.20	0.44	0.48	0.009	0.047
Hematite C	64.94	0.10	2.43	1.65	0.04	0.01	0.028	0.008

Size distribution of these concentrates was determined by laser sizer – Mastersizer 3000, and is shown in Figure 1, where the CITIC concentrate has the finest size with p80 of about 35 µm, and the -0.074 mm portion of about 97 per cent. The Magnetite A and Magnetite B samples are coarser than the CITIC magnetite concentrate, while Hematite C is the coarsest.

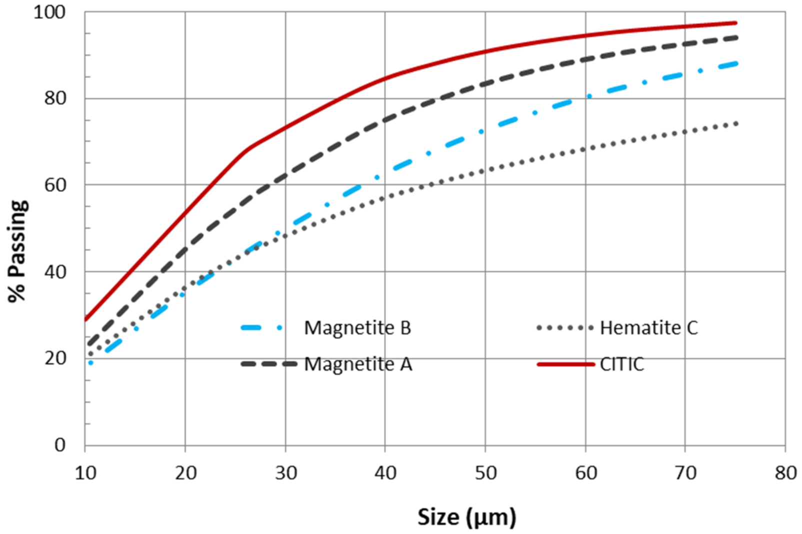

FIG 1 – Size distribution of concentrates.

Specific surface area

Specific surface area is defined as the total surface areas of particles per unit mass. It is an important property related to balling behaviour. Specific surface area of the concentrates was determined by a standard method approved and published by the China National Standardised Management Committee (2008). Table 2 lists the specific surface area of the concentrates studied in this work. Clearly the CITIC concentrate has the largest specific surface area of the four concentrates, implying that it has very good balling properties.

TABLE 2

Specific surface area of the concentrates.

Concentrates	**Density, g/cm^3**	**Specific surface area, cm^2/g**
CITIC	4.59	2043
Magnetite A	4.68	1633
Magnetite B	4.82	1409
Hematite C	4.70	1604

Mineralogy and morphology

Green ball strength is dependent on size distribution and hydrophilic properties of concentrate, as well as the particle shape and particle surface roughness. Mineralogy of CITIC concentrate was studied using X-Ray diffraction and scanning electronic microscopy (SEM). The results confirm that the CITIC concentrate mainly consists of magnetite (>90 per cent), a small amount of hematite, with quartz being the main gangue mineral. CITIC concentrate particles are irregular and rough, and some needle like, as shown in Figure 2. During the balling process, large and small particles readily combine to form balls, and also tend to interlock to increase green ball strength.

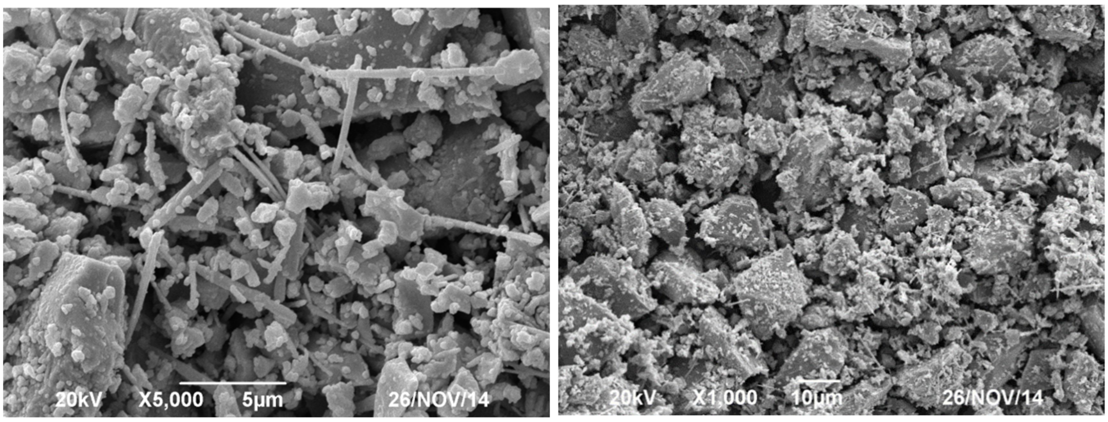

FIG 2 – CITIC concentrate particle morphology.

CITIC CONCENTRATE PERFORMANCE IN PELLETISING

Balling properties

The balling index reflects the ability of a concentrate to form balls under mechanical force when water (and adhesive agent) is added to the concentrates. Capillary moisture, related to particle structure, plays an important role in ball formation while molecular moisture, related to concentrate size distribution and specific surface area, largely determines green ball strength. The static balling index K is determined by both capillary moisture and molecular moisture and calculated by equation $K=W1/(W2-W1)$, where W1 is the maximum molecular moisture; W2 the maximum capillary moisture. Therefore, the balling index can be considered to be an overall index determined by many concentrate properties. Generally, concentrates with smaller size distribution, rougher particle surface and larger specific surface areas have a larger balling index. The higher the index, the stronger ability to form balls, ie the better balling properties.

The measured static balling indexes of a few iron ore concentrates are given in Table 3, showing that the CITIC concentrate has the largest balling index, which is line with the predicted trend from the specific surface area results listed in Table 2.

TABLE 3

Balling properties of the CITIC concentrate.

Concentrates	Max capillary moisture, %	Max molecular moisture, %	Static balling index
CITIC	16.9	8.1	0.93
Magnetite A	15.2	7.0	0.85
Magnetite B	14.2	6.0	0.73
Hematite C	14.3	6.0	0.71

Balling and drying behaviour

Pellets were made from a mix of concentrate and bentonite in a disc pelletiser 0.8 m in diameter and 0.2 m rim depth and inclined at 45° to the horizontal. A small amount of the mix was added to the disc pelletiser, rotating at 28 rev/min, to make pellet 'seeds'. The seeds were moistened with water mist to retain moisture content while adding additional material to enlarge them into pellets. The diameter of the finished green pellets was confined to 8–16 mm by screening. Green ball strength was evaluated with compressive strength and drop number. The procedure for drop number measurement was as follows: a single freshly made green pellet was dropped repeatedly from a height of 0.5 m onto a steel plate until it fractured, or for a maximum of 20 drops if no fracture occurred, and the number of drops was recorded. The drop number is the average of the tests for 30 balls. The compressive strength of the green pellets was determined by the following procedure: a single freshly made green pellet was compressed by a standard compression test machine until it fractured, and the load was recorded. Compressive strength is the average of the load at which green balls fracture for 30 balls.

Green ball strength impacts on product pellet strength and more importantly needs to be high enough to ensure smooth completion of the next stages of the pelletising process, such as drying, pre-heating and induration. Work was then carried out to optimise bentonite and water addition to maximise green ball strength. Figure 3 shows the impact of bentonite addition to green ball strength. As bentonite increases from 0.5 per cent to 1.2 per cent, green ball strength increases, and moisture required increases accordingly. At 1 per cent bentonite, compressive strength is 1.17 kg/p and drop number is 4.8 times, which meets the requirements of the pelletising process.

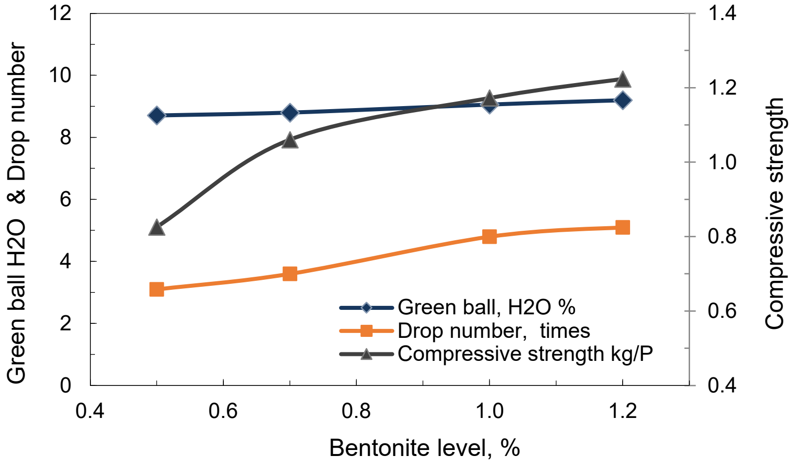

FIG 3 – Impact of bentonite level on green ball strength for the CITIC concentrate.

During pelletising, green pellets go through relatively low temperatures first to dry before going through pre-heating and induration at higher temperatures. It is important for green pellets to survive the drying process without breakdown. Cracking temperature, at which pellets crack/breakup during heating, is used to describe this property of the pellets. Cracking temperature provides guides for the selection of drying and preheating parameters in pelletising.

Fifty green balls of 10–12 mm diameter loaded into a basket were hung in a vertical tube furnace with flowing air at 1.5 m/s and were heated under a given temperature. The temperature at which 4 per cent of green pellets crack or fracture is defined as the cracking temperature. Table 4 lists the cracking temperatures for pellets from the CITIC concentrate at different bentonite levels together with green ball and dry ball strength. The cracking temperature increases with increasing bentonite. At 1 per cent bentonite, the cracking temperature was 550°C for pellets produced from the CITIC concentrate, which meets the production requirements.

TABLE 4

Green pellet strength and cracking temperature for CITIC concentrate.

Bentonite %	Moisture %	Drop number times	Compressive strength kg/p	Cracking temperature °C
0.5	8.71	3.1	0.87	500
0.7	8.80	3.5	1.12	500
1.0	9.06	4.8	1.24	550
1.2	9.20	5.1	1.30	550

Magnetite A and Magnetite B were studied in the same way as the CITIC concentrate. The results are listed in Table 5 for comparison. The optimal bentonite level is the lowest for the CITIC concentrate, again confirming the excellent balling property of the concentrate, while Magnetite A and Magnetite B need 1.5 per cent and 2.1 per cent bentonite respectively. Hematite C needs

1.6 per cent bentonite for optimal balling. At 1 per cent bentonite addition for the CITIC concentrate, green pellet strength and cracking temperature are high enough for the pelletising process, while pellets produced from the other three concentrates have higher cracking temperatures at the optimal moisture and bentonite levels.

TABLE 5

Green pellet strength and cracking temperature for different concentrates.

Concentrates	Optimal bentonite level %	Moisture %	Drop number times	Compressive strength kg/p	Cracking temperature °C
CITIC	1.0	9.06	4.8	1.17	550
Magnetite A	1.5	8.82	5.1	1.09	600
Magnetite B	2.1	8.76	5.3	1.11	700
Hematite C	1.6	10.58	5.0	1.19	580

Induration

Induration tests were carried out at various temperatures for 20 min for the pellets from the concentrates studied in this work, followed by compressive strength determination for product pellets. The results are given in Figure 4. Pellets from the three magnetite concentrates require relatively low induration temperatures of around 1200°C while hematite C needs to fire at a minimum of 1350°C to attain adequate physical strength. This is the main reason why magnetite concentrate pelletising consumes significantly less energy compared to hematite.

Among the magnetite concentrates, CITIC concentrate pellets gain the highest strength at a given induration temperature, eg reaching 204 kg/p at 1100°C, suggesting that CITIC concentrate pelletising has a lower induration temperature and consumes less energy than the other magnetite concentrates. This is because green pellets produced from the CITIC concentrate have higher compressive strength due to its excellent balling properties, making product pellets stronger at a given temperature. Thus, CITIC concentrate has excellent induration property. As expected, hematite pellets from Hematite C need much higher induration temperature for adequate strength compared to the three magnetite pellets.

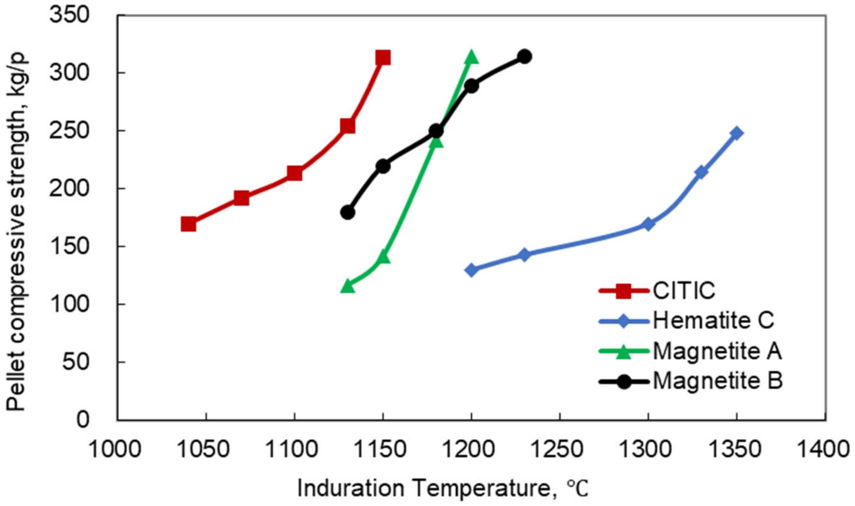

FIG 4 – Temperature impact on strength of product pellets.

Besides compressive strength, pellet hot strength such as reduction degradation index (RDI) and reduction swelling index were examined for pellets made from the three magnetite concentrates. The results, listed in Table 6, confirm that the pellets produced from the CITIC concentrate had high strength during the reduction process, although all pellets have relatively low swelling index and RDI.

TABLE 6

RDI and Swelling index for pellets from concentrates in Table 1.

Pellet	Reduction swelling index, %	RDI, % -3.15 mm
CITIC	9.6	1.8
Magnetite A	7.5	4.4
Magnetite B	10.8	3.3

CITIC CONCENTRATE PERFORMANCE IN SINTERING

Granulation properties of CITIC concentrate

Ore blends used in this study were designed to simulate most of the Chinese sinter plants, as shown in Table 7, where CITIC concentrate was added to blends consisting of Australian fines and Brazilian fines. When finer materials are added to courser fines, the blend granulation could be an issue, so this was studied first.

TABLE 7

Ore blends for sinter pot studies.

Blend	1 Base	2 10%CITIC	3 20%CITIC	4 30%CITIC
CITIC	0	10	20	30
Australian hematite fines	20	18	16	14
Australian goethite fines	40	36	32	28
Brazilian fines	40	36	32	28

Size distribution of the sinter mix is presented in Figure 5 by classifying as nuclei particles (+2 mm), adhering fines (-0.25 mm) and intermediate particles (0.25–2 mm). CITIC concentrate addition increases the portion of adhering fines in the mix. This change is expected to benefit granulation particularly when coarse sinter fines are dominant in blends.

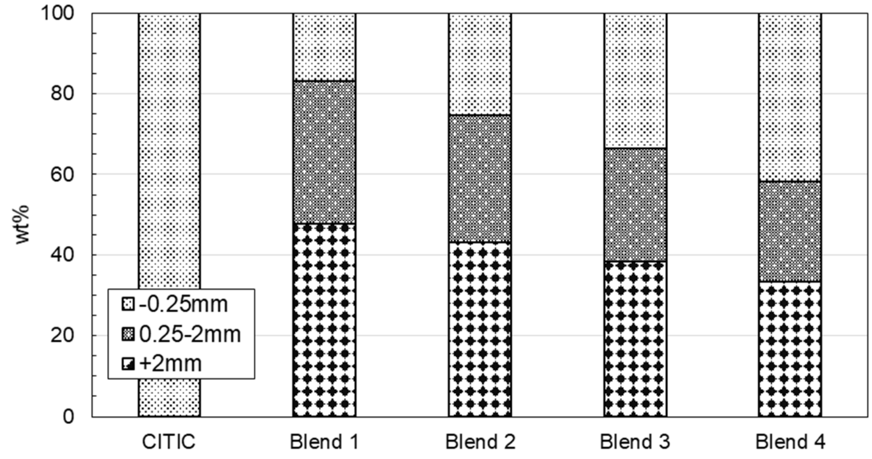

FIG 5 – Size distribution of sinter mix.

Granulation of these four blends were studied by determining the bed JPU (Japanese Permeability Unit) – an index reflecting bed permeability – by a standard method. JPU was calculated using the equation JPU $=F/A \times (H/S)^{0.6}$, where F is air flow rate, m^3/min; A is cross area, m^2; H is bed height, mm; S is suction, mmH_2O. Figure 6 shows the relationship between mix moisture and bed JPU. As the amount of the CITIC concentrate in the blend increases, ie from Blend 1 (no CITIC) to blend 4 with 30 per cent CITIC concentrate, the optimal moisture increases slightly, and importantly, bed permeability improves. This confirms that CITIC magnetite concentrate enhances granulation and improves bed permeability, although it is an ultra-fine concentrate. This is a paradigm switch in some degree in relation to concentrate sintering. This is probably due to the increase in adhering fines, and particularly due to the decrease of intermediate-sized particles in the sinter mix, as displayed in Figure 5. Importantly, the good granulation property of the CITIC concentrate is a result of its very large specific surface area and superb balling properties discussed earlier.

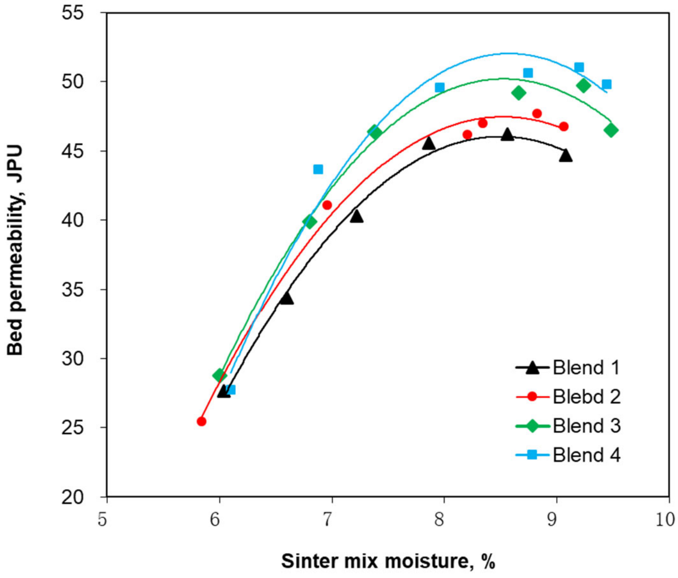

FIG 6 – Bed permeability for the 4 blends.

Pseudo particles after granulation were examined under the reflected light microscope to study the granule structures. A typical granule structure is displayed in Figure 7, where ultrafine particulates adhere on the outer layer of large particles. As the CITIC concentrate level increases, the adhering fines portion of the sinter mix increases, which can accommodate more intermediate particles in the adhering fines layer of granules. In addition, the granules tend to become more spherical as more adhering fines are available. Since the CITIC concentrate has a very fine particle size distribution, the granules formed are dense. These are the main factors contributing to the improved bed permeability, and therefore, sintering performance.

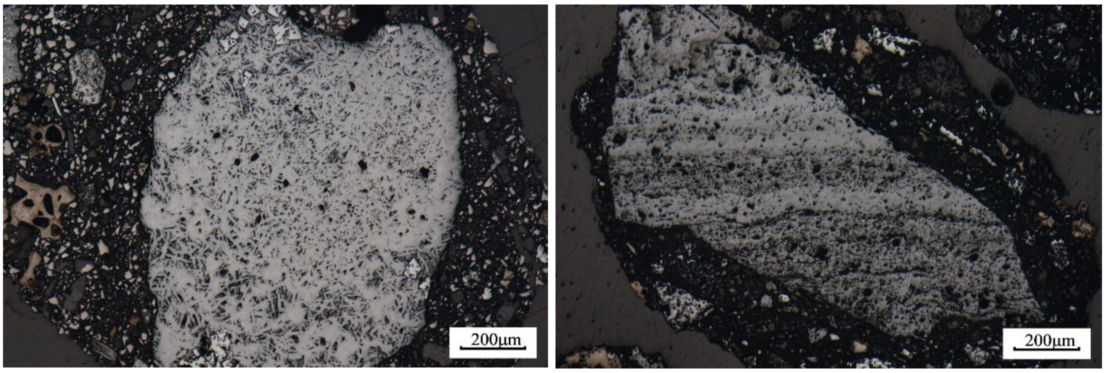

FIG 7 – Granule structure.

The particle size distribution of the sinter mix after granulation was determined by freezing the sinter mix using liquid nitrogen followed by screening the frozen mix. The results are presented in Figure 8, showing that the +3 mm portion in the sinter mix increased with increasing CITIC concentrate, and again confirming improved granulation. This is why bed permeability was also improved (Figure 6).

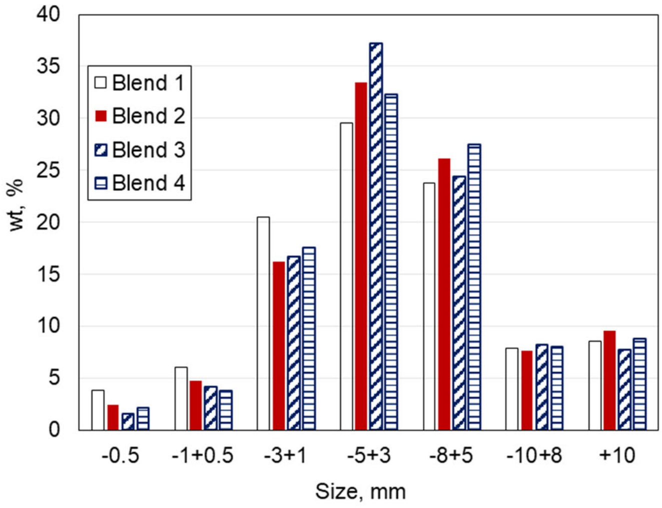

FIG 8 – Sinter mix size distribution after granulation.

Sinter pot tests

Sinter pot tests were carried out on the blends listed in Table 7 to examine the CITIC concentrate performance in sintering, under standard conditions, ie bed height 600 mm, ignition temperature 1150°C, ignition time 90 sec and sintering suction 1450 mmH_2O. A number of pot tests were conducted for each blend under various coke rates and moisture levels to optimise coke and water addition. Sinter productivity, under the optimal coke and moisture levels, increased when 10 per cent CITIC concentrate was added to the ore blend, as did sintering speed (Figure 9). There was no significant change in productivity when the CITIC concentrate level was raised to 30 per cent. The Base blend without CITIC concentrate showed the lowest productivity. The improved bed permeability, discussed earlier, leads to higher flame front speed and ensuring productivity improvement; the improved bed permeability with CITIC concentrate addition also enables charge weight to be increased for a given sinter pot volume – another reason for increased productivity. The same trend has been observed by many sinter plants using CITIC concentrate.

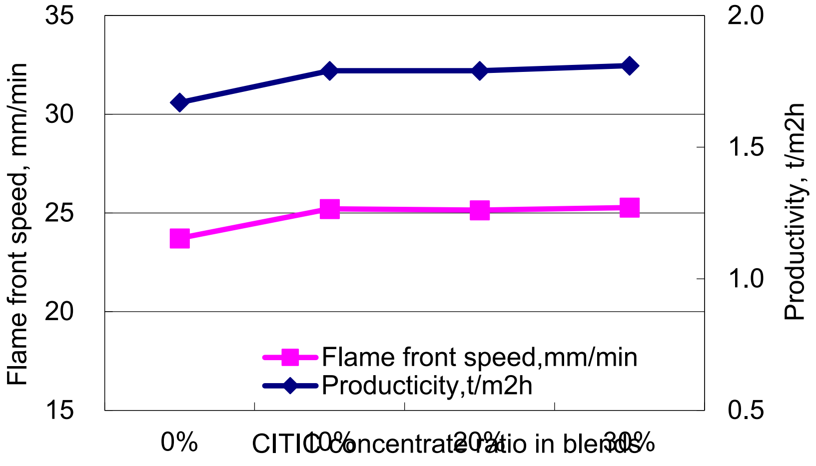

FIG 9 – CITIC concentrate impact on sinter productivity.

Due to the exothermic nature of magnetite, the coke rate drops as the proportion of the CITIC concentrate increases in the blend, providing extra energy saving to steel mills, as shown in Figure 10, eg 64 kg/t coke consumption for the Base blend versus 58 kg/t coke rate for Blend 4 with 30 per cent CITIC concentrate. Sinter strength shows a consistent increase even under reduced coke rate, eg sinter tumble index increasing to 69.0 per cent for Blend 4 containing 30 per cent CITIC concentrate from 66.7 per cent for the Base blend with no CITIC concentrate. Meantime, sinter abrasion also improves with CITIC concentrate addition, ie from 6.4 per cent for the Base blend to 5.8 per cent for Blend 4. This is probably because CITIC concentrate acts as adhering fines, which are oxidised more readily and react with fluxes to form bonding phases during sintering, thus, the addition of CITIC concentrate leads to a texture with better bonded particles and therefore stronger sinter.

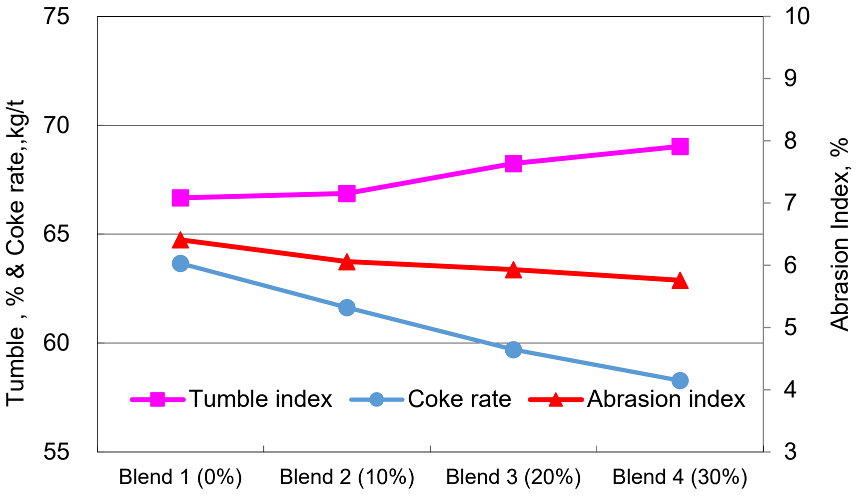

FIG 10 – CITIC concentrate impact on coke rate and sinter strength.

Sinter high temperature properties such as reducibility and RDI are presented in Figure 11 and Figure 12 respectively. Sinter reducibility remains almost unchanged and sinter RDI improves with an increasing proportion of the CITIC concentrate in the sinter blend.

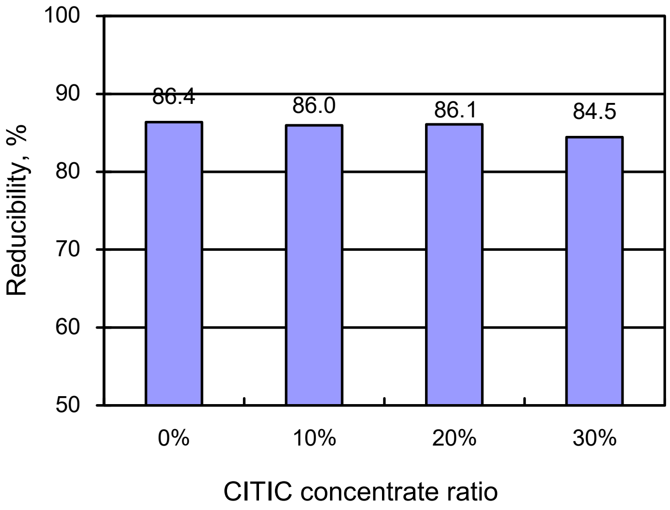

FIG 11 – CITIC concentrate impact on sinter reducibility.

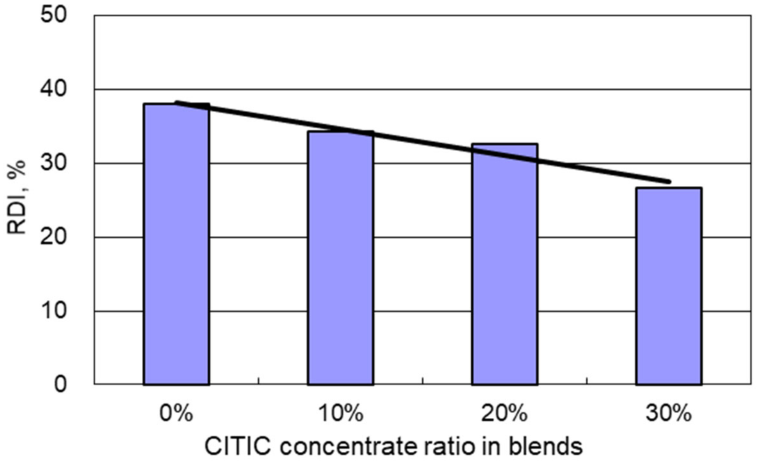

FIG 12 – CITIC concentrate impact on sinter RDI.

The sinter samples were examined under reflected light microscope to study their mineral phases and textures. The proportion of mineral phases was determined by the point-counting technique, and the results are presented in Figure 13. The sinter mineral abundance only shows slight changes, while observations confirm fewer large pores and fewer thin wall textures in sinters with an increasing proportion of the CITIC concentrate. Furthermore, sinter blends containing CITIC concentrate form sinter with a relatively higher proportion of the SFCA and magnetite bonding structures with smaller pores.

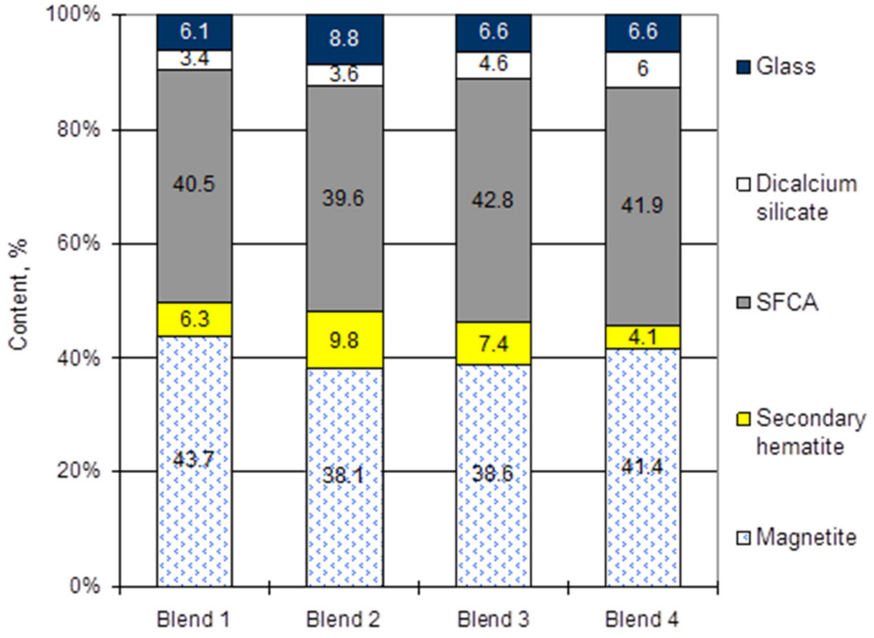

FIG 13 – CITIC concentrate impact on sinter mineral abundance

Obviously, oxidation and granulation are two key aspects in sintering of magnetite concentrates. Since magnetite concentrate is fine in size, naturally, it is perceived that magnetite concentrate has a detrimental impact on sinter mix granulation. This is true for many magnetite concentrates, so efforts have been made to investigate ways to improve magnetite concentrate granulation, such as blending with hematite fines (Adam *et al,* 2017), separate granulation (Matsumura *et al,* 2019), and segregation (Iwami *et al,* 2017). Distinct from many other magnetite concentrates, the CITIC concentrate has very good granulation properties. Test data shows that at blending rations below 30 per cent in sinter blends, CITIC concentrate actually improves sinter mix granulation (Figure 6), which is a key reason why CITIC concentrate improves sintering performance. The good granulation property of CITIC concentrate is explained by its large specific surface area and excellent balling property. Of course, if the concentrate ratio is too high, granulation will be expected to be impacted.

Oxidation is important in magnetite sintering in order to benefit from its exothermic property. Oxidation enables heat to be released to lower energy consumption, and assimilation to be enhanced for SFCA formation. There are many studies on the oxidation process and ways to promote oxidation (Han and Lu, 2017; Yang and Matthews, 1997). Actually, enhancing oxidation is an important stage of assimilation promotion (Morioka, Matsumura and Okazaki, 2019). The key for magnetite to be oxidised is to expose magnetite particles to oxygen, therefore, when magnetite concentrate ratio is low in the blends, oxidation is expected to be more complete. On other hand, when ore blend is rich in magnetite concentrate, magnetite particle exposure to oxygen may be limited and the degree of oxidation is expected to be lower.

Blending is often the best way to use magnetite concentrate effectively to maximise its benefits. Studies have been done on blending magnetite concentrates with hematite ores and goethite ores (Yang *et al*, 2019; Yang, Witchard and Yu, 2000; Yang and Jelenich, 2002; Yang, 2005). Different types of ores are complementary to each other, enabling the metallurgical value of each ore to be maximised if an optimum blend ratio can be established. Typically, around 10–15 per cent of CITIC concentrate is blended with hematite and goethite fines in sinter plants.

CONCLUSIONS

The CITIC magnetite concentrate is a quality feed for both pelletising and sintering. It contains 65 per cent Fe and very low Al_2O_3, P and S. However, the SiO_2 content is high, which may limit its use in some cases. It has a very fine particle size distributions with -0.074 mm of 97 per cent. The CITIC concentrate has a very high specific surface area, large balling index and excellent balling properties, which lead to strong green ball strength.

When used in pelletising, the CITIC concentrate produced the strongest green pellets, even with the lowest bentonite addition, compared to the other concentrates studied in this work, due to its superb balling properties. Product pellets produced from CITIC concentrate had the highest strength under the same induration conditions, implying even more energy can be saved compared to other magnetite concentrates.

When used in sintering at appropriate ratios, the CITIC concentrate improved sinter mix granulation efficiency and sinter bed permeability, thus, leads to increasing flame front speed and sinter productivity. Sinter strength was improved even with a reduced coke rate. Typical blending ratios of CITIC concentrate are observed to be 10–15 per cent in sinter plants.

ACKNOWLEDGEMENTS

The authors would like to thank CITIC Pacific Mining management for permission to publish this work.

REFERENCES

Adam, M, Addai-Mensah, J, Begelhole, J, Quast, K and Skinner, W, 2017. Enhancing magnetite concentrate granulation by blending with hematite ore, in *Proceedings Iron Ore 2017*, pp 17–23, (Australasian Institute of Mining and Metallurgy: Melbourne)

China National Standardisation Management Committee, 2008. GB/T 8074–2008. Testing method for specific surface of cement (in Chinese)

Han, H and Lu, L, 2017. Sintering technologies of sinter mixtures containing high proportions of magnetite concentrates, in *Proceedings Iron Ore 2017*, pp 31–38, (Australasian Institute of Mining and Metallurgy: Melbourne)

Iwami, Y, Yamamoto, T, Oyama, N, Matsuno, H, Saito, N and Nakajima, K, 2017. Improvement of sinter productivity by control of magnetite ore segregation in sintering bed, in *Proceedings Iron Ore 2017*, pp 61–67, (Australasian Institute of Mining and Metallurgy: Melbourne)

Matsumura, M, Takayama, T, Hara, K, Yamaguchi, Y, Ishiyama, T, Huguchi, K and Nomura, S, 2019. Separate granulating efficiency for sinter strength and reducibility based on promotion of magnetite ore oxidation, in *Proceedings Iron Ore 2019*, pp 127–139, (Australasian Institute of Mining and Metallurgy: Melbourne)

Morioka, A, Matsumura, M and Okazaki, J, 2019. Promoting assimilation of magnetite mine ore for CO_2 reduction from sintering process, in *Proceedings Iron Ore 2019*, pp 140–144, (Australasian Institute of Mining and Metallurgy: Melbourne)

Pan, J, Hu, X, Zhu, D and Yang, C-C, 2017. Pelletising performance of Western Australian ultra-fine magnetite concentrate and strengthening technique by optimising ore matching, in *Proceedings Iron Ore 2017*, pp 97–103, (Australasian Institute of Mining and Metallurgy: Melbourne)

Yang, C, Zhu, D, Pan, J, Li, Q and Lu, L, 2019. Influence of the magnetite concentrate properties on sintering performance of magnetite-hematite-goethite iron ore blends and sinter quality, in *Proceedings Iron Ore 2019*, pp 182–188, (Australasian Institute of Mining and Metallurgy: Melbourne)

Yang, L X and Jelenich, L, 2002. Blending Australian ores and Chinese ores for sintering, in *Proceedings 61st Ironmaking Conference,* pp 759–774*, (Iron and Steel Society of America: Nashville)*

Yang, L X, 2005. Sintering fundamentals of magnetite alone and blended with hematite and hematite/goethite ores, *ISIJ International*, 45, 469–476

Yang, L X, and Matthews, E, 1997. Oxidation and sintering of magnetite ore under oxidizing conditions, *ISIJ International*, 37, 885–861

Yang, L X, Witchard, D and Yu, Z N, 2000. Introduction of pisolitic goethite ore into a Chinese ore blend, *ISIJ International*, 40, 647–653

Sustainability and climate change

Sintering for emissions reduction

G S Beros[1]

1. Senior Manager Technical Marketing, Fortescue Metals Group Limited, East Perth WA 6004.
   Email: gberos@fmgl.com.au

ABSTRACT

In 2019 the Chinese Ministry of Ecology and Environment issued guidelines promoting the implementation of ultra-low emissions in the iron and steelmaking industry. These guidelines aim to drive improvements in air quality through the reduction of particulate matter (PM), sulfur dioxide (SO_2) and nitrogen oxide (NO_x). Secondly, it also represents an initial means to commence decarbonisation of the industry. The ultra-low emissions guidelines propose that well over 80 per cent of China's production capacity will achieve these targets by 2025.

In response, many sintering operations have implemented numerous improvements to the process that result in significant efficiency gains. Of note is the adoption of deep bed sintering where, with some modifications to equipment, the sintering bed depth is increased resulting in sizable reductions of SO_2 and NO_x emissions.

This paper will also provide an overview of the requirements to introduce deep-bed sintering into an operation and highlight test work completed which quantifies the resultant reduction in emissions.

INTRODUCTION

Fortescue Metals Group Limited (Fortescue) operates in the Pilbara region of Western Australia. As shown in Figure 1, there are five mine sites; Cloudbreak and Christmas Creek located in the Chichester Hub together with Kings and Firetail in the Solomon Hub. From December 2020 Fortescue also commissioned its new major mine and infrastructure project at Eliwana, located in the Western Hub. Eliwana will supply iron ore for contribution into Fortescue's West Pilbara Fines (WPF) product and will gradually replace iron ore from Firetail mine which is nearing the end of its mine life.

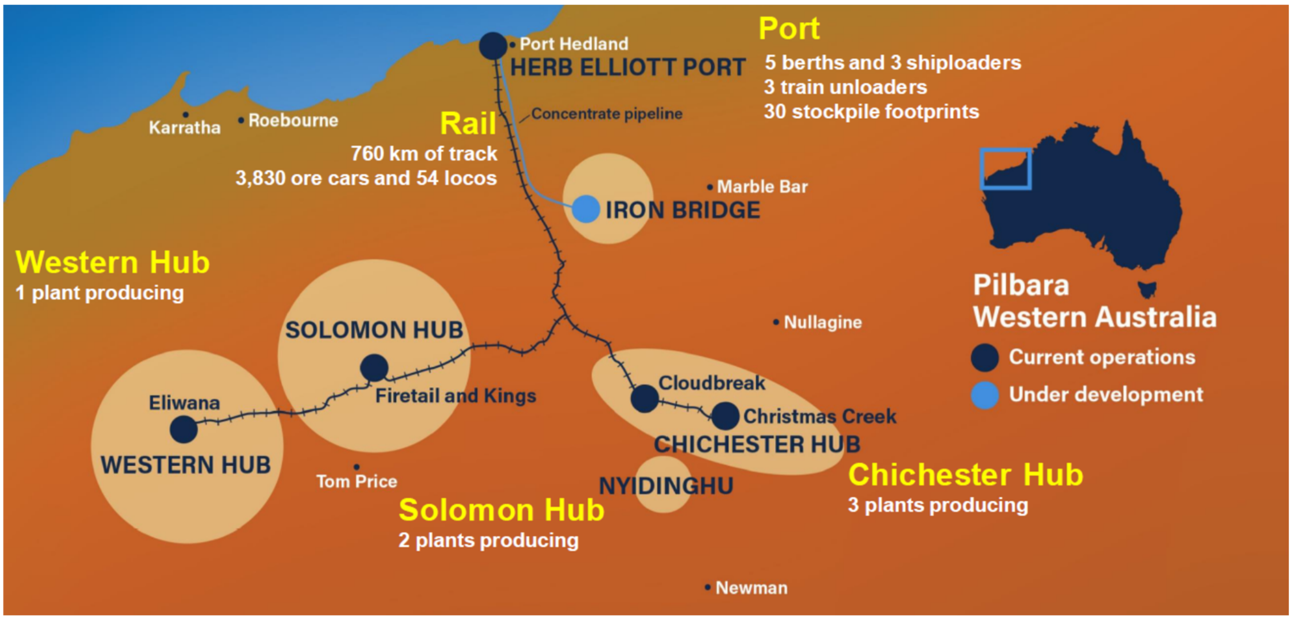

FIG 1 – Location of Fortescue's Operations.

During the June 2021 quarter, Fortescue completed the technical and commercial assessment of the Iron Bridge Magnetite project, a joint venture between Fortescue's subsidiary FMG Iron Bridge and Formosa Steel IB. The capital estimate has been revised to US$3.3 billion to US$3.5 billion which includes Fortescue's share of US$2.5 billion to US$2.7 billion. When completed, the project will deliver 22 Mt per annum of high-grade 67 per cent iron (Fe) magnetite concentrate. First production is scheduled for December 2022 followed by a ramp up period of 12 to 18 months.

Fortescue own and operate the rail and port infrastructure which has 760 km of rail linking the five mines and five berths at Port Hedland. This system is highly efficient and between 15 to 16 trains per day make the journey with a payload of approximately 35 000 t each. The port operations have three inload and three outload circuits where final product stockpile blending is undertaken prior to ship loading and delivery to our customers. For FY21, Fortescue shipped a record 182.2 Mt (wet).

CHINESE STEEL INDUSTRY CARBON REDUCTION

China has committed to a carbon-neutral future by 2060. According to experts, the country's steel industry will play an important role in achieving this goal of reducing emissions by:

- upgrading and modernising facilities,
- increasing the usage of steel scrap in steelmaking, and
- adopting hydrogen-based technologies.

The Chinese government has also indicated that it expects its carbon dioxide (CO_2) emissions to peak before 2030. To accompany this, the China Metallurgical Industry Planning and Research Institute indicated that the Chinese steel industry is working on a plan to peak its emissions by 2025 and reduce them by 30 per cent through to 2030.

In 2019, the Chinese Ministry of Ecology and Environment issued guidelines promoting the implementation of ultra-low emissions in the iron and steelmaking industry. These guidelines aim to drive improvements in air quality through the reduction of PM, SO_2 and NO_x. Secondly, it also represents an initial means to commence decarbonisation of the industry. The ultra-low emissions guidelines propose that well over 80 per cent of China's production capacity will achieve these targets by 2025.

ULTRA-LOW EMISSIONS GUIDELINES

Background Studies

There have been many background studies on the pollution, emissions and air quality emanating from the iron and steel industry which have assisted framing China's ultra-low emissions guidelines (ULEG's). One such study co-authored by Wu *et al* (2015) was entitled 'Primary Air Pollutant Emissions and Future Prediction of Iron and Steel Industry in China' and through an examination of the iron and steelmaking process chain determined:

- ~50–70 per cent of SO_2 comes from the oxidation of sulfur in coal and coke from sintering and pelletising processes.
- ~45–65 per cent of NO_x generation from sintering and pelletising is formed by the reaction between nitrogen with oxygen from air at high temperature and the solid fuel.
- the level of PM is dependent on the uncontrolled emissions from the overall process and the effectiveness of installed control devices.
- coke ovens, sintering and pelletising processes are the major sources of volatile organics (VOC's) and dioxins, generally from fuels.

Guideline scope

The scope of the ULEG's includes all production links commencing with the raw material yard, followed by the processing routes of sintering, pelletising, coking, ironmaking, steelmaking and steel rolling.

As evident from Table 1, the guidelines are very specific to sections within each unit operation. So, for example, the hourly average emission concentrations of PM, SO_2 and NO_x in flue gas of a sintering machine head and pellet roasting or induration plant are not higher than 10 mg/m^3, 35 mg/m^3 and 50 mg/m^3, respectively. To meet the requirement, the average hourly emission concentration should be achieved at least 95 per cent of the time per month.

TABLE 1

Target Average Emission Concentrations (mg/m^3).

Process	Facility	Reference O_2 content	Pollutants		
			PM	SO_2	NO_X
Sintering and Pelletising	Head of Sinter Machine, Pellet Shaft furnace	16	10	35	50
	Grate Kiln, Travelling Grate	18	10	35	50
	Tail of Sinter Machine, Other facilities	-	10	-	-
Coke Making	Coke oven chimney stack	8	10	30	150
	Charging coal and pushing coke	-	10		-
	Coke discharge quenching	-	10	50	-
Iron Making	Stove		10	50	200
	Casting house and bin system	-	10	-	-
Steel Making	Hot metal pre-treatment, Converter (Secondary gas), Electric Arc Furnace (EAF), Lime Kiln, Dolomite Kiln	-	10	-	-
Rolling	Heat treating furnace	8	10	50	200

The production specific nature of the guidelines encourages producers to review processing inputs and operating conditions. For example:

- sintering, pelletising, ironmaking, coking and other processes of material crushing and screening, blending and mixing should operate under closed cover and/or be equipped with dust removal facilities.
- throughout the entire integrated process, the construction of gas collection and scrubbing plants should be installed to ensure that no visible smoke and dust escapes.

Regarding specific pollutants, many mills adopt the following mitigation practices:

- decreasing solid fuel rate and increasing basicity can reduce the emission of SO_2.
- increasing bed height and basicity can reduce the emission of NO_X. It is also important to control the nitrogen level of coke breeze and anthracite.
- installing covered storage yards and dust scrubbing systems to contain particulate matter emissions.
- while VOC's and dioxins are not formally covered by the ULEG's and no target levels have been established for their mitigation, many mills still aim to improve concentration levels by installing effective methods to collect dust and scale, improving the quality of raw materials purchased and switching to dry quenching of coke.

Tangshan City

Tangshan City, with ~180 Mtpa installed pig iron capacity, has been heavily impacted by the ultra-low emission policy. Mills have been enforced with various production restrictions on an ongoing basis since last winter (December 2020). The emissions reduction is met by a combination of:

- production cuts.
- changing raw materials mix.
- increased use of equipment for improved emissions control.

It can be seen from Table 2 that each of the 25 mills in the Tangshan area are placed into various categories according to their measured emissions levels. Category A comprise the operations that have met the ultra-low emissions target guidelines. At the other end of the scale are the Category D operations which have the highest emissions levels. Many of the Category D mills were closed for extended periods of time during the 2020–2021 winter season.

TABLE 2

Emissions category and production curtailment.

Category	# Mills	Production cut
A	2	0%
B	6	30%
C	8	30%
D	9	30%

Following the centenary celebrations of the formation of the Chinese Communist Party, the latest advice for the Tangshan iron and steelmaking hub is that all mills are required to reduce production by 30 per cent through to December 31st, 2021. However, the two mills in Category A are exempt from these product reductions. Both mills have adopted deep-bed sintering techniques to reduce their emissions and achieve the ultra-low emissions targets.

DEEP-BED SINTERING

Deep bed sintering is an increasingly used technology, which has advantages of:

- improving sinter strength.
- increasing sinter yield and productivity.
- reducing fuel consumption and therefore CO_2 emissions.

The technology has been made possible by improved sinter feed preparation, particularly with granulation and mixing. Improved granulation is achieved where an operator reoptimises moisture addition together with using higher quality quicklime to promote an improved nuclei formation and assimilation. About five to ten years ago, a bed depth of between 650 mm to 750 mm was considered a ‘deep sinter bed’. Today there are many sinter plant operations utilising bed depths of between 900 mm to 1000 mm.

Deep bed sintering allows the sinter bed to be maintained at elevated temperatures for a longer period which assists in improving the inherent strength of sinter and enhancing its resistance to particle degradation. Therefore, increasing the bed depth in the sinter plant will not only lower fuel consumption but also improve overall product quality. To increase the trolley wall height to the desired bed depth, some operations may have to raise the ignition hood.

As indicated above, many sinter plants now operate with bed heights more than 750 mm and up to 1000 mm. Because the length of the sinter strand remains fixed, to accommodate the extra height, the speeds of the machine strand and wind boxes must be reprogramed. A sinter bed press, shown in Figure 2, is also installed to gently compact the sinter bed enabling a more uniform flame-front distribution and propagation resulting in an improved melt formation.

FIG 2 – A deep sinter bed fitted with a bed press in operation.

Wang *et al* (2013) published the experience of Shougang Jingtang Iron and Steel plant applying deep bed sintering techniques to two, 500 m^2 sintering machines at Caofeidian Port, Hebei where the sinter bed depth was increased from 750 mm to 860 mm during 2009. The paper provided many engineering insights of the modifications required for converting a sinter plant to a deep-bed process. Due to the extended heating time and higher temperatures created by deep-bed sintering, it was recommended that when adapting the sinter pallet car, consideration is given to the overall pallet structure and materials selection. Through a process of effective management and operation coupled with ongoing continuous improvement, Shougang Jingtang was able to demonstrate that:

- Increasing the sinter bed depth resulted in higher product volume, sinter quality and a lower energy consumption. Benchmarking the Jingtang sinter machines against similar domestic operations, productivity increased by 0.13 t/m^2/h, tumble strength increased by 3.81 per cent +6.3 mm and solid fuel decreased by 11.15 kgce/t. As a result, a significant reduction in SO_2 emissions was achieved.
- Successful development and implementation of various automatic closed loop control systems for sintering alkalinity (basicity), sinter mixture moisture and carbon content together with sinter machine and windbox speeds were essential in achieving the above process improvements.

SUITABLE ORES FOR DEEP-BED SINTERING

Chinese mills who have adopted deep-bed sintering consistently provide feedback that Fortescue ores with its coarse particle sizing, which assists deep bed permeability, and its mineralogy are well suited to the process.

Particle sizing

Liu *et al* (2020) commented that the granulation of a sinter mixture for deep bed-sintering is directly related to the particle size of the raw materials. If the particle size of the iron ore is too fine, the number of nuclear particles is insufficient and the bulk density in the sinter mixture layer increases. This has the effect of deteriorating air permeability and flame propagation throughout the sinter mixture layer, leading to poor sinter productivity and quality. Many Chinese sinter plants use local iron ore concentrates and blend them with imported iron ores. The level of fine iron concentrates and imported iron ores is heavily dependent on the overall granulation performance of a particular blend. In the example provided by Liu *et al* (2020), Tiangang United Special Steel, who operate their sinter plants with a 1000 mm bed depth, control the proportion of iron ore concentrates with a particle size of less than 1 mm at 12 per cent.

Fortescue's iron ore sinter fines products have preferable particle sizing as our wet beneficiation processes creates a product with favourable sizing attributes (Clout, 2013). Fortescue's iron ore sinter fines products dominate the high +6.3 mm and low -0.15 mm percentage product segment, which is shown in the top left-hand side in Figure 3.

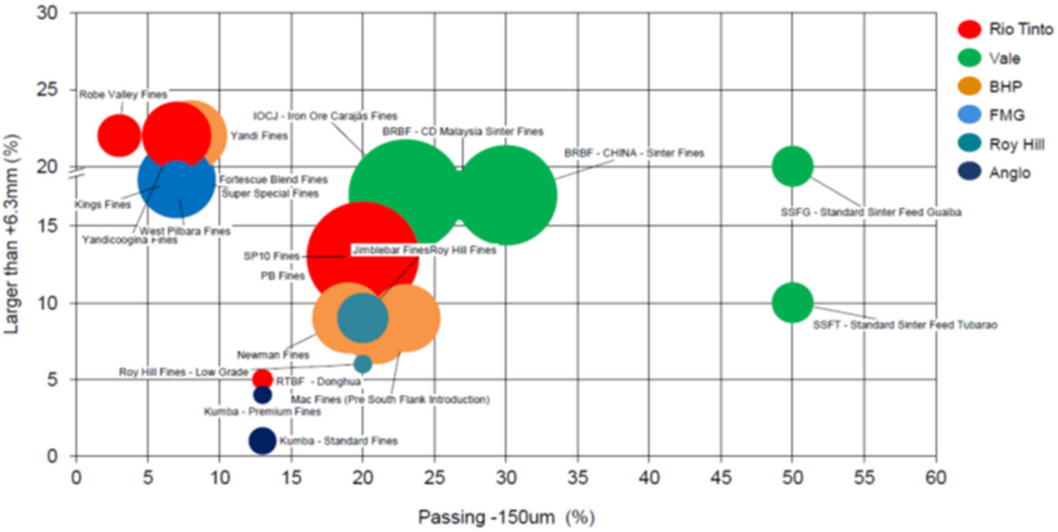

FIG 3 – Global fines particle sizing.

Fortescue's coarse sizing advantage enables many customers, particularly those with domestic iron ore mines, to utilise high levels of their domestic iron ore concentrate in their sinter blends while maintaining sinter productivity and quality. When using Fortescue's iron ore sinter fines, many steel mills in North China blend in domestic products at levels of between 20 per cent to 40 per cent. For example, Shougang Iron and Steel blend Antai concentrate at a level of 40 per cent with Fortescue's iron ore sinter fines, the largest imported component, at 30 per cent of the blend.

Generally, with a re-optimisation of granulation and mixing processes, many Fortescue customers comment that the coarse sizing improves overall sinter productivity through increased sinter strength and yield and lower return fines. Apart from Fortescue, other suppliers of coarse sized sinter fines have flagged diminished production as orebodies approach end of mine life. These current volumes are being replaced with ores that have a much higher ultrafine content such as BHP's replacement of Yandi Fines with South Flank (MAC Fines), as noted in Mining Technology news (May 2021).

Process mineralogy

The OPF's in operation at Fortescue have been designed to process a high proportion of goethite-rich, martite-rich, martite-goethite bedded, detrital and channel iron deposits. Being cognisant of the types of goethite is important for sintering and blast furnace operations to maintain production output that meets their desired metallurgical criteria. The goethite classification proposed by Manuel and Clout (2017) has been used, with the relative properties of the goethite types presented in Table 3.

TABLE 3

Relative physical properties of goethite types (Manuel and Clout, 2017).

Goethite type	Macroscopic image	Colour	Lustre	Streak	Relative geological hardness	Fracture
Brown Goethite		light to dark brown	dull, silky	medium brown	medium to hard	uneven
Ochreous Goethite		yellow	dull, earthy	yellow	powdery to friable	uneven
Vitreous Goethite		dark red-brown to black	vitreous, glossy	dark brown to red-brown	medium to hard	conchoidal

As presented by Beros (2019), each OPF not only improves the grade of the ore but also improves the textural characteristics for enhancing sintering performance. A mineralogical survey of a set of primary hydrocyclones captured the effect on overall mineralogy from the cyclone underflow and overflow streams. This can easily be seen by the coloured textural coding as highlighted in Figure 4. Colours from 'browns and dark blue' represent the harder hematite/goethite material. The lighter colours 'faun' and below represent friable and ochreous goethites plus alumino-silicates and other gangue minerals. Depending on the ore type presented to the primary cyclones, generally 35 to 45 per cent of mass is rejected to the overflow.

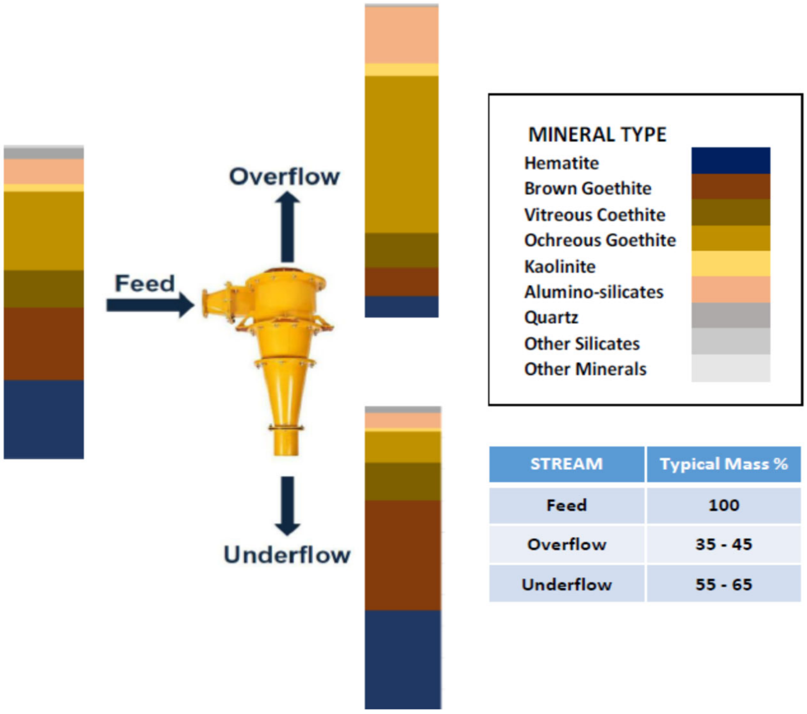

STREAM	Typical Mass %
Feed	100
Overflow	35 - 45
Underflow	55 - 65

FIG 4 – Hydrocyclone mineralogical survey.

The survey clearly indicates that there is a concentration of harder hematite/goethite material to the underflow and rejection of the alumino-silicate minerals and ochreous/friable goethite to the overflow. The hydrocyclone underflow stream is reprocessed by up-flow classifiers and/or spirals which further concentrates the higher grade ‘brown and blue’ streams to the product.

INITIAL DEEP BED SINTERING TEST WORK

Fortescue recently completed initial research with a major customer to evaluate the benefits of deep bed sintering (Beros, 2021). The research also included quantification of SO_2 and NO_x emissions. The base blend, as presented in Table 4, included a 30 per cent mixture of other mainstream Pilbara based ores and a 40 per cent level of domestic concentrate.

TABLE 4

Test work blend.

	Australian blend	South African	Local concentrate	Brazilian
Base	30%	20%	40%	10%

The test work commenced with a bed depth of 750 mm with coke fixed at 5 per cent. While holding coke constant, subsequent firings were undertaken at increments of 50 mm to a total bed depth of 900 mm. Throughout the study, the metallurgical characteristics of the sintering process and product was determined and are shown as relativities to the base blend in Table 5.

TABLE 5

Key sinter results of increasing bed depth.

Bed depth	Productivity	Product yield	Fuel consumption	Tumble index	Reduction degradation	Reducibility
750 mm	100.0	100.0	100.0	100.0	100.0	100.0
800 mm	95.2	99.8	101.2	104.4	92.9	104.0
850 mm	96.0	104.6	95.0	103.8	98.9	100.9
900 mm	92.0	104.0	95.9	107.2	101.3	97.6

As the bed depth increased, the sinter production yield and tumble index increased. Solid fuel consumption significantly decreased which indicated that the quality index of the sinter was markedly improved. However, with the increase of the bed depth, the vertical sintering speed decreased which caused the reduction in sintering productivity. This is counteracted to a certain extent by the improvement in sinter yield and tumble strength.

In a more comprehensive study, Han *et al* (2012) performed sintering pot tests at different bed depths of 700 mm, 850 mm and 1000 mm. The same trends of sinter quality as presented in Table 5 were reported. Regarding emissions, it was noted that as the bed depth increased the oxygen potential increased and the SO_2 and CO_2 (as indicated by solid fuel consumption) emissions per ton of sinter decreased. All these effects are beneficial for improving the process efficiency and providing environmental benefits.

However, despite these efficiency gains in terms of product yield and tumble strength, the decrease in productivity was also associated with an increase in NO_x emissions. The reasoning was that although fuel rate decreased as bed depth increased, the maximum temperature of the bed also increased. The high temperature region became wider which enhanced the ability for production of NO_x from nitrogen and oxygen via the reduced vertical sintering speed and air flow-through the bed.

The study acknowledged that some technical countermeasures were required to improve the deep bed permeability and the solid fuel combustion properties to create a narrowing of the high temperature range and an increase of the vertical sintering speed to ultimately lower NO_x emissions. These countermeasures, some of which have been cited above, include:

- selecting quicklime with the best assimilation and fuel with the best combustion properties.
- use of vertical rods for loosening the sinter feed which can then be gently compacted with a bed press (refer Figure 2).
- diverting a portion (~30 per cent) of the fuel from the feed mixing to improve permeability and improve the sintering temperature range between the upper and lower layers.

All these countermeasures are now well accepted practices of what is required for effective deep bed sintering and importantly satisfy the ULEG targets. The effect of these countermeasures was tested only at a bed depth of 1000 mm and are presented in Table 6, shown as relativities to the results as bed depth increased.

TABLE 6

Key results of study by Han *et al* (2012).

Bed Depth	Productivity	Product Yield	Fuel	TI	SO_2	NO_x
700 mm	100.0	100.0	100.0	100.0	100.0	100.0
850 mm	100.1	93.1	94.4	102.1	74.1	108.1
1000 mm	102.2	80.0	88.2	103.2	53.2	117.2
1000 mm[1]	105.4	100.0	82.1	108.4	41.1	86.9

[1] – Results with countermeasures implemented.

At 1000 mm bed depth, implementing the countermeasures resulted in an overall improvement of all parameters. Compared to the 1000 mm case without the countermeasures, the emission of SO_2 and NO_x decreased which was accompanied by a decrease in CO_2 due to the reduction in fuel rate.

A similar conclusion from the customer study mentioned above was also demonstrated. The exhaust emissions of SO_2 and NO_x were quantified and then calculated in terms of grams per tonne of sinter and presented in Figure 5. Initially bed depth was increased from 750 mm to 900 mm while holding fuel constant at 5.0 per cent. Then at the 900 mm bed depth, fuel levels were reduced from 5.0 per cent to 4.4 per cent. The figure shows the 900 mm depth results for 5.0 per cent and 4.4 per cent.

With the base blend, the test work clearly captured the reduction in emissions of increasing bed depth by 150 mm to 900 mm and then at a bed depth of 900 mm reducing fuel from 5.0 per cent to

4.4 per cent. The test work also showed an additional benefit of reduced emissions when Fortescue's WPF product with its coarser sizing replaced the 30 per cent Australian ore mixture at 900 mm bed depth and 4.4 per cent fuel.

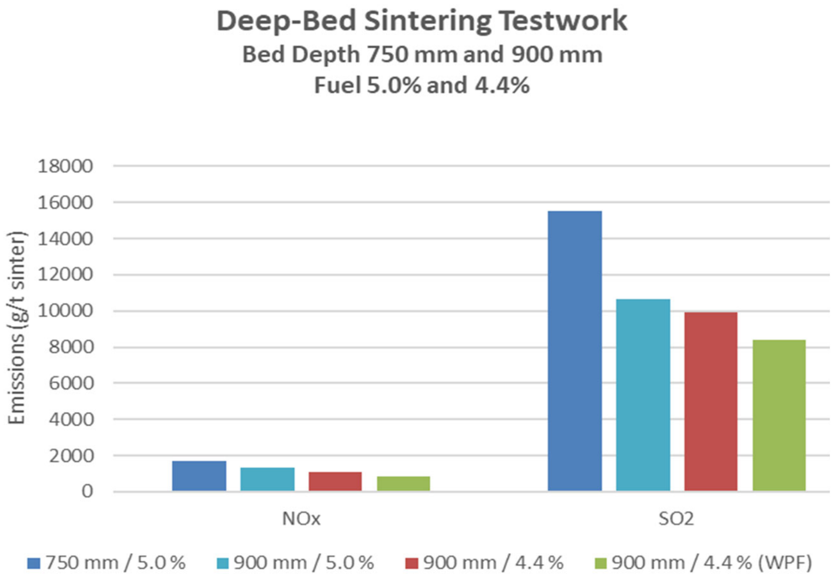

FIG 5 – Initial customer test work.

CONCLUSION

China has committed to a carbon-neutral future by 2060. The Chinese steel industry is working on a plan to peak its emissions by 2025 and progressively reduce them by 30 per cent through to 2030. As an initial means to decarbonise the industry, the Chinese Ministry of Ecology and Environment is promoting and monitoring the implementation of the ULEG's in the iron and steelmaking industry to drive improvements in air quality through the reduction of PM, SO_2 and NO_x.

In response, many sinter plant operators are adopting deep bed sintering which through the studies presented has benefits of:

- improving sinter strength
- increasing sinter yield and productivity
- reducing fuel consumption and therefore CO_2 emissions
- satisfying the requirements to meet the ULEG's for PM, SO_2 and NO_x.

Feedback from customers is that Fortescue products, because of its beneficiation processes, have a preferable particle sizing and goethite mineralogy that is well suited to deep bed sintering.

ACKNOWLEDGEMENT

The author would like to acknowledge Fortescue Metals Group Limited for permission to publish this paper.

REFERENCES

Beros, G S, 2019. Not all Sub-60% Fe Ores are the same: The Link between Processing and Sintering of Fortescue Ores, in *Proceedings Iron Ore 2019,* pp 861 – 869 (The Australasian Institute of Mining and Metallurgy: Melbourne).

Beros, G S, 2021 (in prep). Initial Deep Bed Sintering Characterisation, internal publication, (Fortescue Metals Group: Perth).

Clout, J M F, 2013. Beneficiation of fine iron ores using the desand process, in *Proceedings Iron Ore 2013,* pp 337–347 (The Australian Institute of Mining and Metallurgy: Melbourne).

Han, H, Wu, S, Ma, L, Feng, G and Jiang, W, 2012. Fundamental research on sintering technology with super deep bed achieving energy saving and reduction of emissions, in *Revue de Metallurgie*, Vol 109, pp 249 – 259 (Metallurgical Research & Technology: Paris, France).

Liu, Z, Niu, L, Zhang, S, Dong, G, Wang, Y, Wang, G, Kang, J, Chen, L and Zhang, J, 2020. Comprehensive Technologies for Iron Ore Sintering with a Bed Height of 1000 mm to Improve Sinter Quality, Enhance Productivity and Reduce Fuel Consumption, in *ISIJ International*, Vol 60, pp 2000 – 2007 (Iron and Steel Institute of Japan: Tokyo, Japan).

Manuel, J R and Clout, J M F, 2017. Goethite classification, distribution and properties with reference to Australian iron deposits, in *Proceedings Iron Ore 2017,* pp 567–574 (The Australian Institute of Mining and Metallurgy: Melbourne).

Mining Technology News, 2021. BHP commissions $3.6bn South Flank iron ore mine in Australia (online) Available from: <https://www.mining-technology.com/news/bhp-commissions-south-flank> [Published and Accessed: 20 May 2021].

Wang, D, Wu, S, Li, C and Zheng, C, 2013. Efficient and Clean Production Practice of Large-Scale Sintering Machine, in *ISIJ International*, Vol 53, pp 1665 – 1872 (Iron and Steel Institute of Japan: Tokyo, Japan).

Wu, X, Zhao, L, Zhang, Y, Zheng, C, Gao, X and Cen, K, 2015. Primary Air Pollutant Emissions and Future Prediction of Iron and Steel Industry in China, in *Aerosol and Air Quality Research*, Vol 15, pp 1422 – 1432 (Taiwan Association for Aerosol Research: Taoyuan City, Taiwan).

The production of green steel using HIsmelt

N J Goodman[1]

1. Managing Director, Smelt Tech Consulting, Bateman WA 6153.
   Email: neil.goodman@smelttech.com

ABSTRACT

The HIsmelt technology was developed and proven in Western Australia (WA) after more than 30 years and several billion dollars of research and development. The HIsmelt technology was transferred to China and is now successfully operating at the Molong plant in Shandong Province, China using WA iron ore fines as the major feedstock. Several more plants are under construction in China, and the technology has been approved by the Chinese Government as an environmentally acceptable alternative to the blast furnace. The unique flexibility of the HIsmelt process offers multiple pathways to decarbonise the production of steel in the near future. These pathways include:

- Use of sustainably grown biomass converted to Biochar to replace coal as the reductant.
- Pre-reduction of iron ore fines using hydrogen or biomass to direct reduced iron (DRI) powder.
- Capture of carbon dioxide from the HIsmelt off gas and geo-sequestration underground.

These pathways are highly suitable for the Australian iron ore industry as they utilise:

- The large areas of land and long growing season available in Australia for the production of large tonnages of sustainably grown biomass.
- Coarse iron ore fines directly without the need for fine grinding and pelletising.
- Existing oil, gas and other underground gas reservoirs to store carbon dioxide.

The HIsmelt technology will allow Australia to transition from ‘Asia’s quarry’ to Asia’s supplier of low cost, low carbon and high quality metallics that are required to produce ‘green’ steel with net zero carbon dioxide emissions. In addition, HIsmelt pig iron can be converted locally into steel via electric-arc or basic-oxygen steelmaking furnaces to supply all of Australia’s demand for green steel.

INTRODUCTION

Process description of the HIsmelt technology

The heart of the HIsmelt technology is the Smelt Reduction Vessel (SRV), see Figure 1.

The SRV comprises a steel pressure vessel with a refractory lined hearth, and water-cooled panels around the inside shell of the barrel and roof. During operation, the refractory hearth contains a bath of liquid iron at approximately 1400°C, with a layer of molten slag on top of the hot metal. Iron ore fines, fluxes and coal are injected pneumatically downward through the slag into the hot metal bath via water cooled lances. Hot air blast (HAB) at 1200°C, enriched by oxygen to a total oxygen content of 40 per cent, is supplied by hot blast stoves and injected into the SRV via a water cooled and refractory lined lance to post combust the off gas inside the SRV.

The smelt reduction reaction between the iron oxides and carbon generates a large volume of combustible off gas that erupts from the hot metal bath and throws a large volume of slag droplets into the top space of the SRV. In this top space, the post-combustion of the off gas by the HAB generates a high temperature flame above the slag surface. The energy from the flame is transferred to the slag droplets, which in turn, transfer their heat to the endothermic smelting zone in the hot metal.

The slag layer also insulates the hot metal from the oxygen in the HAB and therefore reduces the back-oxidation of the iron to FeO.

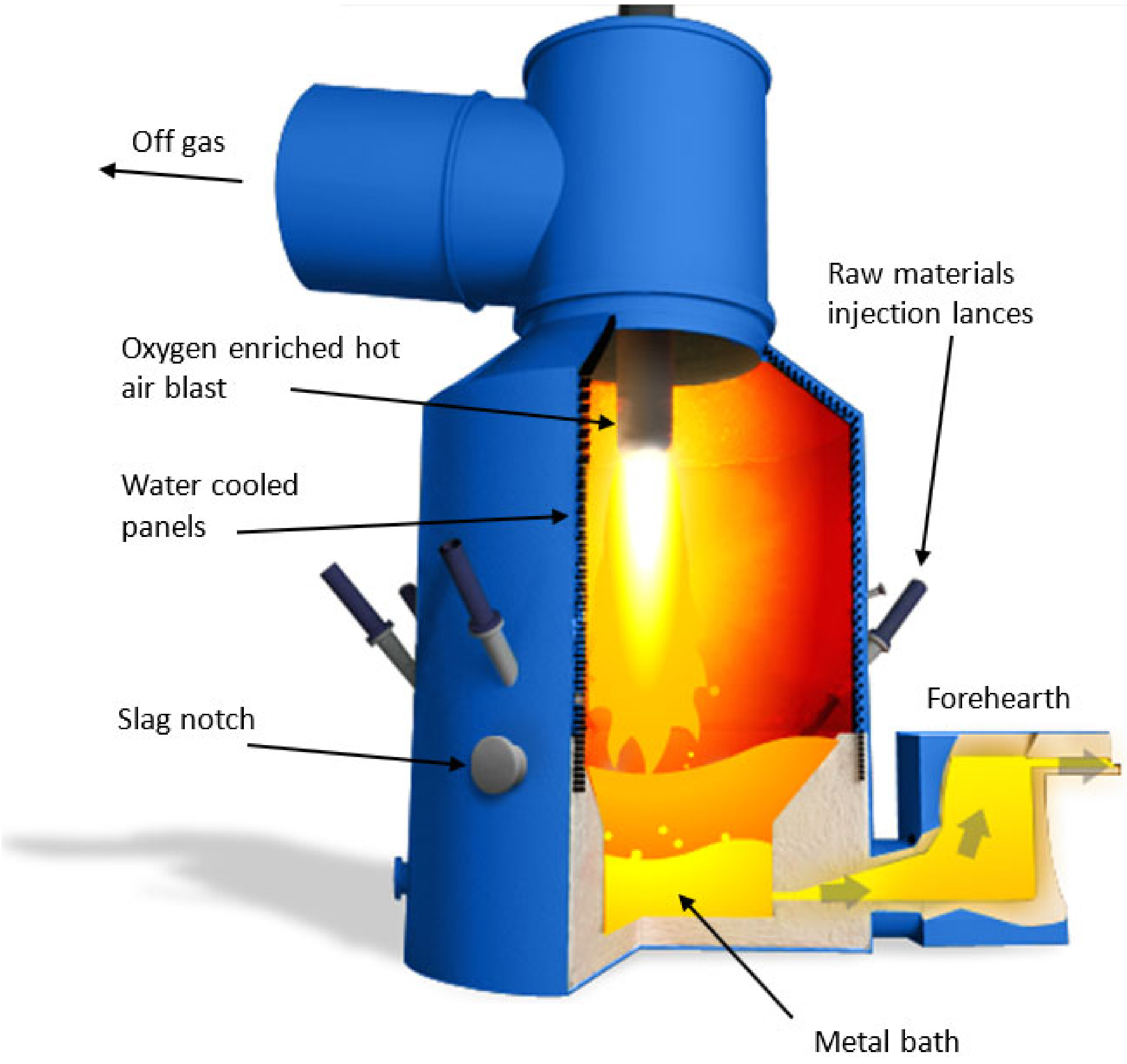

FIG 1 – Smelt Reduction Vessel (SRV).

The liquid iron (hot metal) flows continuously from the SRV via a refractory lined 'forehearth' that keeps the slag separate from the hot metal. The waste gangue from the ore and waste ash from the coal form a liquid slag that is periodically 'tapped' from the SRV via a 'slag notch'.

Development of the HIsmelt technology

The HIsmelt technology was originally developed by Rio Tinto Limited, a British/Australian mining company, from 1982 until 2017, to smelt high phosphorous iron ore fines with non-coking coals. The intellectual property rights for HIsmelt were sold by Rio Tinto to Molong Petroleum Machinery Limited, in 2017.

The first HIsmelt pilot plant, the Small-Scale Pilot Plant (SSPP) was operated in Germany in partnership with Klockner from 1982 to 1986. The SRV was based on a bottom-blown steelmaking vessel with coal and ore injected via bottom tuyeres, and the vessel was rotated to tap metal in batches to produce approximately 1 tonne per hour of hot metal. Figure 2 shows the SSPP being tapped. The results of the SSPP trials showed that smelting iron ore fines with coal in a bath of hot metal was feasible, and the decision was made to build a larger pilot plant.

FIG 2 – The SSSP being tapped.

In 1990, Rio Tinto partnered with Kobe Steel and Midrex to build and operate the HIsmelt Research and Development Facility (HRDF) in Kwinana, Western Australia. The HRDF was designed to produce approximately 10 t per hour of hot metal, and the SRV originally had bottom blown tuyeres that injected coal and iron ore fines, with hot air blast (HAB) from hot blast stoves injected into the top space. The vessel was rotated to tap metal in batches. Although the process operated efficiently, the refractory wear rate was very high, and Kobe Steel and Midrex decided to exit the technology.

Figure 3 shows the horizontal version of the HRDF SRV being tapped.

FIG 3 – HIsmelt Research and Development Facility (HRDF) Smelt Reduction Vessel (SRV) being tapped.

In 1996, Rio Tinto decided to change the SRV to a fixed, vertical design with the following changes:

- injection of coal and ore via water-cooled lances above the hot metal.
- replacement of all refractories above the injection lances with water-cooled panels.

- continuous tapping of hot metal via a 'forehearth' which allows hot metal to flow from the bottom of the SRV via an external refractory lined vessel that acts in a similar manner to a manometer.

The vertical SRV layout is shown in Figure 1.

The results of campaigns with the vertical vessel from 1997 to 1999 were positive, and the SRV successfully smelting a range of ferrous feeds (including iron ore fines, concentrate, steel plant waste and DRI) and coals (ranging from coke breeze to high volatile thermal coals). In 2000 Rio Tinto decided to build a commercial scale HIsmelt plant.

In 2001, Rio Tinto partnered with Nucor Steel, Mitsubishi and Shouguang Steel to form the HIsmelt Kwinana Joint Venture (HKJV) and build a commercial scale HIsmelt plant producing approximately 100 t per hour of hot metal, in Kwinana. The plant was constructed from 2003 to 2005, operated from 2005 to 2008, and produced approximately 400 000 t of pig iron that was delivered to electric arc furnaces in the USA and Asia.

The HKJV plant suffered from a series of problems with ancillary equipment that caused low availability and damaged the refractories. However, the production rate and availability improved steadily, and by Q4 2008, the plant was producing up to 80 t per hour of hot metal with 90 per cent availability.

Unfortunately, the global financial crisis of 2008 forced Rio Tinto to put the HKJV plant into 'care and maintenance', and the plant was mothballed for several years.

In 2012, Rio Tinto signed an agreement with Molong Petroleum Machinery Limited (Molong) to ship a portion of the Kwinana equipment to China, support Molong during the engineering and construction of the new HIsmelt plant, and to train Molong's personnel to operate and maintain the HIsmelt plant.

The Molong plant started construction in 2013 and started operation in 2016.

Molong primarily produces tubular products for the oil industry and makes most of the liquid steel required for the casting of round billets via a basic oxygen furnace. Before the HIsmelt plant was built, Molong would purchase approximately 500 000 t per annum of liquid hot metal from local small blast furnaces (typically less than 500 t per day capacity) that were delivered in 40 t refractory lined ladles via road trucks.

In 2012 the Chinese Ministry of Industry and Information Technology (MIIT) issued a regulation that banned the construction of new small blast furnaces with capacities less than 1 000 000 t per annum and ordered the gradual closure of all small blast furnaces for environmental reasons. However, the MIIT specified that two technologies met the revised environmental standards and could be used to replace small blast furnaces. These technologies were HIsmelt and Finex. After reviewing both technologies, Molong decided to adopt the HIsmelt technology to supply 500 000 t per annum of hot metal their basic oxygen furnace, with excess hot metal delivered to a new foundry facility.

Figure 4 shows the Molong HIsmelt plant at Shouguang Port near Yangkou, Shandong Province.

FIG 4 – Molong HIsmelt plant in Shandong Province, China.

Molong has operated the SRV for more than four years and produced approximately 2 000 000 t of hot metal at an average coal consumption rate of 900 kg per t of hot metal. The cost of the hot metal produced by the HIsmelt plant is approximately 10 per cent lower than the cost of the small blast furnaces previously used by Molong.

A second 6 m diameter HIsmelt plant was started up in Inner Mongolia in 2021, five more 6 m diameter HIsmelt plants are under construction in Hebei Province, and two 6 m diameter HIsmelt plants are under construction in Laos.

PATHWAYS TO SUSTAINABLE STEELMAKING

Replacement of coal with Biochar

The HIsmelt technology was developed to use non-coking coal to reduce the iron oxides to iron, and to provide the fuel for combustion in the top space of the SRV. The coal is injected into the SRV as a powder, and does not have any size and strength requirements, unlike the blast furnace.

Therefore, carbon-containing powders can be used in the HIsmelt technology, and several different carbon-containing powders have been trialled successfully on HIsmelt pilot plants including coke breeze, blast furnace dust and charcoal derived from biomass (Biochar).

The use of biomass products such as Biochar will produce similar carbon dioxide emissions to those from coal. However, the plants that are the source of the biomass consume almost the same amount of CO_2 through photosynthesis while growing, as is released when the biomass is combusted in the SRV. Biochar can be produced from a variety of plant matter, including waste forestry waste, or energy crops, that are considered low carbon biomass sources and are deemed emit a neutral amount of carbon in the atmosphere.

The use of Biochar will comply with the current Australian regulations under the NGER Framework Requirements and the NGA accounting rules to achieve certification of carbon neutrality by Climate Active.

The HIsmelt SRV will emit approximately 1.5 to 2.0 t of CO_2 per t of pig iron when using non-coking coals as the fuel, depending on the Fe content of the iron ore being smelted. With Biochar, the CO_2 emissions will be the same, but the offset of the carbon captured by the biomass will result in a 'net zero' emission of CO_2 from the SRV, and therefore the pig iron production will be 'green'.

Several studies are ongoing worldwide to produce ‘green’ pig iron from a HIsmelt plant from Biochar. These projects are located in areas with large areas of land with forest waste and/or marginal arable land suitable for growing energy crops. These regions include North America, Eastern Europe, North Africa, Australia, Indonesia and New Zealand.

Western Australia is particularly suited to produce ‘green’ pig iron and steel via the use of Biochar because of the large areas of land available for the production of energy crops, and large resources of quality hematite and magnetite present. A recent study has developed a business case for a HIsmelt plant producing ‘green’ pig iron in the Collie region in the South-west region of Western Australia using locally sourced magnetite and biomass from local forestry waste and locally grown biomass energy crops such as Miscanthus or ‘elephant grass’.

The potentially positive factor for WA growers of Miscanthus is that it is already grown for wind breaks and ornamentals in Australia. A Queensland company already produces rhizome stock for planting, and consequently an extensive database exists on the plant and its potential impact in the WA environment.

Miscanthus yields can vary quite widely, between 15 to 50 t per hectare annually after a two to three year growing phase, and as a perennial only needs sowing once and lasts up to 20 years. The periods vary between 10 through 20 years dependent on the climate. It is noteworthy that there is no snowfall in WA, unlike in the US colder states from where a good deal of the reference data comes. The results in warmer climates, such as WA, are anticipated to have yields and life expectancy at the higher end of the range.

The Miscanthus rhizomes store nitrogen like legumes, need little to no fertiliser, and where it is used in large crops has been considered sterile and non-invasive.

Miscanthus is a high yielding crop, grows over three metres tall, resembles bamboo and produces a crop every year without the need for replanting. The rapid growth, low mineral content, and high biomass yield of Miscanthus increasingly make it a favourite choice as a Biomass crop, outperforming Corn Stover and other alternatives.

The benefits of Miscanthus crops may be summarised as follows:

- high yielding
- environmentally friendly
- easy to grow
- low maintenance
- annual growing cycle
- no pesticides or fertilisers
- increases wildlife biodiversity
- eligible for cross compliance
- long lifespan
- excellent cover for wildlife.

Approximately 2–3 t of biomass are required to be produce 1 t of Biochar. The biomass is indirectly heated to approximately 400°C in an oxygen free reactor to drive off the moisture and volatiles, which leaves a carbon-rich ‘char’ comprising approximately 80 per cent carbon, with 20 per cent ash and volatiles. Recent studies in the US and Australia showed that the cost of harvesting the biomass plus pyrolising the biomass will be similar to the long-term price of coal.

Carbon capture and sequestration

In 2009 the HIsmelt technology was selected by a consortium of European steelmakers to smelt liquid FeO produced by the Cyclone Converter Furnace (CCF) developed by Hoogovens (now Tata Steel). The combination of the HIsmelt SRV and the CCF is known as the ‘HIsarna’ process, and a

HIsarna pilot plant was commissioned and operated over several campaigns at Tata Steel Ijmuiden in Holland from 2010 to date.

HIsarna was developed as part of the EU Government's ULCOS (Ultra Low CO_2 Steelmaking) project, with the intention of capturing the CO_2 from the smelter off gas and pumping the CO_2 underground (sequestration). To reduce the capital and operating costs of capturing the CO_2, the nitrogen in the off gas should be reduced as much as possible, preferably to zero. To achieve this, the HIsarna SRV uses 100 per cent oxygen to post-combust the top space gas instead of hot blast.

The successful trials at Ijmuiden showed that a HIsmelt SRV can successfully use 100 per cent oxygen, and therefore offers the opportunity for economically capturing and sequestrating the CO_2 in the off gas. However, the operating and capital costs of capturing and sequestrating the CO_2 are high and require favourable local geological formations such as depleted oil and gas fields to store the CO_2.

Consumption of DRI produced via hydrogen and/or biomass reduction

The flexibility of the HIsmelt process allows the SRV to smelt a wide range of ferrous feeds and the following materials have been successfully smelted in the HIsmelt plants operating in China or Australia; hematite with Fe contents of 55 to 62 per cent, magnetite concentrates with Fe contents of 57 to 68 per cent, and partially and fully pre-reduced directly reduced iron (DRI) with Fe contents of 68 to 90 per cent.

As the Fe content of the ferrous feed increases, the energy required for the reduction reactions is reduced, and the injection rate of the ferrous feed can be increased for a constant energy input. This results in an increased production of liquid iron from the SRV, and a reduction in specific fuel consumption. The approximate production rates and fuel (non-coking coal or Biochar) consumptions of a 6 m SRV for various ferrous feeds are shown below in Table 1.

TABLE 1

Approximate production rates and fuel (non-coking coal or Biochar) consumptions of a 6 m SRV.

Ferrous feed	Pig iron production t per annum	Fuel consumption kg per t of pig iron
60% Fe Hematite	600 000	800
65% Fe Magnetite	1 000 000	700
80% Fe DRI	1 500 000	300

Directly reduced iron (DRI) can be produced in many ways with various reductants. Table 2 shows a range of possible technology routes for producing DRI.

TABLE 2

Possible technology routes for producing DRI.

Furnace type	Ferrous feed	Reductant	Technology status
Shaft	Lump ore or pellets	Natural gas	Proven, more than 100 Midrex or HYL units in operation worldwide
Shaft	Lump ore or pellets	Hydrogen	Pilot plant scale 'HYBRIT' technology
Rotary kiln	Lump ore or pellets	Coal or natural gas	Proven but uneconomic compared to shaft furnaces
Rotary hearth	Lump ore or pellets	Coal or natural gas	Proven but uneconomic compared to shaft furnaces
Fluid bed	Ore fines	Hydrogen	Proven at commercial scale at a single site – 'CircoRed' technology Pilot plant 'HYFOR' technology
Grate kiln	Ore fines	Biomass	R&D laboratory testing

The ‘CircoRed’ process reduces ore fines with hydrogen firstly in a circulating fluid bed (CFB) that produces DRI fines that are pre-reduced to approximately 80 per cent Fe. These pre-reduced fines are then further reduced to >90 per cent Fe in a bubbling fluid bed and then compressed into briquettes and sold as hot-briquetted iron (HBI). The ‘CircoRed’ process was proven at the LTV/Cliffs/Outotec ‘CircoRed’ plant in Trinidad from 1998 to 2002 using hydrogen generated via the steam reformation of natural gas

The combination of a HIsmelt SRV with the first stage CFB of a ‘CircoRed’ plant offers significant advantages for zero-carbon production of pig iron including lower cost ferrous feed (ore fines versus high-grade pellets), lower capital (no second-stage bubbling bed or briquetting required).

The production of DRI via the pre-reduction of ore fines via biomass on a grate kiln potentially offers another route for zero-carbon production of DRI. However, this process is still at the R&D laboratory stage and will require significant investment to develop the technology through the pilot and commercial plant stages.

The economics of hydrogen reduction are not yet favourable and will require significant reduction in the cost of hydrogen production and/or increases in carbon taxes. Approximately 10–15 GJ of energy is required to produce 1 t of DRI, and as each kg of hydrogen contains 120 MJ, 80–120 kg of hydrogen will be required. Assuming 100 kg of hydrogen per t of DRI is required, the cost of hydrogen will have to be less than $1/kg to match the cost of coal or Biochar. Most hydrogen production projects are targeting production costs of $2–$3/kg and therefore carbon taxes will have to be imposed to allow hydrogen production to be economic.

PRODUCTION OF GREEN STEEL IN AUSTRALIA

The HIsmelt SRV produces liquid hot metal comprising 96 per cent Fe and 4 per cent carbon which can be considered to be ‘green’ pig iron when produced using sustainably produced Biochar and/or hydrogen.

‘Green’ pig iron can be easily converted into ‘green’ steel in either an electric-arc or basic oxygen steelmaking furnace.

‘Green’ pig iron can be charged into an electric furnace as a liquid hot metal or as solid ingots or pigs. The electric arc will melt the pigs and scrap steel, and oxygen will be injected to remove the carbon and heat the steel. On a standard electric arc furnace approximately 30 per cent of the charge can be ‘green’ pig, with 70 per cent scrap steel.

‘Green’ pig iron can be charged into basic oxygen furnace as a liquid hot metal and oxygen will be injected to remove the carbon and heat the steel. On a standard basic oxygen furnace approximately 90 per cent of the charge can be ‘green’ liquid pig iron, with 10 per cent scrap steel.

The flexibility of HIsmelt to reduce a wide range of ferrous resources permits the adoption of the technology in all regions of Australia. These regions include:

- The Pilbara, using hematite, magnetite or vanadium-titanium magnetite to produce ‘green’ pig for sale to SE Asia.
- The Mid-West of WA, using magnetite, vanadium-titanium magnetite or calcined hematite from vanadium roasters to produce ‘green’ pig for sale to SE Asia.
- The South-West of WA using hematite or magnetite to produce ‘green’ steel for local consumption and export.
- South Australia using magnetite or goethite to produce ‘green’ steel for local consumption and export.
- NSW and Queensland using hematite or magnetite to produce ‘green’ steel for local consumption and export.

CONCLUSION

The HIsmelt technology is now proven and is future-proofed by offering several pathways to zero-carbon ‘green’ iron and steelmaking. These pathways to sustainable steelmaking include:

- elimination of CO_2 emissions via the injection of sustainable biomass and/or carbon capture and sequestration.
- consumption of DRI produced via hydrogen reduction and/or biomass reduction.

The HIsmelt technology using Biochar can produce ‘green’ steel today for lower cost than blast furnaces using pellets and coke. In future, if low-cost hydrogen becomes available, the production rate of a HIsmelt furnace can be increased while reducing the specific consumption of Biochar.

It never rains but it pours – improving extreme-rainfall resilience in Australia's iron ore regions

J H Hodgkinson[1] and M Grigorescu[2]

1. Senior Research Scientist, CSIRO, Pullenvale Qld 4069. Email: jane.hodgkinson@csiro.au
2. Independent Researcher, Brisbane Qld 4000.

ABSTRACT

The expansive, open cut iron-ore mines in Western Australia typically experience few days of rain per annum, often amounting to less than 250 mm. Unlike mines where rainfall is frequent, they may be less prepared for extreme rainfall events. Such events can cause erosion, flooding and sedimentation, drainage alteration, spoil and stock heaps wetting and effect slope stability. Such impacts may threaten personnel safety, infrastructure, and production.

The CRATER ('Climate Related Adaptation from Terrain Evaluation Results') framework collates and interprets a mine's pre-existing data and semi-quantitative information to assess vulnerability to, and ultimately plan to avoid or minimise, flood-related hazard to infrastructure, people, downtime, environment and revenue. Outputs assist decision makers to design investment strategies for minimising mining operations' vulnerability to climate.

Previously developed for smaller, wetter mines in Queensland's coal region, the outputs provide a hot-spot map, fault tree analysis and an assessment of the mine's capacity to adapt. The multicriteria evaluation (MCE) within a geographic information system (GIS), equally suits iron-ore mines' site-conditions (elevation, slope, drainage, soil and vegetation) to identify critical inundation areas. Hot-spot results provide target zones for in-depth fault-tree analysis that, in turn, present a range of site-specific adaptation options.

Rainfall-intensity and the number of rain days since the 1970s have increased over central and eastern parts of the Pilbara Region. While tropical cyclones may become less frequent, they are projected to increase in intensity. Although some parts of the Hamersley Ranges receive more than 500 mm per annum, rainfall in the Pilbara is generally very low. Therefore, experience of the impacts of extreme rainfall events in the constantly changing topography of Western Australia's iron ore region may be sparse. Minimising potential effects can be proactively assisted using CRATER.

INTRODUCTION

Many mines are situated in climatically inhospitable regions. Mining must take place year-round, and mine owners are committed to a mine site by its geological setting and lease provisions; therefore, it is impossible for them to just relocate to accommodate inclement or extreme weather events. As climate change brings to those regions 'more extreme extremes', decision makers are faced with dealing with new, challenging and changing conditions, needing also to consider the concept of maladaptation in a changing climate (Hodgkinson, Hobday and Pinkard, 2014).

While mining districts familiar with high or frequent rainfall may have more experience with dealing with such weather, or have plans that deal with extreme events, they are still vulnerable. Extreme rainfall events can cause interruptions to production and damage to infrastructure that can be difficult to manage. The 2010–2011 floods in subtropical regions of Queensland for example, disrupted mining for over six months and effected global coal prices. Regions less prone to rain, such as the iron ore district of Western Australia, could be equally disrupted by unforeseen and unplanned-for events. This heightened susceptibility as the climate patterns change, may impact productivity, hazards and environment.

The Pilbara is a key iron ore mining region of the world. It is vast, spanning the width of Western Australia. It has inland ranges, arid desert and a tropical coastline, part of which is the most cyclone-prone area along the Australian coastline (DPIRD, 2021). The Pilbara experiences a semi-arid climate, with high temperatures and low rainfall. The region has two main seasons: notoriously hot summers with the mean maximum temperatures averaging 36–37°C from November to April and mild, dry winters. Rainfall is generally low (~350 mm in the north-east and <250 mm in the south and west) (DPIRD, 2021). While rainfall is variable throughout the year it is highest during summer and autumn when summer storms and tropical cyclones can occur. Cyclones account for up to 34 per cent of the total annual rainfall in the area and can influence up to 450 km inland (DPIRD, 2021). High evaporation rates counter the high, variable rainfall (PDC, 2017) so surface water, while damaging when flowing or flooding, does not persist and the surface can quickly desiccate.

Climate projections for the Pilbara are for temperatures to continue to rise and the intensity of heavy rainfall events to increase (DPIRD, 2021). Over the past ~50 years, rainfall intensity and the number of rain days have increased in the central and eastern parts of the Pilbara and decreased in the west. Annual rainfall is projected to remain largely unchanged to 2090 and, while there is medium confidence that cyclones may become less frequent, their intensity will increase (DPIRD, 2021). Future climate scenarios project that mean annual rainfall could decrease by up to 42 mm or increase by up to 19 mm by 2030 (CSIRO, 2015). In summary, in the next 10 years, fewer extreme events could each deliver greater total rainfall. More intense rainfall, across fewer events in turn may introduce unexpected impacts at mine sites and assets and infrastructure previously not effected by extreme events may be vulnerable.

It is not unusual for mines to build downtime into production plans and consider alternative storage options for stockpiles to mitigate ‘bad’ weather events. Nevertheless, many mines are not yet well-adapted to the changing climate. Vulnerability of mining operations to climate change includes: energy availability and interruptions; water availability (too much or too little); infrastructure and equipment damage; human resources and safety; and impacts on the surrounding community and environment (Moffat, 2009; Hodgkinson *et al,* 2010; Loechel *et al,* 2010; Loechel, Hodgkinson and Moffat, 2011a).

BACKGROUND

Mines typically incorporate weather-related disruption into plans but that is typically developed using climate projections and predictions based on current and historical data and flood-risk mapping. Historical weather data, however, is and inaccurate measure of weather-related risks as climate change is constantly, albeit slowly, altering those events. For instance, the record may not represent changes in frequency or intensity of an area’s infrequent floods, or it may not represent other subtle changes to the climate. There is broad acceptance that climate change is causing changes to climate patterns and extremes, so climate future scenarios are valuable and should be included in future mine planning (Mason *et al,* 2013). Adaptive planning, a process of ‘learning by doing’, provides a means to incorporate new knowledge into future practices (Mason *et al,* 2013). The mine site’s morphology itself, however, is also constantly changing so it is also useful to consider a method that allows a mine to reassess flood – or inundation-vulnerable ‘hot-spots’ prior to a wet season (Hodgkinson, Grigorescu and Alehossein, 2013b).

As extreme weather events are becoming progressively frequent, ‘downtime’ in production schedules factor in costs of risks, hazards, and production interruptions. Increased rainfall intensity and increased rainfall days in otherwise dry regions may include (Liu and Song, 2019, and references therein):

- high intensity rainfall on very dry land triggering overland flow
- high overland flow may lead to toe of slop erosion and under cutting
- pit collapse may occur
- inrush-of-water accidents
- mudslides, damaging mine facilities
- interruption or destruction of transport and power facilities
- ponding of water leading to contaminated water issues.

Pressure on mines to avoid prolonged or frequent downtime also comes from market demand and stakeholder expectations. Adaptation of mine sites or management practices to defend the operations against weather events and the changing climate is becoming an important strategic move for many companies (Hodgkinson, Grigorescu and Alehossein, 2013a).

Here we present a method that utilises commonly available mine site data to explore adaptation options that will assist decision-making around reduced vulnerability to sudden rainfall events and resulting flood. We refer to the method, as 'climate-related adaptation from terrain evaluation results': CRATER.

METHOD AND EXAMPLE

CRATER is a decision-making tool that uses a mine's (typically pre-existing) data to determine locations of the mine that may be vulnerable to flood or inundation, identifies what assets need protecting, and countermeasures to prevent hazards and downtime. It does not predict flood, rainfall or weather-related events, but provides a process for mine planners to consider assets and perform adaptive management.

CRATER was initially tested in the coal regions of Queensland (ACARP project C21041, Hodgkinson, Grigorescu and Alehossein, 2013b) that had previously been badly affected by widespread flooding in 2010–2011. It is a three-stage decision-making tool, that utilises pre-existing data and mine site expertise and knowledge. The three steps are:

- Spatial multicriteria analysis (MCA) using geographic information system (GIS)
- Fault tree analysis (FTA)
- Five-capitals analysis (5CA).

CRATER identifies a mine and its vicinity's most likely flood 'hot-spots' and presents them as a 'traffic lights' warning map. The process then requires a failure analysis approach such as fault-tree analysis to identify both the cause of possible failures and a range of possible failure-avoidance adaptations. In the third step, management can assess the most suitable option for the mine, based on the availability of capital such as time, facilities, labour and money, in addition to social and expert acceptability of the options. CRATER has been tested in an open cut mine environment and has also been tested to identify how subsidence over underground mines may impact on flooding and ponding over the mining life cycle (Hodgkinson and Grigorescu, 2014). Further work is continuing to test larger and more complex mine landscapes to deliver a method to extract more knowledge from existing data.

Stage 1 – Spatial MCA

Multicriteria analysis (MCA) or evaluation (MCE) considers the interaction of numerous and various conditions to assist informed decision-making in a complex system. Developed in the 1960s, the use of the multicriteria approach has become widespread. For the purposes of CRATER, we use spatial MCA to allow cross-analysis of various spatial criteria, many of which may conflict, from both the natural and man-made environment in and around the mine site. Spatial MCA was first presented by Carver (1991), when MCE was integrated with GIS. It has been used widely across the built – and natural environments (for example van Haaren and Fthenakis, 2011; Preda, Wright and Gimber, 2006; Preda, 2009). The mining industry is familiar with GIS, so analysis in a geo-referenced environment suits existing industry skills and data.

In CRATER, multicriteria evaluations are performed by ranking natural conditions such as elevation, slope, drainage and soils, at the mine site. Typical GIS layers that are helpful to the process are:

- Digital elevation model (DEM) priority input – Must have.
- SLOPE derived from DEM – Must have.
- DRAINAGE DENSITY derived from DEM – Must have.
- Mine site infrastructure – Must have.
- VEGETATION – Very good to have.
- SOIL characteristics – Good to have.

The MCE solutions represent an equally or weighted summation of all the parameters that trigger, control or influence the environmental issues being modelled, in this case floods (Figure 1, where ‘w’ signifies the weight that may be applied to each parameter). The areas that show-up in red (with very low scores) have been identified as being of extreme vulnerability and, when overlain by the mine site’s infrastructure GIS layers, the mine in this case, was able to identify the most critical areas, and designated ‘hot-spots’ (Figure 2).

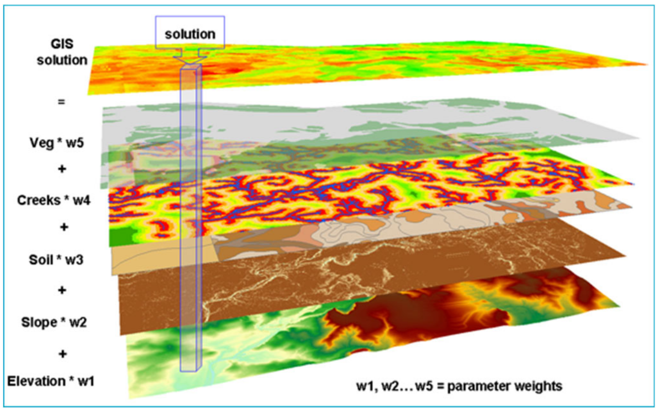

FIG 1 – Parameter summation to generate a MCE solution.

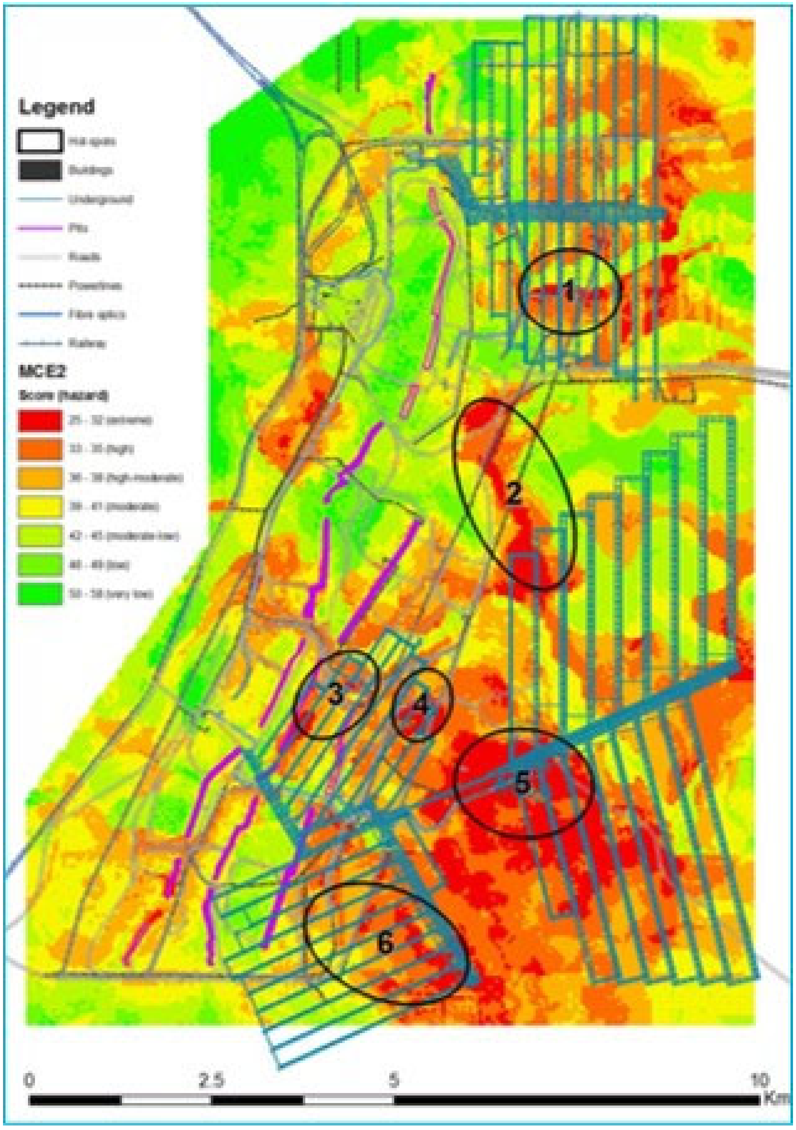

FIG 2 – Model showing vulnerability ratings across the mine site and key hot-spots in relation to infrastructure.

Stage 2 – Fault tree analysis (FTA)

Fault tree analysis (FTA) is used to identify the reasons a failure occurs and the counter measures or adaptation options that are available. Originally designed in the 1960s to study the safety of missile launch-controllers, FTA has since been used for establishing the reliability and safety of other complex systems. For example, it has been used in aviation, the nuclear industry and in mining for equipment reliability, maintainability and safety (for example, Dhillon, 2008; Iverson, Kerkering and Coleman, 2001; Lewis *et al*, 1979).

FTA is a systematic procedure for deducing the basic causes of a fault event, where a single fault is situated at the top of a flow chart and expands to identify the multiple-contributors that can lead to that failure occurring. Each item is ranked, based on the possibilities and likelihood of that fault or failure occurring. Possible control measures are identified for each appropriate hazard or vulnerability. FTA is well-suited to the analysis of specific failures at a mine site, due to the complex system of operation. In CRATER, FTA analysis of specific vulnerabilities at the hot-spots helps to identify why an issue can occur and what options there are available to resolve, reduce or avoid failure. An example FTA diagram is provided in Figure 3.

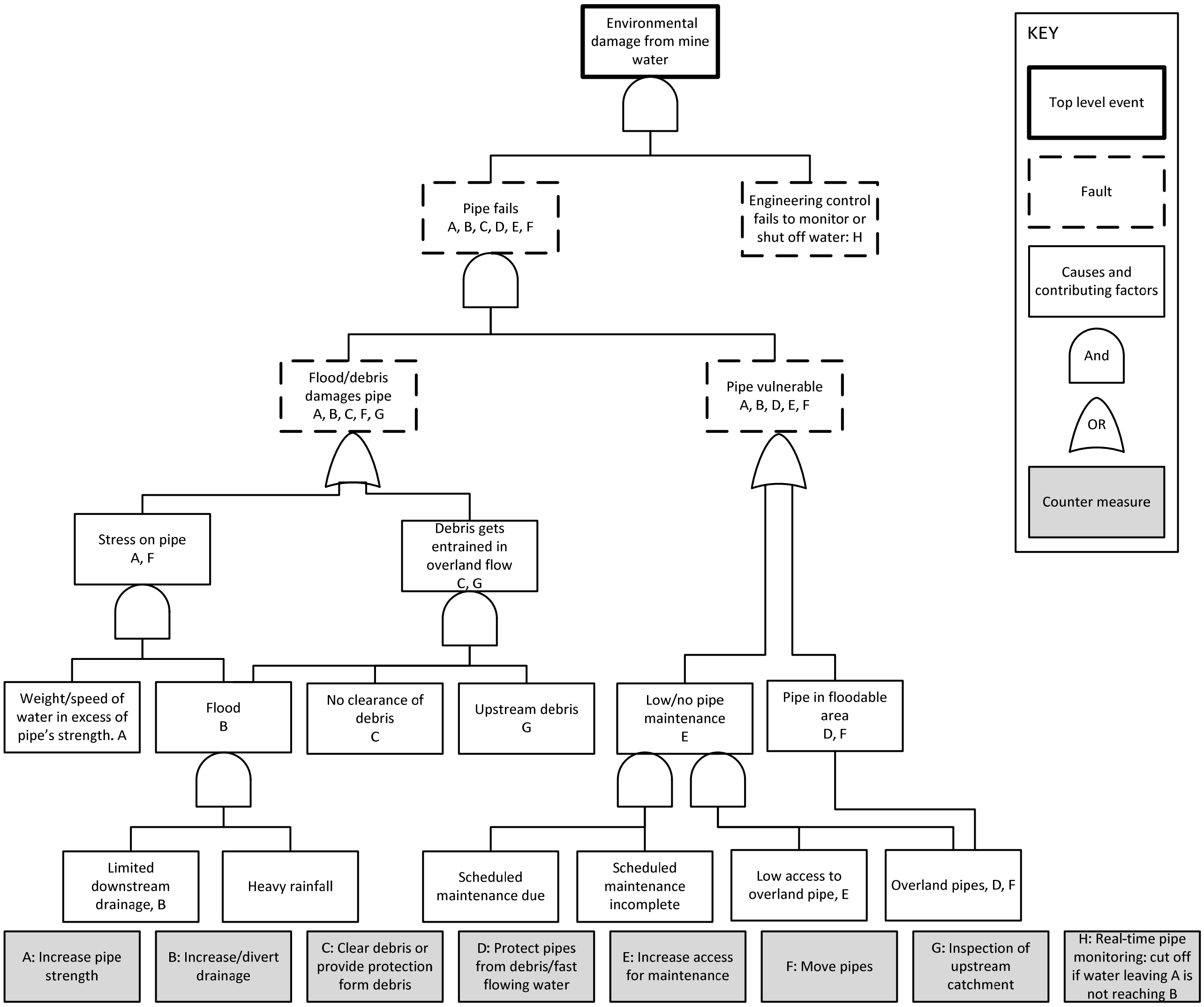

FIG 3 – An example FTA diagram showing the top-down approach, identifying at each node what can go wrong at a hot-spot (faults and contributing factors), and which potential counter measures, or adaptation options (denoted by letter) may reduce the possibility of that node occurring. Counter measures (A to H, grey boxes) can each be assessed for capital availability in Stage 3, 5CA.

Stage 3 – Five-capitals analysis (5CA)

The 5CA method is used to assess the mine's capacity to adapt using each adaptation option. It is important that a mine has the capacity to select an option that can be successfully carried out and that will not cause mal-adaptation (negative impact on someone or something else). An assessment for an option's capacity to be successful will be based on capital availability. The 5CA method was developed initially for assessing capacity to assist with land and water projects (Nelson *et al,* 2010) and has also been applied to the mining context in climate adaptation (Loechel *et al,* 2010; Loechel, Hodgkinson and Moffat, 2011b). The five capitals assessed are:

1. Human (qualified staff availability).
2. Social (mining industry membership, community organisations, community 'buy-in' and acceptance).
3. Natural (leases, groundwater, seedstock, rehabilitation materials).
4. Physical (roads, ports, earth-moving equipment, energy supply lines).
5. Financial (cash reserves, share price, equity position, mine income).

Maladaptation effects are also considered for each of the five capitals, assessing how an option could inadvertently cause damage. This may be that the option could inadvertently cause flood, erosion, pollution, infrastructure damage or untenable long-term costs, for example.

The variables are assessed for each adaptation option or counter measure by an expert panel at the mine, on a scale of 0 to 5 and plotted on a radar diagram, providing a visual to compare what is available against what is required (Figure 4).

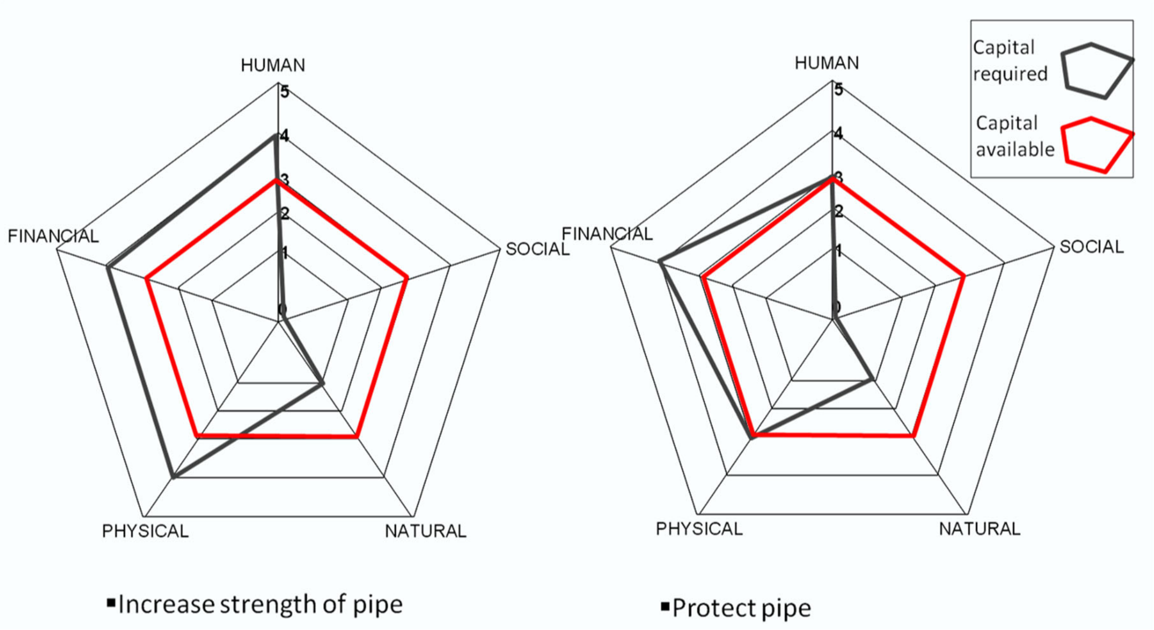

▪Increase strength of pipe

▪Protect pipe

FIG 4 – Radar plot examples showing the difference between capital available and capital required for two adaptation countermeasures selected by mine experts as options for reducing damage at a given hot-spot.

DISCUSSION AND CONCLUSION

CRATER provides a three-stage decision-making tool that allows mines to utilise pre-existing data and mine site expert knowledge to reduce climate-related vulnerability. CRATER uses data that most mines already possess. The primary process assesses the geomorphological features of a site. While the method was initially tested in relatively small, wet-region coalmines, it is also suited to any scale or style of mine including extensive mines in drier regions, such as the iron ore mines of the Pilbara. The outputs provide the decision maker with a set of visual aids that can be used to present stakeholders with decision reasoning and evidence for selecting the most suitable option for the mine at that time.

Iron ore mines are typically large, sprawling, open cut operations that are altering the geomorphology over long time frames. Flood prone areas of concern (hot spots) may not be obvious, especially in regions that do not frequently experience high rainfall. CRATER provides the mine with a relatively quick assessment that does not need new data, which can help decision makers establish the next steps for more detailed planning. The method can also be used for assessing ‘what if’ scenarios for planning under future mine morphologies or future climate scenarios over the life of the mine.

ACKNOWLEDGEMENTS

The author wishes to thank ACARP, the supporting mines and specialists, and the Geological Survey of Queensland for support and resources for project C21041 that led to the development of CRATER. Further, the author acknowledges her colleagues, Dr Habib Alehossein and the late Dr Oswald Marinoni for their expert assistance and encouragement.

REFERENCES

Carver, S, 1991. Integrating multi-criteria evaluation with geographic information systems. *International Journal of Geographical Information Systems* 5, 321–339. https://doi.org/10.1080/02693799108927858

CSIRO, 2015. The Pilbara Water Resource Assessment: past, present and future hydroclimate. An overview report to the Government of Western Australia and industry partners from the CSIRO Pilbara Water Resource Assessment. CSIRO land and Water, Australia, 12 p. https://publications.csiro.au/rpr/download?pid=csiro:EP157487&dsid=DS1

Dhillon, B S, 2008. *Mining Equipment Reliability, Maintainability and Safety* (Springer series in Reliable Engineering). Springer-Verlag, London, 201 p.

DPIRD, 2021. Climate in the Pilbara region of Western Australia, accessed online 7th May 2021 https://www.agric.wa.gov.au/climate-change/climate-pilbara-region-western-australia

Hodgkinson, J H and Grigorescu, M, 2014. “What-if” scenarios for future planning: Climate Related Adaptation from Terrain Evaluation results (CRATER) for protecting mine productivity, *NCCARF 2014, Business as usual? Productivity in a changed climate*. October 2014. https://publications.csiro.au/publications/publication/PIcsiro:EP144865

Hodgkinson, J H, Grigorescu, M and Alehossein, H, 2013a. Staying afloat with CRATER: a decision making tool for mine management under extreme climate conditions, *NCCARF*, June 2013.

Hodgkinson, J H, Grigorescu, M and Alehossein, H, 2013b. ACARP C21041 Preparing a mine for drought ad flood – Stage 1: a vulnerability and adaptive capacity study, CSIRO EP132938 72 p. https://publications.csiro.au/rpr/download?pid=csiro:EP132938&dsid=DS2

Hodgkinson, J H, Hobday, A and Pinkard, E, 2014. Climate adaptation in Australia’s resource-extraction industries: ready or not? *Regional Environmental Change* 14(4):1663–1678 DOI: 10.1007/s10113–014–0618–8

Hodgkinson, J H, Littleboy, A, Howden, S M, Moffat, K and Loechel, B, 2010. Climate adaptation in the Australian mining and exploration industries: Project introduction and initial findings. CSIRO Report P2009/2093, March 2010. DOI: 10.13140/RG.2.1.1005.0407

Iverson, S, Kerkering, J C and Coleman, P, 2001. Using fault tree analysis to focus mine safety research, *108th Annual Exhibit and Meeting, Society for Mining, Metallurgy, and Exploration*, Feb. 26–28, 2001, 10 pp https://www.cdc.gov/niosh/mining/works/coversheet660.html

Lewis, H W, Bunitz, R J, Rowe, W D, Kouts, H J C, von Hippel, F, Loewenstein, W B and Zachareiasen, F, 1979. Risk assessment review group report to the U.S. Nuclear Regulatory Commission, *IEEE transactions on Nuclear Science*, 5:4686–4690. **DOI:** 10.1109/TNS.1979.4330198

Liu, Y and Song, W, 2019. Influences of extreme precipitation on China’s Mining Industry, *Sustainability*. 11, 6719, doi:10.3390/su11236719

Loechel, B, Hodgkinson J H and Moffat, K, 2011b. Pilbara Regional Mining Climate Change Adaptation Workshop: Report on workshop outcomes. 52 p. https://doi.org/10.4225/08/584d966eac088

Loechel, B, Hodgkinson, J H and Moffat, K, 2011a. Regional Climate variability assessment: the Pilbara, Preliminary overview for CSIRO workshop, The Leeuwin Centre, Floreat Park, WA, 21 July 2011, 16 p. https://publications.csiro.au/rpr/download?pid=csiro:EP114812&dsid=DS1

Loechel, B, Hodgkinson, J H, Moffat, K, Crimp, S, Littleboy, A and Howden, S M, 2010. Goldfields-Esperance Regional Mining Climate Vulnerability Workshop: Report on workshop outcomes. CSIRO Report EP106666. Pullenvale: CSIRO Earth Sciences and Resource Engineering. https://doi.org/10.4225/08/584ee639930ab

Mason, L, Unger, C, Lederwasch, A, Razian, H, Wynne, L and Giurco, D, 2013. Adapting to climate risks and extreme weather: A guide for mining and minerals industry professionals, NCCARF Synthesis and Integrative Research, https://nccarf.edu.au/wp-content/uploads/2019/03/Mason_2013_A_guide_for_mining_and_minerals_industry.pdf

Moffat, K, 2009. Climate adaptation in the Australian mining industry: Summary of workshop outputs. Internal CSIRO report. CSIRO Minerals Down Under National Research Flagship, Queensland Centre for Advanced Technology, Brisbane 12 November, 2009.

Nelson, R, Kokic, P, Crimp, S, Martin, P, Meinke, H, Howden, S M, de Voil, P and Nidumolu, U, 2010. The vulnerability of Australian rural communities to climate variability and change: Part II -Integrating impacts with adaptive capacity. *Environmental Science & Policy*, 13 (1),18–27, https://doi.org/10.1016/j.envsci.2009.09.006

PDC, 2017. Selecting sites for irrigation in the Pilbara – climate, land and water considerations, Pilbara Development Commission, Government of Western Australia, Accessed 9th May 2021 online, https://www.pdc.wa.gov.au/application/files/2415/1305/7729/PHADI_FS1_Selecting_site_for_irrigation_single_page.pdf

Preda, M, Wright, P and Gimber, C, 2006. Analysis of nutrient export to waterways using a GIS-based multiple criteria approach. *Environment Institute of Australia and New Zealand Conference*, Adelaide, 18–20 September 2006.

Preda, M, 2009. GIS-based environmental vulnerability mapping of coastal settings, with application to southeast Queensland, *Queensland Coastal Conference. Waves of Change*, 12–15 May 2009, Queensland.

van Haaren, R and Fthenakis, 2011. GIS-based wind farm site selection using spatial multi-criteria analysis (SMCA): Evaluating the case for New York State, *Renewable and Sustainable Energy Reviews*, 15, 3332–3340.

Lime magnetite pellets – an alternative iron ore feedstock for lower carbon footprint ironmaking

S Purohit[1], M I Pownceby[2], G Brooks[3] and M A Rhamdhani[4]

1. Research Scientist, CSIRO, Clayton Vic 3168. Email: suneeti.purohit@csiro.au
2. Senior Principal Research Scientist, CSIRO, Clayton Vic 3168.
   Email: mark.pownceby@csiro.au
3. Professor, Swinburne University of Technology, Hawthorn Vic 3122.
   Email: gbrooks@swin.edu.au
4. Professor, Swinburne University of Technology, Hawthorn Vic 3122.
   Email: arhamdhani@swin.edu.au

ABSTRACT

The current practice of magnetite ore agglomeration involves high temperature oxidation roasting (typically at 1200–1350°C) of magnetite to hematite phase in order to improve the strength and reducibility of pellets. The requirement to pre-oxidise the magnetite before introduction to an ironmaking plant increases the CO_2 emissions generated during the ironmaking process. In our previous papers, a novel, alternative agglomeration route for magnetite ores was presented where magnetite was converted to a reducible $CaFe_3O_5$ (CWF) phase through the addition of lime to produce a Lime-Magnetite Pellet (LMP) feedstock that can be directly charged to ironmaking units. The LMP process eliminates the magnetite oxidation stage, thereby reducing the CO_2 emission during ironmaking. The concept was tested by thermodynamic calculations, high temperature experiments and scaled-down pilot scale test work. In this paper, larger scale synthesis of half-stoichiometric LMPs (1 mole of Fe_3O_4 and ½ mole of $CaCO_3$) were prepared using a balling drum, followed by overnight drying at 110°C and induration at 1050°C for two hours. The LMPs were analysed using X-Ray Diffraction and Scanning Electron Microscope techniques for phase and microstructure characterisation. The LMPs were found to have 14–15 wt. per cent of CWF phase when indurated under a CO_2/CO ratio of 8.5:1. Pilot scale testing of the LMPs was conducted following ISO standard test procedures. The test results indicated the LMP's had a Reducibility Index (RI) of over 91 per cent, a Tumbler Index (TI) of 87 per cent and a Reduction Degradation Index (RDI) of 4.6 per cent. The results indicate LMPs may be useful as an alternative feedstock to ironmaking processes that would result in lower overall CO_2 emissions.

INTRODUCTION

Magnetite ore is one of the most widely used iron ores for ironmaking because of its high iron and low impurity contents after beneficiation. Magnetite, however, has a significantly lower reducibility compared to hematite and is not directly suitable for ironmaking in shaft furnace processes such as the Blast Furnace or a Midrex furnace. The current practice of magnetite ore agglomeration involves high temperature oxidation roasting of magnetite concentrate, typically at 1200–1350°C, to convert magnetite to the more readily reduced hematite phase. The two-stage pre-heating and induration process improves the strength and reducibility of the resulting pellets, making them suitable for ironmaking. However, the requirement to pre-oxidise the magnetite before introduction to an ironmaking plant increases the CO_2 emissions generated during the ironmaking process. In our previous papers, a novel, alternative agglomeration route for magnetite ores was presented where magnetite was converted to a reducible $CaFe_3O_5$ (CWF) phase through the addition of limestone to magnetite and indurating the lime magnetite pellets (LMPs) at 950 to 1100°C under mildly reducing conditions (Purohit *et al*, 2018, 2019, 2020a, 2020b, 2021a, 2021b). The flow sheets for the conventional magnetite pelletisation and the proposed LMP processes are shown in Figure 1.

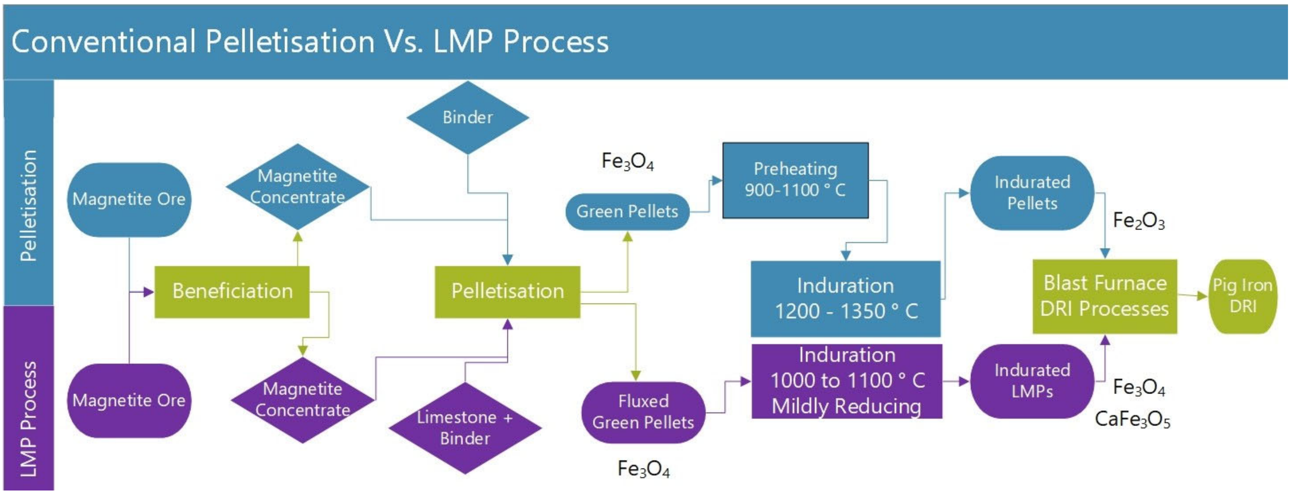

FIG 1 – Schematic flow sheets for magnetite ore agglomeration processes comparing the current magnetite pelletisation route (upper) and the proposed LMP route (lower).

The concept was previously tested by thermodynamic calculations and high temperature laboratory experiments. Experimental results suggested perceptible CWF formation within five mins of reaction at 950–1050°C and reaching near equilibrium percentage after one hour of reaction for pure laboratory grade chemicals (Purohit *et al*, 2020a, 2020b). Microstructural analysis suggested an interconnected platelet shaped morphology of CWF phase and an overall open microstructure of the LMPs (Purohit *et al*, 2020a). Further study on the effect of impurity oxides (laboratory grade) on CWF formation suggested Al and Si impurities led to a reduced CWF percentage due to the formation of larnite (Ca_2SiO_4) and calcium alumino-ferrite/brownmillerite ($Ca_2(Al,Fe)_2O_5$) phases (Purohit *et al*, 2021b, 2021a). In addition to the phase and microstructure analysis, the LMPs were tested using a scaled-down reducibility test and a compact Tumble Index (TI) test and were found to have comparable reducibility and strength to industrial sinters (Purohit *et al*, 2019). In this paper, we extend the laboratory scale test work to a larger scale study by synthesizing, under various experimental conditions, a pilot scale batch of LMPs. The LMP batch that produced the highest amount of CWF phase was selected for pilot testing using standard ISO Reducibility Index (RI), TI, and Reduction Degradation Index (RDI) tests.

PILOT SYNTHESIS OF LMPS

Raw materials

The LMPs reported in earlier literature were synthesized by compacting the raw mix of pure laboratory-grade chemicals (Purohit *et al*, 2021b, 2020b). For the pilot syntheses, LMPs were prepared using magnetite concentrate (sourced from OneSteel) and limestone. The as-received magnetite concentrate had 4.5 wt. per cent moisture with about 94 wt. per cent passing 45 µm. The as-received limestone was milled to -45 µm in a ball mill at 70 rev/min for 50 mins using a 60 per cent slurry. The milled limestone was then oven dried to drive out any remaining moisture. The composition of magnetite concentrate, and limestone are shown in Table 1.

TABLE 1

Chemical composition (by XRF) of the raw materials used to produce the LMPs.

Sample	**Oxide/element wt.%**												
	Fe	FeO	SiO_2	Al_2O_3	P	S	CaO	TiO_2	MgO	Mn	Cl	Na_2O	K_2O
Magnetite	65.52	24.5	4.91	0.15	0.017	0.02	1.13	0.02	1.04	0.06	0.008	-0.01	0.002
Limestone	0.21		0.45	0.17	0.003	-0.001	54.6	0.022	0.44	-0.01	0.004	0.026	0.02

Seeding and balling

A blend of the magnetite concentrate and 20 wt. per cent of the dried and crushed limestone was used to prepare an LMP batch mixture of half-stoichiometric composition (1 mole Fe_3O_4 and ½ mole $CaCO_3$). The half-stoichiometric composition was chosen to produce the LMPs as the overall chemistry was of similar basicity to usual blast furnace sinters. Water was then added to the blend to target 8.5 wt. per cent total moisture. The mix was used to make seeds using a small rotating drum. Using the seeds of size fraction +4.0 mm to -4.35 mm, balling was then done in a balling drum for ten mins. Additional water was added at this stage to bind the blend mix to the seeds. Two batches were made in order to grow the balls using 75 g then 60 g of seeds. This was done to try and achieve larger balls and to minimise waste of material while growing the seeds. The 60 g of seeds produced slightly bigger pellets and the resulting size fraction of the pellets was: 0.4 wt. per cent of +12.5 mm, 82.2 wt. per cent of +10.0 mm, 16.1 wt. per cent of +8.0 mm and 1.3 wt. per cent of +6.3 mm.

Drying and induration

The green LMPs were first dried at 110°C overnight and then were indurated inside a vertical tube furnace. A sample batch of 270 ± 20 g were chosen for each test based on the size of the crucible (5.2 cm Diameter and 13 cm Height) and the measured hot zone of the furnace (about ten cm at the centre of the furnace). The schematic of the experimental set-up is shown in Figure 2. The earlier studies using laboratory experiments and scaled-down pilot testings suggested that the LMPs indurated at 950–1050°C had similar strength and reducibility values to that of industrial sinters. After induration at 1050°C, the LMPs had slightly higher compact TI values than at 950°C and therefore, 1050°C was chosen in this study as the induration temperature required for preparing each pilot testings batch.

A schematic of the experimental set-up for preparing each LMP batch is shown in Figure 2.

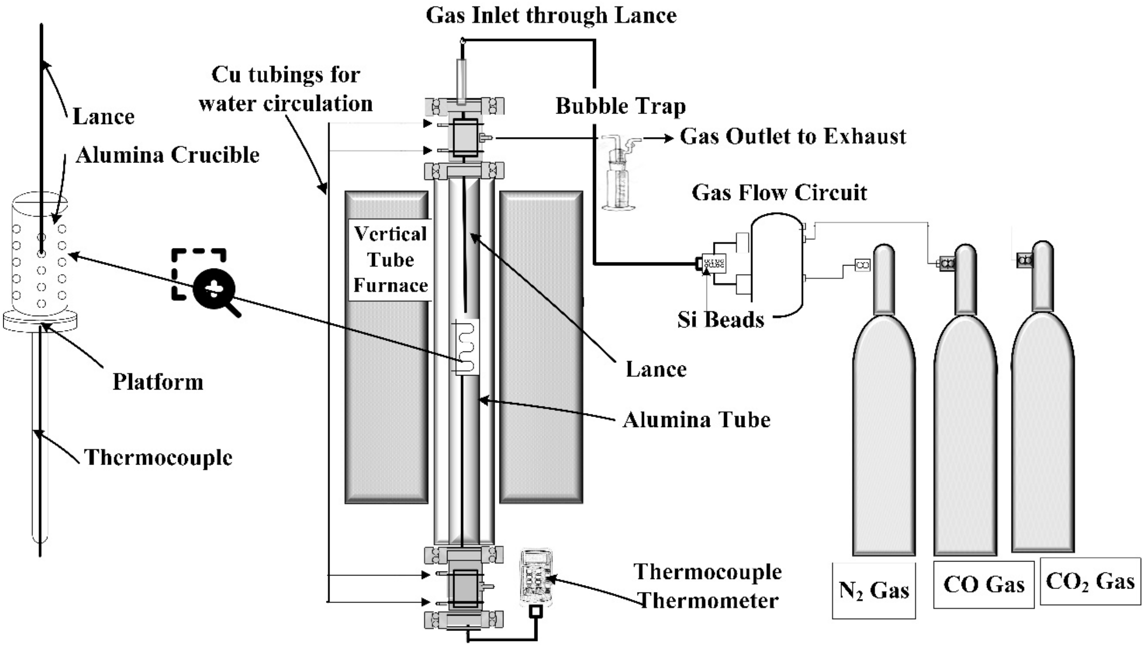

FIG 2 – Schematic of experimental set-up for preparing LMP batch samples.

The induration experiments were conducted inside a vertical tube furnace that had connections to gas inlet and outlet valves. The ends of the furnaces were water-cooled. Three gas lines (CO, CO_2 and N_2) were connected to the gas flow circuit with mass flow controllers used to adjust the composition and flow rate of the furnace inlet gases. The furnace outlet gas line was connected to a bubble trap to check the gas flow before exiting to the exhaust. The experiments were conducted at various oxygen partial pressures by maintaining different CO/CO_2 ratios of the inlet gas. The flow rate of the inlet gas was set to 1.5/L/min.

Each pilot batch of dried, green LMPs were loaded inside an open topped crucible that had perforations base and sides (to improve gas flow within the crucible). The crucible was placed on an alumina platform and loaded inside the furnace so that the crucible was situated in the hot zone of the furnace. The temperature at the bottom of the crucible was measured using an R-type thermocouple that was mounted at the base of the platform (ie base of crucible). The inlet gas was passed through a top lance as shown in Figure 2. To start the experiment, the crucible containing the LMPs was loaded inside the furnace by raising the platform. The furnace was then sealed and N_2 gas was used to purge the furnace. The furnace was initially heated under an inert atmosphere until the thermocouple reached 1050°C. The temperature distribution through the pellet bed was about 1050 ± 30°C. Each experiment was conducted at a fixed CO_2/CO for two hours and after completion, the LMPs were cooled inside the furnace using N_2 gas. Experiments were conducted at various CO_2/CO ratios: 10:1, 8.5:1, 7:1 and 4:1.

Phase and microstructure characterisation

The indurated LMPs from the top, middle, and bottom sections of the crucible were analysed using X-ray Diffraction (XRD) and Rietveld Refinement-Based Quantitative Phase Analysis (QPA) for phase identification and quantification. For the XRD analysis, the samples were micronised using a hand mortar and pestle and then loaded onto low background plates held in PANalytical sample holders for flat plate presentation to the X-ray beam. Diffraction data were collected for 2θ angles ranging from 5 to 140° at 40 kV and 40 mA using a PANalytical Empyrean instrument fitted with a cobalt long-fine-focus X-ray tube. PANalytical HighScore Plus© software (V4.5) was used for phase identification. Rietveld QPA was carried out on the diffraction patterns using TOPAS (V6) software (Hill and Howard, 1987; TOPAS (2009) Version 4.2).

The indurated LMPs were also analysed using Scanning Electron Microscopy (SEM) and Energy Dispersive Spectroscopy (EDS) to identify the chemistry of the key phases and their morphology. For the SEM analysis, the small samples of indurated LMPs were directly analysed under FEI Quanta 400 Field Emission Environmental SEM (ESEM) at a 15 kV operating voltage and a 10 mm working distance. The EDS analyses were conducted on unpolished samples to determine the chemistry of the different phases.

PILOT TESTINGS OF LMPS

Reducibility test

Reducibility Index measures the ease at which the combined oxygen contained in iron ore can be removed. The RI of the indurated LMPs was measured using the ISO 7215 standard RI test (ISO 7215:2015). ISO 7215 is a standard reducibility test applicable for hot-bonded pellets, sinters and lump ores. For the test, 500 g of 10.0 to 12.5 mm sized LMPs were reduced in a fixed bed at 900°C using a reducing gas consisting of 30.0 vol. per cent CO and 70.0 vol. per cent N_2 gas for three hours (Lu, 2015). The flow rate of the reducing gas was maintained at 15/L/min. The final reduction degree was calculated from the measured mass loss after three hours of reduction using the following Equation:

$$R_{180} = \left[\frac{(\Delta m)}{m_0 \times (0.430 \times W_2 - 0.111 W_1)} \times 100\right] \times 100 \tag{1}$$

Where:

m_0	is the mass in grams of the test portion
Δm	is the difference in mass before and after reaction at 900°C ie the mass loss of the test portion after 180 mins of reduction due to oxygen removal
W_1	is the iron (II) oxide content as a percentage of the mass, of the test portion prior to the test)
W_2	is the total iron content, as a percentage of the mass, of the test portion prior to the test

The degree of reduction after three hours reduction is called the Reducibility Index (RI).

Tumble index (TI)

The ISO 3271 standard test is used for evaluating the resistance of iron ore feedstocks (hot-bonded pellets, sinters and lump ores) to size degradation resulting from abrasion and impact (ISO 3271:2015). The TI of the indurated LMPs was measured using the ISO 3271 test. A test portion of 15 kg of LMPs in the size range of 6.3 mm to 40.0 mm were tumbled in a circular rotating drum for a total of 200 revolutions, at a speed of 25 rev/min. The TI was expressed as the mass percentage of materials greater than 6.3 mm remaining after the tumble test (Lu, 2015).

Reduction degradation index (RDI)

After charging the feedstock to the shaft furnace, the permeability of burden is affected by the breakdown of the iron ore feedstock due to reduction. The reduction degradation of the LMPs was measured using the ISO 4696–2 Reduction Degradation Index (RDI) standard test (ISO 4696–2:2007). The test involved isothermal reduction of 500 g of LMPs of 10.0 mm to 12.5 mm size range at 550°C under a reducing gas atmosphere consisting of 30.0 vol. per cent CO and the rest N_2 for 30 min. at a gas flow rate of 15/L/min (Lu, 2015). The reduced sample was tumbled at 30 rev/min for 900 revolutions and then sieved with a 2.8 mm sieve of square openings. The mass percentage of material less than 2.8 mm was considered as the RDI (Lu, 2015).

RESULTS AND DISCUSSION

Phase and microstructure analysis

XRD analysis was conducted on the LMPs from the top, mid and bottom sections of the crucible from the induration experiments at the various CO_2/CO ratios. The XRD patterns of the top, mid and bottom sections from experiments at the CO_2/CO ratio of 8.5:1 are shown Figure 3. As the LMPs were of half-stoichiometric composition, the diffraction patterns are dominated by Fe_3O_4 peaks. All three samples show the formation of CWF phase along with $Ca_2Fe_2O_5$ (C_2F) and Ca_2SiO_4 phases. A small peak of wüstite was also present in all patterns, with slightly more FeO present in the middle layers (shown in Figure 3).

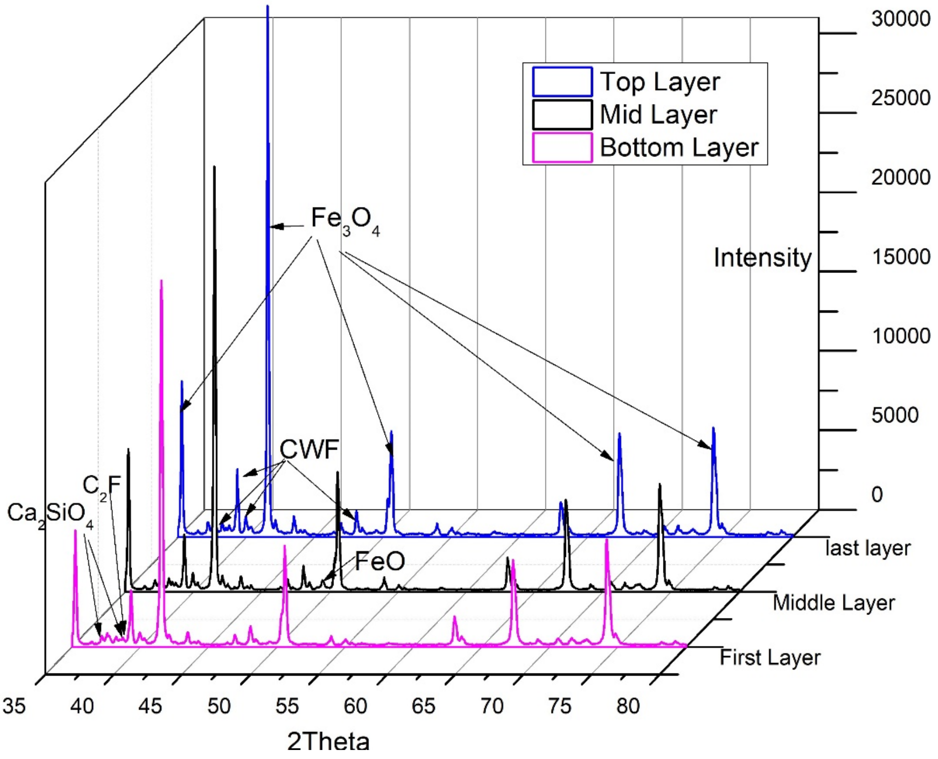

FIG 3 – XRD patterns from the top, middle, and last sections of the crucibles from induration experiments conducted at 1050°C for two hours and a CO_2/CO ratio of 8.5:1.

The Rietveld QPA results quantify the various phases present and the wt. per cent of CWF phase in all samples are summarised in Figure 4. The QPA results indicates that at the higher reduction potentials (ie lower CO_2/CO ratios), the CWF percentage increases. The top section of sample from the induration experiments (marked as red in Figure 4) at a 4:1 CO_2/CO ratio had about 21 wt. per cent CWF phase, but also had about 36 wt. per cent of wüstite (FeO). At a higher CO_2/CO ratio, the FeO percentage decreased and the samples from all three sections of the crucible had a similar composition. For example, at a CO_2/CO ratio of 8.5:1, the samples had a CWF percentage of about 16–17 wt. per cent in all three layers and an FeO content of less than two wt. per cent. Wüstite is a very dense phase and can decrease the reducibility of LMPs. Therefore, the CO_2/CO ratio of 8.5:1 was selected for synthesis of large batches LMPs for pilot testings.

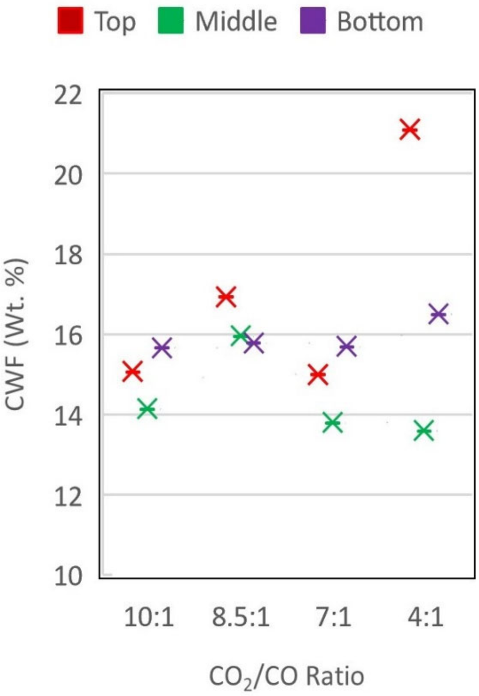

FIG 4 – Plot showing the per cent CWF phase in the LMPs from induration experiments at 1050°C (two hours) and at various CO_2/CO ratios.

A Backscattered Electron (BSE) micrograph from one sample from the induration experiment at a CO_2/CO ratio of 8.5:1 is shown in Figure 5. The microstructure is similar to that observed in the previously reported studies (Purohit *et al*, 2021a, 2020a). The CWF phase has a platelet morphology and the C_2F phase is globular shaped. Overall, the microstructure appears porous with distribution of CWF and C_2F phases throughout the microstructure. SiO_2-containing phases such as Ca_2SiO_4 were found in the LMPs as well (Figure 5).

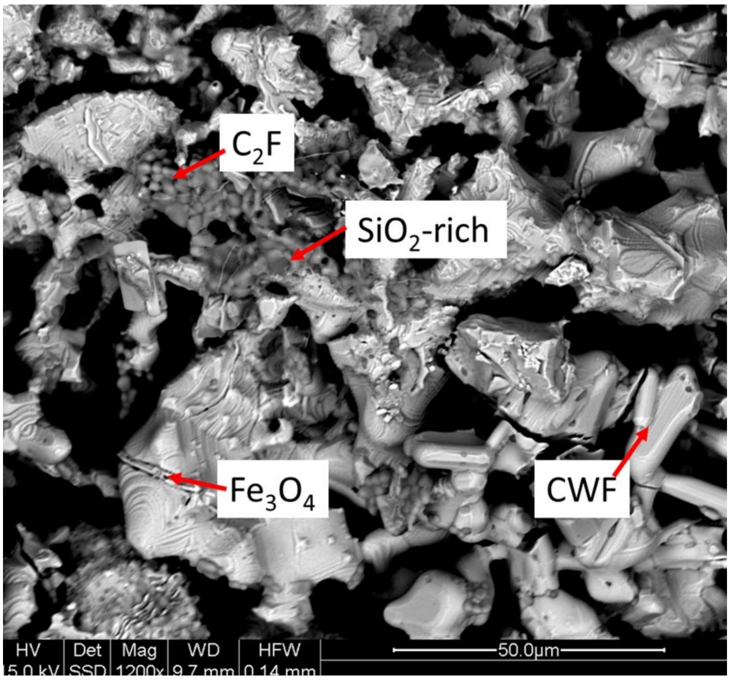

FIG 5 – BSE micrograph of an LMP indurated at 1050°C (two hours) and a CO_2/CO ratio of 8.5:1. CWF has a platelet type morphology whereas C_2F is globular in appearance.

Pilot scale testing results

The reducibility of the LMPs were measured in two batches and the Reducibility Index (RI) was found to be 91.6 per cent and 95.2 per cent. These numbers are significantly higher than the acceptable RI of Blast Furnace feedstocks which is typically >60 per cent for sinters and >70 per cent for pellets (Lu, 2015). The Reduction Degradation Index (RDI) of the LMPs was found to be 4.6 per cent, which is similar to commercial pellets and better than the sinters (<35 per cent) (Lu, 2015). The Tumble Index of the LMPs was 87 per cent indicating they are stronger than sinters (>65 per cent) and of similar strength to pellets (>90 per cent) (Lu, 2015). In summary all the pilot scale testing results suggest that the LMPs would be suitable as a feedstock for blast furnace ironmaking. The quality of LMPs are also likely to be suitable for a DRI operation, but chemistry wise, LMPs will have a higher basicity compared to a typical DRI feedstock.

IMPACT OF LMP PROCESS ON CO_2 EMISSIONS

The CO_2 emissions resulting from the reduction of Fe_2O_3 phase to Fe_3O_4 phase in the current pelletisation process is about 129 kg CO_2 per tonne iron production (Purohit *et al*, 2020b). With the LMP process, magnetite oxidation to hematite is eliminated, resulting in lower CO_2 emissions in the ironmaking stage. The pilot testing results suggest LMPs can be a suitable replacement to the blast furnace sinters. By lowering the sinter percentage in the blast furnace feedstock, the direct and indirect CO_2 emissions (from coke making) associated with sintering will go down, resulting in ironmaking with a lower carbon footprint. Detailed emission analysis of LMP process will be the subject of future study.

CONCLUSIONS

The LMP process eliminates the necessity of magnetite oxidation and hence, reduces the CO_2 emissions in the later ironmaking stage. Several studies have been reported earlier on thermodynamic analysis, LMP synthesis, and scaled-down laboratory testings. In this paper, pilot scale synthesis of LMPs was discussed. The LMPs produced in batches at 1050°C for two hours induration and various CO_2/CO ratios had about 14–21 wt. per cent of CWF phase based on the reduction potential and the position of LMPs in the crucible. At a 8.5:1 ratio of CO_2/CO, the LMPs had limited magnetite to wüstite conversion (<2 wt. per cent) and uniform CWF conversion (about 14–15 wt. per cent) in all the top, middle and bottom sections of the crucible. The microstructure of the batch scale LMPs was similar to the previously reported results with platelet shaped CWF morphology and a porous structure. Pilot tests of the LMPs were conducted using ISO standard tests and the results indicated the LMPs would be suitable as a potential feedstock to ironmaking processes.

ACKNOWLEDGEMENTS

The authors would like to thank Matt Adam and Matt Kilburn for their help in balling and pilot scale testings of LMPs. Keith Vining and Liming Lu are also thanked for discussions involving the potential suitability of LMPs for ironmaking processes.

REFERENCES

Hill, R J and Howard, C J, 1987. Quantitative phase analysis from neutron powder diffraction data using the Rietveld method, *J Appl Crystallogr*, 20:467–474.

ISO – ISO 3271:2015 – Iron ores for blast furnace and direct reduction feedstocks — Determination of the tumble and abrasion indices, https://www.iso.org/standard/62135.html (accessed 5.31.21).

ISO – ISO 4696–2:2007 – Iron ores for blast furnace feedstocks — Determination of low-temperature reduction-disintegration indices by static method — Part 2: Reduction with CO and N2, https://www.iso.org/standard/38077.html (accessed 5.31.21).

ISO – ISO 7215:2015 – Iron ores for blast furnace feedstocks — Determination of the reducibility by the final degree of reduction index, https://www.iso.org/standard/62142.html (accessed 5.31.21).

Lu, L, 2015. *Iron ore: Mineralogy, processing and environmental sustainability, Iron Ore: Mineralogy, Processing and Environmental Sustainability*, Elsevier Inc.

Purohit, S, Brooks, G, Rhamdhani, M A and Pownceby, M I, 2018. Alternative processing routes for magnetite ores, in *AISTech – Iron and Steel Technology Conference Proceedings*, pp 399–406.

Purohit, S, Brooks, G, Rhamdhani, M A, Pownceby, M I and Torpy, A, 2021a. Effect of impurity oxides on CWF ($CaFe_3O_5$) formation in lime magnetite pellets–part II: microstructural analysis and physical and mechanical testing, *Ironmak Steelmak*, 48:313–323.

Purohit, S, Brooks, G, Rhamdhani, M A, Pownceby, M I and Ware, N, 2019. Lime-Magnetite Pellets (LMPs) for Ironmaking, in *AISTech 2019 Proceedings*, pp 687–700.

Purohit, S, Brooks, G, Rhamdhani, M A, Pownceby, M I and Webster, N A S, 2020a. Analyses of CWF ($CaFe_3O_5$) phase formation in lime-magnetite pellets, *Ironmak Steelmak,* 47:852–864.

Purohit, S, Brooks, G, Rhamdhani, M A, Pownceby, M I and Webster, N A S, 2020b. Alternative route for magnetite processing for lower carbon footprint iron-making through lime-magnetite pellets containing $CaFe_3O_5$, *Ironmak Steelmak*, 47:674–685.

Purohit, S, Brooks, G, Rhamdhani, M A, Pownceby, M I and Webster, N A S, 2021b. Effect of impurity oxides on CWF ($CaFe_3O_5$) formation in lime magnetite pellets–part I: thermodynamic assessments and experimental investigations, *Ironmak Steelmak*, 48:299–312.

TOPAS (2009) Version 4.2: general profile and structure... – Google Scholar, https://scholar.google.com/scholar?q=TOPAS %282009%29 Version 4.2%3A general profile and structure analysis software for powder diffraction data%2C Bruker AXS%2C Östl. Rheinbrückenstraße 49%2C 76187 Karlsruhe%2C Germany (accessed 5.28.21).

Solar processing of iron ores

S Purohit[1], M I Pownceby[2], G Brooks [3] and M A Rhamdhani[4]

1. Research Scientist, CSIRO Mineral Resources, Clayton South, Vic 3169.
   Email: suneeti.purohit@csiro.au
2. Senior Principal Research Scientist, CSIRO Mineral Resources, Clayton South, Vic 3169.
   Email: mark.pownceby@csiro.au
3. Professor, Swinburne University of Technology, Hawthorn, Vic 3122.
   Email: gbrooks@swin.edu.au
4. Professor, Swinburne University of Technology, Hawthorn, Vic 3122.
   Email: arhamdhani@swin.edu.au

ABSTRACT

The use of concentrated solar flux for high temperature metallurgical applications is a well-researched area with several reported literatures on solar calcination and metal oxide reduction. This paper presents two such processes with potential to reduce the carbon footprint from ironmaking through using concentrated solar flux. The first process involves solar flux incorporation to the recently developed lime-magnetite pellet (LMP) route of magnetite ore agglomeration. The second process is a hybrid solar-smelting route for iron ore-coal composite pellets that utilises solar flux to provide process heat. Both the concepts of solar agglomeration and solar smelting process were investigated using a solar simulator-hybrid reactor set-up at Swinburne University of Technology. Results from solar agglomeration experiments at 950°C suggested no change in the reaction mechanism of the LMPs under solar irradiation compared to electrical heating. The percentage and morphology of the primary phases (mainly $CaFe_3O_5$) appeared similar for both solar and electric heated LMPs. The solar-smelting of magnetite concentrate-lignite coal composite pellets at 1130°C showed a maximum metallisation of 55 per cent after 1.5 hrs of reaction. The solar-smelt process has about 25 to 35 per cent lower CO_2 emission compared to the blast furnace ironmaking. Techno-economic analysis of implementing a CST facility in an existing composite pellet process suggested a payback period of about ten years at a heliostat cost of \$A100/m^2 and natural gas cost of A\$10/GJ. The economics of CST implementation can be further enhanced by decreasing the thermal losses from the heliostat field and reactor.

INTRODUCTION

The application of concentrated solar thermal (CST) for pyrometallurgical applications is a well-studied area. The most extensively studied materials for solar thermal processing are ZnO, $CaCO_3$, Al_2O_3, MgO, SiO_2 and Fe_2O_3 (Ekman, Brooks and Rhamdhani, 2014; Steinfeld and Meier, 2004; Steinfeld and Palumbo, 2001). Over the years, several directly and indirectly heated solar reactor designs have been proposed and several pilot facilities have been developed for testing and increasing the Technology Readiness Level (TRL) of solar-driven pyrometallurgical processes. Some of the pilot facilities include a 300-kW two-cavity reactor for carbothermic reduction of ZnO (SOLZINC project), a one MW pilot solar calciner with continuous fluidised bed reactor at CNRS (National Centre for Scientific Research, France), a ten kW rotary kiln for continuous operation at DLR (German Aerospace Centre, Germany), a 30 kW bubbling fluidised bed reactor at INCAR-CSIS (Institute of Carbon Science and Technology, Spain), and a 18–28 kW cyclone reactor and ten kW fluidised bed and rotary kiln at PSI (Paul Scherrer Institute, Switzerland) (Abanades and André, 2018; Esence *et al*, 2020; Meier *et al*, 2004, 2006; Moumin *et al*, 2020; Wieckert *et al*, 2007). The SOLZINC project has demonstrated a yield of 50 kg/h of 95 per cent-purity Zn in the temperature range of 1027 to 1227°C (Wieckert *et al*, 2007). Pilot experiments at CNRS showed over 95 per cent calcite conversion at 950 to 1050°C and a 20 kg/hr mass flow rate (Esence *et al*, 2020). The rotary kiln at DLR has been successfully tested for continuous limestone decarbonation as well as for metal oxide granule redox reactions involving CuO/Cu_2O and Co_3O_4/CoO systems for thermal storage (Meier *et al*, 2004, 2006).

The major challenges for implementing pyrometallurgical processes using CST are the high capital costs, limited throughput, maintaining a controlled atmosphere (reducing/inert/pressurised), damage to the transparent windows due to the complex solid-liquid-gas reactions inside the solar reactor, lower thermal/conversion efficiencies and the intermittency of solar flux. However, over the years, major improvements in reactor thermal efficiencies, thermal storage mediums and heliostat designs have progressed, and the commercialisation of CST processes are becoming feasible, particularly in areas such as parts of Australia which have strong solar fluxes.

This paper provides insights towards the potential use of CST applications in the ironmaking industry. A solar-agglomeration process for magnetite ore and a solar composite pellet reduction were investigated using solar simulator experiments. The experimental program was supplemented by a techno-economic evaluation for installing CST facilities at an existing iron ore smelting plant. This paper provides a summary of the work while a more detailed and systematic analysis have been presented elsewhere (Purohit *et al*, 2021).

SOLAR PROCESSING OF IRON ORES

The iron and steelmaking industry is one of the major contributors to the total industrial CO_2 emissions with nearly 1.8 t of CO_2 emitted per tonne of steel. Considering the current global push towards green-steel production, it is high time to evaluate the potential of CST applications in the iron and steelmaking industry. There have been few studies in the past looking at processing of iron ores using CST and these are listed in Table 1.

TABLE 1

List of literatures on solar processing of iron ores.

Sl. No.	Research	Results	Reference
1	Treatment of steel mill waste in a fluidised bed solar reactor at 900–1000°C.	Produced magnetite without any contaminants.	(Ruiz-Bustinza *et al*, 2013)
2	Studied stationary Iron ore sintering at 1200–1400°C and subsequent smelting of sinters using a 1.5 kW vertical axis solar furnace.	Reaction was not uniform throughout sinter the bed. Metallic iron was detected in smelting experiments.	(Fernández-González *et al*, 2017)
3	Reduction of hematite with graphite under solar flux.	Achieved highest metallisation of 77–78 per cent at the temperature range of 1577–1727°C.	(Steinfeld and Fletcher, 1991)
4	Magnetite reduction experiments in a solar furnace consisting of a two-stage concentrator and a solar receiver.	Achieved two-stage reduction of Fe_3O_4 to FeO and Fe, and a maximum metallic iron yield of 68 per cent at 1000°C.	(Steinfeld, Kuhn and Karni, 1993)
5	Carbothermal reduction of Fe_2O_3 using a vertical axis solar furnace.	Reported limited metallisation percentage due to the formation of iron carbide.	(Mochón *et al*, 2014)

There are also significant research activities in the field of syngas or H_2-gas generation using various methods such as water splitting, natural gas cracking, reforming and pyrolysis of methane and coal gasification (Tran *et al*, 2012). Solar-generated reducing gases is another application area for using concentred solar flux in iron ore agglomeration and smelting.

In this paper, two novel routes of solar-iron ore processing are discussed that have the potential to significantly reduce the current emission from ironmaking industry. The first process involves a novel magnetite ore agglomeration process using CST and the second process involves carbothermic reduction of composite pellets using CST.

SOLAR AGGLOMERATION OF MAGNETITE

In our previous papers, an alternative magnetite ore agglomeration route was proposed that eliminates the magnetite oxidation process from the current practise, thereby reducing the overall CO_2 emissions in the ironmaking stage (Purohit *et al*, 2019, 2020a). The process is called the Lime Magnetite Pellet (LMP) process and involves addition of lime to magnetite, forming pellets, and them indurating the pellets in the temperature range of 950–1100°C in a mildly reducing atmosphere. The induration of the LMPs results in the formation of $CaFe_3O_5$ (CWF) phase, which has a platelet morphology making the overall microstructure highly porous. Scaled-down reducibility and tumble tests show that the LMPs have a similar strength and reducibility to industrial sinters. As the process operates at a temperature below 1100°C, LMPs become a suitable candidate for CST application. The LMP process can also be fully operated using H_2 gas or syn-gas produced from solar flux.

Solar induration experiments

In our recent work, solar induration experiments were conducted, and initial results have been reported (Purohit *et al*, 2020c). The LMPs of two different compositions (stoichiometric: 1 mole Fe_3O_4 and 1 mole $CaCO_3$ and half-stoichiometric: 1 mole Fe_3O_4 and ½ mole $CaCO_3$) were prepared using laboratory-grade chemicals. The LMPs were then loaded inside a fused-quartz sample holder (thermocouple attached) and indurated in a solar simulator and hybrid reactor set-up using two 6 kW rated metal halide lamps. The peak flux of each lamp ranges between 117 kW/m^2 to 148 kW/m^2. The experiments were conducted under both electric and solar heating at a reaction temperature of 950 ± 30°C for one hour. The temperature profile of each experimental run is shown in Figure 1. A reducing atmosphere was maintained inside the reactor bypassing CO/CO_2 gas at a 1:4 ratio.

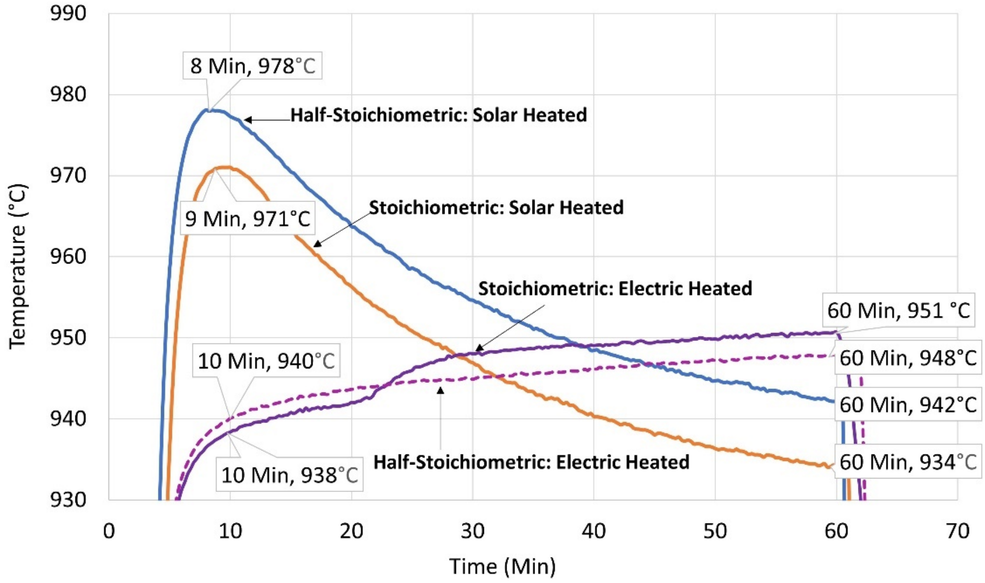

FIG 1 – Temperature profile inside the fused-quartz sample holder at the centre of hybrid reactor.

Analysis of indurated LMPs

The indurated LMPs were analysed to determine their mineralogy and microstructure using both X-Ray Diffraction (XRD) and Scanning Electron Microscope (SEM) instruments. The XRD data for the solar and electric heated samples were quantified using Rietveld quantification and the results are shown in Figure 2. The results indicate higher conversion of Fe_3O_4 to CWF phase in the solar-heated LMPs compared to electric heated samples (eight wt. per cent higher for stoichiometric LMPs and one wt. per cent for half-stoichiometric LMPs). The electric heated sample showed a higher percentage of $Ca_2Fe_2O_5$ (C_2F) phase and over the presence of unreacted Fe_3O_4. The slower reaction kinetics of the electric heated samples was due to the lower reaction temperature at the beginning of the reaction as shown in Figure 1. Previously reported studies on LMPs suggest that at lower reaction temperature of 850°C, LMPs showed higher C_2F and lower CWF compared to that at 950°C (Purohit *et al*, 2020b, 2020a).

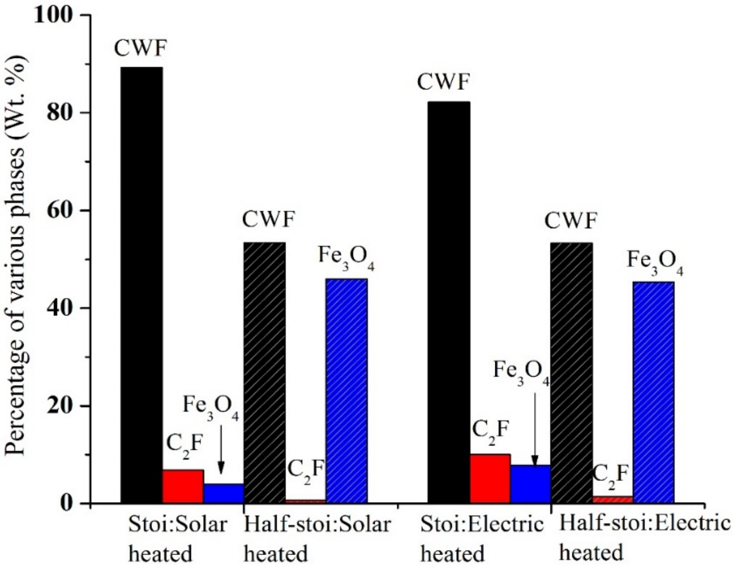

FIG 2 – Rietveld Quantification results of solar and electric heated LMPs.

The SEM micrographs shown in Figure 3 highlight the platelet morphology of CWF phase in both the electric and solar-heated samples. Overall, the microstructures of the indurated LMPs were indistinguishable from each other suggesting no change in reaction mechanism from the electric to solar transition.

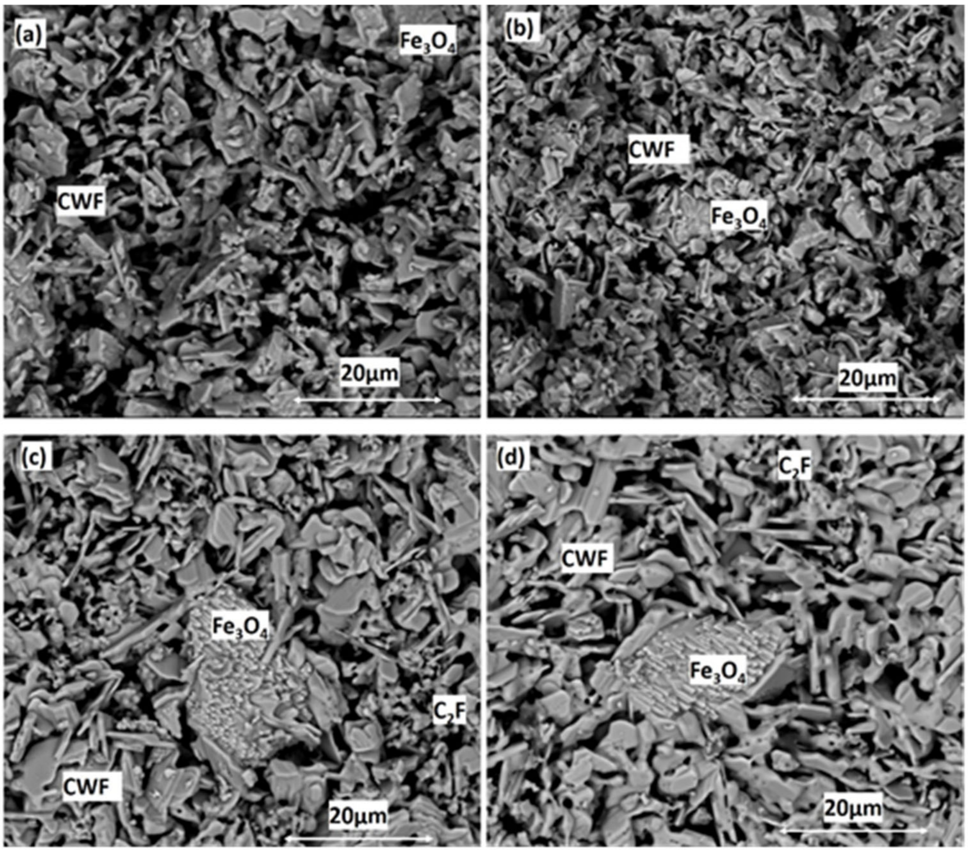

FIG 3 – Backscattered Electron micrographs showing microstructures in (a) half-stoichiometric LMPs reacted under electric heating, (b) half-stoichiometric LMPs reacted under electric and solar heating, (c) stoichiometric LMPs reacted under electric heating, (d) stoichiometric LMPs reacted under electric and solar heating.

SOLAR REDUCTION OF COMPOSITE PELLETS

Iron ore reduction and smelting happens at high temperatures and most of the world's iron is produced using shaft furnace processes such as the Blast Furnace and the Midrex process. Direct utilisation of concentrated solar flux in the shaft furnace ironmaking processes will be very challenging considering the size of reactor and bed depth. In a previous study, we proposed a solar smelting process for iron ores that utilises a hybrid rotary hearth reactor with provision for natural gas heating (similar to the ITmk3 process) and a heliostat field to direct the sunlight towards a reflecting shine-down mirror which redirects the concentrated light to a receiver cavity (Purohit *et al*, 2018). The receiver cavity directs the concentrated solar flux to the hybrid reactor through a quartz window. The schematic of the process is shown in Figure 4.

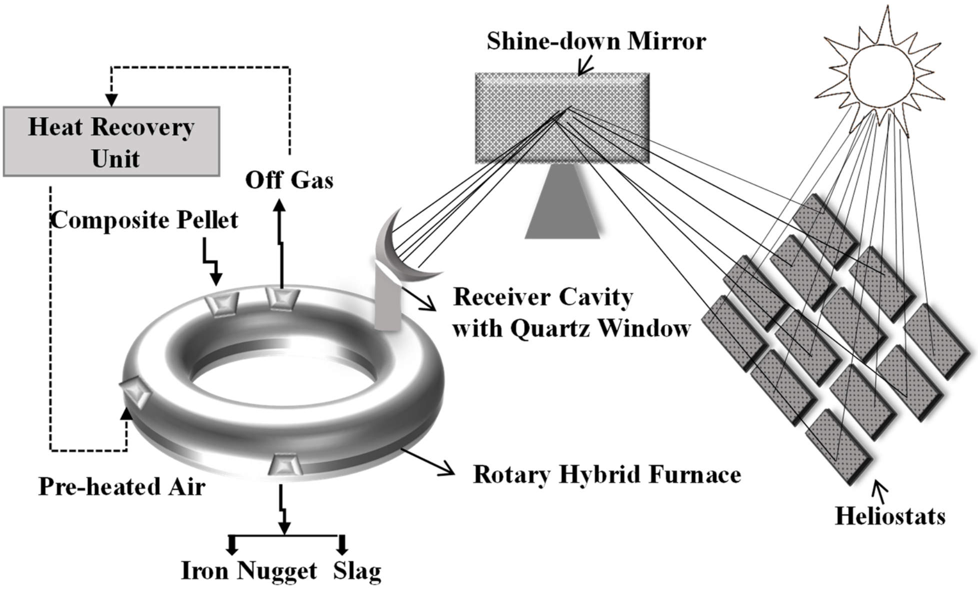

FIG 4 – Schematic of the solar smelting process (Purohit *et al*, 2018).

Solar-smelting experiments and emission analysis

The concept of solar reduction was tested in the laboratory using a solar simulator and hybrid reactor set-up of one MW capacity. The composite pellets of magnetite concentrate (89 wt. per cent Fe_3O_4 and average particle size of 5 µm) and pulverised lignite coal were prepared with a blend composition comprising a 1:1 stoichiometric ratio of Fe_3O_4 and C. The pellets were reduced under solar heating using three lamps (each lamp having peak flux of 117 kW/m^2 to 148 kW/m^2) and a maximum metallisation of 55 per cent was achieved at the average reactor cavity temperature of 1130°C after 1.5 hrs of reaction. The level of reduction in the solar reactor was comparable with results from electrically reduced pellets and hence, at higher reactor temperatures (which was not possible due to limitations in reactor refractory and safety hazards), a higher degree of metallisation is expected.

A mass and energy analysis of the solar smelting was performed that suggested about a 20 per cent reduction in CO_2 emissions compared to the ITmk3 process (an existing composite pellet process) and 25–35 per cent emission reduction from the blast furnace route of iron production (Purohit *et al*, 2018). Over the last few years, various steelmaking plants from around the world have declared a desire to reduce their net CO_2 emissions by 20–30 per cent and the solar-smelt process, using composite pellets of iron ore and metallurgical/non-metallurgical coal or biomass, can potentially provide a suitable alternative towards achieving these targets. Although there are several challenges associated with the operation of a solar-smelt plant, the CST technologies are advancing quite fast compared to the alternative green-H_2 gas (from water electrolysis using renewable energy).

Techno-economic analysis of solar-smelt process

A previous study on the feasibility of the solar-smelt process presented a preliminary techno-economic evaluation for a 200 000-tonne capacity solar smelt plant running nine hours per day. The CAPEX of a rotary hearth type smelting reactor (including all the auxiliary facilities such as disc pelletiser, travelling grate and annular cooler) was estimated to be A$201 M, which values to about A$217 M at the current price. The only component of CST that was included in the CAPEX estimation were the heliostat mirror costs (A$185–195). However, in actual practise, there will be additional costs associated with the shine-down mirror, solar thermal storage for continuous 24 hr operation and the design modification of rotary hearth furnace to incorporate the quartz window/receiver cavity. There will also be additional indirect costs such as legal expenses, costs for engineering supervision, construction expenses and other labour costs. The heliostat field also requires significant amount of land, the cost of which cannot be ignored. The costs of all these direct and indirect items were calculated based on following assumptions:

- The solar-smelt plant shuts down for one month in winter and runs 8000 hrs per annum, ie the production capacity of the plant is 25 t/hr.
- The thermal efficiency of reactor was considered to be 50 per cent.
- A heliostat field efficiency of 62 per cent was sourced from existing literature (Moumin *et al*, 2020).
- The thermal loss from the shine-down tower was assumed as 20 per cent.
- The Direct Normal Irradiance (DNI) used for the calculations was 25 MJ/m^2 or 6.94 kWh/ m^2 (similar to that of an iron ore mining site in Western Australia).
- A specific heliostat field cost of AU$100/m^2 (sourced from Hall *et al*, (2017)) and AU$150/m^2 was considered.
- The size of thermal storage was considered to be 15 hours.
- The cost of the shine-down mirror was assumed to be five per cent of the heliostat field costs (NB: no reported data were found).
- The specific cost of the solar thermal storage was A$14.8/kWh (Moumin *et al*, 2020)
- For directing the concentrated solar flux inside the reactor, a receiver cavity with a transparent window needs to be attached to the rotary hearth furnace. The cost of this additional attachment was assumed to be five per cent of the CAPEX of a rotary hearth smelter.
- The total direct costs of installing a CST facility to an existing rotary hearth smelter was considered to include the total costs of the heliostat mirrors, the shine-down mirror, the thermal storage and the receiver cavity attachment. The indirect costs were assumed to be 20 per cent of the total direct costs.
- The total land area required for heliostat field was considered to be seven times the size of heliostat field (referred from Moumin *et al*, (2020)) and the cost of the land was assumed to be A$1/m^2.

Considering all these assumptions, the heliostat mirror area calculated was 31 ha. Different costs of heliostat mirrors are reported in the literature and therefore, two different mirror costs were chosen for the CAPEX estimation. For a mirror cost of A$100/m^2, the CAPEX of solar facility was estimated to be A$66 M and for a cost of 150 A$/m^2, the CAPEX was estimated to be A$86 M. The cost of various equipment items as a percentage of CAPEX are listed in Figure 5. The figure suggests that the heliostat mirror is almost half of the CAPEX however other direct and indirect costs cannot be neglected. The use of CST eliminates the use of natural gas in the composite pellet smelting process. The only carbonaceous fuel that needs to be used is a solid-state reductant. Based on the annual savings of natural gas from complete solar-flux replacement, the payback period for CST facility installation in an existing plant was calculated. The annual operating and maintenance cost were assumed to be two per cent of CAPEX and was subtracted from the profit from natural gas savings. The resulting payback period estimates are shown in Figure 6. At the current capital cost, the process seems feasible (ten years payback period) when natural gas cost is about A$10/GJ and the mirror cost is $A100/m^2. Assuming a 30 per cent decrease in CAPEX and a mirror cost of below $A150, the CST installation will have a payback period of about five to ten years.

The lower carbon footprint iron nuggets can be sold at premium price to increase the profit and bring down the payback period. As mentioned above however there are subsequent thermal losses from the heliostat field, the shine-down mirror and from the reactor. With improving the field and reactor efficiency, the CAPEX will decrease significantly, and the process will become economically more attractive.

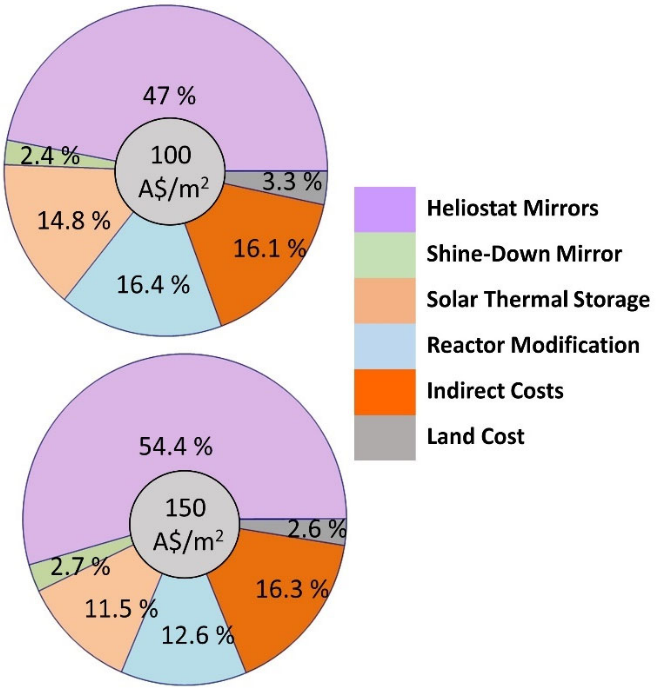

FIG 5 – Capital Cost (CAPEX) Items associated with incorporation of CST in an existing composite pellet process.

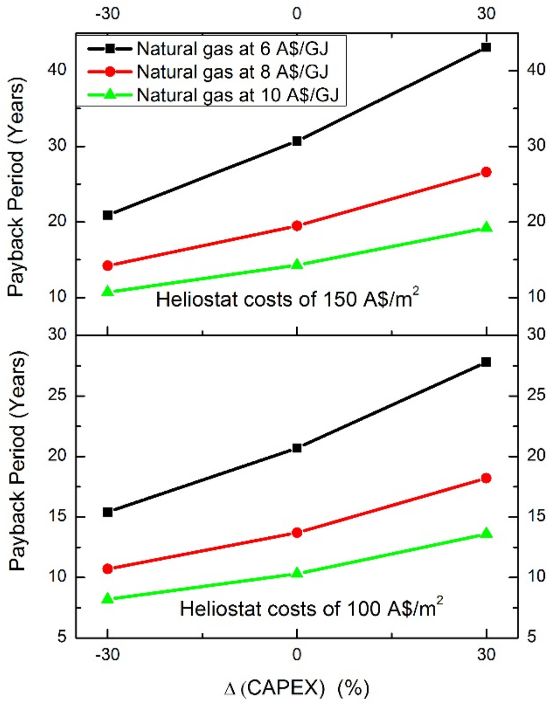

FIG 6 – Effect of natural gas price, heliostat costs and change in CAPEX on payback period.

CONCLUSION

The implementation of CSP for high temperature metallurgical applications is a well-researched area with several reported literatures on solar processing of iron ores. This paper examines two processes for magnetite ores to reduce the overall carbon footprint from the ironmaking industry by using concentrated solar flux – the LMP process and a process involving carbonaceous reduction of magnetite. The solar agglomeration of magnetite ores was investigated using laboratory scale experiments. Results indicated no change in the reaction mechanism of LMPs under solar irradiation compared to electrical heating. The CWF percentage and its morphology appeared similar for both solar and electric heated LMPs. Further study is required for solar agglomeration of a bulk sample quantity under conditions of varying temperature and time to understand the practicality of its commercialisation. A solar-smelting route for magnetite-coal composite pellets was also presented that involves utilisation of solar flux to substitute the part of carbon that is responsible for process heat generation. The solar smelting process has the potential to reduce the CO_2 emissions from the existing blast furnace route by 25–35 per cent. The techno-economics of implementing CST into an existing composite pellet process was evaluated at two different heliostat mirror costs. The results suggest the CAPEX of CST installation is about A$66 M to A$86 M. With about 30 per cent decrease in capital cost items and at natural gas costs of over 10 A$/GJ the payback period is about seven to ten years. Both the experimental and techno-economic analysis results shown in this paper suggest a great potential of CST applications in the ironmaking industry. Large scale testing of these concepts is required to advance these configurations and to scale-up the solar-assisted processes.

ACKNOWLEDGEMENTS

The authors wish to thank Swinburne University of Technology for access to solar simulator-hybrid reactor set-up and for providing financial support for this research through the SUPRA and HDR Publication Scholarships.

REFERENCES

Abanades, S and André, L, 2018. Design and demonstration of a high temperature solar-heated rotary tube reactor for continuous particles calcination, *Appl Energy,* 212:1310–1320.

Ekman, B M, Brooks, G, Rhamdhani, M A, 2014. A review: Solar thermal reactors for materials production, in: *TMS Annual Meeting*, Minerals, Metals and Materials Society, pp 5–14.

Esence, T, Guillot, E, Tessonneaud, M, Sans, J L and Flamant, G, 2020. Solar calcination at pilot scale in a continuous flow multistage horizontal fluidized bed, *Sol Energy,* 207:367–378.

Fernández-González, D, Ruiz-Bustinza, I, Mochón, J, González-Gasca, C and Verdeja, L F, 2017. Iron Ore Sintering: Process, *Miner Process Extr Metall Rev*.

Hall, C, Pratt, R, Farrant, D, Corsi, C, Pye, J and Coventry, J, 2017. Cost analysis of a mini-facet heliostat, in *AIP Conference Proceedings, American Institute of Physics Inc*, p 20005.

Meier, A, Bonaldi, E, Cella, G M, Lipinski, W and Wuillemin, D, 2006. Solar chemical reactor technology for industrial production of lime, *Sol Energy*, 80:1355–1362.

Meier, A, Bonaldi, E, Cella, G M, Lipinski, W, Wuillemin, D and Palumbo, R, 2004. Design and experimental investigation of a horizontal rotary reactor for the solar thermal production of lime, *Energy*, 29:811–821.

Mochón, J, Ruiz-Bustinza, Í, Vázquez, A, Fernández, D, Ayala, J M, Barbés, M F and Verdeja, L F, 2014. Transformations in the iron-manganese-oxygen-carbon system resulted from treatment of solar energy with high concentration, *Steel Res Int*, 85:1469–1476.

Moumin, G, Ryssel, M, Zhao, L, Markewitz, P, Sattler, C, Robinius, M and Stolten, D, 2020. CO2 emission reduction in the cement industry by using a solar calciner, *Renew Energy*, 145:1578–1596.

Purohit, S, Brooks, G, Rhamdhani, M A, Pownceby, M I and Ware, N, 2019. Lime-Magnetite Pellets (LMPs) for Ironmaking, in *AISTech 2019 Proceedings*, pp 687–700.

Purohit, S, Brooks, G, Rhamdhani, M A, Pownceby, M I and Webster, N A S, 2020b. Analyses of CWF ($CaFe_3O_5$) phase formation in lime-magnetite pellets, *Ironmak Steelmak,* 47:852–864.

Purohit, S, Brooks, G, Rhamdhani, M A, Pownceby, M I and Webster, N A S, 2020a. Alternative route for magnetite processing for lower carbon footprint iron-making through lime-magnetite pellets containing $CaFe_3O_5$, *Ironmak Steelmak*, 47:674–685.

Purohit, S, Ekman, B, Mejias, R, Brooks, G and Rhamdhani, M A, 2018. Solar processing of composite iron ore pellets: Preliminary assessments, J Clean Prod, 205:1017–1028.

Purohit, S, Brooks, G, Rhamdhani, M A and Pownceby, M I, 2020c. Solar Agglomeration of Iron Ores, in *APSRC*, December.

Purohit, S, Brooks, G, Rhamdhani, M A and Pownceby, M I, 2021. Evaluation of concentrated solar thermal energy for iron ore agglomeration, *J Clean Prod,* 317:128313.

Ruiz-Bustinza, I, Cañadas, I, Rodríguez, J, Mochõn, J, Verdeja, L F, Garcia-Carcedo, F and Vázquez, A J, 2013. Magnetite production from steel wastes with concentrated solar energy, *Steel Res Int*, 84:207–217.

Steinfeld, A and Fletcher, E A, 1991. Theoretical and experimental investigation of the carbothermic reduction of Fe_2O_3 using solar energy, *Energy*, 16:1011–1019.

Steinfeld, A, Kuhn, P and Karni, J, 1993. High-temperature solar thermochemistry: Production of iron and synthesis gas by Fe_3O_4-reduction with methane, *Energy*, 18:239–249.

Steinfeld, A and Meier, A, 2004. Solar Fuels and Materials, in *Encyclopedia of Energy*, Elsevier, pp 623–637.

Steinfeld, A and Palumbo, R, 2001. Solar Thermochemical Process Technology, *Encycl Phys Sci Technol*, 15:237–256.

Tran, P D, Wong, L H, Barber, J and Loo, J S C, 2012. Recent advances in hybrid photocatalysts for solar fuel production, *Energy Environ Sci*.

Wieckert, C, Frommherz, U, Kräupl, S, Guillot, E, Olalde, G, Epstein, M, Santén, S, Osinga, T and Steinfeld, A, 2007. A 300 kW Solar chemical pilot plant for the carbothermic production of zinc, *J Sol Energy Eng Trans ASME*, 129:190–196.

Tailings

Design considerations for an iron tailings filtration plant and their conveying and disposal systems

J Barrera[1], S Ramirez[2], H Alvarez[3], L Perez[4] and C Garrido[5]

1. Process Engineer, Fluor, Santiago, Chile 7550121. Email: jorge.barrera@fluor.com
2. Process Engineer, Fluor, Santiago, Chile 7550121. Email: sergio.ramirez.letelier@fluor.com
3. Process Engineer, Fluor, Santiago, Chile 7550121. Email: hector.alvarez@fluor.com
4. Process Engineer, Fluor, Santiago, Chile 7550121. Email: leocan.perez@fluor.com
5. Regional Technology Director, Fluor, Santiago, Chile 7550121.
   Email: cristian.garrido@fluor.com

ABSTRACT

In recent years, there has had a greater recurrence of studies and projects that consider tailings filtration followed by dry stacking to reduce the consumption of fresh water, the space required for disposal, and, eventually, to reduce the costs of the project. In addition, this technique could be required to meet new environmental restrictions to extend the life-of-mine of existing plants or to enable the development of new projects, especially in areas of high social interest.

This article is intended to describe the most relevant technical aspects of the design and implementation of an iron ore tailings filtering system and its final overland disposal as well as physical and metallurgical surveys, and laboratory and pilot testing. Furthermore, it is presented how these activities are inserted in the project development to rationalise the resources.

The case under study considers an iron mineral wet magnetic concentration processing plant. The outcome tailings are dewatered by means of thickeners, where the overflow water is recycled back to the plant. The underflow slurry is pumped into intermediate storage tanks before proceeding with further dewatering and final disposal.

The project consists of a tailings filtration plant, belt conveying systems, a temporary stockpiling system, trucking loading and transportation system, moisture-conditioning facilities (spreading and airing), and final disposal facilities (compacting).

Due to the stickiness of the filtered tailings that governs the belt conveying system design, the operating moisture range must be established. Besides, proper technical aspects such as planning, executing, and analysing both the laboratory and the pilot testing data to validate process design parameters; selecting filters; defining spare filtering capacity; handling the out-of-range filtrated moisture; sizing the belt conveying system; configuring the equipment involved, must be considered.

INTRODUCTION

This publication intends to show considerations in the design of tailings filtration plants, including a summary of the environmental regulations applied in Chile, worldwide experiences, and the available filtration technologies trending to ever larger equipment.

Additionally, through a case study are shown the general subjects that must be faced during the engineering design, including the test work, the comparison between various vendors, the flow sheet, layout, and the required testing in a pilot plant operation.

The case study considers the expansion of an existing iron ore magnetic concentrator plant. The tie-in to the existing plant is the tailings thickener underflow.

The expansion of the plant considers taking the thickened tailings and processing them in a new filter plant. The filtrated tailings cake is transported to a specific area reserved for this purpose and piled. This dry stacking facility is located one kilometre from the filter plant.

CHILEAN ENVIRONMENTAL REGULATORY FRAMEWORK

Villanueva (2019) explains that in Chile, the Environmental General Basis Law (No. 19,300) and the updated Law of the General Basis (No. 20,417) establish the environmental regulatory framework and create several governmental organisms, like the Environmental Evaluation Service (SEA by its acronym in Spanish), which is responsible for reviewing the projects through the Environmental Impact Evaluation System (SEIA in Spanish) through the Environmental Impact Evaluation System Regulation. The projects type mentioned in the regulation (mining projects are included) must be presented through an Environmental Impact Study (EIA in Spanish) or an Environmental Impact Declaration (DIA in Spanish), depending on the project type. The EIA is a complete study of the project. The SEA, with the participation of the community, issues the Environmental Qualification Resolution (RSA in Spanish) where the project is approved or rejected. The project must demonstrate that it will not be a risk for the community health, it will not produce a negative effect on the renewable natural resources, it will not affect the cultural legacy, and it will not affect the value of the landscape, among other considerations. The RCA of each project is available to the public and can be found on the internet.

The Environmental Impact Evaluation Regulation also establishes the guidelines for construction, design, operation, and closeout of the tailing deposits, according to the Supreme Decree N° 248, to assure the chemical and physical stability of the waste. Also, it describes the related regulations with storage, transport, installation, elimination, and recycling of dangerous waste that leads to the Dangerous Waste Handling Sanitary Regulation. Massive mining waste like tailings are not generally deemed hazardous waste. However, the authority may require physical and chemical analyses. If analysis demonstrates that the material is harmful, this will be deemed dangerous waste, and it must comply with the regulations for such a waste.

The Mine Closure Regulations (N° 20,551) regulates the phase of closure of a mining installation. It includes measures to avoid abandonment, to assure the physical and chemical stability of the site where the mine operates, controlling water, air, and soil in perpetuity.

The national service of geology and mining (SERNAGEOMIN in Spanish) is a governmental institution with a dedicated department to control the tailing facility's construction, operation, and closure.

TAILINGS FILTRATION EXPERIENCE AROUND THE WORLD

Tailings filtration with subsequent dry stacking is favoured in zones with low rainfall and high evaporation. As shown by Ulrich and Coffin (2013), the main benefits over other tailings storage system are:

- reduces the footprint
- provides a stable structure specially indicated for rugged topography
- does not require a dam wall
- reduces the geotechnical risk
- minimises water infiltration into the soil, and the potential contamination of underground water sources
- maximises water recovery
- allows con-current closure.

However, tailings filtration typically requires high capital cost being justified if there are significant process, environmental, or layout drivers. There are several tailings filtration examples globally, and this technique is being considered in many projects. There are applications in iron, copper, gold, uranium, and aluminium tailings. The filtration equipment selection depends on the test work results, capital and operating costs, industrial experience, and layout, among other considerations. However, typically for coarse particle size distribution (F80 ~400 μm) dewatering screens are used (0.5 mm × 12 mm aperture, for instance) to take out the coarse fraction and to store this in the deposit separately. For a finer particle size distribution (F80 ~200–180 μm) belt filters or pressure filters are used. For ultra-fine particle size distributions (F80 ~45 μm) pressure filters area used. Pressure filters are vertical plate type.

There are different methods of transport of the filtered tailings to the deposit, depending on the production capacity, distance to the deposit, costs, or other considerations, also presented by Lara (2013). The used methods are:

- by dump trucks of 30 to 50 t
- by belt conveyors to the deposit from where, through a small hopper, dump trucks are loaded
- by belt conveyors and stacker.

Stacker can be radial, or bridge conveyors craw mounted with a stacker tripper car or with an additional spreader vehicle after the tripper car.

The filtered tailings moisture is designed in accordance with the requirements of the belt conveying system and the structural requirements of the deposit. The structural requirements of the deposit depend on the topography and the method of deposition. If the method of deposition is by belt conveyor system with a spreader, it cannot accommodate tailings compaction, but if the method by truck is selected, tailings compaction is needed to give structural resistance to allow the transit of vehicles over the surface of the deposit.

Table 1 shows some examples of tailings filtration plants.

TABLE 1

Examples of tailings filtering plants.

Operation	**Country**	**Ore**	**Capacity**	**Moisture (wet*)**	**Technology**	**Particle Size**
Karara	Australia	Fe	35 kt/d	13%	Dewatering screen for coarse fraction. Pressure filters for fine fraction.	Coarse fraction F80 1.5 mm Fine fraction F80 35 µm
La Coipa	Chile	Au	18 kt/d	18%-21%	Belt filters (12). Belt conveyors.	Without Information
Cerro Lindo	Perú	Zn-Pb-Cu	15 kt/d	12%-13%	Belt Filters (3). Truck.	Without Information
Mantos Blancos	Chile	Cu	12 kt/d	18%-20%	Belt filters (2). Belt conveyors and trucks.	F80 190 µm
Manto Verde	Chile	Cu	12 kt/d	17%-18%	Belt conveyor	Without Information

(*): Wet basis is (t water)/(t solids + t water).

VERTICAL PLATE PRESS FILTER TECHNOLOGIES

Filter suppliers currently offer equipment with capacities up to 15 000 tons per day, which will depend on the characteristics of the ore and the expected requirements in the filter cake.

Suppliers have equipment with various plate sizes ranging from 2 × 2 m, 2 × 4 m, 3 × 5 m, 4 × 4.8 m, some under development and soon to be installed, cake thicknesses from 32 mm to 60 mm and with plate numbers from 50 to 200, which will depend on the filter model and requirements based on the capacity and type of material and specifications expected in the filtered cake, to adapt to the different types of materials that can be processed.

Feed pressures vary from 6 to 30 bar depending on the supplier, as each supplier provides different methodologies based on the development of their filters. Some rely on pressure for filtering materials.

Cloth washing water is differentiated into low – and high-pressure washing systems.

For high-pressure cloth washing (~50 barg), the water quality must meet specific requirements, such as maximum particle size (<100 µm), suspended solids (<100 ppm), maximum chlorine content (<300 ppm). For low-pressure washing (0.2 to 0.3 barg), it differs in that it allows slightly larger particle sizes (up to 500 µm) and higher suspended solids content (<500 ppm).

The availability offered by most suppliers for filter operation is in the order of 90 to 92 per cent. This is since some of them incorporate high-pressure cloth washing and simultaneous cloth change systems, improving their availability. However, for design considerations 85 per cent is used, which is typical for these applications.

As mentioned above, the characteristics of the filters to be selected will depend on the features of the material. For example, it is possible to use a chamber for a thickness of 60 mm for a filtered cake, but if the materials to be processed have clays, it will probably be necessary to change the design and use chambers for a cake thickness no bigger than 30 mm.

In summary, the production and capacity of the filters will depend on the density of the material, the concentration of solids in the feed, the rheology of the material to be filtered (less or more clays), the particle size, tailings density, and residual moisture among other characteristics.

Most suppliers have technical services or alliances with local companies to perform maintenance and repairs on the equipment supplied.

PROCESS DEFINITION

In this section will be presented the flow chart definition’s path considering laboratory tests that provide information to select the filtration technology, followed by fluidity tests to rule the cake transports system, from belts to hoppers and chutes.

Once the flow chart configuration is selected, recirculation’s are optimised.

After selecting the flow sheet, plant layout will be designed. Finally, the monitoring and instrumentation system will be present to achieve the filtered tailings for the deposit.

Tailings filtration laboratory test work

Tailings samples must represent the ore of the mine and can be obtained from tailing thickener discharge of the concentrator plant, in the order of a solids concentration of 50 per cent.

Tailings characterisation

The preparation of the samples for the filtration test program includes homogenising each sample, cutting the samples, and leaving one set of samples for the filtration tests and the other for tailings characterisation.

For tailings characterisation, the following measurements are considered in the samples:

- solids concentration and density of the thickened tailings slurry
- particle size distribution
- specific gravity of solids
- mineralogical composition
- chemical composition by elements (for example: Fe, Cu, Al, Ni, Mn, Pb, Zn, Se, Mo, Sn, Cr, As, Cd, and Hg)
- rheology (yield stress, shear stress, viscosity).

Filtration tests

Filtration tests are carried out by all preselected filters suppliers for the different filtration technologies, of which the following laboratory equipment can be considered:

- filter press
- belt filter
- ceramic filter
- hyperbaric filter.

The objective of the tests is to evaluate the filtration capacity of each of the technologies to obtain the following items as design parameters:

- choice of filter media
- optimal thickness of the cake
- times and pressures for pumping, pressing, drying, washing etc
- residual cake moisture
- unit filtration rate (kg/h/m^2)
- filtration area (m^2).

According to the reports submitted by the laboratories for tailings samples, the filters with the highest unit filtration rates, lowest residual moisture, lowest area requirements, and lower pressure requirements are more attractive.

From the laboratory results and through a technical-economic trade-off study, the filtering technology and filter or filters to continue with pilot-scale tests to evaluate the performance in larger equipment, are decided.

Filtered tailings bulk flow test work

To know the bulk flow properties of the filtered tailings is relevant for the design of the conveying belt system because the transport is only possible under a maximum moisture limit. Over this moisture, the material sticks to chutes and hoppers and does not flow, and the system will be blocked. This moisture limit is utilised for the tailings filter design.

The bulk flow properties of the tailings also depend on many other parameters, as presented by Jenike (1964). Some of them are difficult to control or are not possible to be controlled, but all must be known to characterise the tailings and the possible variations of the operating conditions. The tailings filtration plant needs to be designed to these values, and to operate out of this specification may produce operational and maintenance problems.

Bulk flow properties depend typically on the following parameters:

- ore particle size distribution
- particle top size and fines content
- moisture content
- particle shape
- storage time at rest and under pressure
- consolidation pressure and impact (hopper height and impact on chutes)
- ore chemical composition, lithology, mineralogy, clay content
- chemical reagents
- climate conditions (rain, snow, freezing).

Bulk flow properties include the following tests typically:

- tailings sample characterisation as received
- compressive stress and bulk density
- cohesive strength
- wall friction
- hopper discharge minimum aperture
- chute testing
- belt conveying testing.

Samples must be fresh and representative of the different tailings of the plant. The quantity of each sample is 100 kg to 150 kg. Based on benchmarking and filtration results, three moistures may be defined, and samples are prepared for these moistures, and the tests are developed for each moisture. The result of bulk flow properties test work must be the definition of the moisture that allows belt conveying and the design parameters of hoppers, chutes, and conveyors.

Tailings characterisation as received

These tests include samples weight as received, moisture, ore specific gravity, ore size distribution, and saturation under pressure analysis.

Iron tailings are a very fine material. Size distribution is in the order of 99 per cent minus 150 µm, 90 per cent minus 75 µm, and 80 per cent minus 45 µm. Tailing's solids density is around 3000 kg/m^3. The tailings saturation (the capacity of water retention) is high, in the order of 30 per cent moisture (dry basis) at 0.2 kPag pressure.

Compressive stress and bulk density

The compressive stress test (ASTM 6683) allows establishing the modification of bulk density of tailings regarding the subjected pressure. Tailings are very compressible, especially at high moisture. This test defines the bulk density of material for transport system according to moisture and consolidation pressure that it is subjected to.

Tailings sticky strength

Iron tailings sticky strength is very high and increases with moisture content and storage time. Depending on moisture content is not possible to resume flow after 12 or 24 hours of storing. This material must be handled in a continuous flow, avoiding storage, or leaving it resting or under pressure to avoid the requirement of very low moisture. The material has a high tendency to form 'ratholes', and this tendency increases with moisture content. Hoppers should not be conical or with funnel flow. The recommended hopper variety is the wedge type with mass flow (see Figure 1).

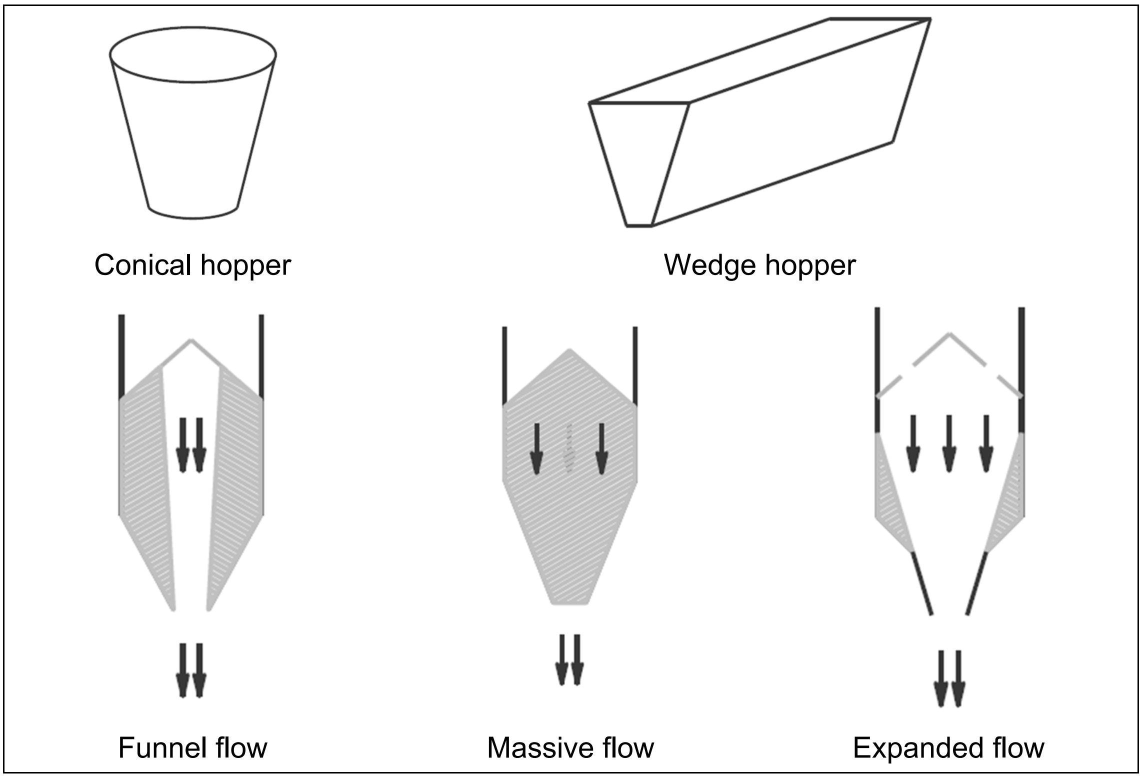

FIG 1 – Hopper and material flow types.

The test, ASTM D 6128 is used to establish the minimum discharge aperture of hoppers and chutes as function of moisture to allow reliable material flow, avoiding 'ratholes' and arcs. The selected moisture is that allows a reasonable minimum discharge aperture size.

Wall friction

This test establishes wall angles (from the vertical) to allow tailings to flow for different moistures and wall materials. Wall materials could be mild steel, anti-adherent rubber, or Tivar-88 (UHMW-PE). Also, tested are different storage time (0, 12 and 24 hours). The tests are developed for conical and wedge hopper types with mass flow. However, usually more extensive angles are achieved with wedge hoppers than conical hoppers. The selected material is that maximise the discharge angle. The selected moisture is that allows the material to flow at a convenient angle.

Discharge aperture

Once the wall material and the angle area selected, the discharge aperture is defined, considering the moisture, the minimum discharge aperture, and the required tailings flow. For a wedge hopper, aperture length of three times discharge aperture width is recommended.

Chute testing

This test consists of establishing the minimum slope angle of a flat surface as a function of the impact pressure of the material that allows material to flow. Different tailings moisture and cover materials are tested. The surface´s material could be mild steel, anti-adherent rubber, or Tivar-88 (UHMW-PE). From the test is selected the chute material that allows the tailings to flow at the minimum angle. The selected moistures are those that would enable the tailings to flow at reasonable angles.

Belt conveying testing

These tests simulate belt conveying with a piece of bench equipment like a belt section, and through vibration and different slopes can simulate belt conveyor transport at different belt speeds and slopes. The test aims to define the belt surcharge angle after long conveyor transport for different slopes and moistures, and the slope where the slip-back condition is generated for different moistures.

DESIGNING THE CASE STUDY WITH PRESS FILTERS

Preselection of a filter for the basic design

This technology is unique to each manufacturer. Each filter design has evolved according to terrain observations and improvements requested by the customers operating their equipment.

Because of this, for the same capability, filters exist with different geometry (height, length, width), capacity (filtration area, chamber volume), filling system (one way, two ways), and others (auxiliary systems) that define the footprint, the size of the building, the head tank, the pump capacity for the filling and pressurising to mention some points.

So, it may seem attractive to have a design independent of the selected manufacturer. But this design will lead to an oversized filter plant that is not real and does not help to optimise Capex and Opex.

Table 2, for the same capacity, shows the characteristics of different filters that also affect the size of the feeder in the download.

TABLE 2

Example of different filters processing the same material.

Parameter	Unit	Filter A	Filter B	Filter C	Filter D
Iron tailings					
Solids	t/d	8000	8000	8000	8000
% Solids	%	50	50	50	50
Specific gravity		3.0	3.0	3.0	3.0
Run time	%	85	85	85	85
Filter					
Dimension					
Length	m	21	26	33	30
Wide	m	6.5	5.5	3.5	5.0
Height	m	4.0	5.5	4.0	3.0
Number of chambers		45	90	150	112
Plate dimension, H × W	m × m	3.5 × 2.5	3.0 × 2.6	2.0 × 2.0	2.5 × 2.5
Effective filtration area	%	77	59	90	82
Filtration area	m^2	593	819	1073	1138
Chamber depth	mm	45	50	45	50
Cake density (theoretical)	t/m^3 wet	2.31	2.31	2.31	2.31
Volumetric capacity	m^3/cycle	13	20	24	28
Dry mass capacity	t/cycle	26	40	47	56
Cycle time	min/cycle	12	19	22	17
Filling time	min/cycle	2.6	4.0	4.8	3.7
Cake discharge time	min/cycle	0.5	0.8	1.0.	0.7
Cycles/day	cycle/d	359	234	199	169
Filtration rate	$kg/m^2/h$	221	158	120	173
Filters required		3	3	3	2
Feed pump capacity	m^3/h	803	796	793	1209
Feed pump pressure	kPag	600	560	2100	1500
Cake					
Moisture (w.b.)	%	15	15	15	15
Cake flow	t/cycle	31	47	56	66
Feeder capacity	t/h	195	180	176	276
Filtrate					
Filtrate flow	m^3/h	380	380	380	380

Due to different capabilities of filters, a comparison between manufacturers goes beyond technical aspects, affecting complete Capex due to the size of the building to house the equipment, and affects Opex due to the energy consumption of pumps and compressors. Because of these differences between manufacturers, it is not possible to design a plant for the maximum capacities of suppliers.

It is necessary to develop a preselection for the basic design through a trade-off study and to preselect a single supplier and develop the plant design for that supplier but considering some possible variations from others. At purchase time, with firm proposals it is again necessary to develop a technical and economic evaluation to finally define the filter supplier. The technical part of the evaluation must be vital because saving money can be a problem in the future. The selection must include equipment that ensures good technical performance and then consider the price of the equipment in the evaluation. It is recommended to visit installations with the filters considered.

Another critical point to consider in the preselection of the vendor is the possibility to provide a pilot plant. Ahead in this document will be presented the importance of pilot plant data to make the best decision to choose the filter for front-end design. Note that once dedicated to one vendor, these kinds of issues no longer exist.

Vertical press filter operation

Typical pressure filtration equipment operate automatically, in batch cycles where the main operations, within the cycle, involve filling the chambers through a centrifugal pump, pressurising using the same centrifugal pump, but now with very little flow and high pressure; then the manifold is washed (the manifold retaining some slurry inside the filter at the same concentration of solids as the feed, so this slurry is removed during washing); then the manifold is blown; then the cake is blown (from the manifold) with compressed air to remove the residual water inside the cake to achieve the required moisture; then the cake is discharged in a very small fraction of time considering the complete filtration cycle with the action of a shaker system of the plates. Later a low-pressure cloth wash is done to remove particles from the clothes with the help of the shaker system. This washing is done from the top through the bottom scrubbing the particles. Finally, the filter closes and is ready to start a new cycle.

Due to low efficiency of the cloth low-pressure water system, different manufacturers have addressed the issue with an additional washing system that allows unblocking cloths. For instance, taking the cloths out to the side of the filter to wash them with a piston system on the floor or in a sort of washing tower above a box to collect the water. Others consider a high-pressure robotic cloth washing system that runs through the filter chamber by chamber. This latter system has become so efficient that it consumes less high-pressure cloth wash water and requires less time from the stopped equipment to wash all filter cloths, thus increasing cloth life, reducing operating cost and increasing mechanical availability of the filter by increasing the period between cloth changes.

Adding filtrate water plus all washing water during the filter cycle, the total final water contains a solid percentage between 3 per cent to 5 per cent if the filter is run perfectly. However, sometimes the filtration process does not run perfectly, and the solids percentage in the total water can increase to 10 per cent or more due to cloth rupture, plate damage, aborted cycles, etc. Then it is necessary to use an agitated tank to receive the water, with slurry pumps to return the water from the filter to the thickener.

Flow sheet configuration

Once the reference supplier has been selected for the design, it is necessary to define the number and the configuration of filters. To avoid affecting plant availability of the upstream concentrator and considering that filters are mechanical equipment that suffer outages for operational issues and maintenance, it is recommended to define standby filtration capacity. Also, this can be combined with a big filter feed tank in the case of small capacity plants. However, for large capacity plants, this is not possible. It is necessary to consider that filters size has increased tremendously, so it is not unreasonable to think of a configuration of one equipment operating plus one on standby (1 + 1). To reduce the budget, other alternative is to consider an arrangement like (1.5 + 0.5), ie one filter operates the whole day, and another one operates half-time, leaving a half-day in standby; the next steps will be (2.5 + 0.5) or (3.5 + 0.5). Over these quantities of filters, it is common to find one complete standby filter, like Karara in Australia (7 + 1), and Palo Alto in Brazil (6 + 1).

Auxiliary systems correspond to the air required for cake blowing, manifold blowing, and washing water for manifold and cloths. This is a short service in the cycle per filter, allowing to overlap the filter cycles so that a common system feeds all filters in a sequence.

It is necessary to feed the filters with solids percentage between 50 per cent and 60 per cent. Therefore, the feed must come from a thickener. To send a diluted slurry below the range indicated makes the filters operate inefficiently and generates problems in the filtration (increasing the cycle time, reducing production, causing leaks between the plates etc).

The thickener underflow is sent to an agitated filter feed tank. Due to filtration timing and cycle time, it is possible to feed 2 or 3 filters with one pump keeping the slurry recycling and controlling the loop feeding of each filter one at a time by on-off valves. However, to increase filter availability, it is preferable to use one pump per filter. In this way, if one slurry feed line fails (pipe breakage, valve failures, or pump failures), the other filters are not affected.

The thickener overflow corresponds to clean water leaving the system to the concentrator, such as process water. This water is stored in a water tank, and by, pumping is distributed for services.

Each filter discharges into the feeder located underneath. If the filters are high-capacity units, an apron feeder can be used to support the cake discharge of each filter. Under the apron feeder, is included a collecting belt for fines. To collect the discharged cake from the feeders, a belt conveyor is used.

Figure 2 illustrates the flow sheet.

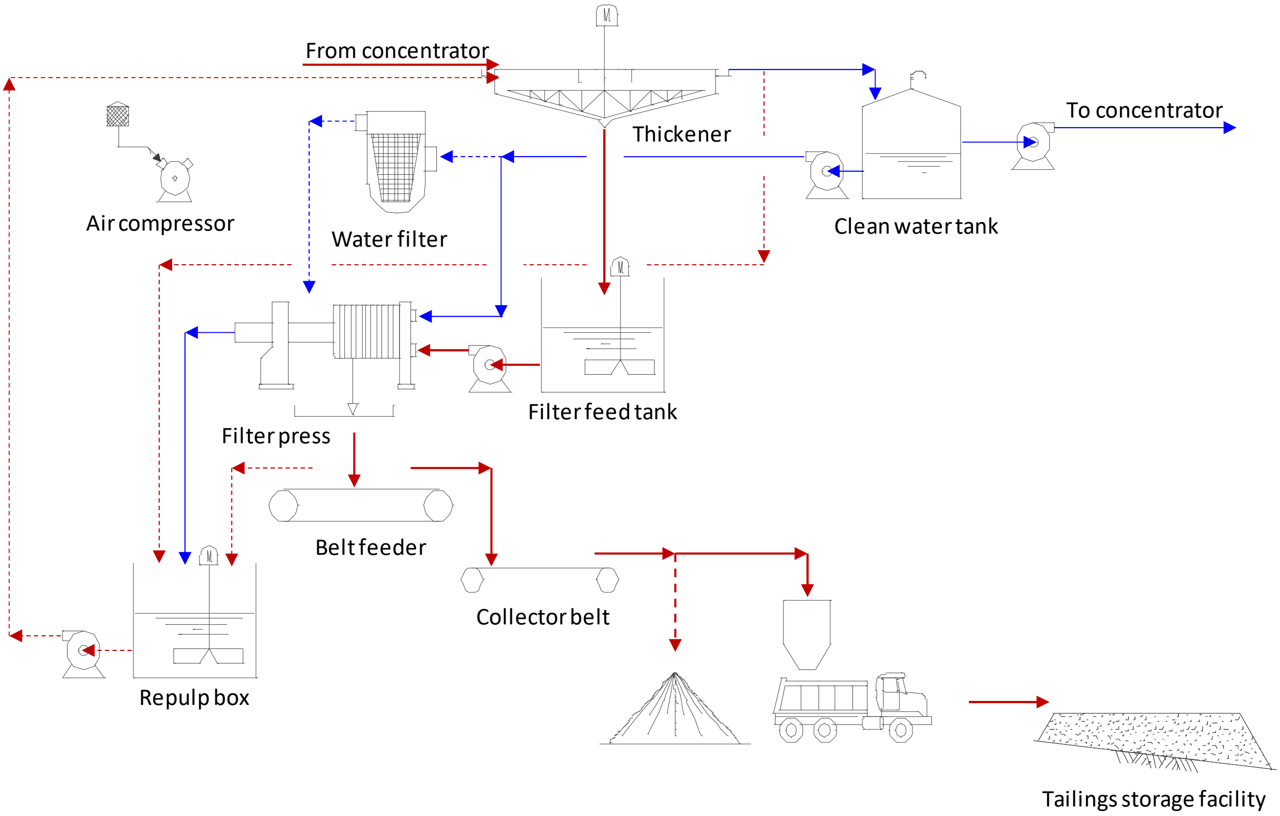

FIG 2 – Example of flow diagram.

Recirculation and slurry reclaim

Recirculation is essential in any process system to maximise target separation, reduce consumption and optimise the process.

In this case, the objective is to minimise the water consumption of the plant and to deliver a cake with the objective moisture. The filter plant recovers water from the tailings slurry and returns it to the process. The clean water requirements for the seal of the pumps and the washing of fabrics at low or high pressure can be satisfied with the same recovered water, subjected to an additional filtration process for a small fraction of the flow.

The water used for filter cloth and manifold washing comes from the thickener overflow. The unique outlets in the system are the filtered cake and the reclaimed water obtained from the thickener overflow; everything else recirculates inside the plant.

Out-of-specification cake should be considered in the plant´s design because can be generated. One solution is to transport the out-of-specification cake to an agitated tank by turning the feeder in the reverse direction of regular operation with water addition to dilute the cake. This agitated tank is also used to receive all the washing water and the filtrate from each filter. All this water contains different and variable quantities of solids and must be sent to a thickener to assure that the final water coming from the filter plant is clean (with a very low quantity of solids).

Water management

When a tailings filtration plant is a brownfield project, it produces an excess of internal water in the plant, and it is necessary to define consumption that requires additional process water.

When tailings filtration is a greenfield project, this issue does not exist.

Moisture sensors

Moisture sensors are located in the filter discharge feeders to determine the cake moisture as soon as the cake is discharged, to confirm that the moisture is under the limit for the process.

Layout

Layout is important because it considers minimising energy consumption in transport, leaving the required space for maintenance considering the entry of the necessary machinery and work equipment, defining floor slopes to manage spillages, and other considerations related to the operation, maintenance, and reliability of the plant.

In expansions of iron concentrator plants, space can be a constrain. Filter buildings are now efficiently designed (slim fit or fit for purpose) to rationalise expansion in the building, earthwork, length of crane bridge, etc. In addition to the filtration building, space is required for a head thickener if it is not available in the concentrator, a slurry feed tank, a seal water tank, a process water tank to return the clarified water, an agitated tank capable of containing, at least, the loading of an out-of-specification cake plus water from filter and dilution water, compressed air system plus accumulators, electrical rooms, and several minor equipment. Also, space must be allocated for filter discharge feeders, collecting belt conveyor, and service crane.

Filters reclaim feeder and conveying capacity

Typical layout of a filter plant considers the filters in parallel discharging over individual feeders and all the feeders discharging to a perpendicular belt conveyor. The feeder capacity is defined by the wet tonnage of the cake discharge in each cycle and a time equal to the cycle time minus the discharge time minus a slack time between discharges where the feeder is running empty. The capacity of the belt conveyor is equivalent to the sum of the feeder discharges. Also, it is necessary to check if it is possible to operate the feeders in a discharge sequence to discharge one filter in the sum of slack times of the others to decrease the capacity of the perpendicular conveyor. Table 3 shows an example with the basic calculation.

TABLE 3

Example of belt feeder and conveyor capacity definition.

Parameter	Value
Filter capacity	2000 t/d dry
Number of filters	4
Run time	84%
Moisture (wet basis)	15%
Cycle time	14 min
Cake discharge	27.2 t wet
Discharge time	0.5 min
Gap between discharges	2 min
Time with charge	11.5 min
Feeder flow rate	2.4 t/min wet
Belt feeder flow rate	9.5 t/min wet

TAILINGS FILTRATION PILOT TESTING AND FILTERED TAILINGS COMPACTION PILOT TESTING

Laboratory and pilot tests on tailings filter cake are performed to determine all the physical, geotechnical, and operational parameters to ensure the tailings filter cake will be safely deposited on land. First, laboratory tests are performed to find out the best group of parameters that represent the behaviour of the handling and the deposition of tailings filter cake. Then, pilot tests are performed to confirm the laboratory measurements. Pilot testing is performed by using an industrial filter size of 10 m^2 or similar. Testing is performed at the plant area where tailings are generated and thickened, and therefore, it is representative enough to design the industrial filtration and deposit facilities.

During piloting tailings filter cake is deposited on a conditioned area above ground to determine potential water infiltration into the soil. The minimum size of the required area to execute the compaction testing is determined by considering the dimensions of the machinery needed for handling, scarping, spreading, and compacting tailings filter cake over the conditioned land, as well as the area required to obtain good representative samples to be taken once tailings filter cake is compacted. The machinery involved is a dump truck, a front loader, a backhoe loader, and a compaction roller. Depositing tailings filter cake on land is performed by using a conditioned rectangular area of 40 m^2 or above. In addition, a nearby space with same dimensions is utilised to accumulate a total volume of tailings material required to build-up one layer. The material is dumped, spread, and quartered, and then its moisture content is monitored to assure that the whole quantity is relatively homogenous. Testing several layers between 0.3 to 0.5 m thick is accomplished. The number of layers to be compacted during testing is a function of the testing results.

Tailings filtration pilot testing plant

The first set of filtering pilot tests is performed to determine the operating parameters required to deliver tailings filter cakes with moisture content below the maximum target value established by bulk flow properties testing. The top target moisture content is kept below the maximum target value to prevent the material from sticking on the equipment while conveying from the filtering area to the deposit facility. See Table 4 for the Operating Parameters that are considered.

The second set of filtering pilot testing is performed to determine the physical and the geotechnical properties of tailings feed, wash water, tailings filter cake, and filtrate water. To perform the filtering pilot testing, the filter is configured to be operated under the parameters determined during commissioning stage. The properties that are measured during the second set of filtering pilot testing are also shown in Table 4.

TABLE 4

Tailings filtration pilot testing.

Filtration Stage	Test/Measurement
Commissioning/Operating Parameters	• Cycle time • Pressure of pressing • Quantity of slurry fed • Quantity of cake • Wash water consumption • Compressed air supply, flow, and pressure • pH of wash water and filtrate
Filter Feed/Thickened Tailings	• Solids content, % (w/w) • Particle sizing analysis, down to 25 μm • Moisture content (%) • Specific gravity of solids • Rheology parameters • Curves of slurry viscosity versus solids % (w/w) and slurry yield stress versus solids % (w/w) • Mineralogy (geology, chemistry, crystal structure, and physical/optical properties)
Filter Wash/Raw Water	• Water chemistry analyses
Tailings Filter Cake	• Moisture content (%)
Filtrate	• Water chemistry analyses

Tailings compaction pilot testing

Once the whole quantity required to build-up one layer of tailings filter cake is accumulated on the conditioning space located nearby compaction testing area, a set of pre-compacting tests is performed (see Table 5). Pre-compacting tests are used to track consistency of the material. Moisture content of material is monitored frequently. Once the target moisture content is reached, the total amount of tailings filter cake is spread over the compaction area to proceed with compaction testing. The optimal moisture content is given by the corresponding moisture content to 95 per cent of the maximum dry density measured by performing a laboratory Modified Proctor compaction test.

After spreading the total amount needed to build-up one layer of conditioned filtrated tailings over the compaction test area, a pilot Modified Proctor compaction test is performed. Samples are taken after each pass of a compaction roller (see Table 5). Same procedure is applied to each of the layers; at least five layers are considered.

TABLE 5

Tailings filtration pilot testing.

Compaction Stage	Test/Measurement
Conditioning Space/Pre-compaction	• Particle sizing analysis, down to 25 µm • Atterberg limits • Specific gravity of solids • USCS, soil classification • Moisture content • Modified Proctor compaction test
Compaction Area/Pilot Compaction	• Modified Proctor compaction test

Moisture infiltration into the soil is measured during the compaction testing period and afterward. The design of the future facility needs to ensure absolute protection of the environment. Therefore, provision to collect and treat infiltration is considered.

Time recording for each of the tests is the most critical parameter because it allows keeping track of tailings batches fed into the filter. Tailings batches travel through the deposit facility to be finally compacted. Therefore, each of tailings batches fed, is characterised at each of the operating stages to establish a well representative function that correlates the tailings filtration and compaction on land against physical, geotechnical, and operational parameters. During operation of the future plant, this correlation will be utilised to predict the stability behaviour of the tailings deposit.

OPERATION AND MAINTENANCE PERSONNEL

The number of people required for a tailings filtration plant depends on the plant capacity, the number, and type of equipment, tailings transport and deposition system, etc. For example, Table 6 shows the personnel for a filtration plant capacity of 8000 t/d (dry), three pressure vertical plate filters, a belt conveying to the deposit, and final transport and deposition with trucks on the deposit. The equipment in the deposit assumes four trucks (50 t), one bulldozer, one roller compactor machine and one crawler excavator.

TABLE 6

Example of personnel for an 8000 t/d tailings filtration plant, belt conveying system and deposition by trucks.

Personnel	Crew/shift
Operation total	**12**
Supervisor	1
Foreman	1
Filter plant operator	2
Control room operator	1
Deposit operator	7
Maintenance total	**4**
Mechanical technician	2
Electrician	1
Instrumentalist	1
Total (*)	**16**

(*) In addition, contracts for equipment maintenance, parts replacements (filter cloths and plates), and support services must be considered.

CONCLUSIONS

Tailing filtration process is a mature technique ready to be applied, with proven technology and many worldwide applications. The technique has several advantages over other types of tailing disposals in low rain climates, relates to environment protection, maximisation of water recovery and reduction of geotechnical risks. The main disadvantage is the extensive mechanical equipment and installation requirements with the high cost and operating and maintenance needs.

ACKNOWLEDGEMENTS

Thanks to Fluor for the support for the article preparation and to Iron Ore 2021 for the opportunity to participate.

REFERENCES

Lara, J L, 2013. Experiencias de operación de Depósito de Relaves Espesados y Filtrados [online]. Available from: <https://www.iimp.org.pe/pptjm/jm20131017_relaves.pdf> [Accessed: 28 March 2021].

Ulrich, B and Coffin, J, 2013. Considerations for tailings facility design and operation using filtered tailings. *Proceedings Paste 2013* (eds: R J Jewell, A B Fourie, J Caldwell and J Pimenta), pp 201–210 (Australian Centre for Geomechanics: Perth).

Villanueva, D E, 2019, Metodología de caracterización geoquímica de residuos mineros aplicable en faena, tesis (unpublished), University of Chile, Chile.

Jenike, A W, 1964. *Storage and Flow of Solids*. University of Utah, Bulletin 123.

Iron ore tailings and value addition – a short review

K Hazarika[1,2] *and G Senanayake*[3]

1. Metallurgical Improvements, Roy Hill, Perth Airport WA 6105.
   Email: kaushika.hazarika@gmail.com
2. College of Science, Health, Engineering and Education, Murdoch University, Murdoch WA 6150.
3. College of Science, Health, Engineering and Education, Murdoch University, Murdoch WA 6150. Email: g.senanayake@murdoch.edu.au

ABSTRACT

The demand for iron-ore is ever increasing with the industry directly employing 60 500 people in a range of highly skilled roles in Australia. In the year 2019, the global iron-ore production was 2.85 billion tonnes. It is estimated that each tonne of beneficiated iron ore produces 400 kg of tailings. The IOTs are fine, dense and stable crystalline material mainly composed of iron oxides, alumina and silica. The current and most applied method of iron-ore tailings (IOTs) disposal is using subaqueous disposal of tailings in dams. The footprint generated by a tailings dam is massive and requires constant monitoring due to the possibility of a failure making the operation and maintenance of tailings dam extremely expensive. This review briefly discusses the known causes of tailings dam failures, their impact to the environment and day-to-day human life and potential applications of IOTs. The increase in water content enhances the pressure on dam walls. This in turn increases the liquefaction potential of the tailings and reduces the overall strength of the dam making it more vulnerable to failure. Potential applications of IOTs are in paints, aggregates in construction materials and bricks. The reuse of IOTs reduce waste and generates further revenue facilitating a path towards a sustainable future for the industry.

INTRODUCTION

Modern society heavily relies on the products of mining and extractive industries. Mining companies provide local employment opportunities, social improvements on a notable scale, which result in socio-economic developments of regional areas by enhancing employment opportunities for the locals, hospitals, schools, airports, roads and accessibility. Nevertheless, the mining industry fails to attract and retain employees. The industry around the world witnesses a shortage of skilled workers ranging from technicians, operators, metallurgists, engineers, specialists, managers and executives. Anthony Hodges, the President of ICMM claimed that 40–50 per cent of the mining industry workforce will reach retiring age within the years of 2015–2020 (Caterpillar Viewpoint N°5, 2014). This problem will worsen due to the time taken to train up new professionals, as someone with up to 10 years' worth of experience will be in short supply (Armstrong, Renato and Carlos, 2019). The boom-bust nature of the industry further adds to this problem as the industry cannot sustain to recruit and train during the tough times as evident from the 1990s when the prices of the commodities plunged which led to shortages of mid-career professionals. Another threat to mining industry is the decreasing ore grades and the mounting waste which demand research into sustainable processing and waste recycling/disposal methods. During the lifespan of a mine, large quantities of earth and rock are moved and processed to acquire the valuable minerals and the rest discarded as waste (Schoenbereger, 2016).

The demand for iron-ore is ever increasing with the industry directly employing 60 500 people in a range of highly skilled roles in Australia. In the year 2019, the global iron ore production was 2.85 billion tonnes. To put things in perspective, a quantitative analysis of iron-ore processed in the world suggests for 2.3 Btpa of ROM feed, 1.6 Btpa is obtained as product generating 700 Mt of tailings (Guimaraes, Araujo and Cuervo, 2017). In 2020, Western Australia, produced a total of 875 Mt of iron-ore, out of which 42–62 Mt was from magnetite mines and the rest from hematite mines (GoWA, 2021). High water content in the waste slurry increases pressure on the dam walls which if turns in to a dam failure enhances the slurry to flow much further downstream with potential risk of reaching habituated and protected areas. The Global Tailings review estimates that the total number of TSFs in the world is 8500 that includes active, inactive and closed TSFs containing

217 km^3 of tailings, suggesting that iron-ore contributes to 19.17 km^3 of tailings and 9 per cent of global tailings as depicted in Figure 1 (LePan, 2021).

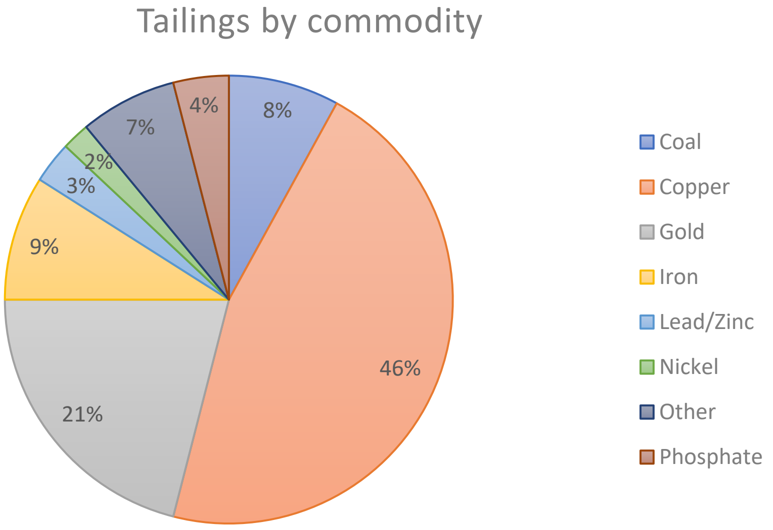

FIG 1 – Iron-ore contributes to 9 per cent of global tailings (217 km^3) in the world by commodity (LePan, 2021).

The waste materials (tailings) left over after processing the minerals and metals of economic value are estimated to be produced at a rate of anywhere from 5–14 billion tonnes per annum. The term 'tailings' is generic as it describes the by-product of several extractive industries including those for aluminium (1 per cent), coal (8 per cent), uranium (<1 per cent), precious and base metals and many other commodities of high value to modern and future technologies. The ratio of discarded tailings to valuable mineral concentrate is normally very high around 200:1 (Kossof *et al*, 2014). The tailings are disposed of in several ways. In the most awful of cases in the past, tailings were dumped into adjacent water bodies such as lakes, rivers, or ocean. However, the current government regulations in many countries prohibit such practices.

The current and most applied method of iron-ore tailings (IOTs) disposal is using subaqueous disposal of tailings in a dam (Guimaraes, Araujo and Cuervo, 2017). Tailings dams are embankments formed by locally collected fills with dams subsequently rising with more waste solid material. Most of the time, tailings are stored in impoundments behind dams constructed of mine wastes. These dams can sometimes fail causing major environmental, health and economic impacts. As a result, the mining industry is often criticized as environmentally destructive as it generates gigantic volumes of waste of magnitude comparable to the same order as that of fundamental geological processes over several thousand tonnes per annum with the principal waste contributor being tailings. It is often observed that once the summit of peak metal production has surpassed, the extraction of lower grade ore is a known long-term trend. Evidence suggests that the period of increasing metal prices show a direct trend with a high rate of tailings dam failure, some occurring within 24–36 months of increased production. It appears that from a boom-time motion point of view, safety and legislative restrictions are not necessarily a priority when it comes to achieving production (Kossof *et al*, 2014). It is predicted that the production of iron-ore in Australia will peak to 905 Mt in the financial 2020–2021 (DoISER, 2020), also reflecting commencement of several new mines in Western Australia. Performing a quick mass-balance, we can conclude that Australia will generate approximately 400 Mt of tailings in this year alone. This short review primarily focuses on iron-ore – the properties of its tailings, dam structure, summary of failures, remedy after failures, measures taken to minimise and prevent the failures and a sustainable future where iron-ore tailings can be reused.

PROPERTIES OF TAILINGS

Tailings are the unwanted rock particles with a grain size distribution from sand to clay sized particles that are stored in slurry form inclusive of chemicals in tailings dams (Raman and Fei, 2019). The particles that constitute tailings are habitually angular to very angular, with the morphology frequently striking high friction angle on dry tailings. The grain size is often variable and difficult to generalise as it is prescribed by specific requirements (Kossof *et al*, 2014). Particle size varies from 2 mm to 625 µm while densities vary according to the parent rock type. The bulk density and specific gravity of tailings ranges from 1.8 to 1.9 t m^{-3} and from 2.6 to 2.8, respectively. An increase in bulk density is often observed in tailings piles with depth because of compaction, dewatering and digenesis (Kossof *et al*, 2014).

In a riverine setting, smaller particles are carried further downstream potentially posing a greater threat either to area of floodplain or allowing for greater dilutions. These smaller particles with higher surface area also become more prone to oxidation and hence become vulnerable to sulfide oxidation and release of heavy metals such as copper and manganese (Kossof *et al*, 2014). The degree of presence of metal and metalloid in tailings entirely depends on the extraction process and the amount of plant investment, efficiency and price of the economic mineral at the time. Since no extraction process is 100 per cent efficient, there are always metals and metalloids other than iron and silicon present in the stream. Tailings minerals can be broadly divided into three categories (Kossoff *et al*, 2014): (i) the gangue fraction, (ii) the residual sulfide-oxide fraction (non-economic) and (iii) the secondary mineral fraction. The secondary mineral fractions form when fresh tailings are exposed to the environment for prolonged periods of time. The secondary mineral also hosts the major contaminant metals and metalloids via structural and surface adsorption and tends to sink in the dam depending on the rate of dissolution. The chemical composition of tailings depends on the four factors described in Table 1. Although 99 per cent of the tailings generated by iron-ore tailings are non-toxic elements, it is usually the large volumes that come into attention that are placed into tailings dams (Guimaraes, Araujo and Cuervo, 2017).

TABLE 1

Factors controlling chemical composition of tailings and reasons for dam failure (Guimaraes, Araujo and Cuervo, 2017).

Factors controlling the chemical composition of tailings	Reasons for dam failure
The mineralogy of the orebody The kind of processing fluids used to extract the economic mineral The efficiency of the extraction process The degree of weathering when stored in dammed impoundments.	Increased volume in plant waste Missing regulations on design criteria Lack of attention to dam stability requirements due to failure in continuous monitoring Lack of control (beginning from emplacement, construction to operations)

GENERAL STRUCTURE OF TAILINGS DAMS AND CAUSES AND IMPACT OF FAILURE

Mining companies often face high financial and reputational costs during TSF failures. The breach of Fundao TSF at Samarco mine in Brazil jointly owned by BHP Billiton Brazil and Vale S.A. saw a joint potential provision for USD2.4 billion under the agreement with Federal Government of Brazil and other public authorities (Larrauri and Lall, 2018). Most TSFs in early days were constructed based on trial and error but the designing process of tailings dams has significantly changed since the 1900s. In recent times, various studies are required to approve TSF design with plans for remediation and closure of impoundments included in the reliability plans. Breach assessments are also increasingly becoming part of many requirements in the permit process of construction (Larrauri and Lall, 2018). The parameters often include volume of tailings (V_F) that could potentially be released and the distance it may travel downstream, called the run-out distance (D_{max}). Generally, TSFs are not emptied in case of failures as only a percentage of the tailings are released. Hence, the methods developed to estimate the release of water from regular dams cannot be applied to tailings dams. Rico, Benito and Diez-Herrero (2008) calculated impounded volume of tailings (V_F in $10^{6\ m3}$) using equation 1 and obtained the run-out distance D_{max} using equation 2 where V_T is Volume of tailings stored at the dam and H is the dam height. Larrauri and Lall (2018) on the other hand have suggested this approach may result in unrealistic estimates when liquefaction is a known risk as it did not consider viscosity or yield stress and have proposed the consideration of potential energy associated with the released volume, contradictory to the whole tailings impoundments volume. The proposed model has a better linear fit using the same data set and is presented in equations 3 and 4.

$$V_F = 0.354 \times V_T^{1.01} \quad R^2=0.86 \tag{1}$$

$$D_{max} = 1.61 \times (H\ V_F)^{0.66} \quad R^2=0.57 \tag{2}$$

$$\mathrm{Log}(V_F) = -0.477 + 0.954 \log(V_T) \tag{3}$$

$$\mathrm{Log}(D_{max}) = 0.484 + 0.545 \log(H_f) \tag{4}$$

A tailings dams' phreatic lines (Figure 2) continuously change due to contributing factors such as rainfall infiltration and discharge of tailings recycling water (Wang *et al*, 2018). Tailings dams also undergo dry-wet cycles along with the appearance of hydro-fluctuation belts. Wang *et al* (2018) proposed a method that purposefully calculated the phreatic lines under dry-wet cycles as shown in Figure 2. Their modelling data suggested that with increasing dry wet cycles the maximum displacement of tailings dam also increased. The displacement was mainly observed at the toe of the tailings dam and at the front edge of the hydro fluctuation belt (Wang *et al*, 2018). Moreover, the safety factor decreases with increasing number of dry-wet cycles.

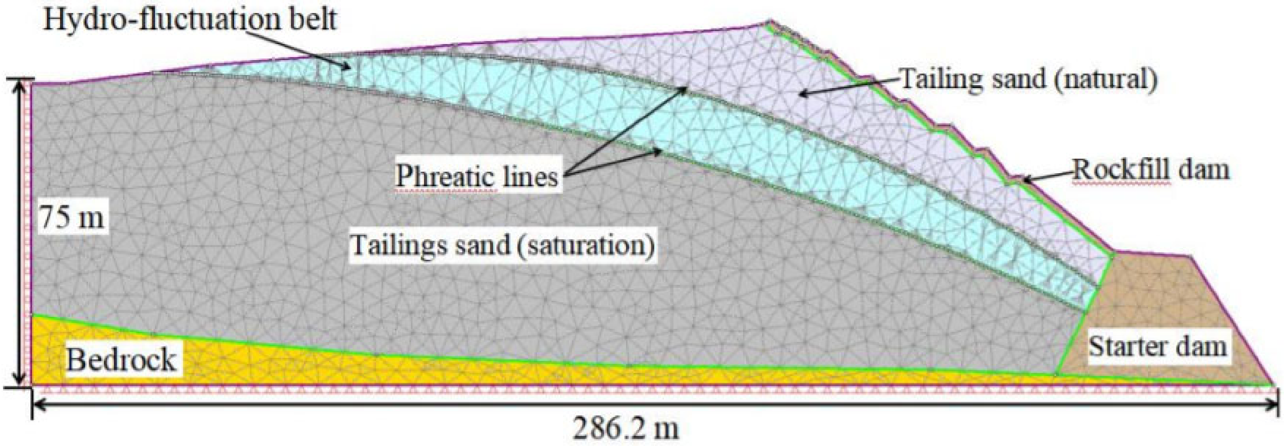

FIG 2 – Calculation model of phreatic lines (Wang *et al*, 2018).

Although TSFs are expected to last forever, history has seen many minor and major spills that have left a lasting environmental menace even after the mines have closed. A tailings storage facility (TSF) occupies several square kilometres of land with dams that can reach heights of tens of metres. Their structure differs from water retention dams, as they are built in stages with the progress of the mine, usually using mine wastes rather than concrete. An upstream dam is built towards the interior of the storage facility so that the embankment crest moves steadily inwards while a downstream dam is built up on the outside face with embankment crest moving outwards (Figure 3). Efforts are still required to establish reliable methodology for coping with hazard prediction from tailings dam failures that serve to classify tailings ponds as per their potential downstream damages.

Tailings dam failures occur from a variety of factors – flooding, piping, overtopping, liquefaction, or a combination of few resulting in spills of polluted water and tailings with different textural and physical-chemical properties further impacting downstream socio-economic activities and ecological systems. A number of particular characteristics (Table 1) make tailings dams more vulnerable to failure such as – embankments formed by locally derived fills, multistage raising of the dam to cope with increase in solid waste and effluent released inclusive of precipitation, the lack of any regulations on specific design criteria, dam stability requiring continuous monitoring and control during emplacement, construction and operation of the dam and the high costs of remediation works following the closure of the mining activities.

There are several factors that affect the deformation and strength of a tailings dam including composition of material, physical and mechanical properties and statistical parameters of the dam such as height, slope ratio, dry beach length, inner water levels, groundwater elevation and seismic activity. As a safe limit, an adequate amount of freeboard must be maintained. If the water is adjacent to the dam itself, erosion or seepage processes may lead to breaching. Hence, TSFs in seismically active or high rainfall areas are very vulnerable to failure.

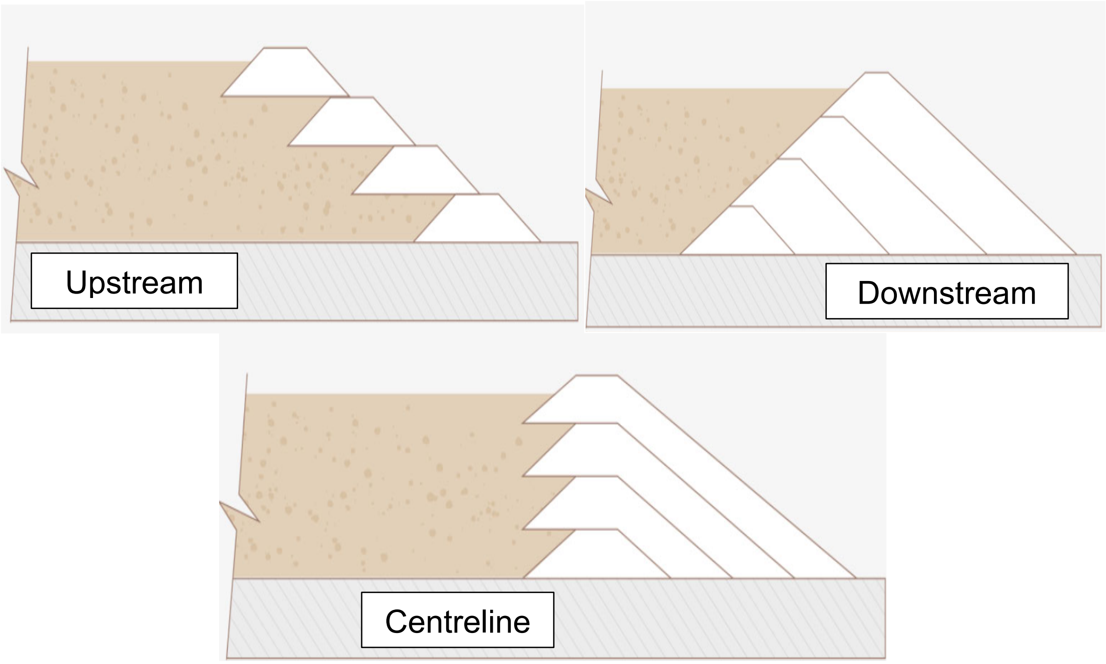

FIG 3 – Illustrations of upstream, downstream and centreline tailings dams (Rio Tinto, 2021).

After the Samarco disaster in 2015, the world's largest mining companies began responding to the issue of tailings dam disaster together. It was then in 2016, the International Council on Mining and Minerals (ICMM) conducted a review of tailings standards, guidelines and risk controls (Owen *et al* 2020). Galvao *et al* (2018) have analysed that the number of disasters due to failures of tailings dams that occurred in Brazil since 1975 was proportional to the price and volume of iron-ore production. All those accidents occurred in the state of Minas Gerais which had the largest number of iron-ore tailings dams and the second largest population of the country.

The causes of failure in active dams often vary but the general conclusions can be drawn and categorised into the groups shown in Figure 4. Upstream raised dams (Figure 3) are the most likely to fall short as such dams are said to be unforgiving structures. They lack a good design practice for its integrity to be maintained. Upstream dams also fail due to static liquefaction which may be defined as the loss of solid properties due to an applied stress causing the tailings to behave in a liquid-like manner causing instability in the structural integrity of the tailings dam. The stress often results from blasting or the moving of heavy equipment. The major concern though is seismically susceptible areas, ie, dams in geographical locations prone to earthquakes.

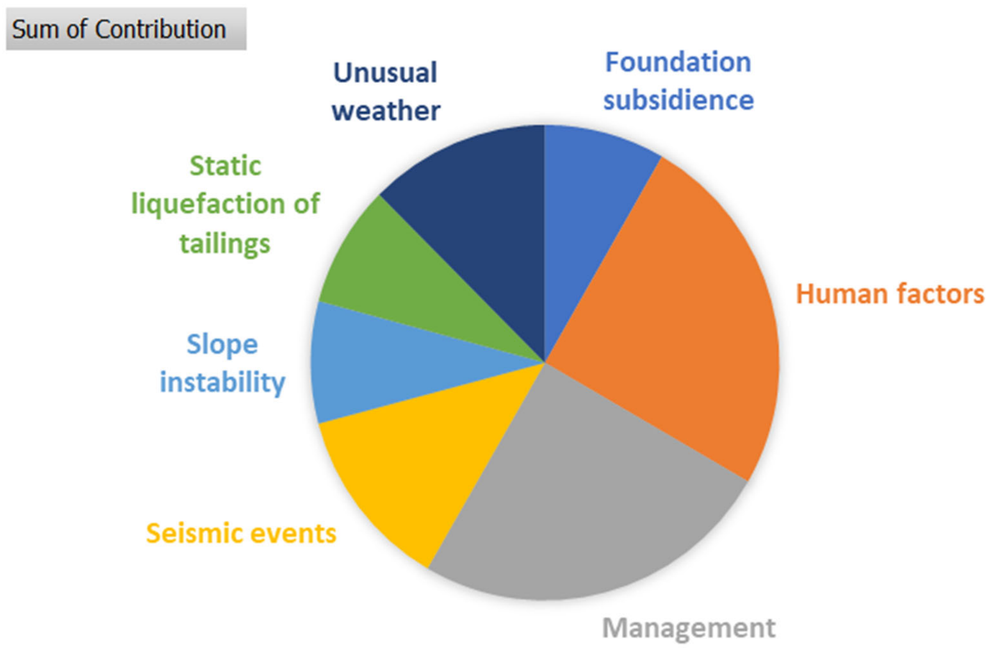

FIG 4 – Causes of iron ore tailings dam failures.

Another common cause of active dam impoundment failure is foundation failure. The permeability of the foundation is an imperative constraint on the stability of the dam structure itself. Low permeability foundation material tends to raise pore pressure rendering the overall structure exposed to shear stress. On the other hand, when the foundation is too pervious a construction material can render its structure vulnerable to piping failure. Such geotechnical factors are often ignored when constructing embankment dams. The following factors rather seem to get more consideration – local topography, mill-impoundment distance and catchment area-size (Schoenbereger, 2016).

The main geotechnical cause of TSF failures is due to water in the wrong place causing either overtopping of the embankment or foundation failure. Backfilling into underground mines and waste disposal in mined-out open pit are increasingly favoured these days. These methods avoid surface storage issues but matters of water management and the surface containment are often ignored. Earthquakes have also caused tailings dam failures; the propagation of seismic waves through a geo-structure can tend to produce seismic inertial forces causing instability of the structure.

Tailings dams are built to store slurry or water from flowing downstream. A dam failure can lead to disastrous results to areas in the downstream due to large gravitational potential energy stored in it. The tailings often tend to flow over a long distance when a break occurs (Raman and Fei, 2019). The failure rate of tailings dams over the last century calculated as 1.2 per cent is a higher figure than that of the conventional water retaining dams which is about 0.01 per cent (Xin, Xiaohu and Kaili, 2011). A study conducted by the International Commission of Large Dams and the United Nations Environment Program in 2001 found that one major tailings dam incident occurred per annum with some caused by slope instability (Nimbalkar, Annapareddy and Pain, 2018). Thus, studies on seismic slope stability analysis is an important factor to be considered prior to designing of tailings dams for earthquake resistance. The reliability of tailings dam is dependent on good design and maintenance. Most failures are preceded by prior symptoms such as structure settlement cracking and wet spots on dam face except for those triggered by earthquakes or major storms. Therefore, good maintenance strategies become an essential part of effective tailings impoundment disaster management (Kossoff *et al*, 2014).

Xin, Xiaohu and Kaili (2011) studied the factors affecting the deformation and stability of the tailings dam including material composition, physical, mechanical properties and the geometric parameters of the dam. They further summarised an analysis of the factors leading to tailings dam failures and subdivided into two modes: overtopping failure and structural failure. The dam structure failure mode was defined into failure due to seepage, instability, or seismic instability. Seismic disaster failure is further categorised into seismic liquefaction and seismic instability failure. Xin, Xiaohu and Kaili (2011) established a risk rate calculation model of each of the above-mentioned failure modes to get probity of tailings dam failure which can be used as a risk assessment tool to predict disasters (Figure 5).

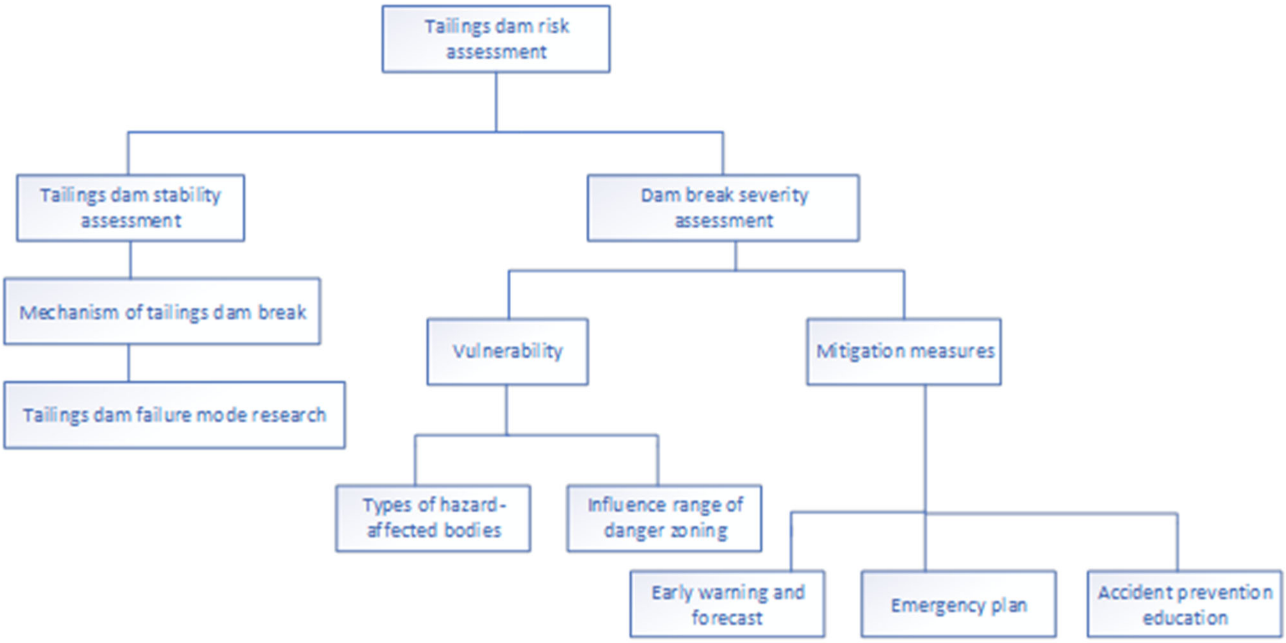

FIG 5 – Risk assessment tool for tailings dams (Xin, Xiaohu and Kaili, 2011).

TAILINGS DAM FAILURES IN IRON-ORE INDUSTRY

Thousands of people have died from iron-ore tailings dam failures (Table 2). The magnitude and the nature of waste material held in tailings dams means their failure and discharge into water bodies invariably affects water and sediment quality as well as aquatic and human life for hundreds of kilometres downstream. The immediate outcome of severe dam failures has been drowning and suffocation. The impact of tailings dams on fish and terrestrial animal and plant life can also be severe (Lemperiere, 2017).

In the year 2015, Brazil saw one of the worst dam failures in its history where 62 million cubic metres of slurry engulfed houses and wiped away the cultural and natural heritage of a village Mariana in the state of Minas Gerais leaving 19 dead, 3 missing and over 600 people homeless. The slurry from this failure reached the Rio Doce river which is one of the main freshwater systems to supply water and nourishment to the endangered Atlantic forest. The turbidity of the river water rose to 12 000 times higher than the allowed limit for consumption with the oxygen level dropping below 1 mg/L causing the death of several tonnes of fish and other living beings forming part of the river ecosystem. This was the seventh tragedy resulting from the failure of tailings in the state of Minas Gerais in less than 30 years (de Oliveira Neves *et al,* 2016).

In August 2018, five months before the Brumadinho collapse, audit results suggested that the dam was stable. The dam was built in 1976 to store iron ore tailings at an average elevation of 86 metres and held over 12 million cubic metres of tailings (Raman and Fei, 2019). Apart from the casualties enlisted in Table 2, the failure destroyed 2.7 million square metres of forests that was in the 98 km path of the slurry flow (Raman and Fei, 2019). The failure occurred during local lunchtime and consequently the slurry ran to the nearby Paraopeba river after about three hours from the first break. Due to the timing of the incident, most casualties took place in the dam worker's cafeteria as it was lunch hour. The event continued for a few more days and during the time, mud kept creeping both downstream and upstream along the river (Raman and Fei, 2019).

TABLE 2

Iron ore tailings dam failures.

Year	Country	Location	Dam height (m)	Storage volume (m^3)	Tailings releases – release volume (m^3)	Runout – tailings travel (km)	Deaths
1969	Spain	Bilbao			115×10^3	0.035	
1976	Sweden	kiruna	15	10^4			
1976	China	Dashihe	37				
1978	Sweden	malmberget	32	20×10^3			
1981	Russia	Balka Chuficheva, Lebedinsky	25	27×10^6	3.5×10^6	1.3	
1984	Ukraine	Mirolubovka	32	80×10^6	none		
1986	Brazil	Itabirito, Minas Gerais	30		62.5×10^3	12	7
1986	Brazil	Pico de São Luis, Gerais	20				
1986	China	Huangmeishan					19
1987	China	Xishimen	31		2230		
1994	China	Longjiaoshan, Daye Iron Ore Mine, Hubei					31
1997	Chile	Algaroobo, Vallenar	18				
1997	Chile	Algaroobo, Vallenar	20				
2001	Brazil	Sebastião das Águas Claras, Nova Lima district, Minas Gerais				8	5
2007	United Kingdom	Glebe Mines			20×10^3		
2008	China	Taoshi, Linfen City, Xiangfen county, Shanxi province	50.7	290×10^3	190×10^3	2.5	277
2011	Canada	Bloom Lake, Newfoundland, Cleveland Cliffs			$200\text{x } 10^3$		
2014	Brazil	Herculano mine, Itabirito, Região Central, Minas Gerais					3
2015	Brazil	Germano mine, Bento Rodrigues, distrito de Mariana, Região Central, Minas Gerais	90	55×10^6	43×10^6	668	19
2019	Brazil	Brumadinho, Brazil					270 deaths, 22 missing

(Glotov *et al*, 2018; Kossoff *et al*, 2014; Raman and Fei, 2019; Larrauri and Lall, 2018; WISE Uranium, 2019).

The Brumadinho collapse (Figure 6) in early 2019 was not a one-off event and it was the 11th most serious tailings dam failure of the decade. Right after this incident Vale raised warnings of another possible failure at the Gongo Soco mine only 65 km away from Brumadinho. Gongo Soco had not been active since 2016; however, it showed movements on its northern slope of the mine pit which may have potentially impacted the Sul Superior dam 1.5 km away. The extraction-site of the Gongo Soco mine is now under 24-hour surveillance, although Vale released a statement in May 2019 that the wall was sinking into the pit posing less of a risk to the tailings dam (Zhou, 2019). In addition, two of BHPs upstream facilities at Samarco in Brazil have been decommissioned following the February 2019 rulings by the Brazilian government on upstream dams in Brazil. According to a recent report in Bloomberg, an audit was conducted by government officials in Brazil after which Vale has received a new warning of a serious and looming risk of rupture due to liquefaction of the dam structure on 9th of June 2021. Officials have since stopped trains to Vale's Mariana complex as a potential collapse could happen any time, affecting about 33 000 kt of daily production for the company. Although Vale has claimed there is no immediate risk, the area around the dam has since been evacuated. Access to the nearby Alegria mine has also since been restricted further affecting 7500 t of daily production (Mariana, 2021).

FIG 6 – View of collapsed tailings dam of Vale SA in Brumadinho, Brazil. Source: REUTERS/Washington Alves (Nogueira, 2020).

RISK AND REMEDIATION

Being in a highly seismic zone, the Chilean regulatory framework has propagated two regulations governing the design and execution of construction and maintenance of tailings dams. The first was the Supreme Decree No 86 that was effective until 2006. In 2007 the second Supreme Decree no. 248 of 2007 came into force (Villavicencio *et al*, 2013). According to the new decree, the new geotechnical requirements are: (i) the strict prohibition of upstream method, (ii) allowing downstream and centreline construction methods, (iii) a degree of compaction based on Proctor test associated with the compaction method for the construction of dams using sand tailings which must have a fine (<80 μm) percentage of less than 20 per cent. There are also several geotechnical design parameters that must be accounted for with the retaining dyke having a mandatory underlying drainage system (Villavicencio *et al*, 2013). This is a remarkable effort as upstream dams have caused the greatest number of failures till date.

The ICMM which is an international auditing organisation dedicated to a safe, fair and sustainable mining and metals industry representing 26 mining and metals industry bodies performed audits and gave a ‘high risk’ rating if the tailings dam failure has the potential to cause 10 or more deaths and an ‘extreme risk’ rating if the tailings dam failure has the potential to cause 100 or more deaths (ICMM, 2019). Regardless of the ICMMs audit identifying risks majority of the companies have assured confidence that they have processes in place to mitigate risk to the public in the following cases within Australia, although not all of them are iron-ore mines: BHP owned Olympic Dam mine (SA), Whaleback iron ore mine (SA), Pilbara mine (WA), the Leinster mine (WA), Rio Tinto’s Andoom and Torro mines at Weipa in Queensland and Glencore’s Mount Isa Mines in which the tailings dam is only 10 km away from Mount Isa’s CBD. Rio Tinto’s Weipa bauxite mine, Glencore’s Mount Isa mine and BHP’s Olympic Dam mine were further approved for expansion, as strategies are in place to avoid/minimise failures (Maguire, 2019).

There are quite a few options available for remediation of tailings dam failures wherein to contain and prevent further spreading, barriers can be constructed. The more common remedial measure often taken for tailings dam spills is the removal of tailings from the affected areas to a storage area carried out in several phases. The Tailings Storage Facility is the last site with active ongoing recuperation and remain under the authority of the mining company. Mines in many jurisdictions must present an environmental management and restoration plan before they can proceed with construction. If the mine owners and operators transfer the risk associated with tailings dam failure to insurance companies, then the insurance companies must be obligated to corroborate and ensure that a calamity can adequately be mitigated by assessing the hazards, downstream effects, impact on the environment and economy by giving an estimate for the losses (Nimbalkar, Annapareddy and Pain, 2018). On a universal scale, insurance companies should also be made aware that highest possibilities of tailings dam failures are associated with active impoundments with the main causes being hydro-geological events, foundation failures and seismic events (Kossoff *et al*, 2014).

There are three basic styles of thickeners these days: (i) High-rate (ii) High density and (iii) Paste. High-rate thickeners are the most used thickener in the industry and provide operations with a relatively inexpensive way to recover water and transport thickened tailings to an impoundment. The mud flow into an impoundment area with the help of gravity and pump flow. Water and solids will further segregate in the impoundment area, which are dealt with either by return to the process plant, evaporation, or discharge. High density thickeners give longer mud residence times to allow for further compaction and the rake drives and supporting structures must be designed to deal with a higher yield stress mud. Paste thickeners offer the operator the ability to produce the highest underflow concentrations and yield stress muds possible with gravity settling alone. The rakes are often equipped with vertical rods or angles that protrude upward in the tank to aid with paste formations. There are, of course, several reasons to consider paste thickeners which includes higher recovery of water and usefulness in mine backfill, but a reason that has great benefit is the stability of the mud once in place posing lower risk of impoundment failure (McLanahan, 2021).

Water management is one of the most challenging concerns in Western Australia. With change in climatic conditions, rainfall patterns and rapid rise in population have created an urgent need to manage and meet a growing demand for water. The challenge in Pilbara is the rapid growth in the iron-ore mining industry with large water needs. It was predicted that in 2020, water usage for every tonne of iron ore shipped at the Port Hedland was 44 litres. Water usage at Port Hedland is also considerably higher than Dampier or Cape Lambert due to the location of stockpiles next the town centre and the need for dust mitigation. It is further estimated that water demand for the Ports will reach an estimated 18 640 mega litres in 2030 (APO, 2007). Hence, optimum water usage and recycling of process water is of utmost importance in ore processing.

A tailings stream in an iron ore process plant is thickened to 45–50 per cent solids in high-rate thickeners whereas the same tailings stream could be thickened to 65–70 per cent solids using a paste thickener. Implementing paste thickeners will not only assist in process water recovery from the tailings stream reducing the requirement of raw water for processing (WesTech, 2021). The paste disposal technique will further help with smaller impoundment area, less water in TSFs, improved water recovery, faster beaching, reduced groundwater contamination and easier rehabilitation. Paste thickeners built in a Mexican iron ore mine, the ArcelorMittal Nippon Steel India Ltd and the Khurmani iron ore mine in West Africa have optimised dam management and water recovery, a huge potential for the Australian iron ore industry.

ECONOMIC IMPACT AND TAILINGS MANAGEMENT

Ample and readily available data is limited and partial on the economic impacts of tailings dams, as most studies focus on impacts on the environment, infrastructure and people. Two major economic constraints are business interruption and environmental damage and clean up. Furthermore, there are the socio-economic and political issues associated with migration of effluent into rivers. Tailings from mining and processing operations specifically represent environmental impacts. The most important liability often results in a polluting party paying for damages caused to the environment. Owners, operators and constructors of tailings dam are exposed to huge environmental liabilities and associated economic losses and hence risk may be transferred via insurance. In addition, tailings dam failures may also lead to further losses arising from business and supply chain interruption particularly when third party property damages or casualties occur and the business closes. Such an example is the impact of business disruption from Vale's mine disaster in 2019 where top executives of the company are facing intentional homicide and environmental damage lawsuits in addition to a $7 billion payout to the casualty victims. Although the actual casualty reported was 270, it is questionable as the actual number may be much higher (BBC, 2021).

On a closer look at the Australian iron-ore industry, it is commendable to mention the steps taken jointly by BHP and Rio Tinto, Fortescue Metals Group (FMG) and a relatively new iron-ore business like Roy Hill not falling far behind when it comes to reduction in generating iron-ore tailings. Australian operators are leading the way in showing the world how to manage TSFs safely.

BHP

Following the tragic Fundao dam failure at Samarco, BHP immediately initiated a Dam Risk review to assess the TSF management of both active and inactive tailings dams. Consequence of the Brumadinho event, BHP further established a Tailings Taskforce accountable for fast-tracking strategies and ensuring best practise is embedded. Updates of BHP standards for TSF governance and controls include (i) key risk indicators set by management to further help monitor tailings performance against data relating to dam integrity and design and (ii) overtopping or flood management and emergency response planning. Out of the 70 TSFs of all commodities operated by BHP, 29 are upstream dams. Four of them have been classified as of extremely high risk and 16 as of very high risk. Currently, BHP is expanding its satellite monitoring program to better manage geotechnical risk using remote monitoring technologies including interferometric synthetic aperture radar (InSAR). This technology monitors ground deformation InSAR technology can detect critical changes that may lead to potential dam failures early and monitor over time. This technique is intended to enable identification, analysis, monitoring and management of ground displacements or any other potential indicators for TSFs. In support for more detailed transparency and integrated disclosure around TSF management, BHP has also contributed to the development of the new Global Industry Standard on tailings management which has been further developed as an international standard for safer tailings management jointly with the ICMM, the UN environment program and the principles for responsible investing (BHP, 2020).

FMG

The TSF design by FMGs includes several aspects: (i) location of mining infrastructure, (ii) employees and communities, (iii) areas of environmental significance, (iv) topography, (iv) geological and climatic conditions, (v) future land use, (vi) tailings characteristics and (vii) seismic activity of the area. It currently operates three active TSFs and manages an additional six inactive facilities, all located in the Pilbara region of Western Australia. Two of FMGs inactive facilities have been rehabilitated, one is in the process and two are being dried for future rehabilitation. The inactive TSFs are in its Iron Bridge mine site which is currently in care and maintenance pending development of the project. The active TSFs are located at Cloudbreak, Christmas creek and Solomon. None of these are large or structurally complex, neither are they in seismically active regions. FMG further ensures none of its TSFs use upstream construction method nor does it use tailings as a structural element for any of its TSFs (FMG, 2021).

Rio Tinto

Rio Tinto aims to protect the health and safety of its people and the surrounding environment in the most transparent way of all the operations. In 2015, Rio Tinto introduced a group standard for all TSFs and water storage facilities ensuring all their managed facilities operate in accordance with one standard. Further in 2016, Rio Tinto joined the ICMM working committee to conduct tailings management review of its member companies. In its iron-ore operations, Rio Tinto has three upstream dams that are currently categorised as high risk of which two are active although they have not reached the planned storage volume, as listed in Table 3. Since the introduction of its Group safety standard, it has mandated detailed control requirements, established surface mining centre of excellence to provide technical expertise and appointed nominated managers and qualified site representatives for TSFs and water dams (Rio Tinto, 2021).

TABLE 3

Rio Tinto’s iron-ore TSFs (Rio Tinto, 2021).

Operations	Status	Date of initial operation	Raising method	Current maximum height (m)	Current tailings storage impoundment volume (m^3)	Planned tailings storage impoundment volume in 5 years’ time (m^3)	Most recent independent expert review	Categorisation based on consequence of failure	Last audited for downstream impacts
Hope Downs 4 – DSP in-pit WFSF	Active	2017	N/A (in-pit)	0; open pit	2164×10^3	2.8×10^6	February 2021	Very Low	January 2016
Hope Downs 4 – Kalgan 2 WFSF	Active	2020	N/A (in-pit)	0; open pit	240×10^3	4.8×10^6	February 2021	Significant	No: In-pit facility
Hope Downs 4 – Kalgan 3 WFSF	Active	2020	N/A (in-pit)	0; Open pit	129×10^3	6.1×10^6	February 2021	Significant	No: In-pit facility
Hope Downs 4 – WFSF Stage 2	Active	2013	Downstream	22	4383×10^3	5×10^6	February 2021	Significant	April 2020
Marandoo – SWFSF	Active	2019	N/A (single embankment)	22	1070×10^3	6.6×10^6	August 2020	High B	January 2020
Marandoo – WFSF	Inactive	2013	Downstream	27.5	7200×10^3	8.5×10^6	August 2020	High C	January 2020
Mesa J – TSF1	Inactive	1998	Downstream	10	14×10^6	$14x\ 10^6$	January 2021	Significant	October 2018
Mesa J – TSF2.5	Closed	2008	N/A (in-pit)	0; open pit	840×10^3	$840x\ 10^3$	July 2018	Very Low	October 2018
Mesa J – TSF3	Active	2009	Downstream	15	7620×10^3	11×10^6	January 2021	High C	October 2018
Mesa J – TSF4 (TSF2)	Inactive	2004	Upstream	21	17×10^6	$17x\ 10^6$	January 2021	High C	October 2018
Mesa J – TSF5 (TSF3 South)	Inactive	2009	Downstream	29	14×10^6	22×10^6	January 2021	High C	October 2018
Nammuldi – NBWT WFSF	Active	2014	Downstream	28	11×10^6	25×10^6	March 2020	Significant	March 2018
Paraburdoo – TSF1	Active	1995	Upstream	21	33×10^6	45×10^6	February 2021	High C	March 2020
Tom Price – TSF1	Inactive	1979	Downstream	40	3500×10^3	3.5×10^6	March 2020	Very Low	No
Tom Price – TSF2A	Active	1992	Upstream	35	21.5×10^6	25.5×10^6	September 2020	High B	February 2021
Yandicoogina – WFC1	Inactive	2005	Downstream	51	10.7×10^6	10.7×10^6	February 2020	Very Low	January 2020
Yandicoogina – WFC2/4	Active	2011	Centreline	44	8.2×10^6	8.2×10^6	February 2020	High C	January 2020
Yandicoogina – WFC3	Inactive	2015	Downstream	55	3.3×10^6	3.3×10^6	February 2020	High C	January 2020
Yandicoogina – WFC3A	Active	2017	Downstream	40	11.9×10^6	20.1×10^6	February 2020	High C	January 2020
Yandicoogina – WFC5	Active	2020	N/A (in-pit)	0; open pit	761×10^3	7.5×10^6	May 2017	Low	No: In-pit facility

Roy Hill

Roy Hill commenced production in 2015 with an initial delivery plan of 55 Mt per annum. The initial annual production of tailings was planned to reach 13.3 million dry t per annum with the TSF designed to contain tailings for the first ten years of production. The TSF was split in to two cells to allow for continuous development of the facility while the other cell was used for deposition. There were seven consecutive raises above the initial TSF embankment before the ultimate storage capacity of the TSF embankment was reached (ANCOLD, 2012).

In 2018, Roy Hill built the wet high intensity magnet separator (WHIMS) (Figure 7) to deliver additional four to five Mt of high-grade iron ore from the mine, in turn increasing its export capacity to 60 Mt. Note that since then Roy Hill has approval to export 70 Mt. A series of electromagnets extract ultrafine iron from their tailing's slurry placing it onto the stockpiles for production. Apart from boosting production at the Pilbara mine, the WHIMS also has significant environmental benefits, as it decreases the amount of waste sent to the tailings pile by up to five Mt per annum. By building the WHIMS plant, the company has clearly reduced 5 Mt of tailings annually which is a major accomplishment. Roy Hill's commitment to efficiency is already making better outcomes for the rest of the industry and community, a win-win. This will be further reflected in the future as the business is driving to further optimise their process plant and improve recovery which in turn will reduce the tailings stored in their TSF (Hancock Prospecting, 2021). With increased production and to allow for tailings to dry before consequent deposition, Roy Hill has since brought an additional in-pit tailings storage facility online.

FIG 7 – Roy Hill's WHIMS plant.

PROCESSING IRON-ORE TAILINGS FOR VALUE ADDITION

A path towards long-term sustainable future is the need of the current hour, as with time, iron ore resources continue to decline with no decline in demand. The industry needs to invest in strategies to increase efficiency in the beneficiation of iron ore, getting higher recoveries and sending lesser material to tailings. The gigantic amount of IOTs incurs a high economic cost for waste management and serious environmental concerns and security risks. Due to these reasons, IOTs may become valuable resources in the future. The conversion of solid industrial waste into other valuable products has received considerable attention for a sustainable future. A few of those options are enlisted below.

Gallium from IOTs

Gallium is considered a strategic element due to its wide use in electronics and energy studies. Gallium based compounds have shown to have potential therapeutic activity against certain cancers and infectious micro-organisms. The average content of Ga in bauxite is 50 mg/kg. Zinc ore deposits may also contain similar amounts although only a fraction of gallium present in bauxite or zinc ores is recoverable and processes are usually private or patented (Macias-Macias *et al*, 2019). The iron ore tailing from a Mexican mine was leached in hydrochloric acid over 48 hours, where the tailing had a total Ga content of 13 mg/kg, achieving total dissolution of Ga in the feed. Solvent extraction using tributylphosphate, trioctylphosphine oxide and a mixture of both with benzene, toluene and hexane as diluents can separate and concentrate gallium. The results suggested that it was possible to extract 100 per cent of Ga present in the iron ore tailings with tributylphosphate and less than 35 per cent of Fe present (Macias-Macias *et al*, 2019), but economic viability needs further attention.

Rare earth elements (REE) from IOTs

Rare earth elements do not occur in nature in an elemental form but are present in various geological environments: (i) carbonates and alluvial deposits which are the main source of production of light REE, (ii) alkaline igneous systems and (iii) deposits of ionic clay which are the main sources of production of heavy REEs. LREEs are light rare earth elements, also known as the cerium group: scandium (Sc), lanthanum (La), cerium (Ce), praseodymium (Pr), neodymium (Nd), promethium (Pm), samarium (Sm), europium (Eu) and gadolinium (Gd). HREEs are heavy rare earth elements, also known as the yttrium group: yttrium (Y), terbium (Tb), dysprosium (Dy), holmium (Ho), erbium (Er), thulium (Tm), ytterbium (Yb) and lutetium (Lu). Their affinity for oxygen makes them appear as oxides although other combinations are also possible with the main minerals being monazite, bastnasite, gadolinite, apatite and zircon. Viability of the use of tailings as valuable resources for extraction of REEs has been tested based on flotation and magnetic separation using hematite tailings containing 58 per cent iron in a feasibility study (Moran-Palacios *et al*, 2019). The quantity of REEs obtained from magnetic separation techniques was six times higher than that from flotation. Thus, the extraction of REEs from tailings would be viable when using magnetic separation techniques. It would also have a great positive impact on the environment proving to be a sustainable method by reducing the volume of the waste disposed and pollution associated with it (Moran-Palacios *et al*, 2019).

Sustainable paint pigments from IOTs

Galvao *et al*, (2018) studied the reuse of IOTs as pigments for sustainable paints. Calcinated iron oxides have been used as pigments for a relatively longer period, however, the use of IOTs as pigments is relatively new. Commercial real estate paints comprise of binders, pigments, fillers and additives. The binder mounds the pigments and varies in cost. Pigments can either be organic or inorganic, whether the inorganic paints are advantageous in the sense that apart from being heat and light resistant, they are cheaper and do not bleach Filler is a mineral additive to opacify paints and reduce costs while additives are added to dissolve the binder and adjust the viscosity of the paint (Galvao *et al*, 2018). It was further observed that IOTs as pigments can be applied with conventional tools and do not require calcination. The tailings underwent drying, particle separation and lump breaking and showed promising results addressing sustainability and mitigating the environmental risks associated with tailings dams.

Concrete composite mixtures from IOTs

Tang *et al* (2019) presented an innovative method using pre-concentration followed by direct reduction and magnetic separation to utilise IOTs as composites for concrete. The process incorporated primary grinding followed by low intensity magnetic separation of IOTs. The bitumen ratio, roasting temperature and time, lime and sodium carbonate ratio and particle size of the roasted IOT were factors that influenced iron recovery. The strength of mortar cement was found to be 33.11 MPa and 50 MPa at seven days and 28 days, respectively, when the number of high-silica residues replacing blast furnace slag was at 20 per cent. Iron was recovered from the IOTs during this pre-concentration step followed by direct reduction and magnetic separation processes (Tang *et al*, 2019). This showed promising results for the use of IOTs with low iron content exhibiting high potential for a sustainable future.

CONCLUSION

The technical demands of safely impounding and storing tailings are abundant and varied, which need a high degree of engineering, training and experience to get it correct. Continuous education of professionals and strict environmental regulations will benefit the industry (Nimbalkar, Annapareddy and Pain, 2018). Tailings dam failures are responsible for multiple impacts in the travel path/distance causing exposure and susceptibility of goods, population, land use, water use and environmental values in the jurisdiction. As such, detailed risk assessment in each case is a necessity. Moreover, with snowballing demand for metals and other commodities for green technology and energy, lower-grade deposits of resources become increasingly driven and the global burden of tailings is projected to be on a steep climb (Figure 1). In metal accounting terms, tailings have been defined as 'hidden flow' which do not add value to the economy, a view changing rapidly. Tailings are hence best kept isolated from the floodplain environment in watertight impoundments or dry stacks if value addition is not an immediate option until future technology become available. In August 2020, Rio Tinto and other International Council on Mining and Metals companies pledged to implement the Global Industry Standard for Tailings Management (GISTM). What is required at this point of time is more companies joining hands to bring transparency to their tailing's storage standards around the world (Zakharia, 2021) and promoting value addition to minimise waste and hazards.

ACKNOWLEDGEMENTS

The authors would like to thank the leaders at Roy Hill for their continuous support and to our peers and colleagues in academia and the mining industry for their contribution to a safe and sustainable future.

REFERENCES

Analysis and Policy Observatory (APO), 2007. Prospective demand for water in the west Pilbara of WA – 2007. Economics Consulting Services. https://apo.org.au/ August, 2021.

ANCOLD, 2012. The Australian National Committee on Large Dams Incorporated, https://www.ancold.org.au/?p=6290

Armstrong, M, Renato, P and Carlos, P, 2019. Why have so many tailings dams failed in recent years?, *Resources Policy* 63 (2019) 101–112.

BBC News, 2021. Vale dam disaster: $7bn compensation for disaster victims. https://www.bbc.com/news/business-55924743. May 2021.

BHP, 2020. BHP Annual Report 2020. www.bhp.com. May 2021.

Caterpillar Viewpoint N°5, 2014. Mining industry employs creative solutions to solve skills shortage: workforce development is critical focus for many companies. http://viewpointmining.com/article/mining-industry-employs-creative-solutions-to-solveskills -shortage.

de Oliveira Neves, A C, Nunes, F P, de Carvalho, F A and Fernandes, G W, 2016. Neglect of ecosystems services by mining and the worst environmental disaster in Brazil. *Brazilian Journal of Nature conservation* 14 (2016) 24–27.

Department of Industry, Science, Energy and Resources (DoISER), 2020. Resources and Energy Quarterly. https://www.industry.gov.au/data-and-publications/resources-and-energy-quarterly. September 2020.

Fortescue (FMG), 2021. Tailings Storage Management. www.fmgl.com.au. May 2021.

Galvao, J L B, Andrade, H D, Brigolini, G J, Peixoto, R A F and Mendes, J C, 2018. Reuse of iron ore tailings from tailings dams as pigment for sustainable paints. *Journal of Cleaner Production* 200 (2018) 412–422.

Glotov, V E, Chlachula, J, Glotova, L P and Little, E, 2018. Causes and environmental impact of the gold-tailings dam failure at Karamken, the Russian far east. *Engineering Geology* 245 (2018) 236–247

Government of Western Australia (GoWA). Department of Jobs, Tourism, Science and Innovation, 2020. Western Australia Iron-ore profile. https://www.jtsi.wa.gov.au/docs/default-source/default-document-library/wa-iron-ore-profile-0520.pdf?sfvrsn=4795711c_4. May 2021.

Guimaraes, F A V, Araujo, A C and Cuervo, J L, 2017. Generation and treatment of Iron ore tailings. Congres de la sim a Metz.

Hancock Prospecting, 2021. Roy Hill Holdings has won the CDE Mining Minerals Processing of the year award for its wet high intensity magnet separator plant, which saves high-grade ultrafine iron-ore units that would otherwise end up on the tailings waste pile. https://www.hancockprospecting.com.au/. May 2021.

International Council on Mining and Metals (ICMM), 2019. Mining and Metals. https://www.icmm.com/en-gb/about-us. August 2019.

Kossoff, D, Dubbin, W E, Alfredsson, M, Edwards, S J, Macklin, M G and Hudson-Edwards, K A, 2014. Mine tailings dams: Characteristics, failure, environmental impacts and remediation. *Applied Geochemistry* 51 (2014) 229–245.

Larrauri, P C and Lall, U, 2018. Tailings dams failures: Updated statistical model for discharge volume and runout. *Environments* 2018, 5, 28.

Lemperiere, F, 2017. Dams and Floods. *Engineering* 3 (2017) 144–149.

LePan, N, 2021. Visualizing the size of mine tailings. https://elements.visualcapitalist.com/visualizing-the-size-of-mine-tailings/. May 2021.

Macias-Macias, K Y, Ceniceros-Gomez, A E, Gutierrez-Ruiz, M E, Gonzalez-Chavez, J L and Martinez-Jardines, L G, 2019. Extractions and recovery of strategic element gallium from an iron mine tailing. *Journal of Environmental Chemical Engineering*, 7 (2019) 102964.

Maguire, K, 2019. Tailings dams failure risks range from high to extreme in audits by Australian mining giants. https://www.abc.net.au/news/rural/2019–06–20/tailings-dam-audit-finds-high-failure-risks-across-australia/11223510.

Mariana, D, 2021. Vale tailings dam at imminent risk of rupture, authorities say. https://www.bloomberg.com/ June.

McLanahan, 2021. Understanding Your Long-Term Vision for Tailings Management. www.mclanahan.com.au.

Moran-Palacios, H, Ortega-Fernandez, F, Lopez-Castano, R and Alvarez-Cabal, J V, 2019. The potential of iron ore tailings as secondary deposits of rare earths. *Applied Sciences*.

Nimbalkar, S, Annapareddy, V S R and Pain, A, 2018. A simplified approach to assess seismic stability of tailings dams. *Journal of Rock Mechanics and Geotechnical Engineering* 10 (2018) 1082–1090.

Nogueira, M, 2020. Murder charges in Vale dam collapse case complicate Brazilian probes. https://www.reuters.com/article/us-vale-disaster-investigation-analysis/murder-charges-in-vale-dam-collapse-case-complicate-brazilian-probes-idUSKBN1ZQ2CM.

Owen, J R, Kemp, D, Lebre, E, Svobodova, K and Perez Murillo, G, 2020. Catastrophic tailings dam failures and disaster risk closure. *International Journal of Disaster Risk Reduction,* 42(2020) 101361.

Raman, A and Fei, L, 2019. An investigation of the Brumhadinho Dam Break with HEC RAS simulation. November, 2019

Rico, M, Benito, G and Diez-Herrero, A, 2008. Floods from tailings dam failures. Science Direct. *Journal of Hazardous Materials* 154 (2008) 79–87.

Rio Tinto, 2021. Tailings. https://www.riotinto.com/en/sustainability/environment/tailings. May 2021.

Schoenbereger, E, 2016. Environmentally sustainable mining: The case of tailings storage facilities. *Resources Policy* 49 (2016) 119–128.

Tang, C, Li, K, Ni, W and Fan, D, 2019. Recovering iron from iron ore tailings and preparing concrete composite admixtures. *Minerals*, 2019.

Villavicencio, G, Espinance, R, Palma, J, Fourie, A and Valenzuela, P, 2013. Failures of sand tailings dams in a seismic country.

Wang, X, Zhan, H, Wang, J and Li, P, 2018. The stability of tailings dams under dry-wet cycles: a case study in Luonan, China. *Water*, 10, 1048.

WesTech, 2021. Tailings Paste thickening. https://www.westech-inc.com/. August 2021

WISE Uranium, 2019. Chronology on tailings dams failures. http://www.wise-uranium.org/. August 2019.

Xin, Z, Xiaohu, X and Kaili, X, 2011. Study on the risk assessment of Tailings Dam Break. *SciVerse Science Direct. Procedia Engineering* 26 (2011) 2261–2269.

Zakharia, N, 2021. Rio Tinto introduces global standard for tailings. https://www.australianmining.com.au/news/rio-tinto-implements-global-industry-standard-for-tailings/

Zhou, V, 2019. Vale raises alarm of potential tailings dam failure. https://www.australianmining.com.au/news/vale-alerts-another-dam-in-risk-of-failure/

Mining iron ore from tailings with minimal use of process water

Y K Leong[1]

1. Professor, University of Western Australia, Perth WA 6009.
   Email: yeekwong.leong@uwa.edu.au

ABSTRACT

Iron ore tailings typically containing 40 to 50 per cent Fe can be beneficiated to iron ore products containing 54 to 60 per cent Fe. The impurities are comprised of clay, quartz, cristabolite and TiO_2. Goethite and hematite are also present. At high concentrations of 55–60 wt% solids, the tailings displayed high yield stress and viscosity and cannot be pumped over long distances. Composite additives comprising of NaOH, phosphate-based additives and sodium metasilicate are found to reduce the viscosity and yield stress very significantly by a few orders of magnitude. The yield stress of 100 Pa can be reduced to almost zero. At this state, dilution of the tailings with its process water to 40 per cent solids causes the coarse and high-density iron ore particles to separate from the colloidal fractions located in the supernatant after a few minutes of sedimentation. Separation by decantation produces a sediment with an Fe content of 54 per cent from tailings with 47 per cent Fe. Another tailings sample with 48 per cent Fe was beneficiated to greater than 57 per cent Fe using NaOH-metasilicate-polyphosphate additives and employing an additional washing step. The use of other composite additives, NaOH and polyphosphates, increased beneficiated product Fe content to greater than 60 per cent from the same tailings. With the current iron ore spot price of more than US$180 per tonne, the cost of this treatment process even including a desalination step, if necessary, is relatively insignificant. This study has given tailings an economic value that should be exploited as soon as possible.

INTRODUCTION

With the spot price of iron ore more than US$180 per tonne, it can be highly profitable mining iron ore from tailings even with the use of chemical additives and desalinated water. The cost of producing desalinated water near a population centre setting is between AU$1.00 to AU$4.00 per kilolitre (kL) according to Australian Water Association (AWA, 2021). The cost of desalinated water production is partially compensated for by a smaller additive requirement. With desalinated water and the appropriate additives, the mining of iron ore from tailings can be performed at a high solids load of 20 to 40 wt%. This will reduce the amount of water needed. The water used in the mineral separation process can be recovered for reuse two or three times, as washed water after the colloidal solids have been removed with the aid of a polymer flocculant as the quality of this water is still high. It was estimated that between 2 and 5 kL of water is needed to produce a tonne of iron ore with 58–60 per cent Fe. The cost of additives was estimated to be as low as US$3.00 to produce a tonne of this iron ore (Leong, 2021). Due to the remoteness of most of these iron ore mines' tailings dams, the cost of producing desalination water must be inflated, let say, US$5.00 per kL. Even at this cost, the cost of extracting the iron ore from tailings is still very favourable. This paper presents results of iron ore recovery from tailings. The details of some of the steps and processes will be left out as commercially sensitive information. The University of Western Australia (UWA)-developed composite additives and applications have been protected under three innovation patents (Leong, 2018, 2020a, 2020b; Leong, Drewitt and Bensley, 2019).

The amount of iron ore tailings in The Pilbara, Western Australia is as high as over a billion tonnes of solids. With Fe content typically at 40–50 per cent in the tailings, the amount of iron ore (Fe_2O_3) resource in tailings is 600–750 Mt equivalent to a US$100–130 billion resource. At the current price of about US$180 per tonne, the cost of recovering this resource is economical provided it is large enough such as a large tailings dam with 20–100 Mt of recoverable iron ore. The cost of recovering this iron ore resource is dependent upon the availability of good quality water and the mineralogy of the tailings. The availability of an iron ore processing plant nearby will make the project even more financially attractive. Results of the use of low cost UWA-developed composites additives and processing steps to enhance the beneficiation of Iron ore will be presented. The advantages and issues for using these additives will also be discussed subjected to certain proprietary information being protected.

The lack of quality water in Pilbara will in the future necessitate the need to process iron ore slurry in a more concentrated form. This paper will illustrate the use of the appropriate surface chemistry tools such as the use of adsorbed additives, to achieve this goal. Beneficiation of iron ore slurries at 30–40 wt% solids will be shown to be possible. Strategies to minimise water usage should also be developed in conjunction such as the recovery of process water for reuse and the use of lower quality bore water for other downstream processing.

RESULTS AND DISCUSSION

Pilbara mine 1 tailings

Figure 1 shows images of 29 wt% solids tailings with and without composite additives. The untreated showed no clear separation in the settled layer as illustrated by its uniform colour. In contrast, the treated slurries showed a darker settled layer which is iron-ore rich. The supernatant layer is clay rich. Clear water was not observed. Essentially the additives separated the colloidal and clay materials located in the supernatant from the coarse particles of iron ore and impurities located in the settled layer.

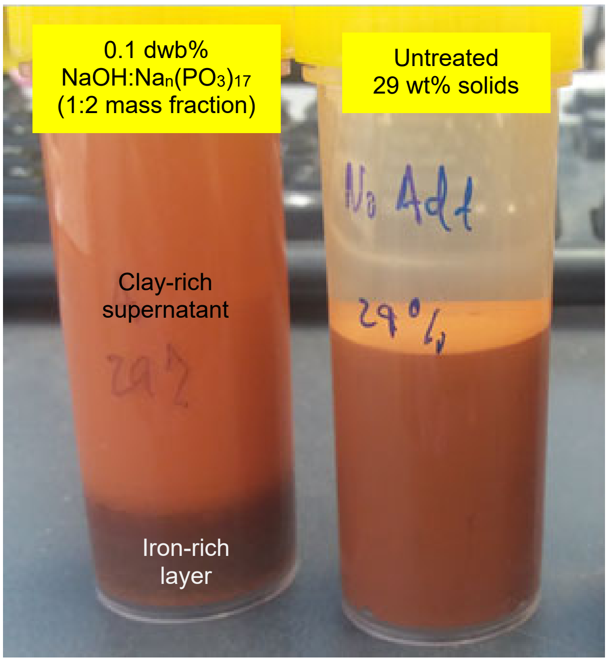

FIG 1 – Sediment properties of 29 wt% iron ore tailing slurries with and without additive treatment (Leong, Drewitt and Bensley, 2019).

The same separation of 40 wt% slurries treated with composite additives of $NaOH$-Na_2SiO_3-$Na_n(PO_3)_n$ is shown in Figure 2. The supernatant and settled layers were separated by decantation. They were then dried in an oven. The dried samples were ground and sent for elemental analysis of Fe, Al, Si and P using ICPAES. The result is shown in Table 1. The untreated slurry contained 47 per cent Fe which was upgraded to 54 per cent Fe upon further treatment. Most of the added P found in the waste supernatant (clay-rich) layer is a desirable outcome. High P content causes the steel to be brittle. A high Al/Si ratio is not desirable in the smelting or refining of beneficiated iron ore due to a high slag viscosity. The Al content is also high in the supernatant waste solids, also a desirable outcome in terms of a better smelting processibility of the beneficiated iron ore. The use of Na_2SiO_3 is thus also beneficial as a Si source in addition to its iron ore beneficiation function.

The decanted settled (iron-ore rich) layer was not washed. Washing and the removal of coarse impurities should increase the Fe content further. These factors are now the focus of the next study.

FIG 2 – Beneficiation of iron ore tailings at 40 wt% solids with NaOH-Na_2SO_3-Na polyphosphate additives (Leong, 2021).

TABLE 1

Fe, Al and P content of processed iron ore.

Iron ore rich layer			Supernatant layer		
Al%	Fe%	P%	Al%	Fe%	P%
2.41	54.0	0.034	7.41	37.3	0.113

The concentration of composite NaOH and phosphate-based additives required to treat the tailings for viscosity reduction and beneficiation for mineral separation ranged from 0.10 to 0.12 dwb%. With the cost of NaOH at circa US$450 per tonne and phosphate-based chemicals at circa. US$900 per tonne, the total additive cost is very low, ranging from US$0.72 to US$0.90, basically less than US$1 for 1 tonne of tailings solids to be treated with a 1:2 NaOH and phosphate-based composite additive.

Pilbara mine 2 slurries

The iron rich layer needs to be further processed to remove coarse impurity if it is to attain a minimum commercial grade of 58 per cent Fe. The tailings generated should be of low solids loading and will need to be concentrated in a thickener.

Another problematic iron ore (55 per cent Fe) slurry from The Pilbara, treated with the same additives achieved an upgrade to more than 58 per cent Fe, now a commercial grade product (Leong, 2021). The separation into an iron ore rich sediment layer and a clay rich supernatant after treatment is shown in Figure 3. With slurries no washing and coarse impurity removal methods were employed. The elemental analysis results are shown in Table 2. The as-received slurry (AF-NT: see Table 2) contained 55.5 per cent Fe, 1.85 per cent Al, 0.07 per cent P and 3.78 per cent Si was upgraded by the treatment of additives to 58.2 per cent Fe, 1.35 per cent Al, 0.09 per cent P and 2.91 per cent (AF0-BL). The recovery of the iron-rich layer was more than 80 per cent. The reduction in Al content in the iron-rich layer is also beneficial. Much of the Al and Si and P elements resided in the clay-rich layer (AF0-TL). A repeat experiment with a fresh sample showed a lower Fe content of 56.9 per cent in the recovered iron rich layer (AF2-BL). Washing of this iron rich layer three times with water in amount equal to the amounts decanted after each wash increased the iron content to 58.9 per cent. The additives were not given the same amount of time to act on the tailings as in the first sample where the separation was conducted after the treated tailings had been rested for three days.

FIG 3 – Beneficiation of iron ore tailings at 40 wt% solids with NaOH-Na_2SO_3-Na polyphosphate additives (Leong, 2021).

TABLE 2

The elemental analysis of iron ore slurries (Pilbara 2 mines) and their separated layers (Leong, 2021).

Sample ID	Al %	Fe %	P %	Si %
AF-NT	1.85	55.5	0.07	3.78
AF0-BL	1.35	58.2	0.09	2.93
AF0-TL	4.30	44.9	0.14	8.20
AF1-BL_3W	1.29	58.9	0.08	2.91
AF2-BL	1.40	56.9	0.09	3.10
AF2-TL	5.14	40.2	0.20	8.92

Pilbara mine 3 slurries

This iron ore slurry from mine 3 contained 54 per cent Fe (RH-NT). After treatment with UWA patented composite additives (NaOH-metasilicate-polyphosphate) to remove clayey colloidal materials, a marginal improvement in the Fe content was found in the iron rich sediment layer, 55.4 per cent Fe (RH-BL). See Table 3 for all the elemental results. Both the Al and Si content decreased slightly. The clay rich colloidal layer (RH-TL) still contains a relatively high Fe content of 42 per cent.

TABLE 3

Elemental analysis of iron ore slurries and separated layers.

Sample ID	Al%	Fe%	P%	Si%
RH-NT	3.19	54.0	0.068	2.95
RH-TL	6.14	42.0	0.22	8.47
RH-BL	2.63	55.4	0.09	5.30
RH-2WTap-MFe	1.62	58.4	0.076	3.30
RH-2WTap-Mwaste	4.75	39.8	0.076	11.07
RH-2WRHH2O-MFe	1.87	59.3	0.071	3.75
RH-2WRHH2O-Mwaste	4.75	40.0	0.078	10.59
RH-BL.MagS	1.86	59.0	0.076	3.73
RH-BL-MagWaste	3.72	46.2	0.084	8.39
RH-BL-MFe	2.00	56.4	0.074	4.08
RH-BL-Mwaste	4.40	41.9	0.084	10.35
RH-BL-2WRHH2O-MFe	1.48	60.4	0.068	2.95
RH-BL-2WRHH2O-Mwaste	3.97	45.9	0.082	8.65

A 1.03 g sample of the dried iron ore rich layer (55.4 per cent Fe-RH-BL) with a recovery of 83 per cent tailings solids was subjected to magnetic separation with a magnetic pan as shown in Figure 4. It has two magnets fixed to the bottom of the pan to collect the hematite rich particles. The magnet produced a 3300 gauss on the collecting side of the pan, directly above the magnet. The magnetic sample (80 per cent recovery) contained a higher Fe content of 56.4 per cent (RH-BL-MFe). The 17 per cent waste contained only 41.9 per cent Fe. A larger sample of this iron rich layer was used in the magnetic separation stage, in which it attained a higher Fe content of 59 per cent (RH-BL.MagS) with a recovery of 57 per cent.

Further experiments were conducted to increase the Fe content in the settled layer after additives treatment and drying by washing with tap or mine water and then magnetic separation. The data showed very encouraging separation results. Iron rich powders with Fe content ranging from 58.4 per cent (RH-2WTap-MFe) to 60.4 per cent Fe (RH-BL-2WRHH2O-MFe) were collected. The additive concentration employed was relatively high and not optimised. The Al and Si contents were generally much lower (compared to RH-NT) in the iron-rich layer while the P content was marginally higher.

(a) (b)

FIG 4 – (a) Locations of magnets fixed to the bottom pan; and (b) the collecting top surface showing the magnetic hematite particles being collected.

Pilbara mine 4 tailings

For the tailings from Pilbara mine 4, only one washing of the iron rich layer was needed to increase the Fe content from 48 per cent to 57–60 per cent Fe. Two composite additives were trialled for this tailings; 1:2 NaOH-$Na_n(PO_3)_n$ and 1:1:1 NaOH-Na_2SiO_3-$Na_n(PO_3)_n$. The raw or as-received tailings and the iron rich layer were dried in the oven. The images of these powders are shown in Figure 5a. The dried tailings lump required the input of significant grinding with a mortar and pestle to produce the powder. However, the iron rich samples produced a non-cohesive powder upon drying. The powders of the iron rich samples were much darker in colour. Microscopic images of the dried powders are shown in Figure 5b. Coarse light colour particles are clearly seen in the iron rich powders. These particles are most likely silica-based impurities.

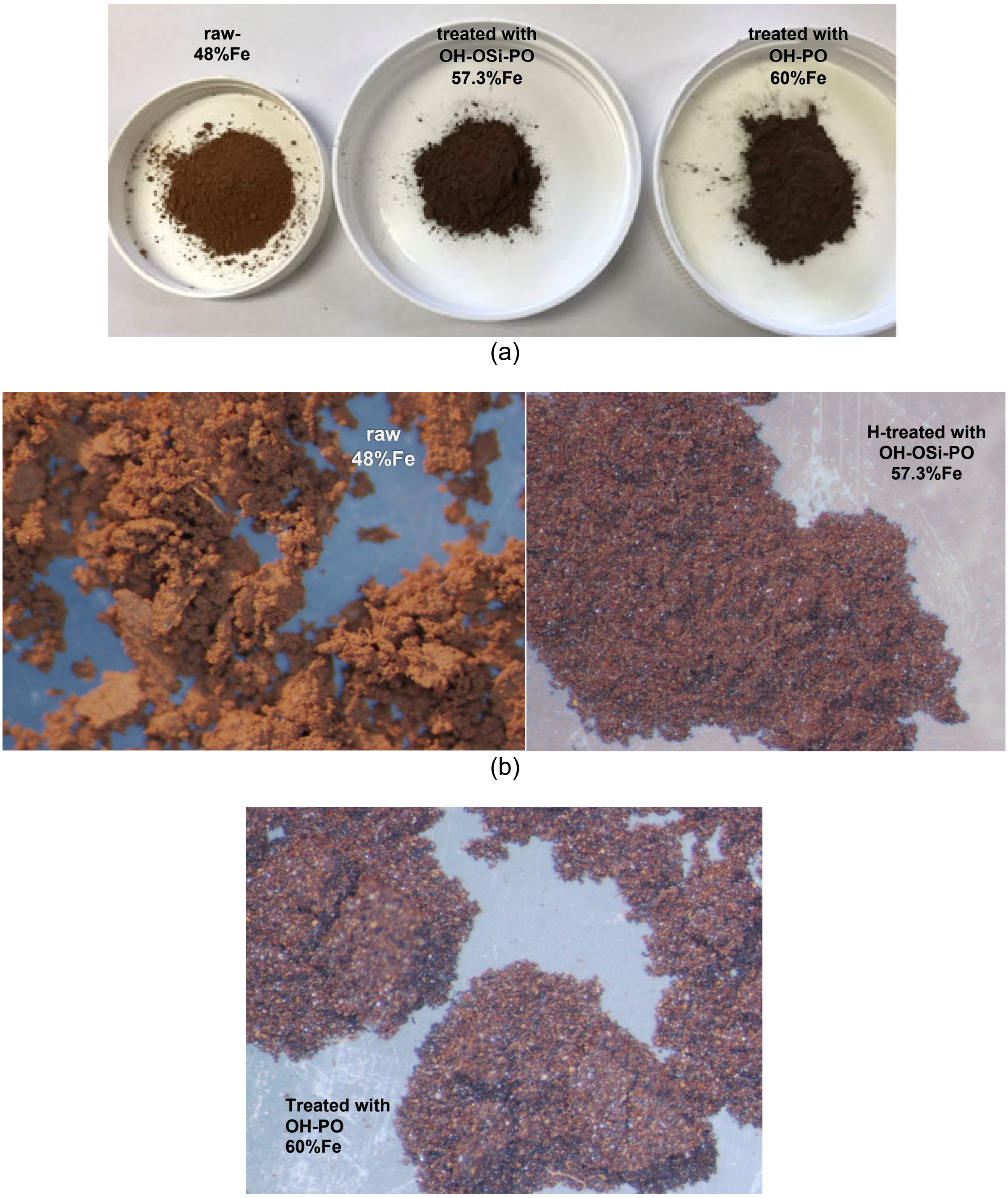

(a)

(b)

(b)

FIG 5 – (a) dried powder of raw tailings and iron rich layer; and (b) the corresponding microscopic image of these powders.

At laboratory scale it has been demonstrated that tailings can be beneficiated to produce commercial grade iron ore product. At plant scale there are several continuous processes that are more efficient that can be used to collect the iron ore particles separating them from colloidal clayey impurities such as WHIMS and classification processes. Note that up to date it has not been possible to upgrade a synthetic or model iron ore slurry with 42 per cent Fe (provided by an iron ore company) to more than 50 per cent Fe. Work is currently underway to find the cause.

CONCLUSIONS

This work has demonstrated knowhow and methods that can be exploited to beneficiate iron ore tailings and slurries at a relatively high solids loading to produce commercial grade iron ore products at laboratory scale. Iron ore tailings dam can now be assigned an economic value and be regarded as a resource. Lower quality iron ore deposits can be economically mine using the knowledge presented in this study. Phosphate-based composite additives have been shown to reduce the usage of process water significantly in iron-ore beneficiation of tailings. The deployment of processes and process strategies to minimise water use will be unavoidable for some mines located in the arid parts of The Pilbara with no appreciable source of high-quality water.

REFERENCES

Australian Water Association (AWA), 2021. Desalination. http://www.awa.asn.au/AWA_MBRR/Publications/Fact_Sheets/Desalination_Fact_Sheet.aspx

Leong, Y K, 2021. Controlling the rheology of iron ore slurries and tailings with surface chemistry for enhanced beneficiation performance and output, reduced pumping cost and safer tailings storage in dam, *Minerals Engineering*, vol 166, 106874.

Leong, Y K, Drewitt, J and Bensley, S, 2019. Reducing the viscosity of concentrated iron ore slurries with composite additives for quality upgrade, reduced power, safer tailings storage and smaller environmental footprint, in *Proceedings Iron Ore 2019: Optimising Value*, pp 738–743 (The Australasian Institute of Mining and Metallurgy: Melbourne).

Leong, Y K, 2018. *Method of Rheology Control*, Innovation Patent No: 2018100304.

Leong, Y K, 2020a. *Controlling Rheology of Iron Ore Tailings Slurries*, Innovation Patent No: 2020103937.

Leong, Y K, 2020b. *Improved Mineral Separation of Tailings*, Innovation Patent No: 2020900408.

Processing of unsaleable ultrafines to potentially reduce the volume of iron ore tailings

E Mare[1]

1. Principal Processing Engineer, Sedgman, Perth WA 6152. Email: elardus.mare@sedgman.com

ABSTRACT

Recent highly publicised incidences of disastrous containment failures, none more pertinent than the 2019 iron ore tailings dam failure in Brumadinho, have focused the world's attention squarely on the often-challenging subject of tailings storage. Unwanted ultrafines, that are deemed to be unworthy of further treatment or not to have further saleable value, are therefore a significant issue for mine owners looking to reduce risks and perceptions associated with long-term storage of tailings.

In this context, there are strong drivers to identify safer approaches to ultrafine tailings management, especially if it can also lead to increased revenue, together with better water stewardship and environmental outcomes.

The better management of tailings needs to be considered from both containment challenge and processing opportunity perspectives. This paper focuses on the latter, reviewing from a technical and economic perspective, the feasibility of more extensive processing and/or reprocessing of specifically iron ore tailings, in a bid to reduce the overall volume for management in long-term storage. Herein the opportunity lies in recovery processing, as much as enhanced thickening and/or mechanical dewatering, and therefore the paper discusses both issues as equally important sides of the same coin.

Recent interest in iron ore ultrafines processing and reprocessing studies suggests that the enhanced processing of iron ore tailings offers multiple perceived advantages. Apart from a potential reduction in tailings volume, associated with safer containment, lower environmental impact and improved water management, the prospect of increased revenue from additional Fe recovery presents supplementary motivation for iron ore players to embrace this approach, as further elaborated in this paper.

A PERSPECTIVE ON TRADITIONAL IRON ORE TAILINGS PRACTICE

With regulators, mining bodies and the public nowadays very much focused on the subject of tailings storage following highly publicised dam failures, it would be ideal if this often-challenging issue could be avoided or at least mitigated to some extent.

In the iron ore world, while DSO (direct shipping ore) operations may escape the issue of tailings storage and its associated risks, an increasing number of non-DSO operations commonly all employing wet processing, face the reality that a part of their ROM (run-of-mine) or plant feed will permanently remain on-site, traditionally as fine wet tailings that will have to satisfy geotechnical and geochemical stability needs in perpetuity.

Compared to commodities such as gold or base metals, where virtually all plant feed conventionally ends up in TSFs (tailings storage facilities), only 5–15 per cent of iron ore ROM typically end up as conventional tailings, at least in the case of non-magnetite operations. While the portion of wet tailings emanating from iron ore processing is therefore relatively small, in absolute terms tonnages can still be fairly large because of the relatively large scale of most iron ore operations. Though never reaching hundreds of kilotonnes per day as for example with large Chilean copper mines, the tailings to be stored at major iron ore mines can still equate to tens of thousands of tonnes per day.

Tailings figures for worldwide mining operations are publicly available from the GRID-Arendal (2020) Global Tailings Portal database that has been compiled since 2020. This shows that in Western Australia alone, the three largest iron ore operators declared tailings volumes for at least 26 storage facilities covering 12 Pilbara sites.

Of these 26 TSFs, 14 were declared as active across 11 sites (Table 1) and projected to keep receiving tailings at calculated average rates ranging between 500 and 20 000 m³ every day for at least five years. The calculated total projected tailings growth over the 5-year period for only these declared facilities is calculated as 60 280 m^3/d, of which the solids component in the as-disposed state is estimated to comprise between 14–20 per cent by volume, equating to roughly 28–40 kt/d dry-basis of ultrafines*.

TABLE 1

Analysis of GRID-Arendal (2020) data for active WA iron ore TSFs (lower case).

Operator/Site	TSFs	Volume (declared values) [Mm^3]	Future volume (declared values) [Mm^3]	5-year volume increase [Mm^3]	Annual volume growth [Mm^3/a]	Volume expansion (daily) [m^3/d]	Mass increase (daily) [t/d]	Solids mass increase (daily)* [t/d]
Totals:	14	196.5	306.6	110.1	22.0	60 280	79 730	27 905
FMG/Christmas Creek	1	10.9	47.1	36.2	7.2	19 822	26 218	9176
FMG/Cloudbreak	1	21.3	27.0	5.7	1.1	3121	4128	1445
FMG/Solomon	1	16.8	40.0	23.2	4.6	12 704	16 802	5881
RT/Hope Downs 4	2	4.8	8.0	3.2	0.6	1752	2318	811
RT/Marandoo	1	7.2	8.2	1.0	0.2	548	724	253
RT/Mesa J	2	31.7	46.5	14.8	3.0	8099	10 712	3749
RT/Nammuldi	1	15.4	30.0	14.6	2.9	7967	10 538	3688
RT/Paraburdoo	1	31.6	34.8	3.2	0.6	1758	2326	814
RT/Tom Price	1	21.0	23.0	2.0	0.4	1095	1448	507
RT/Yandicoogina	2	12.8	14.1	1.2	0.2	676	894	313
BHP/Whaleback	1	23.0	28.0	5.0	1.0	2738	3621	1267

* Solids at assumed density of 3.3 g/cc comprising 35–45 per cent by mass of tailings as disposed to TSFs.

Tailings volumes evidently vary appreciably from large mine to large mine, which would be reflective of ore type differences as well as different extents of existing processing. However, the author believes that at least some of the 28–40 kt/d of ultrafines currently going to TSFs in the Pilbara alone present a well-liberated source of potentially recoverable iron units that can be blended into existing fines production by application of dedicated grade-enhancement treatment.

If only 10 per cent of Western Australia's projected 28–40 kt/d of fine iron ore solids presently going to waste can be converted to product through augmented processing, this represents AU$100–140 m/a additional opportunity for the big three Pilbara producers alone per AU$100 dry tonne value. Obviously capital and operating costs and other operational impacts need to be weighed up, but the aggregate figure is large enough to at least warrant further consideration.

As will be shown later, potentially increasing revenue is only one side of the coin though. Enhanced treatment of the tailings stream also theoretically leads to other, albeit less quantifiable advantages.

While concerns about the extent of realistic tailings moisture reduction can count against the implementation of enhanced tailings processing, potentially smaller amounts of new tailings following such treatment should at least provide some incentive for trying to dewater it to a greater extent than previously untreated tailings. Less tailings mass coupled with improved dewatering thereof will greatly lessen the risks and costs associated with long-term storage through the ensuing reduction in moisture content and volume of material sent to TSFs. Filtered tailings are therefore becoming increasingly common at many mines (Davies, 2011), and even though, due to factors such as potentially restricted energy sources, operational complexity and site-specific characteristics this is not an easy decision for large operations with high tailings production rates (Watson *et al,* 2010), where it may be economical to do so, implementation of filtered tailings will at least be simplified if the amount of tailings are firstly decreased.

Importantly, the adoption of enhanced processing and ensuing options for mechanical dewatering of at least the additional concentrate stream (if not also the reduced tailings stream) would result in more responsible water stewardship through efficient water capture leading to reduced water consumption.

Different approaches to the further processing of tailings

Australia, and in particular Western Australia, is not alone in the production of huge amounts of iron ore and other tailings that occupy large areas. In Russia, for instance, it is estimated that 40 to 80 billion tons of mining-induced waste occupies more than 300 000 hectares polluting the environment (Khokhulya, Fomin and Alekseeva, 2021). This is of concern to many in the mining community especially if it is further kept in mind that these waste materials still contain valuable components that can be used in various industries.

It would be ideal if tailings could simply be reutilised in bulk, such as in the building and construction industry (Kuranchie, 2015), and while such use should be encouraged if it is truly sustainable, according to Khokhulya, Fomin and Alekseeva (2021) this type of recycling addresses less than 10 per cent of the annual generation of mining waste in Russia. Khokhulya and his co-authors therefore advocate enhanced reprocessing of these tailings resources and are of the opinion that, in the case of iron ore, the production of concentrates from previous waste has significant potential in their region for value creation as well as tailings volume reduction.

In another paper, preceding the Brumadinho episode, Dauce *et al* (2018) estimated that magnetite mines in the Quadrilátero Ferrífero mineral province that produces 65 per cent of Brazilian output, on average discharge 29 per cent of plant feed as tailings. They further state that inefficient processing leaves these tailings with grades that are often higher than those of ores now deemed exploitable. They also make the case that historic tailings represent an ideal source for retreatment, not only to enhance revenue, but also to reduce the volume of existing tailings storage.

It follows that tailings are increasingly seen not only as a problem, but in a world of dwindling resources and environmental pressure, is also regarded as an opportunity; an asset to be re-exploited. While this can be as simple as using the bulk material as is (to the extent where that may be feasible and sustainable), it is more likely that serious exploitation of tailings will require enhanced treatment to selectively extract value that has been missed prior to original deposition, or in current upstream processing.

Just like the rest of the iron ore producing world, Australian voices have also been vocal in advocating for better processing of iron ores. Viner, Research Group Leader, CSIRO, in 2017 cautioned that high-grade, valuable hematite and goethite is being lost to tailings during wet processing due to inefficient plant operation as well as inefficient resource utilisation. Maximising of iron ore units should therefore be of growing concern for producers needing to beneficiate lower grading resources in order to meet ever growing demand for Fe units.

While there are many successful examples in base metals and gold where such value re-extraction involves the remining and subsequent re-treatment of historical tailings by more efficient or modern processing, the focus of this paper is to promote the enhanced treatment of tailings, *specifically in iron ore, immediately after they have been generated*. The premise is that it is better, being less expensive and more environmentally responsible, to deal with the issue directly through downstream processing in current production, rather than after it has contributed to the ever-growing bulk of tailings storage that later needs to be disturbed for re-mining.

REFLECTIONS ON THE THEORY OF MASS AND VOLUMETRIC CORRELATIONS FOR ORE AND WATER MIXTURES

Assuming that a binary iron ore mixture such as a slurry, paste or iron ore filtration product consists as a well-saturated mixture of only water and solids particles, predictable physical relationships exist between the relative amounts of the two constituents and their respective densities whereby the overall density and other mixture derivatives can be calculated.

If the density of water is assumed to be unity or close enough to it, the relationship between solids volumetric fraction, solids mass fraction and the density of the binary mix (pulp density) can be expressed as in Equations 1 and 2 and as illustrated in Figures 1 and 2.

$$S_v\,(S_m,\ \rho_s) = 1/\rho_s/(1/\rho_s+1/S_m-1) \tag{1}$$

$$PD\,(S_m,\ \rho_s) = 1/S_m/(1/\rho_s+(1/S_m-1)) \tag{2}$$

Where:

S_v = solids fraction (by volume)

S_m = solids fraction (by mass)

ρ_s = solids density (g/cc or equivalent)

PD = pulp density (g/cc; kg/ℓ or equivalent).

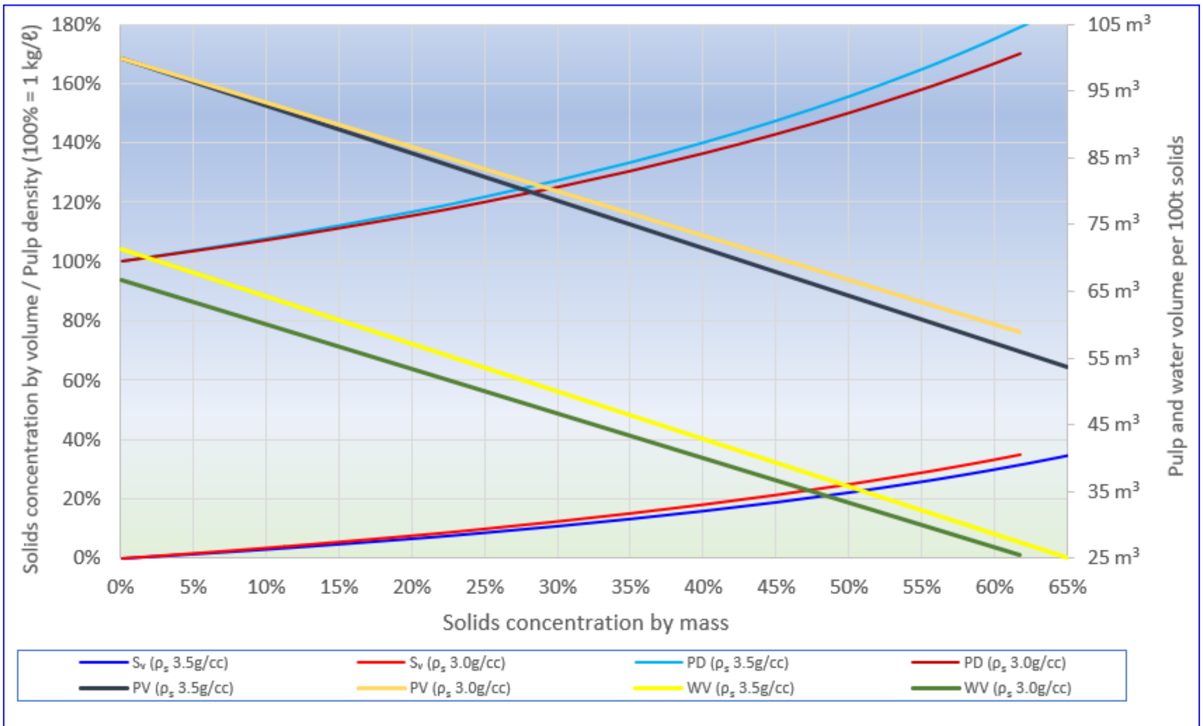

* S_v: solids concentration by volume; PD: pulp density; PV: pulp volume; WV: water volume.

FIG 1 – Mass-based solids concentration slurry dependencies and derivatives.

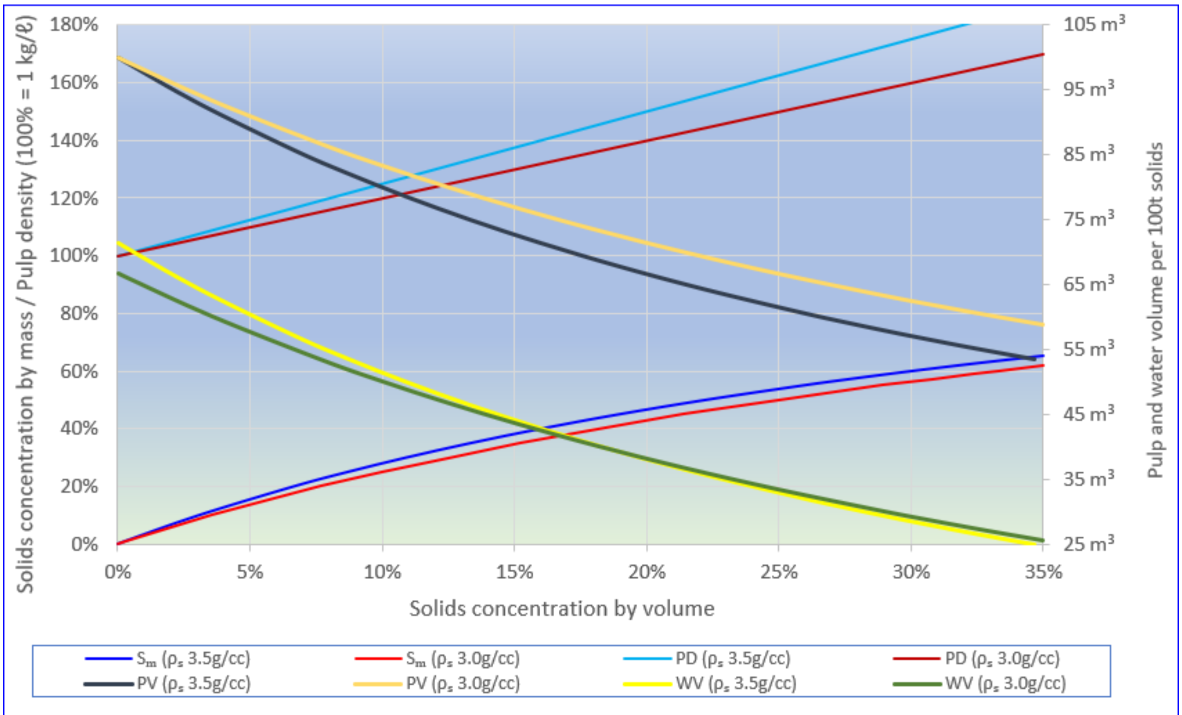

* S_m: solids concentration by mass; PD: pulp density; PV: pulp volume; WV: water volume.

FIG 2 – Volumetric solids concentration slurry dependencies and derivatives.

The dependency of pulp density on solids concentration by mass (Equation 2) is shown in Figure 1 (Figure 2 is shown alternatively as a function of volumetric solids concentration). On their right-hand axes, both graphs also show how pulp and water volumes, per arbitrary choice of 100 t of contained dry-basis solids, decrease as solids concentration of the mixture increases.

Note that Figure 2 has arbitrarily been capped at 35 per cent solids by volume, equivalent to near 65 per cent solids by mass at the two illustrative solids densities chosen for this demonstration (3.0 g/cc and 3.5 g/cc, where the latter is typical of hematite-goethite-kaolinite rich mineralogy). Capping ensures that the plotted relationships remain true, for at some point, as a slurry's solids fraction increases past the transition from pure slurry to paste to eventually 'cake', the binary relationships used here would no longer apply.

Since the density of the solids particles in a water/iron ore mixture is at least three to four times that of water, the volume of a given amount of solids in such a slurry is normally a minor fraction of the total volume even when it is may be a large fraction by mass, as is clearly evident from a comparison of the two figures.

Figure 1 handily illustrates variations that may be appropriate to typical enhanced processing and specifically how densification of the new streams, within the limits of their new particle sizing and solids densities, reduces their volumes for a given amount of contained solids.

For instance (considering the higher hypothetical solids density example here), it can help show that an arbitrary 10 per cent (absolute) increase in solids concentration from say 25 per cent (w/w) to 35 per cent (w/w) increases pulp density by 10 per cent and decreases volume by 9 per cent, while a change from 35 (w/w) to 45 per cent (w/w) increases pulp density by 11 per cent and decreases volume by 10 per cent. The trend for ever decreasing volume is confirmed for the next step change: From 45 per cent (w/w) to 55 per cent (w/w), pulp density would increase by 12 per cent and volume would decrease by 11 per cent.

Importantly, when the binary relationship starts breaking, it can be expected that the slope of the pulp density curve will start to flatten gradually until it plateaus to a bulk density lower than the theoretical solids density. The pulp density and volume changes for a 65 per cent (w/w) to 75 per cent (w/w) step may therefore be less than the 13 per cent and -12 per cent respectively of a 55 per cent (w/w) to 65 per cent (w/w) densification step. Regardless, the graphical presentation conveniently confirms the tendency for volume reduction against increasing solids concentration.

Since equal steps of change in absolute mass concentration equate to identical volumes of water (for instance every 10 per cent (absolute) solids concentration difference equalling a constant difference of 7 m^3 of water in the higher solids density case above), it follows that the percentage of water removed rises as solids concentration increases: From 25 per cent (w/w) to 35 per cent (w/w), 13 per cent of water is removed, while the same metric measures 22 per cent water reduction for changing from 55 per cent (w/w) to 65 per cent (w/w) solids. The increased percentage of water removal hints at potentially increasing difficulty of water removal as the pulp gets thicker.

EVALUATION FROM METALLURGICAL VIEWPOINT

Illustrating the potential outcome for enhanced iron ore tailings treatment

Whilst the potential for enhanced treatment is specific to each operation, a general study of the potential impact of additional tailings processing is possible taking into account a range of outcomes from published papers and case studies. To this effect, credible tailings investigations would involve representative samples appropriately sourced from existing operations and tested sufficiently to assess upgrading as well as subsequent dewatering potential.

Enhanced tailings treatment and/or retreatment to produce saleable concentrates is a popular subject in publications, and those referenced by this paper show that the production of at least blendable Fe grade from previously non-blendable quality, is generally a strong technical possibility.

Depending on the ore type and the grades involved (especially target grade), enhanced tailings processing and reprocessing concepts range from elementary desliming to complex processes involving desliming/gravity/magnetic circuits sometimes requiring intermediate further comminution.

For the purposes of this paper, which is to discuss and graphically conceptualise the bigger picture rather than delve into a discussion of detailed process technology, it is adequate to focus on high-level parameters only: yield (Y), Fe recovery (R_{Fe}) and Fe upgrade factor (UF_{Fe}).

For the upgrading of typical iron ore tailings with P95s lower than 50–100 µm, the author's experience is that for an uncomplicated process deliberately not involving further comminution, Fe recovery estimates of 20–40 per cent are plausible. For example, recoveries achieved by others referenced here to achieve saleable grades, were as follows:

- Dauce *et al* (2018): 64 per cent Fe recovery from 30 per cent Fe tailings.
- Khokhulya, Fomin and Alekseeva (2021): 76 per cent Fe recovery from 19 per cent Fe tailings.
- Murthy and Basavaraj (2012): 79 per cent Fe recovery from 49 per cent Fe tailings.
- Nematollahi (2011): 39 per cent Fe recovery from 33 per cent Fe tailings.
- Tang *et al* (2019): 79 per cent Fe recovery from 13 per cent Fe tailings.

Illustrative simulations that hypothetically assume Fe recovery of 30 per cent at 25 per cent yield are explored below. In the author's view, the implied 1.2 Fe upgrade factor for such a plausible combination would be adequate for the upgrading of many sources of iron ore tailings to at least blendable product grade.

The simulated outcomes for such a case (per 100 t/h of contained solids as an arbitrary starting quantity) are here conveniently illustrated by three simple block flow diagrams that demonstrate related mass and volume flow rates, high-level metallurgical derivatives, and pulp and solids characteristics. *To better illustrate the upgrading progression, Fe grades are shown in relative instead of absolute terms*.

Explanatory notes on assumptions and calculations used for simulated output

The zero redundancy simulations here presented stem overwhelmingly from long-term iron ore experience and pure metallurgical balancing. Some untested assumptions (tailings consolidation performance) are used as explained.

Fe grades

Conventional thickened tailings grade: With absolute Fe grades substituted by relative grades, the feed Fe grade is simply fixed as 100 per cent relative anchoring grade.

Concentrate grade: Calculated relative grade based on enhanced processing upgrade factor.

Consolidated tailings grade: Calculated relative grade based on metallurgical balance.

Solids density/SG

Hypothetical 3.5 g/cc used to calculate feed pulp volume.

Solids concentrations

Conventional thickened tailings: Hypothetical 40 per cent (w/w) solids.

Wet concentrate: Hypothetical 50 per cent (w/w) solids. (Whether achieved with or without thickening is irrelevant to this discussion)

Wet secondary tailings: Hypothetical 10 per cent (w/w) solids.

Thickened secondary tailings: Solids % (w/w) set equal to Conventional thickened tailings in the interest of equal comparison (Ignoring potential for better performance of new thickening operation).

Dry secondary tailings as alternative to Thickened secondary tailings: Hypothetical 75 per cent (w/w) solids.

Blendable concentrate: Hypothetical 85 per cent (w/w) solids.

Consolidated tailings: Hypothetical 90 per cent (w/w) solids assumed after long-term settling.

Process performance derivatives

Yield and upgrade factors: Hypothetical combination via hypothetical 30 per cent Fe recovery as explained.

Solids mass

Conventional thickened tailings solids: Arbitrary 100 t/h contained solids as anchor for simulations.

Simulations

Existing wet processing iron ore operations normally already employ conventional thickening similar to what is detailed by the starting block (LHS centre) in Figure 3 and the other two simulations below. The role of existing thickeners does not disappear when downstream tailings treatment is added to an existing site. In the first-place existing thickeners will still provide immediate capture and clarification of excess upstream process water and in the second place they will offer storage and buffering for stabilisation and optimisation of the new downstream tailings treatment process.

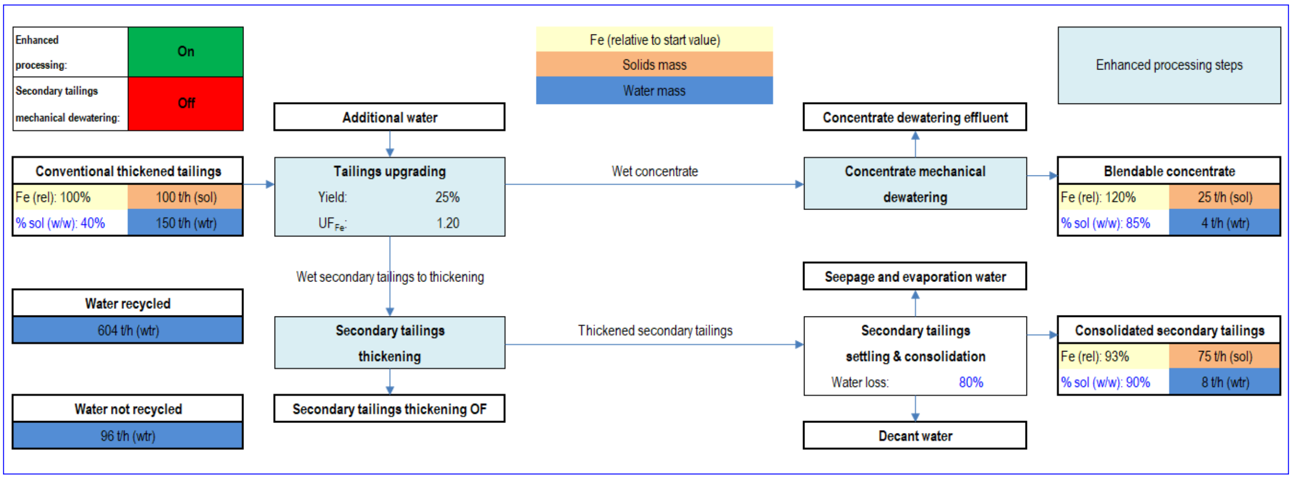

FIG 3 – Enhanced tailings processing with thickening of secondary tailings.

However, when considering the overall process, enhanced tailings treatment is bound to have a positive effect on overall water consumption, primarily due to the superior water capture of mechanical dewatering of the newly created wet concentrate as well as potentially denser secondary thickening underflow from a smaller and likely more modern secondary thickening circuit. *Note, however, that in this analysis, in the interest of an even comparison, secondary thickener underflow density has been left equal to that of primary thickener underflow*.

To fully appreciate the value of enhanced treatment, it is handy to compare it to the case where it does not exist. This is simulated below where enhanced treatment and related dewatering processes have simply been switched off. The process shown in Figure 3 reduces to the simpler one shown in Figure 4 where the conventional tailings simply continue unchanged to the TSF for normal consolidation and final water capture by TSF decanting.

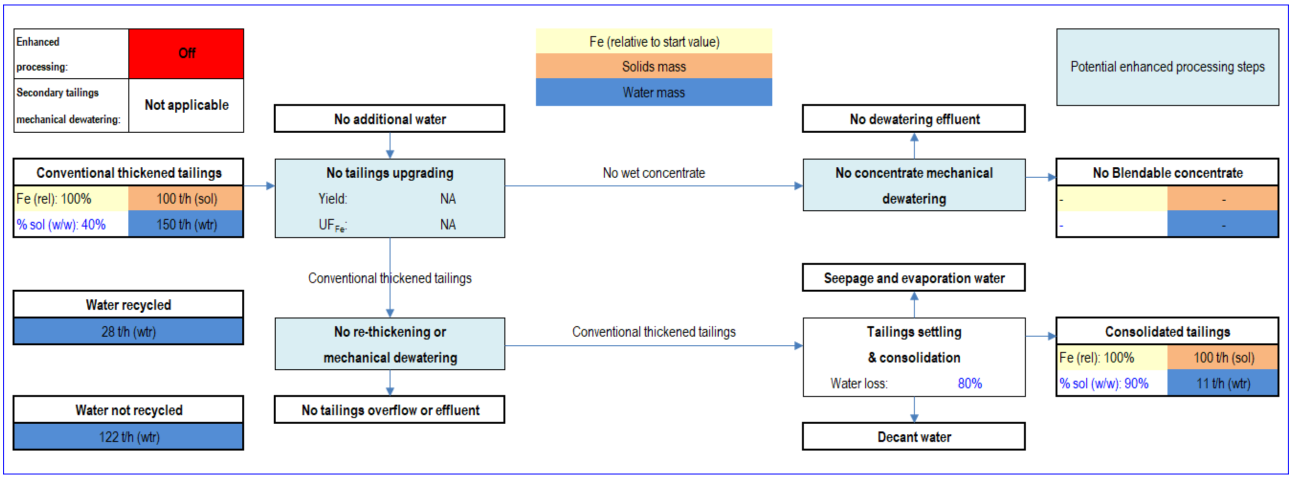

FIG 4 – Typical tailings disposal and consolidation (no enhanced processing).

Selected differences in outcomes between enhanced tailings treatment or not, is summarised in Table 2.

TABLE 2

Comparison of enhanced tailings processing to conventional practice.

Tailings processing	Description	TSF or effective process feed	Secondary tailings to TSF	Consolidated final tailings	Blendable concentrate	Water not recycled
Off	Solids (tph)	100	100	100	NA	
	Water (m³/h)	150	150	11	NA	122
	Pulp (m³/h)	179	183	NA	NA	
On	Solids (tph)	100	75	75	25	
	Water (m³/h)	700	113	8	4	96
	Pulp (m³/h)	729	138	NA	NA	
On v Off	*Solids (tph)*	*- -*	*-25 -25%*	*-25 -25%*	*+25 -*	
	Water (m³/h)	*+550 +367%*	*-37 -25%*	*-3 -25%*	*+4 -*	*-26 -21%*
	Pulp (m³/h)	*+550 +308%*	*-45 -25%*	*NA*	*NA -*	

The main outcome of processing in the illustrated case is obviously the fact that a hypothetical 25 per cent of previously discarded tailings is turned into saleable/blendable concentrate based here solely on increased Fe grade. Not to be overlooked though is the fact that removal of such a mass from the ensuing new tailings also results in a reduction in tailings volume sent to the TSF for potential reduction in consolidated final tailings volume. Further, the fact that less tailings is sent to the TSF, where the loss of water due to seepage and evaporation is normally very high, coupled with the highly efficient water recovery from the concentrate dewatering, results in water saving, conservatively estimated at up to 21 per cent in this illustration.

Apart from tailings storage dam growth and associated long-term geotechnical stability issues, water stewardship in the mining industry is another important sustainability issue that is receiving an increasing amount of public scrutiny. Consequently, enhanced tailings processing does not have to limit itself to efficient mechanical dewatering of only the newly created concentrate.

Figure 5 therefore presents a case for mechanical dewatering of secondary tailings similar to that for newly created concentrate. Not only does this result in even further water saving, but tailings so produced could lend themselves to dry stacking should dammed wet tailings no longer be feasible or deemed desirable.

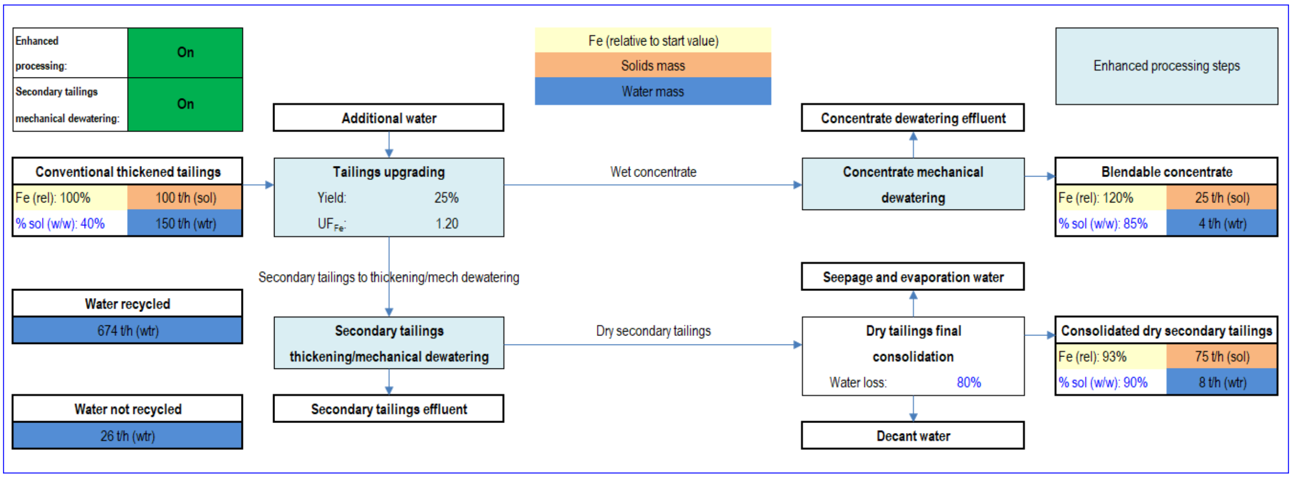

FIG 5 – Enhanced processing including mechanically dried tailings stacking.

Table 3 summarises the further advantages to be achieved with adoption of the ultimate scheme presented in Figure 5 versus the lesser scheme presented in Figure 3.

TABLE 3

Secondary tailings mechanical dewatering/stacking versus regular practice.

Tailings processing	Wet secondary tailings mech dewatering	Description	Secondary tailings to TSF		Recycled water		Water not recycled	
On	Off	Water (m³/h)	113		604		96	
		Pulp (m³/h)	138					
On	On	Water (m³/h)	25		674		26	
		Pulp (m³/h)	50					
On-On v On-Off		*Water (m³/h)*	*-88*	*(-78%)*	*+70*	*(+12%)*	*-70*	*(-73%)*
		Pulp (m³/h)	*-88*	*(-64%)*				

The worth of extending mechanical dewatering to the secondary tailings is mostly evident by the volume of the now stackable tailings being a hypothetical 64 per cent less than the equivalent thickened – only tailings volume. Recycled water has also increased by 12 per cent to reduce water losses by 73 per cent.

Case study – potential iron recovery from Olcon Mine tailings

In a recent paper by Khokhulya, Fomin and Alekseeva (2021), they made a similar well-researched case as discussed above to treat 19 per cent Fe magnetite-hematite historic tailings from Olcon Mine in the Russian Arctic.

A rather elaborate magnetic/gravity process is recommended, requiring additional liberation in the form of two stages of milling. This high-cost processing resulted in the 19 per cent Fe tailings returning 66 per cent Fe product at a yield of 22 per cent (Fe recovery roughly 76 per cent).

Khokhulya, Fomin and Alekseeva (2021) proposes the reprocessing not only for potential additional revenue, but also for the fact that a portion of existing TSFs would be reclaimed, improving the environmental situation in the area.

The author of this paper would rather see the same process also added downstream to the existing Olcon plant to prevent sending the 22 per cent of unnecessary mass to tailings storage in the first place.

Case study – reprocessing tailings into reduced Fe-powder as well as high silica cement block making residue

The reprocessing of iron ore concentrate tailings where both the new concentrate and the new tailings find useful application, is a compelling notion investigated in a 2019 paper (Tang *et al*, 2019).

Tang *et al* (2019) calculate that potentially 750 Mt of metallic iron is lost during the disposal of iron ore tailings containing approximately 8–12 per cent Fe on average from the concentrate production plants of Chinese iron ore mines.

According to Tang *et al* (2019), iron ore tailings utilisation can be divided into two main categories, namely iron recovery and the use of tailings as raw materials.

However, traditional iron recovery reprocessing involving gravimetric, magnetic and flotation techniques, create new waste streams when iron recovery is the only outcome and therefore Tang *et al* (2019) still deem them inefficient for the growing tailings problem in China. Likewise, they caution that re-utilisation of non-reprocessed tailings for making products such as ceramic tiles, engineered cementitious composites, tailings filled polypropylene cement, epoxy composites and underground backfill mining materials, are also inefficient as large amounts of iron resources within the utilised tailings are not recovered.

Consequently, the Tang *et al* (2019) paper demonstrates an innovation called '*pre-concentration followed by direct reduction and magnetic separation*' for the complete re-utilisation of low Fe Chinese iron ore tailings. Admittedly, the process is complex, and it is possibly too expensive for widespread adoption as it involves initial two-stage magnetic separation pre-concentration followed by roasting and another magnetic separation step.

However, all three final outputs (high Fe reduced powder, raw cement 'meal' and high silica powder) are each fully usable in their own right. This paper showcases the kind of 'circular economy' thinking that focuses not only on producing secondary iron ore concentrates, but even complete reuse of tailings to achieve a dramatic reduction of the iron ore tailings storage problem.

The yields and Fe recoveries relating to Tang *et al's* (2019) high Fe reduced powder stream is shown in Table 4.

TABLE 4

Grades and derivatives for treating low Fe Chinese iron ore tailings.

	Pre-concentration	Roasting + magsep	Overall
Fe (process input)	12.61%	36.6%	12.6%
Fe (process output)	36.58%	92.30%	92.3%
R_{Fe}	83.86%	93.96%	79%
UF_{Fe} (calculated)	2.90	2.52	7.32
Yield (calculated)	29%	37%	11%

Case study – reprocessing of tailings of Chador-Malu iron ore, Iran

The Chador-Malu iron ore mine in Iran has been producing hematite-magnetite concentrate for domestic direct reduction consumption since 1997. By 2011, at a yield of 63 per cent and Fe recovery of 79 per cent, 73 Mt of ROM processed at the mine over the 12-year period from 1999, had resulted in 27 Mt of stored tailings (P95 ≈ 40 µm).

With a view of exploiting this material for its inherent value, Nematollahi (2011) from the University of Tehran carried out research on reprocessing of the tailings. With a regrinding and desliming process followed by high gradient magnetic separation and flotation, Nematollahi showed that a low phosphorous concentrate of over 63 per cent Fe could be produced out of this resource at yield and Fe recovery of respectively 21 per cent and 39 per cent as shown in Table 5.

TABLE 5

Reprocessing scheme for Chador-Malu iron ore tailings.

Description	Yield	Tailings attribution	Fe (%)	UF_{Fe}	R_{Fe}
Feed (remined tailings)	**100%**		**33.5**		**100%**
Conc	21%		63.3	1.89	39%
Tailings	79%		25.8	0.77	61%
Desliming overflow	40%	50%			
HGMS non-mags	32%	41%			
Flotation reject	7%	9%			

Like the primary concentrate, the new concentrate would be dewatered by a combination of thickening and filtration. In this case the new secondary tailings would simply be redirected to the TSF, though with 21 per cent of the mass and 39 per cent of the iron units removed.

Case study – generating saleable iron ore Fines through in-line enhanced tailings processing at Sesa-Codli mine in India

In an internal case study report, Mazumdar, Raghavendra and Naik (2021) from Vedanta's Goa operations, describe in-line enhanced tailings processing with the objective of increasing overall plant yield, reduce Fe grade sent to tailings storage and minimise tailings volumes due to the high cost of land and environmental factors.

The most optimal process in their case proved to be magnetic separation, with both MIMS and WHIMS added to -45 µm tailings that had first been through three stages of hydrocyclone desliming.

The additional processing recovers 13 per cent by mass of the deslimed tailings as additional product. The thickened and ceramic filtered additional fines helps increase overall plant yield from 77 per cent to 81 per cent, implying a 5 per cent reduction in overall tailings mass.

Case study – iron recovery from low-grade Australian iron ore fines by up current teeter bed separator

Murthy and Basavaraj (2012), both of CSIRO, in 2012 reported on their objective for producing high-quality iron ore material suitable as sinter feed, from waste material. To this effect, they were successful in upgrading typical -1 mm Pilbara tailings using a Floatex Density Separator (FDS). From a tailings feed measuring 48.7 per cent Fe, their experimental campaign produced a concentrate of 56.9 per cent Fe (1.17 UF_{Fe}). The yield in this case was 67.6 per cent (R_{Fe} therefore 79 per cent), indicating potentially robust upgrading economy.

The two researchers did not elaborate on potential dewatering of their new tailings. Although obviously finer and consisting of lower density solids than the feed source due to both classification and density enhancement brought about by the FDS, the fact that the new tailings was now only about one third of the original dry-basis mass, would be of great importance to further dewatering or just direct storage, whether still in relatively dilute state or an enhanced dewatered state.

STRENGTHS AND WEAKNESSES OF ENHANCED TAILINGS TREATMENT

One of the strengths in favour of further tailings treatment is the fineness indicating a generally good degree of liberation, but the fine sizing may also be its weakness. Though specific particle sizing depends on unique choices made in traditional processing, conventional iron ore tailings typically have an absolute top size in the region of 1 mm but are often heavily skewed towards particles smaller than 50 µm. Whereas such fineness and associated ready liberation may fortuitously avoid the need for expensive further comminution, the downside of it relates to the intended use of the fines product into which it would normally be blended.

Iron ore fines for sintering are namely sold under agreements that set out to manage the level of ultrafines and limits on the amount of sub 150 µm material are normally specified. Even though the 150 µm limits are typically quite generous with most sinter fines seldom in danger of exceeding it, adding more material that will usually be much smaller than the 150 µm contracted size, may therefore seem unwise. However, similar to chemical grade that may only be borderline adequate, this issue as well as a potential increase in product moisture brought about by the increasing fineness, may well prove to simply be commercial decisions to be settled by legitimate quality penalties or price reductions that could be less onerous than the added worth.

Commercial and technical marketers thus are to be brought into operational decisions such as enhanced tailings treatment that can alter qualitative outcomes, whether chemical or physical. However, assuming that the altered characteristics hurdle is not insurmountable, increased production from enhanced tailings processing represents tangible revenue-enhancing potential.

Lower tailings volume and potential lower tailings moisture, with related water savings advantages, present another opportunity in favour of enhanced processing. Tailings storage guardians thus also need to be involved with tailings processing decisions that could significantly affect tailings management. Here, it will be especially important to realise that new tailings, after preferential extraction of higher grading particles, will most likely be finer and less dense at a particle level, than the original tailings material.

The potential effect on thickening, settling and consolidation from new tailings' finer particle sizing is to be balanced against the advantage of lower volume, especially by metallurgists wishing to increase liberation. Apart from potentially prohibitive cost, this is a major reason that the author does not recommend further comminution of the primary tailings prior to further processing.

While it is easy to just focus on potential storage advantages, long-term geochemical stability is of equal importance to long-term geotechnical stability. Enhanced tailings decisions therefore require acknowledgement and understanding of potential mineralogical changes, especially if sulfides like pyrite were already present in the conventional tailings. It also needs to be understood what effect different particle sizing and/or moisture conditions can have on the potential for acid rock drainage. The full suite of ARD-testing should therefore be conducted alongside initial metallurgical testing to ensure that potential geochemical instability does not constitute a fatal weakness.

Finally, no new processing can be implemented without capital outlay and increased operational cost. An assessment of economic feasibility will therefore feature as important as the technical feasibility evaluation with the perceived internal rate of return being the ultimate decider.

A summary of the concluding remarks is presented by a SWOT-analysis as in Table 6.

TABLE 6

SWOT analysis of potential enhanced tailings processing.

Strengths	Weaknesses	Opportunities	Threats
• Tailings represent a readily available ore resource, especially if treated directly in-line. • Comminution likely not required as tailings are potentially well liberated. • Reduced mass of tailings solids and water dictating less tailings storage volume. • More immediate and efficient water capture from concentrate and new tailings leading to water savings and lower overall pumping cost.	• High ultrafines component and possible low Fe grade potentially reducing the grade of sinter fines after blending resulting in possible lower pricing and/or penalties. • Increased overall processing complexity. • Potential risk of materials handling issues on conveyors with blending of high moisture filtered concentrate into saleable ore. • Potential risk of materials handling issues on conveyors and/or trucks upon disposal of high moisture filtered tailings to tailings stockpile.	• Opportunity for increased saleable production and revenue from new concentrate generated from previous wasted tailings. • Opportunity for thickening technology improvement at decreased tailings volumes. • Opportunity for streamlining overall tailings storage activities due to decreased and/or thicker tailings volumes as well as steadier, less intermittent operations following from primary as well as secondary buffering. • Opportunity to mix filtered tailings with mine waste, creating single waste landform rather than separate waste/tailings storage, therefore decreasing rehabilitation cost. • Opportunity to enhance public perceptions of mining by demonstrating commitment to sustainability in terms of recycling, increased employment opportunities and better water stewardship.	• Capex for installation of concentrate mechanical dewatering/materials handling may be too high, without which enhanced processing cannot proceed. • Higher opex compared to conventional tailings processing may make process uneconomical. • Secondary tailings achieving lower thickening and final settling density due to increased fineness and lower solids SG cancelling the effect of lower solids mass. • Increase in contaminant levels and ultrafines rendering blended sinter fines unattractive to the market.

CONCLUSION

Participants in the iron and steelmaking chain are ultimately forced, in the first place by commercial realities but also progressively by sustainability considerations, to optimise their role in this space and in this regard, the beneficiation of iron ore at its source plays an increasingly important part.

The seeming downside of market-driven beneficiation and then having to deal with tailings at the mine site, diminishes from both economical and global environmental perspectives when compared to expensive and environmentally irresponsible downstream pyrometallurgical removal of deleterious material during ironmaking.

However, iron ore tailings that are not necessarily fully exploited for all that it can offer, is equally irresponsible from a resources perspective and probably also less than optimal when viewed from a local economic viewpoint.

Fortunately, iron ore producers are compensated in effective higher iron ore pricing as well as reduced logistic cost for having to put up with tailings and could therefore embrace the further opportunity to ensure proper extraction of all value from their ore while simultaneously minimising their waste to the furthest extent optimally possible.

This paper, like many others on the same subject, proposes that more can and should be done in this regard and that the endeavour may well make sound economic sense while at the same time addressing storage safety and other negative tailings connotations. Mine operators that give enhanced tailings processing further consideration, will find that technologies, especially those associated with dewatering of fine concentrates and wastes are continuously evolving and have become more affordable than last decade or last year. Those that act before being forced to do so by negative circumstances and/or public opinion may indeed find the exercise very rewarding.

ACKNOWLEDGEMENTS

The author thanks Sedgman and parent company CIMIC for the opportunity to publish this paper, but also wishes to acknowledge the input and feedback of colleagues Jenny Agnew, Tina Kavanaugh, Dale Hoffmann, William Potter, Steve van Barneveld and especially Trish Gerrans.

REFERENCES

Dauce, P D, de Castro, G B, Lima, M M F and Lima, R M F, 2018. Characterisation and magnetic concentration of an iron ore tailings, *Journal of Materials Research and Technology 2019,* 8(1):1052–1059.

Davies, M, 2011. Filtered Dry Stacked Tailings – The Fundamentals, in *Proceedings Tailings and Mine Waste 2011*.

GRID-Arendal, 2020. Global Tailings Portal database, [online]. Available from: <dashboard-tailing storage facility> [Accessed: 12 April 2021].

Khokhulya, M, Fomin, A and Alekseeva, S, 2021. Recovery of magnetite-hematite concentrate from iron ore tailings, in *E3S Web of Conferences* 247, 01042 (2021)

Kuranchie, F A, 2015. Characterisation and applications of iron ore tailings in building and construction projects. Available from <https://ro.ecu.edu.au/theses/1623> [Accessed: 29 April 2021].

Mazumdar, S, Raghavendra, M and Naik, S, 2021. Innovative Technique to generate saleable Iron Ore Fines from beneficiation plant Tailings. Available from <https://sesagoaironore.com> [Accessed: 15 May 2021].

Murthy, N and Basavaraj, K, 2012. Assessing the performance of a Floatex density separator for the recovery of iron from low-grade Australian iron ore fines – a case study, in *Proceedings of XXVI International mineral processing congress (IMPC)* / New Delhi, 24–28 September 2012.

Nematollahi, H, 2011. Reprocessing of Iranian iron ore tailings, in *Proceedings Tailings and Mine Waste'10*, pp 335–338 (Taylor & Francis Group, London).

Tang, C, Li, K, Ni, W and Fan, D, 2019. Recovering iron from iron ore tailings and preparing concrete composite admixtures, [online]. Available from <https://www.mdpi.com/journal/minerals> [Accessed: 5 May 2021].

Watson, A H, Corser, P G, Garces Pardo, E E, Lopez Christian, T E and Vandekeybus, J, 2010. A comparison of alternative tailings disposal methods — the promises and realities, in *Proceedings Mine Waste 2010*, pp 499–514 (Australian Centre for Geomechanics: Perth).

Technical marketing

Penetration behaviour of an initial sinter melt into substrates of different ore types

H Han[1], L Lu[2] and S Hapugoda[3]

1. Research Scientist, CSIRO Mineral Resources, Technology Court, Pullenvale Qld 4069. Email: hongliang.han@csiro.au
2. Senior Principal Research Scientist, CSIRO Mineral Resources, Technology Court, Pullenvale Qld 4069. Email: liming.lu@csiro.au
3. Experiment Scientist, CSIRO Mineral Resources, Technology Court, Pullenvale Qld 4069. Email: sarath.hapugoda@csiro.au

ABSTRACT

Sinter quality depends heavily on the mineral phases, textures and physical structure of the sinter, which are formed upon solidification of the sinter melt. The interaction of sinter initial melt with its surrounding materials will impact the properties of the sinter melt and consequently the solidified structure and quality of resultant sinter. Spreading and penetration are two important phenomena dictating the interaction of the initial melt with its surrounding materials, such as nuclei and adhering fines. In the present study, the penetration behaviour of an initial melt into various natural iron ore substrates of different ore types during sintering was studied using a laboratory scale penetration testing procedure. The penetration depth and width were found to increase with temperature and vary with the type of iron ore due to their unique pore structure and mineralogical texture.

INTRODUCTION

Iron ore sinter is a major component of blast furnace feed in Asian ironmaking plants and as a result, sinter quality directly influences the performance of their blast furnaces. Sinter quality depends heavily on the mineral phases, textures and physical structure of the sinter, which are formed upon solidification of the sinter melt. The sinter melt is formed through the interaction of sinter initial melt with its surrounding materials (Ma *et al*, 2013). Hence spreading and penetration phenomena of the initial melt around/into nucleus particles will impact the properties of the sinter melt and consequently the solidified structure and quality of resultant sinter.

Penetration behaviour of different adhering fines into nucleus particles has been widely investigated. Most past research used a method involving two pressed powder tablets (Nakashima *et al*, 2004; Yoshimura *et al*, 2009; Jeon, Kim and Jung, 2015; Wu and Zhang, 2015; Liu *et al*, 2016). The bottom tablet is made to simulate nucleus particles, while the top tablet is pressed from a mixture of adhering iron ore fines and fluxes etc to simulate the initial sinter melt. When the assembly is fired under a sintering heating profile, the initial sinter melt formed from the top tablet is expected to spread on and penetrate into the bottom tablet. The assembly is then sectioned and polished for examining under an optical microscope the penetration ability of the initial sinter melt in terms of width and depth of penetration. However, it is very hard to use the pressed powder method to simulate the mineralogy and porosity of the nucleus particles. Therefore, similar observations were sometimes obtained when the iron ores of interest had similar chemical composition. To overcome this, some researchers used raw or natural nucleus particles which were either coated by (Hida and Nosaka, 2007) or embedded in adhering fines (Debrincat, Loo and Hutchens, 2004; Hida and Nosaka, 2007; Ware and Manuel, 2016; Han *et al*, 2019) to evaluate the penetration ability of initial sinter melt into nucleus particles. However, due to the wide variability in mineralogy and chemistry of the nucleus particles present even in the same ore, extensive tests are often required to obtain meaningful and consistent results.

In addition, with the rapid development of the steel industry, the iron ore reserves of good quality have been depleting quickly all over the world in recent years. As a result, lower quality iron ores with high contents of gangue and combined water have been or are being developed to meet the market demand, and as low cost raw materials, are gradually becoming the main feedstocks in some iron and steel companies. However, the chemical composition, mineral composition and pore structure of these iron ores are extremely complex and very different from those of the traditional iron ores. Hence understanding of the penetration behaviour of these iron ores is urgently needed.

In this paper, natural iron ore substrates were prepared to evaluate the penetration ability of initial melt into different types of nucleus particles. Then the factors affecting penetration behaviour are subsequently discussed.

EXPERIMENTAL

Raw materials

In the present study, the -0.15 mm fraction screened from a typical Australia iron ore was fluxed by a limestone powder (-0.15 mm) to specific CaO content as adhering fines. The chemical composition of the -0.15 mm iron ore and limestone powders are shown in Table 1.

Different types of iron ore, such as dense hematite iron ore, siliceous hematite iron ore, porous hematite iron ore, goethite iron ore, laminated goethitic iron ore (BID hematite with goethite infill) etc, were selected to prepare substrates in the present study. As the ores were sourced from different geological formations, hence they had different chemical compositions and mineralogical characteristics.

TABLE 1

Chemical composition of iron ore and limestone powders (-0.15 mm).

Sample	Fe	SiO_2	Al_2O_3	CaO	MgO	LOI1000
Iron ore	61.39	3.94	2.37	0.05	0.10	4.91
Limestone	Nil	0.92	0.33	54.82	0.40	43.10

Experimental methods

To simulate the penetration behaviour of the initial melt formed from the fines within the adhering layer of pseudo-particles, a sample assembly consisting of a pressed powder tablet of initial melt materials and a natural iron ore substrate was used. Figure 1 shows a schematic diagram of the experiment assembly for penetration test. A mixture of the -0.15 mm iron ore and limestone powders with CaO content of 20 per cent (according to the chemical composition of adhering fines in sinter mixture) was prepared as an initial melt source and pressed into cylindrical tablets of 6 mm diameter and 5 mm height under a pressure of 800N. Large particles of different ore types were selected from drilled core samples and pre-cut into substrates with a dimension of approximately 20 × 20 × 5 mm.

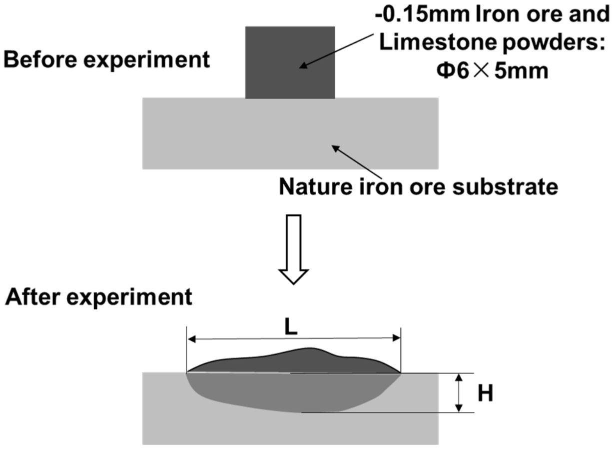

FIG 1 – Schematic diagram of the experimental assembly.

The sample assembly was placed on a Ni foil and loaded onto a sample holder which was positioned at the cold zone of a horizontal heating furnace. During the experiment, the assembly was loaded in an air atmosphere step by step into the hot zone of the furnace to simulate the sintering thermal profile required. The sample assembly was heated from room temperature to 400°C in 1 minute, from 400°C to 850°C in 1 minute, and from 850°C to a specific set temperature (1240°C, 1280°C, 1320°C and 1360°C) in 1 minute. The assembly was then held at the set temperature for 4 minutes before being removed from the furnace and cooled down to room temperature in air. After the experiment, the sample assembly was dissected perpendicularly, mounted in epoxy resin and polished to 1 µm to reveal the melt-substrate interface. Representative cross-sectional images of the interface were then obtained using an optical microscope for determining the length (L) and width (H) of penetration.

During the sintering process, the initial melt first forms within the adhering layer of pseudo-particles, and then spreads out through the adhering layer to react with surrounding adhering fines and nucleus particles to generate the primary sinter melt. These phenomena during sintering can be evaluated by the width and depth of penetration. Larger H values typically correspond to a higher penetration ability.

RESULTS

Penetration behaviour of initial melt into various natural iron ore substrates

The cross-sectional images of the assemblies with various natural iron ore substrates after the penetration experiments at 1280°C are shown in Figure 2. The adhering fines in these experiments comprised 80 per cent iron ore and 20 per cent CaO. As shown in Figure 2, the final shape of the top initial melt tablets was largely influenced by the ore type of substrates. When dense and siliceous hematite substrates were used, the initial melt tablet lost its initial shape and spread widely across the surface of the substrates. On the other hand, the initial melt tablet tended to hold many large pores and maintain its initial shape on the goethite substrate. The final shape and pore structure of the initial melt tablets on the porous hematite and laminated goethite substrates was intermediate between these substrates. In addition, it was clearly shown that the penetration area of melt in the substrates, as marked by the red line, was considerably larger for the goethite and porous hematite iron ore substrates than that for the dense hematite and siliceous hematite iron ore substrates.

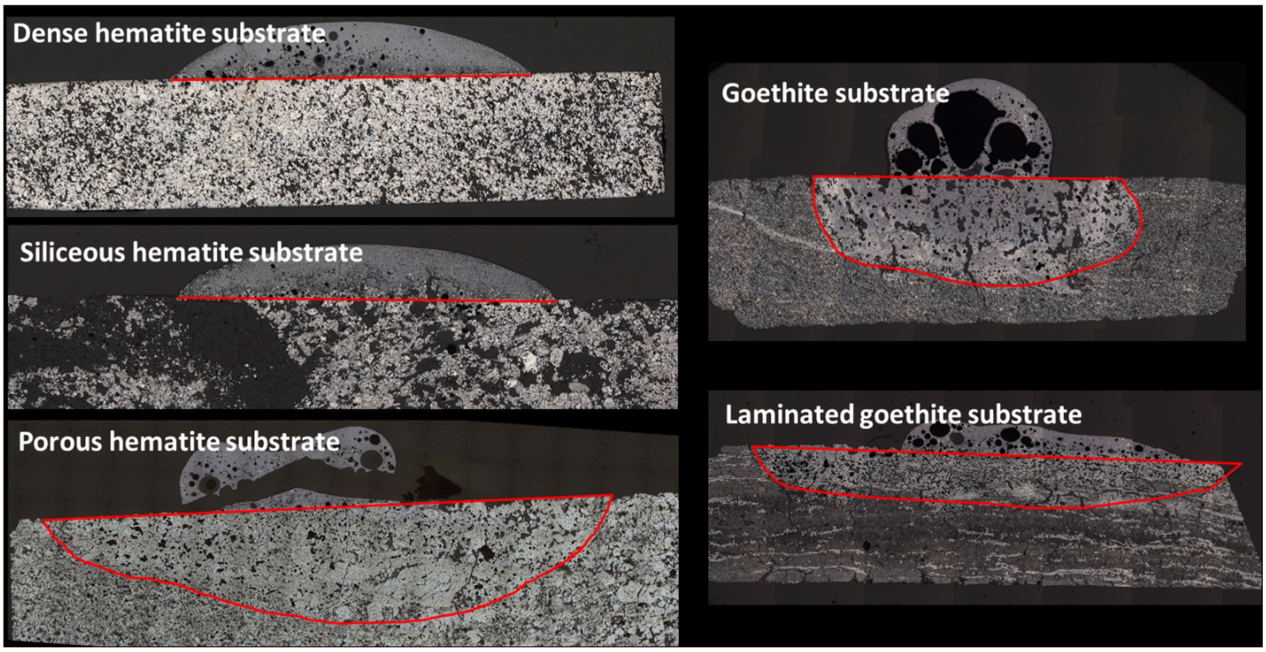

FIG 2 – Cross-sectional images of the sample assemblies of various iron ore substrates after the penetration experiments.

Figure 3 shows the measured results of the spread width and penetration depth, indicating that the penetration depth and width of melt depended on the ore types of substrates. The initial melt achieved its maximum spread width and penetration depth of 15.8 mm and 3.3 mm, respectively, across the porous hematite substrate. For the dense and siliceous hematite iron ore substrates, while the melt spread readily across the substrates, no penetration occurred between the initial melt and substrates. The goethite substrates showed an intermediate behaviour in penetration. However, the melt appeared to spread more and penetrate less into the laminated goethite substrate compared with the goethite substrate.

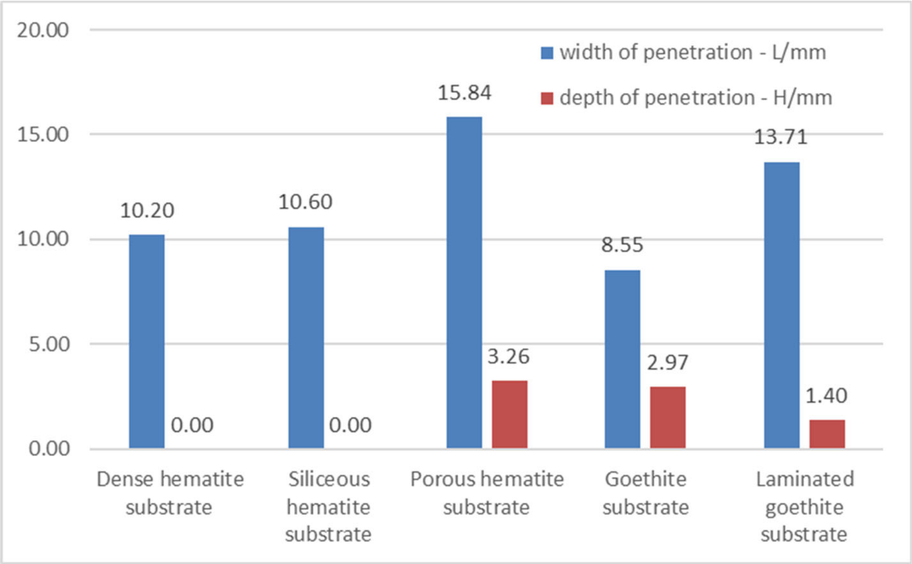

FIG 3 – Results of the penetration experiments with various iron ore substrates.

Penetration behaviour of initial melt at different temperatures

The cross-sectional images and penetration results of the experiments with the selected iron ore substrates at different temperatures are shown in Figures 4 and 5, respectively. For all the substrates tested, the penetration width and depth of melt both increased with temperature consistently. As the temperature increased, both the viscosity and surface tension of initial melt decreased, promoting the penetration of the melt into the substrate.

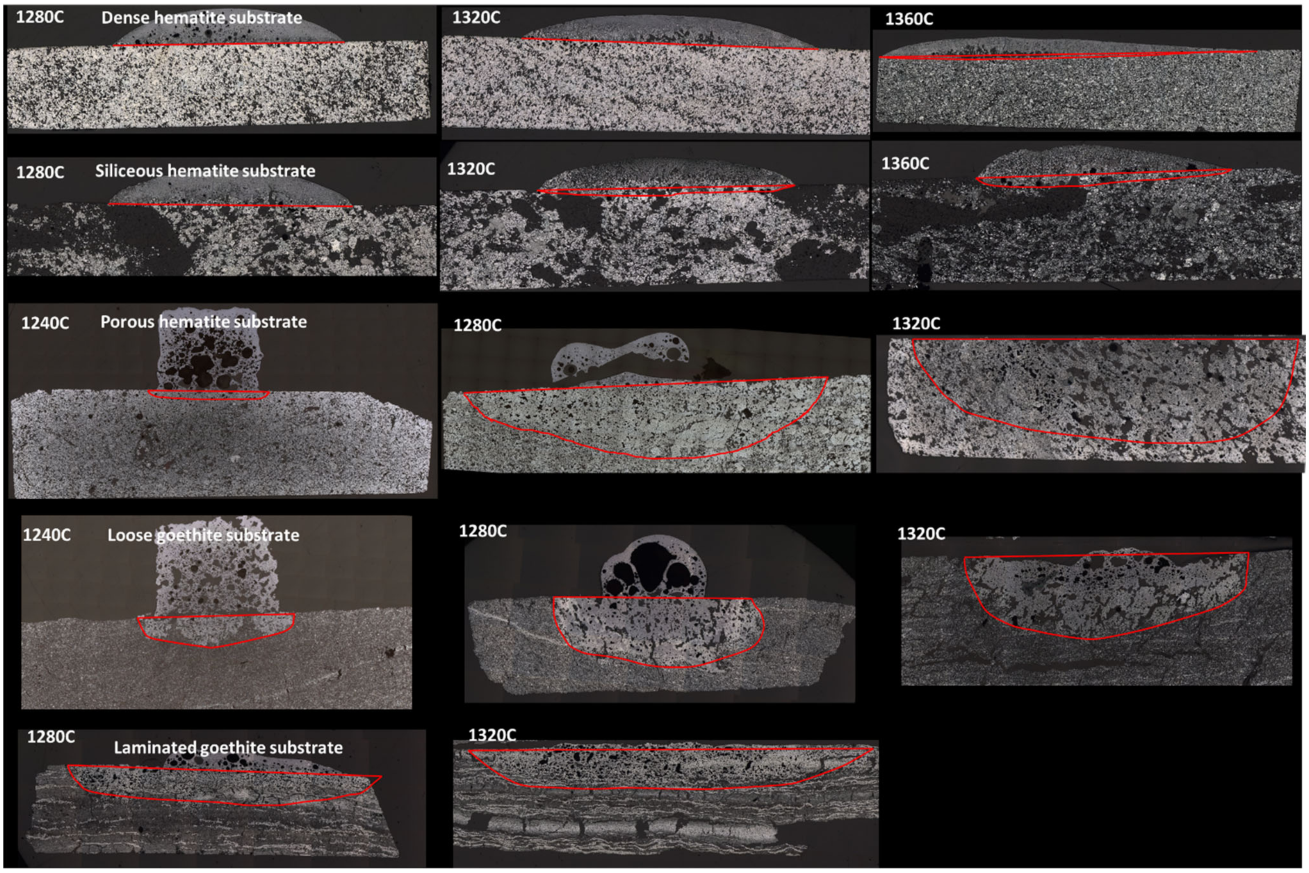

FIG 4 – Cross-sectional images of the sample assemblies after the penetration experiments at different temperatures.

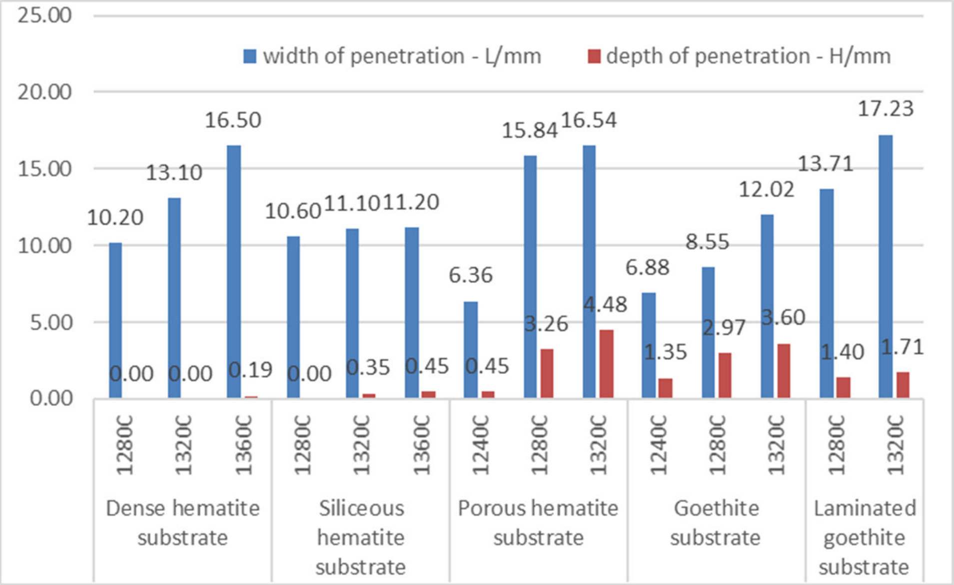

FIG 5 – Results of the penetration experiments with various temperatures.

As shown in Figure 5, the increments of penetration width and depth were both large with increasing temperature using porous hematite and goethite substrate. When the temperature increased from 1240°C to 1320°C, the penetration width increased from 6.36 mm to 16.54 mm and penetration depth increased from 0.45 mm to 4.48 mm for porous hematite substrate, while the penetration width increased from 6.88 mm to 12.02 mm and penetration depth increased from 1.35 mm to 3.60 mm for goethite substrate. In contrast, the increments of penetration width and depth were only 0.60 mm and 0.45 mm with increasing temperature from 1280°C to 1360°C using siliceous hematite substrate. In addition, the penetration width increased more and penetration depth increased less with increasing temperature using dense hematite and laminated goethite substrate.

While the same initial melt material was used in the research, the temperature where the melt started its interaction varied considerably with the ore type of substrates used. As shown in Figure 4, the porous substrate started its interaction at 1240°C, while the siliceous and dense hematite substrates only started their interaction at 1320 and 1360°C, respectively. In contrast, the porous and laminated goethite substrates have already showed substantial interaction at temperatures of as low as 1240°C, indicating a substantially lower interaction temperature for these substrates.

DISCCUSSION – FACTORS AFFECTING MELT PENETRATION BEHAVIOUR

During the penetration process, as the initial melt contacts closely with ore substrate, there are a serial of physical interactions and chemical reactions occurring between the initial melt and ore substrate. Therefore, the physical properties, chemical composition and mineralogical characteristics of the substrates were thought to be the major factors determining penetration behaviour.

Influence of pore structure of iron ore substrates

Penetration process can be considered as the infiltration process of the initial melt into the iron ore substrate. Therefore, the pore structure of ore substrates was one of the major physical properties determining its penetration behaviour. As seen in Figures 2 and 4, the melt hardly infiltrated into the dense hematite substrate which had the lowest porosity, instead it spread out and covered on the surface of the ore substrate, consequently showing the lowest penetration ability. In contrast, the melt was readily to penetrate into the porous hematite substrate, leading to large penetration width and depth.

In addition, the structural change of goethite during dehydration is associated with formation of secondary pores. As the dehydration process of goethite ore substrates took place much earlier before of the initial melt was formed, the secondary porosity formed during the dehydration would directly contribute to the penetration process, leading to a considerably higher penetration ability for the goethite substrates.

Influence of mineral composition of iron ore substrate

As seen in Figure 4, while the porosity of dense and siliceous hematite substrates was similar, these two substrates showed different penetration behaviour with increasing temperature, which is likely due to different mineral composition of the ore substrates. The dense and siliceous hematite substrates showed a different penetration behaviour more than 1280°C. During the penetration process, more silica was expected to dissolve from the siliceous hematite substrate in the melt, which subsequently altered the composition of the melt formed, leading to the difference observed in the penetration behaviour between the siliceous and dense hematite substrates. The melt composition was found to have a major effect on its penetration behaviour due to its influence on the melt property (Ma *et al*, 2013; Yu *et al*, 2015a, 2015b; Liu *et al*, 2016; Yang *et al*, 2018).

Similarly, while the porosity of porous hematite and porous goethite substrates was similar, the penetration behaviour of these two substrates were too different. Compared with porous hematite substrate, the newly generated hematite in the goethite substrate was more readily to react with initial melt and alter the melt composition which made their penetration characteristics different.

CONCLUSIONS

The penetration behaviour of an initial sinter melt into natural iron ore substrates of different ore types was examined at different temperatures. Compared with the dense and siliceous hematite substrates, the porous hematite, porous goethite and laminated goethite substrates was considerably higher in their penetration ability. The penetration depth and width were found to increase with temperature, but different substrates started their penetration at very different temperatures.

The factors affecting the penetration behaviour of melt were discussed. The pore structure and mineral composition of the substrates are the major factors determining the penetration depth and width of the melt on the natural iron ore substrates.

ACKNOWLEDGEMENTS

The authors would like to thank CSIRO Mineral Resources for permission to publish the paper and for the financial support of this work.

REFERENCES

Debrincat, D, Loo, C E and Hutchens, M F, 2004. Effect of iron ore particle assimilation on Sinter structure, *ISIJ International,* 44:1308–1317.

Han, H, Lu, L, Hapugoda, S, Begelhole, J and Holmes, R, 2019. Sintering behaviour of adhering fines and nucleus particles of ores, *Iron Ore 2019,* pp 77–87 (The Australasian Institute of Mining and Metallurgy: Melbourne).

Hida, Y and Nosaka, N, 2007. Evaluation of iron ore fines from the viewpoint of their metallurgical properties in the sintering process, *Institution of Mining and Metallurgy. Transactions. Section C: Mineral processing and extractive metallurgy,* 116:101–107.

Jeon, J W, Kim, S W and Jung, S M, 2015. Utilization of Magnetite Concentrate as an Additive in Adhering Fines of Quasi-particle and Its Effect on Assimilation Behavior, *ISIJ International,* 55:513–520.

Liu, D H, Zhang, J L, Xue, X, Wang, G W, Li, K J and Liu, Z J, 2016. Infiltration behavior of sintering liquid on nuclei ores during low-titanium ore sintering process, *Int J Min Met Mater*, 23:618–626.

Ma, M, Lu, L, Hapugoda, S and Manuel, J, 2013. Effects of melt composition on the interactions of sinter melt on a natural iron ore substrate, *Iron Ore 2013*, pp 431–440 (The Australasian Institute of Mining and Metallurgy: Melbourne).

Nakashima, K, Saito, N, Shinozaki, S, Tanaka, R, Maeda, T, Shimizu, M and Mori, K, 2004. Wetting and penetration behavior of calcium ferrite melts to sintered hematite, *ISIJ International*, 44:2052–2056.

Ware, N and Manuel, J, 2016. Fundamental nucleus assimilation behaviour of haematite and goethite containing ores in iron ore sintering, *T I Min Metall C*, 125:149–155.

Wu, S L and Zhang, G L, 2015. Liquid Absorbability of Iron Ores and Large Limonite Particle Divided Adding Technology in the Sintering Process, *Steel Res Int*, 86:1014–1021.

Yang, M R, Lv, X W, Wei, R R, Xu, J and Bai, C G, 2018. Wetting Behavior of Calcium Ferrite Slags on Cristobalite Substrates, *Metall Mater Trans B*, 49:1331–1345.

Yoshimura, S, Kurosawa, K, Gonda, Y, Sukenaga, S, Saito, N and Nakashima, K, 2009. Penetration Behavior of Calcium Ferrite Melts into Hematite Substrate, *ISIJ International*, 49:687–692.

Yu, B, Lv, X W, Xiang, S L, Bai, C G and Yin, J Q, 2015a. Wetting Behavior of Al_2O_3 Substrate by Calcium Ferrite Series Melts, *ISIJ International*, 55: 483–490.

Yu, B, Lv, X W, Xiang, S L, Bai, C G and Yin, J Q, 2015b. Wetting Behavior of Calcium Ferrite Melts on Sintered MgO, *ISIJ International*, 55: 1558–1564.

Design of a sintering heat profile for accelerating oxidation of magnetite ore

Y Konno[1], T Takayama[2] and M Matsumura[3]

1. Master's student, Tohoku University, Chiba, 293–8511, Japan.
   Email: yuki.konno.r7@dc.tohoku.ac.jp
2. Researcher, Materials Characterization Research Laboratory, Advanced Technology Research Laboratories, Nippon Steel Corporation. Chiba, 293–8511, Japan.
   Email: takayama.9fy.toru@jp.nipponsteel.com
3. Visiting Professor, Tohoku University, Chiba, 293–8511, Japan.
   Email: masaru.matsumura.d6@tohoku.ac.jp

ABSTRACT

The steel industry accounts for 14 per cent of domestic CO_2 emission in Japan, and iron ore sintering process occupies approximately three per cent. While Fe content in iron ore is gradually decreasing. So, the amount of concentrated iron ore will increase in the future. We have focused on magnetite concentrate as sinter materials, because magnetite can be easily magnetically beneficiated. However, it is experienced that blending magnetite ore resulted in increasing Fe^{2+} component in the iron ore sinter, which results in lower reducibility. Therefore, promoting the oxidation reaction from magnetite to hematite in the sintering process is countermeasure for reducibility. In addition, this promotion causes increase of oxidation heat, which results in high sinter strength and reduction of coke. It is assumed that the oxidation of magnetite tends to proceed in the cooling stage, where the oxygen partial pressure increases after the combustion of fine coke, but there are few studies on the effect of heat profile, especially cooling path. The purpose of this study is to design the effective sintering heat profile to promote oxidation of magnetite ore, especially, to investigate the effect of cooling path on sintered ore microstructure. In this study, magnetite ore and magnetite reagent were respectively mixed with calcium carbonate reagent. Then the mixed samples were pressed and formed into cylindrical tablets for simulating the adhesive layer of a pseudo particle. Through examining influence of maximum temperature and cooking rate on oxidation reaction of magnetite, we confirmed that the oxidation reaction of magnetite is suppressed at above 1350°C for maximum temperature, compared to 1300°C. Sintering at lower temperature is desirable because hematite is stable below 1350°C in the Fe_2O_3-CaO phase diagram.

INTRODUCTION

Recently, the steel industry accounts for 14 per cent of domestic CO_2 emission in Japan, and iron ore sintering process occupies approximately three per cent. On the other hand, the quality of iron ore is getting gradually worse due to the decrease of Fe content in iron ore. The use of pulverised and beneficiated fines can be an effective method for processing such materials. So, the amount of concentrated iron ore will increase in the future for maintaining Fe content in sinter. In particular, magnetite ore, which can be easily magnetically beneficiated, is expected to be used as a raw material. However, in the case of high blending ratio of magnetite ore, Fe^{2+} in the iron ore sinter increase, which results in lower reducibility. Therefore, promoting the oxidation reaction from magnetite to hematite is countermeasure for reducibility in the sintering process. In addition, this promotion means increase of oxidation heat, which results in high sinter strength and the reduction of coke. Till now, there are some previous studies on the oxidation reaction of magnetite. Summarising these studies, liquid generated from reacting Fe_3O_4 with CaO suppresses magnetite oxidation by interfering with the O_2 supply. Then it is effective to keeping certain distance between magnetite ore and limestone in sintering packed bed. In other words, these studies focus on melting behaviour in the heating stage of sintering process (Fujino, Murakami and Kasai, 2017; Matsumura *et al,* 2017; Ogi *et al,* 2017).

In contrast, we focus on cooling stage of sintering process based on oxygen potential. Because it is considered that the oxidation of magnetite tends to proceed in the cooling stage, where the oxygen partial pressure increases after fine coke combustion. However, there are few studies on the effect of sintering heat profile, especially cooling rate. The purpose of this study is to design the effective sintering heat profile to promote oxidation of magnetite ore, especially, to investigate the effect of cooling path on sintered ore microstructure.

EXPERIMENTAL METHOD

In this experiment, hematite reagent (-0.125 μm) and magnetite reagent (-0.125 μm) were used. Each of them was respectively mixed with calcium carbonate reagent. These mixed samples were prepared in such a way that the mixing ratio was CaO/t-Fe = 0.143. Then, they were pressed under the compression of 1 MP × 30 seconds and formed into cylindrical tablets (8 mmφ × 10 mm H) for simulating the adhesive layer of a pseudo particle. In order to investigate the effect of the cooling path on the oxidation reaction of magnetite, the tablets were sintered in air atmosphere in an electric resistance furnace through various sintering heat profiles. The sintering heat profiles of furnace temperature are shown in Figure 1 and Table 1. In all series, heating rate is same as 200°C increase in one minute to maximum temperature. In Series 1, the maximum temperature was changed from 1400°C to 1300°C in every 50°C, and the furnace was turned off soon after reaching the maximum temperature. In Series 2, the maximum temperature was 1300°C, and the cooling rate was three minutes for 200°C cooling (66.7°C/min), or six minutes for 200°C cooling (33.3°C/min). In Series 2B, the maximum temperature was 1300°C and cooling to 1100°C with 66.7°C/min rate. During the cooling path, temperature was kept at 1300°C, 1233°C, 1167°C, and 1100°C for three minutes respectively. Chemical analysis was carried out to obtain the FeO concentration of the samples after sintering. The samples were embedded in resin and the minerals and pores in the cross-section were observed by optical microscope. The pores in the cross-section were evaluated by image analysis method. The circularity is an index to evaluate the irregularity of the pores. Under liquid phase, the pores become rounded, and the circularity increases.

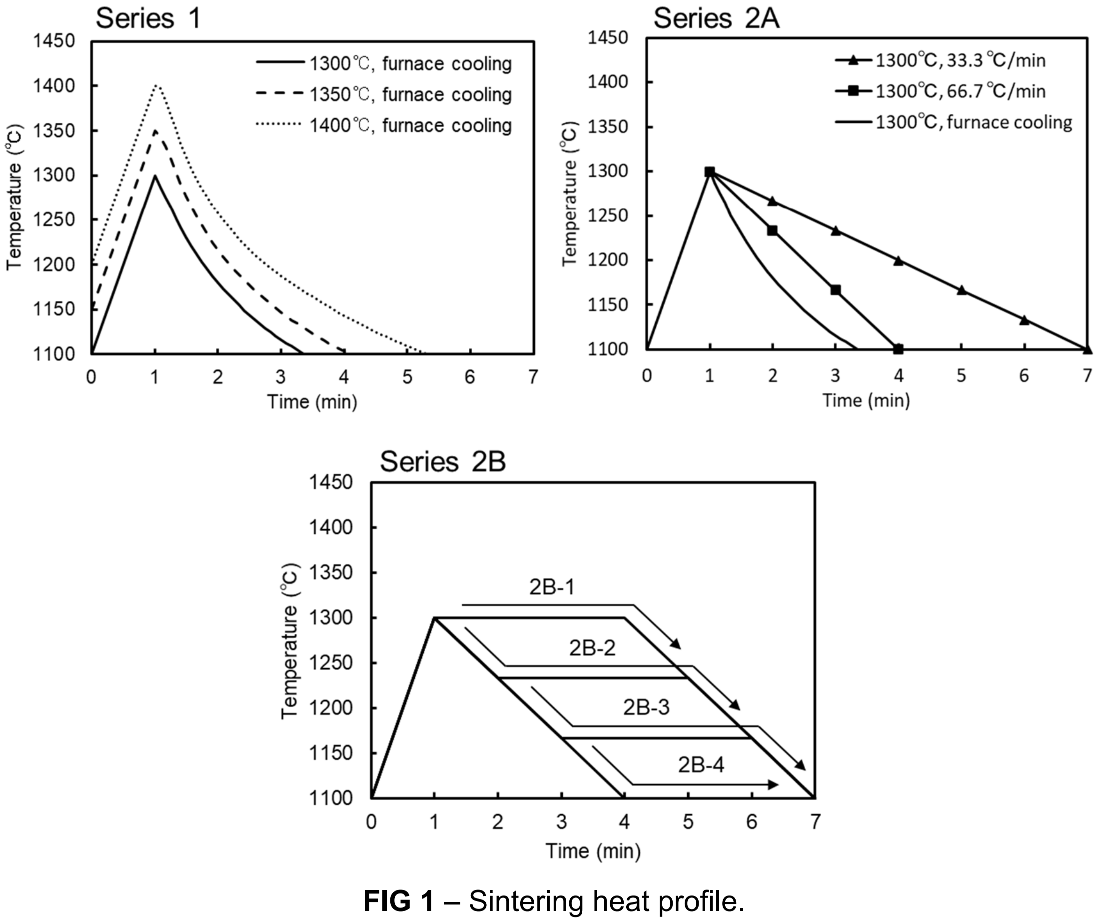
Series 1

Series 2A

Series 2B

FIG 1 – Sintering heat profile.

TABLE 1

Conditions of sintering heat profile.

Sample	Case	Maximum temperature	Cooling condition
H1	Series 1	1350℃	Furnace cooling
M1-1		1300℃	
M1-2		1350℃	
M1-3		1400℃	
H2A	Series 2A	1300℃	66.7℃/min
M2A-1			66.7℃/min
M2A-2			33.3℃/min
M2B-1	Series 2B	1300℃	66.7℃/min 1300℃ (3min)
M2B-2			66.7℃/min 1233℃ (3min)
M2B-3			66.7℃/min 1167℃ (3min)
M2B-4			66.7℃/min 1100℃ (3min)

Results

The effect of maximum temperature on the oxidation reaction of magnetite

Figure 2 shows the cross-sectional view of the samples sintered under the heat profile of Series 1. In the case of the samples sintered at 1400°C and 1350°C there were many rounded pores, while in the case of the sample sintered below 1300°C, there were many small and distorted pores under 50 µm. Figure 3 shows the circularity distribution of the sample of Series 1. In the case of the sample sintered above 1350°C, there were many pores with circularity from 0.8 to 1.0. While, in the case of the sample sintered below 1300°C, there was a peak in the circularity range from 0.4 to 0.6. It is presumed that the integration of the pores above 1350°C was promoted due to melting of the tablets, resulting in rounded pores. As for minerals, in the case of the sample sintered above 1350°C, there was a lot of skeletal hematite, which precipitates from the liquid phase. While, in the case of the sintered below 1300°C, a lot of spotted hematite was found, which precipitates from solid phase.

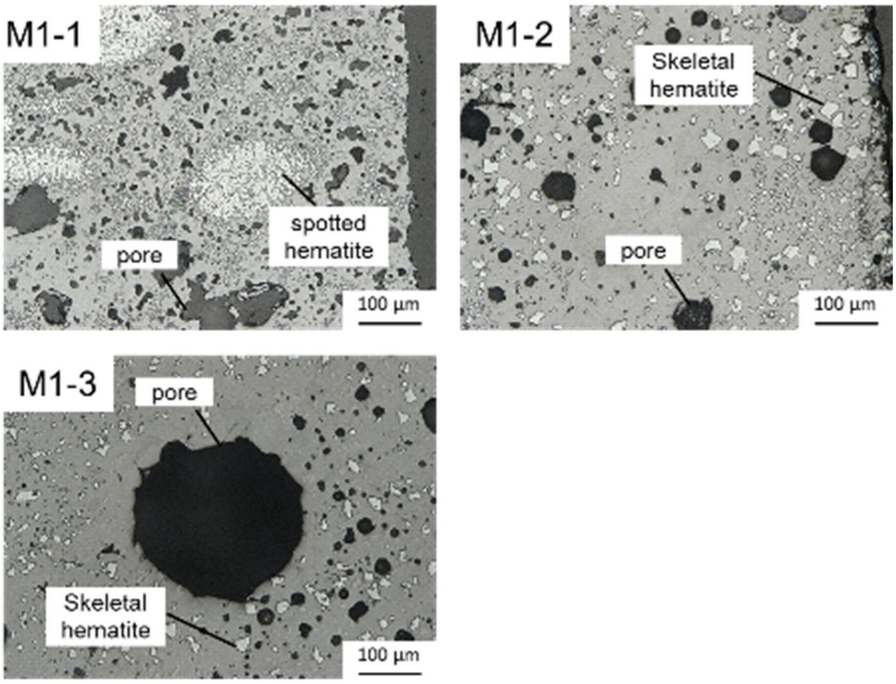

FIG 2 – Cross-sectional view of the sintered samples of M1–1, M1–2 and M1–3.

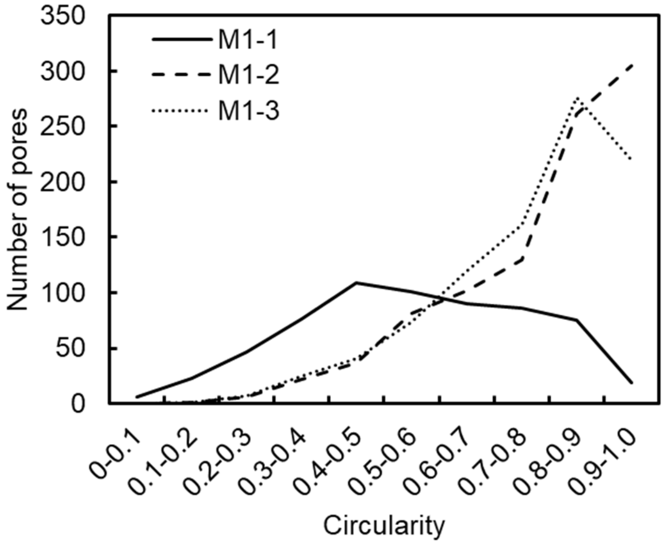

FIG 3 – Circularity distribution of the sample sintered under Series 1.

Figure 4 shows FeO concentration in the samples of Series 1. FeO concentration is an index of the oxidation of magnetite to hematite during sintering, and the decrease of FeO concentration means that the oxidation reaction from Fe^{2+} to Fe^{3+} has proceeded. The FeO concentration of H1, which used hematite reagent, was 1.36, suggesting that some of hematite was dissociated into magnetite during sintering. In the case of sample of magnetite, FeO concentration decreased as the maximum temperature decreased, and especially that of M1–1 was lowest. According to CaO-Fe_2O_3 binary phase diagram in air, magnetite becomes stable above 1358°C (Fujino, Murakami and Kasai, 2017). Therefore, it is desirable to sinter the sample of magnetite below this temperature in order to promote the oxidation of magnetite. However, it is not enough to oxidate by only controlling maximum temperature because FeO concentration of M1–1 was higher than that of case H1.

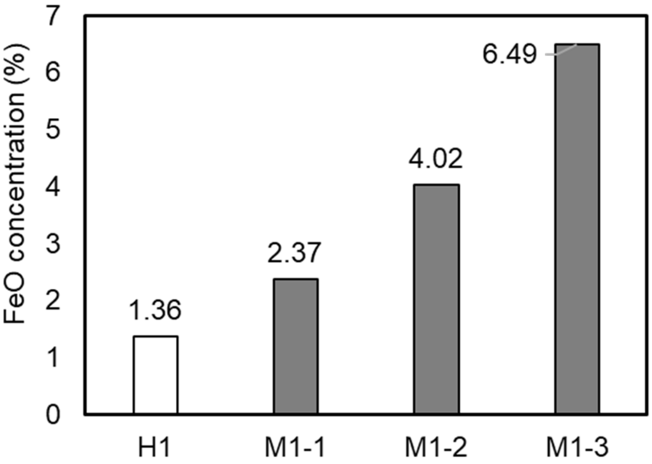

FIG 4 – The effect of maximum temperature on FeO concentration of the sample sintered under Series 1.

The effect of cooling rate on the oxidation reaction of magnetite

Figure 5 shows the cross-sectional view of the samples sintered under the heat profile of Series 2A. As the cooling rate decreases, there are more rounded pores due to the integration of the pores. Figure 6 shows the circularity distribution of the samples of Series 2A and sample M1–1. The circularity of the pores increases as the cooling rate decreases, and the number of pores with a circularity greater than 0.8 is large in M2A-2. This is probably due to the fact that the integration of pore is enhanced as the time of maintaining the liquid phase is extended by decreasing cooling rate. As for the minerals, many spotted hematite was observed in all three conditions regardless of the cooling rate.

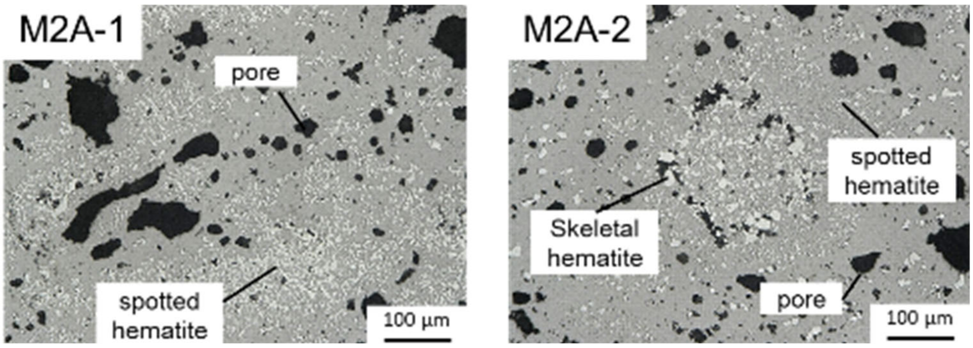

FIG 5 – Cross-sectional view of the sintered samples of M2A-1 and M2A-2.

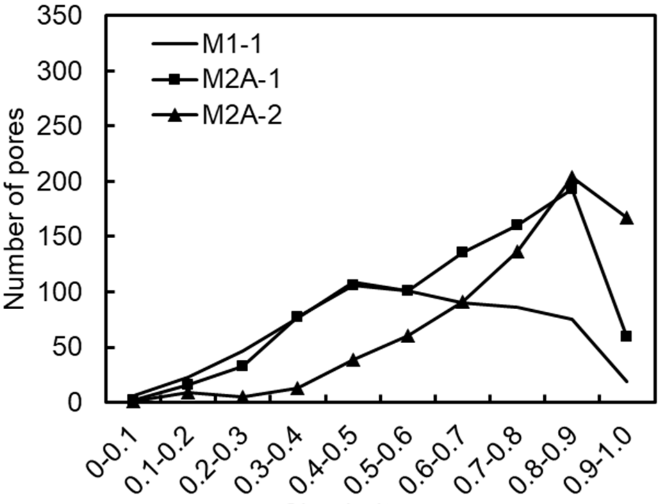

FIG 6 – Circularity distribution of the sample sintered under Series 2A.

Figure 7 shows FeO concentration in the samples of Series 2A and sample M1–1. The FeO concentration of H2A was 1.41, and the dissociation to magnetite was observed even at the maximum temperature of 1300°C. In the case of sample of magnetite, there is no significant difference in FeO concentration regardless of the cooling rate. The decreasing cooling rate means the extension of the high temperature holding time, which has higher potential for magnetite oxidation. However, FeO concentration remained constant. This may be due to the fact that the decrease in the cooling rate increased the amount of melt formation, which suppresses the oxidation of magnetite.

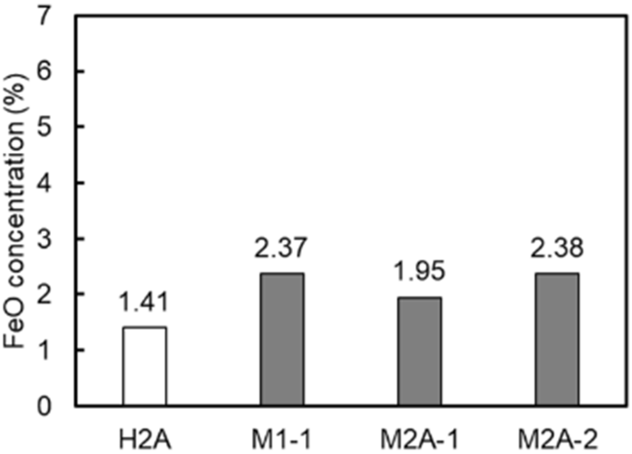

FIG 7 – The effect of maximum temperature on FeO concentration of the sample sintered under Series 2A.

The experiments were conducted under the conditions of Series 2B in order to investigate the effect of the liquid phase on the suppression of oxidation and the effect of prolonged high temperature holding time on the acceleration of oxidation. The eutectic temperature of CaO-Fe_2O_3 is 1205°C. M2B-1 and M2B-2 were kept in the liquid phase, and M2B-3 and M2B-4 were kept in the solid phase. Figure 8 shows the cross-sectional view of the samples sintered under the heat profile of Series 2B. In the case of M2B-1, which was kept in the temperature range where the liquid phase was formed, there were many rounded pores. In the case of M2B-3, which was kept in the solid phase, many small and distorted pores were observed. Figure 9 shows the circularity distribution of the samples of Series 2B. In the case of M2B-1 held at 1300°C, the number of pores with a circularity from 0.7 to 1.0 is large. As for the other three samples whose holding temperature was below 1233°C, there was no significant difference in circularity, and the number of pores in the range from 0.4 to 0.7 was large. As for the minerals, in the case of M2B-1, there were a large number of skeletal hematite outside of the tablet, and spotted hematite was observed inside. In the case of M2B-3, spotted hematite was observed throughout the cross-section.

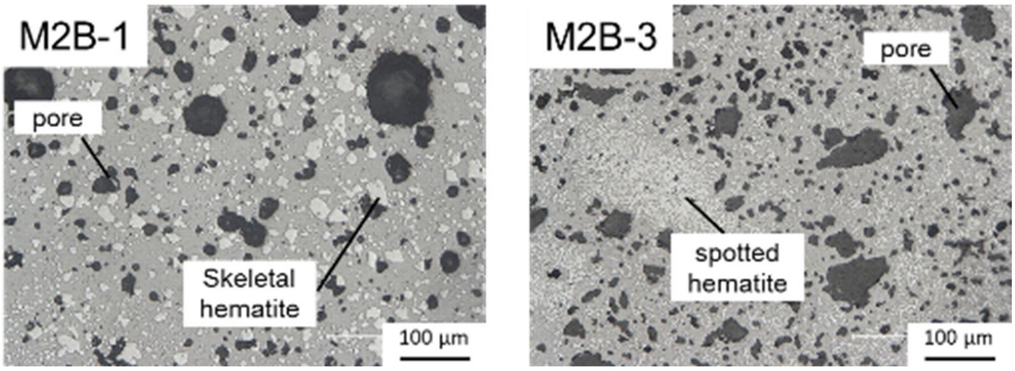

FIG 8 – Cross-sectional view of the sintered samples of M2B-1 and M2B-3.

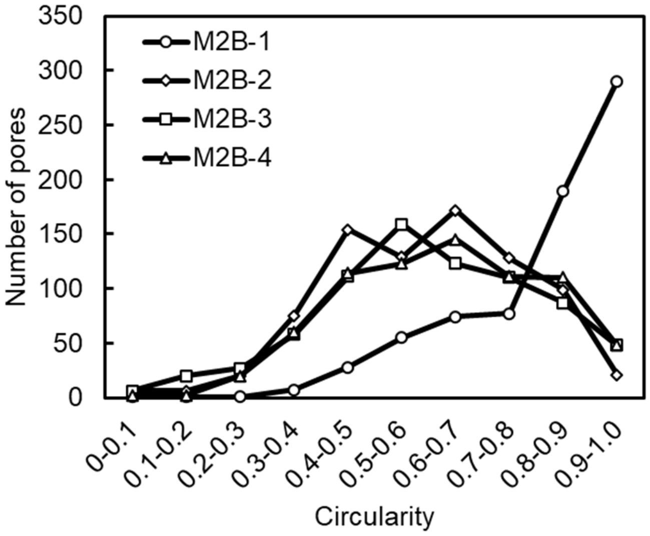

FIG 9 – Circularity distribution of the sample sintered under Series 2B.

Figure 10 shows FeO concentration in the samples of Series 2B. The dotted line in the figure shows the FeO value of H2A. In the case of M2B-1, FeO concentration was 3.03. On the other hand, in the case of the other three samples, FeO concentration was low, and especially that of M2B-3 was lower than that of H2A. This may be due to the fact that the oxidation of magnetite was not suppressed by the liquid phase when it was held at high temperature in the solid phase. Compared with M2B-1 and M2A-1, it seems that the extension of the time of liquid phase leads to increase of FeO concentration. In addition, compared with M2B-3 and M2B-4 the oxidation of magnetite is promoted by holding temperature as high as possible in the solid phase.

In order to achieve the effect of oxidation promotion by extending the high temperature holding time, it is considered that it is effective to shorten the time to pass through the liquid phase stability zone and to cool slowly in the range from 1250°C to 1100°C.

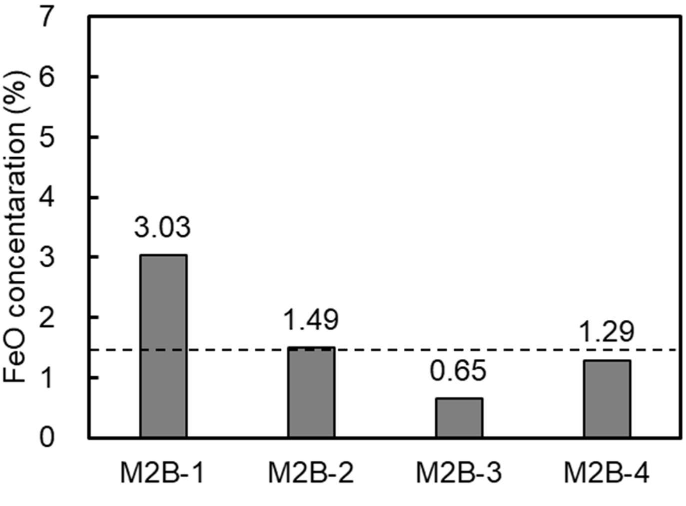

FIG 10 – The effect of maximum temperature on FeO concentration of the sample sintered under Series 2B.

CONCLUSIONS

The purpose of this study was to design the effective sintering heat profile with the maximum temperature and cooling rate to promote the oxidation of magnetite to deal with deterioration of iron ore. The effect of the cooling process on the sintered ore microstructure was evaluated.

- In the case of the sample of magnetite reagent, FeO concentration decreased as the maximum temperature of sintering heat profile decreased from 1400°C to 1300°C. This is because magnetite is stable above 1358°C according to CaO-Fe_2O_3 binary phase diagram, and the oxidation of magnetite was suppressed.

- In the case of the sample kept in the temperature of liquid phase in CaO-Fe_2O_3 system, FeO concentration increased. On the other hand, In the case kept in the temperature of solid phase, FeO concentration decreased and showed as low as that of hematite sample. These results suggest that slow cooling in the temperature range from 1250°C to 1100°C promotes the oxidation of magnetite.

ACKNOWLEDGEMENTS

I would like to thank M Matsumura for useful discussions. I am grateful to T Takayama for assistance with quantitative analysis for mineral phase in sinter ore by Rietveld Method.

REFERENCES

Fujino, K, Murakami, T and Kasai, E, 2017. Promoting Effect on Oxidation Reaction of Iron-bearing Agglomeration Agent by Melt Formation, *Tetsu-to-Hagan’e*, 103:348–356.

Matsumura, M, Takayama, T, Hara, K, Yamaguchi, Y, Ishiyama, O, Higuchi, K, Nomura, S, Murakami, T, Hayashi, M and Ohno, K, 2017. Improvement of Sinter Strength and Reducibility through Promotino of Magnetite Ore Oxidation, *Tetsu-to-Hagan’e*, 103:388–396.

Ogi, H, Ohno, K, Maeda, T and Kunitomo, K, 2017. Effect of Magnetite (Fe2+ source) on Initial Liquid Formation in Sintering Process, *Tetsu-to-Hagan’e*, 103:335–340.

High temperature characteristics of different types of blast furnace ferrous materials

L Lu[1], A Edenton[2] and S Hapugoda[3]

1. Principal Scientist, CSIRO Mineral Resources, Pullenvale Qld 4069. Email: liming.lu@csiro.au
2. Research Project Officer, CSIRO Mineral Resources, Pullenvale Qld 4069.
   Email: alexander.edenton@csiro.au
3. Experiment scientist, CSIRO Mineral Resources, Pullenvale Qld 4069.
   Email: sarath.hapugoda@csiro.au

ABSTRACT

The blast furnace cohesive zone has a profound impact on hot metal productivity and quality, fuel consumption, operational stability and the lining life of the blast furnace. The high temperature properties of ferrous burden materials determine the configuration and location of the cohesive zone and have therefore attracted particular attention. While numerous standard testing methods are in use to assess the quality of ferrous burden materials for the blast furnace, these simple tests are generally conducted under fixed conditions, which often represent the extreme situations encountered by the burden materials in the blast furnace. Furthermore, none of these simple tests provides information on the high temperature properties of the burden materials, such as their softening and melting properties. CSIRO is equipped with a fully computerised testing facility to characterise the high temperature properties of ferrous burden materials under realistic conditions similar to those encountered in the blast furnace. This paper will first review the CSIRO softening and melting test method and then discuss the softening and melting properties of a variety of blast furnace burden materials, including sinter, pellets and lump ore, and their implications for blast furnace operation.

INTRODUCTION

The blast furnace cohesive zone has a profound impact on hot metal productivity and quality, fuel consumption, operational stability and lining life of a blast furnace due to its impact on the total flow and distribution of gas in the furnace burden (Dawson, 1987). Since the identification of the cohesive zone in several quenched blast furnaces in Japan, investigations have been carried out to evaluate the behaviour of blast furnace ferrous burdens during reduction at high temperatures, which is believed to determine the configuration and location of the cohesive zone (Dawson, 1987; Higuchi *et al*, 2004). While numerous standard testing methods are in use to assess the quality of burden materials for blast furnace use, these simple tests are generally conducted at fixed conditions, which often represent the extreme situations encountered by burden materials in the furnace.

The processes occurring in a blast furnace are very complex. The conditions the burden materials are subjected to, such as temperature, gas composition and compressive load, vary widely both vertically and radially. The softening and melting (SAM) test is aimed at simulating the physical and chemical changes occurring in a small volume of sample as it descends in a blast furnace, particularly in the cohesive zone. Over the years, CSIRO has developed a fully computerised testing facility to characterise the softening and melting characteristics of the ferrous burden materials under realistic conditions similar to those encountered in the blast furnace. This paper will first review the CSIRO softening and melting test method and then discuss the softening and melting properties of different burden materials including sinter, pellets and lump ore, and their implications for blast furnace operation.

EXPERIMENTAL PROCEDURE

CSIRO softening and melting testing facility

Figure 1 presents a schematic diagram of the CSIRO softening and melting testing facility. It consists of an induction furnace, a gas distribution system, a loading system, and a data acquisition system. During the test, the sample is sandwiched between two layers of graphite or coke particles and subjected to a programmed and time dependent variation of temperature, gas composition and loading conditions. The physical and chemical changes occurring in the sample during the test are monitored continuously by measuring and recording the changes in bed height, pressure drop across the sample bed, and sample and melt collector temperatures.

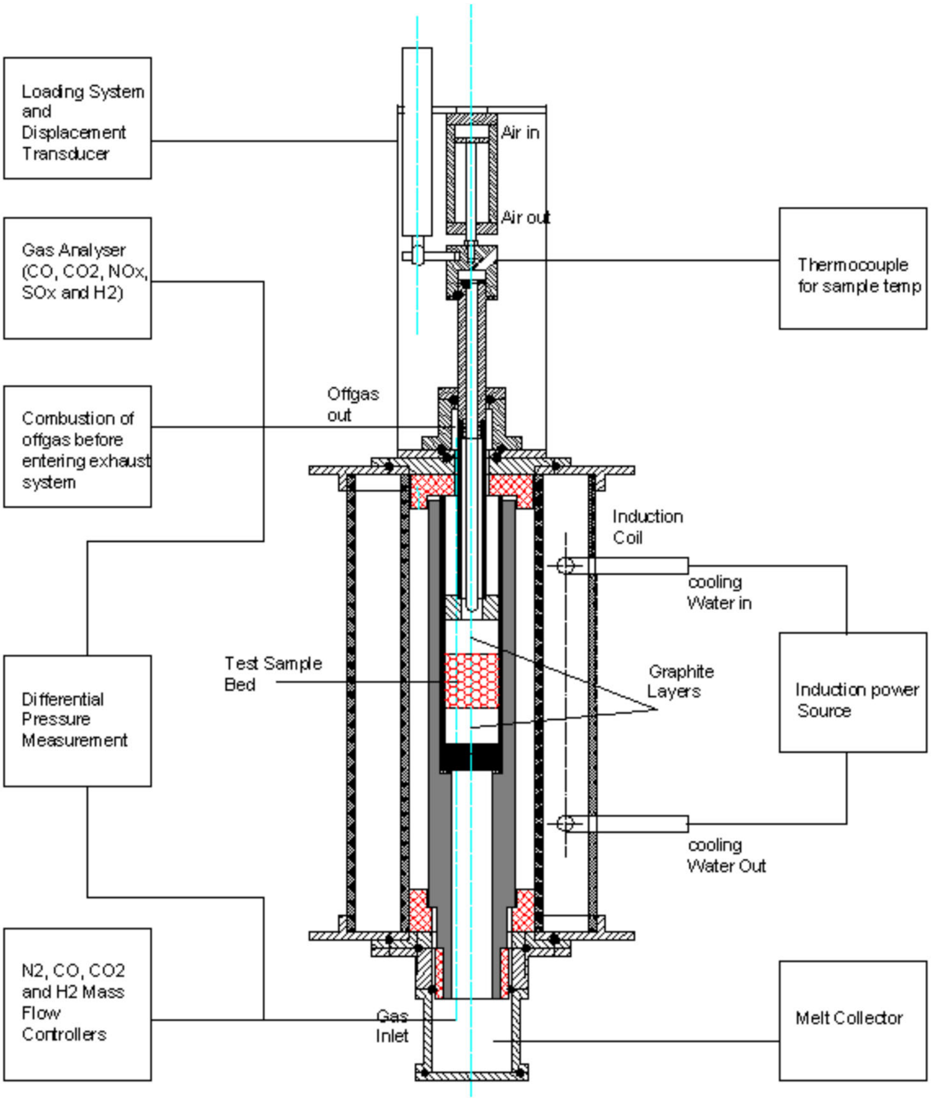

FIG 1 – Schematic diagram of CSIRO softening and melting testing facility.

Table 1 summarises the standard testing conditions used in CSIRO SAM tests. The sample is first heated at about 10°C/min up to 1000°C and then at about 5°C/min to 1550°C or complete meltdown, whichever occurs first, with CO gas being introduced at 400°C.

TABLE 1

Summary of typical CSIRO SAM testing conditions.

Parameters	**Units**	**Conditions**
Sample volume		Fixed, 70 mm diameter and 65 mm height
Sample size	mm	-12.5+10
Graphite layer depth	mm	45 bottom
	mm	40 top
Graphite size	mm	-12.5+10
Gas flow	l/min	11.3
Gas composition	Vol%	30% CO + 70% N_2
Heating rate	°C/min	~10 at temperatures below 1000°C
		~5 at temperatures higher than 1000°C
Load	kN/m^2	98

Figure 2 presents a set of typical softening and melting curves measured for a lump ore under standard CSIRO testing conditions. The softening, melting, and dripping temperatures as well as the cohesive zone temperature range are defined below and illustrated in Figure 2:

Softening temperature (°C), T_S: the sample temperature at 50 per cent bed compaction. Above this temperature, the pressure drop across the sample bed starts to increase rapidly. This temperature usually coincides with the temperature at which direct reduction starts and is defined in this paper as the start of the cohesive zone.

Melting temperature (°C), T_m: the temperature at which the pressure drop across the sample bed returns to that at T_S or 1550°C, whichever is lower. This indicates the end of meltdown and therefore the cohesive zone.

Cohesive zone temperature range (°C), ΔT: the temperature interval between the softening and melting temperatures. It is important to ensure the temperature difference between the softening and melting of the burden is not too great. A thick cohesive zone will result in poor permeability in the furnace burden.

Dripping temperature (°C), T_d: the temperature at which the first drop of molten material is recorded.

S value (kPa×°C): the area under the pressure drop curve above the pressure drop at T_S bordered between the softening and melting temperatures. This is often referred to as the S value in Japan. As shown in the insert in Figure 2, the S value is calculated using the following equation:

$$S = \int_{T_S}^{T_m} (\Delta P - \Delta P_{T_S})\, dT$$

where ΔP and ΔP_{T_S} are the pressure drops across the sample bed at temperatures T and T_S, respectively. The S value indicates the pressure accumulated in the cohesive zone.

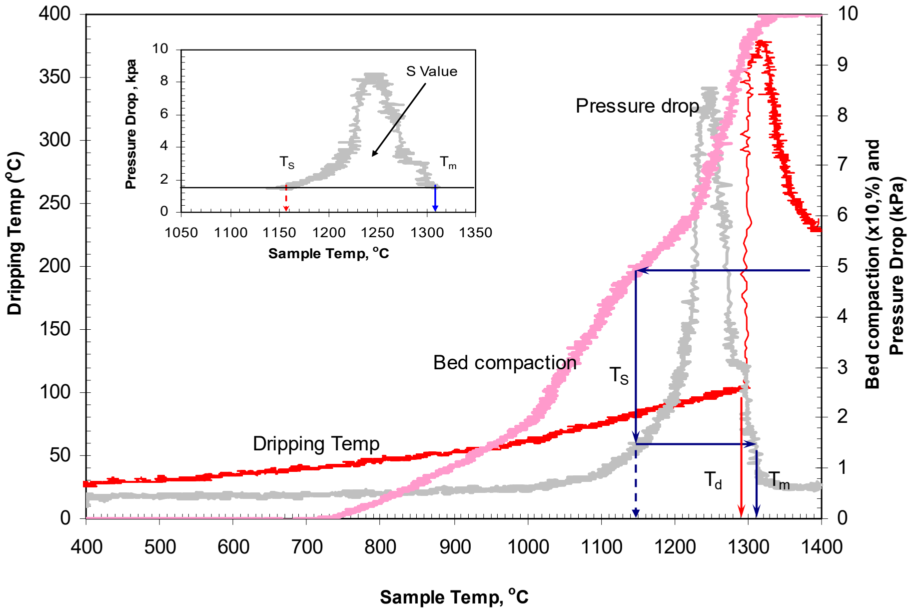

FIG 2 – Typical softening and melting curves measured for a lump ore under standard CSIRO SAM testing conditions $\Delta T = T_m - T_s$

Raw Materials

Three different burden materials, including one lump ore (Sample A), one pellet (Sample C) and one sinter (Sample D), were selected and tested in the paper. Table 2 summarises the chemical compositions of the sized test samples which were prepared from the bulk materials received. The samples were first oven dried at 105°C until a constant mass was achieved. For the lump and sinter samples, the oven dried sample was then screened at 12.5 and 10 mm. While the -10 mm material was discarded, the +12.5 mm material was submitted to staged roll crushing to achieve maximum recovery of the -12.5+10 mm fraction. The pellet sample was not crushed and was only screened at 12.5 and 10 mm to extract the -12.5+10 mm fraction.

TABLE 2

Chemical analyses of the burden materials tested.

Sample code	Sample description	FeO	Fe	SiO_2	Al_2O_3	P	S	CaO	MgO	LOI 900°C
		%	%	%	%	%	%	%	%	%
A	Lump	1.23	64.95	2.41	0.94	0.074	0.011	0.15	0.05	3.09
C	Pellet	1.38	66.20	1.69	0.32	0.011	0.000	0.85	1.36	0.02
D	Sinter	5.63	57.84	4.76	1.78	0.048	0.003	8.91	1.60	-0.15

Figure 3 shows the typical mineralogical characteristics of the burden materials. Sample A was a typical lump ore, comprising mainly of dense to moderately porous microplaty-hematite (H), moderately porous microplaty hematite + goethite (H-G), and moderately porous martite (M), as well as vitreous and earthy goethite (G). Sample C was a fluxed pellet, relatively uniform both in mineral phases and porosity. It was microporous and comprised predominantly of hematite crystals within a glassy matrix. The hematite crystals were well connected and consolidated, indicating well-developed diffusion bonding. There were also particles containing slightly angular hematite crystals with some rounded residual magnetite. These particles were most likely from the core of pellets where insufficient oxidation occurred due to lack of oxygen. Like other iron ore sinters, Sample D was heterogeneous. It consisted of a mixture of mineral phases, including primary hematite, secondary hematite and magnetite, as well as different types of SFCA (silicoferrites of calcium and aluminium). The pore size varied considerably. Clearly the three burden materials selected were very different in terms of chemistry and mineralogy, which was expected to result in different behaviour during high temperature reduction.

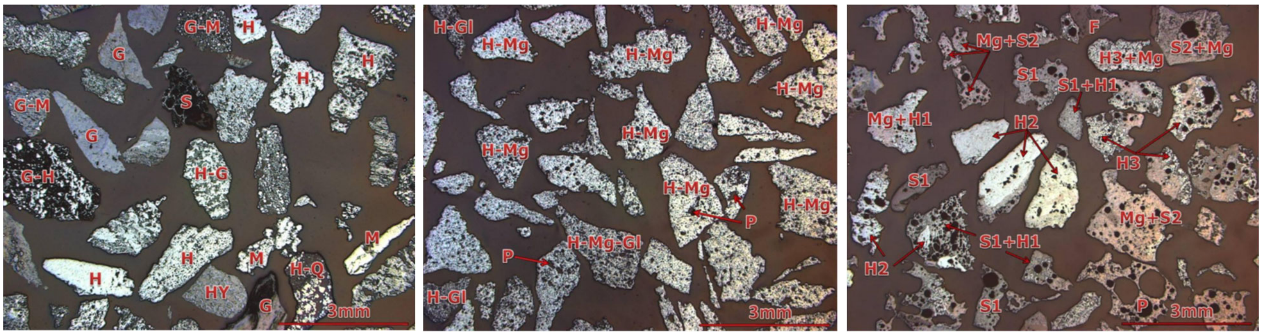

(a) (b) (c)

FIG 3 – Reflected optical micrographs showing mineralogical characteristics of the burden materials tested (-2 to +1 mm fraction): (a) Sample A (Lump), (b) Sample C (Pellet), and (c) Sample D (Sinter). H-Hematite (H1= primary hematite, H2= un-reacted ore, H3= secondary skeletal hematite), Mg= magnetite, M-Martite, G-Goethite, HY-Hydrohematite, S1= SFCA1, S2= SFCA, Gl= glass, P= pore, S-shale, Q-Quartz, F=Flux.

HIGH TEMPERATURE CHARACTERSTICS OF DIFFERENT TYPES OF BLAST FURNACE BURDEN MATERIALS

Figure 4 presents the bed compaction, pressure drop and dripping temperature of the burden materials. The samples have clearly displayed distinct softening and melting characteristics, as shown in Table 3.

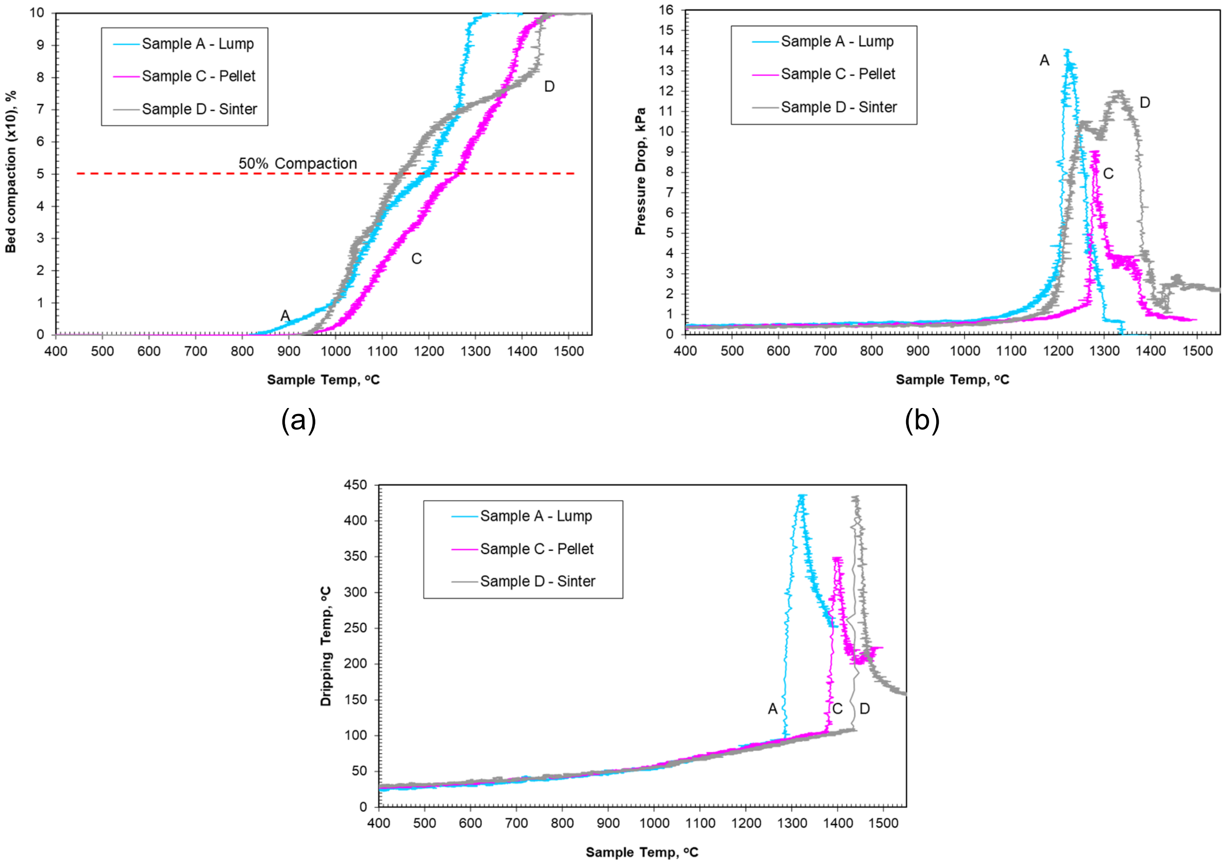

(a) (b)

(c)

FIG 4 – (a) Bed compaction, (b) pressure drop, and (c) dripping temperature of the burden materials tested.

TABLE 3

High temperature properties of the burden materials tested.

Sample code	Sample description	Sample mass	T_S	T_m	ΔT	T_d	S-value
		g	°C	°C	°C	°C	kPa×°C
A	Lump	472.25	1193	1286	93	1286	511
C	Pellet	465.99	1260	1385	125	1375	347
D	Sinter	313.15	1139	1550	411	1435	1907

Lump ore – Sample A

Sample A being a lump ore started to shrink earlier at approximately 810°C. As the sample temperature increased up to 1000°C, the sample underwent slow linear shrinkage. However, as shown in Figure 4b, negligible pressure drop was detected across the sample bed below 1000°C. Therefore, the bed shrinkage observed is believed to be due to the volume change of the lump ore as a result of dehydroxylation of goethite and subsequent brittle deformation and consolidation of the ore particles under load and high temperatures.

At the sample temperature above 1000°C, the bed shrinkage increased more rapidly and the pressure drop across the bed started to increase. However, the pressure drop across the bed was still very low in relative terms and increased only slowly. Hence, it appears that, while the ore particles most likely went through internal structural modification due to reduction and therefore considerable consolidation, the sample has still kept its particle identity. Consequently, the reaction gases could still readily flow-through the remaining gaps between ore particles without causing a significant pressure drop. The bed shrinkage slowed down slightly at the temperature above approximately 1100°C for the sample as the mobility and consolidation of the ore particles was more restricted in an already compacted bed without the onset of softening.

The sample bed reached 50 per cent compaction at around 1193°C. With further increase in temperature, the pressure drop across the sample started to increase rapidly due to collapse of the void space between ore particles resulting from plastic deformation and partial melting of ore particles at the higher temperatures. This occurred because an increasing amount of hematite was reduced to magnetite and wüstite as the sample temperature increased, so the amount of FeO in the sample increased drastically and lowered the solidus of the sample. The particles then underwent plastic deformation under the load and eventually collapsed to form a thick semi-solid mass. The maximum pressure drop was observed at approximately 1225°C for the sample. As the temperature increased further beyond this point, the sample mass became more fluid and started to coat the graphite particles, leading to increased porosity and a decrease in the pressure drop.

The close contact between the relatively fluid sample mass and graphite particles promotes direct reduction of FeO and subsequent carburisation of iron, which lowers the melting point of iron substantially. However, reduction of FeO also increases the liquidus of the molten sample. Melt dripping occurred when the sample temperature reached the liquidus of the molten slag and Fe-C melt formed. The melt started to drip out at 1286°C for the lump sample. The metal that dripped out was collected at the end of each test and its weight is listed in Table 3. More than 80 per cent of the contained iron dripped out for the lump sample (Table 4).

TABLE 4

Calculated masses of metallic iron and slag formed at the end of reduction for the burden materials tested.

Sample code	Sample description	Fe	Total gangue	Sample mass	Metallic Fe	Slag	Metal dripped
		wt%	wt%	g	g	g	%
A	Lump	65.17	3.72	472.25	307.78	17.57	83.3
C	Pellet	66.59	4.78	465.99	310.30	22.26	75.1
D	Sinter	57.91	17.36	313.15	181.34	54.36	42.3

Pellet – Sample C

As shown clearly in Figure 4, the pellet sample did not undergo the initial slow linear shrinkage due to dehydroxylation of goethite observed for the lump sample, but showed clear signs of compaction at temperatures above 980°C. As the sample temperature increased above this point the pellets underwent relatively rapid linear shrinkage. However, no pressure drop was observed across the sample bed until the sample bed reached 50 per cent compaction at 1260°C. Therefore, the sample compaction observed below 1260°C was believed to be mainly due to the internal structure change and consolidation of pellets under load and high temperatures.

Further increases in sample temperature above 1260°C resulted in a drastic increase in the pressure drop across the sample bed. This occurred because as the sample temperature increased still further, the iron shell formed earlier appears to have deformed and the voidage between the pellets has gradually collapsed, resulting in an increase in the pressure drop across the sample bed. Eventually it appears as though the liquid core of the pellets has been put under pressure, squashed out and filled the remaining gaps between deformed pellets, with the maximum pressure drop occurring at approximately 1270°C.

As the temperature increased beyond this point, it looks as though the sample became more fluid due to carburisation and high temperatures and the melt started to fill the gaps between graphite particles, leading to increased porosity and a decrease in the pressure drop. The melt started to drip out of the sample bed at 1375°C with about 75 per cent of the contained iron being collected (Table 4).

Sinter – Sample D

The bed compaction, pressure drop and dripping temperature of the sinter sample (Sample D) are also presented in Figure 4. As for pellets, the sinter sample did not undergo the initial slow linear shrinkage due to dehydroxylation of goethite observed for the lump ore samples, but showed clear signs of compaction at temperatures above 950°C.

As the sample temperature increased further, the sample underwent rapid shrinkage, but no pressure drop was observed across the sample bed until the sample reached 50 per cent compaction at approximately 1139°C. Therefore, the observed sample compaction before 1139°C was considered to be most likely due to internal structure change and consolidation of sinter particles under load, because sinter particles are irregular and hard to compact during sample preparation. Consequently, more rapid compaction is expected initially to optimise the packing.

Further increases in sample temperature above 1139°C resulted in a drastic increase in the pressure drop across the sample bed. It is believed that an increasing amount of hematite is reduced to magnetite and wüstite as the sample temperature increases, so that the amount of FeO in the sample increases rapidly and lowers the solidus of the sample. Hence, the sample underwent plastic deformation under the load and eventually collapsed to form a thick semi-solid mass, the maximum pressure drop occurring at approximately 1330°C.

As the temperature increased still further, it appears that the molten sample became more fluid and started to coat the graphite particles, leading to increased porosity and a decrease in the pressure drop. The melt started to drip out bed at 1435°C, although in this case only 42 per cent of the contained iron was collected (Table 4).

IMPLICATIONS FOR BLAST FURNACE OPERATION

Compared with the lump ore sample, the pellet sample displayed a higher softening temperature with a narrow cohesive zone. The peak pressure drop was also lower and as a result, the pellet sample had the lowest S-value. The higher softening temperature of the pellet sample can be explained by the reduction characteristics of the pellets. Unlike the other burden materials, reduction of pellets is more topological. As a result, a metallic shell is formed around the pellets not long after commencement of reduction. This shell should have sufficient strength to hold the pellets together as separate particles up to relatively higher temperatures and deter further reduction of the pellet core, leading to a high softening temperature compared with other burden materials. From the calculated slag chemistry in Table 5, the slag formed after complete reduction of the pellets had much higher CaO and MgO contents compared with that for the lump sample and hence a higher liquidus and dripping temperature than the lump sample. However, the amount of slag formed is reasonably low, particularly compared with the sinter sample, as shown in Table 4, so the melt can drip out of the sample without much difficulty.

TABLE 5

Calculated slag chemistry of the burden materials after complete reduction.

Sample code	Sample description	SiO_2	Al_2O_3	CaO	MgO	FeO	CaO/ SiO_2
A	Lump	67.89	26.48	4.23	1.41		0.05
C	Pellet	40.46	7.56	19.72	32.26		0.49
D	Sinter	27.76	10.40	52.25	9.59		1.88

Unlike the pellet sample, reduction of sinter was believed to occur relatively uniformly across the sinter particles, leading to formation of FeO earlier. This, together with the basicity of the sample, consequently, leads to a low solidus temperature of the partially reduced sinter sample. Therefore, Sample D was expected to soften first under higher temperature reduction. Compared with the other samples, Sample D also generated a large volume of slag with a very high basicity (Tables 4 and 5). This explains its high dripping temperature and wider cohesive zone.

As a general rule of thumb, burden materials with a high softening temperature and low dripping temperature are desirable for generating a low cohesive zone with narrow width. This reduces the coke consumption by reducing the blast furnace operating temperature and direct reduction in the lower part of the furnace. While many factors, such as composition, pore structure and mineralogy, can affect the softening and melting characteristics of the burden materials, it is thought that the reducibility of the material determines the amount of FeO in the sample during high temperature reduction and therefore the softening characteristics of the material. On the other hand, the liquidus temperature and the amount of slag formed from the burden materials determine the dripping temperature of the material.

Different burden materials have shown very different characteristics of softening, melting and dripping. Comparing the burden materials tested, the pellet and lump ore samples (Samples A and C) had better high temperature characteristics than the sinter sample (Sample D). The sinter sample, on the other hand, was characterised of a dripping temperature and broader cross bed pressure drop profile, consequently a larger S-value. The sinter sample was struggling to drip the melt out with very little melt collected at the completion of the experiment. Therefore, it is particularly challenging to design a single burden material to achieve the overall quality desired. However, it is worthwhile to emphasize that the above observations were made based on the test conditions of 100 per cent burden materials without fluxing. When it is mixed with acidic burden materials such as pellet and lump, sinter is expected to show better high temperature characteristics. Furthermore, sinter is cheaper to produce and raw materials for the sintering process are readily available, which makes sinter very attractive and widely used, particularly in the Asia-Pacific region.

As demonstrated above, the chemistry and reducibility of burden materials have significant impacts on their high temperature characteristics. Therefore, more work is needed to understand these impacts, in order to optimise the high temperature characteristics of burden materials, particularly, sinter, and to study the potential beneficial effects of adding lump ore and pellets on the high temperature characteristics of sinter.

ACKNOWLEDGEMENTS

The authors would like to thank CSIRO Mineral Resources for permission to publish the paper and for the financial support of this work.

REFERENCES

Dawson, P R, 1987. Determination of the high temperature properties of blast furnace burden materials. *SEAISI Quarterly*, (January): pp. 23–42.

Higuchi, K, Naito, M, Nakano, M and Takamoto, Y, 2004. Optimization of chemical composition and microstructure of iron ore sinter for low temperature drip of molten iron with high permeability. *ISIJ International*, 44(12): pp. 2057–2066.

Sinter analogues mineralogy by different heating conditions

T B T Nguyen[1], T Harvey[2], T Honeyands[3], L Matthews[4] and D O'Dea[5]

1. Research Associate, Centre for Ironmaking Materials Research, Newcastle Institute for Energy and Resources, University of Newcastle, Callaghan NSW 2308.
   Email: thibangtuyen.nguyen@newcastle.edu.au
2. Former PhD student, Centre for Ironmaking Materials Research, Newcastle Institute for Energy and Resources, University of Newcastle, Callaghan NSW 2308.
   Email: tobin.harvey@newcastle.edu.au
3. FAusIMM, Associate Professor, Centre for Ironmaking Materials Research, Newcastle Institute for Energy and Resources, University of Newcastle, Callaghan NSW 2308.
   Email: tom.a.honeyands@newcastle.edu.au
4. Research Assistant, Centre for Ironmaking Materials Research, Newcastle Institute for Energy and Resources, University of Newcastle, Callaghan NSW 2308.
   Email: leanne.matthews@newcastle.edu.au
5. Principal Technical Marketing, BHP Marketing Iron Ore, Brisbane, Qld 4000.
   Email: damien.p.odea@bhp.com

ABSTRACT

Productivity and fuel consumption of the blast furnace is driven by the quality of the iron ore sinter, which in turn is related to the sinter mineralogy. The sintering conditions including temperature and gas composition have a significant influence on the formation of melt and finally the mineralogy of the sinter. In this work, analogue sinter tablets were produced from iron ore fines in a laboratory furnace with tightly controlled temperature profile and oxygen partial pressure in the gas. The mineralogy of the sinters was analysed using reflected light microscopy. The results showed that increasing thermal enclosed area (area enclosed by heating and cooling curve above a reference temperature) reduces primary hematite and platy silico-ferrite of calcium and aluminium (SFCA) contents. This is attributed to increasing melt formation, leading to greater assimilation of the iron ore particles. Lower magnetite was found for tablets with greater median pore size, which is thought to be due to greater oxidation of magnetite to hematite during cooling in air. It was also found that higher alumina content was found to result in more SFCA formation under the same heating/cooling conditions, whereas tablets with higher goethite had higher assimilation and produced more secondary hematite on cooling. Finally, it is necessary to relate the enclosed area to the temperature at which the melt formation becomes significant which strongly depends on chemical composition of the ore studied.

INTRODUCTION

Sintering is an important process in the production of steel from iron ore. Iron ore sinter is converted from iron ore fines of less than about 6 mm size into larger agglomerates using a high temperature process. Sinter contributes typically around 70 per cent or more of the ferrous burden in the blast furnace and blast furnaces contribute to about 70 per cent of the world steel production. High quality of sinter is therefore essential for the operation of the blast furnace. The pore structure and mineralogy characteristics of the sinter have been directly linked to the sinter quality especially mechanical strength and reducibility. In sinter plants or sinter pot tests, mineralogy of the sinter is the result of various features such as burden materials' chemical compositions, granulation performance and sintering conditions. For laboratory test such as sinter analogues, the ore's chemistry and heating conditions may be the central influencing factors on the formation of melt, porosity and mineralogy. Pore distribution and total porosity of the sinter was found to be well-linked with the sinter compressive strength and reducibility (Bristow and Waters, 1991; Dawson, Ostwald and Hayes, 1984; Harvey, 2020; Harvey *et al*, 2021). Bristow and Waters (1991) reported that increase in reducibility was due to the formation of micro pores of less than 1 μm during reduction of SFCA. Harvey *et al* (2021) found a strong influence of macro porosity on the reducibility of sinter analogues presented by a linear relationship between reduction degree and median pore diameter up to about 80 μm.

It has been reported that there is always a trade-off between good strength and high reducibility. In sinter pot, high fuel rates may result in stronger sinter but less reducible simultaneously (Dawson, Ostwald and Hayes, 1984). Similar trade-off was also confirmed in the study of (Harvey, 2020) for sinter analogues as laboratory scales. Harvey *et al* (2019) found that increasing the enclosed area (EA) generally increases the sinter strength which achieved a maximum value at EA of ~ 320°C.min. As EA is increased further, the strength reduces accordingly due to the deterioration in strength caused by pores' swelling. Oyama *et al* (2011) claimed that both good strength and reducibility of sinter could be obtained in the sinter pot by increasing the time spent at temperature above 1200°C but less than 1400°C. Other studies investigated the link between two types of SFCA (ie platy/acicular versus prismatic/columnar SFCA) and the compressive strength and reducibility of the sinter (Harvey, 2020; Harvey *et al*, 2021; Ishikawa *et al*, 1983; Ji *et al*, 2019; Mežibrický *et al*, 2021). Ishikawa *et al* (1983) found that the platy/acicular SFCA is more reduced than prismatic/columnar SFCA. However, there was no apparent relationship found between SFCA content and reduction degree in the recent study of Harvey *et al* (2021). For the strength, Higuchi and his co-workers (Higuchi, Okazaki, and Nomura, 2020; Okazaki and Higuchi, 2005) studied the influence of melting characteristics of the bonding phase on the sinter strength (and reducibility) which is well related to the rearrangement of voids or pore structure during sintering. Ji *et al* (2019) revealed that columnar or needle-like SFCA was found to be stronger than platy or sheet-like SFCA. It appears that SFCA is significant to the sinter quality index. The formation as well as the types of SFCA in sinter is known to be dependent primarily on silica, alumina contents in the ores (Ji *et al*, 2019) and of course the sintering conditions. Although there have been many records on the sinter mineralogy reported in the above-mentioned studies, it is still challenging to draw conclusions about the role of SFCA with respect to sinter quality because deviations in the definitions of SFCA phases can be significant depending on the analysis technique used (Honeyands *et al*, 2019). In this study, platy and columnar SFCA are measured using optical microscopy.

It is apparent that mineralogy of sinter made from the same iron ore could behave differently with respect to heating and cooling conditions during sintering. It is also true that of the same heating and cooling conditions, ores of different chemistry could result in distinct pore structure, melt formation and mineral characteristics. Therefore, the aim of this study is using the same technique to investigate independently the influence of heating conditions including Temperature, Time, and Cooling Rate, and the ores' chemistry on the formation of melt and mineralogy of sinter.

EXPERIMENTALS

Sinter analogues designed to simulate the bonding phase in iron ore sinter were prepared from different sources of iron ore fines using an infrared rapid heating furnace which allowed independent control of the maximum temperature, hold time, and cooling rate for each experiment. The temperature profile was based on measurements from sinter pot tests. Two separate series of experiments have been carried out.

In the first series of experiments, the mineralogy and melt formation of the analogue sinter tablets was analysed for a range of maximum temperatures, holding times and cooling rates using the same iron ore nuclei particles. The equipment and procedure are described in a previous work (Harvey *et al*, 2021). The -1 mm fraction of the iron ore was fluxed to a binary basicity (CaO/SiO_2 ratio) of 2.0 using reagent grade $CaCO_3$. The SiO_2 was controlled to 5.4 per cent, MgO to 1.8 per cent, Al_2O_3 to 2.5 per cent, with the remainder being Fe_2O_3. The analogue tablets of the same mass at 0.6 g were heated following the temperature profile given in Figure 1. Conditions used in these experiments are shown in Table 1. Bottled gas with 0.5 per cent O_2 in N_2 (pO_2 = 5E-03 atm) was injected into the furnace at 0.5 LPM during heating and holding, followed by air at the same flow rate during cooling. The thermal enclosed area (EA) is the area enclosed by heating and cooling curve above a reference temperature the integration of the time in minutes which is the shaded area shown in Figure 1. This enclosed area is related to the fuel rate in sinter pot tests. Experiments were carried out to investigate the influence of this EA on the sinter mineralogy characteristics.

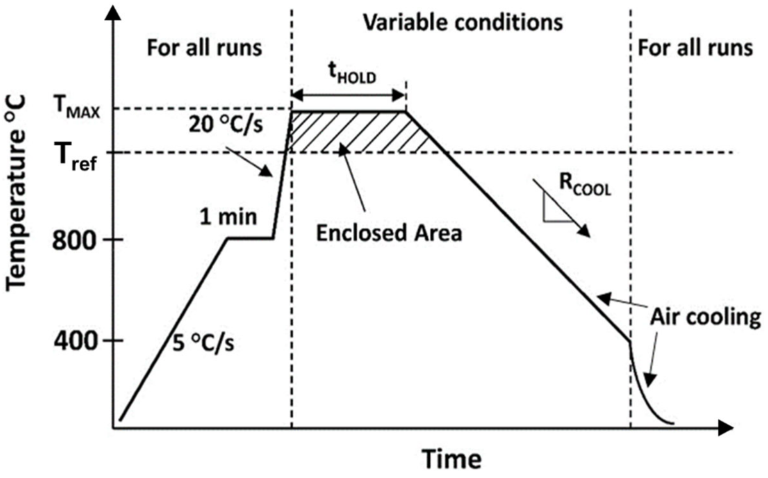

FIG 1 – Temperature profile used in the experiment. Maximum temperature, holding time and cooling rate for each sample of the first series of experiment are shown in Table 1.

TABLE 1

Sinter conditions in the first experiment series. (Asterisk marked for #12 denotes the condition used in the second set of experiments).

Sample #	Maximum temperature (°C)	Holding time (min)	Cooling rate (°C/s)
1	1250	1	5
2	1250	1	1
3	1250	4	5
4	1250	4	1
5	1285	0.167	5
6	1285	1	5
7	1285	2.5	3
8	1285	2.5	3
9	1285	2.5	3
10	1285	4	1
11	1320	0.167	5
12*	1320	1	5
13	1320	1	1
14	1320	4	5
15	1320	4	1

In the second series, mineralogy and melt formation were studied under the same furnace operating conditions using different iron ores, with a range of goethite and alumina contents. The -1 mm fraction of the iron ore was fluxed to a binary basicity (CaO/SiO_2 ratio) of 2.0 using reagent grade $CaCO_3$. The SiO_2 was controlled to 5.4 per cent, MgO to 1.8 per cent, and tablet alumina and LOI content of the tablets varied with the iron ore fines used. The analogue tablets (0.6 g) were heated following the temperature profile given as conditions #12 from Table 1. The range of analogue chemistry regarding alumina content and loss of ignition used in these experiments are shown in Table 2.

TABLE 2

Chemistry of the analogues in the second experiment series.

Sample ID	Maximum temperature (°C)	Basicity	SiO_2	MgO %	Al_2O_3 %	LOI %
UN138	1320	2.0	5.4	1.8	2.37	3.46
UN190	1320	2.0	5.4	1.8	1.87	1.56
UN139	1320	2.0	5.4	1.8	1.86	10.77
UN230	1320	2.0	5.4	1.8	1.43	5.44
UN221	1320	2.0	5.4	1.8	2.03	5.51
UN140	1320	2.0	5.4	1.8	2.35	5.75
UN231	1320	2.0	5.4	1.8	1.27	5.75
UN141	1320	2.0	5.4	1.8	2.51	4.42

RESULTS AND DISCUSSION

Reaction between nuclei ore and the flux results in dissolution of solid into the melt phase. The dissolution extent is expressed as 'assimilation' (Loo and Matthews, 1992) which is related to the chemical composition of the adhering fines layer, basicity of the sinter mixture, sintering conditions and the nuclei ores porosity and mineralogy. In this study, assimilation was determined as the total reacted mineral phases including secondary hematite, magnetite, SFCA, dicalcium silicate and glass. Figure 2a shows a proportional relationship between assimilation and the enclosed area EA which is calculated as given below:

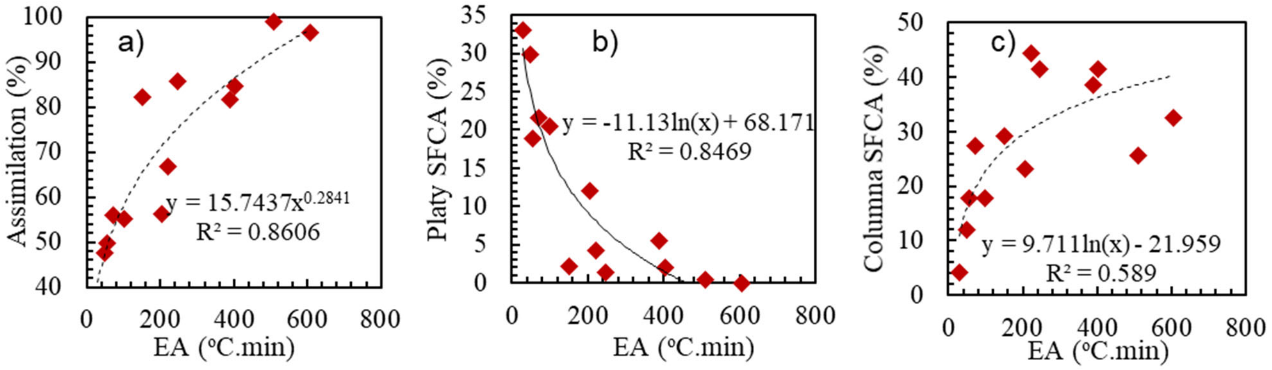

FIG 2 – (a) Assimilation, (b) Primary hematite and c) Platy SFCA as a function of Enclosed Area.

$$EA = \left(T_{max} - T_{ref}\right)\left[t_{hold} + \frac{1}{120}\frac{\left(T_{max}-T_{ref}\right)}{R_{heat}} + \frac{1}{120}\frac{\left(T_{max}-T_{ref}\right)}{R_{cool}}\right] \tag{1}$$

In Equation 1, *EA* is in°C.min, holding time t_{hold} is in minutes, heating rate R_{heat} and R_{cool} is in°C/s. Note that R_{heat} of 20°C/s was fixed for all runs.

The above relationship is apparent because assimilation of ore particles develops as increasing melt formation occurs during sintering due to increasing either maximum temperature or holding time or both factors (ie increasing EA). Note that a greater assimilation by definition results in a smaller relict ore content in the sinter (primary hematite). Assimilation reaches its maximum value of 100 per cent as the ore particles are totally incorporated in the melt, which was observed at EA of above 600°C.min. This behaviour was also reasonably predicted using the correlation shown in Figure 2a.

Platy SFCA was found to reduce with increasing EA (Figure 2b), while columnar SFCA was observed to increase (Figure 2c). This is believed to be due to the coarsening of the crystal structure of SFCA with increasing temperature and time, or EA (Harvey *et al*, 2021).

It is important to note that the best goodness-of-fit of the regression lines (R^2 values) presented in Figure 2 (dashed black lines), of maximum 0.86, were obtained from data analysis using a reference temperature T_{ref} at 1200°C, to calculate EA in Equation 1. The previously used reference temperature of 1100°C was found to give lower R^2 (maximum of 0.77) using the same regression methods. Therefore, it is necessary to relate the enclosed area to the temperature at which a significant amount of melt was formed rather than a generic temperature of 1100°C. This temperature is linked to the chemical compositions of the ore studied. Equilibrium thermodynamic FactSage model was used to estimate the liquid fraction of the chemical composition (~78.77 per cent Fe_2O_3; 4.5 per cent SiO_2; 10.8 per cent CaO; 1.8 per cent MgO and 2.5 per cent Al_2O_3) for temperatures between 1100 and 1350°C (Figure 3). The results showed that there is no melt formed up to temperature of 1160°C whereas the melt fraction reaches nearly 20 per cent at 1200°C. Considering that equilibrium may not be reached in the sintering system due to the dynamic nature of the reactions and the heterogeneous distribution of reactants, the iron ore and limestone flux may react to form calcium ferrite $CaO.Fe_2O_3$ at 1205°C (Scarlett *et al*, 2004) which could be the primary phase to melt. Therefore, it appears appropriate to relate the enclosed area to the temperature at which a significant amount of the melt has formed (about 20 per cent in this study).

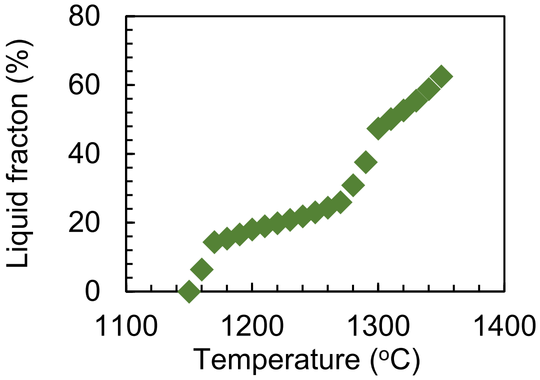

FIG 3 – Liquid fraction estimated using FactSage version 8.0 for the above-mentioned composition at temperature between 1100 and 1350°C.

In the second series of experiments, tablets with higher goethite content (higher LOI) provided higher assimilation and more secondary hematite on cooling (Figure 4a and 4b) which is attributed to the high volume of pores or greater porosity in goethite ores after dehydroxylation, which promotes dissolution in the melt as the temperature increases.

Tablets with higher alumina content were found to result in more SFCA formation under the same heating/cooling conditions (Figure 4c). Although this finding may be obvious as most alumina would exist in the SFCA phase, it appears that the trend is flattening out at higher alumina levels. This is consistent with the study of Ji *et al* (2019), who found that significant increase in total SFCA occurred for alumina below 1.8 per cent whilst a slight increase was found for alumina exceeding 1.8 per cent. Note that the Al_2O_3 shown in Table 2 is the total alumina obtained from aluminium identified by the XRF method regardless of its mineral form. However, ores can contain different alumina mineral types such as kaolinite, aluminous goethite, gibbsite (Webster *et al*, 2017). Therefore, the limit of alumina that exists in the SFCA phase may be linked to the different alumina minerals that exist in the ores, and also the degree of alumina dissolved in the iron oxides on the formation of SFCA. Further work is required to investigate this relationship.

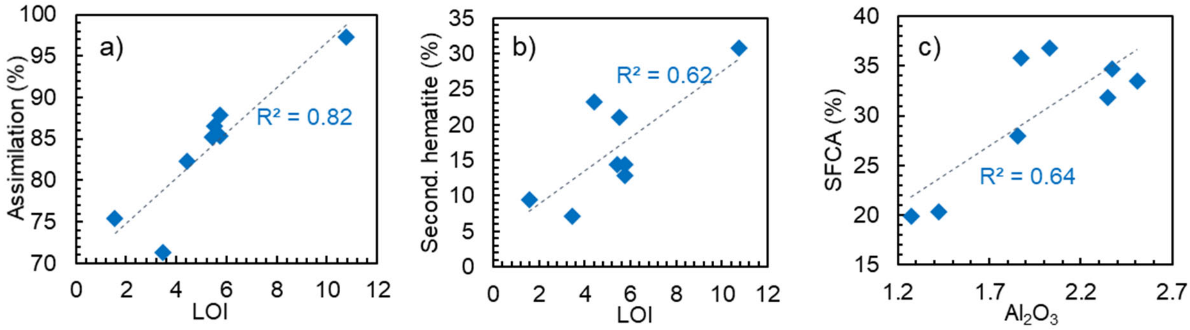

FIG 4 – Effect of LOI on (a) assimilation and (b) secondary hematite. (c) Effect of alumina on total SFCA.

CONCLUSION

The present study investigated the effect of thermal enclosed area and ore chemistry on the mineralogy of sinter analogues. In the first series of experiments, the mineralogy of the analogue sinter tablets was analysed for a range of maximum temperature, holding time and cooling rate using the same iron ore type. In the second series of experiments, mineralogy and melt formation were studied under the same furnace operating conditions using different iron ore nuclei particles, with a range of goethite and alumina contents. The following conclusions were drawn:

- Increasing thermal enclosed area (EA) increases assimilation of the nuclei ores but reduces platy SFCA (whilst increasing columnar SFCA).
- The sinter mineralogy versus EA results in this study were found to be better correlated using a reference temperature of 1200°C. This is close to the melting point of calcium ferrite and is the temperature at which about 20 per cent of the melt is predicted to form using Factsage.
- Ores with higher goethite content, indicated by their LOI, were found to give higher assimilation and secondary hematite phase due to their higher porosity.
- Ores with higher alumina content resulted in a higher total amount of SFCA phases.

There are a number of sinter quality measures, such as strength and reducibility, and direct relationships between each of these measures and sinter porosity and mineralogy are yet to be clearly defined. It is hoped that this work can give guidance to sinter plant operators on the fundamental drivers of sinter mineral formation for a range of ores and sintering conditions, and assist in designing operating conditions to suit the ores used.

ACKNOWLEDGEMENTS

The authors acknowledge the funding of the Australian Research Council in supporting the ARC Research Hub for Advanced Technologies for Australian Iron Ore and BHP for their financial support and permission to publish this paper.

REFERENCES

Bristow, N and Waters, A, 1991. Role of SFCA in promoting high-temperature reduction properties of iron ore sinters, *Transactions of the Institution of Mining and Metallurgy, Section C,* 100.

Dawson, P, Ostwald, J and Hayes, K, 1984. The influence of the sintering temperature profile on the mineralogy and properties of iron ore sinters, *AIMM Bull Proc*, 163–169.

Harvey, T, 2020. *Influence of Mineralogy and Pore Structure on the Reducibility and Strength of Iron Ore Sinter,* University of Newcastle.

Harvey, T, Honeyands, T, O'Dea, D and Evans, G, 2019. Study of Sinter Strength and Pore Structure Development using Analogue Tests, *ISIJ International***,** 247.

Harvey, T, Pownceby, M I, Chen, J, Webster, N A, Nguyen, T B T, Matthews, L, O'Dea, D and Honeyands, T, 2021. Effect of Temperature, Time and Cooling Rate on the Mineralogy, Morphology and Reducibility of Iron Ore Sinter Analogues, *JOM,* 73:345–355.

Higuchi, K, Okazaki, J and Nomura, S, 2020. Influence of Melting Characteristics of Iron Ores on Strength of Sintered Ores, *ISIJ International,* 60:674–681.

Honeyands, T, Manuel, J, Matthews, L, O'Dea, D, Pinson, D, Leedham, J, Zhang, G, Li, H, Monaghan, B and Liu, X, 2019. Comparison of the mineralogy of iron ore sinters using a range of techniques, *Minerals,* 9:333.

Ishikawa, Y, Shimomura, Y, Sasaki, M, Hida, Y and Toda, H, 1983. Improvement of sinter quality based on the mineralogical properties of ores, *Ironmaking Proceedings*, 17–29.

Ji, Z, Zhao, Y, Gan, M, Fan, X, Chen, X and Hu, L, 2019. Microstructure and minerals evolution of iron ore sinter: influence of SiO_2 and Al_2O_3, *Minerals,* 9:449.

Loo, C E and Matthews, L, 1992. Assimilation of large ore and flux particles in iron ore sintering, *Transactions of the Institution of Mining and Metallurgy Section C,* 101.

Mežibrický, R, Csanádi, T, Vojtko, M, Fröhlichová, M and Abart, R, 2021. Effect of alumina and silica content in the calcium aluminosilicoferrite Ca2 (Ca, Fe, Mg) 6 (Fe, Si, Al) 6O20 bonding phase on the strength of iron ore sinter, *Materials Chemistry and Physics,* 257:123733.

Okazaki, J and Higuchi, K, 2005. Marra Mamba ore, its mineralogical properties and evaluation for utilization, *ISIJ international,* 45:427–435.

Oyama, N, Iwami, Y, Yamamoto, T, Machida, S, Higuchi, T, Sato, H, Sato, M, Takeda, K, Watanabe, Y and Shimizu, M, 2011. Development of secondary-fuel injection technology for energy reduction in the iron ore sintering process, *ISIJ international,* 51:913–921.

Scarlett, N V, Pownceby, M I, Madsen, I C and Christensen, A N, 2004. Reaction sequences in the formation of silico-ferrites of calcium and aluminum in iron ore sinter, *Metallurgical and materials transactions B,* 35:929–936.

Webster, N A, O'Dea, D P, Ellis, B G and Pownceby, M I, 2017. Effects of gibbsite, kaolinite and Al-rich goethite as alumina sources on silico-ferrite of calcium and aluminium (SFCA) and SFCA-I iron ore sinter bonding phase formation, *ISIJ International,* 57:41–47.

Analyses of pressure drop in high temperature zone during iron ore sintering

T Singh[1], S Mitra[2], D O'Dea[3] and T Honeyands[4]

1. AAusIMM, PhD candidate, Centre for Ironmaking Materials Research, The University of Newcastle, Callaghan NSW 2308. Email: t.singh@uon.edu.au
2. MAusIMM, Research Associate, Centre for Ironmaking Materials Research, The University of Newcastle, Callaghan NSW 2308. Email: subhasish.mitra@newcastle.edu.au
3. Principal Technical Marketing, BHP Marketing Iron Ore*,* Brisbane, Qld 4000. Email: damien.p.odea@bhp.com
4. FAusIMM, Director, Centre for Ironmaking Materials Research, The University of Newcastle, Callaghan NSW 2308. Email: tom.a.honeyands@newcastle.edu.au

ABSTRACT

Permeability and air flow rate in the bed during iron ore sintering is crucial to controlling the sinter quality and productivity of a sinter plant due to its influence on the flame front speed. In the present work, the permeability of the bed during sintering was analysed by means of measured pressure drop and temperature at multiple points in the bed during sintering. Three different zones were categorised, ie humidified (green) bed, region of maximum resistance (high temperature zone) based on temperature, and sintered bed. Previous work has shown that the maximum pressure drop during sintering was due to several concurrent physico-chemical processes including dehumidification, calcination of fluxes, dehydroxylation of goethite, combustion of coke and melting of granules (>1200°C). To quantify the effect of the different process, sintering experiments were conducted in a milli-pot (diameter 53 mm, height 400 mm) with pressure and temperature measured at same location in bed. The milli-pot was fitted with four equidistant (80 mm apart) taps. Overall, five sections in the milli-pot were analysed for pressure drop at different times during sintering. It was found that in region of maximum resistance, coke combustion and flux calcination were highest contributors with ~35 per cent of the pressure drop when compared to other processes like de-humidification and goethite dehydroxylation which contributed to ~20 per cent and 25 per cent each respectively. The pressure drop contribution of the coke combustion region increased with increasing coke addition rate.

INTRODUCTION

Ironmaking in the blast furnace (BF) is the most widely used method. According to producer companies' annual reports, 74 per cent of total iron ore produced in Australia is in form of fines (-6.3 mm) of different types eg 62 per cent Fe fines, 58 per cent Fe, 58 per cent Fe low Alumina fines. The productivity of the BF highly depends on the permeability of burden fed in the shaft region. High permeability of burden allows furnace gases to rise rapidly without any significant channelling. To maintain the desired degree of permeability in shaft region, fines (-5 mm) cannot be fed to BF (Peacey and Davenport, 2016; Loo and Bristow, 1998). Sintering is the usual method to agglomerate these fines into large size particles to make them suitable for the BF. BF feed typically consists of around 70 per cent or more of sinter with the balance made up of lump ore and pellets. Hence it is important to produce sinter to meet the BF feed requirement and maintain the quality. Good sinter product helps in effective and fast reduction of iron oxide to metallic iron and to maintain the basicity of the BF.

The quality of sinter product like strength and reducibility are very much dependent on the raw material composition, and sintering parameters like sintering temperature, time above ~1100°C, flame front speed, air flow rate. Flame front speed denotes the movement of the high temperature zone from start to end of the sintering and is one of the most crucial parameters to control the sinter quality (Zhou *et al*, 2015; Loo, Tame and Penny, 2012; Loo and Hutchens, 2003; Loo, 2003; Higuchi *et al*, 2000). The flame front speed is driven by the suction applied at the bottom of the bed and the permeability of the bed during sintering. Several zones can be classified based on temperature during sintering which contribute to the total pressure drop during sintering, ie, humidified bed (HB) zone (<~60°C), de-humidification and goethite dehydroxylation zone (~100°C to ~620°C), calcination zone (>~700°C), combustion zone (>~727°C), melting zone (>~1200°C) and sintered bed (SB) zone (<~1200°C on cooling side) (Singh *et al*, 2021; Zhou *et al*, 2012, 2018, 2019; Umadevi *et al*, 2014; Okazaki *et al*, 2003; Loo and Leaney, 2002; Loo, 2000).

Some studies have specifically focused on resistance to air flow in the flame front zone (Zhou *et al*, 2012; Loo, Tame and Penny, 2012; Castro, Sazaki and Yagi, 2012; Oyama *et al*, 2005; Kasai *et al*, 2005; Loo and Hutchens, 2003; Loo, 2003; Mikka and Loo, 1992), however the characteristics of this zone including the bed structure that contributes to flow resistance are complex and still not very clear. In previous work (Singh *et al*, 2021), it has been shown that the maximum pressure drop occurs in a zone termed the region of maximum resistance (RMR), which includes the de-humidification zone and goethite dehydroxylation zone, flux calcination zone, combustion zone and melting zone collectively. The present work explores experimentally the contribution of each process taking place in the RMR. To quantify the effect of each process, pressured drops measured during the sintering process were compared.

METHOD AND MATERIALS

Raw material

An iron ore blend representing a typical chemical composition of sinter in Asia Pacific for ironmaking was used in this work. The ore blend was mixed with coke breeze, limestone, dolomite and the sinter return fines. Coke breeze was used as fuel during sintering while limestone and dolomite were mixed to maintain the basicity of the final sinter product. The sinter chemistry was: TFe = 56.7 per cent, Basicity = 1.9, SiO_2 = 5.0 per cent, MgO = 2.0 per cent and Al_2O_3 = 1.9 per cent. Five different coke rates, ie 5.0 per cent, 5.5 per cent, 7 per cent, 7.5 per cent, and 8.0 per cent were used in the experiments. Raw mixture details are given in Table 1.

TABLE 1

Final raw mixture composition with different coke rates.

Final raw mixture composition	Weight, %
Ore blend	58.8 to 61.0
Coke	5.0, 5.5, 7.0, 7.5, 8.0
Limestone + dolomite	13.7 to 14.2
Return fines	20
Moisture	6.5
Basicity	1.9

Experimental apparatus and procedure

A typical sintering procedure was followed for conducting the sintering experiments in a milli-pot apparatus (internal diameter: 53 mm, height: 400 mm) (Singh *et al*, 2019, 2021; Li *et al*, 2018; Loo and Hutchens, 2003; Loo, 2003). The milli-pot was fitted with four equidistant taps (tap 1 at top and tap 4 at bottom) to record temperature and pressure at the same location using a K type thermocouple, and a pressure transmitter (Dwyer) through a T-piece, as shown in Figure 1a. The sinter pot was fitted to a wind box which was connected to a water ring vacuum pump to create negative pressure in the system (Figure 1b). A hot wire anemometer was fitted at the top of the bed to measure airflow rate. All instruments were connected to an in-house built data logger to log measured data.

For granulation, the raw mixture was first dry mixed for two minutes in a granulation drum and then was wet mixed for 3 minutes after adding the required amount of water. The wet granules were poured into the sinter milli-pot and the filled pot was placed on the wind box and a suction pressure of 4 kPa was generated. The granule packed bed in milli-pot was ignited from the top by an LPG gas burner at a temperature of ~1200°C for 90 seconds. After ignition, the vacuum was set to 8 kPa and the ignition hood was replaced with the flow measuring tube fitted with a hot wire anemometer to measure the flow rate during sintering process. The maximum temperature in the wind box indicated the completion of sintering. The air flow was continued through the bed post sintering to cool the bed down to 40°C. Sintered product was removed afterwards from the milli-pot in its original shape and was tested for further quality measurements. Further details of the sintering equipment are given elsewhere (Singh *et al*, 2021).

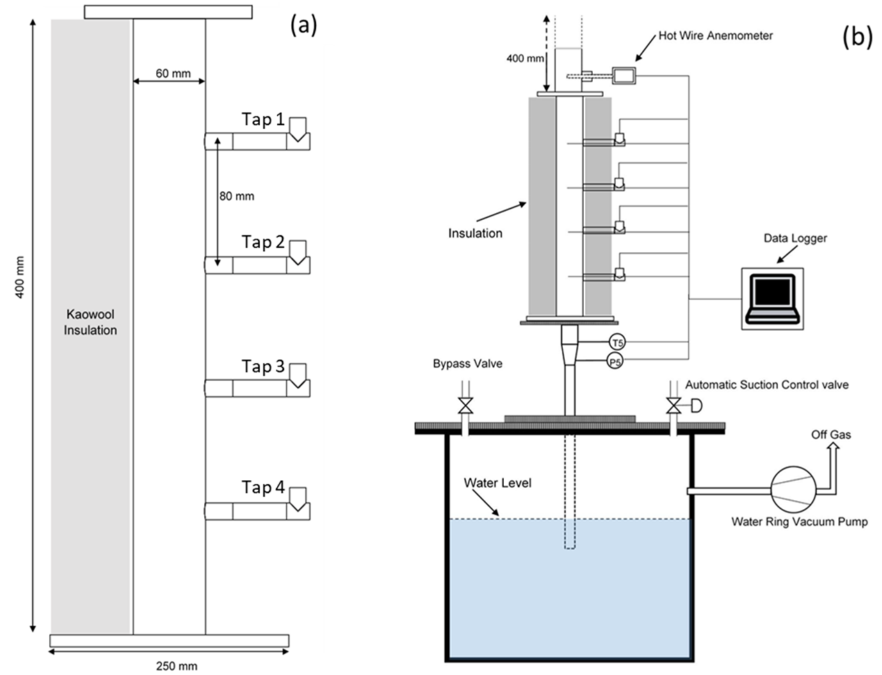

FIG 1 – (a) Schematic diagram of milli-pot used for lab scale sintering experiments. (b) Schematic diagram of sintering equipment.

ZONE IDENTIFICATION DURING SINTERING

In our previous work (Singh *et al*, 2021), the region of maximum resistance (RMR) was defined with help of simultaneous measurement of temperature and pressure in the bed. The flame front zone contributing to RMR was defined as a temperature range from ~100°C at the leading edge of the flame front to ~1200°C at the trailing edge of the flame front. In the present work, the pressure-drop in different processes (distinct or collective) occurring in the RMR were further analysed and their contribution to overall pressure drop was quantified. The temperature range used to the classify different zones was selected from the available literature data (Singh *et al*, 2021; Zhou *et al*, 2012, 2018, 2019; Umadevi *et al*, 2014; Okazaki *et al*, 2003; Loo and Leaney, 2002; Loo, 2000).

With the rapid rise in temperature during sintering and the overlapping temperature range for some of the processes, it was hard to distinguish each process uniquely. It is therefore expected that the measured pressure-drop reflects contributions from some concurrent processes. The starting temperature of the different processes were taken from literature (Walter, Buxbaum and Laqua, 2001) while a numerical model (Zhou *et al*, 2012) was used to estimate the end temperature of a process at which the conversion of a specific species was at least 95 per cent. The approximate temperature range representing various processes are summarised in Table 2.

TABLE 2

Starting and completion temperature of processes during sintering.

Main Process during sintering	Approximate temperature range
De-humidification	~100°C to 220°C
Goethite dehydroxylation	~250°C to 620°C
Flux calcination	~700°C to 1250°C
Coke combustion	~727°C to 1300°C
Granule melting	>1200°C

All processes significantly depend on several factors like reaction rate constant, particle diameter, local gas composition, local absolute pressure etc, hence each process does not have a definite completion temperature, which results in overlap between successive processes, as shown in Figure 2.

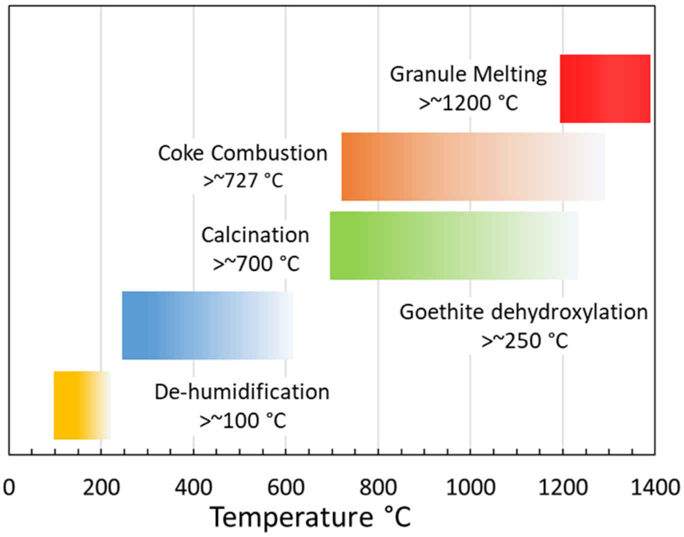

FIG 2 – Temperature range for different processes during sintering (end defined by 95 per cent completion).

PRESSURE DROP QUANTIFICATION METHOD

To quantify the pressure-drop contribution of each process, transient variations in pressure-drop in five different sections of the sinter bed were analysed. The sections were classified as follows section 0: bed top to tap 1, section 1: tap 1 to tap 2, section 2: tap 2 to tap 3, section 3: tap 3 to tap 4 and section 4: tap 4 to wind box (Figure 1).

Pressure-drop in each section was measured at different times and at different temperature of the bottom tap in a particular section. As an example, the method for measuring pressure drop of various processes in section 2 is shown in Figure 3. At time 1 the temperature of tap 3 was ~100°C and hence the pressure drop in section 2 was mainly due to processes happening in RMR. At time 2, the temperature of tap 3 was ~250°C which indicates that the de-humidification region has entered the section below and remaining processes are contributing to the pressure drop in section 2. Subsequently the pressure drop was measured at time 3 and time 4 for tap 3 temperatures of ~700°C and ~1200°C respectively to quantify the pressure drop due to different process during sintering.

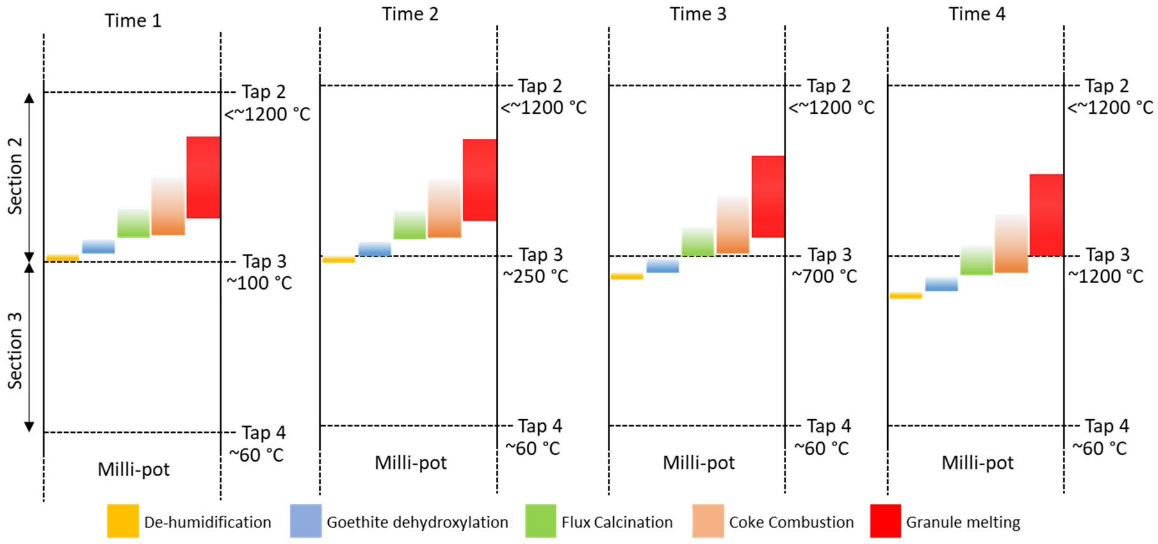

FIG 3 – Method to measure effect of each process on pressure drop during sintering.

The pressure-drop contribution of individual processes was quantified by calculating the pressure difference at two time instances in a section, as shown in Table 3.

TABLE 3

Method for quantifying the effect of individual process on pressure drop during sintering.

Pressure-drop between	Pressure-drop contributing process
time 1 and time 2	De-humidification
time 2 and time 3	Goethite dehydroxylation
time 3 and time 4	Flux calcination + Coke combustion
after time 4	Coke combustion + Granule melting

RESULTS AND DISCUSSION

The pressure-drop in a section of bed was determined by taking the difference between the two adjacent pressure taps. The pressure-drop per unit length of HB (Humidified Bed) and SB (Sintered Bed) was ~20 kPa/m (±10 per cent) and ~5 kPa/m (±15 per cent), respectively. The remaining pressure-drop occurred in the RMR, varying from 35 kPa/m (±10 per cent) in the top section to 80 kPa/m (±10 per cent) in the bottom section as the flame front moved from the top to the bottom of the bed. Pressure-drop of sections in the lower half of the milli-pot ie section 2, section 3 and section 4 were compared at time when the RMR was in a specific section for each coke rate scenario shown in Figure 4. For each corresponding coke rate, the fraction of pressure-drop contribution measured in a section containing the RMR increased down the bed (from section 2 to section 4). As the temperature increased down the bed, the width of HB decreased, and width of SB increased as sintering progressed. An overall increasing trend for pressure-drop contribution with coke rate was observed in the corresponding sections, except for coke rate 5 per cent scenario which was attributed to incomplete and non-uniform sintering of granules. This occurrence was also reported in the previous studies on milli-pot sintering (Singh *et al*, 2021; Li *et al*, 2018).

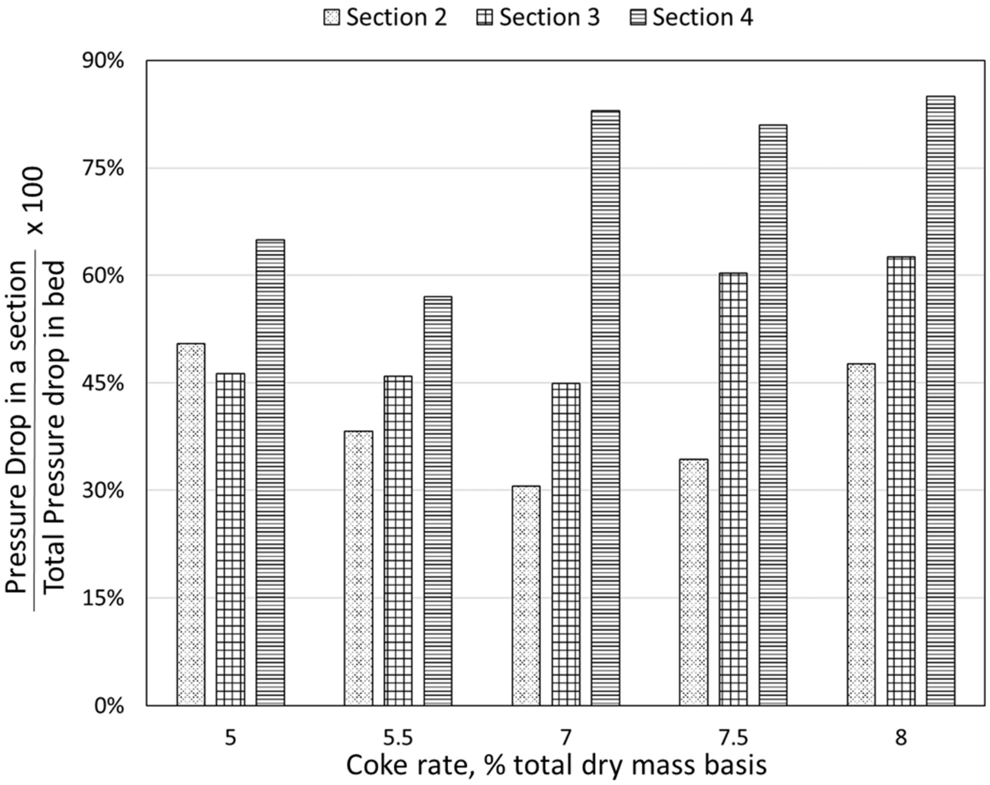

FIG 4 – Pressure-drop contribution percentage in section 2, 3, and 4 to total pressure drop in lower half of milli-pot for coke rate, 5 per cent, 5.5 per cent, 7 per cent, 7.5 per cent, 8 per cent.

The pressure drop within a section was further investigated by quantifying the effect of individual processes using the method explained earlier. The variations in pressure-drop with rapid rise in temperature over small span of time (~1 minute) were plotted at ~60 per cent sintering completion for a coke rate of 7 per cent in Figure 5. During the same period, movement of various processes in RMR are shown in schematic form in Figure 6. From 11.5 min to 12.5 min, the RMR moved from section 2 to section 3, changing the physical and thermal processes occurring in these sections, hence the major pressure drop variations were observed in section 2 and 3 only. In comparison, section 0, 1, and 4 had invariant pressure drop contributions of ~5 per cent for section 0 and 1 (SB) and ~23 per cent for section 4 (HB), due to unchanged physical and thermal processes.

The measured temperatures of tap 4 at time 11.5 min, 11.75 min, 11.9 min, 12.2 min and 12.5 min were 67°C, 146°C, 294°C, 757°C and 1250°C, respectively which marked the movement of various processes from section 2 to section 3, as shown in Figure 6. With the movement of the individual process from section 2 to section 3, the pressure-drop contribution of section 2 started to decrease rapidly from 46 per cent and reached to value equal to 8 per cent within less than 1 minute, even though the majority of the flame front (melting zone) was still in section 3. The pressure-drop contribution of section 3 increased from 23 per cent to 59 per cent as the individual processes entered in section 3. The variation in pressure-drop contribution in section 2 and 3 showed that the pressure-drop was mainly due to the pre-melting processes. The same trend was observed in the lower half section of milli-pot for most of the coke rates except at 5 per cent.

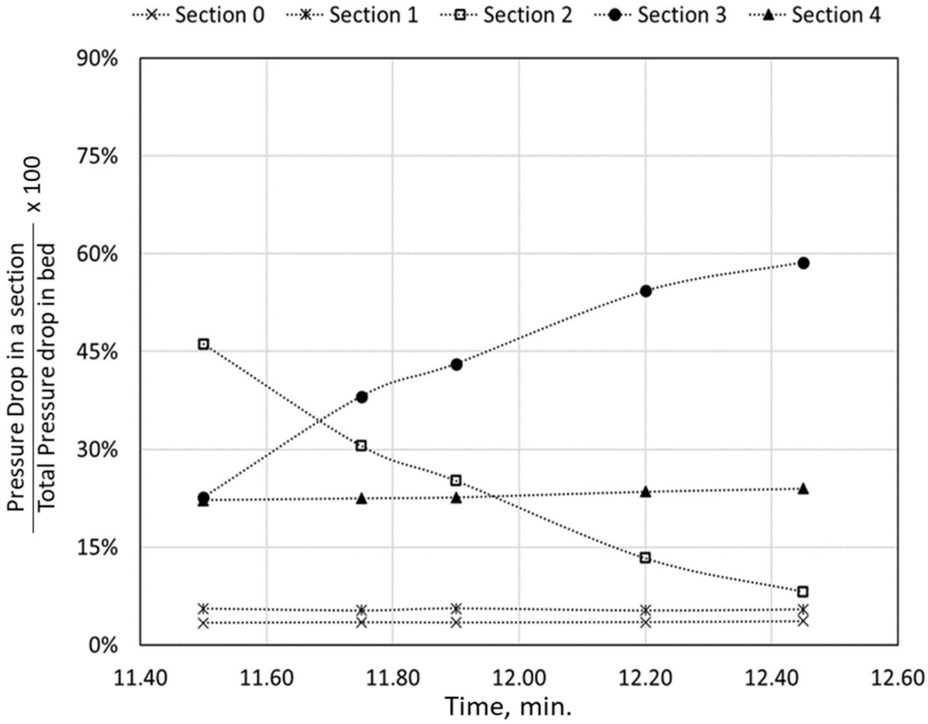

FIG 5 – Graphical representation of variation of pressure drop in section 0, 1, 2, 3 and 4 for coke rate 7 per cent at ~60 per cent sintering.

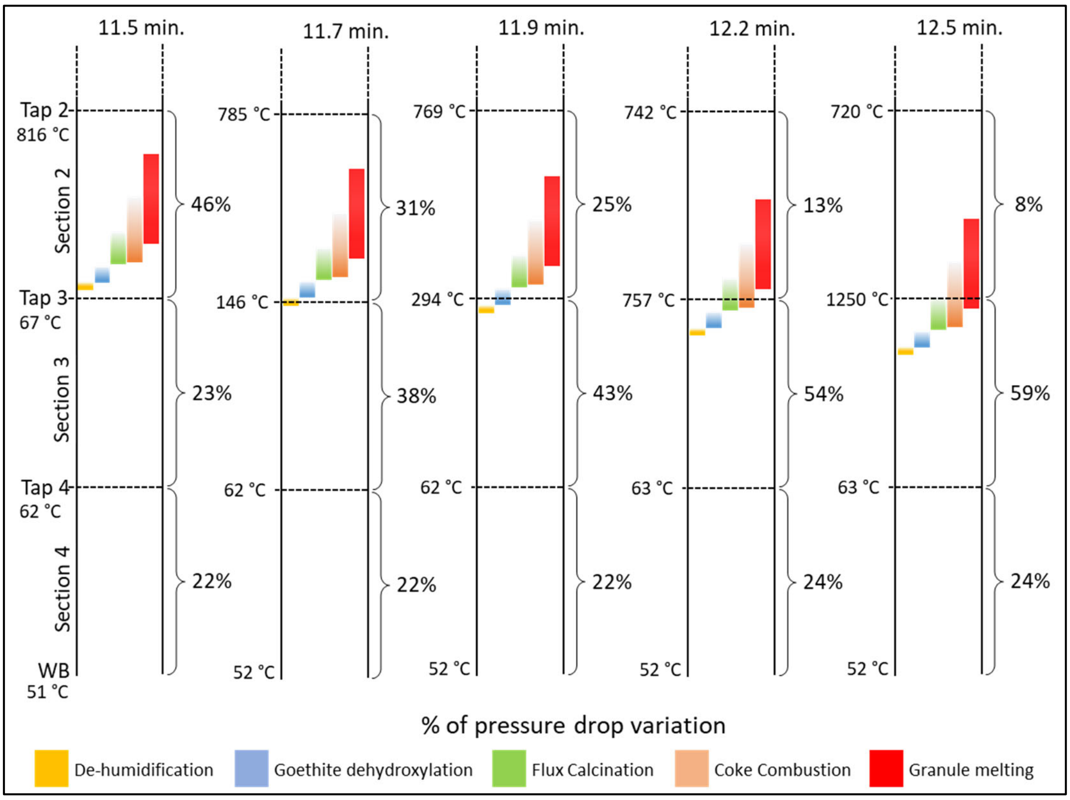

FIG 6 – Schematic representation of variation of pressure drop in section 2, 3 and 4 for coke rate 7 per cent at ~60 per cent sintering.

The changes in temperature and pressure drop shown between section 2 and section 3 in Figure 5 provide an insight into the relative contributions of the different processes in the RMR to the overall pressure drop. The contribution of the individual processes to the overall pressure-drop was as follows: de-humidification – 20 per cent (±5 per cent), goethite dehydroxylation – 25 per cent (±5 per cent), flux calcination zone and coke combustion – 35 per cent (±10 per cent) and melting zone and coke combustion – 20 per cent (±10 per cent). Due to inevitable overlap in the temperature ranges over which these processes occur, and relatively low spatial resolution of the measurements performed, contributions of some processes could not be uniquely identified.

CONCLUSIONS

In the present study, both pressure-drop and temperature were measured at multiple locations in a milli-pot sintering system over a range of coke rates from 5 per cent to 8 per cent to characterise the region of maximum resistance.

It was found that the pressure drop in each section of the bed increases down the bed as sintering progressed due to the increased heat convected down from previous sections. The proportion of the overall pressure drop attributed to the section containing the region of maximum resistance increased with increasing coke rate.

The region of maximum resistance, comprising the de-humidification zone, goethite dehydroxylation zone, flux calcination zone, combustion zone and melting zone, was found to be responsible for ~40 per cent to 80 per cent of the total pressure drop, depending on its location in the bed. The green bed and sintered bed only contributed ~22 per cent and ~5 per cent per 80 mm section respectively.

The pressure drop contributions of de-humidification and goethite dehydroxylation were found to be ~20 per cent and ~25 per cent of the total pressure drop in a section respectively. The contributions of coke combustion and flux calcination together was the highest at ~35 per cent. Finally, the contributions of coke combustion and the granule melting zone was only ~20 per cent.

The quantification of the pressure drop contribution of different processes can be used in potential modifications to the sintering process, such as the design of granules and bed segregation patterns, to allow operators to increase the bed height and increase sinter productivity. Furthermore, the understanding of pressure-drop contribution in various zones can be utilised in developing improved models for control of iron ore sintering.

ACKNOWLEDGEMENTS

The authors gratefully acknowledge BHP for their financial support for the Centre for Ironmaking Materials Research, and permission to publish this work. The authors are also thankful to University of Wollongong for allowing us to use their laboratory facilities for conducting milli-pot experiments, TUNRA workshop staff, University of Newcastle to build the milli-pot and Gareth Penny and Leanne Matthews for their technical assistance.

REFERENCES

Castro, J A D, Sazaki, Y and Yagi, J-I, 2012. Three dimensional mathematical model of the iron ore sintering process based on multiphase theory, *Materials Research,* 15:848–858.

Higuchi, K, Kawaguchi, T, Kobayashi, M, Hosotani, Y, Nakamura, K, Iwamoto, K and Fujimoto, M, 2000. Improvement of productivity by stand-support sintering in commercial sintering machines, *ISIJ international,* 40:1188–1194.

Kasai, E, Komarov, S, Nushiro, K and Nakano, M, 2005. Design of bed structure aiming the control of void structure formed in the sinter cake, *ISIJ international,* 45:538–543.

Li, H, Zhou, D, Pinson, D J, Zulli, P, Lu, L, Longbottom, R J, Chew, S J, Monaghan, B J and Zhang, G, 2018. Sintering of Iron Ores in a Millipot in Comparison with Tablet Testing and Industrial Process, *Metallurgical and Materials Transactions B,* 49:2285–2297.

Loo, C, 2000. Changes in heat transfer when sintering porous goethitic iron ores, *Mineral Processing and Extractive Metallurgy,* 109:11–22.

Loo, C and Bristow, N, 1998. Properties of iron bearing materials under simulated blast furnace indirect reduction conditions:Part 1 – review and experimental procedure, *Ironmaking and steelmaking,* 25:222.

Loo, C and Leaney, J, 2002. Characterizing the contribution of the high-temperature zone to iron ore sinter bed permeability, *Mineral Processing and Extractive Metallurgy,* 111:11–17.

Loo, C E and Hutchens, M F, 2003. Quantifying the Resistance to Airflow during Iron Ore Sintering, *ISIJ International,* 43:630–636.

Loo, C E, Tame, N and Penny, G C, 2012. Effect of iron ores and sintering conditions on flame front properties, *ISIJ international,* 52:967–976.

Loo, C E, 2003. Quantifying the resistance to airflow during iron ore sintering, *ISIJ international,* 43:630–636.

Mikka, R and Loo, C, 1992. Positioning coke particles in iron ore sintering, *ISIJ international,* 32:1047–1057.

Okazaki, J, Higuchi, K, Hosotani, Y and Shinagawa, K, 2003. Influence of iron ore characteristics on penetrating behavior of melt into ore layer, *ISIJ international,* 43:1384–1392.

Oyama, N, Sato, H, Takeda, K, Ariyama, T, Masumoto, S, Jinno, T and Fujii, N, 2005. Development of coating granulation process at commercial sintering plant for improving productivity and reducibility, *ISIJ international,* 45:817–826.

Peacey, J G and Davenport, W G, 2016. *The iron blast furnace:theory and practice*, Elsevier.

Singh, T, Honeyands, T, Mitra, S, Evans, G and O'Dea, D, 2019. Measured and Modelled Air Flow Rates during the Iron Ore Sintering Process:Green and Sintered Beds, in *Proceedings of the Iron Ore Conference 2019*, pp 156–165 (The Australasian Institute of Mining and Metallurgy: Melbourne).

Singh, T, Li, H, Zhang, G, Mitra, S, Evans, G, O'Dea, D and Honeyands, T, 2021. Iron Ore Sintering in Milli-Pot: Comparison to Pilot Scale and Identification of Maximum Resistance to Air Flow, *ISIJ International*.

Umadevi, T, Brahmacharyulu, A, Sah, R and Mahapatra, P, 2014. Influence of sinter grate suction pressure (flame front speed) on microstructure, productivity and quality of iron ore sinter, *Ironmaking & Steelmaking,* 41:410–417.

Walter, D, Buxbaum, G and Laqua, W, 2001. The mechanism of the thermal transformation from goethite to hematite, *Journal of Thermal Analysis and Calorimetry,* 63:733–748.

Zhou, H, Cheng, M, Liu, Z, Zhou, M, Liu, R and Cen, K, 2018. The Relationship between Sinter Mix Composition and Flame Front Properties by a Novel Experimental Approach, *Combustion Science and Technology,* 190:721–739.

Zhou, H, Liu, Z, Cheng, M, Liu, R and Cen, K, 2015. Effect of flame-front speed on the pisolite-ore sintering process, *Applied Thermal Engineering,* 75:307–314.

Zhou, H, Zhao, J P, Loo, C E, Ellis, B G and Cen, K F, 2012. Numerical modeling of the iron ore sintering process, *ISIJ international,* 52:1550–1558.

Zhou, H, Zhou, M, Ma, P and Cheng, M, 2019. Experimental investigation on the flame front resistance of gas channel growth with melt formation in iron ore sinter beds, *Proceedings of the Combustion Institute,* 37:4607–4615.

AUTHOR INDEX